1

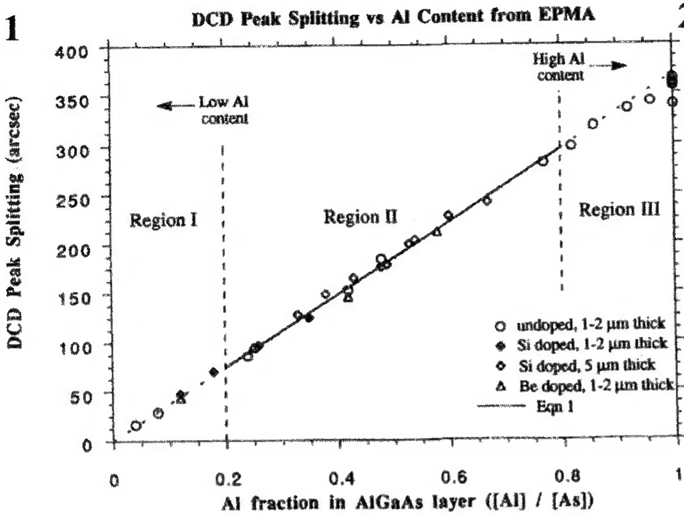

2

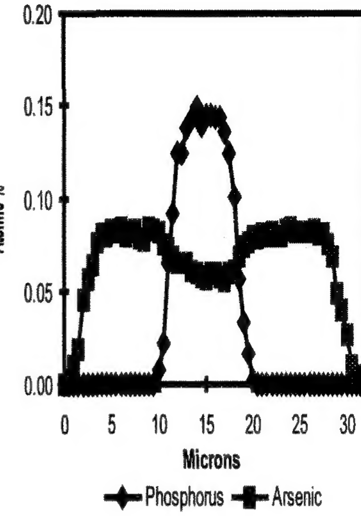

3

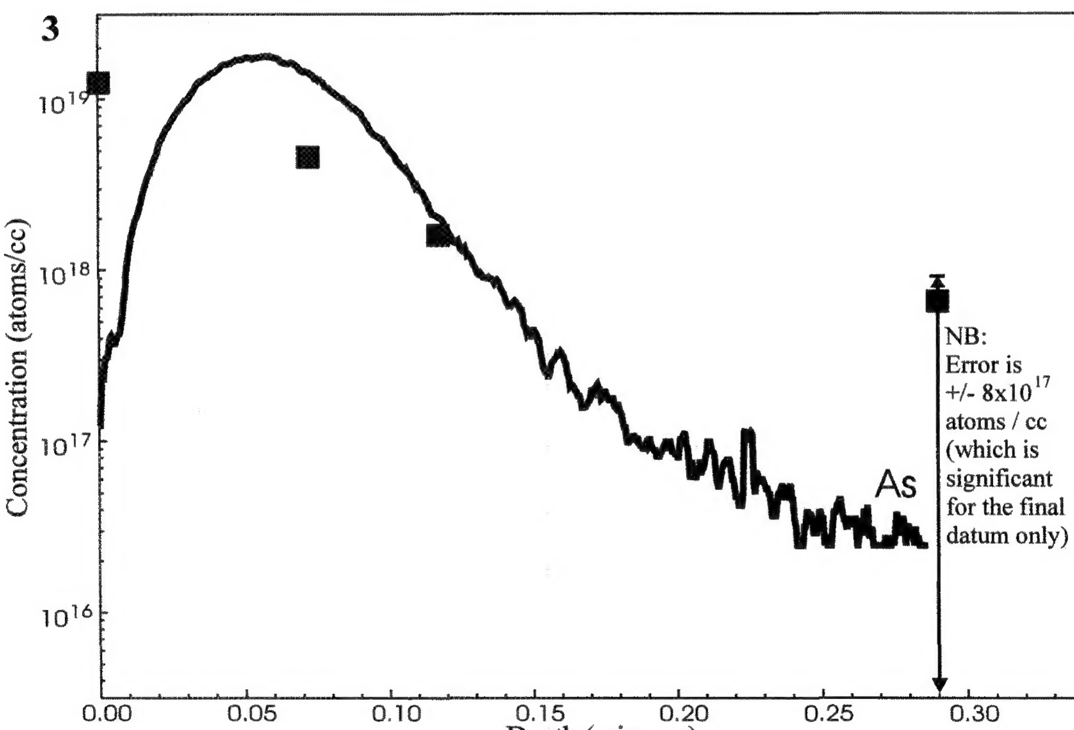

FIG. 1. Double crystal x-ray diffraction (DCD) rocking curve peak separation vs. EPMA concentration.

FIG. 2. EPMA trace across the input protection structure of a commercial IC consisting of an eight micron wide phosphorus-doped polysilicon line sitting on a deep arsenic well.

FIG. 3. SIMS plot of arsenic concentration vs. depth of an 80 keV implant standard. The arsenic concentration, as measured by EPMA at the surface, and in three craters, is shown.

IDENTIFICATION OF PHASES IN CORIUM HELD AT HIGH TEMPERATURE IN A TUNGSTEN CRUCIBLE BY SEM, EPMA,AND EBSD

B. Schneider,* C. Bouchet,* P. Perodeaud,* O. Dugne,* A. Maurizi,** F. Valin,** C. Guéneau,*** G. Bordier***

*DCC/DTE/SIM, CEA VALRHO, 26702 Pierrelatte Cedex, France
**DTA/CEREM/CE2M, CEA SACLAY, 91191 Gif sur Yvette, France
***DCC/DPE/SPEA, CEA SACLAY, 91191 Gif sur Yvette, France

Heat treatments of U - Zr - O mixtures of different oxygen contents (ranging from 1 to 35 at. %) and of a constant U/Zr ratio (U/Zr = 1.35 which is characteristic of the inner part of a pressurized-water reactor) were performed in order to study the high temperature behavior of corium. The selected U-Zr-O mixtures were put in a tungsten crucible and heated to 2050°C. The specimens were thereafter analyzed by Scanning Electron Microscopy (SEM), Electron Probe MicroAnalysis (EPMA) and Electron BackScattering Diffraction (EBSD).

SEM surface analysis showed a complex system (Fig. 1). Four different phases were characterized. The uranium-rich matrix (noted P1) gave no diffraction pattern by EBSD. The average composition of the sharp grains (P2) located near the tungsten crucible surface was 66 at. % of W and 34 at. % of Zr. The diffraction pattern of this phase was accurately indexed with the fcc structure parameters of W_2Zr (Fig. 2). A hexagonal ZrO_x $(0 \leq x \leq 0.3)$ phase (P3) was detected (Fig. 3). Skokan and Hofmann and Politis mentioned it (α Zr(O)) in their high temperature U-Zr-O ternary diagram.[1,2] The grains noted P4 corresponded to the mixed oxide, $(U,Zr)O_2$. Different Zr/U ratio were determined by EPMA in this oxide, particularly in the high oxygen content mixtures. The corresponding diffraction patterns were all accurately indexed with the fcc structure parameters of UO_2. The proportion of the four phases depended on the oxygen content of the initial U-Zr-O mixture. P4 was not observed in the low oxygen content (1 to 5 at. %) mixtures. It was abundant in the 35 at. % O mixture.

EPMA and EBSD were both chosen for their spatial resolution. EPMA was tested as an analytical technique to determine the chemical composition of uranium compounds containing light elements (oxygen). EBSD was used as a microdiffractometer to investigate the local structure of small particles in multi-phase materials. The results obtained by both techniques were consistent.

References

1. A. Skokan, « High Temperature Phase Relations in the U-Zr-O System », *5th Int. Meeting on Thermal Nuclear Reactor Safety*, Karlsruhe, Sept. 9-13 1984, pp 1035-42.
2. P. Hofmann, C. Politis, « Kinetics of UO_2/Zry Reactions at High Temperatures », *J. Nucl. Mater.*, **87** (1979) 375.
3. The authors are indebted to C. Merlet (Université de Montpellier II, France) for useful discussions.

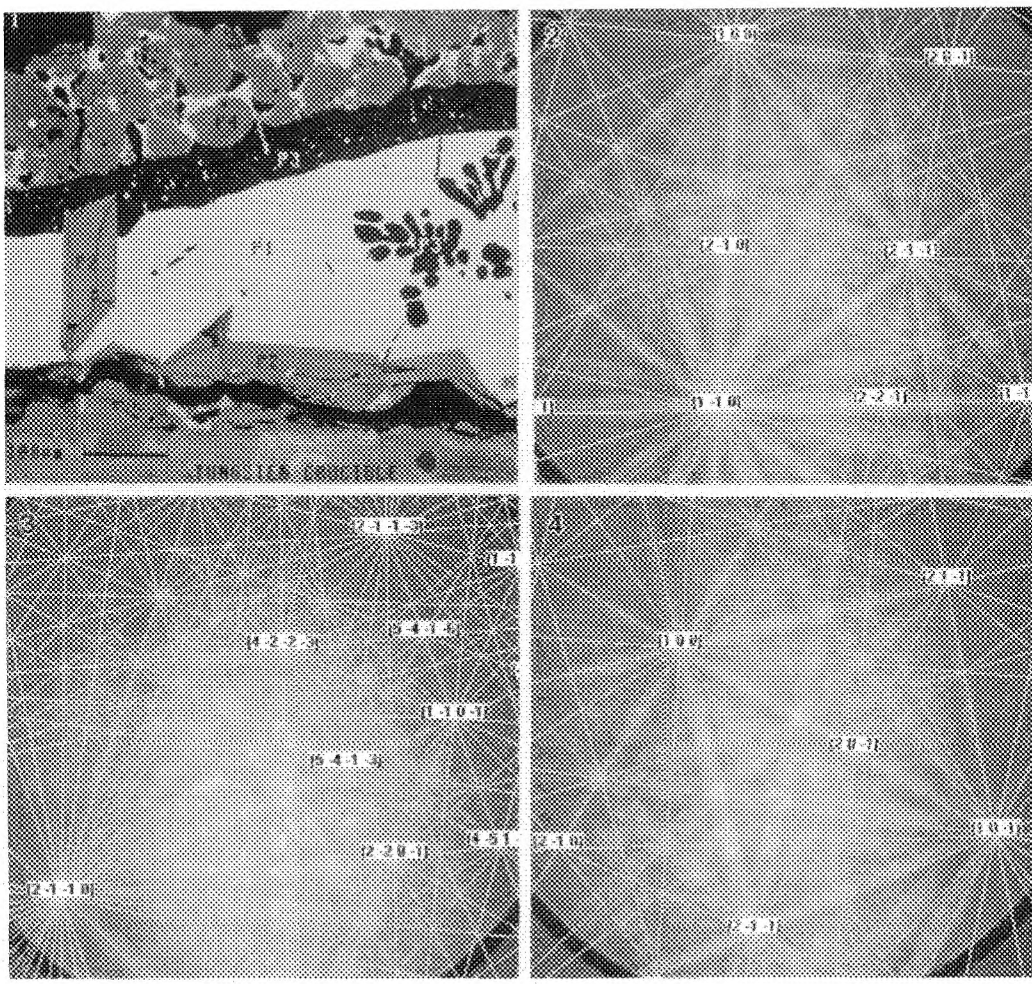

FIG. 1 Location of the different phases in the U-Zr-O mixture with 30 at. % oxygen.
FIG. 2 Electron backscattering pattern of P2 indexed with the fcc structure parameters of W_2Zr.
FIG. 3 Electron backscattering pattern of P3 indexed with the hexagonal structure parameters of α Zr (O).
FIG. 4 Electron backscattering pattern of P4 indexed with the fcc structure parameters of UO_2.

EPMA QUANTITATIVE X-RAY MAPPING

J. F. Thiot* and J. L. Pouchou **

*SAMx, 78280 Guyancourt, France
**Department of Materials Science, ONERA, 92320 Châtillon, France

Quantitative X-ray mapping has always been one of the ultimate goals of many X-ray microanalysis application programs. However, only semi-quantitative X-ray mapping (peak intensities) is commonly used in WDS and EDS techniques. EDS maps are easier to produce, because the multichannel detection gives direct access to the intensities, and also because beam scanning may be used over wide areas without any danger of spectrometer "defocusing". WDS mapping, because of the monochannel detection, has most of the time been limited to one map per spectrometer. A few attempts have been made in both techniques to produce a quantitative map by calibration, i.e. using a few quantitative analyses performed on some pixels to calculate the composition at each pixel of an image. What we propose here is to improve the WDS acquisition scheme and the automation of the quantitation to the point where the user can collect automatically all X-ray maps of the elements in the sample and then run a quantitative routine which automatically calculates the corresponding composition images, through the usual $\phi(\rho z)$ procedures (*PAP/XPP*).

For a few years now, our EPMA automation package (*XMAS*) has been available on a few microprobe configurations. It includes a friendly software to build an analysis file with the analytical parameters: analyzed element, X-ray line, crystal, stage position, physical conditions and standard to be used. An imaging package (*HiMax*) has been added to the standard package for video and X-ray images (beam or stage control). *HiMax* last release includes a link between the analysis file and the image acquisition, so that *HiMax* just needs to know which *XMAS* file to use for automatically acquiring all the X-ray maps (and background images if required).

X-ray intensities are recorded as 16-bit data, and displayed as 8-bit images. Once the images have been acquired and saved into the data base, the *Quantify* function subtracts the background from every image, and uses the standard information saved in the analysis file to compute for each pixel the relative intensity I_x/I_{std} for every element. Then the quantitation is performed with the *PAP/XPP* iteration scheme, including all the features built in this procedure (stoichiometry, element by difference, spectral interference...). With a Pentium 90 MHz, the basic processing time per pixel (including display) is 11 ms, i.e. 3 mn for a 128 x 128 image set. A speed-up option reduces the time to 7 ms per pixel when the current intensities are close to those of a previous pixel.

The capability of *HiMax* to take advantage of the *XMAS* built-in quantitative features is illustrated by the example of a TA6V alloy for which quantitative maps of the minor elements Al, V and Fe have been collected (Fig. 1). The experimental conditions are: 15 kV, 10 nA, 34 µm beam scan, 128 pixels, TAP crystal for Al, PET for V, LiF for Fe, major element Ti by difference. Although Ti is not measured, the interference of V Kα with the Ti Kβ line (Fig. 2) is taken into account by use of a pure Ti "interference standard" measured at the V Kα spectrometer position. In addition, the program creates by difference the concentration map of the element not analyzed (Ti). With the *Spot* mode, one can display the values of any selected pixel (peak count, background, corrected wt.% and at.%) to verify the good performance of the procedure. Table 1 shows the results for one typical pixel in each phase, and the influence of the interference processing on the vanadium concentration.

HiMax offers other specific tools, such as the median filter to eliminate spurious pixels, and a procedure to correct low magnification images for spectrometer defocusing when the beam control mode is used rather than stage control. Usually, the defocusing compensation is done by correlating the position of the WDS crystal to that of the scanned line, in order to approximately fulfil the Bragg condition. The drawback of this method is that a specific orientation of the scanned area is required for each spectrometer, so that the proper conditions cannot be obtained simultaneously for all the elements. In *HiMax*, the correction is presently performed by use of reference images acquired on homogeneous standards. Fig. 3 shows a set of X-ray images acquired at a magnification of 400 (field size ~ 300 µm). Fig. 4 demonstrates the efficiency of the "defocusing correction" (for the Si Kα image, the X-ray intensity loss in the upper-right and lower-left corners was exceeding 80 %).

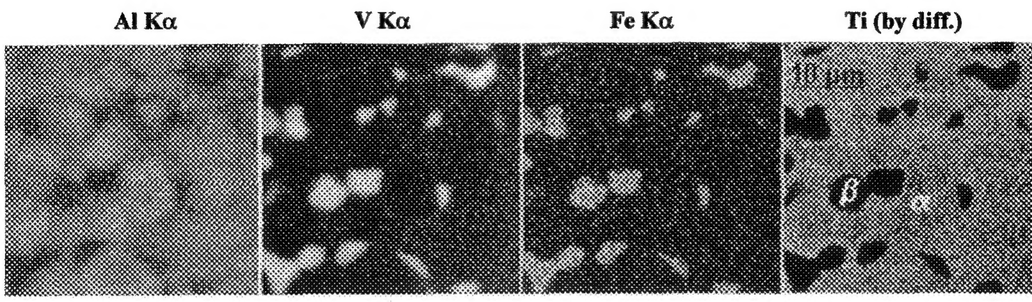

FIG. 1 - Quantitative X-ray maps of the minor elements Al, V, Fe (measured) and of the major element Ti (obtained by difference) in a α+β TA6V alloy (34 x 34 µm² beam scan, 128 x 128 pixels², 300 ms/pixel)

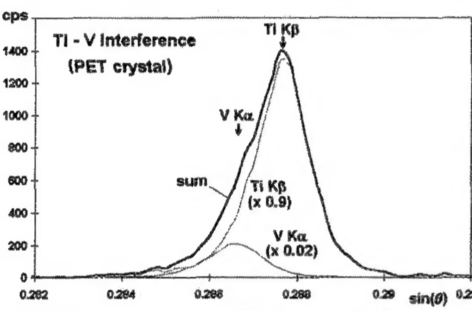

FIG. 2 - Interference of Ti Kβ line with V Kα.

TABLE 1 - Al, V and Fe wt.% for typical pixels of α and β phase selected in composition images of Fig. 1.

	with interference processing			without interference processing		
phase	Al	V	Fe	Al	V	Fe
α	6.25	1.80	0.16	6.27	5.35	0.16
β	4.14	11.36	3.22	4.14	15.59	3.22

The contributions of Y. Amelot and J. Phan (SAMx) to software development and Y.Pioche (ONERA) to experimental work are acknowledged.

FIG. 3 - X-ray maps as acquired (TAP, vertical spectrometer, 300 x 300 µm² beam scan, 256 x 256 pixels²)

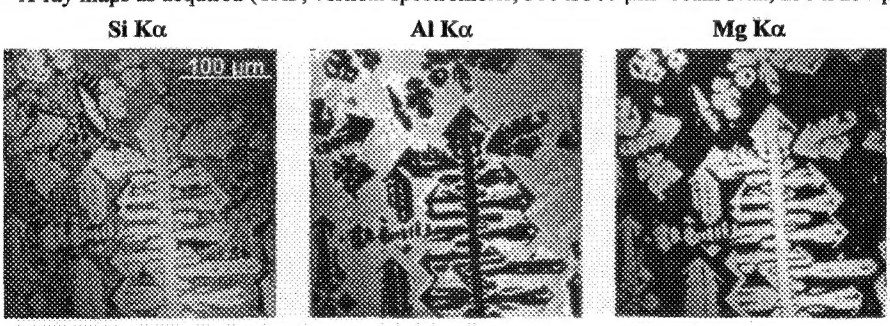

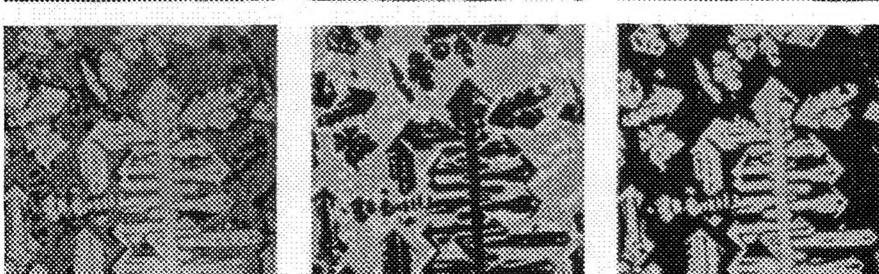

FIG. 4 - Same X-ray maps as in Fig. 3 after compensation for spectrometer defocusing.

MICROSTRUCTURAL CHARACTERIZATION OF CU-SN-NI SOLDER IN MICROELECTRONIC PACKAGING

J. G. Duh, C. C. Young and C. H. Cheng

Department of Materials Science and Engineering, National Tsing Hua University, Hsinchu, Taiwan

Microelectronic packaging has experienced exciting growth in the past years, and solder joints plays important roles in the reliability of package system[1]. Lead-tin (Pb-Sn) alloys are the most prominent solders for the interconnection and packaging of modern electionic components and devices. However, there are environmental concern on the toxicity of Pb. These concerns have inspired a great deal of research to study the feasibility of lead-free replacement alloys[2]. It is known that the presence of intermetallic is often an indication of good wetting in solder joints. Nevertheless, excessive intermetallic growth may be detrimental to joint reliablity. The purpose of this study is to investigate the growth evolution between unleaded Cu-Sn-Ni alloys and metallized layer. These results will help to characterize the effect of aging on the microstructural and mechanical properties of solder / metallized layer / substrate systems.

Pre-treated patterned Pt-Ag / Al_2O_3 substrates were immersed in a Cu electroless plating bath at room temperature. Substrates were dipped into melt solder bath, and taken out perpendicularly, followed by air cooling. For the solder / electroless Cu interface, two kinds of intermetallic compound are observed[3]. Cu_6Sn_5 grows adjacent to the solder, while Cu_3Sn is adjacent to the electroless Cu side. Cu_6Sn_5 layer is generally thicker than the Cu_3Sn layer. It should be pointed out that Cu_3Sn is not observed in the unaged sample using SEM. Thermal aging is always required for Cu_3Sn to become thicker enough to be visible. Figs. 1(a)-(d) exhibit the morphology and X-ray mapping of the Cu-Sn-Ni solder / Pt-Ag / Al_2O_3 assembly after 35-h aging at 150°C. Tin diffuses into the conductor film after soldering according to the micrographs of Sn X-ray mapping.

The electron microprobe analysis (EPMA) for the unleaded solder / electroless Cu / Pt-Ag / Al_2O_3 sample annealed at 150 °C for 0 and 70 hours is shown in Figs. 2 and 3, respectively. The concentration profiles of Cu and Sn traces exhibit a slope within the Cu_3Sn layer for the aged sample. This implies a possible concentration gradient extending from their respective sources. Usually Sn has a faster diffusion rate due to its lower melting point. It is interesting to point that the concentration profiles of Ag and Cu near the interface of the Ag / Cu seem relatively steep even after 70-hour aging at 150°C, indicating a slow diffusion with the constituents.

References

1. D.R. Frear and P.T. Vianeo, Metal. and Mater. Trans. A, 25A(1994)1509.
2. I. Artaki and A.M. Jackson, J. Electronic Material, 23(1994)757.
3. C.C. Young, M. S. Thesis, National Tsing Hua University, Hsinchu, Taiwan(1995).

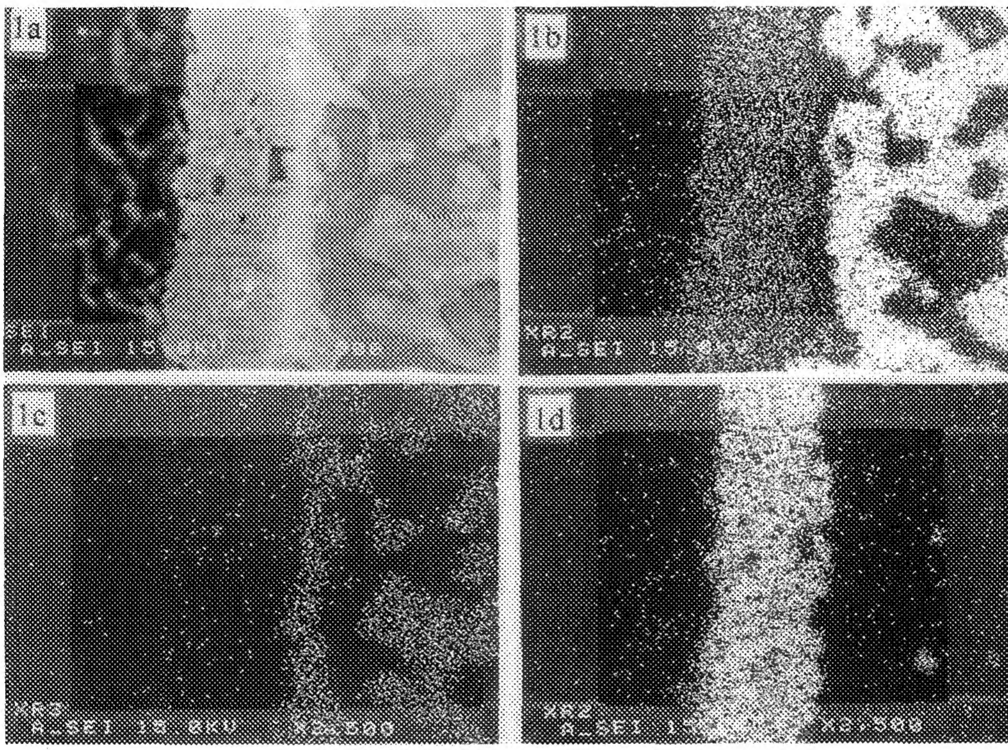

2
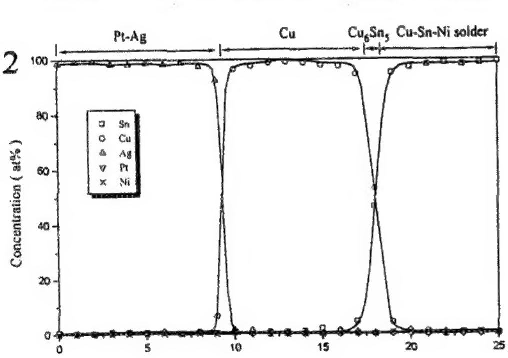

3
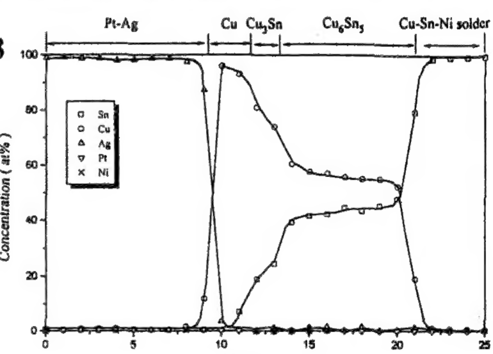

FIG. 1 Cross sectional view of the Sn-Cu-Ni solder/Pt-Ag/Al_2O_3 assembly after 35-hr aging at 150°C, (a) SEI picture, (b) Sn X-ray mapping, (c) Pb X-ray mapping, (d) Ag X-ray mapping.

FIG. 2 Electron microprobe trace across the intermetallic layer of the unleaded solder / electroless Cu / Pt-Ag assembly before aging.

FIG. 3 Electron microprobe trace across the intermetallic layer of the unleaded solder / electroless Cu / Pt-Ag assembly aging at 150°C for 70 hours.

ELECTRON-PROBE QUANTITATIVE ENERGY-DISPERSIVE ANALYSIS OF TRACE MAGNESIUM CONCENTRATIONS IN Ag-Mg ALLOYS

R. B. Marinenko

Microanalysis Research Group, NIST, Gaithersburg, MD 20899

Internally oxidized Ag-Mg alloys are used as sheaths for high Tc superconductor wires because of their superior mechanical properties. The preparation and characteristics of these materials have been reported.[1] Performance of the sheaths depends on the concentration of the magnesium which generally is less than 0.5 wt. percent. The purpose of this work was to determine whether electron probe microanalysis using energy dispersive spectrometry (EDS) could be used to quantitate three different Ag-Mg alloys. Quantitative EDS analysis can be difficult because the AgL escape peak occurs at the same energy (1.25 keV) as the Mg $K\alpha$ peak. An EDS spectrum of a Ag-Mg alloy wire is compared to a pure Ag spectrum in Fig. 1.

EDS spectra were analyzed at 15 keV at a beam current of 1.1 nA using a 20μm beam. Spectra of the alloys were taken at 1000 and 2000 s and Mg was used for the standard. Spectral processing was done with the multiple least squares procedure in the Desk Top Spectrum Analyzer (DTSA) developed in this laboratory.[2] For comparison purposes WDS data was taken at 15 keV, a beam current of 50 nA, and an acquisition time of 100s. Random, point beam samplings taken from each wire showed no or little heterogeneity. Both pure Mg and NBS SRM K-412 glass were used as standards. FRAME-X, a ZAF matrix correction procedure also developed in this laboratory, was used to calculate the concentrations from both the WDS and EDS (in DTSA) data.[3]

In Table I the EDS and WDS results for the three alloys are compared with ICP data provided by the manufacturer and by The American Superconductor Company (ASC) with whom this work was done. Significant uncertainties in accuracy are expected at the low Mg concentrations in these specimens. The uncertainty contribution in the EDS from the low counting statistics for Mg in the unknown which is 2.5% relative or less in spite of the long counting times. This error was kept to less than 1% relative in the WDS analysis by using high count rates and/or long counting times. Errors due to the EDS MLLSQ fitting procedure and the fitted standard are each less than 1% relative. But for both EDS and WDS analyses the largest error is attributed to the ZAF correction procedure which is estimated to be 5% relative because of the large absorption correction of 0.42 for Mg in a Ag matrix. The uncertainties cited in the table are one standard deviation which were obtained from adding all errors in quadrature, including those from counting statistics, specimen inhomogeneity, the matrix correction procedure, and dead time and background corrections.

References

1. A. Charai et. al., Scripta Metallurgica, 17(1983)833.
2. C. E. Fiori et. al., NIST Std. Ref. Database #36. Std. Ref. Data, NIST, Bldg. 221/A322 Gaithersburg, MD 20899.
3. R. L. Myklebust et. al., Electron Probe Quantitation , New York:Plenum (1991)177.

Ag spectrum

Ag-Mg wire spectrum

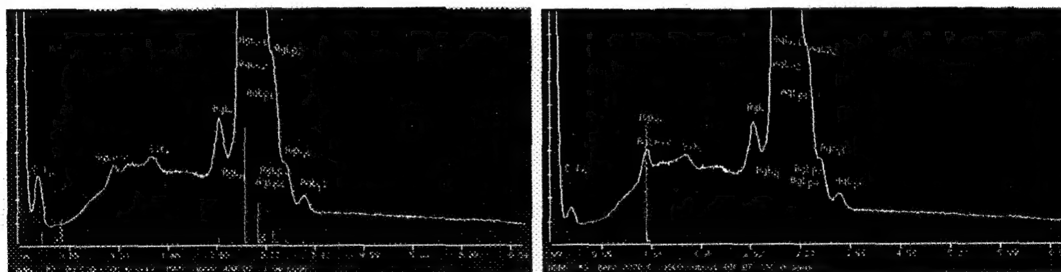

Fig. 1. Comparison of Ag spectrum with a Ag wire containing 0.4 wt.% Mg.

Table 1
Quantitative Analysis of Ag-Mg Alloy Wires
Mg Concentration (wt %)*

Standard Wire	ICP Results** Manu/ASC	EDS (MLLSQ_DTSA) Acq. Time 1000s	2000s	WDS K412	Mg
A	0.107/0.112	0.14 ±0.008	0.12 ±0.007	0.13 ±0.009	0.12 ±0.008
B	0.208/0.223	0.28 ±0.015	0.23 ±0.012	0.23 ±0.013	0.22 ±0.013
C	0.43/0.420	0.44 ±0.023	0.42 ±0.022	0.46 ±0.025	0.43 ±0.024

* Uncertainty is one standard deviation which includes errors from counting statistics, specimen inhomogeneity, the matrix correction procedure, and dead time and background corrections.
** ICP data provided by ASC with no uncertainties; manu=data provided by manufacturer, ASC=data from analysis performed at American Superconductor Corp.

ELECTRON-PROBE MICROANALYSIS OF ALUMINA-SUPPORTED PLATINUM CATALYSTS

R. E. Lakis*, E. P. Vicenzi **, and F. M. Allen***

* LRSM, University of Pennsylvania, 3231 Walnut St., Philadelphia, PA 19104-6202
** Princeton Materials Institute, Bowen Hall, 70 Prospect Ave., Princeton, NJ 08540-5211
*** Engelhard Corporation, 101 Wood Ave., Iselin, NJ 08830-0770

Conventional Electron-Probe Microanalysis (EPMA) requires fully dense, flat polished specimens, and similarly prepared standards of known composition.[1] Most supported catalyst systems do not fit the above criterion, because porosity and large internal surface areas are intrinsic qualities of useful catalyst materials. Many catalysts of commercial importance contain a number of active metals and promoters that are impregnated into porous ceramic support with well controlled concentration profiles relative to the other constituents. It would be of great practical importance to reliably measure the distribution of active materials in a quantitative manner. A previous investigation which focused upon porous alumina, identified a deficit of detected electrons which increased with increasing porosity, and was perhaps due to the roughness of the porous materials surface.[2] This leads to unrealistically low composition totals when traditional correction procedures are employed. This study is a first step towards the collection of high statistical quality data on catalyst materials so that new matrix correction procedures may be developed for these systems.

The alumina supported catalyst specimens were prepared by Engelhard Corporation using routine wet impregnation techniques, and were independently analyzed for platinum content. Fully dense α-alumina was used for the aluminum and oxygen standards, and high purity platinum was used for the platinum standard.

The data was acquired using a five spectrometer Cameca SX50 Microprobe. Aluminum Kα, oxygen Kα, Platinum Mα, and Platinum Lα x-rays were detected using TAP, W/Si multilayer, PET, and LiF crystals respectively. The measurements were made with a stationary probe defocused to 15 micron in diameter. Based upon preliminary investigations, this probe size was found to dramatically reduce the average standard deviation of the data when compared to a focused probe. The fully dense alumina and platinum standards were acquired at 20nA beam current, while the porous catalyst materials were acquired at 200nA. Counting time ranged from 200s to 255s, resulting in at least 100s on peak and 50s on positive and negative backgrounds. The porous material data points are the average of 10 replicate measurements, and the error bars represent ±1 standard deviation of these measurements. The standard values are the average of 5 replicate analysis and had a standard deviation less than $\pm0.5\%$.

Figure 1. is a plot of the aluminum and oxygen x-ray intensities normalized to the fully dense alumina standard. A value of one would indicate the measurement was identical to the standard value at that condition. Similarly, Figure 2. represents the platinum Mα and Lα intensities normalized to fully dense platinum. Figure 1. indicates a substantial x-ray deficit relative to a dense material. Aluminum possessed only 75% of its dense intensity and oxygen was only 60% of the standard value. While this discrepancy is still not understood, the deficit is consistent with previous measurements of porous alumina. Surprisingly though, there was almost no dependence on accelerating voltage. Since the maximum platinum concentration is 1.5 wt% the alumina data is not expected to vary significantly with platinum concentration, and the observed dependence may be an indication that the porosity of these samples is affected by the impregnation process. The data of Figure 2. suggests that this analysis is nearly independent of accelerating voltage, and that higher count rates are achieved for the platinum Lα line. Count rate data for the platinum measurements are presented in Figure 3. The relative differences between Figures 2 and 3 are currently being assessed by comparing the calibration curve data (Figure 3) to matrix correction results based upon the relative intensity values presented in Figures 1 and 2. These results will be the product of our continuing efforts in this area.[3]

References

1. J. I. Goldstein, et al, *Scanning Electron Microscopy and X-Ray Microanalysis,* 2 ed., Plenum Press, New York, 1992.
2. R. E. Lakis, C. E. Lyman, J. I. Goldstein, *Electron Probe Microanalysis of Porous Materials,* Proc. EMSA, 1992.
3. The authors gratefully acknowledge the support of Engelhard Corporation, the Princeton Center for Complex Materials MERSEC, and the Laboratory for Research on the Structure of Matter at the University of Pennsylvania.

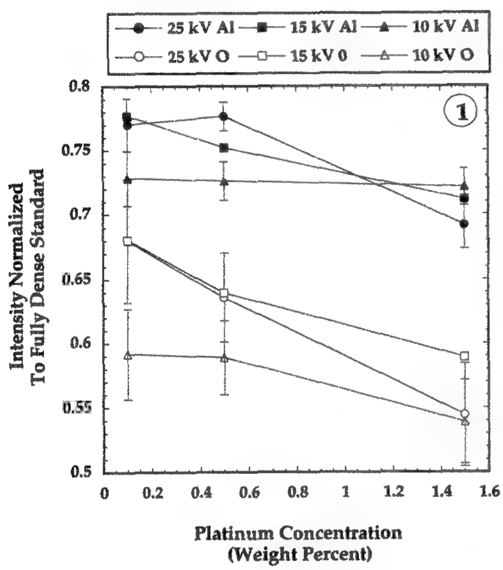

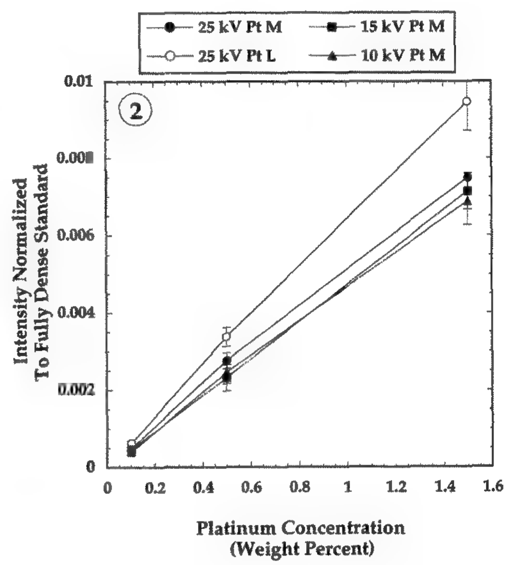

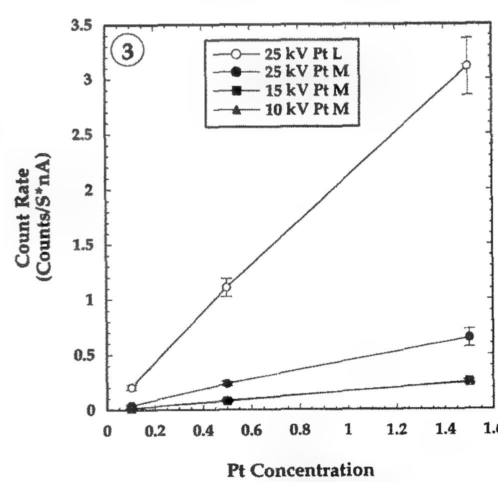

Fig. 1 Aluminum and oxygen intensities normalized to the dense alumina standard vs. platinum concentration.
Fig. 2 Platinum Mα and Lα intensities normalized to the dense platinum standard vs. platinum concentration.
Fig. 3 Platinum Mα and Lα intensities vs. platinum concentration (calibration curve).

LEAD-PHASE DETERMINATION AND DEMONSTRATION OF CONTAMINATED SOIL REMEDIATION MECHANISM BY SCANNING ELECTRON MICROSCOPY AND CHARACTERISTIC X-RAY IMAGING

T. B. Vander Wood

MVA, Inc., 5500 Oakbrook Parkway #200, Norcross, GA 30093

The utility of microscopy and microanalysis in the study of contaminated atmospheres is well established.[1,2] The particulate nature of soils suggests that these methods would be equally useful in the study of contaminated soils and similar materials;[3,4] however, the focus on bulk contaminant concentrations, solution chemistry and leachability has obscured the role of microanalysis in elucidating the chemistry of contamination and in guiding remediation methods.

A case in point is the study of lead contaminated soils and possible remediation strategies. Ma, et al.,[5,6] recognized that reaction of lead with hydroxyapatite provided a possible remediation method for lead contaminated soils by precipitation of hydroxypyromorphite [$Pb_{10}(PO_4)_6(OH)_2$], proposing that the mechanism of lead immobilization in contaminated soils is congruent alteration, that is, dissolution of hydroxyapatite [$Ca_{10}(PO_4)_6(OH)_2$]to give phosphate ion in solution, followed by precipitation of dissolved lead ion as hydroxypyromorphite. No effort was made to microscopically characterize an experimental soil which showed significant reduction in leachable lead after mixing with hydroxyapatite either before or after mixing. Ruby, et al.,[7] also recognized the insolubility of lead phosphates, and conducted an extensive study of a lead ore contaminated sediment, including microcharacterization of the sediment prior to treatment with phosphate rich solution. These authors recognized both congruent alteration and incongruent alteration to lead phosphates occurring naturally in the sediment, but did not evaluate actual remediation techniques.

In the present study, samples of a lead contaminated soil before and after treatment with a proposed remediation technology were examined by scanning electron microscopy/energy dispersive x-ray spectrometry (SEM/EDS) including the use of characteristic x-rays to produces x-ray images of elemental distributions within the samples. In this soil, lead occurred primarily as lead metal and lead oxide (Figure 1a,b). No noticeable phosphate formation had taken place (Figure 1c) and there was no evidence for lead dissolution and reprecipitation as rims or rinds on other particles. This soil was then mixed with a treatment whose principal active component was phosphoric acid, with a resulting dramatic decrease in lead occurring in leaching solutions. Microscopic examination of the treated soil (Figure 2a,b,c) showed extensive formation of lead phosphate rims on the lead metal and lead oxide grains, suggesting incongruent alteration of the lead rich particles. No evidence for congruent alteration (e.g. lead phosphate rich rims on non-lead bearing grains) was observed. Selected area electron diffraction of the rim of a representative treated grain identified the lead rich phase as pyromorphite. The occurrence of incongruent alteration rims on lead rich grains indicates that the principal mechanism of remediation is encapsulation, rather than complete reaction of soluble lead to an insoluble form.

References

1. H. van Malderen, et al., Environ. Sci. Technol., 30(1996)312.
2. K. A. Katrinak, et al., Environ. Sci. Technol., 29(1995)321.
3. E. C. Buck, et al., Environ. Sci. Technol., 30(1996)81.
4. C. Zevenbergen, et al., Microbeam Analysis, 3(1994)125.
5. Q. Y. Ma, et al., Environ. Sci. Technol., 27(1993)1803.
6. Q. Y. Ma, et al., Environ. Sci. Technol., 29(1995)1118.
7. M. V. Ruby, et al., Environ. Sci. Technol., 28(1994)646.

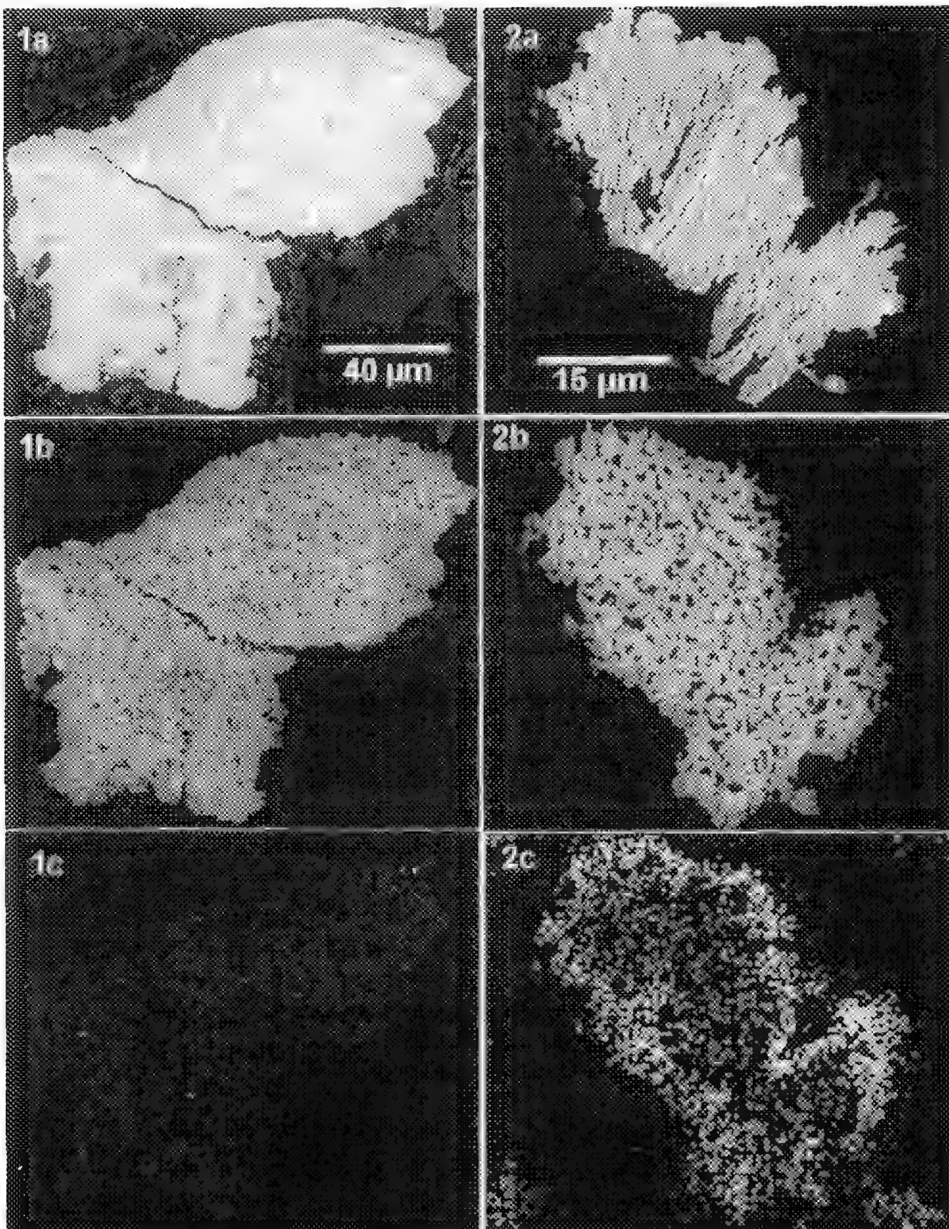

FIG. 1 Typical lead rich particle in untreated soil (a) backscattered electron image (b) lead characteristic xray image and (c) characteristic phosphorous image.
FIG. 2 Typical lead rich particle in treated soil (a) backscattered electron image (b) lead characteristic xray image and (c) characteristic phosphorous image.

CHARACTERIZATION OF LEAD-BEARING PHASES IN MUNICIPAL WASTE COMBUSTOR FLY ASH

L. L. Sutter, G. R. Dewey, J. F. Sandell

Department of Civil and Environmental Engineering, Michigan Technological University, Houghton, MI 49931

Municipal waste combustion typically involves both energy recovery as well as volume reduction of municipal solid waste prior to landfilling. However, due to environmental concerns, municipal waste combustion (MWC) has not been a widely accepted practice. A primary concern is the leaching behavior of MWC ash when it is stored in a landfill. The ash consists of a finely divided fly ash fraction (10% by volume) and a coarser bottom ash (90% by volume). Typically, MWC fly ash fails tests used to evaluate leaching behavior due to high amounts of soluble lead and cadmium species. The focus of this study was to identify specific lead bearing phases in MWC fly ash. Detailed information regarding lead speciation is necessary to completely understand the leaching behavior of MWC ash.

The as-received fly ash was size fractionated[1] and samples were prepared as geological thin sections. This provided a cross-sectional view of the individual particles for analysis using a JEOL 8600 electron microprobe analyzer (EMPA) and an Oxford eXL Phase Distribution Analysis (PDA) system. Additional samples were prepared for x-ray diffraction (XRD) analysis using a Scintag XDS-2000 theta-theta diffractometer.

Using the EMPA, three general forms were found for lead bearing phases including euhedral chloride grains with low concentrations of lead (A in Fig. 1), anhedral grains with very high concentrations of lead (A in Fig. 2), and a chloride particle matrix with low concentrations of lead (B in Fig. 2). The results of typical analyses of the euhedral and anhedral phases are given in Table 1. As shown by these results, the euhedral phases appeared to be near stoichiometric sodium and potassium chlorides with lead occurring as a substitutional element. The anhedral phases were not stoichiometric and had a very high lead content. The chloride matrix was not quantitatively analyzed due its porous physical structure. However, as a result of numerous qualitative analyses, a common group of elements was identified for this matrix phase. The principal elements identified in this chloride matrix include Ca, Cl, K, Na, Pb, S, and Zn.

To confirm the EMPA results, XRD was performed on the fly ash specimens with sylvite, halite, anhydrite, calcite, quartz, rutile, and hematite being identified as the principal phases. Although none of the major diffraction profiles were directly associated with lead bearing phases, a significant shift in profile position was detected for all of the sylvite and halite profiles. The magnitude of profile displacement was approximately 0.2% of the measured d-spacing for sylvite and approximately 0.1% of the measured d-spacing for halite. This peak shift is consistent with an expanded crystal lattice that would result from lead substitution into the halite and sylvite structures.

To determine phase distribution, the electron beam was stepped across the sectioned particles and an x-ray spectrum was gathered at each dwell point[2]. The acquired x-ray spectrum is used to assign the analysis point to a particular phase class. The phase classes used were determined by manually analyzing numerous phases and correlating the measured x-ray intensities for a small group of elements with the actual composition of the phase being analyzed. Selected results from this analysis are presented in Table 2. The results show a concentration of lead bearing anhedral chlorides in the finest and coarsest size fractions. The euhedral phases become more prevalent with increasing particle size.

The results of this study indicate that lead is occurring primarily as a substitutional element in halite and sylvite. Also, lead is present in all size fractions and does not appear to be concentrated in the finest particles. Finally, phase distribution analysis provides an effective method for characterizing materials whose microstuctures include complex phase intergrowths.

References

1. Sutter, L.L., J.F. Sandell, and G.R Dewey, "Applications of Electron Microprobe and Mineral Liberation Analysis Techniques to Municipal Solid Waste Combustor Fly Ash", *Proceedings of the International Symposium on Extraction and Processing for the Treatment and Minimization of Wastes*, February 1994.

2. Sandell, J.F., G.R Dewey, L.L. Sutter, and J.A Willemin, "Evaluation of Lead Bearing Phases in Municipal Waste Combustor Fly Ash", January 1996, Vol. 122, No. 1, *ASCE Journal of Environmental Engineering*.

Figure 1. Euhedral Phases in MWC fly ash.

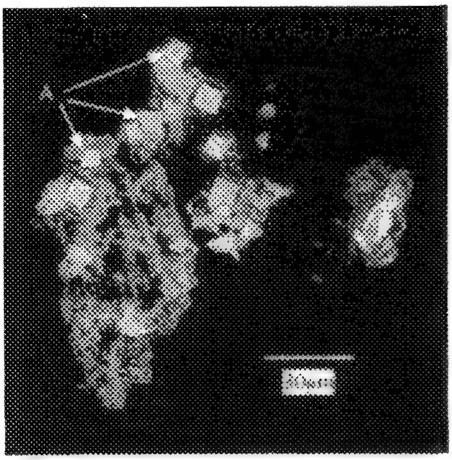

Figure 2. Anhedral Phases in MWC fly ash and a Typical Chloride Matrix.

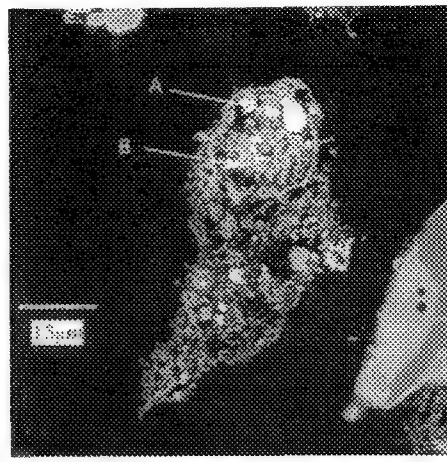

Table 1. Typical EMPA Analyses for Euhedral and Anhedral Phases in MWC fly ash.

Phase	O	F	Na	S	Cl	K	Ca	Zn	Pb
Euhedral	2.1	3.7	55.3	0.2	35.1	2.4	0.3	0.0	0.8
Euhedral	2.7	2.7	51.0	0.4	38.8	1.8	0.7	0.1	1.2
Euhedral	2.7	0.0	49.0	0.1	45.9	1.0	0.0	0.4	0.9
Euhedral	0.0	1.2	49.2	0.0	43.7	3.9	0.7	0.4	0.5
Euhedral	0.2	0.3	0.0	0.0	45.8	51.0	0.0	0.0	3.1
Anhedral	0.4	0.5	0.0	0.9	12.5	7.8	1.6	0.7	74.0
Anhedral	0.0	0.0	0.0	0.0	10.5	10.9	0.3	0.0	76.9
Anhedral	0.0	0.5	0.0	0.0	10.0	9.4	0.3	0.0	78.9
Anhedral	0.0	0.0	0.0	0.0	31.1	29.3	0.7	0.0	38.9
Anhedral	0.0	3.0	0.0	0.0	30.0	25.4	0.8	0.0	40.4

Table 2. Area Fraction of Phase in Each Size Fraction.

Phase Category	Area Fraction of Phase in Each Size Fraction (mesh size)					
	-400	-270 +400	-200 +270	-150 +200	-100 +150	-65 +100
Euhedral	0.06	0.24	0.62	0.45	0.43	0.87
Anhedral	4.48	1.92	3.82	3.33	3.72	6.18

CHARACTERIZATION OF PHASES IN AN AS-CAST Mo-B-Si ALLOY BY WDS EPMA

C.A. Nunes*‡, J.H. Fournelle** and J.H. Perepezko*

* Department of Materials Science and Engineering, University of Wisconsin, Madison WI 53706
**Department of Geology and Geophysics, University of Wisconsin, Madison WI 53706
‡ On leave from FAENQUIL/DEMAR, Lorena 12600-000, São Paulo Brazil

EPMA experiments have been carried out to support an extensive study involving phase equilibria, solidification pathways and diffusion in Mo-rich Mo-B-Si alloys. In this work we have characterized the phases present in an as-cast 60Mo-30B-10Si (at%) alloy by WDS EPMA in order to provide further information to understand some anomalous backscattered electron images of this alloy.[1]

The alloy was produced by arc-melting pure Mo, B and Si under argon. The EPMA analysis was carried out in a CAMECA SX-50 EPMA on a polished and flat surface of the material. In order to avoid additional absorption of the B-Kα radiation the sample was not coated.

The analysis of boron in the presence of Mo presents serious interference between the Mo Mγ line and the B-Kα line (Figure 1). The differential mode of PHA (Pulse Height Analysis), commonly used to suppress multiple order lines, cannot be used here because both lines, Mo-Mγ (λ = 68.95718 Å) and B-Kα (λ = 67.64049 Å), are first order. This problem can be solved by using an on-line overlap correction program[2] which subtracts the Mo-Mγ line from the Boron Kα peak counts on the unknown based upon the empirically determined ratio of Mo-Lα to Mo-Mγ on the Mo standard. Table 1 shows the analysis of a pure Mo (99.95%) specimen with and without this correction program.

The EPMA experiments have been carried out at 7 kV and 20 nA using the crystals PET, PC3 and TAP to determine respectively the contents of Mo (Lα), B (Kα) and Si (Kα). Pure Mo, B and Si have been used as standards. During the calibration a beam current of 5 nA at 7 kV has been used in order to decrease dead time correction error on boron. Due to the spectral interference mentioned above, the background correction for analysis of boron has also presented some difficulty. Based on the analysis of some Mo-B phases of known compositions the following background settings (in sin θ x 10^6) were chosen: Mo: +500, -500; Si: +500, -500; B: +4000 & "slope" = 1.0 (empirically determined). Working at these calibration conditions, the following peak/background ratios have been obtained on the standards: Mo-36.3; Si-123.7 and B-14.8. Our WDS scans on MoB and Mo_2B have not indicated any significant B Kα peak shift in these compounds relative to pure B, in distinction with the observations of Bastin and Heijligers in many other borides.[3] There is some significant change in peak shape (on the long wavelength side) in the Mo-B compounds, primarily we think, due to contribution of Mo Mγ.

A BSE image of the 60Mo-30B-10Si alloy is shown in Figure 2. The location of the points of analysis are indicated and compositions are shown in Table 2. The compositions of the phases are close to MoB, Mo_5SiB_2 (T_2), Mo and Mo_3Si. Powder X-ray diffraction analysis of this alloy has shown the presence of the αMoB, βMoB, Mo_5SiB_2, Mo_3Si and Mo phases (Figure 3). Furthermore, these results confirm that regions of the same composition in MoB can have different BSE contrast; and that the same phenomena exists for T_2.

References

1. J. Fournelle et al. (1996), MAS, this proceeding.
2. CAMECA. (1992) Quantiview 2.0 Reference Guide. Overlapping Correction Program (FILOVL Program). Courbevoie Cedex (France) 16.1-16.6.
3. G.F. Bastin and H.J.M Heijligers. In: *Electron Probe Quantitation*, Edited by K.F.J. Heinrich and D.E. Newbury, Plenum Press, New York (1991) 145-161

1

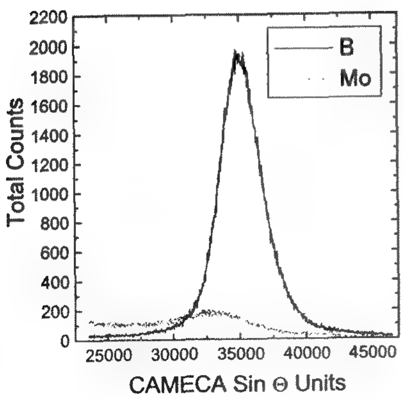

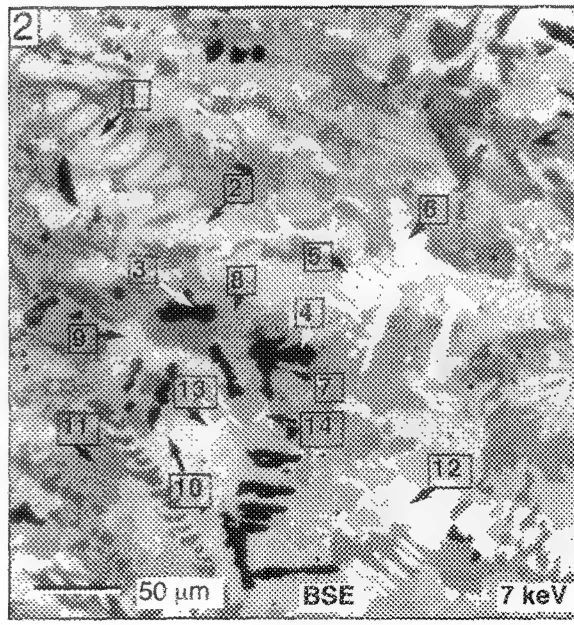

3

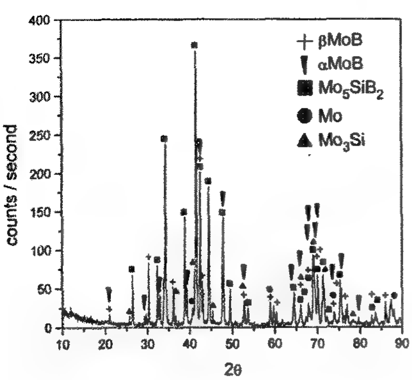

Table 1

Procedure	Mo (at%)	B (at%)
with Filovl	99.77	0.23
without Filovl	81.26	18.74

Table 2

Point	Mo (at%)	B (at%)	Si (at%)
1	54.08	45.75	0.16
2	53.64	46.18	0.18
3	53.41	46.46	0.13
4	53.37	46.50	0.13
5	53.98	45.88	0.14
6	54.04	45.86	0.11
7	62.76	27.11	10.13
8	62.17	27.36	10.47
9	62.57	26.28	11.15
10	62.74	26.58	10.67
11	62.59	26.58	10.83
12	62.20	26.97	10.83
13	91.14	1.83	7.03
14	75.03	3.91	21.06

Fig. 1. WDS scans around B Kα peak position on pure B and pure Mo (7 keV, 5 nA, PC3 xtal)
Fig. 2 BSE image of as-cast 60Mo-30B-10Si alloy, indicating positions of points of WDS electron microprobe analysis (data in Table 2)
Fig. 3 XRD pattern of as-cast 60Mo-30B-10Si alloy (Cu-Kα radiation used)
Table 1. EPMA results of a pure Mo standard, with and without Filovl correction program.
Table 2. Compositions of points in Figure 2, by EPMA (7 keV, 20 nA)

BEYOND FINGERPRINTING: SIMPLE BUT QUANTITATIVE MODELS OF EELS FINE STRUCTURE AND THE COHESION OF INTERFACES

D.A. Muller, D.J. Singh*, S. Subramanian**, S.L. Sass**, J. Silcox and P.E. Batson***

Department of Applied and Engineering Physics, Cornell University, Ithaca, NY., 14853
* Naval Research Laboratory, Code 6691, Washington, DC.
** Department of Materials Science and Engineering, Cornell University, Ithaca, NY., 14853
*** Thomas J. Watson IBM Research Center, NY

Spatially resolved EELS in a STEM provides unique opportunities to examine how local structural and electronic properties can affect macroscopic properties of a solid. Perhaps nowhere else are these connections as pronounced as at interfaces. For instance, H embrittles and B strengthens the grain boundaries in Ni_3Al, a prototypical high-temperature intermetallic. EELS measurements of these boundaries have revealed the changes in electronic structure that correlate with the altered mechanical properties of the material[1].

The interfacial states, which rarely extend more than an atomic layer or so from the boundary, can only be observed with great care. Not only is a stable microscope and very efficient detector required, but also a good understanding of how the probe interacts with the specimen. Artifacts due to radiation damage are a real possibility. If the boundary is examined in a strongly diffracting orientation (as is often the case with special boundaries) probe dechanneling can profoundly alter the measured spectra. This can be avoided by tilting the boundary a few mrad away from the zone axis, which limits the spatial resolution to being sub-nanometer, but not atomic.

The final challenge is the interpretation of the bonding changes. Most of our understanding of the near-edge fine structure in electron energy loss spectroscopy (EELS) comes from the fingerprinting of known materials or by comparison to band structure calculations. However the extrapolation from known metals to their alloys can fail quite dramatically. The Ni_3Al system provides a good many counterexamples to the conventional description and fitting of transition metal EELS spectra. The electronic density of states (DOS), which determines the shape of the EELS fine structure for these alloys, bears little resemble to a superposition of the Ni and Al DOS. Instead, the bonding changes upon alloying must be dealt with explicitly.

First, the measured and deconvolved EELS spectra for bulk Ni, Ni_3Al, NiAl and Al are compared with the s,d local densities of states obtained from linear augmented plane wave (LAPW) calculations (Figs. 1,2). The good agreement (at an energy resolution of 0.8 eV) between theory and experiment suggests, that for *these* materials, a single-particle description of the EELS spectra is appropriate and that core hole effects (which are not included in the LAPW calculations) are minimal for this system. The main trend in the Ni L edge (and hence the Ni d DOS) as Al is added to Ni is a broadening and reduction in height of the sharp peak at the edge onset (the white line). The Al L edge (which measures both Al s,d DOS) shows a transfer of states from the edge onset to higher energies with increasing Ni concentration. This `scooping out' of states in the Ni-Al alloys is seen more clearly in the Al partial DOS where both the occupied and unoccupied states can be studied. Both trends are consequences of hybridization between the Ni d states and the more free electron-like s,p states on adjacent sites.

The division of the spectrum into a `white line' and an atomic continuum not only is a poorly defined process, but worse, it ignores the very contribution that determines the stability and magnetism of intermetallic alloys. Instead, an alternative model that accounts for the changes in band structure due to s-d hybridization is proposed.

A simple sum rule is used to relate the EELS spectra and the core level shifts to changes in the bond energy. Next, careful measurements of the Ni L edges show the Ni-Al alloys to remain charge neutral. In fact, the observed core level shifts are precisely those required to ensure a local charge neutrality (which greatly simplifies the processing of the EELS spectra). Combined, these results lead not only to rules-of-thumb for segregation and bond strength but also to numerical models of heats of formation. As an example, EELS measurements of grain boundaries in Ni_3Al using an atomic-sized probe show that the loss of hybridization can be quantitatively related to the boundary cohesion (Figs. 3,4).[2]

References

1. D. A. Muller et al., Physical Review Letters, 75 (1995) 4744.

2. Supported by the DoE (DE-FG02-87ER45322). The UHV-STEM was acquired through the NSF (DMR-8314255) and is operated by the Cornell Materials Science Center (NSF DMR-9121654). Helpful discussions with E. Kirkland and M. Thomas are acknowledged.

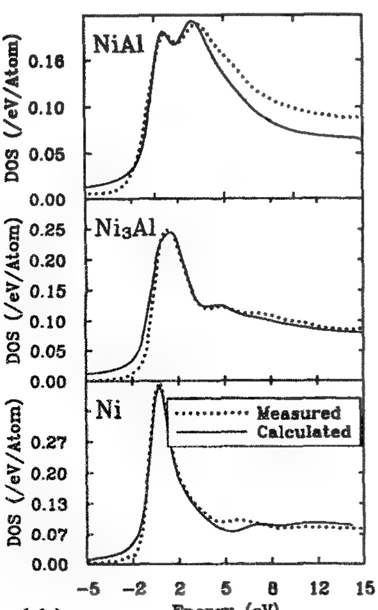

(1)

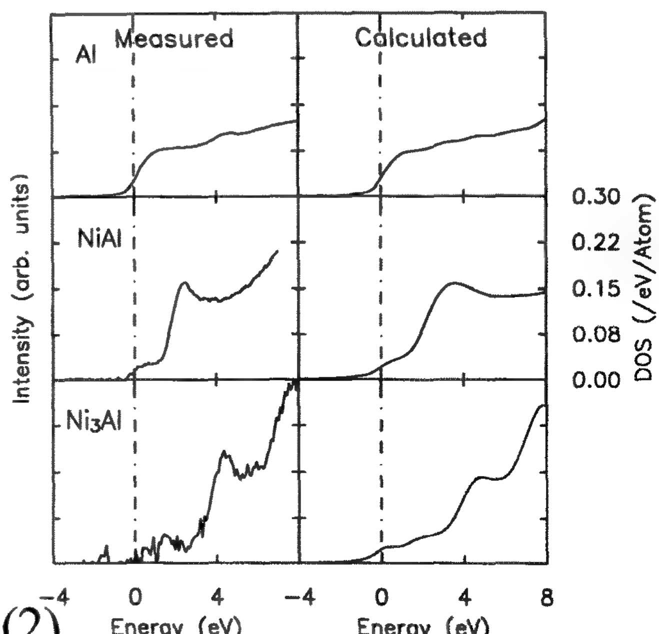

(2)

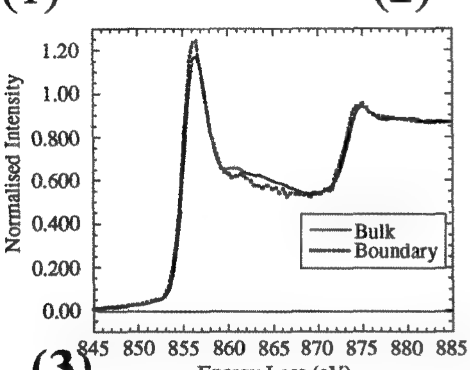

(3)

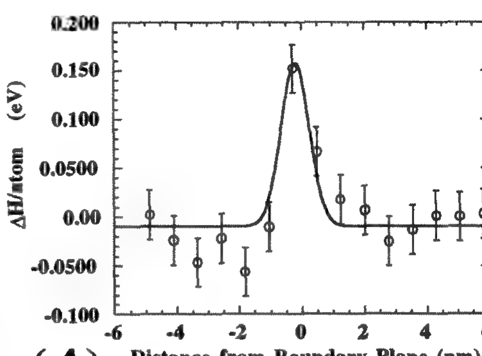

(4)

Fig. 1. Comparison of the LAPW calculated and measured Ni L_3 EELS edges for the Ni-Al system.
Fig. 2. Comparison of the LAPW calculated and measured Al L_3 EELS edges for the Ni-Al system.
Fig. 3. Ni L_3 edge recorded at the large angle boundary in undoped Ni_3Al and compared to a spectrum taken far from the boundary (bulk).
Fig. 4. Spatial variation of the bond energy (per Ni atom) across the boundary in undoped Ni_3Al.

ELECTRON ENERGY LOSS NEAR EDGE STRUCTURES OF INTERMETALLIC ALLOYS AND GRAIN BOUNDARIES IN NiAl

G.A. Botton and C.J. Humphreys

Dept of Materials Science and Metallurgy, University of Cambridge, Pembroke St, Cambridge, CB2 3QZ, UK

Transition metal aluminides are of great potential interest for high temperature structural applications. Although these materials exhibit good mechanical properties at high temperature, their use in industrial applications is often limited by their intrinsic room temperature brittleness. Whilst this particular yield behaviour is directly related to the defect structure, the properties of the defects (in particular the mobility of dislocations and the slip system on which these dislocations move) are ultimately determined by the electronic structure and bonding in these materials. The lack of ductility has been attributed, at least in part, to the mixed bonding character (metallic and covalent) as inferred from ab-initio calculations. In this work, we analyse energy loss spectra and discuss the features of the near edge structure in terms of the relevant electronic states in order to compare the predictions on bonding directly with spectroscopic experiments. In this process, we compare spectra of late transition metal (TM) to early TM aluminides (FeAl and TiAl) to assess whether differences in bonding can also be detected. This information is then discussed in terms of bonding changes at grain boundaries in NiAl.

Alloys were prepared by arc melting high purity starting materials and homogenisation. Energy loss spectroscopy was carried out on a Philips CM30 electron microscope equipped with a Gatan model 666 spectrometer and the grain boundaries were analysed on a VG501 STEM equipped with a Gatan 678 imaging filter. The association of the spectral features with different bands is derived from the modelling of the near edge structure for a series of late transition metal aluminides (FeAl, CoAl, NiAl) using ab-initio electronic structure calculations which have been compared with experiments.[1] Although the density of states of FeAl and TiAl is substantially different, it is worth comparing the spectra providing information on the site decomposed (Al or TM) and symmetry projected (s, p and d) unoccupied density of states for the two materials.

The Al L edges of FeAl and TiAl are very similar at the threshold (fig. 1) both having a onset at 71eV . Differences are observed at about 75.8eV where a sharp peak is present in FeAl. The initial onset is attributed to transitions to mainly *d* states whilst the sharp peak has its origin from the *s* states being pushed away from the Fermi level (E_F) following the interaction of the transition metal *d* bands.[1] The presence of the *d* states near E_F at the Al sites indicates that strong covalent bonding is present in both aluminides but the level of interaction between the *s* bands with the Ti electrons is not as pronounced as in the case of the late transition metal aluminides (similar edges are observed for FeAl, CoAl and NiAl [1]). Larger differences are seen in the Al K edges (probing the *p* final states) where the strong shoulder at the threshold is absent in TiAl (fig. 2). Differences in Al*p*-TM*d* interaction are therefore present between early and late transition metal aluminides. Details of these differences will be described elsewhere. It is worth noting that covalent character in the bonding of TiAl has been deduced recently from charge density maps.[2]

Information of the *s+d* states at the TM sites can be observed by the analysis of the TM $L_{2\text{-}3}$ white-lines. The Fe $L_{2\text{-}3}$ white-line in FeAl presents a well resolved shoulder due to a rapid increase of the *d* partial density of states at about 3.5-4 eV above E_F which is situated near a pseudo-gap in the density of states.[1] This structure is not resolved in the TiAl L_{23} edge but is present in CoAl and NiAl.

Considering the success of the method in retrieving bonding information on "bulk" materials, high spatial resolution analyses at grain boundaries in NiAl have been obtained using a probe size of about 1nm. Spectra "on" and "off" a grain boundary reveal important changes in the Ni $L_{2\text{-}3}$ white-

line (fig. 3). Considering the systematic behaviour of the NiL edge in NiAl as a function of composition and the movement of the E_F associated with the change in chemistry[3], these variations indicate an increase of E_F within the bands (the first peak at the threshold decreases in intensity while in the range 865-870eV the intensity remains constant) which cannot be attributed to either an excess or a deficit of Ni at the boundary. As non-bonding states are being filled in NiAl, this local increase in E_F will result in a decrease of the band filling contribution to the cohesive energy at the interface. Whether this variation will result in a total increase of the cohesive energy will depend, however, on whether other factors which affect the cohesive energy such as the band broadening terms[4] also remain constant.[5]

References
1. G.A. Botton et al., Submitted to Phys. Rev. B.
2. R. Holmestad et al., Philosophical Magazine A 72, (1995)579.
3. G.A. Botton et al., Mat. Res. Soc. Symp, Proceedings, Boston Fall Meeting, 1995, In press.
4. V. Heine, Phys. Rev. 153 (1967)673.

5. This work is supported by EPSRC. We thank Dr. G.-Y. Guo (Daresbury Lab.) for discussions and help in carrying out the theoretical work. We thank Dr R. Holmestad and Z. Horita for providing the TiAl specimen.

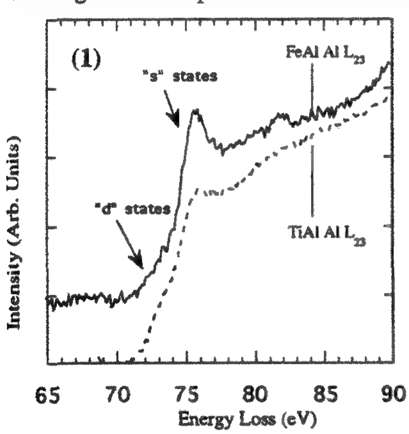

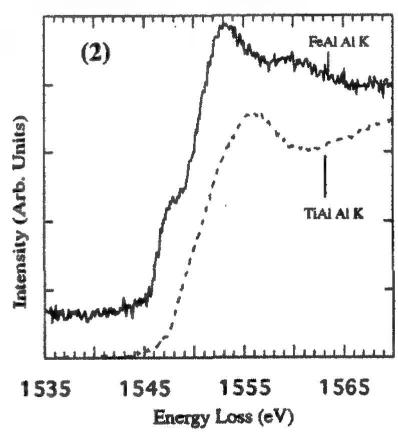

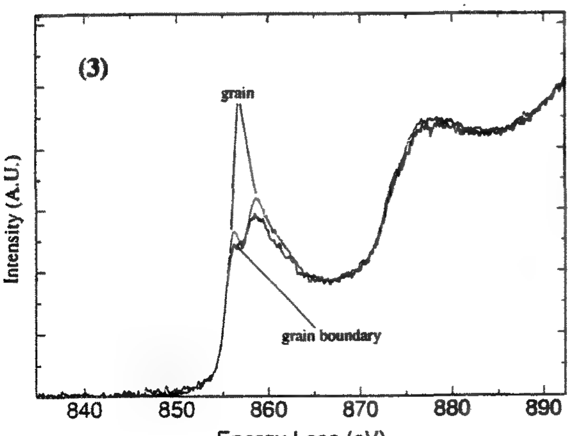

FIG. 1 Al L_{23} edges in TiAl and FeAl.
FIG. 2 Al K edges in TiAl and FeAl.
FIG. 3 Ni L_{23} edge in NiAl. Spectra on a grain boundary and off the grain boundary are shown.

DENSITY OF STATES CALCULATIONS FOR Ni-Al ALLOYS

Jose R. Alvarez and Peter Rez

Department of Physics and Astronomy, Arizona State University, Tempe, AZ 85287-1504

Impurities at grain boundaries can have dramatic effects on the ductility or embrittlement of metals and metallic alloys. The mechanism for these effects is controversial, but it is believed that charge redistribution induced by the impurity atoms is responsible. Electron energy loss spectroscopy (EELS) in the scanning transmission electron microscope (STEM) can be used to measure changes in unoccupied densities of states (DOS) when a small nanometer sized probe is moved across a grain boundary. To interpret the energy loss fine structure band theory is needed to relate the observations, which represent an angular momentum resolved density of states at a particular atomic site, to the local electronic structure in the material.

We compare the Linearized Augmented Plane Wave (LAPW) and layered Korringa-Kohn-Rostoker (LKKR) methods for calculating densities of states relevant for energy loss in Ni-Al alloys. Both methods can give the angular momentum resolved densities of states at a particular site and both use the Local Density Approximation (LDA). The LAPW method allows *ab initio* electronic structure calculations of materials by introducing atomic spheres where the basis wave functions are approximated by solutions of a radial potential; for the interstitial region between the atoms the basis wave functions are approximated by plane waves. Matching of both types of solutions at the surface of the atomic spheres allows the crystal wave function to the determined. A convenient LAPW code which we used in these calculations has been published by Blaha et al[1]. The results were convoluted with a gaussian of half-width 0.3eV to represent instrumental and life-time broadening. The LKKR[2] method uses a generalized Green function that incorporates the symmetry of the crystal to obtain an integral equation. The solution of this integral equation allows the crystal wave function to be determined. The layered KKR method borrows from methods used in LEED theory and first divides the crystal into slices which are considered separately. The LKKR densities of states were calculated with an effective broadening of 0.15eV.

The Ni d density of states reflecting the L_{23} edge is shown for Ni in pure Ni in Fig 1, Ni_3Al in Fig 2a and NiAl in Fig 3a. The total density of states for Al in Ni_3Al, NiAl and pure Al is shown in Figs 2b, 3b and 4 respectively. In all cases the Fermi energy is located at 0 eV. The unoccupied states that would be observed in EELS are to the right of the vertical line. In agreement with previous calculations the Ni d band becomes narrower and the centroid shifts to lower energies as the Al content of the alloy increases. This is due to more localized d-states and greater nearest-neighbor distances between Ni atoms[3]. As can be expected, pure Al shows a DOS quite similar to that for a free-electron gas, which becomes progessively more distorted as the Ni content increases as shown in Figs 3b for NiAl and Fig 2b for Ni_3Al .

Generally the results from LAPW and LKKR calculations are in good agreement. At the Al site there are problems when the LAPW DOS cuts off about 10eV above the Fermi level (Figs 3b and 4). There are also distortions in the Ni unoccupied d DOS above the d band. These discrepancies are caused by the linearization procedure. Care should be excercised in comparing LAPW DOS with EELS experiment.

References

1. P. Blaha et al., *Computer Physics Communications*, 59 (1990) 399.
2. J.M. Maclaren et al, *Computer Physics Communications*, 60 (1990) 365.
3. S.C. Lui et al., *Physical Review B*, 42, 3 (1990) 1582.
4. This work was supported by National Science Foundation grant DMR 930-6253.

1

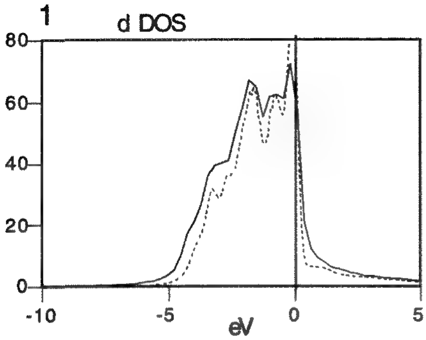

Figure 1: d DOS in Ni.
Figure 2: (a) Ni d DOS and (b) Al total DOS in Ni_3Al.

2a

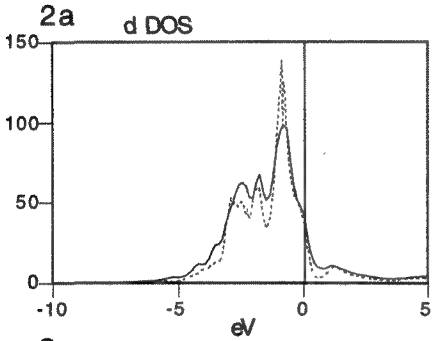

2b

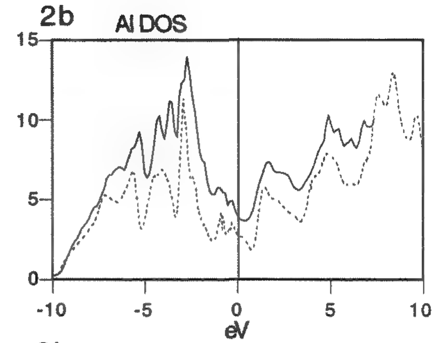

3a

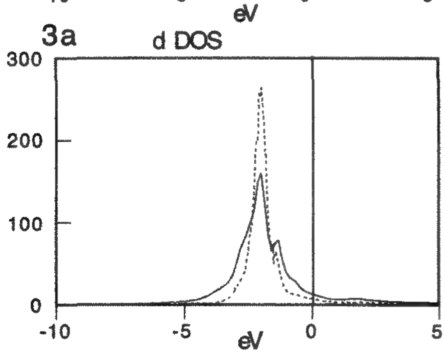

3b

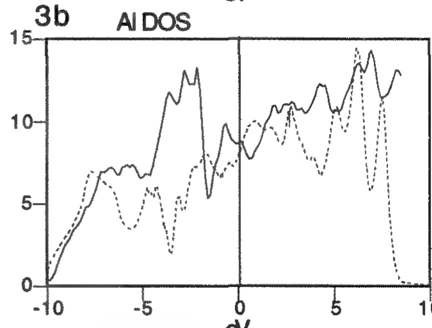

4

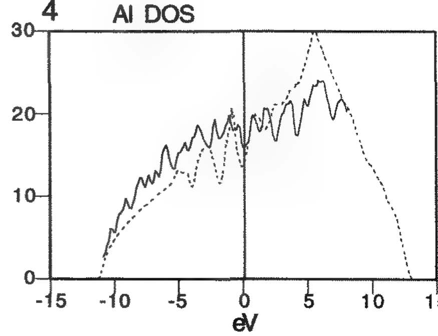

Figure 3: (a) Ni d DOS and (b) Al total DOS in NiAl.
Figure 4: Total DOS in Al.

——— KKR calculation
--------- LAPW calculation

STEM INVESTIGATION OF THE CHEMISTRY AND BONDING CHANGES ASSOCIATED WITH THE GRAIN BOUNDARY EMBRITTLEMENT OF Cu BY Bi

V. J. Keast, J. Bruley and D. B. Williams

Department of Materials Science and Engineering, Lehigh University, Bethlehem, PA 18015

It has long been known that trace amounts of Bi can embrittle Cu after appropriate heat treatments.[1] The Bi segregates to the grain boundaries and weakens them such that failure occurs through intergranular fracture without plastic deformation. This behavior is demonstrated in the scanning electron micrograph of a typical Cu-Bi fracture surface in Figure 1. It is known that the Bi extends for only a few atomic layers into the grains on either side of the grain boundary.[2] This narrow segregation width was been confirmed using Energy Dispersive X-ray Spectroscopy (EDS) on a VG HB603 STEM. Figure 2 shows the ratio of Bi to Cu as the probe is stepped across the grain boundary.

The segregation behavior is well understood, however it is not yet properly understood how the Bi causes embrittlement once it is at the grain boundaries. The Bi must change the bonding at the boundaries so that the boundaries become weak and hence the most likely fracture path. The Electron Energy Loss Near Edge Structure (ELNES) coupled with the small probes and high current density available in a field emission STEM can provide information about the localized electronic structure and hence bonding at grain boundaries. Previous investigations indicated that the near edge structure of Cu was altered at the grain boundaries due to the presence of Bi.[3] Figure 4 shows more recent and convincing evidence obtained from the arrowed region of the grain boundary in Figure 3. The faceting of the boundary seen in Figure 3 is a characteristic of the Cu-Bi system.[5] In Figure 4, two Cu L_{23} edges are displayed after power law background removal. One spectrum was taken with the probe located on the grain boundary and the other with the probe within the adjacent grain. A small amount of extra intensity can be seen above the edge threshold and a spatial difference between the two spectra reveals this feature more clearly.

This feature is related to the white lines seen in the electron energy loss edges or x-ray absorption edges of the transition metals and can be associated with a removal of electrons from the d-band of copper. This is most likely due to the hybridization of the Cu 3d electrons with the Bi 6s and/or 6p states. Pearson et al. have correlated white line intensities to d-band occupancy.[5] Their quantification scheme was applied to a number of our spectra, that demonstrated a white line, to estimate the number of electrons removed from the d-band, Δn, for each Cu atom next to the grain boundary. The results are given in Table 1 along with the Bi contents measured by EDS. Layered KKR electronic structure calculations of the expected occupancy change have been calculated to give an average $\Delta n = 0.27$ which is in reasonable agreement with experiment.[6] This bonding change could be interpreted as a strengthening of the directional d bonds and may provide basis for an understanding of why embrittlement occurs.[7]

References

1. E. Voce and A. P. C. Hallowes, *J. Inst. Metals*, 73(1947)323
2. A. Joshi and D. F. Stein, J. *Inst. Metals*, 99(1971)178
3. J. Bruley, V. J. Keast and D. B. Williams, *J. Phys. D Appl. Phys.*, 29(1996) in press
4. D. H. Pearson, C. C. Ahn and B. Fultz, *Phys. Rev. B*, 47(1993)8471
5. J. M. Donald and L. M. Brown, *Acta Metallurgica*, 27(1979)59
6. P. Rez and J. McLaren, *Proceedings of Microscopy and Microanalysis* 1996
7.This work was funded by NSF 93-06253

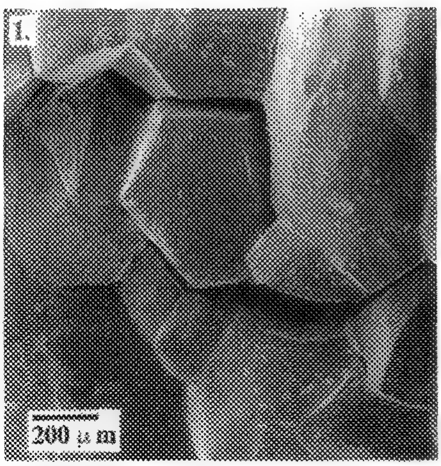

2.

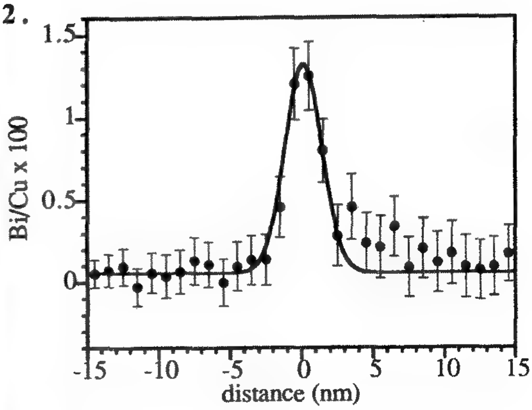

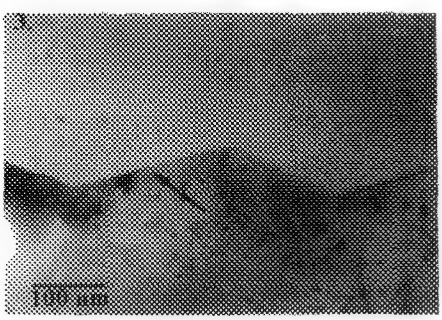

4.

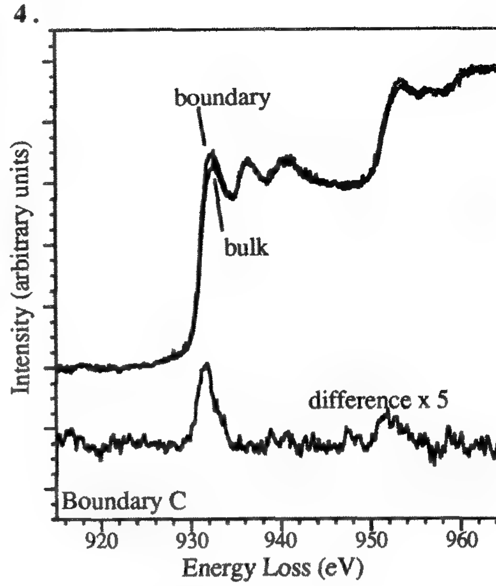

TABLE 1. d-band occupancies and Bi content for different boundaries

boundary	Δn e^{-}/Cu atom	Bi content monolayers
A	0.13	0.21
B	0.15	not measured
C	0.13	0.79

FIG. 1. Typical brittle intergranular fracture surface for Cu-Bi
FIG. 2. Atomic ratio of Cu to Bi as a function of distance from the grain boundary
FIG. 3. STEM bright field image of the boundary used for EELS analysis
FIG. 4. Cu L_{23} edges showing white line at grain boundary

CALCULATIONS OF Cu $L_{2,3}$ FINE STRUCTURE AT GRAIN BOUNDARIES

P. Rez* and J.M. Maclaren**

*Department of Physics & Astronomy and CSSS, Arizona State University, Tempe, AZ 85287
** Department of Physics, Tulane University, New Orleans, LA 70118.

The segregation of impurities to grain boundaries in metals and alloys has been known for some time to make changes in ductility . Examples of this effect are the embrittlement of copper by the addition of bismuth and the ductilization of Ni_3Al by boron impurities. The mechanism by which these dramatic changes in mechanical properties arise is still largely unknown. It has been suggested that embrittling elements draw charge from neighbouring metal atoms while impurities that enhance ductilty act in the opposite way. Changes in the electronic states can be detected as changes in the energy loss spectrum when a small probe in a FEG STEM is moved across the boundary. Recent work by Muller[1] has shown significant differences between the Ni L_3 spectrum from grain boundaries in Ni_3Al with and without boron. Bruley[2] has shown that a "white line", indicative of empty Cu d states, appears in the Cu L_3 edge from Cu atoms near boundaries where bismuth has segregated.

The L_3 energy loss spectrum represents the d symmetry empty states at a given site. To interpret these spectral changes in terms of possible charge transfers it is important to have a theoretical model for calculating local projected densities of states (DOS) in systems with grain boundaries. Standard methods for DOS calculation can be used with supercells. The most appropriate method for transition metals and alloys is the LAPW (linearised augmented plane wave) or LMTO (linearised muffin-tin-orbital) method. As more than 30 atoms would be needed in a realistic calculation computer time would be a serious problem. The DOS would also be unreliable more than about 5ev above the threshold due to the linearisation procedure. We have chosen to use the layered KKR method[3] that is ideally suited to interface and boundary problems. The method owes its origins to theoretical work on LEED and as the perfect crystal regions on either side of the boundary are treated by appropriate reflection and transmission operators there is no need to introduce artificial supercells. Furthermore, it is readily applicable to the determination of symmetry resolved site selected (DOS).

Figure 1 shows the d DOS for copper which should correspond to the structure on the L_3 or L_2 edges. There is no sharp peak ("white-line") present on the edge, in agreement with experiment. The boundary structure from the atomistic calculations and HREM imaging of Yan et al[4] was used as an example of a boundary with Bi segregation. A schematic diagram is shown as Fig. 2. There are 3 planes of copper on either side of the boundary region. The copper plane immediately adjacent to the boundary has a vacancy which sits above the Bi. The calculated d DOS for each plane is given as Figure 3. A white line appears from the planes on either side of the Bi plane, in agreement with experiment. The calculations show a charge transfer of 0.5 electron from the Wigner-Seitz spheres around the copper atoms immediately adjacent to the Bi atoms at the boundary.

Future developments should make it possible to use the same code to calculate not only the effects on near edge structure, but also the boundary energy, making it possible to directly connect atomic and electronic structure with experiment and mechanical properties.

References

1. D.A.Muller, *Physical Review Letters,* 75 (1995) 4744.
2. J. Bruley et al, *J. Phys. D* (1996) in press, and these proceedings.
3. J.M. Maclaren et al, *Computer Physics Communications,* 60 (1990) 365.
4. M. Yan et al, *Physical Review B,* 47 (1993) 5571.
5. This work was supported by National Science Foundation grant DMR 930-6253.

1

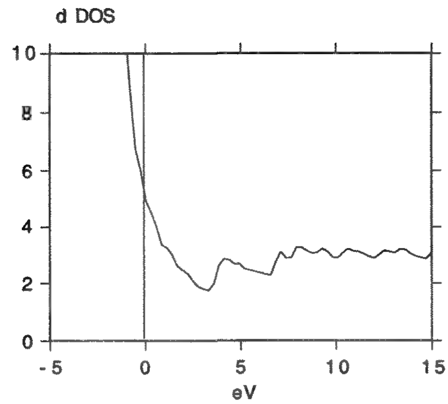

2

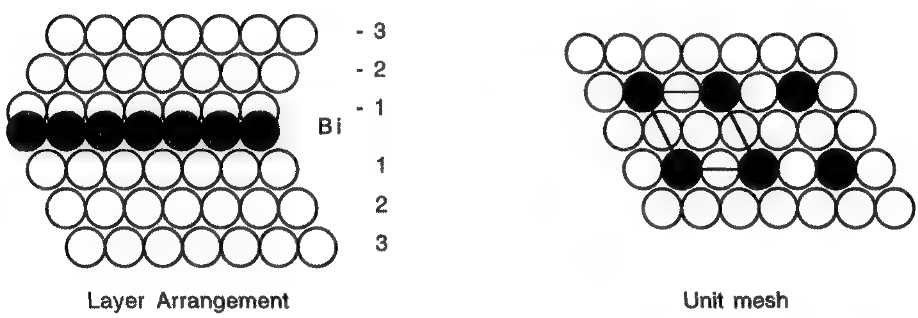

3

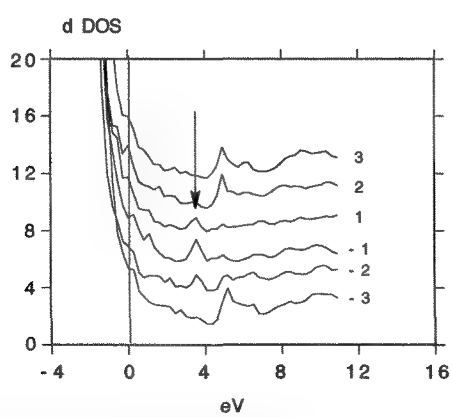

FIG. 1. d density of states representing L_{23} edge in pure copper

FIG. 2. Diagram showing boundary with Bi. There are vacancies in plane -1 above the Bi atoms.

FIG. 3. d densities of states reperesenting Cu L_{23} edge for Cu planes shown in Fig. 2. White line indicated by arrow.

ATOMIC-RESOLUTION EELS FOR COMPOSITION AND 3-D COORDINATION DETERMINATION AT INTERFACES AND DEFECTS

N. D. Browning*, D. J. Wallis*, S. Sivananthan*, P. D. Nellist** and S. J. Pennycook**

*Dept. Physics (M/C 273), U. Illinois-Chicago, 845 W. Taylor St., Chicago, IL 60607-7059. USA
**Solid State Division, Oak Ridge National Laboratory, P. O. Box 2008, Oak Ridge, TN 37831. USA

Materials properties associated with interfaces and defects are dominated by atomic scale fluctuations in composition, structure and bonding. Although electron energy loss spectroscopy (EELS) provides a powerful tool to probe these features, low signal, lens aberrations, image coherence and specimen drift preclude the use of spectrum imaging and energy filtered imaging for these high-resolution problems. However, by utilizing Z-contrast imaging in conjunction with EELS in the scanning transmission electron microscope (STEM)[1,2], these limitations are largely overcome and EELS appears capable of providing fundamental 3-D characterization of defect and interface structures with atomic resolution and sensitivity.

The main premise in utilizing these combined techniques is that the properties of defects and interfaces must be associated with structural differences relative to the bulk. If those structural differences can be located, then it is only necessary to perform spectroscopy in their vicinity to understand the structure-property relationship. For crystalline materials in zone-axis orientations, the Z-contrast image provides this atomic resolution structural map. As this direct image is generated with only the high-angle scattering, it can be used to position the electron probe with atomic precision and does not interfere with the low-angle scattering for spectroscopy. For core-losses (>100eV) the energy loss spectrum has the same atomic resolution and incoherent features as the Z-contrast image, allowing direct correlation of the spectrum with an individual structural feature.

Perhaps the simplest application of this methodology for atomic resolution EELS is in composition profiles of heterophase interfaces. For example, figure 1 shows a Z-contrast image of the interface between a CdTe (111)B film grown by MBE and a Si(100) substrate. This 300kV STEM image (1.3Å probe) clearly shows the polarity of the II-VI material and that the first layer of the film is composed of Te. However, the Z-contrast image cannot by itself give any information on the presence of impurities or any diffusion that occurs between the film and substrate during growth. Figure 2 shows energy loss spectra acquired in single plane steps across the interface. These spectra show that the Te edge at 572 eV extends into the silicon substrate whereas the Cd edge at 404 eV terminates abruptly at the interface. There is also an oxygen edge at 530eV that extends into the silicon substrate for several planes. These results are consistent with the substrate cleaning procedure (< 1/10 of a monolayer oxygen coverage) and establishment of an initial Te flux prior to CdTe deposition. Additionally, the intensity of the Te-edge at the interface gives strong evidence for the formation of a Si/Te compound on the substrate surface[3].

Another application of these techniques involves the detailed analysis of the spectral fine-structure in a characteristic core-edge. In this regard, multiple-scattering (MS) analysis provides an ideal formulation for the low-symmetry of interfaces and defects[4]. MS techniques consider the fine-structure of the spectrum to arise from interference effects occurring when a photoelectron created during the energy loss process is reflected from neighboring atoms. The real-space clusters used in this methodology allow the flexibility to determine whether the contributions to the spectrum arise from single or multiple scattering paths and from which atomic neighbors they originate. This allows the different structural relaxations that can possibly occur, i.e. vacancies or structural distortions, to be distinguished directly from the spectrum. In figure 3, a structural unit identified from asymmetric [001] tilt boundaries in $SrTiO_3$ reveals positions where the Ti-O columns are separated by distances much reduced from the bulk[5]. The incoherence of the Z-contrast image means that these are real features. Using MS theory , the effects of varied occupancy in the boundary can be modelled (figure 4), with the only realistic fit to the experimental data being observed with half-occupied columns. This application of EELS analysis therefore allows us to determine the coordination of boundary atoms in 3-dimensions (figure 5)[6].

References

1. N. D. Browning et al, *Nature* 366 (1993) 146
2. P. E. Batson, *Nature* 366 (1993) 727
3. D. J. Wallis, N. D. Browning, S. Sivananthan, P. D. Nellist and S. J. Pennycook, in preparation
4. D. J. Wallis and N. D. Browning, submitted *Phys. Rev. Letts*
5. N. D. Browning and S. J. Pennycook, in press *J. Phys. D*

6. Research sponsored by NSF under grant no. DMR-9503877 and by DOE-DMS, under contract DE-AC05-84OR21400 with Martin Marietta Energy systems Inc, and by the ORNL Postdoctoral Research Program administered by ORISE.

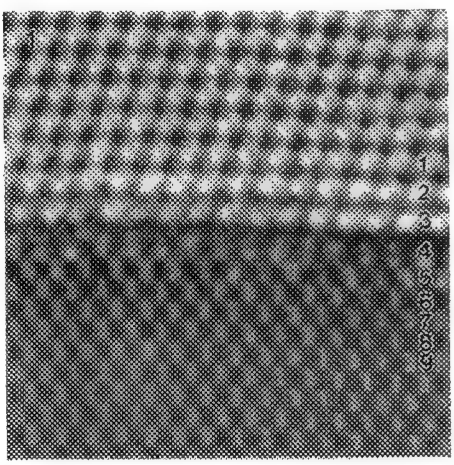

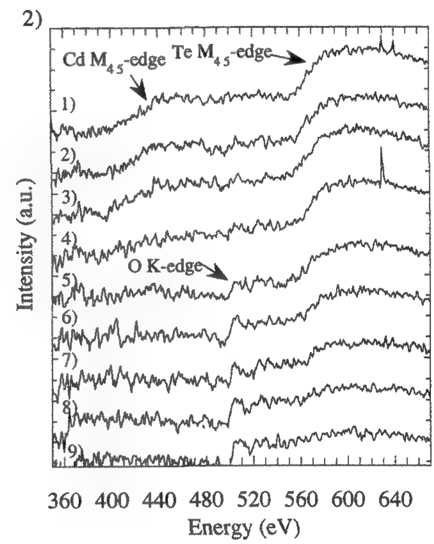

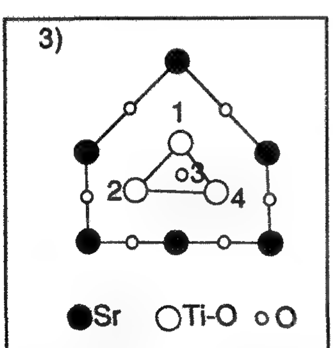

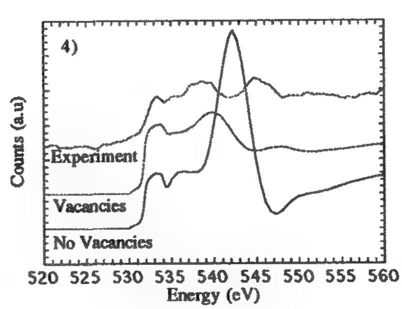

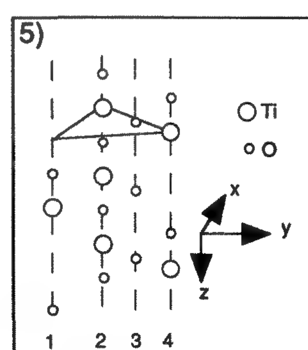

Figure 1: 300kV (1.3Å probe size) Z-contrast image of a CdTe (111)B-Si (110) interface.
Figure 2: Plane-by plane compositional profile of the interface at 100kV (2.2Å probe size).
Figure 3: An asymmetric [001] tilt boundary structural unit for $SrTiO_3$
Figure 4: Multiple scattering calculations for full and half-occupied Ti-O columns
Figure 5: 3-D atomic structure for the Ti-O half-columns

SPECTRUM LINES ACROSS PLANAR INTERFACES BY ENERGY-FILTERED TEM

J. Bentley and Ian M. Anderson

Metals & Ceramics Division, Oak Ridge National Laboratory, PO Box 2008, Oak Ridge, TN 37831-6376

Electron energy-loss spectrum imaging, in which a spectrum is recorded for each pixel as a focused probe is digitally rastered in a two-dimensional pattern on the specimen, has developed into a practical and powerful microanalytical technique.[1] However, even for only a modest number of pixels, acquisition times can become inconveniently long. One-dimensional data (spectrum lines) are often sufficient for many materials science applications, especially for planar interfaces. As well as producing energy-filtered TEM images (or diffraction patterns), the Gatan imaging filter (GIF™) can be used to acquire spectrum lines in the TEM mode, without the need to form a small probe. The basis for this capability is that for the GIF spectroscopy mode a line focus normal to the energy dispersion direction is employed. Spectra as a function of position (TEM operating in the image mode) or scattering angle[2] (TEM operating in diffraction mode) are thus produced. Whereas the effects are present with the usual circular GIF entrance aperture, the use of a slit[2] oriented normal to the energy dispersion direction produces data that can be more readily interpreted. In the image mode, spatial resolution and spectral energy range are coupled through chromatic aberration. Just as the use of TEM image mode is unsuitable for high spatial resolution EELS over an extended energy-loss range,[3] so TEM spectrum imaging may at times be similarly inappropriate. However, the technique appears to be particularly useful for plasmon spectrometry and for studies of energy-loss fine structure with high spatial resolution.

Results from an oxidized CoO-ZrO_2 directionally solidified eutectic that was previously characterized by TEM and electron energy-loss spectrometry[4] illustrate the technique. A near-edge-on CoO-Co_3O_4 interface was oriented normal to the area-selecting slit (a 2 × 0.5 mm slotted washer mounted in the entrance aperture holder of the GIF) with the use of a specimen rotation holder (Fig. 1a). A spectrum line for the low-loss region (Fig. 1b) was recorded with defocused illumination and an exposure time of 0.1 s; spectrum lines for the oxygen K (Fig. 1c) and cobalt L (Fig. 1d) edge regions were recorded with nearly focused illumination and an exposure time of 8 s. Fig. 1b-d and the intensity profiles (energy-loss spectra) of Fig. 2 confirm the differences in spectral information for the two phases (plasmon shapes and shifts; the dramatic differences in oxygen K fine structure; and cobalt L white line shifts, widths, and intensities) described and discussed elsewhere.[4] Subsets (10 spectra symmetrically spanning the interface with 4-nm spacing) of the cobalt L and oxygen K spectrum lines were also analyzed by multivariate statistical analysis (MSA) following the procedure described by Trebbia and Bonnet;[5] some MSA results are shown in Fig. 3. Component E0 is essentially the average spectrum of the sampled region (Fig. 3a,d) and E1 is the principle component of the variation (Fig. 3b,e). The features of E1 indicate the differences in the intensity distributions between Co_3O_4 and CoO, such as the relative prominence of features and peak shifts. All spectra were found to be accurately approximated by linear combinations of E0 and E1. In particular, the analysis yielded no significant component localized at the interface. The relative contributions of E1 in the series of spectra are shown in (Fig. 3c,f) and reflect a smooth transition in the spectral features from one phase to the other. However, the ~12-nm width of the transition is much larger than the sharpness of the interface in Fig. 1a or that estimated visually from Figs. 1c and 1d.[6]

1 M. Tencé, M. Quartuccio, and C. Colliex, *Ultramicroscopy* **58** (1995) 42.
2 K. E. Bagnall et al., *Proc. EMAG95 (Inst. Phys. Conf. Ser. 147)*, ed. D. Cherns (Bristol: IOP, 1995) 183.
3 A. J. Craven, *Proc. EMAG95 (Inst. Phys. Conf. Ser. 147)*, ed. D. Cherns (Bristol: IOP, 1995) 267.
4 J. Bentley et al. *Microbeam Analysis* **2** (1993) S286.
5 P. Trebbia and N. Bonnet, *Ultramicroscopy* **34** (1990) 165.
6 Research at the Oak Ridge National Laboratory (ORNL) SHaRE User Facility sponsored by the Division of Materials Sciences, U.S. Department of Energy, under contract DE-AC05-96OR22464 with Lockheed Martin Energy Research Corp., and by an appointment (IMA) to the ORNL Postdoctoral Research Associates Program, which is administered jointly by the Oak Ridge Institute for Science and Education and ORNL. Thanks to Drs. C. B. Carter and S. McKernan (University of Minnesota) for the CoO-ZrO_2 specimen.

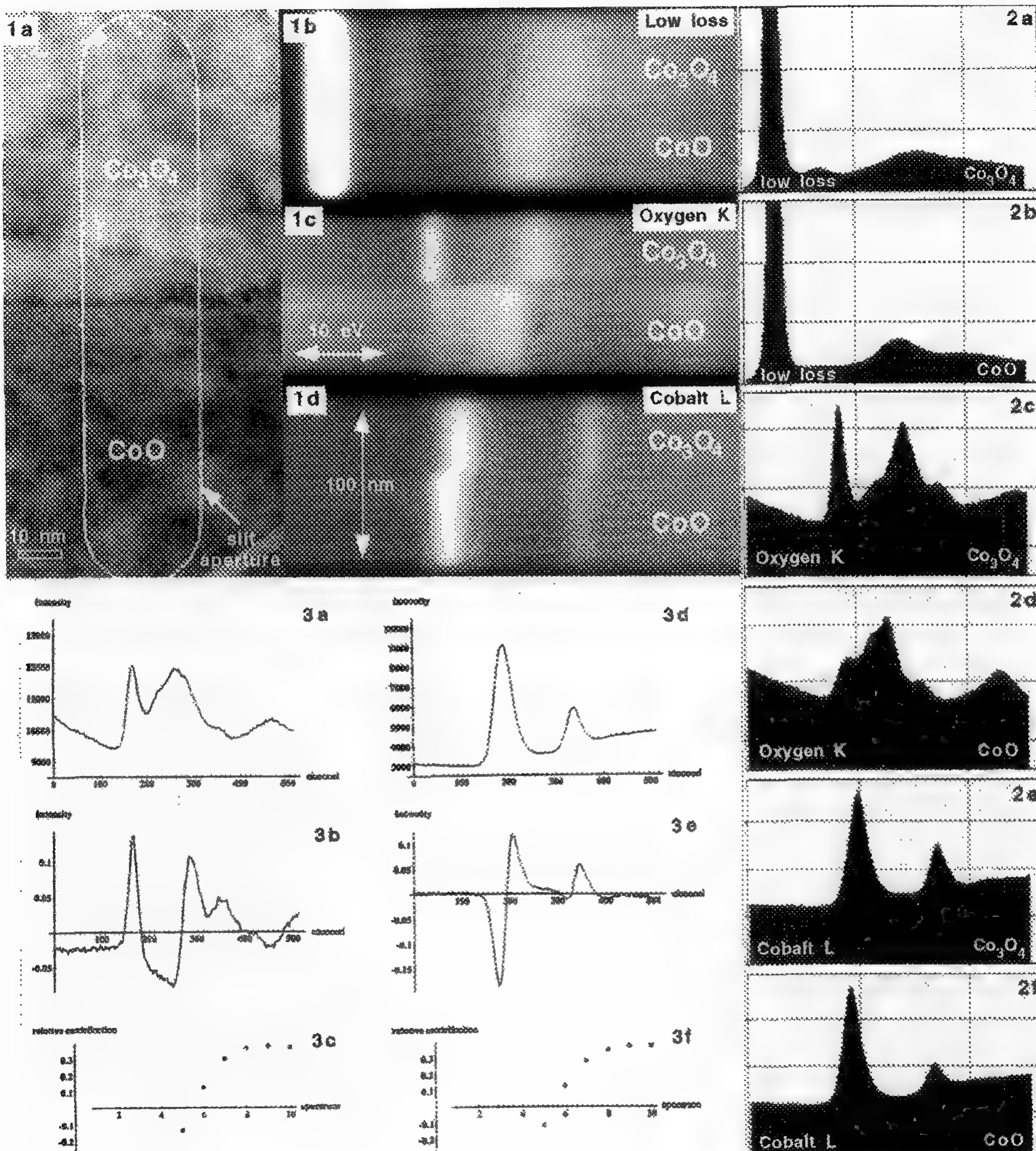

FIG. 1 - (a) Zero-loss bright-field image of near-edge-on CoO-Co_3O_4 interface showing position of area-selecting slit. (b-d) Spectrum lines for (b) low-loss region, (c) oxygen K edge, and (d) cobalt L edge.

FIG. 2 - Intensity profiles (energy-loss spectra) of Fig. 1b,c,d as indicated. Energy range = 50 eV.

FIG. 3 - Multivariate statistical analysis of 10 spectra symmetrically spanning the interface with 4-nm spacing for (a-c) oxygen K and (d-f) cobalt L edge regions. (a,d) E0, essentially the average spectrum; (b,d) E1, the principal component of the variation; (c,f) relative contribution of E1 in each spectrum.

THE EXAMINATION OF YTTRIUM ION-IMPLANTED ALUMINA WITH ENERGY-FILTERED TRANSMISSION ELECTRON MICROSCOPY

E. M. Hunt *, J. M. Hampikian *, N. D. Evans **

*School of Materials Science and Engineering, Georgia Institute of Technology, Atlanta, GA 30332-0245
**Oak Ridge Institute for Science and Education, P.O. Box 117, Oak Ridge, TN 37831-0117

Ion implantation can be used to induce complex alterations in the optical response of insulators through the formation of embedded nano-sized particles. Single crystal alumina has been implanted at ambient temperature with 170 keV Y^+ to a fluence of 5×10^{16} ions/cm^2. Ion channeling, Knoop microhardness measurements, and transmission electron microscopy (TEM) indicate that the alumina surface layer was amorphized by the implant[1]. TEM also revealed weakly diffracting nano-sized crystals ≈12 - 13 nm in diameter as seen in Figure 1. These nanocrystals are randomly oriented, and exhibit a face-centered cubic structure (FCC) with a lattice parameter of 0.41 nm ± 0.003 nm. Energy dispersive spectrometry (EDS) shows that these nanocrystals are rich in aluminum and yttrium and poor in oxygen relative to the surrounding amorphous matrix[1]. The similarity between this crystallography and that of pure aluminum (which is FCC with a lattice parameter of 0.40 nm), coupled with the qualitative nanocrystal composition indicated by EDS, suggests that they are metallic aluminum nanocrystals with a slightly dilated lattice parameter, possibly due to the incorporation of a small amount of yttrium. Energy-filtered transmission electron microscopy (EFTEM) provides an avenue by which to confirm the metallic nature of the aluminum involved in the nanocrystals.

Experiments were performed with a Gatan Imaging Filter (GIF™) interfaced to a Philips CM30 TEM operated at 300 keV. The gain normalized images were 512 x 512 pixels in size, and were recorded with an exposure time of 1 second and an energy window of 5-eV. The component in 15eV loss images due to alumina valence exitation was estimated from adjacent loss images and subtracted[2].

Two single scattering energy-loss distributions from an implanted sample are shown in Figure 2. The spectrum from an area containing particles (a) shows the large volume plasmon feature due to alumina at ~25 eV and a shoulder at ~15 eV resulting from the volume plasmon loss due to metallic aluminum. The spectrum from an area of pure alumina (b) shows only the broad feature at ~ 25 eV. The yttria valence-loss spectrum[3] (c) exhibits a feature at ~15 eV, raising the possibility of the presence of yttria in the implanted region. However, the yttria valence-loss spectrum also contains a strong feature at ~40 eV. This 40-eV-loss feature is not evident in either Figure 2(a) or (b). A zero-loss image of an implanted area is shown in Figure 3a. A 15-eV-loss image, seen in Figure 3b, indicates that the crystals contain metallic aluminum. In a 25-eV-loss image from the same region (Figure 3c), the same features are slightly darker than the surrounding matrix. This image confirms that the particles are not alumina. Figure 4 shows the oxygen "jump-ratio" image (post-edge divided by pre-edge) from an area similar to the one in Figure 3. This image supports the original EDS finding that the particles are oxygen deficient with respect to the matrix material.

EFTEM has confirmed that the particles are not yttria, that the aluminum present in the particles is metallic in nature, and that the particles are oxygen deficient in comparison with the matrix material. The particles thus appear to be a metastable FCC Al -Y alloy with a lattice parameter of 0.41nm. This is an unexpected finding in that the mechanism for metallic aluminum formation must involve the reduction of Al_2O_3, which is a stable oxide, and the Al-Y phase diagram predicts negligible Y solubility in aluminum.

1. E.M. Hunt, et. al., Mat. Res. Soc. Symp. Proc., **396**, p. 403-410 (1995)
2. N.Evans, et. al., Proc. Microscopy and Microanalysis 1995, p. 266-7
3. C.C. Ahn, O.L. Krivanek, "EELS Atlas", (Gatan Inc., Warrendale, PA and Center for Solid State Science, Arizona State Univ., Tempe, AZ , 1983).
4. Research sponsored in part by the Division of Materials Sciences, U.S. Dept. of Energy, under contract DE-AC05-96OR22464 with Lockheed Martin Energy Research Corp., through the SHaRE Program under the contract DE-AC05-76OR00033 with Oak Ridge Associated Universities, and by the Office of Naval Research through the Molecular Design Institute at Georgia Institute of Technology .

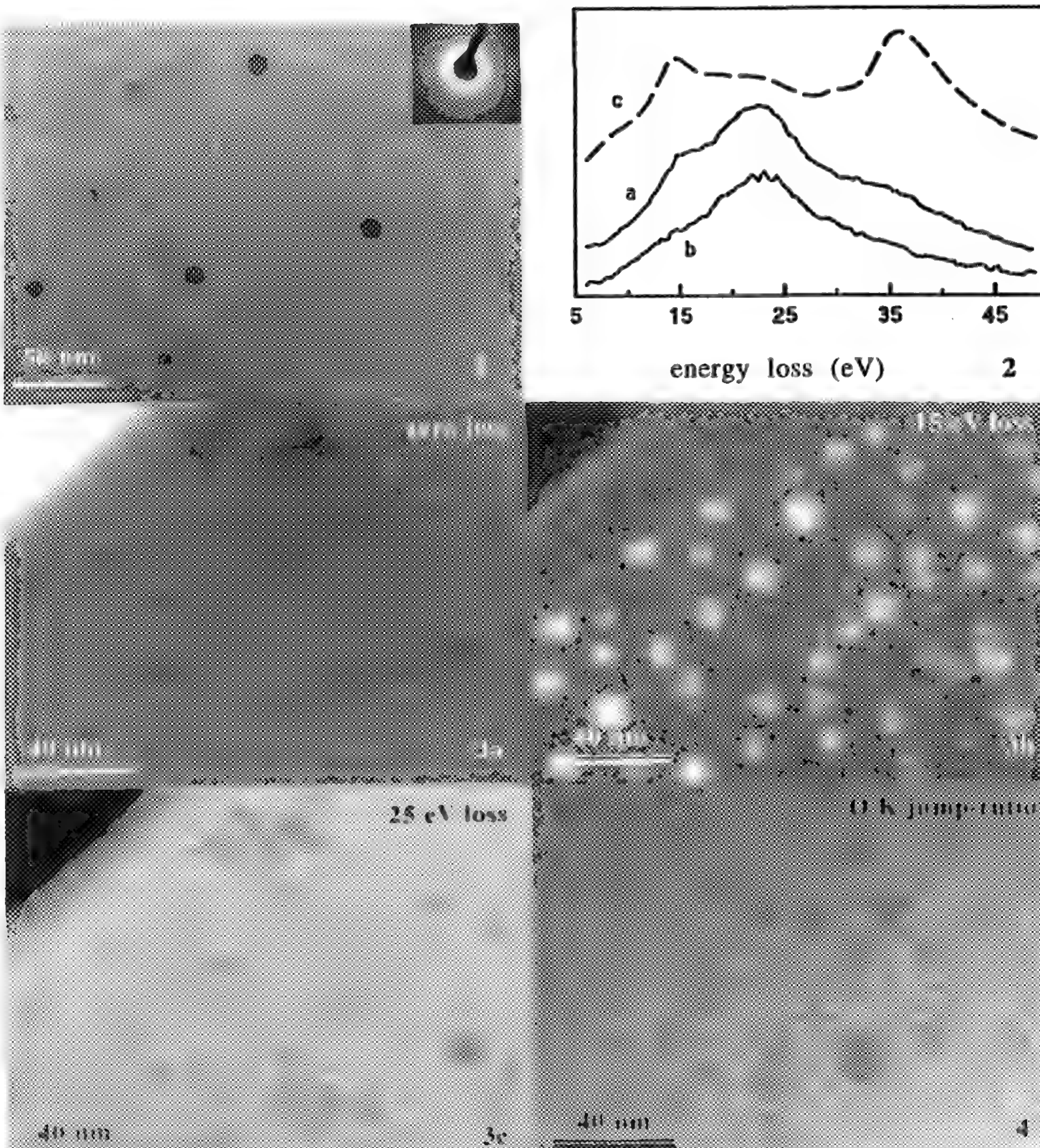

Figure 1: Bright field TEM image of particles and the associated diffraction pattern.
Figure 2: Energy loss spectra from a) a particle bearing region , b) a region of plain matrix and c) the standard energy loss spectrum from yttria.[3]
Figure 3: a) Zero-loss image of a particle-bearing region, b)15-eV-loss image of a particle-bearing region, c) 25-eV-loss image of a particle-bearing region.
Figure 4: Oxygen K jump-ratio image of a similar particle-bearing region

EXELFS STUDY OF THE STRUCTURE OF SILICA AND SODIUM SILICATE GLASSES

Dennis C. Winkler, David B. Williams and Himanshu Jain

Department of Materials Science & Engineering, Lehigh University, Bethlehem, PA 18015

The conventional extended X-ray absorption fine structure (EXAFS) method is not ideal for determining local structure around light elements in a solid.[1] Although the "electron yield" EXAFS technique can be used to increase sensitivity to lighter elements, it is mainly a surface technique.[1,2] We have employed the extended energy-loss fine structure (EXELFS) technique for determining the local structure (partial radial distribution function, inter atomic distance, and disorder parameter) in oxide glasses, specifically around Si and O in silica and sodium silicate glasses. Because a scanning transmission electron microscope is used, EXELFS also allows high spatial resolution which is particularly useful for a glass prone to phase separation.

EXELFS results from the same phenomenon responsible for EXAFS, namely the interference of the outgoing spherical wave of the ejected electron with portions of itself which have been backscattered from the neighboring atoms in the solid. This produces oscillations in intensity beyond the absorption edge.[3,4] These variations in intensity are transformed to radial distribution functions in the same fashion as EXAFS data.[3,4] EXELFS, like EXAFS, provides local atomic environment information that is element specific. This avoids difficulties sometimes found in diffraction methods where structural information involving elements that do not contribute greatly to the total diffraction intensity can be lost. EXELFS also provides higher spatial resolution and better sensitivity for low Z elements than EXAFS. The increased sensitivity to lighter elements is particularly useful for acquiring radial distribution information around oxygen, a major component of the oxide glasses.

The energy-loss data were recorded using a Vacuum Generators HB501 STEM and Gatan Model 666 PEELS. As in other EXELFS studies, the results are dependent on the choice of analysis parameters, such as the degree of the fitting polynomial, ionization potential, and the energy range over which the data are extracted.[5] Parameters for extraction of the radial distribution function from the extended fine structure were chosen to give good agreement with quartz crystal data in the literature. Figure 1 shows the electron energy-loss spectrum of the oxygen K-edge from silica glass. The spectrum has been corrected for channel to channel gain variations by gain averaging and the background has been subtracted. The EXELFS oscillations were isolated by fitting the post-edge region with a smooth polynomial function and subtracting the fit. An energy window above the edge was selected to exclude near-edge structure at the low energy cut off and to avoid domination by noise at the high energy cut off . The resulting data are normalized, transformed from an energy scale to the wavevector (k) scale of the outgoing electron and multiplied by a factor of k^3 (Figure 2). The magnitude of a fast Fourier transform of the data shown in Figure 2 yields the radial distribution function (Figure 3).

In a similar fashion, radial distribution functions were obtained from the oxygen and silicon K-edges for a series of sodium silicate glasses. The results are compared with the information available from

literature and analyzed to verify the so called modified random network model.[2,6] This work will be extended to include the EXELFS study of potassium germanate glasses and the implication of the data for the modified random network model will again be examined.

References

1. J. Stohr, J. Vac. Sci. Technol. 16 (1979) 37.
2. G. S. Henderson, J. Non-Crystalline Solids 183 (1995) 43.
3. R. F. Egerton, *Electron Energy-Loss Spectroscopy in the Electron Microscope*, Plenum Press, New York (1989) 224.
4. P. A. Lee, *EXAFS Spectroscopy Techniques and Applications*, Teo and Joy, Plenum Press, New York (1981) 5.
5. R. D. Leapman, Microbeam Analysis, Heinrich, San Francisco Press, San Francisco (1982) 111.
6. G. N. Greaves, J. Non-Crystalline Solids 71 (1985) 203.

7. This work is supported by the US Department of Energy (Grant No. DE-FG02-95ER45540).

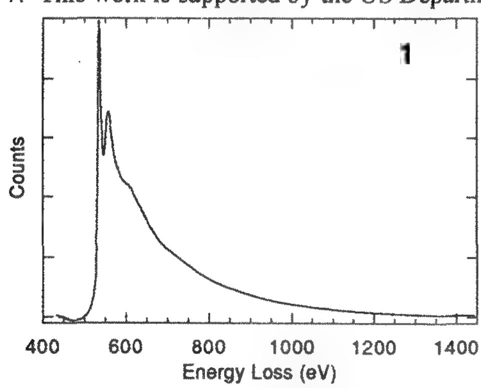

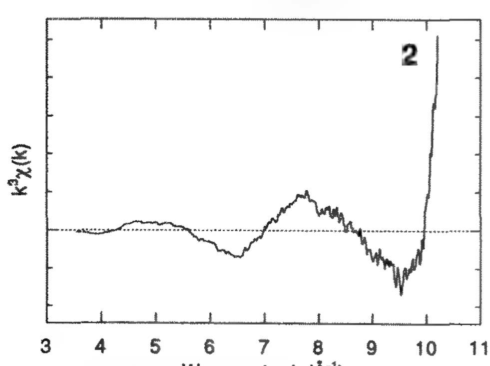

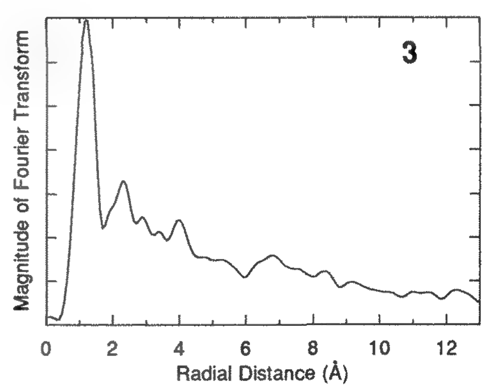

FIG. 1 - Electron energy-loss spectrum of the oxygen K-edge from silica glass.
FIG. 2 - Isolated EXELFS oscillations, $\chi(k)$, multiplied by a factor of k^3.
FIG. 3 - Radial distribution function around oxygen obtained from the fast Fourier transform of the data in Figure 2.

CHEMICAL EFFECTS OF LANTHANIDES AND ACTINIDES IN GLASSES DETERMINED WITH ELECTRON ENERGY LOSS SPECTROSCOPY

Jeffrey A. Fortner, Edgar C. Buck, Adam J. G. Ellison, and John K. Bates

Chemical Technology Division, Argonne National Laboratory, Argonne, IL 60439, USA

The chemical and structural environments of *f*-electron elements in glasses are the origin of many of the important optical, electronic, and magnetic properties of materials incorporating these elements. Thus, the oxidation state and chemical coordination of lanthanides and actinides in host materials is an important design consideration in optically active glasses, magnetic materials, perovskite superconductors, and nuclear waste materials.

The energy loss spectra of the lanthanides are characterized by sharp $3d_{3/2} \rightarrow 4f_{5/2}$ (M_4) and $3d_{5/2} \rightarrow 4f7_{/2}$ (M_5) lines, the relative intensities of which are determined by the 4*f*-shell occupancy of the excited ion. For the light lanthanides, the dependence of these relative peak heights on 4*f*-shell occupancy is quite pronounced. In particular, the ratio of the M_4 to M_5 peak areas in the second derivative spectra is extremely sensitive to the formal valence of the multivalent elements Ce and Pr. In figure 1, the EELS spectra are presented for Ce(III) and Ce(IV) in well-characterized reference materials. The ratio of the M_4/M_5 lines calculated by various methods is plotted against *f*-shell occupancy in figure 2. The present second derivative data are plotted along with those of Manoubi *et al.* [1], who fit their experimental peaks from lanthanide oxides with Lorentzian functions, and also the theoretical multiplet calculations of Thole *et al.* [2] ($A_{3/2}$ and $A_{5/2}$ used instead of M_4 and M_5, respectively). The systematic divergence of the second derivative data from the Lorentzian fits and theoretical peak areas occurs because the M_4 line is broader than the M_5 line, which reduces its relative intensity in the second derivative accordingly.

We have made use of the characteristic line shapes of cerium to determine its oxidation state in alkali borosilicate glasses that are being developed for immobilization of plutonium. Cerium, it should be noted, is often used as a "surrogate" element for plutonium in materials design because of its similar ionic size (for Pu in the +3 and +4 states) and preferred chemical coordination. The solubility of the plutonium (or cerium) in a waste glass will likely be determined by its redox state in the glass. By examining several prototype glass compositions with EELS (figure 3), it was found that the redox state of cerium doped to 7 wt % could be varied by suitable choice of alkali elements in the glass formula.

By analogy with the lanthanides, the intensity ratio of the $N_4$and N_5 lines in actinide elements, which correspond to $4d_{3/2} \rightarrow 5f_{5/2}$ and $4d_{5/2} \rightarrow 5f_{7/2}$ transitions, respectively, might be expected to decrease as occupancy of the 5*f* orbitals increases. For example, by this argument, the uranyl ion should display a N_4/N_5 ratio close to 1.0; instead, the ratio is smaller. In actinides, the relativistic contraction leads to strong hybridization of 5*f* orbits with the 6*d* and 7*s* orbitals. This relativistic contraction is around 2% for the lanthanides but at least 30% for the actinides. Excitation will occur to these 6*d* and 7*s* levels and will complicate the edge shape. Thus, we cannot assume that the same correlation of N_4/N_5 intensity ratios with *f*-orbital occupancy that is seen for the lanthanides will be observed in the actinides. Instead, it is probable that crystal field effects will determine the spectral shape for the actinides. In glasses, however, the flexible local structure may lead to coupling between the oxidation state and crystal field effects, allowing a straightforward interpretation. Preliminary EELS results on a plutonium-doped glass appear in figure 4, illustrating the small actinide N_4/N_5 ratio. This figure also shows that the Pu-$N_{4,5}$ white line cross section is comparable to that of gadolinium $M_{4,5}$ [3].

REFERENCES

1. T. Manoubi, C. Colliex, and P. Rez, *J. Elect. Spec. and Related Phen.* **50**, 1 (1990).

2. B. T. Thole, G. van der Laan, J. C. Fuggle, G. A. Sawatzky, R. C. Karnatak, and J.-M. Esteva, *Phys. Rev. B* **32** (8), 5107 (1985).

3. This work supported by the U. S. Department of Energy, under contract W-31-109-ENG-38.

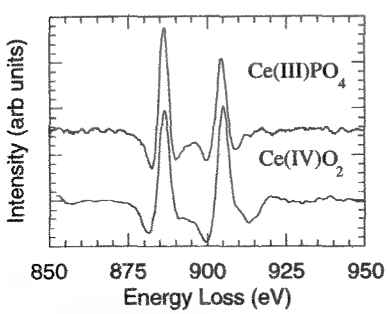

Figure 1. Second derivative EELS spectra of cerium (IV) oxide and cerium(III) orthophosphate. Note the dramatic change in the ratio of the M_4 (903 eV) to M_5 (886 eV) lines.

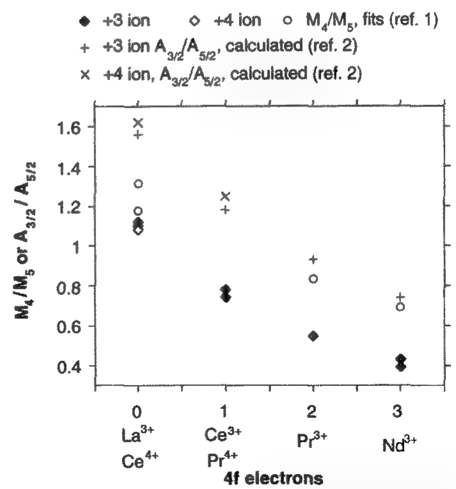

Figure 2. Dependence of the M_4/M_5 spin-orbit group ratio on the occupancy of the $4f$ level for the light lanthanides.

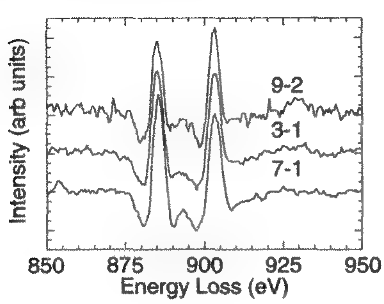

Figure 3. Second derivative EELS spectra of cerium $M_{4,5}$ edges in prototype glasses designed for plutonium disposition. The formal valence of the cerium varies from 3.4 ("7-1") to 4 ("9-2") as a function of the relative proportions of K and Li in the glasses.

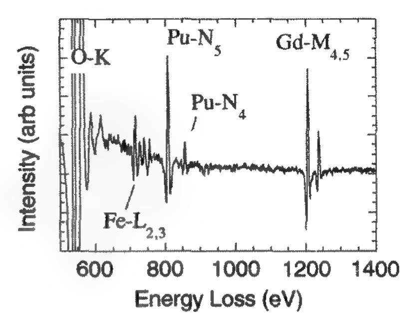

Figure 4. Plutonium N-edges in a glass doped to 7 wt % Pu. Gadolinium is a neutron poison present in a 1:1 ratio with the plutonium, providing a relative measure of the plutonium N-edge cross sections.

DETERMINATION OF LOCAL DIELECTRIC FUNCTION IN DONOR-DOPED BARIUM TITANATE

Kalpana S. Katti, Maoxu Qian and Mehmet Sarikaya, Department of Materials Science and Engineering, University of Washington, Box 352120, WA 98195, USA

Barium titanate ($BaTiO_3$) is one of the basic materials for electroceramic components and is also used for electrooptic applications. When certain donor dopants such as Nb are introduced, it exhibits the property of positive temperature coefficient of resistance (PTCR) wherein there is a jump in resistance of several orders of magnitude at the transition temperature (~120°C).[1] Although considerable work has been done to understand the influence of dopants on bulk samples, it is not clearly known what the detailed distribution of the dopant is and how it affects local properties.

This paper addresses the problem of how the addition of Nb affects local properties of $BaTiO_3$. This is done by using electron energy loss (EEL) spectroscopy which probes the local electronic structure. We use the Kramers-Kronig (KK) analysis to compute the local dielectric function from the low loss electron energy loss data. In this analysis, the interaction of the transmitted electrons with the material is expressed in terms of a dielectric response function which is the imaginary part of $[-1/\varepsilon(q,E)]$ where ε is the dielectric function of the material ($\varepsilon=\varepsilon_1+i\varepsilon_2$) and q and E are the momentum and energy transfer, respectively, in one interaction. The single scattering electron distribution function is proportional to the dielectric response function. The dielectric function can be obtained from KK analysis by determining Re $[1/\varepsilon(E)]$.[2] The dielectric functions $\varepsilon_1(E)$ and $\varepsilon_2(E)$ are calculated from Im $[-1/\varepsilon(E)]$ and Re$\{1/\varepsilon(E)\}$ by:

$$\varepsilon_1(E) = \frac{[Re(1/\varepsilon(E))]}{[Re(1/\varepsilon(E))]^2 + [Im(-1/\varepsilon(E))]^2} \quad \text{and} \quad \varepsilon_2(E) = \frac{[Im(-1/\varepsilon(E))]}{[Re(1/\varepsilon(E))]^2 + [Im(-1/\varepsilon(E))]^2}$$

We modified the KK analysis program by Egerton[3] which accommodated the large signal from the PEELS detector.[4]

Four samples of $BaTi_{1-x}Nb_xO_3$ with x=0.0 to 1.8% are used for this work. Low loss EEL spectra were obtained from within isolated grains (excluding grain boundaries) of the ion beam thinned samples using a GATAN PEELS detector attached to an analytical TEM operated at 200kV. The computed dielectric response functions are shown in Fig 1. The features marked by letters A to E correspond to interband transition (A), single electron core excitation (C, E1 and E) and collective excitations (B and D) where the most prominent feature D corresponds to the volume plasmon. There is a marked shift in the volume plasmon with the dopant concentration which agrees with expected higher valence electron density in doped material. However, the amount of shift, about 0.4eV, is two orders of magnitude higher than the that would be expected from simple free electron model of incorporation of extra electrons from Nb into the $BaTiO_3$ lattice. Fig 2 shows the computed imaginary part of dielectric function from the above data showing marked features in the ε_2 spectrum (A to D) arising from interband transition (A) and core excitations (B,C and D). The ε_2 spectrum is characteristic of the electronic structure of the material and thus a change in ε_2 with dopant is indicative of the influence of the dopant.

In summary, the incorporation of Nb in the $BaTiO_3$ lattice and its influence on local properties was investigated by evaluating the local dielectric function in isolated grains of the material. We found that the addition of dopant influences the electronic structure of the material which is assessed from the shifts in features in the ε_2 spectra. A shift in the plasmon energy to higher energy is observed with increased dopant concentration which is indicative of a large change in valence electron density. The amount of this shift can be explained by regarding the delocalized 'd' electrons from Nb as free electrons contributing to the plasmon. The detailed characterization of donor doped $BaTiO_3$ via the determination of its local dielectric function is an important step towards more rational design of this material for electrooptic applications.

1. A. Amin, *J. Am. Ceram. Soc.*, **72** [3] 369 (1989).
2. J. Daniels, et.al. , *in Springer Tracts in Modern Physics*, (Springer-Verlag, Berlin, 1970)pp 77-135.
3. R. F. Egerton, *Electron Energy Loss Spectroscopy in the Electron Microscope* (Plenum, New York, 1986).
4. K.S. Katti, M. Qian and M. Sarikaya, *to be published in Proc. MRS* (Materials Research Society, Pittsburgh, PA, 1996)

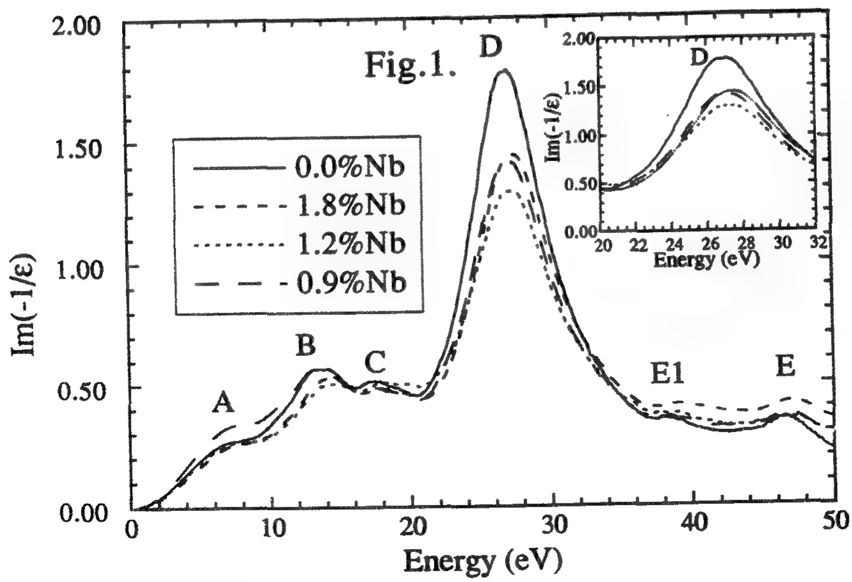

FIG. 1 The dielectric response function of $BaTi_{1-x}Nb_xO_3$ with x= 0.0 to 1.8%. The inset shows the volume plasmon peak D enlarged.

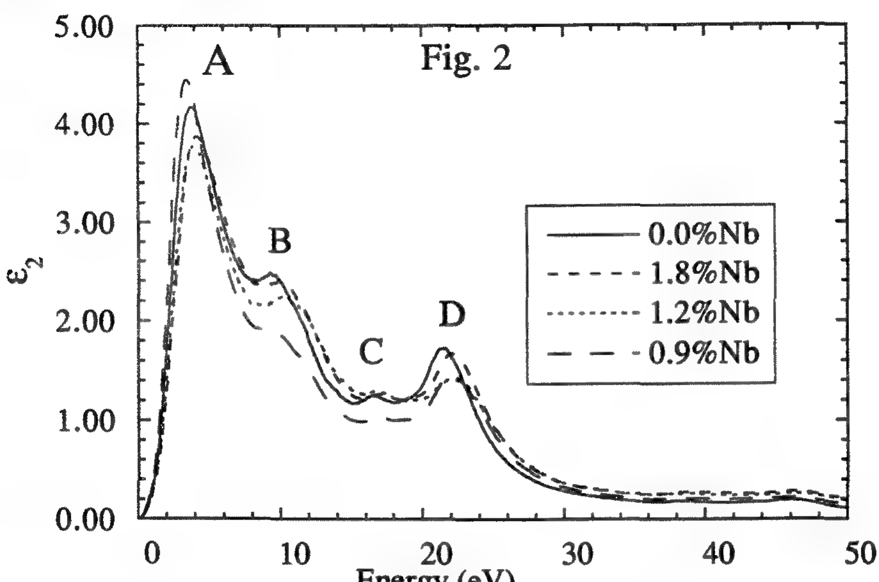

FIG.2 The imaginary part of the dielectric function computed for $BaTi_{1-x}Nb_xO_3$ from the response functions in figure 1.

QUANTITATIVE ENERGY-FILTERED TEM IMAGING OF INTERFACES

J. Bentley, E. A. Kenik, K. Siangchaew,* and M. Libera*

Metals & Ceramics Division, Oak Ridge National Laboratory, PO Box 2008, Oak Ridge, TN 37831-6376
*Department of Materials Science and Engineering, Stevens Institute of Technology, Hoboken, NJ 07030

Quantitative elemental mapping by inner shell core-loss energy-filtered transmission electron microscopy (TEM) with a Gatan Imaging Filter (GIF) interfaced to a Philips CM30 TEM operated with a LaB_6 filament at 300 kV has been applied to interfaces in a range of materials. Typically, 15s exposures, slit width Δ = 30 eV, TEM magnifications ~2000 to 5000×, and probe currents ≥200 nA, were used. Net core-loss maps were produced by AE^{-r} background extrapolation from two pre-edge windows. Zero-loss I_0 ($\Delta \approx 5$ eV) and "total" intensity I_T (unfiltered, no slit) images were used to produce maps of $t/\lambda = \ln(I_T / I_0)$, where λ is the total inelastic mean free path. Core-loss images were corrected for diffraction contrast by normalization with low-loss images recorded with the same slit width, and for changes in thickness by normalization with t/λ maps.[1-2] Such corrected images have intensities proportional to the concentration in atoms per unit volume. Jump-ratio images (post-edge divided by pre-edge) were also produced. Spectrum lines across planar interfaces were recorded with TEM illumination by operating the GIF in the spectroscopy mode with an area-selecting slit oriented normal to the energy-dispersion direction. Planar interfaces were oriented normal to the area-selecting slit with a specimen rotation holder.[3]

In sensitized type 304L stainless steel aged 15 h at 600°C, grain-boundary Cr depletion occurs between Cr-rich intergranular $M_{23}C_6$ particles.[2] Images of net Cr L_{23} intensity show segregation profiles that agree quantitatively with focused-probe spectrum-line measurements recorded with a Gatan PEELS on a Philips EM400T/FEG (0.8 nA in 2-nm-diam probe) of the same regions. Figure 1a shows such a Cr distribution map in which the Cr-rich precipitates and grain boundary depletion are clearly displayed. The grain boundary segregation profile for Cr (Fig. 1b) has a full-width half maximum (FWHM) of ~15 nm. The Cr depletion layer in the matrix adjacent to edge-on carbide interfaces (Fig. 1c) is much smaller (~4 nm FWHM). Figure 2 shows TEM spectrum lines recorded from the same grain boundary regions as in Fig. 1 but at a slightly different specimen tilt (because of the use of a specimen rotation holder). The effects of thickness (grain boundary grooving) and composition differences are readily apparent. The profiles in Fig. 2c,d show the Cr L_3 edge intensity above background (extracted from first difference spectrum lines), for comparison with the profiles in Fig. 1b,c. The spatial displacement due to chromatic aberration is ~5 nm for the Fe L edge. Although, in this case, this shift is smaller than the projected slit width of >20 nm, more generally, such aberrations may severely limit the usefulness of the technique for large ranges of energy-loss. Studies of energy-loss fine structure may be the best use for TEM spectrum lines.[3]

Rare-earth oxide additives that are used for the liquid-phase sintering of Si_3N_4 generate second phases of complex composition at grain boundaries and edges. These grain boundary phases often control corrosion, crack growth and creep damage behavior. High resolution imaging has been widely and effectively used to detect amorphous grain boundary layers that are often only ~1 nm thick. Analyses with focused probes can be compromised by beam damage, but elemental mapping by EFTEM appears not to cause appreciable beam damage. Figure 3 shows an example of Si_3N_4 sintered with a mixture of Sr, Y, and La oxides. The intergranular phase is clearly depleted in N, and although the noise levels in the O and La elemental maps are high, they show that the intergranular films and grain-edge pockets have similar compositions. The correct alignment of the component pre- and post-edge images is critical in avoiding artifacts in such elemental maps of planar features only a few pixels wide.[4]

1 J. Bentley, E.L. Hall and E.A. Kenik, *Proc. 53rd MSA Meeting,* (1995) 268.
2 J. Bentley et al., *Proc. EMAG95 (Inst. Phys. Conf. Ser. 147),* ed. D. Cherns (Bristol: IOP, 1995) 187.
3 J. Bentley and I.M. Anderson, *these proceedings.*
4 Research at the ORNL SHaRE User Facility sponsored by the Division of Materials Sciences, U.S. Department of Energy, under contract DE-AC05-96OR22464 with Lockheed Martin Energy Research Corp., and through the SHaRE Program under contract DE-AC05-76OR00033 with Oak Ridge Associated Universities.

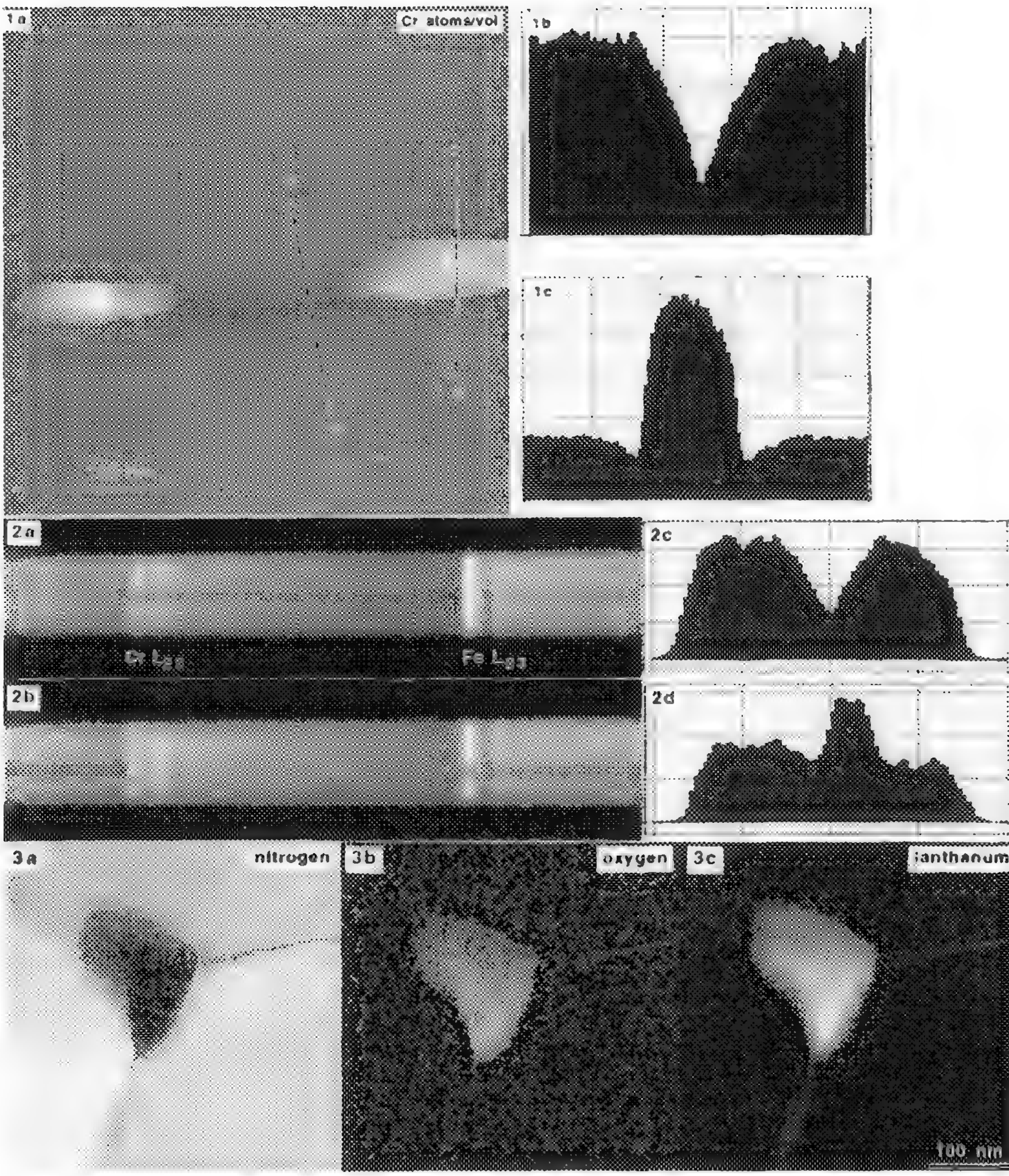

FIG. 1 - (a) Cr L_{23} net core-loss signal normalized to yield Cr concentration in atoms per unit volume, showing Cr depletion between Cr-rich intergranular $M_{23}C_6$ precipitates in type 304L stainless steel aged 15 h at 600°C. (b,c) profiles indicated on (a), 1 pixel ≈ 1 nm.

FIG. 2 - (a,b) TEM spectrum lines [8s exposure, ~1.6 nm/pixel (vertical), 0.5 eV/pixel (horizontal)] and (c,d) profiles of Cr L_3 intensity for (a,c) grain boundary (cf. Fig. 1b) and (b,d) precipitate (cf. Fig. 1c).

FIG. 3 - Images of nitrogen K, oxygen K, and lanthanum M_{45} net core-loss intensity for sintered Si_3N_4.

LOG-POLYNOMIAL BACKGROUND SUBTRACTION IN ENERGY-FILTERED TEM

N. D. Evans and J. Bentley*

Oak Ridge Institute for Science and Education, P.O. Box 117, Oak Ridge, TN 37831-0117
*Metals and Ceramics Division, Oak Ridge National Laboratory, P.O. Box 2008, Oak Ridge, TN 37831-6376

An inverse power relation is widely used to model the background under inner shell ionization edges in both electron energy-loss spectrometry (EELS) and energy-filtered transmission electron microscopy (EFTEM).[1] Proper background subtraction is necessary to obtain correct core-loss integrated intensities in EELS or elemental maps in EFTEM. However, the empirical inverse power relation often does not accurately model the background when losses at slightly lower energies interfere with the edge of interest, or in general, when energy losses are less than ~200 eV. In such cases, the background of EELS spectra has been successfully fitted as a linear least-squares fit to a polynomial, usually a quadratic of the form: $\log(I) = A + BX + CX^2$, where I = intensity and X = log(energy loss).[2] In the present study, this alternative background model, the "log-polynomial," has been applied to pre-edge images for background subtraction from post-edge energy-filtered images.

The technique involves the acquisition of a series of energy-filtered images which covers both pre-edge and post-edge regions of the relevant core-loss edge. All images are aligned to correct for relative drift between images. The pixel-by-pixel intensities in the pre-edge images are fitted to a polynomial (a quadratic) to yield the above coefficients A, B, C and the variance of the fit. These coefficients are then used to extend the background (pixel-by-pixel) to the energies at which the post-edge images were acquired, and the calculated background is then subtracted from each corresponding post-edge image. All image processing (log-polynomial fitting, background calculation and subtraction) is accomplished within DigitalMicrograph software as a series of compiled computer routines (scripts).

For this study, a 304L stainless steel specimen aged 15 h at 600°C has been examined. Chromium segregation has produced Cr-rich $M_{23}C_6$ precipitates at the boundary.[3] Energy-filtered images of an edge-on grain boundary were obtained using a Philips CM30 microscope with an attached Gatan Imaging Filter. Images were acquired 512 x 512 pixels in size (2x on-chip binning) with gain normalization. A series of images was recorded with 10-eV-wide windows and 15 s exposure times; window centers were at 10-eV increments from 613 to 733 eV. Fe elemental maps were constructed from these images; the L_3 edge has an onset at 708 eV. Fitting and processing were performed on drift-corrected 256 x 256 pixel subareas of acquired images.

The log-polynomial fitting procedure was validated by producing two Fe elemental maps from the same filtered series using the two different background subtraction models (the log-polynomial and the inverse power relation, which works reliably in this case). Figure 1a shows an Fe elemental map of the grain boundary region which contains two Cr-rich precipitates. Counting statistics were improved by summing three post-edge images to produce a composite image comparable to one having a 30-eV-wide window centered at 723 eV. Two analogous pre-edge images (having 30-eV-wide windows centered at 653 and 683 eV) were produced by similar image summation. Integrated intensity profiles across a precipitate (AA′) and the grain boundary (BB′) are presented in figures 1b and 1c, respectively. Figure 2a shows the Fe elemental map when the log-polynomial pre-edge background was extended to post-edge energies and subtracted from the post-edge images. Nine pre-edge images were used to determine the fitting coefficients. Identical contrast and brightness levels have been imposed in figures 1a and 2a. The similarity in appearance of these two images, combined with the similarity in corresponding intensity profiles (CC′ with AA′, and DD′ with BB′) indicates the log-polynomial relation correctly determined the background in Fig. 2a. Having validated the log-polynomial fitting procedure, experiments are underway to produce elemental maps where the inverse power relation is not appropriate.[4]

1. R. F. Egerton, *Electron Energy-Loss Spectroscopy in the Electron Microscope*, New York: Plenum Press (1986) 122-25 and 255-62.

2. J. Bentley et al., *Proc. 40th Ann MSA Meeting*, (1982) 496.
3. J. Bentley and E. A. Kenik, *Proc. 52nd Ann MSA Meeting*, (1994) 1000.
4. Research sponsored by the Division of Materials Sciences, U.S. Department of Energy, under contract DE-AC05-96OR22464 with Lockheed Martin Energy Research Corp., and through the SHaRE Program under contract DE-AC05-76OR00033 with Oak Ridge Associated Universities.

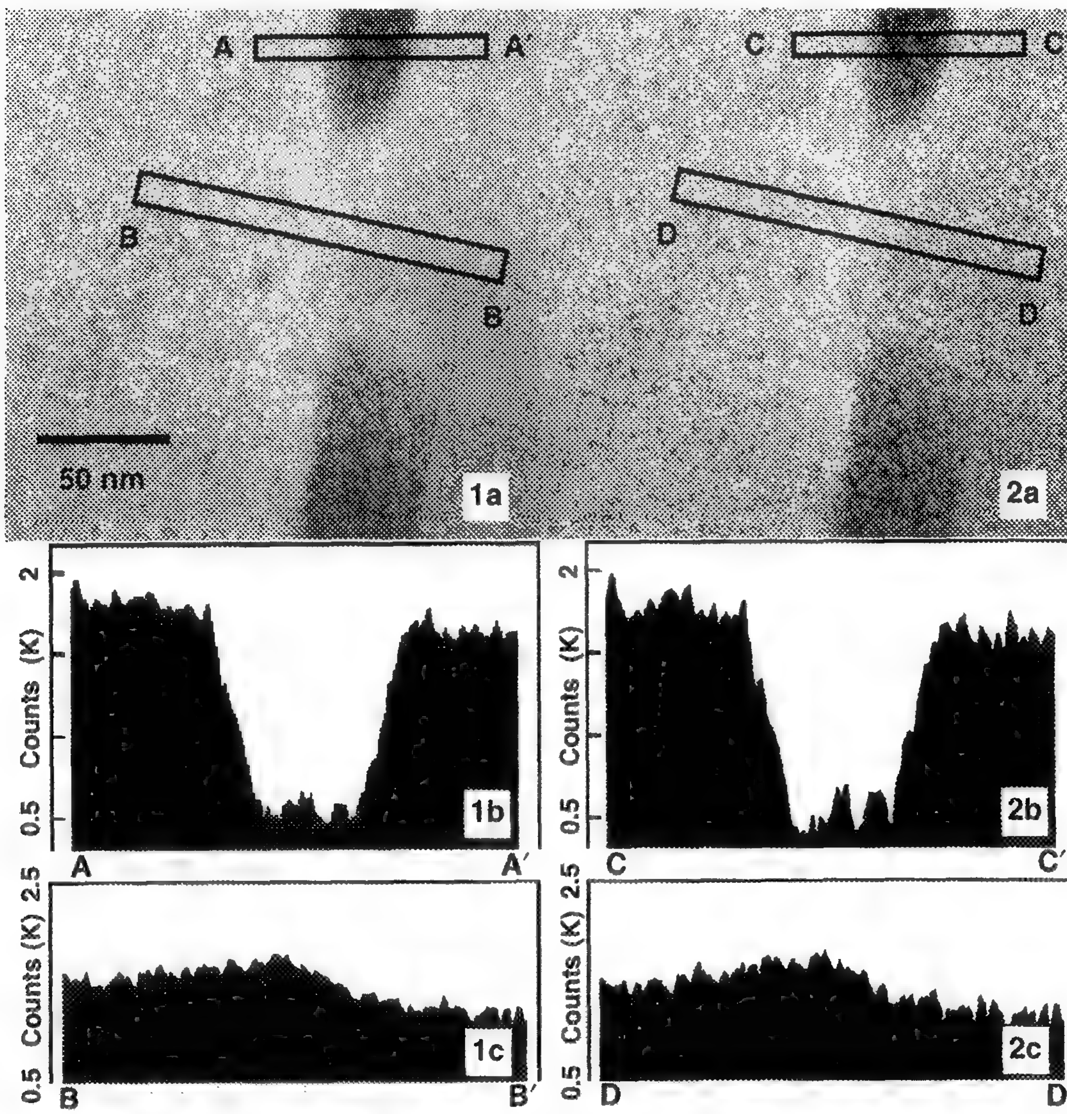

Fig. 1 a) Iron elemental map; background modeled as inverse power relation, b) pixel intensity profile through $M_{23}C_6$ at AA′ and c) pixel intensity profile across grain boundary at BB′.
Fig. 2 a) Iron elemental map; background modeled as log-polynomial relation, b) pixel intensity profile through $M_{23}C_6$ at CC′ and c) pixel intensity profile across grain boundary at DD′.

PLUG-IN SCRIPTS FOR EFTEM AUTOMATION

N. D. Evans and M. K. Kundmann*

Oak Ridge Institute for Science and Education, P.O. Box 117, Oak Ridge, TN 37831-0117
*Gatan Research and Development, 6678 Owens Dr., Pleasanton, CA 94588-3334

Post-column energy-filtered transmission electron microscopy (EFTEM) is inherently challenging as it requires the researcher to setup, align, and control both the microscope and the energy-filter. The software behind an EFTEM system is therefore critical to efficient, day-to-day application of this technique. This is particularly the case in a multiple-user environment such as at the Shared Research Equipment (SHaRE) User Facility at Oak Ridge National Laboratory. Here, visiting researchers, who may be unfamiliar with the details of EFTEM, need to accomplish as much as possible in a relatively short period of time.

We describe here our work in extending the base software of a commercially available EFTEM system in order to automate and streamline particular EFTEM tasks. The EFTEM system used is a Philips CM30 fitted with a Gatan Imaging Filter (GIF).[1] The base software supplied with this system consists primarily of two Macintosh programs and a collection of add-ons (plug-ins) which provide instrument control, imaging, and data analysis facilities needed to perform EFTEM. Of particular interest is the DigitalMicrograph program and its plug-ins. The program itself includes a scripting language (modeled on the C programming language) with which one can create custom routines (scripts) and install them as standard menu items. The plug-ins provide libraries of routines, accessible from any script, for both controlling the filter hardware and the integral slow-scan charge-coupled device (CCD) detector, and performing a variety of high- and low-level mathematical operations on the data. In effect, the DigitalMicrograph script language can be used to further the integrated control of the EFTEM system, thus paving the way for more complete automation as appropriate algorithms are developed.

For the work at the SHaRE User Facility in particular, script routines have been developed to begin automating the following four procedures: 1) aligning the origin of the energy-loss scale (zero-loss peak) with the center of the energy-selecting slit, 2) acquiring data to produce images having pixel intensities that are proportional to concentration in atoms per unit volume, 3) performing arbitrary image arithmetic with automatic correction for image drift, and 4) extracting elemental maps using a log-polynomial background extrapolation technique. These scripts, and their utility, are described here.

1) The energy range (eV) of loss electrons from which images are acquired is controlled by a slit in the filter. The microscopist sets the slit width via software, and then usually centers the zero-loss peak within the slit. However, the zero-loss peak may slowly drift off-center, making it necessary to check and reset this alignment prior to acquisition of a filtered series of images. To center the zero-loss peak in the slit, the filter is typically set to the image mode, slit put in position and set to the desired width, any spectrum offset removed, and the TV-rate CCD camera placed into position. The microscopist monitors the TV image while adjusting the strength (function "energy shift") of the filter's sector magnet. As zero-loss electrons are intercepted by one edge of the slit, image brightness falls off sharply and the value of "energy shift" noted at this extreme. The zero-loss peak is then moved towards the opposite edge of the slit to obtain the corresponding value of "energy shift" at the other extreme. The zero-loss peak is then centered in the slit by setting "energy shift" to the average of the values noted at the two extremes. The script *Center Zero-Loss* assists the microscopist in quickly centering the zero-loss peak. Upon execution, the initial energy-filter configuration is noted. The user is prompted to specify the desired slit-width for centering (the current slit width is offered as a default value). In an interactive manner, the user is prompted to locate first one half-slit and then the second. The correct "energy shift" is imposed, and all other parameters of the filter's original configuration are restored. If the user exits the script, which is

possible at any point during execution, the initial configuration of the filter is restored. This script is particularly useful to the unfamiliar user, or when several filter settings must be changed for zero-loss-peak centering and then reset after centering.

2) For concentration mapping, the script *Acquire ZL and related images* automatically acquires the unfiltered, filtered zero-loss, and low-loss images needed to process a background-subtracted core-loss intensity image, $S_x(\Delta,\beta)$, to yield pixel intensities that are proportional to concentration in atoms per unit volume.[2,3] The microscopist is prompted merely to input the desired CCD exposure time and energy selecting slit widths. The script examines energy-filter parameters (such as mode, energy shift, spectrum offset, TV state, slit width and position) and sets them as needed for image acquisition. The script acquires an unfiltered image, I_T; an image with the zero-loss peak centered in a small energy window Δ_0 (typically 5 or 10 eV), I_0; and a low-loss image, $J_1(\Delta,\beta)$, obtained with energy window (typically 30 eV) and collection half-angle β identical to that used to acquire $S_x(\Delta,\beta)$. For the image $J_1(\Delta,\beta)$, the zero-loss peak is not centered in the energy window Δ, but justified to the high energy side of the window. Appropriate tags (notes and labels) are written to each acquired image. Finally, any changed image filter conditions are returned to their original values. Script execution can be cancelled by the user at any time.

3) A feature common to each image of a filtered series usually does not remain at the same location (pixel) in the series, but its position can "drift" from image to image. This drift can be due to actual specimen drift, high tension instability, and drift in the optics of the energy-filter. Consequently, a set of sequential images must typically be aligned to compensate for this drift, and only the common regions of images then used in analysis. The measurement of relative drift between two images is readily accomplished via routines that are part of the base software, as is the "drift-corrected" division of one image subarea by another (via the "Compute Ratio Image" command). This capability for drift-corrected arithmetic operations has been expanded to include image summation, subtraction, and multiplication via the script *Drift-corrected operations*. Here, the user is prompted to select two images, and the specific mathematical operation. If the relative drift between the images is not on record (i.e., it has not yet been performed), the script initiates this task, updates the drift correction table for these images, performs the requested operation on the subareas it determines to be common to each image, and concludes by displaying the resultant image.

4) Fitting a series of pre-edge images to a log-polynomial function for background subtraction requires use of the common subareas of many images to determine the fitting coefficients.[4] The current procedure for drift-correction is to manually determine the common subareas and then copy each as a new image. This procedure is very tedious. Presently under development is a script for obtaining the largest drift-corrected subareas common in an entire series of images.[5]

1. A. J. Gubbens and O. L. Krivanek, *Ultramicroscopy* 51 (1993) 146.

2. J. Bentley et al., *Proc. EMAG95 (Inst. Phys. Conf. Ser. 147)*, ed. D. Cherns (Bristol: IOP, 1995) 187.

3. J. Bentley et al., *Proc. 53nd Ann. MSA Meeting*, (1995) 268.

4. N. D. Evans and J. Bentley, these proceedings.

5. Research sponsored by the Division of Materials Sciences, U.S. Dept. of Energy, under contract DE-AC05-96OR22464 with Lockheed Martin Energy Research Corp., and through the SHaRE Program under contract DE-AC05-76OR00033 with Oak Ridge Associated Universities.

ALCHEMI OF B2-ORDERED $Fe_{50}Al_{45}Me_5$ ALLOYS

Ian M. Anderson

Metals & Ceramics Division, Oak Ridge National Laboratory, PO Box 2008, Oak Ridge, TN 37831-6376

B2-ordered iron aluminide intermetallic alloys exhibit a combination of attractive properties such as low density and good corrosion resistance. However, the practical applications of these alloys are limited by their poor fracture toughness and low room temperature ductility.[1] One current strategy for overcoming these undesirable properties is to attempt to modify the basic chemistry of the materials with alloying additions.[2] These changes in the chemistry of the material cannot be fully understood without a knowledge of the site-distribution of the alloying elements. In this paper, the site-distributions of a series of 3d-transition metal alloying additions in B2-ordered iron aluminides are studied with ALCHEMI.

A series of seven alloys of stoichiometry $Fe_{50}Al_{45}Me_5$, with Me = {Ti, V, Cr, Mn, Co, Ni, Cu}, were prepared with identical heating cycles. Microalloying additions of 0.2% B and 0.1% Zr were also incorporated to strengthen the grain boundaries, but these alloying additions have little influence on the matrix chemistry and are incidental to this study. The alloys were extruded at 900°C, solutionized at 1000°C for 1 h in vacuum, and annealed at 400°C for 1 week in air. Thin foil specimens were prepared for ALCHEMI analysis with standard electropolishing techniques. Energy-dispersive X-ray (EDX) spectra were acquired with a Philips CM12 operated at 120 kV and equipped with a LaB_6 filament, an EDAX 9900 spectrometer and superUTW Si(Li) detector. ALCHEMI experiments were performed with a beam divergence semiangle of 3 mrad at both {200} and {110} systematic orientations as described in detail elsewhere.[3]

A representative plot of the data is shown in Fig. 1 for the V-containing alloy. Here, the X-ray intensity variations of the host and alloying elements, corrected for the difference in linear response (ionization delocalization), are plotted as a function of crystal orientation. The data indicate excellent discrimination between the intensity variations of the Fe and Al host elements. The extraction of the site-distributions of the alloying elements requires some assumptions to be made concerning the point defect structure of the alloy. The 'Fe'-site occupancies $p^0_{Me'Fe'}$ consistent with the assumption that Fe anti-site defects on the 'Al' sublattice are the only point defects with appreciable concentrations are shown in Fig. 2. Two general features of this plot are noteworthy. The first is the obvious systematic trend in the site-distribution with atomic number: the occupancy of the 'Fe' sublattice increases from Ti through Cu. The second feature is that the elements with atomic number higher than that of the Fe host element have a higher occupancy of the 'Fe' sublattice than do the elements of lower atomic number than Fe of the 'Al' sublattice. These qualitative features are relatively insensitive to the assumptions about the point defect structure, although the point defect concentrations influence the actual values of the site-distributions. The systematic trend in the site-distributions is consistent with the increased thermodynamic stability of the alloys with increasing occupancy of the t_{2g}-type bonding states at the Fermi level.[4] However, thermodynamic considerations alone suggest that Ti, V, and Cr should occupy the 'Al' sublattice exclusively. The residual 'Fe'-site occupancy of these elements can be understood by considering the kinetics of site-equilibration.[5]

References

1. J.H. Schneibel and M.A. Crimp, eds. *Processing, Properties and Applications of Iron Aluminides*, TMS, Warrendale, PA (1994).
2. J.H. Schneibel, E.P. George and I.M. Anderson, in preparation.
3. I.M. Anderson and J. Bentley in *Proc. EMAG 95*, Inst. of Physics, Bristol, UK (1996).
4. C.L. Fu and J. Zou in *High Temperature Ordered Intermetallic Alloys VI*, MRS, Pittsburgh (1995)91.
5. Research at the Oak Ridge National Laboratory (ORNL) SHaRE User Facility was sponsored by the Division of Materials Sciences, U.S. Department of Energy, under contract DE-AC05-96OR22464 with Lockheed Martin Energy Research Corp., and by an appointment to the ORNL Postdoctoral Research Associates Program, which is administered jointly by the Oak Ridge Institute for Science and Education and ORNL. The author thanks Dr. J. Schneibel for specimens and for helpful discussions.

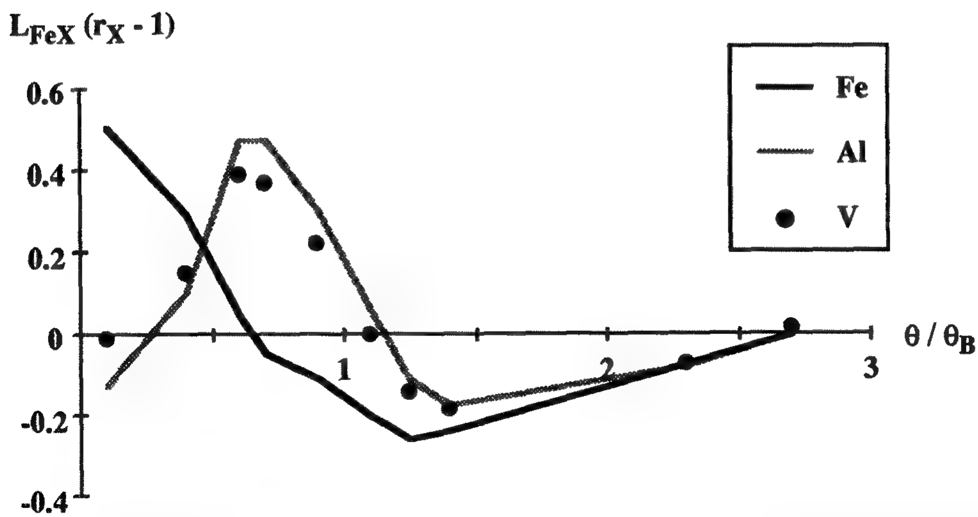

FIG 1 - Plot of X-ray intensity variations as a function of crystal orientation for the host and alloying elements in $Fe_{50}Al_{45}V_5$. The coefficients L_{FeX} correct the data for differences in linear response to the electron channeling (ionization delocalization). θ_B is the Bragg angle for the {200} fundamental reflection.

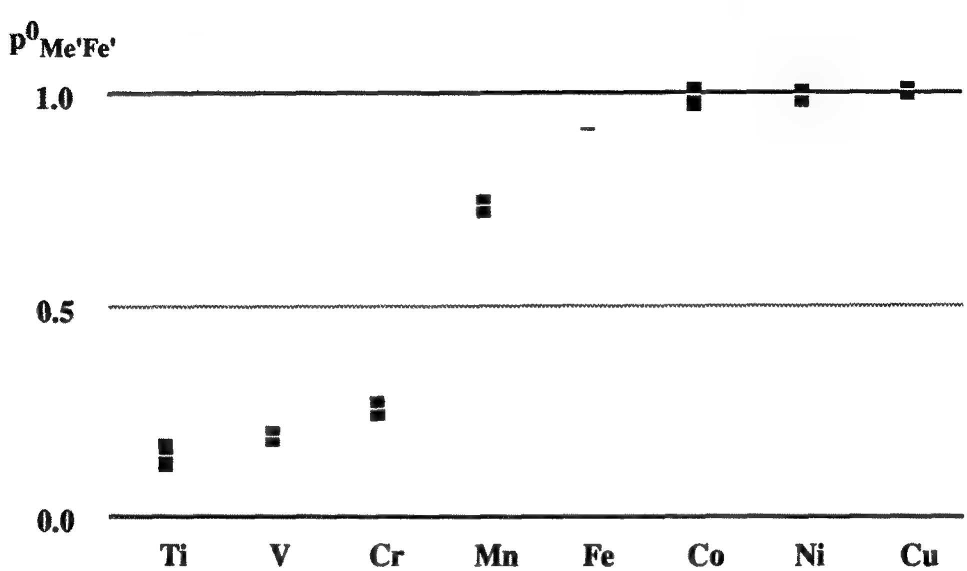

FIG 2 - The 'Fe'-site occupancies $p^0_{Me'Fe'}$ consistent with the assumption that Fe anti-site defects on the 'Al' sublattice are the only point defects with appreciable concentrations (± one standard error).

MULTIVARIATE STATISTICAL ANALYSIS OF A SERIES OF ALCHEMI SPECTRA

Ian M. Anderson and J. Bentley

Metals & Ceramics Division, Oak Ridge National Laboratory, PO Box 2008, Oak Ridge, TN 37831-6376

Multivariate statistical analysis (MSA) of a series of spectra or images offers an objective and quantitative way to characterize the features of the spectra that vary in a correlated fashion and to determine the number of independently varying components in the series. For example, in a series of spectra showing grain boundary segregation, there may be only one independently varying spectral component, which signifies an increase in the concentrations of the segregants and a corresponding decrease in the concentrations of some of the matrix constituents. The basis of the MSA method has been outlined by Trebbia and Bonnet, with application to the analysis of electron energy-loss spectrum images.[1] Titchmarsh et al. have applied this analysis to a series of energy dispersive X-ray (EDX) spectra for the study of grain boundary segregation.[2] The present paper illustrates the application of MSA methods to a series of EDX spectra acquired for ALCHEMI analysis.[3] The basic method has been modified slightly for the analysis of ALCHEMI data. For the procedure outlined by Trebbia and Bonnet, the origin (zero intensity in every pixel) is assumed to lie in the plane of the data and variations in the average signal level are assumed to convey no information. Neither assumption applies to ALCHEMI analysis. These differences can be accommodated by measuring the variation of the ALCHEMI data with respect to the average of the spectra.

The ALCHEMI data are well approximated by the sum of this average spectrum and a linear combination of the two largest moments of the variation. The remaining moments of the variation are essentially noise-bearing. The physically relevant analogs of the three components are (i) the weakly diffracting reference spectrum (WDRS), which is acquired at an orientation with negligible channeling, (ii) the response of the continuum and characteristic X-ray intensities to the electron channeling, which conveys information often described by the expression "ionization delocalization", and (iii) the site-distribution information. These components are shown in Figs. 1 and 2 for a data set acquired at the <111> axial orientation from an $L1_2$-ordered γ' particle in a René 95 nickel-base superalloy.[4] Fig. 1 shows a section of the WDRS from 0 to 20 keV that has been reconstructed from the average spectrum and the two significant moments of the data. This reconstructed spectrum is noise-filtered relative to the raw data. Figs. 2a and b show sections of the corresponding components for delocalization and the site-distribution, respectively, from 0 to 10 keV. The relative amplitudes of these components as a function of specimen orientation are shown in Figs. 2c and d, which are plotted on the same scale. Note that only a fraction of the large channeling effect at the zone axis conveys the site-distribution. The mean electron intensity at the atomic columns undergoes irregular variations as the Bragg conditions of the various reflections near <111> are satisfied (Fig. 2c), whereas site-discrimination is observed only when all superlattice reflections are excited with a negative excitation error, in close proximity to the <111> zone axis (Fig. 2d). The relative intensities of soft ($\leq$ 4 keV) characteristic X-rays in Fig. 2a are small in comparison with those of the WDRS in Fig. 1, consistent with the classical notion of ionization delocalization. Fig. 2b shows that an increase in the X-ray intensities characteristic of the Ni host element is accompanied by a corresponding decrease in that for Al. The intensities of the other elements are consistent with the measured site-distribution. Adaptation of this method for the extraction of quantitative site-distributions is under investigation.[5]

References

1. P. Trebbia and N. Bonnet, *Ultramicroscopy* 34(1990)165.
2 J.M. Titchmarsh et al., *Microbeam Analysis* 4(1995)S259.
3. I.M. Anderson and J. Bentley, these proceedings.
4. J. Bentley and I.M. Anderson, these proceedings.
5. Research at the Oak Ridge National Laboratory (ORNL) SHaRE User Facility was sponsored by the Division of Materials Sciences, U.S. Department of Energy, under contract DE-AC05-96OR22464 with Lockheed Martin Energy Research Corp., and by an appointment (IMA) to the ORNL Postdoctoral Research Associates Program, which is administered jointly by the Oak Ridge Institute for Science and Education and ORNL.

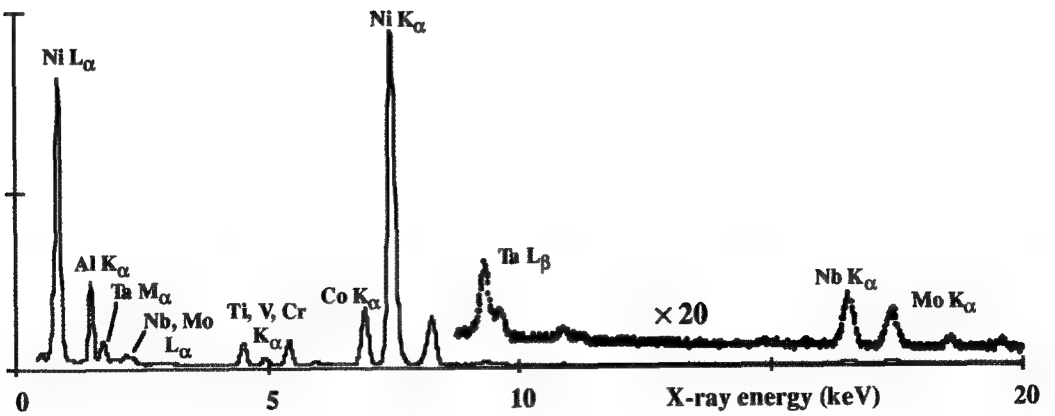

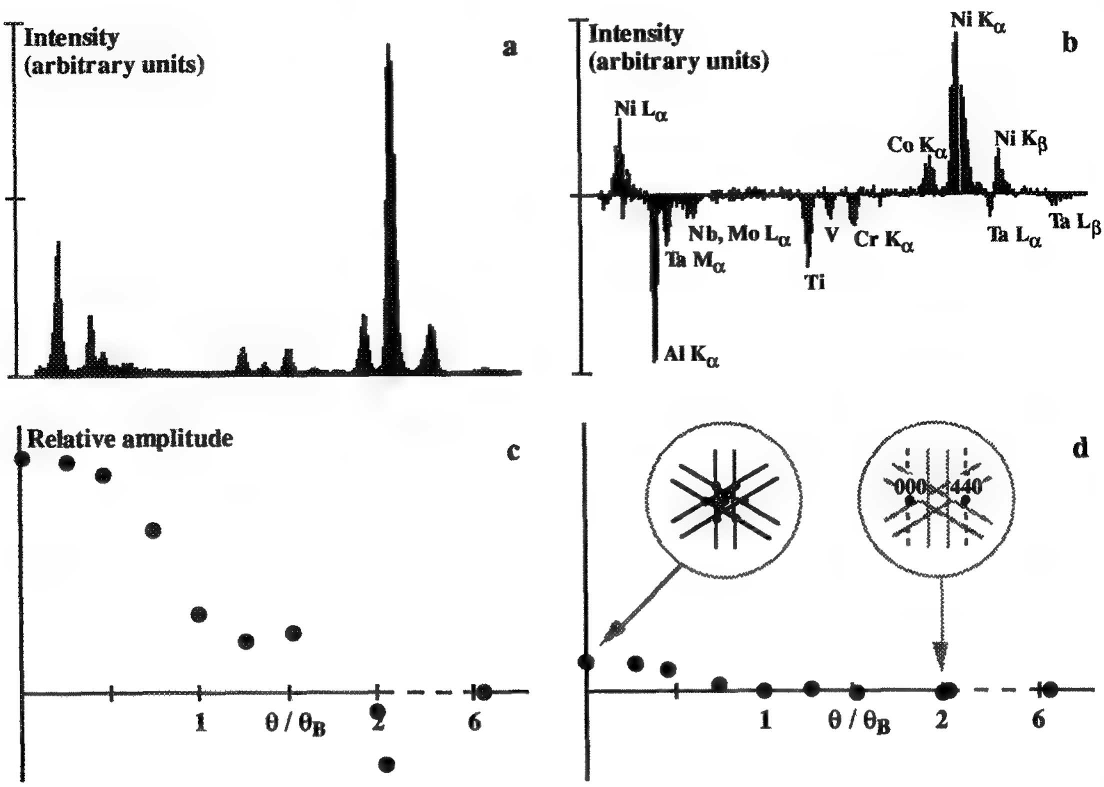

FIG 1 - The weakly diffracting reference spectrum, reconstructed from the average spectrum and the two most significant MSA components of the ALCHEMI data set. Full scale is 10,000 counts / ch.

FIG 2 - Component spectra corresponding to (a) response to electron channeling ("delocalization") and (b) site-distribution; (c), (d) relative amplitudes of components as function of orientation.

ALCHEMI OF $L1_2$-ORDERED $Ni_{76}Al_{21}Hf_3$ AND GAMMA PRIME PARTICLES

J. Bentley and Ian M. Anderson

Metals & Ceramics Division, Oak Ridge National Laboratory, PO Box 2008, Oak Ridge, TN 37831-6376

Recent improvements to the atom location by channeling-enhanced microanalysis (ALCHEMI) technique now allow reliable measurements of site distributions in ordered alloys.[1,2] Early zone-axis ALCHEMI of $L1_2$-ordered Ni_3Al-based alloys[3] was plagued by ionization delocalization; for $Ni_{76}Al_{21}Hf_3$ at <001> the fraction of Hf on the Al sublattice, $p_{Hf'Al'} = -127\%$. Reanalysis[4] by statistical ALCHEMI was no better, giving $p_{Hf'Al'} = -220 \pm 190\%$, contrary to the claims that delocalization effects should be minimized.[5] The same data set analyzed with the reformulated ALCHEMI method[1,2] yields $p_{Hf'Al'} = 80 \pm 25\%$.[4]

Further experiments have been performed at ~140K in a Philips CM12 operated at 120 kV and equipped with an EDAX 9900 spectrometer and superUTW Si(Li) detector. The diffracting conditions were carefully adjusted with the beam (not specimen) tilt, a probe size of ~200 nm and beam divergence of ~3 mrad were used, and the current in the probe was monitored and held constant at ~1 nA. Based on the methods developed and optimized for B2-ordered alloys,[2] planar ALCHEMI at a 200 systematic yielded $p_{Hf'Al'} = 76.9 \pm 6.6\%$. (The necessary relative "localization" of Ni and Al, $L_{NiAl} = 1.433 \pm 0.057$, was obtained at a 111 systematic.) However, the poor site discrimination under 200 planar conditions (there are no planes of pure 'Al') limits the precision of the extracted site occupancy. Therefore, ALCHEMI data were obtained for <001> and <111> zone axes (where the 'Ni' and 'Al' sites are on separate atomic columns). The <001> data indicated hardly any site discrimination; the previous nonphysical results[3] from this orientation arise because the delocalization effect swamps the site discrimination. As in previous <001> studies, the Al/Ni intensity ratio was highest for channeling exactly at the zone-axis; this situation prevails for accelerating voltages from 100 to 300 kV. The data from <111> indicated site discrimination only within ~0.5 θ_{220} of the zone axis, where θ_{220} is the (220) Bragg angle. For data acquired at greater misorientations from <111>, the linear variation on 3D-plots[4] of the relative intensities of Ni, Al, and Hf, (indicating no site discrimination between the 'Ni' and 'Al' sites), yielded $L_{NiAl} = 1.601 \pm 0.110$. Applying this delocalization correction to the entire data set yielded $p_{Hf'Al'} = 78.0 \pm 4.3\%$, in excellent agreement with the (200) data and with atom probe results,[6] and consistent with ternary phase diagrams.[7]

Exploiting its high spatial resolution and applicability to multiphase alloys, ALCHEMI has been applied to the γ' phase in a René 95 nickel-base superalloy. The microstructure consists of a trimodal distribution of coherent misfitting $L1_2$-ordered γ' particles (~50 vol%) in a Ni solid solution γ matrix. A ~0.5-µm diameter γ' particle free of matrix overlap was selected for analysis. Following the success with $Ni_{76}Al_{21}Hf_3$ described above, zone-axis ALCHEMI at <111> was used. Delocalization-corrected intensity ratios $L_{NiX}(r_X - 1)$, where $r_X = I_X^{(\xi)} / I_X^{(0)}$ is the ratio of the characteristic X-ray intensity of element X at an orientation (ξ) to its intensity at the weakly diffracting reference orientation (0), are shown in Fig. 1 for selected elements as a function of the incident beam tilt θ from the exact axial condition in units of θ_{220}. As for $Ni_{76}Al_{21}Hf_3$, the site discrimination is confined to data with $\theta/\theta_{220} \leq 0.5$; delocalization correction coefficients were obtained from the data with $\theta/\theta_{220} > 0.5$. From Fig. 1, Co strongly prefers the 'Ni' sublattice, Ta strongly prefers the 'Al' sublattice, and Cr is distributed over both sublattices. Quantitative site occupancies for seven minor constituents were extracted assuming that there are no Ni or Al anti-site defects: $p_{Ti'Ni'} = 11.8 \pm 3.7\%$, $p_{V'Ni'} = 32.3 \pm 7.6\%$, $p_{Cr'Ni'} = 58.3 \pm 2.9\%$, $p_{Co'Ni'} = 100.2 \pm 1.0\%$, $p_{Nb'Ni'} = 18.0 \pm 4.0\%$, $p_{Mo'Ni'} = 32.0 \pm 5.7\%$, and $p_{Ta'Ni'} = 0.5 \pm 5.1\%$. The K lines were used for all elements except Ta, where the Lβ was used (Ta Lα is severely overlapped by Ni Kβ). The slightly larger error for the V result is due to both its low concentration and the severe peak overlaps among the Ti, V, and Cr K series. Once again, the site occupancies are consistent with phase diagrams[7] and there are some clear trends: an increasing 'Ni' site preference moving from left to right on the periodic table (Ti, V, Cr, Co), (Nb, Mo); and an increasing 'Al' site preference in moving top to bottom in columns V and VI (V, Nb, Ta), (Cr, Mo). The former trend is similar to the increasing 'Fe' site preference for the 3d transition metals (Me = Ti to Cu) in $Fe_{50}Al_{45}Me_5$ B2-ordered alloys.[8]

The <111> γ' ALCHEMI data have also been subjected to multivariate statistical analysis (MSA).[9] One result of this analysis that conveys site-occupancy information in a spectral format is shown in Fig. 2. The solid curve represents the spectral response to the electron channeling: its peak intensities are inherently corrected for ionization delocalization.[9] The shaded spectrum is a linear combination of the spectral response and site-distribution components[9] of the MSA that has the same Ni K intensity as the solid curve and zero Al K intensity. The ratio of peak intensities conveys the fractional 'Ni'-site occupancy.[10]

1 I.M. Anderson and J. Bentley, *these proceedings.*
2 I.M. Anderson and J. Bentley, *Proc. EMAG95, Inst. Phys. Conf. Ser.* ***147***, (Bristol: IOP, 1995) 531.
3 J. Bentley, *Proc. 44th EMSA Meeting* (1986) 704.
4 J. Bentley et al., *Microbeam Analysis* **3** (1993) S191.
5 P.S. Turner et al., *J. Microsc.* **162** (1991) 369.
6 M.K. Miller and J.A. Horton, Jr., *Scripta Metall.* **20** (1986) 1125.
7 S Ochiai et al., *Acta Metall.* **32** (1984) 289.
8 I.M. Anderson, *these proceedings.*
9 I.M. Anderson and J. Bentley, *these proceedings.*

10 Research at the Oak Ridge National Laboratory (ORNL) SHaRE User Facility sponsored by the Division of Materials Sciences, U.S. Department of Energy, under contract DE-AC05-96OR22464 with Lockheed Martin Energy Research Corp., and by an appointment (IMA) to the ORNL Postdoctoral Research Associates Program, which is administered jointly by the Oak Ridge Institute for Science and Education and ORNL. The authors thank Drs. E.L. Hall (GE Corp. R&D) and J.A. Horton, Jr. (ORNL) for providing specimens.

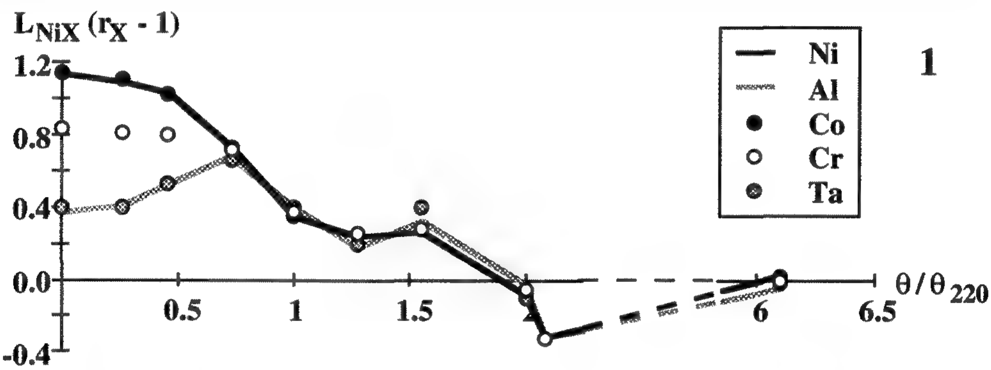

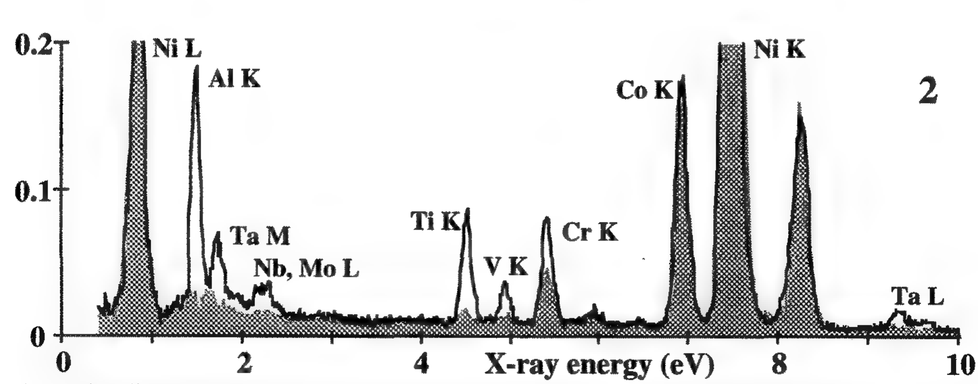

FIG. 1 - Delocalization-corrected, normalized X-ray intensities as a function of tilt from the <111> axial orientation in units of 220 Bragg angle.

FIG. 2 - Spectra reconstructed from the multivariate statistical analysis (see text).[9] The ratio of the peak intensities in the shaded spectrum to those of the solid line represents the fractional 'Ni' site occupancy.

ALCHEMI OF $NbCr_2/V$ C15-STRUCTURED LAVES PHASE

P.G. Kotula,* I.M. Anderson,† F. Chu,* T.E. Mitchell,* and J. Bentley†

*Center for Materials Science, Los Alamos National Laboratory, Los Alamos, NM 87545
†Metals & Ceramics Division, Oak Ridge National Laboratory, PO Box 2008, Oak Ridge, TN 37831-6376

Laves-phase intermetallics are of potential interest for use as high temperature structural materials, of which $NbCr_2$-based C15-structured Laves phases are particularly attractive.[1] Vanadium-alloyed $NbCr_2$ Laves phases have been studied.[2] The defect mechanism of a ternary Laves phase is crucial to understanding its physical metallurgy and deformation behavior.[3] It is suggested based on the Nb-Cr-V phase diagram and first-principles total energy and electronic structure calculations for $NbCr_2$ that V should occupy the B sites in C15-structured AB_2.[2] In this paper, ALCHEMI[4] is employed to examine this assumption for one composition of a V-alloyed $NbCr_2$ C15 Laves phase.

A Nb-Cr-V alloy of composition $Nb_{33}Cr_{42}V_{25}$ was prepared by arc-melting followed by annealing at 1400°C for 120 h. Specimens were prepared for microanalysis by cutting 3 mm discs followed by dimpling and ion milling. Energy-dispersive X-ray (EDX) spectra were acquired with a Philips CM30 operating at 300 kV and equipped with a Kevex Quantum detector. Fourteen spectra were collected near <014> over a range of {400} excitations between symmetry and beyond {12 0 0}. Owing to the high accelerating voltage (and therefore relatively flat Ewald sphere) used for these experiments, it was difficult to eliminate non-systematic reflections, although attempts were made to minimize this effect. Spectra were also acquired with a Philips CM12 operating at 120 kV and equipped with an EDAX superUTW detector. Nine spectra were collected near <334> over a range of {440} excitations between symmetry and {880}. Site-distributions were extracted from the data by multivariate statistical analysis (MSA)[5] with delocalization correction[6] as described elsewhere.[7,8]

The C15 Laves phase structure is essentially the same as the oxide spinel structure without oxygen. Therefore, for the compound AB_2 ($NbCr_2$ in this case) there are two distinct sublattices: A (the tetrahedral site in spinel) and B (the octahedral site in spinel). Figure 1 shows X-ray spectra collected at {400} under conditions that maximized the electron fluence on the A and B sublattices. The correlated variation of the V and Cr characteristic X-ray peaks gives qualitative evidence of similar site-distributions for these elements. However, the precision of the site-distribution extracted with MSA was poor. This imprecision can be explained by the similarity of the variations of all X-rays to the channeling, as shown in Fig. 2. Although the variation of the Nb $K\alpha$ intensity is opposite to those of the V and Cr $K\alpha$ intensities, the shapes of the three curves are similar. The three curves do not therefore vary independently, as required by MSA. The lack of site-discrimination at {400} can be attributed to the similar elastic scattering powers of the alternating planes, of composition Nb and Cr_2 in the stoichiometric binary alloy. Indeed, the intensity of the 400 reflection was relatively weak. ALCHEMI was therefore performed at the {440} systematic row, with alternating planes of composition NbCr and Cr. Here, the intensity of the 220 reflection, due entirely to scattering from the A sublattice, was pronounced. Figure 3 shows the variation of the delocalization-corrected intensity ratios[8] with orientation. The correction coefficients L_{CrX} were all within 2% of unity for the medium energy X-rays used for quantification. In contrast to the data in Fig. 2, the signals for the two host elements vary independently of one another. Multivariate statistical analysis indicated a 99.3 ± 3.9% correlation between V and Cr. The relatively large statistical error arises because the two sublattices are not completely separated onto alternating planes at {440}.[8] However, the result is consistent with exclusive site-occupancies of Nb for the A sublattice and Cr and V for the B sublattice.

In the C15 structure, the ideal ratio of atomic radii for the A and B sites is $\sqrt{3/2} \approx 1.225$. Ratios of ~1.1 to 1.6 are observed. In binary $NbCr_2$, the ratio of the Nb (2.08Å) to Cr (1.85Å) radii is ~1.13. It is expected from size effects that V (1.92Å) would substitute for Nb on the A sublattice. As the V is found to substitute for Cr, it is clear that electronic effects must be more important than size effects in this case.[9]

References

1. D. J. Thoma and J. H. Perepezko, *Mater. Sci. & Eng.* A156(1992)97.

2. F. Chu, D. J. Thoma, P. G. Kotula, S. Gerstl, and T. E. Mitchell, in preparation.
3. F. Chu and D. P. Pope, *Mater. Sci. & Eng.* A170(1993)39.
4. J. C. H. Spence and J. Taftø, *J. Microscopy* 130(1983)147.
5. C. J. Rossouw et al., *Phil. Mag. Lett.* 60(1989)225.
6. M. G. Walls, *Microsc. Microanal. Microstruct.* 3(1992)443.
7. I. M. Anderson and J. Bentley, *Proc. 13th ICEM: Electron Microscopy 1994* 1(1994)609.
8. I. M. Anderson and J. Bentley, *Proc. EMAG 95. Bristol: Inst. of Physics (1996).*
9. Research at Los Alamos National Laboratory (LANL) was sponsored by the US Department of Energy (DOE)-OBES. Research at Oak Ridge National Laboratory (ORNL) SHaRE User Facility was sponsored by the DOE Division of Materials Sciences under contract DE-AC05-96OR22464 with Lockheed Martin Energy Research Corp. and by an appointment (IMA) to the ORNL Postdoctoral Research Associates Program, which is administered jointly by the Oak Ridge Institute for Science and Education and ORNL. PGK acknowledges a Director-funded postdoctoral fellowship from LANL.

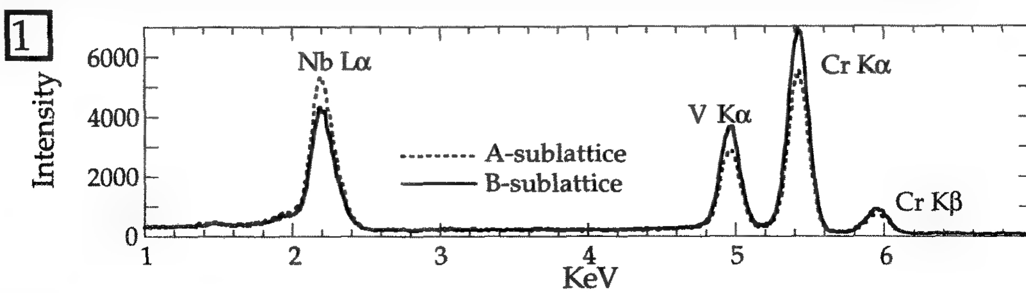

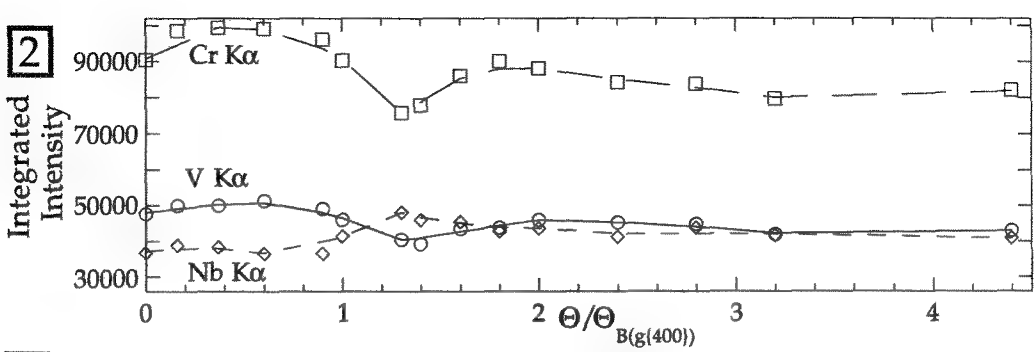

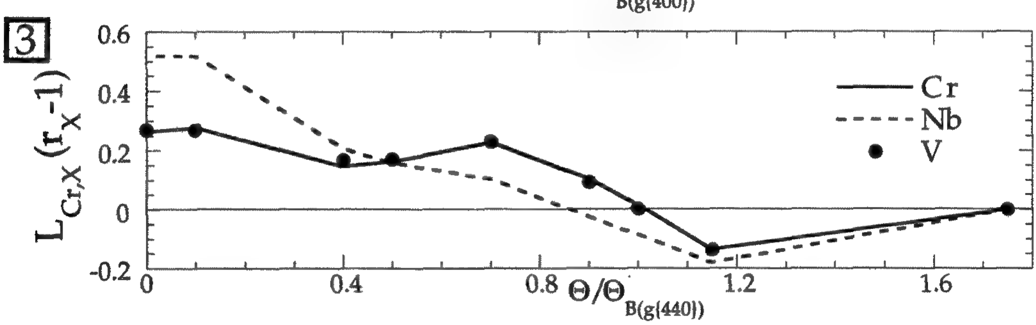

FIG 1 - EDX spectra acquired at {400} with electron fluence on the A and B sublattices.
FIG 2 - Variation of integrated X-ray intensities with orientation at the {400} systematic row.
FIG 3 - Variation of delocalization-corrected intensity ratios with orientation at the {440} systematic row.

EXELFS Analysis of Natural Diamond and Diamond Films on Si Substrates

A. Duarte Moller
Centro de Investigación Científica y de Educación Superior de Ensenada (CICESE),
Km. 107 carretera Tijuana-Ensenada, Ensenada B. C., México

L. Cota Araiza and M. Avalos Borja
Instituto de Física, Universidad Nacional Autónoma de México
Km. 107 carretera Tijuana-Ensenada, Ensenada B. C., México

In this work, we report the EXELFS results obtained from a polycrystalline diamond film grown on smooth silicon substrates using the Hot Filament Chemical Vapor Deposition (HF-CVD) technique in a two-step deposition process published elsewhere [1]. In order to evaluate the quality of the thin film obtained, these results were compared with results obtained from natural diamond.

The diamond sample was prepared in cross-section by ion milling where the nominal size of diamond particles was about 1 μm. The EXELFS experiments were performed in a JEOL-2010 Transmission Electron Microscope with a GATAN-666 PEELS attachment. A primary energy of 200 KeV was used with an average acquisition time of 5 minutes. The extended fine structure (EFS) energy range was 300 eV. In order to obtain the local structure, the standard procedure developed for EXAFS [2] was applied here. The natural diamond particles with a nominal size of 1 μm were taken from commercial powder.

Figure 1 shows the energy loss spectra around the ionization carbon K-edge corrected for background and plural scattering procces. The near edge structure is almost indistinguishable between both diamond samples. The absence of the π^* transition indicates that no significant amount of graphite or amorphous carbon is present. Thus, through these spectra one may estimate the quality of the diamond film grown by the HF-CVD technique.

Figure 2 shows the radial distribution functions obtained by applying the Fourier transform to the diamond energy loss spectra showed in figure 1. The values obtained for the nearest neighbors in the two diamond samples are in good agreement with the respective accepted values [3]. In order to evaluate the capability to resolve straighforwardly the atomic position of the nearest neighbors in the different systems, the correction by EXAFS phase shifts [4] was not applied here. The difference among the values obtained here and the expected values is 0.001 nm and 0.001nm for the first and second nearest neighbors in the diamond film and 0.002 nm and 0.001nm for the first and second nearest nerighbors in the natural diamond sample. The average difference between our results and the expected values is 0.00125 nm (1 %). The position of the third main peak is not reliable like a third nearest neighbor, because the extended fine structure results from a short range process.

We conclude that the diamond film grown through HF-CVD technique on non-scratched Si substrates, are of good quality as demonstrated by the energy loss spectra in figures 1. The capability to analyze regions with dimensions less than 1 mm is not available with regular EXAFS. This renders TEM-EXELFS as a simple, precise and available technique in most surface physics laboratories. We believe, however, that the combination of EXELFS with others established surface spectroscopies may help to give a better description of a number of physical-chemical phenomena in surfaces and interfaces.

We thank F. Ruiz for technical help, CONACyT for the finantial support and GATAN Inc. for assistance in specimen preparation..

References

1. G. A. Hirata, L. Cota Araiza, M. Avalos Borja, M. H. Farias, O.Contreras, W. Ma, H.Okamoto, Y. Hamakawa, Y. Matsumoto, M. J.Massey, R. S Katiyaand, R. K. Brydson. Diam. and Relat. Mat. 3 (1993)
2. C. A. Ashley and S. Doniach. Phys. Rev. B. Vol. 11, 4 (1975) 1279
3. Charles Kittel. Introduction to Solid State Physics., Wiley and sons Inc. New York. Chichester sixth edition, 1986, p.19
4. Boon K. Teo and P. A. Lee. Jour. Amm. Chem. Soc. 101-111 (1979) 2815

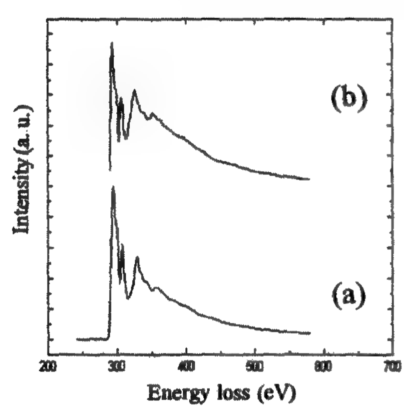

Figure 1. Extended fine structure above the carbon K edge from (a) natural diamond and (b) ours poly-crystalline diamond thin film in cross section.

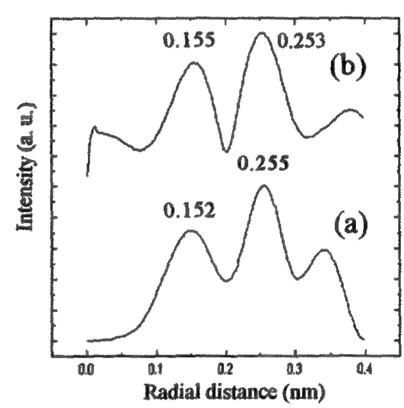

Figure 2 Radial distribution functions F(r) as obtained from direct Fourier transform of the extended fine structure presented in figure 1.

RADIATION DAMAGE AND SPATIAL RESOLUTION IN THE EXELFS OF INORGANIC MATERIALS

D. Haskel,* M. Sarikaya,** M. Qian,** and E. A. Stern*

* Department of Physics, Box 351560, University of Washington, Seattle WA 98195 ,USA
** Materials Science and Engineering Department, University of Washington, Seattle WA 98195 ,USA

EXELFS, the extended energy loss fine structure superimposed on the high energy loss side past an inner-shell electron excitation in an EELS spectrum, contains quantitative information about the local structure around the scattering atom from which the core electron is excited, similar to that contained in the x ray absorption fine structure (XAFS).[1] Main advantages of the EXELFS technique over XAFS include the relative ease in the former to study the local environments of low Z elements coupled to the higher spatial resolution, imaging and diffraction capabilities of the TEM.
Radiation damage to the sample caused by the energetic electron beam, however, has been an important concern to whether EXELFS can be safely applied to study materials at the nanometer scale. To investigate this question we chose to study Al, SiC and MgO as representatives of three different classes of binding: metallic, covalent and ionic, with the belief that these should exhibit different sensitivities to different mechanisms of radiation damage and hence will be fair representatives of a wide variety of materials.

We recorded EXELFS spectra at the Al, Si, C, Mg and O K-edges as a function of electron dose, either by increasing the electron flux or by reducing the illuminated area of the specimen. All the experiments were done in a Philips 430 TEM equipped with a LaB_6 filament and with a 666 GATAN parallel detector EELS spectrometer. Data were collected in the diffraction mode with a nominal camera lenght of 250 mm and a 3 mm entrance aperture to the GATAN spectrometer. Data collection was divided in seven time intervals and data scans within each interval were aligned and added on-line. The different intervals were needed to monitor any time dependent changes in the EXELFS due to either radiation damage or changes in experimental conditions. A total of 10^6 counts were acquired at each current condition to achieve sufficient counting statistics. The highest electron current attained in our experiments was $I = -12.4nA$ and the smallest probe size used was $0.5\mu m$ in radius, given a maximum current density of $J \approx 10^{23}e^-/(sec\ m^2)$. We could not observed any radiation damage in the Al and SiC samples, even after accumulating 10^6 counts at the highest current density and smallest area (highest dose). For the MgO case, however, even though the EXELFS did not show any time dependent changes, changes were evident in the diffraction pattern (DP) as well as in the image after a total dose of $J\Delta t \approx 3 \times 10^{26}e^-/m^2$ was administered to the sample. A uniform ring pattern passing through the single crystal spots appeared in the DP and dark spots about 100Å in size appeared in the image. After corroborating that no changes ocurred in the EXELFS signal of each material as a function of time, the different groups were aligned and summed together. The EXELFS data were analyzed in a way described previously[2] using XAFS theory, and excellent agreement with the known structures was obtained. XAFS theory can be used to analyze the EXELFS provided the dipole approximation is satisfied. This requires that $q_m a_0 \lesssim 0.2$ (q_m is the maximum momentum transfer in the inelastic scattering

and a_0 the radius of the K-shell electron[3]), which can be obtained by a proper choice of collection geometry in the TEM.

Table. 1 summarizes the main findings of this work and the parameters used in determining the validity of the dipole approximation and the ultimate spatial resolution attainable. The spectrometer acceptance semiangle , $\theta_m = 6$ mrad, is determined by the camera length and the spectrometer entrance aperture (diffraction mode). The maximum wave number transfered is given by $q_m = \sqrt{(q_{m,\perp})^2 + (w/v)^2}$; $q_{m,\perp} = \frac{2\pi}{\lambda}\theta_m = 1.5\text{Å}^{-1}$ is the maximum transverse momentum transfer, $\lambda = 0.0251\text{Å}$ is the 200 KeV electrons wavelength, $\hbar w$ is the energy loss and v is the velocity of the incoming electrons. w/v is given 500 eV above the edge. $a_0 \approx \sqrt{\hbar/(2\ w_0 m_e)}$ is the radius of the K shell electron, $\hbar w_0$ being its binding energy and m_e its mass. $J\Delta t$ is the total dose needed to accumulate 10^6 counts at the given edge using a probe $0.5\mu m$ in radius and the highest current density. Δt is about 1 hr. at the Al and Si K-edges and about 15 min. at the C and O K-edges. $J\Delta t_{max}$ is the threshold doses for radiation damage. For Al and SiC these values are taken from the literature (we could not observe any damage at the doses used to record the EXELFS because a field emission gun is required to observe damage in a reasonable time exposure). For MgO we use for the threshold the value at which we started seeing changes in the image and DP, even though the EXELFS did not show changes and the nature of the changes are presently unknown. The ultimate probe size achievable is estimated from improvements in collection efficiency (a factor of two when going from 3mm to 5mm spectrometer entrance aperture for edges where the validation of the dipole approximation is not compromised) and by improvements in counting rates attainable with a faster computer (a factor of six if our Macintosh IIci is replaced by a Power Macintosh).

References

1. E. A. Stern, M. Qian, M. Sarikaya; *Proceedings of the Material Research Society*, vol.332, M. Sarikaya, K. Wickramasinghe and M. Isaacson (eds.) (MRS, Pittsburgh, 1994) 1-12.
2. D. Haskel *et al.*; *Ultramicroscopy* **58** (1995) 353.
3. E. A. Stern; *Optik* **61** (1982) 45.
4. T. J. Bullough, R. W. Devenish, C. J. Humphrey; *The EMAG 1989*, *Institute of Physics Conference series*, No. 98, P. J. Goodhew and H. Y. Elder (eds.) (IOP, Bristol, 1990) 267.
5. D. L. Medlin, L. E. Thomas, D. G. Howitt; *Ultramicroscopy* **29** (1989) 228.

Table 1. Ultimate probe size for EXELFS

Edge	$(\omega/v)(\text{Å}^{-1})$	$q_m a_0$	$J\Delta t(e/m^2)$	$J\Delta t_{max}(e/m^2)$	Ultimate probe radius (Å)
Al (Al metal)	1.45	0.1	3.4×10^{26}	10^{28} [a]	250
Si (SiC)	1.7	0.104	3.8×10^{26}	5×10^{27} [b]	384
C (SiC)	0.57	0.186	8×10^{25}	5×10^{27} [b]	256
O (MgO)	0.68	0.139	1.2×10^{25}	3×10^{26} [c]	400
Mg (MgO)	1.31	0.107	3×10^{26}	3×10^{26} [c]	2000

[a]Ref. 4
[b]Ref. 5
[c]Our measurements

EXELFS χ-DATA RENORMALIZATION

M. Qian, M. Sarikaya, and E.A. Stern

Materials Science and Engineering and Physics, University of Washington, Seattle, WA 98195

Extended Electron Energy Loss Fine Structure (EXELFS) spectroscopy is useful not only because it contains the same local atomic structure information as XAFS (X-ray Absorption Fine Structure), but also it has good low Z element sensitivity, up to nanoscale spatial resolution, and the capability of combining other high spatial resolution TEM measurements together with EXELFS[1]. Until presently, due to poor quality of the EELS data, however, the EXELFS technique has not been developed to its full advantage. We have introduced various new methods to improve the data acquisition technique which includes removal of channel to channel gain variation and correction of dark-current background under real conditions; on-line aligning and accumulation, of virtually unlimited number of spectra while monitoring the thickness change (sample drift), radiation damage, electron beam energy drifts, and change in energy resolution during measurements[2]. We have also developed a systematic data analysis procedure which utilizes the sophisticated UWXAFS[3] data analysis software package after correction of the differences between EXELFS and XAFS data[4]. In this paper we will discuss one of the fundamental differences, the background between the two types of data and how to renormalize the EXELFS χ-data to ensure the correct usage of XAFS programs.

In general, the data should be normalized by the background signal, contributed solely by the core electron being excited. In XAFS, it is standard to normalize the χ by the edge step instead of the background as a function of energy because the background is not accurately determined and also it is quite flat within the interested energy range. McMaster correction than is applied to compensate the slight decay of the background in higher energy region. In EXELFS, we work on much lower energy region and the background decreases dramatically with energy, i.e., exponential decay $(1 + \Delta E / E_0)^{-b}$ Here, $\Delta E/E_0$ could be 2 and b could be 3 in carbon K-edge which gives a factor of 1/27 decay. In this case, normalization with background function is preferred. This, however, requires an extremely accurate method to determine the correct background. The modeling of the true background necessitates to separate the contribution of the excited core electron from that contributed by all the rest of the energy loss processes. One possible way to accomplish this is to very accurately fit the pre-edge background and then extrapolate this beyond the edge and then subtract it from the total signal. Unfortunately, the core electron background decreases by more than an order of magnitude for the energy range of interest past the edge. Thus, small errors in the extrapolated background can give serious errors in the core electron background. In most cases, therefore, edge-step normalization is still used.

The background so obtained has a different energy dependence than that obtained by X-ray absorption. The ratio of the two backgrounds is:

$$n_e / \mu = \frac{\omega_0}{\omega} ln(\frac{q_m^2 v^2}{\omega^2} + 1) / ln(\frac{q_m^2 v^2}{\omega_0^2} + 1)$$

Here n_e/μ is the ratio of backgrounds between EXELFS and XAFS, ω (ω_0) is the angular frequency of electron energy loss ($\hbar\omega$, $\hbar\omega_0$), q_m is the maximum electron wave number

transverse to the beam introduced by scattering, and v is the speed of the fast electrons. n_e/μ could vary from $(\omega/\omega_0)^3$ to ω/ω_0, depending whether q_m is much less or much large than ω/v. To normalize correctly to the X-ray absorption χ, it is necessary to divided the χ value obtained from EXELFS by a n_e/μ factor[5]. Fig. 1 shows a comparison of the renormalized EXELFS χ-data of Al to the one obtained from XAFS. It is clear that the renormalization do reduce the difference between the EXELFS χ and XAFS χ. The reason for the remaining difference in low k area is not clear. This and the consequence of the results will be discussed in relation to quantitative EXELFS.

References

1. R. D. Leapmam, and V. E. Cosslett, *J. Phys.* D **9**, L.29-32 (1976).
2. M. Qian, M. Sarikaya, and E. A. Stern, *Ultramicroscopy*, **59**, 137-147 (1995).
3. E.A. Stern et al, the copyrighted UWXAFS 3.0 software.
4. M. Qian, M. Sarikaya, and E.A. Stern, submitted to *Micron*, (1996).
5. E. A. Stern, M. Qian, and M. Sarikaya, *MRS Symposium Proceedings* **332**, M. Sarikaya, et al. (eds.) (MRS, Pittsburgh, PA, 1994) pp. 3-14.
6. P. Lagarde, unpublished (1992).

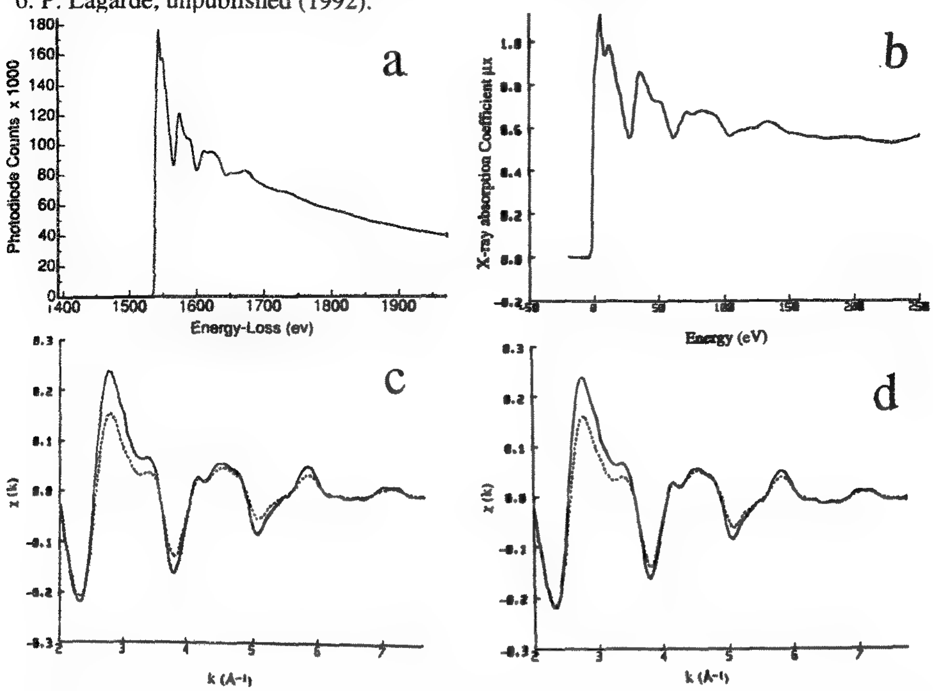

Figure 1 A comparison of EXELFS and XAFS data from Aluminum K-edge. (a) Al K-edge EEL spectrum, pre-edge background removed. (b) Al K-edge x-ray absorption spectrum[6], pre-edge background removed. (c) χ-data from XAFS (solid line) and EXELFS (dotted line). Both are normalized by edge step and no renormalization has been applied to the EXELFS data yet. (d) Same as (c) but the EXELFS data was renormalized.

CORRODED SPENT NUCLEAR FUEL EXAMINED WITH EELS

Edgar C. Buck, Nancy L. Dietz, and John K. Bates

Chemical Technology Division, Argonne National Laboratory, 9700 South Cass Avenue, Argonne, IL 60439

Direct disposal of spent nuclear fuel (SNF) into the proposed unsaturated geologic repository at Yucca Mountain, NV is being studied at several laboratories, including Argonne National Laboratory [1]. Corrosion tests with SNF are being conducted to understand the long-term behavior of SNF under conditions designed to simulate the unsaturated conditions at the site. The SNF used in this study was the Approved Testing Material (ATM)-106 with a burn-up of 43 MW•d/kg U [2]. A sample of ATM-106 fuel was exposed to dripping simulated groundwater for 271 days; after this time the experiment was terminated and the material removed for further study. Details of the testing methodology have been given by Finn et al. [1].

Previous attempts to study SNF with TEM have used ion milled samples [3], in this study we prepared the samples by ultramicrotomy which reduced the radiological hazard substantially. Particles of the reacted SNF were carefully removed from the surface with the aid of an optical microscope and diamond scribe and then embedded in a Medcast epoxy block. The selection of suitably sized particles (<5 μm in diameter) and correct orientation was critical to producing usable ultramicrotomed thin sections of SNF for TEM (see Fig. 1a). We have successfully produced TEM thin sections which can be used for detailed EELS. Analyses were performed on a JEOL 2000FXII/ Gatan 666 PEELS with a LaB_6 filament. The energy resolution was 1.6-1.8 eV.

Figure 1b shows the reacted fuel and an attached alteration phase. The objective of the TEM investigations has been to determine the nature of SNF corrosion through the identification of alteration phases and determination of the distribution of neutron capture and fission products. The alteration phase was identified by electron diffraction, x-ray energy dispersive spectroscopy, and EELS as a layered cesium molybdenum uranyl oxide hydrate, structurally related to phases of the becquerelite group uranium minerals. These uranyl oxide hydrate alteration phases will control the solubility of uranium and, hence, determine the long-term durability of the solid SNF waste form.

The large number of elements in SNF can make TEM/EDS analysis a challenge. As well as removing channel-to-channel gain variation in parallel detectors, the second-difference EELS technique serves as a frequency filter that selectively enhances the high frequency features, such as the $M_{4,5}$ absorption edges ("white lines") of rare earth elements (REE) and transuranics (TRU). In Figure 2, second-difference EELS of REE within the corroded particle of SNF is shown. The technique allows detection of REE that are present at < 20 ppm. In Figure 2a, the TRU M_4 and M_5 edges, which correspond to $3d_{3/2} \rightarrow 5f_{5/2}$ and $3d_{5/2} \rightarrow 5f_{7/2}$ transitions, respectively, have been used to detect low levels of TRU in the SNF. Overlap of TRU $N_{4,5}$ edges with the more intense REE $M_{4,5}$ edges effectively excludes this lower energy region from being used. An extremely high intensity, coupled with relatively long integration times (5-20 s) and repetitive runs, can allow detection of individual TRU elements, Np, Pu, and Am (see Fig. 2b). The calculated concentrations of TRU elements in ATM-106 SNF are 2590 ppm Pu and 115 ppm Am [2].

With ultramicrotomed TEM samples, we have been able to study a very hazardous material. The sections prepared were of such quality that highly detailed EELS analysis was possible allowing for the detection of low levels of transuranics in the reacted fuel. This work will assist in gaining an improved understanding of the corrosion mechanism of spent fuel in an aqueous environment [4].

References

[1] P. A. Finn et al., *Radiochimica Acta*, 66/67 (1994) 189

[2] R. J. Guenther et al., Characterization of Spent Fuel Approved Testing Material-ATM-106, *Pacific Northwest Laboratory Report*, PNL-5109-106 (1988)

[3] L. E. Thomas et al., *J. Nucl. Mater.*, 166 (1989) 243

[4] Spent fuel tests performed by P. A. Finn, D. J. Wronkiewicz, J. W. Emery, and J. C. Hoh. Work supported by the U.S. Department of Energy under contract W-31-109-ENG-38.

1a **1b**

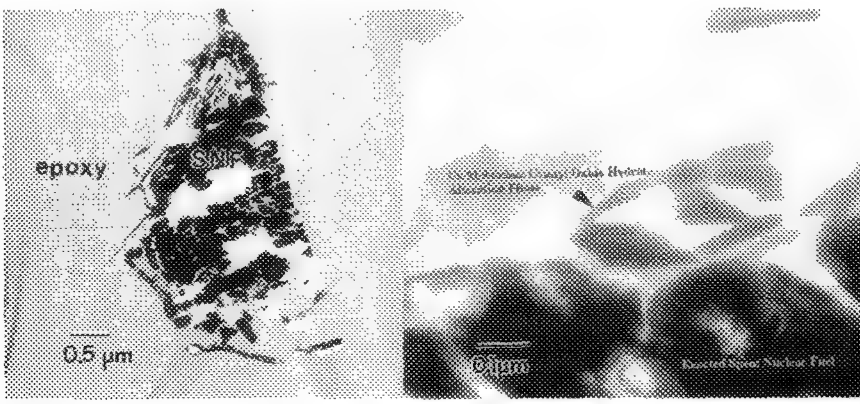

2a **2b**

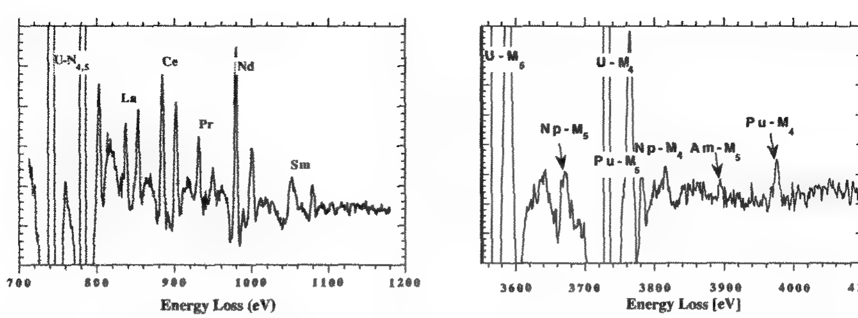

Fig. 1 (**a**) Low Magnification Image of Thin Sectioned SNF and (**b**) Image of Reacted SNF and attached Cs Mo Uranyl Oxide Alteration Phase.

Fig. 2 Second-Difference EELS of SNF Showing REE $M_{4,5}$ edges of La, Ce, Pr, Nd, and Sm. The major component of SNF, uranium, is visible in the two energy loss ranges analyzed. In (**a**) $N_{4,5}$ edges of U at 738 eV and 780 eV along with a number of REE and in (**b**) $M_{4,5}$ edges of U at M_5 = 3552 eV, M_4 = 3728 eV, along with the TRU elements, Np (M_5 = 3666 eV and M_4 = 3850 eV, Pu (M_5 = 3778 eV, M_4 = 3973 eV), and Am (M_5 = 3887 eV, M_4 = 4092 eV).

EFFECT OF THICKNESS VARIATIONS ON EELS SPATIAL-DIFFERENCE PROFILES

J. Bruley and D. B. Williams

Department of Materials Science and Engineering, Lehigh University, Bethlehem, PA 18015

This paper concerns the influence of sample thickness on spatial-difference spectra, and seeks to identify if an interface dependent signal may be generated as an artifact of grain boundary grooving. The spatial-difference profiling technique may be used to identify variations in composition and electronic structure across interfaces at sub-nanometer length scales.[1] The signal-to-background ratios and hence visibility of small changes to the near-edge structure and edge intensities are enhanced using this technique by removing intense energy dependent backgrounds. These backgrounds are assumed to be only slowly varying with respect to the electron probe position. A spatial-difference spectrum is generated from the difference between two spectra after suitable normalization or scaling. This scaling is achieved by either matching intensities of the background prior to a characteristic absorption edge (for compositional profiles) or by normalizing to some characteristic structure of the near-edge structure (for bonding profiles). The latter is performed typically after subtraction of a smooth power-law background modeled in the region immediately preceding the edge.

An increase in foil thickness increases the probability of plural scattering and thereby influences the core-loss absorption edge spectra in two ways: The first is through an increase and shape change of the smooth background relative to the signal intensity. The second involves plural scattering of the core-loss plus a valence (i.e., interband or plasmon) excitation and is given by the convolution between the single scattering edge structure with the low-loss valence spectrum. We have modeled the effect of a groove by generating a series of spectra of Al_2O_3 with a range of thicknesses, t, varying between 0..25 and 0.5 times the inelastic mean free path, λ. This is accomplished from the single scattering spectrum, S(E), using the following expression:[2]

$$P(E)=FT\{ZL(E)*\exp(FT\{S(E)\}*t/\lambda)$$

where FT{ } represents a Fourier transform and P(E) and Z(E) represents the plural scattering spectrum and zero-loss spectrum respectively. Figure 1 shows the $L_{2,3}$ edges for two thicknesses modeled in this series. The spectra are displayed with power-law backgrounds removed. The resultant edges have been normalized between 78 and 86 eV. A slight but visible difference is evident in the first near-edge peak at 79 eV. This difference might be mistaken for an interface-dependent effect. The lower curve of figure 2 shows the thickness profile of a model of a reasonably deep grain boundary groove. The integrated counts within 8 eV of the edge following the plural scattering analysis is shown in the upper curve and follows the trajectory of the foil thickness profile, as expected.

The spatial-difference spectrum, ΔI(E), between neighboring pixels having $\Delta t/\lambda=0.05$ were determined after normalizing the peak integral within a window, dE, 2 eV wide centered on the 79 eV resonance. The resultant spectrum is shown as the upper curve of figure 3. By re-normalizing the second spectrum with respect to the first by a factor, f = 1.0025, the near-edge structure characteristic of the bulk Al_2O_3 phase is completely removed (lower curve in figure 3). The residual intensity is equal to the difference in the systematic error of the two power-law background fits, dI^b.

$$\Delta I(E)=\frac{I_1(E)+dI_1^b(E)}{\sum(I_1+dI_1^b)}-f.\frac{I_2(E)+dI_2^b(E)}{\sum(I_2+dI_2^b)}$$

where, I, represents the counts within the edge. Figure 4 shows the r.m.s. value of the integrated counts across the grain boundary groove for the two normalization schemes. As anticipated, the profile generated using the re-normalized difference spectrum is constant across the grain boundary demonstrating that the thickness variation creates no interface signal at the near-edge region. The slight but finite increase in the absolute intensity seen at the interface with the normalized spectrum profile amounts to about 2 parts in 10^5 with respect to the integrated Al signal. For an experimental

spectrum with about 10^6 photodiode counts/channel, the noise level is over an order of magnitude higher than this and so such variations would probably remain invisible in the profile. Of course more sophisticated data processing routines, such as multiple least squares fitting, would avoid such errors due to incorrect normalization. However they are more time consuming and may not be much better at identifying real interface dependent signals.[3]

1. J. Bruley, V. Keast, D.B Williams, J.. Phys. D (Appl. Phys). **29** (1992) in press; J. Bruley et *al.*, J. Mater. Res. **9** (1994) 2574
2. D.L. Misell and A.F. Jones, J. Phys. D **2** (1969) 540
3. This work was funded by NSF DMR 93-06253

1

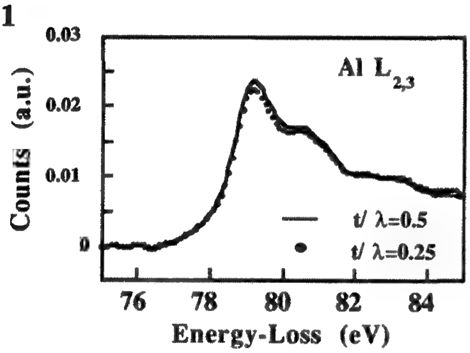

2

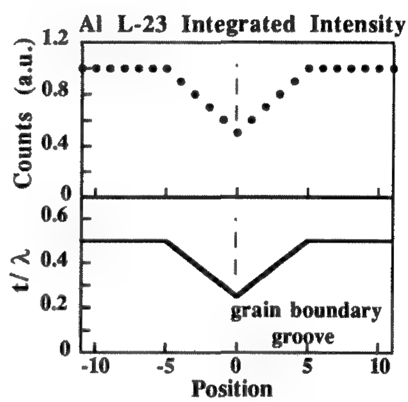

3

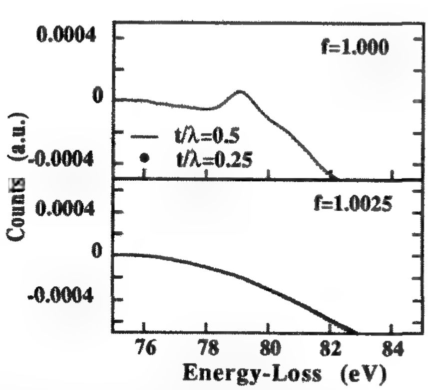

4

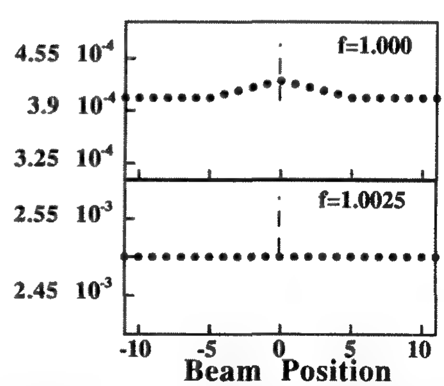

FIG 1 Al $L_{2,3}$ edge for t/λ=0.25 and 0.5 after AE^{-r} background removal and normalization (ΔE=20eV)
FIG 2 Profile of the integrated edge counts (before normalization) and the thickness profile of the proposed grain boundary groove.
FIG 3 The spatial difference spectra after signal normalization between 78-80 eV (upper curve) and after re-normalization to remove residual near-edge structure (lower curve).
FIG 4 Profiles of the r.m.s. spatial-difference signal across the groove (signal normalized to unity)

INTERLABORATORY STUDY OF K FACTOR DETERMINATION BY ASBESTOS-ANALYSIS LABORATORIES

S. Turner,* E.B. Steel,* and O.S. Crankshaw**

*Surface and Microanalysis Science Division, Chemical Science and Technology Laboratory, National Institute of Standards and Technology, Gaithersburg, MD 20899
**Center for Environmental Measurements and Quality Assurance, Research Triangle Institute, Research Triangle Park, NC 27709

The National Voluntary Laboratory Accreditation Program (NVLAP) of the National Institute of Standards and Technology (NIST) has been accrediting laboratories for the analysis of asbestos by transmission electron microscopy since 1990. As part of the quality assurance procedures for the program, laboratories are required to determine k factors for Na, Mg, Si, Al, Ca and Fe.[1] An interlaboratory study has been conducted by NIST and the Research Triangle Institute (RTI) in which laboratories analyzed thin film standards SRM 2063 or SRM 2063a.[2,3] This work reports results of initial analysis of the data.

For this study, laboratories were required to collect three spectra from the thin film SRM, to determine average k factors and standard deviations and to supply information concerning instrumentation, software and the setup for data collection (eg., take-off angle, tilt of grid, keV of transmission electron microscope). The laboratories collected data at either 80, 100, or 120 keV. All but two laboratories used energy dispersive x-ray detectors that have Be windows with a reported thickness ranging from 4 to 12 micrometers.

Seventy-two laboratories returned results; the data from three laboratories was incomplete. K factor determinations were reviewed and were corrected for errors in calculation. Histograms and plots of the corrected k factor data are given in Figures 1 and 2. For comparison purposes, k factors for Mg, Ca and Fe relative to Si and for Mg to Fe were determined from spectra generated from the NIST Desktop Spectrum Analyzer program (DTSA) for the reported range of transmission electron microscope voltages, Be window thicknesses and detector take-off angles with the assumptions of 0.1 μm ice, 0.1 μm Si dead layer, and a 90° angle between the direction of the x rays and the detector window and chip.[4] The k factors from generated spectra are indicated on the histograms and plot. The k factors for many of the laboratories are outside the expected range. The reasons for the outlier values are not known in all cases but likely reasons include absorption problems, fluorescence, excessive beam dosage and incorrect determination of background-subtracted counts.

References

1. E.B. Steel, S. Turner, and H.W. Berger, *NVLAP Program Handbook for Airborne Asbestos Analysis,* NISTIR 89-4137 (1989).
2. Certificates of Analysis for SRMs 2063 and SRM 2063a, Microanalysis Thin Film Mg-Si-Ca-Fe, Standard Reference Materials Program, NIST, Gaithersburg, MD 20899.
3. E.B. Steel, D.E. Newbury, and P.A. Pella, *Analytical Electron Microscopy-1981,* (1981)65.
4. C.E. Fiori, R.L. Myklebust and C.R. Swyt, "NIST-NIH Desktop Spectrum Analyzer" Standard Reference Program Database 36, NIST, Gaithersburg, MD 20899.

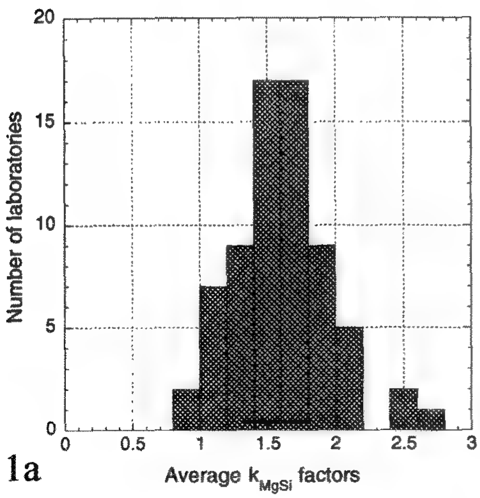

1a

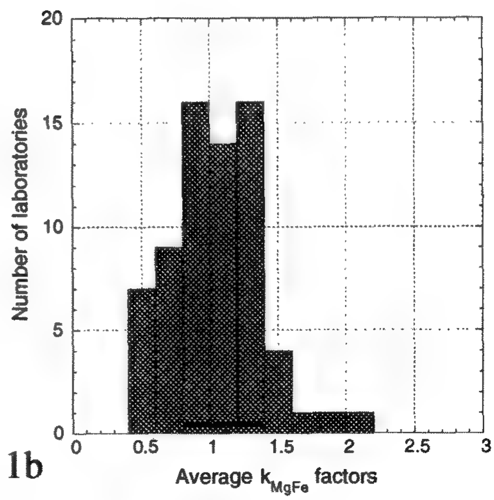

1b

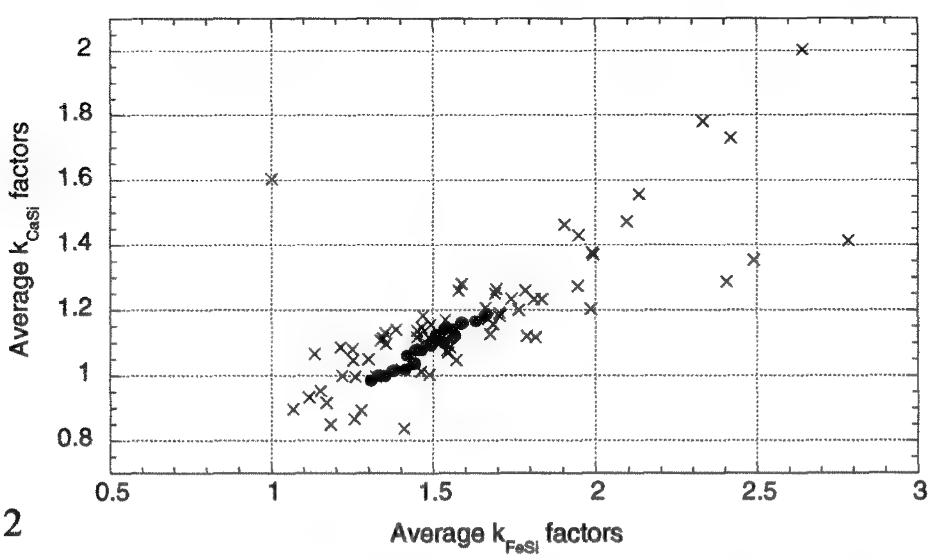

2

FIG. 1. Histograms of Mg k factors relative to Si (a) and Fe (b). The black bars indicate the range of k factors obtained by generation of spectra using DTSA.
FIG. 2. Ca k factors relative to Si plotted against Fe k factors relative to Si ("x"s indicate values reported by the laboratories; black dots indicate k-values calculated from generated spectra). Many of the laboratory values to the left of the k factors from generated spectra likely result from absorption of x rays or fluorescence of the sample. Many of the laboratory values to the right of the k factors from generated spectra likely relate to background-subtraction problems.

CHARACTERIZATION OF Mo/SiO_2 INTERFACIAL REACTIONS IN METAL HALIDE ARC TUBE BY ANALYTICAL TEM

S.J. Jeon*, C. Sung* and Chung Chao**

*Department of Chemical and Nuclear Engineering, Center for Advanced Materials, University of Massachusetts, Lowell, MA 01854, **Osram Sylvania Inc., Manchester, NH.

The purpose of this study is to investigate the interfacial reactions between Mo foil and quartz in metal halide arc tubes. After welding to a tungsten cathode, the Mo foil was specially treated before Mo/SiO_2 pinch seal operation. Mo foils in arc tubes show different performance in lamp depending on the type of the treatment. Mo/SiO_2 interfacial reactions and amounts of Mo diffusion into the SiO_2 were analyzed using TEM, SEM and EDS in order to understand the different properties of arc tubes.

Arc tubes were treated with one of the following conditions : (A)untreated, (B)dry hydrogen fired, (C)process "B" plus humidity exposure. Cross-sectional TEM and SEM samples in the longitudinal direction of the arc tube through the center of Mo foil were prepared. Two Mo/SiO_2 interfacial areas, one near the end of the W cathode and the other the longitudinal center of the foil were compared each other.

Fig. 1 shows the cross-sectional SEM image in the longitudinal direction of the arc tube. The long, narrow image in the center area is a cross-section of Mo foil which was sealed in SiO_2. Both sides of the foil are welded to a W cathode(right side) and Mo wire(left side). Fig. 2 shows TEM micrograph of the Mo/SiO_2 interfacial reactions of center area treated with method A. Amorphous Si-rich Mo oxide(Fig. 3) layers were formed and Mo-rich Si oxides(Fig. 4) were revealed as a microcrystalline phases or amorphous layers. The Mo/SiO_2 interfacial area of samples treated with method B or C showed similar phases and reactions while the amorphous Mo-rich Si oxide layer was not observed in samples treated with method B and microcrystalline Mo-rich Si oxide was not found in samples treated with method C. This result implies that rate of Mo/SiO_2 interfacial reactions are decreased by hydrogen or humidity treatments. Inhibition of reaction by these treatments was especially remarkable near the end of the W cathode. Fig.5 shows complex Mo/SiO_2 interfacial reactions of the edge area near the W cathode treated with method A. Complicated phases were observed in this region: amorphous layers such as Mo-rich W oxide and Si-rich Mo-W oxide, W-rich particles, Mo-rich particles, crystalline Mo-rich Si oxide with and without W element(see schematic diagram, Fig. 6). On the other hand, only amorphous Si-rich Mo oxide layer was found at the reaction zone treated with method B or C.

The thickness of Mo diffusion layer into the SiO_2 were measured using EDS to conform the amount of interfacial reactions. Large content of Mo was detected upto 15um from the interface in sample treated with method A. It was of significance that the Mo diffusion layer thickness was decreased to 1um in sample treated with method C. Reduction of interfacial reactions by hydrogen or humidity treatment implies good adherence of Mo/SiO_2 interface based on our microstructural observation.

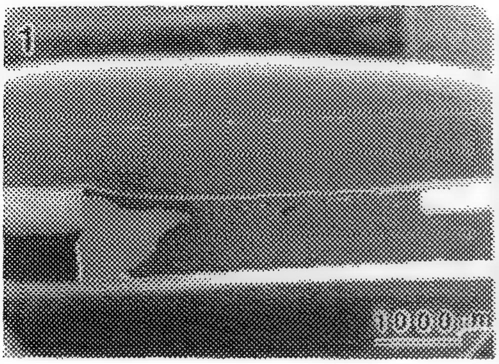

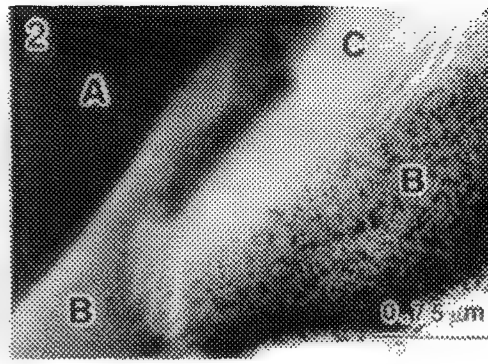

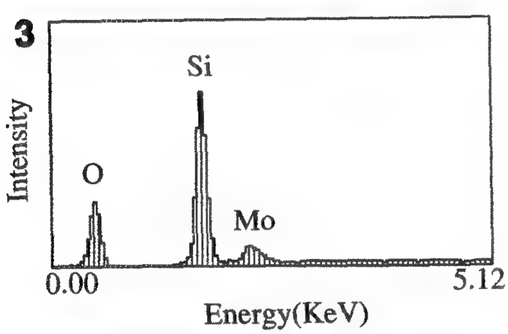

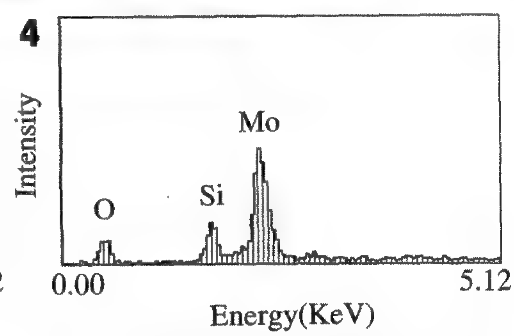

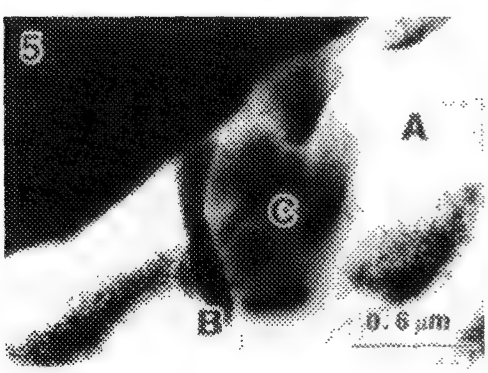

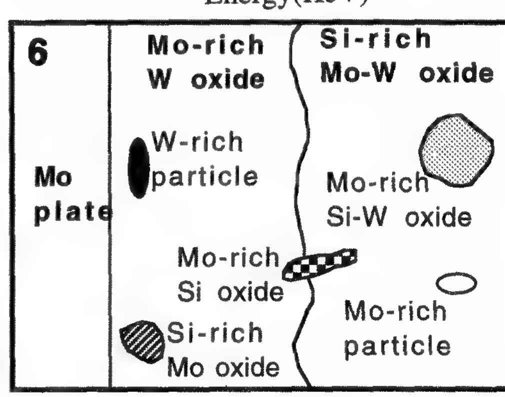

FIG.1 Cross-sectional SEM image of arc tube treated with methode A.

FIG.2 TEM micrograph showing Mo plate(A), microcrystalline Mo-rich Si oxide(B) and amorphous Si-rich Mo oxide(C).

FIG.3 EDXS spectrum from Si-rich Mo oxide.

FIG.4 EDXS spectrum from Mo-rich Si oxide.

FIG.5 TEM micrograph showing amorphous Mo-rich W oxide(A), crystalline Mo-rich Si oxide(B) and amorphous Si-rich Mo-W oxide(C).

FIG.6 Schematic diagram showing Mo/SiO_2 interfacial reactions.

INTEGRATED COMPUTER DATA ACQUISITION AND CONTROL IN ANALYTICAL ELECTRON MICROSCOPY

J. K. Weiss, W.J. de Ruijter and Douglas. W. Cosart

EMiSPEC Systems, Inc., 2409 S. Rural Rd., Suite D, Tempe, AZ 85282

Computers were considered to be mainly "add-on" equipment for analytical electron microscopes until only the last several years. Before that time, although most microscopes had been microprocessor-controlled for at least five years, the only use of more conventional computers was for controlling spectrometers connected to the microscope. The fundamental limitation of computers for scanned imaging was mostly one of speed. Spectra could be acquired and displayed in real time even by computers of early 1980's vintage, whereas only modern computers are capable of acquiring and displaying video rate digital scanned images.

The result of this fundamental difference in signal rates between imaging and spectroscopy is that separate computer systems have been developed for imaging and spectroscopy. Even in the cases where spectroscopy systems (most notably EDX systems) have integrated some image acquisition capabilities, or where imaging systems have integrated some spectroscopy, the design of the systems is virtually always centered around either imaging or spectroscopy. Even recent systems which do a reasonable job of integrating imaging with spectroscopy are still centered on one type of spectroscopy, even though a large percentage of microanalytical instruments are equipped with more than one spectroscopic detector.

There are several problems with this "one computer per detector" design. First, a user must learn each system, which involves learning about both the software and the computer platform. Unfortunately, for example, it has developed that the most common computer platforms on a microanalytical TEM are a PC-based computer for microscope control, a UNIX workstation for EDX control, and a Macintosh for PEELS control. In addition to learning each of these systems, the user must also struggle with interchanging data between the acquisition computers and off-line processing computers. A second problem which becomes obvious is the expense of equipping a lab with all of the above systems and their necessary peripherals.

The most serious limitation of discrete computers for acquisition and control lies in the poor communication between those systems. Even on the systems where there is some communication (for example using the serial communications port to the microscope CPU) the speed of the communication link (usually between 0.1 and 1 sec. per command) makes real-time interaction between the computers unfeasible. The net drawback of the poor inter-system communication is the lack of synchronous acquisition using all of the signals available on the microscope.

Within the last two years, technological advances in computer hardware and software have eliminated the need for discrete computer data acquisition systems. Fast CPU's, inexpensive memory and hard disk space, high-resolution video cards and monitors, fast 32-bit I/O buses and multitasking 32-bit operating systems allow a single computer to do everything from slow serial spectroscopy to real-time digital scanned imaging. There are currently several commercial and academic development efforts under way to take advantage of computer advances in order to provide integrated data acquisition and control.[1]

The most obvious techniques promised by integrated AEM data acquisition are interactive spectroscopic surveying, multi-spectroscopic elemental mapping, and spectrum imaging. Spectroscopic surveying has existed in some form on some EDX acquisition systems for several years. Using this technique, the user can position the electron beam interactively by moving a marker on an acquired image, while observing in real time the spectra acquired from that position. This technique has proven to be extremely useful for quickly identifying regions of interest from which to acquire maps. In many cases, the user can quickly reject an area which is unsuitable for a time-consuming map, and in other cases enough information is available from the survey so that an entire map is not necessary.

On analytical microscopes with more than one spectroscopic detector, much can be gained by acquiring all spectroscopic signals synchronously.[2] The information from the different detectors is in general complementary, and the synchronous acquisition provides spectroscopic information which is exactly registered in position and/or time. The type of complementary information which is available includes:

1) EDX and Auger - bulk and surface information
2) EDX and PEELS - high sensitivity for low- and high-Z elements
3) EDX and CL - localized composition and electronic structure

Spectrum imaging is attracting renewed interest lately, mainly because it is now technologically feasible. There are obvious advantages to saving the spectra at each point in a scan, as opposed to discarding the original data after processing each point because it gives the user the opportunity to process the data as many times as are necessary to extract the useful content.[3] The ability to perform sophisticated post-processing not possible during real-time acquisition makes spectrum imaging very attractive, especially for systems with significant spectroscopic peak overlap, low signal-to-background ratios, low elemental concentrations or spectral artifacts. Although a typical spectrum image uses 5-10 megabytes of storage space, the advent of fast, inexpensive (< $0.25/MB), high capacity (> 100 MB) removable storage media allows current users to always store all spectra acquired during elemental mapping.

Multi-spectroscopic surveying, mapping and spectrum imaging requires a single computer to coordinate beam scanning with acquisition from all of the detectors. To perform these techniques with "one computer per detector" control systems, those systems must be capable of accepting real-time external control and data transfer. Although it is technologically possible to transfer spectral data (even for multiple spectroscopies) in real time over an interface such as ethernet or SCSI, none of the commercial data acquisition systems provides such an option in their control software.

We have developed a data acquisition system that is capable of both directly driving scanning microscopes and also acquiring from most of the spectroscopic detectors in common use. The system consists of hardware providing the signals necessary for rastered scanning and for controlling and acquiring from the imaging and spectroscopic detectors. The hardware generally interfaces directly to each detector, as opposed to interfacing through that detector's control system, in order to acquire data at the full rate available from the detector.

One cannot underestimate the importance of advances in software interfaces, which have typically lagged well behind hardware improvements. We have taken advantage of modern graphical user interfaces available on PC computer platforms which make complex control and acquisition setup approachable by non-experts. A single application integrates control panels for all available hardware with data display, manipulation, and processing. With such a software interface, and the appropriate hardware interface, we can approach the ideal of controlling all aspects of microscope control and acquisition from a single workstation.

1. M. Tence et al., *Ultramicroscopy*, 58(1995)42.
2. P. J. Wright, *Proc. Microscopy and Microanalysis 1995*, (1995)392.
3. J. Bruley et al., *Proc. Microscopy and Microanalysis 1995*, (1995)312.

RECENT PROGRESS IN ALCHEMI ANALYSIS

Ian M. Anderson and J. Bentley

Metals & Ceramics Division, Oak Ridge National Laboratory, PO Box 2008, Oak Ridge, TN 37831-6376

The scope of microanalysis encompasses a variety of the charactersitics of a small volume of material, from its composition to its electronic structure. One such characteristic is the local environment of the elements in the volume, including the identity and coordination of the near-neighbors of each element. For multisublattice crystals, this level of the chemistry is characterized by the site-occupancies of the elements composing the crystal. Atom-location by channeling-enhanced microanalysis (ALCHEMI) is a powerful technique for the experimental measurement of these site-occupancies. Following its introduction,[1] ALCHEMI enjoyed initial successes for the study of cation distributions in oxide minerals.[2] However, the technique was prone to large systematic errors for analyses that required soft (≤ 4 keV) X rays, because of so-called ionization delocalization.[3,4] Improvements to the original formulation of ALCHEMI have aimed to improve the low statistical confidence level of the technique,[5] to explicitly address ionization delocalization,[6,7] and to correct for anti-site defects.[7-9] The present paper will illustrate these improvements while emphasizing the basis underlying ALCHEMI analysis.

ALCHEMI can be performed on any transmission electron microscope (TEM) equipped with an energy-dispersive X-ray (EDX) detector, thus benefitting from both the high spatial resolution and wide availability of TEM. The technique exploits the variation in the thickness-averaged electron intensity within the unit cell that arises due to dynamical electron diffraction (electron channeling) when the specimen is oriented such that one or more low-index reflections of the crystal are strongly excited. This variation effects a corresponding variation in the characteristic X-ray intensities of the elements composing the crystal. However, there are two additional requirements for the variation in these X-ray intensities to discriminate between two sublattices of the crystal: (1) that the two sublattices be separated onto alternating atomic planes or columns at the channeling orientation and (2) that there be a difference in the electron intensities at the sublattices of the crystal, which occurs only if a superlattice reflection of the crystal is strongly excited. Fig. 1 shows the variation of the delocalization-corrected intensity ratios $L_{FeX}(r_X - 1)$ with specimen orientation at (a) {110} and (b) {200} systematic orientations for B2-ordered $Fe_{50}Al_{45}Cu_5$. The effect of the channeling on the X-ray intensity of elements X = {Fe, Al, Cu} is characterized by $(r_X - 1)$, where $r_X = I_X^{(\xi)} / I_X^{(0)}$ is the ratio of the characteristic X-ray intensity of element X at a given orientation (ξ) to its intensity at a reference orientation (0) that is ideally free of channeling effects. The delocalization correction coefficients for these plots are $L_{FeAl} \approx 1.4$ and $L_{FeCu} \approx 1.0$, and θ_{110} and θ_{200} are the Bragg angles for the {110} and {200} fundamental reflections, respectively. Fig. 1 shows that there is no site-discrimination at the {110} systematic, where all planes are of equal composition and no superlattice reflection of the alloy is excited, but that at {200} where the 'Fe' and 'Al' sublattices are separated onto alternating planes there is a pronounced difference in the responses of the Fe and Al host elements over the range of orientations where the {100} superlattice reflection is strongly excited. However, a superlattice reflection may not be strongly excited under any conditions if the elastic scattering powers of the alternating planes are similar. In this case, the corresponding systematic orientation may exhibit lower site-discrimination than an orientation having a stronger superlattice reflection but at which the sublattices of the crystal are less separated.[10] Similar considerations limit the benefits of axial relative to planar orientations for ALCHEMI analysis. The size of the channeling effect at a zone axis is usually greater than the corresponding effect at a systematic row because more low-index reflections are strongly excited. However, this larger effect may not indicate better site-discrimination. Multivariate statistical analysis methods have been used to separate the delocalization and site-distribution components in a series of ALCHEMI spectra acquired at the <111> axial orientation from an $L1_2$-ordered γ' particle in a René 95 nickel-base superalloy.[11] These studies indicate that site-distribution information is conveyed by only a small fraction of the large channeling effect at <111>. Similar studies at the <001> and <011> zone axes of B2-ordered iron aluminides show that although the channeling effect is larger at the zone axes than at the {200} systematic orientation, the extracted site-distributions have poorer precision.[12]

References

1. J.C.H. Spence and J. Taftø, *J. Microsc.* 130(1983)147.
2. J.C.H. Spence et al. in *Mater. Res. Soc. Symp. Proc. 62*, MRS, Pittsburgh, PA (1986)153.
3. S.J. Pennycook et al., *Appl. Phys. Lett.* 44(1984)547.
4. J. Bentley, *Proc. 44th Ann EMSA* (1986)704.
5. C.J. Rossouw et al., *Phil. Mag. Lett.* 60(1989)225.
6. M.G. Walls, *Microsc. Microanal. Microstruct.* 3(1992)443.
7. I.M. Anderson and J. Bentley, *Proc. 13th ICEM: Electron Microscopy 1994* 1(1994)609.
8. M.G. Walls, *J. Physique* 4(1993)2155.
9. D.H. Hou and H.L. Fraser, *Proc. 53rd Ann MSA* (1995)128.
10. P.G. Kotula et al., these proceedings.
11. I.M. Anderson and J. Bentley, these proceedings.
12. Research at the Oak Ridge National Laboratory (ORNL) SHaRE User Facility was sponsored by the Division of Materials Sciences, U.S. Department of Energy, under contract DE-AC05-96OR22464 with Lockheed Martin Energy Research Corp., and by an appointment to the ORNL Postdoctoral Research Associates Program, which is administered jointly by the Oak Ridge Institute for Science and Education and ORNL.

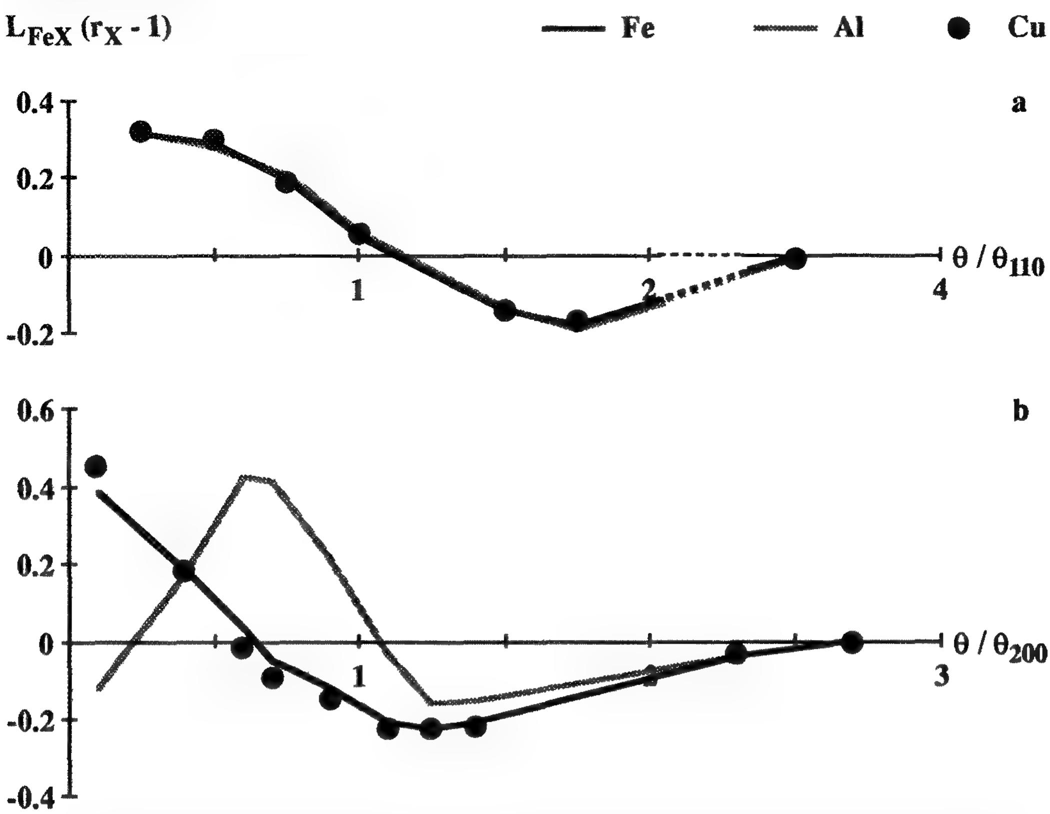

FIG 1 - Variation of delocalization-corrected intensity ratios $L_{FeX}(r_X - 1)$ with specimen orientation at the (a) {110} and (b) {200} systematics in B2-ordered $Fe_{50}Al_{45}Cu_5$. See text for details.

ANALYTICAL ELECTRON MICROSCOPY OF NANOMETER-SIZE PRECIPITATES IN Al ALLOYS WITH A 200-kV FIELD-EMISSION TEM

J. M. Howe,* S. P. Ringer,** B. C. Muddle** and I. J. Polmear**

*Department of Materials Science and Engineering, University of Virginia, Charlottesville, VA 22903
**Department of Materials Engineering, Monash University, Clayton 3168, Victoria, Australia

Certain trace elements are known to have a pronounced effect on the nucleation kinetics of metastable phases in Al alloys.[1] This provides many opportunities for alloy design. Understanding the role of trace elements in the precipitation process is difficult because they are typically present at levels of less than 0.1 at.% and involve early stages of clustering or segregation to precipitates.[2,3] This paper presents recent results from the application of a 200 kV thermal field-emission gun (FEG) transmission electron microscope (TEM) to study trace element additions and the early stages of precipitation in Al alloys, using the case of an experimental alloy designated ALMAGEM as an example.[4]

An Al-2.41Cu-0.34Mg-0.1Si-0.04Ge alloy was cast into a book mold, homogenized, solution treated at 525°C, water quenched and aged for 12.5 h at 170°C to peak hardness. Disks 3 mm in diameter were electropolished in a HNO_3/methanol solution and examined at 200 kV in a JEOL 2010F FEG TEM with a high-tilt (±30°) pole piece. The microscope has an information limit of about 0.14 nm. A probe size of 0.4 nm full width at half-maximum was used to obtain energy-dispersive X-ray (EDX) spectra and electron diffraction data from nanometer-size precipitates in the alloy.

In the peak hardness condition, the alloy is comprised of at least three metastable phases, including Cu-rich G.P. zones and θ' plates on the {100} planes, and rods along the <100> directions.[5] The origin of the <100> rods and their role in alloy strengthening is of primary importance in this alloy. Figure 1 shows a typical bright-field TEM image of the alloy in a <100> orientation. The dark spots (arrows) are the <100> rods seen end-on. Figure 2 shows a HRTEM image of two rods in the alloy about 2 nm in diameter. In contrast to the surrounding Al matrix, the <100> rods do not look crystalline but display an amorphous structure. High-resolution TEM images of similar amorphous looking GPB zones have been observed in an Al-Cu-Mg alloy.[6] Electron diffraction patterns taken with a 0.4 nm probe at locations A and B in Fig. 2 are shown in Fig. 3. The fundamental <200> and <220> matrix reflections are evident in both patterns. Pattern B from the <100> rods displays additional intensity which appears as diffuse speckles throughout the pattern, again indicating a lack of crystallinity in the rods. An EDX spectrum obtained by accumulating counts from several rods such as those in Fig. 2 is shown in Fig. 4. The rods are clearly enriched in Cu and Mg in roughly equal amounts. In addition, Ge and Si are present in the precipitates at quite detectable levels even though there is less than 0.1 at.% of either element in the alloy. These results are in good agreement with recent atom-probe field ion microscopy on the same alloy.[5] The electron diffraction patterns and EDX spectrum in Figs. 4 and 5 were typical of many of the rod-shaped precipitates examined and illustrate the capability of a 200 kV FEG TEM for analyzing segregation of trace elements to nanometer-size precipitates in Al alloys. Analysis of trace additions to other alloys will also be presented.[7]

References

1. A. Mukhopadhyay et al., in *Proc. Morris E. Fine Symp.*, TMS, Warrendale, PA (1991) 283.
2. K. Hono, T. Sakurai and I. J. Polmear, *Scripta Metall. Mater.*, 30 (1994) 695.
3. J. M. Howe, *Phil. Mag. Lett.*, 70 (1994) 111.
4. G. B. Brook, *Aircraft Engineer*, 1 (1975) 32.
5. S. P. Ringer et al., to be published in *Proc. 5th Intl. Conf. Al Alloys* (1996).
6. V. Radmilovic et al., *Scripta Metall.*, 23 (1989) 1141.
7. This research was supported by the National Science Foundation under grant DMR-9302439 (JMH) and by the Australian Research Council (SPR, BCM and IJP).

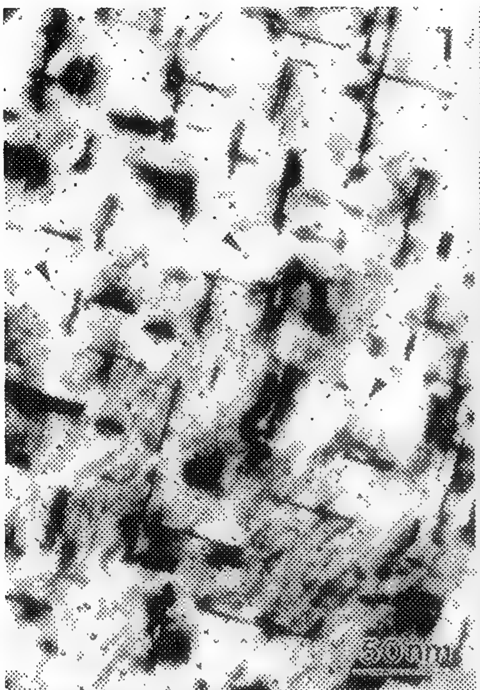

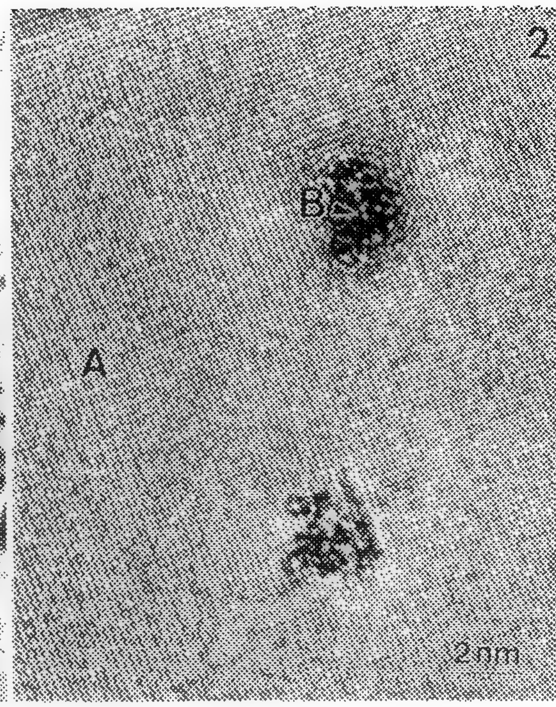

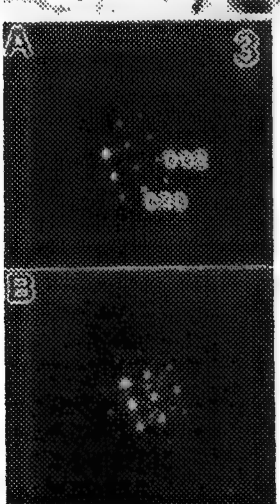

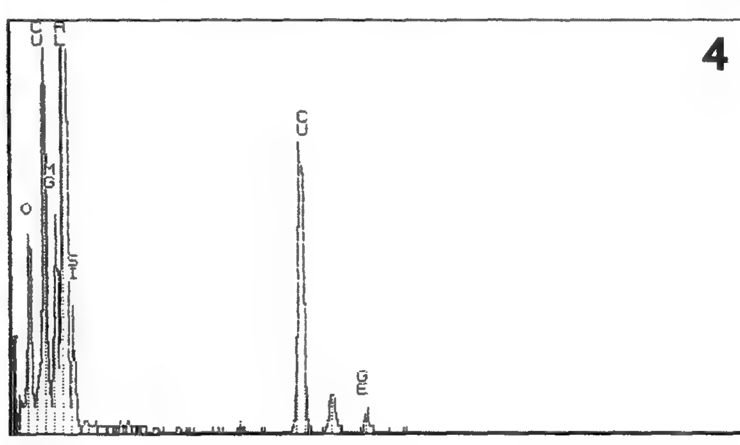

FIG. 1 - Bright-field TEM image of G.P. zones, θ' plates and <100> rods in ALMAGEM alloy.
FIG. 2 - High-resolution TEM image of <100> rods seen end-on in the JEOL 2010F microscope.
FIG. 3 - Electron diffraction patterns obtained from (A) the matrix and (B) the <100> rod in Fig. 2.
FIG. 4 - EDX spectra showing segregation of trace elements Si and Ge to the <100> rods.

QUANTITATIVE HIGH-SPATIAL-RESOLUTION MICROCHEMICAL ANALYSIS OF Fe-Co-Ni TRANSFORMATION-TOUGHENED STEELS

H.E. Lippard, V.P. Dravid, G.B. Olson

Department of Materials Science & Engineering, Northwestern University, Evanston, IL 60208, USA

Superior strength-toughness combinations can be obtained in AerMet100 by an austenite→martensite phase transformation of small intralath austenite precipitates. The enhanced toughness in these alloys has been attributed to the presence of "metastable" austenite precipitates, the stability of which is intimately related to the size and composition.[1] The austenite precipitates require high stability to resist transformation under all stress conditions except when in the triaxial stress field of a crack tip. The two primary factors determining austenite stability are size and composition. Thus the microstructure-property correlations and further alloy development require quantitative microchemical analysis of austenite precipitates in the 4-10nm size range.

Of the possible analytical techniques, only analytical electron microscopy (AEM) and atom probe-field ion microscopy (AP-FIM) merit consideration by achieving quantitative composition analysis with very high spatial resolution. After exploring both avenues, AEM was chosen as the analytical technique based on its superior speed, counting statistics, and versatility. However, this alloy microstructure pushes the limit of analytical energy dispersive spectrometry (EDS) analysis. Specimen preparation by electropolishing yields high quality electron transparent samples but thicknesses less than 10nm can not be reliably achieved. This necessitates analysis of precipitates embedded in a matrix of similar composition where more than half of the interaction volume is the matrix. Both the matrix and precipitates contain all of the major alloying elements listed in Table 1. The largest composition difference between matrix and precipitate is ~30wt% in the FCC stabilizing element nickel.

The data necessary for deconvolution of the precipitate EDS signal is collected by STEM annular dark field (ADF) imaging for precipitate size, low-loss parallel electron energy loss spectroscopy (PEELS) for local foil thickness, and EDS. The precipitate composition is extracted using a calibrated matrix composition, a measured local foil thickness, and a known spherical precipitate geometry. This method allows analysis of any particles where the precipitate fraction of the interaction volume is greater than 0.1. Monte Carlo simulations were conducted using parameters matching the experimental conditions to confirm the EDS results. The effect of probe size, foil thickness, precipitate composition, and precipitate position were evaluated in the simulations.

Figure 1 is a dark field TEM image displaying the two morphological forms of austenite: (A) large interlath precipitates and (B) small intralath precipitates. EDS analysis reveals the interlath austenite is too large and insufficiently enriched in FCC stabilizing elements (25wt% nickel) to provide transformation toughening. The intralath precipitates show 35-40wt% nickel enrichment levels and their 4-5nm size is sufficient to provide an transformation toughening enhancement. Figure 2 displays the EDS results from both types of austenite precipitates. The nickel content of the matrix is 10wt%. Results from the Monte Carlo simulations and EDS analysis of an Fe-15Co-10Ni ternary alloy will be presented. The ternary alloy allows the austenite precipitation to be studied without the effect of simultaneous carbide nucleation and growth.

References

1. G.B. Olson, in *Innovations in Ultrahigh-Strength Steel Technology*, Washington, D.C.:U.S. Government Printing Office (1990) 3.
2. This work was supported by ARO Grant # DAAH04-93-G-0471/P01 and an NSF Graduate Fellowship (HL).

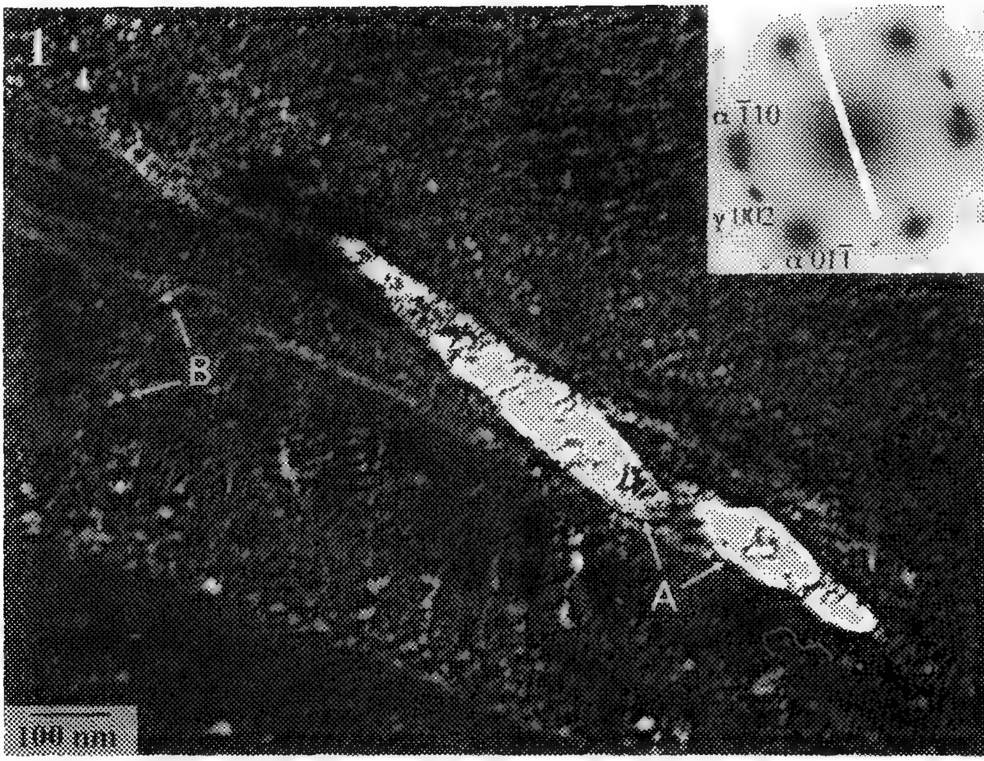

Table 1. - AerMet100 composition

	Composition (wt%)
Fe	balance
Co	13.42
Ni	11.03
Cr	3.00
Mo	1.18
C	0.238

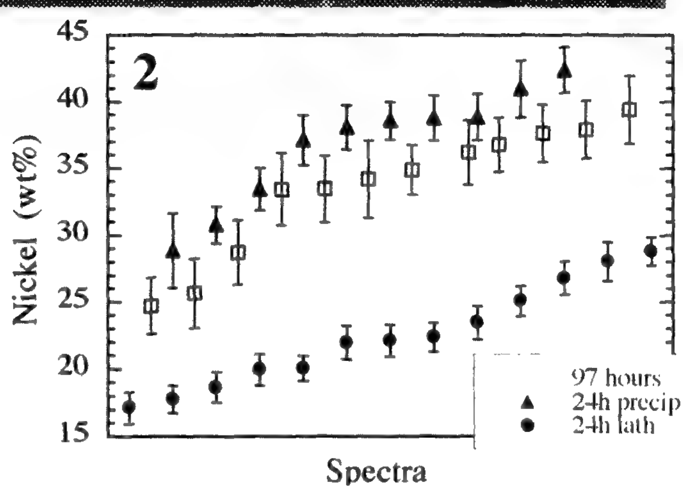

FIG. 1. - TEM dark field of austenite precipitates showing: (A) large interlath precipitates, (B) small intralath precipitates.
FIG. 2. - Nickel content of intralath and interlath precipitated austenite acquired by STEM EDS analysis.

INVESTIGATION OF CoPt AND CoPt + ZrO_x THIN FILMS FOR MAGNETIC STORAGE MEDIA USING HIGH-RESOLUTION ANALYTICAL ELECTRON MICROSCOPY

R. A. Ristau and K. Barmak

Department of Materials Science and Engineering, Lehigh University, Bethlehem, PA 18015

Materials for very high density magnetic storage media, with capacities of 10 Gbits/in^2 and beyond, require high coercivity and high signal to noise ratio. To achieve storage densities of this level engineering of the material to produce very fine, magnetically decoupled domains is necessary. We have characterized the microstructure and microchemistry of 10 nm thick CoPt and CoPt + ZrO_x thin films, as deposited and annealed, using transmission electron microscopy (TEM) and nanometer-scale energy dispersive x-ray spectroscopy (EDS).

CoPt has a very high coercivity (H_c) when annealed to produce the ordered $L1_0$ phase.[1] Annealing also increases grain size which reduces the signal to noise ratio.[2] Co-sputtering CoPt with ZrO_x was intended to reduce grain size. TEM micrographs in Figure 1 show that grain growth was dramatically reduced in the CoPt + ZrO_x films. Essential to the development of optimum material properties are quantified grain size measurements, yet owing to the small grain size and the complexity of TEM images due to diffraction contrast there are few systematic studies of grain size in thin films.[3] Accurate grain size statistics in our films were obtained using a semi-automated image analysis technique, whereby hand-traced composites of several TEM images were digitally analyzed. In this way, data was routinely collected from more than 1000 grains per specimen to grain sizes below 1 nm. This represents at least an order of magnitude improvement in the lower limit of grain size measurements over previous thin film studies.[3] A plot of the mean grain size for CoPt and CoPt + ZrO_x films at several anneal temperatures in Figure 2 shows the reduction in grain size in the latter for all anneal temperatures. Also, the distribution of grain sizes was far narrower in the CoPt + ZrO_x films, as shown in the histograms in Figure 3. It is believed that a large distribution in grain size as well as a large mean grain size both have the undesired effect of reducing the signal to noise ratio.

Co-sputtered CoPt + ZrO_x films show a microstructure in the as-deposited state that is near the desired form of isolated regions of ferromagnetic material (CoPt) surrounded by nonferromagnetic material (ZrO_x), shown in Figure 4a. After annealing to produce the $L1_0$ ordered phase, however, the interconnected structure of the ZrO_x was observed to be broken up into particles (Figure 4b). Using EDS at ~1 nm resolution with Lehigh University's VG HB603 STEM, elemental maps of Co, Pt, and Zr were obtained. These show (Figure 5) that the ZrO_x forms discrete islands either between or above/below the CoPt grains. From this data it is clear that the present annealing conditions do not allow both the desired microstructure and magnetic properties to persist. Analysis techniques on this scale will have a major impact on the optimization of the material properties of high density magnetic storage media.

1. J. A. Aboaf et al., *IEEE Trans. Mag.*, 19 (1983) 1514.
2. T. P. Nolan et al., *J. Appl. Phys.*, 73 (1993) 5566.
3. H. P. Longworth and C. V. Thompson, *J. Appl. Phys.*, 69 (1991) 3929, and references therein.
4. The authors gratefully acknowledge Kevin Coffey, J. Kent Howard, and Michael Parker at IBM System Storage Devices, San Jose, CA for their assistance and for providing the samples. This research is supported by NSF grants DMR-9256332 and DMR-9458000.

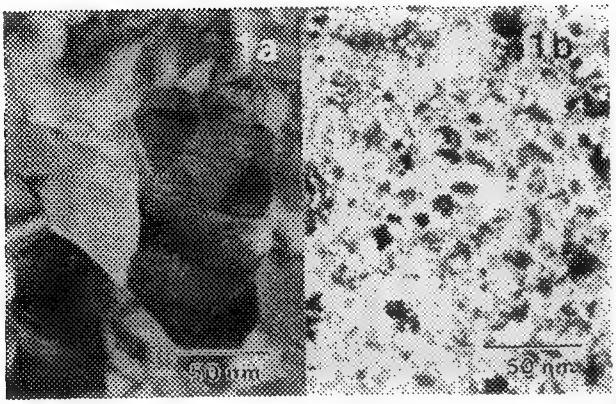

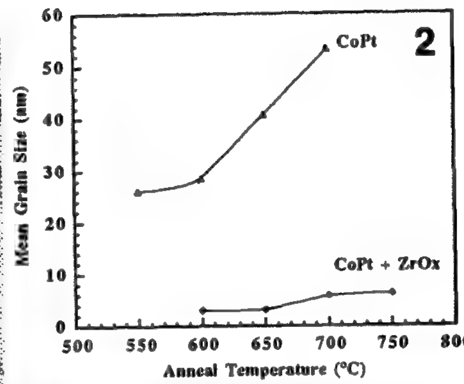

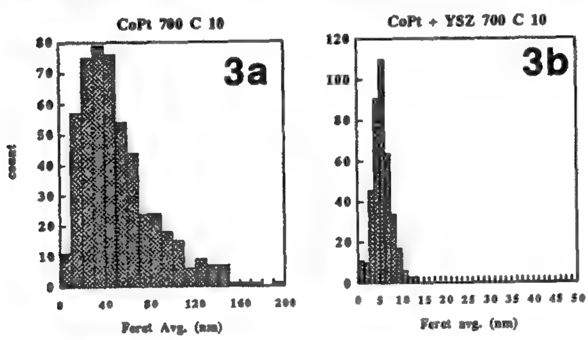

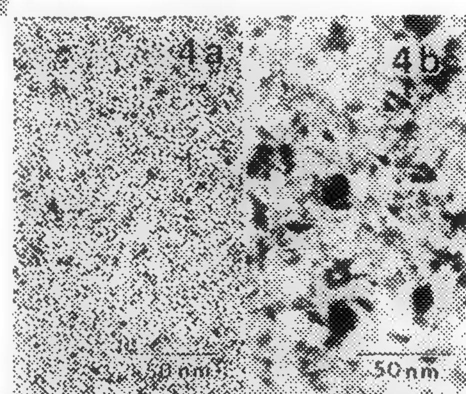

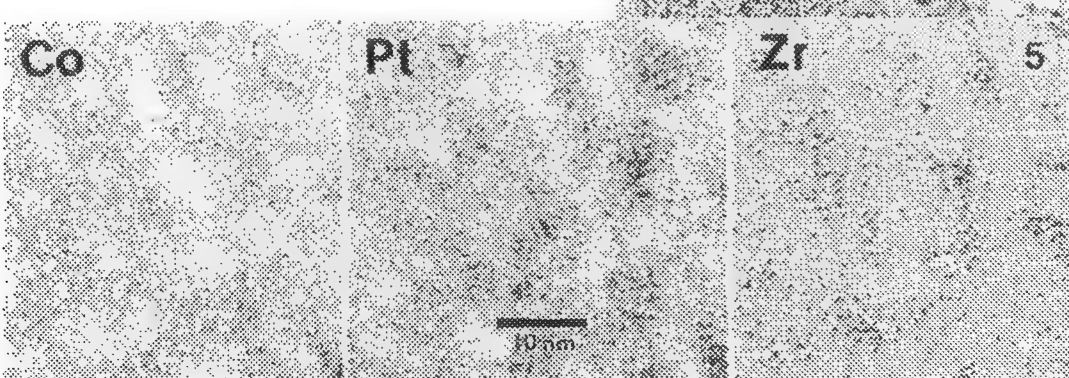

Figure 1. Bright field TEM images of annealed CoPt (1a) and CoPt + ZrO_x (1b) thin films.
Figure 2. Plot of mean grain size verses anneal temperature for CoPt and CoPt + ZrO_x thin films.
Figure 3. Grain size distribution for CoPt (3a) and CoPt + ZrO_x (3b). Note different scales used.
Figure 4. Bright field TEM images of CoPt + ZrO_x as deposited (4a) and annealed 700° C 10 min. (4b).
Figure 5. Energy dispersive X-ray maps of elemental Co, Pt and Zr for sample in Figure 4b. Darker contrast indicates stronger signal.

QUANTITATIVE X-RAY MICROANALYSIS AND THICKNESS DETERMINATION USING ζ FACTOR

M. Watanabe*, Z. Horita†, and M. Nemoto†

*Department of Materials Science and Engineering, Whitaker Laboratory #5, Lehigh University, Bethlehem, PA 18015-3195 USA.
†Department of Materials Science and Engineering, Faculty of Engineering 36, Kyushu University, Fukuoka 812, Japan.

X-ray absorption in quantitative x-ray microanalysis of thin specimens may be corrected without knowledge of thickness when the extrapolation method[1] or the differential x-ray absorption (DXA) method[2,3] is used. However, there is an experimental limitation involved in each method. In this study, a method is proposed to overcome such a limitation. The method is developed by introducing the ζ factor and by combining the extrapolation method and DXA method. The method using the ζ factor, which is called the ζ-DXA method in this study, is applied to diffusion-couple experiments in the Ni–Al system.

For a thin specimen where incident electrons are fully transparent, the characteristic x-ray intensity generated from a beam position, I, may be represented as $I = (N\rho W/A)Q\omega aist$. Here, N is the Avogadoro's number, ρ and W are the density and the weight fraction at the beam position respectively, A is the atomic weight, ω is the fluorescence yield, Q is the ionization cross-section, a is the ratio of K_α (or L_α, M_α) intensity to the total K (or L, M) intensity, i is the beam current density, s is the area of beam illumination, and t is the thickness at the beam position. The mass thickness ρt is then related to normalized x-ray intensity as $\rho t = \zeta(I/W)$ and the ζ factor is defined as $\zeta = A/NQ\omega ais$. Thus, with use of the relationship of $\rho t = \zeta(I/W)$, the absorption correction is achieved through the equation

$$\frac{W_J}{W_A} = k_{J(j)A(i)} \left(\frac{I_{J(j)}}{I_{A(i)}}\right)_m \left\{\frac{(\mu/\rho)_s^{J(j)}}{(\mu/\rho)_s^{A(i)}}\right\} \frac{1-\exp[-(\mu/\rho)_s^{A(i)}\zeta_{A(i)}\{(I_{A(i)})_m/W_A\}\operatorname{cosec}\theta]}{1-\exp[-(\mu/\rho)_s^{J(j)}\zeta_{A(i)}\{(I_{A(i)})_m/W_A\}\operatorname{cosec}\theta]} \quad (1)$$

Here, A and J represent the quantities associated with elements A and J (= B, C, ...), (i) and (j) represents the characteristic x-ray lines associated with i shell and j shell (i, j = K, L, or M), m signifies the measured x-ray intensity, $k_{J(j)A(i)}$ is the k factor, $(\mu/\rho)_s^{J(j)}$ and $(\mu/\rho)_s^{A(i)}$ are the mass absorption coefficients of lines A(i) and J(j) at the beam position respectively, and θ is the x-ray take-off angle. For the proportionality between ρt and (I/W), the x-ray absorption should be negligible in the specimen. In this study, thus, we consider that the absorption is negligible for line A(i) but significant for line J(j).

If the k and ζ factors are known, it is possible to correct the absorption of J(j) line without knowledge of density and thickness. The determination of each weight fraction is achieved through eq.(1) with the combination of $W_A + \sum W_J = 1$. The determination of the k and ζ factors is made using a standard specimen. Since the composition is known in a standard, eq.(1) is solved for the $k_{J(j)A(i)}$ and $\zeta_{A(i)}$ factors from more than two measurements of characteristic x-ray intensities. This determination is achieved by a non-linear least square fitting method. If the density is known, it is also possible to determine the thickness at the beam position through the relationship of $\rho t = \zeta(I/W)$. The thickness determination is possible not only in the specimen with a known composition (standard) but also with an unknown composition. For the specimen with a known composition, the determination is straightforward using the relationship of $\rho t = \zeta(I/W)$. For the specimen with an unknown composition, the thickness is determined using the same relationship after the composition is determined.

The characteristic features of the ζ-DXA method proposed in this study are that (1) it does not require knowledge of the thickness nor the density for absorption correction, (2) it is possible to measure thickness if the density is known, (3) the thickness range effective for the method is much greater than that for the extrapolation method, (4) the method permits using the combination of the K shell plus K shell lines which is inapplicable to the DXA method, and (5) the determinations of composition and thickness are achieved by a single measurement of x-ray intensities. The requirement for the ζ-DXA method is that it is necessary to keep the beam current density the same between the determination of k and ζ factors from standards and the determination of composition and thickness in the specimens of unknown compositions.

Pure Ni coupled with Ni–51.8mol%Al (Ni/Ni–51.8mol%Al) was subjected to diffusion annealing at 1173 K for 7.2 ks (2 hours). A thin specimen for transmission electron microscopy was prepared from the diffusion couple by an electropolishing technique. A detailed procedure for the preparation of thin specimens was described earlier.[4,5] Figure 1 plots (a) the concentration profiles measured across the diffusion-couple interface with and without absorption correction and (b) the corresponding thickness variation determined using the $\zeta_{Ni(K)}$ factor. The $k_{Al(K)Ni(K)}$ and $\zeta_{Ni(K)}$ factors were determined in the diffusion-couple end-member of Ni–51.8mol%Al where the beam positions were far away from the interface so that no change in composition took place during diffusion annealing. Without absorption correction, the level of C_{Al} cannot reach 51.8mol% and the variation of C_{Al} is likely to be affected by the variation of thickness. Inspection of the concentration profile reveals that the Ni_3Al intermetallic phase ($\gamma\prime$ phase) formed at the couple interface and there are abrupt changes in C_{Al} at the $\gamma/\gamma\prime$ and $\gamma\prime/\beta$ interphase interface. Here, γ is the Ni-rich solid solution phase and β is the NiAl intermetallic phase. There is also a rapid change in C_{Al} in the b phase which corresponds to the pseudo-boundary. The presence of such a boundary arises because the interdiffusivity takes a minimum at $C_{Al} \simeq 49mol\%$.

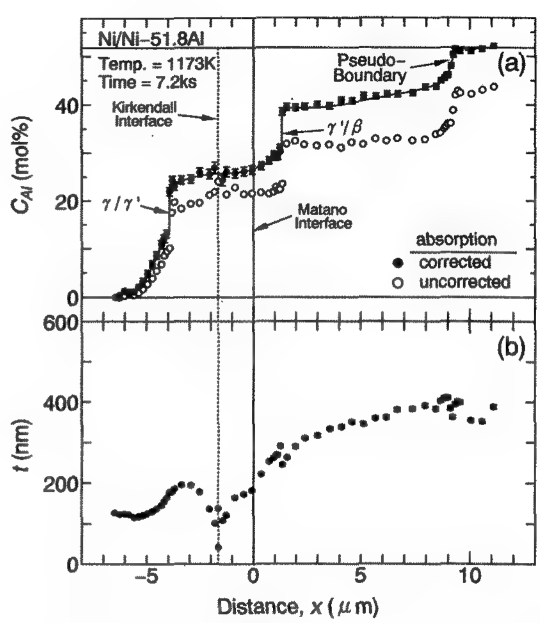

FIG. 1: Variations of (a) C_{Al} and (b) t across the Ni/Ni–51.8mol%Al diffusion-couple interface.

References

1. Z. Horita, T. Sano and M. Nemoto, *Ultramicroscopy*, **21**(1987)271.
2. P. L. Morris, M. D. Ball and P. J. Statham, *Inst. Phys. Conf. Ser* **52**(Ed. T. Mulvey), (1980)94.
3. Z. Horita, K. Ichitani, T. Sano and M. Nemoto, *Phil. Mag. A*, **59**(1989)939.
4. M. Watanabe, Z. Horita, D. J. Smith, M. R. McCartney, T. Sano and M. Nemoto, *Acta Metall. Mater.*, **42**(1994)3381.
5. N. Komai, M. Watanabe and Z. Horita, *Acta Metall. Mater.*, **43**(1995)2967.

6.This work was supported by the Grant-in-Aid for Scientific Research from the Ministry of Education, Science, Sports and Culture of Japan. A JEM-2000FX analytical electron microscope in the HVEM Laboratory of Kyushu University was used in this study.

OPTIMIZATION OF THE PRODUCTION OF A CHROMIUM THIN-FILM AEM CHARACTERIZATION STANDARD BY THERMAL EVAPORATION

K. A. Repa and D. B. Williams

Department of Materials Science and Engineering, Lehigh University, Bethlehem, PA 18015

The need for a chromium standard to characterize the performance of an analytical electron microscope (AEM) and its associated x-ray energy-dispersive spectrometer (XEDS) in quantitative terms which can also be used to realistically compare AEM-XEDS systems has long been recognized[1] and becomes increasingly important as advances in the technology of electron microscopy are made. Previous thermal evaporation of a 100 nm thick chromium film onto a 20 nm carbon support film by the National Institute of Standards and Technology (NIST)[2] provided a useful standard, but attempts to reproduce these results encountered difficulty in achieving consistent adherence to 200 mesh copper grids. These difficulties are attributed to preexisting stresses in the carbon support film [Fig. 1] and as a result production of self-supporting Cr films was chosen, with the NIST standard serving as a model against which the present specimens were evaluated. Relevant properties of a characterization standard have been well defined[3] and include the thickness, XEDS profile and grain size.

The Cr was deposited by a Denton 501 thermal evaporator from a tungsten coil onto a temporary 0.3% formvar support film. The formvar solution was poured onto a glass slide pretreated with a detergent release agent. After drying, the formvar film was scored along the edges and steamed to pre-shrink and relieve film stress. The formvar was then floated off the slide in distilled water and picked up on copper grids supported by a steel mesh. The amount of Cr deposited was determined by the weight (0.38g) experimentally found as a function of evaporator geometry to be necessary to yield an XEDS peak profile comparable to that generated by the NIST standard on a Philips EM400T scanning transmission electron microscopy (STEM) unit. The STEM unit was operated at 120 keV with constant spot size (~20 nm) and consistent column location by focusing with the eucentric height adjust. After an evaporator vacuum of 4×10^{-6} torr was reached, the Cr was heated to a dull red glow for approximately ten minutes. A shutter, placed near the tungsten coil to act also as a heat shield, was then opened and the Cr was quickly evaporated by a 20 to 25 Amp current through the coil. After removal from the evaporator the formvar support film was dissolved in chloroform.

The XEDS profile of the self-supported Cr film (SS-Cr) compared well with the NIST profile [Fig. 2]. The most notable difference was the presence of primarily Si contamination in the NIST standard and primarily W contamination in the self-supported sample. W contamination was reduced to approximately the same level as the Si contamination by pre-coating the W coil with Cr before the actual evaporation. Thickness of the films were further measured by electron energy loss spectroscopy (EELS) and the bright field images of grain size and diffraction patterns recorded by the Philips EM400T were also compared [Fig. 3]. The thermal evaporation of the self-supported Cr films is found not only to be a viable alternative to the NIST carbon supported films, but also has the added advantage that EELS analysis is simplified. The only noted area of compromise is the increase in the grain size of the self-supported films, which is expected because the carbon support film which increases nucleation density has been removed.[4]

References
1. D. B. Williams, *Microbeam Analysis - 1986,* ed. by A. D. Romig, Jr. and W. F. Chambers, San Francisco Press, San Francisco, CA, (1986), 443.
2. D. B. Williams and E. B. Steel, *Analytical Electron Microscopy - 1987,* ed. by D. C. Joy, San Francisco Press, San Francisco, CA (1987), 228.
3. S. M. Zemyan and D. B. Williams, *J. Microscopy,* **174**: 1, (1994) 1.
4. Acknowledgment is gratefully given to Mr. David Ackland for technical advice.

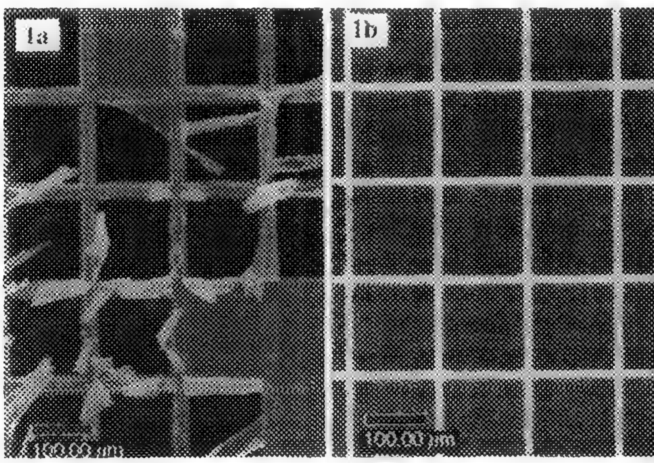

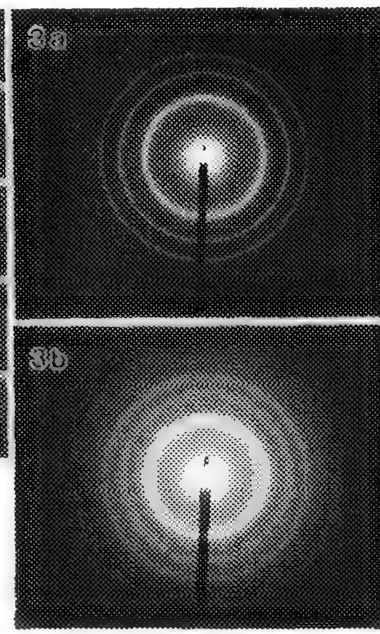

2(a) XEDS Window Integral Counts:

Regions (keV):	NIST Gross	NIST Net	SSCr Gross	SSCr Net
Cr Kα: 5.0 to 5.7	53816	51962	53922	51978
Bkg 1: 4.1 to 4.8	1617	339	1507	121
Bkg 2: 6.3 to 7.0	1493	143	1264	292

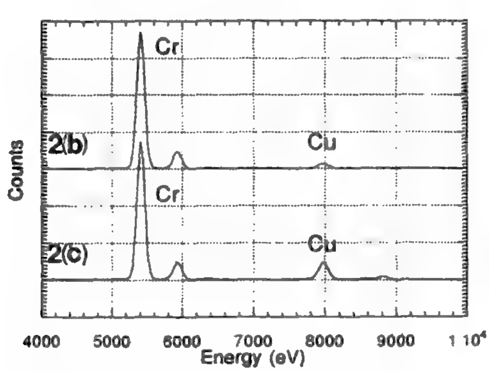

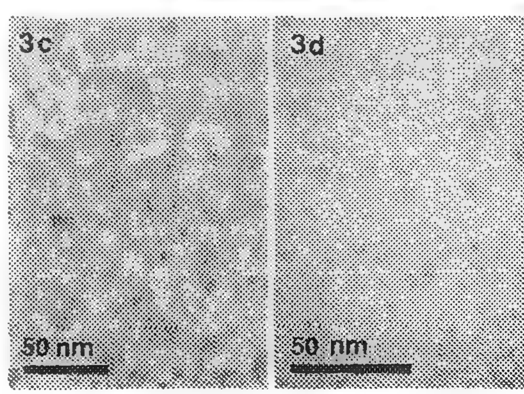

Figure 1. Low magnification SEM image of (a) 100 nm Cr film on 20 nm C support film and (b) Self-supported Cr film showing improvement in adherence to TEM grid.
Figure 2. Comparison of XEDS profiles. (a) Window integrals at 120 keV STEM mode, 120 sec live time acquire; Profiles of (b) SS-Cr film and (c) NIST film.
Figure 3. Comparison of TEM diffraction patterns and brightfield images of grain size of (a, c) SS-Cr film and (b, d) NIST film.

COLOR IMAGE ANALYSIS IN OPTICAL MICROSCOPY

Sylvain Laroche

CLEMEX Technologies, 800 rue Guimond, Longueuil (Qc) Canada, J4G 1T5
(e-mail: slaroche@clemex.com, Web page: www.clemex.com)

Most of the applications in microscopic image analysis are still solved by a heuristic method that focuses on the specificity of each problem. This is particularly true for applications involving color images. Because of this, the design of robust algorithms has remained time consuming and is usually performed by an image analysis expert with many years of experience. How then can the knowledge of the expert be transferred to the less specialized microscopist? How can the specificity of a typical application be related to general color image analysis tools?

Only a general approach can work towards decreasing the heuristic aspect of the design phase and help the common user perform image analysis without the assistance of an expert. To illustrate such an approach, two typical applications, one in material science, and the other in the biomedical field are presented:

Segmentation of aluminum grains seen under polarized light
Detection of DNA-multi-probes in fluorescence imaging in-situ hybridization (FISH)

Although these applications are very different in nature, the image analysis framework is the same. The implementation of such a framework in a fully integrated image analysis system is also discussed.

Detecting and measuring objects of interest described by specific colors, shape and contrast requires tools that fall within the following categories:

1) Color acquisition and color space conversion
2) Color Filtering
3) Color Segmentation
4) Edge Detection
5) Measurement and mapping over the full sample

Several color models are available to process color images. The well-known RGB format is very common for display purposes. However, it is inadequate for image analysis since the linear combination of the three components is not easily deduced for expressing a region with similar colors. Consequently, the process of color segmentation is very difficult. An alternate color space, HSI (Hue, Saturation, Intensity), is more suitable and is closer to the way color is expressed in everyday life. Because video cameras deliver an RGB signal, a conversion from RGB to HSI is required. Since display systems are restricted to RGB output, representing an HSI image is not a simple issue. Specifically, a further conversion back to the RGB space becomes necessary.

Other factors also mitigate the acquisition process. For example, uneven lighting at the microscopic level must be compensated by a special form of shading correction performed in the HSI space. In FISH applications, low-light fluorescence imaging also demands a special acquisition mode because standard CCD cameras are not sensitive enough to capture as many photons as required. Consequently, increasing the exposure time of the CCD element is often necessary to deal with such conditions.

The raw HSI image contains objects of interest as well as artifacts, background structures, etc. To facilitate the segmentation process, color filtering can be used to enhance the objects of interest while discarding other features. Mathematical Morphology has proven to be a very powerful approach to segment and filter gray-tone and binary images. However, common operations such as erosion, dilation, opening and closing do not have clear counterparts in color imaging. Such transforms can nonetheless be implemented into the HSI space by performing morphological operations on the intensity component and propagating the Hue-Saturation pair over the neighborhood of the structuring element. The generalization of Mathematical Morphology to color image processing has lead to the creation of several very powerful non-linear filters.

After proper filtration, objects having specific colors are detected by segmentation in the HSI color space. Low and high limits for hue, saturation and intensity can easily be defined as long as the HSI space is presented to the user in a relevant manner. An HSI color histogram can also be used to facilitate the color thresholding process.

Performing color thresholding immediately, even after filtering, is not always the most efficient approach however. For example, when adjacent color structures are in contact, color segmentation can be more easily obtained by detecting the color boundary. In such cases, a color edge gradient can be performed. The resulting noisy image is then further processed by applying a watershed operation to yield a clear boundary structure despite the poor local contrast of the gradient image. This image can then be segmented by thresholding.

Filtering is usually required to clean the binary image obtained by the color segmentation before measurements and shape factors can be computed for the objects of interest. Once the filtering is complete, object measurements can be performed to yield a final classification. The amount of data generated can be somewhat overwhelming, particularly if data was gathered over several fields. This can make the review and validation process tedious if the proper tools are unavailable. One effective approach is to map the results over the full sample and superimpose the map over the original image. The operator then inspects the map to validate the results.

References

1. Laroche S., Forget C., Grain Sizing of Anodized Aluminum by Color Image Analysis, MC95, International Metallography Conference, May 1995
2. Serra J., Image Analysis and Mathematical Morphology, Academic Press, 1982, 610 p.
3. Breen E.J. Regression methods for automated colour image classification and thresholding, Journal of Microscopy, vol. 174. Pt 1, April 1994, 23-30

TOMOGRAPHY OF PARACRYSTALLINE SPECIMENS

Kenneth A. Taylor and Hanspeter Winkler

Institute of Molecular Biophysics, Florida State University, Tallahassee, FL 32306-3015

3-D image reconstruction of objects with no symmetry are produced by combining images of specimens tilted at finely spaced intervals about a single tilt axis. Image fiducials, usually gold particles applied to the surface of the specimen, are used to orient and align the separate views and 3-D images calculated by back projection methods. Electron microscope tomography has developed into a powerful method for producing a 3-D image of objects lacking crystalline symmetry.[1] Crystalline objects are usually reconstructed using Fourier based methods that produce averaged 3-D images. Electron crystallography has become a powerful tool for solving the 3-D structure of proteins at atomic resolution.[2,3]

Paracrystalline objects lie between crystalline and nonperiodic specimens because part of their structure is often well ordered but they have as well a significant disordered part. Muscle is one of the more notable members of this type of specimen because often the actin and myosin filaments form a well ordered array but the crossbridges, i.e. the motor domain of myosin, are much more disordered. Other examples include 2-D actin bundles or gels which have well ordered actin filaments but a somewhat disordered arrangement of crosslinking proteins (Taylor & Taylor, 1994). The more disordered the specimen, e.g. contracting muscle, the less information will be obtained from an averaged reconstruction. Thus, a method is needed that can image the disordered part of the structure in 3-D.

To address this problem, we have extended the standard crystallographic reconstruction protocols to facilitate imaging of the disordered component of the structure.[4] The method has several attractive characteristics for tomography of unstained specimens. The reference image for alignment becomes statistically better defined as more images are merged into the reconstruction data base. In addition, since the reference is formed from all previously merged images, accumulation of alignment errors is minimized. In order to obtain the highest signal to noise ratio in the individual unit cells, averaging is required, especially if images are obtained by low dose imaging techniques on unstained specimens. Thus to obtain the most information on the components of a paracrystalline array, tomography must incorporate methodology for 3-D correlation averaging. For disordered specimens, such as muscle, averaging will require analysis of the classes of molecular structure using correspondence analysis.[5,6]

In principle, correlation averaging on disordered crystals can be done more effectively from a tomogram than it can be from the individual 2-D images that make up the data set. Correlation averaging is commonly done on 2-D projections[7] but in a tilt series from a disordered specimen, can lead to superposition problems as increasing tilts bring ostensibly different material into the projected unit cell. This problem can be circumvented if the 3-D image is obtained first and the separate molecules then aligned and averaged by a 3-D correlation averaging protocol.

Tomograms can also reveal low resolution defects in the specimen that can later be corrected thereby facilitating the calculation of an average. Flatness is a common problem in electron crystallography of 2-D crystals.[8] Tomograms of insect flight muscle, have shown that the sections are not flat. However, it was possible to computationally correct for the wrinkling in the tomogram to produce a flat "specimen".[9] Straightness of helical filaments is also a common problem, but difficult to correct with just 2-D images which do not reveal the bending out of the image plane. In a tomogram, just as it is for wrinkling, information on out-of-plane bending would be available allowing the filament to be straightened in 3-D. Finally, in multilayer crystals, a tomogram would reveal the number of layers and any disorientation between the layers.

While these possibilities exist, the resolution limitations have yet to be established. The dose fractionation theory of Hegerl and Hoppe may provide a framework for tomography of unstained specimens.[10] This theory has been scrutinized recently as the desire to obtain 3-D images of ice embedded specimens has increased.[11] The application of this principle may provide a solution to the radiation damage limitations in tomography of unstained specimens.

References

1. J. Frank, *Electron Tomography*, Plenum Press: New York, (1992).
2. R. Henderson et al., *J. Mol. Biol.* 213(1990)899.
3. W. Kühlbrandt et al., *Nature*, 367(1994)614.
4. K. A. Taylor and H. Winkler, *Proc. 53rd Ann. MSA Meeting*, (1995)734.
5. M. Van Heel and J. Frank, *Ultramicroscopy* 6(1981).
6. J. Frank and M. Van Heel, *J. Mol. Biol.* 161(1982)107.
7. W. O. Saxton et al., *Ultramicroscopy*. 13(1984)57.
8. R. M. Glaeser et al., *Ultramicroscopy*. 55(1994)1.
9. K. A. Taylor and H. Winkler, *Ultramicroscopy* (in press)
10. R. Hegerl and W. Hoppe, *Z. Naturforsch.* 31a(1976)1717-1721.
11. B. F. McEwen et al., *Ultramicroscopy* 60(1995)357.

RADON TRANSFORMS, ALIGNMENT, AND 3D-RECONSTRUCTION FROM RANDOM PROJECTIONS

Michael Radermacher

Wadsworth Center, New York State Dept. of Health, Albany, N.Y. 12201-0509 and Department of Biomedical Sciences, State University of New York at Albany, 1400 Washington Ave, Albany, N.Y. 12222.

Since their inception three-dimensional reconstruction techniques have been based on the theory of Radon transforms [1,2]. Only much later have Radon transforms been recognized as powerful tools for image processing and pattern recognition [3,4,5]. Techniques like the "common lines" technique for finding the orientation of projections of highly symmetrical particles [6], which had been developed using Fourier transforms, can easily be translated into a technique that uses Radon transforms. In contrast to Fourier transforms Radon transforms have the advantage of being real valued which simplifies many interpolation steps. The central section theorem known for Fourier transforms also applies to Radon transforms. The two- or three-dimensional Fourier transform on a polar grid can be obtained from the two- or three-dimensional Radon transform by a one-dimensional (radial) Fourier transforms and vice versa. Fourier transforms obtained by a one-dimensional transformation of the Radon transform will be referred to a Fourier/Radon transforms. The shifting property of Radon transforms has no equivalent for Fourier transforms and can be exploited for simultaneous translational and rotational alignment. Correlation techniques have been developed for alignment of a single noisy projection relative to a three-dimensional model [7], and many of the additional ideas set forward in [7] have been realized.

The three-dimensional Radon transform is defined as

$$\hat{f}(p,\vec{\xi}) = \int f(\vec{r})\delta(p-\vec{\xi}\cdot\vec{r})\, d\vec{r},$$

where $\delta(p-\vec{\xi}\cdot\vec{r})$ specifies a plane over which the integration is carried out and $\vec{\xi}$ is the unit vector that determines the direction of this plane. For the twodimensional Radon transform $\vec{\xi}$ and $\vec{r}$ are replaced by two-dimensional vectors and the integration becomes a line integration instead of an integration over planes.

Alignment in two dimensions: Let $\hat{g}_i(p,\epsilon)$ be the Radon transform of the projection P_i, and $\hat{f}(p,\vec{\zeta})$ be the Radon transform of a reference image, $\vec{\zeta} = (\cos(\epsilon), \sin(\epsilon))$. The cross-correlation function $C(\alpha, r, \eta)$, with α being the rotation angle and (r, η) the shift vector in polar coordinates, is:

$$C(\alpha, r, \eta) = \int\int \hat{f}(p,\vec{\zeta}) \cdot \hat{g}_i(p - r\sin(\epsilon+\eta), \epsilon+\alpha)\, dp\, d\epsilon$$

The rotation α_0 and shift (r_0, η_0) of the image relative to the reference is determined from the maximum of C.

Alignment in three dimensions: In three dimensions the cross-correlation function is five-dimensional. It is determined by calculating all two-dimensional cross-correlation functions between $\hat{g}_i(p,\epsilon)$, the Radon transform of the projection P_i, and $\hat{f}_{\beta,\gamma}(p,\vec{\zeta})$, the crossections through the three-dimensional Radon transform at angles β, γ.

$$C(\alpha, \beta, \gamma, r, \eta) = \int\int \hat{f}_{\beta,\gamma}(p,\vec{\zeta}) \cdot \hat{g}_i(p - r\sin(\epsilon+\eta), \epsilon+\alpha)\, dp\, d\epsilon$$

The alignment and reconstruction in three dimensions starts with a preliminary three-dimensional reference, which can be a reconstruction from the projection set $\{P_i, i = 1, N\}$ with preliminary angle assignments. The procedure is iterative and is carried out using two and three-dimensional Fourier/Radon transforms. In step i projection P_i is subtracted from the three-dimensional model, $C_i(\alpha, \beta, \gamma, r, \eta)$, the cross-correlation function for projection P_i is calculated and the orientation $(\alpha_i, \beta_i, \gamma_i)$ and translation (r_i, η_i) of projection P_i are determined. P_i is shifted by (r_i, η_i) and added back to the model in its orientation $(\alpha_i, \beta_i, \gamma_i)$. All subtractions and additions of P_i are done as averaging procedures, using indices that keep track of the number of projections that contribute to each radial line in the Fourier/Radon transform. The procedure is done for each i, $i = 1, N$ and repeated several times.

A very fast two and three-dimensional Radon inversion algorithm has been written that allows the performance of the iterative process to be observed. This inversion algorithm also can be used reconstructions from random projections independent of the alignment procedures.

1. Radon J., Über die Bestimmung von Funktionen durch ihre Integralwerte längs gewisser Mannigfaltigkeiten. Berichte Über die Verhandlungen der Kőniglich Săchsischen Gesellschaft der Wissenschaften zu Leipzig, Math.Phys. Klasse 69, 1917, 262-277
2. Deans S.R. The Radon transform and some of its applications. John Wiley & Sons, New York, 1983.
3. Van Heel M., Angular reconstitution: a posteriori assignment of projection directions for 3D reconstruction. Ultramicroscopy 21, 1987, 111-124
4. Sanz J.L.C., Hinkle E.B., Jain A.K., Radon and projection transform-based computer vision. Springer Verlag, Berlin, 1988
5. Pintsov D.A., Invariant pattern recognition, symmetry and Radon transforms. J. Opt. Soc. Am. A, 6, 1988, 1544-1554.
6. Crowther R.A., DeRosier D.J., Klug F.R.S. The reconstruction of a three-dimensional structure from projections and its application to electron microscopy. Proc. Roy. Soc. Lond. A. 317, 1970, 319-340.
7. Radermacher M., Three-dimensional reconstruction from random projections: orientational alignment via Radon transforms. Ultramicroscopy 53, 1994, 121-136.

8. Supported by Grants from NSF, BIR 9115534, and NIH, RO1 GM29169 and P41 RR01219.

EXAMPLES OF 3D MORPHOLOGICAL IMAGE ANALYSIS IN MICROSCOPY

D. Jeulin*

*Centre de Morphologie Mathématique, Ecole des Mines de Paris, 35 rue St-Honoré, F77300 Fontainebleau, FRANCE

Image analysis of materials microstructure is a complementary means of characterization in addition to more usual properties, such as chemical analysis or physical measurements. In this lecture are introduced some of the most recent developments in the implementation of 3D morphological image analysis. Usually, the available information in Quantitative Microscopy is two-dimensional, as obtained from polished sections. However 3D data may be obtained: the topography of rough surfaces can be accessed from a stylus instrument or from a confocal optical microscope; serial sections can be prepared and examined in the optical microscope; sometimes serial sections can be obtained in a non destructive way, using the optical confocal microscope for transparent media [2], or X-ray tomography. With these data, 3D morphological processing can be used [16] to get more specific information on the microstructure. Mathematical Morphology operations, defined in a more general background [18, 19], are easily performed on 3D images by software developed on standard computers [2, 4]. We will present the following classes of problems that can be solved by the basic tools of Mathematical Morphology: image filtering, segmentation, measurements, and random image models. This is illustrated by examples.

Since most sources of images of microstructures (electron microscope or microprobe) provide a large range of noisy data, the first step in image analysis is most often the application of a filter to remove the noise. Morphological non linear filters can be used to improve such images [19]. Optimized linear filters, based on a geostatistical approach, minimize the variance of estimation from second order statistics models; they were used to make a deconvolution of noisy confocal microscope images [2] in the z direction. The use of 3D neighborhoods of every voxel can provide improved filters, but in many cases 2D filters give a satisfactory image restoration. In some cases, the z resolution of 3D images is much lower than the x-y resolution. It can be interesting to recover equal x-y-z spacings by interpolation of plane sections; this can be performed by a morphological (non linear) or by a linear interpolation.

A powerful approach for the segmentation of images (providing domains with similar morphological properties) was proposed and applied to many practical problems [1, 17]. Its principle lays on the extraction of pertinent markers in images, and on the construction of divide lines of watersheds in two dimensions or of divide surfaces in thee dimension, which draw the boundaries between the different regions in an image. This method is very efficient to separate overlapping objects. The segmentation is also a useful tool to solve some problems of 3D reconstruction. In [4], the walls of the cells of a foam are reconstructed by means of a 3D watershed reconstruction using the calculation of the distance of every voxel to the edges of the foam. The 3D segmentation, that can be used as an input in a 3D size distribution measurement, gives good result in a situation where a separate 2D segmentation of every section fails, due to the very poor information seen on sections. In [1], the topography of steel fracture micrographs is reconstructed from stereo SEM micrographs; this involves a segmentation procedure to extract the boundary of facets seen on the micrographs, with a matching of homologous markers in the stereo pair. The final reconstruction is obtained by a trian-

gulation. In [12], this principle is extended to the reconstruction aggregates of carbon spheres with 30nm diameter examined in the TEM: every image of a sequence of images separated by 5^0 tilts is thresholded, then segmented to recover characteristic points on the aggregates; the 3D coordinates of the centers of spheres in the aggregates are evaluated by a stereographic reconstruction.

Measurements on 3D images can be made directly without any stereological model: in [2], the volume of osteocyte lacunae is estimated; size distributions of particles of any shape can be estimated; furthermore, 3D connectivity measurements can be obtained for characterizing a porous network [13]; in [3] the distribution profiles of polyamide particles in a wood varnish is obtained from 3D imaging obtained by a confocal microscope.

Finally, random image models [6, 14, 15] are a useful tool to estimate morphological properties of 3D microstructures, even from 2D images. In [2], a Boolean model is used to estimate the number of osteocyte lacunae per unit volume, from 3D images; this technique enables us to count the number of objects in a texture, without segmenting the objects that it contain. Random function models were developed in [10] to simulate the rough surface of electric discharge textures obtained for the skin pass roll. Random models are also useful to analyze the morphology of powders from packing observed with the SEM; for this purpose the dead leaves model can provide an estimation of powder size distributions from SEM images without polishing the specimens, as illustrated for spherical powders in [7, 8, 11]; in [9], this model was used for UO_2 powders of complex shapes to study their coalescence and the content of binary mixtures.

References

[1] Beucher S. *Thèse de Doctorat en Morphologie Mathématique*, ENSMP, 1990 .

[2] Conan V.et al. (1992) *J. Microsc.* **166**, 169-184.

[3] Girault S. et al. in *ICEM 13-Paris*, 17-22 July 1994, pp. 541-542.

[4] Gratin C. *Thèse de Doctorat en Morphologie Mathématique*, ENSMP, 1993.

[5] Jeulin D. (1988) in *D.E. Newbury, Ed. Microbeam Analysis (San Francisco: San Francisco Press)* 9-13.

[6] Jeulin D. *Thèse de Doctorat d'Etat ès Sciences Physiques*, University of Caen, 1991.

[7] Jeulin D., Terol Villalobos I. (1992) *Acta Stereol.* **11**/Suppl I: 105-110.

[8] Jeulin D. (1993) *J. Microsc.* **172**,(1), 13-21.

[9] Jeulin D. et al., *Microsc. Microanal. Microstruct.* 6 (1995) 371-384.

[10] Jeulin D., Laurenge P. (1996), in *Proc. ISMM'96*, Atlanta.

[11] Jeulin D., Squillaci E., *Colloque sur le traitement des poudres et leurs conséquences, SF2M-Paris*, 18-20 Mars 1996.

[12] Le Coënt A. *Thèse de Doctorat en Géostatistique*, ENSMP, 1995 .

[13] L'Espérance G. et al. in *Proc. Microscopy & Microanalysis'96.*

[14] Matheron G. *Eléments pour une théorie des milieux poreux* (Masson, Paris, 1967).

[15] Matheron G. *Random Sets and Integral Geometry* (Wiley, New York, 1975).

[16] Meyer F. (1992) *J. Microsc.* **165** (1), 5-28.

[17] Meyer F., Beucher S. (1990) *J. Visual Comm. Image Represent.* **1** (1), 21-46.

[18] Serra J. *Image analysis and Mathematical Morphology* (Academic Press, London, 1982).

[19] Serra J.(ed) *Image analysis and Mathematical Morphology*, vol. 2 (Academic Press, London, 1988).

Extracting 3-D information from SEM and TEM images: approches and applications in the physical sciences

Gilles L'Espérance*, Martin Dionne*, D.Jeulin, C. H. Demarty**, S. Tremblay* and E. Perrier***

*** Centre for Characterization and Microscopy of Materials, (CM^2), École Polytechnique de Montréal, (Québec), Canada, H3C 3A7.**
**** Centre de Morphologie Mathématique, École des mines de Paris, 35 rue St-Honoré, F77300 Fontainebleau, France**

Techniques for extracting 3-D information from TEM samples in life sciences have considerably progressed in recent years. One approach has been the use of serial sections prepared by ultramicrotomy from which the volume of the sample and of various constituents can be reconstructed.

In the case of engineering materials, however, ultramicrotomy generally induces severe deformation resulting in a large density of structural defects (dislocations, stacking faults etc.). This leads to significant diffraction contrast effects which mask microstructural features such as second phase particles, precipitates etc. Recently, a series of TEM bright field images taken at different tilts have been used in combination with image analysis to determine the volume fraction (V_f) of second phase particles in thin foils of aluminum alloys (1). Although the technique was successful to remove most of the diffraction contrast effects and to make the particles visible, the need to acquire and process a large number of images makes the technique laborious and can lead to artefacts (1).

In cases when the required hardware and software are available, Plasmon Energy Shift Images (PESI) are very powerful to remove diffraction contrast effects in thin foils of highly dislocated (cold worked) aluminum alloys thus making the second phase particles visible (figures 1 and 2). These images can then be combined with PEELS thickness maps and image analysis (2, 3), to determine the volume fraction of the particles (4) embedded in thin foils of varying thicknesses. A comparison of the results obtained with the two techniques will be presented as well as results of the work carried out to determine proper acquisition parameters to achieve good sampling statistics.

In the case of a bulk and opaque sample observed in the SEM, successive sections obtained after repeated polishing of the sample (figures 3a and 3b) can be used to characterize the microstructure of the sample in 3-D. From the 3-D images obtained, it is possible to measure size distributions of phases (even connected) by morphological openings; it is also interesting to simulate the propagation of a front within the porous network or within the matrix by geodesic operations; this type of transformation is useful to characterize the 3-D connectivity of porous media by measuring a kind of propagation time to connect two opposite facets of a sample by 3-D paths remaining in a single phase of the medium. In addition, the set of shortest paths in the

medium can be extracted for display or for further characterization. This will be illustrated on porous metal images.

1) G. Botton and G. L'Espérance, J. of Microscopy, vol. 173 (1994) 9-25.
2) G. Botton et al., submitted to J. of Microscopy.
3) S. Tremblay, M.Sc.A. thesis, École Polytechnique de Montréal, (1995).
4) S. Tremblay and G. L'Espérance, proceedings of ICEM 13, Paris, (1994), 627.

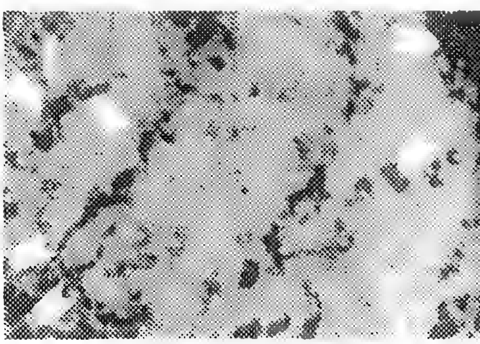

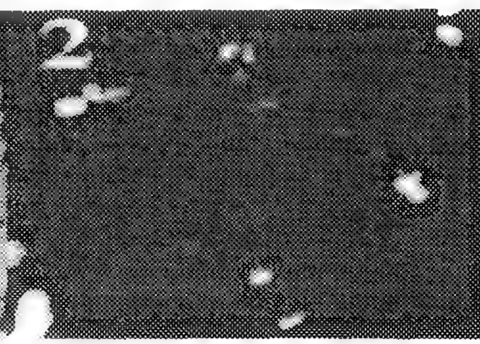

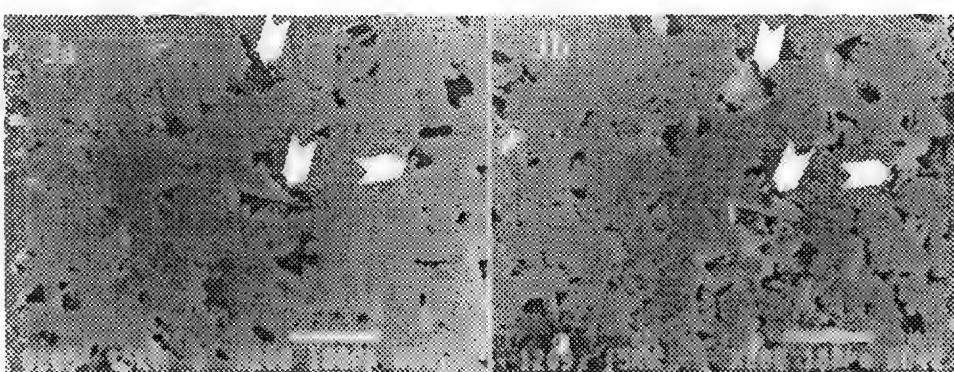

Figure 1:TEM bright field image showing second phase particles (arrowed) and diffraction contrast effects in Al thin foils.

Figure 2:Plasmon Energy Shift Image of the same area as in figure 1 showing the particles.

Figures 3a and 3b: Two successive SEM sections of a porous sample obtained after repeated polishing. The change of the pores size and morphology (see arrows) can be observed as a function of depth.

A "FILMLESS" METHOD OF ACQUIRING AND MEASURING ELECTRON DIFFRACTION PATTERNS

D. C. Dufner

Electron Microscopy Center, Texas A&M University, College Station, TX 77843

Electron diffraction is one of most widely used techniques in the characterization of specimens in the TEM. With the advent of computerization, there is a growing trend toward automation of the measurement and analysis of electron diffraction patterns (EDPs). There are a number of computer programs used for measuring, indexing, and simulating EDPs, some of which are now commercially available. Many of these programs are stand-alone programs which either perform a specific aspect of EDP analysis or require significant user interaction, particularly in the measurement phase. In some cases, the lack of suitable algorithms for measuring EDPs usually limit these programs to the extent that users still have to perform standard procedures of measuring EDPs from negatives or prints to obtain the necessary values needed to complete the execution of these programs. Here, a more convenient means for online acquisition and measurement of EDPs is presented.

The basic experimental setup consists of a video framegrabber (Targa+16 by Truevision, Indianapolis, IN), an image processing and analysis software (Image-Pro Plus for Windows, v. 1.3, by Media Cybernetics, Silver Spring, MD), and a spreadsheet program (Excel v. 7.0 by Microsoft, Redmond, WA) operating in a standard 486 PC workstation. The computer system can be used to capture images from either a TV camera on a TEM, a videocassette recorder, or a scanner as shown in a schematic in Figure 1. Since this system operates in a Microscoft Windows environment, there is a much better integration of the hardware/software components than the MS-DOS-based system previously described at the 1993 MSA meeting.[1] Image-Pro Plus is used to drive the capture utility of the framegrabber to obtain EDPs, and after an image is saved, a macro sequence written as a script file in Image-Pro Plus initiates the measurement process. During the measurement, Image-Pro Plus counts the spots as bright objects within a specified area of interest (AOI), measures the areas, and determines the centroid positions. The measurements are then exported to an Excel worksheet, where the distances between the spots are determined and converted into d-spacing values. Since the transmitted beam spot usually has a larger area than the diffracted beam spots, the area measurements are sorted by Excel in a descending order to bring that spot up as a point of reference for the distance measurements. At the completion of the measurements, a "print screen" utility is invoked to produce a hardcopy of the EDP along with the numbered spots as shown in Figure 2. The results are shown in Figure 3 with the d-spacing values for [100] beta-Sn displayed in the last column. The only interactive step for the user to perform is to select an AOI in the form of a circle, square, or another user-defined shape.

With the current configuration operating in the Windows environment, many of the compatibility problems associated with the previous MS-DOS-based system have been eliminated. One notable feature is the ability to obtain hardcopy images of EDPs with the spots numbered for user reference which was not possible with the earlier version of the program. The measurement process is more streamlined with fewer user-interactive steps, which translates into greater time savings particularly in the analysis of large number of EDPs obtained from well-populated sample grids.[2]

References

1. D.C. Dufner and J.M. Ehrman, *Proc. 51st Ann. MSA Meeting*, (1993)700.
2. The use of the instrumentation in the Texas A&M University Electron Microscopy Center is gratefully acknowledged.

1

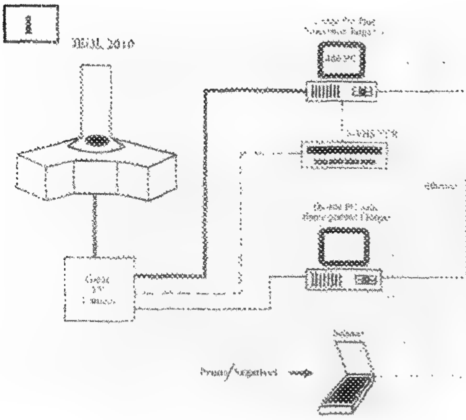

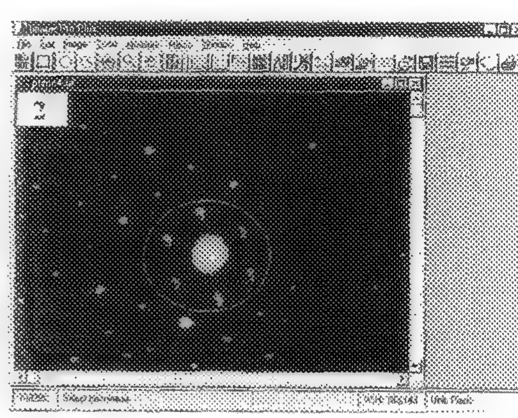

3

Image: ptsn4.tif

Object #	Area	Centr-X	Centr-Y	Distance	d-sp (nm)
4	1487	244.836	202.58		
1	82	232.476	148.96	55.0238	0.2809
8	74	255.297	256.77	55.1899	0.2800
3	65	190.385	181.83	58.2710	0.2652
5	41	296.342	223.63	55.6422	0.2777
7	39	201.949	235.79	54.2446	0.2849
2	28	285.107	169.96	51.8230	0.2982

FIG. 1 Schematic drawing of hardware/software configurations used for acquisition and measurement of EDPs.
FIG. 2 Hardcopy of screen output showing measured spots in [100] zone pattern of beta-Sn.
FIG. 3 Printout of Excel worksheet showing measurement results from diffraction pattern in Fig. 2. Values of d-spacings are calculated from distances between transmitted spot (#4) and diffracted spots.

AN APPROXIMATION TO THE DYNAMICAL CALCULATION OF RHEED PATTERNS FROM ROUGH SURFACES

S. Lordi *, J.A Eades**

*Department of Physics, University of Illinois at Urbana-Champaign, Urbana , IL 61801
**Frederick Seitz Materials Research Lab, University of Illinois at Urbana-Champaign, Urbana , IL 61801

RHEED (reflection high energy electron diffraction) is a technique widely used in molecular beam epitaxy (MBE) and for the characterization of surfaces in other contexts. Despite its widespread use, however, the interpretation of RHEED has largely been limited to the use of positions of the reflections with no attempt made to use the intensities in the patterns.

The reasons for this are related to the complexity of RHEED computations. There are several methods which can be used to calculate RHEED intensities from flat surfaces.[1] However, in MBE (and other crystal growth methods) where RHEED is most often used, the surfaces are rough. Of the dynamical methods for calculating RHEED intensities from flat surfaces, only the modified Cowley-Moodie multislice method with the edge patching algorithm can be applied to rough surfaces without making severe approximations.[2] This method is computationally intensive because the ensemble average over the statistical parameters of the surface cannot be done before the dynamical calculations. Separate dynamical calculations have to be performed for each realization of the surface and the results averaged at the end.

Unforutnately the kinematic approximation is of less use in RHEED than in transmission because there is no experimental parameter in RHEED, equivalent to thickness in TEM, which can be varied to make the kinematic approximation more reasonable. Since the dynamical calculations are so time consuming there is a strong case for the reformulation of RHEED calculations in a way that speeds up computation as well as providing a description of diffraction which gives a feel for the process.

Such a reformulation for rough surfaces has begun to be developed. The method requires full dynamical calculations be performed for surfaces with single steps. The diffraction from a surface with an arbitrary population of steps is then calculated in a "kinematical" way using the results of these dynamical computations as inputs.

The coordinate system used in this work is shown in figure 1. The incident wavepacket is assumed to have a convergence angle small enough to be treated as a plane wave with wavevector **k** nearly parallel to the z axis. Only surfaces with steps parallel to the y direction (approximately perpendicular to the incident beam) are treated. For this case, the surface is periodic only in the y direction and the standard Bloch formalism is used in a slightly modified form to write the wavefunction outside the crystal:

$$(1) \qquad \Psi(x,y,z) = \Sigma_{Gy} \exp\{i\,(K_y + G_y)\,y + i\,(k_x\,x + K_z\,z)\}\ \Phi_{Gy}(x,z)$$

where G_y is a reciprocal lattice vector of the surface parallel to the step edges and $\Phi_{Gy}(x,z)$ is the plane wave decomposition of the Bloch function outside the crystal. The core of the method is that instead of calculating the $\Phi_{Gy}(x,z)$ from a full dynamical simulation, they are approximated by:

$$(2) \qquad \Phi_{Gy}(x_p,z) = \Sigma_i\, M(\,z - z_i\,, \Delta z_i\,)\ \{\,P_{Gy}(h_s - h_i\,, z - z_i\,) \otimes \varphi_\alpha(\,x_p\,, z - z_i\,)\,\}$$

The surface consists of terraces of height h_i and width Δz_i which start at z_i.(figure 1) The three terms have the following meanings: M is a shape function which broadens the scattering as the width of the terrace is reduced; $\varphi_\alpha(\,x_p\,, z - z_i\,)$ is the scattering from a surface with a single step at z=0 ending on a

terrace of height h_s taken from full dynamical reference calculations; and P is a function which accounts for the phase shift between terraces of different heights. The $\otimes$ indicates a one dimensional convolution in the z coordinate. A more restrictive approximation can be made by replacing the φ_α with the scattering from a flat surface.[3]

Test calculations using equation 2 were performed for Fe(100) surfaces with monatomic steps parallel to [010] and compared to the results of full dynamical calculations performed with the Cowley-Moodie multislice method and the edge-patching algorithm. The dynamical reference calculations required for the application of equation 2 were also performed with the Cowley-Moodie multislice method with the edge patching algorithm. A single rod (or systematic row) model was used in which the potential was constant parallel to the step edges. The incident beam azimuth was [001], the energy was 10 keV, and the incident angle was 30.2 mrad. The steps were evenly spaced with consecutive steps in opposite directions. Figure 2 shows the comparison between the full dynamical calculation and the calculation done using the approximation represented by equation 2 for a step spacing of 9.2 nm. The agreement at the specular peak (24.7 nm^{-1}) is very good and less good at the satellite peaks (which are due to the step period). When the step spacing is increased to >= 18 nm the curves are indistinguishable across the whole range.

The range of step sizes for which this approximation is valid can be expected to depend on the material, beam energy , and diffraction conditions. Under the conditions of this test this approximation is valid for rough Fe (100) surfaces with minimum terrace sizes on the order of 10 nm to 15 nm.[4]

1. Z.L. Wang, *Elastic and Inelastic Scattering in Electron Diffraction and Imaging*, Plenum Press:New York (1995).
2. Y. Ma and L.D. Marks, *Acta Cryst*, A47 (1991) 707.
3. A. Ichimiya, *Surface Science*, 187 (1987) 194.
4. This work was performed at the Materials Research Lab with the support of Department of Energy Grant DEFG02-91ER45439.

1

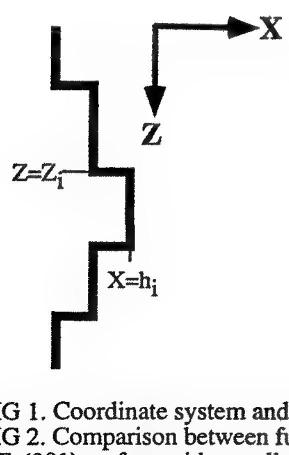

2

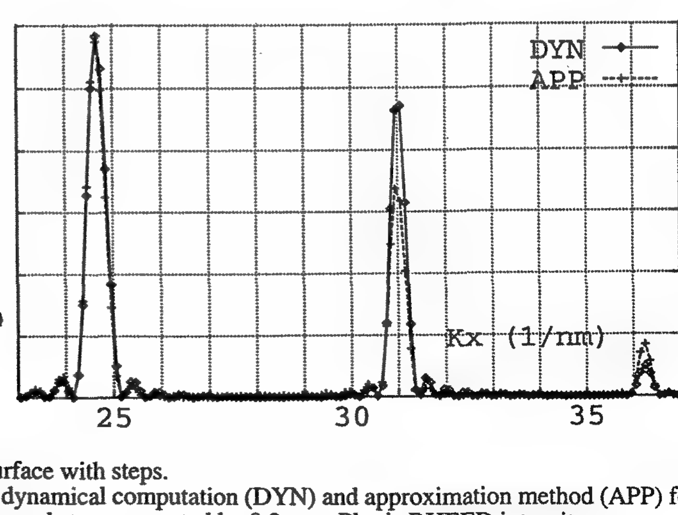

FIG 1. Coordinate system and surface with steps.
FIG 2. Comparison between full dynamical computation (DYN) and approximation method (APP) for a Fe(001) surface with equally spaced steps separated by 9.2 nm. Plot is RHEED intensity versus normal component of the scattered wavevector.

Improving X-Ray Map Resolution With Image Restoration Techniques

Richard B. Mott, John J. Friel, and Charles G. Waldman

Princeton Gamma-Tech, Princeton, NJ 08540

X-rays are emitted from a relatively large volume in bulk samples, limiting the smallest features which are visible in X-ray maps.[1] Beam spreading also hampers attempts to make geometric measurements of features based on their boundaries in X-ray maps.[2] This has prompted recent interest in using low voltages, and consequently mapping L or M lines, in order to minimize the blurring of the maps.[1,3]

An alternative strategy draws on the extensive work in image restoration (deblurring) developed in space science and astronomy since the 1960s. A recent example is the restoration of images from the Hubble Space Telescope prior to its new optics. Extensive literature exists on the theory of image restoration.[4,5] The simplest case and its correspondence with X-ray mapping parameters is shown in Figures 1 and 2.

Using pixels much smaller than the X-ray volume, a small object of differing composition from the matrix generates a broad, low response. This shape corresponds to the point spread function (PSF). The observed X-ray map can be modeled as an "ideal" map, with an X-ray volume of zero, convolved with the PSF. Figure 2a shows the 1-dimensional case of a line profile across a thin layer. Figure 2b shows an idealized noise-free profile which is then convolved with the PSF to give the blurred profile of Figure 2c.

In principle, the ideal profile can be recovered from the observed profile if the PSF is known. The simplest procedure uses the Fourier transform property that convolution in space corresponds to multiplication in the Fourier domain. Therefore, the deconvolution problem becomes a division in Fourier space (ignoring the possible problem of zeros in the transformed PSF). Figure 2d shows the result after transforming back to the spatial domain with the Inverse Fourier Transform (IFT). The same procedure is easily generalized to two dimensions for X-ray maps. In practice, direct Fourier division will result in an extremely noisy image because the pixel counting statistics of X-ray maps are often poor, and small errors in the estimated PSF result in large errors in the reconstructed map. It is necessary to apply various least-squares constraints on the restored image, such as those used in Weiner filtering.[6]

For the special case of small objects in a known uniform matrix, application of constrained Weiner-type restoration should substantially improve limits of detectability, assuming the PSF is spatially invariant. For more general cases of X-ray mapping, this assumption is false because the X-ray volume and therefore the PSF depends on the composition at each pixel. General restoration of X-ray maps needs the full spectrum at each pixel in order to derive the composition, and the restoration will be an iterative process in which successive restored maps will be used to update the composition and PSF estimates. The PSF also depends on the energy of the line being mapped. In the limit, as computing capacity advances, perhaps we may look forward to X-ray spectrum image restoration, from which compositional images may be derived at better spatial resolution than is now considered possible.

References

1. J. J. Friel, *X-Ray And Image Analysis In Electron Microscopy*, N.J.: Princeton Gamma-Tech(1995)24.
2. C. Blais, G. L'Esperance, E. Baril, C. Forget, Microbeam Analysis -- 1995, 377.
3. C. Nockolds, Microbeam Analysis -- 1995, 371.
4. R. Gonzales and P. Wintz, *Digital Image Processing*, Reading, MA.:Addison-Wesley (1977)183.
5. A. K. Jain, *Fundamentals of Digital Image Processing*, Englewood Cliffs, NJ: Prentice Hall(1989)267.
6. Ibid., 276

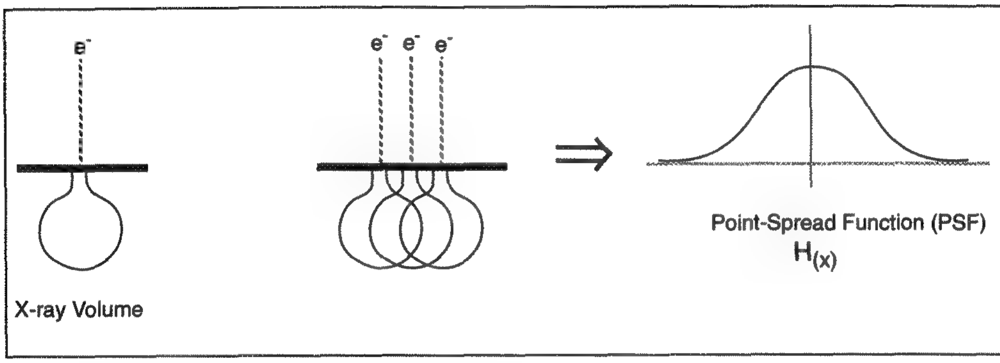

Figure 1. The point spread function (PSF) corresponds to the X-ray intensity detected as the beam is scanned in very fine steps over a point source.

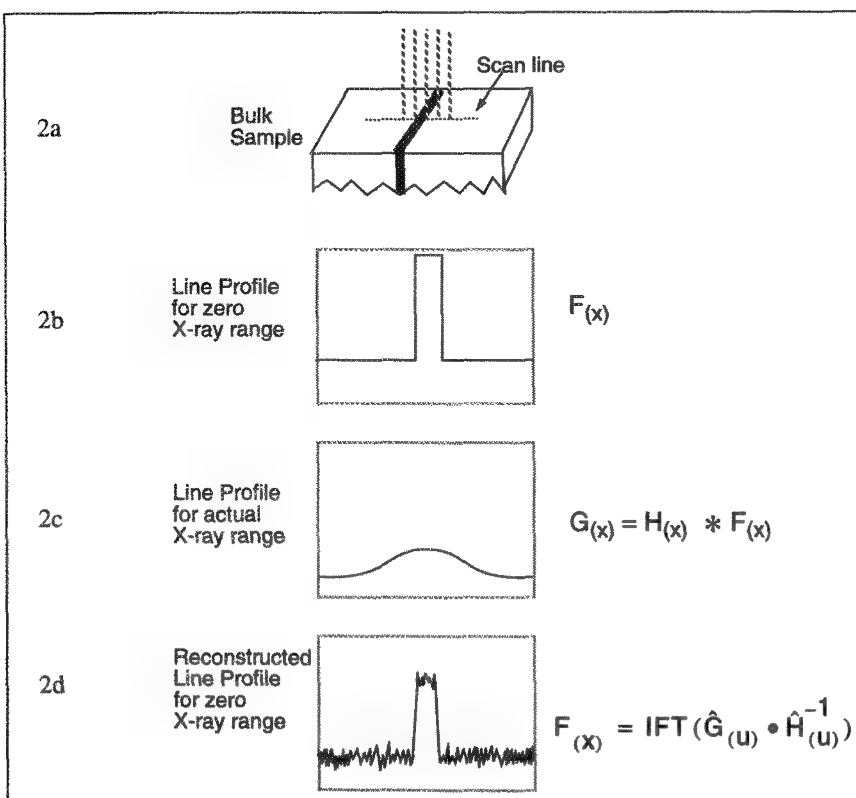

Fig. 2. The observed line profile of 2c results from the convolution of the ideal line profile of 2b with the PSF. An estimated ideal profile is recovered by dividing the Fourier transform of the observed profile 2c by the Fourier transform of the PSF, and inverting the Fourier transform.

THE SYNTHETIC APERTURE MICROSCOPE

William R. Franklin,* Terry M. Turpin,* Jeffrey R. Lapides,* Craig Price,* Paul Woodford,* and Lee D. Peachey**

*Essex Corporation, 9150 Guilford Road, Columbia, MD 21046-1891
**Dept. of Biology, University of Pennsylvania, Philadelphia, PA 19104-6018

It is well known that the resolution of a microscope depends critically on the aperture of its objective lens. Achieving wide apertures requires the lens to be extremely close to the sample being imaged, which is often inconvenient. We describe an optical microscope, currently in breadboard form, that achieves a large aperture, and thus high resolution, with a large (theoretically unlimited) working distance, based on the principles of synthetic aperture radar (SAR).

The synthetic aperture microscope (SAM)[1] makes time sequential measurements of the complex three-dimensional Fourier components of the transmissivity or reflectivity of an object. An individual component is sensed by illuminating the object with a plane wave of coherent light and interferometrically measuring the amplitude and phase of the scattered wave. Physically, the system utilized a Bragg scattering condition to select each component. By using rotating transmitters and receivers, the three dimensional k-space of the object is recorded. It is shown that the resolution in each dimension is inversely proportional to the bandwidth sampled in that k-space dimension. The best resolution obtainable is 1/4 the wavelength of the illuminating light, twice that achievable with an objective lens.

It is further shown that the spherical or polar symmetry of desirable collection geometries for SAM result in curvilinear samplings of k-space. Consequently, in order to utilize the fast Fourier transform algorithm, it would be necessary first to interpolate the samples onto a linear grid in k-space. An adequate interpolation process would add enormous computational complexity to the reconstruction procedure, rendering it impossible to perform real-time image reconstruction, even with the most powerful workstations. The approach presented here is to reconstruct the image using a high performance, optoelectronic processor (originally inspired by the needs of SAR) which performs a discrete inverse Fourier transform on the data, thus avoiding the interpolation entirely. It is the enormous computational capacity of this processor that permits the real time reconstruction of three-dimensional images independent of the k-space sampling scheme.

A control module selects the field (or several sub-fields) of view to image, selects the Fourier components of the object to measure, controls the measurement of the complex scattered optical waves, implements image processing algorithms in the frequency domain prior to image formation, and selects the Fourier components to be used in forming the final image and the viewing angle for this image. This independent selectability in both spatial and frequency domains, without a need either to collect data on a rectangular grid or to interpolate the data onto such a grid before inverse transformation, effectively provides a microscope with a programmable lens. In that sense, this is the most general form of microscopy.

The advantages of SAM over conventional microscopy include ease of correcting systematic errors in the sensing process, reliance on optical designs that function in the paraxial approximation, the ability to generate full, three-dimensional complex images from any arbitrary viewing angle, the possibility to image from large distances, the simplicity of implementing filters and other image processing algorithms by direct manipulation of the Fourier data, and the ability to choose multiple sub fields of view that can vary in both shape and spacing.

References

1. T. Turpin et al., SPIE Proceedings, 2566B-34, July 1995, San Diego, CA.
2. T. M. Turpin (1992) "Sequential Image Synthesis" U.S. Patent 5,079,565 Jan 7, 1992.
3. The work of L. D. Peachey was supported by Grant No. RR2483 from the National Institutes of Health, and that of the other authors by the Essex Corporation.

1

2

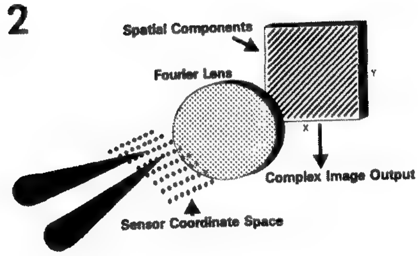

3

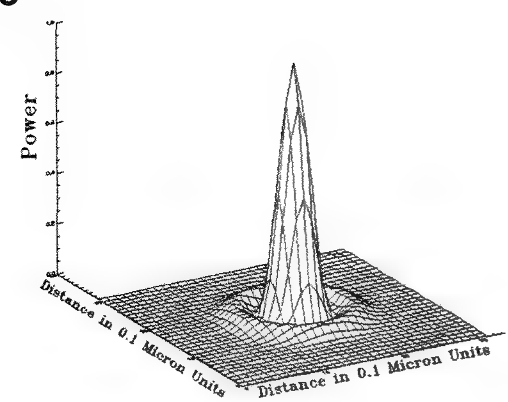

4

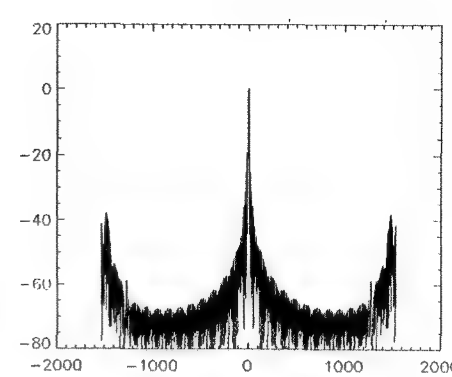

FIG. 1-The mechanical and optical arrangement used for data collection. The transmitter and receiver can consist of single or multiple elements. Our breadboard design uses a single element transmitter and an array for photosensing.

FIG. 2-The ImSyn™ processor performs discrete Fourier transforms interferometrically. By interfering two mutually coherent point sources of light in the front focal plane of a lens, sinusoidal fringe patterns are produced in the back focal plane which represent individual Fourier components. Altering the source amplitudes, relative phase, separation and angular orientation of the sources with acousto-optic devices (not shown), creates arbitrary spatial frequency components which are sequentially written and summed on a photosensing array, building up the image.

FIG. 3-Theoretical point spread function (PSF) for a SAM. The PSF resulting from 128 horizontally positioned detectors rotated through 1024 angles is shown. Vertical scale is power scaled to the peak. A full width at half power maximum value of 0.4 microns is obtained for 0.83 micron illumination.

FIG. 4-A wide view of the PSF for a SAM - The same PSF from FIG. 3 is displayed to show side lobe structure and aliasing contributions. The vertical scale is power in dB from peak, and the horizontal scale is distance in units of 0.1 micrometer. An alias free field of view of 100 micrometers is obtained.

Digital Imaging: When should one take the plunge?

John F. Mansfield
Electron Microbeam Analysis Laboratory, University of Michigan, 413 SRB,
2455 Hayward, Ann Arbor MI 48109-2143
Email: John.F.Mansfield@umich.edu
URL: http://emalwww.engin.umich.edu/people/jfmjfm/jfmjfm.html

The current imaging trend in optical microscopy, scanning electron microscopy (SEM) or transmission electron microscopy (TEM) is to record all data digitally. Most manufacturers currently market digital acquisition systems with their microscope packages. The advantages of digital acquisition include: almost instant viewing of the data as a high-quality positive image (a major benefit when compared to TEM images recorded onto film, where one must wait until after the microscope session to develop the images); the ability to readily quantify features in the images and measure intensities; and extremely compact storage (removable 5.25" storage devices which now can hold up to several gigabytes of data).

The problem for many researchers, however, is that they have perfectly serviceable microscopes that they routinely use that have no digital imaging capabilities with little hope of purchasing a new instrument. The question for them is: should I wait until I can get funding to purchase a new instrument at a later date, or should I try and take advantage of the benefits of digital imaging now? The answer to that question depends on several criteria; the dynamic range of the images to be recorded, the desired resolution, whether real-time acquisition is desirable and, of course, how much one can afford to pay for a system.

Digital imaging requires the connection of a TV camera to the microscope and a computer system to capture the image that is output by the camera (SEM digital imaging is slightly different and discussed below). Since they are light, compact, offer the capabilities of slow-scan capture, and on-chip integration, CCD TV cameras are the most popular type of camera used. Prices range from several hundred dollars to tens of thousands of dollars and are commensurate with the number of features. The lower priced cameras typically will deliver images at regular TV rate, i.e. 30 frames per second, and offer no cooling of the CCD chip for noise reduction or on-chip integration to improve low intensity images. Higher priced cameras will offer digital slow-scan output direct to a computer with 8, 10, 12 or even 16 bit intensity resolution, on-chip cooling and integration, and will be packaged with a controller card that is inserted into a personal computer or workstation.

Optical microscopy's transition to digital imaging may be a very straightforward processwith the purchase of a TV adapter for the microscope, a suitable TV camera and a computer system with an image acquisition board or frame-grabber. If 8-bits of information (256 grays or colors are sufficient for recording and analyzing the images in question) then such a system could cost less than $4000, however, if more than eight bits are required and/or a slow scan camera is necessary, the price can quickly climb into the tens of thousands of dollars.

TEM has the added complexity that the camera must be interfaced with the column of the microscope. Initially there were only one or two vendors who were able to offer such systems, but, as the market has expanded a number of vendors now offer systems. This competition between vendors coupled with a reduction in cost of the basic hardware has driven prices down. It is possible to buy a basic slow scan imaging system for a TEM for less than $35,000.

Digital image acquisition in SEM is performed in one of two ways. Passive recording involves synching the computer based acquisition system with the raster of the SEM probe, whereas active acquisition requires the computer system to take control of the SEM probe. In either system the secondary electron signal is digitized by an analogue to digital acquisition board in the computer and displayed on the computer screen. X-ray Energy Dispersive Spectroscopy (XEDS) systems manufacturers have been offering this capability for decades, but, with the introduction of the inexpensive desktop computers, and provided that the scanning system of the microscope in question can be controlled remotely, such systems can be purchased for less than $20,000 (including the price of the computer).

The Electron Microbeam Analysis Laboratory (EMAL) at The University of Michigan is a good example of where low-cost digital acquisition systems have been added to existing scopes. The EMAL analytical electron microscope, a JEOL 2000FX, has a Gatan model 673 TV-rate CCD camera mounted on the 35mm camera port. This relatively inexpensive camera (less than $20,000) was purchased to allow the video-taping of dynamic experiements conducted with the hot, cold and straining stages of the microscope. Connection of this camera to a Scion LG-3 video frame-grabber in an Apple Macintosh computer running the NIh-Image software has allowed a number of groups acquire digital images with this camera for grain and particle size measurement and dislocation density determinations.

The JEOL 2000FX can be used to acquire digital images in the scanning transmission (STEM) and secondary electron (SEM) modes. The XEDS system on this microscope is a Tracor/Noran TN5500 with the digital imaging option. Although this system is far from state-of-the-art, it performs flawlessly for the acquisition of digital images. The images are transferried via Ethernet to external workstations for manipulation and analysis. The Tracor/Noran system does not support such networking and so a secondary operating system and file transfer software have been installed on the TN5500 PDP-11. Networking the TN5500 cost approximately $2500, and it was the most cost effective way of accessing the digital images recorded on the 2000FX.

The EMAL high resolution electron microscope, a JEOL 4000EX, has an image-intensified Gatan model 622 TV camera mounted beneath the camera chamber. This camera has also been connected to a Scion LG-3 frame grabber and Macintosh combination. Moderate quality images may be recorded with this system, particularly when one uses the real-time capture capability of the LG-3. With 16 megabytes of on-board memory it is possible to perform frame averaging from 32 consecutive video frames. Users are able to check the scope alignment by Fourier analysis of the digitized images before committing their data to film. The 32 video frames can also be used to study dynamic events in the microscope, Martin et al have used the system to study the *in-situ* polymerization of their polydiacetylene samples[1].

EMAL also houses an Environmental Scanning Electron Microscope (ESEM), an ElectroScan model E3. While this instrument is computer controlled, it is one generation removed from having a completely integrated image acquisition, manipulation and storage system. Digital images and XEDS maps are acquired with a 4Pi Analysis Spectral Engine, installed in an Apple Macintosh computer. The 4Pi system drives the scanning system of the ESEM directly and can record 8-bit images up to 4096 by 4096 pixels in size. Since such images are 16 megabytes in size, routine images are recorded at 512 by 384 pixels or 1024 by 768 pixels.

A single microscope user may be able to generate tens or even a hundred images in a single session. If each image is between 0.25 and 1.0 megabytes in size, then even the 1 gigabyte hard disks of today's typical desktop computers cannot store more than about 20 days worth of data for a single user. Serious thought has to be given to off-line storage and archive options. Since EMAL is a multi-user facility serving twenty to thirty departments on campus for their microscopy and microanalysis needs, efficient storage of data has been absolutely essential. Each of the data acquisition computers in the laboratory not only has a removable storage option (Iomega ZIP drives), but also has access to the campus computer network and is capable of communicating via a variety of network protocols. The principle here is that the users may transfer their data to their local PCs or workstations where it is their responsibility to archive their data or save it directly to a removable disk. The data storage space on the laboratory hard disks is viewed as temporary and is purged frequently.

It is clear from the experience of The University of Michigan EMAL one can use digital imaging effectively without having to purchase all new instrumentation. While it is still necessary to use film for high quality publication images, much of the routine data may be recorded on the low cost systems described above.

References

1. J. Liao& D.C. Martin, Science 260 (1993) pp1489-1491.

METHODS AND MORALITY OF DIGITAL MANIPULATION OF MICROSCOPIC IMAGES

J. C. Kinnamon[*†] and Terri A. Sherman-Crosby[*†]

[*]Department of Biological Sciences, University of Denver, Denver, Colorado 80208 and [†]The Rocky Mountain Taste and Smell Center, Denver, CO 80262

In recent years dramatic increases in both the computational power of personal computers and the ability of image enhancement software to "retouch" acquired images have provided the structural biologist with capabilities that were undreamed of less than a decade ago. Possessing the power to manipulate acquired images, however, does not necessarily mean that it is appropriate to do so. The goals of this presentation are: 1) to describe how images can be enhanced using commonly available software (*e.g., Adobe Photoshop*) and 2) to present some of the ethical issues related to the manipulation of microscopic images.

First of all, it should be stated that manipulating images did not begin with the introduction of the computer. The ability to adjust the appearance of microscopic images has been around as long as the darkroom. Several options for image manipulation were available to the skilled darkroom technician. One could adjust the contrast level by using different grades of paper, or increase the contrast level and sharpness or "snap" by using a point source illumination instead of an opal light source. A scratch on a negative might be covered by retouching the print using *Spotone*. Dodging and burning were used to even out poorly exposed images.

Instead of altering images in the darkroom, we can now use *Adobe Photoshop, NIH Image* or other software to enhance scanned microscopic images. Common operations include the following: 1) *Unsharp Mask* is used to sharpen the apparent focus of an image, 2) *Gaussian Blur* is used to even out an unevenly exposed negative, 3) the *Rubber Stamp* tool is used to retouch images by removing blemishes or artifacts, 4) the *Dodge/Burn* tool has similar results to the traditional darkroom technique, 5) the *Dust and Scratches* filter can be used to reduce noise due to dust or scratches by searching a selected area of pixels for "different" pixels and blurring those different pixels to match the surrounding pixels, and 6) the *Levels* command can be used to adjust the gamma curve of the image. Probably the two most commonly used procedures are the *Unsharp Mask* and the *Levels* command.

Under what circumstances is it appropriate to manipulate digitized images? We posed this question to several principal investigators, EM facility directors, and editors of journals whose primary subject matter is structural biology. It is manifest that no consensus exists concerning the manipulation of microscopic images. Some are comfortable with almost any kind of manipulation so long as the information content of the image is not altered and a description of the filters and operations used is included in both the *Materials and Methods* and the *Figure Legends* of the manuscript. Others are emphatic in their belief that any manipulation with the computer is inappropriate. We believe that the time has come to reach a consensus on this very sensitive and contentious issue.

Supported in part by NIH grants DC00285 and DC00244.

Figure 1. Dye sublimation print created from a scanned negative of a transmission electron micrograph of a hamster taste bud before enhancement. Staining artifacts (white arrows), hole in section (black arrow), poorly exposed region (asterisk).
Figure 2. Digitally manipulated image of Figure 1 in which the *Unsharp Mask*, *Gaussian Blur*, *Rubber Stamp*, and *Levels* operations in *Adobe Photoshop* were used to remove artifacts and enhance the image.

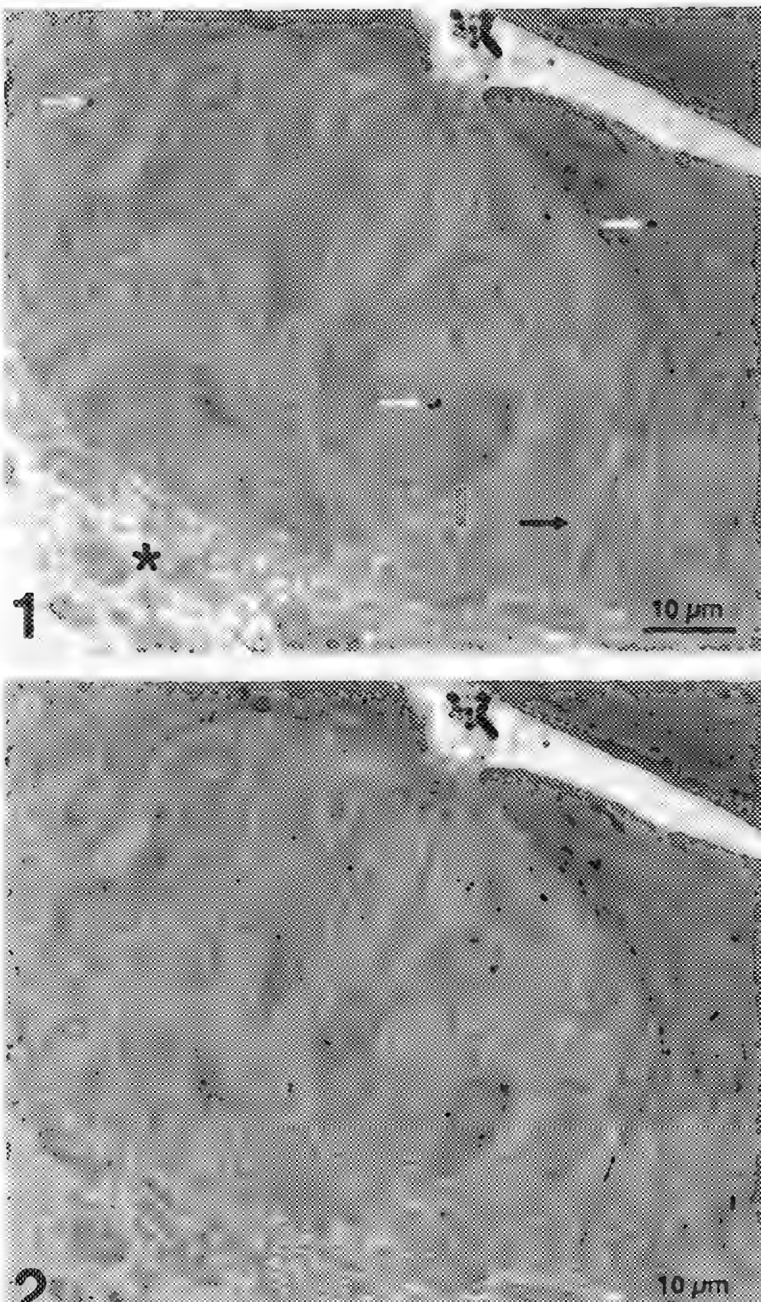
1
10 μm
2
10 μm

PRACTICAL CONSIDERATIONS AND APPLICATIONS OF DIGITAL IMAGING IN A CORE MICROSCOPY FACILITY

R.L. Price

Department of Developmental Biology and Anatomy, School of Medicine, University of South Carolina, Columbia, SC 29208

The Integrated Microscopic Analysis Facility (IMAF) at the University of South Carolina School of Medicine is a core research and imaging facility that provides service for the faculty, staff and students of the medical school and associated hospitals. The IMAF currently houses one scanning and two transmission electron microscopes, a confocal scanning laser microscope, and several image processing computers and programs. While not yet totally converted to digital technology, we have been successful in introducing digital imaging to several areas of our imaging capabilities during the last few years. The purpose of this abstract and subsequent presentation is to present some practical considerations and problems we have encountered in the conversion of the IMAF to digital imaging microscopy, and to present brief results from some projects which were not possible before the introduction of digital imaging to the facility.

There is little doubt that in the past few years one of the major advances for those of us who work in the areas of light and electron microscopy has been the development of digital imaging technology. The ability to collect, store, enhance and analyze digitized images has reduced the per project time many of us spend in the collection and analysis of data, and in some cases eliminated the need for tedious darkroom work. However, as with the rapid advancement of technology in many areas, new problems are introduced as quickly as old problems are minimized or solved. Problems which have arisen in the conversion to digital imaging in the IMAF include compatability of data storage devices, the ability of various programs to read the large number of image storage formats that exist, requirements for additional computer literate staff, and additional expenses associated with the maintenance and upgrade of computers and programs.

Figure 1 illustrates the current configuration of our networked instrumentation and shared hardcopy devices. Networking of the computers and associated hardware has minimized many of the initial problems we encountered with the management of large files, various file formats and data storage devices, but as we have added components to the system, we have also found it necessary to add two graduate assistants with computer engineering backrounds. One graduate assistant is currently responsible for maintaining and troubleshooting the computer

network and for transmitting data to remote locations. The second graduate assistant is responsible for the operation of the Silicon Graphics workstation and assisting users in reconstruction of data sets collected on the confocal microscope.

The addition of the graduate assistants has been essential in freeing time for other staff members to perform microscopy tasks associated with the research projects submitted to the IMAF. The majority of these projects are heart, brain, or eye related and encompass a full range of techniques from cell and whole embryo culture to observation of specimens that have developed *in vivo*. Brief results from some of these projects will be presented to illustrate the capabilities and advantages of digital imaging techniques in our ongoing research projects.

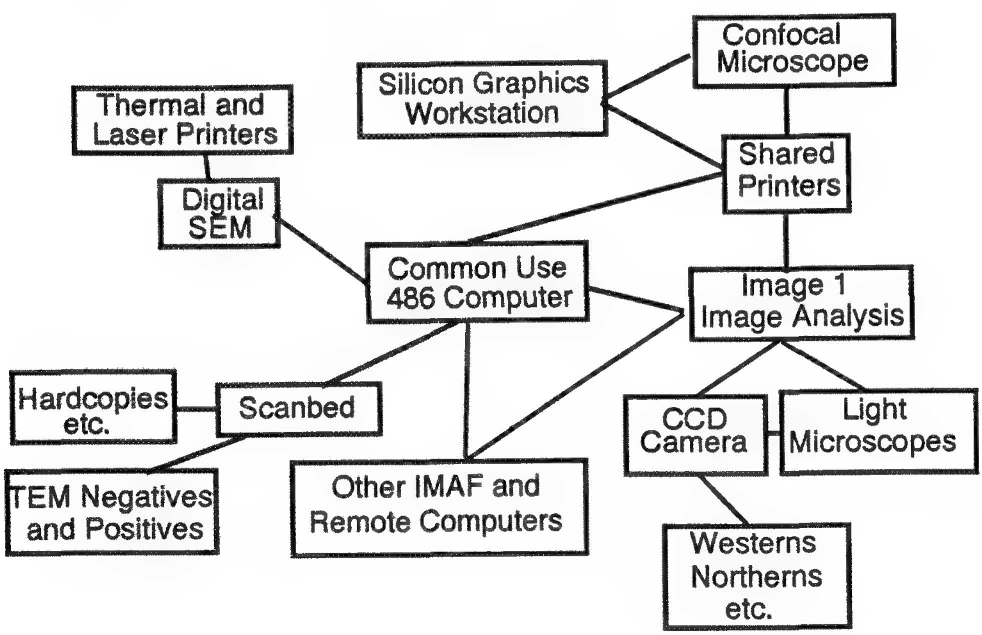

Figure 1. Schematic diagram of the networked computers and shared devices used in the Integrated Microscopic Analysis Facility.

MIGRATING TO DIGITAL IMAGING FROM FILM

J. R. Minter, K. Schlafer, G. Sotak, and L. Thom

Eastman Kodak Company, Analytical Technology Division, Rochester, NY 14652-3712

Since the invention of the microscope, most images were recorded on photographic film. For transmission electron images, Hamilton and Marchant recognized that most photographic films are "nearly perfect detectors, in that they record the input signal without appreciable loss and do not seriously add to the input noise."[1] Despite film's efficiency as an image recorder, microscopists complained about the long cycle time between image recording and completion of the final print. Quantitative image analysis of images recorded on film is also time-consuming and expensive because microdensitometers capable of producing high quality and high resolution scans of negatives are slow and expensive.

Over the past few years several new technologies to record light and electron images have been commercialized.[2,3] The oldest of these are video-rate cameras and TV-rate cameras built with charge coupled devices (CCDs). These are limited by small image size (512 x 478). Larger format digital cameras built using slow-scan CCD cameras have recently been applied to light and transmission electron microscopy. Digital scan generators and frame buffers have been added to scanning electron microscopes.

With all the new choices of image recorders available, the microscopist is faced with a complicated choice of the optimum sensor for a particular project. No single sensor has been demonstrated to be the optimum sensor for all applications. This presentation will compare the performance of film to digital cameras for image capture. Sensor performance is judged on the basis of the spread function, signal-to-noise characteristics, and the sensitometric curve shape. Digital image capture may also include hybrid systems where the original image is captured on film and digitized with one of a variety of scanners. The performance of several of these scanners will also be discussed.

Image capture is just the first step in the microscopy imaging chain. The microscopist's job is not complete until the images have been shared with the appropriate audience and properly stored for later retrieval. This presentation will compare the various hard-copy output methods available to microscopists today, including thermal dye printers, ink-jet printers, and laser printers. The appropriate choice of one of these printers depends upon the resolution, image tone, and cost requirements of the particular project. There are a myriad of digital image storage options available to the microscopist. These include magnetic and digital audio tape (DAT), removable magnetic media, magneto-optic media, and writable CD-ROM. The appropriate choice of one of these media depends upon the requirements for useful life of the images, frequency of access, input/output rate, cost, and the hardware used by collaborators. Our laboratory uses removable magnetic media for short-term transport and magnetic tape and writable CD for long-term storage.

---

1. J. F. Hamilton and J. C. Marchant, J. Opt. Soc. Amer., 57(2), 232-239 (1967).
2. O. L. Krivanek and P. E. Mooney, Ultramicroscopy, 49, 95-108 (1993).
3. J. C. Russ, The Image Processing Handbook, 2nd Ed., pp. 1-77, CRC Press, Boca Raton, FL (1995).

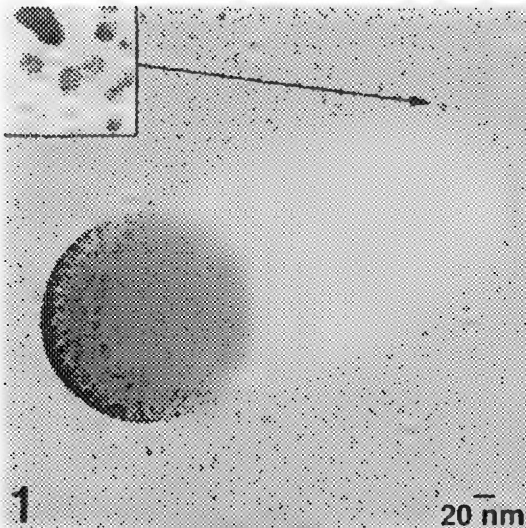

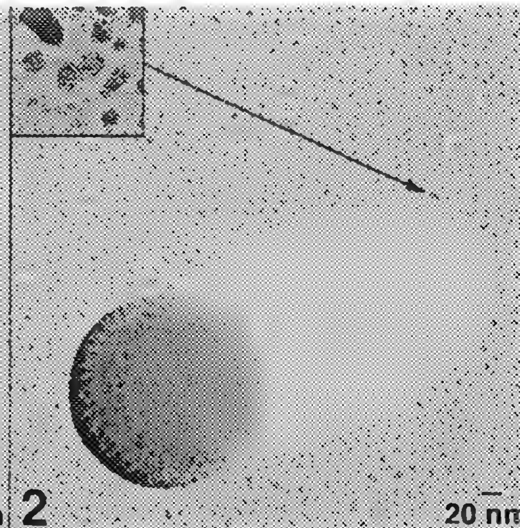

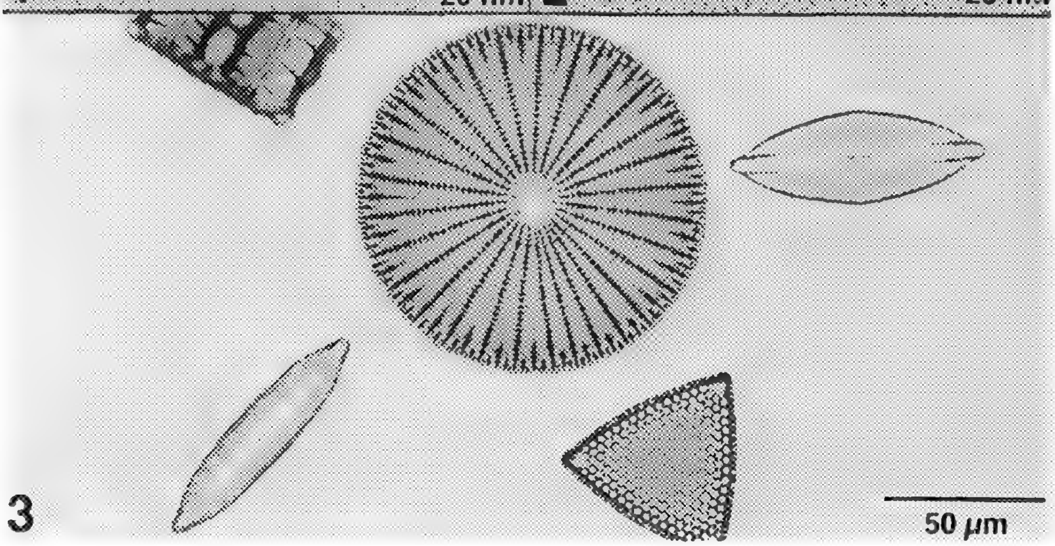

Figure 1. Image of a Au-shadowed latex recorded with a Gatan Model 694 Slow Scan CCD camera [38kX nominal mag., 120kV]. Inset: area enlarged 4X by pixel interpolation. This camera has a total mag. 1.35X nominal. All figures printed with a KODAK XLT 7720 Digital Continuous Tone Printer.

Figure 2. Image of the same area as Figure 1 recorded on KODAK Electron Image Film SO-163 and digitized at 25 μm resolution on a Optronics P1000 rotating drum microdensitometer. Inset: area digitized at 5 μm resolution on a Perkin Elmer flat-bed microdensitometer.

Figure 3. Image of diatoms recorded on a KODAK Professional Digital Camera System, DC3 [600X nominal mag., 40X 0.95 N.A. objective].

UNIX-BASED WORKSTATIONS FOR DIGITAL IMAGE PROCESSING AND ANALYSIS

Eddie B. Prestridge

Princeton Gamma-Tech, 1200 State Road, Princeton, NJ 08540

The modern workstation, with its inherent high speed and massive memory, allows the use of complicated image analysis and processing algorithms and artificial intelligence programs not available to current PCs and mini-computers.[1,2]

There is no single feature that differentiates the UNIX based workstation from a PC. Rather, it is its fundamental design that gives the workstation superior performance. This superiority in no small part is the result of the UNIX operating system.[3] UNIX is a word that sometimes strikes fear into the hearts of mortal men! There is no reason to fear, however. Users of UNIX-based systems have no more interaction with the operating system than say users of WordPerfect running on a MS-DOS or MAC OS machine.

UNIX is the only operating system that runs on a wide range of systems from laptops to mainframes. It is unique in at least five areas: 1) massive data sets handling, 2) multitasking, 3) multi-user, 4) security, and 5) networking. Let me give you what I think are usable descriptions for these five areas.

Data Sets: UNIX allows the use of what is known as demand page virtual memory. This feature allows the computer to operate on programs or massive data sets much larger than its physical memory. Artificial intelligence (rule based) programs would not be possible without this feature, which is absent in MS-DOS and MAC OS.

Multitasking: The UNIX operating system is designed so that many active applications or utilities can run simultaneously. Regardless of the "hype" for some windowed environments for the other operating systems, they simply are not multitasking. Every time a new operation is started something else has to stop. For example, with a UNIX based system you can backup your whole system while continuing to do image collection and analysis. Try that on your PC.

Multi-user: Multiple users can access a workstation using terminals and other workstations over a network. Also, the look and feel of the system can be changed to suit each individual user.

Security: Users are given personal security parameters that ensure sensitive files are given unique read, write, and execute permissions. UNIX workstation users must use a password to log-in. In other words, I may let you look at my images but you can not keep them or change them. This is very important in situations where you have open use (many users) of the system.

Networking: Unlike MS-DOS, many networking applications are bundled in the UNIX operating system. One of these is standard/integrated ethernet. PC systems have to use third party software/hardware for which there is no standard.

References

1. J. J. Friel et al., MiCon 90: *Advances in Video Technology for Microstructural Control*, ASTM STP 1094, American Society for Testing and Materials, Philadelphia (1990)170.

2. J. J. Friel and E. B. Prestridge, *Artificial Intelligence for Twin Identification*, ASTM STP 1165, American Society for Testing and Materials, Philadelphia (1993)243.

3. B. Ritchie and K. Thompson, *The UNIX Time Sharing System*, Bell System Technical Journal, 57, #6, pt 2, AT&T(1978).

THE IBM-PC IN ELECTRON MICROSCOPY

James F. Mancuso

Advanced Microscopy Techniques Corp., Danvers, MA 01923

IBM PC compatible computers are widely used in microscopy for applications ranging from control to image acquisition and analysis. The choice of IBM-PC based systems over competing computer platforms can be based on technical merit alone or on a number of factors relating to economics, availability of peripherals, management dictum, or simple personal preference.

IBM-PC got a strong "head start" by first dominating clerical, document processing and financial applications. The use of these computers spilled into the laboratory where the DOS based IBM-PC replaced mini-computers. Compared to minicomputer, the PC provided a more for cost-effective platform for applications in numerical analysis, engineering and design, instrument control, image acquisition and image processing. In addition, the sitewide use of a common PC platform could reduce the cost of training and support services relative to cases where many different computer platforms were used. This could be especially true for the microscopists who must use computers in both the laboratory and the office.

"Ease of use" was one area that involved intense debate concerning the characteristics of the DOS operating system. Great strides have been made in this regard - spurred by the adoption of the Windows and OS-2 interfaces. Today the ease of use issue is mostly based on personal preference, the local environment and the past experiences of the user. Other deficiencies in the DOS operating system were limitations in memory usage, the lack of multitasking, and limits in the number of devices that could be installed on a given platform. Again these limitations have been reduced or eliminated with the modern operating systems.

The major advantage of the IBM-PC is its unmatched installed base and the wide choice of both hardware and software that is available for it. For microscope control especially, the PC offers the greatest number of options for A/D - D/A conversion, digital I/O, digital communications, industrial grade electronics, display and hard copy output devices, automation and motion control. Although the graphics capability initially lagged traditional "workstations" and Macintosh systems, the gap has closed substantially, if not completely, in terms of both price and performance.

Intense competition among PC equipment suppliers drives down the purchase price of both peripheral devices and applications software. The microscopist can choose from large number of pre-packaged image processing packages for image analysis, archiving and enhancement. In addition there are numerous companies that customize these packages for specific applications. A multitude of software development packages are available, and PC programmers can be found in most technical organizations. The rapid progress in computer hardware has allowed today's PC to run image processing and

graphics applications at speeds that, up until recently, could only be achieved by expensive workstations.

The large number of suppliers and possible configurations can lead to problems with hardware and software compatibility. Although all computer platforms face this issue, PC systems integration needs to be done with more care. A conservative approach in upgrading a system is usually a good idea.

The PC can stand alone, or it can be part of a network of similar PCs, or it can be "mixed and matched" with Macintoshes and UNIX based systems. Purely PC based networks are popular, but it is often useful to have a UNIX based network server. Because the PC is so commonly used, all other computer platform manufacturers have been forced to provide a means to communicate with the PC. In general, PC users can be assured that their files can be transferred to and read by other types of computer systems.

Today the computer evolved from the DOS based IBM-PC is a strongly competitive choice for use in the microscopy laboratory which can be easily integrated into the office environment.

PLATFORM WARS: MACINTOSH-BASED DIGITIZATION SYSTEMS

O. L. Krivanek and J. A. Hunt

Gatan Research & Development, 6678 Owens Drive, Pleasanton, CA 94588 USA

Improvements over the past few years in essentially all modern operating systems coupled with the blurring of the boundaries between mainframes, workstations, and personal computers make the choice of platform often one of personal preference other than of necessity. A decade ago there were very distinct differences between the features offered by IBM PC and clones, the Apple Macintosh, and UNIX workstations. These differences included price, processing performance, OS features, look and feel, graphical capabilities, memory and disk limitations, networking capabilities, ease-of-use, system stability, development tools, etc. Since then many of these distinguishing differences have evaporated making platform selection a more subtle issue, but also much less important. However, there are still a great many users that tend to make such decisions based on their "religious" preference of platform rather than based on objective information.

How does one choose the appropriate platform for image acquisition and processing? The question should first be - "What software packages do what is needed?" From this list the choice of platform can be narrowed. The next questions should then be: "What else is to be done with the system?", "What other systems will communicate with this platform?", "What kind of maintenance will the system need and who will do it?", "What platforms are the users comfortable with and how much time will it take to train the users to begin to use the system?".

The Macintosh has several image acquisition and processing packages available that cover the entire range of image processing and analysis needs. NIH Image (National Institutes of Health) is a good general purpose microscopy image processor (IP) that supports light and other microscopies where images are acquired through TV cameras or scanners. It also has the advantage of being free of charge. IDT makes a high-end, general purpose IP that has excellent scripting capabilities and analysis routines. Photoshop (Adobe) is good for acquiring and processing scanned or other images with limited dynamic range. DigitalMicrograph (Gatan) is a high-end IP that is tailored to electron microscope (EM) image acquisition and processing, allows data processing in floating-point resolution (desirable for high-quality data that is attainable in the EM), computer control of the EM and detectors, user scriptability, etc. These packages have other important features, and there are other excellent Macintosh IP software packages, but we of course can not mention them all here.

In the 1980's and even up until the mid-1990's, Macintosh programmers have had one extremely important advantage over PC programmers called "flat memory space". This feature allowed Macintosh programmers to use large amounts of memory in a very simple way. PC programmers had to resort to complicated methods to effectively use memory greater than 64K at a time and, before Windows 3.0, more than 640K total. Because the scientific community often requires processing data of several megabytes or more, the Macintosh became a natural choice of personal and laboratory computer for many scientists. For instance, image processing is a very memory intensive practice. A very basic IP system today may require only 16MB of RAM, whereas more state-of-the-art systems may require 128MB or more. The Macintosh (and workstations) handle arrays of memory approaching these sizes easily. However, software written for Windows 3.x (before Win32s) cannot address arrays of greater

than 64K in a straightforward manner. The increase in complexity impacted the quality and capability of most PC based image processing packages. This limitations have been removed in Windows NT and 95 but some manufacturers have not yet managed to purge their software of this older "16-bit" code.

Since its inception, the Macintosh users and developers have enjoyed a well defined set of graphical user interface (GUI) guidelines. This feature has allowed Macintosh software to be easy to use, because most Macintosh programs have common elements that work in similar ways - thus requiring the user to learn less about each application. It has also allowed Macintosh applications to work and share data together more easily than its Windows and UNIX counterparts. Strict GUI guidelines are now also available for Windows (3.0+/NT/95) but UNIX platforms still have several GUI variants. Macintosh programmers have also had the luxury of being able to access all hardware through a unified series of OS calls. The PC and UNIX worlds have been fragmented from the very beginning making these machines often difficult for the user to setup and difficult for the application programmer to support. This is the case for all types of hardware from printers to video cards to network access. The situation has been mitigated for the PC platform with recent improvements in OS technology (i.e., plug-and-play approaches), but the Macintosh still has fewer variations for programmers to consider. The Macintosh has long been considered the easiest platform to setup, use, and maintain.

The Macintosh has featured flat memory space, well defined GUI standards, and common access to peripherals such as display models and printers for such a long time - much longer than other platforms. Thus there is a very mature base of quality image processing, image manipulation, and image analysis software available for the Macintosh. The Macintosh integrates easily with the other platforms via seamless networking with most Network Operating Systems (NOS) and the ability to exchange portable disk media.

All the major OS and computer hardware manufacturers, including Apple, have been systematically correcting weaknesses in their platforms. Apple has made two major changes to its hardware recently. The most important change has been adopting the PowerPC RISC processor which has given the Macintosh a much needed increase in speed. The PowerPC 604 chip set used in the most recent Macintosh computers compares favorably with the P5 & P6 generation processors used in the most recent PC computers, particularly for floating point calculations. The second important hardware change has been moving to the PCI bus which allows manufacturers to design cards that operate on both the Macintosh and the PC. This has brought down the price and increased the availability of interface cards such as graphics accelerators and frame grabbers, particularly for the Macintosh. Apple will soon be releasing an important improvement to their OS called "Copland" which will significantly improve the Macintosh OS speed, the look and feel of the interface, and provide better multitasking capabilities.

Macintosh clones have now become important choices both in terms of price and performance. Power Computing currently makes the fastest single processor personal computers of any manufacturer. Daystar makes multiprocessor Macintosh clones that exceed 600 million floating-point operations per second. The PREP platform that IBM will be offering in the near future will allow a single machine to run UNIX (AIX), Windows NT/95, OS/2, and the Macintosh OS. The PREP strategy further blurs the distinctions between platforms further emphasizing that platforms are becoming less important than the software products themselves. Nevertheless, the Macintosh remains an excellent platform for image processing and analysis because of its mature base of IP packages, ease of use, ease of administration, ease of networking with other platforms, OS features, and high processing performance.

USE OF DIGITAL MICROSCOPY IN PROCESS CONTROL DURING THE MANUFACTURE OF RUBBER-MODIFIED THERMOPLASTICS

M. T. Dineen

Analytical Sciences Laboratory, The Dow Chemical Company, Midland, MI 48667

The production of rubber modified thermoplastics can exceed rates of 30,000 pounds per hour. If a production plant needs to equilibrate or has an upset, that means operating costs and lost revenue. Results of transmission electron microscopy (TEM) can be used for process adjustments to minimize product loss. Conventional TEM, however, is not a rapid turnaround technique. The TEM process was examined, and it was determined that 50% of the time it took to complete a polymer sample was related to film processing, even when using automated equipment. By replacing the conventional film portion of the process with a commercially available system to digitally acquire the TEM image, a production plant can have the same TEM image in the control room within 1.5 hours of sampling.

A Hitachi H-600 TEM Operated at 100 kV with a tungsten filament was retrofitted with a SEMICAPS™ image collection and processing workstation and a KODAK MEGAPLUS™ charged coupled device (CCD) camera (Fig. 1). Media Cybernetics Image-Pro Plus software was included, and connections to a Phaser II SDX printer and the network were made. Network printers and other PC and Mac software (e.g. NIH Image) were available.

By using digital acquisition and processing, the time it takes to produce a hard copy of a digital image is greatly reduced compared to the time it takes to process film. The digital image can be delivered rapidly and directly via the computer network to the operators of the production plant, whether locally or at another geographic location. Another benefit of digital acquisition is the immediate quantification of morphology via image analysis software (Fig. 2). Digital image archiving is an option and the inclusion of digital images for reports is easy. The system can also be quickly converted between film and digital modes.

However, with the system as described here, there is a cost for speed. The quality of the image is reduced compared to film. At low magnifications, the digital system is of marginal utility for rubber modified thermoplastics. Image analysis cannot resolve internal structure and cannot accurately measure particle size (Fig. 3). At increased magnification, however, this system is more suitable and the necessary information is extracted. For instance, both the morphology and particle size are resolved and accurately measured (Fig. 4). Networking of the microscopy lab and production plant must be utilized for the digital system to be most effective in saving time and effort. Additionally, the acquisition,, analysis, transfer, and storage of digital images is memory intensive.

By equipping a TEM with a digital acquisition and analysis system, turnaround time for sample analysis was reduced by 50%. With this reduction in time, significant cost savings are realized when TEM is applied as a process control tool for the manufacturing of rubber modified thermoplastics.

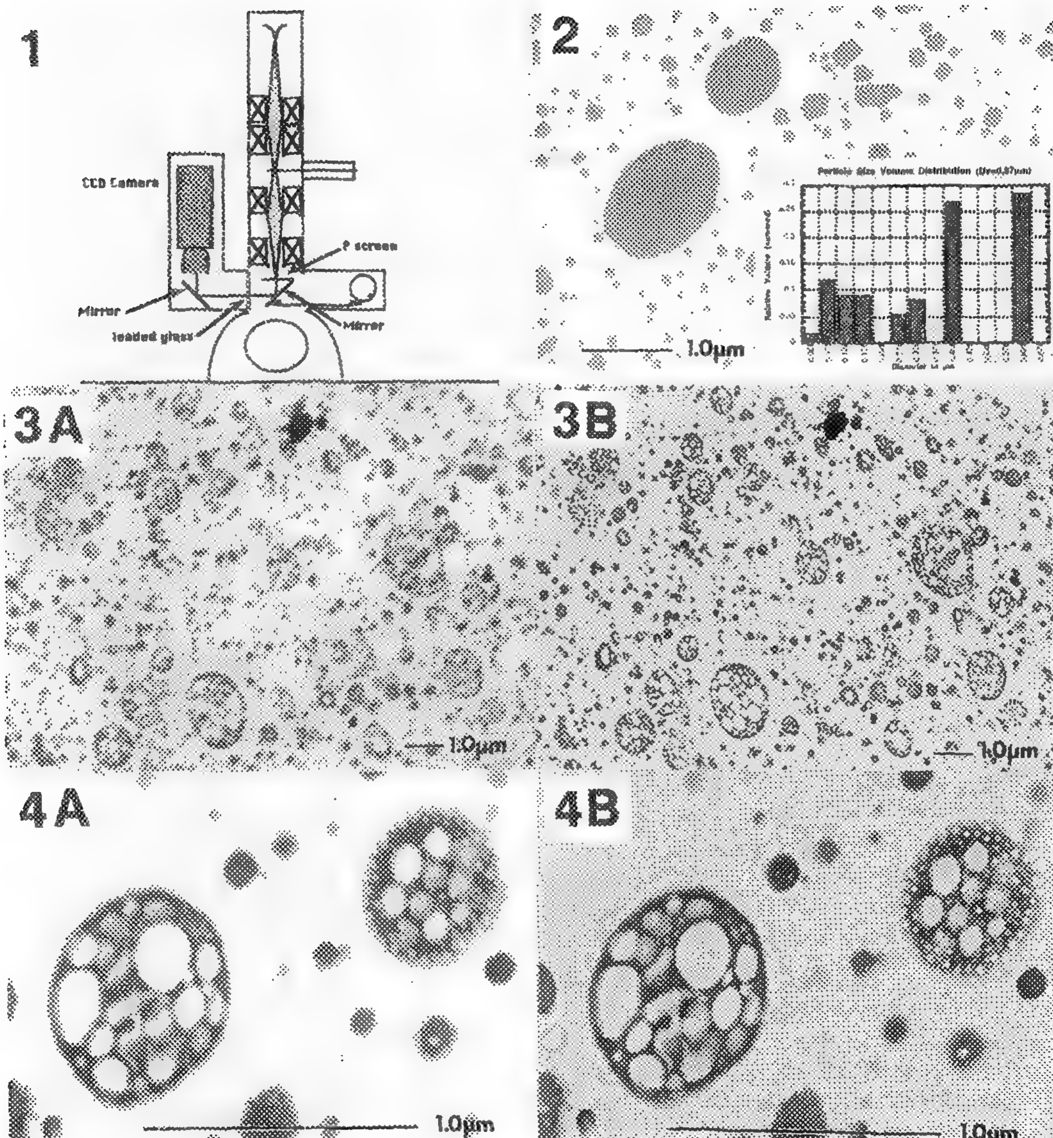

FIG. 1 Schematic of TEM/CCD camera interface.
FIG. 2 Digital image analysis of rubber modified thermoplastic.
FIG. 3A Digitally acquired image of rubber modified thermoplastic; low magnification (7,500x).
FIG. 3B Conventional film image of same area as FIG. 3A.
FIG. 4A Digitally acquired image of FIG. 3A at higher magnification (45,000x).
FIG. 4B Conventional film image of same area as FIG. 4A.

WIDEFIELD DIGITAL IMAGES IN BIOLOGICAL TRANSMISSION ELECTRON MICROSCOPY (TEM) OBTAINED BY AUTOMATIC IMAGE MONTAGE

F.M.S. Haug,* V. Desai**, J. Laake,* P.O. Nergaard,*** O.P. Ottersen*

* Department of Anatomy, Institute of Basic Medical Sciences, University of Oslo, Norway
** Soft Imaging Software Gmbh, Münster, Germany.
*** Norsk Philips AS, Oslo, Norway

A transition to digital recording is taking place in microscopy, including TEM.[1,2] Biological TEM often requires nanometer resolution within micrometer fields of view, i.e., image widths between 1 and 5 (10) Kpixels in digital terms. Electron dense particles between 1 and 15 nm are used in immunolabelling and in neurohistology, micrometer-sized objects such as synaptic boutons or glial processes are often studied with a need to clearly resolve membranes and filaments.

We needed larger fields of view in an image processing system (IPS) to quantify neuroactive amino acids in immunogold labelled ultrathin sections.[3] At startup of our project (1991) megapixel cameras for TEM were few and expensive and we designed a system for on-line image montage.[4]

A Gatan 673 Mk3 Wide angle TV camera is adapted to the lateral port of a Philips CM10 TEM. Pixel noise is reduced by frame averaging in a fully equipped Matrox Image 1280 board (EISA version) that also supports variable offset and gain of the analogue signal, real time mapping of gray values 0 and 255 to specific colours, and full handling of 1280 x 1024 pixel images. An MS Windows based IPS, analySIS (TM), is used for image processing and remote control of the TEM. The host PC has a 90 MHz Pentium CPU, 64 MB RAM and two 1 GB EISA - SCSI disks.

The video camera allows positioning and focusing in real time. A single function then reads the magnification from the TEM, calculates the required number of tiles and their relative position, shifts the electron image relative to the sensor to locate each tile, frame averages, mounts the image almost seamlessly (there are 70 tiles in Fig. 1) and calibrates it. To a calling macro, this simulates the recording of a single video-image. The operator must comply with a live image smaller than the final mounted image. A utility function calibrates the 2-dimensional image shift to different linear magnifications and rotation states of the microscope. These calibrations are generally stable for weeks. Another utility allows the user to specify final image size, clipping of the tiles to remove edge defects, and number of frames to average per tile.

Figs. 1 - 3 illustrate the range of field sizes achieved by the recording system. Brain tissue is from a hippocampal slice culture, post-embedding labelled for glutamate (small 15 nm particles) and glutamine (large 30 nm particles).[5] M= magnification (nominal) displayed by CM10. Wo= object field width in um. Wi= image width in pixels. Nt= number of tiles in image depend on the size of the tiles and of the final image. Nf= number of frames averaged per tile. R= recording time in seconds. For the present standard format of 1280 x 1024 (8-bit) pixels, total recording time is 13-14 seconds, which to us is acceptable when compared to the time spent in other operations. For routine counting of gold particles these images are adequate and comfortably handled by current hardware. Processing, display and storage, not acquisition, restrict the usefulness of larger images (16 - 32 MB).

The present system renders fields of view to approximately 20 x 20 micrometers and 4000 x 4000

pixels. The tiling system can be interfaced to other microscopes and to scientific grade slow scan cameras, permitting the selection of sensors with higher sensitivity, dynamic range or other advantages, in return for fewer pixels.[1] Then, total resolution and contrast transfer will depend on the selection of camera and the actual electron optic magnification.

References

1. G.Y. Fan et al., in *Proc. 49th Ann. EMSA Meeting,* (1991)524.
2. O.L. Krivanek and P.E. Mooney, Ultramicroscopy 49(1993)95.
3. O.P. Ottersen, Anat. Embryol 180(1989)1.
4. F.M.S. Haug et al., Analyt. Cell. Pathol 6(1994)297.
5. J.H.Laake et al., J. Neurochem. 65(1995)871.

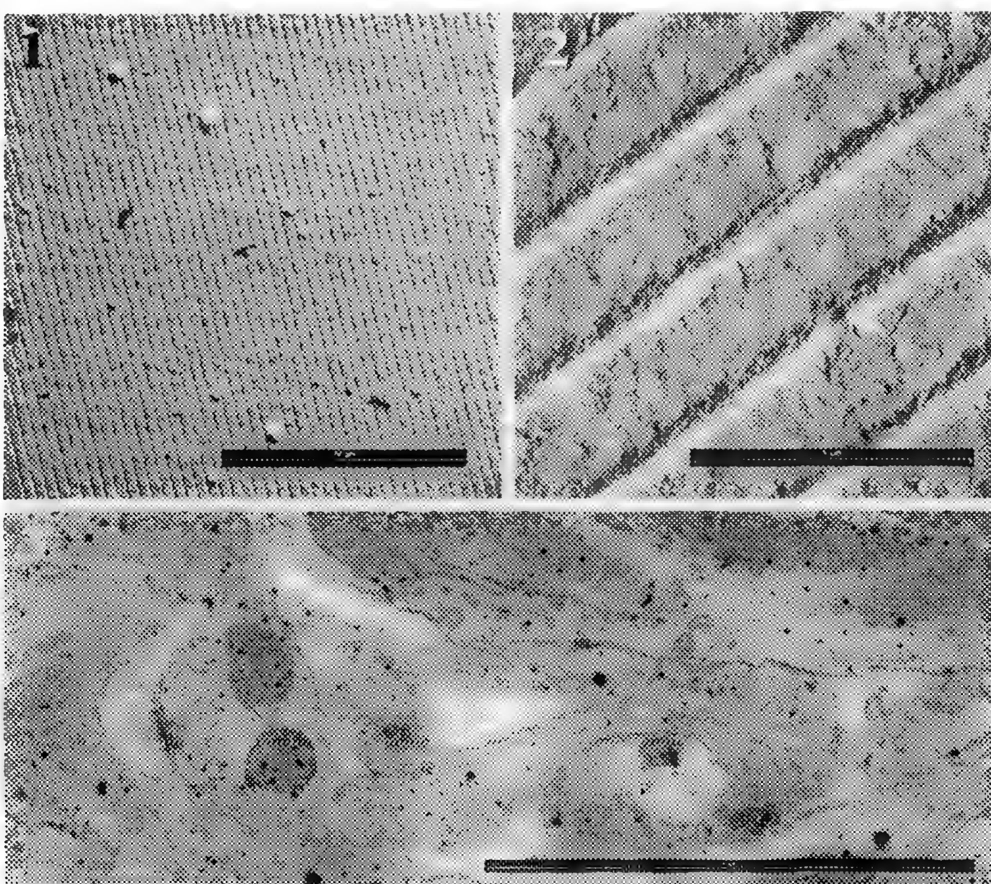

FIG. 1 Grating 2160 l/mm. M= 7900, Wo= 21.1, Wi= 4000, Nt= 70, Nf= 1, R= 140. Scale line 10 um.
FIG. 2 Grating 2160 l/mm. M= 92000, Wo= 1.79, Wi= 4000, Nt= 56, Nf= 1, R= 115. Scale 1 um.
FIG. 3 Brain tissue (see text). M= 25000, Wo= 4.21, Wi= 2560, Nt= 16, Nf= 1, R= 38. Scale 2 um.

SOFTWARE TOOLS FOR 4D LIVE CELL MICROSCOPY

C. Thomas, P. DeVries, J. Hardin*, and J.G. White

Integrated Microscopy Resource and *Dept. of Zoology, University of Wisconsin - Madison, Madison WI 53706

The Integrated Microscopy Resource has developed a trio of Macintosh-based software tools which allow the user to collect digital 4D microscopy (3D over time) of live cells. To demonstrate the program, high-resolution Nomarski DIC images were collected from an inverted microscope using a video camera. The output of the camera can be averaged and contrast-enhanced before the resulting signal is digitized using a framegrabber card installed in a Macintosh computer (Figure 1). Collection, subsequent processing, and analysis of the resulting data sets are handled by the following three software tools:

4D Acquisition Software - This IMR-designed software system is based on the popular shareware image processing program "NIH-Image" (author Wayne Rasband, NIH) and controls the actual image acquisition through a series of graphic user interfaces. A framegrabber card, a stage drive motor, and an illumination shutter are manipulated to allow the imaging of either a single focal-plane of the specimen over time, or the acquisition of 3-dimensional volumes at each timepoint. After selecting the top and bottom of the sample, the user can specify the number of focal planes to acquire, the increment for the focus motor between focal planes, the number of timepoints to collect, and a file format in which to save the images. The software will automatically move through the sample from the top to the bottom gathering images of each focal plane as it goes. The result is a stack of images representing the 3D structure of the sample. The software will wait a defined amount of time and the process will be repeated for as many timepoints as the user has designated.

A "variable time-interval" feature allows the delay between timepoint acquisitions to change during the course of the experiment such that the sample interval of the software matches the developmental rate of the organism being studied. Up to five different experiment times and interval times can be set with a graphic interface. In this way the user collects neither too much nor too little data.

4D Turnaround - It is not unusual for several thousand images occupying a Gigabyte or more of hard disk space to result from the kind of data acquisition runs described above. In order to organize the data into a format and size with which we can more easily work, we have developed the 4D Turnaround application. A memory-efficient, small, stand-alone application written in C, the 4D Turnaround processes the multiple 3D data stacks into Quicktime movies (Quicktime is a file format that allows multiple images to be viewed and stored on the computer as movies). At the same time as these movies are being created, the user can apply a variety of compression schemes to get the size and quality of data set that is desired. Compression ratios of up to 15:1 are possible with typical light-microscope images (Figure 2). The original, raw data is not destroyed during this conversion, so it can be kept or discarded as the user sees fit. A variety of input file formats are supported.

4D Viewer - The quicktime movies that result from the 4D Turnaround process can be loaded into the 4D Viewer application. This application allows the user to roam backwards and forwards in time as well as up and down in focus through a 4D data set. In this way, cellular dynamics can be observed at smooth animation speeds. Additionally, the user can create color overlays for each individual image in the data set which can be saved to and read from the computer's hard disk (Figure 3). These overlays are very memory efficient (6000 average sized overlays take up only about 9 Mb of disk space) and can be played back at a very rapid pace.

Clicking on any object in an overlay (a circled nucleus, for example) will show text associated with that object describing the structure in more detail. This text can be searched so that, for example, any overlay with "P1 Nucleus" in it can be brought forward automatically. Sub-movies can be produced featuring dynamic, color annotations that follow the movement of selected features in the data set. These movies can be played on any QuickTime movie player, even in a Windows environment. Other features allow the user to set bookmarks in 4D space that can be saved/loaded to the disk, and any of the frames of a 4D data set can be saved as individual PICT files for later processing.

The programs are freely available to all and can be down-loaded from an FTP site at the IMR. A fuller description of the programs and downloading instructions are obtainable at the IMR's World Wide Web site: http://www.bocklabs.wisc.edu/imr/imr.html

This work was supported by NIH Grant P41 RR00570-25A to the Integrated Microscopy Resource.

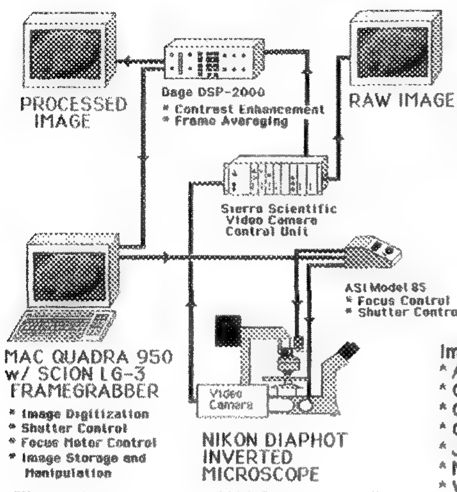

Figure 1

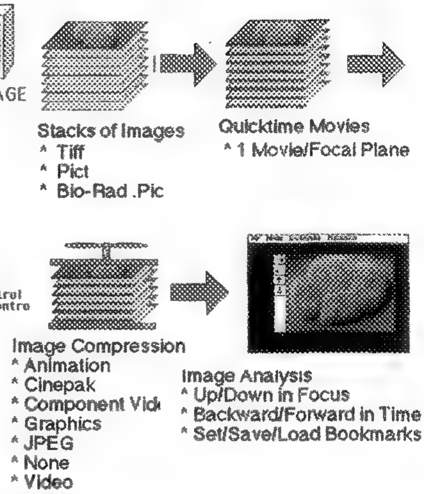

Figure 2

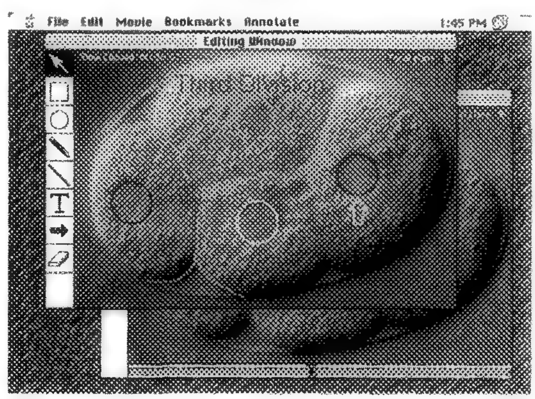

Figure 3

FIGURE LEGENDS:

Figure 1: The hardware portion of the 4D Live Cell Imaging Workstation as it exists at the Integrated Microscopy Resource. This is where data acquisition takes place under the control of the 4D Acquisition Software.

Figure 2: Functional diagram of the 4D Turnaround application. During the processing of multiple 3D timepoints into Quicktime movies, the user's choice of compression schemes can be added to reduce the size of the resulting data set.

Figure 3: The 4D Viewer in use. The viewer allows the user to roam forward and backward in time as well as up and down in focus through a 4D data set. Here an image of a four-cell *c. elegans* embryo has been augmented with a color overlay using the viewer's annotation suite. The image is only one of 6000 that can be viewed in this particular data set.

DIFFERENTIAL CONTRAST IMAGING WITH DIFFERENTIAL HYSTERESIS PROCESSING

Klaus-Ruediger Peters

Molecular Imaging Laboratory, Biomolecular Structure Analysis Center, University of Connecticut Health Center, Farmington, CT 06030-2017

The spacial information of images can be characterized with contrast patterns. We analyzed the spacial contrast distribution in micrograph data with differential hysteresis processing[1] using a PiXISION-AP128 imaging workstation (JEOL USA Inc., Peabody, MA) and found that discrete spacial image components have discrete contrast characters which are defined by specific contrast levels and specific contrast ranges. Consecutive contrast segmentation at increasing contrast levels produced a limited number of contrast patterns which were discretely recognizable and distinguishable. These contrast patterns have an unique accumulative property, i.e., a digital image can be segmented into contrast patterns and reassembled from its contrast patterns. Contrast patterns can be mathematically defined by a differential hysteresis range (DHR). The DHR (DHR x-y) describes differential contrasts of a pattern with two intensity values as contrasts which are larger than the first value (x) and smaller than the second value (y). The contrast patterns can be visualized as images through linear scaling to the maximum visual perception range (8-bit).[2] The DHR provides an universal imaging parameter since it applies to all images independent of source, size, bit depth, and spacial content.[3]

Visualization of digital image information is often hindered by the limitations of the visual system.[2,3] Fine structural contrasts may be so small in size (only a few pixels wide) or so weak in contrast (only a few intensity levels strong) that they cannot be "seen" in a displayed image. Digital zoom and contrast segmentation can overcome these limitations. As an example, a gold labeled cryosection of eye tissue is used. These sections are known to have low contrast and limited fine structural details. The pertinent labeling information has to be deduced from correlating the marker distribution with the cytoplasmatic ultrastructure. However, these image components are often masked by contrasts from uneven section thickness, ice contamination, partial drying as well as uneven background illumination (Fig. 1a). These structural components produced discrete contrast patterns which could be easily segmented under interactive visual control. One of the patterns represented the cytoplasm, e.g. bilayered membranes, ER details and vesicle fine structures (Fig. 1b). The other pattern represented the gold label (Fig. 1c). Structural information of both contrast patterns were used with different weighting for a descriptive imaging of the labeling result. The morphological aspect relied more on a visibility of cellular structures whereas the quantitative aspect relied more on a visibility of the gold label. Both differential contrast patterns could be overlaid (mixed) at any proportion adequate for the image purpose (Fig. 1d). Contrast imaging provided a practical way for "seeing" micrograph data. It furnished intuitive access to the contrast functions of the microscope fostering an objective "knowledge-based" image understanding.[4]

1. K.-R. Peters, *Proc. Microscopy Microanlysis 1995*: 642-643
2. D.E. Newbury et al., *Advanced Scanning electron Microscopy and X-Ray Microanalysis*, Plenum Press: New York and London (1986)181
3. K.-R. Peters, "http://panda.uchc.edu/htklaus/index.html"
4. The digital TEM image data set was kindly provided by James O'Rourke, University of Connecticut Health Center, Farmington, CT.

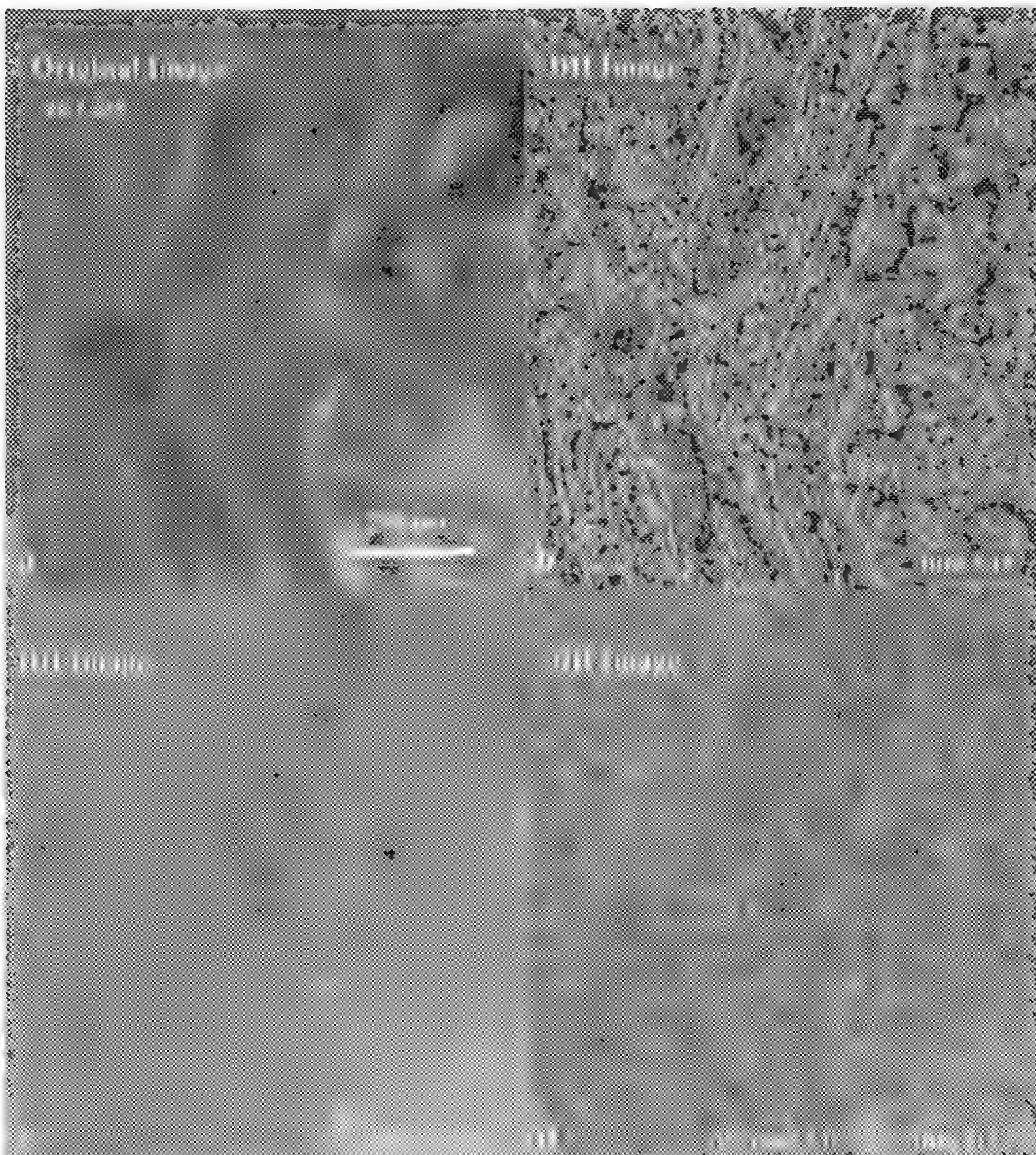

FIG. 1.- (a) TEM image of a cryosection of eye tissue labeled with 10 nm gold particles (TEM negative digitized with a flatbed scanner to 685x755x8-bit). The correlation of cellular ultrastructure and gold labeling is not clearly recognizable. (b) Contrast pattern of the cytoplasmic ultrastructure segmented at DHR 5-19. (c) Contrast pattern of the gold label segmented at DHR 115-235. (d) Selective imaging of both contrast patterns through overlay at a proportion which emphasized the cytoplasm. DH = Differential Hysteresis, DHR = Differential Hysteresis Range, IR = Intensity Range.

[3]PERFORMANCE EVALUATION OF A SECOND GENERATION METAPHASE FINDER FOR CHROMOSOME-BASED RADIATION DOSIMETRY.

[1]Pollitt, D., [2]McLean, J., [3]Johnson, F., [1]Rivest, J-F. and [1]Gibbons, D.
[1]University of Ottawa, Faculty of Engineering, 161 Louis Pasteur St., Ottawa, K1N 6N5, Canada. [2]Radiation Protection Bureau, 775 Brookfield Rd. Ottawa, K1A 1C1, Canada and [3]Ottawa Instrumentation, 169-5th Ave., Ottawa, K1S 2M8, Canada.

To be useful, a metaphase chromosome finder must be able to quickly identify chromosome spreads, rank them in terms of analysability and relocate them for visual examination at high magnification. In addition, the system should use state-of-the-art technology which is commercially available at competitive prices. The metaphase finder described here uses an 8-bit CCD camera (640 x 480 pixel resolution) and an Olympus BX-50 microscope with a x 20 apochromat objective. The camera composite video signal is connected to an image processing card (Matrox "COMET" card) for a final image resolution of 2.4 x 2.4 µm (5.8 μm^2) per pixel for a 100 x 80 µm field of view. The microscope stage movements and focusing are under software control (illumination and filter selection are manual). Miniature motors (MicroMo 1616 series) and reduction gearboxes were retrofitted to a standard Olympus microscope stage and to the fine focus control shaft. X and Y movements of the stage and focus (Z) are controlled by a Precision Motion card. Resolution is better than 0.5 µm in X and Y, and 0.05 µm in the focus (Z) plane. A 486-DX100MHz IBM compatible computer with 8 MBytes RAM was used to control the acquisition and manipulation of data. A 2 GByte DAT drive was used to archive data. The autofocus algorithm, a crucial component of the scanning microscope system, adjusts the focus for mechanical drift and for variations within successive fields of view. The autofocus algorithm is both fast and accurate and is relatively insensitive to other system parameters such as the mean brightness of the image. The autofocus is based on maximizing a function. For the system described here, the independent variable is the number of focus steps from the optimal focal plane, and the dependent variable is a "figure-of-merit" which reaches a maximum when the image is in focus. When metaphase chromosomes are prepared on microscope slides for visual examination, they appear as clusters or "spreads" of rod shaped objects. The radius of a cluster must be within pre-determined limits for the chromosomes to be analysable; too small and some chromosomes can overlap making analysis difficult or impossible; too large and some chromosomes could be missing from the field of view. The x 20 objective, while unable to resolve individual chromosomes, can scan a relatively large area of the slide and extract clusters of chromosomes from background noise. Data reduction occurs early in the analysis to minimize overall processing time. In

general, the image is reduced to a number of regions of interest by use of a dynamic brightness threshold which is selected once by the analyst at the beginning of the slide. The size of the selected regions and the distance between regions depends on the magnification used in scanning the slide, the intensity of the staining and the physical spreading of the chromosomes. The metaphase-finding algorithm is a two-phase band-pass filter which removes unwanted picture elements on the basis of size, shape and proximity to other picture elements. The first phase removes metaphases that are too widely dispersed, and the second, removes those that are too clumped to be analyzed. In phase I, the dynamic brightness threshold, which was previously set by the analyst, is used to reduce the image to a number of region of interest. The next step is an opening (an erosion followed by a dilation) which removes small picture elements (the chromosomes and small isolated debris). Next, this new image, which only contains large picture elements, is subtracted from the original thresholded image leaving only the chromosomes and the small isolated debris. A medium sized dilation produces clumps from the small picture elements which are in close proximity to each other. Then a large erosion removes the smaller clumps. The clumps that remain are dilated back to their original size and shape. In phase II, further filtering is accomplished by a large erosion which removes any small clumps that may have survived previous filtering. This image is then used for a geodesic reconstruction of the appropriately sized picture elements produced at the end of phase I. The final result will be the identification of analysable metaphase chromosome spreads if present in the original image. For the large dilations and erosions, a distance function is used to increase data processing speed. Rapid acquisition and processing of metaphase spreads using commercially available hardware and customized software can make computer-assisted cytogenetic-based radiation dosimetry cost-effective reality.

A COMPUTER-GENERATED THREE-DIMENSIONAL VIEW OF THE DEVELOPING HUMAN BILIARY SYSTEM

V. Vijayan & CEL Tan

Department of Pediatric Surgery, Singapore General Hospital, Singapore 169608

With the advent of computers, microscopy has entered an exciting new era of computerised three dimensional (3D) reconstruction. Using serial sections, it is now possible to generate complex 3D images, that can be rotated at various angles to study the organ systems of interest. In this project, the first of its kind, we have used computer generated 3D reconstruction to study the developing human biliary system.

The human biliary system consists of the extra and intrahepatic components. The extrahepatic system develops from the embryonic hepatic diverticulum and is tubular from the start. The intrahepatic bile ducts arise from the Ductal Plate. The Ductal Plate comprises of sheets of biliary epithelium, with discontinuous luminal spaces, that appear within the mesenchyme along the portal vein branches. The Ductal Plate is remodelled into tubular definitive bile ducts by an orderly process of epithelial deletion and selection which occurs between 11-13 weeks of gestation[1,2]

METHODOLOGY

MATERIALS AND EQUIPMENT: Fetuses were obtained from medical termination of pregnancies, carried out for psychosocial reasons, with the consent of the mother and the ethical committee of the Singapore General Hospital. The specimens were embedded in paraffin, the porta hepatis region was identified and serially sectioned at a thickness of 5 μ. Sections were stained with toluidine blue. Every third section was used to perform 3D reconstruction.

An Axiophot microscope (Carl Zeiss, Germany) connected through a digital camera (Progress 3012) to a 386 PC with image processing hardware and software (IBAS 2.5 and MIPRON 2.0, Kontron Elektronik, Germany) was used.

ALIGNMENT OF SECTIONS: The sections were viewed under an upright microscope and images were digitised. Alignment was done manually for every section in the series. Alignment was done using a RGB monitor connected to the VIOB output of the IBAS 2.5 system. In order to align an image, the preceding image was converted to overlay and the current image aligned according to the overlay. Alignment was done at low magnifications of 2.5 using the outline and other clearly visible structures in the image as references.

IMAGE PROCESSING: Images were stored in grey scale (0-255). The only image processing required was correction of uneven staining intensities. Biliary structures and blood vessels, were selected and the other structures erased.

3D RECONSTRUCTION: 3D reconstruction was performed using the voxel based reconstruction technique of distance shading. With this technique the object that is closest to the viewer appears brightest and vice versa. The biliary structures and blood vessels were reconstructed as separate images, the reconstructed images were put together later by simple arithmetic functions. Look-up tables were used to add colour to the reconstructed biliary structures and blood vessels.

RESULTS

Reconstructed 3D image (figure 2) shows the very early Ductal Plate of a 7 week fetus. Figure 3 shows a 11 week fetus with abundant Ductal Plate structures and figure 4 shows a 16 week fetus with more adult-like morphology. Figure 1 is a photomicrograph of the Ductal Plate in tissue section.

CONCLUSION

Computer generated 3D reconstruction offers a very valuable technique for demonstrating the change in morphology from Ductal Plate to tubular well defined bile ducts during the intrauterine development of the human biliary system.

REFERENCES

1. Desmet VJ. J Hepatology, 1: 427-447, 1985
2. Tan CEL & Moscoso GJ. Pathology International, 44: 29-40,1994
3. V Vijayan & CEL Tan. Zoological Studies, 34(S1): 199-201, 1995

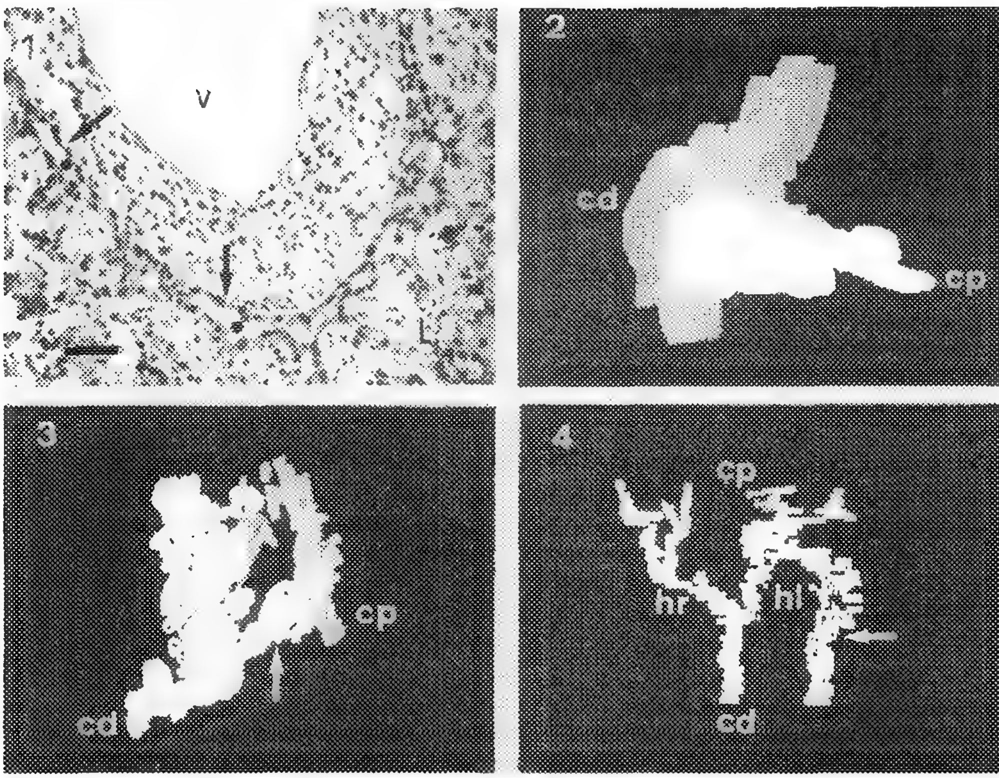

FIG. 1 Photomicrograph of a tissue section from a 11 week fetus showing a portal vein branch (v), liver parenchyma (l) and the Ductal Plate (arrow). Discontinuous luminal spaces can be seen in the Ductal Plate (*). Scale bar= 50 μ

Figures 2-4 are computer generated 3D images (not to scale). The caudal and cephalic ends are marked as cd and cp respectively.

FIG. 2 Very early Ductal Plate structures in a 7 week fetus, showing finger like projections into the liver. Seven sections 15 μ apart were included in this reconstruction.

FIG. 3 Image of a 11 week fetus showing abundant Ductal Plate structures. One prominent bile duct (arrow), which is continuos with the exrtahepatic system, is already beginning to develop. Forty six sections 15 μ apart were included in this reconstruction.

FIG. 4 Image of a 16 week fetus, showing well defined bile ducts and few Ductal Plate remnants. The right (hr) and left (hl) hepatic ducts can be seen. One Ductal Plate structure (arrow) can be seen extending from the left hepatic duct to the periphery of the liver. Forty six sections 15 μ apart were included in this reconstruction.

PRACTICAL METHODS FOR TEM

K. Chien, R. Gonzalez, R. C. Heusser, H. Shiroishi and M. L. Heathershaw

Pathology & Laboratory Medicine, Cedars-Sinai Medical Center, Los Angeles, California 90048

Multiple sectioning: Two or more core specimens from a kidney needle biopsy can be embedded in single block using an 8-facet silicone rubber embedding mold. Tissue blocks are softened by placing them face down on an 85°C hot plate for one minute and then trimming with a Teflon coated razor blade. This prevents the block face from being deeply fractured which can affect section quality. If glomeruli are found within different cores in a single block, the block face can be retrimmed into multiple mesas and simultaneously thin-sectioned.[1] This method greatly increases the efficiency of both thick and thin sectioning which is extremely helpful when handling more than 1600 cases of renal biopsies in our EM laboratory each year.

Knife Spacer: Due to the difference in thickness between a glass and diamond knife, and also depending on which portion of the diamond knife is being used, the knife stage has to be moved laterally over a long distance when changing from one knife type to the other. Placing a L-shaped spacer, 3 to 5 mm in thickness, on the left side of the stage when sectioning a glass knife will greatly reduce this lateral adjustment.

Thick before thin sectioning: ASCP requires a 1 micrometer section after thin sectioning to show the precise area cut for EM. However, cutting a 1 micrometer section first has the following advantages: 1.The rough block surface from previous thick sectioning (especially from a large block) is resectioned to provide a smooth surface for thin sectioning. 2. If knife marks appear in the same spot on the thick sections even after moving to new areas of the glass knife, it is an indication that foreign particles are in the tissue block. These particles must be removed prior to thin sectioning. 3. Due to the pre-alignment by glass knife, all that is required is a lateral tilting adjustment for diamond knife sectioning.

Specimen Retrieval: Polymerized epoxy blocks firmly attached to a glass slide can be easily "peeled off" by heating on a 100°C hot plate for approximately 30 seconds.[2] Once this technique is mastered, many other specimens can be retrieved for EM examination: 1. Histologically stained paraffin sections on glass slides can be fixed with OsO4/xylene and infiltrated with epon/xylene as previously discussed.[3] This rapid processing method not only eliminates the rehydration and dehydration steps but also maintains the stains within the sections for precise localization of cells for thin sectioning. A modification can be made by clearing the xylene with acetone and infiltrating with epon/acetone. Another approach is to dissolve OsO4 crystals in propylene oxide for fixation, and then infiltrating with epon/propylene oxide. Both methods improve section quality. 2. Cell suspensions from cytology can be cytocentrifuged onto glass slides with 1 drop of 22% specific albumin (Baxter), immediately fixed in glutaraldehyde and processed for TEM.[4] 3. Cryostat sections can be picked up with polylysine coated glass slides and immediately fixed and processed for TEM with excellent morphological preservation.[5] 4. When retrieving Glycol Methacrylate embedded specimens, a different approach is used. Instead of dissolving the GMA away, 3 μm sections are cut and stained on glass slides. Sections are directly infiltrated with 1:1 epon/acetone. Epoxy resin sufficiently penetrates the GMA and produces adequate blocks for thin sectioning.

Serial thin sectioning: Many methods have been described to make thin sections “adhere” to each other and form a ribbon so that they will not float apart and can be picked up sequentially. A different approach has been developed by “freezing” thin sections on the surface of the water so that they can also be sequentially picked up: Approximately 2ml of distilled water is added to a 30ml Sample Cup (Baxter) (fig.1). After a little agitation, the water is then poured into the diamond knife trough. When thin sections come off the knife edge, they may or may not form a perfect ribbon, but will be held stationary on the surface of the water by a substance released from the Sample Cup (fig.2). Sections can then be transferred onto grids as preferred. The actual chemical composition of this substance is uncertain but possibly it is an SDA approved silicone mold releasing reagent. No contamination of sections or the electron microscope has been detected. This simple method can also be applied to routine thin sectioning and provided better control of thin sections within the knife trough.

Projection slides: The best quality projection slides can be obtained directly from electron micrograph negatives. The image of a negative is reduced by an enlarger to 35mm and then exposed on Kodalith 2556 negative film for approximately 2 seconds and developed in D-19 for approximately 1.5 minutes. One major problem is that the concentrated light becomes too bright to focus by eye. Rotating a polarization filter on the mirror of the enlarging magnifier will cut down the brightness for precise focusing.

References

1. K. Chien et al., Ann. Proc. EMSA Meeting 43(1985)714.
2. K. Chien, Ann. Proc. EMSA Meeting 38(1980)644.
3. K. Chien et al., Ann. Proc. EMSA Meeting 40(1982)356.
4. K. Chien et al., Ann Proc. EMSA Meeting 44(1986)220.
5. K. Chien et al., Ann. Proc. EMSA Meeting 43(1985)460.

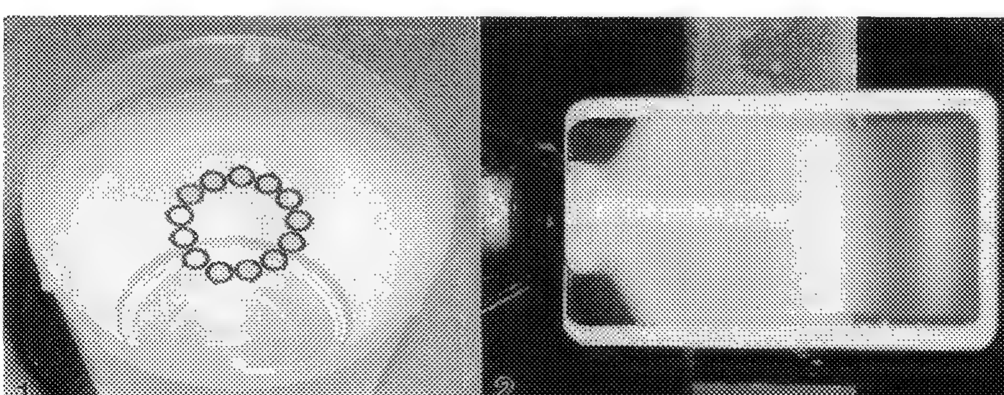

FIG. 1 - Copper grids are held in place on the surface of water by substance released from Sample Cups.
FIG. 2 - Five hours after sectioning, ribbon of thin sections remains stationary by the use of same substance released from Sample Cup.

TEM CHARACTERIZATION OF CMR THIN FILM ON [001] $SrTiO_3$ SUBSTRATE

Y.Y. Wang[1], A. Gupta[2], and V.P. Dravid[1]

1) Department of Materials Science and Engineering, Northwestern University, Evanston, IL 60208
2) IBM T.J. Watson Research Center, Yorktown Heights, NY 10598

Due to its potential magnetic device application, giant/colossal magnetoresistant (GMR or CMR) material, (bulk material as well as thin film), have been under intense investigation in recent years. In the bulk material, the changes of the resistivity under 4T magnetic field is about 80% at the metal-insulate transition temperature for $La_{0.7}Ca_{0.3}MnO_3$ (LCMO).[1] In 1994, S. Jin et al reported thousandfold change in resistivity in magnetoresistive La-Ca-Mn-O films on a $LaAlO_3$ substrate.[2] It is suspected that such a large magnetoresistivity change in the thin film is due to the defect structure in the epitaxially grown thin film.

The base structure of LCMO is an MnO_6 octahedral perovskite cubic structure. Because of its strong static Jahn-Teller (JT) distortion, the compound is metrically orthorhombic, with $a \sim b \sim \sqrt{2}\, a_p$ and $c \sim 2a_p$, where a_p is the lattice constant for the base cubic structure. X-ray diffraction study on this compound shows that it belongs to *Pnma* space group.[3]

In this report, we study the structure as well as the chemical composition of an epitaxially grown $La_{0.7}Ca_{0.3}MnO_3$ (LCMO) thin film by transmission electron microscopy. The thin film on [001] $SrTiO_3$ single crystal substrate was prepared by laser ablation. The resistivity measurement of the film shows 54% resistivity changes at the metal-insulator transition temperature under 4T magnetic field.[4]

The energy dispersive x-ray spectroscopy (EDX) study shows that the thin film has the right composition as $La_{0.7}Ca_{0.3}MnO_3$ and as shown in Fig.1. Fig.2 shows the cross-sectional TEM picture, where a clear epitaxial growth of the LCMO thin film is shown. The figure shows that *c*-axis is along the growth direction. However, in the other region examined, we observed that *c*-axis is perpendicular to the growth direction. This observation is consistent with the plan-view HREM images from different area of the film, shown in Fig.3 and Fig.4, in which the crystal orientations pendicular to the film surface are $[1\bar{1}0]$ and [001], respectively. The $[1\bar{1}0]$ image shows that the unit cell doubles from a_p to $2a_p$; while the [001] image shows the $\sqrt{2} \times \sqrt{2}\, a_p$ structure. The difference of *a* and *b* is estimated to be about 2% in the [001] image (Fig.4), which is consistent with the neutron diffraction studies on the bulk material with the similar composition.[3] These indicate that the thin film has a domain structure. Comparing with bulk materials examined by HREM along the $[1\bar{1}0]$ axis as well as along the [001] axis, where there was no distortion observed, we observed a weak zigzag atomic distortion along the [110] direction and the $[1\bar{1}0]$ direction in both Fig.3 (the $[1\bar{1}0]$ axis image) and Fig.4 (the [001] axis image). In addition, we observed shear displacement defects in the high resolution images from all regions. Nano-meter scale precipitates were also observed in the plan-view images. However, these precipitates do not seem to affect the electric properties of the thin film.

Since electron energy loss spectroscopy can be used to determined the composition as well as the electronic structure, we show the EELS spectrum of the thin film in Fig.5. The calculated L_3/L_2 ratio for Mn is about 2.3, which is close to Mn^{+3} state. In this spectrum, we also observed a hole state pre-edge at O K-edge, which is similar to the hole state at O K-edge in the doped high temperature cuprate superconductors.

In conclusion, we examined a high quality LCMO thin film by high resolution electron microscopy, energy dispersive x-ray spectroscopy, and electron energy loss spectroscopy. Specifically, we observed hole states on the O site by electron energy loss spectroscopy.[5]

References:

1. P. Shiffer et al., *Phys. Rev. Lett.* 75, 3336, (1995); 2. S. Jin et al., *Science*, **264**, 413, (1994); 3. P.G. Radaelli et al., *Phys. Rev. Lett.* **75**, 4488, (1995); 4. A. Gupta et al., to be published; 5. This work was partly supported by National Science Function under the contract No DMR 91-20000.

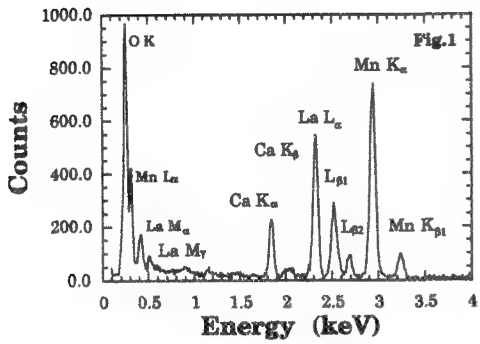

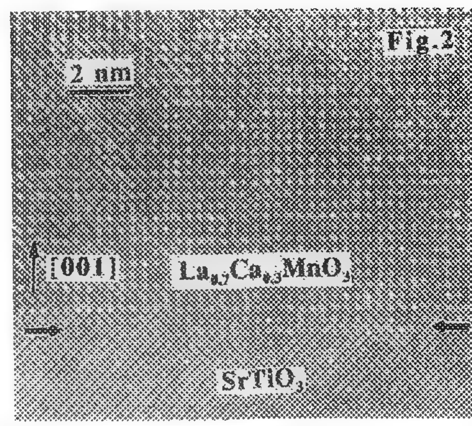

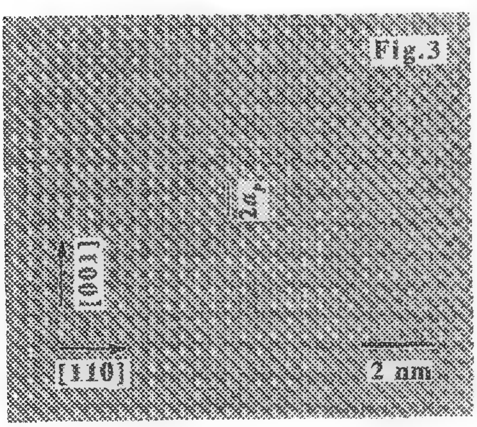

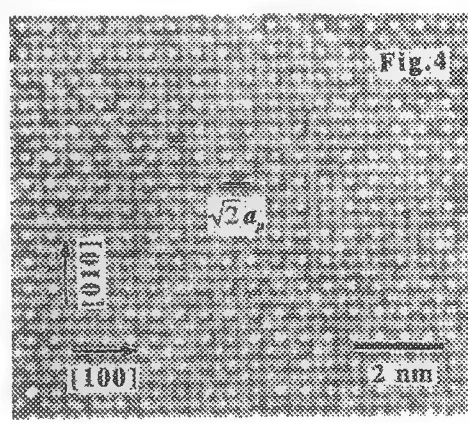

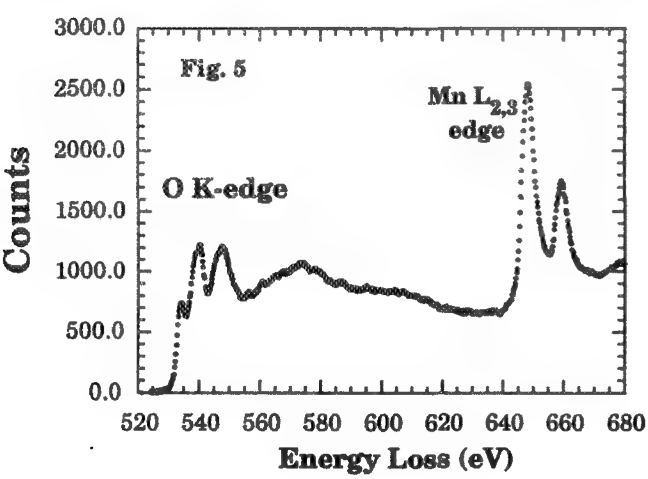

Fig.1: EDX spectrum of the LCMO thin film.

Fig.2: HREM image of the cross section. It shows that c is along the growth direction.

Fig.3: Plan-view image of LCMO along the [110] direction. c~$2a_p$ is visible in the figure.

Fig. 4: Plan-view image of LCMO along the [001] direction. The $\sqrt{2} \times \sqrt{2}\, a_p$ structure is visible in the figure.

Fig.5: Energy loss spectrum of LCMO thin film. A pre-edge is observed at the O K-edge onset.

ROLE OF MICROSTRUCTURE IN DETERMINING THE TRIBOLOGICAL PROPERTIES OF CERAMIC MATERIALS

C.P. Doğan[*] and J.A. Hawk[*]

[*]Albany Research Center, Albany, OR 97321

It is well known that experimentally-determined values of wear resistance are not materials' constants, but rather measured responses to a particular set of conditions imposed by a specific wear environment. Nonetheless, a material's tribological performance is often estimated based on its bulk material properties. For applications requiring abrasive wear resistance, for example, ceramic materials are traditionally selected based on their hardness and fracture toughness, which are assumed to be proportional to the wear resistance (1). However, recent studies (2,3) have indicated that for many commercially-important ceramic materials, subtle differences in the microstructure (not always reflected in measured values of bulk hardness and fracture toughness), can lead to large variations in the abrasive wear resistance.

A number of microstructural variables can influence the tribological properties of a ceramic material: matrix grain size, matrix grain shape, the presence of intra-and inter-granular second phases, and the presence of transforming second phases (in zirconias and zirconia-toughened ceramics, for example). Generally these microstructural features influence the tribological properties by influencing the internal stress state of the ceramic. Those features which increase the internal tensile stresses, particularly at the grain boundaries, tend to degrade the overall tribological performance of the bulk ceramic through a decrease in the short-crack toughness of the material. Similarly, microstructural features which reduce internal tensile stresses will have a positive influence on the tribological performance of the ceramic.

The importance of understanding the microstructure when selecting a ceramic for a wear application is illustrated by comparing two apparently similar, commercially-produced Si_3N_4 ceramics: Both materials, are primarily β-Si_3N_4, with a yttrium-aluminosilicate boundary phase, and both have an average matrix grain size of ~ 0.5μm, a hardness of ~14GPa, and a bulk fracture toughness of between 5.7 and 6.0 MPa$\sqrt{m}$ (as reported by the manufacturer). However, their microstructures and abrasive wear resistances (measured in a pin-on-drum test against 150-grit SiC) are somewhat different. Material A (Fig. 1a) has a partially-crystalline boundary phase and a specific wear rate of 1.34×10^{-2} mm^3/N-m. Material B (Fig. 1b) has a (near) fully crystalline boundary phase and a specific wear rate of 0.90×10^{-2} mm^3/N-m. This 49% improvement in wear resistance originates in the magnitude of the stresses created by thermal expansion mismatch as the boundary phase devitrifies during cool-down from the sintering temperature. Figure 1a clearly shows the presence of stress in Material A, at points where crystalline $Y_2Si_3O_3N_4$ and the matrix meet. While stresses are also apparent at the heterophase Y_2SiO_5-Si_3N_4 boundaries in Material B, they do not appear to be as large, and they are diffused over larger areas. Although the magnitude of this residual stress in Material A is not, by itself, sufficient to cause failure, it becomes determinative when combined with stresses imposed by the wear environment. The short crack toughness is decreased, and material is easily removed from the wear surface.

In liquid-phase sintered, high-alumina ceramics, on the other hand, a fully devitrified boundary phase is generally not desirable for wear applications, although the actual values of wear resistance will depend

upon the matrix grain size and the composition and nature of the boundary phase(s). In a 94% alumina with magnesium aluminosilicate boundary phases, an increase in alumina grain size, combined with devitrification of the boundary glass, translates into a 140% degradation in the abrasive wear resistance of the material. A comparison of the wear surfaces of these two materials (Figs. 2) illustrates the effect that an increase in internal stresses has on the material removal mechanisms under abrasive wear conditions.

References

1. A.G. Evans and D.B. Marshall, Fundamentals of Friction and Wear of Materials, D.A. Rigney, Ed.; ASM, Metals Park, OH, USA, 439-452 (1981).
2. C.P. Doğan and J.A. Hawk, Wear 181-183, 129-137 (1995).
3. J.A. Hawk and C.P. Doğan, Advanced Ceramics for Structural and Tribological Applications, H.M. Hawthorne and T. Troczynski, Eds.; CIM, Montreal, Quebec, Canada, 139-150 (1995).

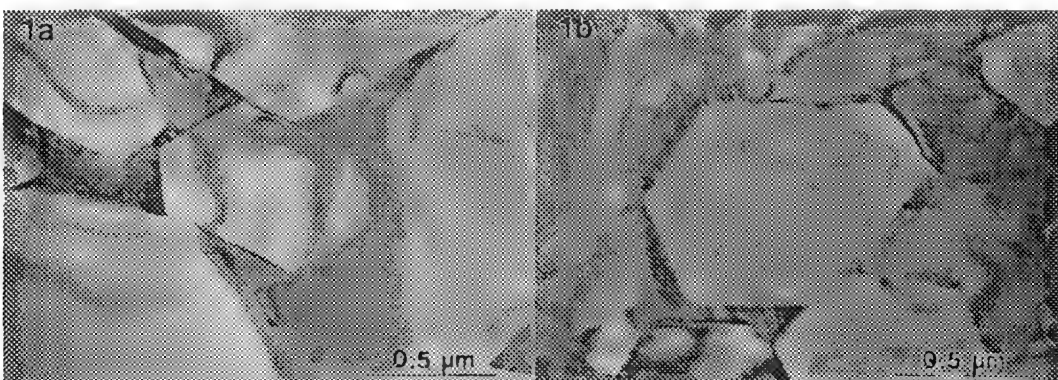

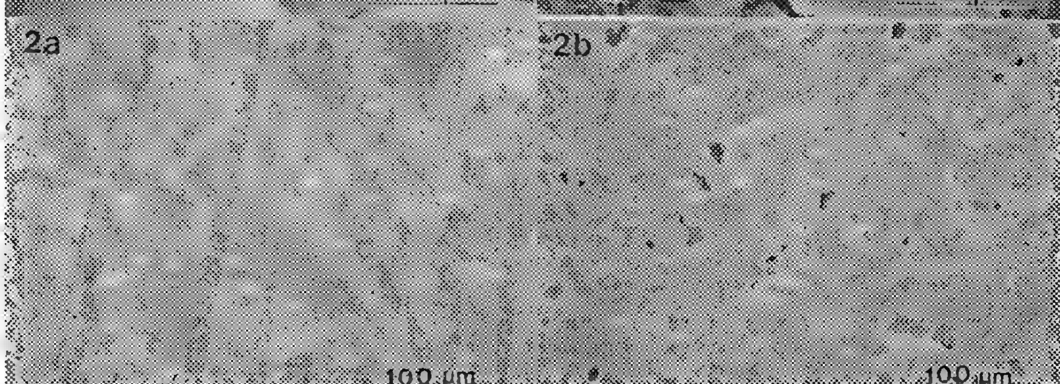

FIGURE 1. Microstructure of the boundary regions within the two Si_3N_4 ceramics, illustrating (a.) the partial devitrification of the glass in Material A, and (b.) near complete devitrification of the boundary regions in Material B.

FIGURE 2. Wear surfaces of two 94% aluminas. (a.) A fine-grained alumina with amorphous boundary phase. (b.) A larger-grained alumina with a crystalline boundary phase.

THE CRITICAL ROLE OF MICROSCOPY AND SPECTROSCOPY IN THE DEVELOPMENT OF NEW MATERIALS FOR MICROELECTRONICS PACKAGING

R.A. Youngman

Carborundum Corporation, 10409 S.50th Place, Phoenix,AZ 85044

It has been over thirty years since sintered aluminum nitride (AlN) has been the focus of many research and development activities in Japan, the U.S., and Europe. Only in the past 5 years has there been significant use of this material in microelectronics. There are many reasons for this considerable time for application including, technology needs and acceptance of a new material. Also important has been the role of materials understanding of AlN through the use of microscopy and spectroscopy. We illustrate the use of both standard and unique characterization techniques to elucidate the nature of the crystalline defects which control the important property of thermal conductivity.

The thermal conductivity of pure AlN is 320 W/mK. This value has never been achieved in a sintered ceramic. In order to develop a sintered AlN with a high thermal conductivity it is necessary to understand the factors which control the thermal conductivity. We have addressed this through the use of optical spectroscopy and connected these results with the microstructure of the material via cathodoluminescence (CL) imaging. It is well established that impurity oxygen controls the thermal conductivity of AlN.[1] Extensive studies of the nature of the oxygen-impurity defect (an oxygen atom substituting on the N sublattice with resultant, charge balancing Al vacancies) including the use of photoluminescence (PL) spectroscopy, has lead to a detailed model for the evolution of this defect as a function of oxygen content and therefore thermal conductivity.[2] Fig.1 is a summary of the photoluminescence of oxygen-impurities in AlN as a function of thermal conductivity. One pertinent observation from this data is that the position (energy) of the luminescence peak is directly related to the thermal conductivity . The peak position can therefore define the thermal conductivity of the area being sampled. With respect to the development of a sintered ceramic material one needs information on a microscopic (<20 micrometers) scale. This cannot be accomplished with photoluminescence. Cathodoluminescence (in an SEM or TEM) however, can routinely spatially resolve at this level. Fig.2 is the cathodoluminescence spectrum from a typical oxygen-doped AlN ceramic. Note the similarity to the photoluminescence spectra of fig.1. This allows one to utilize the cathodoluminescence signal in a direct way to establish, on a microscopic scale, both the oxygen content and the spatial distribution of the oxygen within the AlN grains. Fig.3 is a pair of micrographs of the same region of an AlN ceramic utilizing the backscattered electron signal (BSE) (fig.3a) and the 375nm (+/- 40nm) cathodoluminescence signal combined with the BSE signal. The bright areas in fig.3a are the Y-Al-O compounds which form during sintering from the Y-based sintering aids, and the darker areas are the AlN grains. In fig.3b, the additional intensity is due to the cathodoluminescence of the oxygen impurities in the AlN grains. It is clear that utilizing this spectroscopy-based microscopy one can perform detailed analysis of the exact peak position (i.e. oxygen content) and the spatial distribution of the oxygen in the microstructure. In the case illustrated here there is a non-uniform distribution of oxygen in the AlN grains. These observations are of fundamental importance in the development of a process which will yield a high thermal conductivity sintered AlN.

In conclusion, it is important to point out that the relative ease with which these data have been collected is in substantial contrast to the extreme difficulties associated with the detection and spatial resolution of low atomic number elements in ceramic materials. The use of this unique technique represents a powerful tool for microstructural analysis in otherwise complex and difficult-to-analyze systems.

References

1. G.A. Slack et al., J. Phys. Chem. Solids, **48**, 641-7 (1987).
2. J.H. Harris, R.A. Youngman, and R.G. Teller, J. Mater. Res., **5**,1763-73 (1990).

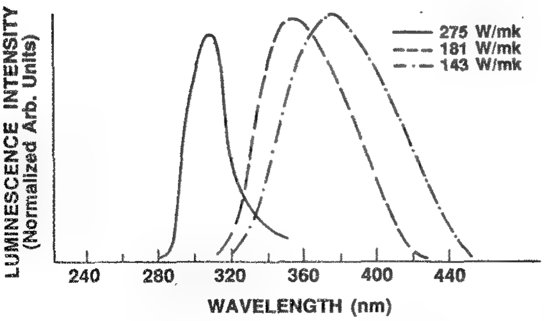

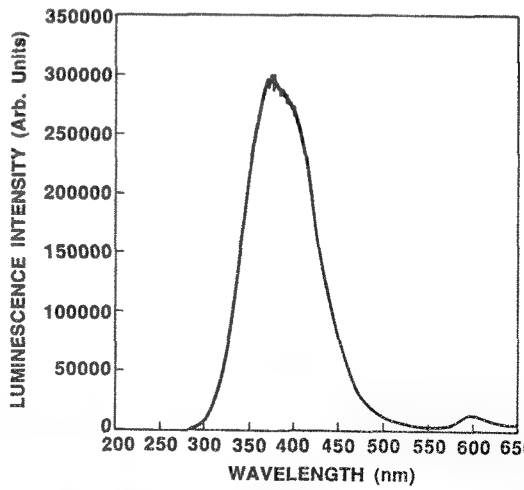

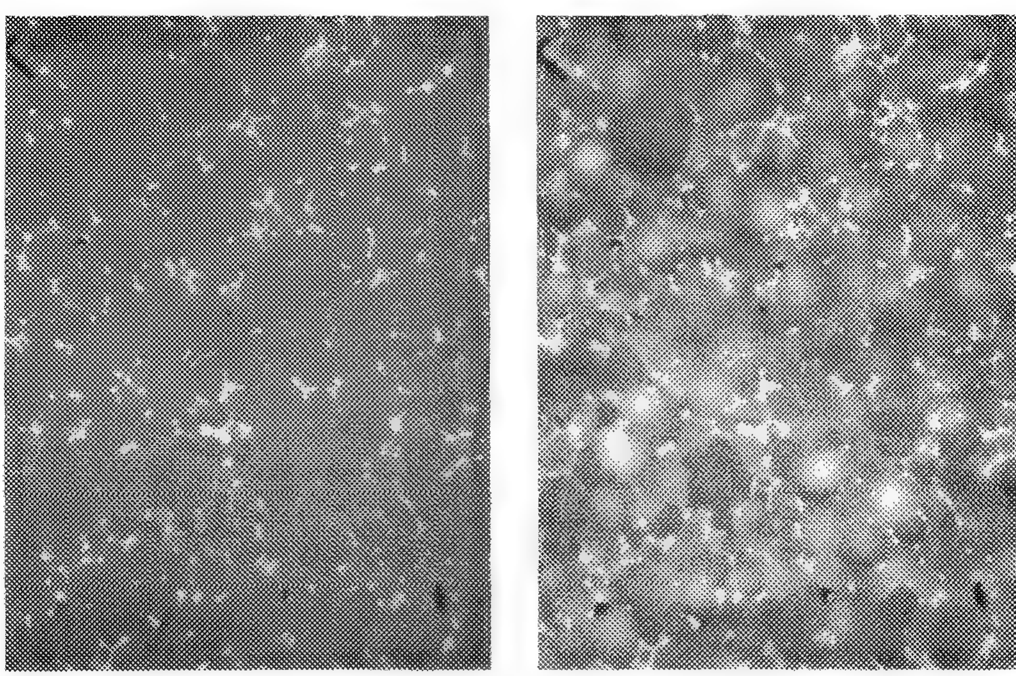

Fig. 1 PL spectra of three AlN specimens with different thermal conductivities.
Fig. 2 CL spectrum of an AlN specimen in an SEM.
Fig. 3 A pair of micrographs from the same region of an AlN ceramic utilizing the (a) BSE signal and (b) the 375nm (+/- 40nm) CL signal combined with the BSE signal.

Construction of Plastic Contact Deformation Maps on Ceramics: a Case Study on Aluminum Nitride

D. L. Callahan

Department of Mechanical Engineering and Materials Science, Rice University, Houston, TX 77251-1892

Modern polishing, precision machining and microindentation techniques allow the processing and mechanical characterization of ceramics at nanometric scales and within entirely plastic deformation regimes.[1] The mechanical response of most ceramics to such highly constrained contact is not predictable from macroscopic properties and the microstructural deformation patterns have proven difficult to characterize by the application of any individual technique. In this study, TEM techniques of contrast analysis and CBED are combined with stereographic analysis to construct a three-dimensional microstructure deformation map of the surface of a perfectly plastic microindentation on macroscopically brittle aluminum nitride.

The bright field image in Figure 1 shows a 1g Vickers microindentation contained within a single AlN grain far from any boundaries. High densities of dislocations are evident, particularly near facet edges but are not individually resolvable. The prominent bend contours also indicate the severity of plastic deformation. Figure 2 is a selected area diffraction pattern covering the entire indentation area. This pattern is the convolution of 5 distinct crystalline orientations representing the undeformed surface, the four facets, and the continuous intermediate orientations; there is no evidence of high pressure phase transition as observed in silicon and at least theoretically possible in AlN.[2-4]

The surface rotations resulting from indentation are analyzed beginning with a precise starting orientation measured from a CBED pattern from the undeformed grain. Orientations within the plastic zone are not so simply determined: the severe plastic strain makes CBED patterns from within the plastic zone indeterminate. However, bright field / dark field analysis of the bend contours based on the reflections in Figure 1b can be used to determine the operating Bragg reflections and hence locate plane traces on the indentation surface.

Stereographic analysis is then used to model the effect of various orientation transformations on this starting orientation as consistent with the known indentation geometry. These projections are used to simulate the specific orientations indicated by the various dark field images. For example, Figure 3 represents a stereographic triangle consistent with the broad facet illuminated in the dark field image Figure 4: the deformed orientation has been obtained by rotating the initial matrix orientation (point **0**) 11° about an axis in the plane of the image and parallel to the facet-surface edge. The facet orientation (point **X**) is seen to lie on the $(0\bar{1}\,1\,0)$ plane trace as consistent with the presence of the $(0\,\bar{1}\,1\,0)$ bend contour.

A deformation solution requires that all four facets exhibit orientations consistent with symmetrically-equivalent transformations consistent with the known three-dimensional indentation geometry. Furthermore, these transformations must also allow continuous, symmetric transitions across all facet edges. The complete deformation solution for this surface is internally self-consistent and also consistent with the basic surface morphology as predicted from elastic-plastic mechanics and observed in a variety of systems by atomic force microscopy.

References:

1. P. N. Blake and R. O. Scattergood, J. Am. Ceram. Soc. 73[4] 949 (1990).
2. D.R. Clarke, M. C. Kroll, P.D. Kirchner, R.F. Cook, and B. J. Hockey, Phys. Ref. Lett. 60, 2156 (2988).
3. J.J. Gilman, J. Mater. Res. 7, 535 (1992).
4. J. C. Morris, J. Kulik, J. A. Patten, and R. O. Scattergood, J. Am. Ceram. Soc, 78[8] 2013 (1995).

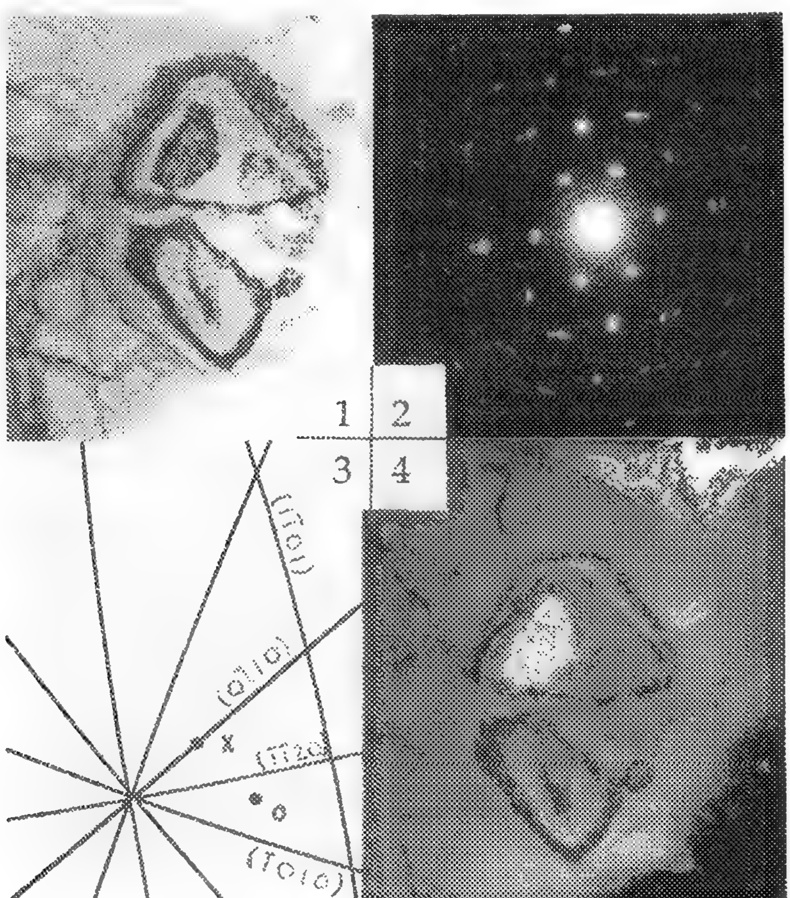

FIG. 1 Vickers microindentation on AlN: diagonal length is ~ 2 µm.
FIG. 2 Selected area diffraction pattern from indent shown in FIG. 1
FIG. 3 Stereographic triangle illustrating orientation (X) of the facet shown in FIG. 4
Fig. 4 $(0\,\bar{1}\,1\,0)$ Dark Field TEM micrograph corresponding to FIG. 1

CHARACTERIZATION OF BORON NITRIDE THIN FILMS SYNTHESIZED BY PLASMA-ASSISTED CHEMICAL VAPOR DEPOSITION TECHNIQUE

J. Liu, S. H. Lin and B. J. Feldman

Department of Physics, University of Missouri, St. Louis, MO 63121

Boron nitride (BN) is a well-known non-oxide ceramic that has interesting and useful properties for potential industrial applications. The attractive properties of BN include its high-temperature shock stability, high electrical resistivity, anisotropic thermal conductivity and desirable mechanical properties.[1] The potential uses of BN films include oxidation-resistant and anti-corrosive coatings, sensors, optical devices, and high temperature electronics. Thin films of BN have been obtained by a variety of growth techniques including sputtering, ion plating, evaporation, and chemical vapor deposition and associated techniques. To optimize the growth parameters and the performance of BN films, advanced electron microscopy techniques have been employed to study the structural evolution of BN films synthesized by plasma assisted chemical vapor deposition technique (PACVD).

The BN films were grown in a capacitively coupled rf plasma reactor with a feedstock of diborane (B_2H_6), ammonia (NH_3), and hydrogen (H_2). The growth parameters were the same as previously reported.[2] Chemical analyses of the grown BN films showed that they had significantly more boron (44 at.%) than nitrogen (33 at.%) and contained a large amount of hydrogen (23 at.%). Samples suitable for high resolution transmission electron microscopy (HRTEM) were prepared by gently grinding the BN films between two glass slides and were then dry-dispersed onto a holey carbon film. HRTEM observations were carried out on a Topcon 002B microscope with a 0.18 nm resolution. Surface morphology of the BN films was obtained by directly examining the samples in a high resolution field emission scanning electron microscope (FESEM) (Hitachi-4500) without prior coating. Low incident beam voltage (2 kV) was used to prevent charging of the samples.

Low magnification FESEM images revealed that BN films grown on silicon wafers were smooth and largely unstructured. At high resolution, however, small domains with sizes ranging from 5 to 30 nm were observed. Figure 1 shows a typical high resolution FESEM image of the BN films. Figure 2 shows a typical HRTEM image of the crushed BN films. It can be clearly seen that the majority of the BN film was crystalline and that nanometer-size crystallites were oriented randomly in an amorphous matrix. By analyzing many such HRTEM images and selected area electron diffraction patterns it was determined that the small crystallites had a hexagonal boron nitride (h-BN) structure. The structure of h-BN is analogous to the graphitic form of carbon, with strong bonding within the atomic layers and week bonding between layers. Electron microscopy results clearly showed that turbostratic BN materials were produced by the low temperature PACVD growth process. Many h-BN crystallites were bent to have an arc shape as clearly seen in FESEM images. HRTEM images also showed the bending of individual BN layers. Boron nitride nanotubes were occasionally observed. The formation of different shapes of the BN nanocrystallites will be discussed. It is noteworthy that small BN crystallites were imaged with bright contrast in FESEM images (figure 1). One explanation is that the bright contrast of the h-BN crystallites is due to topographic effect. This suggests that the h-BN crystallites were grown faster than the amorphous matrix during the growth process. Furthermore, based on the chemical analyses of the BN films it was determined that the composition of the amorphous matrix consisted primarily of boron and hydrogen. The growth mechanism(s) of the turbostratic BN films by PACVD technique will be discussed.[3]

References

1. R. T. Paine and C. K. Narula, *Chem. Rev.*, 90 (1990)73.
2. S. H. Lin and B. J. Feldman, *Mat. Res. Symp. Proc.*, Vol. 358 (1995)817.
3. The authors are grateful to Dr. Peter Crozier for assisting with HRTEM work which was conducted at the Center for HREM at Arizona State University.

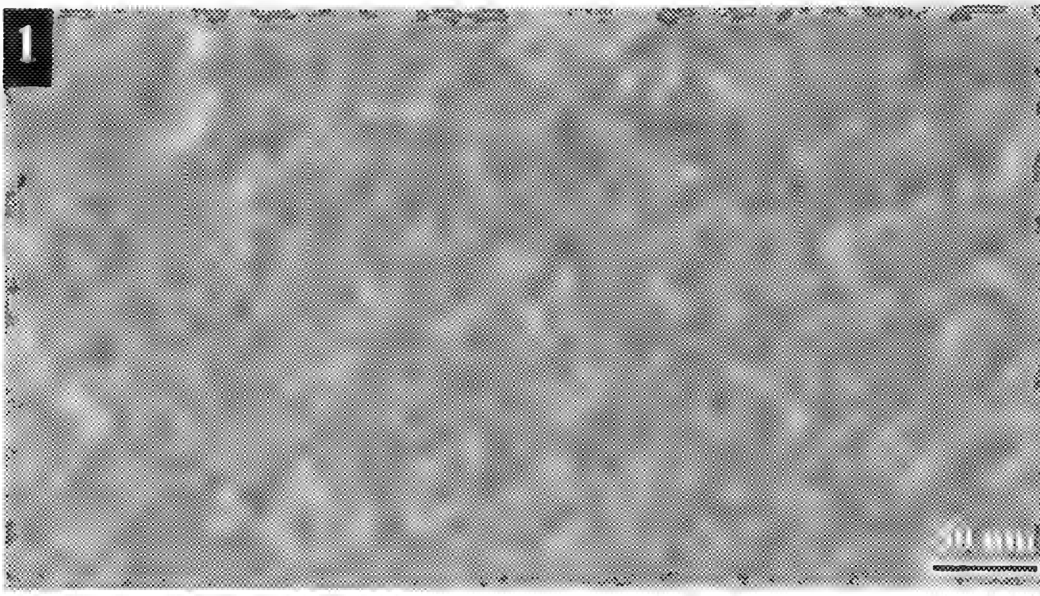

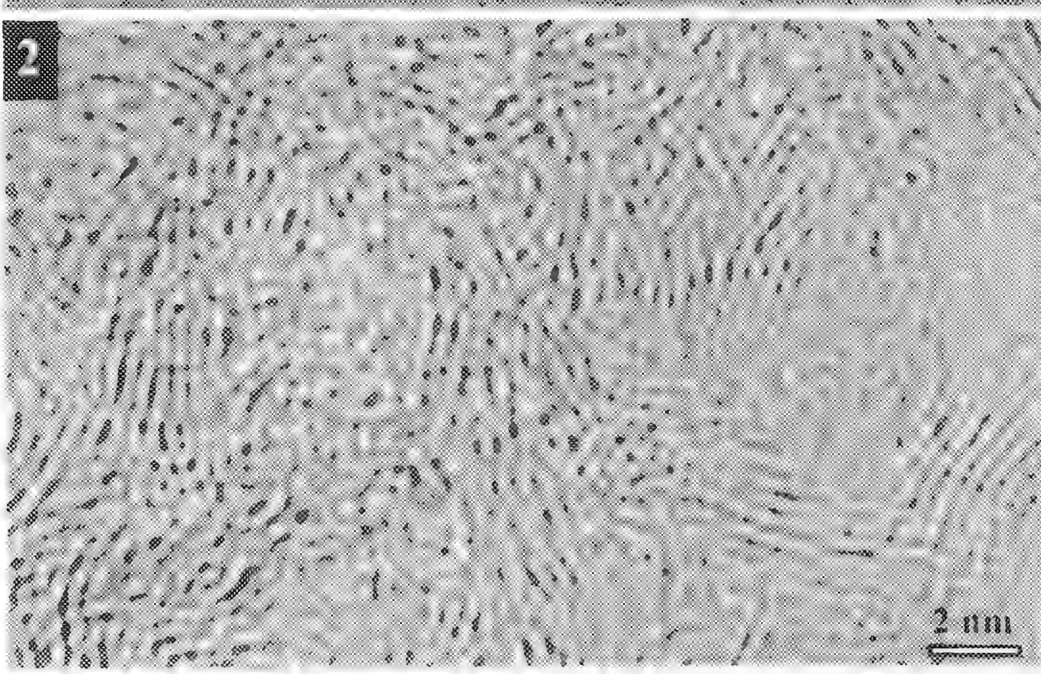

Fig. 1----High resolution low voltage (2 kV) FE-SEM image of BN film deposited on Si wafer.
Fig. 2----HRTEM image of BN film showing small crystallites of hexagonal boron nitride.

CRITICAL ISSUES IN CERAMIC MICROSTRUCTURES

D. R. Clarke

Materials Department, University of California, Santa Barbara, CA 93106-5050

As the number and variety of ceramic materials have grown so rapidly in the last few decades, ranging from silicon nitride structural ceramics to the perovskite superconductors to the ferroelectric oxides to semiconducting sensors, the number of scientific and technical issues has also grown rapidly. Many of the basic questions relate to the role the microstructures play in determining the observed physical behavior but increasingly it is not the geometric properties of the microstructure that are of central concern but rather compositional variations and associated electrical characteristics. These require the continued development of microscopy techniques to complement the tremendous advances in microstructural understanding that have already been made possible by microscopy in the past.

Since the role of microscopy is such a broad one, only a few of the most generic problems in microstructure characterization will be described in this talk. The topics selected include the characterization of intergranular films in liquid-phase sintered ceramics, the charge distribution at interfaces and the associated space charge, the epitaxial growth of oxides on oxide substrates, and the use of fluorescence imaging to identify phases and non-destructively measure local strains.

Relatively speaking, the characterization of thin (~1 nm) intergranular films in liquid phase sintered ceramics is an old topic. Since the first identification of the presence of such thin films coating the grain boundaries in silicon nitride ceramics in 1974, a wealth of observations in a wide variety of other ceramics have been reported. It is now known that the films are a remanent, generally silica-rich, phase left wetting the grain boundaries after cooling from the sintering process used to densify the ceramic. It is also known from high-resolution electron microscopy that, rather unexpectedly, the thickness of the intergranular film does not vary from one grain boundary to another despite changes in the grain boundary plane and changes in the relative crystallographic misorientation of the grains on either side of the boundary. The reason for this is not known and represents an important challenge to our understanding of the densification of ceramics as well as the origin of grain boundary wetting by a liquid phase. One model proposes that the intergranular film is stabilized by the action of van der Waals forces and is present as a result of a gradient energy contribution to the overall free energy of the grain boundary. On the basis of the predictions of this model a number of critical observations have been proposed including accurate, high spatial resolution measurements of the composition across intergranular films and into their adjoining grains. Such measurements require the use of field-emission STEMs with EELS but without the radiation damage associated with the use of such high power densities. There is a continuing need for a microscopy that reveals, in quantitative detail and high resolution, the charge distribution along a grain boundary or interface as well as in the

associated space charge region. The lack of such a microscopy remains a major impediment to a wide range of subjects, including the charge distribution in Schottky barriers, the potential distribution at grain boundaries in varistor ceramics and solar cells, and the charge depletion at free surfaces. Traditionally the principal technique that has provided some of the required data, primarily the location of recombination centers, has been EBIC in the scanning electron (and optical) microscope. Defocus imaging in the TEM has also been used to examine field distributions at low magnifications in simple structures such as p-n junctions. There is, thus, a tremendous opportunity for electron beam holography once the imaging methodologies, the image reconstruction techniques and image contrast theory have been fully developed.

The successful epitaxial growth of defect-free oxides on oxide substrates is an essential pre-requisite for the use of high-Tc superconductors in device applications and the incorporation of ferroelectric memories in devices, to name just two. It can be argued that with continued process development the defect level will fall, just as occurred through largely empirical development in the silicon industry. However, it is important to recognize that microscopy played a key role in the identification of defects introduced during processing helping to define the direction of process development. Undoubtedly it will be again so for the epitaxial oxides but given that the bonding is different, the crystal structures more complex and the importance of charge effects, microscopies of all types will be required in defect identification.

The fact that most ceramics are, in actuality, wide band-gap semiconductors and hence transparent in the visible makes it possible to use optical based microscopies for analysis. One such methodology uses photoluminescence (fluorescence) in an optical microscope to form images of phases and uses piezospectroscopic shifts to determine local strains. Cr3+ fluorescence has proven to be particularly suited to the study of alumina-based ceramics, composites and coatings since the R-line fluorescence is both intense and sharp. On account of its similar size and same valence, Cr3+ is a substitutional solute for Al3+ in aluminum oxide. When the d3 outer electrons are excited, by an argon ion laser for instance, to higher energy states they return to the ground state emitting principally R-line fluorescence -- a doublet at frequencies of 14448 and 14419 cm-1. Other polymorphs, for instance, Q have similar fluorescence but at different frequencies. It is thus possible to map out the distribution of the polymorphs, and has recently been used to study the kinetics of the Q-a transformation in oxide scales formed on NiAl high temperature alloys. One of the surprising findings was that as distinct from the usual linear kinetics of interface controlled transformations, the kinetics were logarithmic. The R-line fluorescence also is suited to strain measurement. When the host lattice, for example a-alumina, is strained the crystal field at the Cr3+ ions is altered thereby changing the energies of the excited states and hence the frequency of the R-line fluorescence. These changes are relatively small (~ 1 cm-1 per GPa) but by measuring the frequency shift the local strain can be calculated.

HETEROGENEOUS SOLID-STATE REACTIONS BETWEEN MgO(001) AND IRON OXIDE

Matthew T. Johnson*, Hermann B. Schmalzried** and C. Barry Carter*

*Department of Chemical Engineering and Materials Science, University of Minnesota, Minneapolis, MN 55455
**Universität Hannover, Institut für Physikalische Chemie and Elektrochemie, Hannover, Germany

The transport properties of the diffusing species in heterogeneous solid-state reactions are affected by concentration gradients, temperature gradients, stress fields and electric fields. In the present study, interfacial reactions between thin films of iron oxide and bulk monocrystalline MgO{001}, resulting in the formation of the spinel product $MgFe_2O_4$, were carried out separately as a function of time and temperature, applied external electric field and partial pressure of oxygen. Electron microscopy techniques have been utilized to investigate the reaction kinetics and interface morphology.

The reaction couples were produced by means of pulsed-laser deposition (PLD). The setup for PLD has been described elsewhere.[1] By depositing high-quality oxide films on bulk substrates, a well controlled geometry can be fabricated which is conducive to the study of fundamental processes in solid-state reactions. In producing the reaction couples, 600nm of iron oxide was deposited on monocrystalline MgO{001}. The reaction couples were then reacted under varying conditions and analyzed, using both scanning (SEM) and transmission electron microscopy (TEM).

In order to gain an understanding of the reaction rates for this system, the evolution of the spinel layer was followed as a function of time and temperature in air, using backscatter SEM imaging. Figure 1 is a graph depicting the growth of the spinel layer at 750°C. This graph shows that the growth kinetics of the spinel layer follow a parabolic rate law, indicative of diffusion control. Figures 2 and 3 are cross-section backscatter SEM images of two diffusion couples that were reacted for the same time at a temperature of 1100°C. The difference between the two is that the reaction couple in figure 2 was placed in an applied electric field, film side toward the cathode. In analyzing the resulting microstructure, iron has diffused into the bulk, where on cooling it has nucleated and reacted in the MgO to form dendrites of $MgFe_2O_4$ spinel. In the diffusion couple that was reacted under the applied field, the iron has diffused deeper and in greater concentration into the bulk in comparison to the standard. This effect can be attributed to the formation of an associate pair between the Fe^{3+} on the Mg^{2+} site and the vacancy created on the MgO lattice in order to maintain charge neutrality. Because the associate pair possesses a negative effective charge, it is repelled from the cathode. The other major difference between the two is that because of the applied field, Mg^{2+} ions have been driven past the spinel layer where they have reacted with ambient oxygen and formed a layer of MgO on the surface; a result which is consistent with previous work.[2] Figures 4 and 5 are cross-section backscatter SEM images showing the effect of the partial pressure of oxygen on reaction kinetics. The diffusion couple in figure 4 was reacted for 1hr at 800°C in vacuum were the diffusion couple in figure 5 was reacted for the same time and temperature in a pure oxygen atmosphere. As can be seen from the two images, the spinel layer of the diffusion couple reacted in vacuum is much thicker. This effect can be attributed to the increase in point defects in the oxide film. This increase in defects results in an increase in the diffusivity and the growth of the reaction product.

References

1. P. G. Kotula and C. B. Carter, Proc. 2nd Int. Conf. on Laser Ablation, AIP Conf. Proc., **288** (1993)231-236 .
2. J. R. Martinelli, E. Sonder, R. A. Weeks and R. A. Zuhr, Physical Review B, **32** [10](1985)6756-6763 .
3. The authors wish to acknowledge the Center for Interfacial Engineering(CIE), an NSF Engineering Research Center. The authors also thank Stan Erlandson for access to the Hitachi S-900 and Chris Frethem for technical assistance.

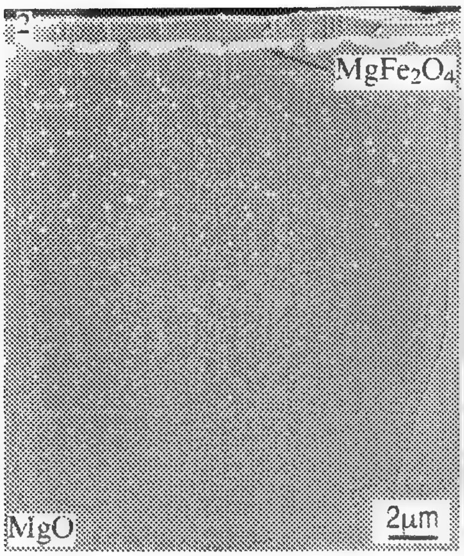

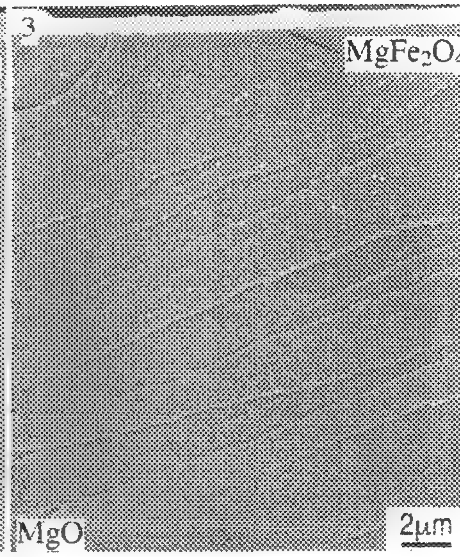

1

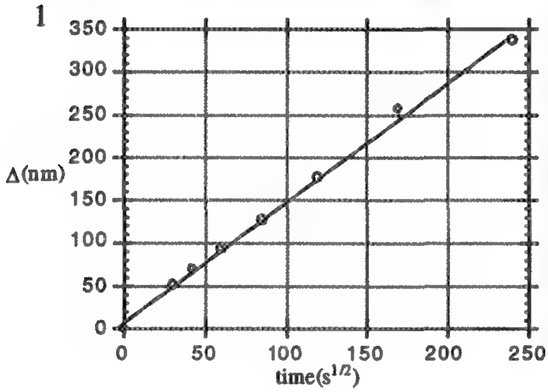

Fig. 1 Graph depicting the growth rate of the spinel layer at a temperature of 750°C.

Fig. 2 Cross-section backscatter SEM image of thin-film reaction couple reacted at a temperature of 1100°C in an applied electric field.

Fig. 3 Cross-section backscatter SEM image of thin-film reaction couple reacted at a temperature of 1100°C.

Fig. 4 Cross-section backscatter SEM image of thin-film reaction couple reacted at a temperature of 800°C in vacuum.

Fig. 5 Cross-section backscatter SEM image of thin-film reaction couple reacted at a temperature of 800°C in pure oxygen at atmospheric pressure.

CHARACTERIZATION OF CRYSTALLINE TITANIUM DIOXIDE SYNTHESIZED AT ROOM TEMPERATURE

Mani Gopal

Department of Materials Science and Mineral Engineering, University of California, Berkeley CA 94720 and Center for Advanced Materials, Lawrence Berkeley National Laboratory, Berkeley, CA 94720

A process has been developed to synthesize crystalline titanium dioxide powders from aqueous solutions at low temperatures ($T \leq 100°C$) and atmospheric pressure[1]. Processing at slow reaction rates causes the formation of the thermodynamically favored rutile phase. Faster reaction rates promote the formation of anatase, the statistically favored phase. Processing at intermediate rates causes a mixture to be formed (Fig. 1). This paper reports the TEM and SEM characterization of rutile, precipitated at 40°C.

Specimens for TEM were collected on holey carbon grids suspended vertically in the stirred solution. After removal, the grids were washed in isopropyl alcohol and dried under a heat lamp. For SEM analysis, a drop of the solution was placed on the specimen holder and dried. The top surface was then washed with isopropyl alcohol to remove any contamination and observed.

The bright field image (Fig. 2b) of the rutile precipitates shows them to have a nominal size of 50-100 nm. The sharpness of the (002) ring in the electron diffraction pattern (Fig. 2a) indicates the needles are elongated in the [002] direction. The corresponding dark-field image (Fig. 2c) shows that individual needles are comprised up of smaller particulates (HR-TEM shows them to be ~3 nm in size). It is important to note that in each needle, all the particulates diffract together or they all do not, indicating a common orientational relationship.

The higher-than-theoretical intensity of the (002) ring in the electron diffraction pattern (Fig. 2a) corresponds to the propensity for the needles to "lie" on the holey-carbon TEM substrate. This is confirmed by the diffraction pattern obtained from a tilted specimen (Fig. 3). The (002) ring in incomplete and shows two arcs, due to diffraction from the precipitates whose [002] direction is parallel to the tilt axis. The [002] directions of other precipitates are not perpendicular to the electron beam and hence do not diffract.

At a later stage of the precipitation process, the number density of needle-like precipitates in the solution increases. The needles then agglomerate into spheroids, as imaged by SEM (Fig. 4). Although the SEM image suggests these clusters are dense, TEM images determine they are not. Electron diffraction patterns taken from the cluster show it to contain a disordered collection of rutile needles. Fig. 5 is an SEM image of a different batch of rutile precipitates taken after they were coated with gold. The acicular features of the precipitates have been covered, resulting in an erroneous morphology.

References

1. M. Gopal *et al.*, submitted to *J. Mater. Sci.*
2. The author would like to thank Dr. W. MoberlyChan, Prof. L. C. De Jonghe and Prof. G. Thomas for their help and guidance. This work was funded by ARPA, Project Number 8672.

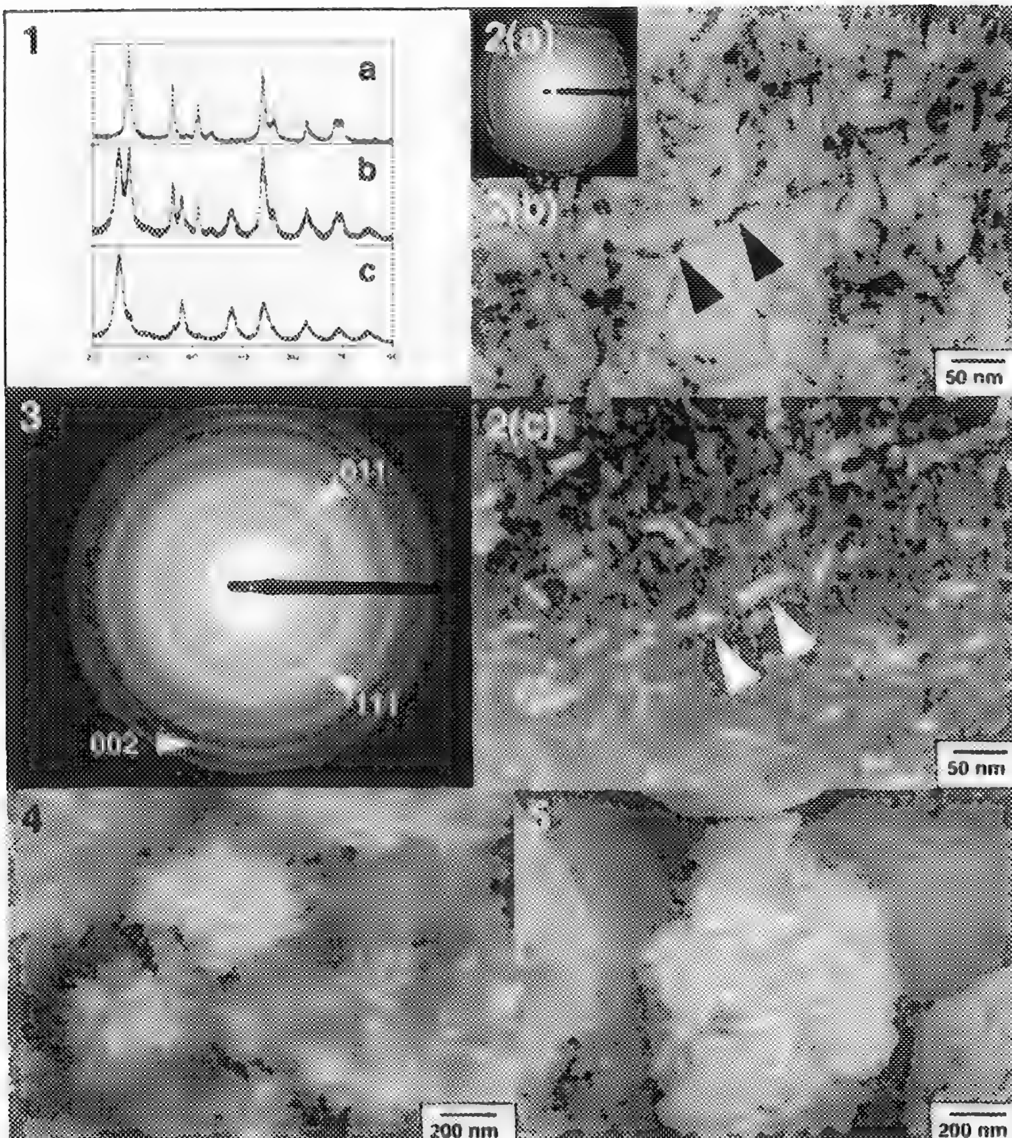

Figure 1 - X-ray diffraction patterns showing the effect of heating rate on the phase formed. (a) Slow reaction rate produces rutile, (c) fast reaction rate produces anatase. **Figure 2** - Bright-field (b) and dark-field (c) images showing rutile needles made up of smaller particulates. **Figure 3** - Electron diffraction pattern from a tilted specimen showing discontinuous (002) ring. **Figure 4** - SEM image of an agglomerate of rutile needles. **Figure 5** - SEM image of agglomerate after gold coating.

THE ROLE OF MIXED CUBIC/HEXAGONAL NUCLEATION LAYERS ON THREADING DISLOCATION REDUCTION IN EPITAXIAL GAN FILMS

X. H. Wu*, L. M.Brown**, D. Kapolnek*, S. Keller‡, B. Keller‡, S.P. DenBaars*‡, and J.S. Speck*
*Materials Department and ‡Electrical and Computer Engineering Department,
University of California Santa Barbara, California 93106 ; **University of Cambridge, UK

The defect density and their configuration in epitaxial GaN films on sapphire are strongly related to the optical and electrical properties of the films. The crystalline quality of GaN on sapphire can be greatly improved by introducing a low temperature GaN buffer layer. However, recent studies in our group demonstrate that the pre-growth substrate treatment can significantly change the defects structure and electron properties of the films [1,2]. In this paper, we present our results on studies of the film microstructures and their corresponding nucleation layers. We propose a novel mechanism for dislocation reduction for GaN on sapphire.

The growths for this study were achieved in a horizontal flow reactor operating at atmospheric pressure. Basal plane Al_2O_3 (Union Carbide) substrates were first cleaned in solvents and then heated in flowing H_2 at 1050°C. Sample A was exposed to an ammonia flow of 3 l/min for 60s, sample B for 400s before the temperature was then reduced to 600°C and a nominal 190 Å thick GaN layer was grown. Subsequently, the reactor temperature was increased to 1080°C and ~1 μm thick films were grown at a rate of ~7 Å/s. Cross sectional and plan view TEM sample were prepared by the wedge polishing method and Ar ion milled at 4 kV. The TEM investigation were carried out on either a JEOL 2000FX or a JEOL 2010 TEM operating at 200 kV.

The only difference for sample A and B is that the substrate of sample B was exposed to a longer duration ammonia flow than sample A. The increased exposure time for sample A may promote the formation of a very thin layer of AlN layer on the sapphire substrate. As a consequence of the ammonia exposure time, the defect structures of thick layer of these two samples are completely different. For sample B, the threading dislocation (TD) density is about $2x10^{10}cm^{-2}$ - more than 99% of the threading dislocations have pure edge character with Burgers vectors $1/3\langle 11\bar{2}0\rangle$. The threading dislocations in sample B organize into low angle grain boundaries. For sample A, the TD density is $\sim 7x10^{8}cm^{-2}$ with half of the threading dislocations having pure edge character and half having mixed or pure screw character. For sample A, the threading dislocations do not organize into low angle grain boundaries. Additionally, sample A has a high density of partial dislocations (both Frank and Shockley type) near the film/substrate interface. Further TEM studies show that for sample A (Fig. 1a) that the small grains in as-grown nucleation layer have a highly faulted cubic structure, whereas for sample B (Fig. 1b) the as-grown nucleation layer shows two discrete regions: there is a continuous thin pure hexagonal GaN layer of thickness 20-50 nm near the interface; above this layer, the nucleation layer has a highly faulted cubic structure with a rough morphology very similar to that in sample A. After these two as-

grown nucleation layers were annealed at 1050°C, the film in sample A (Fig. 2a) showed some smoothing, but overall it still had a rough morphology - the grain size increases and the structure is more hexagonal with high density of partial dislocations [3]. However the film in sample B (Fig. 2b) after heating develops into a continuous hexagonal layer. Collectively, these results demonstrate that the dislocation reduction from sample B to sample A is associated with the high density of near interfacial stacking disorder in sample A. Partial dislocations must form during island coalescence in sample A. The Shockley partials react with pure edge threading dislocations to give complete annihilation. However, for sample B, the nucleation layer transforms into a smooth hexagonal layer with minimal stacking disorder, thus there is little possibility of annihilation reactions between pure edge threading dislocations and Shockley partials.

References

1. B. Heying *et al.*, *Appl. Phys. Lett.* **68**, 643 (1996).
2. S. Keller*et al.*, *Appl. Phys. Lett.* **68**, 1525 (1996).
3. X.H. Wu *et al.*, *Appl. Phys. Lett.* **68**, 1371 (1996).

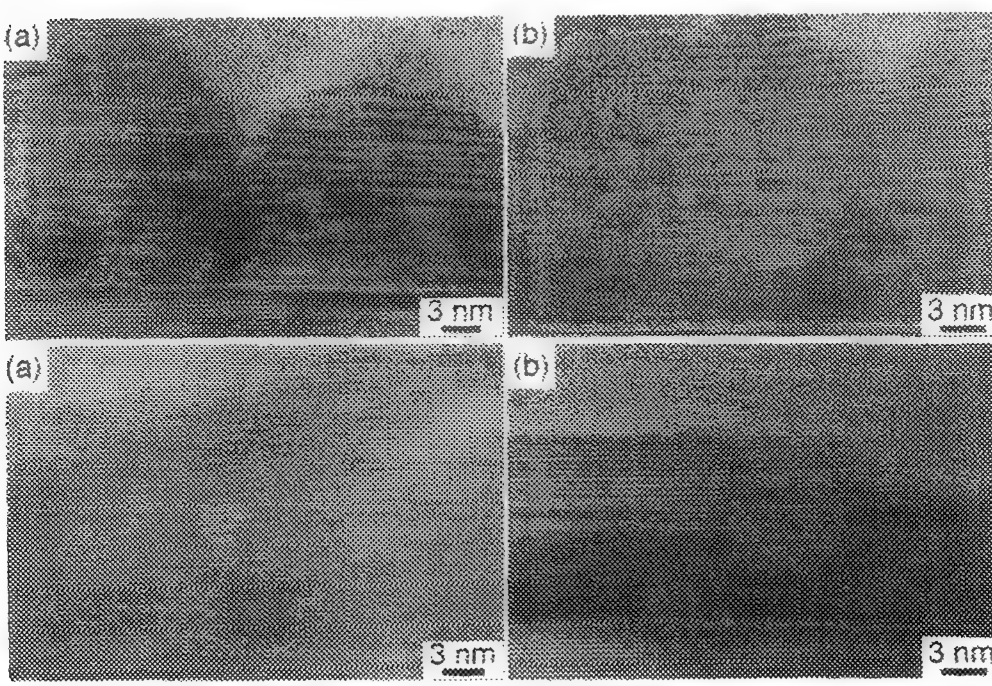

Fig. 1 HREM cross sections of GaN/Al_2O_3 as-grown nucleation layers. (a) sample A, (b) sample B.

Fig. 2 HREM cross sections of GaN/Al_2O_3 annealed nucleation layers. (a) sample A, (b) sample B.

ON the CRYSTALLOGRAPHY of TRIPLE POINTS in NONOXIDE CERAMICS: EPITAXIAL RELATIONSHIPS ARE a FUNCTION of STATISTICS and GEOMETRY

Warren J. MoberlyChan

Materials Science Division, Lawrence Berkeley Laboratory, 1 Cyclotron Road, Berkeley, CA 94720

Covalent ceramics, such as SiC and Si_3N_4, can have superior mechanical properties for high temperature structural materials. However, densification difficulties and poor fracture toughness have hindered use. Traditionally, the choice of sintering additives has been a "hit and miss" method to improve properties. The primary purpose of an additive is to provide good density, as residual pore size relates to critical flaw size. Another feature of an additive has recently been to invoke fracture around the matrix grains, thereby enhancing toughness [1]. Most reported nonoxide ceramics include upwards of 10% secondary phase(s) as a continuous phase between many matrix grains and causing poor high temperature strength. Even when this secondary phase is crystallized [2], thin amorphous interfaces are observed [3, 4]. The ABC-SiC processed for this study incorporates <5% total Al, B, and C as additions. The Al enhances densification, as well as the β-to-α phase transformation at lower temperatures (1600-1900°C); and controlling the microstructural development has provided record toughness [1].

Secondary phases that result from the sintering additives are classified in 3 geometries. At the largest scale, there are crystalline phases ($Al_8B_4C_7$, Al_4O_4C, and Al_2O_3) which wet amongst numerous matrix grains. The size of these large phases are comparable to the size of the original additive [5]; however, the volume fraction of these large phases in ABC-SiC is substantially less than in most ceramics. At the smallest scale, HR-TEM (Fig. 1a) observes a 1 nm-thick amorphous phase at grain boundaries and very small triple points. EDS, Auger [1], and PEELS determine the amorphous grain boundaries are enriched in Al and O. Fig. 1b maps Al in an energy-filtered image, using a Gatan Imaging Filter [6]. Integrating signal intensity determines concentrations and thicknesses of amorphous phase are the same for normal (Fig. 1c) and tilted (Fig. 1d) boundaries; whereas tilted interfaces are difficult to interpret with HR-TEM.

The third geometry of secondary phases are small, isolated, crystalline triple-point channels that adjoin only three matrix grains. As the volume fraction of secondary phases is decreased (<5% total), these isolated triple points become more prominent, as well as influential to the mechanical properties [1]. Fig. 2a and 3a are BF-TEM images of dual-phase, plate-like, α-4H grains of ABC-SiC hot pressed at 1900°C [1]. Small triangular triple point phases are present where two adjoining grains intersect the planar surfaces. Fig. 2b is an intergranular fracture surface that shows triple points crystallize over many microns in length but only a few nanometers in width. Fig. 2c and 3b are HR-TEM images of crystalline triple points surrounded by a thin residual amorphous phase. The triple points are too small for traditional microdiffraction; thus crystallographic analysis, as well as orientation relationships, are determined by computer [6] diffractograms (Fig. 2d, 2e, and 3c). Often a thin amorphous phase is present between the crystalline triple point and the matrix grain on which it nucleated, even though an epitaxial relationship exists. During cooling, the liquid-phase additives nucleate on a matrix grain. As the crystalline phase grows down a triple point channel, it pushes undesirable solutes ahead of it and to the sides. Eventually the crystalline phase will grow over a step in the planar surface of the matrix grain, at which time undesirable solutes are pushed beneath the triple point phase. The triple point phase becomes detached from the matrix grain and continues growing without a mismatch strain. Surrounding regions enriched in undesirable solutes remain amorphous. The orthorhombic structure of Al_4O_4C and the hexagonal structure of $Al_8B_4C_7$ result in 4 and 2 observed orientation relationships, respectively.

References
1. W. J. MoberlyChan, et al., in this *MSA Proceedings* (1996).
2. C. Koehler & G. Thomas, *MSA Proceedings* , **V2** (1992) 1070-1071.
3. H. Gu, J. Mayer, H. Müllejans, & M. Rühle, *MSA Proceedings* , (1994) 976-977.
4. W. J. MoberlyChan, et al., to be submitted to *Acta metall. mater.*
5. W. J. MoberlyChan, et al., *MAS Proceedings* , (1994) 49-50.
6. W. J. MoberlyChan, S. Gubbens, & Gatan, Inc., work in progress.
7. The authors gratefully acknowledge the NCEM staff. Support was by DOE #ACO3-76SF00098.

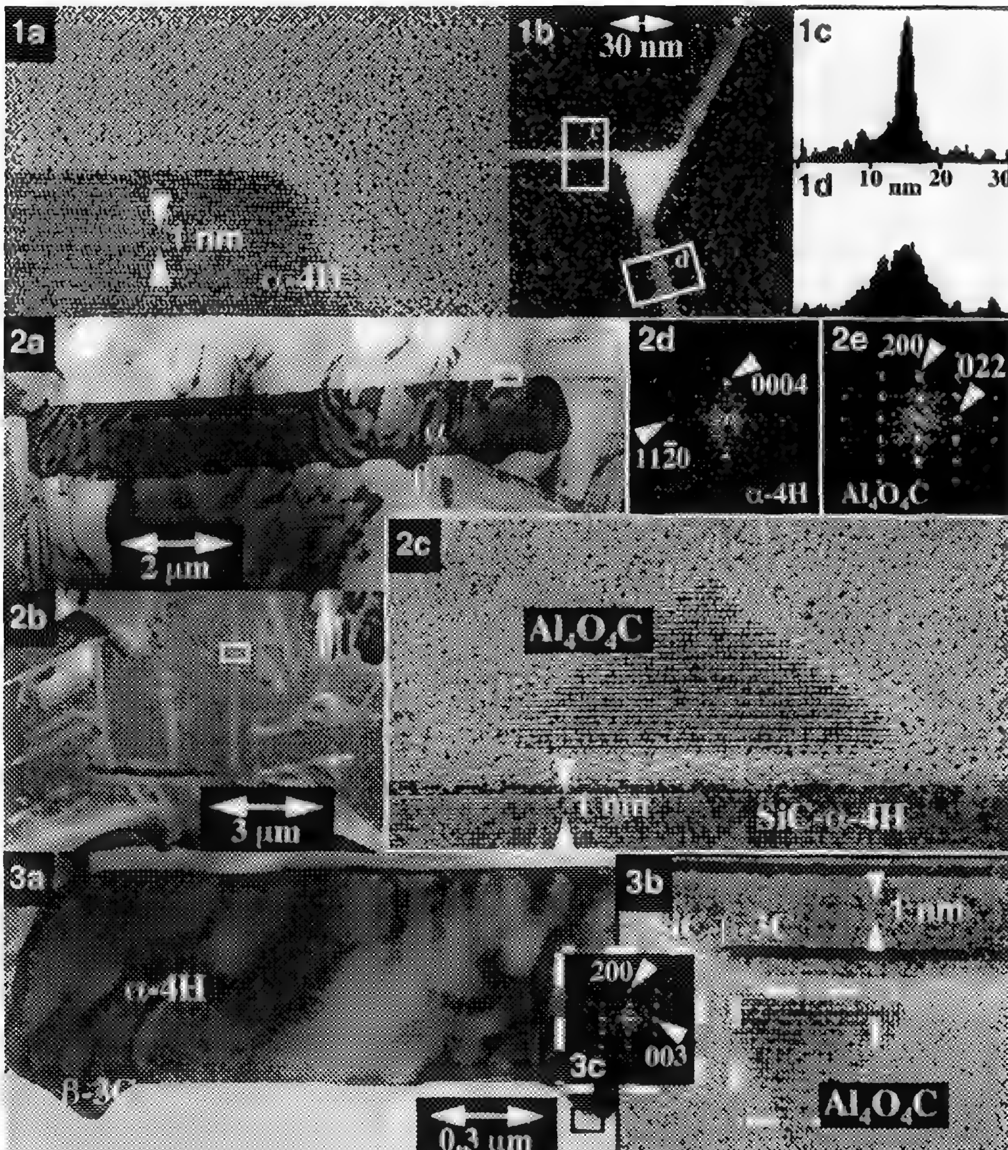

Fig. 1: (a) HR-TEM of amorphous grain boundaries and triple point. (b) Energy-filtered (GIF) map shows Al with equal concentration/thickness for (c) normal and (d) tilted grain boundaries. Oxygen map parallels Al.
Fig. 2: (a) BF-TEM cross-section of plate-like ABC-SiC, processed at 1900°C/4hr. (b) SEM fracture surface with triple point phases (predominantly $Al_8B_4C_7$). (c) HR-TEM and (d and e) diffractograms determine phase and orientation relationship: $(100)_{Al_4O_4C}$ //$(0001)_{SiC}$ and $[011]_{Al_4O_4C}$ //$[1100]_{SiC}$.
Fig. 3: (a) BF-TEM of plate-like SiC; 1900°C/1hr. (b) HR-TEM of crystalline triple point; (c) [010] Al_4O_4C.

SPIRAL CARBON TUBES GROWN BY A MIXED-VALENT OXIDE-CATALYTIC CARBONIZATION PROCESS

Z. L. Wang and Z. C. Kang

School of Material Science and Engineering, Georgia Institute of Technology, Atlanta, GA 30332-0245

Synthesis of carbon tubes is vitally important in carbon research and applications. In this paper, spiral carbon tubes are grown by a mixed-valent oxide-catalytic carbonization (MVOCC) process [1]. The carbon tubes are highly twisted and have many growth induced nodes. (Fig. 1). The product has high purity and no catalyst particle is found in the product. With the presence of inter-lock structure, the mechanical properties of the material made using the spiral carbon tubes could be significantly improved. The inner tube is not completely hollow but interconnected by graphitic layers. The surfaces of the tubes have many open graphitic edges, thus, a high chemical activity of the tubes is expected. Figure 2 shows a low-magnification TEM image at the initiation side of a carbon tube, where a spiral node is formed. The non-uniform contrast across the node region reflects the spiral geometry at the node. In the growth front (Fig. 3), the inner tube is not hollow and is interconnected by graphitic "bridges". The graphitic layers composing the inner-wall region of the tube have larger sizes, while the graphitic flakes in the outer-wall region are rather small, with sizes ranging from 1-10 nm. The growth front has a shape similar to a "cowboy hat", where the graphitic layers across the top of the hat are severely bent, indicating the non-equilibrium shapes at the growth front. A sharp turn of the graphitic layers at the edge of the hat may be produced by a "boat-type" line defect proposed for interpretation of a 90° bending of carbon layers [2]. The alignment between graphite layers is also visible at the left-side of the hat, suggesting a coherent layer-by-layer growth at the growth front.

The nucleation of a carbon node is believed to be initiated from a pentagonal carbon-ring, which causes the hexagonal network to be bent inward. If a few pentagon carbon-rings are introduced in the graphite lattice, a quasi-icosahedral spiral shell can be formed (Fig. 4a). The continuation of the spiral growth requires a proper supply of a certain fraction of pentagonal carbon-rings in order to accommodate the inward curvature of the spiral core (Fig. 4b). In practice, however, the nucleation rate of carbon-rings, as determined by experimental conditions, such as temperature and gas-flow rate, may not create the fraction of pentagonal carbon-rings required to force the growing layer following the curvature of the inner graphitic layers. If no pentagonal carbon-rings are created for a very short period of time and the hexagonal carbon-rings are over supplied, the spiral layer will grow outward forming a "conical-type" partially closed structure with consideration of the three-dimensional spiraling geometry (Fig. 4c). The formation of this "conical" protrusion is the beginning of the tube growth and the termination of the growth of the spiral core. If the shortage of pentagonal carbon-rings continue, the newly arrived large-size hexagonal networks tend to distribute on the top of the conical protrusion, forming a hat-top structure (Fig. 3). The hat-top can be closed if pentagonal carbon-rings exist at the edge of the large graphite layers, it will be open otherwise (Fig. 4d). The edge of the hat-top may be produced either by pentagonal carbon-rings or the boat-like line defects, depending on the angle of bending. The closed hat-top forms the bridge structure, while the unclosed hexagonal networks create many open edges and dangling bonds, as observed in Fig. 6. In the mean while, small size graphitic flakes nucleated in the growth chamber are arriving on the surface, resulting in the transverse growth of the tube. It is expected that the growth rate of the large graphitic layers at the growth front will be very high, forming a long tube (Fig. 4e). The piling-up growth phenomenon is similar to a stack of piled ice-cream cups with open and/or closed bottom faces. The small size graphitic flakes tend to pile up on the outer surface. Therefore, the inner-wall of the tube is composed of larger size graphitic layers, and the outer-wall region is composed of smaller size graphitic flakes (Fig. 3).

The formation of the node can be interpreted using the creation of paired pentagonal and heptagonal carbon-rings in the hexagonal networks. If a pair of pentagonal and heptagonal carbon-rings is created, the tube will be forced to turn clockwise for approximately 60°. Another 60° turn is introduced if the second pair of pentagonal and heptagonal carbon-rings occurs, resulting in the twisted spiral growth of the tube. The number of pentagon and heptagon pairs determines the total twist angle.

In summary, the carbon tubes are nucleated on spherical carbon cores, created by unclosed polyhedron carbon shells containing pentagonal carbon-rings. The conical growth of graphitic layers along the tube is a result of a temporary shortage in supply of pentagons. The pairing of pentagons and heptagons is the key to nucleate the nodes. The growth mechanism of these tubes is different from those straight nanotubes, which are directly nucleated on the catalyst surface and the contact area between catalytic particles determines the inner diameter of the tube [3]. Our experiments prove that the fraction and nucleation rates of pentagons, hexagons and heptagons determine the surface geometry of the product. If large fractions of pentagons and heptagons are continuously produced, carbon spheres will be formed. If the creation rate of pentagonal and heptagonal carbon-rings is much smaller than the rate at which the hexagonal carbon-rings is created, a tube-like product will be formed. A fluctuation in the creation rate of the pentagons and heptagons results in a growth of separated nodes along the tube which force the tube to grow into a spiral shape.

[1] Z.C. Kang and Z.L. Wang, Phil. Maga. B, in press (1996); US patent pending; in these proceedings.
[2] H. Hiura et al., Nature **367** (1994) 148.
[3] S. Iijima et al., Phys. Rev. Lett. **69** (1993) 3100; S. Iijima, MRS Bulletin **XIX**, No. 11 (1994) 43; S. Amelinckx et. al., Science **265** (1994) 635.

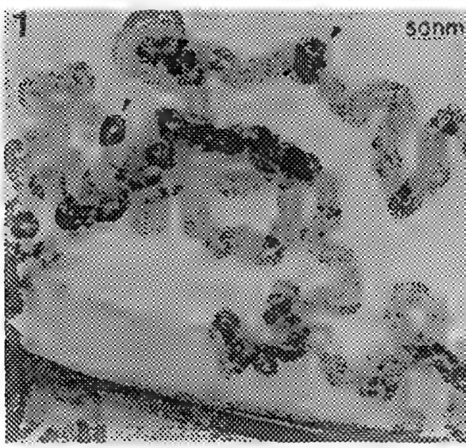

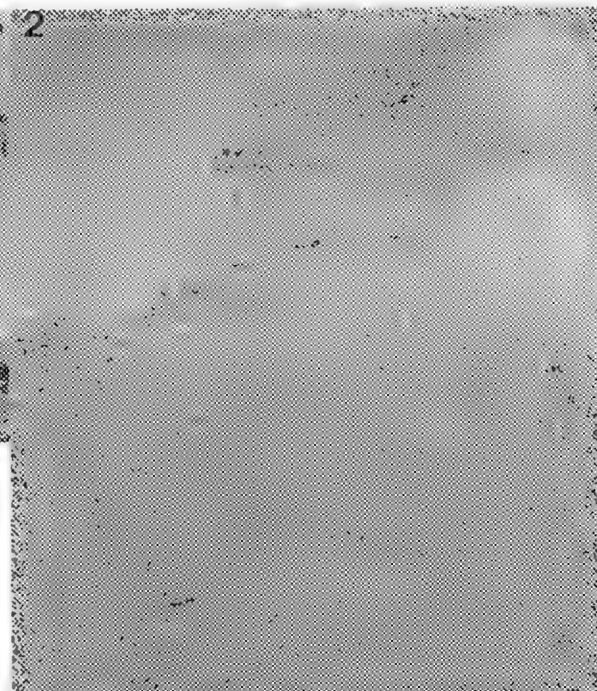

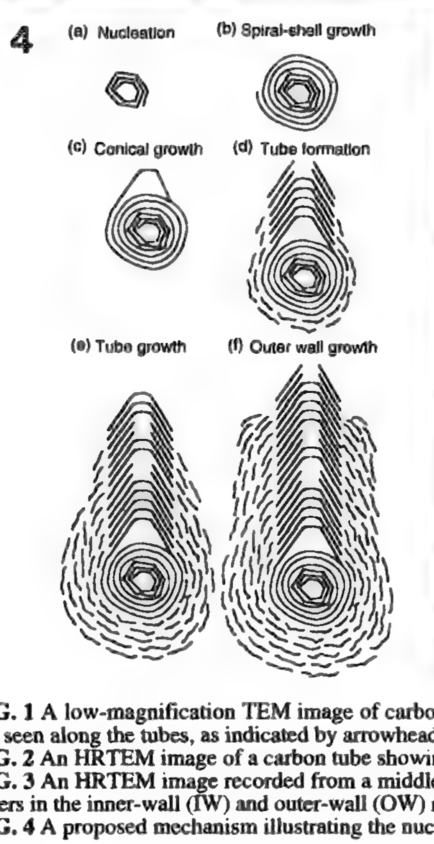

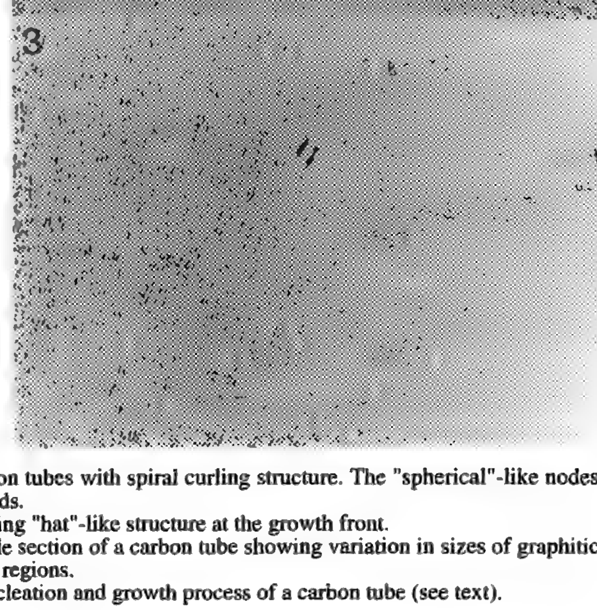

FIG. 1 A low-magnification TEM image of carbon tubes with spiral curling structure. The "spherical"-like nodes are seen along the tubes, as indicated by arrowheads.
FIG. 2 An HRTEM image of a carbon tube showing "hat"-like structure at the growth front.
FIG. 3 An HRTEM image recorded from a middle section of a carbon tube showing variation in sizes of graphitic layers in the inner-wall (IW) and outer-wall (OW) regions.
FIG. 4 A proposed mechanism illustrating the nucleation and growth process of a carbon tube (see text).

TEM STUDY OF FRANKLINITE-HETAEROLITE ($ZnFe_2O_4$-$ZnMn_2O_4$) EXSOLUTION INTERGROWTHS

W.L. Gong, L.M. Wang and R.C. Ewing

Department of Earth and Planetary Sciences, University of New Mexico, Albuquerque, NM 87131

The spinel structure-type is derived from *ccp* oxygen packing by cation occupation of one quarter of the tetrahedral and one half of the octahedral interstices with a general stoichiometry of AB_2O_4. Franklinite, ideally $ZnFe_2O_4$, was the dominant ore mineral of zinc at the great Franklin and Sterling Hill zinc deposits, New Jersey. Although the chemistry of franklinite conformed to the spinel formula, the composition showed a wide range in the proportions of iron, zinc, and manganese.[1] The microscopic examination of polished sections of the Franklin spinel revealed oriented exsolution intergrowths of franklinite, magnetite ($Fe^{2+}Fe^{3+}{}_2O_4$), and gahnite (ideally $ZnAl_2O_4$).[2,3] In this contribution, the exsolution intergrowths of franklinite and hetaerolite (ideally $ZnMn_2O_4$) are well characterized using JEM 2000FX and JEM 2010 electron microscopes operated at 200 keV.

Two groups of oriented hetaerolite lamellae with different generation occur in the franklinite host (Fig. 1). The early-formed is the coarse hetaerolite lamella with ~1 μm in width, which may be oriented on (100) of the franklinite. Another is the thinner hetaerolite lamellae with only 0.2 μm in thickness, which may be oriented on (111) of the franklinite host. Thinner lamellae all terminate at the coarse lamellae. EDS analysis indicates all the hetaerolite lamellae have a constant composition of $Zn(Mn^{3+}{}_{1.65}Fe^{3+}{}_{0.29}Cr^{3+}{}_{0.05}Al_{0.01})_2O_4$. The host franklinite is of $Zn(Fe^{3+}{}_{1.31}Mn^{3+}{}_{0.68}Al_{0.01})_2O_4$. The interfaces between the hetaerolite exsolution lamellae and the host phase are usually lattice-coherent as revealed by HRTEM (Fig. 2). The coarse hetaerolite lamellae are periodically spinel-twinned along (111) as shown by Fig.3. The modulated strucutre which has been explained for spinodal decomposition in the literature exists in the background (Fig.4). Spinel-twining is also observed in the background franklinite (Fig. 5).

The subsolidus in the system of Fe_3O_4-Mn_3O_4-$ZnMn_2O_4$-$ZnFe_2O_4$ has been described by Mason (1947).[4] At the peak temperature of regional metamorphism (760 °C), what are now exsolution intergrowths were homogeneous Zn-Mn iron-rich spinel. Assuming slow subsolidus cooling at a rate of ~2 °C per million years, this chemically complex spinel exsolved into a franklinite solid-solution and a hetaerolite solid-solution with (001) as the plane of exsolution at relatively high temperatures. Subsequently, at relatively low temperatures, the hetaerolite lamellae developed in the franklinite solid-solution with (111) of the spinel lattice as the common plane. These two unmixing processes were probably heterogeneous and were nucleation-and-growth controlled. The lamellar width may depend on different cooling rates. Finally, at an even lower temperature, spinodal decomposition occurred leading to the formation of the background modulations and "tweed' textures in the spinel solid-solution system.

References

1. C.B. Sclar and B.F. Leonard, Econ. Geol. 87, 1180 (1992).
2. A.J. Valentino, A.V. Carvalho III, C.B. Sclar, Econ. Geol. 85, 1941 (1990).
3. C. Frondel and C. Klein, Am. Miner. 50, 1670 (1965).
4. B. Mason, Am. Miner. 32, 426 (1947).
5. This work was supported by BES/DOE grant DE-FG03-93ER45498.

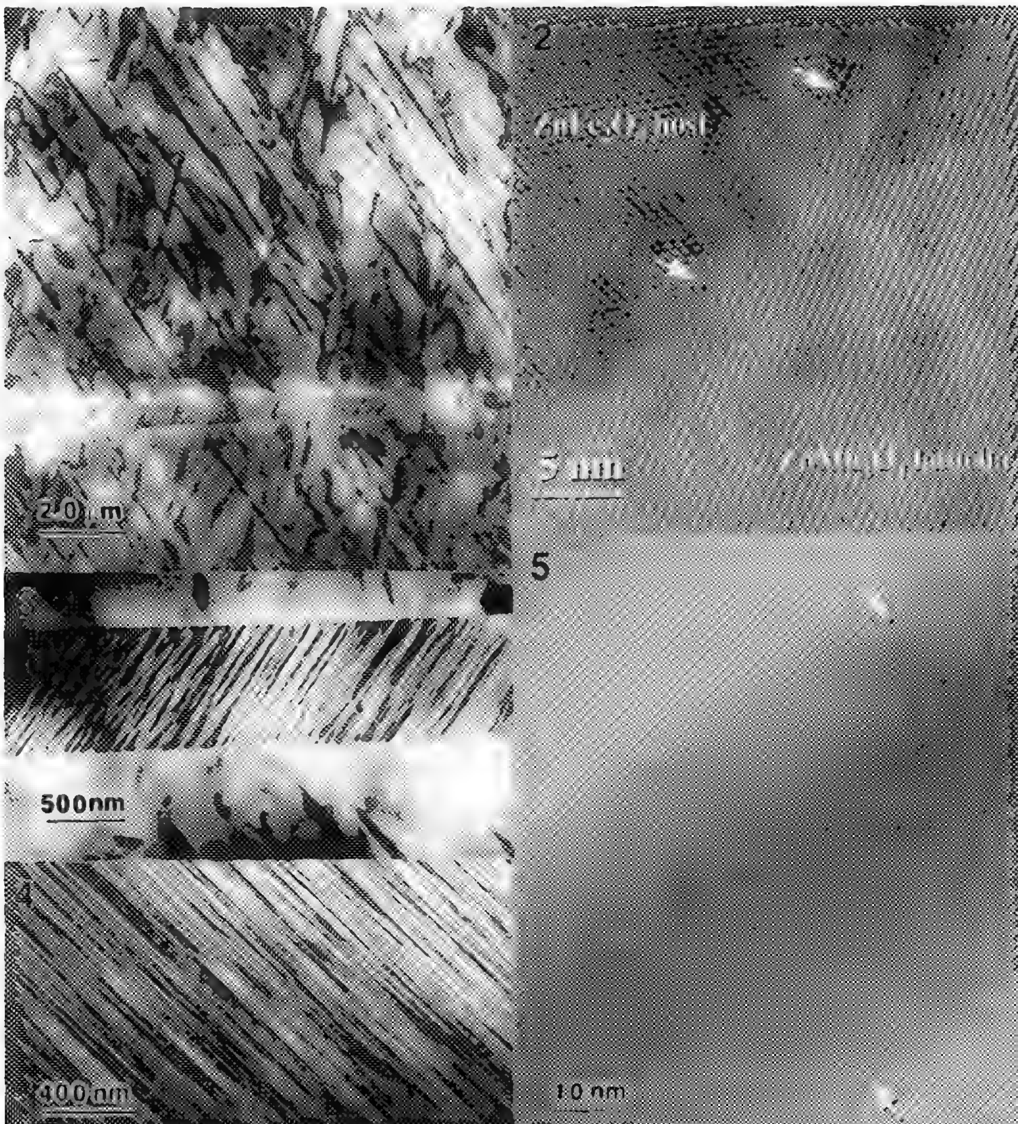

FIG. 1. BF image showing two groups of the hetaerolite lamellae exsolved from the franklinite host.
FIG. 2. HRTEM image showing the lattice coherency between the thinner hetaerolite lamella and the franklinite host.
FIG. 3. Periodic spinel-twins in an early exsolved hetaerolite lamella.
FIG. 4. Modulated structure in the franklinite background.
FIG. 5. HRTEM image showing the spinel-twin microstructure in the franklinite matrix.

SITE OCCUPANCY IN GAMMA ALUMINA

C.A. Bateman, A.Z. Ringwelski, and R.W. Broach

UOP, 50 E. Algonquin Road, Des Plaines, Il 60017-5016

Gamma (γ) alumina is referred to as a defect spinel because it has a tetragonally distorted spinel structure (AB_2O_4) and an insufficient number of cations to fill all cation sites. In the spinel structure, the oxygen lattice is cubic close packed with A- and B-site cations in tetrahedral and octahedral coordination, respectively.[1] The 21⅓ Al atoms per unit cell of γ alumina can distribute themselves across 16 octahedral and 8 tetrahedral sites.

The literature differs on where the 2⅔ cation vacancies per unit cell are located. Wilson and McConnell proposed that the vacancies in γ alumina, as first formed by calcining boehmite, are predominantly on the tetrahedral lattice but, with further heat treatment, move to occupy random positions on both octahedral and tetrahedral lattices.[2] One study using NMR showed that the vacancies lay exclusively on the tetrahedral lattice, independent of the calcination temperature.[3] A more-recent study using Rietveld refinement of powder neutron diffraction data suggested that both octahedral and tetrahedral lattices were partially occupied.[4]

A γ alumina that had been calcined from a hydrothermally grown boehmite was examined to determine if the cation vacancies lay on the octahedral, tetrahedral, or both lattices of this material. To determine which lattices (O, Al_{tet}, Al_{oct}) scattered into which reflections, the structural data of Zhou and Snyder was used for calculations (a = 7.911 Å, Fd3m).[4] The X-ray structure factors squared (F^2) are shown in Table 1, along with the relative phases of the different contributions to each reflection. Full occupancy of each lattice was assumed for the sake of calculations.

Mottled contrast is shown in (022) centered dark field (CDF) images taken from the [100] zone axis. Mottling on a scale of about 1.5 nm indicates that the tetrahedral lattice is not fully occupied but contains ordered microdomains. The cation contribution to (044) is predominantly octahedral, and (044) CDF images taken along [100] also show mottled contrast with a scale of about 20 to 50 nm. Both cation lattices are partially occupied, with the ordered microdomains being substantially smaller on the tetrahedral lattice, as also evidenced by the broad (220) peak in the XRD pattern.

References

1. R.W.G. Wyckoff, *Crystal Structures*, 3, Interscience 1965, 75.
2. S.J. Wilson, and J.D.C. McConnell, *J. Solid State Chem.*, 34, (1980) 315.
3. C.S. John, N.C.S. Alma, and G.R. Hays, *Applied Catalysis*, 6, (1983), 341.
4. R.S. Zhou, and R.L. Snyder, *Acta Cryst.*, B47, (1991) 617.

TABLE 1. X-ray F^2 for different reflections and lattices.

Atoms	{111}	{220}	{222}	{400}	{440}	{444}
Al_{tet}	- 6.2	9.0	0 0	- 6.5	+ 4.2	- 2.9
Al_{oct}	+ 12.3	0.0	- 29.9	+ 26.2	+ 16.9	+ 11.5
O	+ 0.2	0.0	+ 42.4	+ 33.0	+ 14 6	+ 8 3
γ Al_2O_3	2 0	9.0	1.1	68.9	100	20 9

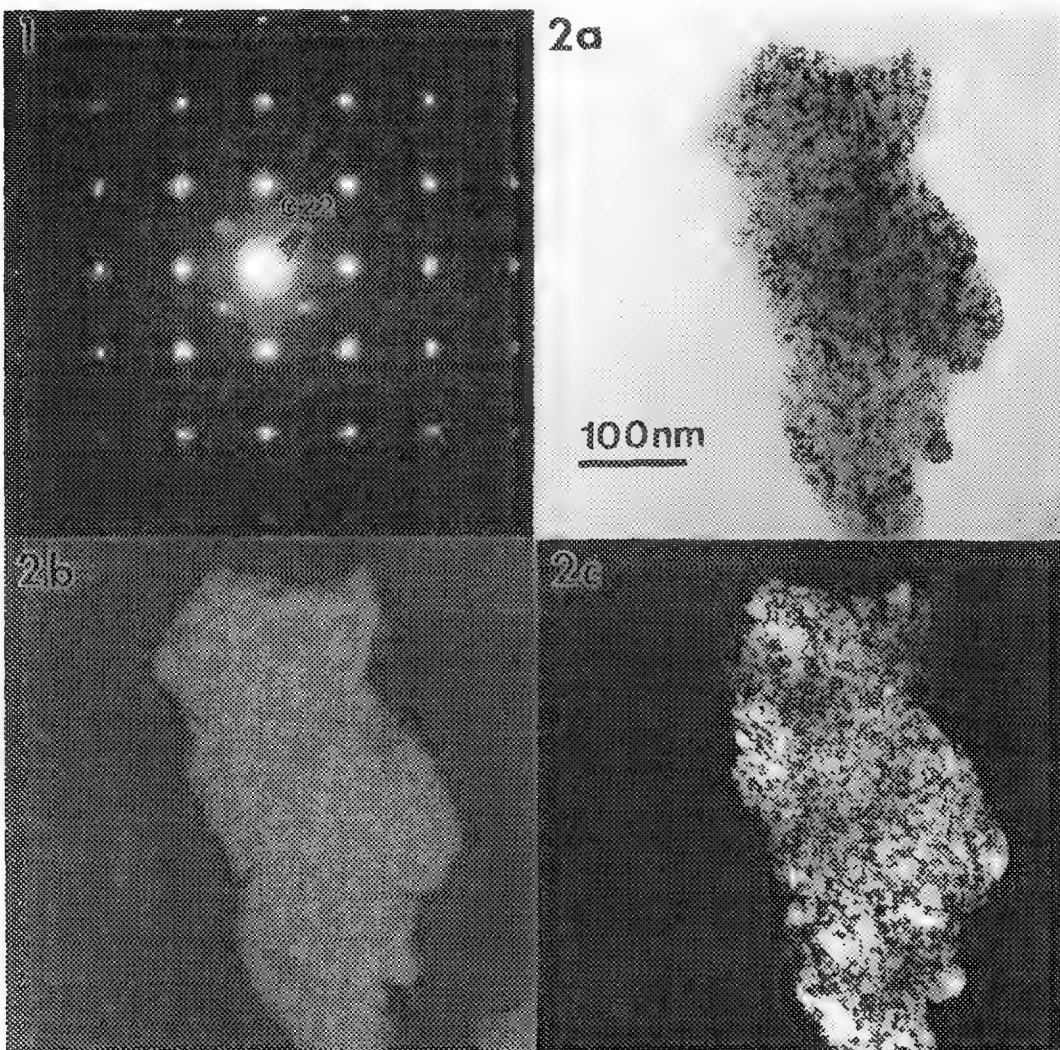

FIG. 1 [100] SADP. Only tetrahedral cations contribute to the {220} reflections.
FIG. 2 Bright field (a), and (022) and (044) CDF images, (b) and (c) respectively.

NUCLEATION AND GROWTH OF $SrTiO_3$ ON NANOMETER-SIZED $BaTiO_3$ PARTICLES

C. M. Chun,[*,†] A. Navrotsky,[*,†] and I. A. Aksay[*,#]
*Department of Geological and Geophysical Sciences, [#]Department of Chemical Engineering, and
[†]Princeton Materials Institute, Princeton University, Princeton, New Jersey 08544-5211

The hydrothermal processing of either $BaTiO_3$ or $SrTiO_3$ can result in the formation of nanometer-sized particles. Despite agreement on the mechanism of dissolution and precipitation, there remains some controversy concerning the nucleation and growth mechanism of the particles, particularly on the appearance of "raspberry-like" $BaTiO_3$ particles in the early stage of growth. The controlled aggregation of primary particles by multiple clustering[1] or morphological instability of continuous growth by molecular addition[2] have been proposed as possible mechanisms. Similarly, the role of supersaturation during precipitation leading to the formation of colloidal $BaTiO_3$ particles is not yet understood. Our TEM studies using the growth of $SrTiO_3$ on $BaTiO_3$ seed particles reveal that two different morphologies for the growing $SrTiO_3$ exist and that the form taken by the $SrTiO_3$ depends on the degree of supersaturation.

Nanometer-sized $BaTiO_3$ seed particles were hydrothermally treated in both dilute (0.4M) and concentrated (2.0M) supernatant solutions prepared by reacting TiO_2 (Degussa, P-25) in an aqueous solution of $Sr(OH)_2$ at 80°C for 4 hours followed by centrifugation. About 20 wt% $BaTiO_3$ seeds with respect to TiO_2 were placed in supernatant solutions and aged at 80°C for 4 hours, 2 days, and 7 days respectively. The resulting particles were recovered by centrifugation, rinsed with CO_2-free deionized water, and redispersed in methanol for TEM (Philips, CM200 FEG) observations.

In the early stage of growth in concentrated solution, the surface of the $BaTiO_3$ seeds was roughened by the adherence of primary $SrTiO_3$ nuclei 5~10 nm in size (Fig. 1a, b). In contrast, in dilute solution the surface of $BaTiO_3$ seeds was fairly smooth (Fig. 2a, b). During the final stage of growth, the size of the $BaTiO_3$ seeds was increased to 100 nm by heteroepitaxial $SrTiO_3$ coatings in both concentrations (Fig. 1c, 2c). A HREM image corresponding to the early stage of growth in concentrated solutions shows non-perfect alignment between the growing $SrTiO_3$ phase and the $BaTiO_3$ seeds, consisting of unusual contact angles (Fig. 3). In dilute solutions completely matched crystal lattices form (Fig. 4). A HREM image from the final stage of growth in concentrated solutions shows that the $SrTiO_3$ coating has the same crystallographic orientation as the $BaTiO_3$ seeds, an observation confirmed by electron diffraction (ED) (Fig. 5).

Homogeneous nucleation and growth by aggregation seem to occur when solutions are highly supersaturated because the $SrTiO_3$ primary nuclei are initially misaligned with the $BaTiO_3$ seeds. Final restructuring results in a single crystal. The attractive interaction between primary $SrTiO_3$ particles nucleated in solution and $BaTiO_3$ seeds leads to the growth of particle clusters by controlled aggregation, resulting in a rough "raspberry-like" appearance. In contrast, heterogeneous nucleation and continuous growth occurs when solutions are moderately saturated, promoting epitaxial film growth without precipitation. In this case the high surface mobility of the depositing ions and molecules permits alignment with the seed in a minimum energy configuration, i.e., the growth is epitaxial. The orientation relationship is apparently one that allows for good atomic matching between the two different crystals, minimizing the interfacial energy. Therefore, the chemistry in the solution determines the level of supersaturation, which controls the nucleation and growth of $SrTiO_3$ on nanometer-sized $BaTiO_3$ seed particles under hydrothermal conditions.[3]

References

1. C. M. Chun et al., *Proc. 53th Ann MSA Meeting* (1995)188.
2. A. T. Chien et al., *J. Mater. Res.*, **10**(1995)1784.
3. This study used MRSEC Shared Facilities supported by the NSF under Award Number DMR-940032 and was supported by a U. S. Air Force Office of Scientific Research grant, AFOSR-F49620-93-1-0259.

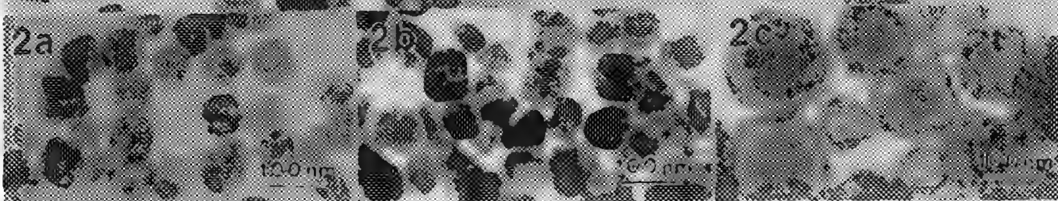

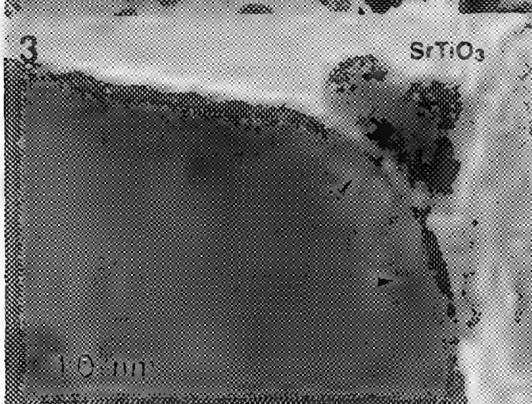

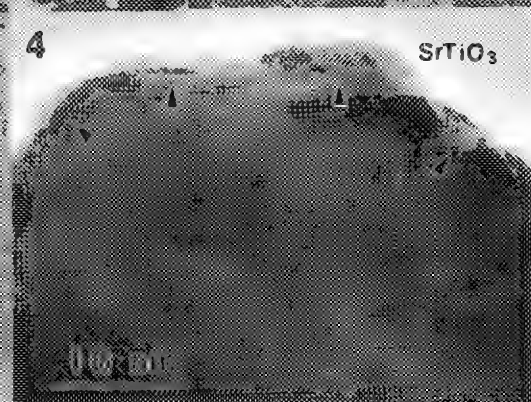

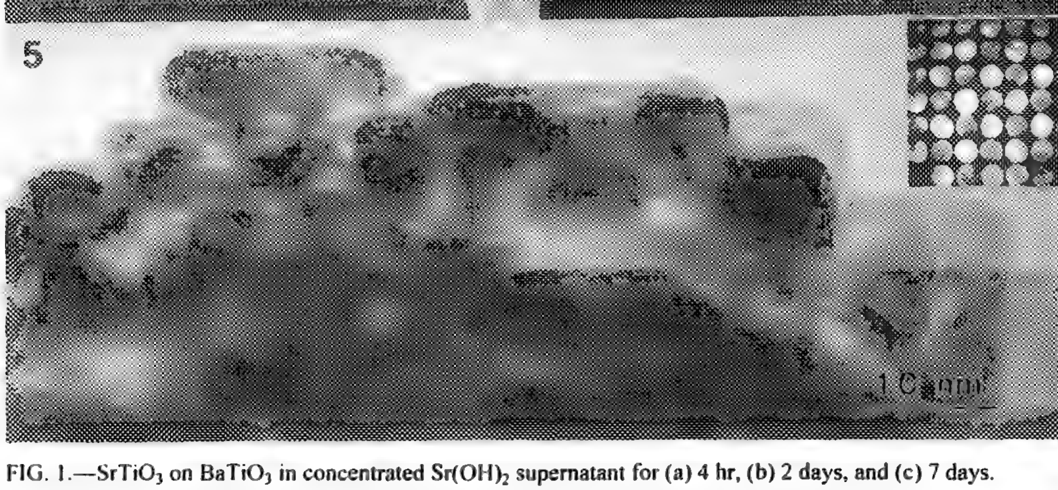

FIG. 1.—$SrTiO_3$ on $BaTiO_3$ in concentrated $Sr(OH)_2$ supernatant for (a) 4 hr, (b) 2 days, and (c) 7 days.
FIG. 2.—$SrTiO_3$ on $BaTiO_3$ in dilute $Sr(OH)_2$ supernatant for (a) 4 hr, (b) 2 days, and (c) 7 days.
FIG. 3.—HREM of $SrTiO_3$ on $BaTiO_3$ particle in concentrated $Sr(OH)_2$ supernatant at 80°C for 4 hr.
FIG. 4.—HREM of $SrTiO_3$ on $BaTiO_3$ particle in dilute $Sr(OH)_2$ supernatant at 80°C for 4 hr.
FIG. 5.—HREM of $SrTiO_3$ on $BaTiO_3$ in concentrated $Sr(OH)_2$ supernatant for 4 hr and ED pattern.

THE β - 3C to α - 4H TRANSFORMATION in SiC with Al, B, and C ADDITIONS: KINETICS DOMINATED by GROWTH AKIN to OSTWALD RIPENING

Warren J. MoberlyChan, J. J. Cao, & L. C. DeJonghe

Materials Science Division, Lawrence Berkeley Laboratory, 1 Cyclotron Road, Berkeley, CA 94720

The cubic-to-hexagonal phase transformation upon heating SiC has been a focus and/or precondition of hundreds of research studies [1-4]. In single (or large) crystal SiC, partial dislocation motion propagates stacking faults to invoke the transformation, analogous to the classic FCC-HCP transformation in Co. The hexagonal phase can exist in >200 [1, 4] different stacking modulations of planes of Si-C tetrahedra, with the α-6H polytype regarded as the high temperature equilibrium phase [2, 5]. ("6" is the repeat stacking in a unit cell [1, 2].) The propensity of stacking faults in all SiC materials provide the nuclei for the transformation. Most transformation studies of polycrystalline SiC cite the work of Heuer, et al. [3], which describes a transformation similar to that in single crystals. The Heuer model incorporates grain growth by observing the nucleated alpha phase as sandwiched between "sheaths" of beta phase, with the sheaths continuing to grow and "protect" the growing alpha phase throughout the transformation. Grain growth incurred during processing is typically treated as kinetically independent of the transformation.

The β-to-α transformation in SiC has recently been utilized by several research groups to judiciously process an *in situ* toughened ($K_{1c} > 9$ MPa$\sqrt{m}$) microstructure [6, 7]. Processing of this ABC-SiC starts with cubic (β) powders (~0.2 microns), to which < 5% total Al, B, and C are added. Liquid-phase sintering occurs while hot pressing (50 MPa) at 1600-1950°C for 1-4 hr. Materials characterization includes XRD, SEM of etched and fracture surfaces, TEM, and accessory spectroscopies [4, 6].

When densified at lower temperatures, SiC retains the cubic structure, but with grains growing to ~1 μm. For higher processing temperatures, SiC transforms to the hexagonal phase, with the fraction transformed being a function of temperature, time, and additive concentration; and grain growth develops an interlocking, plate-like microstructure. Fig. 1a depicts the original powders in the green compact. Fig. 1b & 1c are micrographs of etched SiC processed at 1780°C and 1900°C, respectively. (Etching SiC in molten salt at >500°C for >2 days reveals the grain morphology but preferentially removes smaller grains.) XRD indicates hot pressing at 1780°C/1 hr. produces <20% transformation to the α-SiC, 1900°C/1 hr causes ~75% transformation, and 1900°C/4 hr. produces ~100% transformation to α-4H. TEM of the 1780°C material determines the majority of the grains are cubic, with an ~1 μm grain size and many stacking faults and microtwins. The (111) faults within any grain are all parallel, thereby disrupting the cubic symmetry and causing the beta grains to grow with an aspect ratio of ~2. The diffracting grain in Fig. 2a represents one of the few large (>1 μm) grains in the 1780°C material. Electron diffraction of the lower portion of this grain exhibits a faulted cubic structure (Fig. 2b), whereas the upper portion has the hexagonal (α-4H) structure (Fig. 2c). As the grain grows up (as temperature increases), the basal plane stacking converts to the thermodynamically favored hexagonal structure [6]. The anisotropy of the hexagonal structure promotes elongation of the grain; and the lower beta planes are "pulled" along to develop a plate-like, dual-phase grain. As other beta grains undergo this growth-induced transformation, a microstructure of interlocking, plate-like, dual-phase grains develops (Fig. 3a). Whereas all the background grains in Fig. 2a are β, the surrounding grains in Fig. 3a are α-4H. Fig. 4 presents schematics of the densification, grain growth, and growth-induced transformation [4]. Even when processed at the highest temperatures and/or longest times, beta persists at the bottom of grains, indicating insufficient activation energy for stacking fault propagation to transform these original β-seed portions of the grains. The bottom β portions of grains exhibit irregular, {111}-faceted interfaces, while the top of the α portion grows with an atomically planar (0001) surface (Fig. 3b). A 1 nm-thick amorphous phase enriched in Al and O invokes intergranular fracture and high fracture toughness [8].

References
1. N. W. Jepps & T. Page, in Prog. Crystal Growth and Characterization, Pergamon, **V7** (1983) 259-307.
2. P. Pirouz & J. W. Yang, *Ultramicroscopy*, **51** (1993) 189-214.
3. A. H. Heuer, et al., *J. Am. Ceram. Soc.*, **61** [9] (1978) 406-412.
4. W. J. MoberlyChan, et al., submitted to *Acta metall. mater.*
5. C. Cheng, V. Heine, & I. L. Jones, *J. Phys. Condensed Matter*, , **2** (1990) 5097-5113.
6. J. J. Cao, et al., *J. Amer. Ceramic Soc.*, **79** [2] (1996) 461-469.
7. W. J. MoberlyChan, et al., in this *MSA Proceedings* (1996).
8. The authors gratefully acknowledge the NCEM staff. Support was by DOE #ACO3-76SF00098.

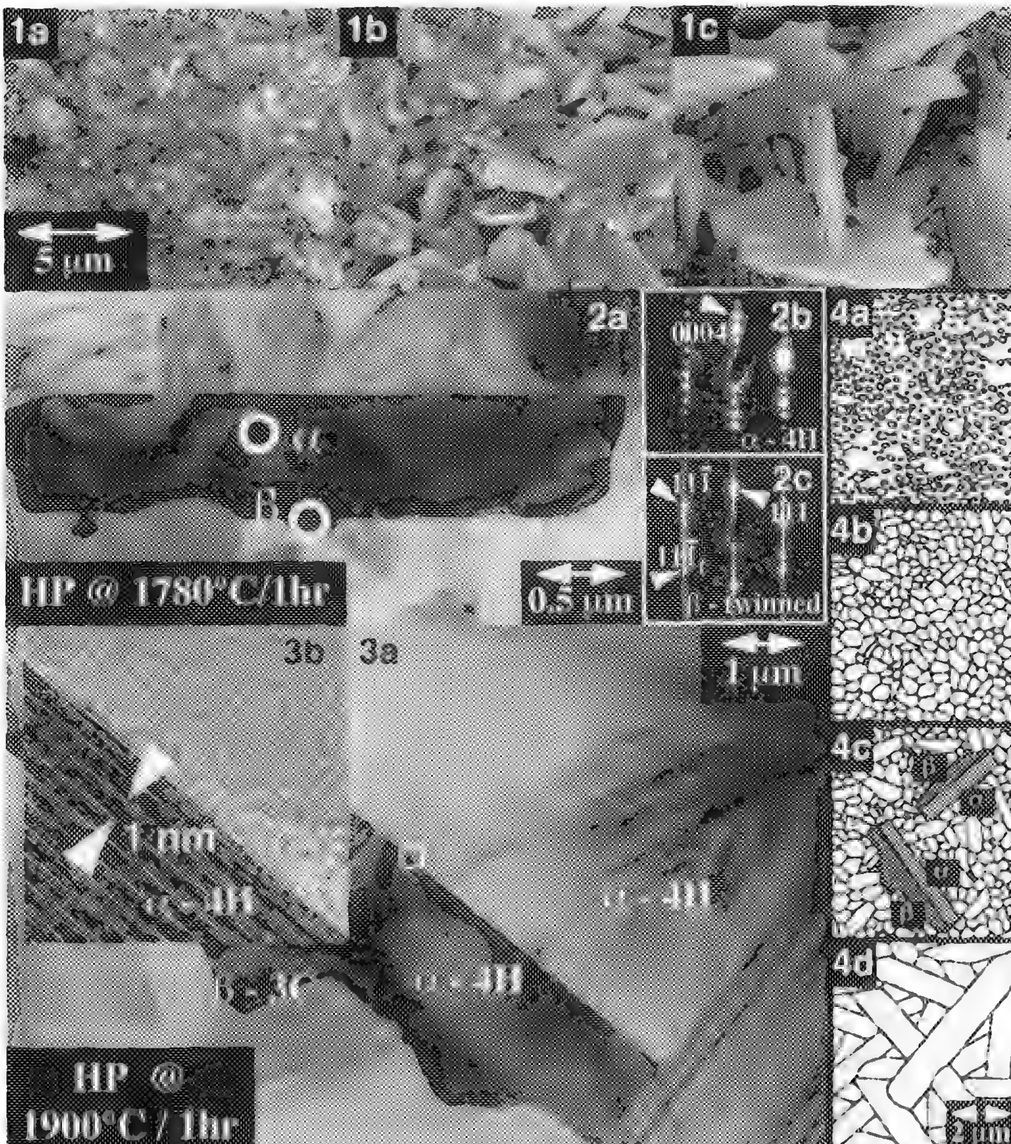

Fig. 1: SEM of (a) β-SiC powders, (b) α/β-SiC pressed at 1780°C/1-hr., and (c) α-SiC at 1900°C/4-hr.
Fig. 2: (a) BF-TEM and SAD of (b) α-4H and (c) β-3C regions of dual-phase, plate-like SiC grain.
Fig. 3: (a) BF-TEM of interlocking, plate-like SiC; and (b) HR-TEM of amorphous grain boundary.
Fig. 4: Schematic of (a) initial powders, (b) densification of β-SiC via liquid-phase sintering, (c) growth to form dual-phase grains, and (d) final transformation to interlocking, plate-like α-4H-SiC.

IN-SITU AND EX-SITU AFM IMAGING OF μN LOAD INDENTS ON SILICATE GLASS/ALUMINA INTERFACES

A. V. Zagrebelny, E. T. Lilleodden, J. C. Nelson, S. Ramamurthy, and C. B. Carter

Department of Chemical Engineering and Materials Science, University of Minnesota, 421 Washington Ave., SE, Minneapolis, MN 55455-0132

Contact which only involves a small volume of material is becoming increasingly important to many industries including micromachines, microelectronics, and magnetic recording[1]. The ability to characterize surface roughening on the micro- and nanoscopic scale is invaluable in understanding microplasticity due to indentation, scratches, wear, fatigue and epitactic mismatch. It has been demonstrated that AFM studies are appropriate for developing a mechanistic approach to μN load indentation analysis since they allow deformation volumes and residual depths to be measured and characterized directly and unambiguously.[2]

In the present study, interfaces between silicate glass and single-crystal α-Al_2O_3 have been studied using AFM and nanoindentation. The interfaces between the glass and the crystalline grains were prepared by growing films of anorthite ($CaAl_2Si_2O_8$) composition with thickness ranging 100-200 nm on single-crystal sapphire substrates of $\{11\bar{2}0\}$ (A-plane) and $\{1\bar{1}02\}$ (R-plane) crystallographic orientations by pulsed-laser deposition (PLD).[3] Some specimens were subjected to heat treatments in a conventional box furnace causing films to dewet the substrates. Fig. 1 shows schematically the morphology of the dewetted film which has resulted in the formation of distinctive islands, 0.5-2 μm in size. Both types of specimens were tested with two different micro/nanomechanical testers.

AFM studies were performed on Nanoscope III (Digital Instruments) using microfabricated Si_3N_4 cantilevers (Ultralevers, Park Inc.). All images were recorded in air with a normal applied force of 10-15 nN in a contact mode. Fig. 2 shows the AFM surface-type plot of the deformed regions produced *ex-situ* with the nanoindenter. The analysis of the indent features, such as cracks radiating from edges and buckling of the film, together with irregularities on load-displacement curves produced with an indentation instrument allow the failure mechanisms associated with delamination of the film from the substrate to be explored fully.

The mechanical properties of interfaces between crystallized islands of anorthite and alumina substrates were also probed *in-situ* with a newly developed indentation device which combines indentation of the nanometer scale with an AFM. The specimens were probed with a specially designed force-displacement transducer (Hysitron Inc.), combined with modified AFM set-up.[4] The force transducer was mounted on the AFM base, and the specimen then mounted on the transducer. The indenter probe was also used as an imaging probe, thereby eliminating the ambiguities of locating the indentation after unloading. For these purposes, standard AFM cantilevered tips were replaced with three-sided diamond pyramid tips in order to support the force compression of the column rather than by the bending of a cantilevered beam. The primary advantage of the surface testing and imaging with the AFM-based instrument is the ability to eliminate ambiguity in quantifying the mechanical properties because specific features on the surface can be image probed and reimaged **selectively**. This approach uniquely enables the characterization of submicron features such as dewet islands which necessitate small displacements and exact positioning of the indentations.[5]

References

1. S. E. Harvey, Ph.D. Thesis. University of Minnesota, (1995).
2. E. T. Lilleodden et al., *J. of Mat. Res.*, **10** [9] 2162-2165 (1995).
3. M. P. Mallamaci, Ph.D Thesis. Cornell University, (1995).
4. W. W. Gerberich et al., *Acta Met., in press,* (1996).

5. Research is supported by the U.S. DoE under Grant No.DE-FG02-92ER45465. The AFM and Hysitron indenter are part of the University of Minnesota Characterization Facility supported in part by Center for Interfacial Engineering, an NSF Engineering Research Center.

Fig.1

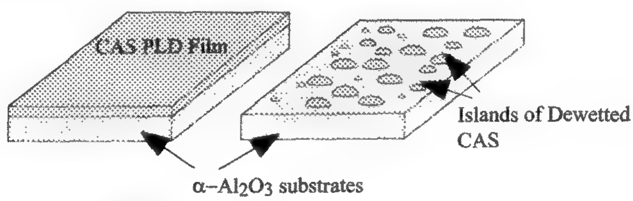

Fig.2

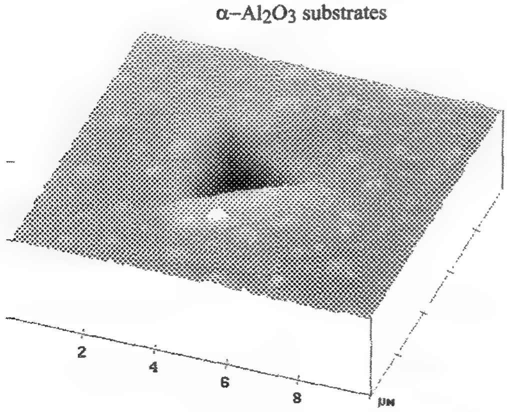

Fig.3

a.

b.

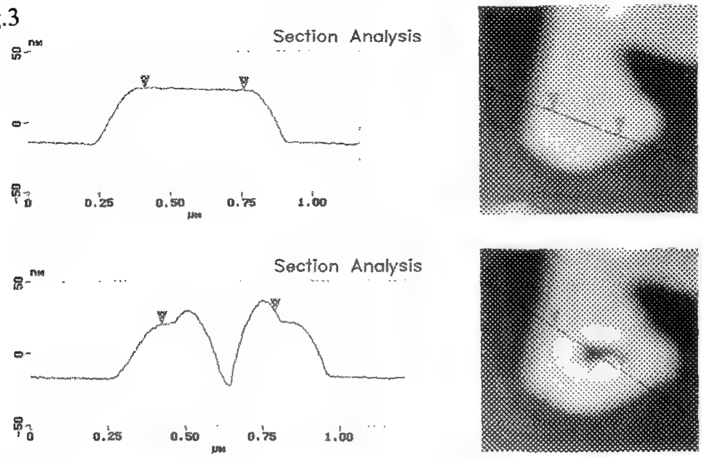

Fig.1. Schematic representation of PLD films, as-deposited (continuous) and after heat treatments.
Fig.2. Surface-plot AFM image of the deformed region on 150 nm anorthite film on single crystal sapphire (R-plane).
Fig.3. AFM images produced with Hysitron nanoindenter. The same region of the dewetted CAS film was imaged before (a) and after (b) indentation. Section analysis shows that the actual size of the CAS island is less than 0.5μm.

SILICATE-GLASS/SAPPHIRE INTERFACES PROBED WITH MICROMECHANICAL TESTING INSTRUMENTS: SEM AND TEM COMBINED CHARACTERIZATION

A. V. Zagrebelny, J. C. Nelson, S. Ramamurthy, and C. B. Carter

Department of Chemical Engineering and Materials Science, University of Minnesota, 421 Washington Ave., SE, Minneapolis, MN 55455-0132

The presence of intergranular phases is a common feature in today's polycrystalline ceramics prepared through traditional sintering routes. Although it has been shown that the chemistry and the microstructure of these phases may be altered, for example, by manipulating the heat treatments to tailor the final material's properties, very little is known about the mechanical properties of the interfaces on the microscopic scale.

The mechanical behavior of the interfaces between calcium-alumino-silicate (CAS) glasses and single-crystal α-Al_2O_3 substrates has been studied with two different types of micromechanical testers. The emphasis of this work is to correlate irregularities observed in the load-displacement curves produced using these testing instruments with the morphology of the deformation regions observed for the microindentations and microscratches. The effect of the substrate orientation on the interfacial properties has also been studied. Scanning electron microscopy (SEM) and transmission electron microscopy (TEM) have been used to characterize the deformation structures associated with the microscratches and microindentations.

The interfaces between the glass and the crystalline grains were prepared using a thin-film geometry developed previously.[1,2] Films of anorthite ($CaAl_2Si_2O_8$) composition with thickness ranging from 100nm to 200nm were grown on single-crystal α-Al_2O_3 substrates of $\{11\bar{2}0\}$ (A-plane) and $\{1\bar{1}02\}$ (R–plane) orientations by pulsed-laser deposition (PLD).[2] The introduction of such a glass as a thin film allowed the use of the newly developed experimental approaches and techniques for micromechanical testing of thin films.

SEM observations illustrated in Fig. 1a revealed features that are representative of microscratch tracks. The typical microscratch track consisted of three distinctive regions. Initially, the scratch track is smooth, as the indenter penetrates into the film. Later, extensive spallation occurs which is recognized by delamination from the substrate. Finally the spallation of the film stops, since the maximum stress that has occurred during the scratch process is then below the interface.[3] The SEM observations directly correlate with load-displacement measurements shown in Fig. 1b where the transitions between those regions were also recorded.

To analyze the deformation mechanisms in the substrates, the film was chemically etched away from the scratched specimens. Then, TEM specimens were prepared by conventional dimpling and ion milling methods. TEM observations were made using standard bright-field (BF), centered dark-field (CDF), and weak-beam dark-field (WBDF) modes. Fig. 2a,b shows a BF/CDF pair of the images from the scratch track. The deformation structure beneath the scratch tip showed a high density of dislocations on both sides of the scratch track.[4]

References

1. A. Zagrebelny et. al., *Mat. Res. Symp. Proc.*, **401**, (1995).
2. M. P. Mallamaci, Ph.D. Thesis. Cornell University, (1995).
3. W. W. Gerberich et al., *Acta. Met., in press,* (1996).
4. Research is supported by the U.S. DoE under Grant No. DE-FG02-92ER45465. The SEM and TEM are part of the University of Minnesota Characterization Facility supported in part by Center for Interfacial Engineering, an NSF Engineering Research Center.

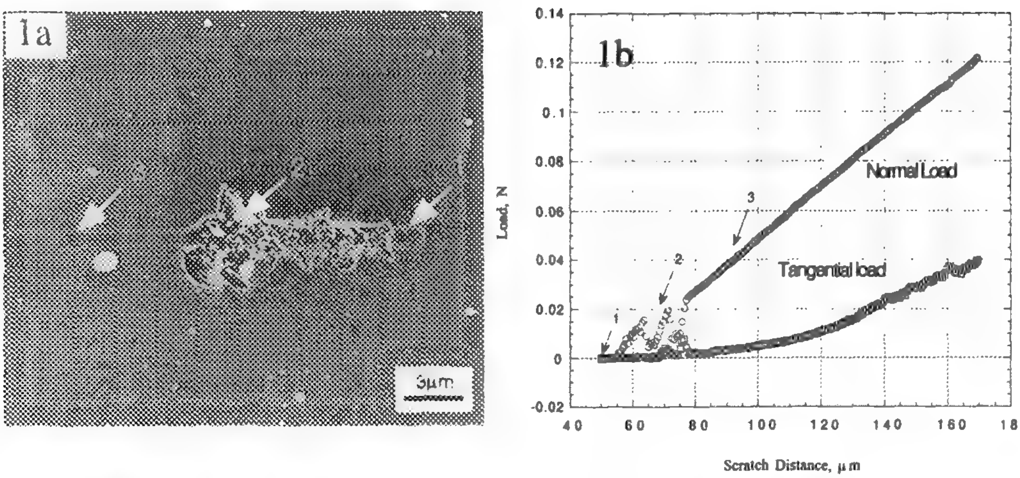

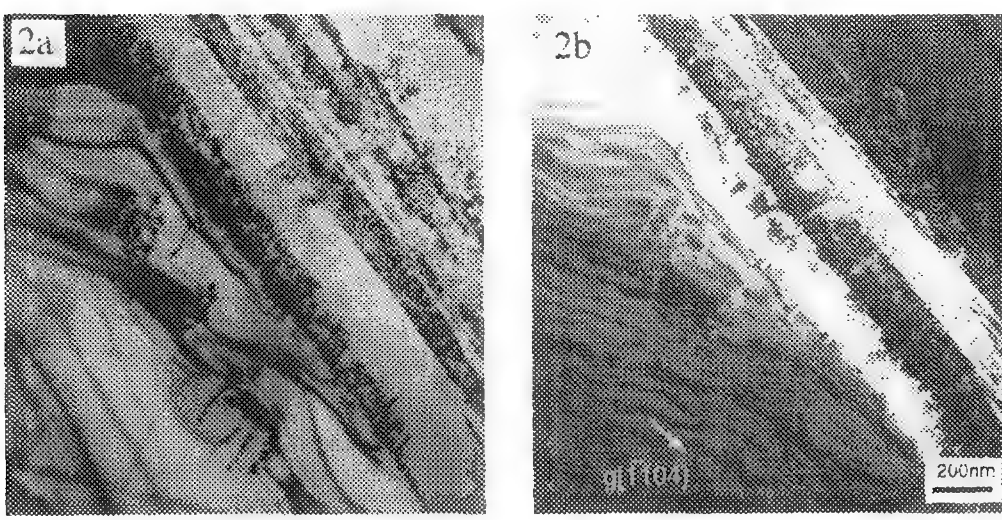

Fig.1a,b. SEM micrograph (5 keV, 1nm Pt coating) of the scratch track on the R-plane of the sapphire with CAS film on it. Three distinctive regions associated with different failure mechanisms are clearly pronounced. Load-displacement measurements directly correlated with SEM observations.

Fig.2a,b. TEM BF and CDF pair of the scratch track showing the deformation of the sapphire substrate beneath the tip of the indenter.

PENTAGONAL AND HEPTAGONAL CARBON-RINGS IN GROWTH OF NANOSIZE GRAPHITIC CARBON SPHERES

Z.C. Kang and Z.L. Wang

School of Material Science and Engineering, Georgia Institute of Technology, Atlanta, GA 30332-0245 USA.

Fullerene C_{60} [1] and nano-tubes [2] are a group of unique structures of carbon. These structures are produced using a carbon electrode arc-discharge technique, but it has not been successful in producing carbon spheres. Recently, a new mixed-valent oxide-catalytic carbonization (MVOCC) process has been invented that can be used to synthesize monodispersed nano-size graphitic carbon spheres at low cost and with large quantities [3]. The carbon spheres were produced at 1100° C by decomposition of natural gas (methane) under the catalytic assistance of transitional/rare earth metal oxides with mixed valences. The product is pure and separated from the catalyst, thus, no purification is needed. The MVOCC process does not produce any environmental hazardous chemicals, and the catalyst is reusable. The carbon spheres are expected to have extraordinary mechanical, physical and chemical properties and potential applications in the areas such as high-strength composite materials, environmental filtering, catalysis, lubrication and surface coating.

The carbon spheres have an average diameter of 210 nm (Fig. 1). More than 85% of the carbon spheres have almost the same size. The sphere is composed of curling graphite layers with random twisting (Fig. 2). The graphitic layers forming the carbon spheres are not closed shells but small size waving flakes, ranging in sizes from 1 - 30 nm. The carbon atoms can form hexagonal, pentagonal and heptagonal carbon-rings. A pentagonal carbon-ring causes the hexagonal network to curve inward (with + 60° disclinations), forming a surface with positive curvature. The heptagonal carbon-ring forces the hexagonal lattice to be curved outward (with - 60° disclinations) [4]. The curving produced by a heptagon is opposite to that by a pentagon. Thus, if a pair of pentagon and heptagon appears in the hexagonal lattice, the curving of the entire lattice would be dramatically reduced, possibly resulting in lower energy. These different types of atom-rings are the structural units for forming the graphitic layers with different curling structures [5].

The sphere is nucleated from a pentagon carbon-ring followed by a spiral shell growth. When the sphere grows larger, graphitic layers are nucleated on the surface due to arrival of the paired pentagonal-heptagonal (P-H) carbon-rings (Fig. 3). Euler's theorem shows that a perfect closed shell can be formed if exact 12 pentagonal carbon-rings are introduced in the hexagonal network although the number of hexagons is arbitrary. The unclosed graphitic layers are composed of many pairs of pentagonal-heptagonal carbon-rings. A spherical particle cannot be formed if all the arriving species are pure pentagons, because a pentagonal carbon-ring will lead to the growth of large faceted polyhedrons. Therefore, pentagons need to be paired with heptagons in order to nucleate a non-faceted graphitic layer that follows the topology of the inner layers, provided the sizes of the graphitic layers can be changed. The two very adjacent paired pentagon and heptagon should be unstable and tend to recombine to form two hexagonal carbon-rings. However, when the two paired pentagon and heptagon are separated by hexagonal network, various structural configurations can be formed (Fig. 4). The combination of the pentagonal, hexagonal and heptagonal carbon-rings can make any required geometrical shape. A total of 8 different waving structural configurations have been found, as indicated by the model numbers in Fig. 3. Large size spheres cannot be grown without a large fraction of P-H carbon-rings.

Therefore, a large graphitic carbon sphere, excluding the central core with spiral structure, is composed of graphitic segments containing the P-H pairs. The formation of the P-H pairs is determined by the synthesis technique and experimental conditions. If the experimental conditions are changed so that the pentagons and heptagons are not paired, the carbon particles might grow into different geometrical shapes, such as large curved and twisted tubes. The presence of a large numbers of unclosed graphitic layers on the surface can create many unbalanced carbon bonds. Thus, the sphere surface is chemically active and may exhibit useful catalytic behavior [6]. In our technique, the experimental conditions can be controlled to produce either spheres or tubes with high purity (> 95%).

[1] H.W. Kroto et al., Nature **318**, 162 (1985).
[2] S. Iijima, Nature **354**, 56 (1991).
[3] Z.C. Kang and Z.L. Wang, US patent pending.
[4] S. Iijima, P.M. Ajayan and T. Ichihashi, Phys. Rev. Lett. **69**, 3100 (1992).
[5] Z.C. Kang and Z.L. Wang, Phil. Maga. B, in press (1996).
[6] Z.C. Kang and Z.L. Wang, J. Phys. Chem., in press (1996).

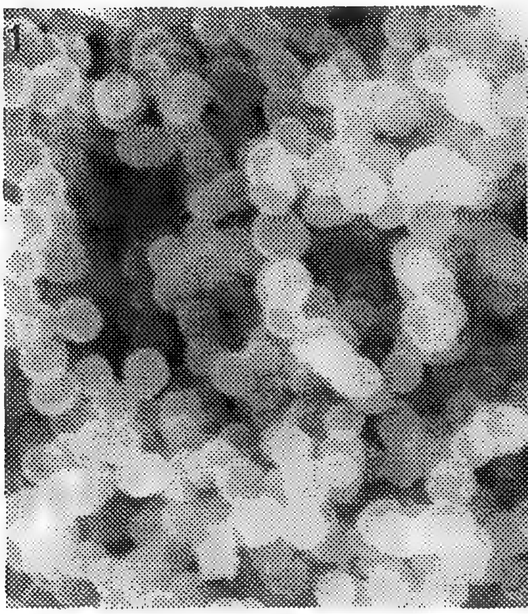

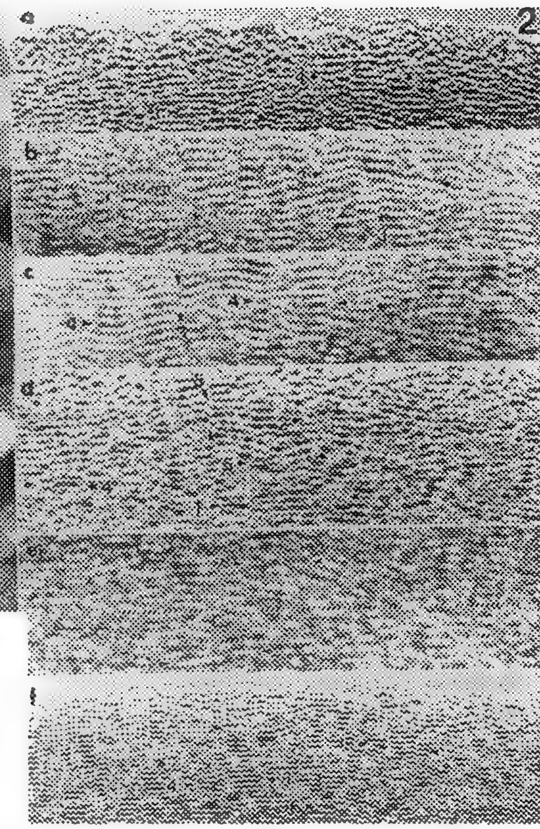

3
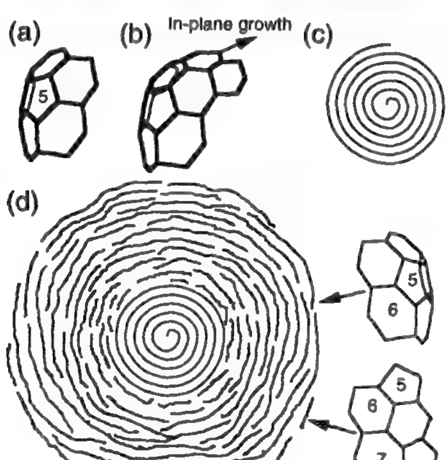

4
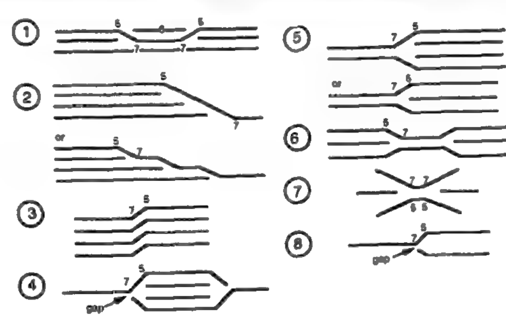

FIG. 1 A scanning electron microscopy (SEM) image of synthesized carbon spheres showing monodispersive size distribution. The image was recorded at 15 kV using a Hitachi S800 SEM.
FIG. 2 HRTEM images of spherical carbon particles showing various types of graphitic waving structures in areas indicated by arrowheads. The sequence numbers appearing in areas represent structural models described in Fig. 4. The interlayer distance is 0.34 nm in each image.
FIG. 3 The nucleation of pentagon, growth of quasi-icosahedral shell and formation of graphitic layers as a result of combining hexagonal, pentagonal and heptagonal carbon-rings.
FIG. 4 Two-dimensional structural models of graphitic layers produced by combinations of pentagonal (5), hexagonal (6) and heptagonal (7) carbon-rings. The pentagons are paired with heptagons.

LIQUID-PHASE SINTERING OF BN DOPED Fe-Cu/TiC COMPOSITES

Nuri Durlu,* Nan Yao,‡ David L. Milius,§,‡ and Ilhan A. Aksay§,‡

*Materials Research Division, Marmara Research Center, Tübitak, Gebze-Kocaeli, Turkey
§Department of Chemical Engineering and
‡Princeton Materials Institute, Princeton University, Princeton, New Jersey 08544-5263

Fe-Cu composites are commonly produced by liquid phase sintering (above the melting temperature of Cu, 1085°C).[1] The wear resistance of these Fe-Cu alloys can be enhanced by introducing hard particles, e.g., TiC, into the matrix. In such cases, however, the densification of Fe-Cu/TiC composites by liquid phase sintering becomes difficult mainly due to the high wetting angle (110° at 1100-1200°C in argon) of liquid Cu with TiC particles.[2] Especially when the amount of the TiC phase is high enough to form a continuous network of TiC grains, full densification is only achieved through hot pressing. We have recently overcome this problem in an [(Fe-4 wt% Cu) + 30 wt% TiC] composite by the addition of small amounts of BN. Composites with BN additives have been successfully sintered at 1275°C under vacuum or argon by additions of 1 wt% BN. Electron microscopic characterization of these composites has shown that this success is due to the modification of the liquid phase by the addition of BN, which also promotes the liquid phase sintering of the TiC phase.

Thin slices of samples were cut from the composites sintered at 1275°C either under vacuum or argon for 1 h. Mechanically polished samples were thinned with 6 kV argon ions. During ion-milling, the specimens were cooled with liquid nitrogen. Specimens were then examined using a Philips CM 200 FEG-TEM at 200 kV.

The most direct way of providing evidence for liquid phase sintering is to show the remnants of a thin layer liquid phase between the grains of network forming solid phases. This liquid phase would provide a pathway for the dissolution and transport of the components of the solid particles. A typical example of this process is the liquid phase sintering of silicon nitride.[3] In our case, a typical grain boundary phase between two Fe grains is shown in Fig. 1a. Cu precipitates of 30-50 nm are observed within the Fe grains and at the grain boundary. Parallel electron energy loss spectroscopy (PEELS) data obtained from the grains and the grain boundaries showed that the grain boundary phase is rich in C (Fig. 1b). Similarly, a thin layer of a different phase is observed between TiC grains (Fig. 2a). EDS spectra obtained from the region between two TiC grains showed the presence of an amorphous Fe-B or Fe-B-C phase (Fig. 2b). The characterization of these grain boundary phases is not complete. However, the evidence obtained so far strongly suggests that the addition of BN to Fe-Cu\TiC composites leads to enhanced densification through liquid phase sintering as evidenced by the presence of the amorphous thin film between TiC grains.

References

1. R.M. German and K.A. D'Angelo, *International Metals Reviews* **29**(1984)249.
2. R. Ramquist, *Int. J. Powder Metall.* **1**(1965)2.
3. D.R. Clark and G. Thomas, *J. Am. Ceram. Soc.* **60**(1977)491.
4. This research was supported by NATO under grant SFS-TU-POWMETAL, and by a grant from the U.S. Air Force Office of Scientific Research, AFOSR-F49620-93-1-0259.

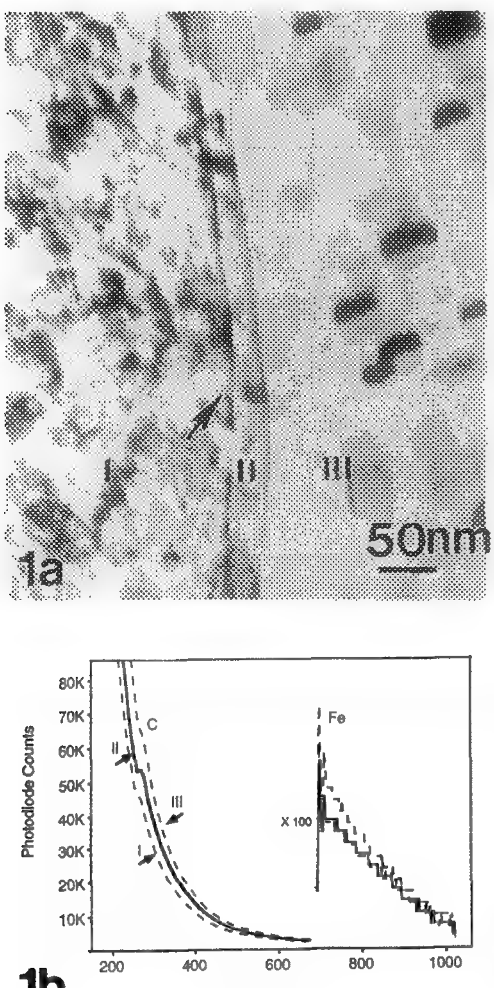

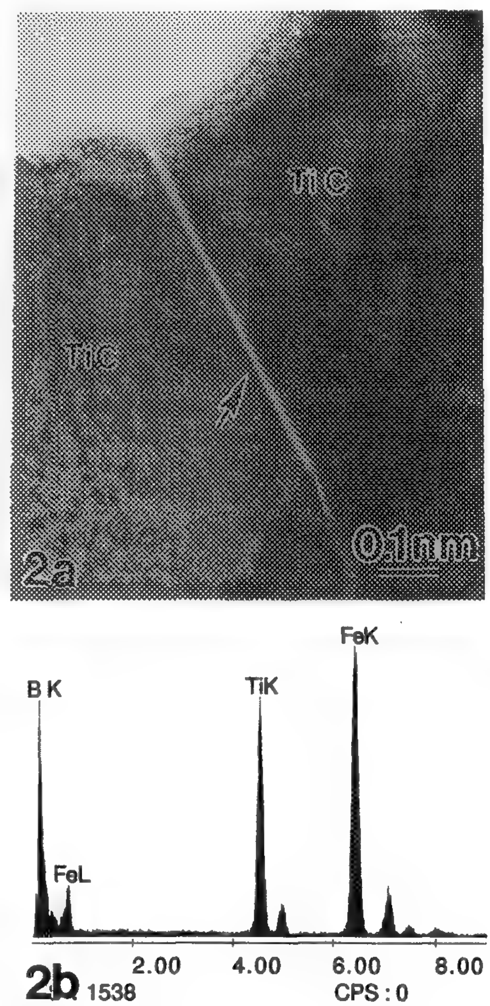

FIG. 1.—(a) BF-TEM image of grain boundary phase between two Fe grains and (b) PEELS spectra which shows the presence of C in the grain boundary phase.
FIG. 2.—(a) BF-TEM image of an amorphous phase in between two TiC particles and (b) EDS spectrum which shows the presence of Fe-B or Fe-B-C within this phase.

HRTEM STUDY OF ZIRCON FROM ELISEEV ANORTHOSITE COMPLEX, ANTARCTICA

R. Wirth*, H. Kämpf* and A. Höhndorf**

* GeoForschungsZentrum Potsdam, Telegrafenberg A 17, D-14473 Potsdam, Germany
**Bundesanstalt für Geowissenschaften und Rohstoffe, Stilleweg2, D-30631 Hannover, Germany

Zircon is a common accessory mineral in magmatic, metamorphic and sedimentary rocks. The crystal structure is tetragonal with space group $I4_1/amd$. Zircon contains minor amounts of U and Th and can be dated by a variety of techniques yielding ages of crystallization, cooling, and redistribution of radioactive isotopes and their daughter products. The precision of the radiogenic age determination strongly depends on the ability of zircon to retain the daughter products which were produced by the radiogenic decay of U and Th.

Zircon-bearing rocks of this study are metamorphic oxide-apatite gabbronorites (OAGN) from the Eliseev Anorthosite Complex, Wohlthat-Massif, East Antarctica (Kämpf et al., 1995). These unusual rocks are strongly enriched in accessory minerals (apatite: < 10 vol.%; zircon: < 1 vol.%, Owens & Dymek, 1992). Three steps in the evolution of these rocks are distinguished: a magmatic formation, followed by a granulite facies metamorphism and finally a tectonomagmatic overprint. The zircon crystals of this study are brown colored, up to 12 mm in length and up to 3 mm wide (Fig.1). Petrological investigations show that zircon has formed during the granulite facies event. Optical microscopy and cathodoluminiscence microscopy reveal a rhythmic zoning and many microcracks. The concentrations of uranium and thorium are low (U: 34-89 ppm and Th: 3-9 ppm). The radiation damage by radioactive decay of U and Th is expected to be minor due to the low uranium and thorium content.
The investigations were carried out in a Philips CM200 transmission electron microscope. Analytical electron microscopy was performed by energy dispersive analysis (EDAX).

Results: High resolution lattice fringe images of zircon exhibit undisturbed lattice fringes and no significant radiation damage features (Fig.2).
Cracks with different width (50 nm - > 1000 nm) are very common in zircon. They are oriented parallel to the {100} and {010 } lattice planes. The narrow cracks (width < 100 nm) are filled with amorphous zirconium oxide and amorphous SiO_2 (Fig.3, 4). The amorphous state of the layers was confirmed by convergent beam electron diffraction (CBED). Wider cracks (> 100 nm) show an enrichment in Fe, Ti and Zn additionally to zircon oxide and SiO_2.

Conclusion: The cracks in zircon minerals filled with amorphous zirconium oxide, SiO_2, Fe, Ti and zink show that zircon hase to be considered as an open system. Age determinations using zircon may produce significant uncertainties because most of the age determination methods use whole grains including cracks and submicroscopically altered areas. The fracturing of the zircon crystals is correlated with the tectonomagmatic event mentioned above because this event is characterized by a chemical overprint (Fe+Ti+Sc+Zn). The reason for the occurrence of amorphous layers of zirconium oxide and SiO_2 remains unknown.

References

H. Kämpf et al., in : P. Bormann & D. Fritsche (eds.): The Schirmacher Oasis, Qeen Maud Land, East Antarctica and its surroundings, Justus Perthes Verlag Gotha, (1995) 133-146.
B.E. Owens & R.F. Dymek, Canadian Mineralogist, **30**, (1992)163-190.

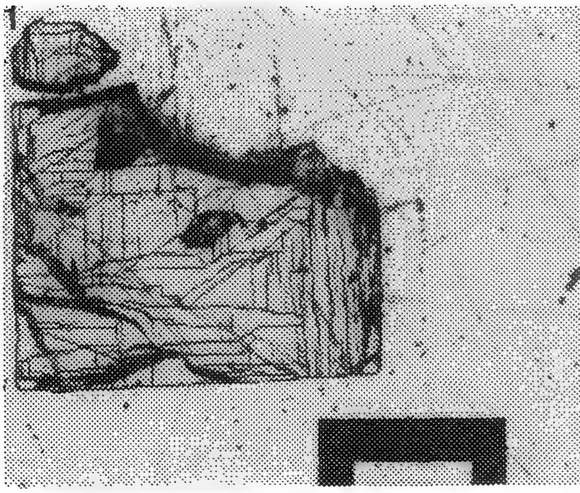

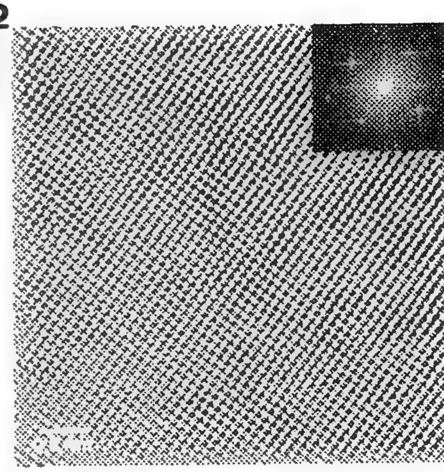

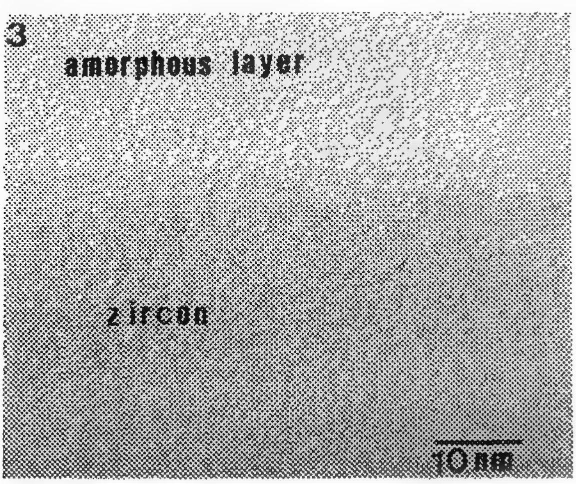

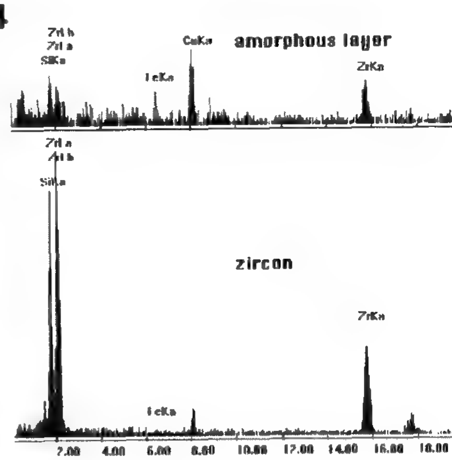

Fig.1 Optical micrograph of a prismatic zircon single crystal with numerous cracks (scale bar = 970 micron). Sample WMX, thin section cut perpendicular to [001] .

Fig.2 HRTEM image of zircon with zone axis [001]. Fourier-filtered image.

Fig.3 Lattice fringe image of zircon .The bright area in the upper part of the micrograph shows a microcrack filled with amorphous ZrO and SiO2 (zone axis [001]).

Fig.4 X-ray spectra from the amorphous layer and zircon corresponding to Fig.3.

OBSERVATION OF A NETWORK STRUCTURE IN ASPHALT CEMENTS

S. J. Rozeveld, E. E. Shin, A. Bhurke, and L.T. Drzal

Composite Materials and Structure Center, Michigan State University E. Lansing, Michigan 48824

Paving asphalts are often judged and selected based on their rheological behavior at prescribed temperatures or aging response. Asphalts are considered as a colloidal mixture, where clusters of polar, aromatic molecules are dispersed in a less polar solvent[1]. Thus, the extent to which the solvent phase disperses the associating molecules will determine many of the fundamental asphalt properties. Asphalts are typically divided into four major groups, namely: asphaltenes, resins, aromatics, and saturates[2]. Asphaltenes are the highest molecular weight group and constitute ~25% of the total asphalt. Resins are very polar in nature and act as a dispersing agent or peptisers for the asphaltenes. The solvent or oily phase (aromatics and saturates) are the lightest molecular weight group and are the bulk of the total asphalt (40-50%)[2].

The dispersion of the asphaltenes within the oily solvent is an important property and has been studied by separation and titration methods[1,3]. In this study, asphalt cements were examined using an Environmental Scanning Electron Microscopy (ESEM) (*ElectroScan 2020)*, and confocal Laser Scanning Microscope (LSM) (*Zeiss 10*).

During electron microscopy studies of asphalt cements, a network structure was observed in the asphalt films after they were exposed for several minutes by the electron beam[4]. It is envisioned that the beam volatilizes the low molecular weight oils on the surface of the asphalt and thereby reveals the network of high molecular weight asphaltenes and resins. A typical network consists of a random entanglement of asphaltene and resin strands (fibrils) as shown in Fig. 1 while the unexposed regions remain featureless.

It was originally thought that the network was a beam induced artifact; however, further investigations on deformed asphalt films suggest otherwise. Asphalt films were elongated uniaxially at room temperature and then examined in the ESEM. The resulting network, shown in Fig. 2, is more ordered and resembles a "ladder" network with the longest chains aligned parallel to the tensile axis. This suggests that the network is a natural component of asphalts and provides a measure of the state of asphaltene dispersion.

Asphalts blended with 5% styrene-butadiene-rubber (SBR) latex were also investigated using ESEM and LSM. As shown in Fig. 3, the fibrils in the network of the SBR modified asphalt are strongly aligned compared to the unmodified asphalts. Similarly, a LSM image of the SBR modified asphalt, presented in Fig. 4, reveals a strongly fluorescing SBR phase with a string-like texture. Thus, the final network arrangement is strongly influenced by the addition of the SBR polymer phase.

References

1. J. F. Branthaver et al., *Trans. Res. Record*, 1323 (1991) 22.
2. D. Whiteoak, *The Shell Bitumen Handbook*, Riversdell House, U.K.: Shell Bitumen U.K. (1990).
3. J. C. Petersen, *Trans. Res. Record*, 999 (1984) 13.
4. E. E. Shin et al., *Proc. of the 75th Annual Meeting of the Trans. Research Board*, in press.
5. This work was supported by the Research Excellence Fund and Composite Materials and Structures Center at MSU, and the Michigan Department of Transportation.

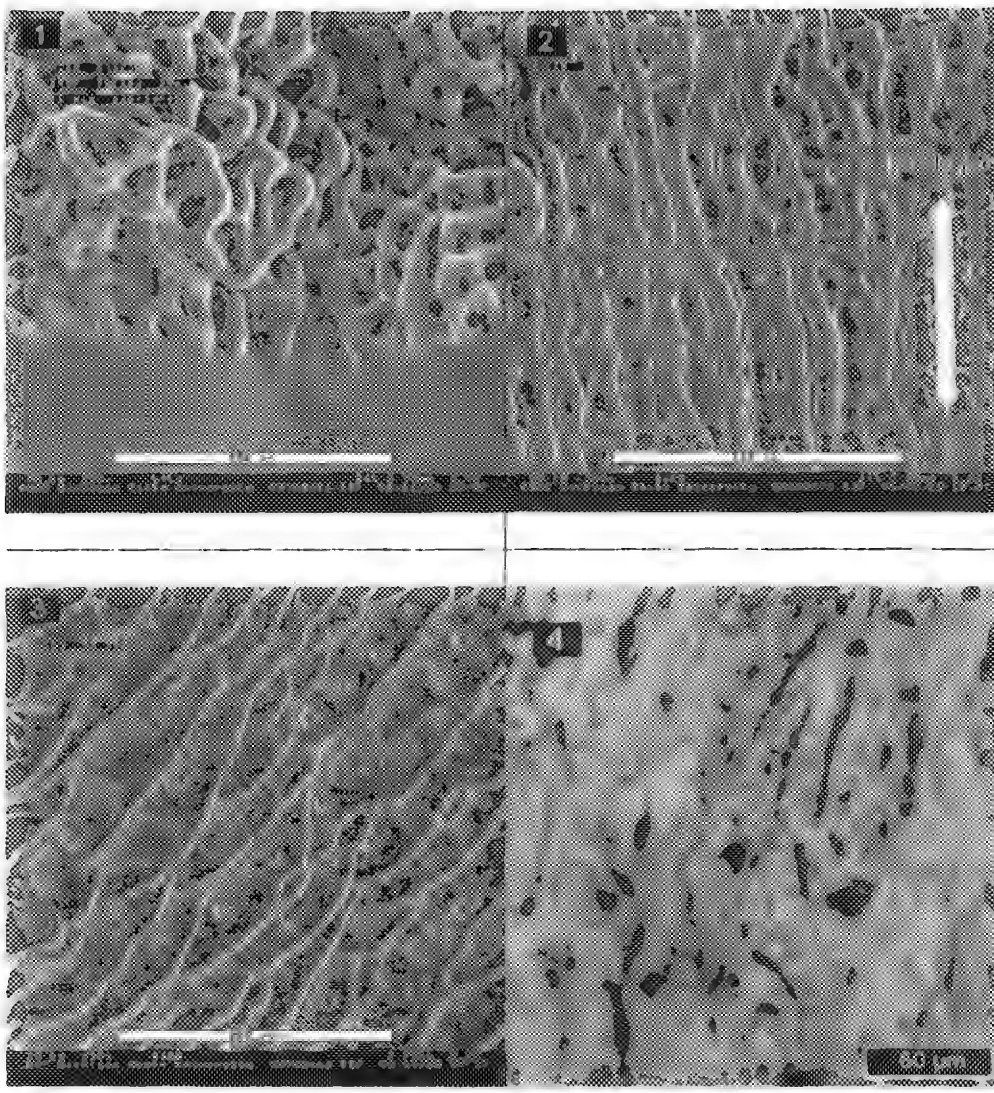

FIG 1 ESEM image of a network in an asphalt film after 10 minutes of beam exposure.
FIG 2 ESEM image of an elongated aphalt film after beam exposure
FIG 3 ESEM image of an asphalt modified with 5% SBR after beam exposure
FIG 4 LSM image using fluorescent light of an asphalt modified with 5% SBR (contrast inverted for clarity).

TIME-RESOLVED HIGH-RESOLUTION ELECTRON MICROSCOPY OF STRUCTURAL STABILITY IN MgO CLUSTERS

T. Kizuka and N. Tanaka

Department of Applied physics, School of Engineering, Nagoya University, Furo-cho, Chikusa-ku, Nagoya, 464-01, Japan

Structure and stability of atomic clusters have been studied by time-resolved high-resolution electron microscopy (TRHREM). Typical examples are observations of structural fluctuation in gold (Au) clusters supported on silicon oxide films,[1] graphtized carbon films[2] and magnesium oxide (MgO) films.[3] All the observations have been performed on the clusters consisted of single metal element. Structural stability of ceramics clusters, such as metal-oxide, metal-nitride and metal-carbide clusters, has not been observed by TRHREM although the clusters show anomalous structural and functional properties concerning to solid state physics and materials science.

In the present study, the behavior of ceramic, magnesium oxide (MgO) clusters is for the first time observed by TRHREM at 1/60 s time resolution and at atomic resolution down to 0.2 nm.

MgO and gold were subsequently deposited on sodium chloride (001) substrates. The specimens, single crystalline MgO films on which Au particles were dispersed were separated in distilled water and observed by using a 200-kV high-resolution electron microscope (JEOL, JEM2010) equipped with a high sensitive TV camera and a video tape recorder system.

Figure 1 shows a time-sequence series of high-resolution images of morphological change of a MgO cluster supported on a Au particle. Figure 2 shows the image simulation (a) corresponding to fig. 1a, and its structure model determined (b). The number of atoms is estimated to be about 500 from the analysis. The MgO cluster has a NaCl type structure. The MgO cluster is prepared through the following characteristic process: a Au particle breaks into an edge of the MgO film by intense electron beam of 100 A/cm^2 and then a piece of the MgO film, i.e., a MgO cluster, is separated as shown in fig. 3a. The MgO cluster has an undefined shape. The Au particle moves back to the edge surface of the MgO film and the edge recovers when beam density is decreased to $10 A/cm^2$ (fig. 3b). Figure 1a shows the initial state: the MgO cluster has a chair-like shape. The constituent atoms at corners and steps desorp preferentially due to the electron beam irradiation. Such desorption was found in the nanometer-scale electron beam processing.[4] The shape of the MgO cluster changes to a rectangular prism or a chair-like shape (fig. 1b-f) when the cluster size decreases to about 1 nm (fig. 1f). The MgO cluster showed translational motion and rotation when the size decreased and the external shape changed.

It is for the first time found in the present study that the MgO cluster keeps the NaCl type structure which is stable as the bulk structure, down to about 1 nm in size, although the cluster changes frequently the external shape. It is well known that single-element metal clusters show structural fluctuation even if its size is larger than 2 nm.[1-3]. The present observation shows clearly that the ceramic MgO cluster is rather stable in comparison with the metal clusters.[5]

References

1. S. Iijima and T. Ichihashi, Phys. Rev. Lett., **56**(1986)616.
2. K. Takayanagi, et al., Jpn. J. Appl. Phys., **26**(1987)l957.
3. T, Kizuka et al., Z. Phys., **D26**(1993)S58.
4. T. Kizuka et al., Phil. Mag., **A71**(1995)631.
5. Financial supports were provided to the present study from Yazaki Memorial Foundation for Science and Technology and Research Foundation for the Electrotechnology of Chubu. The present study is partly supported by Grant-In-Aid of the Ministry of Education, Science and Culture, Japan.

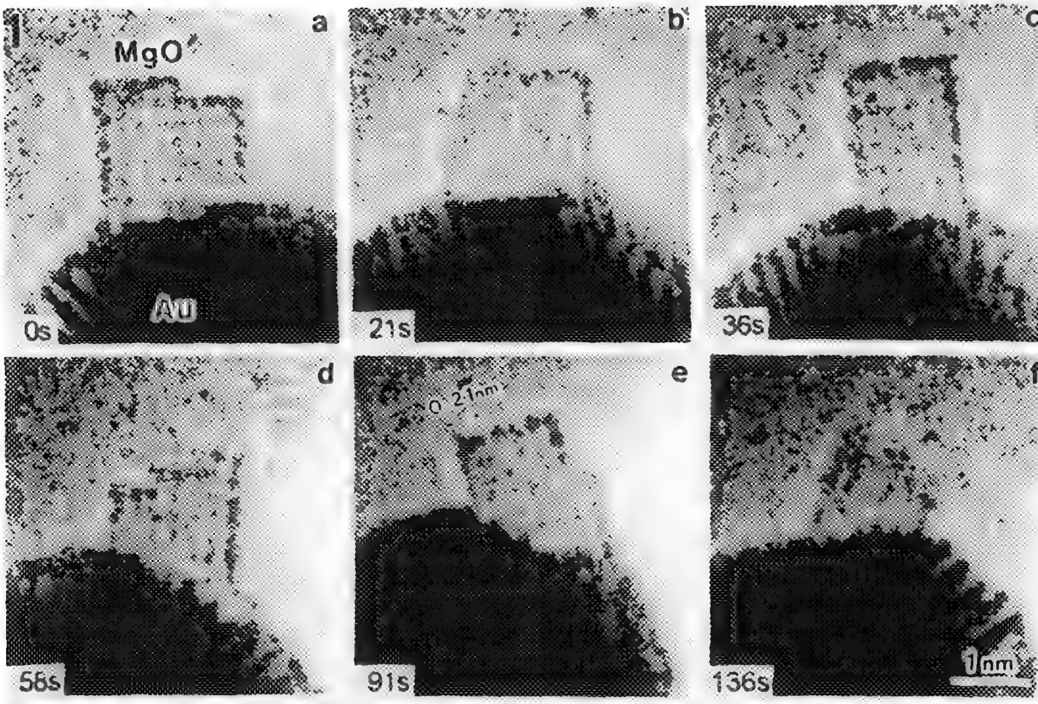

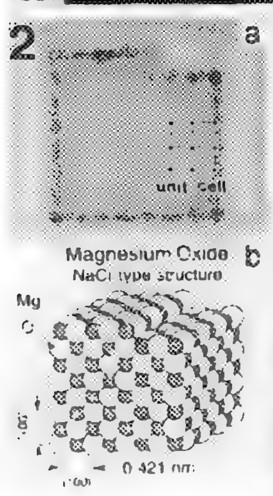

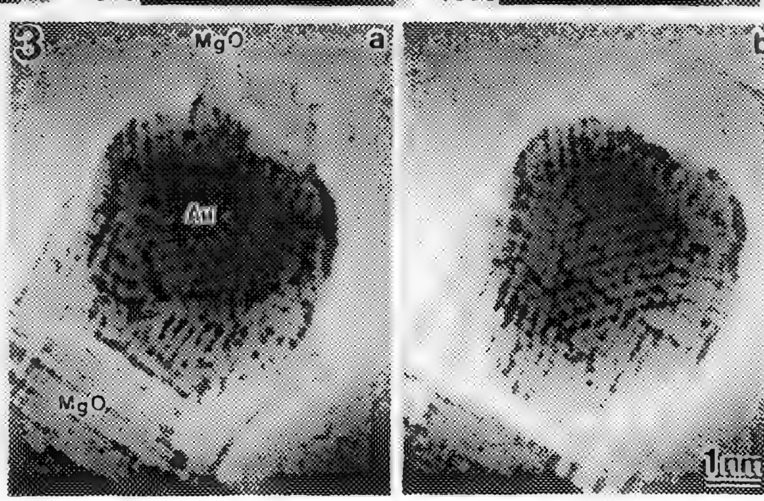

FIG. 1 - A time-sequence series of high-resolution images of the morphological change of a MgO cluster supported on a Au particle.

FIG. 2 - The image simulation (a) corresponding to fig. 1a, and its structure model (b).

FIG. 3 - Formation process of a MgO cluster. Electron beam density was $100A/cm^2$(a) and 10 A/cm^2(b).

TIME-RESOLVED HIGH-RESOLUTION ELECTRON MICROSCOPY OF GRAIN BOUNDARY MIGRATION PROCESS IN MgO FILMS

T. Kizuka, M. Iijima and N. Tanaka

Department of Applied Physics, School of Engineering, Nagoya University
Furo-cho, Chikusa-ku, Nagoya, 464-01, Japan

High-resolution electron microscopy (HREM) has been employed intensively to analyze the atomic structures of grain boundaries and interfaces having two dimensional structures inside polycrystalline and composite materials.[1] Furthermore time-resolved HREM (TRHREM) is required to analyze the behavior of grain boundaries and interfaces at atomic scale.[2,3] The grain boundary migration, which is a typical grain boundary behavior, is a fundamental process relating to structural stability of polycrystalline materials. The mechanism of the migration has been still unknown.

In the present study, the variation of atomic arrangement at the grain boundary migration of a MgO [001]$\Sigma 5$ boundary was analyzed by TRHREM.

Magnesium oxide polycrystalline films were prepared by vacuum-deposition on air-cleaved (001) surfaces of sodium chloride at 300°C. TRHREM was carried out at room temperature using a 200-kV electron microscope (JEOL, JEM2010) equipped with a high sensitive TV camera and a video tape recorder. The spatial resolution of the system was 0.2 nm at 200 kV and the time resolution was 1/60 s. Electron beam density was 30 A/cm^2.

A preferential orientation relationship was observed between crystallites in the films and the substrate. The relationship was $(001)_{MgO}$ // $(001)_{NaCl}$. Incident electron beam direction was perpendicular to a $(001)_{MgO}$ plane. A lot of tilt grain boundaries were observed cross-sectionally. The grain boundary migration was enhanced by the increase of atomic diffusion due to electron beam irradiation.

Figure 1 shows a time-sequence series of high-resolution images of grain boundary migration of a [001]$\Sigma 5$ grain boundary with a rotation angle of 36.9°. Structural model for each image is also shown. First, the boundary was composed of several structural units arrayed non-periodically along a curved line at the starting time (0 s)(fig. 1a). The units surrounded with {120}, {130} and {140} crystal planes had columnar voids with cross-section of 1 - 3 atoms at the centers. Most of the {120} units and the {140} units then transformed successively into the {130} units (fig. 1b,c). Each unit shifted by several atomic distances at the transformation. The time of each transformation was less than 1/60 s. The interval of time of transformation was a few seconds. The {130} units aligned periodically along (310) plane at 410 s (fig. 1d). Subsequently the {130} units transformed into the {120} units aligned along (120) plane at 615 s (fig. 1e). It was thus concluded that the present grain boundary migration consisted of two processes; (1) the transformation from non-periodic array containing several units into periodic alignment of the {130} units along (310) plane, and (2) the transformation into the periodic alignment of the {120} units along (120) plane. In both of the processes, the migration speed was limited by the intervals of time of the parallel-translation or the structural transformation of the units.[4]

References

1. Grain Boundary Structure and Related Phenomena, Trans. JIM, **27**(1986).
2. T. Kizuka et al., Phil. Mag. Lett., **69**(1994)135.
3. T, Kizuka et al., Z. Phys., **D26**(1993)S58.
4. Financial supports were provided to the present study from Yazaki Memorial Foundation for Science and Technology and Research Foundation for the Electrotechnology of Chubu. The present study is partly supported by Grant-In-Aid of the Ministry of Education, Science and Culture, Japan.

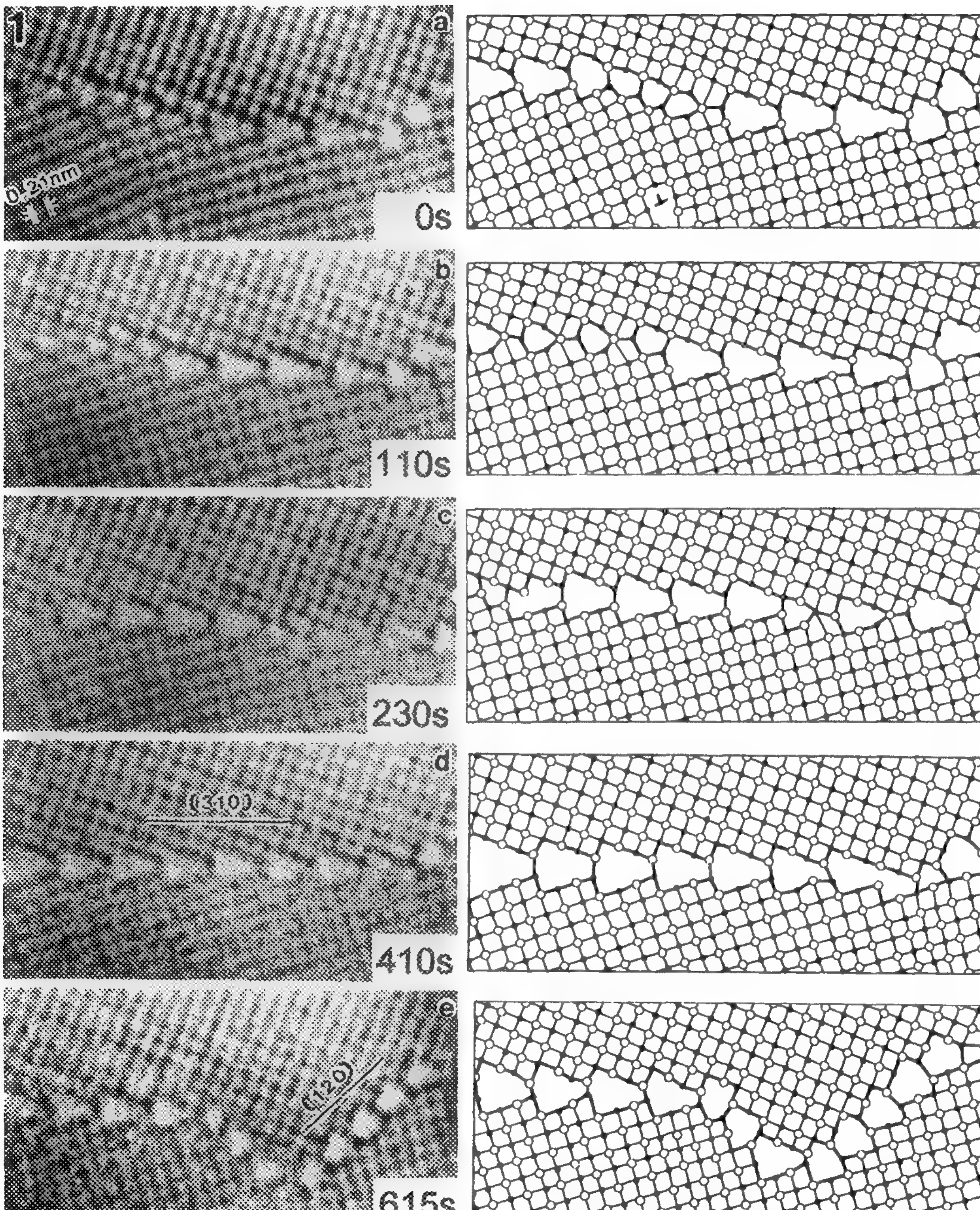

FIG. 1 - A time-sequence series of high-resolution images of grain boundary migration of a [001]Σ5 grain boundary with a rotation angle of 36.9°. Structural models for the images are also shown.

MORPHOLOGICAL EVOLUTION OF NANOMETER-SIZED $BaTiO_3$ PARTICLES

C. M. Chun,*,† A. Navrotsky,*,† and I. A. Aksay*,#
*Department of Geological and Geophysical Sciences, #Department of Chemical Engineering, and
†Princeton Materials Institute, Princeton University, Princeton, New Jersey 08544-5211

Highly pure, stoichiometric, nanometer-sized, and fairly monodispersed anhydrous crystalline $BaTiO_3$ particles are synthesized under hydrothermal conditions in a single process step without further heat treatment by reacting titanium isopropoxide [$Ti(OC_3H_7)_4$] precursor in aqueous solutions of $Ba(OH)_2$ at 80°C.[1] Traditional considerations of solution hydrolysis, solute condensation, and nucleation only partly explain the generation of the "raspberry-like" $BaTiO_3$ particles composed of 5~10 nm primary crystalline particles. Consequently, the colloidal interaction of the precipitating particles and, therefore, controlled aggregation of freshly nucleated particles must be taken into account. Our TEM studies show aggregation growth of small subunits to form uniform, rounded polyhedral particles, suggesting colloidal stability may play a key role in controlling precipitate size and shape.

In order to investigate the evidence supporting the aggregation growth,[2] $Ti(OC_3H_7)_4$ precursor (Aldrich) has been added to 1.0M $Ba(OH)_2$ solution and hydrothermally reacted at 80°C in polyethylene bottles. Four molecules of water and two hydroxyl ions attach through their oxygen atoms to the titanium of $Ti(OC_3H_7)_4$ in a nucleophilic process. One proton from each water molecule interacts with one oxygen of the alkoxide groups through hydrogen bonding, and, following electronic rearrangements, four molecules of propanol are expelled. The result of this hydrolysis step is an anion of the formula, $Ti(OH)_6^{2-}$, which is neutralized by the Ba^{2+} (aq) ions in alkaline solution. The protonated species undergoes stabilization by condensation, with the release of water, forming primary $BaTiO_3$ particles (Fig. 1). The resulting particles are recovered by centrifugation after reaction, rinsed with CO_2-free deionized water, and freeze-dried.

The primary $BaTiO_3$ particles formed homogeneously in solution are unstable due to their small size (5~10 nm). They are attracted together by van der Waals forces. This interaction leads to the growth of primary particle clusters and yields a "raspberry-like" appearance. During aggregation, clusters of misaligned nuclei form first, and can be subsequently stabilized to form a single crystal. Because randomly oriented primary nuclei collide with each other, there is a disregistry between the particles equivalent to the insertion of a row of dislocations (Fig. 2). The aggregate contains fine scale subunits, a multiplicity of low or high angle grain boundaries, and other types of stacking defects on the scale of the observed surface roughness. For a stabilized aggregate, primary particles have the same crystallographic orientation as indicated by the continuity of lattice fringes throughout the aggregate (Fig. 3). The mechanism leading to the observed crystallographic alignment is not fully understood, but factors such as the directionality of Hamaker constants and inhomogeneous charge distribution are envisaged as inducing a tendency to align between primary particles during aggregation. Eventually the aggregate surface begins to smooth through rearrangement of surface species via dissolution and recrystallization (Fig. 4). The rough primary particles with a smaller radius of curvature have a higher rate of dissolution and so preferentially dissolve and recrystallize on the neck areas. This stabilization process decreases the total surface free energy and maintains crystallinity in the overall aggregate. Particle formation, crystallographic alignment within particles, and particulate uniformity can then be explained in terms of solution reactions and colloidal behavior.[3]

References

1. J. Menashi et al., U.S. Patent # 4,832,939 (1989).
2. C. M. Chun et al., *Proc. 53th Ann MSA Meeting* (1995)188.
3. This study used MRSEC Shared Facilities supported by the NSF under Award Number DMR-940032 and was supported by a U. S. Air Force Office of Scientific Research grant, AFOSR-F49620-93-1-0259.

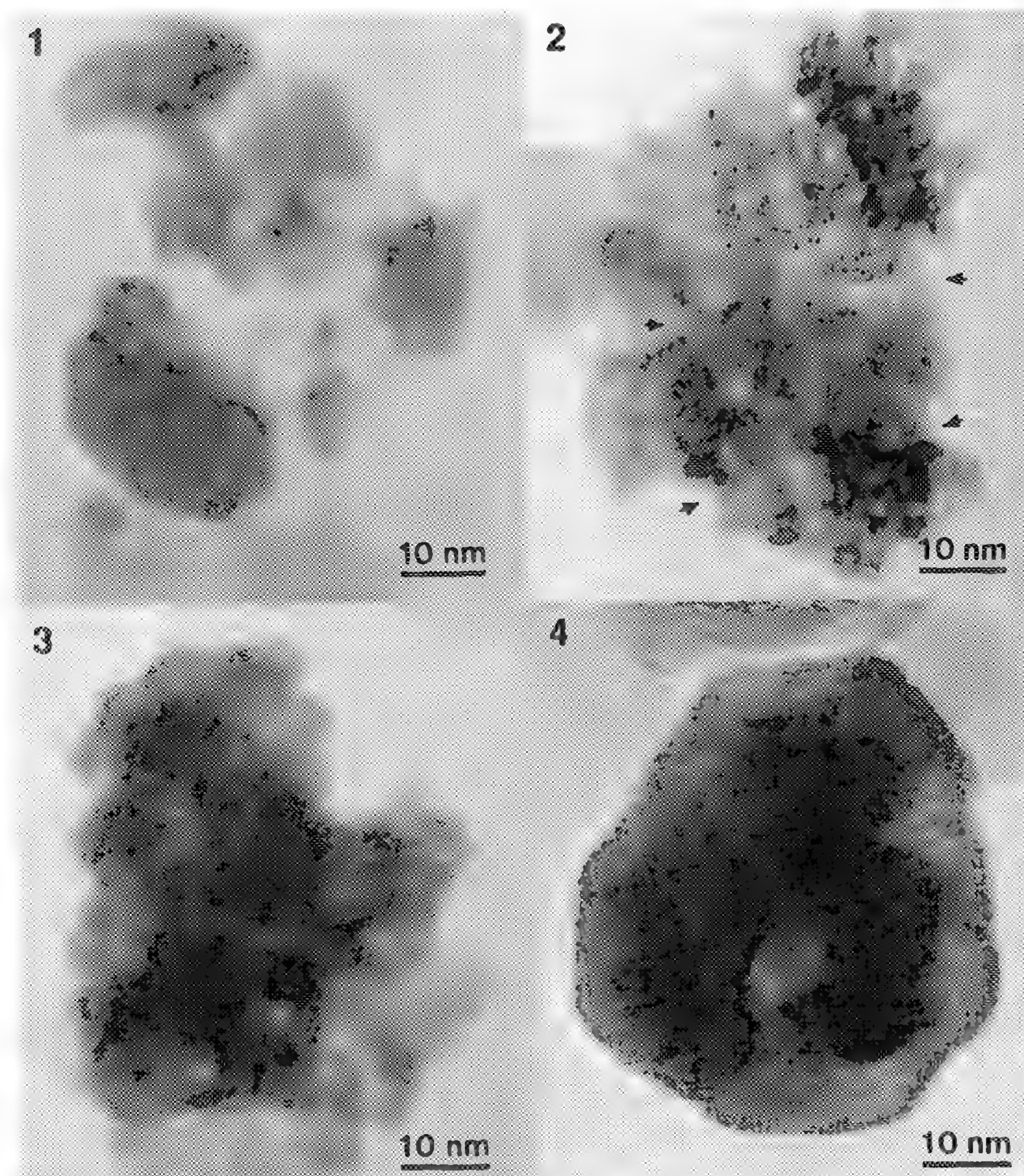

FIG. 1.—Primary $BaTiO_3$ particles formed homogeneously in 1.0 M $Ba(OH)_2$ at 80°C after 1 min.
FIG. 2.—A cluster of misaligned $BaTiO_3$ particles formed in 1.0 M $Ba(OH)_2$ at 80°C after 10 min.
FIG. 3.—An aligned $BaTiO_3$ single crystal formed in 1.0 M $Ba(OH)_2$ at 80°C after 1 hour.
FIG. 4.—A rounded polyhedral $BaTiO_3$ particle formed in 1.0 M $Ba(OH)_2$ at 80°C after 48 hours.

PROBING VACANCIES AND STRUCTURAL DISTORTIONS AT INDIVIDUAL DEFECTS IN CERAMICS USING EELS

D. J. Wallis[1] and N. D. Browning

Dept. Physics (M/C 273), U. Illinois-Chicago, 845 W. Taylor St., Chicago, IL 60607-7059. USA

In electron energy loss spectroscopy (EELS), the near-edge region of a core-loss edge contains information on high-order atomic correlations. These correlations give details of the 3-D atomic structure which can be elucidated using multiple-scattering (MS) theory. MS calculations use real space clusters making them ideal for use in low-symmetry systems such as defects and interfaces. When coupled with the atomic spatial resolution capabilities of the scanning transmission electron microscope (STEM), there therefore exists the ability to obtain 3-D structural information from individual atomic scale structures. For ceramic materials where the structure-property relationships are dominated by defects and interfaces, this methodology can provide unique information on key issues such as like-ion repulsion and the presence of vacancies, impurities and structural distortion.

An example of the use of MS-theory is shown in fig 1, where an experimental oxygen K-edge from $SrTiO_3$ is compared to full MS-calculations[2] for successive shells (a shell consists of neighboring atoms, so that 1 shell includes only nearest neighbors, 2 shells includes first and second-nearest neighbors, and so on). For an excited oxygen, shell 1 contains only Ti atoms meaning that as only the peak labeled d is reproduced for a single shell cluster it must arise from scattering by Ti. In the 2 shell cluster, it can be seen that all the gross spectral features are reproduced with the addition of subsequent shells modifying their spectral intensities. Both long and short range effects are therefore revealed in the energy loss spectrum. At 8 shells the calculations become convergent and the intensity and position of most of the spectral features are reproduced. The slight error in the intensity of peak b and position of peak c can be attributed to the muffin tin approximation[2] used to model the atomic potentials. However, in the study of interfaces and defects the bulk structure always exists as a reference, so by comparison with the bulk data these inaccuracies can be accounted for.

At interfaces and defects, two distinct relaxation mechanisms may occur: distortion of the atomic positions or the presence of vacancies. In general, the distortion of atomic positions leads to a damping of spectral features. However, the amount of damping is dependent on the order of scattering giving rise to a feature (higher order scattering gives more severe damping[3]). In fig 2, it can be seen that different peaks are reproduced by scattering of different orders. Peak b has strong single scattering contributions and will be relatively unaffected by distortion compared to peak d which contains mainly 5th order scattering. Vacancies on the other hand may result in very different changes in features as scattering paths are removed entirely. In figure 3, the results of vacancies in the $SrTiO_3$ bulk structure are investigated. In particular, it is noted that the peak labeled b is enhanced by oxygen vacancies. Such an enhancement can not occur due to structural distortions. From this analysis it is possible to make the following structural assignments of peaks in the oxygen K-edge: peak a arises from long-range atomic correlations as its full intensity is not reproduced until 8 shells are included; peak b is affected by the distances to atoms within shell 2; peak c is dominated by oxygen-oxygen correlations in shell 2; peak d arises from high-order Ti-Ti correlations in shell 1; and peak e is dominated by local high-order atomic correlations.

Fig 4a shows an experimental spectrum from the bulk and a 45° asymmetric [001] tilt grain boundary in $SrTiO_3$. The experimental changes in spectral intensity between the bulk and the boundary are well reproduced by the calculation for a bulk cluster contains 4 oxygen vacancies in shell 2 (fig 4b). Most noticeably, enhancement of peak b is reproduced, indicating that the changes result from vacancies, and not distortion. Reduced intensity in peak a is not reproduced by this calculation since the loss of long range symmetry concomitant at the boundary is not present in the bulk cluster. These

calculations also suggest that the symmetry aspects emphasized by the MS calculations are very bulk like, i.e. the boundary tries to reproduce as closely as possible the lowest energy structure of the bulk.

In conclusion, using EELS in the STEM in conjunction with multiple scattering theory it is possible to obtain direct experimental details of the 3-D structure at individual defects. This information is unique and places strong constrains on atomistic models by indicating the presence of vacancies and the degree of possible distortions. The results shown here are consistent with model atomic structures determined for grain boundaries in $SrTiO_3$[4,5].

References
1. Contact address, ORNL, Solid State Division, P.O. Box 2008, Oak Ridge, TN 37831-6031.
2. Rehr J.J. et al, Phys. Rev. Lett. **69**, 3397 (1992).
3. Wallis D.J. and Browning N.D. submitted to Phys. Rev. Lett.
4. N. D. Browning and S. J. Pennycook, in press J. Phys. D
5. This research is funded under NSF grant No. DMR-9503877.

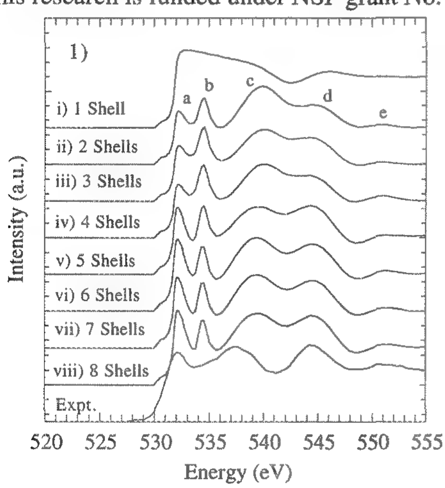

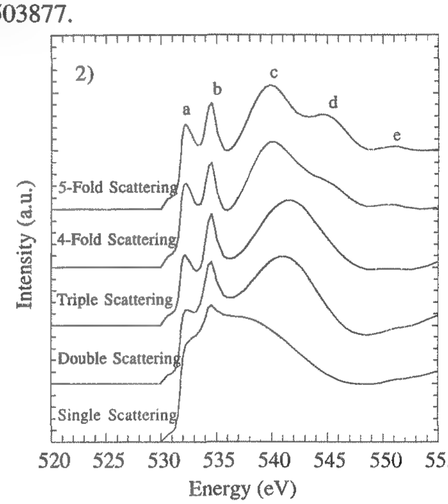

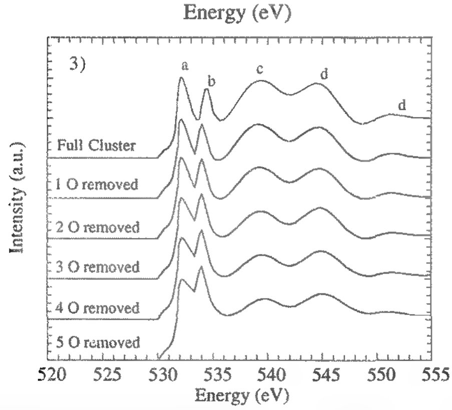

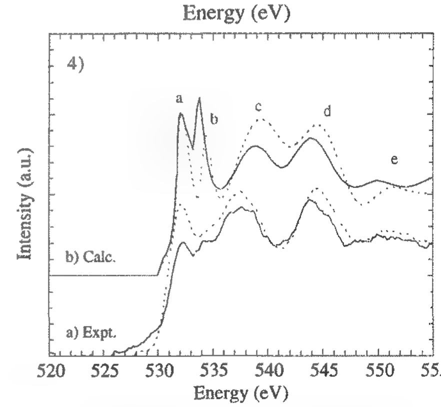

FIG 1. Expt. O K-edge and full MS calcs for $SrTiO_3$. i)-viii) include successive shells of atoms.
FIG 2. Calcs for a 2 shell cluster of $SrTiO_3$ with restrictions on the maximum order of scattering.
FIG 3. Effects on ELNES of oxygen vacancies in shell 2 of an 8 shell cluster for $SrTiO_3$.
FIG 4. a) bulk (dotted line) and grain boundary (solid line) O K-edges. b) comparison of calculations for a bulk cluster (dotted line) and a cluster containing 4 oxygen vacancies in shell 2 (solid line).

DIRECT IMAGING OF CHARGE TRANSFER [1]

Yimei Zhu* and J. Tafto**
*Brookhaven National Laboratory, Upton, NY 11973, ** University of Oslo, Blindern, Oslo 3, Norway

The electron holes confined to the CuO_2-plane are the charge carriers in high-temperature superconductors, and thus, the distribution of charge plays a key role in determining their superconducting properties. While it has been known for a long time that in principle, electron diffraction at low angles is very sensitive to charge transfer, we, for the first time, show that under a proper TEM imaging condition, it is possible to directly image charge in crystals with a large unit cell. We apply this new way of studying charge distribution to the technologically important $Bi_2Sr_2Ca_1Cu_2O_{8+\delta}$ superconductors.

Charged particles interact with the electrostatic potential, and thus, for small scattering angles, the incident particle sees a nuclei that is screened by the electron cloud. Hence, the scattering amplitude mainly is determined by the net charge of the ion. Comparing with the high Z neutral Bi atom, we note that the scattering amplitude of the hole or an electron is larger at small scattering angles. This is in stark contrast to the displacements which contribute negligibly to the electron diffraction pattern at small angles because of the short **g**-vectors.

In electron diffraction, however, superstructure reflections are seen near the forward direction, Fig. 1(a) and (e), and they should not be there in a kinematical diffraction pattern if the super-cell, Fig.1(b), commonly described by the introduction of a displacement field is used. To address the question of displacement of atoms versus charge transfer we minimized the multiple scattering by studying very thin areas of the crystal and also carried out dynamical calculations, which include multiple scattering of electron diffraction and images. We modified a multislice program to include the scattering amplitudes of holes and electrons, and made calculations for three different models of the crystal in the (100) projection. In Column II of Fig.1, the model is based on neutral atoms using the displacement parameters reported by Ref.2. In the model of Column III, we introduced charged atoms and used the charge distribution from the electron structure calculations of Ref.3. In the third model of Column IV, we maintained the average concentration of charge in each CuO_2 plane and BiO plane at the same level as in the previous model, but let the charge in the BiO layer be modulated along the b-axis. With reference to formal valence, this model shows pileup of electron charge in the region of the BiO double layer where the atomic planes expand along the b-direction. In our comparisons, the calculated diffraction pattern (Fig.1(h)) with the pronounced {011} reflections and HREM image (Fig.1(f)) with the distinct black cage-contrast show the best agreement with observations, Fig.1(e) and Fig.1(i), respectively. Fig. 1(m) is a low-resolution image formed by using a small objective aperture (apt.1, Fig.1(e))) so that in addition to the direct beam only the four innermost superstructure spots {011} and the two fundamental reflections {002} were included. Primarily, modulation along the c-direction is seen in the calculated images for the models without charge modulation in the b-direction, Figs.1(n) and 1(o), since the dominating beams are {002} and (000). When charge modulation along the b-direction is introduced (Fig.1(p)), good agreement with the observed image is achieved. Our study demonstrates that electron microscope images on the nanometer scale and electron diffraction patterns are very sensitive to charge transfer over a few tenths of a nanometer, and suggests that there is a considerable modulation of the valence electron density in the BiO double layer, and this may, at least partly, be caused by additional oxygen in this layer.

Reference
1. Y. Zhu and J. Tafto, *Phys. Rev. Lett.*, **76** 443 (1996).
2. S. Horiuchi,et al *Jpn. J. Appl. Phys.*, **27** L1172 (1988). 3. R.P. Gupta et al , Phys. Rev. B, **49** 13154 (1994).
4. This work was supported by US DOE under contract No.DE-AC02-76CH00016.

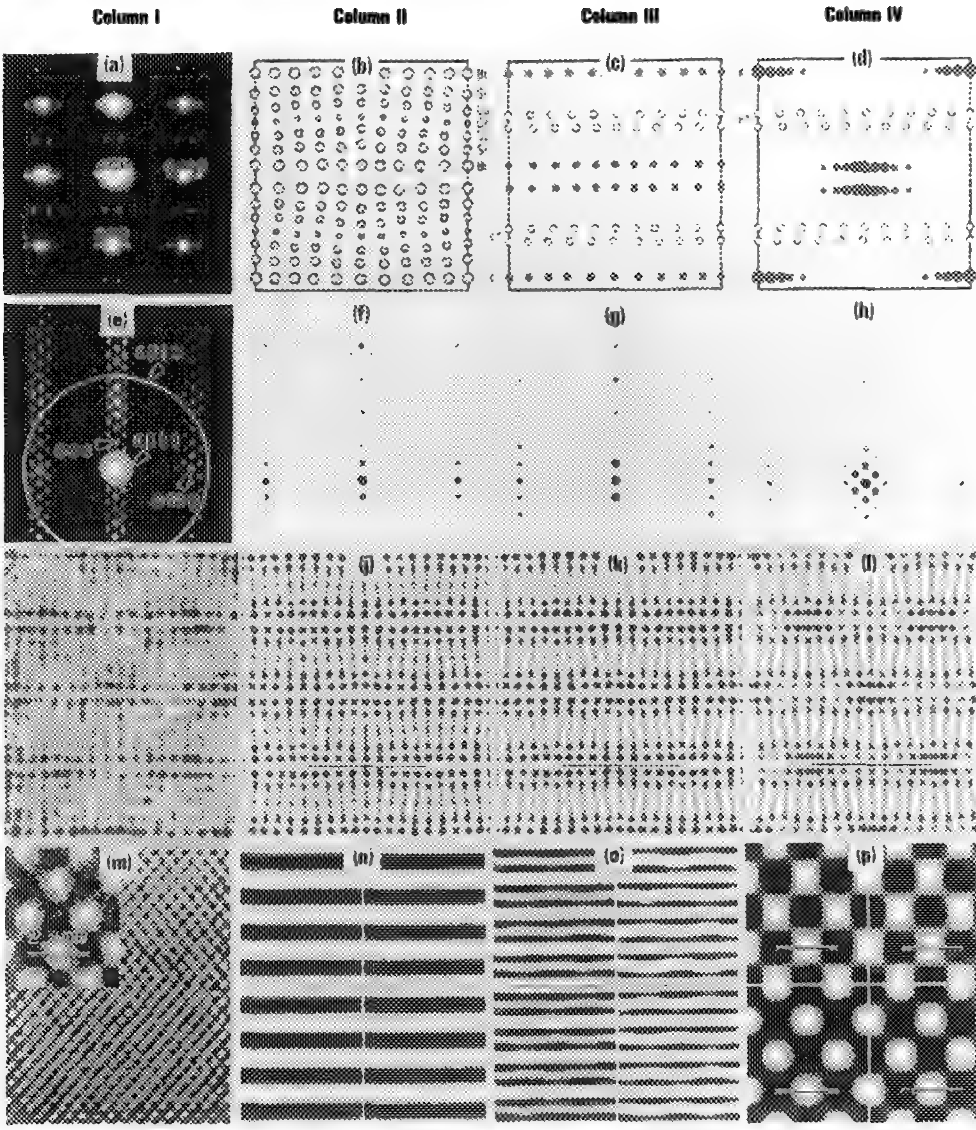

Fig.1 Electron diffraction patterns and images. Experimental ones in Column I, and calculated ones in Column II, III, and IV, based on three different models of the charge distribution. All the figures refer to the (100) projection, except for (a) to the (001) projection. Column II: based on a model with displacement only without charge modulation; Column III: based on a model same as in (b) except for addition of charge modulation along the c-direction; Column IV: with additional modulation of the charge in the b-direction as well as in the c-direction; Row II: diffraction patterns, circles in (e) indicate the sizes of the objective aperture; Row III: high-resolution images using the big objective aperture (apt 2); Row IV: low-resolution images using the small objective aperture (apt 1). The bar in the experimental (inset of (m)) and calculated ((j), (k), (l) and (p)) images indicates the size of the crystal unit cell along the b-axis.

LOW-VOLTAGE MICROSCOPY AND POSITION-TAGGED SPECTROMETRY OF CERAMIC MICROSTRUCTURES

J. J. Friel,*and V. A. Greenhut**

*Princeton Gamma-Tech, 1200 State Rd., Princeton, NJ 08540
**Department of Ceramics, Rutgers University, Piscataway, NJ 08855

Ceramic microstructures are ideally suited for low-voltage field emission microscopy on uncoated samples. Most elements of interest in ceramics have useful X-ray lines below 5 keV, thus permitting the use of accelerating voltages between 3 and 8 kV. One analytical consequence of the use of low voltage is a reduced interaction volume with the electron beam, so that X-ray maps can be collected at submicrometer resolution. To produce usable maps at low voltage, the SEM must be capable of sufficient beam current, and the X-ray detector geometry must be optimal. Another way to optimize X-ray microanalysis is to collect an entire spectrum at every point in the microstructure even at high resolution. Although this capability would permit an X-ray spectrum to be displayed from one pixel, a much more productive approach is to create a spectrum based on all pixels of a particular phase.

We used a LEO 982 FESEM and PGT EDS system with a 60mm^2 Si(Li) crystal. The technology to collect simultaneous digital images, X-ray spectra, and X-ray maps is called position-tagged spectrometry (PTS).[1] The technique works as follows: With the electron beam scanning the sample continuously at several frames/second or faster, the analytical system tags each photon measured by the EDS detector with the beam's position when the photon was generated. These data are streamed to a computer at high speed. The result is a file containing the x, y, and energy of each photon. As photons are counted over time, the X-ray intensity at each energy adds a fourth dimension.

Fig. 1 shows a ceramic-matrix composite consisting of SiC fibers in a $ZrTiO_4$ matrix. The composite has been previously described by Jessen.[2] At a magnification of 500×, one can see both the fibers and the matrix, and it is even possible to discern inhomogeneity in the matrix. Fig. 2 is a higher magnification digital image and shows two phases clearly separated in the matrix. The composite was produced by sol-gel methods, and the matrix has exsolved over time. The data were collected by scanning the beam while collecting a PTS file consisting of position and energy. Maps for Zr, Ti, Si, and C were constructed from the file after the collection and are shown in Fig. 3. On the basis of the Zr and Ti maps, all pixels not associated with the SiC fibers were classified into either a Zr-rich phase or a Ti-rich phase. The average size of these phases is between 500 and 1000 nm, and the X-ray range for the Zr Lα line is about 300 nm at the 7kV accelerating voltage used. It would be difficult to position the beam in one point and collect a representative EDS spectrum, but PTS enabled us to sum the spectra from all pixels comprising each phase. These spectra are shown in Fig. 4 for the Zr-rich and Ti-rich regions. Quantitative analysis yielded 57 mol% ZrO_2 in the Zr-rich phase and 59 mol% TiO_2 in the Ti-rich one. Note that in Fig. 4, the counts/full scale is over 30,000 because the spectra were derived from the entire microstructure divided into two phases.

The low-voltage high-resolution capabilities of the FESEM let us image this composite at both the scale of the fibers and of the exsolved matrix. By combining the FESEM with the new PTS technology, we were able to characterize the microstructure thoroughly as to 1) what phases were present, 2) how much of each was present, 3) where they were, and 4) what their compositions were.

References
1. R. B. Mott et al., Proc. 53rd Ann. MSA Meeting, (1995) 592.
2. T. L. Jessen, Ph. D. Dissertation, Rutgers U. (1995).

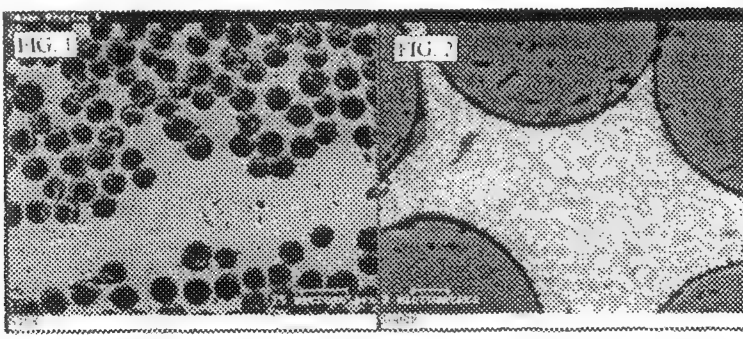

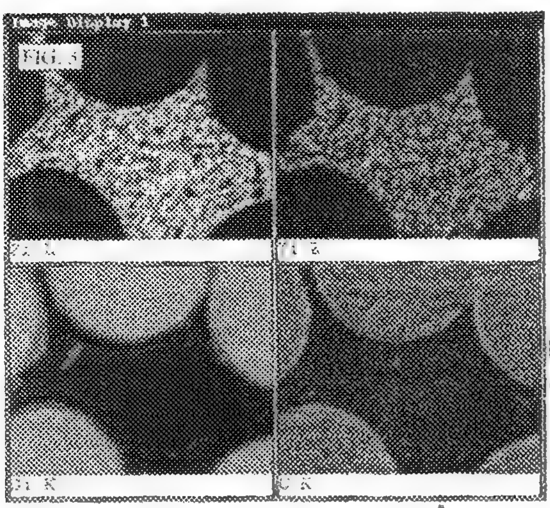

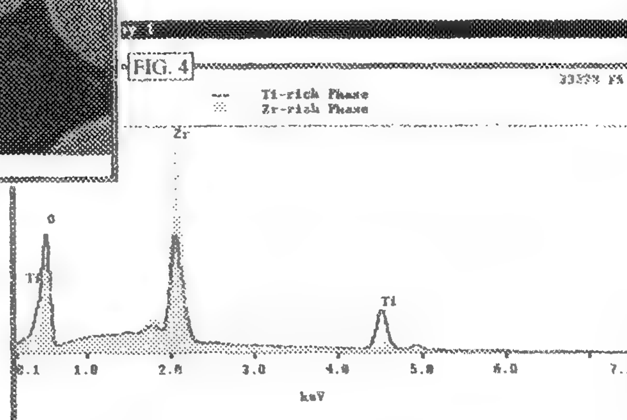

FIG. 1. Secondary electron digital photomicrograph showing overall microstructure of the composite.
FIG. 2. Higher magnification photomicrograph showing the structure within the matrix phase.
FIG. 3. Digital X-ray maps constructed at 512×400 resolution by position-tagged spectrometry.
FIG. 4. EDS spectra obtained by summing the spectra from each pixel in the Zr-rich phase and in the Ti-rich phase.

ELECTRON-MICROSCOPY STUDIES OF GRAIN BOUNDARY PHASES AND FRACTURE IN YTTRIA-ZIRCONIA CERAMICS

S.E. Lash, H. Pham, A. Cooper, and M.L. Mecartney

Materials Science & Engineering Program, Department of Chemical and Biochemical Engineering, University of California at Irvine, Irvine, CA 92717-2575

Trace amounts of intergranular silicate phases in zirconia ceramics are known to be significant factors in modifying the ionic conductivity of cubic yttria stabilized zirconia[1] and in enhancing high temperature superplastic deformation behavior of tetragonal yttria stabilized zirconia[2]. This work studies how the composition and distribution of the intergranular phase affect fracture.

Samples were prepared of yttria stabilized zirconia ceramics with 3 mol% yttria (3Y-TZP, metastable tetragonal zirconia) and 8 mol% yttria (8Y- FSZ, fully stabilized cubic zirconia). Additions of 1 wt.% of a barium silicate glass or a borosilicate glass were made prior to sintering so that different intergranular phases could be formed. Samples were sintered at 1400-1600°C for 2-21 h. SEM images of fracture surfaces were digitized and analyzed using Adobe Photoshop and Prismview programs.

Figure 1a shows the SEM analysis of a fracture surface of a 3Y-TZP sample sintered 1500°C for 10 hours. Transgranular fracture is indicated by the rough and wavy surfaces. Approximately 30% of the fracture is transgranular fracture. A 3Y-TZP sample sintered at 1500°C for 10 hours with 1 wt.% of a barium silicate glass added shows a markedly different surface, with intergranular fracture being dominant (95%), and the smooth facets of the grains clearly evident (Figure 1b).

Analyzing a series of SEM micrographs of fracture surfaces for different samples indicated that pure 3Y-TZP samples all had a high degree of transgranular fracture (ranging from 30% to 90%), while samples with intergranular barium silicate phases had predominantly intergranular fracture (93-96%). Samples with the borosilicate phase sintered for short times had a high amount of transgranular fracture (25-80%), but with long sintering times (21 hours) the amount of transgranular fracture dropping to 4%.

The intergranular phase distribution in 8Y-FSZ samples was analyzed by TEM. (Grains are an order of magnitude larger in the 8Y-FSZ samples than in the 3Y-TZP samples so observation of the intergranular phases was much easier.) Micrographs of the two intergranular phases in 8Y-FSZ showed markedly different wetting behavior for short sintering times. Measurement of the dihedral angles of wetting for the pure samples and the intergranular borosilicate samples showed a range of angles from 45° to 60° (Figures 2a and 2b). Dihedral angles of 60° were observed at triple grain junctions (Figure 3). In contrast, the barium silicate glass wet the boundaries with extremely low dihedral angles (Figure 4).

It is postulated that during sintering the barium silicate glass wet the boundaries and upon cooling the continuous intergranular film that was formed provided an easy path for fracture. Pure zirconia and the material containing the borosilicate intergranular phase both had significant transgranular fracture because the melted borosilicate glass did not wet the boundaries significantly. Another factor of importance in transgranular versus intergranular fracture may be the role of residual stress due to thermal expansion anisotropy with residual stress relief provided by the flow of the intergranular phase above the glass transition temperature.[3]

1. M. Godickemeier et al., *J. Mater. Res.* 9 (1994) 1228.
2. M.C. Gust et al. *J. Am. Ceram. Soc.*, 73 (1993) 1681.
3. This work is supported by grant #STB-UC95-141 from the DOE Los Alamos National Scientific Lab under the Combined UC Los Alamos Research program. Collaboration with T.E. Mitchell of the Center for Materials Science at Los Alamos is gratefully acknowledged.

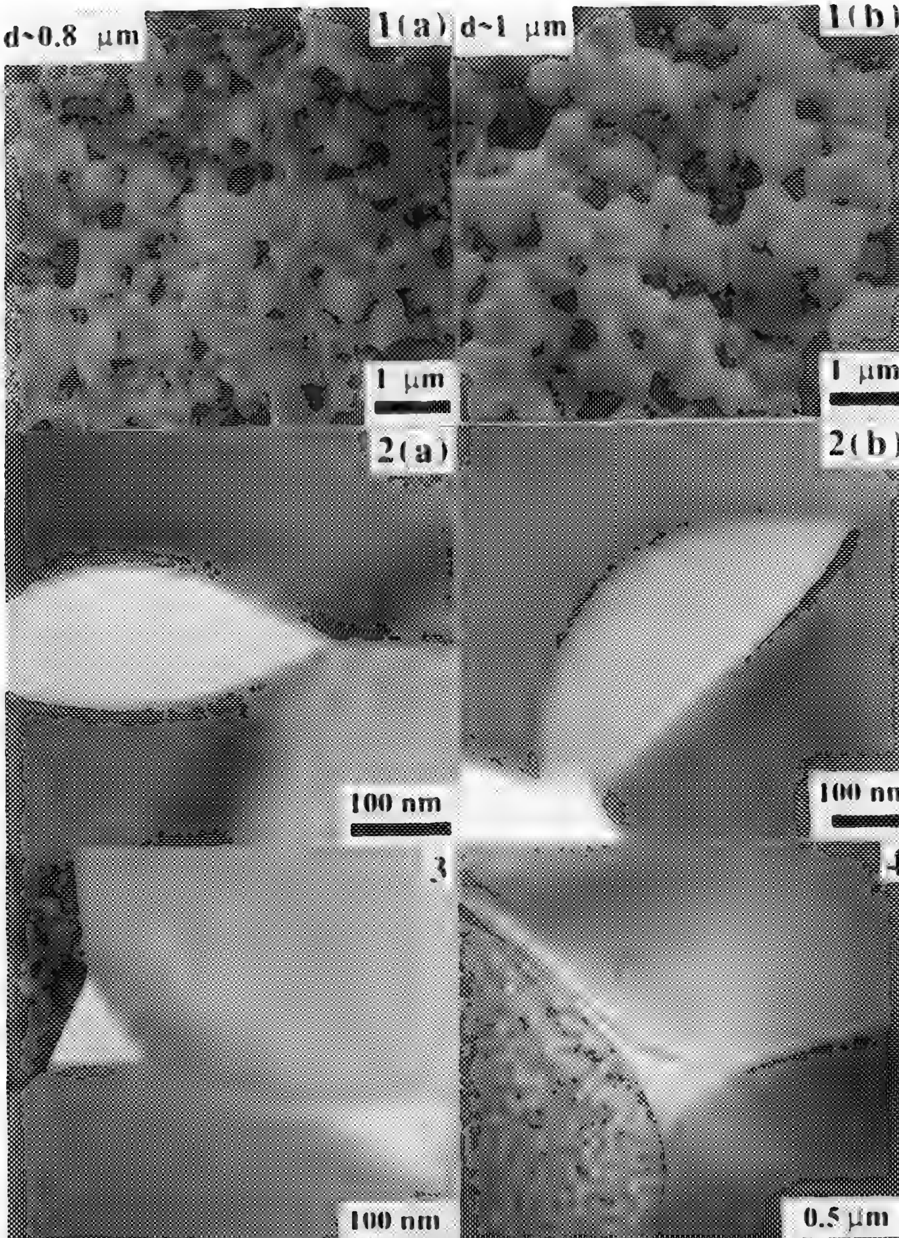

Figure 1. Fracture surfaces (a) 3Y-TZP only (b) with 1 wt.% of an intergranular barium silicate phase.
Figure 2. (a) Intergranular porosity in pure sample, (b) intergranular pore filled with borosilicate phase.
Figure 3. Porosity at triple grain junctions in pure sample.
Figure 4. Wetting of barium silicate intergranular phase at triple junction.

ATOMIC STRUCTURE OF INTERNAL Cu/Al_2O_3 INTERFACES

G. Dehm*, C. Scheu*, and M. Rühle*

*Max-Planck-Institut für Metallforschung, Institut für Werkstoffwissenschaft, Seestrasse 92, 70174 Stuttgart, Germany

Metal/Ceramic compounds show a wide range of applications, ranging from electronic packaging to bio-medical implants [1]. A detailed knowledge of the bimaterial interface is therefore necessary in order to understand the compound properties and their dependence on microstructure and atomic configuration. In this study, thin overlayers of Cu on (0001) α-Al_2O_3 were grown by molecular beam epitaxy. The films possess a fixed $(111)_{Cu} <110>_{Cu} \parallel (0001)_S[10\bar{1}0]_S$ (index S: Al_2O_3) orientation relationship to the substrate [2]. High resolution transmission electron microscopy (HRTEM) and electron energy loss spectroscoppy (EELS) were applied to obtain information about the interface structure and the bonding mechanism of the interface at an atomic level. The HRTEM studies were performed on the Jeol JEM ARM1250, an atomic resolution microscope operated at 1250 kV [3]. The bonding mechanism between Cu and Al_2O_3 can be determined by an analysis of the energy-loss near-edge structure (ELNES) of the internal interfaces. Those investigations were carried out in a VG HB501 dedicated scanning transmission electron microscope equipped with a parallel EELS (Gatan 666PEELS).

HRTEM of the Cu/Al_2O_3 interface confirms that the close-packed planes and close-packed directions of Cu and Al_2O_3 are parallel (FIG. 1). Lattice micrographs were taken with the incident beam direction parallel to the $<21\bar{1}>_{Cu}$ and $<2\bar{1}\bar{1}0>_S$ zone axis. The (022) Cu planes, with a spacing of 0.128nm, are clearly resolved. The (111) Cu planes and (0006) Al_2O_3 planes are lying parallel to the interface as indicated in the micrograph. Furthermore, the lattice image shows that the interface is atomically sharp. Due to the low substrate temperature of 200°C used for the Cu growth in ultra high vacuum conditions no interfacial phases caused by chemical reactions are observed.

The (0001) basal plane of α-Al_2O_3 can be either terminated by an oxygen layer or aluminum layer. Either Cu-O bonds or Cu-Al bonds can be established at the interface. The type of bonding can be determined by an EELS analysis of the fine structure of the Al, O, and Cu edges. The ELNES contains the information about local coordination and electronic structure [4]. Thus, local changes of the oxidation state of Cu at the interface due to bonds with the oxygen sublattice of Al_2O_3 or a metallic interface bonding between Cu and the Al-sublattice will modify the ELNES.

The spectra were recorded by applying the spatial difference technique [5]. The interface was aligned edge-on and spectra recorded in the substrate, in the film and at the interface with the beam scanning an area of $10*12nm^2$. All spectra were rectified for dark current and read-out pattern of the parallel detector. The pre-edge background was extrapolated by a power law and subtracted from the raw data. The EELS spectrum of the interface was corrected following the method described in ref. [5] for both the bulk substrate and film contributions which are present due to the width of the measured area. The remaining difference spectrum represents the ELNES of interfacial atoms possessing a different oxidation state and/or environment compared to the bulk. In FIG. 2 the measured $Cu_{L2,3}$ spectra of the Cu-film (I_{Cu}) and the interface (I_{IF}) are presented. The difference spectrum of the interface (ΔI_{IF}) is shown in FIG. 2(c). The spectrum was obtained by $\Delta I_{IF} = I_{IF} - \alpha I_{Cu}$, with the scaling factor $\alpha = 0.4$. Since no electron transitions occur in Al_2O_3 within that energy-loss, contributions of bulk Al_2O_3 need not be considered. The difference spectrum of the interface reveals a $Cu_{L2,3}$ ELNES which is clearly different from bulk Cu. At an energy loss of 933eV a L_3 white line is observed which reveals that unoccupied 3d-states exist for interfacial Cu-atoms [5]. Thus, Cu-atoms at the interface change their oxidation state from metallic Cu^0 to either Cu^{1+} or Cu^{2+}. Comparing the interfacial $Cu_{L2,3}$ ELNES (FIG. 2c) to reference spectra of Cu_2O (Cu^{1+}) and CuO (Cu^{2+}, FIG. 2d,e) indicates that the oxidation state of Cu at the interface is Cu^{1+}, since no chemical shift which is typical for Cu^{2+} is detected. Examination of the O_K interface difference ELNES reveals a broadening of the main peak at 540eV, whereas the intensity of the $Al_{L2,3}$ difference spectrum of the interface remains zero within the detection limit. This indicates that Al doesn't change its local coordination and so is not involved in bonding at the interface. However, the interface specific component

found in $Cu_{L_{2,3}}$ and O_K edge imply the presence of Cu-O bonds across the interface.

A simulation of the experimental HRTEM micrograph (FIG. 3) under the assumption of Cu-O bonds at the interface as found by our ELNES studies, provides a bonding distance of 0.2nm ± 0.02nm between the terminating oxygen layer and copper layer at the interface. The simulated image is presented in FIG. 3b and the corresponding atom positions of the interface model are shown in FIG. 3c.

References

1 D. Wolf and S. Yip, *Materials Interfaces*, Chapman & Hall: London, Uni. Press, Cambridge (1992)
2 F. Phillip et al., *Ultramicroscopy 56*, (1994)1
3 G. Dehm et al., *Philos. Mag. B 71*, (1995)1111.
4 R.F. Egerton, *Electron Energy Loss Spectroscopy*, Plenum Press: New York (1986)
5 C. Scheu et al., *Microsc. Microanal. Microstruct. 6*, (1995)19
6 We acknowledged valuable discussions with Prof. Rishi Raj (Cornell University). Dr. Hui Gu (Orsay, France) provided the reference spectra of Cu_2O and CuO.

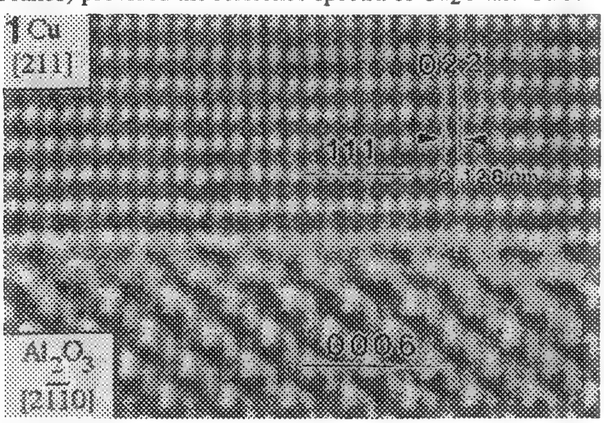

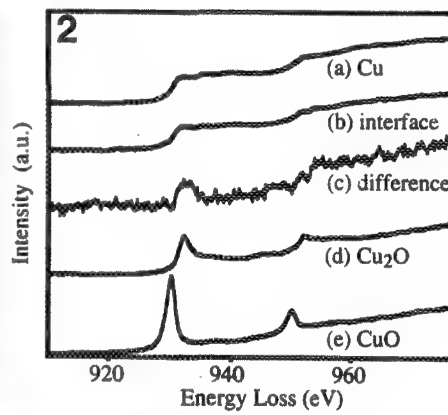

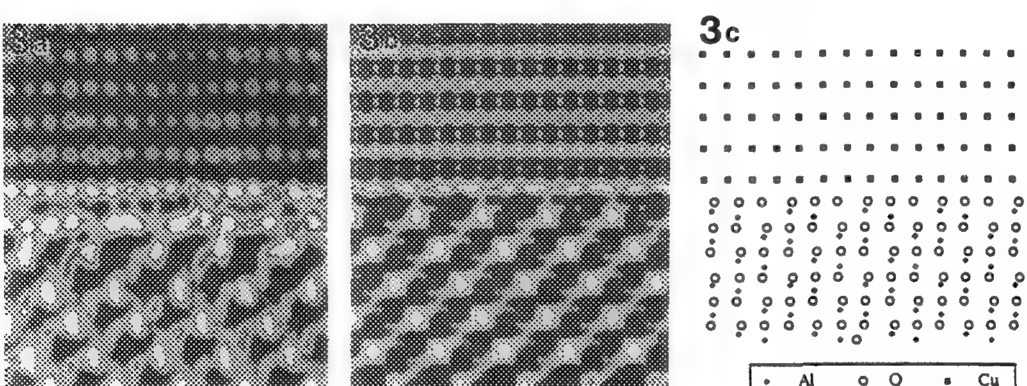

FIG. 1 - Atomic resolution TEM micrograph of the Cu/Al_2O_3 interface edge-on.
FIG. 2 - $Cu_{L_{2,3}}$ edge ELNES of (a) bulk Cu, (b) interface region, (c) and interfacial atoms. Reference spectra of (d) Cu_2O and (e) CuO.
FIG. 3 - HRTEM micrograph (a) of the Cu/Al_2O_3 interface and (b) simulated image assuming the (c) atomistic model with Cu-O bonds at the interface.

ELECTRON DIFFRACTION FROM ANTHRACENE

W. F. Tivol* and J. H. Kim**

*Wadsworth Center and the School of Public Health, the University at Albany, Empire State Plaza, PO Box 509, Albany NY 12201-0509, USA

**155-67 71st Ave., Flushing NY 11367

Collection of a three-dimensional data set from anthracene illustrates some of the difficulties which can be encountered. Since the crystals are grown from solution their orientation is not certain, and the crystals are very bendy, so a range of orientations is encountered at a given tilt setting. Anthracene is moderately labile to irradiation, so care must be taken to avoid radiation damage during data collection. Anthracene will sublime at room temperature under vacuum, so the data must be collected at reduced temperature. Flat, well-ordered areas of the crystals are rare, so collection of high-resolution data is time-consuming. The thickness of the crystals is difficult to control, so finding areas which have minimal multiple scattering is also formidable.

The structure of anthracene is already known, so simulations of the diffraction patterns along various zone axes can be made. Cerius^2 2.0® was used to produce simulated zone axis patterns for all combinations of indices whose absolute values were 3 or less.[1] The preferred orientation for the untilted grid is [102].[2] Scans of several preparations resulted in patterns which matched the simulation for [102]. The angles for each of the Miller planes with respect to [102] were calculated from the formula given by Dorset.[3]

Data were collected at 1.2 MV on the AEI-EM7 high-voltage electron microscope (HVEM). A dilute solution of anthracene was prepared, and about 25 μl was placed on a carbon-coated 200-mesh grid. When this procedure was done at room temperature (~23°C), the resulting crystals were usually too thick to give useful diffraction patterns, so subsequently the procedure was done in a warm room at 37°C. Figure 1 shows a typical area of crystals. The grid was placed in a Gatan Model 626 cryostage, inserted in the HVEM and cooled to about -150°C (the anti-contaminator was at -180°C). When the temperature had stabilized, the specimen was tilted to the desired orientation and scanned at low magnification for a grid square which had apparently suitable crystals. N.b., since only one tilt axis was available, only a small fraction of the crystals were properly oriented in the grid plane, so apparently suitable crystals were not necessarily aligned with a zone axis parallel to the incident beam. The specimen was positioned so that the incident beam illuminated one corner of the grid square, the HVEM was switched to diffraction mode and a smaller condenser aperture was inserted. This aperture produced a beam which was approximately the same size as the area selected by the diffraction aperture--350 nm in diameter. The specimen was scanned in diffraction mode until a zone-axis pattern was seen, at which point the beam was shut off until the camera shutter had opened. All the scans performed in imaging mode used a low electron dose--total beam current was about 20 pA--and were monitored by the intensified CCD camera mounted under the HVEM. The current used in diffraction mode was about 2 pA, and the patterns were recorded on Cronex LoDose mammography film.

Figure 2 shows four of the zone axis patterns found. The zone axes for these patterns were confirmed by measuring the a^*-to-b^* ratios and noting the similarity of the intensities to those predicted by the simulations.[4]

Referrences

1. Distributed by Molecular Simulations, Inc., 16 New England Executive Park, Burlington MA 01803-5297, USA.
2. D.L. Dorset, personal communication.
3. D.L. Dorset, *Structural Electron Crystallography*, Plenum Press: New York and London (1995)34.

4. Supported by Biotechnological Resource grant RR01219, awarded by the National Center for Research Resources, Department of Health and Human Services/Public Health Service, to support the Wadsworth Center's Biological Microscopy and Image Reconstruction Facility as a National Biotechnological Resource.

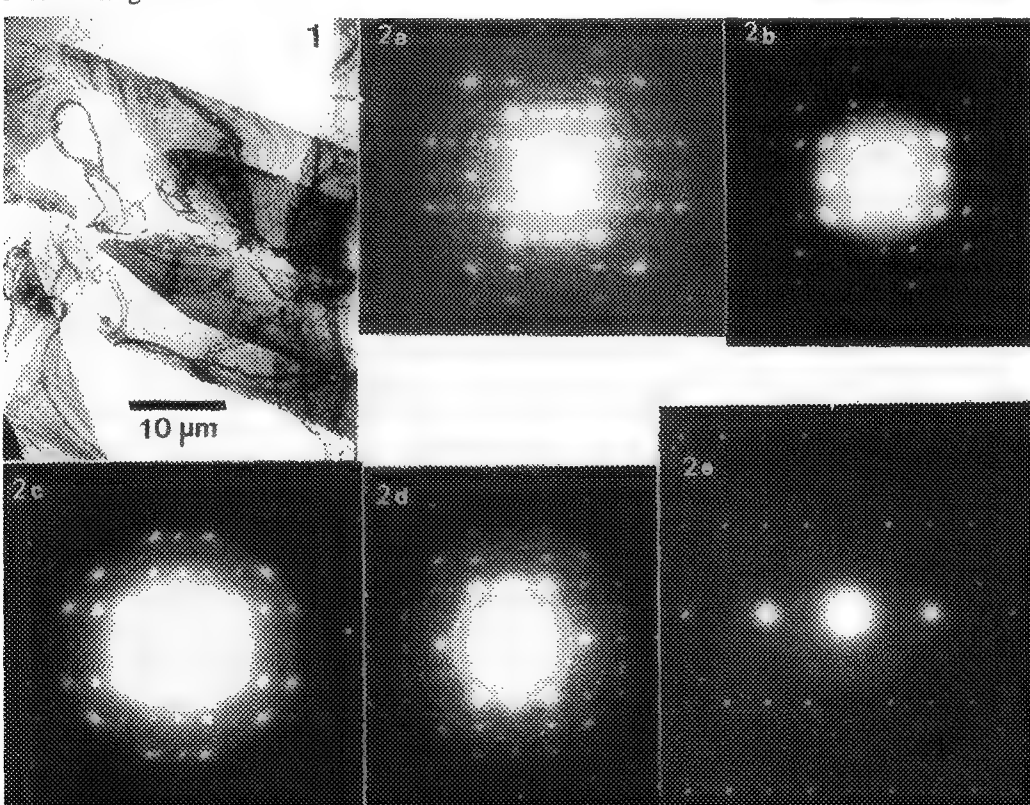

FIG. 1 Anthracene crystals. Note thick areas and bend contours.
FIG. 2 Zone-axis patterns. a) [100], b) [001], c) [001], lighter print showing higher-order spots, d) [101], e) [203].

ELECTRON-BEAM-INDUCED TRANSFORMATIONS IN ZIRCONIA-ALUMINA NANOLAMINATES: AN *IN SITU* HIGH-RESOLUTION ELECTRON-MICROSCOPY STUDY

M.A. Schofield, M. Gajdardziska-Josifovska, R. Whig, and C.R. Aita

Laboratory for Surface Studies, U. of Wisconsin-Milwaukee, P.O. Box 413, Milwaukee, WI 53201

Composite systems containing zirconia have been used extensively as transformation-toughening materials based on a stress induced martensitic transformation of the metastable tetragonal phase of zirconia to the monoclinic phase.[1] Recently it has been shown that tetragonal zirconia can be stabilized in zirconia-alumina nanolaminates grown by reactive sputter deposition, when the zirconia layer is less than 6 nm thick.[2] Cross-section high resolution transmission electron microscopy (HRTEM) of these nanolaminates revealed localized tetragonal-to-monoclinic transformation caused by sample preparation.[3] In this study, quantitative HRTEM is used to analyze the zirconia nanocrystallite transformation *in situ*, by controlled exposure of the sample to the electron beam of the microscope.

The irradiation conditions used in this study to induce the zirconia transformation are summarized in Table 1. The mildest irradiation condition corresponds to normal imaging illumination used in this study to obtain high resolution images. Under these normal illumination conditions, the first condenser lens (C1) is used to form a 0.1 μm sized probe which is over focused on the sample by the second condenser lens (C2). Additionally, a 50 μm condenser aperture (CA) is inserted into the beam path. The digital quantum efficiency of the CCD camera used to record images was determined to be ~1 electron per count, so that mild irradiation of the sample corresponds to an electron flux of 8×10^3 electrons s^{-1} $Å^{-2}$. Moderate and extreme irradiation conditions used in this study correspond to electron fluxes of 3×10^5 electrons s^{-1} $Å^{-2}$ and 8×10^6 electrons s^{-1} $Å^{-2}$, respectively.

Experiments were performed for the three different irradiation conditions, whereby, sequences of high resolution images were obtained of selected zirconia nanocrystallites. Fig. 1 is an HRTEM image showing a typical region of the polycrystalline zirconia layer in the as-prepared sample. The amorphous native oxide layer of the silicon substrate is shown at the bottom of the image, while part of the first amorphous alumina layer is shown at the top. The lattice fringes parallel to the substrate in Fig. 1 are an overwhelming feature of tetragonal nanocrystallites of this layer and correspond to the tetragonal {111} planes of zirconia. No observable changes were introduced in zirconia nanocrystallites similar to the one shown in Fig. 1 under extended periods of normal imaging illumination.

Fig. 2 is an HRTEM image showing typical characteristics of the stress induced transformation produced under extreme irradiation conditions corresponding to an electron dose of 5×10^8 electrons/$Å^2$. Typical features in Fig. 2 are the broad-band contrast across the zirconia layer (region A), and the tilt between the {111} lattice fringes and the substrate (region B). The phase assignment of these lattice fringes is discussed below. The extreme irradiation experiments invariably produced significant changes in the sample, therefore, experiments with moderate irradiation were undertaken to examine the details of the nanocrystallite transformation.

Fig. 3a-c show HRTEM images of identical regions of the sample recorded in sequence with 10 seconds of moderate irradiation of the sample (electron dose of 3×10^6 electrons/$Å^2$) between each image acquisition. Observable changes of a continuous nature in the zirconia layer can be seen in region A of Fig. 3a-c. Careful lattice spacing measurements of region B in Fig. 3a-c (and in additional images of the sequence) are plotted in Fig. 4 as a function of image acquisition time. At early times the spacing agrees with the high temperature bulk tetragonal {111} spacing 2.96 Å.[4] At later times in Fig. 4 the spacing is about 2% larger than the tetragonal {111} spacing, but smaller than the monoclinic bulk {11-1} spacing (3.16 Å) by 4.5%. The transformation of the tetragonal {111} spacing parallel to the substrate to this intermediate regime in spacing was commonly observed, but no stable monoclinic phase was found, suggesting that the tetragonal nanocrystallites are quite resistant to electron beam irradiation. Further studies are needed to determine if the zirconia nanocrystallites transform to the monoclinic phase during moderate exposures, but undergo a relaxation to the tetragonal phase under imaging conditions, or whether the tetragonal-to-monoclinic transformation has a higher threshold than provided by the moderate irradiation of these experiments.[5]

References

1. D.J. Green et al., *Transformation Toughening of Ceramics*, CRC Press, Boca Raton, FL (1989).
2. C.M. Scanlan et al., *Appl. Phys. Lett.*, 64(1994)3548; C.R. Aita, U.S. Patent No. 5472795 (5/12/95).
3. M. Gajdardziska-Josifovska and C.R. Aita, *J. Appl. Phys.*, 79(1996)1315.
4. ASTM Joint Committee on Powder Diffraction Standards, 1974, File Nos. 13-307 and 17-923.
5. Work supported under U.S. ARO Grant Nos. DAAH04-93-G-0238 and DAAH04-95-1-0242, NSF Grant Nos. DMR-9553148 and BIR-9413762, and by gift from the Johnson Controls Foundation to the Wisconsin Distinguished Professorship of CRA.

Table 1. Irradiation conditions

	Condenser Aperture (CA)	First Condenser Lens (C1)	Second Condenser Lens (C2)	Electron Flux [electrons s^{-1} $Å^{-2}$]
Mild (Imaging)	50 μm	0.1 μm spot size	over focused	8×10^3
Moderate	50 μm	0.3 μm spot size	focused	3×10^5
Extreme	none	0.1 μm spot size	focused	8×10^6

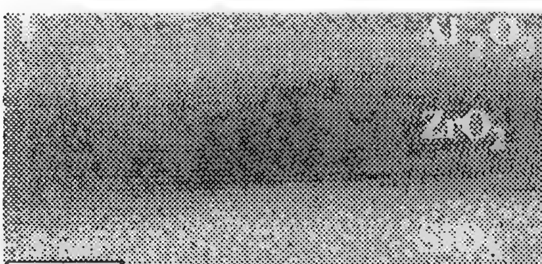

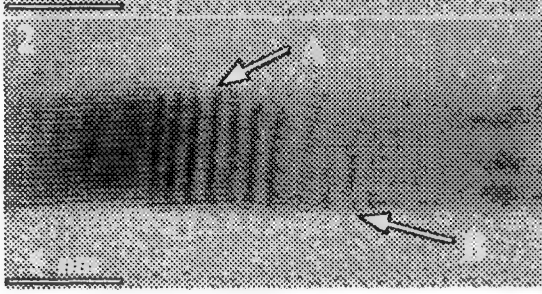

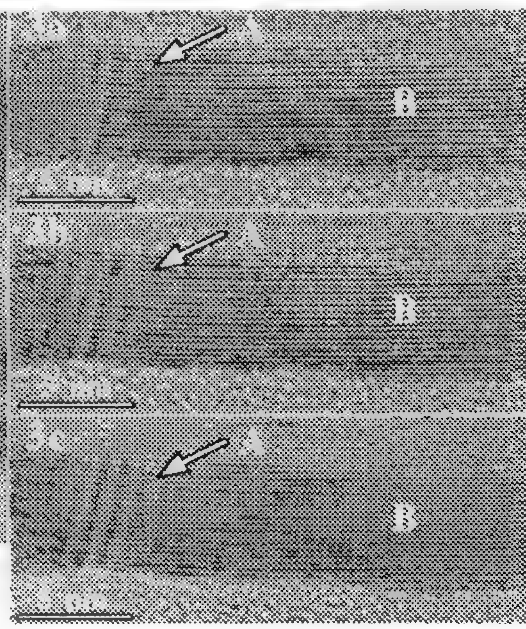

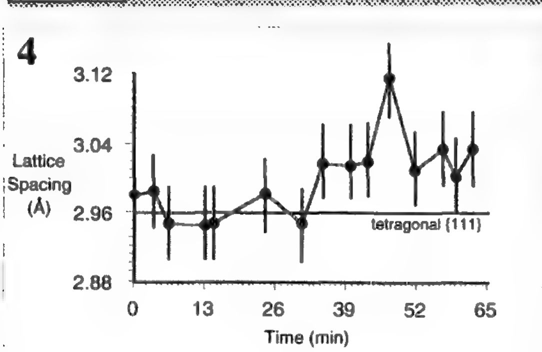

FIG. 1 HRTEM image showing typical region of zirconia layer before irradiation.

FIG. 2 Broad contrast (A) and lattice fringe rotation (B) produced under extreme sample irradiation.

FIG. 3 Partial set of images from moderate irradiation sequence showing two typical structures (A and B).

FIG. 4 Lattice spacing measurements of region B of Fig. 3 for complete irradiation sequence.

CONTROLLING MICROSTRUCTURAL EVOLUTION to *IN SITU* TOUGHEN AND STRENGTHEN SILICON CARBIDE

Warren J. MoberlyChan, J. J. Cao, & L. C. DeJonghe

Materials Science Division, Lawrence Berkeley Laboratory, 1 Cyclotron Road, Berkeley, CA 94720

Nonoxide ceramics are desirable for high temperature structural applications, however, they have typically exhibited inferior room temperature fracture toughness. Similar to processing developments to toughen Si_3N_4[1], SiC has recently been processed via control of a phase transformation [2-4] to produce *in situ* toughened microstructures [2, 5, 6]. An elongated grain shape, coupled with a tortuous fracture path around grains, can provide bridging behind an advancing crack tip, which increases the crack resistance (rising R curve) and halts crack propagation. Most *in situ* toughened nonoxide ceramics incorporate upwards of 10-20% secondary phase(s) [1, 5], which simplifies crack propagation through this weaker phase to improve toughness, but typically at the expense of substantially reducing strength at high temperatures. The ABC-SiC in this study can be processed with <3% secondary phases and consequently exhibits record toughness and higher strength than commercial (Hexoloy SA) SiC [2, 6].

Starting with submicron beta-SiC powders and minimal additives (<5% Al, B, and C), these ABC-SiC materials are hot pressed at temperatures between 1700°C and 1900°C for ~1 hour. The Al-based additives not only ensure full densification, but also activate a cubic-to-hexagonal phase transformation at temperatures a couple hundred degrees below typical processing temperatures for other SiC materials. For this study hot pressed discs are sectioned to provide beams for bend tests to measure strength and toughness based on controlled surface flaws. Materials analysis includes XRD, optical microscopy, SEM fractography, TEM, and associated spectroscopies [2-4].

During hot pressing a phase transformation occurs via the growth of the alpha-4H phase from the beta grain, thereby developing dual-phase grains [3, 4]. The α-4H structure encourages anisotropic grain growth to develop an interlocking, plate-like morphology (Figure 1). While grain size increases with processing time, the strength increases due to an increase in interlocking with aspect ratio. The additives, in particular Al, react with the native oxide on powders to enhance liquid-phase sintering, and upon cooling persist as a ~1 nm-thick amorphous phase. (See HR-TEM image in Figure 2a.) This amorphous phase is enriched in Al and O and invokes intergranular fracture. (See Auger Spectra in Figure 2b.)

Hexoloy, a commercial, equiaxed, α-6H SiC, exhibits transgranular fracture (Figure 3a), poor toughness (K_{1c} <3 MPa$\sqrt{m}$), and a strength of ~400 MPa at room temperature. Similarly, a submicron β-ABC-SiC (processed at 1700°C, below the transformation temperature) with intergranular fracture (Figure 3b) exhibits a limited improvement in toughness and strength (K_{1c} <5 MPa$\sqrt{m}$ and ~600 MPa, respectively). However, an ABC-SiC processed at 1900°C for 1 hour to develop an interlocking microstructure with intergranular fracture (Figure 3c) has superior properties (K_{1c} >9 MPa$\sqrt{m}$ and ~700 MPa bend strength). Figures 4a and 4b depict indentation crack paths in polished surfaces of Hexoloy and ABC-SiC, respectively; with crack deflection and elastic bridging behind the crack tip evident in Figure 4b. The planar surfaces of plate-like grains are disrupted by β $\{\bar{1}11\}$-facets [3] and crystalline triple point phases observed by SEM fractography and HR-TEM at grain boundaries [4, 7]. These asperities disrupt a frictional pullout mechanism, thereby indicating toughening is due to elastic bridging and/or "pinning".

References

1. P. F. Becher, *J. Am. Ceram. Soc.*, **74** [2] (1991) 256-269.
2. J. J. Cao, et al., *J. Amer. Ceramic Soc.*, **79** [2] (1996) 461-469.
3. W. J. MoberlyChan, et al., submitted to *Acta metall. mater.*
4. W. J. MoberlyChan, et al., in this *MSA Proceedings* (1996).
5. N. P. Padture & B. R. Lawn, *J. Amer. Ceramic Soc.*, **77** [10] (1994) 2518-2522.
6. C. J. Gilbert, et al., *Acta metall. mater.*, in press.
7. W. J. MoberlyChan, et al., in this *MSA Proceedings* (1996).
8. The authors gratefully acknowledge the NCEM staff. Support was by DOE #ACO3-76SF00098.

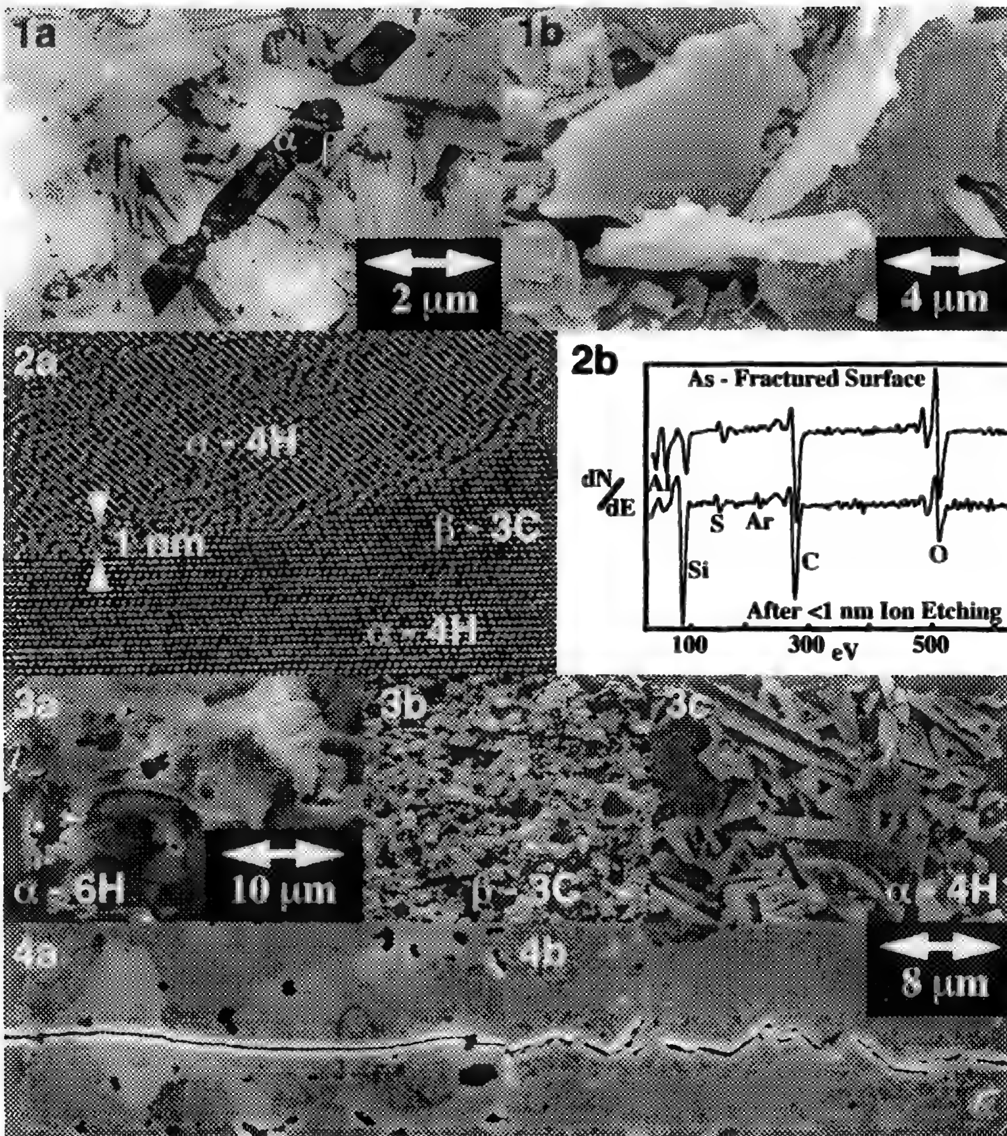

Fig. 1: (a) BF-TEM and (b) SEM (surface etched in molten salt) images of interlocked, plate-like grains.
Fig. 2: (a) HR-TEM of amorphous grain boundary phase and (b) Auger of intergranular fracture surface.
Fig. 3: SEM fractographs; (a) transgranular in equiaxed α-6H-SiC Hexoloy, (b) intergranular in fine-grain, equiaxed β-SiC, (c) transgranular in plate-like α-4H-SiC. (c) is >3 times tougher than (a) or (b).
Fig. 4: SEM of indentation crack paths; (a) transgranular in Hexoloy, (b) intergranular in ABC-SiC.

TEM/AEM CHARACTERIZATION OF FINE-GRAINED CLAY MINERALS IN VERY-LOW-GRADE ROCKS: EVALUATION OF CONTAMINATION BY EMPA INVOLVING CELADONITE FAMILY MINERALS

Gejing Li*, D. R. Peacor*, D. S. Coombs**, and Y. Kawachi**

*Department of Geological Sciences, University of Michigan, Ann Arbor, MI 48109
**Geology Department, University of Otago, P. O. Box 56, Dunedin, New Zealand

Recent advances in transmission electron microscopy (TEM) and analytical electron microscopy (AEM) have led to many new insights into the structural and chemical characteristics of very fine-grained, optically homogeneous mineral aggregates in sedimentary and very low-grade metamorphic rocks. Chemical compositions obtained by electron microprobe analysis (EMPA) on such materials have been shown by TEM/AEM to result from beam overlap on contaminant phases on a scale below resolution of EMPA, which in turn can lead to errors in interpretation and determination of formation conditions.[1] Here we present an in-depth analysis of the relation between AEM and EMPA data, which leads also to the definition of new mineral phases, and demonstrate the resolution power of AEM relative to EMPA in investigations of very fine-grained mineral aggregates in sedimentary and very low-grade metamorphic rocks.

Celadonite, having end-member composition $KMgFe^{3+}Si_4O_{10}(OH)_2$, and with minor substitution of Fe^{2+} for Mg and Al for Fe^{3+} on octahedral sites, is a fine-grained mica widespread in volcanic rocks and volcaniclastic sediments which have undergone low-temperature alteration in the oceanic crust and in burial metamorphic sequences. In Triassic sediments of the Gavenwood Tuffs in the Hokonui Hills, Southland Syncline, New Zealand, it occurs typically in microvesicles in altered glass shards as 10 μm thick rims with inner fillings of further celadonite, chlorite, and/or the zeolite heulandite.

EMPA of micron-sized areas gave celadonite compositions with a range of K, Si, and other elements, apparently suggesting celadonite/chlorite mixtures.[2] TEM/AEM show that the Gavenwood Tuffs "celadonites" are actually intergrowths of two different 10-Å celadonite family minerals, in packets a few to a few hundred layers thick, with similar sized packets of 14-Å chlorite and some probable berthierine, the 7-Å polymorph of Fe-rich chlorite (Figs. 1 and 2). The mixing scale of intergrown phyllosilicates is well below the resolution of EMPA (a few μm) and optical microscopy. AEM analyses show that the celadonite packets are virtually ideal dioctahedral tetrasilicic micas, dominated by $Fe^{2+}Fe^{3+}$ and $Fe^{2+}Al$ octahedral components rather than $MgFe^{3+}$ (celadonite), defining the two distinct new phases $KFe^{2+}Fe^{3+}Si_4O_{10}(OH)_2$ and $KFe^{2+}AlSi_4O_{10}(OH)_2$ and suggesting nearly complete solid solution among all four end members of the family (Fig. 3). Further EMPA data demonstrate a few analyses in the $Fe^{2+}Fe^{3+}$ field of celadonite-family quadrilateral. However, as shown in Fig. 4, the presence of only 5-10% of chlorite displaces projection points for analyses with average of $Fe^{2+}Fe^{3+}$ and $Fe^{2+}Al$ components into the $MgFe^{3+}$ (celadonite) field. The plotted points for EMPA trending toward the upper left quadrant result from this effect, and the properly reinterpreted EMPA data confirm the formulae of $Fe^{2+}Fe^{3+}$ and $Fe^{2+}Al$ members determined by AEM analysis.

References

1. W.-T. Jiang et al., Clays and Clay Minerals, 42(1994) 593.
2. J. R. Boles and D. S. Coombs, *Geol. Soc. Amer. Bull.,* 86(1975) 163.
3. G. S. Odin et al., in G. S. Odin, Ed., Green Marine Clays, Elsevier, New York, (1988)337.

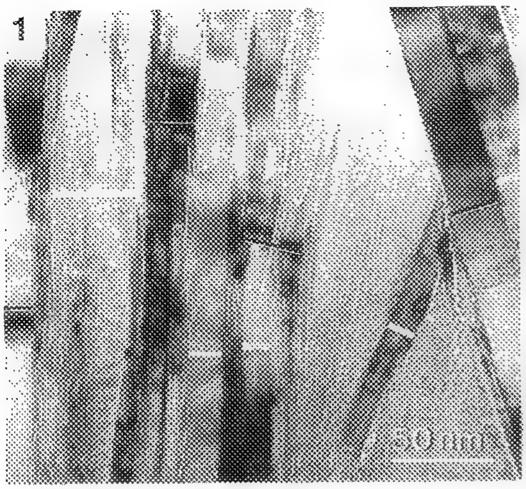

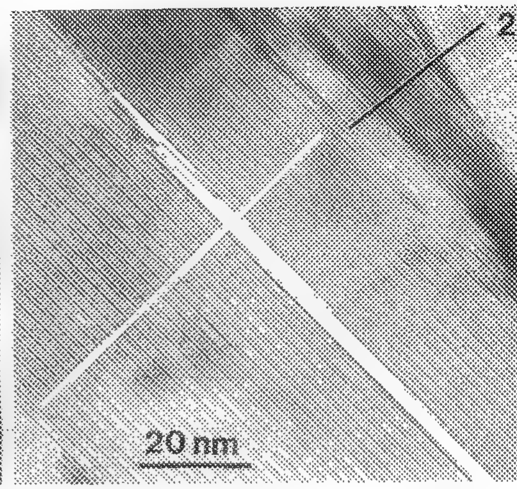

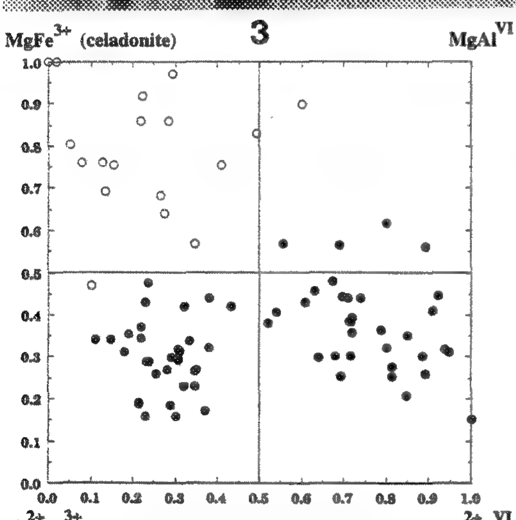

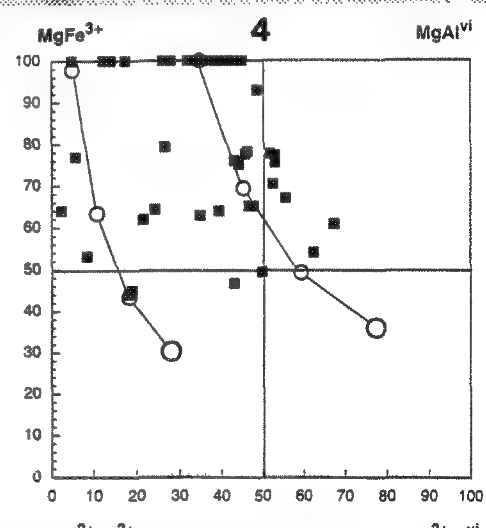

FIG. 1 TEM image showing intergrown discrete packets of chlorite (thin white bars) and celadonite-family minerals (thick white bars), each a few tens nanometers in thickness.

FIG. 2 TEM (001) lattice fringe image showing packets of celadonite-family minerals (thick white bar) and mixed-layered chlorite/berthierine (thin white bar).

FIG. 3 Plot of compositions for octahedral cations of celadonite family minerals. • : this study, ○ : reference.[3]

FIG. 4 Compositions (■) of mixtures of chlorite and celadonite-family minerals by EMPA, compared with average AEM analyses ( ) of discrete celadonite-family minerals, these being joined to points (O) corresponding to the addition of 5%, 10%, and 15% of average chlorite as analyzed by EMPA.

PROGRESS IN ELECTRON-PROBE MICROANALYSIS OF BORON IN GEOLOGIC SAMPLES

James J. McGee

Geologic Division, U.S. Geological Survey, Reston, VA 22092

Despite the availability of modern instrumentation with improved detection and correction systems, the analysis of boron in geologic samples by electron probe microanalysis (EPMA) is often avoided. Many studies resort to using calculated or assumed concentrations of B based upon mineral stoichiometry rather than attempt to quantify the B contents by measurement. Assuming stoichiometric behavior for B is not always valid and disregards the possibility of variations in B content of minerals. Such assumptions can contribute to misleading crystal chemical substitution models for the other mineral constituents.

With modern EPMA instrumentation, analysis of B in minerals where B is present in major concentration levels (such as in tourmaline) is possible and should be incorporated into routine analytical procedures by the mineralogical community. The effort to make B measurement routine will reinforce itself, as techniques, standards, and problems are addressed by the geologic community interested in refining the measurement application. Progress in this effort, and some of the factors in need of further consideration are discussed here.

Perhaps the most significant development in the measurement of B (and other light elements) during the past decade has been the introduction and continued refinement of layered synthetic microstructures (LSM) as analyzing crystals.[1-3] For B, the LSM crystals commonly available consist of NiC (2d ~60Å) and MoB_4C (2d ~145Å to 200Å). The use of LSM crystals in geologic applications has been demonstrated during the past few years.[4,5] In comparison with traditional analyzing crystals such as lead stearate, peak intensities for B using LSM crystals are higher by a factor of 10 to 50, depending on the material measured and the analytical conditions. Along with the increased peak intensity, there is a broadening of the B peak using LSM crystals.[2,4] Such broad peaks require that backgrounds be measured at large offsets from the peak (± 6 to 10Å).

Potential problems of utilizing LSM crystals, such as wavelength shifts, peak shape variations, overlapping spectra, and orientation effects have been evaluated.[1-5] Because the peaks are relatively broad, overlapping spectra from other elements in the analyzed material can be problematic. For instance, Cl spectral lines occur close to the B K_α peak, and there is a relatively high yield of Cl X-ray intensity in comparison with B X-ray intensity.[4] Therefore, a small amount of Cl in a material could introduce large errors in the B measurement.[4] Contributions from higher order X-ray lines (e.g. 3rd order O K_α) and from internal fluorescence of the LSM material (MoB_4C) are also possible.[3] Although LSM crystals suppress many higher-order X-ray lines, the spectral contributions of these higher-order lines must be assessed and corrected, if present, especially when low-level concentrations are of interest (which is nearly always the case in mineralogical studies). Variations in B peak position and shape in different materials may reflect different crystallographic orientation of the sample.[1] These spectral variations may require the use of techniques such as peak integration, rather than simple measurement of peak maximum intensity, or "area peak factors" in which the ratio between correct peak integral intensity and the peak intensity is determined.[1]

Use of well-characterized, homogeneous standards that are structurally and compositionally similar to the samples, if possible, should minimize the effects of peak shift/shape variations and matrix corrections. Possible standards include various tourmalines as well as other rarer, but more B-rich minerals, such as danburite and datolite. In addition, some non-geologic materials, e.g. the NIST borosilicate glass standards, may be usable for geologic applications.

A review of the geologic literature shows some studies where the B contents have been measured by EPMA in a variety of minerals, including tourmaline, kornerupine, vesuvianite, dumortierite, and reedmergnerite.[4-10] Continued application of B analysis in mineralogy, utilizing careful measurement techniques and optimized matrix correction procedures, will enable accurate and precise measurement of B, even at the low levels commonly present in minerals. In addition, EPMA compositional mapping of B in geologic samples can provide valuable qualitative and quantitative information on B-bearing mineral assemblages (Fig. 1). Future efforts in EPMA to improve the measurement of B in minerals should include development and characterization of a suite of suitable B mineral standards as well as correction or minimization of the factors (overlaps, spectral variations, etc.) influencing B measurement. These efforts to establish routine EPMA for B will be invaluable in studies of various geologic materials and petrologic problems.

References

1. G.F. Bastin and H.J.M. Heijligers, *Microbeam Analysis,* 1(1992)61.
2. K. Kawabe et al., *Microbeam Analysis,*(1988)341.
3. H. Kobayashi et al., *Advances in X-Ray Analysis,* 38(1995)307.
4. J.J. McGee et al., *American Mineralogist,* 76(1991)681.
5. M. Raudsepp, *Canadian Mineralogist,* 33(1995)203.
6. J.D. Grice and G.W. Robinson, *Canadian Mineralogist,* 27(1989)199.
7. F.C. Hawthorne et al., *Canadian Mineralogist,* 33(1995)389.
8. L.A. Groat et al., *Canadian Mineralogist,* 32(1994)505.
9. B.S. Hemingway et al., *American Mineralogist,* 75(1990)1370.
10. E.S. Grew et al., *European Journal of Mineralogy,* 5(1993)971.

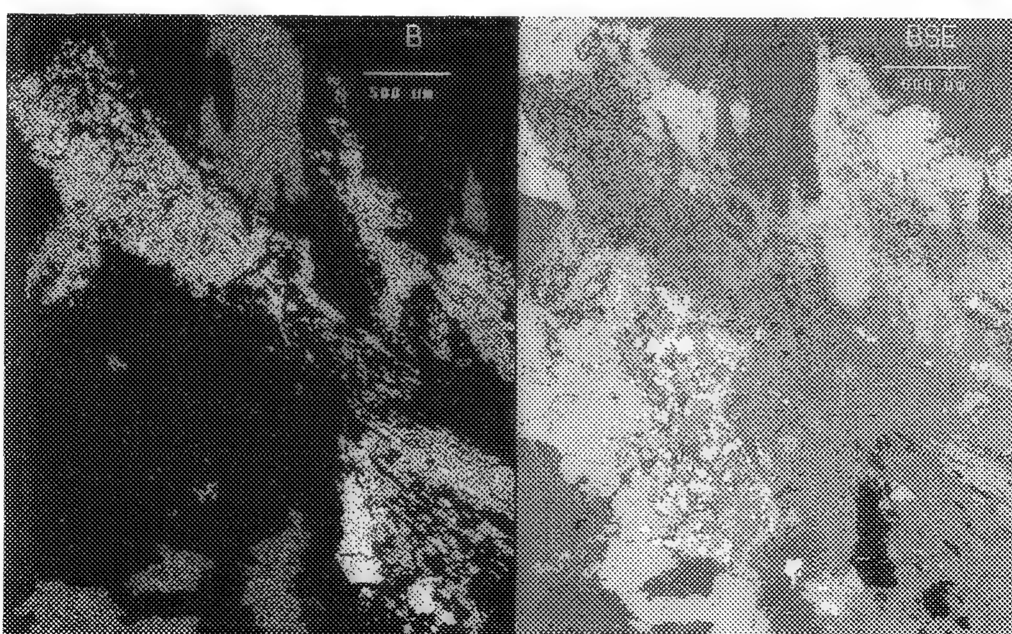

FIG. 1 B K_α X-ray and backscattered electron (BSE) maps of B-bearing minerals, including werdingite, dumortierite, grandidierite, and an unnamed hi-Al-B-silicate in pegmatite from the Rogaland complex, Norway.

SIMS DIRECT ION IMAGING IN THE MINERALOGICAL SCIENCES

G. McMahon* and L. J. Cabri**
* Materials Technology Laboratory, Natural Resources Canada, 568 Booth St., Ottawa, Ont. CANADA
** Mining and Mineral Sciences Laboratory, Natural Resources Canada, 555 Booth St., Ottawa, Ont. CANADA

The use of secondary ion mass spectrometry (SIMS) has enjoyed increasing popularity in the mineralogical sciences owing to its high sensitivity to all elements in the periodic table with detection limits in the parts per million to parts per billion regime, coupled with the ability to display maps of elemental distribution at these detection levels with a spatial resolution of 1 μm. A description of the technique and its application to a wide variety of mineralogical problems has recently been reviewed.[1,2]

The drawback of SIMS is the rather complicated nature of quantification schemes necessitated by sample matrix effects, which refer to differences in the sensitivity for a given element in samples of different composition. These differences result from changes in the ionization efficiency and sputtering yield (sample matrix specific) as well as changes in secondary ion transmission and ion collection efficiencies (instrument specific). Therefore, the use of matrix-matched standards of known concentration is required to establish a calibration factor known as the relative sensitivity factor (RSF) which can be used to convert the experimentally measured secondary ion intensity into concentration values. Furthermore, the effect of changes in ion intensity caused by variations in primary beam current or analysis at different sample positions is removed by normalization to an ion species which represents the matrix material.

Although SIMS has been widely used to determine trace amounts of precious metals and platinum-group elements in a number of minerals, these studies are only infrequently combined with direct ion imaging to obtain a further understanding of the distribution of the element in question.[3-5] This can lead to problems in certain circumstances because the reference standards are by design selected to be as homogenous as possible. However, for the unknown samples this is often not the case. For example, Figs. 1a-c show direct ion images for $^{56}Fe+^{32}S$, ^{197}Au and $^{75}As+^{32}S$, respectively. The diameter of the image field is 62 μm, and the images were acquired using a Cameca ims 4f under conditions enabling high mass resolution ($m/\Delta m = 2500$). Within this image field, three different sulfide minerals, pyrite, pyrrhotite and arsenopyrite, were present, with the gold being present only in the arsenopyrite. In a case such as this, errors can arise in the quantification procedure if for example Fe+S or S was selected as the matrix mass. Both of these matrix species as well as the gold would be uniformly distributed within the same field of view in the reference standard, but in the unknown, the Au would be assumed to be uniformly distributed as well. This is not the case as can be seen in Fig. 1b, and thus the Au concentration in the arsenopyrite would be underestimated. However, if As+S is selected as the matrix mass in both the standard and the unknown, the problem can be circumvented.

Another example of how direct ion imaging can be used to alert one of potential errors in concentration calculations is shown in Figs. 2a and 2b. In this case, only a single arsenopyrite grain is present (Fig. 2a), and thus the selection of the matrix mass is of lesser concern. However, the distribution of gold is so strongly segregated as observed in Fig. 2b that the Au-carrying regions will again be underestimated. In order to resolve this problem, the use of imaging depth profiles of the standard and unknown with subsequent definition of specific regions of interest for the

the reconstruction of selected area depth profiles is being investigated.

1. S.J.B. Reed, *Mineralogical Magazine*, 53(1989)3.
2. N.D. MacRae, *The Canadian Mineralogist*, 33(1995)219.
3. P. Neumayr et al., *The Canadian Mineralogist*, 31(1993)711.
4. M.E. Fleet et al., *Contributions to Mineralogy and Petrology*, 115(1993)36.
5. E.M. Ripley and S.L. Chryssoulis, *Economic Geology*, 89(1994)201.

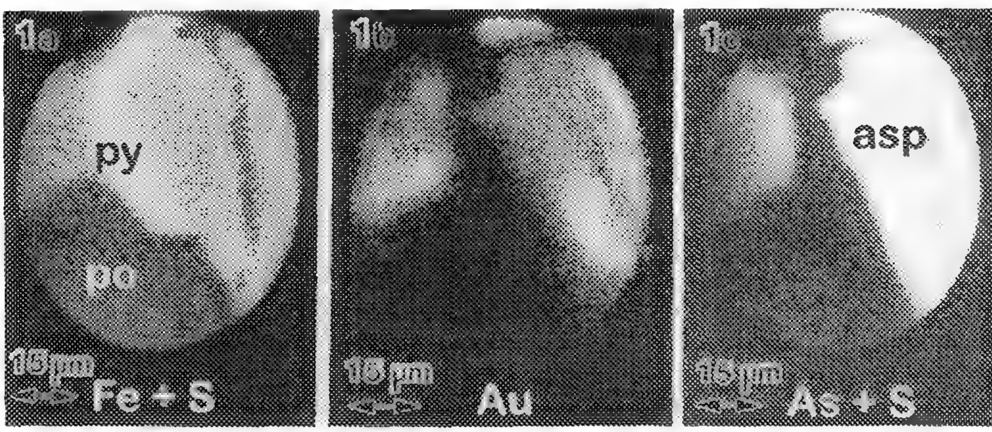

FIG. 1 SIMS direct ion images from a region containing pyrite, pyrrhotite and arsenopyrite for (a) $^{56}Fe+^{32}S$, (b) ^{197}Au and (c) $^{75}As+^{32}S$.

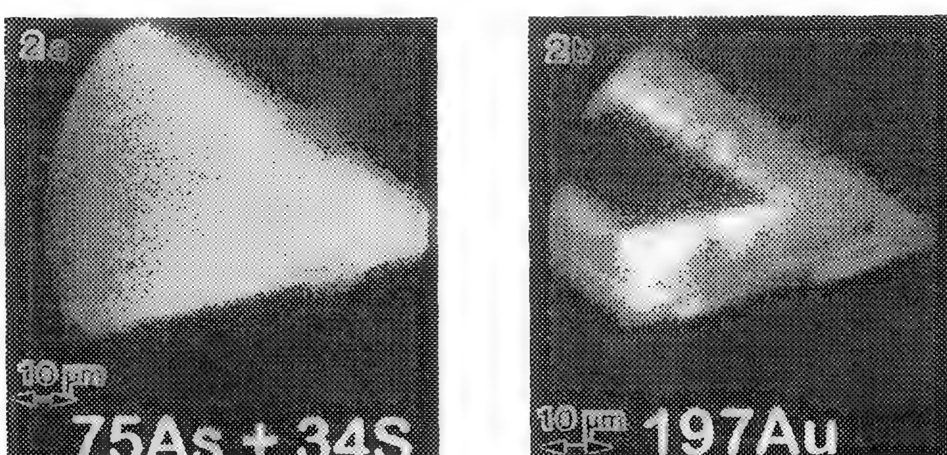

FIG. 2 SIMS direct ion images of an arsenopyrite grain for (a)^{197}Au and (b)$^{75}As+^{34}S$.

TRANSMISSION ELECTRON MICROSCOPE OBSERVATION OF DIAMOND / WC INTERFACE

Geun-Hong Kim and Chang-Hwan Chun

Agency for Defense Development, P.O.Box 35-4, Taejon 305-600, Korea

Commercial diamond coated WC-Co cutting tool has been investigated by transmission electron microscope (TEM) to understand the nucleation and growth of diamond on WC substrate. Cross-sectional specimens have been prepared by mechanical polishing followed by ion milling. TEM observations have been performed using analytical TEM, JEM 4000FX (JEOL Ltd.).

The surface of the coated diamond is composed of grains of 2 - 5 μm in diameter. Each main grain is formed by columnar subgrains of 10 - 50 nm in diameter with similar orientations. Cobalt, a binder in cemented carbide, within 5 μm in depth from the carbide surface has been found to be removed to increase the adhesion of diamond.

One of diamond subgrains, which has been grown large in [001] orientation on WC grains is shown in Fig.1. High density of twins are found on (111) plane starting from WC grain boundaries. It is thought that the interfacial stress between diamond layer and WC grains is accommodated by these twins.

Graphite layers of 10 - 40 nm in thickness are also found between diamond and WC as shown in Fig.2. However these graphite layers were scarcely observed revealing that most of diamond has grown from WC grains directly. Micro-diffraction pattern of graphite layer shows together the diffraction pattern of diamond with [01-1] symmetric axis which exists near graphite. The (200) interplanar spacing of diamond increased by 8% compared with theoretical value. This is in good agreement with high resolution observation. High resolution image of diamond grown on WC and micro-diffraction pattern of WC grain are shown in Fig.3. It is known that diamond has grown with coherency between (01-1) plane of WC (d = 0.1884 nm) and (200) plane of diamond (theoretically, d = 0.178 nm, measured, d = 0.192 nm). The observation that (200) interplanar spacing of diamond increased by 8% compared with theoretical value is similar to other result on diamond/Si interface showing 13% increase in (200) interplanar spacing of diamond [1]. It is thought that further study is required on this abnormal diamond structure.

Stacking faults are also observed in WC grains adjacent to diamond implying that these imperfections relieve the interfacial stress as twins do in diamond layer.

References

1. K. Kobayashi, S. Karasawa and T. Watanabe, J. Crystal Growth, 99, 1211 (1990)
2. The authors are grateful to Prof. Changmo Sung, University of Massachusetts Lowell, for providing samples investigated in this work.

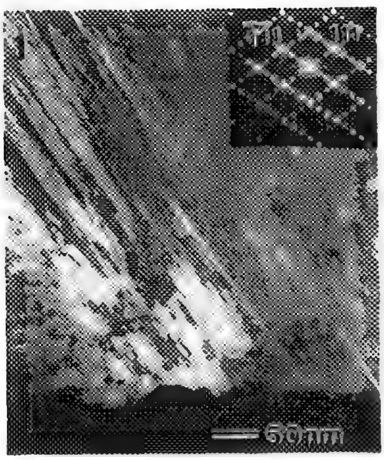

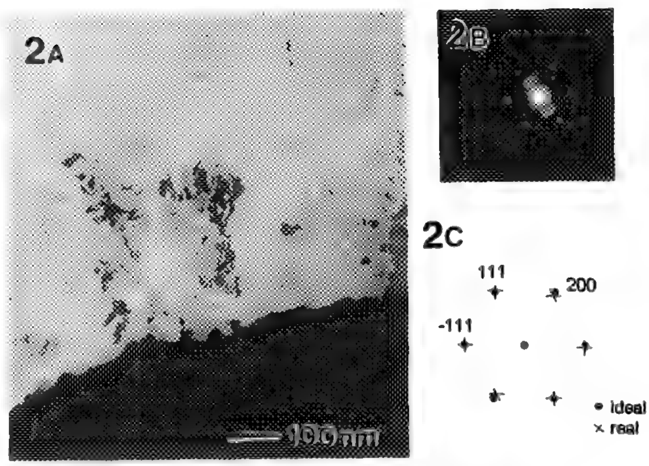

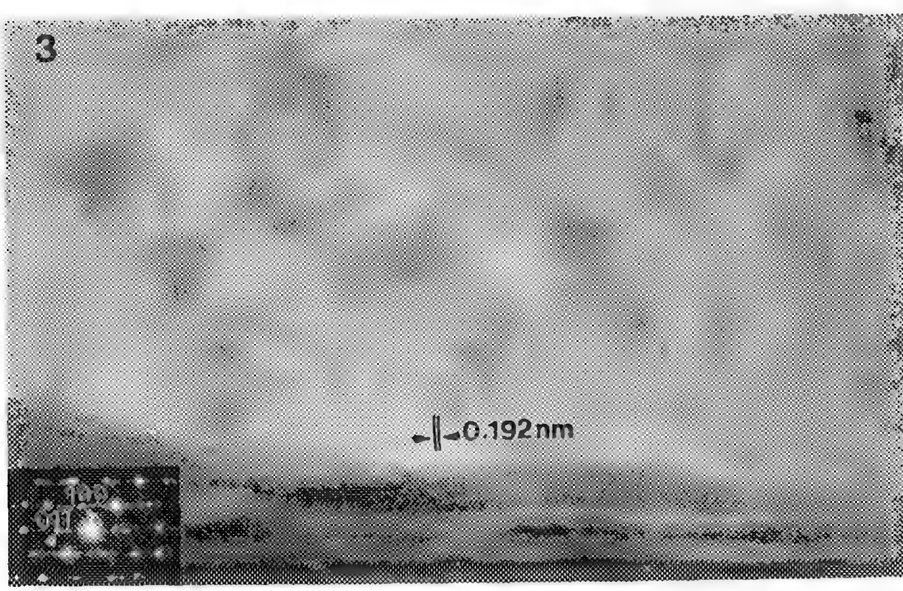

FIG.1. Dark field image with micro-diffraction pattern of twins in a diamond subgrain on WC.

FIG.2. (a) Dark field image, (b) micro-diffraction pattern of thin graphite layers between WC and diamond and (c) comparison of diamond [01-1] axis pattern in (b) with ideal pattern.

FIG.3. High resolution electron micrograph of diamond and WC interface with inserted micro-diffraction pattern of WC grain.

ENERGY-FILTERED ELECTRON DIFFRACTION FROM AMORPHIZED SOLIDS IN THE DEDICATED SCANNING TRANSMISSION ELECTRON MICROSCOPE (STEM)¶

A. N.Sreeram[†*], L.-C. Qin[†‡], A. J. Garratt-Reed[§] and L. W. Hobbs[†]

[†]Department of Materials Science & Engineering, [§]Center for Materials Science & Engineering, Massachusetts Institute of Technology, Cambridge, MA 02139 *now at David Sarnoff Research Center, Princeton, NJ 08543 [‡]now at NEC Corp., Tsukuba 305, Japan

There is significant current interest in understanding the structure of aperiodic solids, such as originally crystalline material amorphized by ion implantation, impact or application of massive pressures, or deposited amorphous thin films, which occupy small volumes. Radially-averaged real-space distribution functions can be derived from diffraction data, the best of which come from thermal neutron diffraction, which inconveniently requires large volumes. Neutron data are collectable in reciprocal space out to $q = 2\sin(\Theta/2)/\lambda = 70\ \mathrm{nm}^{-1}$, where Θ is the scattering angle and λ the wavelength, or about twice as far as for X-rays, which also require large diffracting volumes. Electron diffraction is the only recourse for very small volumes because of the much stronger interaction of the electron, but spectra must be energy filtered to remove the large inelastic scattering component. Recently, it has been shown[1] that useful electron diffraction data can be collected conveniently to at least $q = 16\ \mathrm{nm}^{-1}$ in the VG HB5 dedicated 100-kV field-emission STEM. This contribution details our experiences with improved collection in the VG HB603 instrument operating at 250 kV.

The HB5 used initially was fitted with a VG-designed serial EEL spectrometer, while the HB603 was initially fitted with a similar spectrometer, which was later replaced by a Gatan model 766 digi-PEELS parallel system. At the time the experiments were performed, spectrum imaging was not possible with the latter system. In order to acquire energy-filtered diffraction patterns, it was therefore necessary to remove the PIN-diode array, make an optical "slit" (out of black electrical tape: it was quite easy to apply two pieces of tape to the outer surface of the optical window, with a gap of about 0.5 mm between them), and arrange for a photomultiplier to detect the light passing through the slit. The parallel-detection EELS system was therefore effectively converted into a serial system. Although the slit was of fixed width, the lenses built into the Gatan optics allowed the dispersion, and hence the energy resolution, to be varied.

System control and data logging was performed initially by a Link Systems AN10000 computer, capable of recording up to 1024 data points in a line scan and incorporating a 10MHz voltage-to-frequency converter for image digitization. It was only capable, though, of pixel dwell times up to 65ms, 16-bit data and single line scans. All data from the HB5 and early data from the HB603 were recorded with this unit. A system was later assembled from commercial time/counter and digital/analogue expansion cards in a personal computer, running simple in-house software. This arrangement was capable of 32-bit data acquisition, 4096 data points per line, dwell times from 5 μs to 64 s, and counting input frequences up to 10MHz. The 10MHz voltage-to-frequency converter in the Link AN10000 was used with this system too. Data were logged to disk in ASCII format, ready for further processing. A signal conditioning amplifier (gain up to 10X and time constant up to 10 s) was used in the analog signal path in all cases. On the HB5, this amplifier was integral to the microscope; on the HB603 it was home-built.

Linescans through the (radial) diffraction patterns were obtained by setting the microscope to selected area diffraction mode and using the data logging system to generate the scan line and record the output of the scintillator. In a STEM, the camera length is determined by the scan amplitude, and the angular resolution by size of the collector aperture (modified by post-specimen optics, if fitted). In the HB5, a 100-μm aperture was typically used. In the HB603, a 1 mm aperture was used, but the post-specimen optics allowed this to be demagnified. The actual effective size, for the optical conditions employed, was not determined, but the size of the 000 spot was subjectively assessed to be significantly smaller than the width of the first diffuse scattering ring in the diffraction pattern.

Diffraction pattern line scans were calibrated against a crystalline reference, for example to the initial

crystalline state for solids undergoing amorphization in the electron beam. The diffracted intensity distribution was rendered into the form of a Zernicke-Prins interference function $S(q)$ normalized by a sharpening function representing the average atomic scattering factor in a composition unit [1]. Radial density (distribution) functions $g_e(r) = 4\pi r^2[\rho_e(r)-\rho_e] = 8\pi r \int_{-\infty}^{\infty} qS(q)\sin(2\pi qr)\, M(q)\, dq$ were derived from $S(q)$ using the Lorch modification function $M(q)$ [2]. Fig. 1 shows a result for $AlPO_4$, amorphized in the 250-keV electron beam of the HB603, from diffraction data collected out to 18 nm^{-1} using a < 2 eV window centered on zero loss [3]. Superimposed is the RDF deduced for the silica polymorph quartz (with which $AlPO_4$ is isomorphous) using data collected to 16 nm^{-1} in the HB5. The peak markings are from an X-ray study of hydrothermally-grown amorphous $AlPO_4$ [4] and agree well with the electron-deduced peaks.

Difficulties can be experienced while taking data of a serial nature on microscopes with field-emission guns because of poor emission stability. The HB5 had a particularly good gun vacuum and, provided the tip was flashed shortly before data acquisition was started, the emission stability was adequate in most cases. In early experiments with the HB603, the tip noise was a problem, evidencing itself as random noise in the data. The first attempt to overcome this problem was to acquire and sum multiple scans; the limit was set by the speed of the scintillator, but 10ms/pixel was usuable, allowing a single 1024-pixel line to be acquired in about 10 s. 100 lines could therefore be summed in a little over 1000 seconds. Later, as the new microscope settled, the gun vacuum improved, and the tip noise was a less significant problem; the multiple-line scanning technique continued to be used, however.

Another problem encountered was that of high-voltage and spectrometer stabilities. In both microscopes, an apparent energty drift of about 1 eV/minute was initially experienced. We believe that this drift was due to thermal instability of the high-voltage generator; on the HB603, the drift become insignificant once the high voltage was left on 24 h/day.

References

1. L. C. Qin and L. W. Hobbs, *J. Non-Cryst. Solids* **192&193** (1995) 456. 2. E. Lorch, *J. Physique* **C2** (1969) 229. 3. A. N. Sreeram, L. W. Hobbs, N. Bordes and R. C. Ewing, "Irradiation-induced amorphization of $AlPO_4$" *Nucl. Instrum. Meth.* **B** (1996, in press). 4. G. D. Wignall, R. N. Rohon, G. W. Longman and G. R. Woodward, *J. Mater. Sci.* **24** (1977) 1039.

¶This research was supported by the Basic Energy Sciences Division, U.S. Department of Energy under grant DE-FG02-89ER45396, utilizing MRSEC shared facilities supported by the National Science Foundation under award DMR94-00334.

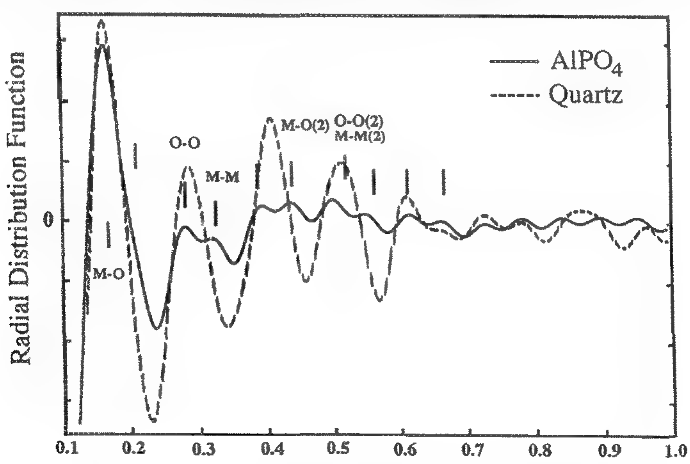

Fig. 1. RDFs derived for electron-amorphized $AlPO_4$, using the HB603, and quartz, using the HB5. The peak positions and ascriptions are from an X-ray study of hydrothermally-grown amorphous $AlPO_4$ [4].

CBED AND HREM STUDY OF DECAGONAL QUASICRYSTALS

M. Tanaka, K. Tsuda, and K. Saitoh

**Research Institute for Scientific Measurements,
Tohoku University, Sendai 980-77, JAPAN**

Decagonal quasicrystals have been investigated by convergent-beam electron diffraction (CBED) and transmission electron microscopy. Figure 1 shows possible pentagonal and decagonal point groups.[1] The CBED method has revealed that the decagonal quasicrystals found so far belong to the space groups of noncentrosymmetric $P\overline{10}m2$ and centrosymmetric $P10_5/mmc$.

Dark-field microscopy has revealed the existence of inversion domains with an antiphase shift of $c/2$ at the domain boundaries in the alloys with space group $P\overline{10}m2$.[2] High-resolution electron microscopy (HREM) has revealed the existence of specific pentagonal atom clusters in the Al-Ni-Fe, Al-Cu-Co and Al-Ni-Co alloys. Figure 2 shows a HREM image of $Al_{70}Ni_{15}Fe_{15}$ belonging to space group $P\overline{10}m2$.[2] The atom clusters of an about 2nm diameter are clearly seen as indicated by a black circle. The clusters are polar or noncentrosymmetric due to the dark pentagon at their centers. All the clusters in domain A have one sense of polarity and those in domain B the other sense. It should be noted that the HREM image of the cluster columns was found to be pentagonal at an accelerating voltage of 200kV but nearly decagonal at higher than 300kV.[3]

A phase transformation from $P\overline{10}m2$ to $P10_5/mmc$ was found to occur in Al-Ni-Fe alloys with changes of Ni and Fe compositions.[4] The transformation occurs through the mixing of atom cluster columns with the positive and negative senses, as schematically shown in Fig.3. The 10_5 screw axes appear in space group $P10_5/mmc$ between the neighboring two pentagonal cluster columns as seen in Fig. 3.

Al-Ni-Rh and Al-Ni-Ir alloys were found also to belong to space group $P10_5/mmc$.[5] However, they do not have pentagonal cluster columns but have decagonal cluster columns. 10_5 screw axes exist at the centers of the columns as well as between the neighbouring two columns. This implies that there exist two types of quasicrystal structures under space group $P10_5/mmc$.

Structural models were reported for Al-Ni-Co and Al-Cu-Co alloys with space group $P10_5/mmc$ by assuming the projection of the cluster column to be decagonal. We have constructed structural models for Al-Ni-Fe, Al-Ni-Co and Al-Cu-Co alloys with space groups $P\overline{10}m2$ and $P10_5/mmc$ on the basis of the pentagonal atom cluster columns.[6]

References

1. M. Saito *et al.*, *Jpn. J. Appl. Phys.* 31 (1992) L109.
2. K. Tsuda *et al.*, *Jpn. J. Appl. Phys.* 32 (1993) 129.
3. K. Tsuda *et al.*, *Phil. Mag.* A, to be published.
4. K. Saitoh *et al.*, *Phil. Mag.* A73 (1996) 387.
5. K. Tsuda *et al.*, *Phil. Mag.* Lett., in press.
6. K. Saitoh *et al.*, in preparation.

7. The authors are grateful to the Dr. A. P. Tsai, Dr. A. Inoue and Prof. T. Masumoto for supplying the good quality quasicrystals.

1

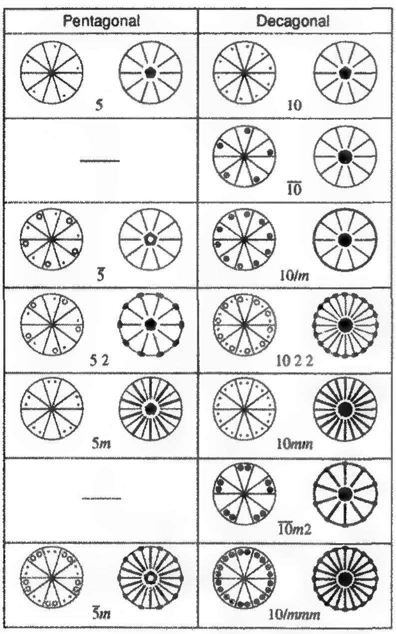

3

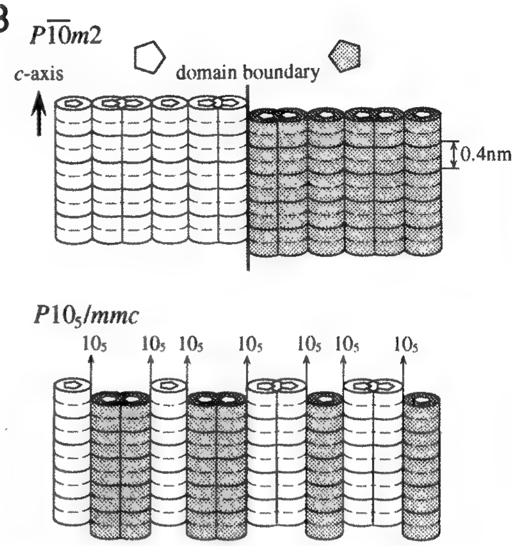

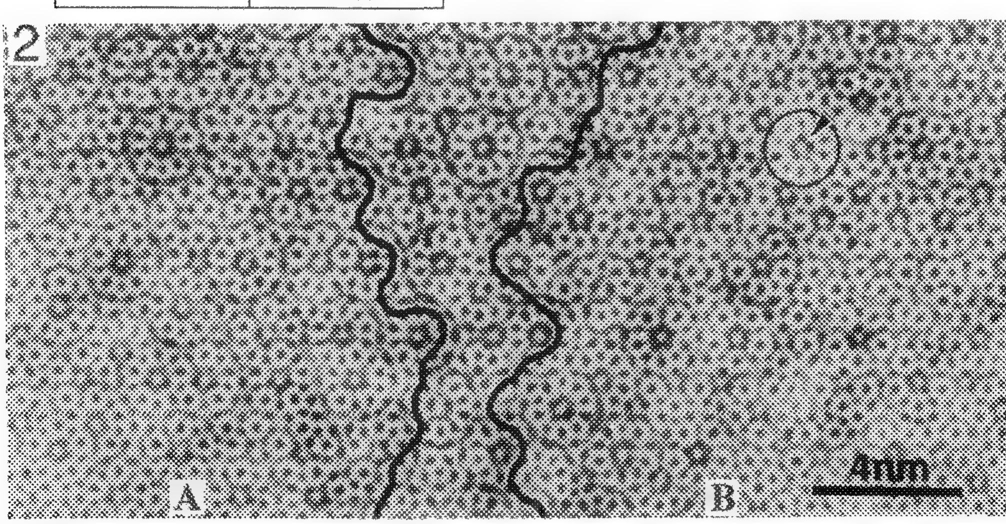

FIG. 1 Pentagonal and decagonal point groups constructed by analogy with trigonal and hexagonal point groups.

FIG. 2 High-resolution electron micrograph of $Al_{70}Ni_{15}Fe_{15}$ taken at an incidence parallel to the decagonal axis. The polarity of the pentagonal cluster columns is opposite between areas A and B.

FIG. 3 Schematic diagrams of cluster column arrangements in the $P\overline{10}m2$ and $P10_5/mmc$ phases.

CHARGE-DENSITY WAVE MODULATIONS IN THE TRANSITION METAL CHALCOGENIDES

J.C. Bennett* and F.W. Boswell**

*Department of Physics, Acadia University, Wolfville, Nova Scotia, Canada B0P 1X0
**Deptment of Physics, University of Waterloo, Waterloo, Ontario, Canada, N2L 3G1

The transition metal chalcogenides, due to the typically large covalency of the metal-chalcogenide bonds, often adopt low-dimensional structures and exhibit charge-density wave (CDW) modulations[1]. Incommensurate (IC) or commensurate (C) modulations structures are observed as well as a rich variety of phase transitions driven by the temperature dependence of the CDW amplitude and phase. Defects of the CDW modulation, including antiphase boundaries (APB) and discommensurations (DC), are of determinate importance for the mediation of these phase transitions. The microstructural phenomena occurring in the quasi-one-dimensional chalcogenides will be surveyed with emphasis on two representative systems: the $Nb_{1-x}Ta_xTe_4$ solid solution and the $M_xNb_3Te_4$ (M = In or Tl) intercalation compound.

The $Nb_xTa_{1-x}Te_4$ compounds are based on a tetragonal subcell with axes (a x a x c) and consist of an extended chain of metal atoms centered within an antiprismatic cage of Te atoms. At room temperature, the CDW modulations are commensurate ($2a$ x $2a$ x $3c$) for $TaTe_4$ and incommensurate ($\sqrt{2}a$ x $\sqrt{2}a$ x $\sim 16c$) for $NbTe_4$. A full spectrum of composition- and temperature-dependent CDW phase transitions is observed including C to IC, C to C and IC to IC transitions. Two interdependent processes are at work: (i) lock-in, involving changes in the modulation periodicity along each chain, and (ii) relative phase adjustments of the CDW on adjacent chains leading to changes in the unit cell dimensions perpendicular to the chain axis. Satellite dark-field (SDF) images reveal a fascinating array of microstructural phenomena accompanying the CDW transitions. For example, in $TaTe_4$ a three-dimensional network of APBs associated with phasing errors of the CDW on neighbouring chains is observed at room temperature (Fig. 1a). On heating, these APBs become mobile and interact to reduce the defect density (Fig. 1b). At ~ 450 K, a new C phase based on a ($\sqrt{2}a$ x $\sqrt{2}a$ x $3c$) supercell is observed to nucleate and grow out from the remaining APBs producing new defects where the various domains meet (Fig. 1c, d). On further heating, these defects evolve into multiple fringes, eventually forming a regular array of discommensurations walls above the C to IC transition at ~ 550 K (Figure 2). Similar behaviour, although differing substantially in detail, is observed for the other members of the $Nb_xTa_{1-x}Te_4$ series and reflect the subtle interplay of Fermi surface and interchain coupling effects in determining the CDW modulation structures.

In Nb_3Te_4, zigzag chains of Nb atoms are modulated by a commensurate CDW with onset temperature of ~100 K.[2] Hexagonal tunnels large enough to accommodate In or Tl ions lie adjacent to the chains. In-situ electron diffraction experiments reveal the CDW transition temperature is sharply increased for both intercalates while the modulation periodicity is significantly decreased and adopts an incommensurate value (Fig. 3). SDF images reveal the CDW microstructures differ in character and for In and Tl intercalation (Fig. 4). Diffraction effects attributed to ordering of the intercalate in the tunnels are observed for $In_xNb_3Te_4$ (Fig. 3). Thus the $M_xNb_3Te_4$ system allows unique insight into the effect of neighbouring intercalate rows on the CDW of a quasi-one-dimensional metal.

1. Charge-density Waves in Solids, Eds. L. Gorkov and G. Gruner, North Holland Pub., Amsterdam (1989)
2. Y. Ishihara and I. Nakada, Sol. State Comm. 45, 129 (1983).

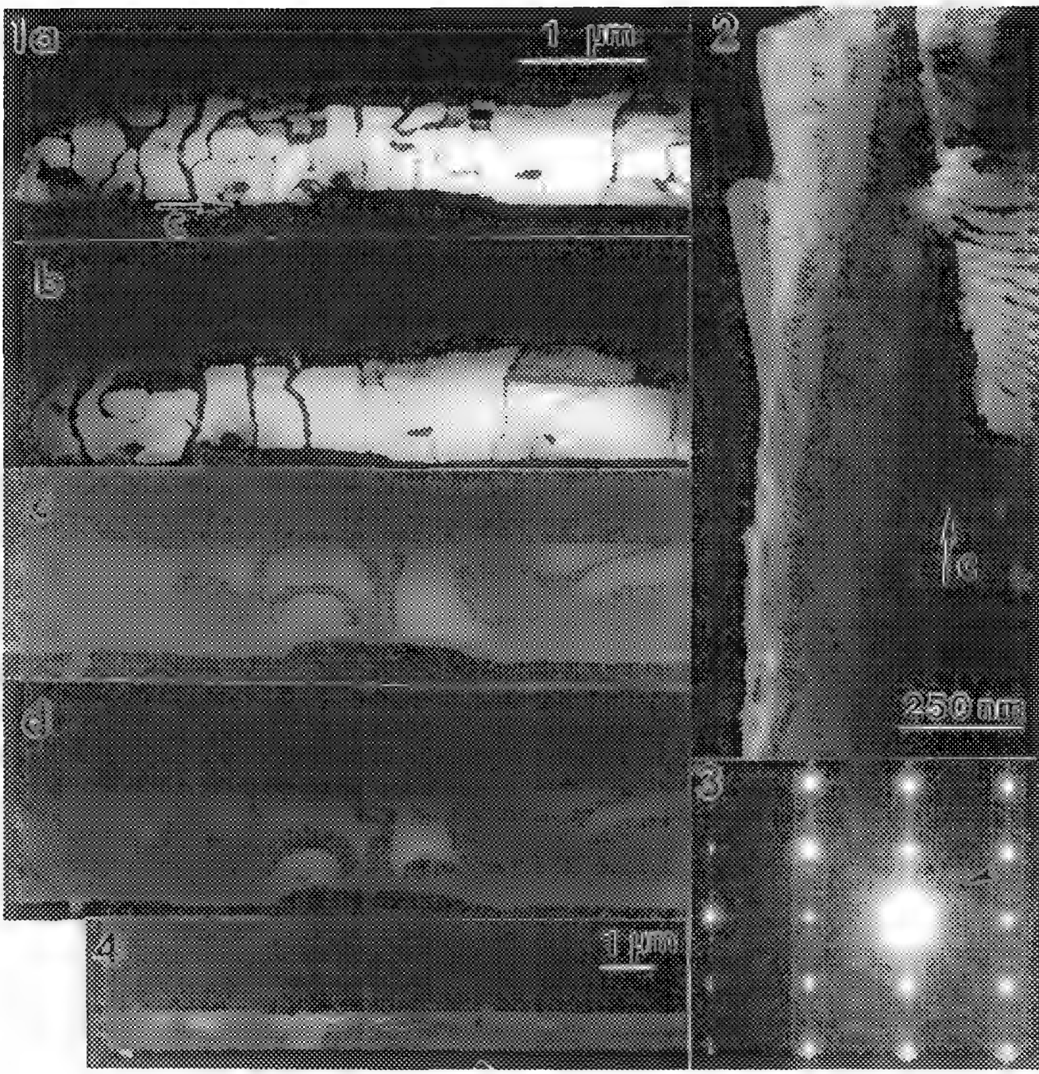

Fig. 1: SDF images of the same region of a $TaTe_4$ crystal observed during heating to the C to C transition. a) at room temperature, b) ~400 K, c) an d) ~450 K. The regions with dark contrast have transformed to the high-temperature C phase. The direction of the c-axis is indicated by an arrow.

Fig. 2: SDF image of a $TaTe_4$ crystal heated into the IC state at ~550 K.

Fig. 3: $[1\bar{1}00]$ zone axis electron diffraction pattern of $In_xNb_3Te_4$ at 43 K. The superlattice reflections (arrow) appear due to the CDW at ~100 K while the streaks, also present at room temperature, are associated with intercalate ordering.

Fig. 4: SDF image of $Tl_xNb_3Te_4$ crystal. Large irregular domains showing light and dark contrast are visible.

THE STRUCTURE AND PROPERTIES OF MISFIT LAYER COMPOUNDS

A.E. Curzon

Physics Department, Simon Fraser University, Burnaby, British Columbia, Canada, V5A 1S6.

The purpose of this article is to provide an introduction to the class of compounds known as misfit layer compounds.

An example of a misfit layer compound is $(NdS)_{1.2}NbS_2$. In the present study this material was made by heating appropriate amounts of sulphur powder, niobium powder and neodymium chips in an evacuated quartz tube at 850°C for 12 hours.[1] A subsequent five day process involving transport and back transport at 1000°C in the presence of iodine as transport agent led to the formation of lustrous crystal platelets suitable for electron microscopy and electron diffraction studies. The orthorhombic material consists of alternate layers of NdS (two atoms thick) and layers of NbS_2 (three atoms thick) each perpendicular to the c-axis. Fig. 1 shows a [100] view of the structure observed in recent studies.[1] Though it differs from the structure reported in other work[2], both reported forms have features in common which are characteristic of all misfit layer compounds. The NdS and NbS_2 layers have the same periodicity along the b and c directions but the periodicities along the a direction are different and incommensurate. It is this difference in periodicities in one direction which distinguishes the misfit layer compounds from other layer compounds. The a lattice parameters in $(NdS)_{1.2}NbS_2$ are a = 0.5625 nm for the NdS layers and a = 0.331 nm for the NbS_2 layers.[1,2] In order to calculate electron diffraction patterns the structure may be represented by an orthorhombic super unit cell with b = 0.5733 nm, c = 2.266 nm and a = 1.671 nm, which corresponds approximately to three unit cells of NdS and five unit cells of NbS_2 along the [100] direction. An [010] view of this model structure is shown in fig. 2. The chemical formula represented by the super unit cell is $(NdS)_{1.2}NbS_2$ because the cell contains 24 sets of NdS and 20 sets of NbS_2.

Notice that the Nb atoms in the upper layer of the two layers of NbS_2 in the unit cell of fig. 1 are not directly above Nb atoms in the lower layer. In the alternative structure[2], the Nb atoms in the upper layer appear directly above those in the lower layer when the cell is viewed along [100] as is the case for fig. 1 (i.e. their co-ordinates along the c direction differ by z = 1/2). This is the only difference between the two structures. Both the NdS sublattice and the NbS_2 sublattice of the alternative structure have the same Fm2m symmetry so that, for example, the 110 reflection from each sublattice is forbidden and such reflections cannot occur by double diffraction. In the structure of fig.1 the NbS_2 sublattice has Am2m symmetry and its 110 reflection is allowed. The corresponding reflection in the super cell description is 510. This diffraction reflection was observed in the present studies which justified the assumption that the Nb atoms in one of the two layers in a unit cell were displaced with respect to the structure reported by others.[2] The nearest neighbour distances and bond angles are the same in both structures so that there is little energy difference between the two forms. Their occurrence in different experiments is presumably associated with slightly different methods of manufacture.

There are many other misfit layer compounds of the type $(MS)_nTS_2$ where M = metal and T = transition metal. They occur with various structures (including triclinic[3]) and some of these will be discussed. The adjacent arrays of sulphur atoms of the MS and of the TS_2 layers have rectangular symmetry and

hexagonal symmetry, respectively. This gives rise to the possibility of orientation variants and complicated electron diffraction patterns such as those reported for $(SnS)_{1.17}NbS_2$.[4] The MS layers are intercalated between the metal-dichalcogenide layers and therefore staging and polytypes occur.[5]

A wide range of the physical properties of the misfit layer compounds has been studied. These include electrical transport[6,7], optical absorption and reflectivity[8,9], Raman spectroscopy[10] and magnetic properties[3,7]. Fractional superconductivity in $(LaS)_{1.2}NbS_2$ has been reported[6] by which is meant that a part of the specimen enters the superconducting state. Resonant photo emission and x-ray absorption spectra studies indicate that the valence of the metal M is 3 in those misfit layer compounds with M = La, Ce or Sm.[11] A selection of these physical properties will be reviewed in order to show that the misfit layer compounds are an interesting class of compounds well worth further intensive study.

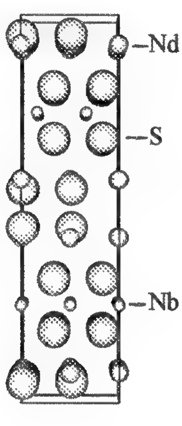

FIG 1 - The idealised orthorhombic structure of $(NdS)_{1.2}NbS_2$ viewed along [100]

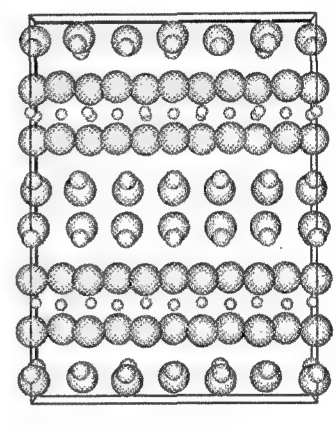

FIG 2 - The idealised orthorhombic structure of $(NdS)_{1.2}NbS_2$ viewed along [010]

References

1. X. Meng-Burany and A.E. Curzon, *Micron*, (1996) - accepted for publication.
2. A. Lafond et al., *J. Solid St. Chem.*, 103(1993)458.
3. G.A. Wiegers et al., *J. Phys: Condens. Matter*, 3(1991)2603.
4. S. Kuypers et al., *Acta Cryst.*, A45(1989)291.
5. S. van Smaalen and J. L. de Boer, *Phys. Rev. B*, 46(1992)2750.
6. T. Terashima and N. Kojima, *J. Phys. Soc. Japan*, 63(1994)658.
7. G.A. Wiegers and R.J. Haange, *J. Phys: Condens. Matter*, 2(1990)455.
8. T. Takahashi et al., *J. Phys. Chem. Solids*, 34(1973)1131.
9. C. H. Rüscher et al., *J. Phys: Condens. Matter*, 6(1994)2117.
10. M. Hangyo et al., *Phys Rev. B*, 48(1993)11291.
11. A.R.H.F. Ettema et al., *Phys Rev. B*, 49(1994)10585.
12. The author thanks the Natural Sciences and Engineering Research Council, Ottawa, for research funds.

SUPERSTRUCTURES AND ORDERING PHENOMENA IN CERAMIC SUPERCONDUCTORS

R. Gronsky

Department of Materials Science and Mineral Engineering, and Materials Sciences Division, E.O. Lawrence Berkeley National Laboratory, University of California, Berkeley, CA 94720-1760

It is now well established that the phase transformation behavior of $YBa_2Cu_3O_{6+\delta}$ is significantly influenced by matrix strain effects, as evidenced by the formation of accommodation twins, the occurrence of diffuse scattering in diffraction patterns, the appearance of tweed contrast in electron micrographs, and the generation of displacive modulation superstructures, all of which have been successfully modeled via simple Monte Carlo simulations.[1] The model is based upon a static lattice formulation with two types of excitations, one of which is a change in oxygen occupancy, and the other a small displacement of both the copper and oxygen sublattices. Results of these simulations show that a displacive $\sqrt{2} \times \sqrt{2}$ superstructure forms very rapidly in a morphology of finely textured domains, followed by domain growth and a more sharply defined modulation wavelength, ultimately evolving into a strong <110> tweed with 5 nm to 7 nm period. What is new about these findings is the revelation that both the small-scale deformation superstructures and coarser tweed morphologies can result from displacive modulations in ordered $YBa_2Cu_3O_{6+\delta}$ and need not be restricted to domain coarsening of the disordered phase. Figures 1 and 2 show a representative image and diffraction pattern for fully-ordered ($\delta = 1$) $YBa_2Cu_3O_{6+\delta}$ associated with a long-period <110> modulation.

In thin film morphologies, $YBa_2Cu_3O_{6+\delta}$ assumes other metastable structures associated with deviations from stoichiometry, the most characteristic being multiple CuO layers in the ordered stacking sequence. Films were deposited as c-oriented $YBa_2Cu_3O_7$ on both magnesia and alumina substrates by laser ablation under 200 millitorr of oxygen and a substrate temperature of 750°C. A buffer layer of approximately 10 nm of calcium titanate promoted the growth of 300 nm thick films with a critical current density in the range of 10^6 A/cm^2 at 74 K. Cross-sectional specimens prepared by ion milling were examined at 200 kV and 800 kV at the LBNL's National Center for Electron Microscopy, and compared to simulations of mixed-phase microstructures using the same Monte Carlo methodologies described above.[2] The theoretical and experimental results compared in figures 3 and 4 show excellent agreement, and indicate the mechanism of transformation from $Y_2Ba_4Cu_7O_{14}$ to $YBa_2Cu_3O_7$ is one of CuO loss via out-diffusion to grain boundaries and free surfaces. Orphan CuO segments remain in the microstructure as extrinsic stacking faults, and these are believed to be strong flux-pinning sites. The inverse reaction does not generate such favorable homogeneous distributions of stacking faults because elastic compensation at surfaces and grain boundaries pins the strained segments of the microstructure containing multiple CuO layers (note considerable lattice strain visible in figure 4), and forbids their uniform distribution throughout the film.

Parallel attempts at nanostructural engineering in the compliant Bi-Sr-Ca-Cu-O system by inert ion intercalation have brought new understanding of the effects of CuO layer spacing on superconducting behavior.[3]

---

[1]M. Goldman, C.P. Burmester, L.T. Wille, and R. Gronsky, *Phys. Rev. B* **50** (2), 1137 (1994).
[2]M. Fendorf, M.E. Tidjani, C.P. Burmester, L.T. Wille, and R. Gronsky, *in* High T_c Superconductor Thin Films, L. Correra (Editor), Elsevier Science Publishers B.V., (1992), p. 771.
[3]X. Xiang, W. Vareka, A. Zettl, J. Corkill, T. Barbee, M. Cohen, N. Kijima, and R. Gronsky, *Science* **254**, 1487 (1991).

This work is supported by the Division of Materials Sciences, Offices of Basic Energy Sciences, U.S. Department of Energy under contract No. DE Ac03 76 SF00098.

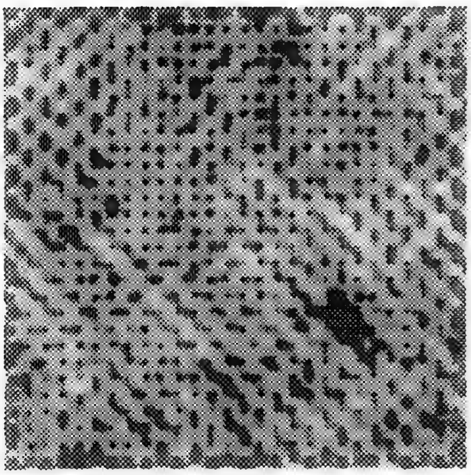

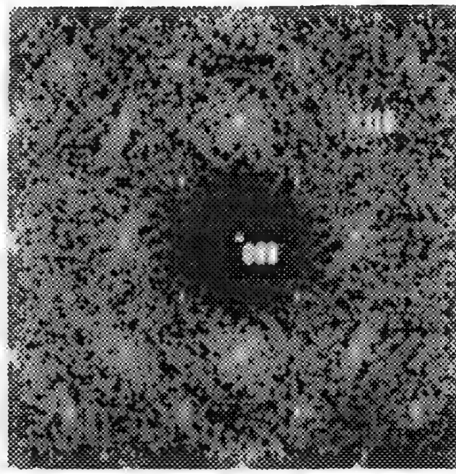

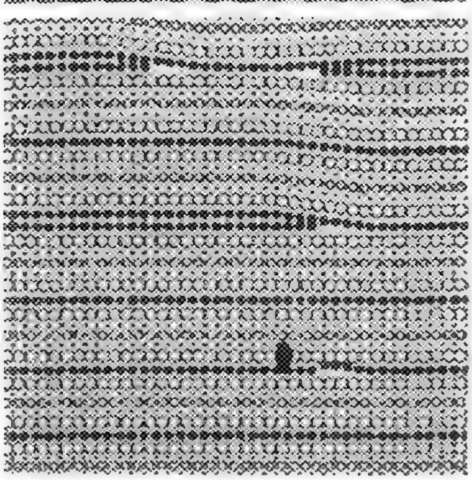

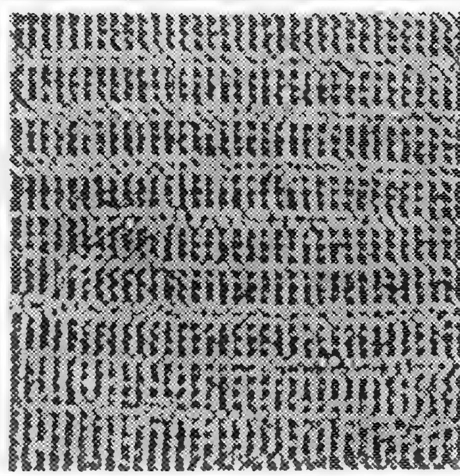

FIG. 1 Simulated microstructure of $YBa_2Cu_3O_7$ after several thousand Monte Carlo steps per atom showing evolution of tweed contrast due to a long period <110> modulation.

FIG. 2 Fourier transform of simulated microstructure showing classic <110> striations in reciprocal space associated with the soft-mode deformation that leads to tweed.

FIG. 3 Simulation-generated snapshot of mixed phase $Y_2Ba_4Cu_7O_{14}$ + $YBa_2Cu_3O_7$ microstructure. Filled circles correspond to CuO planes (Cu sites), and show several bifurcation events.

FIG. 4 Experimental high resolution image showing Cu sites as white dots. Note bifurcation to entrapped double CuO layer in center of image. Extended sections of double CuO layers are representative of the $Y_2Ba_4Cu_7O_{14}$ phase.

SHORT-RANGE ORDER OF OXYGEN VACANCIES IN STABILIZED CUBIC ZrO_2

Z.-R. Dai* and Z.L. Wang#

* Beijing Laboratory of Electron Microscopy, Chinese Academy of Sciences, P.O. Box 2724, Beijing 100080; and Department of Materials Physics, University of Science and Technology Beijing, Beijing 100083, China; currently at: Department of Materials Science and Enginering, University of Washington, Seattle WA 98198, USA.

School of Materials Science and Engineering, Georgia Institute of Technology, Atlanta Georgia 30332.

Diffuse scattering of stabilized cubic zirconia is an interesting subject for many years because it is correlated to the local atomic arrangements that deviate from the average structure, thus, it is responsible for many important physical properties of the material, such as electric conductivity and structural stability. Much research work was performed using X-ray and neutron diffraction. As limited by the nature of these techniques, however, large size crystals are required to perform the experiments, thus, the results are a statistical average over a larger volume containing defects, interfaces and dislocations. In this paper, electron diffraction is used to characterize the diffuse scattering of submicron size cubic ZrO_2 partially stabilized with MgO and Y_2O_3. Kinematical electron diffraction theory is applied to calculate the diffuse scattering patterns and the Cowley's short-range order (SRO) parameters. Discussion relating to short-range correlation between oxygen and vacancy, vacancy and vacancy is given.

A partially stabilized zirconia ceramics with MgO (10% mol) and Y_2O_3 (1% mol) was prepared by sintering and solution-treatment at 1700 °C for 4 h after milling and shaping under isostatic pressure [1]. TEM observations were made at 120 kV in a Philips CM12 transmission electron microscope.

The specimen is composed of cubic, tetragonal and monoclinic phases. These phases are oriented following $(100)_m\ [010]_m \parallel \{100\}_t <100>_t \parallel \{100\}_c <100>_c$ [2]. Figures 1(A)-(C) show a set of experimental electron diffraction patterns of the specimen. In addition to the strong Bragg reflections, diffuse scattering is clearly seen, which is highly intensive and confined in reciprocal space to a regular geometrical pattern exhibiting the translation symmetry of the b.c.c. reciprocal lattice. Dark-field imaging showed that diffuse scattering came only from the cubic phase (Fig. 2). Extensive data analysis indicated that the local order of oxygen vacancies is the major source for producing diffuse scattering [1]. Diffuse scattering is an indication in change of transition state from a disordered cubic fluorite structure to an ordered superstructure. Kinematical electron scattering theory is applied to analyze the observed diffuse scattering, and the result shows that Cowley's SRO parameters are related to the Fourier coefficients of the diffuse scattering intensity distribution in three-dimensional reciprocal space [3]. Geometrical analysis showed that the diffuse scattering in reciprocal space can be described by a model composed of 8 ellipsoids (Fig. 3). An experimentally observed diffuse scattering pattern is the intersection of the Ewald sphere with the ellipsoidal model. If the width of the ellipsoid surface is truncated by a Gaussian function, the calculated diffuse scattering patterns are shown in Figs. 1(a-c). The main features of the diffuse scattering are clearly shown. The SRO parameters were calculated and the results are given in Table 1. The values of $\alpha(lmn)$ specify the degree to which the neighbors of one sort of atom tend to be preferably of the same sort or of the opposite sort. If $\alpha(lmn)$ is positive, the vacancies tend to clump together with vacancies and oxygen tend to clump together with oxygen. If $\alpha(lmn)$ is negative, the vacancies tend to clump together with oxygen. Therefore, the values of $\alpha(lmn)$ reflect the short-range order in the considered system. The decrease of $\alpha(lmn)$ with the increase of inter-ion distance gives the range of order. For ZrO_2, it is concluded that the oxygen vacancy-oxygen vacancy pairs are preferably linked by the $\mathbf{r}_{<200>}$ and $\mathbf{r}_{<310>}$ position vectors of anionic sublattice of f.c.c. fluorite structure, and oxygen anion-oxygen vacancy pairs are preferably linked by $\mathbf{r}_{<110>}$, $\mathbf{r}_{<211>}$ and $\mathbf{r}_{<220>}$, where $\mathbf{r}(lmn) = l\mathbf{a}/2 + m\mathbf{b}/2 + n\mathbf{c}/2$ indicates the position of oxygen anions in the sublattice. The order is limited to approximately 0.8 nm (the lattice constant of cubic zirconia a = 0.517 nm). Dynamical diffraction theory for a system containing SRO has been developed [4] to quantitatively simulate the diffraction patterns.

[1] Z.-R. Dai, Z.L. Wang, Y.R. Chen, H.Z. Wu and W.X. Liu, W.X., Philos. Mag. A (1996), in press.
[2] Z.-R. Dai et al., Metall. Sinica, A4 1991) 471.
[3] Z.-R. Dai, Z.L. Wang and W.X. Liu, Philos. Mag. A (1996), in press.
[4] Z.L. Wang, Acta Cryst. A, in press (1996).

1

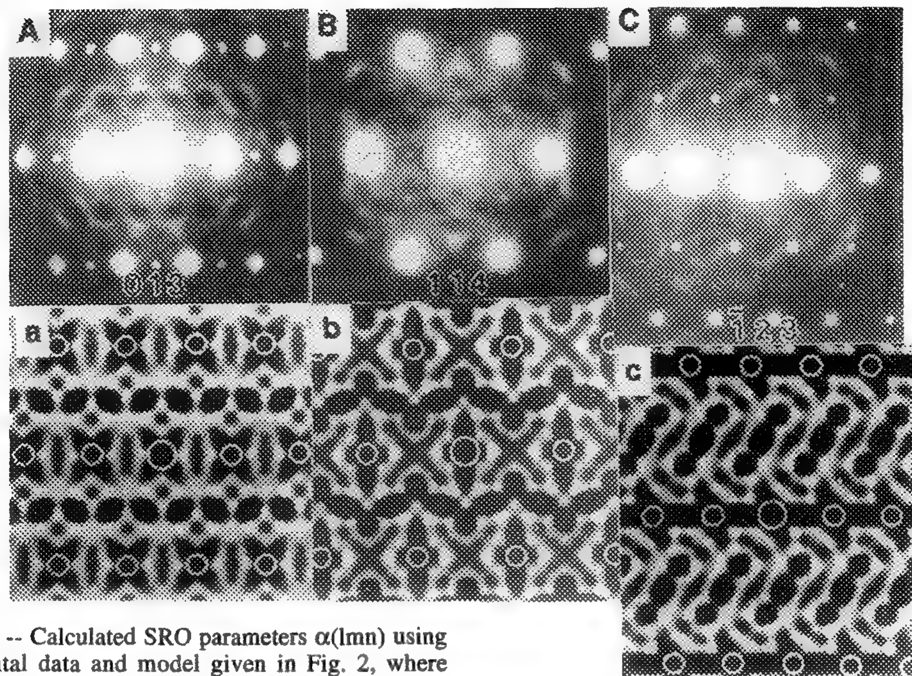

TABLE 1 -- Calculated SRO parameters α(lmn) using experimental data and model given in Fig. 2, where **r**(lmn) = l**a**/2 + m**b**/2 + n**c**/2 is relative position of the anion sublattice.

j	*lmn*	α(*lmn*)	j	*lmn*	α(*lmn*)	j	*lmn*	α(*lmn*)
1	100	0.000	5	210	0.000	8	300	0.000
2	110	-0.087	6	211	-0.051		221	0.000
3	111	0.000	7	220	-0.116	9	310	0.071
4	200	0.122				10	311	0.000

2

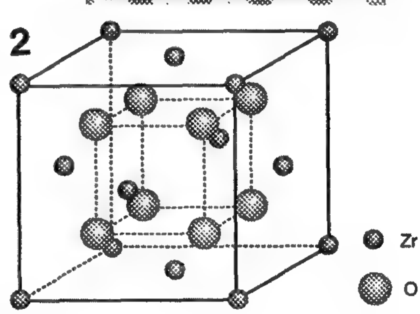

3

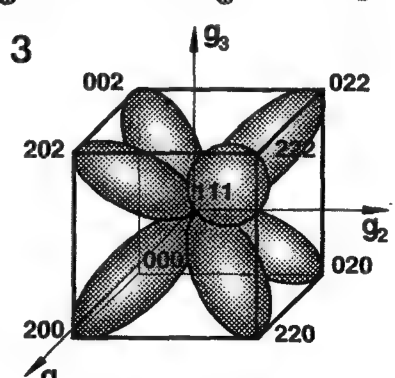

FIG. 1 Experimental electron diffraction patterns (A-C) with diffuse scattering and corresponding simulated patterns (a-c) using the kinematical diffraction theory.
FIG. 2 The unit cell structure of the cubic ZrO_2, where the oxygen cage is shown.
FIG. 3 A three-dimensional geometrical shell model of diffuse scattering intensity distribution in the reciprocal unit cell.

STACKING SEQUENCES OF THE CRYSTALLITES IN Co-Sm FILMS

B. W. Robertson and Y. Liu

Center for Materials Research and Analysis, and Department of Mechanical Engineering, University of Nebraska, Lincoln, NE 68588-0656.

Magnetic thin films sputtered from the Co-Sm system have been shown to be promising as recording media. High coercivities of up to 4.0 kOe [1] have been obtained from Co-Sm films. Recent microstructure characterization of Co-Sm films deposited by the DC magnetron sputtering has shown that the microstructure is composed of the amorphous matrix and crystallites with a grain size of about 5 nm [2]. As different sputtering processes have different dynamics for the formation of the nanostructure, phases formed could be different from those predicted by the equilibrium phase diagram. Crystal structure determination is important for understanding the high anisotropy and epitaxy growth of the Co-Sm films. The crystal structure of the crystallites was identified to be a close-packed structure. However, the stacking sequence changes from crystallite to crystallite. This paper describes the detailed high resolution electron microscopy (HREM) study of the stacking sequence of the crystallites in Co-Sm films. It is found that the stacking near the Cr underlayer tends to be hexagonal (ABAB) stacking. As the film grows, the stacking sequence is disturbed and three layer stacking, four layer stacking and random stacking are formed.

Figure 1 shows the crystallites distributed in the amorphous matrix of a Co-Sm film. The grain size of the crystallites is about 5 nm. In the $[1\bar{2}0]$ orientation, if the stacking direction is set horizontal, the relative stacking positions of A layers, B layers and C layers of the close-packed structure are projected at three levels with equal spacing. The A layers, B layers and C layers are then identified by their relative positions. Figure 2-4 show the stacking sequence taken from three different crystallites. The crystallite in Figure 2 is located next to a Cr grain in the underlayer. The Co-Sm crystallite is epitaxially $(\bar{1}100)$ $[0001]$ // Cr $(\bar{1}2\bar{1})[\bar{1}01]$ grown on the Cr grain. The Co-Sm layer is basically a two-layer stacking, ABAB (or ACAC), with a stacking fault as indicated by the arrows. The crystallite images in Figures 3 and 4 were recorded in a region about 25 nm away from the Cr underlayer. Three repeating unit cells of the stacking ABAC and some random stacking are observed in Figure 3. Three repeating unit cells of ABC stacking (FCC structure), four repeating unit cells of AB stacking (HCP structure) and some random stacking are observed in Figure 4. The simulated HREM images based on the close-packed structure models mentioned above show excellent match with the TEM images.

Acknowledgments The Authors wish to thank X. Zhao for TEM specimen preparation, G. Krichau for effort in maintenance of the CMRA CFEM, Professor Z.S. Shan for preparing the films, Professor D. J. Sellmyer and S.H. Liou for discussions. Research is supported by ARPA/NSIC under Grant MDA 972-93-1-0009, and NSF under grants DMR 9222976 and OSR 9255225.

1. D. J. Sellmyer, Z. S. Shan, Y. Liu, S. H. Liou, S. Malhotra and B. W. Robertson, Scripta Metall. et Mater. Vol.33, pp 1545-1552, 1995.
2. Y. Liu, B.W. Robertson, Z. S. Shan, S. Malhotra, M. J. Yu, S. K. Renukunta, S. H. Liou, and D. J. Sellmyer, IEEE Trans. Magn., Vol. 6. 4035-4037, 1994.

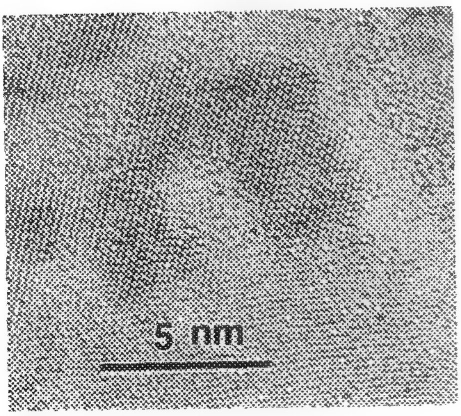

Figure 1. HREM micrograph showing the crystallites in the Co-Sm film.

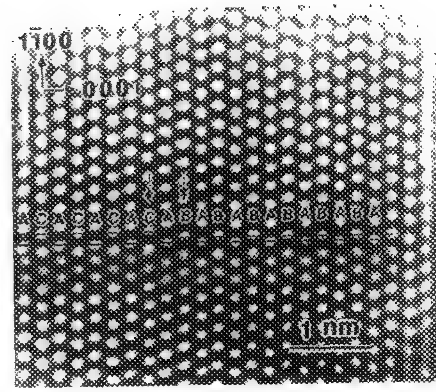

Figure 2. A [11$\bar{2}$0] zone axis HREM image taken from a crystallite grown on a Cr grain in the Cr underlayer. The structure is mainly ABAB stacking with a stacking fault.

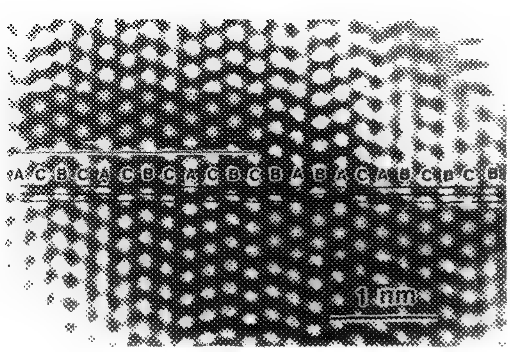

Figure 3. A [11$\bar{2}$0] zone axis HREM image taken in a region about 25 nm away from the Cr underlayer. Three repeating unit cells of the stacking ABAC are observed.

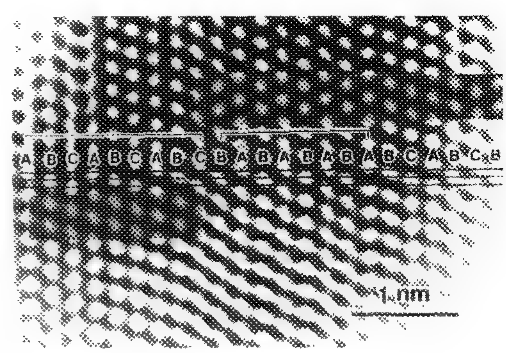

Figure 4. A [11$\bar{2}$0] zone axis HREM image taken in a region about 25 nm away from the Cr underlayer. Three repeating unit cells of the stacking ABC and four repeating unit cells of the stacking AB are observed.

CAN THE ICOSAHEDRAL PHASE BE MODELED AS A CRYSTAL ?

Weimin Bian and Yimei Zhu
Materials Science Division, Brookhaven National Laboratory, Upton, NY 11973

We propose a crystal model that is in excellent agreement with the experimental electron diffraction patterns and high-resolution electron microscopy images of the icosahedral phase in Mn-Al and related systems. Structurally, the model has long-range translational order with a large unit-cell ($Im\bar{3}$ space group) containing 10038 atoms, as well as orientational order characterized by symmetry close to the $m\bar{3}\bar{5}$ point group which is commonly assigned for quasicrystals.

Fig.1(a)-(c) show, respectively, the SAD patterns of the so-called twofold, threefold, and fivefold axes observed in rapid quenched Al-14at%Mn. Simulation of the corresponding SAD patterns (Fig.1(d)-(h)) suggested that they did not result from a single zone-axis diffraction, but from several closely orientated zone axes. For example, Fig.1(f) was generated by the superposition of the [305], [508], and [8 0 13],.... axes (denoted as N-<305>); the rotation angles from the [001] axis to each axis are 30.96°, 32.01°, and 31.61°, respectively. All are very close to 31.71°, which is the angle between a twofold and a fivefold axis in the $m\bar{3}\bar{5}$ point group. In a conventional electron diffraction experiment, if the [001] axis of the crystal is rotated 31.71° around the [010] axis, these three zone axes would simultaneously satisfy the Bragg conditions and cannot be separated. Such superposition in the projected diffraction pattern, especially when the unit-cell is large, can yield a pseudo-fivefold symmetry which is indistinguishable with a true fivefold symmetry in SAD.

Similar pseudo-symmetries were found in Fig.2(g) (twofold) and Fig.2(e) (threefold) which were attributed to the reflections from [358], [5 8 13], [8 13 21],.... (denoted as N-<358>), and [038], [0 5 13], [0 8 21],... (denoted as N-<038>) zone axes, respectively. We also found that the <001> pattern (Fig.1(b)) and <111> (Fig.1(h)) pattern is almost identical to that of the N-<358> and N-<038>, respectively. Based on our analyses, we conclude that the six "fivefold" axes previously reported for the icosahedral phase ($m\bar{3}\bar{5}$) are actually six N-<305> axes (pseudo-fivefold) in $m\bar{3}$. The ten "threefold" axes are six N-<038> (pseudo-threefold) and four <111> (true threefold) axes, and the fifteen "twofold" are twelve N-<538> (pseudo-twofold) and three <001> (true twofold) axes.

Our structural model also agrees well with the observations of HREM. Fig.2 shows a HREM image recorded along the pseudo-fivefold axis of the icosahedral phase in the Al-Cu-Fe alloy. The periodicity of the image along the [010] and the [503] directions. The inset is the calculated unit-cell projection along the N-<305> zone axis, showing good agreement with the experimental one. Here, each dot does not represent a single atom-column, but the projection of a cluster of dodecahedron. In fact, for most of the published high-quality HREM images of the icosahedral phase including Al-Mn-Si, Al-Cu-Fe, and Al-Ru-Cu alloys,[1] we found similar unit-cell with a periodicity about 5nm in these images. Such a periodic structure can address the origin of the sharp diffraction-peaks and their unusual symmetries, and suggests that the icosahedral phase can be considered as a complex cubic crystal, rather than a quasicrystal.[2]

References

1. See, for example, K. Hiraga, *J. Microscopy*, **146** 245, (1987).
2. Work partially supported by the U.S. DOE DE-AC02-76H00016.

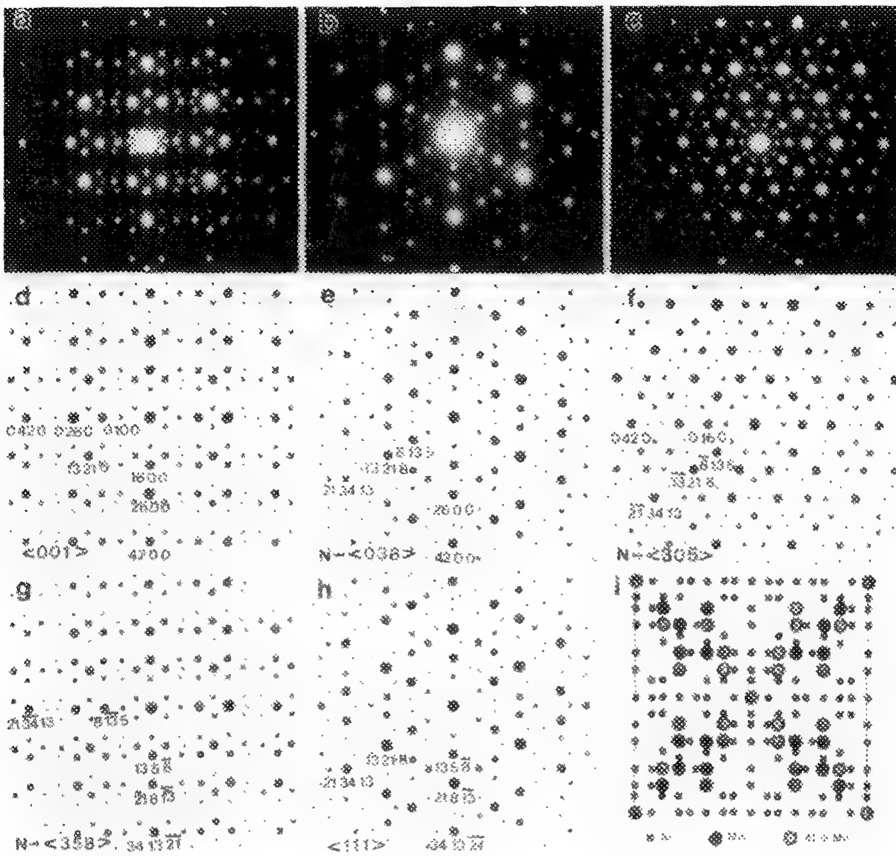

Fig.1 Experimental (a)-(c) and calculated (d)-(h) SAD patterns. Note the similarity of the patterns between (d) and (g), and (e) and (h). The <001> projection of the unit-cell is shown in (i).

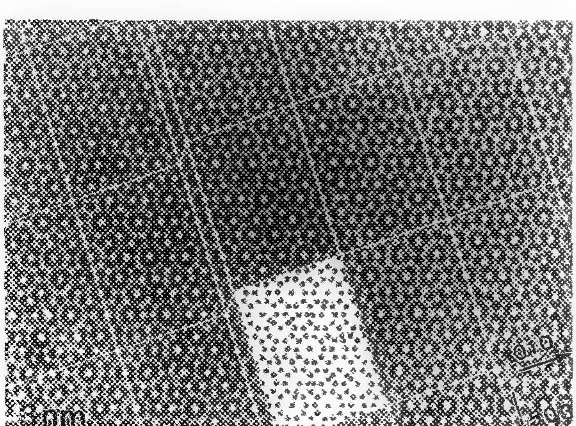

Fig.2
HREM image along the pseudo-fivefold axis showing a potential map of the local structure in Al-Cu-Fe. Inset is the N-<305> projection of the unit-cell of the proposed model. The periodic translational order in [010] and [503] direction is marked by the parallel white-lines. Note, there is a planar defect which yields a lattice displacement in the area.

DECOMPOSITION OF AN Al-Cu-Ru QUASI-CRYSTAL AT 1420 K

Y. Kitano * , Y. Fujikawa ** and T. Watanabe ***

*Dept.of Mat. Sci., Shimane Univ., Nishi–Kawazu–Machi 1060, Matsue 690, Japan.
**Dept. of Mat. Sci., Hiroshima Univ., Kagami–Yama 1–3–1, Higashi–Hiroshima 739, Japan.
***Device Development Center of Hitachi Ltd., Ohme, Tokyo 198, Japan.

Quasi–crystals of $Al_{65}Cu_{20}Ru_{15}$ alloy are known to be an icosahedral–phase (I–phase) of the F–type. This state has been confirmed to be stable near 1100 K, but perhaps not at temperatures higher than around 1300 K. In this paper we report high temperature behavior of this alloy. We have found that the stable I–phase would decompose into three or four phases at 1420 K, one of which is an I–phase having a different composition. We denote the lower temperature I–phase, I–phase(L), and this high temperature one, I–phase(H).

5N Al and Cu and 3N Ru were arc–melted in Ar. The nominal composition of the alloy was 65Al, 20Cu and 15Ru. In order to obtain homogeneous materials, the ingot was annealed at 1020 K for 100 hours. The X–ray powder diffraction pattern confirmed that the heat–treated ingot was only I–phase(L). This is the starting material in this study. DTA and EPMA analysis, and SEM and TEM observations were carried out in order to investigate subsequence thermal reaction. Experimental results with brief discussion are as follows.

1. The composition of the starting material (I–phase(L)) is 67.5 at%Al, 18.7 at.%Cu and 13.8 at.%Ru. A structure image and diffraction pattern are given in Figs. 1(a) and 1(b).
2. A number of quasi–crystallites having a shape of the icosahedron or its modification are observed in the optical microscope at the surface of the ingot. The diameter of the crystallites is several tens μm. In order to obtain larger quasi–crystals, annealing at higher temperature for a longer time or with slow cooling is required. In this case some additional phases appear. (Fig. 2)
3. In the heating process, thermal absorption occurs near 1320 K. This suggests that decomposition of the I–phase(L) may start at this temperature.
4. By annealing the I–phase(L) at higher temperature, the surface topograph changes, suggesting partial melting. (Fig. 3)
5. When the I–phase(L) is annealed at 1420 K for 5 hours, the materials decompose into three or four phases. This is confirmed by an EPMA image, Fig. 4.
6. The area marked A in Fig. 4, is a crystal with composition of 73.8 at.% Al, 6.4 at.% Cu and 19.8 at.% Ru. The crystal belongs to the cubic system and to one of three space groups; $F\bar{4}3m$, F432 and $Fm\bar{3}m$. The lattice parameter is 1.49 nm. An electron diffraction pattern is given in Fig. 5, for [110] orientation
7. The area marked B in Fig. 4 is the quasi–crystal I–phase(H). The composition of this phase is 69.6 at.% Al, 14.8 at.% Cu and 15.6 at.% Ru.
8. The areas C and D contain only Al and Cu. The melting temperature of this Ru–free area is between 900 and 1200 K.
9. By re–annealing the specimens used above at 1020 K for 10 hours. The I–phase(L) is recovered.

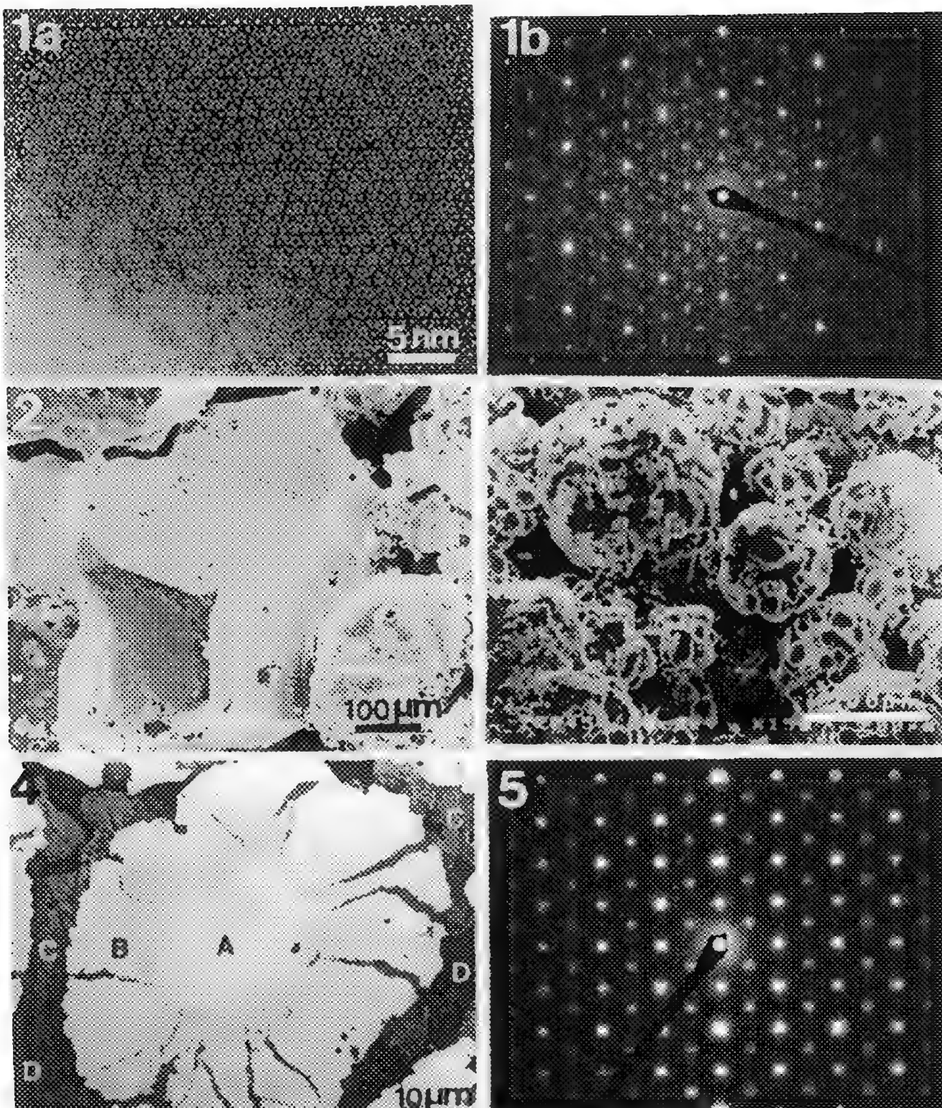

FIG. 1. (a) HRTEM image and (b) diffraction pattern of I–phase(L).
FIG. 2. SEM image of rather large quasi–crystals.
FIG. 3. SEM image of the surface of a specimen annealed at 1460 K.
FIG. 4. EPMA image of the phase decomposed at 1420 K from the I–phase(L).
FIG. 5. Diffraction pattern for the cubic crystal, marked A in Fig. 4.

α-AlMnSi PHASE TO A BCC STRUCTURE BY XE$^+$ ION-BEAM IRRADIATION

Y.X. Guo, L.M. Wang and R.C. Ewing

Department of Earth and Planetary Sciences, University of New Mexico, Albuquerque, NM 87131

AlMnSi alloy system has attracted great attentions since the first report on the icosahedral quasicrystal materials in 1984. The rapidly quenched AlMnSi alloy around the stoichiometry of the α-AlMnSi phase (α-phase below) may form icosahedral quasicrystals. And the structure unit of the α-phase is of near icosahedral symmetry. The α-phase has a cubic structure with space group Pm3 (a=1.268 nm)[1]. In each unit cell there are 138 atoms. The most important structure unit in this phase is the so-called MacKay icosahedron. In such a structure unit, 12 Al atoms are decorating the vertices of an icosahedron. Surrounding this icosahedron is another same oriented icosahedron of 12 Mn atoms, which is about twice the diameter of the former. Furthermore, 30 Al atoms define a shell outside the two inner icosahedra with each atom sitting at the midpoint just out of the Mn icosahedron edges. In the structure of α-phase, the icosahedra are slightly distorted and are connected along those of their three fold axes that coincide with the <111> direction of the cubic lattice. The two triangular faces of the Mn icosahedron make up an Mn octahedron. Hence, two MacKay icosahedra define two basic positions as if in a bcc cell with a total of 108 atoms. The rest 30 atoms of light elements (Al or Si) in the structure serve as glue atoms that fill up gaps among the slightly distorted icosahedra. Electron diffraction pattern of this primitive cubic phase is shown in figure 1a, which is in [001] zone axis.

We here report our preliminary study on the structure change of α-phase under Xe$^+$ ion beam irradiation. TEM specimens of α-phase were made by mechanical grinding and ion milling. The as-milled TEM specimens were examined with a JEOL2010 microscope. No discernible structure disordering was found (figure 1a, b). In-*situ* irradiation with 1.5MeV Xe$^+$ ion beam was performed using the HVEM-Tandem Facility at Argonne National Laboratory. Irradiation dose ranged from 0 up to 5.1×10^{14} ions/cm^2. Specimens were irradiated at room temperature. When irradiated at 5.1×10^{14} ions/cm^2, the α-phase becomes completely amorphous. The amorphization should be the result of point defects accumulation.

Irradiated after a dose of 5.1×10^{13} ions/cm^{2}s, the primitive cubic cell of α-phase transforms to a body-centered cubic cell (figure 2a). Although the electron diffraction would be difficult to distinguish the difference in lattice parameters, the diffraction pattern in figure 2a follows the bcc diffraction procession, for instance, the 100 spot in the unirradiated α-phase is absent after irradiation. High resolution electron image from irradiated specimen (figure 2b) has slightly mottled contrast as compared with one from unirradiated specimen (figure 1b). This should be due to the introduction of the defects, such as Frenkel pairs, by irradiation. If we reconsider that the α-phase is near bcc structure, the bcc phase should be of two undistorted MacKay icosahedra decorating the two lattice points. In this sense, the α- and bcc phase must have a very close structure relationship. This also implies that the incident ions displace those glue atoms more efficiently than to displace atoms in the MacKay icosahedra. The slightly distorted icosahedra in the α-phase may have become more icosahedrally symmetrical. In other word, the MacKay icosahedron is a relatively stable atomic cluster in the AlMnSi system. Figure 1c and 2c are a pair of diffraction patterns along the five-fold axis of the icosahedron clusters from unirradiated and irradiated α-phase respectively. In figure 1c, there is only one ring of ten diffraction spots slightly away from a five-fold rotation symmetrical positions with obvious unevenly distributed diffraction intensities. On the other hand, near five-fold rotation axes were found in the irradiated specimen (figure 2c). This confirms the relative stability of the MacKay icosahedron exposing to the high energy ion beam irradiation.

The irradiation on the α-AlMnSi phase may lead to a crystalline to quasicrystalline phase transformation. And the study provides evidence that the MacKay icosahedron is relatively stable atomic cluster in the α-phase. The icosahedron may be used in the modelling for the icosahedral quasicrystals.

1. M. Cooper and K. Robinson, Acta Cryst. 20, (1966) 614
2. This work was supported by BES/DOE under contract DE-FG03-93ER45498

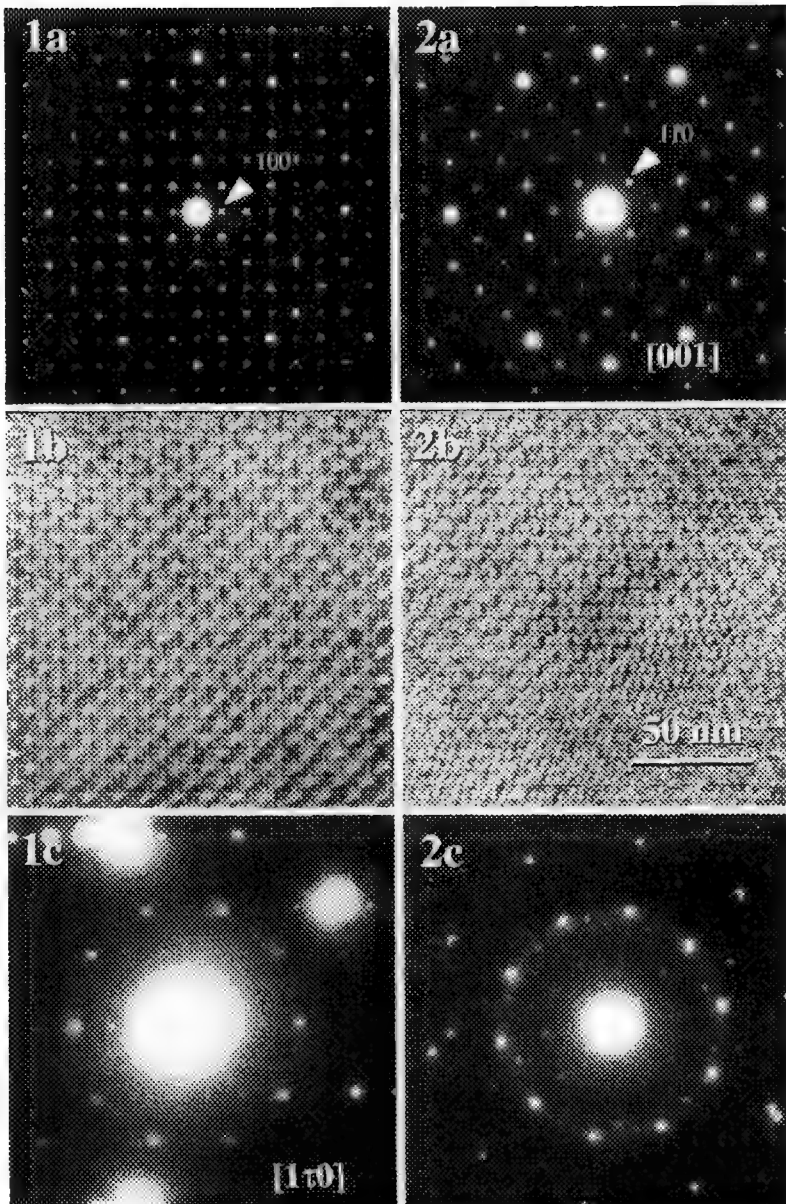

FIG.1 Unirradiated α-AlMnSi phase. a) electron diffraction along [001] showing a primitive cubic crystal structure, b) perfect crystal periodicity, and c) diffraction along [1τ0], τ=1.618..., showing only one ring of ten spots without evenly distributed diffraction intensity.

FIG.2 Irradiated α-AlMnSi phase. a) diffraction pattern of a bcc structure (note the missing of 100 spot, b) defects may have been introduced by irradiation, and c) diffraction pattern of a near five-fold rotation symmetry indicating a transition from α-AlMnSi phase to icosahedral quasicrystal structure.

HREM STUDY OF PHASE TRANSFORMATION INDUCED BY ION IRRADIATION IN Al-Cu-Co-Ge SINGLE DECAGONAL QUASICRYSTAL

L.F. Chen, L.M. Wang and R.C. Ewing

Department of Earth and Planetary Sciences, University of New Mexico, Albuquerque, NM 87131

Irradiation-induced phase transformation in crystals has been an interesting research field for the past twenty years[1]. Since the discovery of quasicrystals in Al-based alloys[2], there have been some reports on irradiation-induced phase transformation in quasicrystals by *in situ* TEM observations[3,4]. However, detailed study on phase transformation in quasicrystals under ion irradiation at atomic level using HREM is necessary for the fundamental understanding of the process. In this paper, we report the results from a systematic HREM study on phase transformation induced by ion irradiation in Al-Cu-Co-Ge single decagonal quasicrystal (31.4 wt.% Cu, 21.8 wt.% Co and 5.4 wt.% Ge).

The TEM specimens of single decagonal quasicrystal were prepared perpendicular to the tenfold axis. The transformation in single quasicrystal was studied by *in situ* TEM during 1.5 MeV Xe^+ ion irradiation at room temperature using the HVEM-Tandem Facility at Argon National Laboratory and examined in detail by HREM using a JEM2010 microscope at the University of New Mexico after the irradiation.

The progressive phase transformation process was observed in both electron diffraction and HREM images. Before ion irradiation, typical single decagonal quasicrystal HREM image and electron diffraction pattern along the tenfold axis can be seen (Fig. 1a). Fig.1b is the inverse Fourier transform of Fig.1a's Fourier transform after filtering out the noise in Fourier space. The filtered HREM image (Fig.1b) shows the decagonal quasicrystal structure more clearly and revealed no apparent defects and damages in the unirradiated single decagonal quasicrystal. A faint diffuse ring was observed in the diffraction pattern after an ion dose as low as 1.7×10^{14} ions/cm^2, and it became more intense with the increasing dose. Meanwhile, the quasicrystal spots in the diffraction pattern faded. This indicated the formation and expansion of the amorphous volume. In the HREM image, mottled contrast were observed due to damage build-up. However, it is difficult to perform a quantitative analysis of the damaged volume from the HREM image because the appearance of the damaged structure varies greatly with the specimen thickness[5]. When the dose was increased further to 4.3×10^{14} ions/cm^2, only a few spots coexisted with two typical amorphous rings in the diffraction pattern, and these spots remained even after the ion dose reached 1.7×10^{15} ions/cm^2. This observation indicated that the original quasicrystal has transformed into an amorphous component and possibly a crystalline component after the irradiation. This crystalline component is much more resistant to amorphization than the quasicrystalline structure. The HREM image taken after 4.3×10^{14} ions/cm^2 and the corresponding Fourier transform are shown in Fig.2a. It is apparent that the volume fraction of amorphous phase has increased greatly and the tenfold symmetry has disappeared in the Fourier transform. After the contribution from the amorphous component was filtered out in Fourier space, it is obvious that the remaining volume has a crystalline periodicity as shown in Fig.2b. The phase transformation and separation observed in the Xe^+ ion irradiated Al-Cu-Co-Ge quasicrystal are due to irradiation induced defect build-up and possible compositional segregation.

References

1. F.V. Nolfi, Phase Transformations During Irradiation (Applied Science, London, 1983).
2. D. Shechtman, I. Blech, D. Gratias and J.W. Cahn, Phys. Rev. Lett. 53 (1984) 1951.
3. K. Urban, N. Moser and H. Kronmüller, Phys. Status Solidi (a)91 (1985) 411.
4. J. Mayer, K. Urban and J. Fidler, Phys. Status Solidi (a)99 (1987) 467.
5. L.M. Wang, M.L. Miller and R.C. Ewing, Ultramicroscopy 51 (1993) 339.
6. This work was supported by U.S. DOE/BES under Contract DE-FG03-93ER45498.

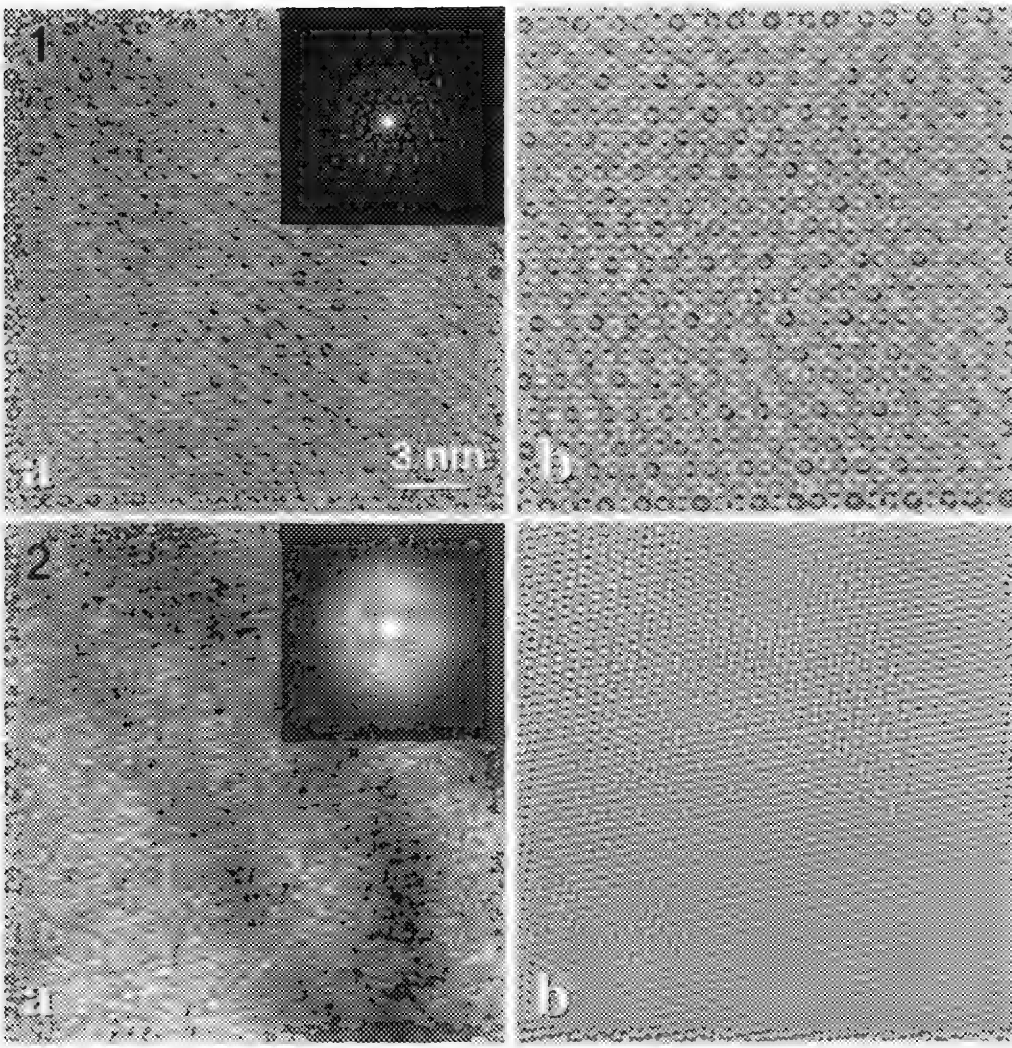

FIG. 1. (a) HREM image of Al-Cu-Co-Ge single decagonal quasicrystal and its corresponding electron diffraction before ion irradiation; (b) inverse Fourier transform of Fig.1a's Fourier transform after filtering out the noise in Fourier space. The sample was a near perfect quasicrystal before ion irradiation.

FIG. 2 (a) HREM image of Al-Cu-Co-Ge single decagonal quasicrystal and its corresponding Fourier transform after 1.5 MeV Xe^{+} irradiation to a dose of 4.3×10^{14} ions/cm^2 at room temperature; (b) inverse Fourier transform of Fig.2a's Fourier transform after the contribution from amorphous component in Fig.2a is filtered out in Fourier space. The quasicrystal has transformed into an amorphous component and a crystalline component after the ion irradiation.

ON THE INFLUENCE OF SPECIMEN THICKNESS IN TEM IMAGES OF SUPERCONDUCTING VORTICES

J. Bonevich,* D. Capacci,** G. Pozzi,** K. Harada,*** H. Kasai,*** T. Matsuda,*** and A. Tonomura***

*National Institute of Standards & Technology, Metallurgy Division, Gaithersburg, MD 20899
**Physics Dept. and Istituto Nazionale di Fisica per la Materia, viale B. Pichat 6/2, 40127 Bologna, Italy
***Advanced Research Laboratory, Hitachi Ltd., Hatoyama-machi, Saitama-ken 350-03, Japan.

The successful observation of superconducting flux lines (fluxons) in thin specimens both in conventional and high T_c superconductors by means of Lorentz[1,2] and electron holography[3,4] methods has presented several problems concerning the interpretation of the experimental results. The first approach has been to model the fluxon as a bundle of flux tubes perpendicular to the specimen surface (for which the electron optical phase shift has been found in analytical form[1,5]) with a magnetic flux distribution given by the London model,[6] which corresponds to a flux line having an infinitely small normal core. In addition to being described by an analytical expression, this model has the advantage that a single parameter, the London penetration depth, completely characterizes the superconducting fluxon. The obtained results have shown that the most relevant features of the experimental data are well interpreted by this model. However, Clem has proposed another more realistic model for the fluxon core that removes the unphysical limitation of the infinitely small normal core and has the advantage of being described by an analytical expression depending on two parameters (the coherence length and the London depth).[6] Therefore, simulations with this improved and physically more appealing model have been carried out, with the conclusion that both in the Lorentz and holographic cases the predictions of the two models are very similar[7,8] and that discrimination on the basis of the experimental data can be done reliably only using the holographic high resolution mode.[8]

Nonetheless, still a noticeable discrepancy exists between predicted and experimental results when the commonly accepted values for the various lengths are inserted into the simulations. In the Lorentz mode, noticeable contrast is reached at larger defocuses that those predicted on the basis of the curves of the contrast versus defocus, a fact that can be accommodated by taking a larger value for the two characteristic lengths than those quoted for the bulk material, whereas in the holographic mode the best fitting of the line scans of the reconstructed phase across the core is again achieved with larger values of the lengths. The reconstructed phase of a fluxon in a thin film of Nb (bulk value of λ_L=30 nm) and the corresponding line scan across the core are shown in Figure 1. Whereas it cannot be excluded that in thin films these lengths can take larger values than those obtained from indirect measurements in bulk specimens, we would present a more physical explanation of the observed discrepancy by considering the effect of surfaces on the field lines, as shown by Hasegawa et al.[9] who solved numerically the Ginzburg-Landau equations for a thin superconducting film.

Fortunately, also an approximate, but analytical, solution exists for this problem, found by Clem,[10] and we have applied it to the interpretation of our data. Figure 2 shows the projected phase maps of the magnetic field calculated according to our previous bulk model (a) and the new Clem[10] model (b) taking into account the specimen thickness. It can be ascertained that the field lines begin to fan out near the surfaces, giving an external field topography broader than the bulk one. By considering that the contrast in the out-of-focus images is predominantly affected by the external field, it turns out that defocus series calculated with the broader topography of the surface field shows good contrast at larger values of the defocus distance, in better agreement with the experimental findings.

References

1. K. Harada et al., *Nature* 360 (1992) 51.
2. J.E. Bonevich et al., *Phys. Rev. B* 49 (1994) 6800.
3. J.E. Bonevich et al., *Phys. Rev. Lett.* 70 (1993) 2952.

4. J.E. Bonevich et al., *Phys. Rev. B* 50 (1994) 567.
5. A. Migliori, G. Pozzi and A. Tonomura, *Ultramicroscopy* 49 (1993) 87.
6. R.P. Huebener, *Magnetic Flux Structures in Superconductors*, Springer, Berlin (1979).
7. G. Pozzi et al., in *Electron Holography*, A. Tonomura et al.: Elsevier, Amsterdam (1995) 12.
8. G. Pozzi et al., *Microsc. Microanal. Microstruct.* 6 (1995) 559.
9. S. Hasegawa et al., *Phys. Rev. B* 43 (1991) 10.
10. J.R. Clem, in *Inhomogeneous Superconductors-1979 (Berkeley Springs, WV)*, D.U. Gubser et al.: AIP Conf. Proc. No. 58, AIP, New York (1979) 245.

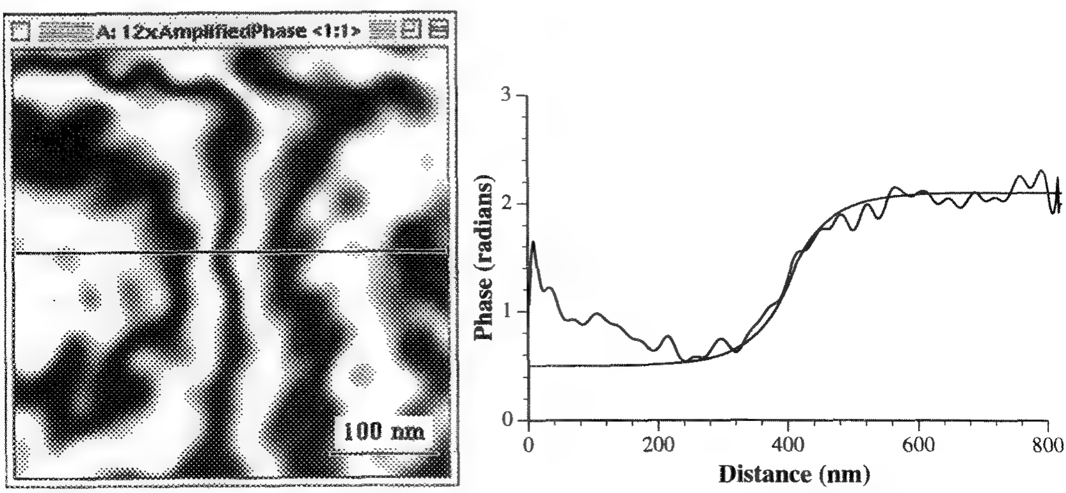

FIG. 1 - (a) Reconstructed interference micrograph of single fluxon (phase amplified 12×). Phase profile across fluxon core can be fit with London parameter of 50 nm, larger than bulk value 30 nm (b). Phase difference across fluxon is 0.5π and the phase on the left is affected by bend contours in the foil.

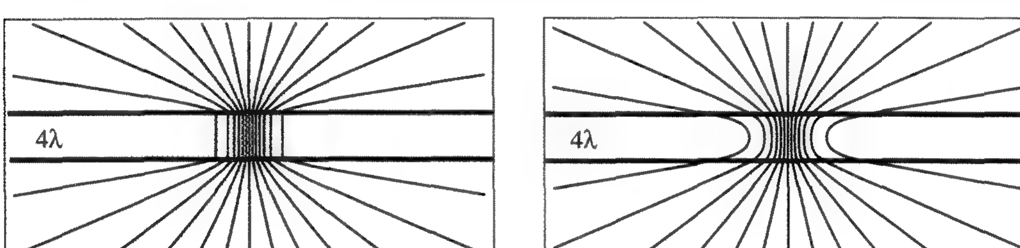

FIG. 2 - Projected phase maps of fluxon's magnetic field according to previous bulk model (a) and Clem model (b) for a fluxon in superconductor of thickness $4\lambda_L$. The magnetic field lines far out near the specimen surfaces causing apparent broadening of the fluxon.

DISTINGUISHING BETWEEN $YBa_2Cu_3O_{7-x}$ AND Y_2BaCuO_5 IN MELT-PROCESSED $YBa_2Cu_3O_{7-x}$

J.D. Riches*, J.C. Barry* and P.J. McGinn**

* Centre for Microscopy and Microanalysis, University of Queensland, QLD 4072, Australia
** Department of Chemical Engineering, University of Notre Dame, IN 46556-5637, U.S.A.

Much of the work in high temperature superconducting ceramics in the last few years has been aimed at improving the critical current density (J_c). By melt-texturing samples it is possible to achieve a significant increase in the J_c of bulk $YBa_2Cu_3O_{7-x}$ (Y123). It has been known for some time that additions of Y_2BaCuO_5 (Y211) in the Y123 superconductor can improve the J_c.[1] However, for the maximum improvement the Y211 particles must be very fine and well distributed throughout the sample.[2] Thus it is clearly of considerable interest to be able to examine a bulk sample and be able to easily distinguish between the Y123 and Y211 particles. By a combination of scanning electron microscopy (SEM) and transmission electron microscopy (TEM) it is possible to study grain size, inclusion size and dislocation structure in the same sample.

In these experiments we examined a TEM specimen with a JEOL 6400F SEM. A micrograph showing the TEM specimen and the holder which allowed it to be examined in the SEM are shown in Figure 1. At the standard operating voltage of 20kV it was not possible to distinguish the Y123 from the Y211, in either the secondary electron imaging (SEI) mode or the backscattered electron imaging (BEI) mode. However, when the accelerating voltage was reduced to 1kV there was distinct contrast between two phases in the sample. Figure 2 shows the difference in the images obtained at the two different operating voltages. Figure 2(a) is a micrograph of an area taken at 20kV in the BEI mode while Figure 2(b), an image of the same specimen area, shows the contrast visible between two phases at 1kV in SEI mode. The composition of these phases was investigated by examining the same specimen in a JEOL 4000FX TEM with EDS detector. It was found that the two phases in question were Y211 and Y123, as expected. EDS spectra of these phases are shown in Figure 3. Although it was possible to clearly distinguish the Y211 phases from the Y123 phases using the 6400F SEM, the resolution was insufficient to examine the sub-micron particles that were of primary interest for this study. For this reason it was decided to examine the samples in another microscope, namely a JEOL 890F in-lens SEM. It was thought that the superior resolution available on this instrument would allow us to determine if the sub-micron sized Y211 particles were present in the samples. However, while the resolution in this microscope was better than that of the 6400F the contrast between the Y123 and Y211 phases was not seen (Fig. 4). Figure 4 shows images of the same region, for an accelerating voltage of 1kV, in both the 6400F and 890F SEMs. Although the magnification level is somewhat different it is quite clear that the Y211 particles are not visible in the 890F image. The result was confirmed by taking higher magnification images of specific regions in the sample. The difference between the 6400F and 890F images was unexpected. The 6400F and 890F have different SEI detector geometry and it may be that the 6400F detector "sees" a significant backscatter signal while the 890F detector does not.

References

1. M. Murakami et al., *Superconducting Science and Technology*, 4 (1991) S43.
2. D.F. Lee et al., *Physica C*, 202 (1992) 83.

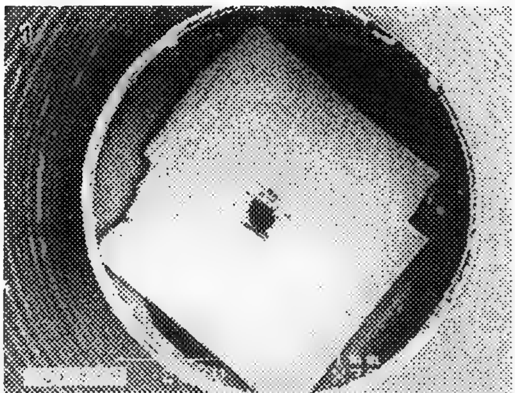

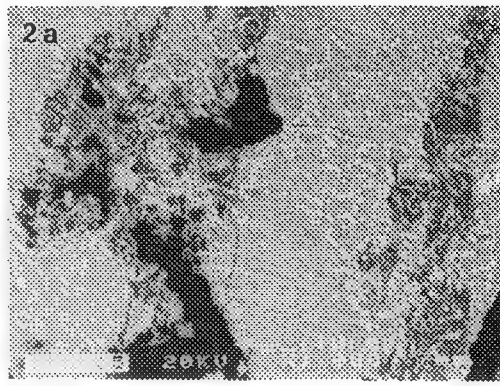

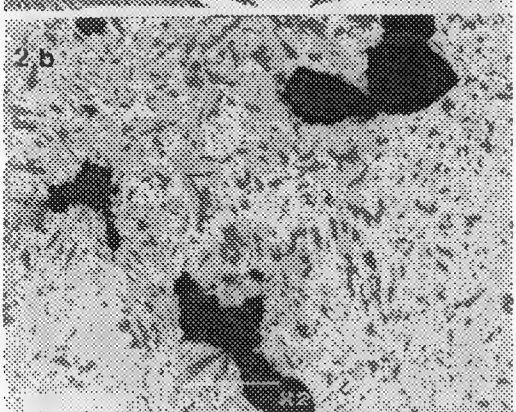

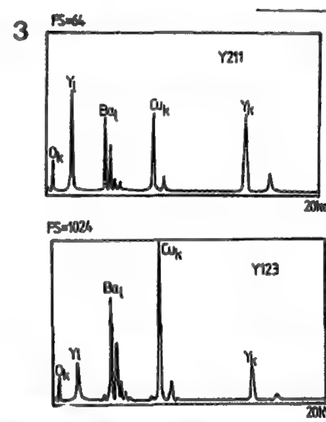

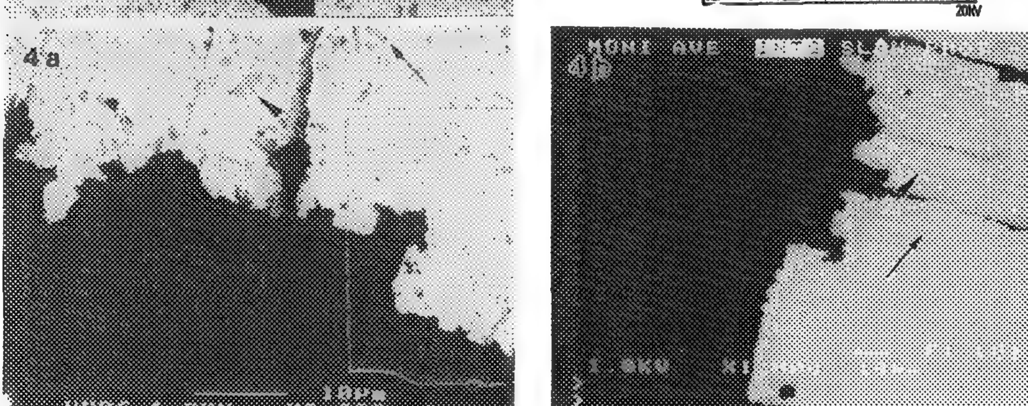

FIG. 1 TEM specimen in special holder for SEM examination.
FIG. 2 (a) Area of sample imaged with backscattered electrons at 20kV.
(b) Same area imaged with secondary electrons at 1kV.
FIG. 3 EDS spectra showing Y211 and Y123 phases.
FIG. 4 (a) Sample imaged in the 6400F SEM at 1kV.
(b) Same area imaged in the 890F SEM at 1kV.

MICROSTRUCTURES AND TRANSPORT PROPERTIES: A COMPARISON BETWEEN GRAIN BOUNDARIES ARTIFICIALLY PRODUCED IN $YBa_2Cu_3O_y$ BICRYSTAL THIN FILMS AND BULK CRYSTALS

X.F. Zhang,* V.R. Todt,* D.J. Miller,* M. St. Louis-Weber,** J. Talvacchio***

*Materials Science Division and Science and Technology Center for Superconductivity, Argonne National Laboratory, Argonne, IL60439.
**Department of Materials Science and Engineering, Northwestern University, Evanston, IL60208.
***Westinghouse Science and Technology Center, Pittsburgh, Pennsylvania 15235.

In order to establish the link between grain boundary (GB) structures and transport properties in superconducting materials, electromagnetic measurements and detailed microstructural studies of carefully prepared GBs are required. Frequently, artificially induced GBs prepared by thin film deposition onto bicrystal substrates are used for such studies. Recently, transmission electron microscopy (TEM) studies have revealed a meandering configuration for GBs in $YBa_2Cu_3O_y$ (YBCO) thin films grown on [001] tilt $SrTiO_3$ bicrystal substrates (Fig. 1a).[1-4] The deviation of the meandering GBs away from the underlying substrate GBs varies from a few tens to hundreds of nanometers. We have demonstrated that the magnitude of the meander in terms of amplitude and wavelength can be reduced by lowering the film deposition rate. The meandering GBs were shown to consist of various straight facets which are a few tens to hundreds of nanometers in length. It is possible that the various segments have very different current transport behavior due to a variable misfit dislocation density. Thus, an unambiguous correlation between the microstructure and global transport properties is difficult to attain.

The origin of meandering in the YBCO thin film bicrystals has been concluded to be mainly a consequence of three-dimensional island nucleation and growth in the YBCO films. However, GBs formed in bulk materials do not generally show this type of short period meandering. We have developed a dual-seeded-melt-processing technique in an attempt to engineer more planar GBs in [001] tilt YBCO bulk bicrystals.[5] TEM images show remarkably straight GB planes between the two halves of the YBCO bicrystal, and such samples have been prepared for a variety of misorientation angles. Fig. 1b shows the morphology of a 18.5° GB grown by this method. In comparison with the morphology shown in Fig. 1a for a bicrystal film, this type of boundary is remarkably straight with deviations consisting only of a few straight facet segments. In addition, these planar GBs can extend over a scale of millimeters. In this process, $Nd_{1+x}Ba_{2-x}Cu_3O_x$ crystals are used as the seeds and the misorientation between two halves of the YBCO bicrystals can be controlled by the seeding process as schematically shown in Fig. 2. The microstructures of the GBs may be affected by various process parameters during the solidification procedure. Critical current densities (J_c) across the [001] tilt bicrystal GBs were measured and a nearly two orders of the magnitude difference has been found between GBs with the tilt angles less than 10° and larger than 20°, respectively.

References

1. C. Traeholt et al., Physica C **230** (1994) 425.
2. J.W. Seo et al., Physica C **245** (1995) 25 .
3. D.J. Miller etal., Appl. Phys. Lett. **66** (1995) 2561.
4. X.F. Zhang et al., J. Mater. Res., submitted.
5. V.R. Todt et al., 1995 MRS, Boston, MA.
6. This work was partially supported by the National Science Foundation Office of Science and Technology Centers under contract DMR 91-20000 and the U.S. Department of Energy, Basic Energy Sciences-Materials Sciences, Conservation and Renewable Energy - Advanced Utility Concepts - Superconducting Technology Program, under contract #W-31-109-ENG-38.

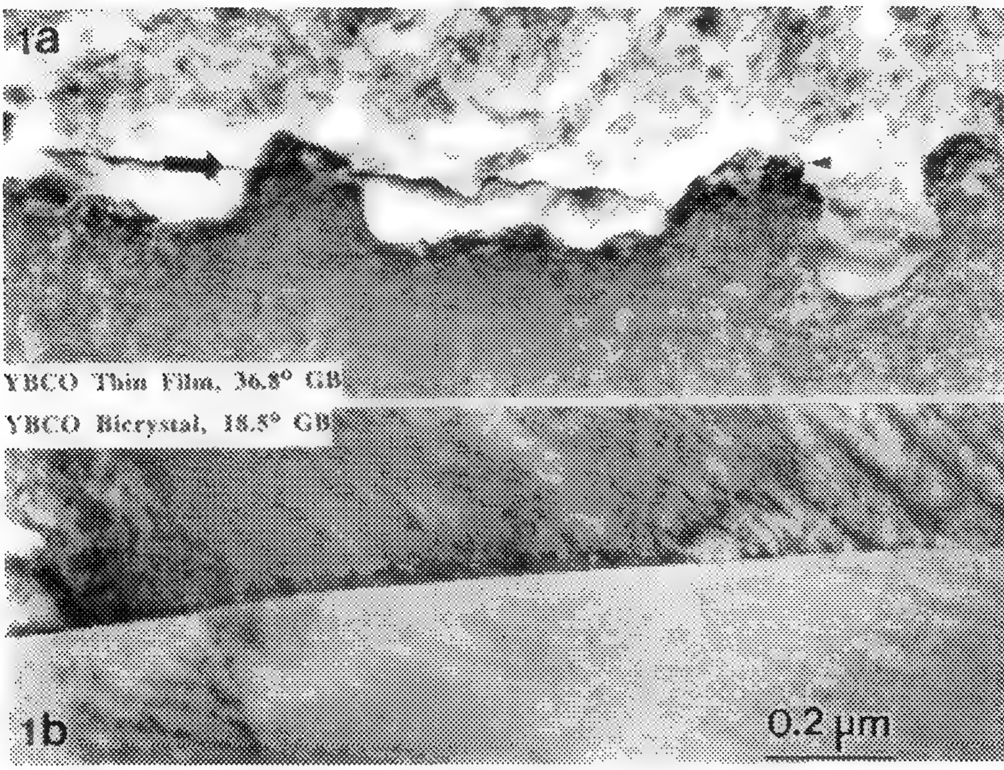

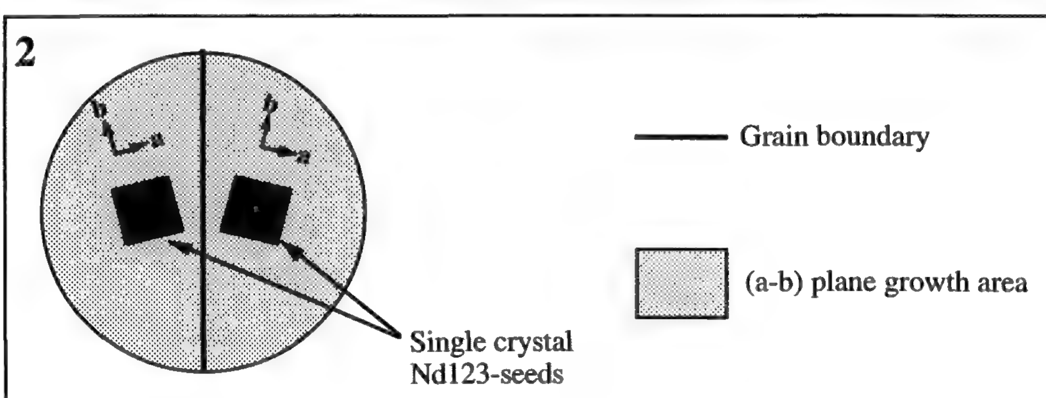

FIG. 1 Bright-field images for (a) a meandering grain boundary formed in a [001] tilt 36.8° YBCO bicrystal thin film, and (b) a flat grain boundary produced in a [001] tilt 18.5° YBCO bulk bicrystal. Arrow and arrowheads in (a) indicate substrate GB and YBCO film GB, respectively.

FIG. 2 Schematic top-view illustration of the double seeded pellet. Nd123 denotes $Nd_{1+x}Ba_{2-x}Cu_3O_x$. The (**a-b**) plane of the YBCO is parallel to the paper plane.

MULTI-MODE LIGHT MICROSCOPY OF MICROTUBULE ASSEMBLY DYNAMICS AND CHROMOSOME MOVEMENT *IN VIVO* AND *IN VITRO*

E. D. Salmon, J. C. Waters and C. Waterman-Storer

Department of Biology, University of North Carolina, Chapel Hill, NC 27599-3280

We have developed a multi-mode digital imaging system (1, 2) which acquires images with a cooled CCD camera (Figure 1). A multiple band pass dichromatic mirror and robotically controlled filter wheels provide wavelength selection for epi-fluorescence. Shutters select illumination either by epi-fluorescence or by transmitted light for phase contrast or DIC. Many of our experiments involve investigations of spindle assembly dynamics and chromosome movements in live cells (1-4) or unfixed reconstituted preparations in vitro (5) in which photodamage and phototoxicity are major concerns. As a consequence, a major factor in the design was optical efficiency: achieving the highest image quality with the least number of illumination photons. This principle applies to both epi-fluorescence and transmitted light imaging modes. In living cells and extracts, microtubules are visualized using X-rhodamine labeled tubulin. Photoactivation of C2CF-fluorescein labeled tubulin is used to locally mark microtubules in studies of microtubule dynamics and translocation. Chromosomes are labeled with DAPI or Hoechst DNA intercalating dyes. Example applications will be presented including high resolution imaging of mitotic spindle and nuclear dynamics in the cell division cycle of the yeast *Saccaromyces cerevisiae* (3); analysis of how microtubule assembly/disassembly at kinetochores and at spindle poles is coupled to chromosome movement (2,4); measurements of microtubule dynamics and chromosome movement for spindles assembled in the test tube in vitro (1,5); and visualization of the assembly dynamics of individual microtubules and the movement of tubular ER relative to microtubules in newt lung epithelial cells.

References

1. E. D. Salmon, T. Inoué, A. Desai and A. W. Murray, High resolution multimode digital imaging system for mitosis studies in vivo and in vitro, *Biol Bull.* (1994) 187, 231.
2. E. D. Salmon and J. C. Waters, A High Resolution Multimode Digital Imaging System for Fluorescence Studies of Mitosis. In: *Analytical Use of Fluorescent Probes in Oncology*, E. Cohen, ed., Plenum Press, New York, (In Press).
3. E. Yeh, R. Skibbens, J. Cheng, E. D. Salmon and K. Bloom, Spindle dynamics and cell cycle regulation of dynein in the budding yeast, *Saccaromyces cerevisiae. J. Cell Biol.* (1995) 130, 687.
4. J. C. Waters, C. L. Rieder, T. J. Mitchison and E. D. Salmon, Taxol inhibits kinetochore microtubule subunit exchange at their plus-ends, but not minus end disassembly at the poles, *Mol. Biol. Cell* (1995) 6, 364a.
5. A. Murray, A. Desai, and E. Salmon, Real time observation of anaphase in vitro, *Molec. Biol. Cell* (1995) 5, 255a.
6. Supported by NIH grant GM24364.

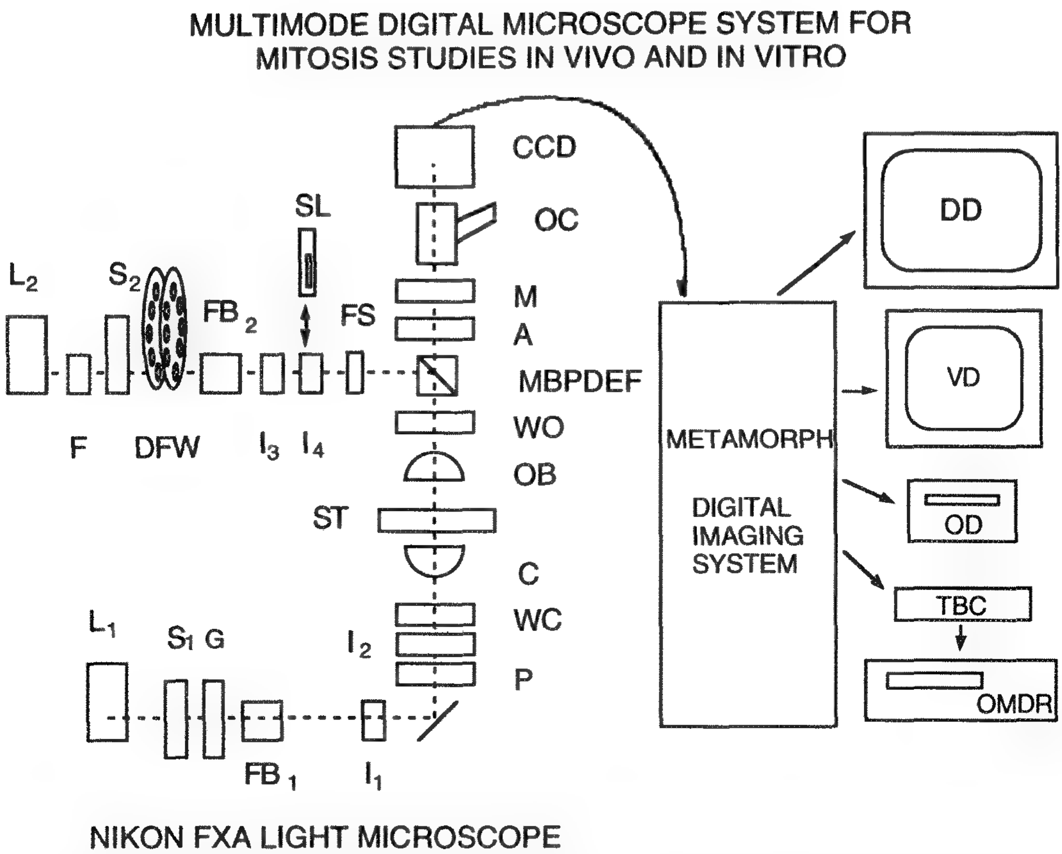

Figure 1. Component parts are: L1, 100 W quartz halogen lamp; S1, Uniblitz shutter (#225L2A1Z523398;Vincent Associates, Rochester, NY); G, ground glass diffuser; FB1, manual filter changers including KG4 heat cut and green interference filters; I_1, field iris diaphragm; I_2, condenser iris diaphragm; P, AP, high transmission Nikon polaroid polarizer and removable analyzer; WC, WO, DIC Wollaston prisms for condenser and objective; C, Nikon NA = 1.4 CON A, Achr-Apl condenser; ST, rotatable stage with focus position controlled by z-axis stepper motor (Mac2000, Ludl Electronic Products, LTD., Hawthorne, NY); OB, 20x/NA= .75 or 60x/NA=1.4 Nikon objectives; MBPDEF, epi-filter block with multiple bandpass dichromatic mirror and emission filter (#83101 and #83100, Chroma Technology Corp., Brattleboro, VT); L2, 100 W HBO Hg lamp; F, KG4 heat cut filter; S2, DFW, shutter and dual 8 position filter wheel (Metaltek, Raleigh, NC), one wheel containing neutral density filters (#FNQ011, Melles Griot, Irvine, CA), and the other a series of narrow bandpass excitation filters (#83360, #83490, #83570, Chroma Technology Corp.); FB_2 manual filter changer; I_3, epi-condenser iris diaphragm; I_4, epi-field diaphragm slider; SL, slit (25 μm width, #04PAS004, Melles Griot, Irvine, CA) cemented to Nikon pinhole slider (#84060) for photoactivation; FS, filter slider; M, optivar magnification changer, 1X-2X; OC, oculars; CCD, cooled CCD camera (#C4880, Hamamatsu Photonics, Bridgewater, NJ); DD, 1024 x 768 pixel, 20 inch digital graphics display monitor (#2082, Viewsonic); VD, RGB video display monitor (#PVM1271Q, Sony); MetaMorph digital imaging system (Universal Imaging Corp., West Chester, PA) using a EISA bus, 64 MByte RAM memory, Imaging Technololgy AFG digital and video image processing card, Hamamatsu C4880 CCD controller card, Matrox MGA Ultima graphics display card, graphics display to S-VHS converter card (Hyperconverter, PC video conversion Corp., San Jose, CA), 1.4 MByte floppy drive, 580 MByte hard drive, ethernet card, parallel port cards for controlling shutter S1 and driving laser printer; 8 serial port card for controlling MetalTek filter wheel, Ludl z-axis stepper, CCD camera, and OMDR; OD, Pinnacle Micro 650 MByte optical drive; TBC, Personal Time-Base Corrector III, Digital Processing Systems, Fluorence KY; OMDR, Panasonic 2028 Optical Memory Disk Recorder (1,2). Modified from 1,2.

MEMBRANE TRAFFIC: MICROTUBULE MOTOR CYCLES AND KINECTIN

Michael P. Sheetz

Department of Cell Biology, Duke University Medical Center, Durham, NC 27710

Although membrane traffic can occur in the absence of microtubules, the rapid metabolism of many eucaryotic cells requires that vesicular organelles are actively transported. Microtubule-dependent transport is particularly robust in actively growing cells and the volume of membrane transported increases dramatically in going from static to growth conditions. Both inward and outward movement are regulated simultaneously implying coordinate activation of both motors or a transport cycle. Relatively large complexes of the microtubule motors and associated proteins are responsible for powering the movements (reviewed in Vallee and Sheetz, 1996). Of the many motors that have been described, kinesin and cytoplasmic dynein are the most abundant and have been the focus of these studies. Included in the microtubule motor complexes are motor receptors and activating factors. A membranous motor receptor, kinectin, was identified on the basis of its interaction with kinesin (Toyoshima et al., 1992). An antibody to kinectin blocks both kinesin binding to organelles and kinesin-dependent motility of those organelles (Kumar et al., 1995). In addition, the same antibody partially inhibits cytoplasmic dynein-dependent motility. We find that loading of VSP4D into chick embryo fibroblasts inhibits approximately 80% of intercellular organelle movements as viewed by video-enhanced DIC microscopy. Further, the reassembly of the Golgi after Brefeldin A induced disassembly and movement of the viral G glycoprotein to the cell surface were also impaired.

Thus kinectin appears to be an important component for the rapid processing of proteins in the secretory pathway. The suggestion that it serves as a receptor for both kinesin and cytoplasmic dynein is supported by in vitro binding data wherein the two motors compete for binding to vesicles (Yu et al., 1992) and the alpha helical portion of kinectin (Yu et al., 1995) will bind strongly to both kinesin and cytoplasmic dynein. To explain these findings and the linkage between the regulation of motility and other steps in vesicle processing, we have suggested that kinectin is a central component of the control of the microtubule motor cycle (Sheetz and Yu, 1995). In the membrane traffic process, the steps of fission, transport, fusion and processing could be coordinated through a protein such as kinectin which is part of the membrane being transported.

References

Kumar, J., H. Yu, and M.P. Sheetz. (1995) Kinectin, an essential anchor for kinesin-driven vesicle motility. *Science* 267: 1834-7.

Sheetz, M.P., and H. Yu. (1995) Regulation of kinesin and cytoplasmic dynein-driven organelle motility. *Semin. Cell Biol.* In Press.

Toyoshima, I., H. Yu, E.R. Steuer, and M.P. Sheetz. (1992) Kinectin, a major kinesin-binding protein on ER. *J. Cell Biol.* 118: 1121-31.

Vallee, R. and M. Sheetz. (19996) Targeting of motor proteins. *Science* 271:1539-1544.

Yu, H., C.V. Nicchitta, J. Kumar, M. Becker, I. Toyoshima, and M.P. Sheetz. (1995) Characterization of kinectin, a kinesin-binding protein: primary sequence and N-terminal topogenic signal analysis. *Mol Biol Cell.* 6: 171-83.

Yu, H., I. Toyoshima, E.R. Steuer, and M.P. Sheetz. (1992) Kinesin and cytoplasmic dynein binding to brain microsomes. *J. Biol Chem.* 267: 20457-64.

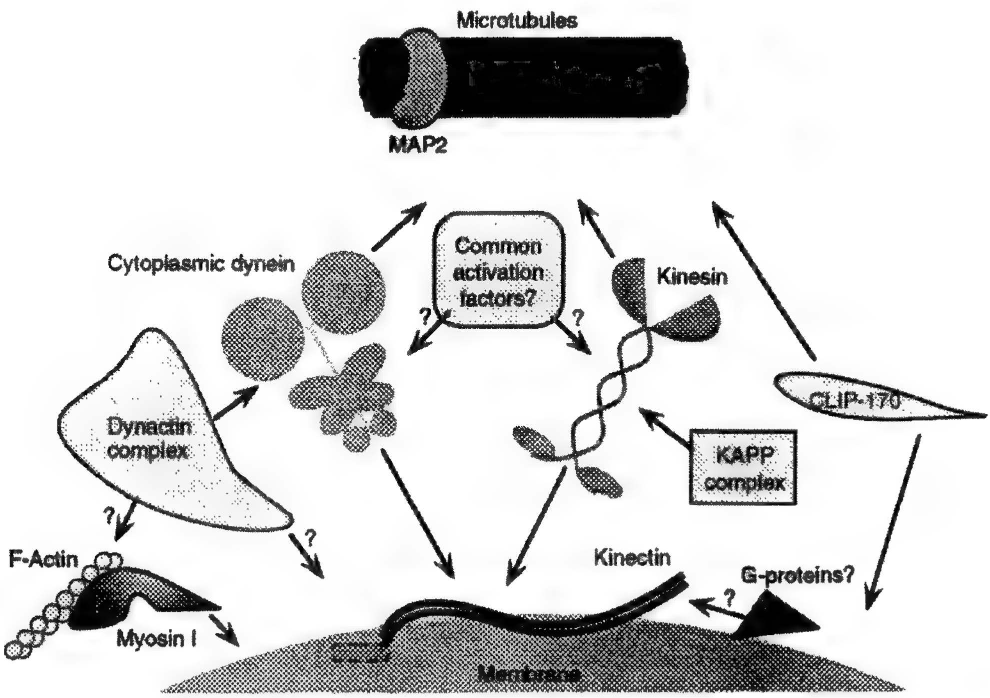

Figure 1 Components of the organelle motor complex. All the currently defined components of the complex are schematically illustrated and labeled here. An arrow indicates the site of known interaction for that component. A question mark (?) by the arrow means that the function for that component is not certain and a question mark by the name of the component means that is not certain whether that component is part of the complex. The entire dynactin complex is illustrated as one block without details of its component parts because the dynactin complex is reviewed elsewhere in this issue. Common activation factor(s) and KAPP complex also have no details because we have yet to understand these components.

LIGHT - MICROSCOPIC ANALYSIS OF THE PHYSICAL PROPERTIES OF CYTOPLASM IN LIVING CELLS

Masatoshi Hori*, Jeffrey D. Jones*, Lee Janson*, Keith Ragsdale* and Katherine Luby-Phelps*

*Department of Physiology, The University of Texas Southwestern Medical Center, Dallas, TX 75235-9040

We have used a variety of optical techniques to explore the intracellular constraints on diffusion, cytoplasmic compartmentalization and biomechanics of living tissue culture cells. Fluorescence ratio imaging measurements of solvent viscosity in single cells indicate that the solvent viscosity of cytoplasm does not differ detectably from bulk water.[1] Nevertheless, data obtained by fluorescence recovery after photobleaching (FRAP) of inert tracer molecules suggest that macromolecular crowding and molecular sieving retard the long-range translational diffusion of protein-sized molecules from 4 to 50-fold relative to their diffusion in dilute aqueous solution.[2]

Transient binding interactions with intracellular components may additionally retard the diffusion of proteins. Recent FRAP studies of fluorescent analogs of calmodulin suggest that as little as 5% of this protein is freely diffusing, even in unstimulated cells where intracellular [Ca^{2+}] is below the threshold for activation of calmodulin binding to calcium-dependent targets *in vitro*.[3] Preliminary data show that binding is mitigated or abolished by charge reversal mutations in the central helix of calmodulin or by a point mutation in calcium binding loop 4 that greatly reduces the affinity of calmodulin for Ca^{2+}. Mutations in either the N- or the C-terminal hydrophobic pockets of calmodulin that reduce the affinity of calmodulin for its targets *in vitro* have no apparent effect on binding to intracellular components at resting [Ca^{2+}].

In addition to hindering diffusion, cytoarchitecture also restricts the distribution of inert tracers in a size-dependent manner. Fluorescence ratio imaging of the subcellular distribution of 30 nm radius relative to 3 nm radius tracer particles reveal that the large particles are excluded from sub-compartments of the cytoplasm. Whole mount electron microscopy and immunofluorescence microscopy of the excluding compartments shows that they are devoid of microtubules, vimentin intermediate filaments and organelles, but contain abundant microfilament bundles and meshworks.[4] Although these regions are also vertically very thin, ratio imaging measurements of the partition coefficient of tracer particles into these compartments as a function of particle size are consistent with exclusion by molecular sieving rather than exclusion by a slit pore (Fig. 1). Based on these data, the percolation cutoff for partition into these compartments is 54 nm radius (Fig. 1).

Single particle tracking of 200 nm green fluorescent beads microinjected into the cytoplasm of living cells suggests that in non-excluding regions the diffusion of organelle-sized particles may also be restricted. Plots of mean squared displacement of the beads (MSD) vs. time yield diffusion coefficients $\leq 10^{-9}$ cm^2/sec, which is from 15 to 100 times slower than in dilute solution. In addition, the plots for many beads exhibited a plateau indicating that their diffusion was limited to "cages". The diameter of cages typically was on the order of several square micrometers (Fig. 2).

Green fluorescent beads can also be microinjected as passive markers of cytoplasmic deformation. We have recently measured the strain rate of cultured fibroblasts under tensile stress. Even at low cell

density, neighboring cells form contacts that resemble adherens junctions in morphology. Actin, α-actinin and β-catenin were localized in these junctions by fluorescent analog cytochemistry and immunofluorescence. The junctions are sufficiently strong that when one cell undergoes spontaneous centripetal contraction, its partner is deformed parallel to the substratum. Plots of strain vs. time for the deforming cells were well fit by the Kelvin-Voight viscoelastic solid model with mean values of σ/E = 0.62 and E/η = 3.4×10^{-3} (Fig. 3).

1. K. Luby-Phelps et al., *Biophys. J.* ,65(1993)236.
2. L. Hou et al., *Biophys. J.* , 58(1990)31.
3. K. Luby-Phelps et al., *J. Biol. Chem.* 270(1995)21532.
4. D.W. Provance et al., *J. Cell Science.* 106(1993)565.

5. This work was supported by NSF grant MCB-9304603 and American Heart Association Grant-in Aid 93011130. Dr. Luby-Phelps is an American Heart Association Established Investigator.

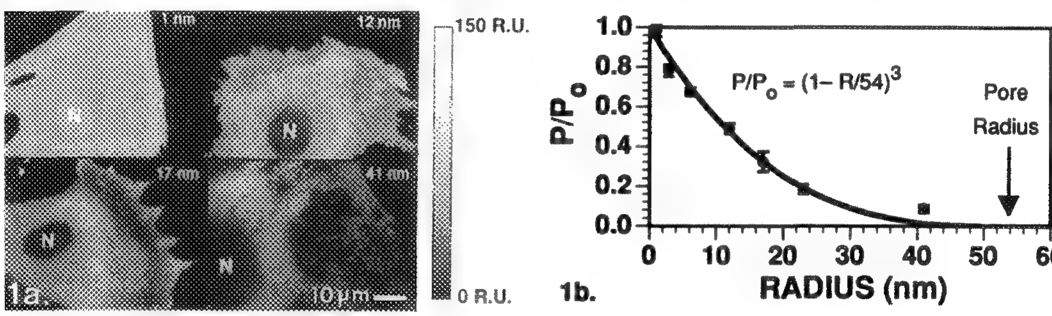

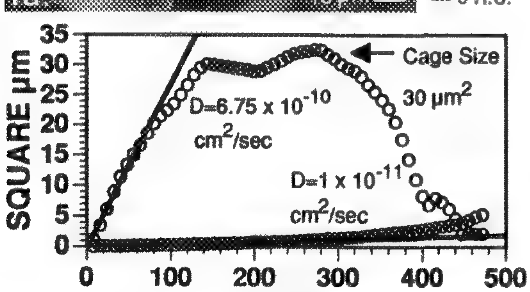

2.

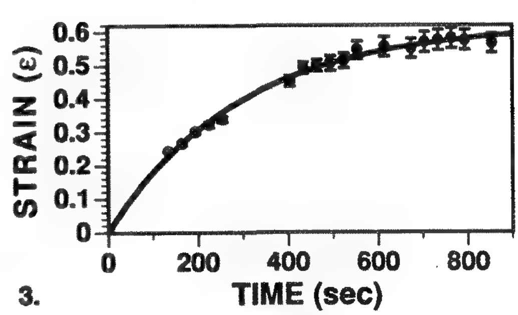

3.

FIG. 1 (a) Ratio maps of the relative concentration of fluorescent tracer particles of varying size in different regions of fibroblast cytoplasm (b) Partition coefficient (P/P_0) vs. Radius for fluorescent tracer particles in excluding regions of fibroblast cytoplasm. Data fit curve $P/P_0 = (1-\alpha)^3$, indicating molecular sieving is the mechanism of exclusion.

FIG. 2 MSD vs. Time for two 200 nm beads within a non-excluding region of fibroblast cytoplasm. Slope of linear initial portion of each curve was used to calculate 2-D diffusion coefficients. Plateau value was used to estimate cage size.

FIG. 3 Strain vs. Time for a single fibroblast under tensile stress through adherens junctions with a contracting neighbor. Data fit a Kelvin-Voight viscoelastic solid model with correlation coefficient of 0.99 and $\chi 2$ of 0.002.

SUBCELLULAR AND MULTICELLUAR ORGANIZATION OF CALCIUM SIGNALING IN LIVER

A.P. Thomas, and L.D. Robb-Gaspers

Department of Pathology, Anatomy and Cell Biology, Thomas Jefferson University, Philadelphia, PA 19107

Cytosolic Ca^{2+} ($[Ca^{2+}]_i$) is a ubiquitous intracellular messenger in mammalian cells, and imaging studies of single living cells loaded with fluorescent Ca^{2+} indicators have demonstrated that the $[Ca^{2+}]_i$ changes induced by extracellular agonists are often organized in complex temporal and spatial patterns. A number of hormones that regulate hepatic metabolism, including vasopressin and α_1-adrenergic agonists, bring about their effects through a rise in $[Ca^{2+}]_i$ mediated by the Ca^{2+}-mobilizing second messenger IP_3. Imaging studies of isolated hepatocytes have demonstrated that the $[Ca^{2+}]_i$ responses during continuous exposure to these hormones consist of a series of discrete $[Ca^{2+}]_i$ spikes, the frequency of which is determined by the dose of agonist.[1] By contrast, the amplitude and kinetics of the individual $[Ca^{2+}]_i$ spikes are not affected by changing the agonist dose. In addition to the temporal organization in the form of $[Ca^{2+}]_i$ oscillations, the $[Ca^{2+}]_i$ changes are also spatially organized into regenerative $[Ca^{2+}]_i$ waves that propagate throughout the cytoplasm and nucleoplasm of the cell from a discrete plasma membrane locus. These oscillatory $[Ca^{2+}]_i$ waves are generated by the complex interplay of $[Ca^{2+}]_i$ and IP_3 in regulating the gating properties of the IP_3-receptor Ca^{2+} channel, which is located in the endoplasmic reticulum Ca^{2+} store.

Most studies of $[Ca^{2+}]_i$ signaling in response to IP_3-dependent hormones have been carried out using isolated cell preparations. However, we have recently established methods to obtain imaging measurements of $[Ca^{2+}]_i$ from intact perfused livers loaded with fluorescent Ca^{2+} indicator dyes.[2] Isolated perfused rat livers were immobilized on the stage of an inverted epifluorescence microscope and a time series of images was recorded from a focal plane 20-50 µm into the tissue. In agreement with the isolated hepatocyte studies, continuous perfusion with low doses of vasopressin induced oscillatory $[Ca^{2+}]_i$ waves in the individual hepatocytes of the perfused liver. Remarkably, the $[Ca^{2+}]_i$ oscillations were coordinated across entire lobules of the liver by cell to cell propagation of the $[Ca^{2+}]_i$ waves along the hepatic plates. These intercellular $[Ca^{2+}]_i$ waves initiated in a small number of cells of the periportal zone of the liver and then propagated radially into the pericentral zones. Thus, the oscillation frequency of the initiating cells determined the frequency and spatial pattern of the $[Ca^{2+}]_i$ oscillations for the entire lobule. Although $[Ca^{2+}]_i$ waves propagated with constant velocity within each cell, there was a significant delay at each cell-cell boundary. This delay period was inversely related to agonist dose, such that the rate of intercellular $[Ca^{2+}]_i$ wave propagation increased with increasing agonist dose. The time series shown in Fig. 1 was recorded using low magnification confocal microscopy of a liver loaded with fluo3 and perfused continuously with 0.125 nM vasopressin.[2] Similar data could also be obtained using conventional epifluorescence from fura2-loaded livers if these data were subsequently deconvoluted to remove out of focus information. This approach allows the calculation of calibrated $[Ca^{2+}]_i$ levels.[2] Comparison of the vasopressin-induced $[Ca^{2+}]_i$ oscillations measured in isolated hepatocytes (Fig. 2) and individual hepatocytes of the intact liver (Fig. 3) demonstrates that the properties of these $[Ca^{2+}]_i$ signals are very similar between the two preparations. However, the cells of the intact liver are more sensitive to the hormone.

Intracellular $[Ca^{2+}]_i$ waves provide a mechanism to transmit signals detected at the plasma membrane to targets within the cell, whereas the intercellular $[Ca^{2+}]_i$ waves of the intact liver may serve to coordinate responses across the functional lobular units of this organ. The present approach is not limited to studies of $[Ca^{2+}]_i$ signaling in the intact perfused liver. We are currently using fluorescence imaging of the perfused liver to monitor metabolic responses using the intrinsic fluorescence of pyridine and flavin nucleotides. In addition, it is possible to use this preparation to monitor other hepatic functions such as bile secretion. Fig. 4 shows images of fluorescent dye pumped into the bile canaliculi.

References

1. T.A. Rooney et al., *Cell Calcium.* 12(1991)111.
2. L.D. Robb-Gaspers and A.P. Thomas, *J. Biol. Chem.* 270(1995)8102.

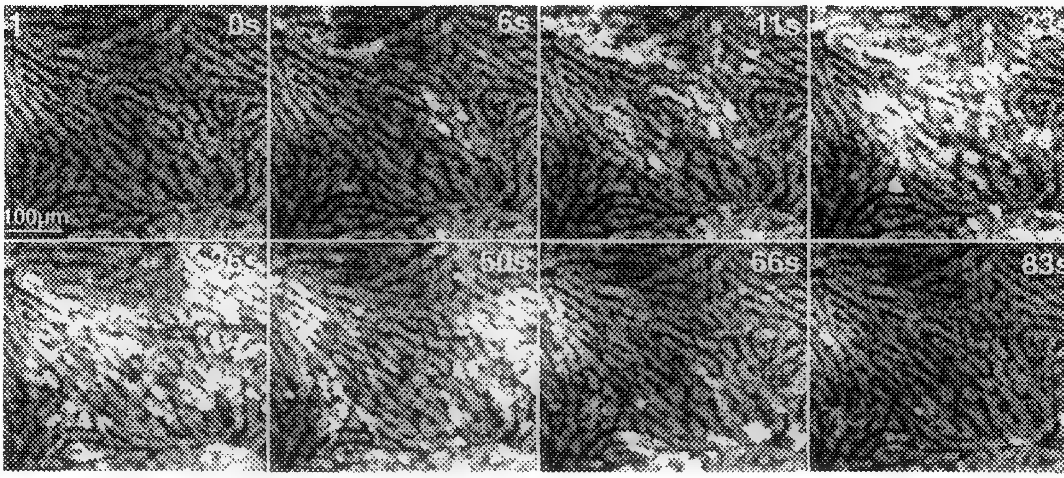

2

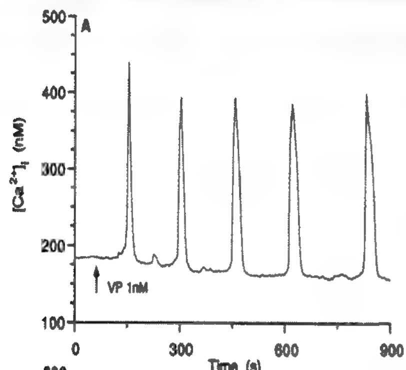

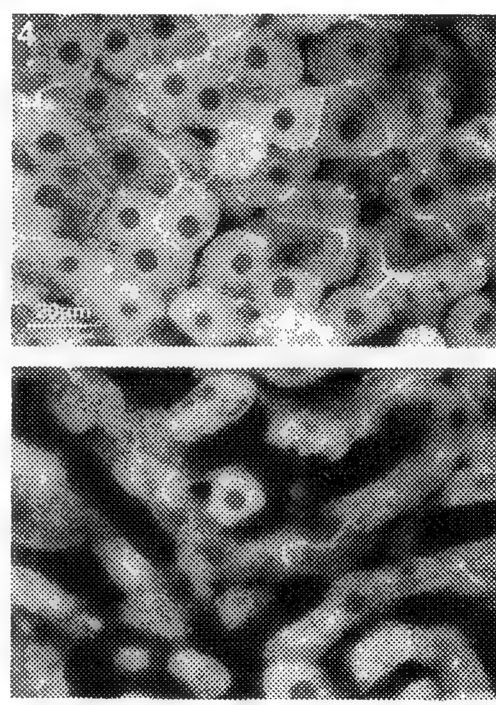

3

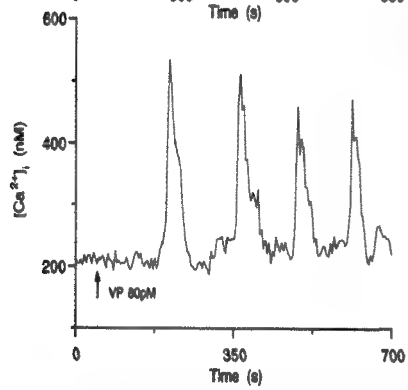

FIG.1 Coordinated intercellular $[Ca^{2+}]_i$ waves propagating between hepatocytes in a fluo3-loaded rat liver perfused with 0.125 nM vasopressin.

FIG.2 $[Ca^{2+}]_i$ oscillations in a single isolated hepatocyte stimulated with 1 nM vasopressin (VP).

FIG.3 $[Ca^{2+}]_i$ oscillations in a single hepatocyte of the perfused liver stimulated with 80 pM VP.

FIG.4 Two confocal sections of a perfused liver showing fluorescent dye in bile canaliculi.

CONFOCAL IMAGING OF CALCIUM IN INTACT VENTRICULAR MUSCLE PROVIDES A NEW VIEW OF EXCITATION-CONTRACTION COUPLING

W.G. Wier

Department of Physiology, University of Maryland School of Medicine, 655 West Baltimore St., Baltimore MD 21201

A fundamentally new understanding of cardiac excitation-contraction (E-C) coupling is being developed from recent experimental work using confocal microscopy of single isolated heart cells. In particular, the transient change in intracellular free calcium ion concentration ($[Ca^{2+}]_i$ transient) that activates muscle contraction is now viewed as resulting from the spatial and temporal summation of small (~ 8 μm^3), subcellular, stereotyped 'local $[Ca^{2+}]_i$-transients' or, as they have been called, 'calcium sparks'[1]. This new understanding may be called 'local control of E-C coupling'.[2] The relevance to normal heart cell function of 'local control' theory and the recent confocal data on spontaneous Ca^{2+} 'sparks'[1] and on electrically evoked local $[Ca^{2+}]_i$-transients [2-5] has been unknown however, because the previous studies were all conducted on slack, internally perfused, single, enzymatically dissociated cardiac cells, at room temperature, usually with Cs^+ replacing K^+, and often in the presence of Ca^2-channel blockers. The present work was undertaken to establish whether or not the concepts derived from these studies are in fact relevant to normal cardiac tissue under physiological conditions, by attempting to record local $[Ca^{2+}]_i$-transients, sparks (and Ca^{2+} waves) in intact, multicellular cardiac tissue. In addition, the ability to study $[Ca^{2+}]_i$ with confocal imaging in intact cardiac tissue is expected to facilitate the study of diseased heart muscle and to open the way to study phenomena, such tissue arrhythmias and disturbances of vascular perfusion (blood flow), that are not possible to study in single isolated heart cells.

Spherical aberration is the main optical problem in imaging living cells deep in tissue with objectives designed for oil immersion , and spherical aberration increases proportionately with depth into the aqueous media and cellular material. Therefore , we used the new Nikon water immersion objective (60 X, N.A. 1.2) on our MRC-600 Confocal Imaging System. This objective has a working distance of 220 μm (above 170 μm of coverslip glass). Trabeculae from the atrioventricular border of the right ventricle of normal brown rats (LBN-F1) were obtained as described originally by ter Keurs[6]. The trabeculae selected for study were approximately 2000 μm in length and less than 150 μm in diameter.

Confocal imaging was performed in quiescent trabeculae as illustrated in Fig. 1. Either full-frame images (*x,y,* constant *z)* (A) or 'line-scan' images (*x*(*t*), constant *y,z*)(B) were obtained. Calcium sparks are readily visible in the full-frame image as spatially localized bright regions, and, in the line-scan images as localized, transient changes in fluorescence. In the quiescent muscle Ca^{2+} sparks were similar in time course and spatial spread to those recorded previously in single isolated cardiac cells. As we have pointed out previously, a number of factors shape the confocal image of Ca^{2+} sparks and a substantial variation in amplitude and time course can be seen in the Figure. Ca^{2+} waves were also recorded in some of these quiescent trabeculae. In general, the Ca^{2+} waves recorded in these preparations appear similar to those we have recorded previously, in single cells.

We have shown that $[Ca^{2+}]_i$ can be visualized with confocal microscopy in individual muscle cells within a ventricular trabecula, under physiological conditions, including mechanical loading.

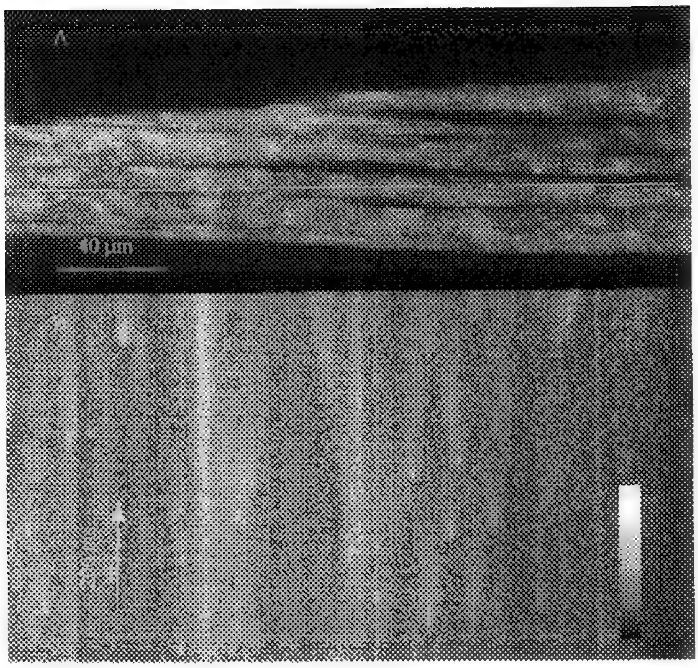

Fig. 1 Confocal images of calcium sparks in intact mammalian cardiac muscle (rat ventricle)

Through the use of an appropriate objective lens, adequate spatial resolution of subcellular structures can be obtained, even deep within multicellular cardiac tissues. The present results are that spontaneous calcium sparks are common in resting rat ventricular trabeculae. $[Ca^{2+}]_i$ waves occur sporadically, and, surprisingly, they can be limited to single cells. They seemed to occur randomly (*i.e.* not in a focus of damage), and their presence was correlated with microscopically visible waves of contraction of sarcomeres within cells in the muscle. Finally, the existence of Ca^{2+} sparks in muscles generating normal $[Ca^{2+}]_i$-transients and twitch force implies that the concepts of local control of E-C coupling do apply to intact normal cardiac muscle.

References

1. Cheng, H., Lederer, W.J. & Cannell, M.B. (1993). *Science* **262**, 740-743.
2. Lopez-Lopez, J.R., Shacklock, P.S., Balke, C.W. & Wier, W.G.. (1994) *The Journal of Physiology*, **480.1**; 21-29.
3. Cannell, M.B., Cheng, H., & Lederer, *Biophysical J.* **67**;1942-1956.
4. López-López, J.R., Shacklock, P.S., Balke, C.W. & Wier, W.G. (1995) *Science*, **268**;1042-1045.
5. Cannell, M.B., Cheng, H. & Lederer, W.J., (1995). *Science*, **268**;1045-1048.
6. ter Keurs, H.E.D.J., Rijnsburger, W.H., Van Heuningen, R., & Nagelsmit, M.J. (1980). *Circulation Research*. Vol. 46, pp. 703-714.

DIRECT MEASUREMENT OF CHROMATIN DIFFUSION AND CONSTRAINT IN LIVING CELLS USING A GFP-LAC REPRESSOR FUSION PROTEIN

W.F. Marshall, A.F. Straight, A. Murray, J.C. Fung, J. Marko*, D.A. Agard, and J.W. Sedat

Dept. Biochemistry and Biophysics, University of California, San Francisco, CA 94143

*Center for Studies in Physics and Biology, Rockefeller University, New York, NY 10021-6399

The polymer dynamics of interphase chromatin is at present a poorly understood aspect of nuclear organization, but one with profound consequences on events within the nucleus. The rates of many important processes, such as meiotic homolog pairing, site-specific recombination, and chromatin condensation, all involve the motion of chromatin within the nucleus. How fast can such rearrangements occur? Because interphase chromatin is likely to behave as a tangle of random-walk polymers, there is likely to be a substantial hindrance to diffusion. Therefore, the rate at which a given site on a chromosome can diffuse within the nucleus may limit the rate at which events requiring chromatin motion can occur. Furthermore, the polymer physics of interphase chromatin is an interesting line of theoretical research in its own right, and knowledge of diffusion rates is an important experimental parameter to consider when evaluating physical models. Finally, a fundamental aspect of nuclear architecture is the extent to which chromatin is anchored to a nuclear skeleton. Such matrix attachments would result in constrained diffusion, which can be detected by analysis of chromatin motion.

We have developed a method to track chromatin in living cells of the budding yeast *S. cerevisiae*. The first requirement for tracking chromatin diffusion is a way to mark a specific site on a chromosome and follow it in 3D in living cells. We employ yeast cells containing genomic insertions of a lac operator array (developed by A. Belmont) and expressing a fusion of the green fluorescent protein (GFP) with the lac repressor protein. When the GFP-lac repressor molecules bind at the site of the lac operator array, a single fluorescent spot is formed in the nucleus. These cells are imaged using time-lapse wide-field 3D fluorescent microscopy. Stereo pairs of such time-lapse images are given in Figure 1.

Diploid cells carrying two lac-operator insertions are routinely imaged. The distance between the two fluorescent spots is then measured as a function of time. The mean-squared change in this distance should be a linear function of time for free diffusion. At short time intervals (Figure 2) this is indeed the case and from this type of plot an approximate diffusion constant can be calculated. However, when longer time intervals are considered (Figure 3), it is clear that the plot reaches a plateau. This indicates a constraint on the diffusion, which could result from attachment to a nuclear skeleton.

We have developed a similar strategy for tracking chromatin in *Drosophila* embryos, which takes advantage of the fact that topoisomerase II binds specifically to a particular heterochromatic satellite block, so that if fluorescent anti-topoII antibodies are injected, a bright fluorescent spot is seen, allowing motion of the underlying heterochromatic block to be tracked in vivo. Unlike the situation in yeast, no constraint to diffusion is observed. The calculated diffusion constant is similar to that seen in yeast. In *Drosophila* we have also measured directly the rate of several types of chromosome rearrangement including homolog pairing, and we are thus able to compare the observed rates of these events with those predicted from the diffusion measurements.

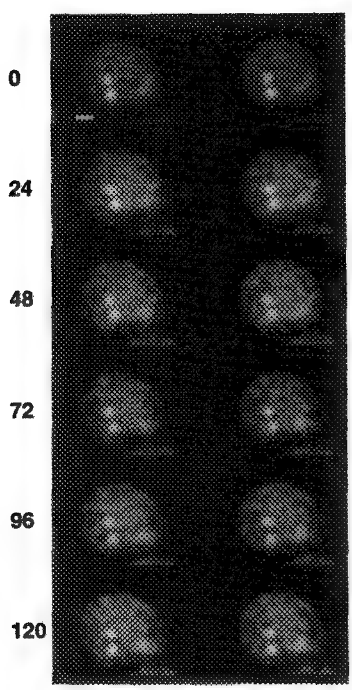

Figure 1. Stereo pairs of time-lapse images of yeast cells expressing GFP-LacI. Time is given in seconds.
Scale bar 1.0 μm.

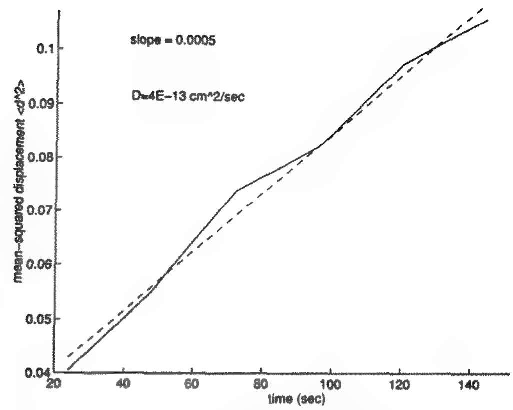

Figure 2. Free diffusion observed for short time-scale.

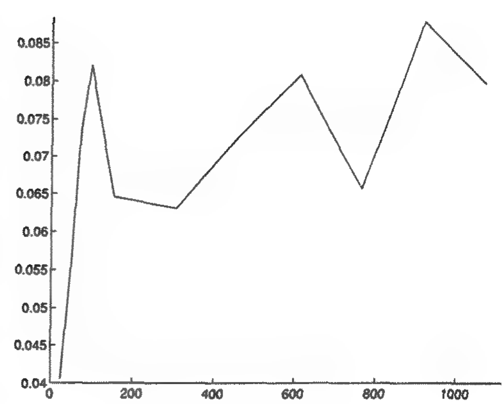

Figure 3. Constrained diffusion observed on longer time-scales

EFFECTS OF PACING AND ISOPROTERENOL ON MITOCHONDRIAL Ca^{2+} TRANSIENTS IN ADULT RABBIT CARDIAC MYOCYTES DURING THE CONTRACTILE CYCLE

Hisayuki Ohata, Brian Herman and John J. Lemasters

Department of Cell Biology & Anatomy, University of North Carolina, Chapel Hill, NC 27599-7090.

Using laser scanning confocal microscopy, we have developed methods to measure mitochondrial free Ca^{2+} in cultured adult rabbit cardiac myocytes during excitation-contraction.[1,2] Here, we examined the effect of isoproterenol and the rate of electrical pacing on the magnitude and duration of mitochondrial Ca^{2+} transients. The mitochondria and cytosol of myocytes were loaded with the Ca^{2+}-indicating fluorophore, Fluo-3-AM, at 4°C. Subsequently, the mitochondria were labeled with tetramethylrhodamine methylester (TMRM). In line scans, red TMRM fluorescence and green Fluo-3 fluorescence were simultaneously imaged by laser scanning confocal microscopy. Large transients of Fluo-3 fluorescence after electrical stimulation were observed both in cytosol and mitochondria (Figures 1). Isoproterenol (1 μM) increased the magnitude of Ca^{2+} transients caused by field stimulation and their subsequent rate of decay (Figure 2). This effect of isoproterenol was more marked in the cytosol than in mitochondria. In particular, the effect of isoproterenol on Ca^{2+} transients was least in perinuclear mitochondria. In the absence of isoproterenol, diastolic Fluo-3 fluorescence steadily increased in each region as pacing frequency increased from 0.5 Hz to 2 Hz (Figure 2). Additionally, peak systolic values increased gradually in mitochondria but not in cytosol as pacing increased. In the presence of isoproterenol, Ca^{2+} transients in each region became sharper, and diastolic fluorescence did not rise as markedly as pacing increased. Moreover, peak systolic fluorescence was relatively unaffected by pacing. We conclude that rapid mitochondrial Ca^{2+} transients occur during the contractile cycle in adult rabbit cardiac myocytes, which may be important in matching mitochondrial metabolism to myocardial ATP demand during changes in cardiac output. The shape of these transients is modified by the rate of pacing and adrenergic stimulation.

REFERENCES

1. Lemasters, J.J., E. Chacon, H. Ohata, I.S. Harper, A.-L. Nieminen, S.A. Tesfai and B. Herman (1995) Measurement of electrical potential, pH, and free Ca^{2+} in individual mitochondria of living cells by laser scanning confocal microscopy. In *Methods in Enzymology, Volume 206, Mitochondrial Genetics and Biogenesis: Part A*, G.M. Attardi and A. Chomyn, Eds., Academic Press, New York, pp. 428-444.
2. Chacon, E., H. Ohata, I.S. Harper, D.R. Trollinger, B. Herman and J.J. Lemasters (1996) Mitochondrial free calcium transients during excitation-contraction coupling in rabbit cardiac myocytes. *FEBS Letters*, in press.
3. This work was supported, in part, by Grant HL48769 from the National Institutes of Health.

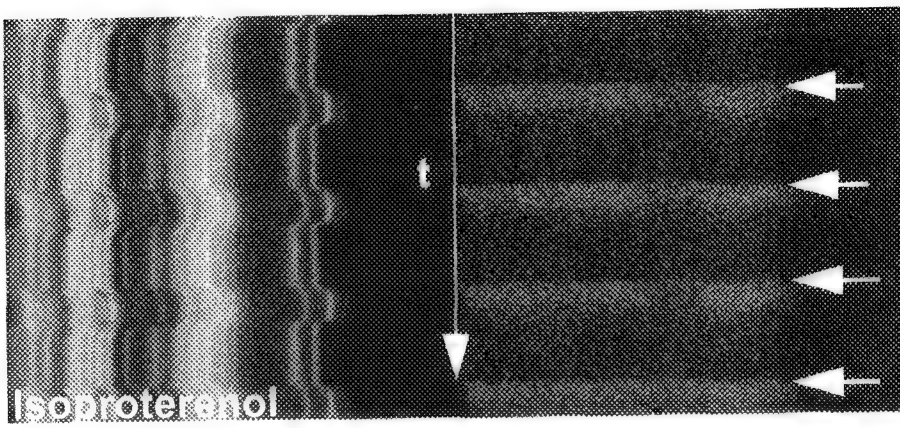

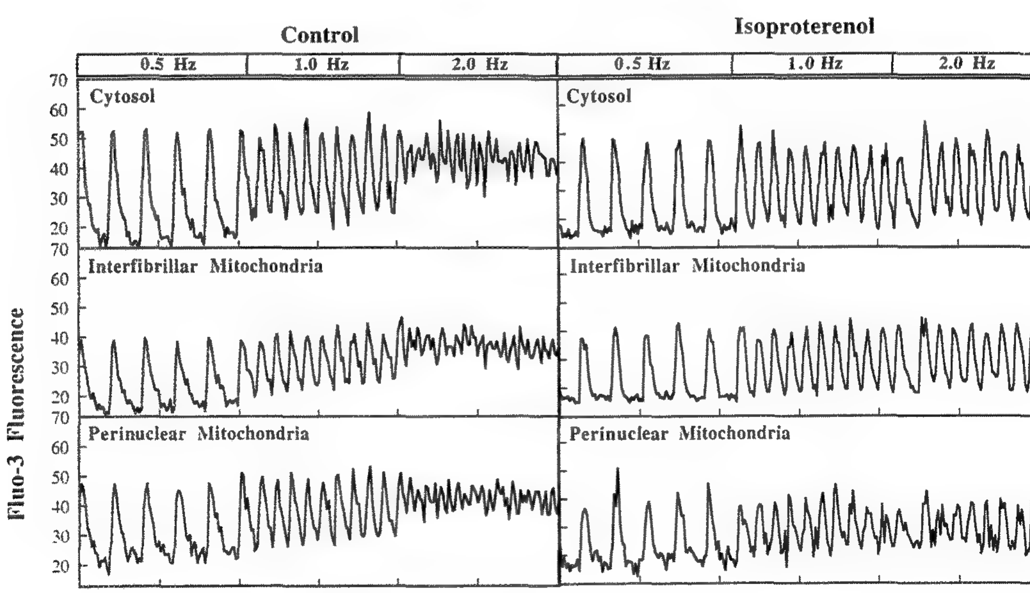

Figure 1. **Mitochondrial and cytosolic Ca^{2+} transients during field-stimulation.** A myocyte was loaded with Fluo-3 and TMRM at 4°C and stimulated (arrows) at 0.5 Hz in the presence of 1 μM isoproterenol. TMRM (left) and Fluo-3 (right) fluorescence is shown for a line-scan image collected at 25 msec per line.

Figure 2. **Effect of increasing pulse frequency on Fluo-3 fluorescence.** Pixels corresponding to cytosol, interfibrillar mitochondria, and perinuclear mitochondria were determined from TMRM fluorescence. Average pixel values of Fluo-3 in each region were calculated and plotted *versus* time for a myocyte incubated in the absence (left) and presence of 1 μM isoproterenol.

REAL-TIME CONFOCAL IMAGING OF CALCIUM CHANGES UPON EXOCYTOSIS IN *PARAMECIUM*

Sergei Levin, Birgit H. Satir

Department of Anatomy and Structural Biology, Albert Einstein College of Medicine, Bronx ,NY 10461.

Exocytosis in the unicellular eukaryote *Paramecium* occurs rapidly upon stimulation with the biological secretagogue lysozyme (100 μM) in a Ca^{2+}-dependent manner. Prior to stimulation each cell contains several thousand dense core secretory vesicles (trichocysts) docked beneath the cell membrane which can be induced to fuse with the plasma membrane either globally or locally. Fusion of the vesicle is followed by secretion and expansion of the trichocyst content from a 4 μm protein crystalline array to a 40 μm spear-like protein structure that are visible in the light microscope. The exocytosis microdomain of the cell membrane has been well characterized in earlier freeze fracture studies. The specific site of exocytosis was shown to consist of a rosette (fusion rosette) of 9 to 11 intramembrane particles surrounded by two outer rings of smaller sized particles. It is below these fusion rosettes that each of the secretory vesicles is docked and primed to release upon stimulation. In the absence of assembled fusion rosette normal release of trichocysts is blocked, as demonstrated with rosette defective mutants[1]. The fusion rosette has been postulated to function as calcium gates involved in exocytosis[3]. *Paramecium* has three known distinct Ca^{2+} channels: 1) the ciliary voltage-gated channel, 2) the hyper-polarization-activated channel, and 3) the anterior mechanosensory channel. Recently, we have described experiments indicating the presence of a fourth type of Ca^{2+} channel, a specific receptor operated Ca^{2+} conductance associated with lysozyme stimulated exocytosis[2]. In this study we have visualized local (temporal and spatial) calcium fluxes associated with discrete exocytic events, using real time confocal microscopy (Nikon, RCM 8000) and calcium imaging with Indo-1 dual emission dye.

Axenic cultures of late log phase cells were harvested, washed twice in calcium containing PIPES buffer and transferred to PIPES buffer containing 1mM KCl, 5mM $CaCl_2$, pH 7.2. After washing, cells were exposed to Indo-1 (0.01 μg/ml) for 40 min at room temperature, followed by $Ni(Ac)_2$ (100 μM) for 10-20 min in order to immobilize the cells. Localized exocytosis was stimulated by using a minispritzer to apply secretagogue (lysozyme/lucifer yellow mixture, 100:1) onto a selected region of the immobilized cell. Cells treated with $Ni(Ac)_2$ secreted normally (Fig. 1). $Ni(Ac)_2$ did, however, inhibit cell motility in a time and concentration dependent manner with 50 % of cells immobile after 15 min exposure to 100 μM (Fig. 2). Exocytosis was accompanied by a local transient increase in Indo-1 emission ratio (calcium concentration, Fig. 3). Calcium concentrations returned to pre-stimulation levels in approximately 60 sec, corresponding to the time of calcium sequestering. An example of our initial spatial resolution is depicted for a region of the cell membrane before (A) and after (B) stimulation (Fig. 4). These results demonstrated that stimulation of exocytosis was accompanied by a three-fold increase in local ionic calcium concentrations.

References

1. Beisson et al., J. Cell Biol 69(1):126-43, 1976
2. Hennesey et al., J. Membrane Biol 148:13, 1995
3. Satir and Oberg, Science 199:536, 1978
4. This research was supported by MSA undergraduate scholarship.

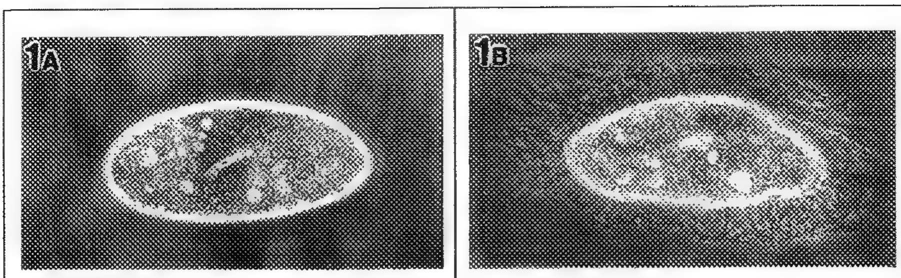

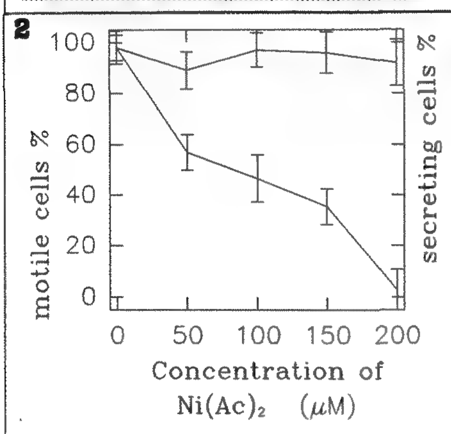

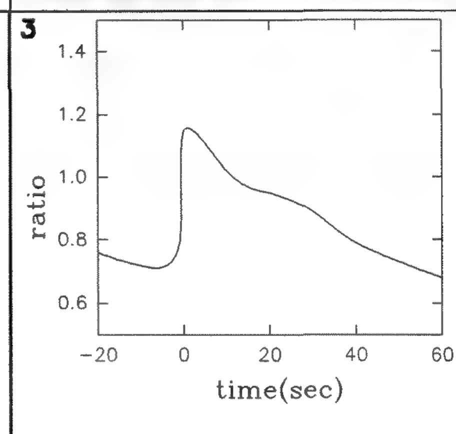

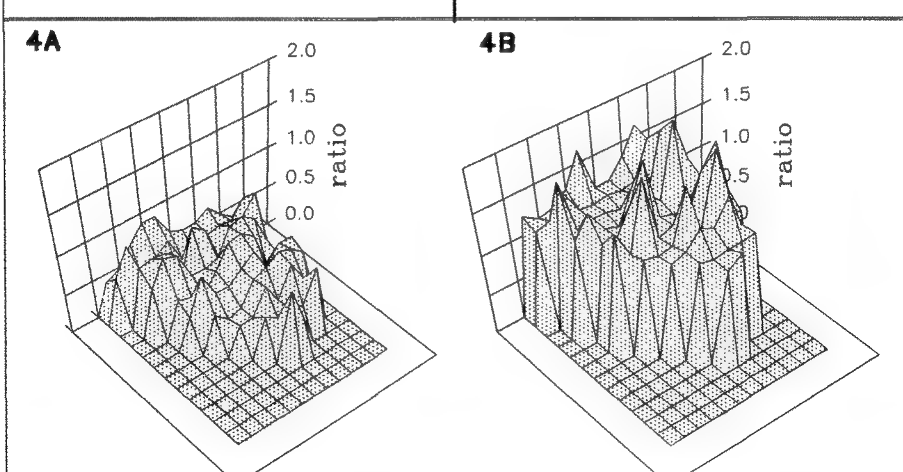

FIG 1. Light micrographs of *Paramecium tetraurelia* immobilized with Nickel Acetate (100μM), before (A) and after (B) stimulation of secretion with lysozyme (100μM).
FIG 2. $Ni(Ac)_2$ inhibits motility but does not inhibit secretion. Motility and secretion were measured after 20 minutes of exposure to $Ni(Ac)_2$.
FIG 3. Calcium concentration increase after lysozyme stimulation of a single cell. Lysozyme was added at time 0 and Ca^{2+} concentration was followed by Indo-1 emission ratio.
FIG 4. Local calcium concentration before (A) and after (B) addition of lysozyme. Ca^{2+} concentration was measured by Indo-1 emission ratio.

ULTRASTRUCTURAL MORPHOLOGY OF THE DORSAL LOBE OF THE PROSTATE GLAND IN CADMIUM-AND ZINC-TREATED RATS

Z.M. Bataineh*, N. Hailat**, S. Lafi, and I. Bani Hani***

*Department of Anatomy, ***Department of Urosurgery, Faculty of Medicine, **Department of clinical medicine, Faculty of Veterinary Medicine, Jordan University of Science and Technology, Irbid, JORDAN.

We have demonstrated in previous study that the nucli of the cells of the posterior lobe of the prostate gland sequesters less zinc in cadmium and zinc treated rats compared to the normal ones(1). In this study we will evaluate if the variation in the nuclear zinc concentration is associated with a concomitant variation in ultrastructural morphology. Two groups of animals were injected with 2mg/kg and 10 mg/kg cadmium chloride and zinc sulfate, respectively(2). Another group served as control. Dorsal lobe of the prostate gland from the three groups were prepared for conventional E.M study. Grids were examined and photographed by Hitachi-700 electron microscope.

Figure (1) shows prostatic cells from the posterior lobe of the prostate gland of a normal rat. The rough endoplasmic reticulum form a narrow continuous cisternae, most abundant at the lateral portion of the cell and sometimes acquired whorl-shaped appearance. Well-developed Golgi apparatus with abundant secretory vesicles are shown. Mitochondria are oblonged in shape and are dominant at the apical membrane of the cell. The apical portion is studded with short microvilli. Figure (2) shows prostatic cells of the dorsal lobe of the rat prostate gland. Rough endoplasmic reticulum shows a dilated cisternae, but show some discontinuity. Golgi apparatus is less profound with a narrow cisternae. Mitochondria vary in shape and are fewer in number. Microvilli are short but fewer, and the secretory vesicles are less abundant than those in normal rat.
Figure (3) shows cells from the dorsal lobe of the rat prostate gland. Rough endoplasmic reticulum shows few, but dilated cisternae with discontinuity. Golgi apparatus is profound filling the upper portion of the cell. Mitochondria are few in number, but evenly distributed all over the cell. Also, secretory vesicles are fewer in number. Microvilli are long but very few in number.

The variation in the ultrastructural morphology of the epithelial cells with different treatment, may reflect the ability of these cells to sequester zinc from the metabolic pool(3). These changes may be attributed to the synthesis of the protein metallothionein which is induced by the zinc and cadmium treatment(4). These metals have shown the ability to induce the metallothionein synthesis if injected to animals(2).

References:

1.Z.M. Bataineh et al., unpublished data.

2.A.M. Scheuhammer et al., Toxicology 36(1985)101-108.
3.J.A. Chandler et al., 9(1977)103-120.
4.Z.M. Bataineh et al., Prostate 9(1986)397-410.

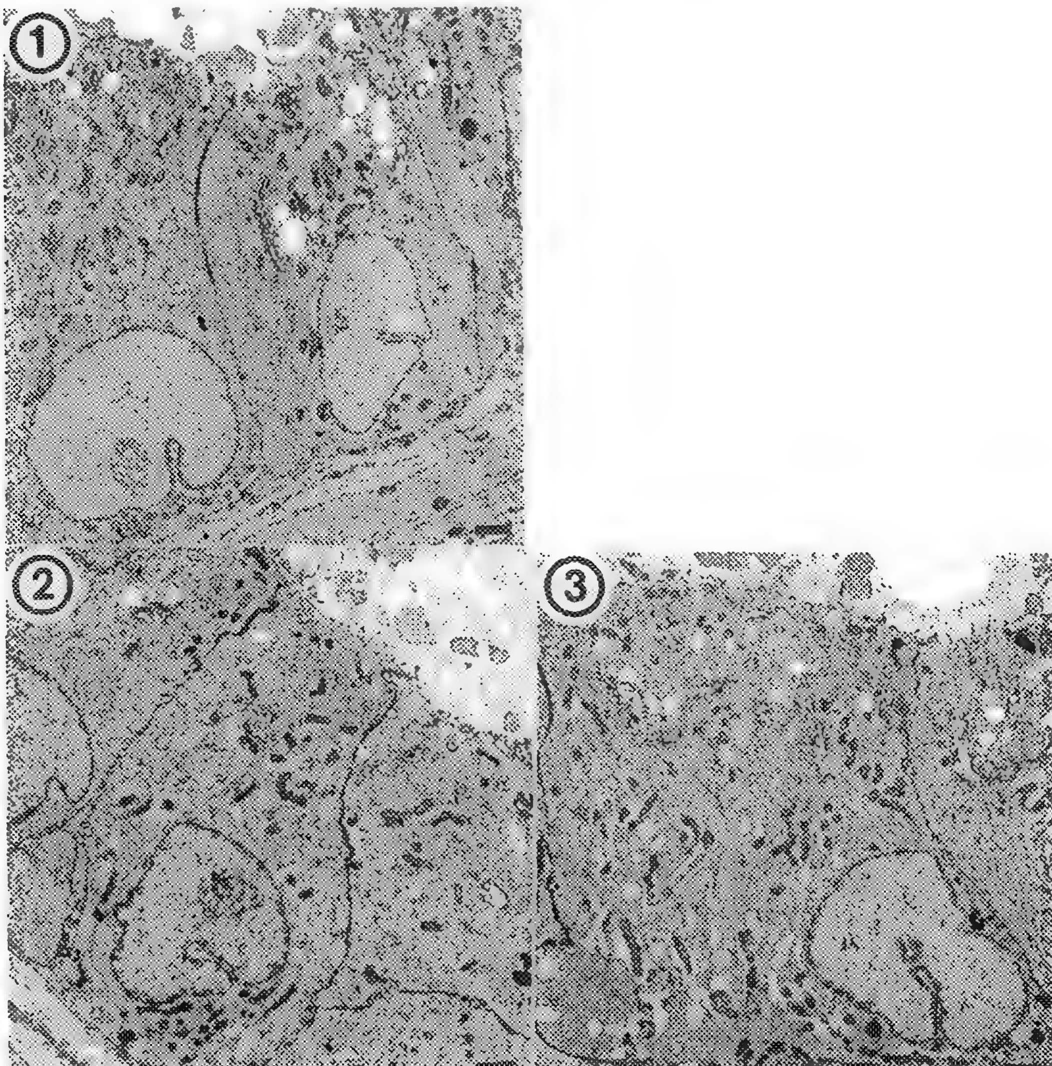

FIG.1 Shows epithelial cells from the posterior lobe of the prostate gland of the normal rat.
FIG.2 Shows epithelial cells from the posterior lobe of the prostate gland of the zinc treated rat.
FIG.3 Shows epithial cells from the posterior lobe of the prostate gland of the cadmium treated rat.

ADRENAL GLAND ULTRASTRUCTURAL PATHOLOGY IN *PLASMODIUM BERGHEI* PARASITIZED MICE

M. Pulido-Méndez,* H.J. Finol,** A. Rodríguez-Acosta,° A. Márquez,* I . Aguilar,° M.E. Girón,° N. González,** and J. García-Tamayo°°.

*Institute of Experimental Medicine, **Center of Electron Microscopy, Sciences Faculty, °Institute of Tropical Medicine, °°Institute of Pathological Anatomy. Central University of Venezuela. Apartado 47114, Caracas 1041 A, Venezuela.

The use of animal models is widely accepted in malaria research. *Plasmodium berghei* has been extensively studied because it produces a mortal malaria in rodents. Electron microscopic studies on brain and liver pathology have been performed in this infection[1,2]. In a previous ultrastructural work[3] we reported the capillary alterations observed in adrenal cortex in *P. berghei* infected mice. In this work we describe the cell and capillary changes we found in adrenal cortex and medulla in this infection.

Male mice weighing 18-22 g were inoculated intraperitoneally with *P. berghei* infected erythrocytes. At the ninth day animals were sacrificed when parasitemia ranged between 80-90%. Adrenal gland samples were processed by routine techniques and observed in a Hitachi H-500 transmission electron microscope .

Alterations were observed in both adrenal cortex and medulla. Capillary abnormalities included widening of fenestrae, swollen mitochondria and existence of autophagic vacuoles. Parasitized erythrocytes attached to endothelial cells were seen in some areas (Fig. 1). Necrotic capillaries were also observed (Fig. 2). Cortical and chromaffin cells showed alterations. Some cortical cells were seen disrupted. Parasitized erythrocytes were seen into cortical cells with altered cytoplasm (Fig. 3). Erythrocytes were also seen into some chromaffin cells (Fig. 4).

This work represents the first electron microscopic study on adrenal gland pathology in *P. berghei* infected mice. Our results, together with others obtained in *P. knowlesi* infection[4] suggest that adrenal gland could be an important target organ in malaria.

References

1. J. R. Rest and D. H. Wright. *J. Pathol.*, 127(1979)115.
2. J.F.G.M. Meis et al. *Am. J. Trop. Med. Hyg.*, 37(1987)506.
3. M. Pulido et al. *Acta Microsc.*, 4A(1995)45.
4. C. Natali. *Riv. Malariol.* 13(1934)563.
5. This work was supported by grants from the CDCH of UCV (Nr. 09.34.0173.93) and DIFMUCV.

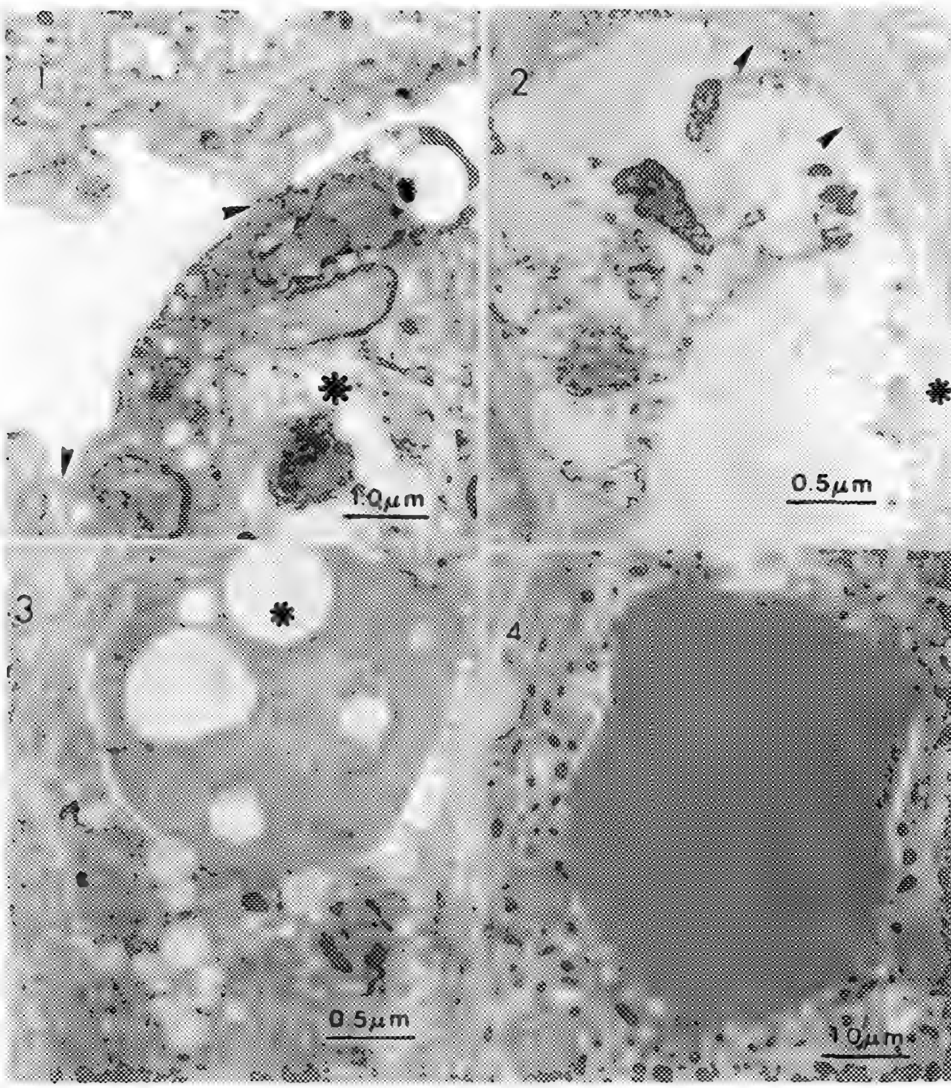

FIG 1 Arrowheads show zones of adherence between an altered parasitized erythrocyte (asterisk) and the endothelial cell.

FIG 2 A destroyed capillary with cell debris into the lumen Note rests of plasma (arroheads) and basement (asterisk) membranes.

FIG 3 A parasitized erythrocyte (asterisk) is surrounded by altered cortical cell cytoplasm

FIG. 4 An erythrocyte is located into a chromaffin cell.

Brain Homogenate Standards for Analysis of Aluminum in Alzheimer's Disease

C.R. Swyt*, Q.R. Smith**, and Q.S. Deng**

*Biomedical Engineering and Instrumentation Program
**National Institute on Aging
National Institutes of Health, Bethesda MD 20892

Aluminum doped brain homogenates have been proposed as a common set of standards to help resolve the disparity among the reported measured concentrations in plaques and tangled neurons in post-mortem Alzheimer's Disease brain specimens.[1] Among the many analytical techniques utilized electron probe microanalysis (EPMA) alone provides both the capability to identify, by backscattered electron imaging, cells in unstained sections and to achieve, using wavelength dispersive x-ray spectrometry (WDS), a sensitivity for aluminum approaching the higher reported normal aged brain concentrations.[2] We have prepared a set of freeze-dried 30 μm cryosections of aluminum doped homogenized rat brain. We report here the preliminary results of analysis by EPMA and briefly discuss some of the practical considerations in using such homogenates as a standard set for quantitation by WDS.

Stepwise distilled water dilutions of J.T. Baker Al Standard Solution #6917-04: Al 10 mg/ml in 0.3 M HCl were prepared giving aluminum concentrations from 1 mg/ml to 1 μg/ml. Two grams of rat brain were homogenized in 3 ml of each dilution and in 3 ml distilled water as a control. WDS data and energy dispersive spectra (EDS) were acquired concurrently from one carbon substrate mounted cyosection of each homogenate. At least three 50 μm by 50 μm areas on each section were scanned with a beam 15 keV in energy. Peak counts were determined by summing 5 or ten 60 second WDS measurements at the aluminum peak position (TAP crystal) and two settings each above and below peak, fitting a line to the four background values, and subtracting the predicted background value from the sum at peak. All values were between 1000 and 1500 counts. The standard deviation of ten repeated measurements giving a mean count of 1046 was 47 counts. The average normalized peak values are presented in Table 1. The estimated aluminum dry weight concentrations shown were obtained using the accepted value of 78% total brain weight for water content. Measured values were determined from WDS peak to background ratios using National Institute of Standards and Technology (NIST) reference glass K412.[3]

Mean peak counts were found to vary linearly with dilution ($r = 0.99$). However, inhomogeneity in the section aluminum distribution is apparent with concentration greater than 10 μg/ml. WDS background counts indicated changes with dilution in the sample average atomic number Z. Estimates of Z for quantitation were made using the NIST-NIH Desktop Spectrum Analyzer (DTSA) program.[4] Spectra were generated by adjusting an average brain composition until a good match to the average EDS spectrum for each standard was obtained (Fig. 1). DTSA reports the average Z for the composition. Detector parameters, etc. for spectrum generation were previously determined by comparing generated spectra to those from a suite of NIST standard reference materials. Inhomogeneity and variable composition of the matrix, illustrated by the EDS spectra in Fig. 2., contributed to the differences between estimated dry weight concentrations and those calculated for the WDS analytical volume.

These results show that aluminum doped brain homogenates must be utilized carefully for quantitation. They should be homogenous at better than analytical volume size, and aluminum concentrations in the analytical volume should be verified using certified standards taking into account the total composition.

References

1. M.A. Lovell et al., *Journal of Toxicology and Environmental Health*, (in press).
2. W.R. Markesbery, et al., *Neurobiology of Aging*, 5(1984)19.
3. J.I. Goldstein et al., *Scanning Electron Microscopy and X-ray Microanalysis*, Plenum Press: New York (1992)490.
4. C.E. Fiori et al., (National Institute of Standards and Technology, Gaithersburg MD 20899). Desktop Spectrum Analyzer U.S. Patent 529913, 1993.

TABLE 1. - Preliminary analysis: Aluminum in brain homogenates.

μg Al/ml	pk counts±stdev	SEM(samples)	avg Z (EDS)	ppm (WDS)	ppm (calc)
1000	10419 ±1293	747 (3)	7.49	6861	6303
100	1354 ± 112	45 (6)	7.04	1204	676
10	102 ± 22	15 (3)	7.16	88	68
1	11 ± 31	11 (8)	7.16	10	7
control	15 ± 32	18 (3)	7.00	13	9

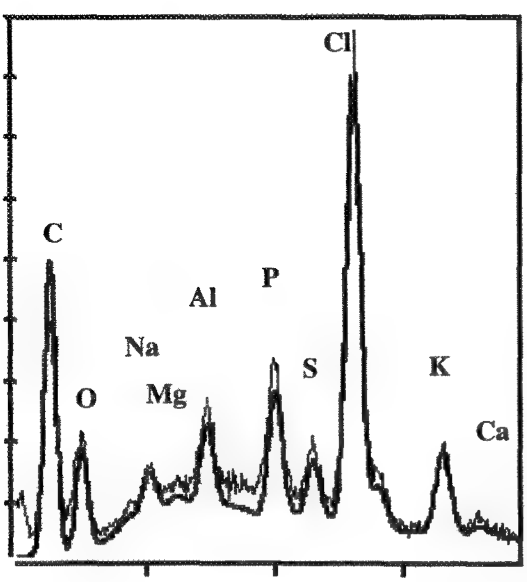

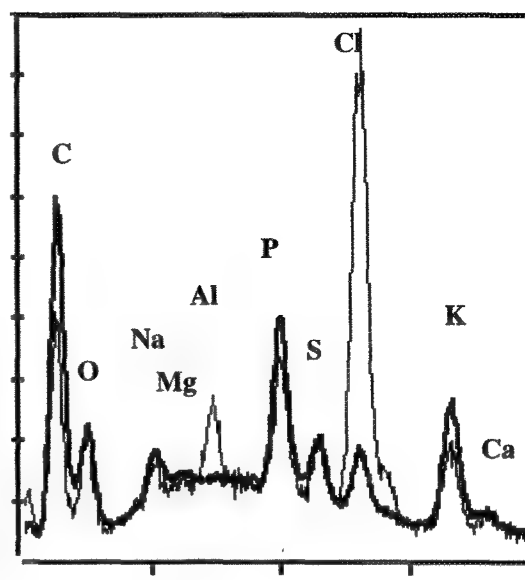

Fig. 1 DTSA generated spectrum (thick line) and EDS spectrum from freeze-dried 30 μm thick aluminum doped brain homogenate cryosection (1 mg Al/ml homogenate).
Fig. 2 EDS spectra illustrating compositional variations among freeze-dried 30 μm thick aluminum doped brain homogenate cryosections (thick line, 1 μg Al/ml of homogenate; thin line, 1 mg Al/ml).

EFFECT OF pH AND INHIBITORS ON BETA-AMYLOID FIBRIL ASSEMBLY

Beverly E. Maleeff[1], Timothy K. Hart[1], Stephen J. Wood[2] and Ronald Wetzel[2]

SmithKline Beecham Pharmaceuticals, Departments of Toxicology[1] and Macromolecular Sciences[2], King of Prussia, PA

Alzheimer's disease is characterized post-mortem in part by abnormal extracellular neuritic plaques found in brain tissue[1]. There appears to be a correlation between the severity of Alzheimer's dementia *in vivo* and the number of plaques found in particular areas of the brain. These plaques are known to be the deposition sites of fibrils of the protein β-amyloid. It is thought that if the assembly of these plaques could be inhibited, the severity of the disease would be decreased. The peptide fragment Aβ, a precursor of the β-amyloid protein, has a 40 amino acid sequence, and has been shown to be toxic to neuronal cells in culture after an aging process of several days. This toxicity corresponds to the kinetics of *in vitro* amyloid fibril formation[2]. In this study, we report the biochemical and ultrastructural effects of pH and the inhibitory agent hexadecyl-N-methylpiperidinium (HMP) bromide, one of a class of ionic micellar detergents known to be capable of solubilizing hydrophobic peptides, on the *in vitro* assembly of the peptide fragment Aβ[2,3].

The Congo red binding assay was used to quantitate *in vitro* peptide assembly into fibrils[2]. Aβ was prepared and incubated for 2 hours with or without inhibitor in a microtiter plate well. Congo red solution was then added to each well and allowed to bind to the peptide for 30 minutes. The plate was then shaken briefly and the absorbance read at 540 and 480 nm. The amount of Congo red bound was calculated and compared to values for control wells containing no inhibitor. A panel of 4300 compounds was initially screened for inhibitory activity. Of those, 29 agents were found to exhibit good apparent inhibitory activity. These compounds were subjected to a secondary assay in which Aβ aggregation was determined by the turbidity of the suspension. From this assay, HMP bromide was found to be the most potent inhibitor.

We examined the morphology of fibers formed in the presence or absence of inhibitors. Samples of peptide were prepared for transmission electron microscopy either by incubation *in vitro* or *in situ* with or without inhibitors. *In vitro* samples were incubated at pH 5.8, 25°C for 2 hours or at pH 7.4, 37°C for 48 hours, conditions under which fibrillization is known to occur, and were then applied to carbon-stabilized, collodion-coated copper grids. An *in situ* procedure was developed to study fibrillization using conditions similar to those used in the Congo red binding assay. The *in situ* procedure consisted of applying an aliquot of the peptide solution at pH 5.8 to a grid, and incubating in a moist chamber for 2 hours. All samples were negatively stained with 2% aqueous uranyl acetate and examined.

Microscopically, there were differences between Aβ aggregates formed *in vitro* at pH 7.4 and pH 5.8 (Figure 1). At pH 7.4 the aggregates appeared as classic amyloid fibrils, approximately 10-15 nm wide and of indeterminant length. The pH 5.8 aggregates appeared either as rope-like structures, approximately 50-70 nm wide, or as aggregated globules approximately 40-50 nm in diameter. Addition of HMP bromide at pH 7.4 inhibited fibril formation, but clustered globules, approximately 50-60 nm in diameter, and short filaments, approximately 5-10 nm wide and 200 nm in length, were present (Figure 2). At pH 5.8, HMP bromide caused the peptide to appear as a mass of short fibrous segments, approximately 5-8 nm wide and 20 nm long. Examination of Aβ assembly *in situ* revealed an absence of any fibril-like forms (Figure 3). Control samples contained globular aggregates, approximately 30-40 nm in diameter, whereas inhibitor-treated samples contained globular aggregates that were about half the diameter (approximately 15 nm). The microscopic findings substantiate the biochemical results that HMP bromide inhibits the assembly of Aβ peptides into multimeric forms under a number of conditions. Microscopic analysis provides a sensitive secondary assay for screening compounds for use in treating Alzheimer's disease.

References

1. Crowther, RA, 1991. Structural aspects of pathology in Alzheimer's disease. Biochim. Biophys. Acta 1096:1-9.
2. Wood, SJ, et al., 1996. Selective inhibition of Aβ fibril formation. J. Biol. Chem., in press.
3. Wood, SJ, et al., 1996. Physical, morphological and functional differences between pH 5.8 and 7.4 aggregates of the Alzheimer's amyloid peptide Aβ. J. Mol. Biol., in press.
4. This work has been supported by SmithKline Beecham Pharmaceuticals.

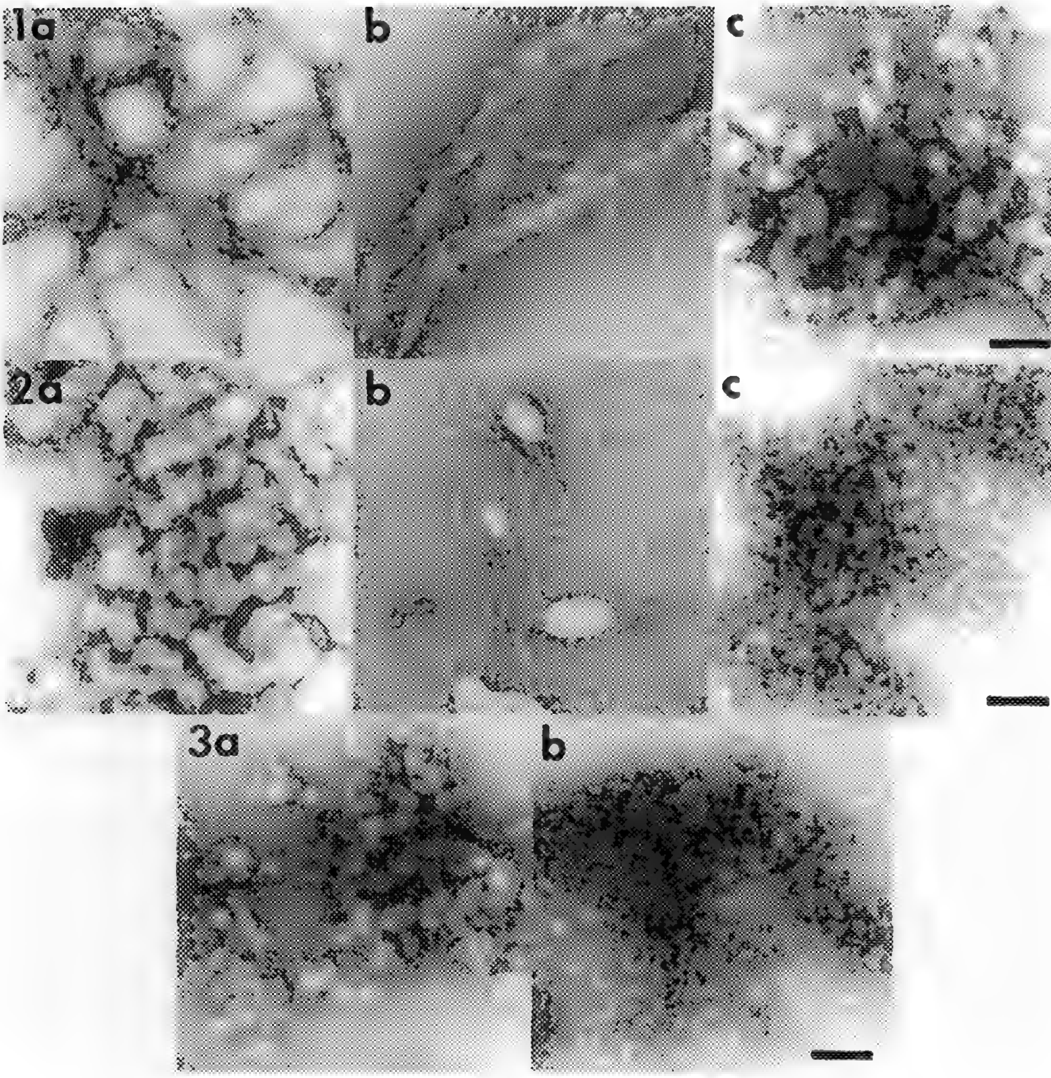

Figure 1. Negative stain preparations of Aβ aggregates formed in vitro at (a) pH 7.4 and (b,c) pH 5.8. The pH 7.4 aggregate is representative of the classic amyloid fibril. Bar = 100 nm.

Figure 2. Addition of the inhibitor HMP bromide prevents fibril formation at pH 7.4, but (a) globular aggregates and (b) short filaments are present. At pH 5.8, aggregates are composed of short filamentous segments (c). Bar = 100 nm.

Figure 3. Assembly of Aβ peptides *in situ* at pH 5.8. Control aggregates are globular clusters (a), while peptides incubated with HMP bromide (b) are globular, yet smaller and less likely to clump. Bar = 100 nm.

Distensibility and Wall Composition of Rat Cerebral Arterioles in Hypertension Induced by Chronic Blockade of Nitric Oxide Synthase

S. M. Ghoneim, J. M. Chillon, and G.L. Baumbach

Department of Pathology , and Cardiovascular Center, University of Iowa College of Medicine, Iowa City , IA, 52242

We have previously reported that, during chronic hypertension, cerebral arterioles undergo hypertrophy of the vessel wall, accompanied by a paradoxical increase in passive distensibility.[1,2]
We have proposed that this increase may be due to a reduction in the proportion of nondistensible (collagen and basement membrane) to the distensible (smooth muscle, elastin and endothelium) components of the vessel wall.[3,4] We have recently observed in stroke-prone spontaneously hypertensive rats(SHRSP), that an endothelium derived factor, endothelin, may contribute to hypertrophy, but not to increases in passive ditensibility, of cerebral arterioles vessel wall.[5]

The goal of this study was to examine wall mass, composition and passive ditensibility of cerebral arterioles in chronic hypertension induced by decreased availability of another endothelium derived factor, nitric oxide (NO).

Four weeks old male Sprague-Dawley rats were treated with L^G- nitro-L-arginine methyl ester (L-NAME; 10 mg /kg/day) in the drinking water . We examined distensibility of maximally dilated cerebral arterioles in 4 months old Sprague-Dawley rats. Arterioles were then fixed at physiological pressure(2.25% gluterladehyde in 0.10 mol/L cacodylate buffer) , the arteriolar segment used for distensibility measurements was removed then immerse fixed , rinsed briefly in 0.1M cacodylate buffer,osmicated and processed routinely for electron microscopy (TEM).

One micron thick , cross sections were cut from all specimens and stained with Richerson's stain for light microscopical examination. Cross sectional areas (CSA), inner/outer diameter of vessels were calculated via a digitizer and mean & pulse pressure measured. Thin sections were subsequently obtained ,stained with Phosphotungstic acid and examined under a Hitachi 7000 EM. Ten micrographs were taken from each specimen at X9000 magnification and enlarged X3 for a final magnification of X 27000. Micrographs were point counted via Weibel single investigator technique,and data analyzed. Volume density of smooth muscle , elastin,collagen, basement membrane , and endothelium was quantitated from elctronmicrographs of the vessel wall.

Our results showed that pial arterioles mean and pulse pressures and cross-sectional area of the vessel wall were significantly greater in L-NAME treated Sprague-Dawley rats than in untreated rats.(Fig 1). Thus during L-NAME induced hypertension, cerebral arterioles undergo hypertrophy of the vessel wall. The stress-strain curve in pial arterioles from L-NAME treated rats was similar to the curve in control rats (Fig.2). This finding suggests that despite hypertrophy of the vessel wall, L-NAME induced hypertension was not accompanied by alterations in passive distensibility .

We also observed that cross sectional area (CSA)of smooth muscle(SM),elastin (E)and basement membrane(BaseM) were significantly greater in L-NAME treated than in untreated rats(Fig.1,3a,b). CSA of collagen (C) was not significantly increased, whereas CSA of endothelium (Endo)was similar in L-NAME treated and untreated Sprague-Dawley rats(Fig. 1). The ratio of nondistensible-to-distensible components of the arteriolar wall ({C+BaseM}/{E+SM+Endo}) was similar in treated and untreated Sprague-Dawley rats(Fig.1). Thus when all of the major components of the arteriolar wall were taken into account, hypertrophy in Sprague-Dawley rats with L-NAME induced hypertension was not accompanied by modification of the arteriolar wall components.

The findings in this study would appear to support the concept that proportional composition influences vascular dispensability of cerebral arterioles.

References:

1. G.L. Baumbach, D.D.Heistad., Hypertension, 13(1989)968.
2. G.L. Baumbach, M.A.Hajdu. , Hypertension, 21(1993)816.
3. G.L. Baumbach, et al., Journal Physiology(Lond), 416(1989)123.
4. G.L. Baumbach, et al., American Journal of Pathology, 133(1988)464.
5. J.M. Chillon, et al., Hypertension, 27(1996)794.

6. This work was supported by NIH Grants HL-22149 and NS-24621 and funds from the Iowa Affiliate of the American Heart Association.

Table: Baseline values and pial arteriolar wall composition in untreated Sprague-Dawley rats and Sprague-Dawley rats that were treated with L-NAME.

Parameter	Untreated	L-NAME
Pressure		
Systemic Arterial Mean Pressure (mmHg)	103±2	170±9*
Pial Arteriolar Pressure (mmHg)		
Mean	42±2	87±6*
Pulse	13±2	25±2*
Wall composition		
Cross-Sectional Area of Vessel Wall (μm^2)	1019±58	1839±70*
Cross-sectional Area (μm^2)		
Smooth Musle Cells	660±46	1347±57*
Elastin	71±9	129±10*
Collagen	4.7±1.3	8.7±2.0
Basement Menbrane	69±7	99±8*
Endothelium	217±24	250±21
Ratio of nondistensible to distensible components		
(C+BaseM)/(E+SM+Endo)	0.079±0.008	0.063±0.006

Values are mean±SEM in 6 untreated Sprague-Dawley rats, and 8 Sprague-Dawley rats treated with L-NAME. *p<0.05 vs untreated.

C: Collagen; E: Elastin; BaseM: Basement Menbrane; SM: Smooth Muscle; Endo: Endothelium

1

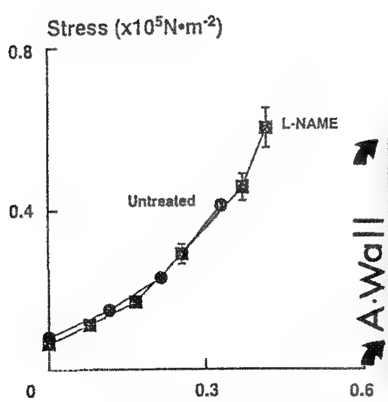

2

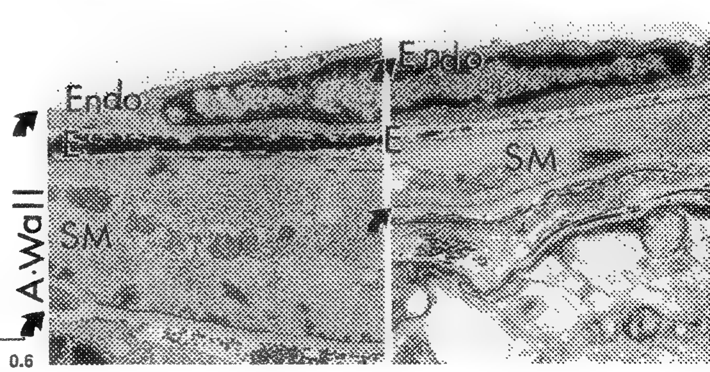

3a 3b

FIG.1 Table showing pial arteriolar wall composition values in treated & untreated rats.

FIG.2 Stress-strain curve shifts to the right in treated rats indicates increase in arteriolar distinsibility.

FIG.3 Pial arteriolar (CS) wall samples showing increase wall thickness in treated than untreated rats.

DIRECT WHOLE MOUNT ELECTRON MICROSCOPIC DEMONSTRATION OF INHIBITION OF FIBRINOGEN-GOLD BINDING BY ANTAGONISTS OF THE PLATELET GLYCOPROTEIN IIB-IIIA RECEPTOR

J. C. Mattson,* S. Khurana,** D. M. Farrah,* H. K. Hatfield*

*Department of Clinical Pathology, William Beaumont Hospital, Royal Oak, MI 48073
**Division of Cardiology, Department of Medicine, William Beaumont Hospital, Royal Oak, MI 48073

Glycoprotein IIb-IIIa (GPIIb-IIIa) is an externally exposed membrane complex on platelets which serves as an activation-dependent receptor for fibrinogen, fibronectin, von Willebrand factor and vitronectin. These ligands share an RGD sequence which binds to a specific site on GPIIIa. In addition, fibrinogen has a gamma chain dodecapeptide sequence that also interacts with GPIIb. Binding of fibrinogen to GPIIb-IIIa is directly responsible for cross-bridging adjacent platelets leading to platelet aggregate formation. In the search for pharmacologic anti-thrombotic agents, there has been considerable interest in drugs that inhibit platelet function, aspirin being the classic example. Recent efforts have been directed to the development of agents that target GPIIb-IIIa. Several synthetic peptides and peptidomimetic agents have been developed to compete with the RGD binding site on GPIIb-IIIa.[1] Monoclonal antibodies directed against sites at or near the fibrinogen binding domains on GPIIb-IIIa have also been of considerable interest. The chimerised Fab fragment of the monoclonal antibody 7E3 (ReoPro, Centocor) has been approved by the US FDA to reduce the thrombotic complications of high risk angioplasty.[2] The monitoring of these anti-GPIIb-IIIa drugs has traditionally been with platelet aggregation, an assay with considerable biologic variability and lack of specificity. We have examined the ability of several peptides and peptidomimetic agents to inhibit gold-labeled fibrinogen binding in a whole mount electron microscopy assay.[3] Gel-filtered platelets were allowed to adhere and spread on formvar-coated, carbon-stabilized nickel grids for 20 minutes at 37 °C. Grids were then incubated with fibrinogen-gold in the presence or absence of GPIIb-IIIa antagonist. The concentration range for each antagonist was selected to include doses currently being tested clinically and the known in vitro inhibitory concentrations of RGDS and dodecapeptide (Table 1). Results indicate that inhibition of fibrinogen binding using a gold-labeled ligand and whole mount electron microscopy is an effective measure of GPIIb-IIIa blockade by all peptides and peptidomimetics tested (Figures 1-3). The pharmacologic agents MK-383 (Merck) and SC-54701 (Searle) performed as well as the prototype RGDS and demonstrated inhibition comparable to c7E3 monoclonal antibody.

1. J. Lefkovits et al., NEJM (1995) 332: 1553.
2. The EPIC investigators, NEJM (1994)330: 956.
3. D. W. Estry et al., Eur J Cell Biol (1991)54: 196.
4. This work was funded by the William Beaumont Hospital Research Institute

Table 1 . Concentrations (A-D) of Inhibitors to Glycoprotein IIb-IIIa

ANTAGONIST	A	B	C	D
RGDS (μM)	0.05	0.5	1.0	4.0
DODECAPEPTIDE (μM)	20	40	80	100
c7E3 (μg/mL)	0.25	0.5	1.0	3.6
MK-383 (ng/mL)	50	100	250	500
SC-54701 (ng/mL)	10	20	40	400

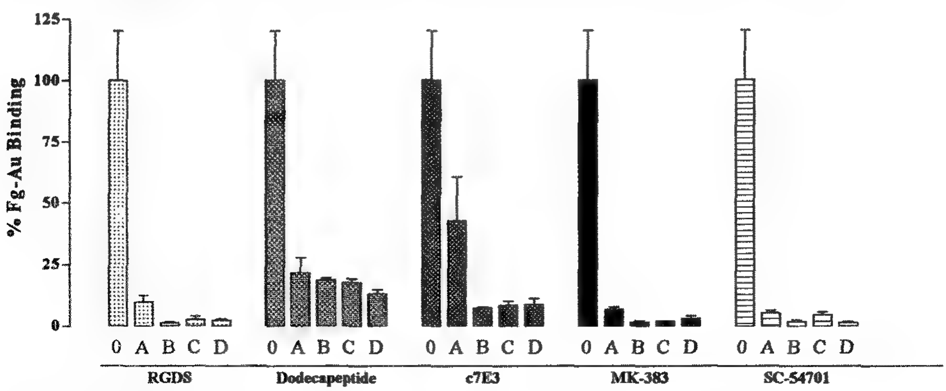

FIG 1. Effect of Glycoprotein IIb-IIIa blockade on Fibrinogen-Gold Binding

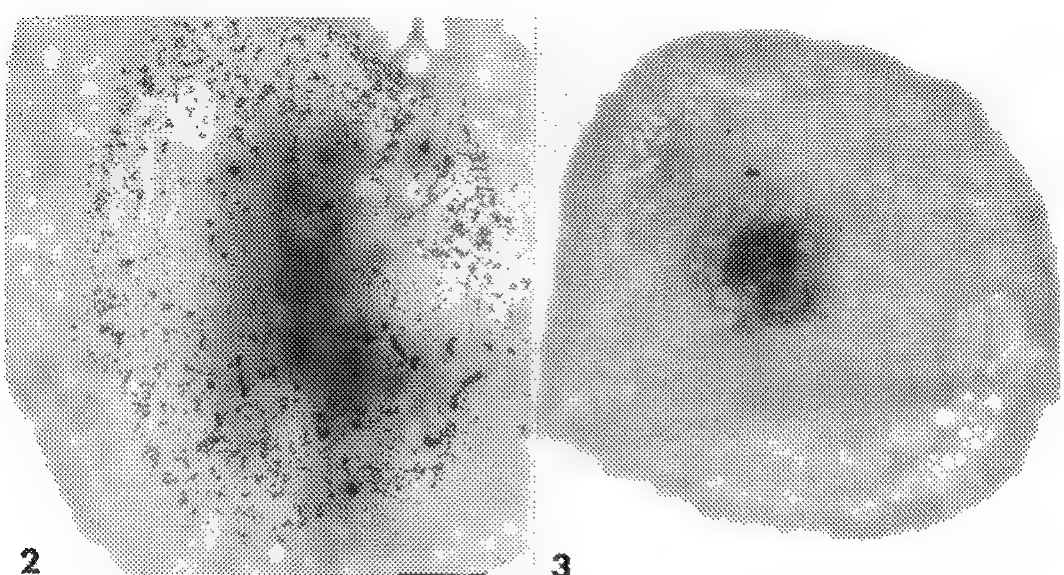

FIG. 2 Fibrinogen gold binding in the absence of Glycoprotein IIb-IIIa antagonist. Bar =1 μ

FIG 3 Inhibition of fibrinogen-gold binding by 500 ng/mL MK-383. Bar =1 μ

ABSENCE OF TEMPORAL ORDERING OF APOPTOTIC FEATURES IN HEAT-SHOCK TREATED LEUKEMIA AND LYMPHOMA CELL LINES

D.W. Fairbairn*, M.D. Standing**, and K.L. O'Neill*

*Department of Microbiology, Brigham Young University, Provo, UT 84602
**Microscopy Laboratory, Brigham Young University, Provo, UT 84602

Apoptosis is a genetically defined response to physiological stimuli that results in cellular suicide. Features common to apoptotic cells include chromatin condensation, oligonucleosomal DNA fragmentation, membrane blebbing, nuclear destruction, and late loss of ability to exclude vital dyes.[1] These characteristics contrast markedly from pathological necrosis, in which membrane integrity loss is demonstrated early, and other features of apoptosis, which allow a non-inflammatory removal of dead and dying cells, are absent. Using heat shock-induced apoptosis as a model for examining stress response in cells, we undertook to categorize a variety of human leukemias and lymphomas with regard to their response to heat shock. We were also interested in determining whether a common temporal order was followed in cells dying by apoptosis. In addition, based on our previous results[2], we investigated whether increasing heat load resulted in increased apoptosis, with particular interest in relatively resistant cell lines, or whether the mode of death changed from apoptosis to necrosis.

Several cell lines exposed to heat shock (43°C for one hour) exhibited differential apoptosis induction using DNA fragmentation as an endpoint by the DNA comet assay (reviewed in ref. 3) 12 hours after treatment, and using cell shrinkage or pyknosis as an endpoint by trypan blue exclusion 24 hours after induction. Cells displaying less than 15% apoptosis were considered insensitive (BJAB and K562), 15-30% of low sensitivity (Raji and Louckes), 30-50% of moderate sensitivity (B95-8 and Namalwa), 50-75% of high sensitivity (HL-60R), and above 75% of extremely high sensitivity (YAC-1). Examination of routine resin-embedded light sections, stained with Toluidine Blue O and Azure II, confirmed the chromatin condensation. Increasing treatment temperature from 37°C by 2°C increments resulted in a change of cell death from apoptosis peaking at 43°C, to necrosis, which became apparent at 45°C and was predominant in almost all cells in all cell lines tested at 49°C. Interestingly, cell lines relatively resistant to heat shock-induced apoptosis did not show an increase of apoptosis at higher temperatures before being killed by pathological temperatures. This argues against a window of sensitivity for apoptosis, and indicates the presence of protective factors; or alternatively, the absence of apoptosis-predisposing factors common to the other cells. We were unable to describe a common temporal morphological pathway leading to eventual death, as some features were more predominant in some lines and absent in others, and the order of events was not conserved across the cell lines.

1. E. White, *Genes and Development*, vol. 10 pp. 1-15
2. D.W. Fairbairn et al., *Scanning* (1996) in press.
3. D.W. Fairbairn et al., *Mutation Research* (1995) 339:37.

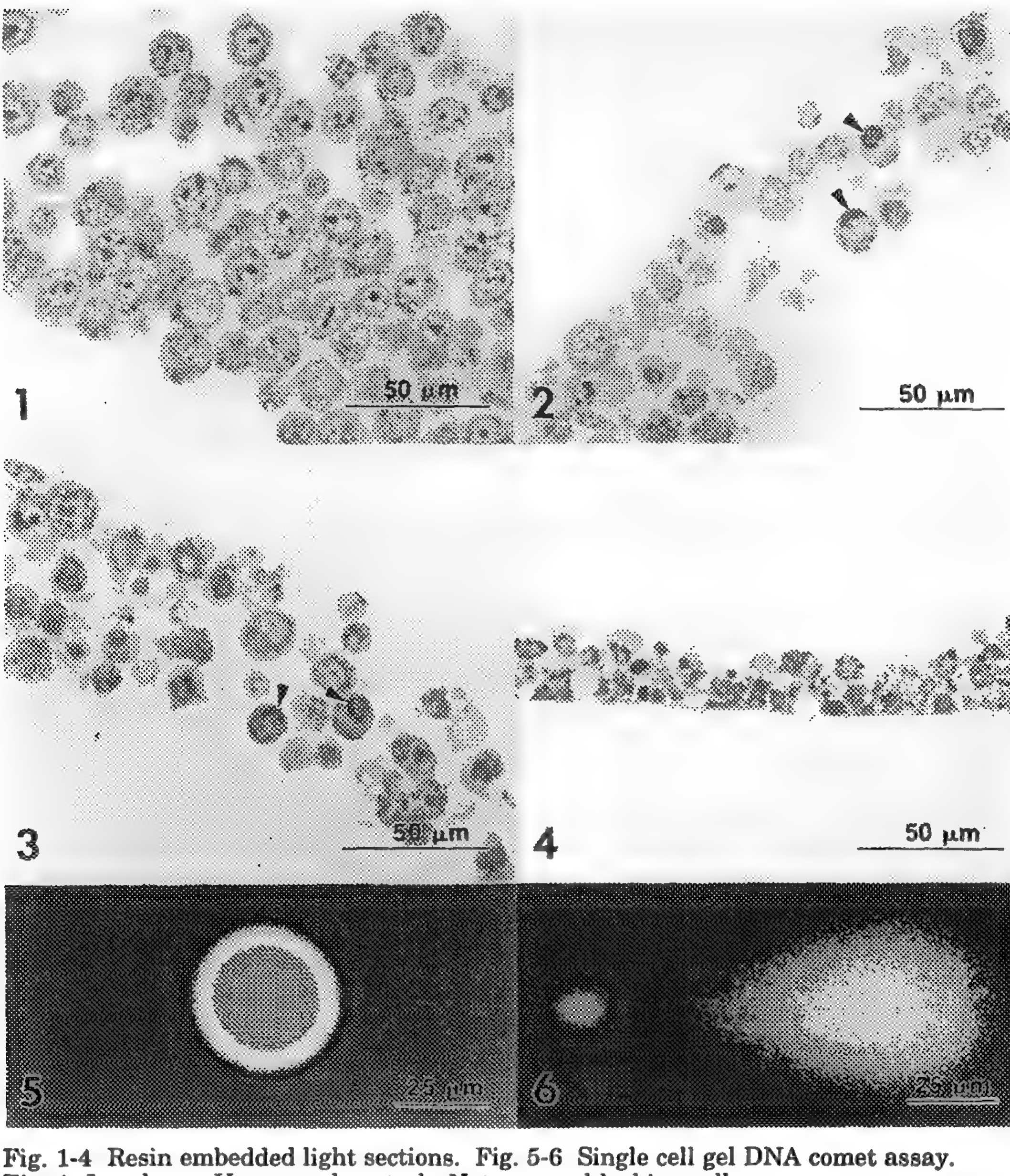

Fig. 1-4 Resin embedded light sections. Fig. 5-6 Single cell gel DNA comet assay.
Fig. 1 Louckes -- Unexposed control. Note normal looking cells.
Fig. 2 Louckes -- Heat shocked. Note condensed chromatin (arrows).
Fig. 3 HL60R -- Heat shocked. Note condensed chromatin (arrows).
Fig. 4 YAC-1 -- Heat shocked. Note general cellular degradation.
Fig. 5 Raji -- Unexposed control. Circular appearance of DNA indicates no damage.
Fig. 6 Raji -- Heat shocked as above. Long comet indicates DNA fragmentation.

ACTIVATION OF ISOLATED HETEROPHILS FROM CHICKS STIMULATED IN VIVO WITH *SALMONELLA ENTERITIDIS*-IMMUNE LYMPHOKINES

R. B. Moyes, R. E. Droleskey, M. H. Kogut, and J. R. DeLoach

USDA, Agricultural Research Service, Food Animal Protection Research Laboratory, College Station, TX 77845

Salmonella enteritidis (SE) is of great concern to the poultry industry due to the organism's ability to penetrate the intestinal mucosa of the laying hen and subsequently colonize the ovaries and yolk membrane. The resultant subclinical infection can lead to SE infection of raw eggs and egg products. Interference with the ability of the organism to invade has been linked to the activation and recruitment of inflammatory polymorphonuclear cells, heterophils, to the lamina propria of the intestinal tract.[1]

Recently it has been established that heterophil activation and increased resistance to SE organ invasion can be accomplished by the administration of SE-immune lymphokines (SE-ILK) obtained from supernatants of concanavalin-A stimulated SE immune T lymphocytes from SE hyperimmunized hens.[2] Invasion of SE into the lamina propria provides a secondary signal for directing activated heterophils to the site of SE invasion.

In suspension culture, normal and SE-ILK lymphokine stimulated heterophils isolated from peripheral blood were found to be morphologically similar when observed by scanning electron microscopy (SEM) (Figs. 1, 2). Cells were spherical with limited cytoplasmic projections. Activated heterophils however, displayed increased receptor-mediated, CD11b/CD18, adherence in vitro to BSA-coated slides as compared to control heterophils from PBS-injected birds. Since antibodies to the Mac-1 complex (CD11b/CD18) inhibit adherence of SE-ILK activated but not normal heterophils, it can be surmised that these adhesion molecules play a major role in the enhanced response to SE invasion. In preparations of cells incubated with a BSA matrix examined by SEM, unstimulated control heterophils were sparse and of generally round or flattened morphology with few cellular projections. In contrast, SE-ILK stimulated heterophils were evident at a greater population density and displayed increased numbers of filamentous projections of cell cytoplasm (Fig. 3). SE-ILK stimulated heterophils which migrate to and were isolated from the peritoneal cavity of immunized birds also exhibited increased in vitro attachment as compared to the cells isolated from peripheral blood although a greater degree of cytoplasmic extension was evident in stimulated cells (Fig. 4). These findings indicate that similar to other animal models, transendothelial migration of activated heterophils is an adhesion molecule mediated event specifically CD11b/CD18, and this activation can be discerned by morphological traits as demonstrated in this study.[3,4,5]

References

1. M. H. Kogut et al., 1994, *Microb. Pathog.*, 16:141-151.
2. M. H. Kogut et al., 1995, *J. Leukocyte. Biol.*, 57:56-62.
3. T. K. Kishimoto et al., 1994, *Adv. Pharmacol.*, 25:117-169.

4. C. W. Smith et. al., 1989, *J. Clin. Invest.*, 83:2008-2017.
5. T. Morisaki et. al., 1991, *Clin. Immunol. Immunopathol.*, 61:365-375.

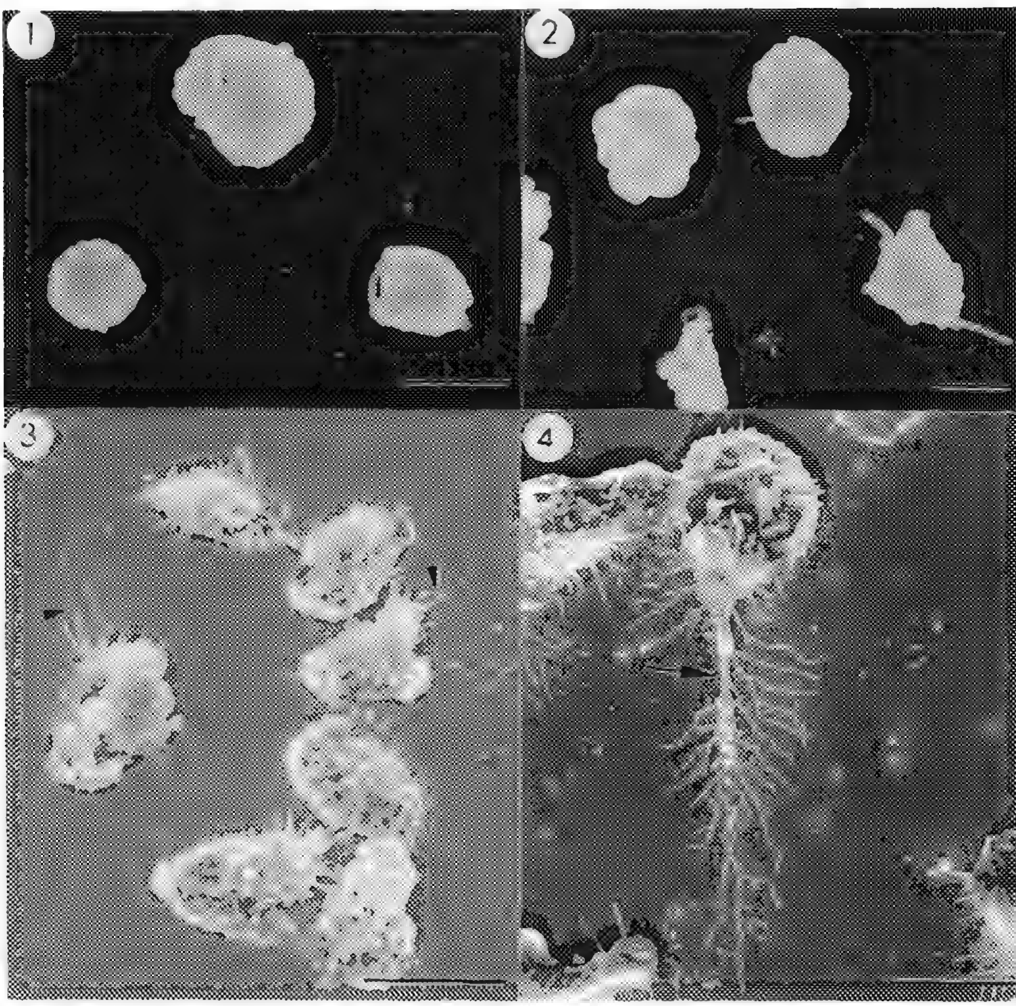

Fig. 1. Isolated peripheral blood heterophils from control chicks. Bar = 5 μm.

Fig. 2. Isolated peripheral blood heterophils from SE-ILK immunized chicks. Bar = 5 μm

Fig. 3. BSA-attached peripheral blood heterophils from SE-ILK immunized chicks with projections of cell cytoplasm (arrowheads). Bar = 10 μm

Fig. 4. BSA-attached SE-ILK activated heterophil isolated from the peritoneal cavity of SE-ILK immunized chicks containing an extended projection of cell cytoplasm (arrow) with numerous smaller projections radiating from it. Bar = 10 μm.

CYPRINELLA LUTRENSIS GILL LESIONS AFTER EXPOSURE TO TERBUFOS

Ibrahim A. Messaad* and Edward J. Peters*

*Dept. of Forestry, Fisheries and Wildlife Science, University of Nebraska--Lincoln, NE 68583-0814.

Terbufos (O,O-diethyl, S-(((1,1-dimethylethyl)thio)methyl) phosphorodithioate), purity 98% acts as anticholinestrase. Commercial formulations are applied to soil as an insecticide-nematicide throughout the United States to control corn root-worm larvae and other pests, preventing an economical loss to producers.[1,2] Terbufos is highly toxic to fish species (e.g., fathead minnows 96 hr's LC_{50} is 150 $\mu g\ L^{-1}$) and toxicity increases as temperature increase.[3] There have been no reports on its effects on fish gills.

Red shiners (*Cyprinella lutrensis*) were collected from the Platte River, Nebraska using a seine and maintained in 30-L glass aquaria (10 fish /tank) for a 14-d acclimation period at 22 °C on a 12:12 photoperiod and fed a commercial fish food once daily except for 24-h before and at the beginning of bioassays. During the 14-d bioassay, fish were exposed to terbufos concentrations of 0, 1, 10, and 100 $\mu g\ L^{-1}$. At the conclusion of the bioassay, fish were fixed in 3% glutaraldehyde with 0.1 M phosphate buffer. Gills were removed, washed in 0.1 M phosphate buffer and post-fixed in 1% OsO_4 for 2-h, gills were rinsed in water and dehydrated in a graded ethanol series. After critical point drying using liquid CO_2, gill tissues were mounted on stubs, coated with gold-palladium and examined using a Cambridge S-90 stereoscan at 15 kV.

Normal gills from control specimens (Fig. 1) are made up of primary lamellae (filaments) arranged in double rows on each of the arches and many secondary lamellae found on both sides of each filament. Surface morphology of arches, filaments and lamellae is made up of epithelium which is characterised by pavement cells, chloride cells, and goblet cells. In comparison to the control, gill tissues from treated fish showed fusion of secondary lamellae (Fig. 3), a rupturing of epithelial cells, hyperplasia causing fusion of lamellae (Fig. 5), and hypertrophy of both filamental and lamellar epithelium (Fig. 4 and 6). Pavement cells from control specimens (Fig. 2) were characterized by numerous microridges which aid in respiration and osmoregulation. However, pavement cells from treated specimens (Fig. 4,6) showed a significant loss of or pronounced changes in the length of microridges. With hypertrophy, microridges tended to become fragmented or shortened giving the appearance of microvilli and disappeared at highest terbufos concentrations.

Qualitative pathomorphological changes shown in this study clearly indicate the direct toxicological impacts of terbufos on *C. lutrensis* gill normal structures. Similar degenerative changes of gill morphology have been responsible for respiratory and osmoregulatory dysfunction in other species from a variety of chemicals.[4]

References

1. A. S. Felsot and A. Lew, J. Econ. Entom. 82(1989)380.
2. R.J. Little et al., J. Econ. Entom. 85(1992)1413.
3. G. E. Howe et al., Environ. Toxicol. Chem. 13(1994)51.
4. B. S. Khangarot and D. M. Tripathi, Ecotoxicol. Environ. saf. 22(1991)291.

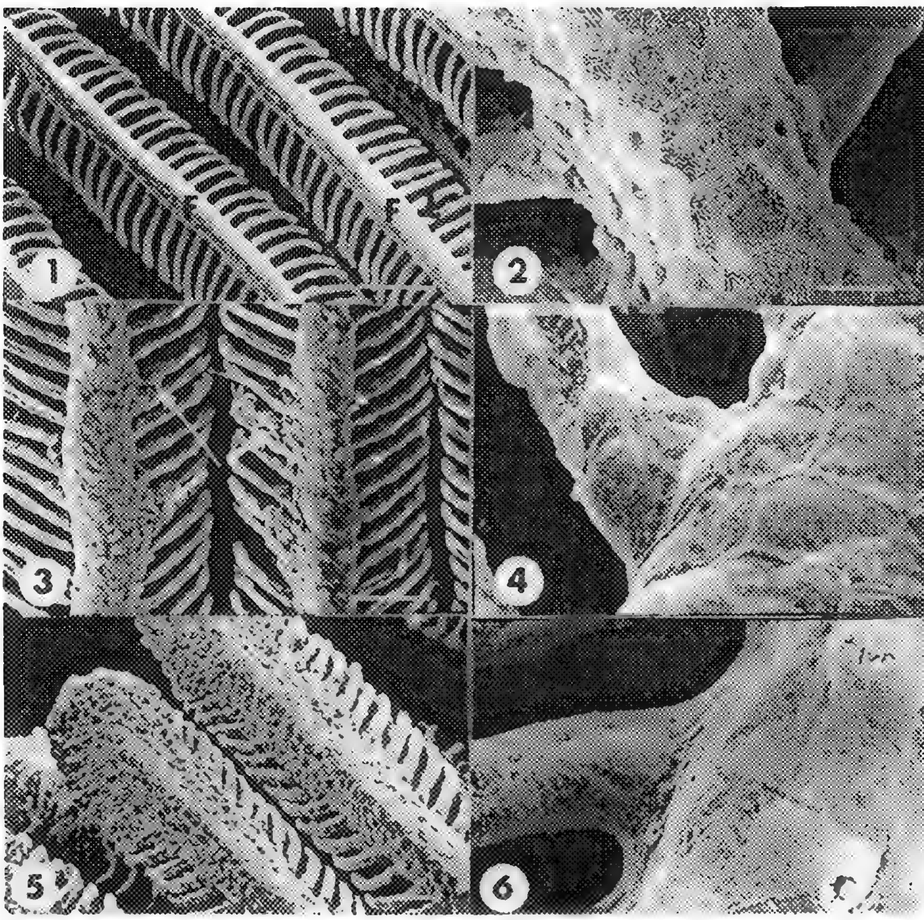

FIG. 1.--Normal gill filaments of C. lutrensis Note filaments (F) and lamellae (L). Bar = 100 μm.
FIG. 2.--Part of gill filament and lamellae showing pavement cell microridge patterns. Bar = 10 μm.
FIG. 3.--Several gill filaments. Fusion of lamellae (arrows) at 10 μg L^{-1} terbufos. Bar = 100 μm.
FIG 4.--Part of gill filament and lamella. Show cell boundaries and loss of pavement cell microridge patterns at 10 μg L^{-1} terbufos. Bar = 5 μm.
FIG. 5.--Gill filaments showing bronchial or hyperplasia leading to fusion of lamellae at 100 μg L^{-1} terbufos. Ba = 1 μm.
FIG. 6.--Part of gill filament and lamella. Complete loss of cell boundaries and microridge patterns at 100 μg L^{-1} terbufos. Bar = 5 μm.

SKELETAL-MUSCLE ULTRASTRUCTURAL PATHOLOGY IN PATIENTS WITH SEPSIS AND MULTIPLE ORGAN FAILURE SYNDROME (MOFS)

A. Márquez*, N.L. Díaz**, H. J. Finol**, and M. E. Correa

* Institute of Experimental Medicine, and ** Center of Electron Microscopy, Sciences Faculty, Central University of Venezuela, Apartado 47114, Caracas 1041A, Venezuela.

To date the most accepted definition of sepsis includes the suspicion of infection plus the systemic response to it (tachypnea, tachycardia and hypothermia or hyperthermia)[1]. This condition could lead to the so called multiple organ failure syndrome (MOFS) when there are evidences of functional compromise in two or more systems[1]. Muscle weakness and wasting are common findings in those patients. The skeletal muscle histopathology in patients with those two conditions has been poorly studied. The only electron microscopic investigation we could find describes alterations in muscle fibers and endplates [2]. In this work we describe the whole spectrum of changes found in skeletal muscle of patients suffering from sepsis and MOFS.

Five patients recluded in an Intensive Care Unit were selected, two had a diagnosis of sepsis, and three presented MOFS. Needle muscle biopsies from *quadriceps femoris* muscle were obtained. Tissue samples were processed with routine techniques for transmission electron microscopy and observed in a Hitachi H-500 electron microscope.

Patients with sepsis showed moderate alterations in muscle fibers including sarcomeric disorganization, swelling of sarcoplasmic reticulum and mitochondrial abnormalities (fig. 1). Thickening of capillary basement membrane was also observed. Patients with MOFS exhibited severe abnormalities in muscle fibers including nuclear destruction, sarcomeric fragmentation and necrosis (fig. 2). Sarcolemma was absent in some areas (fig. 3). Muscle atrophy varied from slight to total. Sometimes, severely atrophied fibers were beside almost normal ones (fig. 4). Intramuscular nerve twigs showed myelin disorganization and axonolysis (fig. 5). Microvasculature was highly affected exhibiting thickened basement membrane, endothelial hypertrophy, and lumen occlusion. In some cases capillary necrosis was evident (fig. 6). In both groups a mononuclear cell infiltration formed by macrophages, lymphocytes and mast cells was observed.

This study shows that patients with sepsis present an inflammatory myopathy with mild to moderate changes in muscle fibers and capillaries. Patients with MOFS exhibited more severe alterations in muscle structure, microvasculature and innervation. Additional studies are necessary in order to establish the ethiopathogenic mechanisms of these damages.

References

1. R. C. Bone, *Critical Care Medicine,* 19(1991)973.
2. J. H. J. Wokke, et al., *Journal of Neurological Sciences,* 88(1988)95.
3. This work was supported by the CDCH of UCV (N° 03-003421-95) and DIFMUCV.

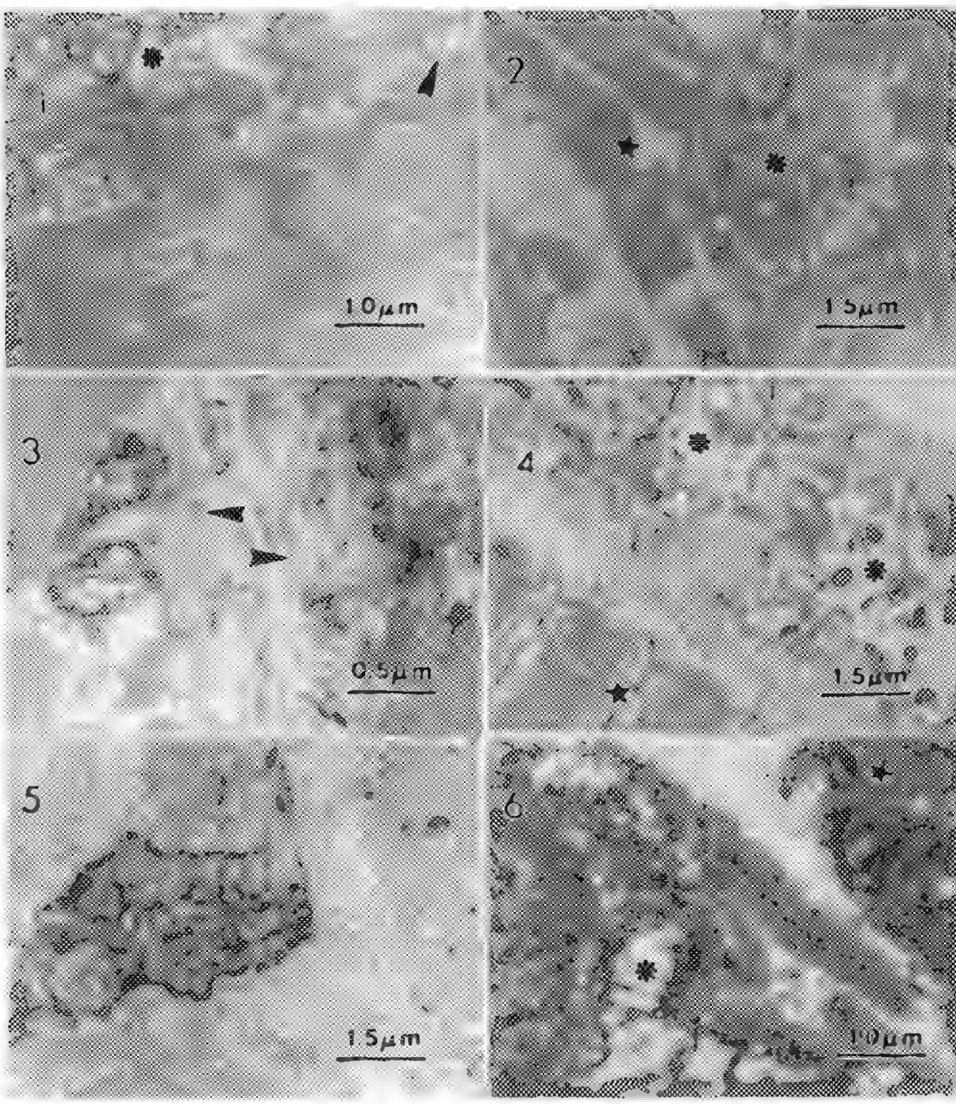

FIG. 1 Mitochondrial alterations (asterisk), swollen triad (arrowhead), and sarcomeric disorganization are shown.

FIG. 2 Note nuclear destruction (asterisk) and sarcomeric fragmentation (star).

FIG. 3 Note zones with no sarcolemma (arrowheads).

FIG. 4 Two severely atrophied fibers (asterisks) are beside an almost normal one (star).

FIG. 5 An intramuscular nerve twig shows myelin disorganization and axonolysis.

FIG. 6 Capillary rests (asterisk) are next to a necrotic fiber (star).

REVIEW OF ULTRASTRUCTURAL AND HISTOPATHOLOGIC FEATURES OF LIVER DISEASE IN α_1-ANTITRYPSIN DEFICIENCY IN A PEDIATRIC POPULATION

James P. Barrish and M. John Hicks
Department of Pathology, Ultrastructural Pathology Laboratory, Texas Children's Hospital, Baylor College of Medicine, Houston, Texas 77030-2399.

α_1-antitrypsin (α_1AT) deficiency (serum concentration <11 μmol/L) is one of the most common hereditary disorders in the United States and Europe with an incidence of 1 in 2,000 Caucasians of northern European descent. α_1AT is the major inhibitor of neutrophil elastase and is synthesized by the liver, released into the plasma and diffuses into organ systems thereby providing protection against the effects of neutrophil elastase. Deficiency of this antiprotease occurs when an aberrant homozygous form (most commonly PiZZ) is inherited. While α_1AT deficiency is associated with emphysema in adults, liver disease is seen most often in young α_1AT deficient children. Liver disease occurs in approximately 10% of neonates with α_1AT deficiency, and this is characterized as a neonatal hepatitis syndrome with cholestasis, hepatosplenomegaly, conjugated hyperbilirubinemia, and elevated liver transaminases in a small for gestational age neonate. Typically, there is spontaneous regression of clinical symptoms by 6 months of age with persistence of mild biochemical abnormalities. However in about 3% of these neonates, the liver disease progresses resulting in cirrhosis and rapid onset of liver failure. Liver transplantation in these cases is the only alternative available.

During the past 10 years, eleven pediatric cases of α_1AT deficiency with tissue submitted for both light and transmission electron microscopy were identified. The histopathologic and ultrastructural features were reviewed. In addition, immunogold labeling for detection of α_1AT was carried out on selected cases. The histopathologic examination consisted of routine H&E, PAS with and without diastase, trichrome and immunocytochemical staining for α_1AT.

The histopathologic features (Fig 1) were variable depending upon the individual's state of disease. In some cases, there was periportal fibrosis and proliferation of bile ducts along with cholestasis, resembling biliary atresia. Periportal hepatocytes did demonstrate PAS-positive diastase-resistant fine intracytoplasmic globules. Ultrastructurally (Fig 2a), the hepatocytes showed accumulations of fine proteinaceous material slightly to moderately distending the cisternae of the rough endoplasmic reticulum (RER). This material was highlighted by immunogold labeling for α_1AT. Peroxisomes were noted to be increased in size and number. In children with more advanced liver disease (Fig 1), there was obvious cirrhosis with micronodular formation and bridging fibrosis. Large PAS-positive, diastase-resistant intracytoplasmic globules were seen with most hepatocytes. Immunocytochemical stains for α_1AT showed diffuse immunoreactivity. Ultrastructurally (Fig 2b, 2c), hepatocyte cytoplasm showed merging and confluence of the dilated RER cisternae and frequent areas of large aggregates of proteinaceous material which was reactive with α_1AT immunogold labeling.

Although α_1-antitrypsin deficiency in adults results in lung injury due to the uninhibited influence of neutrophil elastase, such a mechanism has not been proven to be responsible for liver disease in the α_1AT deficient neonate. As illustrated in the current study, the detrimental effect of α_1AT deficiency on the liver is believed to be due to the accumulation of the aberrant protein within the rough endoplasmic reticulum. The subsequent cirrhosis and liver failure in α_1AT deficiency are thought to occur via extensive hepatocellular damage similar to the mechanism of injury involved in other inherited metabolic storage diseases.

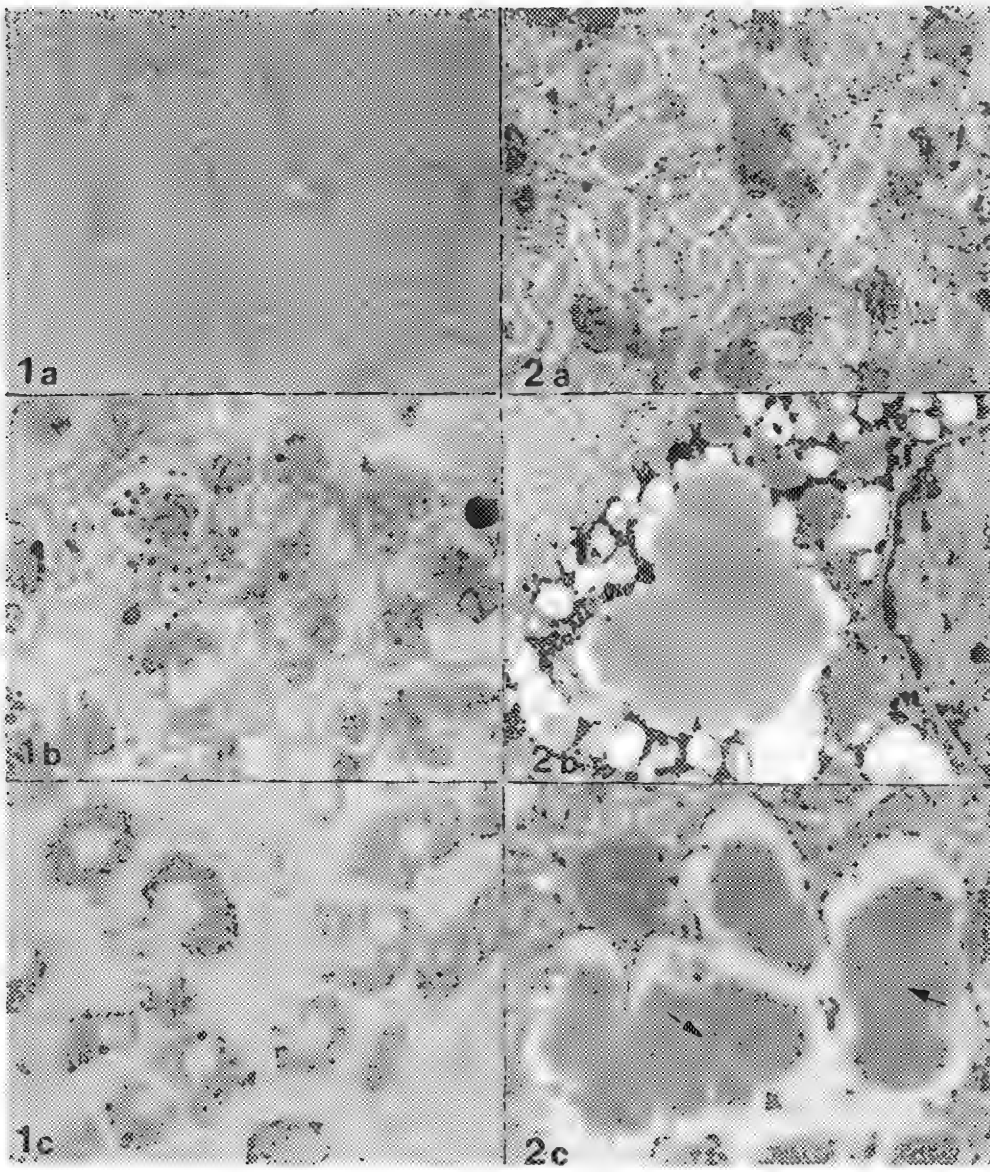

Figure 1 Histopathologic Features of Liver Disease in α_1-Antitrypsin Deficiency
a) Micronodular cirrhotic pattern (H&E, X280); b) PAS-positive, diastase-resistant intracytoplasmic globules (PAS, X2,800); c) Cytoplasmic immunoreactivity for antibody to α_1-antitrypsin (X2,800).
Figure 2 Ultrastructural Features of Liver Disease in α_1-Antitrypsin Deficiency
a) RER cisternae mildly dilated with proteinaceous material and increased peroxisomes (X8,000); b) Confluent large aggregates of proteinaceous material (X10,500); c) α_1-Antitrypsin immunogold labeling (arrows) of proteinaceous material (X24,000).

HEPATOCYTE ULTRASTRUCTURAL ALTERATIONS IN PERIMETASTATIC AREAS

H.J. Finol,* M.E. Correa,* L.A. Sosa,** A. Márquez,*** and N.L. Díaz.*

*Center of Electron Microscopy, Sciences Faculty,**Departament of Histology, Medicine Faculty, and ***Institute of Experimental Medicine, Central University of Venezuela. Apartado 47114, Caracas 1041A, Venezuela.

In classical oncological literature two mechanisms for tissue aggression in patients with cancer have been described. The first is the progressive invasion, infiltration and destruction of tissues surrounding primary malignant tumor or their metastases (1); the other includes alterations produced in remote sites that are not directly affected by any focus of disease, the so called paraneoplastic phenomenon (2). The non- invaded tissue which surrounds a primary malignant tumor or its metastases has been usually considered a normal tissue (3). In this work we describe the ultrastructural changes observed in hepatocytes located next to metastases from diverse malignant tumors.

Hepatic biopsies were obtained surgically in patients with different malignant tumors which metatastized in liver. Biopsies included tumor mass, the zone of macroscopic contact between the tumor and the surrounding tissue, and the tissue adjacent to the tumor but outside the macroscopic area of infiltration. The patients (n = 5), 36-75 years old, presented different tumors including rhabdomyosarcoma, leiomyosarcoma, pancreas carcinoma, biliar duct carcinoma and colon carcinoma. Tissue samples were processed with routine techniques for transmission electron microscopy and observed in a Hitachi H-500 electron microscope.

The study of the biopsies showed diverse hepatocyte alterations which were the same in all cases.

In some patients tumor cells were observed beside hepatocytes and no invasion was evident (Fig. 1). Mitochondrial alterations included the existence of marked pleomorphism which bizarre forms (Fig. 2). In some areas the mitochondria showed different electron densities. Some mitochondria with scarce cristae showed paracristalline inclusions (Fig. 3) and granules probably formed by calcium phosphate (Fig. 4). Rough and smooth endoplasmic reticulum looked swollen in some areas (Fig. 5). Proliferation of lysosomes was also observed (Fig. 6). When primary malignant tumors or their metastases grow into an organ two different tissues are considered to exist, the tumor tissue and the non-neoplastic tissue forming the organ which is usually called normal tissue. This last denomination is used even with the tissue that is in intimate contact with neoplastic cells (3). As the capacity of malignant tumor to produce damage in non-invaded organs, the so called paraneoplastic phenomenon, has been amply demonstrated (2), the possibility that the tissues which surround malignant tumors could be altered should be considered. In our cases, the ultrastructural analysis of hepatocytes that surrounded metastases from diverse malignant tumors exhibited a wide spectrum of abnormalities, these alterations were observed in hepatocytes which were not invaded by tumor cells and their ethiopathogenic mechanism are not well understood. This study indicates that the denomination of normal for the non-neoplastic tissue which surrounds primary malignant tumor or their metastases could be inadequate. This theme deserves additional investigation including other tumors and tissues.

References

1.R.S.Cotran et al. Robbin's Pathologic Basis of Disease. Philadelphia, W.B. Saunders, (1989)246

2.H.J. Finol et al. J. Exp. Clin. Cancer Res. 12 (1993) 53.

3.G.C. Easty. Biology of Cancer. New York: John Wilkins & Sons (1975) 58.

4. This study was supported by grants from the CDCH of UCV (Nr. 03-00-3421-95) and DIFMUCV.

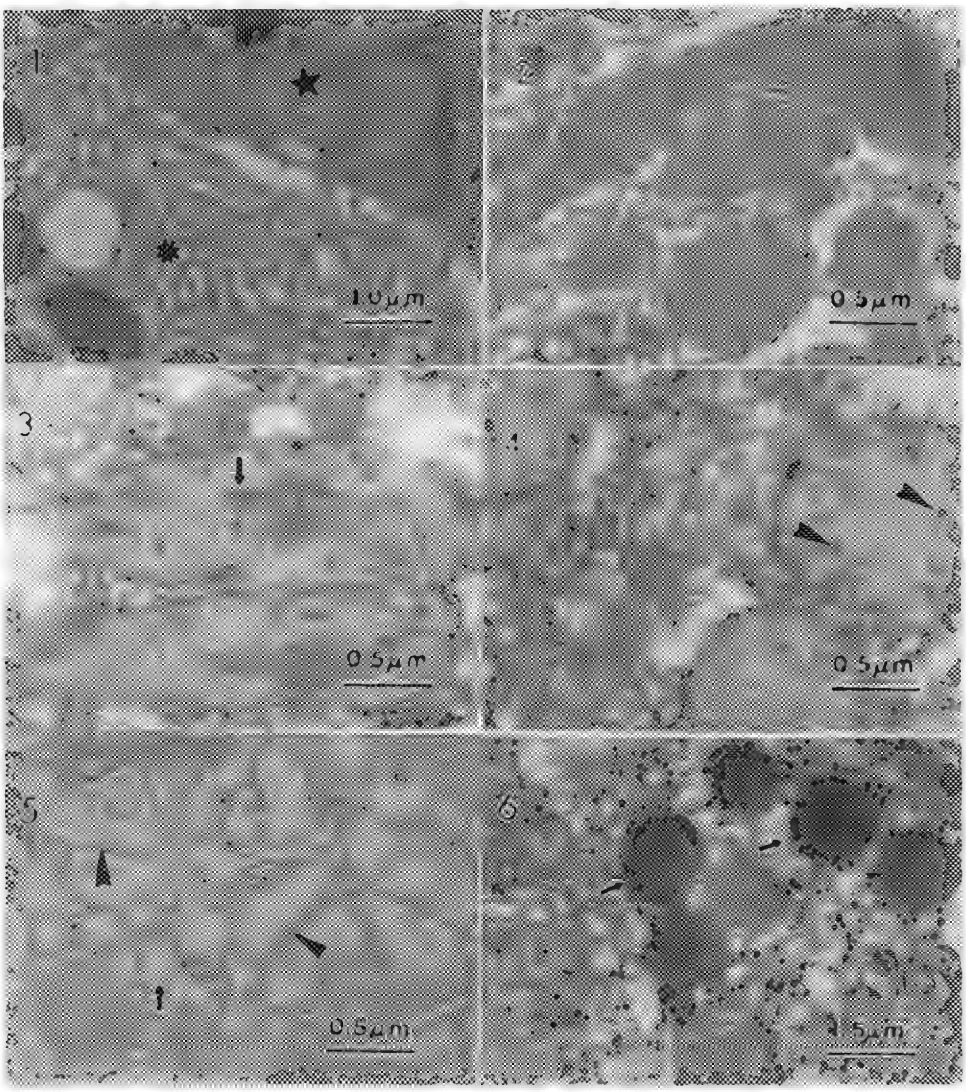

FIG 1 A tumor cell from a pancreas carcinoma (star) is beside a hepatocyte (asterisk)
FIG. 2. Mitochondria show different sizes and shapes.
FIG. 3. Paracristalline inclusions inside mitochondria (arrow).
FIG. 4. Arrowheads show granules into the mitochondria.
FIG 5. Note swollen rough (arrowhead) and smooth (arrow) endoplasmic reticulum.
FIG. 6. Note abundance of lysosomes (arrows).

EVALUATION OF PLATELET DENSE GRANULES FOR DETERMINING STORAGE POOL DEFICIENCIES BY HVEM IMAGE AND QUANTITATIVE ANALYSIS

W.T. Gunning[*], J.N. Turner[**], K. Buttle[**], E.P. Calomeni[*], N.A. Lachant[***], and M.R. Smith[****]

[*]Department of Pathology, Medical College of Ohio, Toledo, OH
[**]Wadsworth Center, New York State Department of Health, Albany, NY
[***]Department of Medicine, Wayne State University, Detroit, MI
[****]Department of Medicine, Medical College of Ohio, Toledo, OH

There are a variety of conditions which have been associated with prolonged bleeding times. If other etiologies including von Willebrand's disease have been ruled out, a platelet function disorder must be considered[1]. The best, if not only, technique to make this diagnosis is the electron microscopic evaluation of whole air dried platelets. Bull first described the presence of dense granules in whole platelets in 1968[2] and the technique has been utilized extensively[1,3-5] The electron dense or delta granules are easily distinguished from the larger more numerous alpha granules which are electron lucent. The significance of the dense granules is that they are known to be "storage pools" of serotonin, calcium, adenosine di- and triphosphate, and pyrophosphate. Prolonged bleeding times may be directly related to an insufficiency of these substances. The diagnosis of a storage pool deficiency is made when either the storage content of the dense granules is abnormal or their number is diminished. We observe normal platelets to have 4-6 dense granules, which agrees with the literature[5].

The pathophysiology of some patients that have prolonged bleeding times but normal dense granule counts is not understood. Our initial impression is that their dense granules are smaller than normal. Thus, it is important to determine volume as well as number of these granules. Since the granules are small in size and number most quantitative approaches are very tedious. Figs. 1 & 2 show images of the typical whole mount and thin section preparations imaged at 100 keV. The image quality of the whole mount is obviously not optimal and no volume information is available. The thin section image has excellent image quality and demonstrates all the normal platelet ultrastructure but quantitation is difficult and tedious due to the granules' small size and sparseness. We are circumventing these problems by using high-voltage electron microscopy to image sections thick enough to contain whole platelets. Figs. 3 and 4 are stereo images of sections 2 and 0.75 μm thick respectively. It is clear that the images are of good quality throughout the section thickness and while not showing the ultrastructural detail of Fig. 2 are appropriate for quantitation of the dense granules. We plan to perform 3-D analysis using our reconstruction system, STERECON, and will compare dense granule number and total volume per platelet with clinical parameters in an attempt to better understand unusual bleeding disorders.

References:

1. Israels, S.J., et al. Brit. J. Haematol. 75:118-121, 1990.
2. Bull, B.S. Blood 28:901-913, 1968.
3. Weiss, H.J., et al., Brit. J. Haematol. 83:282-295.
4. White, JG. Blood 33:598-606, 1969.
5. Witkop, C.J., et al. Scand. J. Haematol. 26:305-311, 1987.
6. Work partially supported by: NIH RR01219.

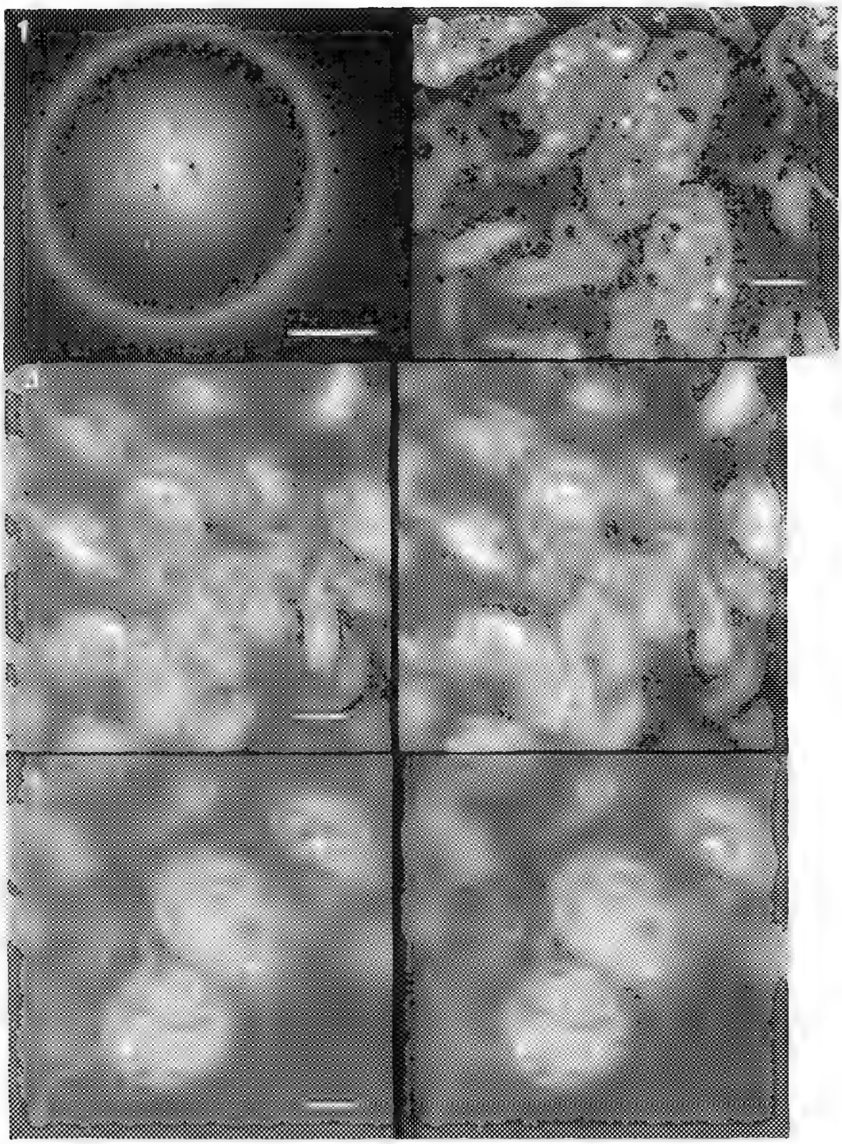

All bars are 2 μm

Fig. 1. CTEM of a whole mounted air dried platelet with obvious dense granules.
Fig. 2. CTEM image of a thin section of platelets with storage pool deficiency.
Figs. 3 & 4. HVEM stereo images of 2 and 0.75 μm sections respectively.

ELECTRON MICROSCOPY STUDY OF SKELETAL MUSCLE MICROVASCULATURE IN THE PARANEOPLASTIC PHENOMENON

P. Tonino,* H.J. Finol,* A. Márquez,** B. Müller,*** M. Correa,* and L.Sosa**

*Center for Electron Microscopy, Faculty of Science, A.P. 47114, Caracas 1041A.
**Faculty of Medicine and ***Dentistry Faculty, Central University of Venezuela.

In addition to signs and symptoms at sites of primary and metastatic disease, cancer can cause manifestations in remote sites that are not directly affected by any focus of disease. Such manifestations of malignancy are collectivelly known as paraneoplastic phenomenon. Muscular manifestations consist of slight to severe and usually proximal wasting and weakness.[1] In our laboratory we described the ultrastructural pathology of skeletal muscle in the paraneoplastic phenomenon in patients with bronchogenic and cervix carcinoma.[2,3] In these studies a brief report on capillary alterations was made. The present investigation was undertaken in order to extent the study on the microvasculature in the skeletal muscle paraneoplastic phenomenon.

Muscle biopsies were obtained in patients suffering from bronchogenic carcinoma (n= 10), gastric carcinoma (n= 7), cervix carcinoma (n= 1) and lymphoma (n= 4). Tissue samples were processed by routine transmission electron microscope techniques and observed in a Hitachi H-500 EM.

A varied spectrum of capillary damage was observed including an almost normal endothelium with thickened basement membrane (Fig. 1) and endothelial proliferation with progressive lumen occlusion (Fig. 2). In these capillaries endoplasmic reticulum proliferation, abundant mitochondria and lysosomal structures were seen (Fig. 2). A different process observed was the degeneration of the endothelial cells with presence of autophagic vacuoles (Fig 3 and 4). The pericyte also suffered from degeneration. Capillary necrosis was also seen. The mononuclear cell infiltrate was formed by macrophages, lymphocytes and mast cells.

This study demonstrates that the skeletal muscle paraneoplastic phenomenon includes an important microvascular compromise. This fact indicates the existence of a vascular etiopathogenic factor in the muscle damage in the paraneoplastic phenomenon. The capillary alterations we observed are similar to those reported in several autoimmune myopathies with different etiologies.[4,5] Additional studies including immuno-electron microscopy techniques should be used in order to elucidate the mechanisms of muscle microvessels damage in this syndrome.

References

1. S. Lakhanpal et al., *Clin. Proc.*, (1986)645.
2. P. Tonino et al., *J. Exp. Clin. Cancer Res.*, (1991)283.
3. H.J. Finol et al., *J. Exp. Clin. Cancer Res.*, (1993)53.
4. H.J. Finol et al., *J. Rheumatol.*, (1990)210.
5. H.J. Finol et al., *J. Submicrosc.* Cytol. Pathol., (1994)245.
6. This research was supported by grants from CDCH-UCV and DIFMUCV.

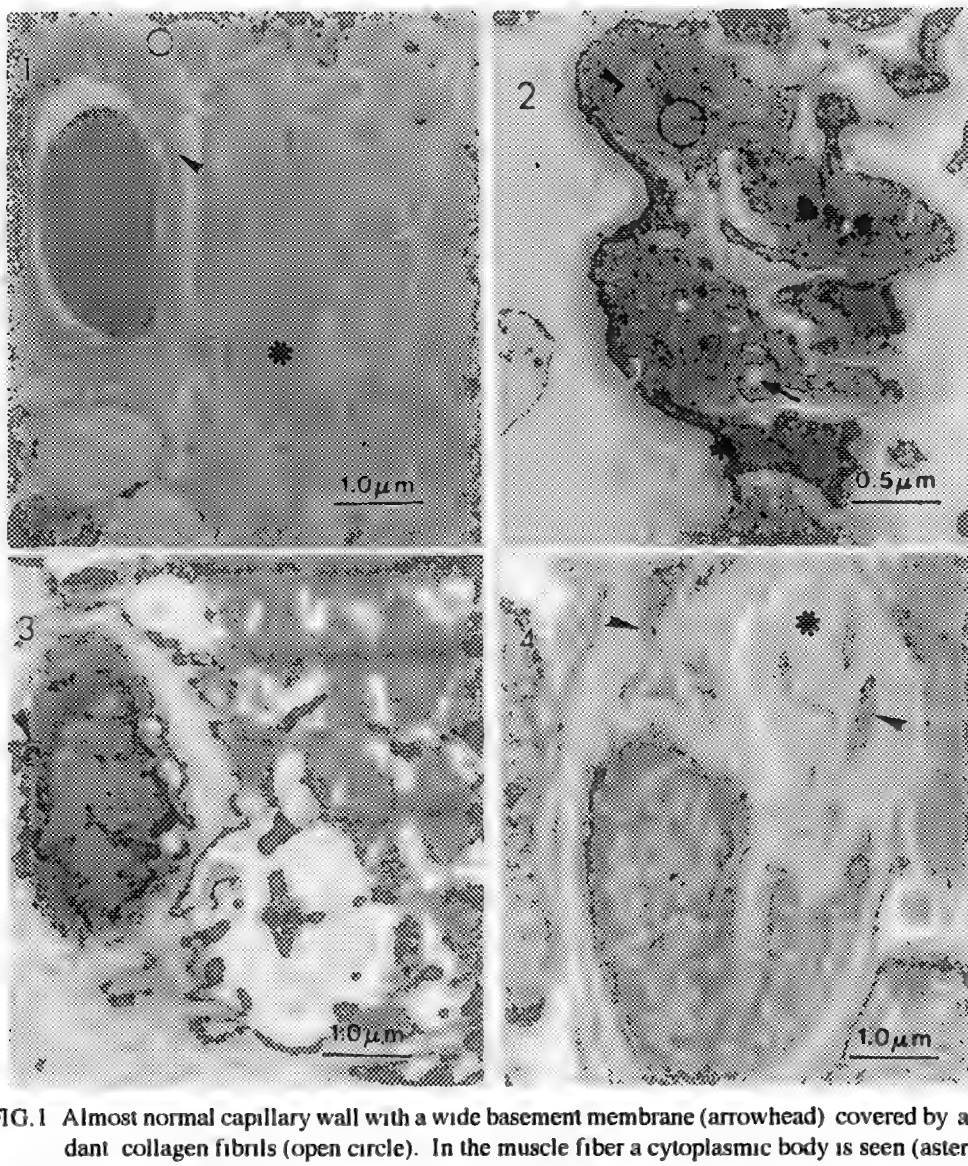

FIG. 1 Almost normal capillary wall with a wide basement membrane (arrowhead) covered by abundant collagen fibrils (open circle). In the muscle fiber a cytoplasmic body is seen (asterisk).

FIG. 2 In this capillary the lumen is lost and in endothelial cytoplasm are seen abundant vesicles (open circle), vacuoles (arrow) and lysosomes (arrowhead). Pericyte has homogeneous cytoplasm (asterisk).

FIG. 3 In the endothelial cytoplasm autophagic vacuoles are seen (arrowhead).

FIG. 4 Additionally to the endothelial cell nucleus rests of the cytoplasm are seen inside the thickened basement membrane (asterisk).

SEMINAL CYTOLOGY IN INFERTILE MEN WITH *Chlamydia trachomatis* AND *Ureaplasma urealyticum* INFECTIONS. OBSERVATIONS THROUGH ELECTRON MICROSCOPY

M. G. Gallegos A., O. G. Díaz G., M. J. Vazquez H., R. Rositas M., E. Ramirez B.
School of Medicine, Universidad de Nuevo León. Ave. . Mty., N. L. **MEXICO**. C.P. 64,440

Among non gonococcic uretritis 60 % of them are caused by *C. trachomatis* and *U. urealyticum*, organisms transmited by sexual contact (1). These are frecuently presented like asymptomatic infections and involved a diminish sperm quality. The defects in motility and morphology of spermatozoa associated with these infections have not to date been explained clearly (2), although, in the case of *U. urealyticum* it has been shown that sperm motility is decreased by the physical adherence of the organism to the tail of the spermatozoon (3).

Although, some descriptions of the ultraestructure of semen in pacients with *U. urealyticum* (4) and *C trachomatis* (5) infections exist, there has not been a detailed description of alterations of the fine structure of the spermatozoa that can or can´t be related to astenozoospermia.

In this study we selected a group of 26 patients, who presented infertility with an alteration in sperm motility and morfology proven with a seminogram under the parameters recomended by the WHO (6). All patients were microbiologicaly tested for *U. urealyticum* (Mycotrim GU, Irving Sc.), and to nine of them a direct test with fluorescent monoclonal antibodys for detectionl of *C. trachomatis*, was done using uretral exudates (Syva Microtrac). A Sample of seminal liquid was fixed in glutaraldehyde at 2.5% and osmium tetraoxide at 1%, before washing in 0.2 molar phosfate buffer pH of 7.4, and then were embedded in epoxic resine and sectioned at 90 nanometers for examination under the electron microscope. These sample sections were stained with uranile acetate and lead citrate.

RESULTS. The microbiological studies showed four individuals infected with *U. urealyticum* and two individuals infected with *C . trachomatis*, the spermatic observation under the electron microscope in these individuals showed similar findings: heavy intranuclear vacuolization, chromatine decondensation, nuclear and acrosomal deformities, alterations in the flagellar ultrastructure and binucleation. Along with this spermatic alterations we also observed the constant presence of polymorfonuclear cells. Phagocytosis of spermatozoa and the presence of infectious elements such as bacterias, dense chlamydial bodies, and pleomorfic mycoplasmic elements. In the cases of negative microbiological test some of the alterations observed were also present in the individuals only in a diminished rate of incidence.

In 10% of the patients with negative microbiological test, were found, at electron microscopy level, seminal chlamydial dense bodies and pleomorfic mycoplasmic elements; this would indicate the ineffectiveness of microbiological test to detect genital urinary infections caused by these infectious agents.

The altertions in the spermatic ultrastructure observed in association with infections by *C. trachomatis* and *U. urealyticum* can be associated although no specifically with spermatic motility problem and reproductive failure of the affected individuals.

1.Hellstrom, W.J.G.; Facts M.D. and Neal D.E.: Diagnosis and therapy of male genital tract infections. Infertlity and reproductive Medicine. Clinics of North America (3):339-427, 1992.

2.Fowlkes D. M.; McLeod j.: T-mycoplasmas and human infertility: Correlation of infection with alterations in seminal parameters. Fertility Steril. 26:1212. 1973.

3.Swenson, C.E. and W.M.O´Leary. Examination of human semen infected with *Ureaplasma urealyticum* by fluorescence microscopy. Arch. of Androl. (5), 373-377, 1980.

4.Busolo F.; Zancheta and Bertolini. Mycoplasmic localization patterns on spermatozoa from infertile men. Fert. and Steril.(42), 412-417, 1984.

5.Villegas-Castrejon H, Villanueva-Díaz CA, Solórzano-Santos SKK: Esterilidad conyugal por *Chlamydia trachomatis*. Estudio ultraestructural. Perinatol Reprod Hum. 8:70-77, 1989.

6.WHO.Laboratory Manual for the examination of human semen and semen-cervical mucus interaction. Cambridge University Press-London. 1989.

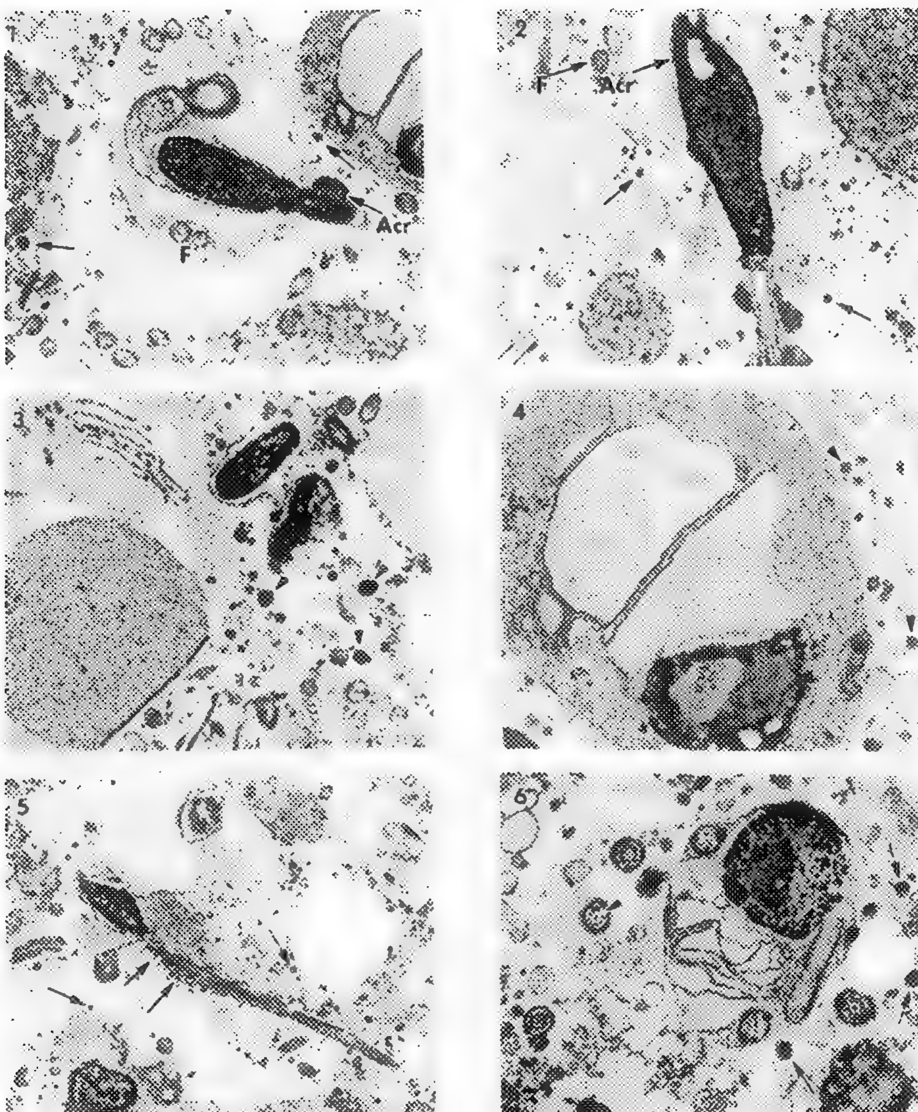

Figs. 1 and 2. Sperm cells with acrossomal alterations (Acr.), and remanent perinuclear citoplasma. Arrows pointout pleomorfic electrondense elements that represent *Ureaplasma urealyticum*.

Figs. 3 and 4. Inmadure spermatids with nuclear and acrosomal abnormalities that are present concomitantlly to pleomorfic electronense elements (Arrows heads).

Fig. 5. Sperm cell with autolytic changes and pleomorfic electrodense elements of *U. urealyticum* adhered to midle piece of the tail.

Fig. 6. Abnormal sperm with cromatinic decondensation, acrossomal agenesia, folded flagellae, and membranous structures like lamellae. With arrows are noted mycoplasmic particles and with the arrow head indicates abnormal flagellar structure.

SPERMATIC MULTINUCLEATION IN INFERTILE AGRICULTURE WORKERS EXPOSED TO CARBOFURANYL PESTICIDE

G. Gallegos de L., M.M. Arizpe S.,L.E. Alvarado C.and E. Ramirez B.
Pathology Dept., School of Medicine,Univ. de Nuevo León;A.P. 1563

It is known that the exposure to gonadotoxic agents cause male infertility in agricutural workers (1). Pesticides provoke a detrimental effect on the spermatogenesis characterized by low count of sprematozoa, as well as sperm motility and morphology alterations (2). Simultaneosly an increase in FSH seric levels is present (3).

The semen analysis was proposed in 1975 to detect sperm quality and function alteration induced by chemical agents (4).There are many morphologic anomalies related to the noxious action of some gonadotoxic agents, ie. head deformities, microcephalia, tail defects, etc. (5 , 6).

We detected in our laboratory a pair of cases of infertile patients, that presented high levels of teratozoospermia with a high percentage of multinucleated spermatozoa and spermatids, and referred exposure to Carbofuranyl (Furadan 300). Since this agent has not been classified as gonadotoxic, we tried to show it´s posible causal relationship with spermatic multinucleation phenomenon observed and the fertility of these patients.

STUDY OF CASES:

CASE No. 1 : A 30 years old male agronomist had primary infertility since 8 years ago, and estimated 10 years exposure to pesticides with the last 3 years exposed to Carbofuranyl. He had a history of a gonorrhoea infection 6 years ago treated with antibiotic therapy. In a seminogram the patient presented astenozoospermia registering 28% of binucleated spermatozoa, and 10% multinucleated spermatids.

CASE No. 2 : A 37 years old male agricultural worker with a history of 10 years primary infertility and recent exposure to Carbofuranyl (Furadan 300). He also mentioned exposure to hot baths. At seminogram presented lower than 5 million per mililiter of spermatozoa, and progressive sperm motility diminished (6%). Thenmore it was found 98% morphological sperm abnormalities and presented inmature cells. These included 26% of multinucleated spermatozoa and 6% of multinucleated spermatids.

To confirm the multinucleation and to describe the sperm ultraestructural alteration concomitantly present in both patients, we processed a seminal pellet obtained by centrifugation and then included in epoxy resin. Semithin and thin sections were analyzed at ligth and electron microscopy respectively. Characteristic images of our observations are shown in plate 1.

CONCLUSIONS:

Between one and two percent of seminal spermatozoa from infertile and fertile men are binucleated while spermatic multinucleation is even rarer. This phenomenon, originated from the cariokinesis without cytokinesis, has not been associated with any preexisting condition. In view of this we considered outstanding the coincidence between the two cases of infertile men and the exposure to Carbofuranyl, that to date has not been reported to have a gonotoxic efect or cronic toxicity.

1.-Thompson St. Preventable causes of male infertility. World J. Urology. 11:p111-119. (1993).

2.-Wayland J. Hayes, Jr. MD. PH. D. Pesticides Studied in Man. (1987).

3.-Sandifer S. H. , Wilkins R. T. Spermatogenesis in Agricultural Workers Exposed to Dibromochloropropane (DBCP) . Bull. Environm. Contam. Toxicol. 23:p703-710. (1979).

4.-Wyrobeck, A. J. and W. R. Bruce. Chemical induction of sperm abnormalities in mice. Proc. Natl. Acad. Sci. U.S.A. Vol: 72: 4425-4429.(1975)

5.-Ratcliffe Jennifer , Scrader S. M. , Steenland K. Semen quality in papaya workers with long term exposure to ethylene dibromide. British J. of Industrial Medicine. 44:p317-326. (1987).

6.- Wyrobeck, A.J. ; G. Watchmaker; L. Gordon; K. Wong; D. Moore II and D. Whorton Sperm shape abnormalities in Carbaryl exposed employees. Enviromental Health Perspectives 40:255-265 (1981).

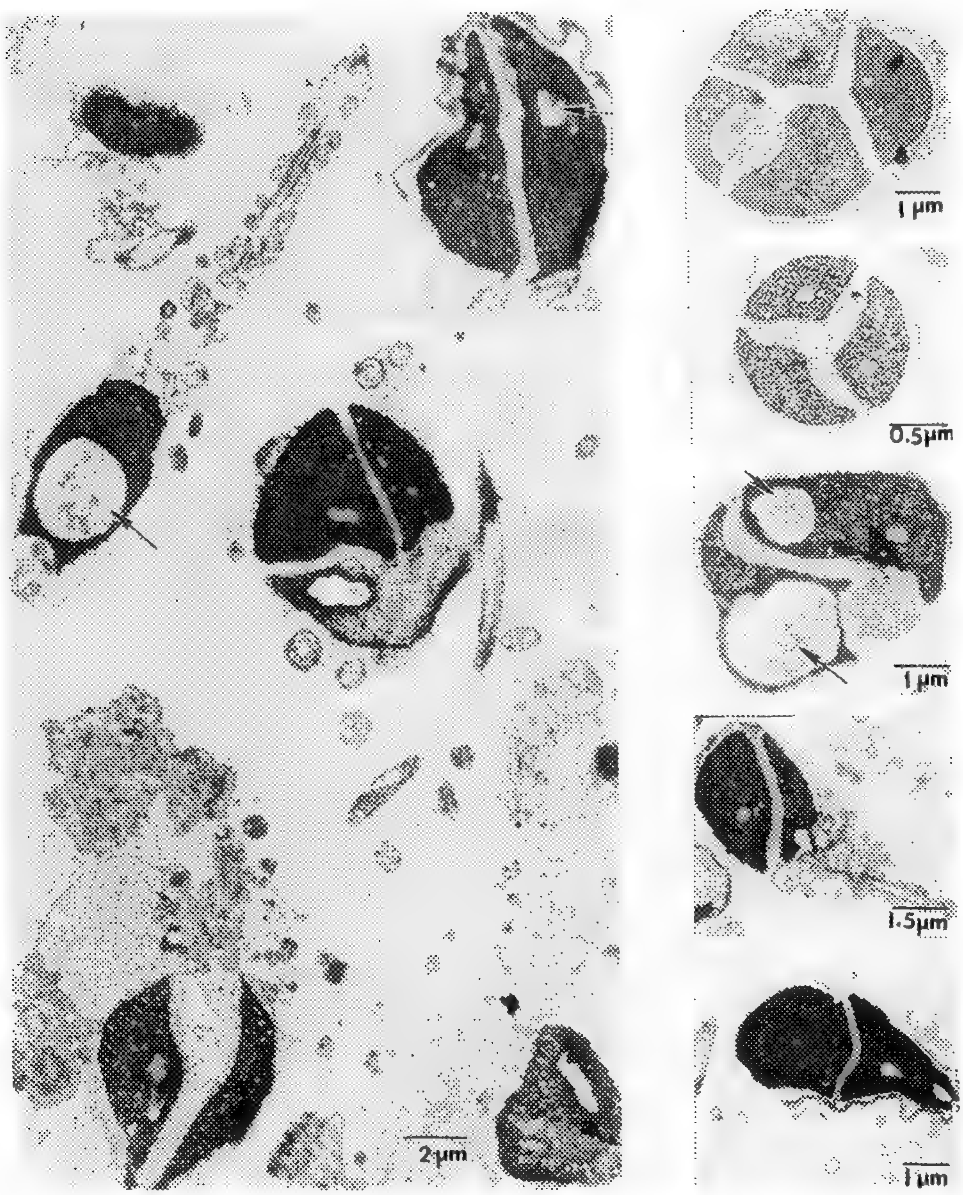

SPERMATIC MULTINUCLEATION

Electron micrographs of spermatozoa, that shown cromatinic descondensation and celular autolysis. Notice the intranuclear vacuole (arrow).

SEMINAL PHAGOCYTES DETECTION AT LIGHT-MICROSCOPY LEVEL USING THREE DIFFERENT TECHNIQUES

L. Benítez A.; O. Díaz G.; R. M. Eguía M. and M. G. Gallegos A.
School of Medicine. University of Nuevo León. Monterrey, N.L. **MEXICO.** AP 1563

The phagocytes are normally present in the conective tissue at different organs, and their number increased in immunological or inflammatory processes. In these cases, they are present too in corporal fluids (1).

The presence of phagocytes in semen was referred by several authors (2,3), but that phenomenon has not been suficiently analysed. At smear Papanicolaou stained analysis, the seminal phagocytes can be inadverted thus, their relationship to the male infertility or another reproductive tract pathology can not be established.

In this study we implemented three techniques to detect the presence of phagocytes in semen of 28 infertile patients: Myeloperoxidase for polymorphonuclears (leukocyte), Neutral red for macrophages (4) and the semithin sections analysis at light microscopical level of the seminal pellet obtained by centrifugation and included in epoxyresin (5).

Inflammatory cells (polymorphonuclear or macrophages) were observed in 89% of the patients; 57% were neutral red positive (Fig. 1) and 32% were detected by myeloperoxidase (2). The semithin section observed with light microscope allowed the identification of polymorphonuclear cells in 82% of the cases and macrophages in 11% (Figs. 3 y 4). While in half of the cases, the semithin sections exam reported polymorphonuclear myeloperoxidase negative for them. Likewise, the seminal pellet sections could not demostrate the presence of macrophages in 21 % of the cases that were positive to neutral red. All techniques were negative for inflammatory cells in 7%of the patients.

Our results showed a false negative results of myeloperoxidase reaction for polymorphonuclear cells in semen. Regard macrophages they are efficiently detected by neutral red stain. The semithin sections of seminal pellet included in epoxyresin, were adequated to evaluate the presence of inflammatory cells, even though the cell autolysis could difficult the macrophages identification. Thus we considered that the three techniques that we proved are complementary but not rejectant.

BIBLIOGRAPHY

1.-Rubin,E.; Farber,J.L. Patología. Fundamentos. Editorial Médica Panamericana. (1992). Pág. 55.
2.- Phadke, A.M. Occurrence of macrophage cells in the semen and the epididymis in cases of male infertility. J. Reprod. Fert. (1961). 2:400.
3.- Blanco, A.M. et al. Phagocytosis of ejaculated spermatozoa. Acta Cytol. (1992). 36(2). 251-258.
4.- Gonzáles,G.F. Andrología. Fertilidad e Infertilidad: Técnicas Especializadas Avanzadas. Editorial Instituto de Investigaciones de la Altura. (1992). Pág. 301.
5.- Hayat,M.A. Basic electron microscopic techniques. Van Nostrand Reinhold Co. (1972).

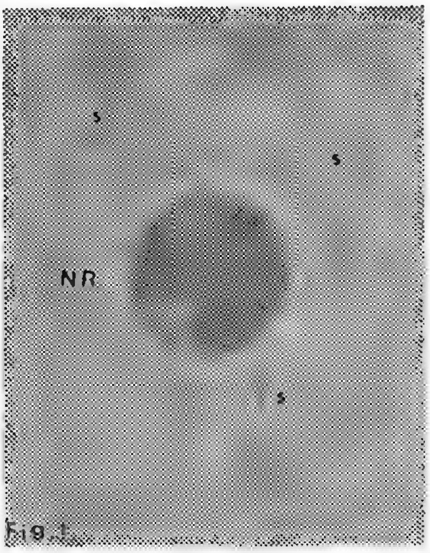

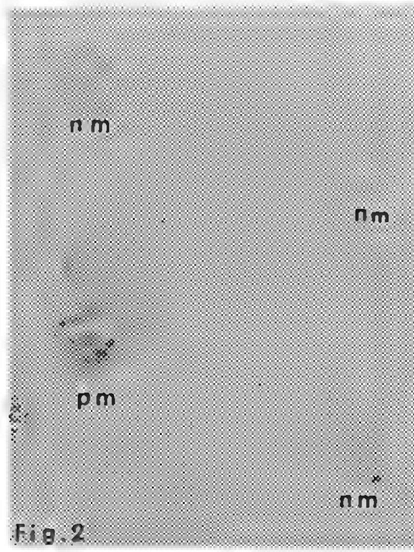

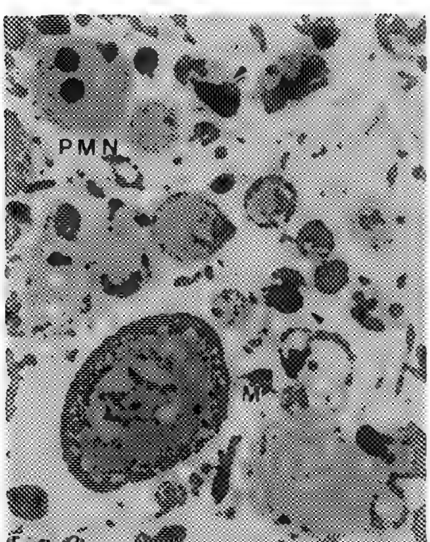

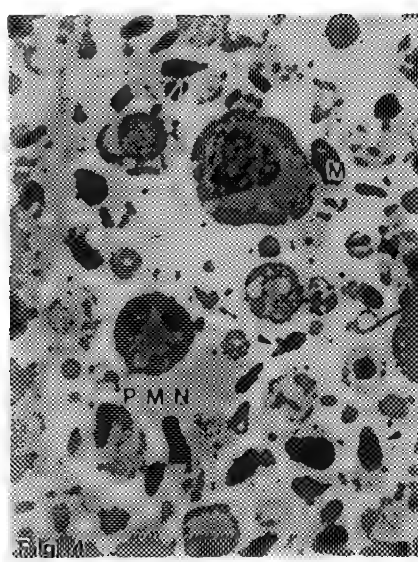

Fig.1 Neutral red supravital stain,that demostrate a macrophage cell (NR). Some sperm cells are indicated (s). Magnification: 1,000 X in negative.
Fig.2 Polymorphonuclear leukocyte positive to myeloperoxidase reaction (pm) and negative to it (nm) are seen in this light micrograph. Magnification: 1,000 X in negative.
Figs.3 y 4 Light microscopy image of semithin section shown macrophages (M) and polymorphonuclear leukocytes (PMN). Sperm cells are indicated (arrows head). Magnification: 1,000X in negative.

FATE OF CORONARY-ARTERY SIDE BRANCHES IN BALLOON ANGIOPLASTY AND WIKTOR STENT PLACEMENT

Michael F. Wolf and Michael R. Coscio
Center for Biomaterials Research (CBR), Medtronic Inc., Promeon Division

In healthy coronary arteries an extensive network of sidebranching exists to support the high vascular requirement of the surrounding tissue. The size of such side branches is quite broad, ranging from 10 to over 1000μ in diameter extending away from the major vessel (typically 3-4 mm diameter). In the region of balloon expansion during angioplasty, these vessels may be compromised by damage or stripping away of the natural and normally-healthy nonthrombogenic lining (endothelium). This injury exposes potentially thrombogenic subendothelial tissue about the vessel and side branch entrance points. Side branches become further threatened by potential overlap of stent material upon stent placement. Using scanning electron microscopy, this investigation reports on the chronology of the healing response as observed following stent implantation in a porcine model. Particular attention is paid to the fate of local side branches.

Methods: Using a porcine model, standard angioplasty with Wiktor stent placement in either the LAD, RCA, and/or the CCA coronary artery was conducted. At time points of 6 hr, 1, 7, 30, 90, and 180 days post implantation, in situ perfusion fixation was performed using standard methods.[1-3] The devices were then carefully removed en bloc with the surrounding vasculature and trimmed for standard gross photography, histology, and SEM analysis. For the latter, samples were prepared by post fixation with osmium tetroxide, dehydration in ethanol, and critical point drying. Specimens were then examined with or without gold coating using a JEOL JSM-6301 FXV FESEM microscope.

Results and Conclusions: Over time (7-30 days), damaged or stripped-away endothelium was completely replaced by endothelium growing in from surrounding areas (Figure 1). Stents placed around or on top of side branches did not appear to markedly affect sidebranch patency. Often, the stent material became completely incorporated into developing neointimal tissue. The patency of side branches in the vicinity of balloon angioplasty and Wiktor stent placement therefore appeared minimally affected by the procedure and the device placement.

References:

1. M.F. Wolf and M.R. Coscio, *Comparison of Luminal Surface Observations of the Healing Response of an Experimental Small Diameter Woven Dacron and Expanded Polytetrafluoroethylene Arterial Prosthesis*, 49th Annual Meeting of the Electron Microscopy Society of America, August 1991.
2. M.F. Wolf, M.R. Coscio, L.A. Cheevers, E. Irwin, *Morphological Features of Cardiovascular Implants Preserved Using Simple In-situ Perfusion Fixation Techniques,* Implant Retrieval Symposium, Society for Biomaterials, September 1992.
3. M.F. Wolf, P. Cahalan, L. Cahalan, J.R. Keogh, M.R. Coscio, M. Overend, *Thrombotic Potential of Surface-Modified Biomaterials Using Human Blood Under In Vitro Mock Recirculation and an In Vivo Intravascular Catheter Model,* Transactions of Surfaces in Biomaterials Annual Meeting, Scottsdale, AZ, 1994.

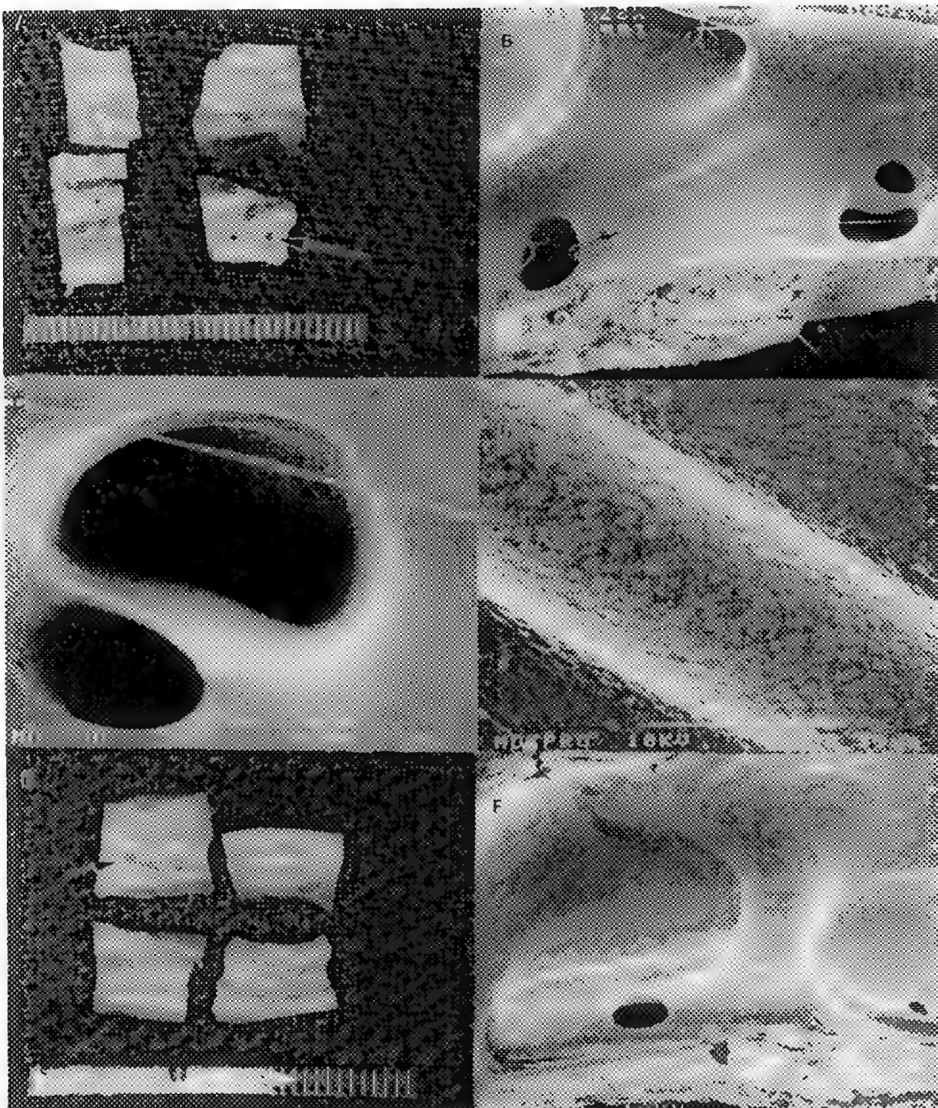

Figure 1. Healing response of stented coronary artery 30 days post implantation. **A:** Gross photograph showing a LCA-placed stent. Close inspection of the lower right portion shows at least one segment of stent wire passing directly over a 500-1000μ sidebranch (arrow). **B:** Low magnification micrograph showing how the stent wire healed over the sidebranch and effectively bifurcated the opening. Two other patent sidebranches are seen in the vicinity. The long string that spans the image and follows down into a sidebranch is a long strand of fibrin of unknown upstream origin. **C:** High magnification micrograph of bifurcated sidebranch opening showing passing stent wire to be completely covered by neointimal tissue. **D:** High magnification micrograph showing a segment of stent wire completely covered by neointimal tissue. **E:** Gross photograph showing an RCA-placed stent. Close inspection of the upper left portion shows a stent wire passing directly around a 500-1000μ sidebranch. **F:** Low magnification micrograph of E that reveals an even smaller sidebranch further downstream. Both sidebranches appear patent.

OXIDATIVE INJURY AND ENDOTHELIAL CELL DYSFUNCTION IN DIABETIC RETINOPATHY: A COMBINED CYTOCHEMICAL AND IMMUNOCYTOCHEMICAL STUDY

E. Ann Ellis,* Maria B. Grant,* Frederick T. Murray,** and Martha B. Wachowski**

*Department of Medicine, University of Florida, Gainesville, FL 32610
**Pharmacia & Upjohn, Kalamazoo, MI 49007

Endothelial cell dysfunction has been implicated in a number of microvascular complications of diabetes. Microvascular changes in diabetic retinopathy present initially as leaky vessels in the neural retina which lead to deterioration of vision. Oxidative injury as a result of free radical production has been suggested as a mechanism of endothelial cell dysfunction caused by hyperglycemia.[1,2]

The NADPH oxidase complex catalyzes the formation of superoxide ($O_2^{\cdot -}$); hydrogen peroxide (H_2O_2) is formed by dismutaion of $O_2^{\cdot -}$. Cytochemical localization of the free radical derived oxidant, H_2O_2, was done by the cerium NADPH/NADH oxidase method[3,4] in eyes of obese, noninsulin dependent diabetic BBZ/Wor rats[5] with diabetes of five and ten months duration. Age matched, nondiabetic controls were eyes from BB/Wor^{DR} rats. Endothelial cell dysfunction, indicated by leaky vessels, was documented by colloidal gold immunocytochemical localization of extravasated endogenous serum albumin[6] on sections of retina in which H_2O_2 had been localized.[7]

Cerium perhydroxide is an electron dense reaction product of cerium and H_2O_2. Peroxide localized in endothelial cells, basement membranes, and vessel lumens in eyes of diabetic rats (Figs. 1 and 2). There was minimal to no localization of H_2O_2 in comparable sites in eyes from nondiabetic, age matched controls (Fig. 3). Colloidal gold localization of extravasated endogenous serum albumin was extensive around vessels in the retina of diabetic rats (Fig. 4) as compared to nondiabetic rats (Fig. 5). Extravasation of serum albumin was increased at sites of oxidative injury (Fig. 6).

The study presented here demonstrates morphological evidence of oxidative injury in diabetic retinopathy which correlates with endothelial cell dysfunction as indicated by leakage of serum albumin at sites of free radical derived oxidant localization. In addition, the activated endothelial cell is documented as a source of free radical derived oxidants as a result of hyperglycemia in diabetes.

References

1. R. A. Cohen, *Circulation*, 87[suppl. V](1993)V-67.
2. B. Tesfamariam, *Free Radic. Biol. Med.*, 16(1994)383.
3. R. T. Briggs et al., *J. Cell Biol.*, 67(1975)566.
4. J. Guy et al., *Arch. Ophthalmol.*, 108(1990)1614.
5. D. L. Guberski et al., *Diabetologia*, 36(1993)912.
6. M. Bendayan et al., *Diabetologia*, 29(1986)868.
7. E. A. Ellis and J. R. Guy, *Proc. 50th Ann. EMSA Meeting*, (1992)808.

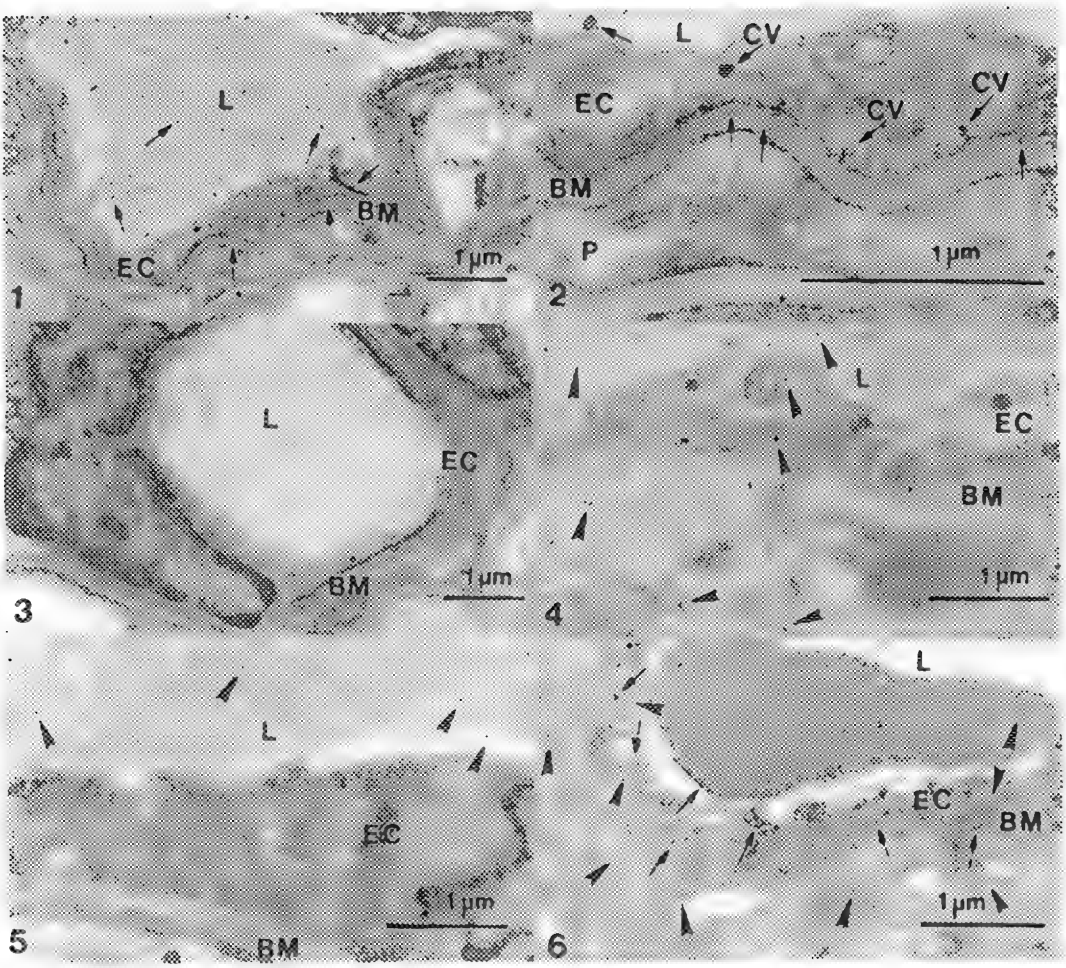

FIG. 1 Localization of H_2O_2 (arrows) in vessel lumen (L), endothelial cell (EC), and basement membrane (BM) of a capillary in the retina of a BBZ/Wor rat after 5 months of diabetes.
FIG. 2 Higher magnification of Fig. 1 showing fine cerium perhydroxide precipitate (arrows) in cytoplasmic vesicles (CV) which discharge their contents into basement membrane. Note the absence of precipitate in the basement membrane (*) of the adjacent pericyte (P).
FIG. 3 Age matched, nondiabetic control of comparable area to that shown in Fig. 1.
FIG. 4 Localization of serum albumin with 20 nm colloidal gold particles (arrowheads) showing leaky vessel with extravasation of serum albumin beyond basement membrane in retina of rat after 5 months of diabetes.
FIG. 5 Localization of serum albumin in age matched, nondiabetic control.
FIG. 6 Colocalization of serum albumin (arrowheads) and H_2O_2 (arrows) in retina of rat after 10 months of diabetes.

ULTRASTRUCTURAL CHANGES IN ENDOTHELIAL CELLS CULTURED IN HEPARIN-ENRICHED MEDIA

C.A. Taylor,* S. Lemley-Gillespie,** S.M. Xu,**J. George,* and A.K. Mandal**

*Department of Anatomy, Wright State University, Dayton, OH 45401
** Department of Medicine, Wright State University and Veterans Affairs Medical Center, Dayton, OH 45428

The widespread use of heparin is due to its ability to reduce clotting and prevent thrombosis. An additional biological property of heparin is the reduction of blood pressure in rat models.[1] This lowering of blood pressure is endothelin-1 dependent[2,3] and results in cell cytoskeleton reorganization, which suggests a mechanism for vascular relaxation.[4]

Endothelial cells (CRL 1998 ATTC) reach confluency within 3 days when fed media 199/10% FCS (Sigma) and incubated at 37°C with 5% CO_2 at 80% humidity. This growth medium is replaced with fresh medium containing 0-100 U/ml heparin, and the incubation continued for 24 hours. The cells are removed with 0.25% trypsin and pelleted for 2 minutes in a microfuge. Routine procedures for TEM include fixation in 2% buffered glutaraldehyde followed by 1% aqueous OsO_4, dehydration in a graded series of acetones, and embedding in Medcast (Pella). Thick and thin sections are cut with a Diatome diamond knife and mounted on bare 300 mesh grids. Contrast is enhanced with uranyl acetate followed by lead citrate before examination with the Philips 400 transmission electron microscope. Our procedures for immunofluorescence histochemistry, enzyme-linked immunosorbent assay (ELISA), and flow cytometry were published previously.[4]

Untreated control cells have an extensive fringe of microvilli, although many cells are in direct apposition. Increasing the concentration of heparin decreases the microvillar fringe: the blunting of microvilli seen in SEM and the relocation of vimentin intermediate filaments toward the nucleus seen in immunofluoresence[4] are consistent with the TEM findings. The composition of an extracellular, amorphorous material found with higher levels of heparin is being analyzed.

References

1. D. Susic et al., *Hypertension* (1982) 4, 681-685.
2. J. Yokokawa et al., *Am J. Physiol.* (1992) 263, R1035-R1041.
3. A.K. Mandal et al., *Kidney International* (1995) 4,1508-1516.
4. A.K. Mandal et al., *Kidney International* (1995) 47:1017-1022.
5. This work was supported in part by Bristol-Myers-Squibb Pharmaceutical Company.

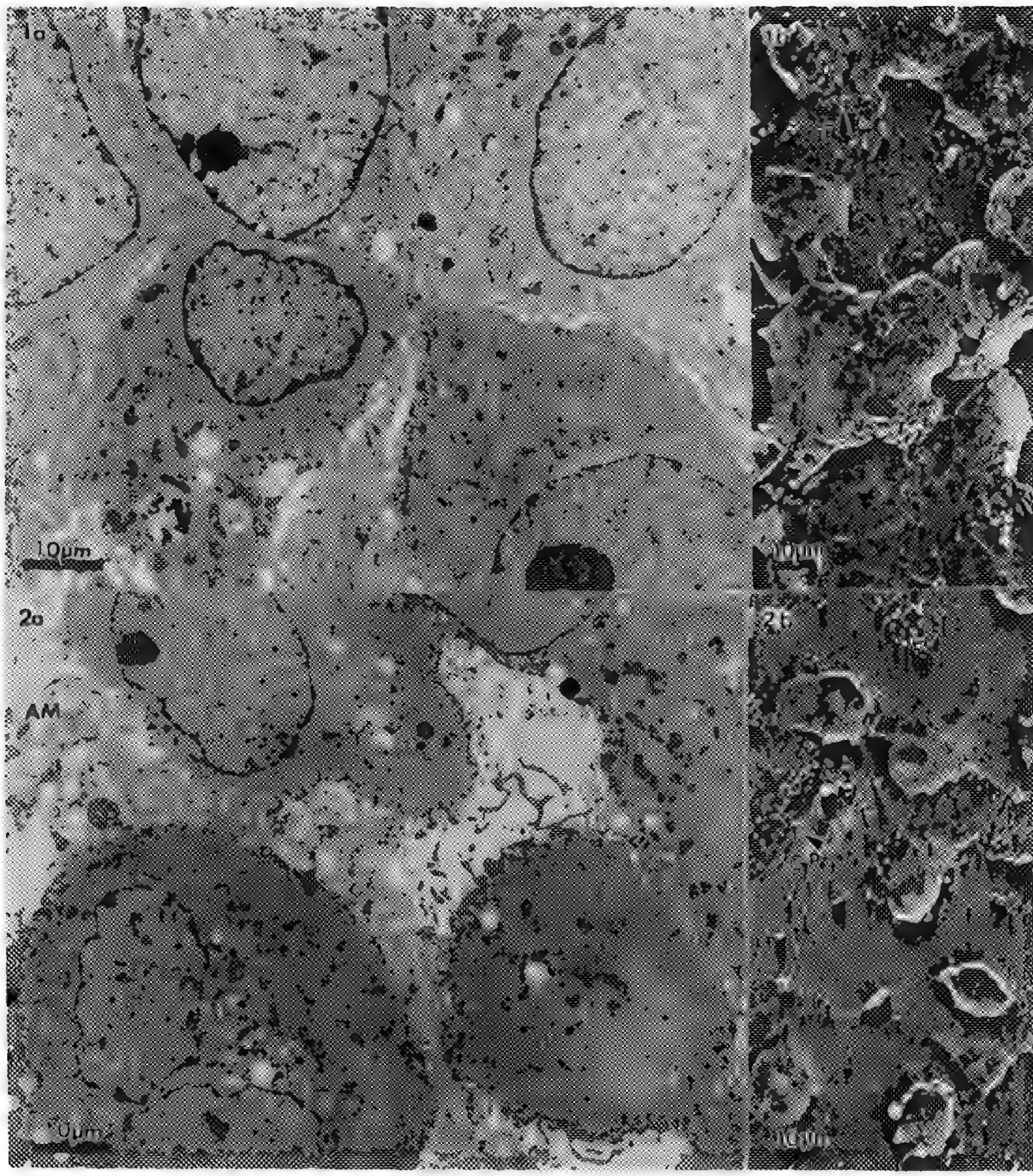

FIG. 1 Endothelial cells cultured without addition of heparin. (a) TEM of microvillar fringe and cell apposition (b) SEM of microvilli and granular projections (GP).
FIG. 2 Endothelial cells cultured for 24 hours with 100 U/ml heparin. (a) TEM of blunted microvilli and extracellular amorphous material (AM) (b) SEM showing increase in granular projections (GP) and decrease in cell contact.

LOCALIZATION OF ENDOTHELIAL NITRIC OXIDE SYNTHASE IN THE NORMAL AND FAILING HUMAN ATRIAL MYOCARDIUM

Chi-Ming Wei, Margarita Bracamonte, Shi-Wen Jiang, Richard C. Daly
Christopher G. A. McGregor, Shaobo Zhang, Charles Y. F. Young.
Mayo Clinic and Mayo Foundation, Rochester, MN 55905

Nitric oxide (NO) is a potent endothelium-derived relaxing factor which also may modulate cardiomyocyte inotropism and growth via increasing cGMP. While endothelial nitric oxide synthase (eNOS) isoforms have been detected in non-human mammalian tissues, expression and localization of eNOS in the normal and failing human myocardium are poorly defined. Therefore, the present study was designed to investigate eNOS in human cardiac tissues in the presence and absence of congestive heart failure (CHF).

Normal and failing atrial tissue were obtained from six cardiac donors and six end-stage heart failure patients undergoing primary cardiac transplantation. ENOS protein expression and localization was investigated utilizing Western blot analysis and immunohistochemical staining with the polyclonal rabbit antibody to eNOS (Transduction Laboratories, Lexington, Kentucky).

In Western blot analysis, the membranes of human cardiac tissue was solubilized with 10 mM CHAPS, the purified antibody probe was subjected to 7.5% SDS-PAGE and electrotransferred to nitrocellulose membrane. The nitrocellulose membrane was treated overnight at 4°C with anti-eNOS antibody, then washed and treated with goat anti-rabbit IgG peroxidase. Immunohistochemical Staining for eNOS was performed in cardiac tissue as we have previously described. Tissues fixed in 10% buffered formalin were dehydrated and embedded in paraffin. Serial sections were cut at a thickness of 5 μm. The presence of eNOS in cardiac tissues were examined utilizing a modified two-stage protocol as we previously described.

Western blot analysis (Figure 1) demonstrated eNOS signaling in normal and failing human heart with similar levels and no cross reaction with other type NOS antibodies. Positive immunohistochemical staining was observed within the cytoplasm and para-nuclear region of cardiomyocytes. No significant difference in eNOS immunoreactivities between normal (Figure 2) and failing (Figure 3) human myocardium were detected. As negative control (Figure 4), the sections treated with normal rabbit serum (NRS) instead of primary antibody, demonstrated no immunoperoxidase activity.

The present studies demonstrate the distribution of eNOS in normal and failing human hearts. These studies suggest that NOS mediated paracrine and autocrine pathways continue in the control the myocardial function in the failing human hearts.

References

1. S. Moncada et al., Pharmacol Rev (1991) 43, 109.
2. R. Schulz et al., Br J Pharmacol (1992) 105, 575.
3. A.J. DeBelder et al., Lancet (1993) 341, 84.
4. C.M. Wei et al., Circulation (1994) 89, 1580.
5. K. Nishida et al., J Clinic Invest (1992) 90, 2092.
6. This research was supported in part by grants from the Minnesota Affiliate of the American Heart Association (MHA-123), Astra/Merck Group, American Society of Hypertension (MMD Clinical Fellowship) and National Institute of Health (HL03174).

1

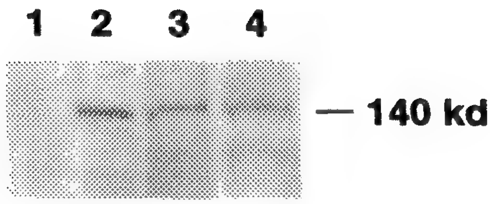

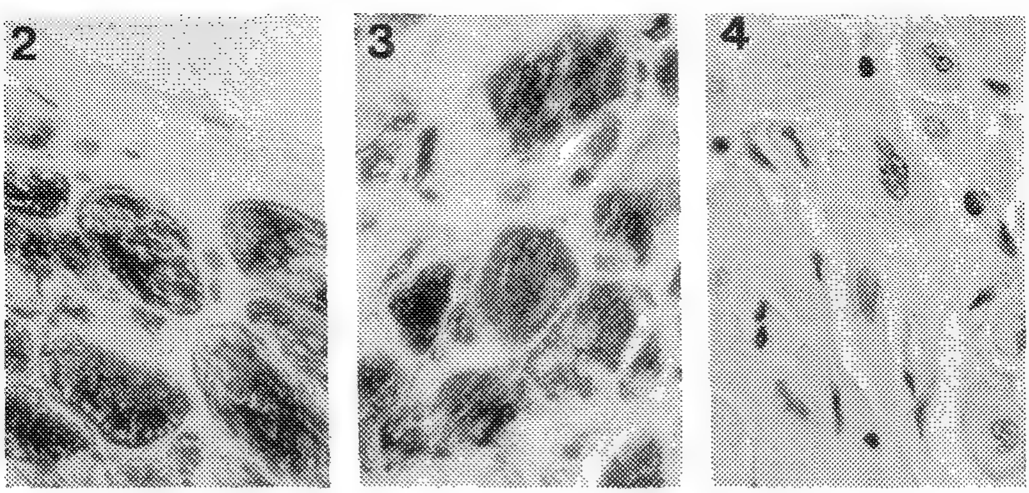

LEGEND:

Figure 1: Western blot analysis with eNOS antibody. 1) mouse macrophage for negative control; 2) human endothelial cell for positive control; 3) normal human right atrium; 4) congestive heart failure patient right atrium.

Figure 2: Immunohistochemical staining with eNOS antibody in normal human right atrium demonstrates positive staining in cytoplasm of normal human myocardium. (x1000)

Figure 3: Immunohistochemical staining with eNOS antibody in failing human right atrium demonstrates positive staining in cytoplasm of failing human myocardium. (x1000)

Figure 4: As negative control, normal rabbit serum (NRS) reveals no immunoreactivities in cytoplasm. (x1000)

THE EFFECTS OF CISPLATIN, TAXOL, AND CISPLATIN PLUS TAXOL ON NON-SPECIFIC ESTERASE AND ALKALINE PHOSPHATASE ACTIVITY IN RAT KUPFFER CELLS

B.N. Johnson, and S.K Aggarwal

Department of Zoology, Michigan State University, East Lansing, MI 48824-1115

Cisplatin (*cis*-diamminedichloroplatinum II) and taxol (paclitaxel) are two chemotherapeutic agents used to combat various types of cancers. Cisplatin, although effective at inhibiting cell division via cross-linking of DNA, is extremely toxic to both the liver and the kidney.[1] Taxol, a diterpene analog, interferes with cell division by specifically binding to the beta subunit of the tubulin protein, promoting the formation of these microtubule polymers.[2] In combination, cisplatin and taxol have proven to be more effective against ovarian cancers compared to the individual use of the respective drugs.[3] These drugs are known to influence a variety of changes within the tissue, including activation of the murine peritoneal macrophages[4,5] The effects of cisplatin, taxol, and cisplatin plus taxol on the liver Kupffer cells were studied using non-specific esterase and alkaline phosphatase as markers.

Wistar rats (160-180 g) were given intraperitoneal injections of cisplatin (1.8 mg/kg/day x 5), taxol (4 mg/kg/day x 5), and cisplatin plus taxol (0.9 mg/kg/day x 5; 2 mg/kg/day x 5) using a .85% saline solution as the vehicle for administration. The liver was excised, freeze sectioned and incubated in an incubation medium specific for each enzyme for 40 minutes at room temperature. The tetrazolium staining method was employed for both enzymes.

Histochemically, all variations in drug treatment produced an increase both in the number of Kupffer cells and in the concentration of the non-specific esterase and alkaline phosphatase enzymes in the liver sinusoids, compared to the control. In the normal liver, Kupffer cells appear discoid in shape (Fig.1). Following cisplatin treatment however, these cells demonstrated increased cytoplasmic extensions, as well as an increase in the population approximately 10 times that of normal (Fig.2). Sections from animals treated with taxol also demonstrated an increase in Kupffer cell population, approximately 3 times that of normal. These Kupffer cells appeared larger than the Kupffer cells in other treated animal liver sections and were discoid in shape without the cytoplasmic extensions exhibited by the cisplatin treated tissue (Fig.3). The Kupffer cells of the cisplatin plus taxol treated sections showed both an increase in population and cytoplasmic extensions, intermediate to the cisplatin treated and taxol treated animals (Fig. 4).

These results suggest that cisplatin, taxol, and cisplatin plus taxol treatment influences both the number of Kupffer cells as well as the degree of extension formations within the rat liver. The Kupffer cells lining the sinusoids of this organ serve to phagocytose bacterial invaders and other toxins harmful to the body.[6] Due to their immunologic importance, the increased population and extension formations observed in the treated tissues correlates well with their function in tissue preservation.

References

1. S.K Aggarwal and J.M. Fadool., *Anti-Cancer Drugs*, 4(1993)149.
2. H.J Guchelaar et al., *Clin-Oncol-R-Coll- Radiol*, 6(1994)40.
3. E. Reed et al., *Semin-Oncol*, 22(1995)90.
4. J.P. Palma et al., *Anti-Cancer Drugs*, 3(1992)665.
5. D.H. Pluznik et al., *Cancer Research*, 54(1994),4150.
6. S.A. Price and L.M Wilson., *Pathophysiology*, St. Louis, Mosby-Year Book,(1992)337.

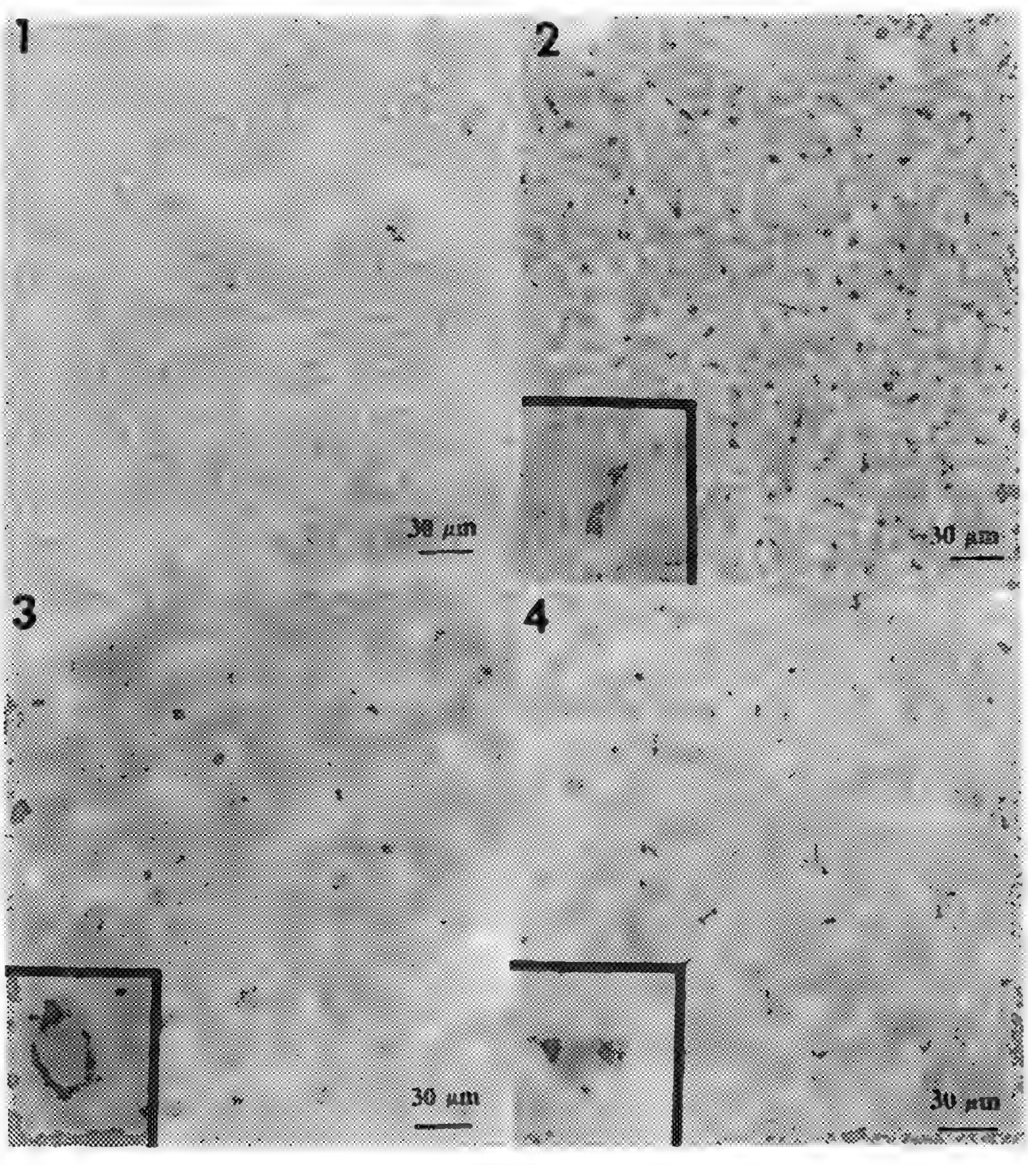

FIG. 1 Light micrograph showing the normal distribution of Kupffer cells in the rat liver after esterase staining. x 896.

FIG. 2 Distribution of Kupffer cells after cisplatin treatment. x 896. Insert showing a Kupffer cell enlarged with its extensions. x 2240.

FIG. 3 Distribution of Kupffer cells after taxol treatment. x 896. Insert demonstrating the discoid appearance of the Kupffer cell. x 2240.

FIG. 4 Distribution of Kupffer cells after cisplatin + taxol treatment. x 896. Insert demonstrates an intermediate size and extension formations between the taxol and cisplatin treated specimens. x 2240.

FT-IR Microspectroscopic Mapping of Diseased Brain Tissue

D. L. Wetzel*, L-'P Choo**, H. H. Mantsch**, M. Jackson**, S. M. LeVine***

* Kansas State University, Microbeam Molecular Spectroscopy Laboratory, Shellengerger Hall Manhattan, KS 66506
** Natural Research Council Institute for Biodiagnostics, Winnipeg Manitoba, R3B 1Y6, Canada
***University of Kansas Medical Center, Dept. of Physiology, 3901 Rainbow Blvd, Kansas City, KS 66106

Multiple frozen sections of brain tissue representing three diseased cases and two normal cases were prepared for examination by microtoming and thaw mounting on barium fluoride optical windows (2mm x 13mm). Chosen from the microtomed sections were those from each of the diseased brains that included both a lesion site typical of that disease and surrounding tissue to allow contrast in functional group mapping between the adjacent tissue in the microscopic field. Among sections prepared from one specimen frozen to the microtome specimen holder one or more were used for staining to support the visual selection process. Remaining sections mounted on barium fluoride windows were tested for infrared optical transmission by scanning the spectra at selected sites of interest. The range of infrared absorbance and the sample scattering characteristics affected the quality of individual spectra. With visible light microscopy it was necessary to verify consistency of focus throughout the part selected for potential mapping since with the programmed moving stage experiment spectra are collected from all points at the same distance of the objective from the stage once focussing has been set. Conservation of the intensity of radiation transmitted through the sample and hence the quality of the spectra obtained are highly dependant on consistently good focus with the front surface cassegrainian mirror lens condenser and objective. From the criteria described and the preliminary optical testing a section and a specific area within that section were chosen for mapping. Similarly a mapping region to represent the brain of each case (multiple sclerosis, and alzheimer disease) also two normal brain as controls. Prior to these experiments the Kansas workers reported mammal, mouse, and rat brain tissue microbeam molecular mapping of both normal[1,2] and pathological specimens[3,4] at the Kansas State University and Brookhaven National Laboratory. The Manitoba research group previously reported results for many individual spectra of human neuropathological samples[5,6] including those from multiple sclerosis and alzheimer victims. This human brain mapping is a cooperative effort of the two groups. Bright, low noise, low divergence synchrotron infrared radiation used as a source for microspectrocopy in these experiments allowed scans from a large number of points to provide detailed mapping in a reasonable acquisition time. For each diseased brain (multiple sclerosis, adrenoleukodystrophy, alzhemier) the infrared functional group features were coincident with lesion sites in the tissue. The type of response is emphified by peak area data at select wavelengths for one 160 point line map taken in 12μm increments and one 520 point map in 24μm increments. Fig. 1 shows the highest concentration of lipid in the white matter (WM) (1469 and 2927 cm^{-1} peak areas) a reduced amount in the plaque (P) and a minimum concentration in gray matter (GM). The distribution in WM and GM is consistant with that in normal brain tissue. Three dimensional plots (Fig. 2) from data obtained from a different section from the same case study, in a rectangular pattern from GM (left) through WM and into plaque (right) clearly show reduced lipid (1469 and 1740 cm^{-1}) in the plaque compared to the unaffected

WM. A detailed analysis and discussion of data from these mapping efforts will be reported in the future.

REFERENCES

1. D. L. Wetzel and S. M. LeVine, *Proc. SPIE- Int. Soci. of Optic. Engin.*, 575(1992)435.
2. D. L. Wetzel and S. M. LeVine, *Spectroscopy*, 8(1993)40.
3. S. M. LeVine and D. L. Wetzel, *Am. J. Path.*, 145(1994)1041.
4. S. M. LeVine et al., *Int. J. Dev Neuroscience*, 12(1994)275.
5. L-'P. Choo et al., *Proc. SPIE - Int. Soci. of Optic. Engin.*, 2089(1993)134.
6. L-'P. Choo et al., *Proc. SPIE - Int. Soci. of Optic. Engin.*, 2089(1993) 494.

Support is acknowledged from the National Sciences Foundation EPSCoR: OSR-9255223.
Contribution no. 96-409-J Kansas Agricultural Experiment Station, Manhattan.

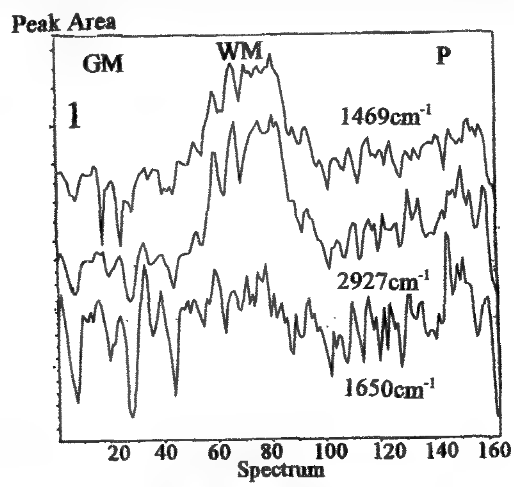

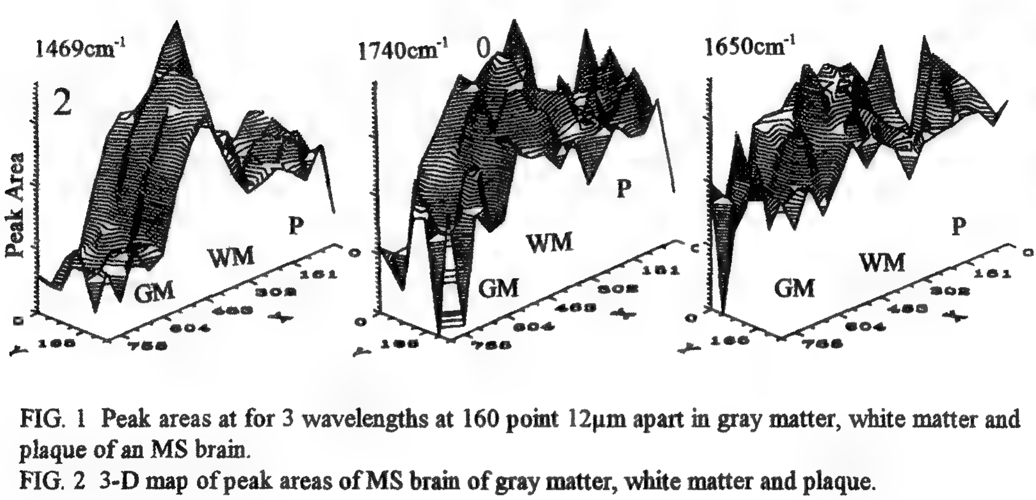

FIG. 1 Peak areas at for 3 wavelengths at 160 point 12μm apart in gray matter, white matter and plaque of an MS brain.
FIG. 2 3-D map of peak areas of MS brain of gray matter, white matter and plaque.

ULTRASTRUCTURE OF A SERTOLI-LEYDIG CELL TUMOR OF THE OVARY

S. Siew*, S. Katlein**

*Pathology Department, Michigan State University, East Lansing, MI 48824

**St. Lawrence Hospital, Lansing, MI 48915

Sertoli-Leydig cell tumors of the ovary are comparatively rare, comprising less than 0.1% of ovarian neoplasms. It has been generally accepted that they are derived from remnants of primitive male directed cells of the indifferent stage of gonadal development. However, another postulate is that they originate from specialized ovarian stromal cells through different stages of differentiation. At the gross level, they tend to be nodular and solid with only focal evidence of cystic change. The histopathologic features vary with the degree of differentiation, ranging from tumors with well differentiated tubular structures lined by Sertoli cells with intertubular Leydig cells (Type I) to an undifferentiated sarcomatoid pattern (Type III) consisting of spindle shaped cells.

We report a case of an intermediate type (II) which showed a mixed pattern on light microscopy. A tubular structure could be identified in plastic embedded sections, cut at 1 μm and stained with toluidine blue. However, most of the tubules were solid and a luminal space was identified only in a few instances. The intratubular cells showed the features of Sertoli cells. The tubules were closely packed but there were occasional blood vessels and scattered Leydig cells in the intertubular tissue.

Transmission electron microscopy confirmed the presence of tubular structures, subtended by a basal lamina. The tubules contained only Sertoli cells showing the characteristic features of nuclei with deep indentation, a nucleoplasm of finely dispersed euchromatin and prominent, well developed nucleoli (Fig. 1). The nucleocytoplasmic ratio varied, but it was large, in some of the cells. Junctional complexes were present at points of close cytoplasmic apposition. However, there was evidence of widening of intercellular spaces, which may be an artifact of fixation. The cytoplasm contained attenuated profiles of smooth endoplasmic reticulum, elongated mitochondria, lipid vacuoles and droplets and some intermediate filaments. Charcot-Botcher crystalloids were not observed.

Varying numbers of cells with the ultrastructural features of Leydig cells were observed in the extra tubular tissue. They occurred singly and as aggregates in a loose stroma. They were elongated on polygonal with some irregular cytoplasmic processes. There was a lack of basal lamina formation. The nuclei tended to be ovoid with some evidence of indentation. They contained scattered aggregates of heterochromatin, Nucleoli were present, mostly in a peripheral location. Smooth endoplasmic reticulum was well developed and the rounded mitochondria had tubular cristae (Fig. 2). Reinke crystals were not observed. Scattered lipid droplets and small myelinoid figures were present.

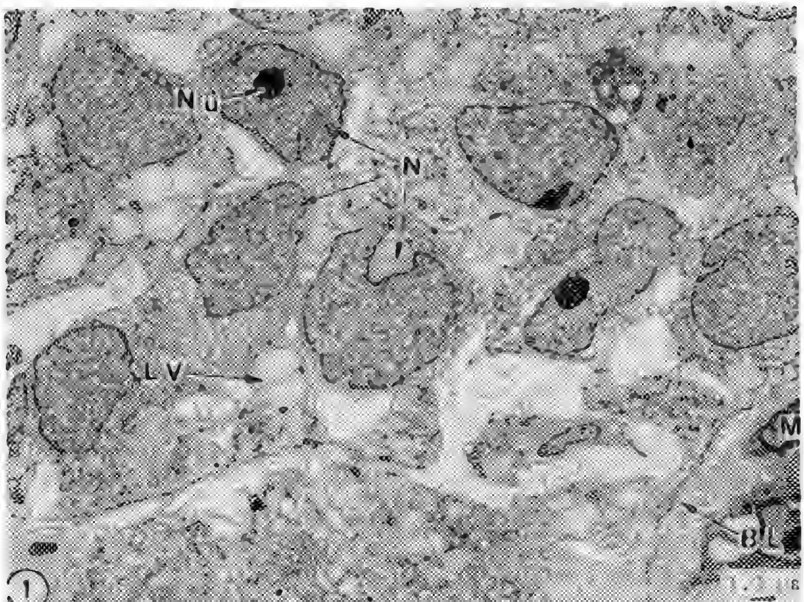

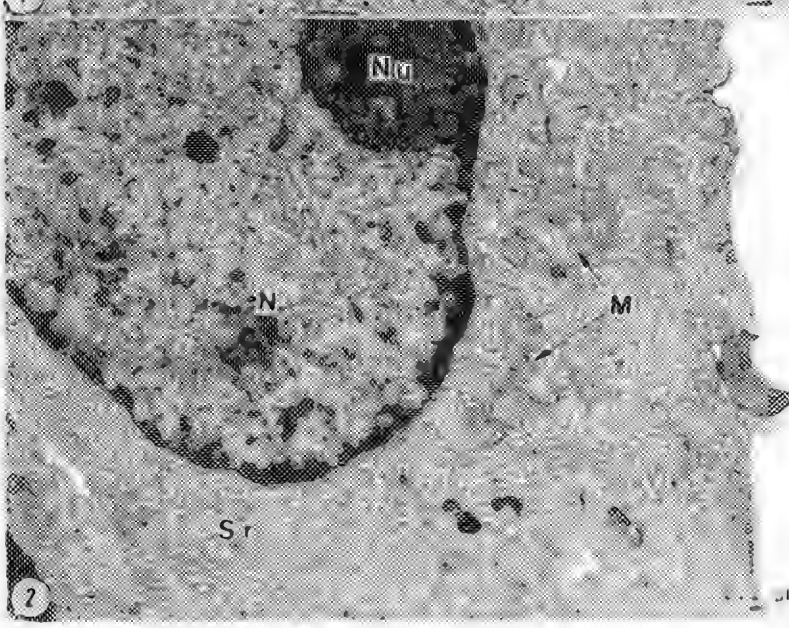

FIG. 1 Tubular structures containing only Sertoli cells BL-Basal lamina, LV-Lipid vacuoles, M-Myoid cell, N-Indented nuclei, Nu-Nucleoli, (Widened intercellular spaces may be an artifact of fixation).

FIG. 2 Leydig cell, M-Mitochondria, N-Nucleus, Nu-Nucleolus, Sr-Smooth endoplasmic reticulum

INTERACTION OF INTERNALIZED, VIABLE *LISTERIA MONOCYTOGENES* WITH MHC CLASS II MOLECULES AND LOW PH COMPARTMENTS

Linda Iadarola, and Paul Webster

Center for Cell Imaging, Department of Cell Biology, Yale University School of Medicine
New Haven, CT 06520. *http://info.med.yale.edu/cellimg*

Listeria monocytogenes, an aerobic, non-sporulating, gram-positive bacillus, is a contaminant of the food we eat [1] and is capable of surviving in the cytoplasm of infected cells. Ingestion of contaminated foods by susceptible individuals (newborn, elderly and immuno-compromised) can result in severe systemic disease resulting from opportunistic infections.[2] There is a high case fatality rate in immunocompromised individuals.[3]

During the course of infection, *L. monocytogenes* invades cells by adhering to the cell membrane from where the bacteria are internalized into membrane bound phagosomes. Disruption of the phagosome membrane allows the bacteria to gain access to the cell cytoplasm where they grow and multiply.[4] In the cytoplasm, actin polymerization on the bacteria surface cause them to move in the cell and form long cytoplasmic protrusions at the cell surface.[4] The protrusions, with a bacterium at the tip, are taken up by adjacent, uninfected cells which then become infected.[4]

Both CD4 and CD8 T cell responses are required for protection against listeriosis, indicating an interaction with both class I and class II MHC molecules. The interaction of listeria with MHC class II molecules is examined in this study using a macrophage-like cell line (J774) as a model system.

The early events of macrophage invasion by *L. monocytogenes* were studied by applying specific antibodies to either whole cell mounts (LM) or thin cryosections (TEM). Low pH compartments were visualized by incubating cells in 30μm 3-(2,4-dinitroanilino)-3'-amino-*N*-methyldipropylamine (DAMP) at 37°C. Antibodies to dinitro phenol (DNP) were used to visualize the accumulated DAMP on the thin cryo sections. Biotin was visualized using monoclonal antibodies.

We demonstrate that the bacteria adhere to the plasma membrane of the host cell (Fig 1), exclude plasma membrane proteins from the bacterium-membrane junction (Fig 1) and the early phagosome (Fig 2). Intracellular compartments containing MHC class II (Fig 3), LAMP 1 and low pH (Fig 4), fuse with the phagosome membrane soon after internalization. Vesicles that contained MHC class II but not LAMP 1 were seen in close proximity to phagosomes containing newly entered listeria (Fig 5). The majority of the intracellular listeria were present first in MHC class II positive compartments but then colocalized with LAMP 1 positive compartments after 2 hr infection (Fig 6).

These data suggest that listeria is able to exclude surface proteins such as MHC class II from the phagosome. However, the internalized bacteria are not able to prevent subsequent delivery of these molecules to the phagosome membrane. It appears that MHC class II responses during listeriosis may be triggered in macrophages only during the first 25 min. after bacterial invasion. Cytoplasmic listeria pass from cell to cell via LAMP 1 positive compartments but do not re-enter compartments containing MHC class II.

References

1. P. Cossart & J. Mengaud,Mol. Biol. Med. 6 (1989) 5164.
2. J. M. Farber & P. I. Peterkin, Microbiol. Rev. 55 (1991) 476.
3. R. L. Jurado *et al.*, Clin. Infec. Dis. 17 (1993) 224.
4. L. G. Tilney & D. A. Portnoy, J. Cell Biol. 109 (1989) 1597.

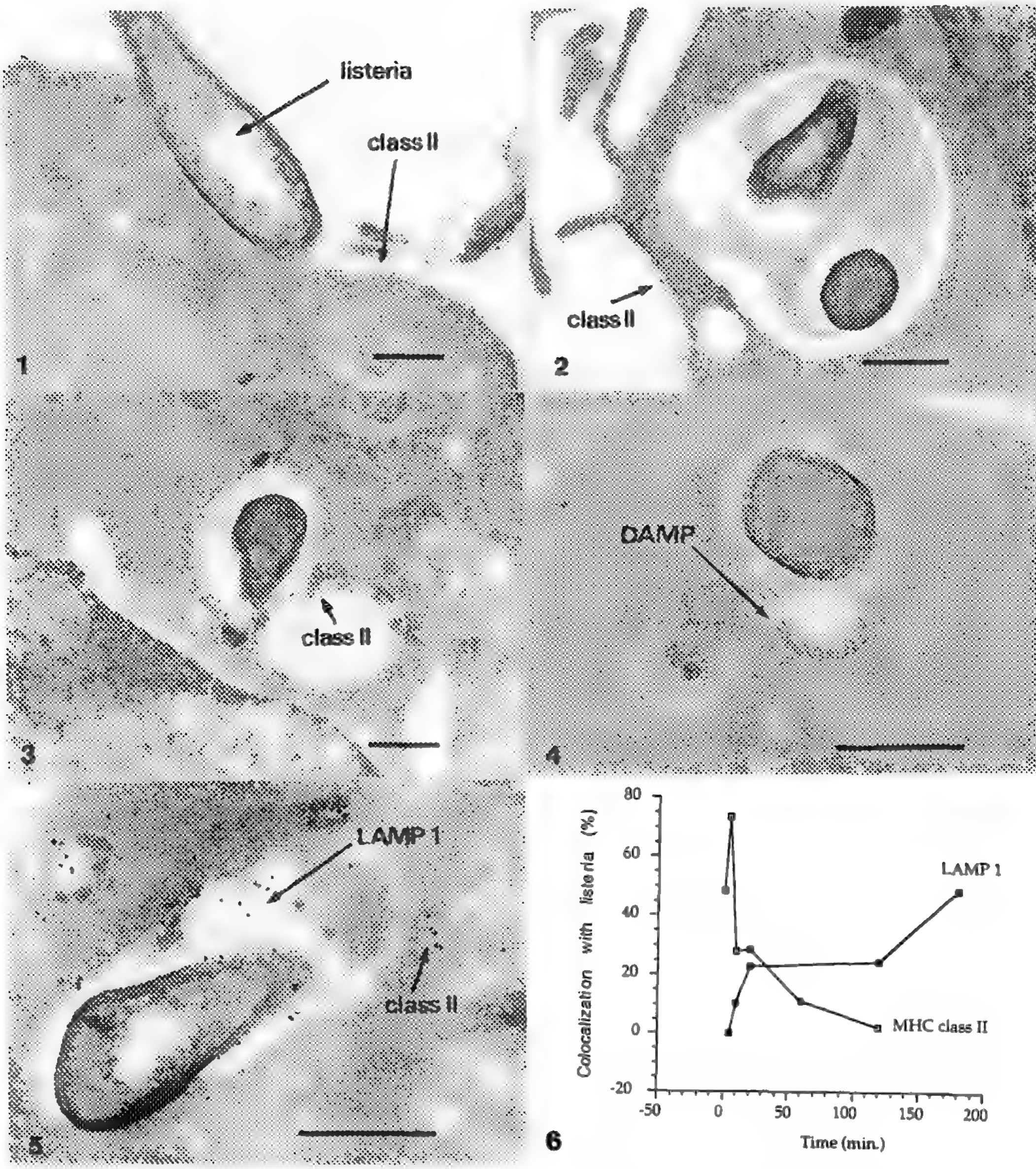

scale bar = 0·5um

FIG 1 Surface MHC class II is absent from the junction beween listera and plasma membrane.
FIG 2 MHC class II molecules are absent from the membrane of the early phagosome.
FIG 3 Intracellular vesicles that label for MHC class II fuse with the early phagosome.
FIG 4 Low pH compartments, containing accumulated DAMP, fuse with the early phagosome.
FIG 5 MHC class II-positive, LAMP 1-negative structures are seen close to the early phagosome.
FIG 6 Quantified LM data show that listeria first colocalize with MHC class II and then with LAMP 1.

IDENTIFICATION OF A BACULOVIRUS POLYHEDRON FORMATION MUTANT WITH A NOVEL PHENOTYPE

James M. Slavicek, Melissa J. Mercer, and Mary Ellen Kelly

USDA Forest Service, Northeastern Forest Experiment Station, Forestry Sciences Laboratory, 359 Main Road, Delaware, OH 43015

Nucleopolyhedroviruses (NPV, family *Baculoviridae*) produce two morphological forms, a budded virus form and a viral form that is occluded into a paracrystalline protein matrix. This structure is termed a polyhedron and is composed primarily of the protein polyhedrin. Insects are infected by NPVs after ingestion of the polyhedron and release of the occluded virions through dissolution of the polyhedron in the alkaline environment of the insect midgut. Early after infection the budded virus form is produced. It buds through the plasma membrane and then infects other cells. Later in the infection cycle the occluded form of the virus is generated (reviewed by Blissard and Rohrmann, 1990).

The processes of polyhedron formation and virion occlusion are likely to involve a number of viral gene products. However, only two genes, the *polyhedrin* gene and *25K FP* gene, have been identified to date that are necessary for the wild type number of polyhedra to be formed and viral particles occluded. Mutations in the *polyhedrin* gene will prevent normal polyhedron formation and virion occlusion. Two polyhedron formation mutants have been described that contain point mutants in the *polyhedrin* gene. The *Autographa californica M*NPV (Ac*M*NPV) M29 mutant produces small particles composed of polyhedrin protein that lack a paracrystalline lattice (Duncan and Faulkner, 1982; Duncan et al., 1983; Carstens et al., 1987). The Ac*M*NPV M5 mutant produces a few large cuboidal shaped polyhedra in infected cells (Brown et al., 1980; Carstens, 1982; Carstens et al., 1986).

During serial passage in cell culture a class of viruses termed few polyhedra (FP) mutants arises at a high frequency and become predominant. These mutants have the characteristics of an altered plaque morphology, production of few polyhedra that contain very few viral nucleocapsids, increased production of budded virus (BV), and in the Ld*M*NPV, decreased percentage of cells producing polyhedra (Hink and Strauss, 1976; MacKinnon et al., 1974; Potter et al., 1976; Fraser and Hink, 1982; Slavicek et al., 1992; Slavicek et al., 1995). DNA insertions and deletions in the Ac*M*NPV *25K FP* gene will generate the FP mutant phenotype (Fraser et al., 1983, Fraser, 1987 for review). The *25K FP* gene is essential for polyhedron formation and virion occlusion since deletion of this gene is sufficient to generate the FP mutant phenotype (Beames and Summers, 1988, 1989).

Proteins other than the 25K FP and polyhedrin have been identified that are part of the polyhedron or are involved in polyhedron formation; however, deletion of the genes that code for these proteins did not impair polyhedron formation or virion occlusion. The polyhedral envelope protein is a major component of the polyhedron envelope (Whitt & Manning, 1988; Gombart et al., 1989; Russell and Rohrmann, 1990). Deletion of the *polyhedral envelope* gene from the Ac*M*NPV genome generated a virus that produced polyhedra viral occlusions (Zuidema et al., 1989). Another protein found in the polyhedron is the p10 protein. However, deletion of the p10gene from the Ac*M*NPV genome did not impair polyhedron formation suggesting that this protein is not essential for that process (reviewed by Rohrmann, 1992; van Oers et al., 1993).

In this study, we have characterized a novel *Lymantria dispar* nucleopolyhedrovirus (Ld*M*NPV) polyhedron formation mutant (PFM-S). This isolate, PFM-S, produced approximately 3.5 fold fewer and 5.0 fold more polyhedra compared to wild type virus and a FP mutant, respectively. Polyhedra generated by isolate PFM-S were normal in shape, but contained very few viral occlusions and were approximately one-half the size of polyhedra generated by a Ld*M*NPV FP mutant (Figure 1A and C, respectively). Approximately 33% of polyhedra generated by isolate PFM-S contained a diffuse structure that encapsulated the polyhedra (Figure 1A). This structure was absent on polyhedra produced nucleopolyhedrovirus isolates A21-MPV and A21-2 (Figure 1B and C, respectively). Isolate PFM-S released approximately the same amount of budded virus as a Ld*M*NPV FP mutant. In contrast to a FP mutant, most intranuclear viral nucleocapsids produced by isolate PFM-S lacked envelopes. The phenotype of PFM-S appears unique in comparison to previously described baculovirus polyhedron formation mutants.

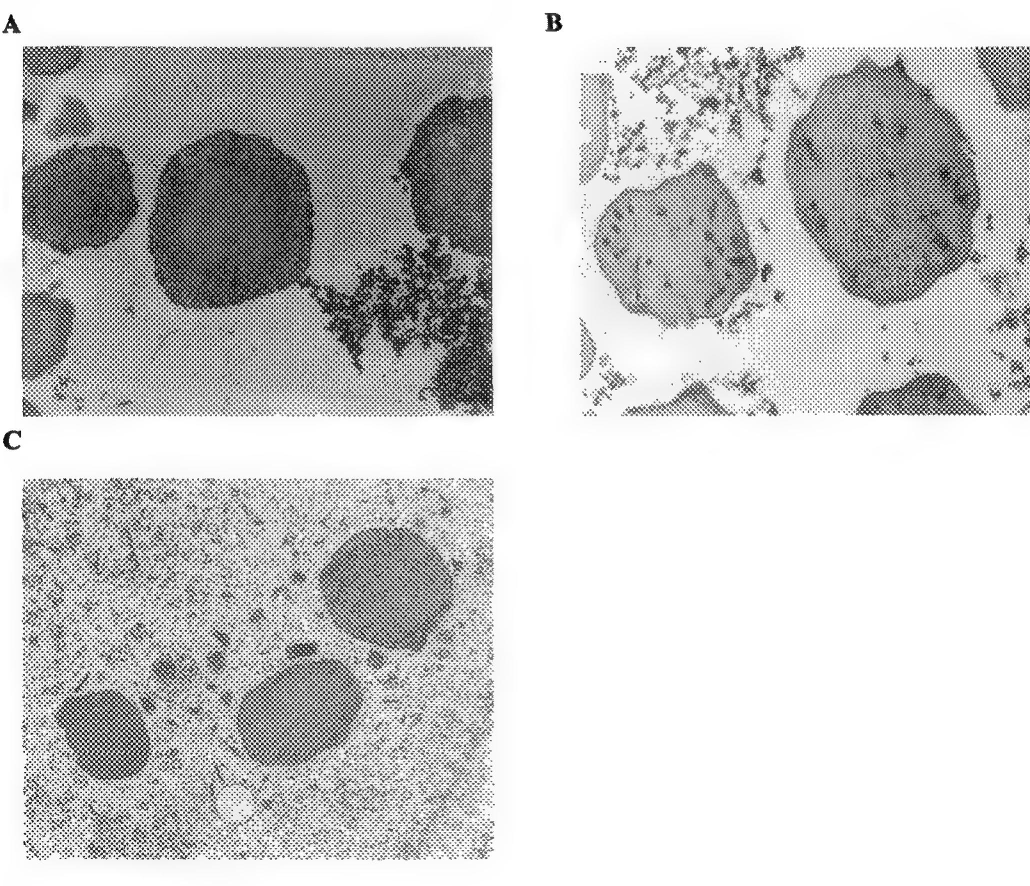

Figure 1. Electron micrographs of representative cross-sections of polyhedra generated by isolates PFM-S (A), A21-MPV (B), and A21-2 (C). The bar marker represents 1 μm.

CYTOPLASMIC DYNAMICS OF THE TUBULIN AND ACTIN CYTOSKELETONS DURING TELIOSPORE GERMINATION AND BASIDIOSPORE FORMATION IN A RUST FUNGUS

Robert W. Roberson, William P. Sharp, John P. Shields*, Steve Sayegh, and Bader F. Al-Anzi

Department of Botany, Box 871601, Arizona State University, Tempe, AZ 85287-1601 and
*Department of Botany, University of Georgia, Athens, GA 30602-7271

Gymnosporangium clavipes C. & P. is a basidiomycetous fungus belonging to a common and destructive group of plant pathogens known to as the rusts.[1] The rusts are best known for their damage to economically important crops including corn, wheat, oats, and barley[1] and have become important model organisms in cell biology studies.[2] Of all the stages in their complex life cycle, perhaps the most interesting are those involved in teliospore germination and basidiospore formation.

As illustrated with scanning electron microscopy teliospores of *G. clavipes* are ellipsoidal spores consisting of an apical and basal cell (Fig. 1). Upon germination of the teliospore, four discrete morphological events occur that give rise to mature basidiospores. These events include: i) emergence of germ tubes (Fig. 2), ii) formation of three septal cross walls segmenting the germ tube into four compartments (Fig. 3), iii) growth of a single sterigma from each compartment, (Fig. 4) and iv) enlargement of sterigmal tips to form individual basidiospores (Fig. 5). The objective of this research was to determine whether these developmental stages were temporally correlated with changes in the organization of the tubulin and actin cytoskeletons.

The cytoskeletons were visualized using light (LM) and transmission electron (TEM) microscopic methods. For LM, cells were prepared using indirect immunofluorescent (IIF) staining protocols and images recorded with standard epifluorescence microscopy or scanning laser confocal microscopy. Cryofixation (slam or high pressure freezing) and freeze-substitution methods were employed in preparing samples for TEM.

Actin staining revealed an accumulation of brightly fluorescent plaques located within the cortical cytoplasm throughout all stages of growth and development (Figs. 6-11). Actin plaques are believed to represent filasomes (Fig. 12). Unlike actin, the tubulin cytoskeleton exhibited numerous organizational changes which corresponded to specific morphological and cytoplasmic events during teliospore germination and basidiospore formation (Figs. 13-18).

References

1. C.J. Alexopoulos, C.W. Mims, and M. Blackwell, *Introductory Mycology*, John Wiley & Sons, Inc. (1996).
2. Y.H. Kwon, H.C. Hoch, and R.C. Staples, *Protoplasma*, (1991)37.

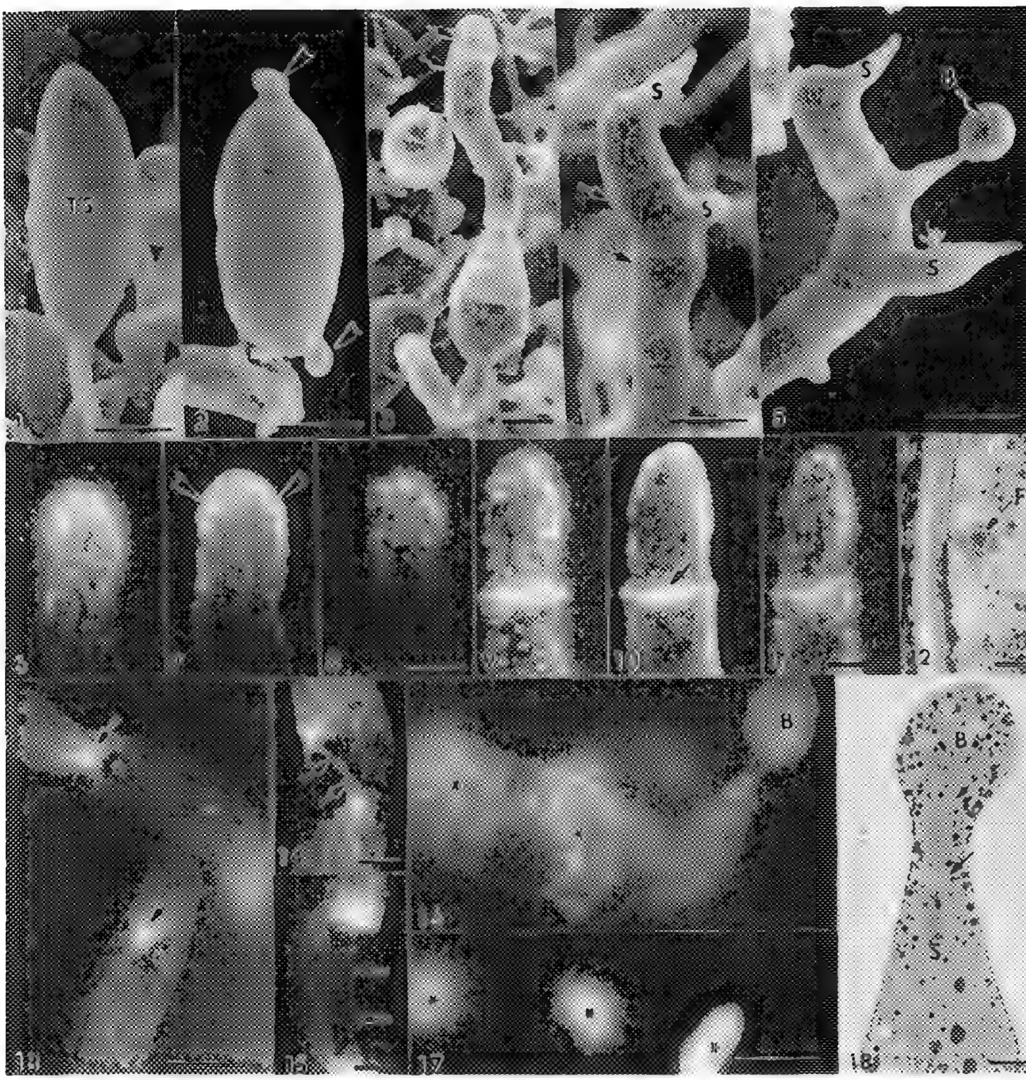

FIGS. 1-5 SEM of teliospore (TS) germination and basidiospore (B) formation. Note germ tube (arrowheads), septa (arrows) and sterigma (S). Bars = 10 μm.
FIGS. 6-12 IIF and TEM of actin. Figures 6-8 show three focal planes through germ tube (asterisks). Note abundant actin plaques (arrowheads). Figures 9-11 show focal planes of septa (arrows) formation. Bars = 15 μm. Figure 12 is high-pressure frozen germ tube illustrating filasome (F). Bar = 0.1 μm.
FIGS. 13-18 IIF and TEM of microtubules. Figure 13 shows nuclei (asterisks) and MTOCs (arrows) in two germ tubes. Figures 14 and 15 illustrate meiotic spindles (arrows). Figures 16-17 shows basidiospore (B) and nuclear locations (asterisk). Figure 17 is DAPI stained. Bar = 20 μm for figures 13, 16, 17; Bar = 10 μm for figures 14, 15. Figure 18 is slam frozen basidiospore (B). Note sterigma (S) and numerous microtubules (arrows). Bar = 1.0 μm.

ADHERENCE OF TEMPERATURE AND IRON-STRESSED ENTEROHEMORRHAGIC *ESCHERICHIA COLI* GROWING AT 9.5°C TO HEp-2 CELLS

Tina S. Schwach and E. A. Zottola
Department of Food Science and Nutrition, University of Minnesota

Conditions in the intial growth environment are known to effect growth and expression of numerous bacterial virulence factors[1]. Thus, we were interested in studying whether growth and adherence of enterohemorrhagic *Escherichia coli* (EHEC) to intestinal-like epithelia was affected by temperature and the amount of available iron in the initial growth environment. Adherence of *E. coli* 026:H11, strain 400, to HEp-2 cells was quantified using the assay of Sherman and Soni[2] and monitored by both SEM and TEM. Bacteria were grown at 9.5°C with and without iron-restriction in 0.3% Trypticase Soy Broth plus 1% Nobel Agar (TSBA). Ethylenediaminedihydroxyacetic acid was added (0.75 mM and 2.0 mM) to induce both low (EL) and high (EH) levels of iron-restriction and 100 µM $FeCl_3$ was added to induce iron-replete conditions.

Microbial populations from the 4 TSBA treatments were enumerated on Eosin Methylene Blue (EMB) agar at 37°C. A slow increase was noted over the 12 d of incubation from 10^4 to 10^9 CFU/ml for both control (T) and iron-replete (I) treatments. Both EL and EH iron-restricted treatments showed less than a 0.5 log increase in population during the first 3 d followed by a gradual decrease to at or just below initial inoculum levels (Fig. 1). HEp-2 cells were grown in Dulbecco's Minimal Essential Media/Ham's F12 (DMEM/F12) with 10% serum in 24-well tissue culture plates for 2 d. One or more mls from each TSBA treatment were centrifuged and the pellet resuspended in fresh DMEM/F12 to an estimated concentration of 10^5-10^6 bacteria/ml. Bacteria and HEp-2 cells were incubated together for 5 h or 24 h at 37°C. Non-adherent bacteria were removed by continuous rinsing in phosphate-buffered saline. The HEp-2 monolayer was lysed, freeing adherent bacteria, which were enumerated on EMB at 37°C. Results showed a gradual increase in adherence from 1 to 12% for the control and 0.8 to 16% for the iron-replete sample over the 12 days. Adherence of iron-restricted EHEC showed only slight increases, from 0.1 to 2%, during the study (Fig. 2).

Sterile 13 mm-round Thermanox® cover slips, added to tissue culture wells, were used as growth substrates for the EM samples. Cover slips were cut in half, one half processed for low-voltage SEM and the other half for TEM. EHEC organisms adhere to human intestinal epithelial by a characteristic attaching and effacing (AE) lesion as viewed by TEM[3]. *In vitro*, AE lesions are both bacterial strain and tissue culture cell line dependent[4]. *E. coli* strain 400 did not appear to exhibit AE lesions in any treatment in this study (Figs. 3 and 4). Adherent bacteria were most often associated with microvilli (Fig. 5). Prolonged iron-stress resulted in fewer adherent or healthy bacteria (Fig. 6).

Results suggest that EHEC growing with both temperature and iron-stress exhibit metabolic changes which effect their ability to grow at 9.5°C and recover, grow and adhere to HEp-2 cells at 37°C.

REFERENCES:

1. J.J. Mekalanos, *Journal of Bacteriology*, (1992)1.
2. P. Sherman and R. Soni, *Journal of Medical Microbiology*, (1988)11.
3. S. Knutton et al., *Infection and Immunity*, (1987)69.
4. T.A. Oelschlaeger et al., *Infection and Immunity*, (1994)5142.

All scanning micrographs were taken on a Hitachi S-900 Field Emission Low-Voltage SEM at 1.5 KeV. All transmission micrographs were taken on a Philips CM-12 at 60 KeV.

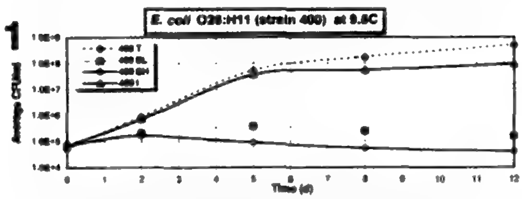

Fig. 1. Growth of EHEC strain 400 in 0.3% TSBA at 9.5C T is control. EL is low iron-stress. EH is high iron-stress. I is iron-replete.

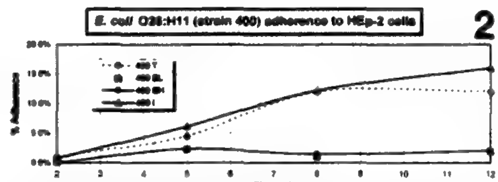

Fig. 2. Percent adherence of EHEC strain 400 from 0.3% TSBA at 9.5C to HEp-2 cells at 37C. T is control. EL is low iron-stress. EH is high iron-stress. I is iron-replete.

Fig. 3. Day 7 Control (T). Inset: Bacteria at arrow showing beginning of AE lesion.

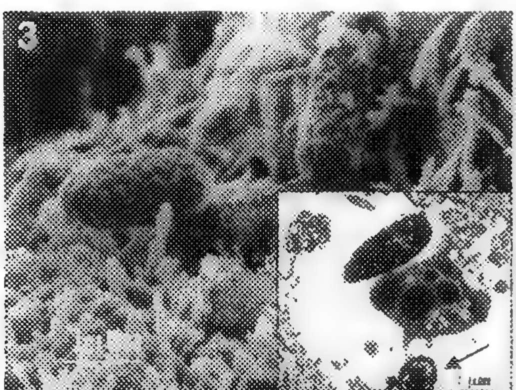

Fig. 4. Day 11 Iron-replete (I). Bacteria (SEM and inset TEM) adherent to HEp-2 cell surface.

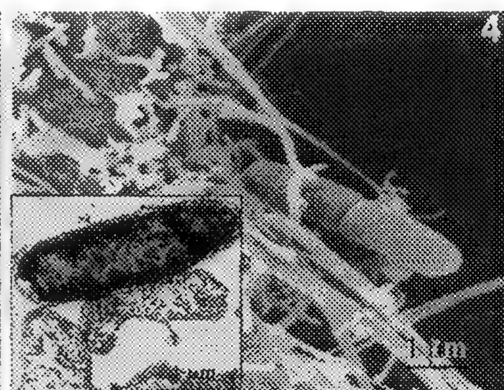

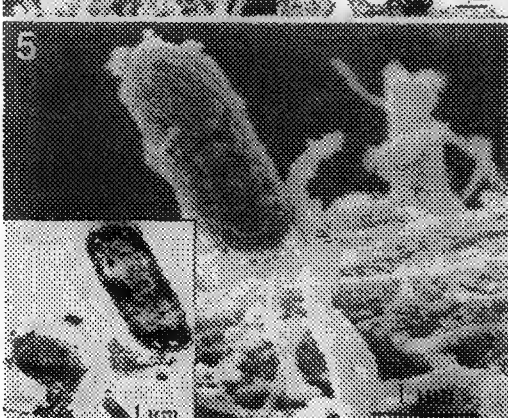

Fig. 5. Day 3 Low iron-stress (EL). Bacteria adherent to microvilli.

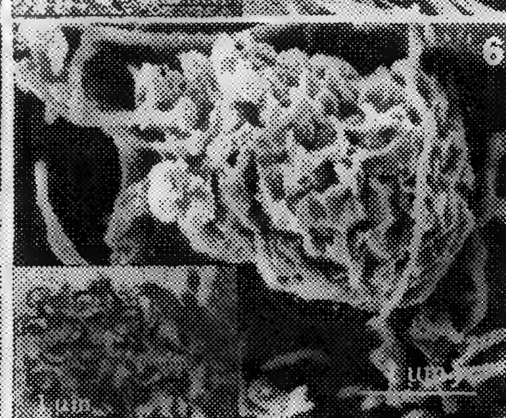

Fig. 6. Day 5 High iron-stress (EH). Disintegrating bacteria adherent to HEp-2 cell surface.

QUANTITATIVE ELEMENTAL ANALYSIS OF BACTERIAL POLYPHOSPHATE BODIES USING SCANNING TRANSMISSION ELECTRON MICROSCOPY AND ENERGY-DISPERSIVE X-RAY SPECTROSCOPY

J. Goldberg*, H. Gonzalez*, T.E. Jensen*, and W.A. Corpe**

*Department of Biological Sciences, Lehman College of CUNY, Bronx, NY 10468
**Department of Biological Sciences, Columbia University, NYC, NY 10027

The elemental composition of polyphosphate bodies (PPB's) has been determined qualitatively previously using energy dispersive x-ray spectrometers (EDX) and in bodies isolated from cells. In this present study we determine in several bacteria their quantitative elemental composition using EDX in conjunction with a STEM.

Bacteria were grown as previously described or were collected from natural sources.[1,2] Portions of each sample were air dried on formvar coated grids. Separate samples were fixed and embedded in Epon. For x-ray analysis cells of interest were first located using the TEM mode. The microscope was then switched to the STEM mode. Analysis of cell components was carried out in the spot mode (75 kV) of the STEM. The spot diameter at 100,000x is approximately 20nm. The objective lens current was adjusted so a total x-ray count of 600 to 1,000 cps was attained for the 100 sec. count time. Spectra were collected on a PGT IMIX (EDX). The data was analyzed using a bulk sample analysis program (ZAF method) in standardless mode (w/w). Latex spheres of known density (1.05 g per cu cent) and volume were analyzed to obtain a standard (mass/weight).[3,4]

Approximately 40 bodies in each sample were analyzed and averages of the elements present were calculated in various laboratory grown stock cultures of photoautotrophs and heterotrophs as well as isolates from Lake Arthur in Black Rock Forest, NY. The quantitative analysis of laboratory grown organisms revealed (bulk analysis) that a typical invivo PPB contains on average O (65%), C (19%), P (10%) and 6% of the minor elements. Minor elements include Mg (2%) and Ca (1%) and frequently K (1%), Fe (0.9%), S (0.8%) and Al (1%). When this data is used in the equations provided by Heldal[3,4] it translates to O (4.3×10^{-8}ug), C (1.2×10^{-8}ug), P (6.7×10^{-9}ug), Mg (1.3×10^{-9}ug), Ca (6.7×10^{-10}ug), K (6.7×10^{-10}ug), Fe (6.0×10^{-10}ug), S (5.4×10^{-10}ug) and Al (5.9×10^{-10}ug). PPB's in thin sectioned material had essentially the same composition as those from laboratory cultured air dried preparations.

Quantitative x-ray analysis of samples from nature indicate that there are more minor elements present than in the cultured cells particularly Zn. The PPB's in the natural samples had O (66%), C (19%), P (7%). On average they were composed of 8% minor elements with Mg (4%), Ca (1%), Zn (0.5%), S (1%), K (1%) and Fe and Al together (0.5%). When these mass percentages are converted to actual amounts with the Heldal equations[3,4] they are O (1.63×10^{-8}ug), C (4.75×10^{-9}ug), P (2.50×10^{-9}ug), Mg (5.0×10^{-10}ug), Ca (2.50×10^{-10}ug), K (2.50×10^{-10}ug), Fe (2.25×10^{-10}ug) and S (2.0×10^{-10}ug).

The presence of C at 19% of the bodies and the excess O in relation to the ratio P to O in PO_4 units indicates an organic component. In a study of isolated bodies from *Micrococcus lysodeikticus* they found 24% protein and 30% lipid in addition to the other elements. These and our results indicate

that the PPB's may have other unknown functions in addition to essential element storage and acting as a detoxification method by sequestering heavy metals. [1,2]

References

1. T.E. Jensen and W.A. Corpe, Arch. Hydrobiol. 127(1993)385.
2. T.E. Jensen and W.A. Corpe, Arch. Hydrobiol./Suppl. 75, Algological Studies 75(1994)149.
3. M. Heldal et al., App. Environ. Microbiol. 50(1985)1251.
4. M. Heldal et al., in P.F. Kemp et al., Aquatic Microbial Ecology, Lewis Publishers, Boca Raton (1993), 387.
5. I. Friedberg and G. Avigad. J. Bacteriol. 96(1968)544.

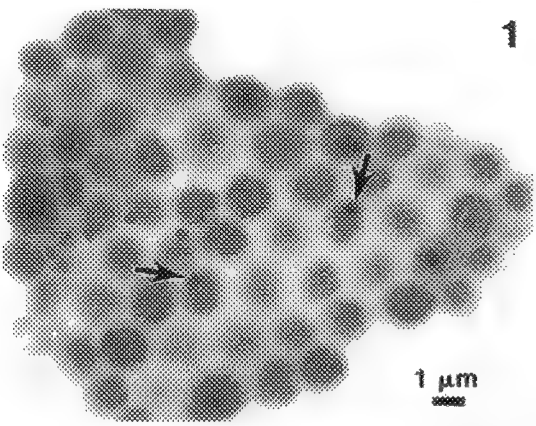

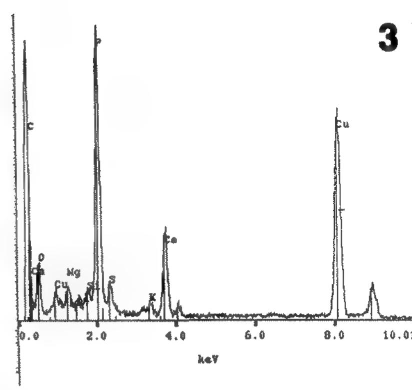

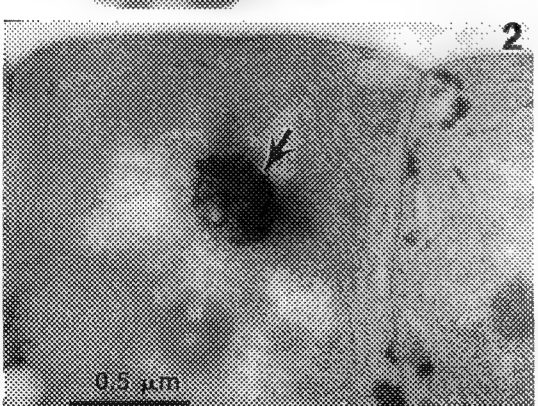

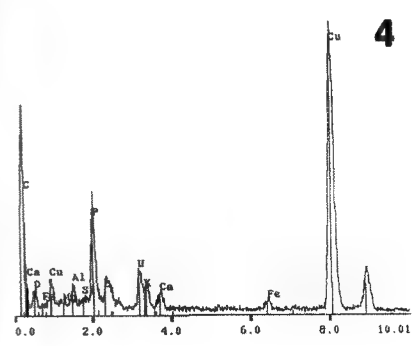

Fig. 1 Whole cells air dried of *Staphlococcus aureus*. Dense bodies at arrows are PPB's.
Fig. 2 Thin section of *Plectonema boryanum* . Dense body at arrow is a PPB.
Fig. 3 Spectrum of a PPb
Fig. 4 Spectrum of a PPB with a significant Fe peak.

NEGATIVE-STAIN ELECTRON MICROSCOPY (EM) OF SELF-ASSEMBLED ASTROVIRUS AND CALICIVIRUS CAPSIDS

Charles D. Humphrey,* Jose P.G. Leite,** Baoming Jiang,**
Stephan S. Monroe,** Jacqueline S. Noel,** and Roger I. Glass**

*Molecular Pathology and Ultrastructure Activity
**Respiratory and Enteric Viruses Branch, Div. of Viral and Rickettsial Diseases, CDC, Atlanta, Ga 30333

Astroviruses (AstV) and caliciviruses (CacV) are members of a group of 20-40nm infectious gastroenteric viruses.[1,2] These viruses often have few distictive morphologic features and occur only in small numbers, making them difficult to detect by EM or serology. Specific antisera in animals or production of monoclonal antibodies has only recently been achieved for a few serotypes. The genomes of AstV (AstV genotype 2) and CacV (Toronto virus genotype) have recently been characterized.[3-6] The complete genome of each virus consists of three open reading frames (ORF). ORF-2 of each virus codes for a capsid precursor.[3-6] We have expressed capsid protein of each virus in *Autographica californica* nuclear polyhedrosis virus (AcNPV) infected *Spodoptera fruigiperda* (Sf9) cells. Capsid protein precursors expressed in AcNPV-infected insect cells self-assembled into virus-like particles (VLPs) that were antigenic by immunofluorescence and enzyme-linked immunosorbent assays as well as immunogenic in laboratory animals. Purification of the VLPs was monitored by negative stain direct EM (2% phosphotungstic acid pH 6.5 or 0.5% uranyl acetate) or by immune EM. AcNPV expressed preparations were examined by using monoclonal antibodies, antisera raised in animals, or from humans previously infected with the respective AstV or CacV.

VLPs were readily seen in negative stain preparations of CacV infected culture supernatants (Fig. 1). These VLPs were 30nm in diameter and had characteristic Toronto virus structure. Stain penetrated empty-appearing VLPs and VLPs without stain penetration were observed. VLPs were also seen in AstV preparations (Fig. 2). However, typical AstV structure was not observed because the VLPs seen, which were not AcNPV associated, seemed damaged and had a collapsed appearance. These collapsed VLPs labeled readily with antisera to AstV genotype 2 antisera. Both CacV and AstV VLP preparations were antigenic by enzyme-linked immunosorbent assays and were immunogenic in laboratory animals.

The above described studies will aid in the development of sensitive, specific assays and increase understanding of CacV and AstV capsid structure.

References

1. C.R. Madeley and B.P. Cosgrove, Lancet 2(1975)441.
2. A.Z. Kapikian and R.M. Chanock. Norwalk Group of Viruses. in Virology 2nd ed., B.N. Fields et al. eds. New York: Raven Press, Ltd 1990:671-693.
3. X. Jiang et al, J. Virol. 66(1992)6527.
4. S.S. Monroe et al., J. Virol. 67(1993)3611.
5. T.L. Lewis et al., J. Virol. 68(1994)77.
6. J.F. Lew et al. MMWR 39(1990)1.

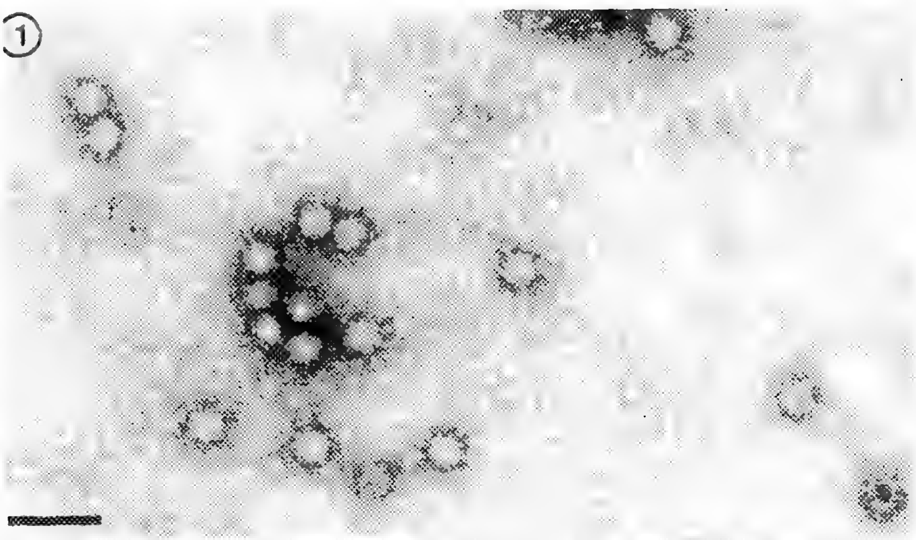

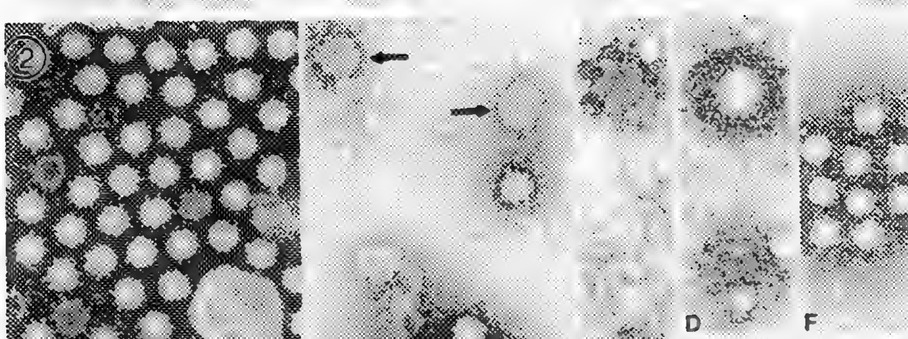

Fig. 1 Negative stain EM of self-assembled recombinant Toronto virus capsid protein VLPs obtained from supernatants of AcNPV infected Sf9 cells. Bar represents 100nm for all images. Fig. 2 Negative stain EM of self-assembled VLPs obtained from recombinant AstV-2 capsid protein that was expressed in AcNPV infected Sf9 cells. AstV propagated in LLCMK2 cell culture were examined for comparison (panels A,B; arrows show collapsed AstV). Recombinant AstV (rAstv) trapped with AstV antibody (panels C,D). rAstV trapped with primary antibody and coated with IgG conjugated to 5nm colloidal gold (panel E). AstV propagated in LLCMK2 cells aggregated with AstV antibody (panel F). LLCMk2 propagated AstV aggregated with antibody and labeled with IgG conjugated to colloidal gold (panel G).

BACTERIOIDS IN THE RECTAL ORGAN OF THE LANTERN BUG *PYROPS CANDELARIA* LINN (HOMOPTERA: FULGORIDAE)

W.W.K. Cheung and J.B. Wang
Biology Department, Chinese University of Hong Kong, Hong Kong

The lantern bug harbours three symbionts, namely a, x and i in its body.[1,2] These microorganisms are supposed to be transmitted transovarially to the future progeny. The x-symbionts are found in a special pair of organs called the x-organ which bulges to form a rectal organ in adult females. The purpose of this study is to investigate into the fine structure of the x-symbionts. This will serve as a basis for understanding the interactions of this microorganism with its host.

The rectum of the lantern bug *Pyrops candelaria* Linn. was dissected out in buffered insect saline and fixed in 2.5% glutaradehyde in 0.1M sodium cacodylate buffer (pH 7.2) for 1 hr. The rectal organ was subsequently post-fixed in 1% osmium tetroxide (pH 7.2) and dehydrated in alcohol/acetone series. These were blocked in Spurr resin and cut with a Reichert Ultratome. Sections were stained with uranyl acetate and lead citrate and examined with a JEOL JEM-1200EX electron microscope. Thick sections (1 µm) were stained with 1% toluidine blue and examined under a Nikon Optiphot light microscope.

In the light microscope transverse section of *Pyrops* rectum showed a bulging organ consisting of large cells having numerous granular materials (Fig. 1). These granular materials were x-bacterioids under the electron microscope (Figs. 2-4). A host cell had a large, irregular-shaped nucleus having scattered patches of chromatin materials, scattered mitochondria, and rough endoplasmic reticulum (Fig. 2). Bacterioids were oval-shaped, measured 2-3 µm, and had patches of osmiophilic materials containing nucleoproteins. High power magnification of a bacterioid showed it had a membranous surface coat enclosing a mass of granular cytoplasm (Fig. 4). The cytoplasm contained specks of ribosomes, scattered mitochondria, and crystalline materials of unknown function. X-organ bacterioids increase in number throughout the life history of their host and are transmitted transovarially from generation to generation[2]. Their role in *Pyrops* is unknown. They probably have intimate nutritional relationship with their host which might depend on them to synthesize some essential nutrients such as vitamins, proteins, and steroid compounds that are not found in the plant sap taken in by the host.[3,4,5]

References
1. H.J. Muller, 1949, Zoologica 98:1-220.
2. P. Buchner, 1965, Endosymbiosis of animals with plant microorganisms. Interscience, New York.
3. W.W.K. Cheung, 1979, J. Chinese Uni. Hong Kong 5:523-533.
4. A.E. Douglas, 1989, Bio. Rev, 64:409-434.
5. We thank the Research Grant Council (Hong Kong Government) for financial support.

Fig. 1. Transverse section of *Pyrops* rectum with rectal organ. Light micrograph. Showing rectal organ (ro), host cell nuclei (n), rectal epithelium (rm) and midgut epithelium (mg). Bar=10µm.

Fig. 2. Electron micrograph of part of rectal organ cell. Showing nucleus (n), x-bacterioids (b), vacuoles (v). Bar=2μm.
Fig. 3. As above. Showing mitochondria (m), x-bacterioids (b), rough endoplasmic reticulum (rer), vacuoles (v). Bar=0.5μm.
Fig. 4. Transverse section of x-bacterioid. Showing membranous coat (c), ribosomes (r), nucleoproteins (np), crystalline materials (ct). Bar=0.2μm.

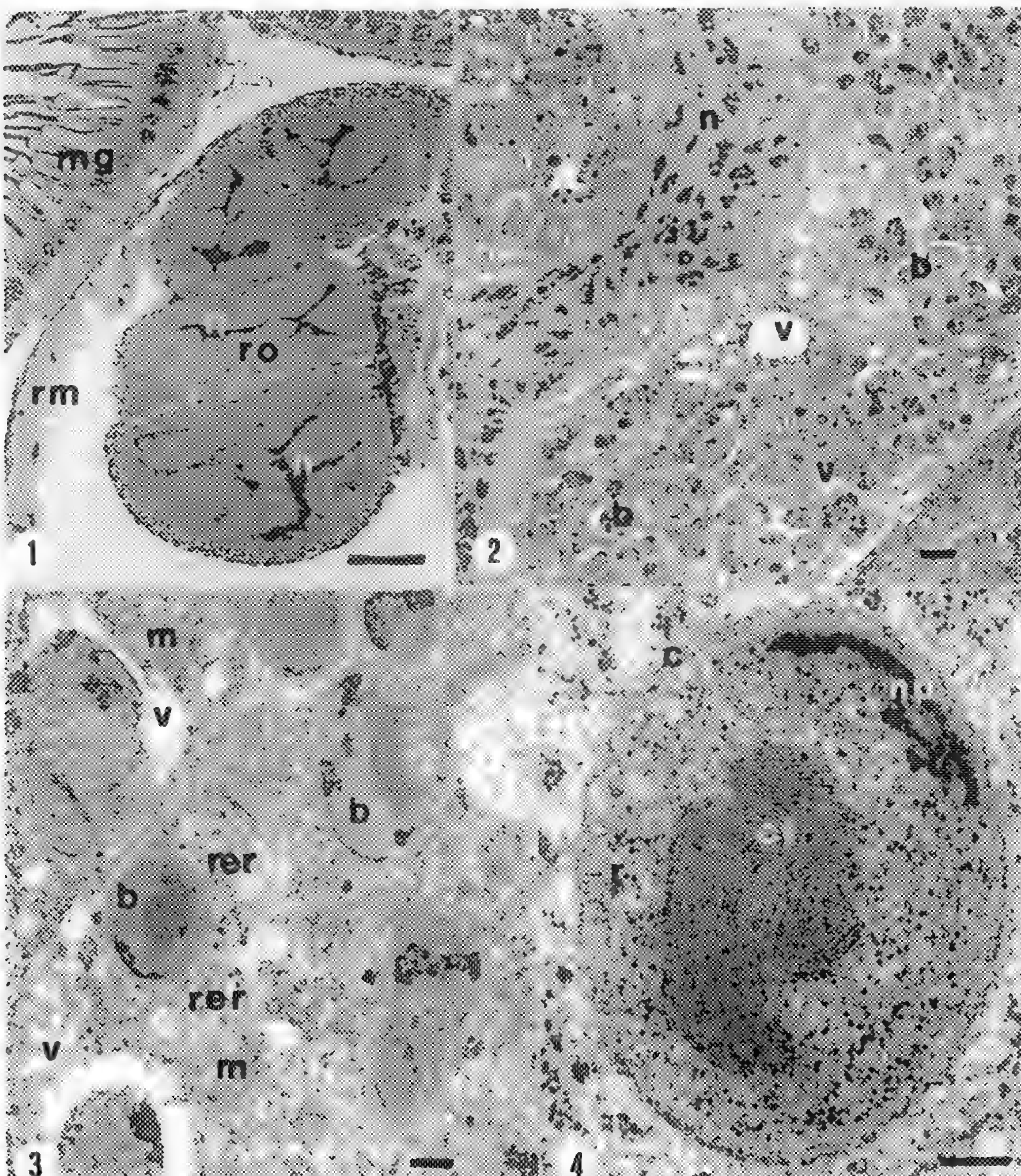

ATTACHMENT, ENTRY, AND DESTRUCTION OF CULTURED HUMAN B-LYMPHOCYTES BY THE LYME-DISEASE SPIROCHETE *BORRELIA BURGDORFERI*

Elizabeth R. Fischer and David W. Dorward

National Institute of Allergy and Infectious Diseases, National Institutes of Health, Rocky Mountain Laboratories, 903 South Fourth Street, Hamilton, Montana 59840

The most prevalent tick-borne disease in the United States, Lyme disease, is caused by the spirochete *Borrelia burgdorferi*[1]. Studies have suggested that Lyme disease spirochetes, like other bacteria, may enter host cells thereby evading the immune system.[2,3]

In order to investigate possible interactions between Lyme disease spirochetes and immune system cells, we co-incubated *B. burgdorferi* strain Sh-2-82 with cultured human B- and T-cells (TIB-215 and H9, ATCC, respectively) and primary lymphocytes at an MOI of 100:1.

Nomarski interference microscopy revealed that as early as 10 minutes after coincubation, as previously described with other cell lines[3,4], low passage spirochetes (<8 in vitro passages) attached tip first to the B-cells and then invaded the B-cells (Fig. 1,4). Scanning electron microscopy revealed that by 24 hours post-infection, 90+% of B-cells had spirochetes attached to their surfaces (Fig.2). Transmission electron microscopy suggested that intracellular spirochetes may exist both in vacuoles and free in the cytoplasm of primary lymphocytes (Fig. 3a-b). Surface penetration by low passage spirochetes corresponded with a dramatic loss of filopodia and other surface projections (Fig. 4), followed by disruption of the host cell membrane and cell death (Fig. 5). These effects were not observed with high passage spirochetes (>30 in vitro passages) (Fig.6). Similarly, these changes were not observed with the cultured T-cell line, with B-cells coincubated with *B. hermsii* (agent of relapsing fever), with heat killed or sonicated *B. burgdorferi*, or with the culture supernatants of the spirochetes.

At 24 hours post-infection, trypan blue exclusion revealed less than 50% viability in the cultured B-cells, and the surviving B-cell population showed reduced susceptibility to further infection by low passage spirochetes (data not shown). The factors involved in B-cell attachment, entry and destruction have not yet been determined.

These studies document that *B. burgdorferi* has cytopathic effects on select cultured B-cells. This work may provide an effective model system for investigating the pathogenesis of Lyme disease.

References

1. Centers for Disease Control, *U.S. Morbid. and Mortal. Weekly Report.* **34**(1985)376-384.
2. B.B. Finley, et al., *Microbial Rev.* **53**(1989)210-230.
3. K.E. Hechemy, et al., *Med. Microbiol.* **36**(1992)229-238.
4. D.Denee Thomas, et al., *Infect. and Immun.* **57**(4)(1989)1324-1326
5. The authors would like to acknowledge Ted Hackstadt for his assistance with the Nomarski differential microscopy.

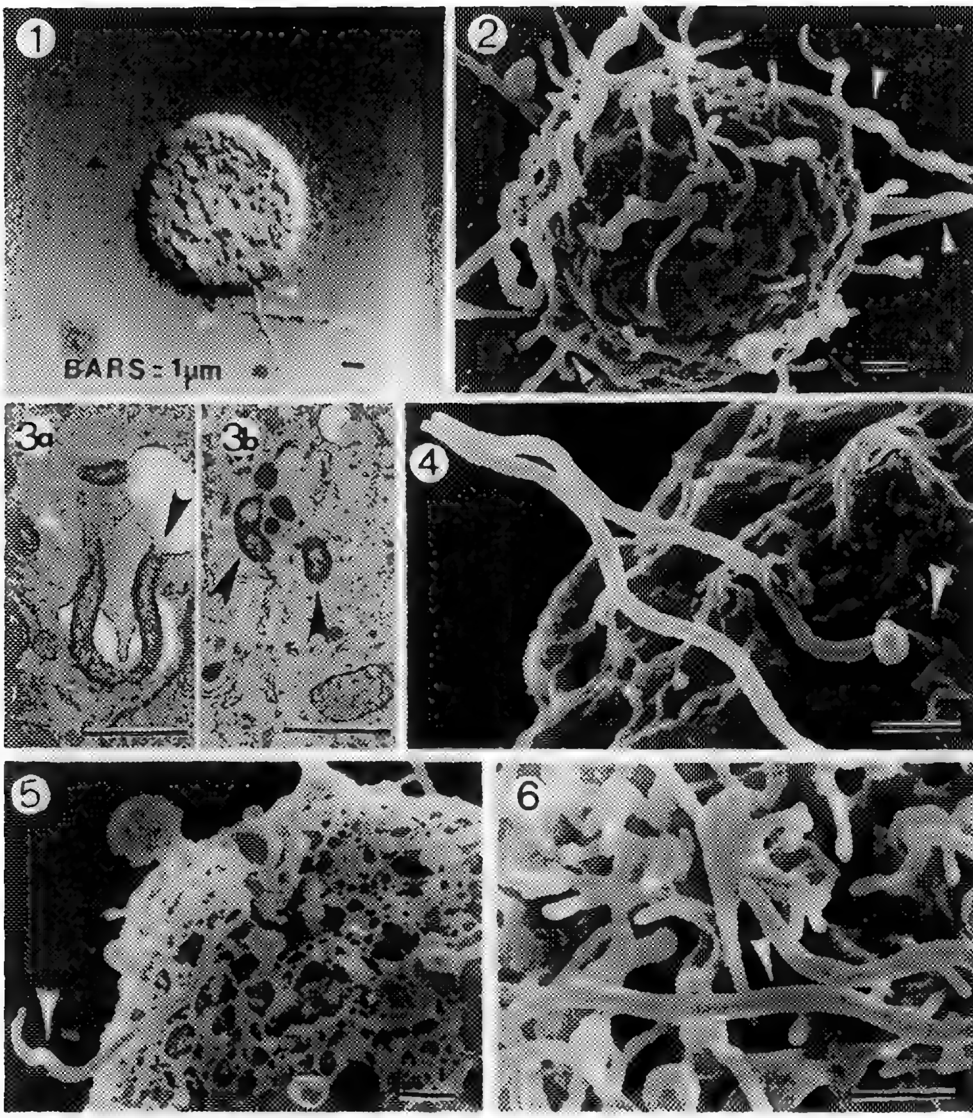

FIG. 1 Attachment of spirochete tips with cultured B-cells.

FIG. 2 Spirochetes readily attach to majority of B-cells.

FIG. 3 Intracellular spirochetes in vacuoles (a) and possibly free in the cytoplasm (b) of primary human lymphocytes.

FIG. 4 Evidence of invasion of spirochete resulting in loss of cell surface projections.

FIG. 5 Demonstration of cell membrane disruption and cell death after 24h coincubation of spirochete (arrow) with B-cells.

FIG. 6 B-cells coincubated with high passage spirochetes (arrow) or uninfected (not shown) did not result in the loss of surface projections.

MOVEMENT OF SPOTTED FEVER RICKETTSIAE THROUGH TICK HOST CELLS IN VITRO

U. G. Munderloh,* S. F. Hayes,** J. Cummings,* and T. J. Kurtti*
*Department of Entomology, University of Minnesota, St. Paul, MN 55108
**Microscopy Branch, Rocky Mountain Laboratories, NIH, Hamilton, MT 59840

Spotted fever group (SFG) rickettsiae are obligate intracellular prokaryotes that include tick-borne pathogens of animals and man as well as organisms that live in symbiotic association with their tick hosts. A striking feature of the behavior of pathogenic rickettsiae in the vertebrate is their ability to quickly disseminate between cells from the original site of entry shortly after infection, and before severe lesions are detected. Similarly, ticks become systemically infected with SFG rickettsiae, indicating that an efficient mechanism of dispersal also exists in the vector. This is accomplished despite the fact that rickettsiae are not motile.

Kadurugamuwa et al. (1991)[1] have used light and electron microscopy to show that *Shigella flexneri* utilize host cytoskeletal components to travel through cytoplasmic extensions and penetrate into neighboring cells. Using mammalian cells cultured in vitro, Heinzen et al. (1993)[2] have demonstrated that SFG rickettsiae cause host cell actin polymerization at one rickettsial pole causing them to be propelled through the cytoplasm, and to transfer rapidly from cell to cell.

We have developed a tick cell culture model to investigate the ability of SFG rickettsiae to cross from cell to cell within the tick vector. This was done using an SFG rickettsia isolated from the Lone Star tick (*Amblyomma americanum*), and tick cell lines established from the brown ear tick (*Rhipicephalus appendiculatus*) and the black-legged tick (*Ixodes scapularis*). Electron microscopy demonstrated that upon entry into tick cells, SFG rickettsiae briefly become enveloped in host membrane (Fig 1). This is rapidly broken down into vesicular structures (Fig. 2), and intracellular rickettsiae come to lie in direct contact with the host cell cytoplasm. In some instances, they may be found entrapped within endoplasmic reticulum. Similarly, when rickettsiae exit, host membrane becomes stretched around them (Fig. 3), but is lost before re-entry. Studies using fluorescent labeled phalloidin indicated that SFG rickettsiae take advantage of the tick host cytoskeleton in a manner similar to that described for mammalian cells (2). During early stages of infection, when cells harbored only one or a few organisms, "comet tails" of f-actin formed on one end of rickettsial cells, presumably pushing them forward. Actin tails were not seen in later stages of infection when tick cells became completely filled with rickettsiae. Possibly, such heavy infections disrupt the cytoskeleton, or exhaust the host cell supply of actin.

1. J.L. Kadurugamuwa et al., *Infection and Immunity*, 59 (1991) 3463.
2. R.A. Heinzen et al., *Infection and Immunity*, 61 (1993) 1926.

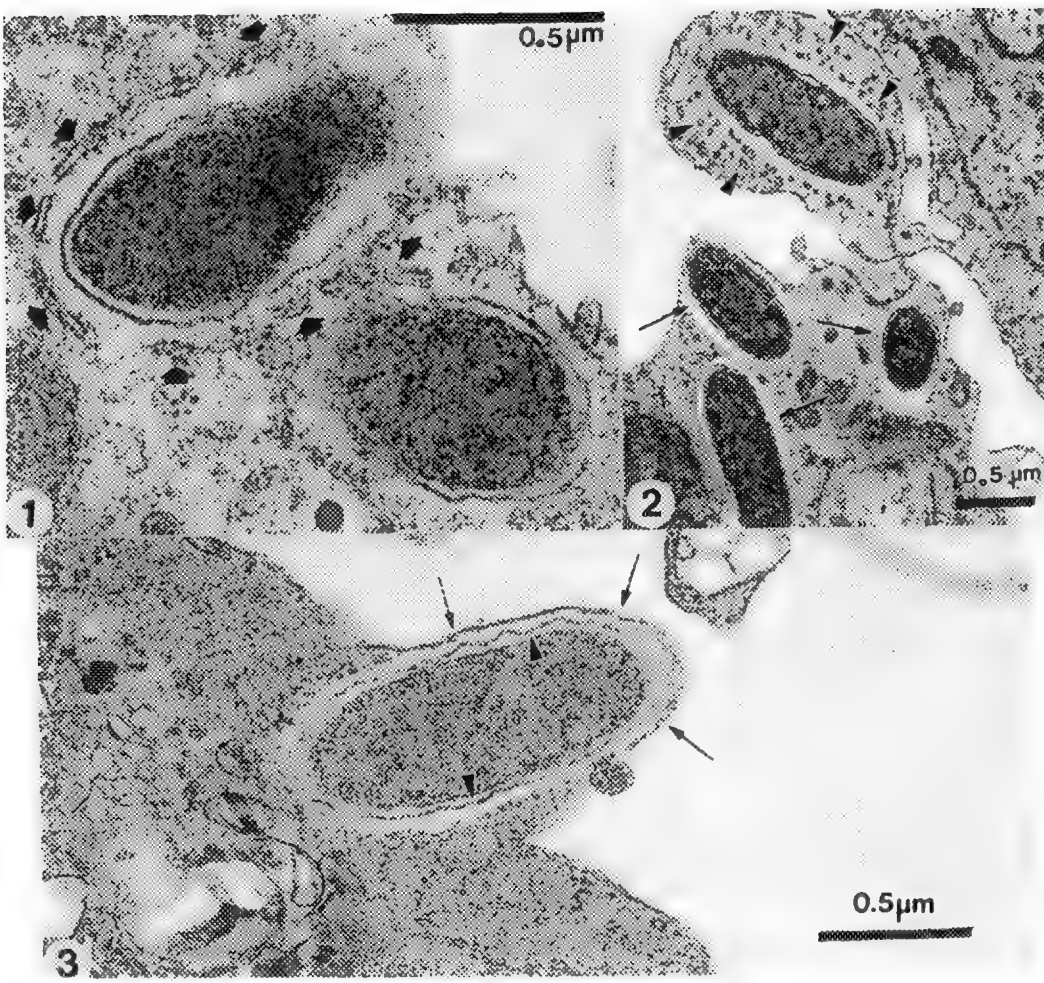

FIG. 1 Entry of a spotted fever group rickettsia into a tick cell cultured in vitro. Arrows indicate remnants of the invaginated host cell membrane which is already in the process of disintegrating.
FIG. 2 Completely internalized rickettsia surrounded by small vesicular structures (arrow heads) representing further degradation of the host cell membrane. Arrows indicate rickettsiae within a neighboring cell that are devoid of such structures, and are in free contact with the host cell cytoplasm.
FIG. 3 Rickettsia in the process of exiting from a tick host cell. Note host cell membrane being pushed outward (arrows), and which is distinct from the rickettsial outer membrane (arrow heads).

HIGH-RESOLUTION SEM AND CLOSTRIDIAL ATTACHMENT

B. Panessa-Warren, G.T. Tortora, J.Warren*

School of Health Technology and Management, Div. of Diagnostic and Therapeutic Sciences, SUNY Stony Brook, N.Y. 11794-8205
*Div. of Instrumentation, Bldg 535B, Brookhaven National Laboratory, Upton, N.Y 11973

Since the mid 1960's when the TEM was a new and primary tool for elucidating the classification of the various strains of microorganisms, investigators around the world have been reporting morphological surface aberrations (such as hairs, ribbons, tubular appendages and feather-like structures) of the clostridial endospore that facilitate and verify the classification of these organisms [1,2,3,4]. Yolton [1], Pope [2], Samsonoff [3] and others were unable to discern the function, of these appendages and stated that the "functional role of spore appendages remains obscure".

Today, there is still no information on the functional role, if any, of these "appendages" and "hairs". For the past few years we have been examining the endospores from two clostridial species that are pathogenic in man and higher mammals, **C.sporogenes ATCC3584**, and **C.difficile ATCC 9689 and 43594.** These organisms cause wound infections, pseudomembranous colitis, and nosocomial diarrhea. Our previous work strongly suggested that the outer envelope of these spores, the exosporium, had a "morphological plasticity" that allowed the spores to attach to a surface that supported bacterial growth [5,6]. With current advances in high resolution SEM using LaB6 and field emission sources, it is now possible to study these extremely small and complex spore appendages at all stages of germination with spacial orientation capabilities not possible when the original studies were done. Over the past 2 yrs, the advances in software technology and improved SEM resolution and image enhancement capabilities, make it possible to work with fields of intact spores still attached to a nutritive surface and examine the exosporium and membrane contacts with the nutrient surface at resolution and magnifications formerly reserved for TEM. This investigation combines attachment studies using agar substrates (Trypticase Soy agar + 5% glucose, and Blood CDC agar) and human cells (lung fibroblasts and colon cells), with high resolution imaging of intact spores on their nutritive substrate (agar and human cell)to determine the ultrastructural changes that accomplish clostridial colonization. Studies were also done to determine if attachment was altered as a result of exposure to cation substitution, cation chelation, or colchicine treatment.

Filtered, purified spore preparations of C.sporogenes ATCC 3584 and C.difficile ATCC 9689 & 43594 were resuspended in distilled water and stored at 4°C until needed. Ten microliters of spore suspension was inoculated on agar covered SEM stubs or within a circumscribed region on agar plates. Plate studies for attachment were also done with each test solution. Spores were anaerobically incubated for 1.5hrs for C.sporogenes and 3 hrs for C.difficile to allow the spores to begin the germination process. Two ml of each test solution were placed on the agar-coated SEM stubs inoculated with spores and allowed to react with the spores on the agar in the incubator, after which 3 ml of 2.8% glutaraldehyde in buffer were added to the stub. After 20 min fixation in the incubator the stubs were removed and placed in fresh fixative for several hrs before acetone dehydration and critical point drying. SEM samples were either given an 8-10nm thick AuPd coating (sputter coated), a 2-4nm thick tungsten (W), or 2-4nm thick chromium coating at high vacuum.

In summary, attachments and colonization by C.sporogenes and C.difficile were unaffected

by agitation in PBS, sterile water, colchicine and EDTA in 1M HEPES. However,when subjected to 1% $BaCl_2$, EDTA in phosphate buffered saline, or EDTA in water, attachments were disrupted and bacterial colonization did not take place. Morphologically each spore type revealed unique exosporial morphologies once germination began, supporting the early premise that the appendage structures of clostridial spores could be used for taxonomic classification.[1,2,3] Field emission SEM revealed that in all cases very delicate exosporial projections were initially observed extending from the spore to a nutritive substrate. The test solutions that prevented clostridial colonization also produced marked alterations in the exosporial projections and highly reactive surface of the endospore. Charging, beam penetration and stabilization of the membranous structures of the spores during electron beam bombardment were continual problems whether the spores were grown directly on stubs or prepared with human cells. Very thin metal coatings were essential for visualization of these delicate structures, but even at 0.5KV specimen instability made it necessary to use frame integration.

1. D.Yolton et al.Journal of Bacteriol. 95(1968)231.
2. L.Pope et al. Journal of Bacteriol. 94(1967)1206.
3. W.Samsonoff et al.,Journal of Bacteriol.101(1970)1038.
4. J. Hoeniger and C. Headley, Can.J.Microbiol.15(1969)1061.
5. Panessa-Warren, B. et al. SCANNING, 16(1994)227.
6. Panessa-Warren, B. et al. Proc.52 Ann. MSA Meeting(1994)354.

7. The authors would like to thank AMRay Inc. and JEOL, Inc. for their assistance in doing the field emission work.

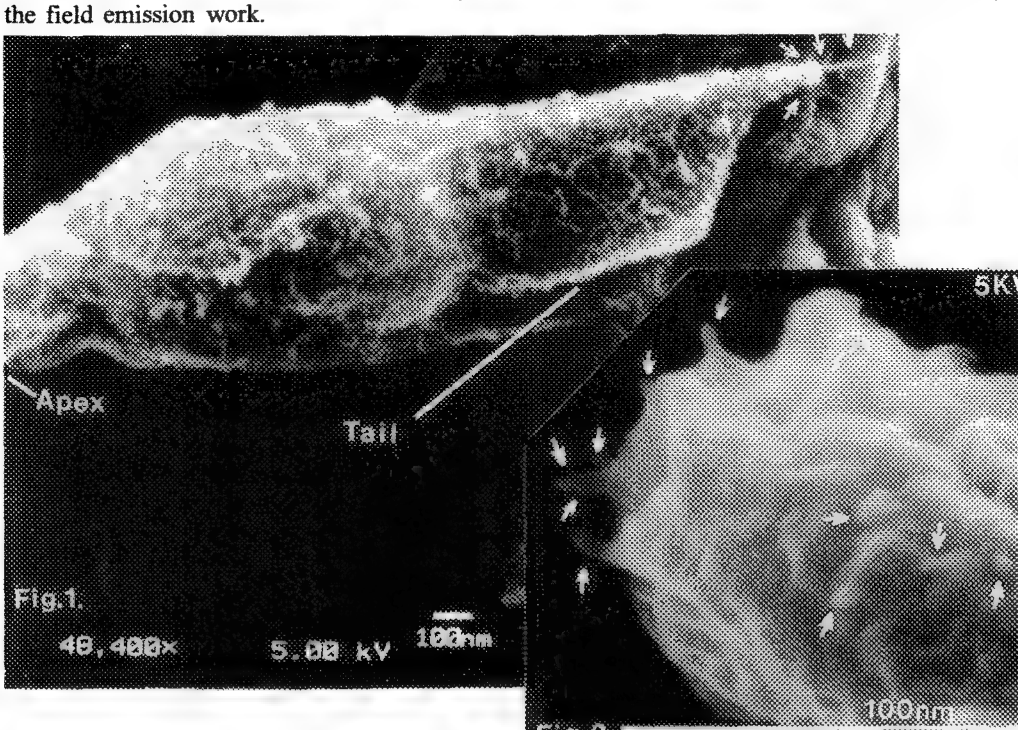

Figure 1. W-coated C.sporogenes with exosporial attachments(arrows) to agar substrate.
Figure 2. Apical tip of C.difficile with exosporial projections(arrows). Cr coated.

EVALUATION OF ALTERNATIVE FIXATIVES/PROTOCOLS FOR THE ULTRA-STRUCTURAL PRESERVATION OF FAST AND SLOW GROWING MYCOBACTERIA

S. F. Hayes* and P. L. C. Small*

*Microscopy Branch, Rocky Mountain Laboratories, National Institute of Allergy and Infectious Diseases, Hamilton, MT 59840 (USA)

Various fixation formulas and protocols were examined to determine a routinely optimal fixation of Mycobacterial species in and out of tissues. These were evaluated by TEM and compared to results obtained using freeze substitution methods upon other Mycobacteria such as *Mycobacterium aurum* CIPT 1210005, *M. fortuitum, M. phlei* 425, *M. kansasii* and *M. thermoresistible* ATCC 19527[1-3].

Samples consisted of two slow growing mycobacterial species, both human pathogens; *Mycobacterium tuberculosis*, grown in M7H9 broth, and *Mycobacterium marinum* (1218 R & S variants), grown on M7H10 agar, with the latter also grown in tissue culture, and in guinea pig skin. Fixatives included: (1) glutaraldehyde/paraformaldahyde/tannic acid in a phosphate/sucrose buffer, (2) paraformaldehyde/polylysine/periodate/glutaraldehyde (PLPG) in phosphate buffer followed by tannic acid and reduced osmium respectively, (3) PLP followed by tannic acid only without osmium, and (4) fixative 84-40 containing carbodiimide, glutaraldehyde and ruthenium red[4]. Protocols varied in the length of time for fixation, types of buffers, solvents and in embedding schedules for Spurr's low viscosity resin.

Thin sectioned materials illustrated in figures (1-7) show ultrastructure comparable to that obtained by freeze substitution as reported by Paul and Beveridge[1-3]. Consistency in results were obtained primarily by extending the fixation time, adding excess volumes of fixative or successive changes of fixative over a period of 24-48 h. Extended washes with tap water to remove phosphates from reaction with uranyl salts was imperative. Solvent choice, *i.e.*, alcohol as a dehydrating agent yielded poor infiltration, polymerization and distortions to the ultrastructure, when temperatures below 65°C were used. When low polymerization temperatures were necessary, acetone proved best. Tests for the extraction of specific lipids and proteins were not done. Morphologic preservation was assessed empirically by direct comparison to published freeze substitution images.

We feel that the above data reinforces the observations of Paul and Beveridge, giving other alternatives for adequate preservation of Mycobacterial components.

References:

1. T.R. PAUL & T.J. BEVERIDGE, Journal of Bacteriology, 174 (1992) 6508.
2. T.R. PAUL & T.J. BEVERIDGE, Zentralblatt Fur Bakteriologie, 279 (1993) 450.
3. T.R. PAUL & T.J. BEVERIDGE, Infection and Immunity, 62 (1994) 1542.
4. P.J. HITCHCOCK et al., Infection and Immunity, 48 (1985) 94.

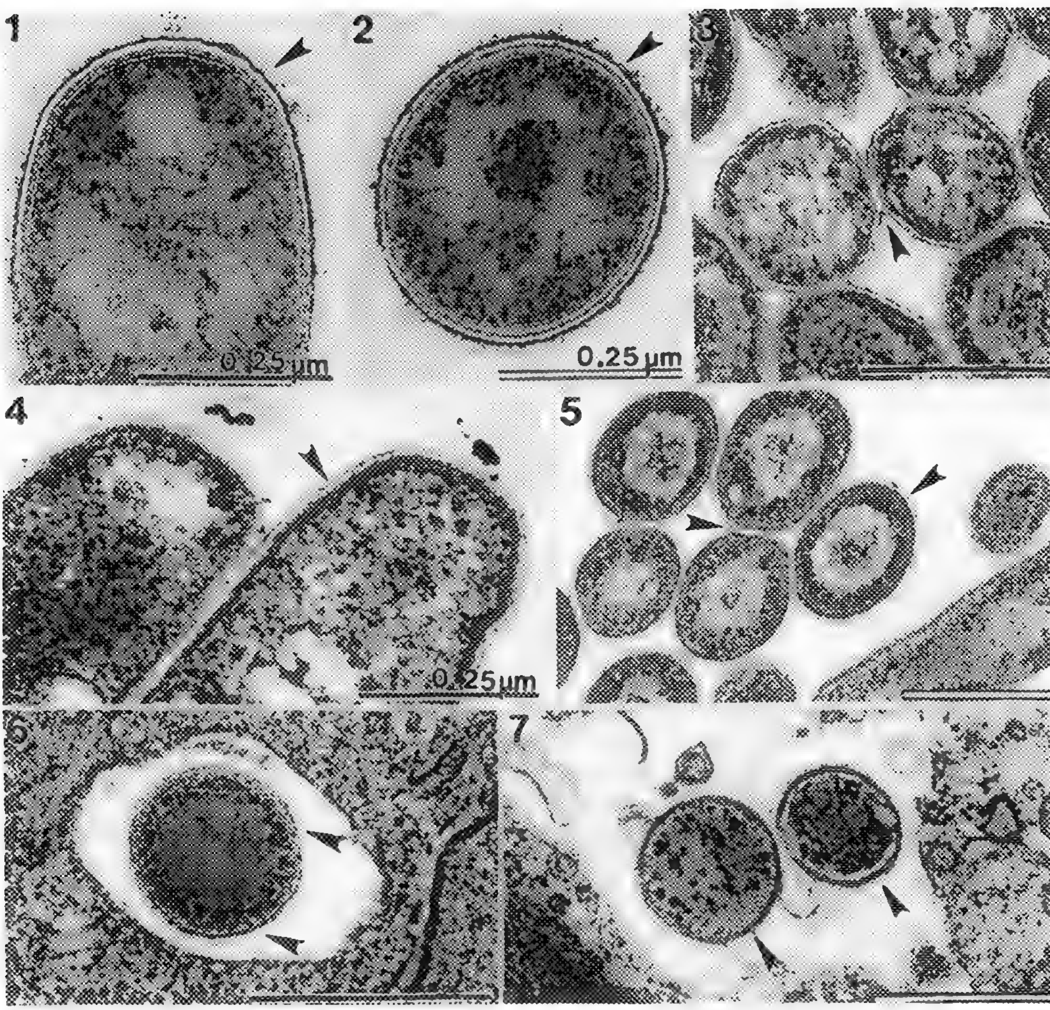

Arrows in all figures denote the OL and all bar markers equal 0.5µm, unless noted.

FIG. 1 & 2. *M. tuberculosis*, RV strain GTP/PS fixed, showing a prominent outer layer and associated extended fuzzy material.

FIG. 3 *M. marinum*, 1218R variant fixed by method (2). Prominent OL with organism to organism/ fusion of this layer is noted. Differentiation of the peptidoglycan/outer layer of periplasmic membrane region and different pattern of nucleoplasmic matrix differ from fig.s 1 & 2.

FIG. 4 *M. marinum* fixed by method (3), ethanol dehydrated, and stained with $KMnO_4$. Note the bilaminar status of the plasma/peptidoglycan dispersed nucleoplasmic matrix.

FIG. 5 *M. marinum* fixed by method (4). Profiles display the same prominent fusion of the OL and cytoplasmic matrix as noted between organisms referred to in ref. 1, fig.s 3-6.

FIG. 6 & 7. *M. marinum*, RAW cell monolayer and guinea pig skin respectively fixed by PLP, by $K_3Fe(CN)_6$ reduced osmium and then dehydrated by ethanol or acetone.

AN IN-LENS CRYOSTAGE FOR HIGH-RESOLUTION SECONDARY-I AND SCANNING TRANSMISSION ELECTRON MICROSCOPY

Robert P. Apkarian

Integrated SEM & Microanalytical Facility, Emory University, Atlanta GA 30322

A newly designed cryo-holder was built for the in-lens top stage of a Topcon DS-130 field emission scanning transmission and high resolution secondary electron-I microscope (STEM/HRSEM). The modified Oxford CT-3500 cryo-holder was designed to fit into the narrow bore in-lens of the DS- 130F. The cryo-holder was designed to shuttle from the freezing chamber, to the high vacuum chamber of the Denton DV-602 magnetron sputter system for metal coating, and then to the interlock of the DS-130F upper stage. The intention was to provide a single cryo-holder to image frozen specimens by either HRSEM or STEM modes. In this electron optical design, many specimens, prepared by different cryo-preparation procedures, could be imaged by either or both imaging modes. The upper stage of the DS-130F was modified to accept a second liquid nitrogen (LN_2) cold trap and a Varian cold cathode ion discharge gauge for monitoring the vacuum at the specimen (Fig.1).

Cell or phospholipid vesicle suspensions were prepared for cryo-HRSEM by placing a droplet onto a dome shaped Balzers BU012 129-T 3 mm gold specimen carrier and plunge freezing in either freon-22 or liquid ethane. The carriers were loaded onto the cryo-holder and the specimen surface was fractured under LN_2 with a chilled blade (Fig.2). Alternatively, 3 mm gold specimen carriers with a flat surface BU012 128-T, may be used for freezing and cryo-HRSEM imaging of macromolecular specimens. Another option is to cut frozen sections and place them onto grids and load onto the cryo-holder for cryo STEM imaging. Low contrast frozen specimens loaded in the Oxford cryo-holder were protected from frost by closing the shutters above and below the specimen and transferring in a dry nitrogen gas sleeve to the Denton system for chromium coating (Fig.3).[1] Both Balzers specimen carriers and TEM grids on the cryo-holder were within the focal plane while the shutters were open in-the-lens of the DS-130F (Fig. 4).

Continued development of cryo-electron microscopy extends the image accuracy of biological structure at the macromolecular level.[2] Cryo-EM methods provide superior specimen preservation over chemical fixation and drying methods, provided that biological samples in the aqueous phase are frozen rapidly enough to avoid ice crystal formation. Virtuous samples can be contrast enhanced by ultrathin metal coatings prior to cryo-HRSEM or cryo-STEM imaging in order to provide high quality recordings.

References:

1. Apkarian R.P. 1994 Scanning Microsc.8:2;289.
2. Hermann R. and Muller M. 1994 Scanning Microsc. 7:1;343.
3. The author thanks Art McCanna and Material Analytical Services for their technical support, and to Denton and Oxford Instruments for their efforts and equipment development.

FIG 1.-- The DS-130F in-lens stage fitted with the Oxford cryoholder (X), cold cathode gauge(C) and two cold traps (1&2).
FIG 2.-- The Oxford cryo-holder (*) in LN_2 freezing chamber.
FIG 3.-- The Denton DV-602 sputter chamber with side entry cryo-holder (arrow).
FIG 4.-- The cryo-holder with (a) bulk and (b) grid specimen carriers. Cold trap(*) and shutter (arrow).

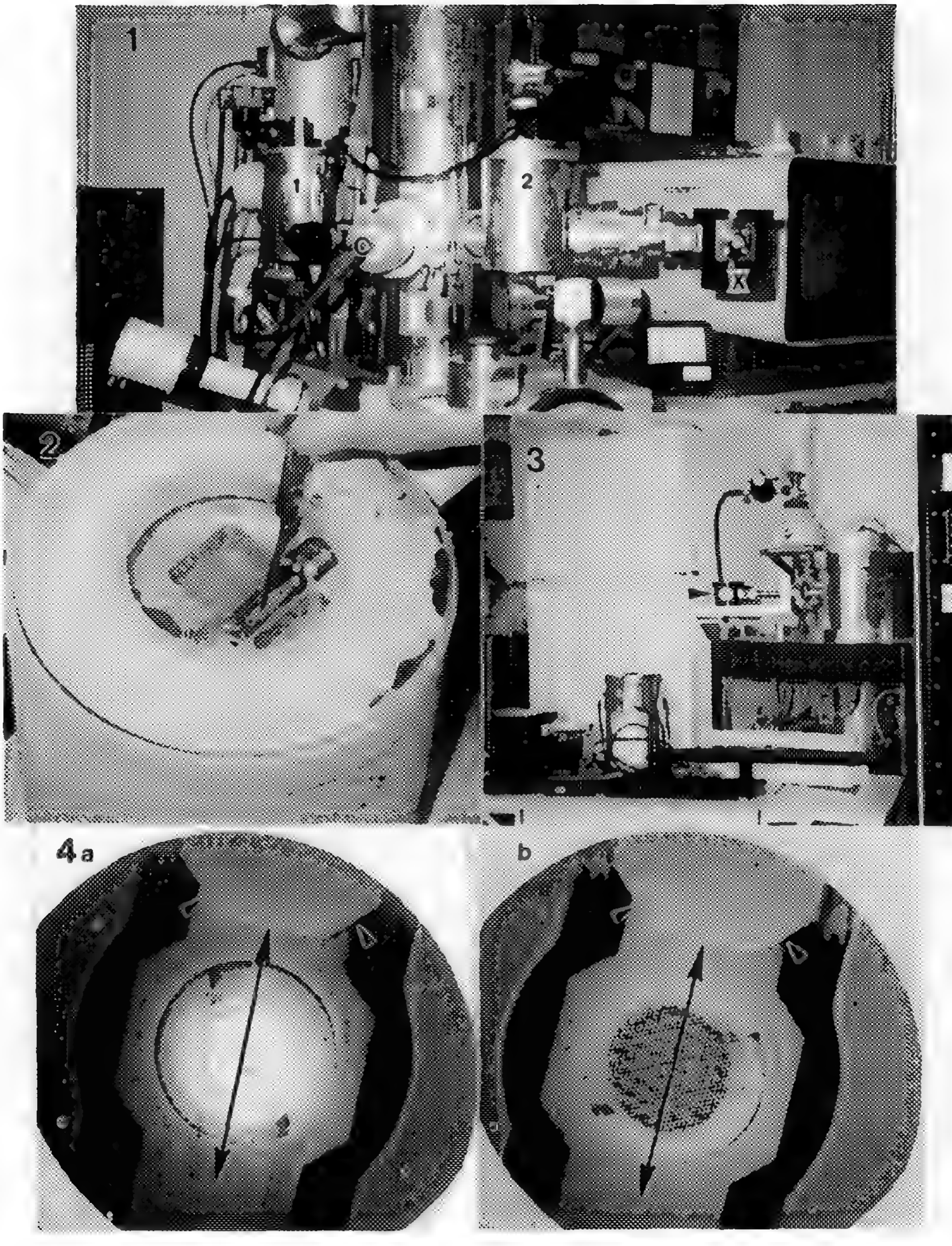
1
1
2
2
3
4a
b

PROGRESS IN HIGH-RESOLUTION CRYO-SEM IMAGING OF VIRAL PARTICLES

Ya Chen*, Geoffrey Letchworth† and John White*

*Integrated Microscopy Resource (IMR), and †Department of Animal Health and Biomedical Sciences, University of Wisconsin, Madison, WI 53706, USA

Low-temperature high-resolution scanning electron microscopy (cryo-HRSEM) has been successfully utilized to image biological macromolecular complexes at nanometer resolution[3-5,7-9,11]. Recently, imaging of individual viral particles such as reovirus using cryo-HRSEM[1,2,4] or simian virus (SIV) using HRSEM, HV-STEM and AFM[6] have been reported. Although conventional electron microscopy (e.g., negative staining, replica, embedding and section), or cryo-TEM technique are widely used in studying of the architectures of viral particles, scanning electron microscopy presents two major advantages. First, secondary electron signal of SEM represents mostly surface topographic features. The topographic details of a biological assembly can be viewed directly and will not be obscured by signals from the opposite surface or from internal structures. Second, SEM may produce high contrast and signal-to-noise ratio images. As a result of this important feature, it is capable of visualizing not only individual virus particles, but also asymmetric or flexible structures[1,2,4]. The 2-3 nm resolution obtained using high resolution cryo-SEM made it possible to provide useful surface structural information of macromolecule complexes within cells and tissues[1,3]. In this study, cryo-HRSEM is utilized to visualize the distribution of glycoproteins of a herpesvirus.

A knowledge of the 3-dimensional structure and distribution of herpesviral membrane glycoproteins of virions is important for understanding virus-cell infection. Reliable prediction by computer algorithms or experimental visualization by X-ray crystallography is virtually precluded for most of these molecules because they are large, contain one or more very hydrophobic sequences, are heavily and heterogeneously glycosylated, and most form homo- or hetero-oligomers on the virion surface.

Bovine herpesvirus type 1, the cause of infectious bovine rhinotracheitis, was inoculated into Madin-Darby bovine kidney cells at a multiplicity of 1 and harvested from the culture medium at 24 hours. The medium was cleared of debris by low speed centrifugation and virus was pelleted by ultracentrifugation through 30% sucrose in PBS and then repelleted in distilled water. Virus was attached to grids coated with formvar/carbon/0.1% poly-L-lysine (70,000 molecular weight), fixed in 1% glutaraldehyde to stabilize structure followed by rinsing it in distilled water to remove salts. The grids were then blotted with filter paper to remove excess water, plunge-frozen in liquid ethane maintained close to its freezing-point by liquid nitrogen. The specimen was then transferred to a Gatan cold-stage and freeze-dried under controlled conditions at 188K for 30 min using MED010 (Bal-Tec) cryo-sputtering device. A mass thickness of 2 nm tungsten was sputtered at 163K. The specimen was finally cryo-transferred to a Hitachi S-900 FESEM and examined at 163K[1,3].

Preliminary results (Figure 1) show that structures consistent with individual glycoprotein dimers can be visualized by cryo-HRSEM. The structures present as short, uniform structures covering the entire virion envelope. A stereo pair of cryo-HRSEM images reveal the 3-dimensional distribution of glycoprotein on viral surfaces. However, the distinct 10, 14, and 24 nm spikes shown by transmission EM[10] are absent.

The application of cryo-HRSEM to image herpes virions has demonstrated the possibilities and limitations on semi-thin samples (> 100 nm). Although more background signals are generated, the

contrast and signal-to-noise ratio of the surface details are reduced, compared to imaging of the beam transparent thin sample[7-9], the resolution obtained in this study is still adequate to visualize surface molecules. Future immunolabeling will help to identify surface proteins. In conclusion, cryo-HRSEM is a useful addition method to other techniques for studying virus particles.

References:

1. Centonze, V.E., Chen, Y., Borisy, G.G. and Nibert, M.L., *J. Struct. Biol.*, 115(1995) 215-225.
2. Chen, Y., Centonze, V.E., Nibert, M.L. and Borisy, G.G., *Proc. 52th Ann MSA Meeting*, (1994)134-135.
3. Chen, Y., Centonze, V.E., Verkhovsky, A. and Borisy, G.G., *J. Microsc.*, 179(1995)67-76.
4. Chen, Y., Centonze, V.E., Verkhovsky, A., Nibert, M.L. and Borisy, G.G., *Proc. XIIIth Int'l Cong. Electr. Microsc. Vol.1*, (1994)25-26, Paris.
5. Chen, Y., Verkhovsky, A. and Borisy, G.G., *Proc. 51h Ann MSA Meeting*, (1993)120-121.
6. Cuevas, L., Herrera, M.I., María, I.S., *et al*, *Proc. XIIIth Int'l Cong. Electr. Microsc. Vol.1*, (1994)113-114, Paris.
7. Hermann, R. and Müller, M., *Scanning Microsc.*, 5(1991)653-664.
8. Hermann, R. and Müller, M., *J. Electr. Micros. Tech.*, 18(1991)440-449.
9. Müller, M. and Hermann, R., *Hitachi Instrument News*, 19(1990)50-57.
10. Stannard, L.M., Fuller, A.O. And Spear, P.G., *J.Gen.Virol.*, 68(1987)715-725.
11. Wepf, R., Bremer, A., Amrein, M., Aebi, U. and Gross, H., *Proc. 10th EUREM,* (1992) 751-753.

12. This research was supported by NIH Grant DRR-0570 to the Integrated Microscopy Resource (IMR), Madison, Wisconsin.

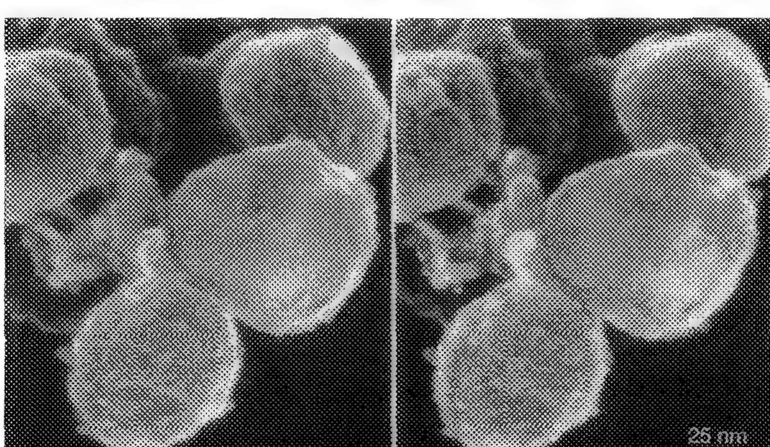

FIG. 1 Stereo pair of cryo-HRSEM micrographs of herpesvirus revealed the 3-dimensional distribution of glycoprotein on virion envelope. x 350,000.

MULTIPLE-FRACTURING AND VIEWING OF THE SAME FROZEN SAMPLE AT DIFFERENT DEPTHS USING A LOW TEMPERATURE FESEM

M.V. Parthasarathy* and C. Daugherty*

*Section of Plant Biology, Division of Biological Sciences, Cornell University, Ithaca, NY 14853

The versatility of Low Temperature Field Emission SEM (LTFESEM) for viewing frozen-hydrated biological specimens, and the high resolutions that can be obtained with such instruments have been well documented[1,2,3,4]. Studies done with LTFESEM have been usually limited to the viewing of small organisms, organs, cells, and organelles, or viewing such specimens after fracturing them.

We use a Hitachi 4500 FESEM equipped with a recently developed BAL-TEC SCE 020 cryopreparation/transfer device for our LTFESEM studies. The SCE 020 is similar in design to the older SCU 020 except that instead of having a dedicated stage, the SCE 020 has a detachable cold stage that mounts on to the FESEM stage when needed. Since the SCE 020 has a precisely controlled lock manipulator for transferring the specimen table from the cryopreparation chamber to the cold stage in the FESEM, and also has a motor driven microtome for precise control of specimen fracture, we have explored the feasibility of using the LTFESEM for multiple-fracture studies of the same sample. Such a technique could be of potential use in spatial and temporal studies of cell differentiation or maturation in small organisms, organs and tissues.

Our preliminary results indicate that successful multiple-fracturing and viewing of the same sample after each fracture is to some extent specimen-dependant. Fig. 1 illustrates an image obtained from the first fracture of a yeast pellet and Figs. 2 & 3 show high magnification images of the protoplasmic fracture faces of the plasma membrane that are from a subsequent fracture. Successful multiple-fracturing of unembedded and relatively large specimens was difficult and inconsistent. We are still in the process of optimizing the necessary parameters for obtaining consistent results. An improved optical and lighting device that would permit a brighter and a higher magnified view of the specimen during fracturing is one of the factors that could help in obtaining consistent multiple-fractures.

References

1. P. Echlin, *J. Mirosc.* 112(1978)47.
2. N.D. Read and C.E. Jeffree, *J. Microsc.* 161(1991)59.
3. W.P. Wergin and E.F. Erbe, *Scanning Microscopy* 5(1991)927.
4. R. Hermann and M.Müller, *Scanning Microscopy* 7(1993)343.
5. This work was conducted at the Cornell Integrated Microscopy Center.

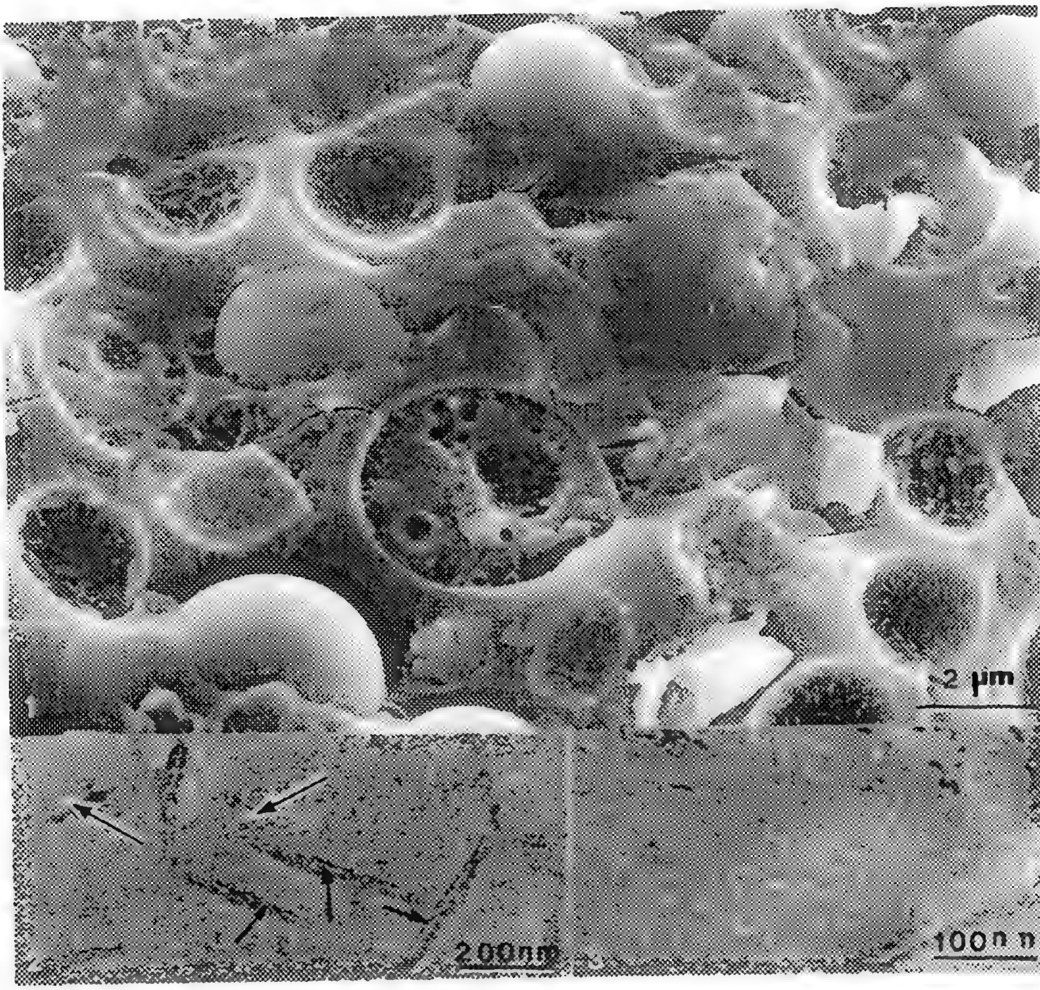

FIGS. 1-3 Low Temperature FESEM images of frozen-hydrated yeast cells viewed at -180^0 C after fracturing and sputter-coating with 3 nm of platinum.
FIG. 1 Low magnification view of fractured yeast cells.
FIG. 2 High magnification images of the protoplasmic fracture face obtained from a subsequent fracture of the same yeast pellet in Figure 1. Large arrows indicate the characteristic intramembranous particles present in such fractures. Small arrows indicate cracks that develop in the frozen specimen when it is exposed to electron beam for relatively long periods of time.
FIG. 3 Protoplasmic fracture face intramembranous particles.

INTERNAL ORGANISATION OF THE NUCLEAR PORE COMPLEX BY SURFACE IMAGING WITH FIELD EMISSION IN LENS SEM (FEISEM)

Allen, T.D., Kiseleva, E.V., Goldberg, M.W.

CRC Dept. Of Structural Cell Biology, Paterson Institute, Christie Hospital, Manchester M20 9BX, UK.

We have been working towards a 3 dimensional structural understanding of the Nuclear Pore Complex (NPC) with a view to investigating structural alterations associated with the molecular mechanism of transport across the nuclear envelope. FEISEM allows direct visualisation of changes in individual NPCs which will complement information from TEM 3D reconstructions (1). FEISEM has produced significant new information on the more peripheral elements of the NPC, most notably the nuclear pore basket or 'fishtrap' and the nuclear envelope lattice (2,3). NPC baskets have been recognised in both avian and insect species as well as amphibia and are likely to be evolutionarily conserved (4). In the salivary gland nuclei of *Chironomus* different configurations of basket structure have been recognised undergoing interaction with Balbiani Ring particles during mRNA export (5). (Fig 1).

The ability to observe and directly compare large numbers of NPCs on isolated NEs from either the cytoplasmic or nucleoplasmic face, at equivalent biological resolution to TEM has enabled us to access internal NPC organisation by surface imaging (3).This approach involves mild proteolysis, detergent extraction, mechanical fracture, or combinations of these methods. Mild proteolysis of isolated unfixed NES from *Xenopus* oocytes produces a consistent and progressive dismantling or disassembly of the NPC, removing peripheral elements first, followed by membrane associated structures, then progressive exposure of 'core' elements of the NPC (3,6). At the cytoplasmic face loss of cytoplasmic filaments, and progressive removal of the ring lead to the exposure of internal pore components. At the nucleoplasmic side however, some coaxial ring elements may well be removed before complete breakdown of the NPC basket.While detergent extraction will remove the membranes of the NE without any apparent effect on NPC structure we have found that the combination of detergent and proteolytic effects will expose direct interaction between the NPC core structure (spoke ring) and the nuclear lamins (3). (Fig.2).This directly observed NPC core structure bears significant similarity to that proposed from TEM computerised 3D reconstruction (1).

A further method of removal of peripheral NPC structure has been to merely roll the freshly isolated nucleus or NE over the substratum, effectively 'wet fracturing' unfixed NPCs from the cytoplasmic side. This process leaves both the surface faces of the 'wet fracture' available for inspection. The most novel structure revealed in this manner is a characteristic ring made up of eight subunits of pronounced triangular shape, termed the 'star' ring. (3). (Fig 3). Due to its 'incurved' nature, it has not yet proved possible to 'roll' the nucleoplasmic face of the NE. Iin this situation we have uncovered internal NPC structure from the nucleoplasmic side after fixation, dehydration and critical point drying of isolated NEs, by touching them to double-sided adhesive ttape. This 'dry' fracture will remove, or at least distort NPC baskets, allowing direct visualisation of NPC internal structure from the nucleoplasmic side. (Fig 4).

1. C.W. Akey, J. Mol. Biol. 1995, **248**, 273-293.
2. H. Ris, EMSA Bull. 1991, **21**, 54-56.
3. M.W. Goldberg & T.D. Allen, J. Cell. Biol. 1992 **119**, 1429 - 1440.
4. T.D. Allen, *et al*, Proc. MSA 1994, 12-13.
5. E.V. Kiseleva, *et al* (submitted Nature, 1996).
6. M.W. Goldberg & T.D. Allen, J. Cell. Sci. 1993, **106**, 2610174.

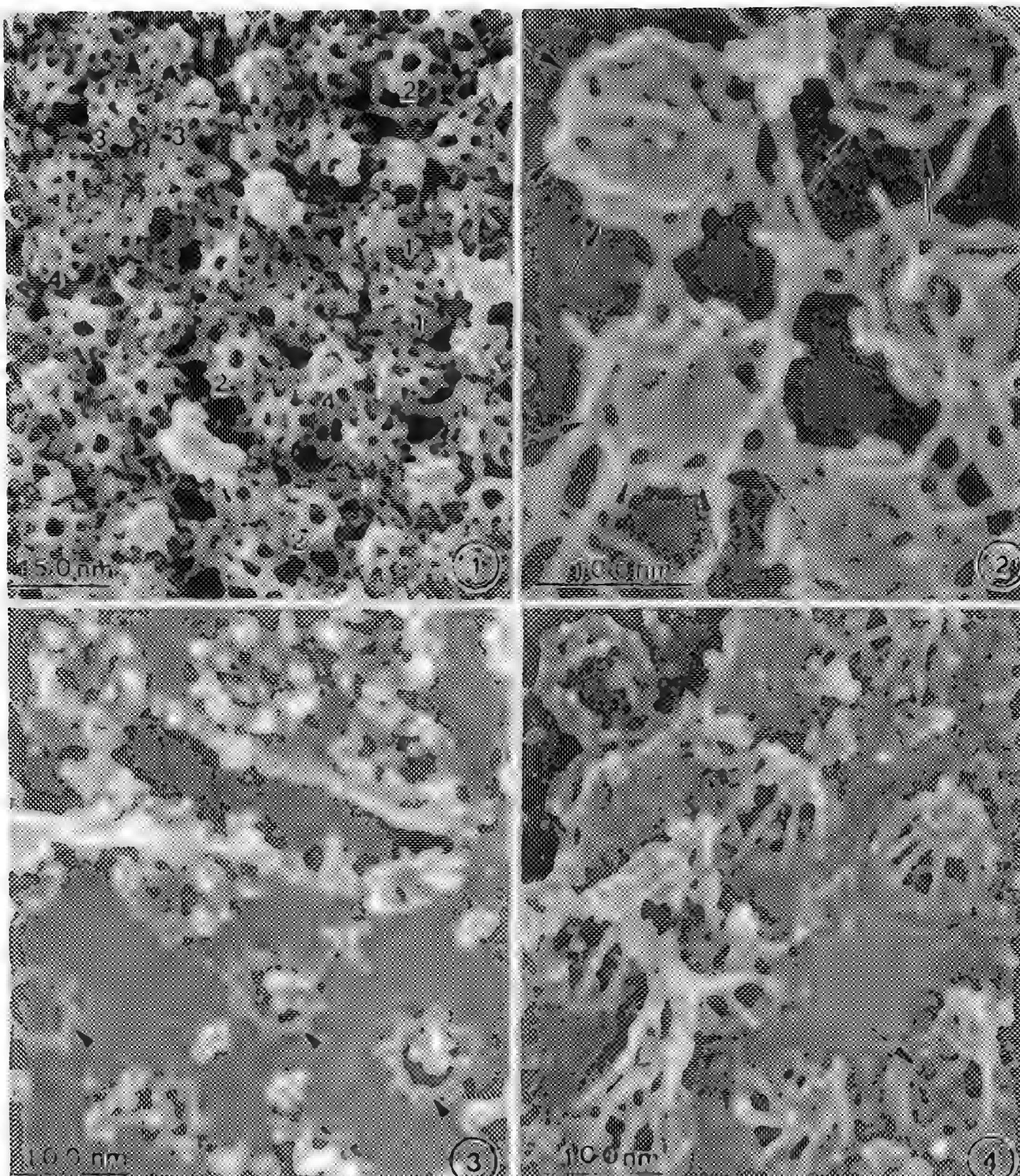

Fig. 1. Nucleoplasmic surface of NE isolated from *Chironomus* salivary gland. NPC baskets have the following configurations "Closed" (1) "Open" (2) RNP attached (3) RNP in transit (4).
Fig. 2. Core structure of NPC from *Xenopus* oocyte displaying peripheral radial arms (arrowed) after conbined proteolysis and detergent extraction.
Fig. 3. 'Wet fracture' exposing 'Star ring', after removal of the cytoplasmic coaxial ring.
Fig.4.'Dry fracture'of nucleoplasmic side of NE, showing sub NPC basket structure. (arrowed).

PROBLEMS IN OBSERVATION OF NATURAL BIOLOGICAL SURFACES WITH HIGH-RESOLUTION SCANNING ELECTRON MICROSCOPY

René Hermann and Martin Müller

Labor für Elektronenmikroskopie 1, ETH, 8092 Zürich, Switzerland

High resolution scanning electron microscopy can contribute a lot to the understanding of events occurring on biological surfaces even at a molecular level (either natural or artificially produced surfaces, e.g. by freeze-fracturing). In order to reach this goal, significant structural elements, down to dimensions of 2 - 4 nm have to be preserved as a function of the physiological state. Cryotechniques are important tools to fulfil this task.

A natural biological surface is often not easily accessible to scanning electron microscopic observation. The surface is the part of the specimen where an exchange with the surroundings takes place. Removal or replacement of the surrounding medium can strongly influence the surface structure. Surrounding fluids normally contain non volatile components (only a few organsisms, e.g. yeasts,[1] survive in distilled water without damage). Drying procedures - out of the native milieu - therefore result in deposition of solutes onto the specimen surface, sometimes mimiking natural biological structures.[2]

Fig. 1 shows a tetrachloro-ethylene dechlorating bacteria, stem PER-K23.[3] It has been rapidly frozen in the growth medium and subsequently freeze-etched, platinum/carbon and carbon coated. The sample was observed in a Hitachi S-900 field-emission SEM at -150° C in the BSE imaging mode.[4] The surface of the bacteria, exhibiting a regularly arranged surface layer, is partially covered, most likely by deposited solutes of the medium.

There have been a few attempts to overcome the problem of deposition of solutes on natural surfaces by using freeze-substitution combined with either critical point drying[5-7] or freeze-drying[8]. Structural resolution in the nm range has so far only been achieved on thin, beam-transparent samples after freeze-substitution followed by freeze-drying (critical point drying did not succeed when using the same samples).[9] Various freeze-substitution protocols followed by freeze-drying are tested in order to get a similar structural resolution on surfaces of bulk biological samples.[10]

References

1. P. Matile et al., *The yeasts I*, Rose and Harrison: Academic Press, New York (1969)219.
2. K.R. Miller et al., *J. Ultrastruct. Res.*, 82(1983)123.
3. C. Holliger et al., *Appl. Environ. Microbiol.*, 59(1993)2991.
4. P. Walther et al., *J. Microsc.*, 179(1995)229.
5. M. Baba, M. Osumi, *J. Electron Micr. Techn.*, 5(1987)249.
6. D.I. Barlow and M.A. Sleigh, *J. Microsc.*, 115(1979)81.
7. P. Walther and J. Hentschel., *Scanning Microsc. Suppl.*, 3(1989) 201.
8. P.C. Bridgman and T.S. Reese, *J. Cell Biol.*, 99(1984)1655.
9. R. Hermann and M. Müller, *Scanning Microsc.* 5(1991)653.
10. We thank Rolf Germann , Laboratory for EM 1, ETH Zürich for his help with the manuscript. PER-K23 were kindly supplied by Christof Holliger, EAWAG, Kastanienbaum, Switzerland. We also thank Alex Wild, Microbiology, ETH Zürich for his help in culturing the cells.

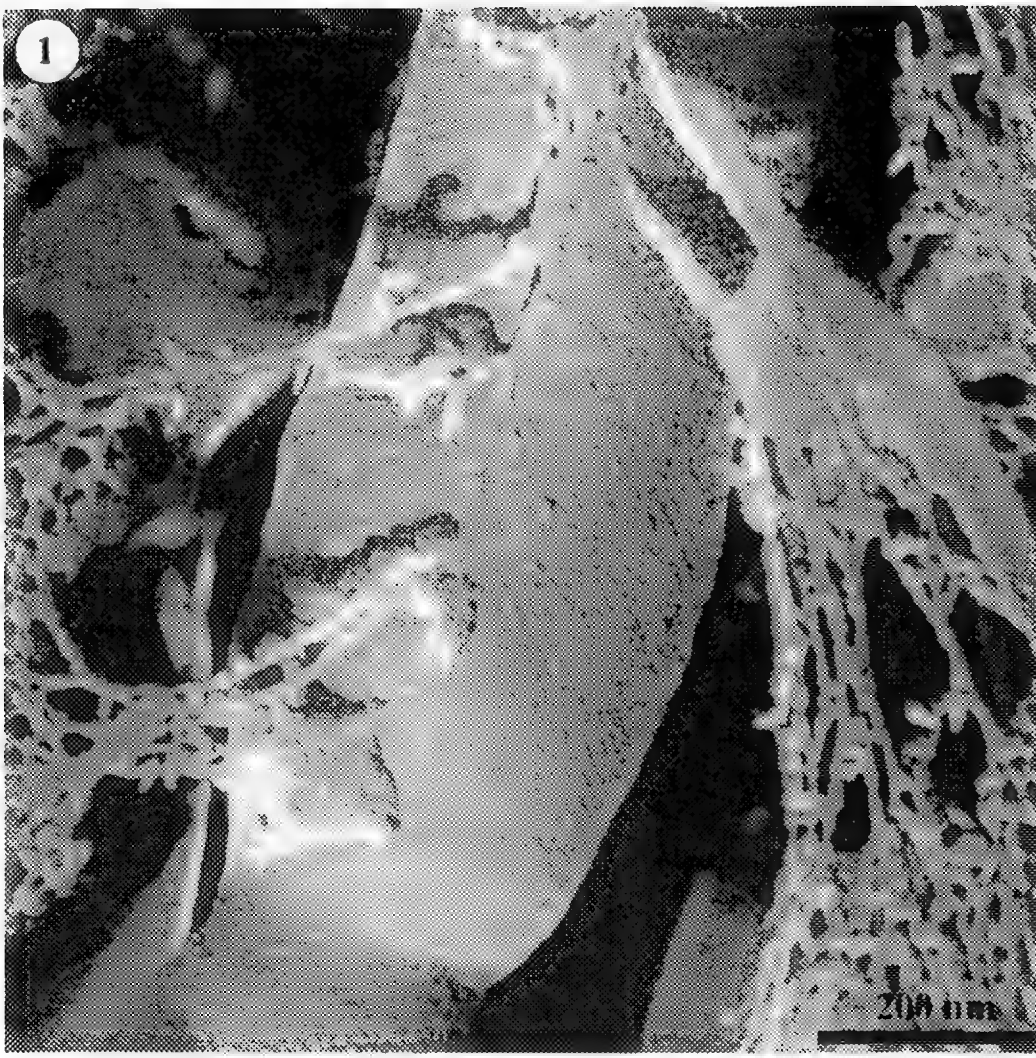

FIG. 1. Scanning electron micrograph of stem PER-K23, a tetrachloro-ethylene dechlorating bacteria. The sample has been rapidly frozen in the growth medium by plunging into liquid ethane, subsequently freeze-etched at -100° C in a Balzers freeze-etching device. The sample has subsequently been coated with platinum/carbon and carbon. It was then transfered in liquid nitrogen to the microscope and finally observed in a Hitachi S-900 field-emission SEM at -150° C using the BSE imaging mode. The surface of the bacteria, exhibiting a regularly arranged surface layer, is partially covered, most likely by deposited solutes of the medium.

Low-Temperature Field-Emission Scanning Electron Microscopy of High-Pressure Frozen Samples Reveals Structural Information Below 10 nm

Paul Walther and Martin Müller

Laboratory of Electron Microscopy, Swiss Federal Institute of Technology, Zurich, Switzerland

High-pressure-frozen samples can be imaged in the frozen hydrated state with a low temperature scanning electron microscope (LTSEM) thereby preventing many of the fixation and drying artifacts related to chemical fixation and dehydration. One limiting factor of high resolution LTSEM, however, is mass loss of the hydrated specimen due to electron beam irradiation. This effect is significantly reduced by using double layer coating and backscattered electron imaging (Walther et al., 1995). Thereby the sample is first coated with a contrast forming heavy metal layer (1 - 3 nm thick) and afterwards with a stabilising carbon coat (5 - 10 nm; Walther and Hentschel, 1989). The heavy metal layer is imaged with backscattered electrons that penetrate the carbon layer. Using this method structural information comparable to the TEM-replica ("freeze-etch") technique can be achieved, without the need of replica cleaning. The method has been especially useful for samples where replica cleaning is difficult; e. g. investigation of new materials for filling cavities in dentistry, or the effects of drug application to human skin, or investigation of new materials in polymer science.

In this work we used high pressure freezing and LTSEM for preparation of cells in suspensions. In analogy to the propane-jet sandwich method (Müller and Moor, 1984) a 10 µm thick gold grid was dipped into the cell suspension and afterwards clamped in between two flat 3 mm aluminum discs. This thin aqueous layer was usually very well frozen by high pressure freezing, so that even extra cellular areas did not show any indications of ice crystal formation. The sandwiches were fractured in a BAF 300 freeze-etching device (Bal-Tec, Princ. of Liechtenstein) at a temperature of 163 K and partially freeze dried ("etched") for 2 min. Afterwards, the samples were coated with 3 nm of platinum-carbon at an angle of 45° and with 5 nm of carbon (perpendicularly) and then the bulk sample was cryo-transferred to the Hitachi S-900 field emission in-lens SEM on a Gatan cryo-stage. Images were recorded digitally at a temperature of about 140 K using the backscattered electron signal.

The table on the next page shows fracture faces of the green algae *Euglena gracilis*. Fig. 1 is a cross fractured chloroplast exhibiting the membrane stacks. Due to the relatively strong "etching" the water is partially sublimated, and small particles can be seen in between the linear membrane structure (Fig. 2 is the labelled portion of Fig. 1 at higher magnification). Fig. 3 shows the periodic cell wall structure of the same bulk sample at high magnification (primary magnification is 300,000 x). The diffraction spots (Fig. 3, insert) show that a periodicity of about 6 nm and a periodicity of about 3.2 nm can be resolved.

We thank Dr. Barbara Baldan, University of Padova, Italy for providing the *Euglena* sample.

References:
Müller M. Moor H. (1984). Proc. 42nd annual meeting of EMSA, San Francisco Press: 6-7.
Walther P, Hentschel J. (1989). Scanning Microsc 1989, 3, Supplement 3: 201-211.
Walther P, Wehrli E, Hermann R, Müller M. (1995). J Microsc. 179, 229-237.

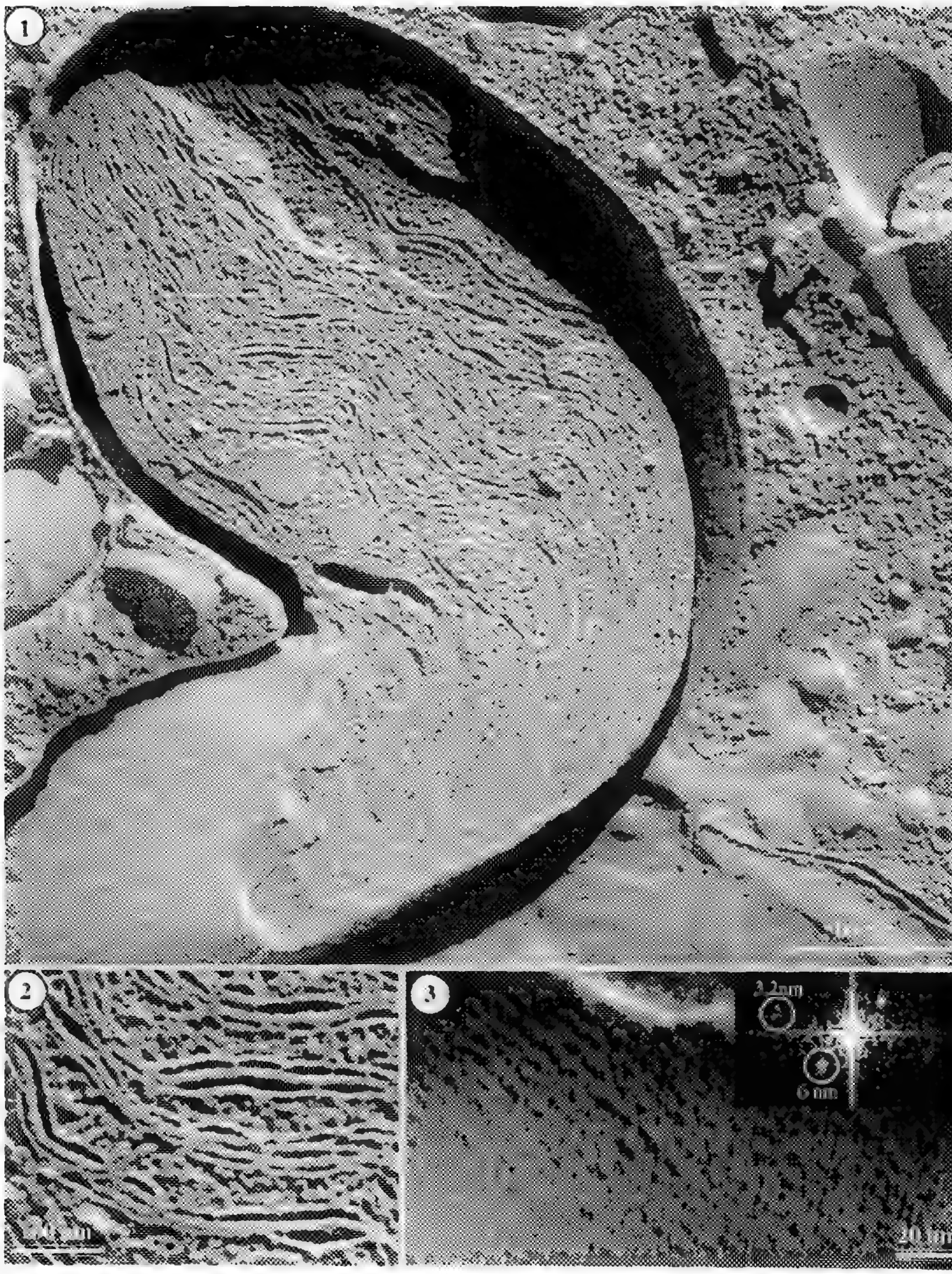
1
2
3
3.2nm
6 nm
20 nm

APPLICATION OF A CORRECTED LVSEM IN BIOLOGY: ARTEFACTS IN IMAGING OF UNCOATED BIOLOGICAL MATERIAL

R. Wepf, M. Haider, M. Kroug, D. Mills and J. Zach

European Molecular Biology Laboratory, Postfach 10 22 09, D-69012 Heidelberg, Germany

In Biology high resolution SEM has become of special interest to study the surface representations of isolated macromolecular complexes as well as the organisation of such complexes and organelles in their natural context.
Apart from the probe size, surface imaging in the nm-scale is limited by the interaction volume of the primary electrons, which directly increases with increasing primary energy. On one hand at low voltages (200-1000eV) the interaction volume can be kept minimal, but a probe size of 1-2 nm can only be obtained by a correction of the spherical and chromatic aberrations (Zach, 1990; Haider et al., 1994). On the other hand, the probe size at high voltages is mainly limited by diffraction and spherical aberation but nevertheless a probe sizes <1 nm at 30keV can be routinely achieved (Nagatani et al., 1987). To overcome the resolution limitation by the large interaction volume in bulk samples, biological specimens are coated with a very thin (1-2 nm) metal film to localize the SE-signal at the surface of the specimen (Joy, 1990). Such a coating film can blur fine details and obscure the material contrast of the specimen itself. Imaging of uncoated and unstained biological specimens could become possible if charge free imaging conditions can be found. The insulating and inhomogenous nature of biological samples and their sensitivity to irradiation complicates the finding of charge free imaging conditions even at low beam energies.
Surprisingly, we observe negative charging at high magnification and therefore strong imaging artefacts, even if at low magnification the SE-yield of the specimen is >1 and hence the specimen reaches a positive charge. To overcome charge induced imaging artefacts we tested different imaging and signal detection strategies as well as different preparation techniques for biological samples. TV mode averaging can overcome charging artefacts but due to the instability of the scan generators at such high speed the images are blured compared to slow scan imaging (Fig. E vs. D). For slow scan imaging with little influence of charging a beam current of ≤15 pA has turned out to be essential (Fig.B & D) even for LVSEM. To scope with the very low SE-signal obtainable from beam currents ≤10pA we use a microchannel plate incorporated into the detector objective lense.
We will present the current resolution achievable with the corrected LVSEM on test specimens and compare it with results obtained by HVSEM and TEM. Further we will discuss some problems of imaging insulators at low beam energies (500-2000eV) and we will discuss in more detail some aspect of charging in respect to different imaging conditions and specimen preparation.

References:

1) Haider M.,Zach J. and Wepf R. (1994), ICEM, Paris, les éditions de physique.
2) Joy D. C. (1990), " J. Microsc. **161**:
3) Nagatani T.,Saito S.,Sato M. and Yamada, M.(1987), Scanning Microsc. **1**(3): 901-909.
4) Zach J. (1990) " Nuclear Instrum. and Methods in Physics Research **A298**: 255-259.
5) This work was funded by the German Science Foundation (DFG -Za173). The aid of Dr. M. Diakonova is gratefully acknowledged.

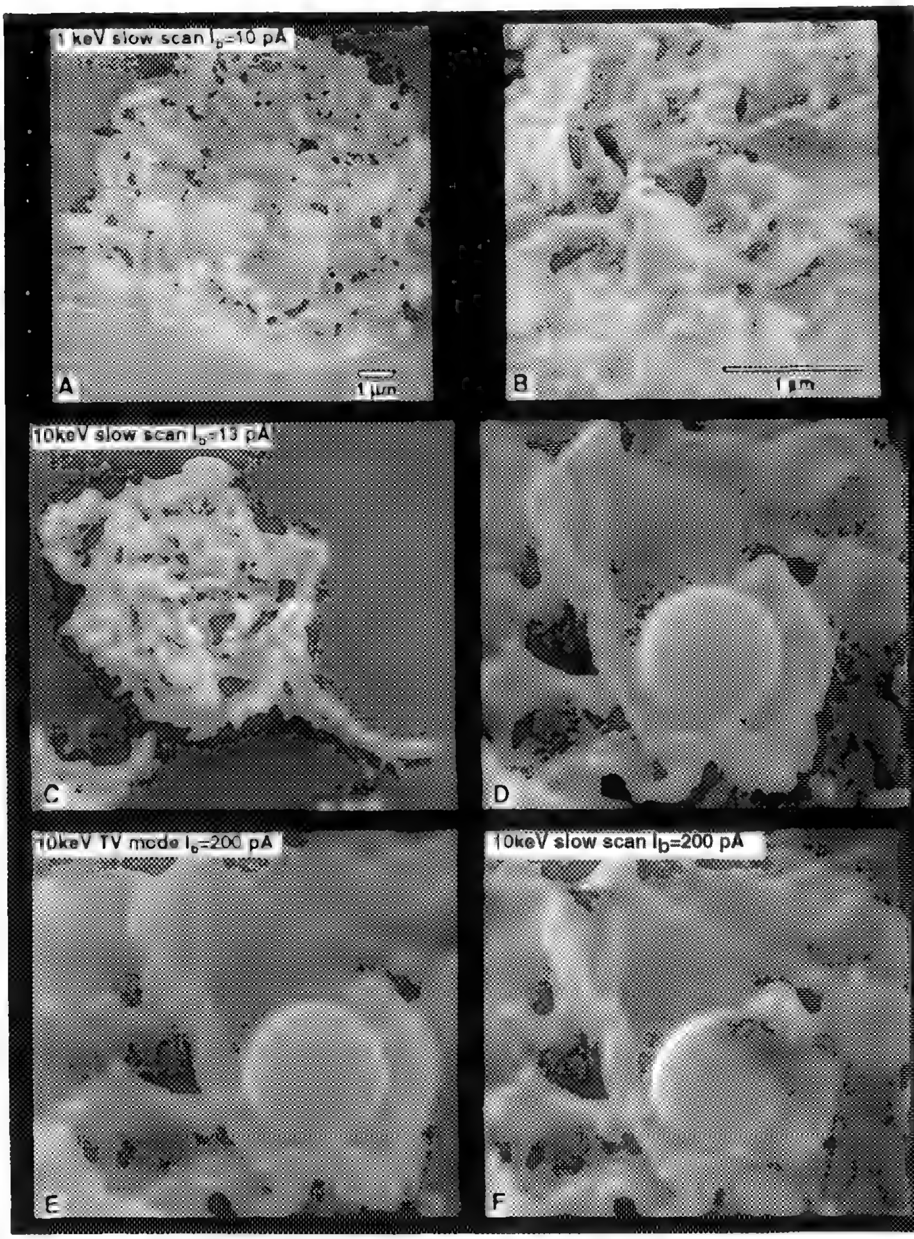

SE-Images of rapid froozen, freeze-substituted uncoated and coated Macrophages durn
Phagocytosis of Latex-beads imaged under different conditions:
A&B) imaged in the corrected LVSEM at 1keV and with a beam current of 10pA.
Note that at large magnifications (>30'000*) charging artefacts are nearly vanished.
C-F) imaged in a XL-30 FEG prototype (Philips) at 10keV either at 14pA (C&D) or at 200pA (E&F
Note: charging artefacts can be avoided by using a TV averaging mode (256frames)but the ima
is blured compared to slow scan imaging at much lower beam current (D).

FESEM IMAGING OF THE XENOPUS OOCYTE NUCLEAR ENVELOPE

H.Ris

Dept.of Zoology and Integrated Microscopy Resource,University of Wisconsin,Madison WI.53706

The transport of proteins and nucleic acids into and out of the nucleus is controlled by a unique membrane transport system, the nuclear pore complex (NPC), a large macromolecular assembly inserted into the pores of the nuclear envelope (NE). The large nucleus of the Xenopus oocyte has been a favorite object for both functional and structural studies. TEM of thin sections and negatively stained membranes had revealed the eightfold symmetry of the NPC, but the complex anatomy of the cytoplasmic and intranuclear surface of the NPC was first revealed by high resolution, field emission SEM[1,2,3] .On the cytoplasmic side, the NPC is limited by a flat ring, about 20 nm wide and 120 nm in diameter. It carries 8 twisted filaments which, in the presence of divalent cations are condensed into 20x40 nm cylinders. On the nuclear side there is a similar ring with 8 long , thin filaments attached to its outer rim. The distal ends of these filaments terminate in a smaller ring, about 50 nm in diameter, forming a "fishtrap"- like structure. These structures were confirmed by TEM of rapidly frozen and freeze-dried envelopes after heavy metal coating[4] . In most published pictures the small ring of the fishtrap is poorly defined, because in situ a 50 nm thick, fibrous cylindrical structure is attached to it (fig 3b)[5]. In this side view of the NPC in a thick section after epon extraction, the fishtrap filaments end in a 10 nm particle and these 8 particles form the top of the fishtrap. Rarely, this structure is also seen in whole mounts. In the commonly used isolation buffers, this 50 nm fiber is usually torn off the fishtrap, leaving distorted remnants attached to it.In Fig.2 , at the arrows, we see short remnants of this structure, which is in fact a hollow tube. I have used McGregor's isotonic buffer to avoid stretching of the NE, and added 5% sucrose to disperse the nuclear gel. FESEM imaging of the intranuclear surface now reveals a new nuclear structure , a branching cable system which connects groups of NPCs with the nuclear interior(Fig.1, arrowheads). It is suggestive that this hollow cable system could be involved in transport between the NPCs and the nuclear interior. The fibrous lamina is another regular component of the nuclear envelope .It consists of 10 nm fibers composed of lamins, a family of intermediate filament like proteins. In Xenopus, the lamina forms an orthogonal net of 10 nm fibers which becomes visible if the NE is extracted with Triton X-100[6]. This protocol does not preserve the fishtraps. I have modified the procedure so that the lamin net, the fishtraps inserted in it and the fishtrap connecting cables are all preserved (Fig.1). Such preparations can now provide information on the relationship between the NPC and the lamina.

References

1. H.Ris.Inst.Phys.Conf.Ser.No 98 16 (1989) 657.
2. H.Ris. Electron Microsc.Soc. Am.Bull.21 (1991) 54
3. M.W.Goldberg and T.D.Allen. J.Cell Science 106 (1993) 261.
4. M.Jarnik and U.Aebi. J.Struct.Biol.107 (1991) 291
5. H.Ris and M.Malecki. J.Struct.Biol.111 (1993) 148
6. U. Aebi et al. Nature 323 (1986) 560.

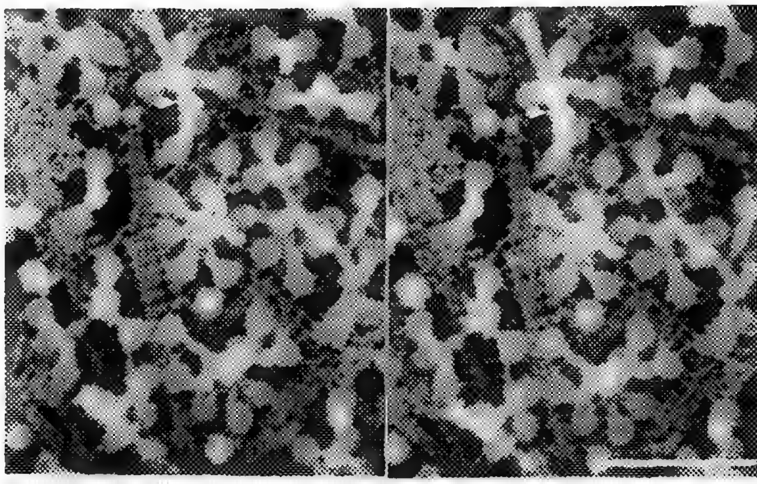

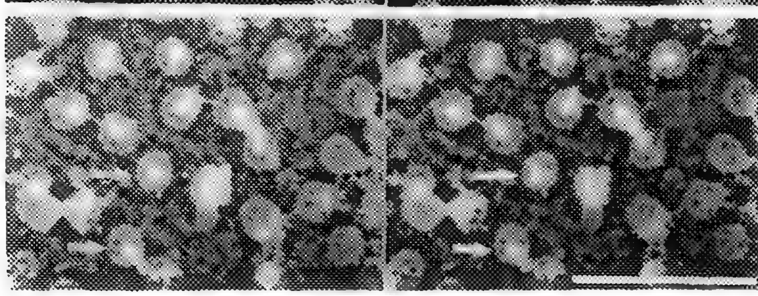

Fig.1. Stereo-image of intranuclear surface of an isolated Xenopus oocyte nuclear envelope.The nucleus was isolated in McGregor buffer containing 5% sucrose, attached to carbon coated coverslip and spread to expose the intranuclear surface.The membrane was extracted with 0.1% Triton X-100 in isolation buffer containing 1% glutaraldehyde .Fixation: 1%glutaraldehyde and 0.2% tannic acid in isolation buffer, followed by 1% OsO_4 and 1% uranyl acetate. Critical point dried. Branching 50 nm thick fibers with a 50 nm periodicity interconnect groups of fishtraps.The fishtraps are inserted in the meshes of the lamin net.
Hitachi S-900 FESEM, 1.5 kV. Bar = 500 nm

Fig.2. Stereo-image of intranuclear surface of a Xenopus oocyte nucleus isolated in McGregor buffer, attached to carbon coated coverslip and transferred to low salt buffer. Nucleus spread open to expose intranuclear surface. Fixation as in Fig.1. Critical point dried. The 50 nm fibers on the fishtraps are torn off close to the top of the fishtrap. The hollow center of these fibers is seen at the arrows.
Hitachi S-900 FESEM, 1.5 kV. Bar=500 nm

This research was supported by grant DRR-570 from NCRR-NIH to the Integrated Microscopy Resource (IMR) Madison,WI

A SURVEY OF DETECTOR OPTIONS FOR THE "LEAKY-VACUUM" SEM

Stuart McKernan* and John F. Mansfield**

*Department of Chemical Engineering and Materials Science, Amundson Hall, University of Minnesota, Minneapolis, Minnesota 55455.
**North Campus Electron Microbeam Analysis Laboratory, 413 SRB, University of Michigan, 2455 Hayward, Ann Arbor MI 48109-2143.

Since the inception of the "Leaky-Vacuum" SEM (known by various manufacturers as environmental-, wet-, variable-pressure-, high-pressure- SEM) samples may be imaged with environmental conditions which are radically different from those in traditional SEMs. The presence of a (relatively) high pressure in the sample chamber affects the ability of the microscope to form a small, well defined electron probe on the surface of the sample, thereby affecting the ultimate resolution of the microscope. The environment also affect the operation of most SEM detectors. In this contribution the operation of different SEM detectors will be surveyed, and their performance in the "Leaky-Vacuum" SEM environment will be examined.

The most common detector in the SEM, the Everhart-Thornley (E-T) secondary electron (SE) detector, suffers most strongly from the effect of the residual chamber gas at high pressures. SEs emitted from the sample are low in energy and frequently collide with the residual chamber gas. This causes an electron cascade which ultimately overloads the E-T detector. At pressures less than ~1-2 torr, however, the E-T detector still produces useful results. The Electroscan SE detectors (the environmental secondary detector and the gaseous secondary electron detector) both make use of the electron cascade in the specimen chamber to provide the signal amplification.[1] At very low pressures (< ~0.5 torr) there is insufficient gain in these detectors to produce an image except at very long working distances. At high pressures (> ~10 torr) the incident beam is so broadened that good imaging conditions are not easily achieved. The working range of these detectors, however, does encompass a very useful range of operating pressures. The situation for the various backscattered electron (BSE) detectors is less affected by the presence of the residual gas. The higher energy backscattered electrons are scattered less by the residual gas than are the lower energy secondary electrons. The secondary electrons produced by collision of both the secondary and backscattered electrons with the residual gas in the specimen chamber are predominantly too low in energy to be efficiently detected by the BSE detectors. The main effect of the higher pressure in the sample chamber on the image quality is a slight loss of resolution due to the broadening of the incident beam.

Energy dispersive X-ray detectors are affected in a number of ways by the presence of a residual gas in the specimen chamber, as has been examined by many authors.[2] As the pressure in the chamber rises, more of the incident beam is scattered from the area under investigation by collisions with the gas. These scattered electrons may generate X-rays from the specimen at positions very far (> 1mm) from the investigated area. This poses problems for quantification of inhomogeneous samples. However, provided that the major contribution to the signal comes from the electron probe, rather than the 'skirt' of scattered electrons, reasonable spatial resolution for X-ray mapping can be obtained. In practice this limits the maximum chamber pressure to 1-2 torr. One final effect visible at high pressures is the presence of characteristic X-rays generated from the residual gas in the specimen chamber.

Cathodoluminescence (CL) signals may benefit from "leaky vacuum" technology as non-conductive samples do not require coating, thus reducing attenuation of the light as it leaves the sample. The chamber gas has little effect on the emitted light, but may provide some cathodoluminescence of its own if it is present at a high enough pressure.[3] Electron Backscatter Patterns (EBSP) can be used to determine individual grain crystallography in the SEM. The information comes from a very thin surface region of the specimen.[4] For non-conductive samples the use of higher pressure microscopy to reduce the charging will obviate the necessity to coat the specimen, thus reducing the EBSP signal. The backscattered electrons will still suffer some scattering between the specimen and the scintillator screen, giving an optimum pressure of

1-2 torr, although recognizable EBSPs can be obtained at pressures as high as 6 torr.[5] This variation is illustrated in figure 1.

For many other, less frequently used, signals such as specimen current, voltage contrast, and EBIC. The image quality is hardly affected al all by the higher pressure in the specimen chamber. Examples of the influence of the specimen chamber pressure on these different signal detection schemes will be presented.[6]

References
1. Electroscan Corporation, 66 Concord Street, Wilmington, Massachusetts 01887
2. B. J. Griffin et al., in E. S. Etz Ed., Microbeam Analysis (1995) 383
3. G. D. Danilatos, Scanning; **8**, 279 (1986)
4. J. R. Michael and R. P. Goehner, Proc. Ann. EMSA Meeting 52, 596 (1994)
5. V. Thaveeprungsriporn et al., J. Mater. Res., **9**, 1887 (1994)

6. Support was provided by the Center for Interfacial Engineering, an NSF Engineering Research Center.

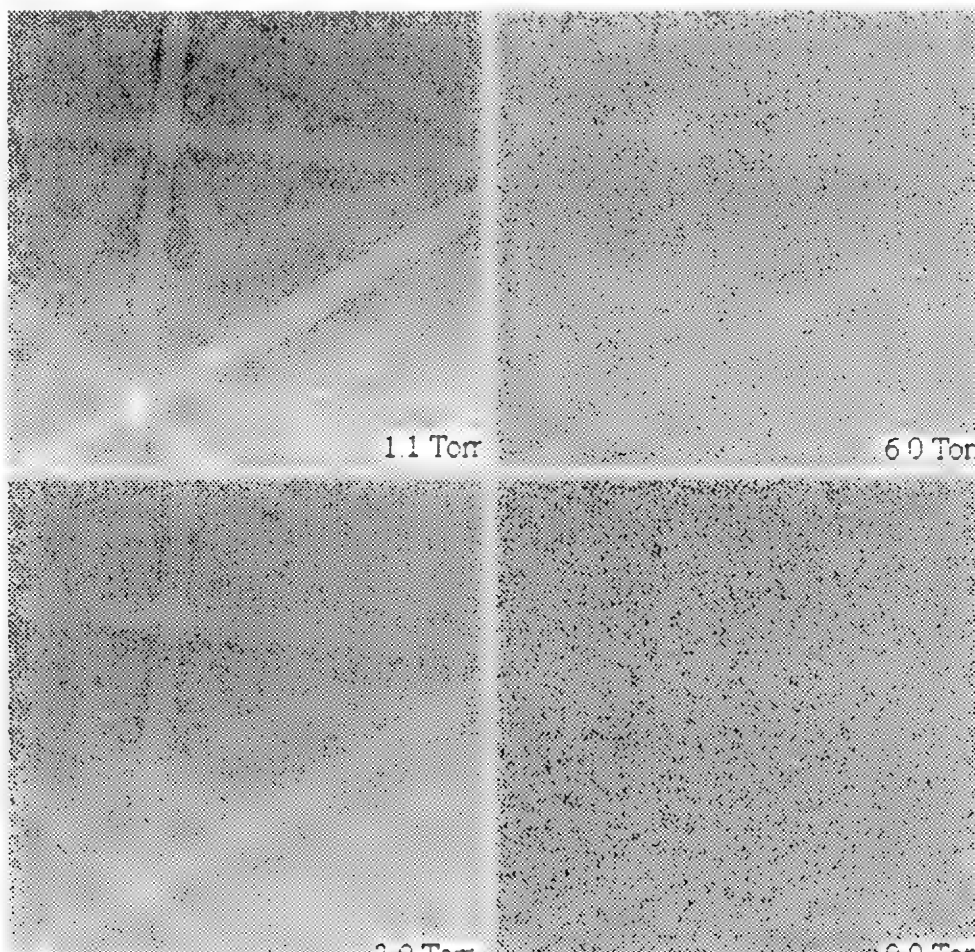

Figure 1 EBSPs obtained from a Si (001) Single crystal at four different residual gas pressures.

MONTE CARLO SIMULATIONS OF THE ION-CASCADE PROCESS IN THE ESEM

B.L. Thiel, I.C. Bache, A.L. Fletcher, P. Meredith and A.M. Donald

Polymers & Colloids Group, Cavendish Laboratory, University of Cambridge, Cambridge, U.K.

Our Monte Carlo simulations and experimental measurements show the Townsend Gas Capacitor (TGC) model[1] to be highly inappropriate for describing the electron cascade process in the Environmental SEM (ESEM). Previous workers have described the signal collected by the Gaseous Secondary Electron Detector (GSED) as having contributions from secondary as well as backscattered and primary electrons, all being amplified by gas cascade.[2-4] Although these models are qualitatively correct, they require a more sophisticated description of Townsend's First Ionisation Coefficient, α. Figure 1 illustrates the short-comings of the TGC models when compared to experimentally obtained amplification curves. (Details of the amplification measurements made with various imaging gases will be given elsewhere, along with specifics of the Monte Carlo Calculations.[5])

The major flaw in applying the TGC model to the ESEM stems from the assumption that the secondary electrons and their environmental daughters reach a steady-state kinetic energy distribution en-route to the detector. Under that assumption, α (the probability of ion-pair generation per unit path length) is constant between the sample and detector. However, useful combinations of GSED bias and gas pressure do not typically satisfy these criteria. It is necessary to consider α as a function of position along the sample-to-detector path, *i.e.*, $\alpha(z)$. Figure 2 shows that substantial deviations from TGC behaviour can occur, although the Townsend value is eventually reached.

For proper interpretation of the ion-pair creation profile it is necessary to consider the scattering cross-sections as presented for water in figure 3, bearing in mind that the average kinetic energy of the electrons increases as they approach the detector.[6,7] The "cathode fall region" immediately after the secondary electrons leave the sample is of particular interest. Initially, no ion-pairs can be produced until the electron has gained enough momentum to exceed the ionisation threshold of the gas molecules (12.6 eV for H_2O). Under conditions of low detector bias, the cathode fall region can occupy a significant fraction of the sample-to-detector distance, and thus lower the effective amplification path length. Once the ionisation threshold has been passed, ion-pair production jumps dramatically, followed by an exponential decrease to a limiting (TGC) value. It is noteworthy that in some cases the non-linear region can account for over half of the sample-to-detector distance. Since the total amplification is an integral function of $\alpha(z)$, the importance of this region cannot be understated!

From our studies it has emerged that the most significant factors in determining the shape and magnitude of the amplification curves are molecular and atomic excitation losses. A simple gas such as helium has only electronic excitations and ionisations for absorbing collision energy, and does not exhibit an amplification maximum in the ESEM operating range (Fig. 4). The result is a low total amplification of secondary electrons, and effects due to primary beam ionisations begin to dominate the signal at high pressures. Conversely, complex molecules (*e.g.*, water) have vibrational normal modes covering a broad energy spectrum (specifically at low energies) which absorb a significant portion of the imaging electron's momentum. Ironically, these excitation losses are necessary for attaining appreciable amplifications, as they keep the average electron kinetic energy much closer to the maximum in the ionisation cross-section (refer to figure 2). Accordingly, complex gases do exhibit a peak in amplification as a function of pressure, as indicated in figure 1.

In addition to the daughter-electron creation profile, Monte Carlo calculations can also provide insight into the electron energy distributions and the collision statistics. An understanding of these behaviours is needed to consider second order effects such as space-charge effects, recombination, and production of

secondary electrons due to positive ion impact. More importantly, though, having $\alpha(z)$ parameterised as a function of gas type, pressure, working distance, and detector bias will allow a more detailed analysis of the contributions from secondary, backscattered, and primary beam electrons, resulting in improved image interpretation.[8]

1.) A. von Engel in *Ionized Gases*, Clarendon Press, Oxford (1965).
2.) D.A. Moncrieff and V.N.E. Robinson, *J. Phys. D: Appl. Phys.*, 11 (1978) 2315.
3.) A.N. Farley and J.S. Shah, *J. Microsc.*, **158** (1990) 389.
4.) G.D. Danilatos, *Scan. Microsc.*, **4** (1990) 799.
5.) B.L. Thiel, et al., to be submitted to J. Microsc.
6.) Dayashankar and A.E.S. Green, *Radiat. Phys. Chem.*, **40** (1992) 523.
7.) A. Jain, *J. Phys. B: At. Mol. Opt. Phys.*, **21** (1988) 905.

8.) The authors wish to acknowledge helpful discussions with Prof. A. Howie. Support for this work was provided by the BBSRC and the Colloid Technology Programme, jointly funded by the DTI and Unilever, Schlumberger, Zeneca and ICI.

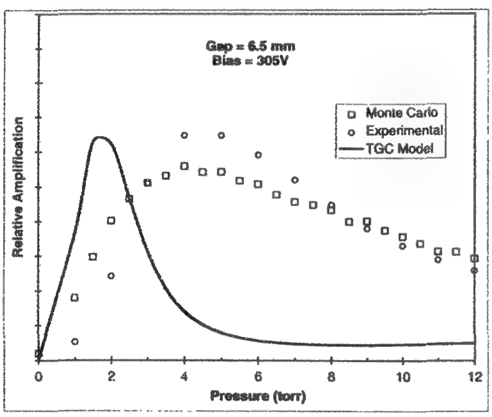

Figure 1.

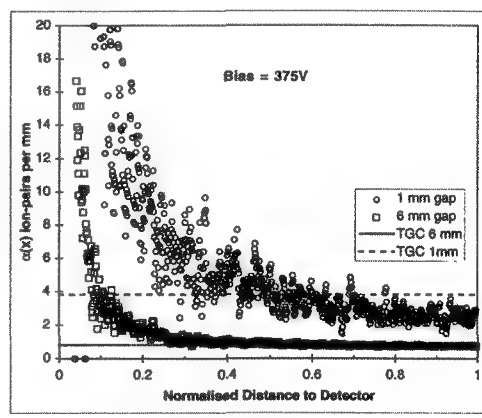

Figure 2.

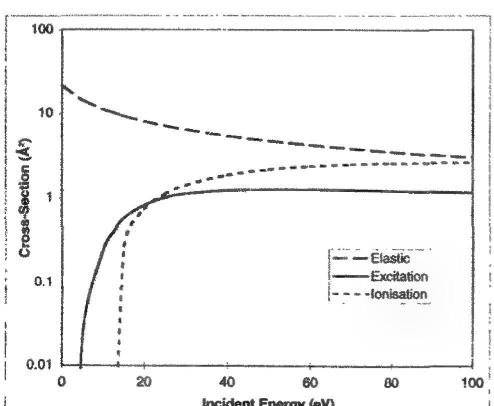

Figure 3.

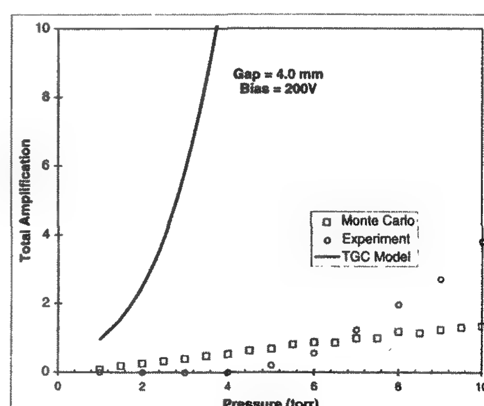

Figure 4.

MODELING THE ELECTRON-GAS INTERACTION IN LOW-VACUUM SEMS

David C Joy
EM Facility, University of Tennessee, Knoxville, TN 37996-0810, and
Oak Ridge National Laboratory, Oak Ridge, TN 37831

The passage of a beam of electrons through the low pressure gas atmosphere in an environmental SEM results in a scattering - and hence a broadening - of the probe, a reduction in the current available for imaging and analysis, and in the production of secondary ions which can also impact the specimen and modify the production of secondary and backscattered electrons. In order to optimize and fully exploit the capabilities of low vacuum SEMs it is desirable to be able to accurately predict these effects. The first step in achieving this aim is to be able to quantitatively predict the behavior of the incident beam.

At a gas pressure of 100Pa. the mean free path for 20keV electrons is of the order of 1cm. For a typical working distance of 1cm., therefore, the average electron is only scattered once. In this condition a first approximation to the modification of the incident probe can be made by estimating a mean scattering angle and assuming that this event occurs at the mid-point of the trajectory and several authors have demonstrated that this gives a useful estimate of the beam broadening[1]. However to adequately describe the beam profile as it reaches the specimen surface a Monte Carlo simulation must be used[2]. Although the cross-section for elastic scattering is generally larger than that for inelastic events, it is the small angle inelastic events which determine the form of the beam profile close to (i.e within a few micrometers of) the axis, while it is the higher angle elastic events which determine the width and magnitude of the large scattered region which surrounds the beam. The program GASSEM therefore accounts for both elastic and inelastic scattering, permits all the experimental variables (gas composition, pressure and temperature; working distance, and energy) to be selected and tracks each electron from the point where it enters the low vacuum region until it reaches the sample surface, allowing the detailed beam profile to be determined.

Computations show (figure 1) that under typical operating conditions a substantial fraction - from 10% of a 10keV beam after 15mm of air at 500Pa, to 90% of a 15keV beam after 5mm of air at 100Pa - reaches the specimen unscattered. This component is the core around which the rest of the profile is formed.The radial intensity distribution I(r) of the profiles, typical examples of which are shown in figure (2), is to a good approximation the sum of two exponentials - a result which makes it possible to conveniently parameterize the profile shape with the experimental variables. As the pressure or the working distance is increased the unscattered fraction falls and this intensity is transferred to the skirt of the distribution which may extend for 1 to 2mm from the axis. These computed profiles can be compared with profiles measured by scanning the beam over an edge[1], but a more sensitive test is to compare computed and measured values of the fraction of the beam intensity falling within a specified radius of the axis[3]. Figure (3) shows such a comparison with published data for 25keV beams in nitrogen demonstrating that the Monte Carlo procedure accurately predicts the observed profile over a wide range of conditions.

It is also possible to use the Monte Carlo model to understand the processes of ion formation and multiplication in the gas which are responsible for the reduction of charging, and the unique contrast effects, observed in this type of SEM. Since all of the electrons (primary, secondary, and backscattered) that are present can generate ionization in the gas a complete solution of the imaging problem would require tracking an electron as travelled through the gas from the gun to the specimen, following in the specimen and then, if necessary, continuing to track it as a backscattered or secondary

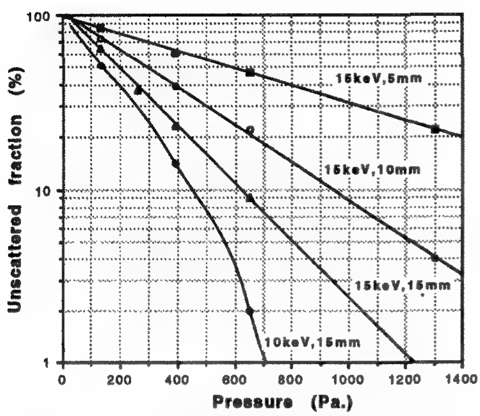

Fig.1 Computed unscattered fraction of beam in air vs energy and path length

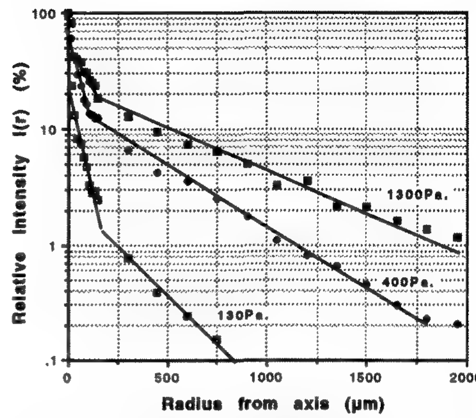

Fig.2 Computed beam profiles in air at 15keV vs gas pressure

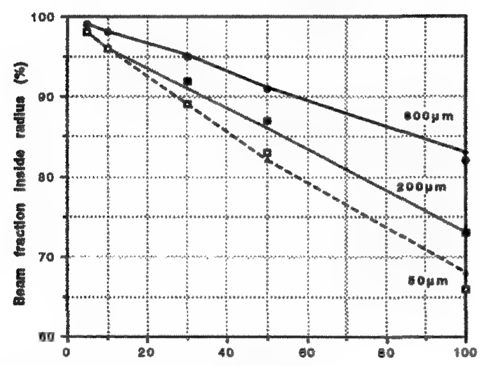

Fig.3 Current fraction falling inside given radius and comparison with experiment.N2, 25keV,15mm

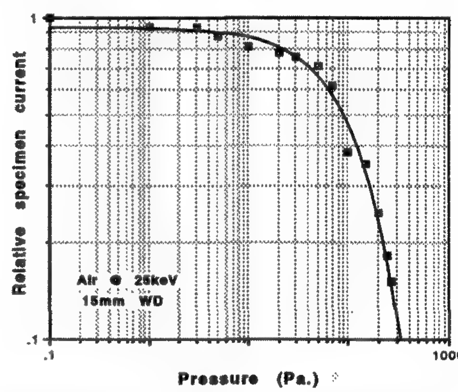

Fig.4 Measured variation of specimen current with gas (air) pressure.

electron as it again moves through the gas. A simplified problem for test purposes is to consider the net variation in specimen current as a function of gas pressure (figure 4). At the high vacuum limit the specimen current I_{sp} satisfies the usual relation $I_{sp} = I_B (1 - \delta - \eta)$ where I_B is the incident current and δ,η are the secondary and backscattered yields respectively, but as the gas pressure increases this equation is modified by the flux of positive ions which impinge on the sample causing the specimen current to fall and eventually to change sign. An initial goal is to be able to compute the gas conditions at which I_{sp} becomes zero as this is the optimum point for imaging providing charge balance at the lowest gas pressure and hence the smallest beam broadening.[4]

1. A.N.Farley and J S Shah, J.of Microscopy **158**, (1990), 379-388
2. D C Joy, *Monte Carlo Modeling for Microscopy and Microanalysis*, OUP:NY, (1995)
3. D.A.Montcrieff et al., J.Phys.D.Appl.Phys. **12**, (1979), 481-488
4. Oak Ridge National Laboratory is operated by Lockheed Martin Energy Research Corp. for the U.S. Department of Energy under contract number DE-AC05-96OR22464

ELECTRON BEHAVIOR IN THE GASEOUS ENVIRONMENT OF THE ENVIRONMENTAL SCANNING ELECTRON MICROSCOPE CHAMBER

S.A. Wight (email: scott.wight@nist.gov)

NIST, Microanalysis Research Group, Bld 222, Rm A113, Gaithersburg MD 20899.

Measurements of electrons striking the sample in the Environmental Scanning Electron Microscope (ESEM)[1] are needed to begin to understand the effect of the presence of the gas on analytical measurements. Accurate beam current is important to x-ray microanalysis and it is typically measured with a faraday cup.[2] A faraday cup (Figure 1) was constructed from a carbon block embedded in non-conductive epoxy with a 45 micrometer bore platinum aperture over the hole. Currents were measured with an electrometer and recorded as instrument parameters were varied.

Instrument parameters investigated included working distance, chamber pressure, condenser percentage, and accelerating voltage. The conditions studied were (1) low vacuum with gaseous secondary electron detector (GSED) voltage on; (2) low vacuum with GSED voltage off; and (3) high vacuum (GSED off). The base conditions were 30 kV, 667 Pa (5 Torr) water vapor, 100,000x magnification with the beam centered inside aperture, GSED voltage at 370 VDC, condenser at 50%, and working distance at 19.5 mm. All modifications of instrument parameters were made from these conditions. The effect of varying the working distance from 18 to 24 mm on measured current is shown in figure 2. A remarkable difference is found between the "GSED on" and "off" conditions. Secondary electrons are generated by primary electrons that have been scattered out of the beam by gas molecules. The secondary electrons cascade as they accelerate towards the positively biased GSED. The positive cup current ("GSED on" plot) is the result of positively charged gas molecules that migrate away from the positively biased GSED and are collected by the aperture. This effect is negligible when the GSED voltage is reduced to it lowest setting of 28VDC. The plot of this "GSED off" condition is similar in shape and magnitude to the high vacuum case. Assuming the number of positive ions is directly proportional to the number of secondary electrons striking the GSED, then the plot represents secondary electron signal strength. The shape of the low vacuum, "GSED on" case shows that there is an optimum working distance for a given set of instrument parameters. Varying the chamber pressure from 66 to 2933 Pa (0.5-22 Torr) yields a similar result, Figure 3, where the maximum represents the optimum chamber pressure for maximum secondary electron signal. Figure 4 depicts the secondary electron response rise with the condenser settings below 50%. Similarly the accelerating voltage, graphed in Figure 5, depicts the increased secondary electron response at lower accelerating voltages. Varying the GSED voltage from 28 to 450 VDC results in a non-linear response in secondary electron production (Figure 6) as expected.[3]

These graphs allow ESEM users to choose instrument parameters that minimize scattering of the primary electron beam in the gas for analytical measurements; low chamber pressure, high accelerating voltage, and high condenser settings. Beam current measurements should not be attempted with the GSED voltage applied.

References

1. Certain commercial equipment, instruments, or materials are identified in this report to specify adequately the experimental procedure. Such identification does not imply recommendation or endorsement by the National Institute of Standards and Technology, nor does it imply that the materials or equipment identified are necessarily the best available for the purpose.

2. J.I. Goldstein et al., *Scanning Electron Microscopy and X-Ray Microanalysis*, 2nd Ed., Plenum Press, New York(1992)65.

3. G.D. Danilatos, *Advances in Electronics and Electron Physics*, 78(1990)1.

1

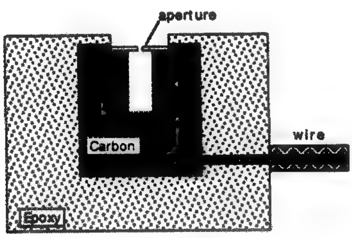

2

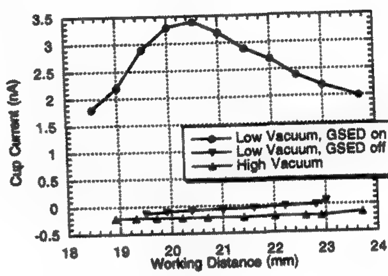

3

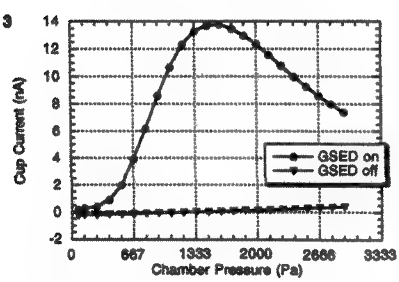

4

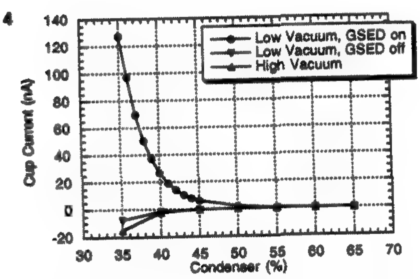

5

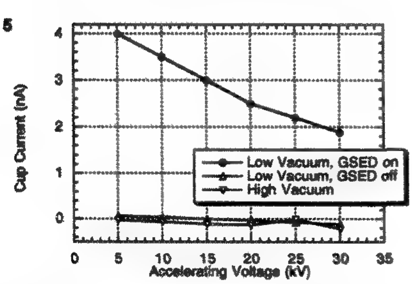

6

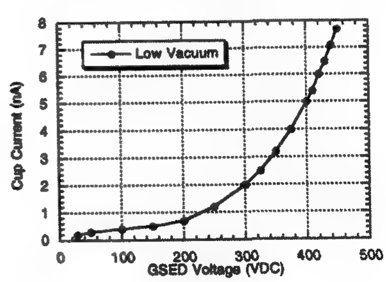

FIG. 1 Schematic of Faraday Cup
FIG. 2 Plot of Working Distance versus Cup Current
FIG. 3 Plot of Chamber Pressure versus Cup Current
FIG. 4 Plot of Condenser Setting versus Cup Current
FIG. 5 Plot of Accelerating Voltage versus Cup Current
FIG. 6 Plot of GSED Voltage versus Cup Current

ENVIRONMENTAL SCANNING ELECTRON MICROSCOPE (ESEM) OBSERVATION OF SUBSURFACE CHARGE EFFECTS IN INSULATORS: IMPLICATIONS FOR ELECTRON IMAGING AND X-RAY MICROANALYSIS

Griffin, B.J.[1] and Nockolds, C.E.[2]

[1]Centre for Microscopy and Microanalysis, The University of Western Australia, Nedlands, W.A., Australia 6907
[2]E.M. Unit, The University of Sydney, Sydney, N.S.W., Australia 2006

The nature of subsurface charging in non-conductive samples has been investigated and modelled by a number of authors. Potential effects of subsurface charging include modification in electron range and interaction volume, variation in secondary electron yield, and reduction in incident electron beam energy and consequent modification to the emitted x-ray signal.

During an unconnected experimental series on large surface area, polished mineral samples unusual images were observed following spot x-ray analysis. On these specimens, a bright circle centred on the analysis point was observed at low magnification in the secondary electron image. Around this bright circle was a concentric dark zone with diffuse edges. This effect was noted to be time variant, with the scanned area progressively increasing in brightness until the contrast with the circle was lost. Curiously however the perimeter of the circle was defined at this stage by a narrow 'dark' ring. This serendipitous observation has led to the observation and definition of subsurface charging in insulators, albeit at a preliminary stage.

To examine this phenomena a series of experiments have been undertaken using various beam conditions and samples. The following initial observations can be made:

(i) for a given specimen, the diameter of the enhanced brightness circle about the analysis point is linearly proportional to accelerating voltage,
(ii) the decay rate of the relative contrast is very slow in the test specimens, the effect being observable over periods in excess of 30 minutes and up to 5 days,
(iii) the decay rate is reduced if the area is exposing to a scanned beam at low magnification or at low magnification areas require a significant period (> 1-2 minutes) to equilibrate, ie the equilibration is dose dependent,
(iv) the decay time is a function of accelerating voltage, ie depth of electron penetration,
(v) on a fracture in the sample an elongation of the bright area is observed along the fracture
(vi) on a strongly cleaved sample the bright area is an ellipse whose long axis parallels the cleavage direction,

and (vii) in a sample containing isolated non-conductive grains in a conductive matrix the non-conductive grains show an enhanced SE brightness relative to the matrix which is not observable in the BSE image.

The observations are consistent with the development of a negatively charged region below the surface of the sample, surrounded by a positively charged zone. The emission of secondary electrons is enhanced above this region due to a mean path length increase for the SE, and with an opposite effect from the concentrically arranged positively charged zone.. The black 'ring' effect observed with time may define a 'compression' of the positive charge due to the build up of negative charge from the scanning of the surrounding area.

These observations concur with previously reported 'voltage contrast' effects observed in SEM and ESEM and with analytical discrepancies in non-ideal samples. Direct correlations with Monte Carlo models have been achieved however these models do not take into consideration beam dose, as a function of time or beam current.

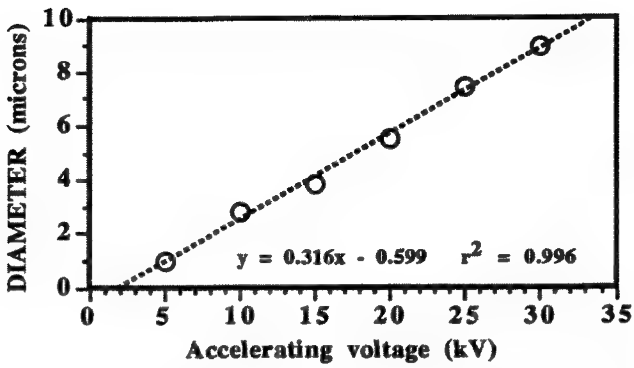

Figure 1: variation of spot diameter with accelerating voltage in uncoated garnet

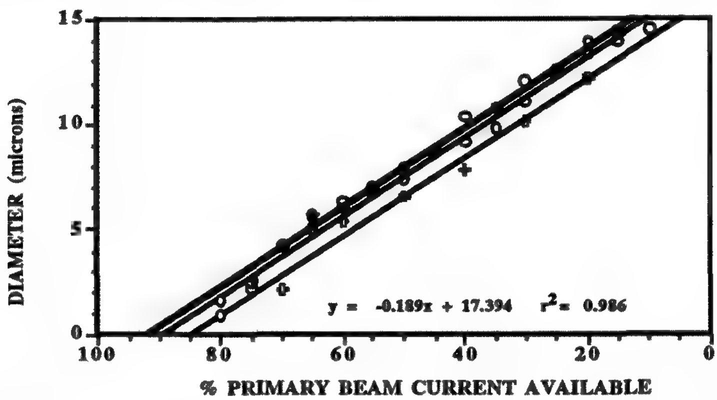

Figure 2: variation of spot diameter with beam current in uncoated garnet

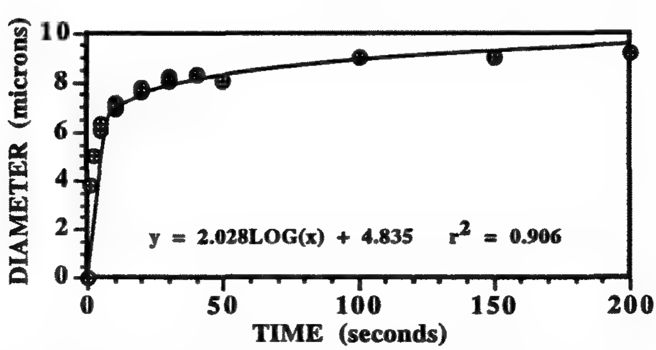

Figure 3: variation of spot diameter with time in uncoated garnet

QUANTITATIVE EDS ANALYSIS IN THE ENVIRONMENTAL SCANNING ELECTRON MICROSCOPE (ESEM) USING A BREMSTRAHLUNG INTENSITY-BASED CORRECTION FOR PRIMARY ELECTRON BEAM VARIATION AND SCATTER

Griffin, B.J.[1] and Nockolds, C.E.[2]

[1]Centre for Microscopy and Microanalysis, The University of Western Australia, Nedlands, W.A. 6907
[2]E.M. Unit, The University of Sydney, Sydney, N.S.W., Australia 2006

Quantitative EDS analysis of bulk samples in the scanning electron microscope (SEM) or electron microprobe requires, as a fundamental parameter, a stable and reproducible primary electron beam current. Beam current is usually measured with a Faraday cage positioned in the electron column below the objective aperture or in the specimen holder. Reproducibility and stability within 1%/hour is a minimum condition.

Primary beam current measurement in the ESEM or any high pressure SEM is difficult to measure. Electron-gas interaction in the biased chamber generates a positive ion flow highly amplified relative to the primary beam (Danilatos, 1990) and generates an x-ray signal from the gas. The latter signal amplitude is dependent on primary beam current, chamber pressure and backscatter electron signal from the specimen (Griffin et al. 1993). These interactions prevent quantification of EDS data standardised to Faraday cage primary beam current measurements or x-ray counts from a reference standard.

Nockolds (1987) and then Griffin and Nockolds (1991) used the relationship between the intensity of a region of the Bremstrahlung and the mean atomic number of the sample to derive a correction for variations in primary electron beam current from a calibrated value. Routinely, this correction is located within the conventional ZAF data reduction algorithm and is invisible to the operator. The correction was demonstrated to correct for irregular variations in beam current of up to 50%.

A set of mineral standards of large surface area has been used to calibrate selected elements and the specifics of the relationship between the intensity of a region of the Bremstrahlung and the mean atomic number of the sample. The standards were constructed to be sufficiently large to contain the beam scatter (Griffin, 1992). The data (figure 1) give the following relationship, for the current analytical conditions:

$$BGD = 1079\,(Z^*) + 995 \qquad r^2 = 0.994$$

[BGD = integral counts in energy range; Z^* = mean atomic number]

Application of this relationship to quantitative EDS analysis of a range of silicate minerals was successful in providing analyses of conventional accuraccy using conditions of 30kV and 1.0 torr water vapour pressure. The analysis procedure is simple and routine as no account has to be made of the primary beam current value, within normal instrument reproducibility. Initial measurements indicate an analytical spatial resolution, based on beam scatter, of around 60 microns (figure 2).

G D Danilatos, *Advances in Electronics and Electron Physics*, 78(1990)1-102.
B J Griffin, *Proc. 50th Annual Meeting of the Electron Microscopy Society of America (Eds.: Bailey, Bentley & Small)*, (1992)1324-5.
B J Griffin, R L Trautman and J Coffey, *Microbeam Analysis*, 2(1993)S37-8.
B J Griffin and C E Nockolds, 1991, *Scanning*, 13:307-312.
C E Nockolds, *Microbeam Analysis*, (1987)9-11.

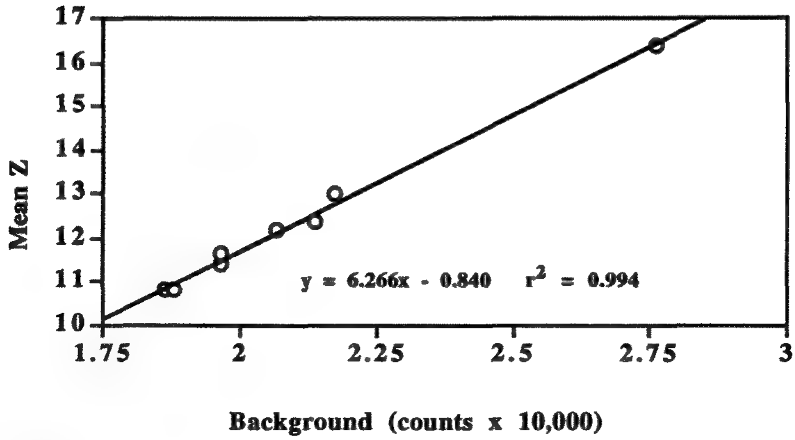

Figure 1: Relationship between Bremsstrahlung background and mean atomic number

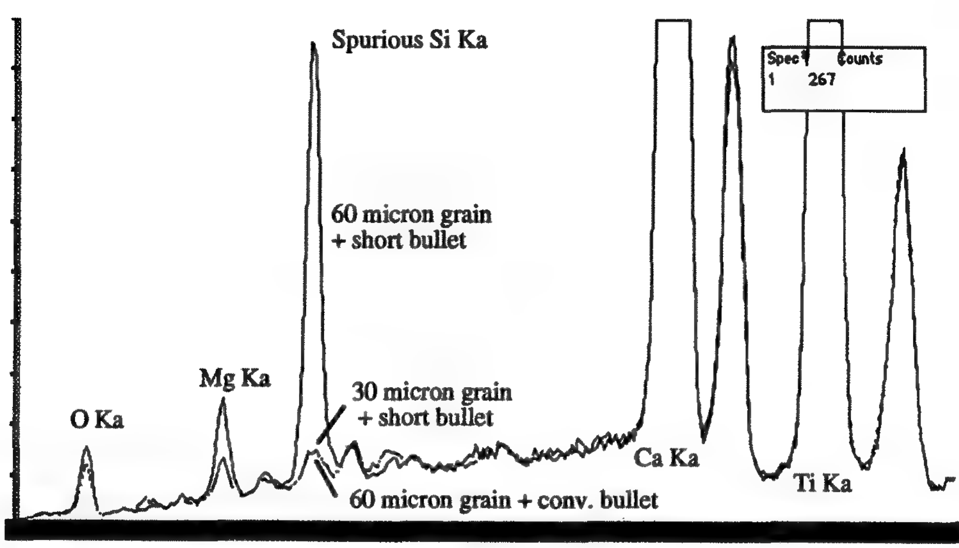

Figure 2: x-ray spectra at 30 kV and 1 torr from perovskite grains of different size showing the effects of scattering of the primary beam on x-ray resolution

BIOLOGICAL APPLICATIONS OF ENVIRONMENTAL SCANNING ELECTRON MICROSCOPY: EXAMINATION OF FULLY HYDRATED SAMPLES

Gilpin, C.J.

Biological Sciences Electron Microscope Unit, G452 Stopford Building, University of Manchester Oxford Road, Manchester, M13 9PT, U.K.

The environmental scanning electron microscope (ESEM) utilises a secondary electron detector capable of operating at pressures in the range of 1 ~ 20 Torr (130 ~ 2700 Pascals). By use of differential pumping apertures the electron gun and column can be maintained at "normal" vacuum levels of 10^{-5} Torr. A pressure of 10^{-2} Torr exists within the secondary electron detector separated from the specimen chamber by another differential pumping aperture. The specimen chamber pressure is produced by admitting a gas to the chamber under operator control. The gas can be any ionisable gas. Water vapour is a commonly used chamber gas. By controlling chamber gas pressure and sample temperature, by means of a Peltier effect stage, condensation and evaporation can be produced. The ability to maintain samples in a fully hydrated state in this way singles out the Electroscan ® ESEM as a unique instrument. ESEM presents an opportunity to examine biological samples with their natural water content present.

In an attempt to evaluate the benefits of ESEM artificial arterial grafts have been examined using both conventional SEM and ESEM. Woven Dacron tubes infused with gelatine were internally coated with a variety of substances designed to promote adhesion and growth of endothelial cells. Such samples were examined using both conventional SEM and ESEM. With conventional SEM, using either freeze drying or critical point drying, the gelatine substrate was poorly preserved preventing an assessment of endothelial cell attachment and growth. ESEM examination, however, revealed the smooth nature of the coated gelatine and endothelial cells could be clearly be identified. At the present time different methods of harvesting endothelial cells are being undertaken in the knowledge that their distribution and structure can be successfully examined.

Mushroom spores have been examined using both ESEM and cryo-SEM. As with many samples the extracellular matrix surrounding mushroom spores is well preserved using ESEM (Figure 1). Such a matrix is often seen in a partially dehydrated state even when using cryo-SEM (Figure 2). The spores themselves are seen as smooth surfaced structures using ESEM whereas with cryo-SEM an irregular surface encrustation seems to be present. The results seen using cryo-SEM may be a reflection of the difficulty in controlling sublimation of surface ice rather than an inherent weakness of the technique. Similar results have been observed when examining biofilms.[1] Extracellular matrix is only successfully preserved with ESEM. The micro-organisms which make up the biofilm can, however, only be successfully imaged using dried preparations.

Frequent use is made of X-ray microanalysis in biology. Many difficulties are encountered in using this technique in the ESEM. Beam spread due to the scattering effect of chamber gas has been studied.[2,3] X-ray data is collected over an area of up to 1 mm when chamber pressures of ~ 5 Torr are used. In addition X-rays are generated from the chamber gas. Area or point analysis of non-homogeneous samples is not possible. X-ray mapping does, however, provide usable data.

A range of other biological samples will be considered. Fresh water pollution studies have been undertake
and organisms which take up heavy metals have been studied. Blue green algae and diatoms have been observed by controlled evaporation of water until the organisms are clearly visible in the wet state. Delicat structures such as spider's webs are particularly suited to study by ESEM as there is no preparation necessa and handling is kept to a minimum. It is often more convenient to study chemically fixed, hydrated sample: Preliminary data are available from a study of human spermatozoa in cases of infertility which have been fixed with glutaraldehyde and washed in distilled water prior to examination in the ESEM
Enormous potential exists for further examination of biological specimens, in the hydrated state, using ESEM.

1. Sutton, N.A., Hughes, N. and Handley, P.S. Journal of Applied Bacteriology, 76, 5, 448-454 (1994)
2. Sigee, D.C and Gilpin, C.J. Scanning Microscopy Supplement 8 219-229 1994
3 Gilpin, C.J. and Sigee, D.C. Journal of Microscopy 179 22-28 (1995)

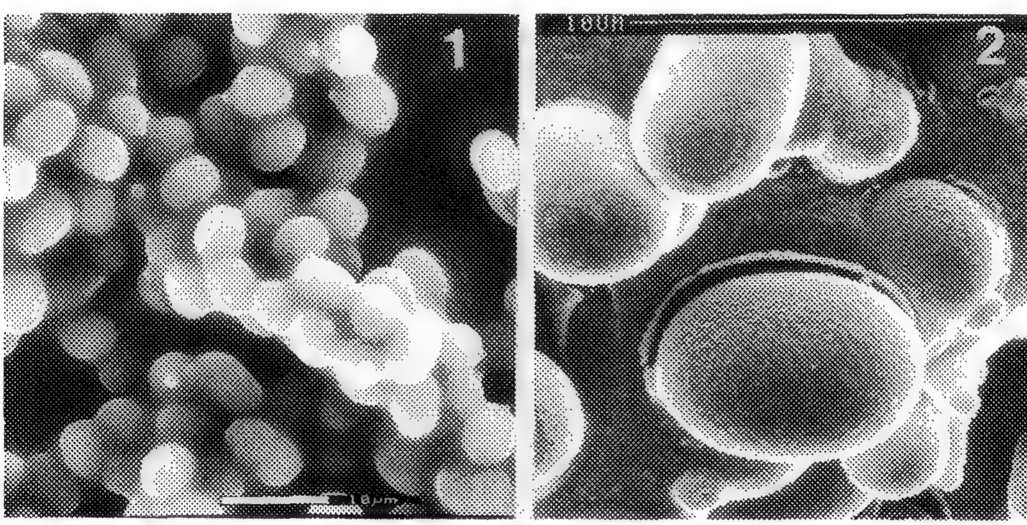

Figure 1. ESEM of mushroom spores showing intact extracellular matrix

Figure 2. Cryo SEM of mushroom spores showing partial dehydration of extracellular matrix

'LEAKY VACUUM' SEM FOR MATERIALS SCIENTISTS

A. Horsewell, C.C. Appel and J.B. Bilde-Sørensen

Materials Department, Risø National Laboratory, DK-4000 Roskilde, Denmark

'Leaky vacuum' SEM is carried out at Risø using the Electroscan™ E-3 Environmental SEM and the low vacuum JEOL 5310 LVSEM. In our laboratory, a wide variety of materials problems has led us to develop several novel 'leaky vacuum' SEM methods which will be described here; a) in-situ fracture mechanics experiments, b) utilization of charge contrast to characterize local conductivity of insulators, c) removal of beam skirting error in energy dispersive X-ray analysis.

In-situ fracture-mechanics experiments

Crack tip processes in non-conducting materials such as ceramics and polymer composites cannot be observed in the conventional SEM because the vacuum deposited conductive coatings peel away around the edges of the growing cracks. Charge prevention is readily achieved in the ESEM through ionization of the 5-10 torr atmosphere around the specimen surface. Not only is the large specimen chamber convenient for special rigs, but the poor vacuum means low demands on the rig construction with respect to out-gassing of lubricants, strain gauges and electrical monitors.

For in-situ crack growth studies we use a specially designed tension / compression / 4-point bending rig which is capable of applying loads of up to 1000 N. To measure crack growth resistance we have developed a double cantilever beam loaded by pure moments. This allows growth of stable cracks of several centimetres in length even in very brittle materials. We measure applied load while concurrently observing and measuring crack tip opening, crack opening mode and crack wake effects such as bridging and friction. In composite materials, laminates and layered structures, the majority of testing is carried out on plane polished cross-sectional surfaces in which contrast arises from differences in SE yield between the constituents of the specimens. The observations provide invaluable input to fracture mechanics modelling[1].

Charge contrast characterization in non-conductors

When poor conductors are imaged in the SEM, electron beam charging occurs when a fraction of the injected charge leaks away too slowly and causes a build-up of surface potential. It is therefore usual to coat specimens by sputtering with carbon or gold. For uncoated poorly conducting specimens as typically used in 'leaky vacuum' SEMs, local differences in the electrical conductivity of the specimen can cause variations in electrical potentials at the specimen surface. These local differences in electrical potential can in turn cause local differences in the collection of the low energy, secondary electrons.

The basic considerations for the creation of the initial local variations in surface potential build-up in poorly conducting specimens are unchanged in the ESEM as compared to the SEM. Differences do occur, however, in the mechanisms of dissipation of the surface charges. Two mechanisms of charge dissipation occur in the ESEM. The first is direct charge neutralization from the cloud of ionized gas molecules and water vapour which is concentrated between the specimen and the gas amplification detector. Charged areas of the specimen surface attract oppositely charged gas ions in suitable quantities for charge neutralization. Secondly, ionized gas molecules provide a path for the leakage of charge build-up to a nearby electrical ground connected to the specimen stage.

An example of the use of this type of direct characterization of electrical conductivity in ceramics by ESEM arises in materials for Solid Oxide Fuel Cells. These fuel cells consist of porous

electrodes on both sides of the fully dense ceramic electrolyte. The anode is a cermet composite consisting of roughly equal parts of zirconia, Ni-metal and pores. The ceramic and metal phases have almost identical backscatter coefficients and are therefore impossible to distinguish from each other by contrast differences in the BSE signal. We can however use the SE signal in the ESEM to characterize the material. The zirconia is electrically insulating whereas Ni is a good electrical conductor. When the pressure in ESEM is adjusted to be just too low to prevent charging of the zirconia, areas which do begin to charge will appear bright with respect to non-charging areas; it is thereby possible to get an image of the electron conductive path in the cermet[2]. This method has also been used to image grain boundaries in a plane polished zirconia sample. Here, a gas pressure was chosen to just produce charging in the grains. Since there was no charging at the more conductive, impurity containing grain boundaries, they became visible.

Beam skirting error-correction in energy dispersive X-ray analysis

Characterization of materials in the ESEM and LVSEM often involves chemical analysis by energy dispersive X-ray spectrometry. However, a major problem has been that the spatial resolution of energy dispersive X-ray spectroscopy (EDS) is strongly degraded by the presence of gas in the specimen chamber because the gas scatters the primary electrons on their way from the last pressure limiting aperture towards the sample. To illustrate the extent of the problem we note from the work of Bolon[3] that 45% of the electron beam was scattered beyond 25μm in an ESEM operated at 3 torr water vapour pressure with an acceleration voltage of 30 kV and a working distance of 15 mm. The skirting effect is of course minimized by working at the lowest possible pressure and working distance, but this may not be practicable and may still not lead to acceptable spatial resolution of the X-ray analysis. Two correction methods have been suggested and used successfully in our laboratory[4]: one is termed the 'beam stop method' and will be described here. The other method, termed the 'pressure variation method' utilizes changes in skirt geometry with gas pressure and is described in more detail elsewhere.

The 'beam stop method' requires the insertion of a fine needle of a known element, which is not present in the sample, into the beam path just above the specimen surface at the point of analysis. The EDS spectrum which results consists of the spectrum from the known element of the needle (typically Pt or W) plus the spectrum created from the skirt of the scattered primary electron beam. A spectrum obtained without the needle yields the spectrum that would have been obtained in high vacuum plus the spectrum from the skirt of scattered electrons. Clearly, the pure spectrum may then be obtained by removing the characteristic peaks of the known element from the first spectrum and finally subtracting the remaining spectrum from the second spectrum. The method may be adapted for line scans by replacing the beam stop needle by a beam stop foil close to the specimen surface. Here, line scan spectra are obtained, one close to the edge of the beam stop foil in the specimen and one along the beam stop foil. Skirt contributions are so large that the two spectra will contain almost the same information from the skirt; subtraction once again yields the pure line scan spectrum.

References

1. A. Horsewell, B.F. Sørensen & O. Jørgensen (1995) Proc. 7th Int Conf on Intergranular and Interphase Boundaries in Materials, Lisbon, June 26-29, 1995. Materials Science Forum. *In print.*
2. C.C. Appel, A. Horsewell (1995) Proc. 47th Annual Meeting of the Scandinavian Society for Electron Microscopy, Trondheim, Norway, June 12-14, 1995, pp. 50-51.
3. R.B. Bolon (1991) Microbeam Analysis, (D.G. Howitt, ed.) San Francisco Press, 199-200.
4. J.B. Bilde-Sørensen, C.C. Appel (1996) Proc. 48th Annual Meeting of the Scandinavian Society for Electron Microscopy, Aarhus, Denmark, June 2-5, 1996. *To be published.*
• This work forms part of an ongoing programme within the Engineering Science Centre at Risø for Structural Characterization and Modelling of Materials.

Application of High-Pressure Scanning Electron Microscopy (ECO-SEM) in Forensic Sample Analysis

Thomas A. Kubic, MS, JD, and JoAnn Buscaglia, MS***

**AMRAY/ATOMIKA, 160 Middlesex Turnpike, Bedford, Massachusetts 01730-1491*
*** TAKA Analytical Services, Inc., P.O. Box 208, Greenlawn, New York 11740-0208.*

Traditionally to obtain satisfactory images and reasonable resolution with a Scanning Electron Microscope (SEM), it has been necessary to employ a high vacuum within the sample chamber.

High vacuum can result in the dehydration of materials with an alteration of sample morphology and in some cases the introduction of artifacts. In such an environment, samples that are non-conductive experience extensive charging with image degradation. Samples of forensic concern, such as textile bundles or swatches, exhibit this problem even after the application of metal coating. The problem is even more pronounced when carbon coating is used, as is often the preference of forensic microscopists in order to simplify interpretation of the EDX spectra.

The commercial availability of "high pressure" or controlled environment SEMs that operate with sample chamber pressures from 50 to 4000 millitorr, while the electron guns and columns are kept at high vacuum conditions have solved these problems. The presence of this "higher" pressure retards dehydration while charging effects are nearly eliminated. Since most forensic applications of SEM-EDX are conducted at magnifications substantially less than 10,000X, high vacuum within the sample chamber is not required.

Quality images are obtained by employing modem detector technology. Elemental analysis is readily performed because excitation energies in the 15 keV range are employed resulting in efficient excitation of most elements.

This paper presents the results obtained on a number of sample types of forensic import, including textile fibers and fabrics, hair, gun shot residue (GSR) and paint. Previously considered difficult samples are shown to be easily analyzed with a minimum of sample preparation. Other advantages of the system in dealing with unclean samples will be explained.

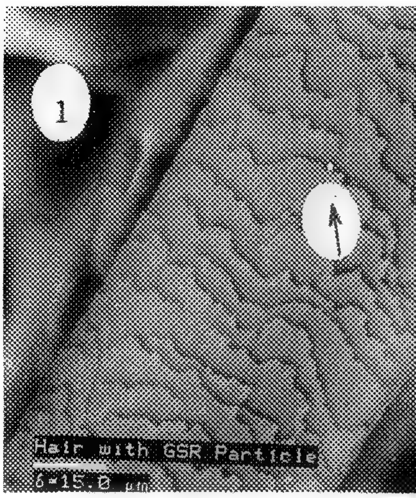

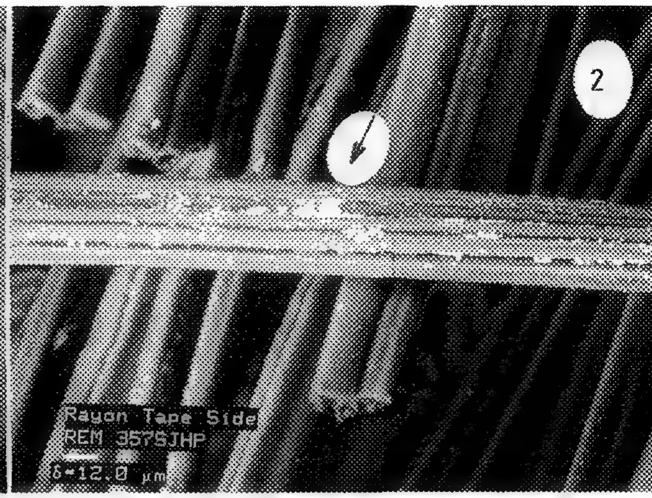

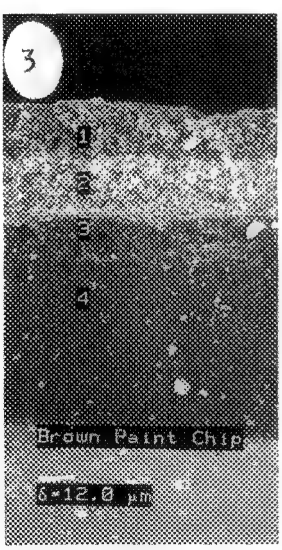

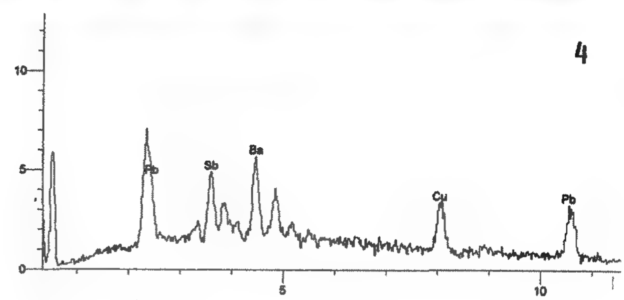

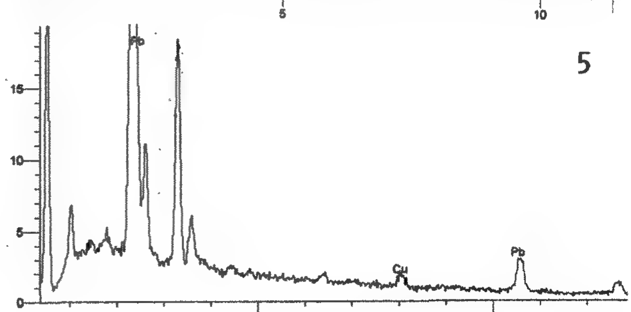

Figure 1 Human Hair with Gun Shot Residue (GSR) particle adhering at scale edge.

Figure 2 Rayon fiber exhibiting bright areas due to "Bullet Wipe".

Figure 3 Multi layer paint chip exhibiting easily discernable average atomic number contrast due to chemical composition differences.

Figure 4 X-Ray spectra of GSR particle (Figure 1)

Figure 5 X-Ray spectra of "Bullet Wipe" (Figure 2)

ENVIRONMENTAL MICROSCOPY OF CAPILLARY STRESS-INDUCED STRAIN BEHAVIOR IN AMBIENT-PRESSURE AEROGELS

Sudeep M. Rao[1], Joshua Samuel[2], Sai S. Prakash[3], C. Jeffrey Brinker[4]

[1] University of New Mexico/Sandia National Laboratories' Advanced Materials Laboratory, 1001 University Blvd., SE, Albuquerque, NM 87106

[2] Ceramic Processing Science Department 1841,

[3] Department of Chemical Engineering, University of Minnesota, 421 Washington Ave., SE, Box 137, Minneapolis, MN, 55455

[4] Ceramic Synthesis and Inorganic Chemistry Department 1846, Sandia National Laboratories, Albuquerque, NM 87185

Ambient pressure silica aerogel thin films have recently been prepared by exploiting reversible drying shrinkage caused by derivatization of the internal gel surface [*1*]. Aerogels have porosities of upto 99.9% and due to the small size of the pores (few nanometers), large capillary stresses are produced in gels that are partially saturated with a wetting liquid. As a result of these capillary stresses, the flexible silica network undergoes strain which has been observed using environmental microscopy. This technique allows variation of the equilibrium vapor pressure and temperature, and a simultaneous monitoring of the deformation of the unconstrained film thickness. We have observed >600% deformation during the pore-filling and pore-emptying cycles. In this presentation, we discuss the unique stress-strain behavior of these films.

Ref.: [*1*] Sai S. Prakash, C. Jeffrey Brinker, Alan J. Hurd & Sudeep M. Rao, "Silica aerogel films prepared at ambient pressure by using surface derivatization to induce reversible drying shrinkage", *Nature.* Vol. 374, 30 March, 1995, 439-443.

This work was supported by the US Department of Energy Basic Energy Sciences Program. Sandia National Laboratories is a US Department of Energy Facility.

Department of Energy Basic Energy Sciences Program. Sandia National Laboratories is a US Department of Energy Facility.

References

1. Sai S. Prakash, C. Jeffrey Brinker, Alan J. Hurd & Sudeep M. Rao, "Silica aerogel films prepared at ambient pressure by using surface derivatization to induce reversible drying shrinkage", *Nature*, Vol. 374, 30 March, 1995, 439-443; Erratum: Nature, Vol. 375, 1995, p 431.

2. Sudeep M. Rao, "http://www.unm.edu/~sudeep/esem.html".

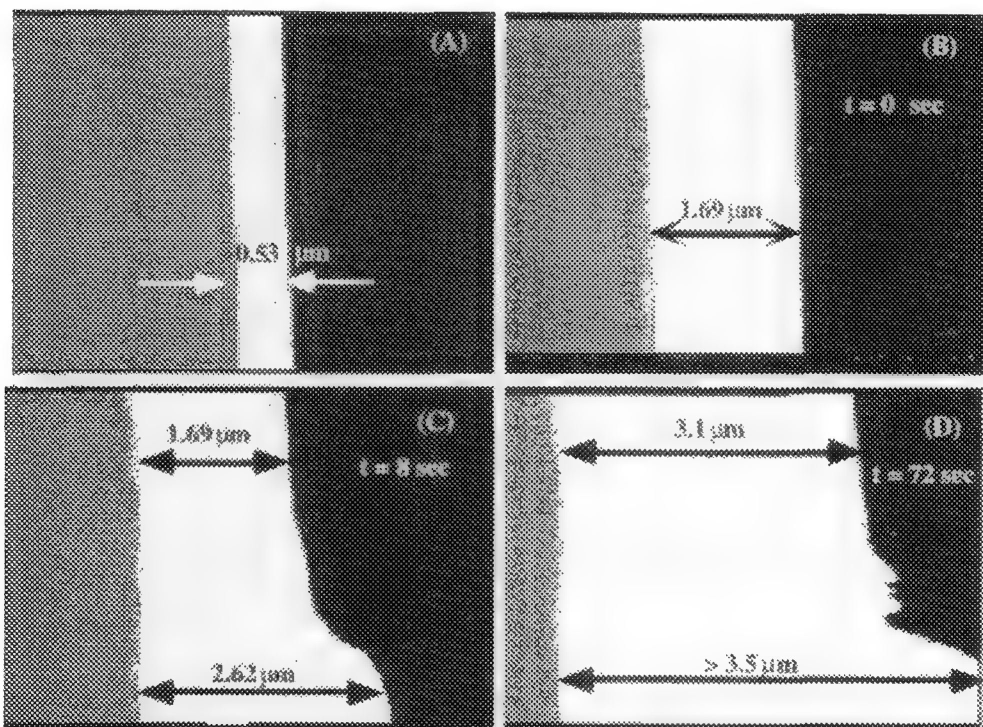

Figure 1. Image 1A shows the ambient pressure silica aerogel film at its minimum thickness of 0.53 μm. Images 1B to 1D show drying of film and the resulting "springback". Images were digitized from video recorded at 7 secs/frame. Grey area is the silicon substrate.

Advanced Applications and Instrumentation for Scanning Probe Microscopy (SPM)

D. A. Grigg

Digital Instruments, Inc.
Santa Barbara, CA 93103

Scanning probe microscopy (SPM) has continued to advance into new applications and disciplines every year. The development of new techniques and instrumentation for SPM's have enabled researchers to study sample surfaces in a variety of ambient conditions and using a number of contrast mechanisms. A review of new SPM techniques and instrumentation will be presented.

Phase imaging is a new technique that provides nanometer-scale information about variations in surface properties, such as adhesion, friction, viscoelasticity, composition and perhaps others, not revealed by any other single SPM technique. An example using phase imaging to differentiate component phases of composite materials is shown in Fig.1 of wood pulp fiber.[1] The left image is a normal topographic image acquired using the TappingMode™ technique.[2] The right image is the simultaneous phase image. The phase image highlights cellulose microfibrils and a lignin component atop the cellulose component not seen in the topographic image. The details of phase imaging will be discussed.

Until recently, the study of liquid-solid interfaces using atomic force microscopy (AFM) was primarily limited to contact mode imaging. However, contact mode AFM can affect the resolution and image quality of samples, particularly biological samples, due to large lateral forces. TappingMode under liquids has recently allowed the study of sensitive samples with the same advantages as in air. Fig. 2 is a 700 nm image of 400 base pair DNA molecules in a $NiCl_2$ buffer solution on mica.[3] This example demonstrates that a relatively mobile molecule at the solid liquid interface can be easily imaged using TappingMode under fluid.

Other advances in SPM techniques that have recently become available include scanning capacitance microscopy (SCM) and enhanced surface force measurements such as force volume measurements and nano-indentation. Each of these techniques, and others, will be discussed.

The SPM instruments that have been developed to utilize the above techniques have rapidly advanced within the past couple of years. SPM instruments are now built for applications ranging from biological research to semiconductor wafer inspection utilizing wafer handling robots. The second half of this paper will review the past year's improvements in SPM instrumentation from microbiology to metrology.

References

1. Image acquired by D. Chernoff, Advanced Surface Microscopy and sample supplied by D. E. Doro Pereira, Aracruz Cellulose.
2. Q. Zhonget al., Surface Science, 290(1993)L688.
3. H.G. Hansma et al., Biophysical Journal, V68 N5(1995)1672.

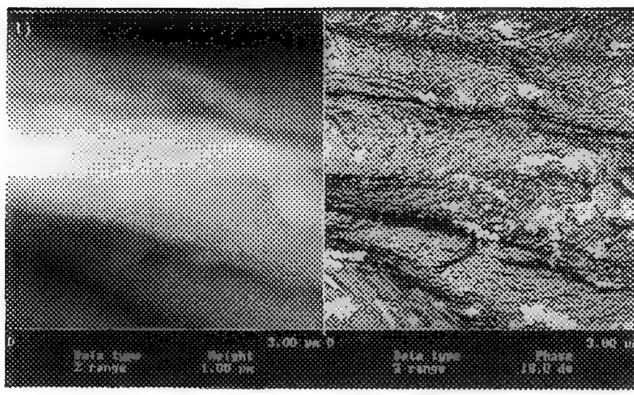

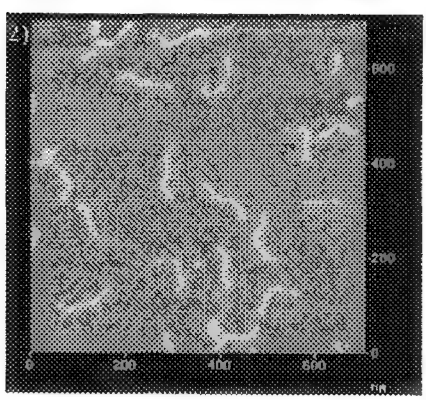

FIG. 1. Phase (right) and TappingMode (left) images of wood pulp fiber. The phase image highlights cellulose microfibrils. In addition, a lignin component appears as light areas in the phase image, but not apparent in the topography image. 3μm scan.[1]

FIG. 2. 700 nm TappingMode under fluid image of 400 base pair DNA molecule in $NiCl_2$ buffer solution on mica.[2]

TIP-SAMPLE FORCE INTERACTION AND SURFACE LOCAL HARDNESS IN STM AND AFM IMAGING

M.-H. Whangbo,[a] H. Bengel,[b] and S. N. Magonov [c]

[a] Department of Chemistry, North Carolina State University, Raleigh, North Carolina 27695-8204

[b] Freiburger Materialforschungszentrum, Albert-Ludwigs Universität, D-79104 Freiburg, Germany

[c] Digital Instruments Inc., 520 E. Montecito St., Santa Barbara, California 93103

STM and AFM images of various layered inorganic compounds, organic conducting salts and polymers were examined to assess the role of the tip-sample force interaction in scanning probe microscopy. To a first approximation, the AFM image of a sample surface is described by the total electron density plot $\rho(r_0)$, and the STM image by the partial electron density plot, $\rho(r_0, e_f)$.[1,2] In these calculations, the structures of the surface layers are taken from the bulk crystal structures, so that a surface deformation induced by the tip force is neglected.

During the scanning in STM and AFM measurements, a sample surface often undergoes a geometry relaxation due to the tip-sample force interactions. As depicted in Fig. 1a, the macroscopic deformation of a sample surface caused by the tip force is explained in terms of classical theories in which the interacting solids are treated as materials with uniform density distributions. For a surface with several different chemical environments, the extent of the surface atom depression is determined by the local hardness. This introduces an atomic scale corrugation into the macroscopically depressed surface (Fig. 1b), and such a tip-force induced corrugation is detected with STM and AFM. The variation of the surface local hardness in layered compounds can originate from the atomic arrangements within each layer and/or from those between adjacent layers.

To estimate a possible surface reconstruction, a systematic study of AFM images with different applied forces is desirable. Force-dependent AFM contrast changes exhibit the local hardness variation of the surface, from which one can guess the deformed surface structure. In AFM imaging with tip forces of several hundreds nN, the surface deformation is expected to be similar to that found in ambient-condition STM measurements. The knowledge of atomic scale surface relaxation obtained from AFM and STM experiments is critical in understanding the mechanical properties of materials in nanometer scale.

References

1. S. N. Magonov, M.-H. Whangbo, *Surface Analysis with STM and AFM*, **1996**, VCH, Weinheim.
2. S. N. Magonov, M.-H. Whangbo, *Adv. Mater.* **1994**, *6*, 355.
3. The work was supported by the Office of Basic Energy Sciences, Division of Materials Sciences, U.S. Department of Energy, under Grant DE-FG05-86ER45259 and also by Alexander von Humboldt Foundation.

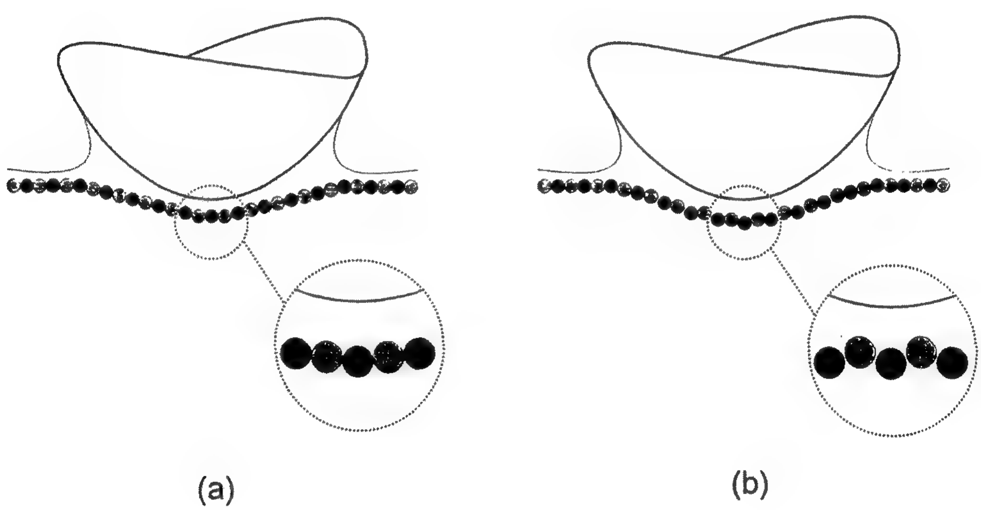

Figure 1. Schematic representation of the surface deformation induced by the tip force: (a) The presence of chemically non-equivalent atoms on the surface is ignored in the macroscopic deformation. (b) Under the tip force, the "hard" atomic sites of the surface are depressed less than the "soft" atomic sites leading to an atomic-scale surface corrugation. Under ambient condition, the tip-force is transmitted to the sample surface through the liquid contamination layer.

CORRELATION OF FILM STRESS AND THE MECHANICAL RESPONSE OF Au THIN FILMS

K.F. Jarausch,* J.E. Houston** and P.E. Russell*

*Materials Science Department, North Carolina State University, Raleigh NC 27695-7918
**Department 1114, Sandia National Laboratories, Albuquerque NM 87185

The investigation of the mechanical properties of nanostructured materials is critical to the continuing development of thin film technology. For example, the semiconductor industry must understand how stress and strain effect the electronic properties of superlattices and cause the delamination of metal interconnect films. A variety of nano-indentation techniques have been developed as tools to investigate the mechanical behavior of thin films.[1] In a previous study the interfacial force microscope (IFM)[2] was used to survey the mechanical response of 200nm thick Au films deposited on various substrates under various deposition conditions.[3] By combining the methods of contact mechanics and classic indentation techniques, quantitative investigations of the effective elastic modulus and the maximum shear-stress at the plastic threshold were tabulated. The results indicated a large variation in these parameters for the various film/substrates, while the values were consistent over a single film/substrate. The observed variation could be explained by several factors: differences in the films' morphology, adhesion to the substrate, or residual stress. In this paper we describe an investigation of the mechanical response of similar Au thin films as a function of residual and imposed film stress.

In the earlier work, 200nm thick polycrystalline Au films were prepared by thermal evaporation onto clean 300C glass and mica substrates at a rate of 0.2nm/sec, and by e^--beam evaporation at 0.5nm/sec onto 25C Si substrates which had been coated with 20nm adhesion layers of Cr or Ti. The Au films were coated with self-assembling monolayer films which passivate the adhesive interaction between the W probe and Au surface, thereby allowing the direct application of contact mechanics to analyze the deformation response.[4] A single crystal <111> Au surface was prepared in the same manner as a reference for comparing the thin film properties to bulk properties. All of the measurements were taken with the same IFM sensor and 200nm W probe.

We illustrate the procedure for analyzing the values of elastic modulus and shear-stress threshold for plastic deformation with the typical loading-cycle shown in Fig. 1 (taken on <111> Au). In region 1 no hysterisis for peak loads less than ≈44μN was observed and no change in the film's morphology was evident in the subsequent image. For this region of the loading-cycle, the relationship between load and deformation closely follows the classical Hertzian model for a rigid, non-interacting parabolic punch deforming an elastic half space.[5] The Hertzian model is fitted in this region and plotted as the dashed line (in Fig. 1) for comparison. The effective elastic modulus was determined from this fit. The point at which the loading curve deviates from Hertzian behavior (≈44μN) marks the onset of plastic deformation (region 2). The maximum shear-stress threshold for plastic deformation was calculated from this transition point.

Previous analysis of 200nm thick Au films demonstrated the consistency of the measurement technique from location to location on a film/substrate, or sample, as is illustrated in Table 1.[3] Although consistent for an individual sample, the average values of effective elastic modulus and shear-stress threshold were found to vary by as much as a factor of three from sample to sample. Despite this variation, the ratio of the latter to the former was nearly identical, at a value of 4%, for all samples. In addition, it was found that the deformation to the plastic threshold was approximately 11nm for all the samples and substrates suggesting that the mechanical response of Au remained very consistent. Note also that the data in Table 1 did not identify a dependence of the variation on the films' morphology, or adhesion to the substrate.

In recent experiments the mechanical properties of similar 200nm thick Au films on Ti and Cr coated Si substrates were compared. With identical thicknesses, grain sizes, and roughnesses, the films differed only in their adhesion layer and residual stress. The residual film stress was evaluated using a commercial laser scanning technique[6] which measures the change in wafer curvature caused by the application of a thin film. The Au/Ti/Si sample was measured to have tensile residual stress (≈+140MPa) while the Au/Cr/Si was compressive (≈-325MPa). The IFM measurements of effective elastic modulus and shear-stress threshold appear to correlate with this difference in residual stress (48,2.1 and 110,4.5 respectively as compared to Au <111> with 70,2.9 where these values are expressed in GPa).

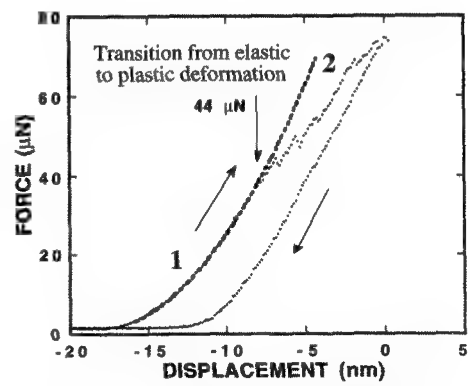

FIG. 1 - A typical loading-cycle curve taken on and Au <111> sample. The dashed line represents the fit based on the Hertzian model for a parabolic punch deforming an elastic half space.

Experiments are now underway to isolate the contribution of film stress to the mechanical response of Au thin films. A diaphragm device has been built with which it is possible to mechanically and controllably change the stress-state of the film. In this way the IFM measurements of effective elastic modulus and shear-stress threshold are correlated directly with the stress, while the film's morphology and adhesion to the substrate remain constant. The observed dependence of the mechanical response on stress will be discussed in terms of possible mechanisms, identifying just how the stress alters the measurement process and causes the variation of the films' mechanical response. These experiments suggest that the IFM has a potential for being able to measure residual thin-film stress on a very local level which could prove critical in controlling both the positive and negative aspects of this important parameter.

Sample	Grain Diameter (nm)	Mean Surface Roughness (nm)	Adhesion to Substrate	Elastic Modulus (GPa)	Threshold Shear Stress (GPa)
Au/Mica	250	5.4	Very Weak	36±5	1.7±0.2
Au/Ti/Si	60	1.8	Strong	48±5	2.1±0.3
Au <111>				70±6	2.9±0.1
Au/Glass	500	4.1	Weak	75±15	2.7±0.5
Au/Cr/Si	150	2.4	Strong	110±19	4.5±0.4

TABLE 1 - Summary of the values for the surface morphology and the mechanical properties of polycrystalline gold films on various substrates, values for Au <111> are included for reference (after Ref.3).

REFERENCES

1. G.M Pharr and W.C. Oliver, *MRS Bulletin*, July(1992)28
2. S.A. Joyce and J.E. Houston, *Rev. Sci. Instrum.*, 62(1991)710.
3. P. Tangyunyong et al, *J. Adhesion Sci. Technol.*, 8(1994)897.
4. R.C. Thomas et al., *Science*, 259(1993)1883.
5. I.N. Sheddon, *Int. J. Eng. Sci.*, 3(1965)47.
6. Flexus Inc., Sunnyvale CA.

SURFACE PHOTOELECTROCHEMISTRY USING NEAR-FIELD SCANNING OPTICAL MICROSCOPY (NSOM)

Patrick J. Moyer

Department of Physics, City University of New York - Brooklyn College, Brooklyn, NY 11210

Near-field scanning optical microscopy (NSOM) has been used to characterize and modify surfaces[1] with lateral spatial resolution as high as 50 nm. Some of these experiments were performed under electrochemical conditions. Progress towards this goal involved several important steps. They include proving adequate operation of the shear force feedback mechanism in liquids[2] and fabrication of appropriate NSOM fiber probes.

With regards to shear force feedback, which is used to maintain the fiber probe within the near field of the sample, there has been ample discussion regarding the physics of the tip-sample interaction. It is important for biological and photoelectrochemical applications that the feedback mechanism operates successfully in liquid environments. Our results indicate that shear force operation in water allows for high spatial resolution NSOM characterization while providing high force sensitivity. When comparing the frequency spectra of the probe resonances in air and water, the water resonance is broadened. The broadened resonance peak when completely immersing the probe in water indicates an increase in damping. Using the forced, damped harmonic oscillator model, this suggests a decrease in the force sensitivity of the probe, which is expected. Figure 1 shows corresponding (top) transmission NSOM and (bottom) shear force topography images of an aluminum pattern on glass. Each image is 5 μm x 5 μm. Of interest is the fact that the NSOM image is of high resolution while the shear force mechanism does not image the pattern. Rather, the force probe appears to be sensitive to contamination on the surface. Imaging the same sample under the same conditions using contact and non-contact mode atomic force microscopy shows clearly the underlying aluminum pattern while showing less sensitivity to the surface contamination.

In order to use NSOM under electrochemical conditions, the standard aluminized fiber probe must be replaced by a less reactive (yet still metal-coated) probe. To this end, we will discuss efforts to fabricate probes with various metal coatings, including chromium and gold. Additionally, some of our electrochemistry experiments prevent us from using conventional glass (SiO_2-based) fibers. Alternative probes will also be discussed.

1. Patrick J. Moyer, Karsten Walzer, and Michael Hietschold, *Appl. Phys. Lett.* **67**, 2129 (1995).
2. Patrick J. Moyer and Stefan B. Kämmer, *Appl. Phys. Lett.*, in press.

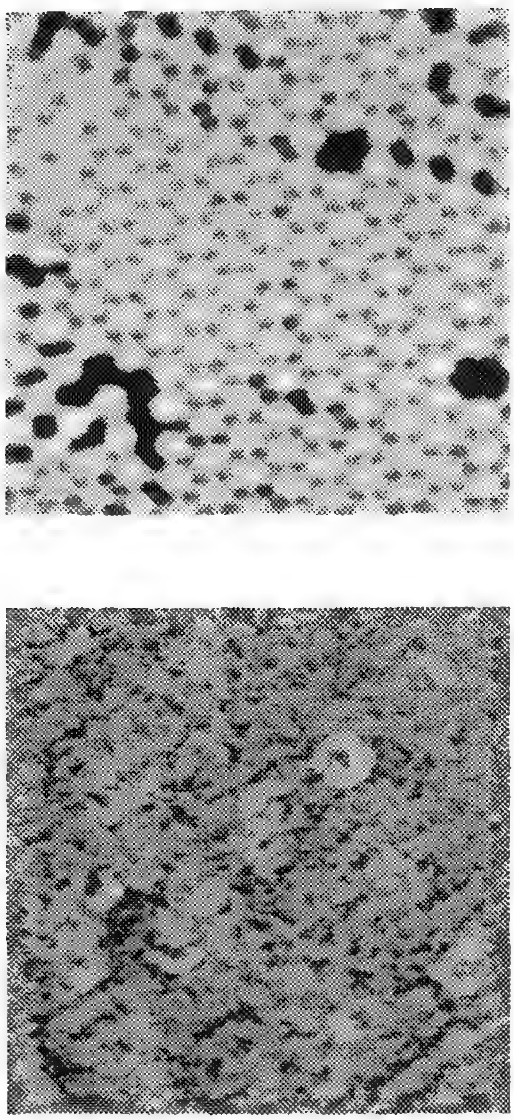

FIG. 1 Simultaneously acquired (top) transmission-mode NSOM image and (bottom) shear force topography images of aluminum pattern on glass obtained while scanning in water. Each image is 5 μm x 5 μm and the total height of the shear force topography image is 75 nm.

Near-Field Scanning Optical Microscopy Imaging of Luminescent Polymers

J. Kerimo,* D. A. Vanden Bout,* D. A. Higgins,* and P. F. Barbara*

*Department of Chemistry, University of Minnesota, Minneapolis, MN

Conjugated polymers such as poly(*p*-pyridyl vinylene)(PPyV) have interesting photoluminescence and electroluminescence properties. These polymers have a high quantum yield of luminescence and are of great practical importance as light-emitting diodes or organic semiconductors.[1] We have performed studies on thin films(about 50nm) of these polymers using the high spatial optical resolution of NSOM.

The luminescent polymer film was excited with 488nm light and the fluorescence was collected with a high numerical aperture microscope objective. Topography and NSOM fluorescence images were collected simultaneously and used for studying the morphology and optical properties of the film. An example of topography and fluorescence NSOM images of the film is shown in Fig. 1a. The films are very flat (2nm rms variations in topography) and have very few features. The NSOM fluorescence image shows great film inhomogeneity with bright features varying in size from 80-250nm observed throughout (Fig. 1b). These features do not correlate with the topography, indicating they may be located in the bulk of the polymer or are simply not resolvable in the topography image.

We have also done polarization-dependent fluorescence NSOM where linearly polarized fluorescence was collected. Two images of orthogonal polarizations were collected simultaneously and are shown in Fig. 2. The two polarization images show features that are emitting linearly polarized fluorescence which is evidence of ordered and oriented domains. The domains are due to aggregation of the luminescent polymer chains in the thin films which has also been proposed by other workers.[2] Further evidence for aggregation comes from transmission images at 488nm where similar features were observed. We also performed transmission imaging at 488nm on a non conjugated polymer (poly(4-vinyl-1-methyl pyridinium Bromide) film of a similar thickness. These nonluminescent films showed only uniform images with no evidence of domains. We concluded that the aggregation is intrinsic to the PPyV polymer film and not an artifact that may have been introduced by the NSOM imaging.

1.M. Aldissi Editor, *Intrinsically Conducting Polymers: An Emerging Technology*, Nato ASI Series, Kluwer Academic Publishers, Boston (1993).

2. U. Lemmer et al., *Chemical Physics Letters*, 240(1995)373-378.

3. The authors gratefully acknowledge Dr. Epstein and Jim Blatchford for providing the samples. This work was funded by the ONR.

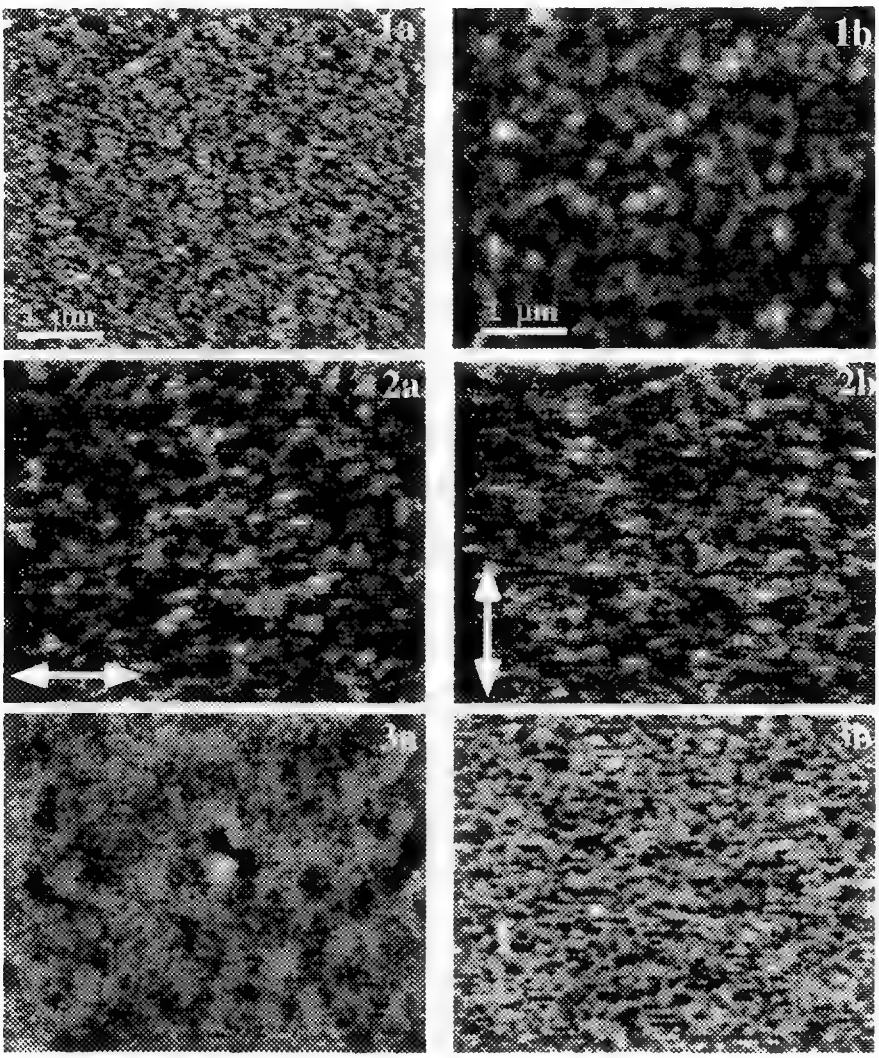

Fig. 1 The topography of the PPyV is less than 10nm in Fig. 1a and the corresponding NSOM fluorescence image is shown in Fig. 1b, and notice the domains are easily observed in the NSOM image but not on the topography image.
Fig. 2 The linearly polarized fluorescence of the PPyV film was collected in the noted directions. Note that the images are very different from each other indicating the orientation and order of the domains
Fig. 3 Transmission images at 488nm of the PPyV fim (Fig 3a) and a nonluminescent polymer film (Fig 3b) of similar thickness(50 nm).

POLY(3-ALKYLTHIOPHENE) MEMBRANES FOR GAS SEPARATION

I. H. Musselman,* L. Washmon,* D. Varadarajan,* B. J. Tielsch,** J. E. Fulghum**

*Programs in Chemistry, The University of Texas at Dallas, Richardson, TX 75083-0688
**Chemistry Department, Kent State University, Kent, OH 44242

The separation of gases is a commercial process conducted primarily via cryogenic distillation. An alternative method involves the use of solvent cast polymer membranes. Unlike distillation, membrane processes are energy efficient, easy to scale-up, and require only electrical energy in their operation.[1] Current membrane separation applications include oxygen or nitrogen enrichment of air, the separation of carbon dioxide from natural gases, and the recovery of hydrogen from refinery and purge streams.[2] In our laboratory, gas separation membranes are being developed based on conducting, soluble and processable polymers such as poly(3-n-alkylthiophene)s. The chemistry of these membranes is being altered by changing the R group (e.g. octyl, dodecyl), the oxidation state, and by incorporating zeolites and molecular sieves to facilitate gas transport.[3] An important aspect of this project concerns establishing the relationship(s) between the structure of poly(3-alkylthiophene) membranes and their bulk properties, specifically permeabilities and selectivities for various gases. It is anticipated that this understanding will help to elucidate the mechanism by which gas separation occurs in these membranes. The use of microscopy and surface and microanalysis methods to characterize membrane morphology, microstructure and chemistry is clearly critical to the project.

The measurement of membrane permeability and selectivity depends on being able to reproducibly cast membranes so that multiple measurements can be made and on knowing the membrane thickness. Poly(3-octylthiophene) (POT) and poly(3-dodecylthiophene) (PDDT) membranes are cast onto glass substrates (Accu-Lab™ Jr. Drawdown Machine) using sonicated solutions of 10% w/w polymer in tetrachloroethylene. Membrane thickness and surface roughness are measured by light microscopy (LM) (Wild-Leitz Ergolux) and TappingMode™ atomic force microscopy (TMAFM) (Digital Instruments, Inc.), respectively. POT and PDDT membranes were found to be of uniform thickness, 21.7 ± 0.7 µm and 17.1 ± 0.6 µm, respectively, in the center 3.5 cm of each membrane (Fig. 1). This extent of uniformity exceeds the 2.5 cm diameter membrane requirement of the permeation cell. The average root-mean-square roughness (R_{rms}) value, measured from 4 samples taken from the center portion of 5 identically prepared POT membranes, was 0.7 ± 0.1 nm. Based on these results, the casting technique was determined to be reliable and reproducible.

The microstructure and surface chemistry of PDDT membranes in the neutral, oxidized (1 hr in 1% w/w solution of $NOBF_4$ in dry acetonitrile) and reduced (0.5 hr in 10% w/w solution of H_2NNH_2 in water) states were investigated by LM, scanning electron microscopy (SEM) (Philips XL30), and TMAFM and x-ray photoelectron spectroscopy (XPS) (Kratos Axis HS), respectively. The neutral membrane surface was defect-free (Fig. 2a) and able to withstand the oxidation (Fig. 2b) and reduction (Fig. 2c) processes. For neutral PDDT, XPS revealed the presence of C, O, and S (thiophene) as well as small amounts of F, Cl and Si. The Cl is consistent with the presence of anhydrous ferric chloride ($FeCl_3$) used in the polymerization reaction. The F is difficult to identify based on a weak signal. The Si could be a siloxane or silicone (both common contaminants) although a non-stoichiometric silicon oxide is also possible. In contrast to the neutral membrane, TMAFM revealed raised features 10 to 20 nm in height on the surface of the oxidized membrane (Fig. 2b). The presence of such nm-scale features were not recognized by the traditional microscopy techniques LM and SEM. Possible contributions to these features include residual oxidant or physical changes to the polymer surface. XPS showed the presence of N, B and F, in addition to the elements detected for the neutral membrane. This new chemistry is consistent with the oxidizing agent, however, it is expected that BF_4^- is distributed uniformly through the membrane. Interestingly, a similar structure has been observed for vapor deposited polythiophene films subjected to alternate

oxidationchemistry.[4] Angle-dependent XPS is in progress to determine whether, in fact, the raised features are due to the presence of residual oxidant. TMAFM revealed a smooth surface for the reduced PDDT membrane (Fig. 2c). As expected, XPS spectra exhibited much lower levels of the oxidant.

Initial data indicates good reproducibility of gas permeability and selectivity. Neutral PDDT provides O_2 to N_2 selectivity of 2.49.

Microscopy and surface analysis results will be presented which establish the structure-function relationships present in these polymer membranes. It is anticipated that these relationships will help to elucidate the mechanism by which gas separation occurs. Knowledge of this mechanism will greatly aid in the design and tailoring of membranes for use in specific separation applications.

References

1. J. L. Humphrey, *Chemical Engineering Progress*, October 1995, 31.
2. W. J. Koros, *Chemical Engineering Progress*, October 1995, 68.
3. I. H. Musselman, K. J. Balkus, Jr., J. P. Ferraris, L. Washmon, D. Varadarajan, M. Hmyene, J. DeRouchey, S. J. Riley, manuscript in preparation.
4. T. R. Dillingham et al., 42nd National Symposium of the American Vacuum Society, Minneapolis, MN, October 16-20, 1995, poster presentation.
5. This research is funded by DOE Pittsburgh Energy Technology Center DE-FG22-94PC94222.

1

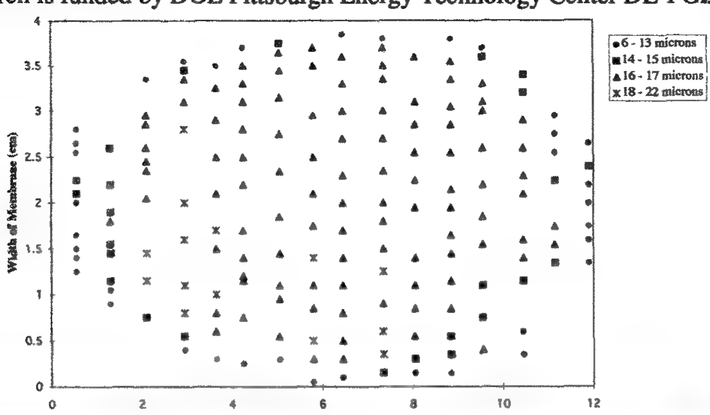

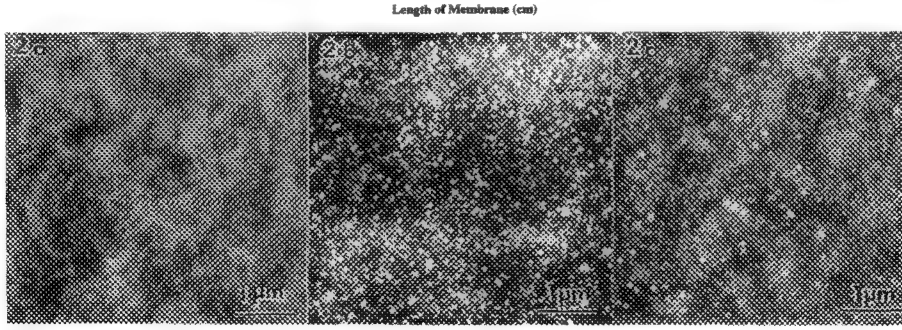

FIG. 1 Thickness map for 10% PDDT membrane.
FIG. 2 TMAFM images (5 x 5 μm) of (a) neutral (b) oxidized and (c) reduced PDDT membranes.

ATOMIC FORCE MICROSCOPY STUDIES OF MICROSTRUCTURE AND PROPERTIES OF SELF-ASSEMBLED MONOLAYERS

J. F. Richards,* E. B. Troughton,** R. A. Dennis** and P. E. Russell*

* Materials Science and Engineering, Box 7907, North Carolina State University, Raleigh, NC 27695

**Lord Corporation, 405 Gregson Drive, Cary, NC 27511

Self-assembled monolayers are unique structures and have received considerable attention from microscopists seeking to image the predicted molecular level structure. More recently, practical engineering applications of SAMs have been proposed in areas ranging from corrosion barriers to adhesion promoters to lithographic resists.[1] While some of the applications of interest, most notably the lithographic resists, can be developed on substrates close to the ideal; such as single crystal Si wafers or thin epitaxial films; many others will require the coating of very non-ideal surfaces. These may range from materials such as Al or ferrous based metals to engineering polymeric materials. In this study we have taken a two-pronged approach to develop reliable systematic atomic force microscopy (AFM) techniques for the determination of both microstructure and properties of SAMs on various substrates of interest.

We have chosen to investigate n-alkanethiols ($SH\text{-}(CH_2)_{n-1}\text{-}CH_3$) on single crystal gold as our reference system for technique development. This is due to the relative simplicity of the system, combined with the large literature base of research into the preparation and characterization of the thiol-Au system.[2] Previously reported scanned probe microscopy studies on this system have included both scanning tunneling microscopy (STM) and contact mode AFM. Although there are some discrepancies in the published data, most authors find that it is possible to image the molecular order of the SAM for chain lengths ranging from 4 to 15. There are several questions we have chosen to address based on previous works. One is based on the importance of imaging force, whether in STM or contact mode AFM. It appears that the molecular structure of the SAM itself can be imaged at sufficiently low force, whereas at high forces, the gold lattice can be imaged through the SAM (or with the SAM pushed away by the tip). The interesting aspect is that upon returning to low force conditions, the larger SAM structure is again observed; i.e.. the process is completely reversible.[3] Thus, the tip sample interaction is clearly capable of modifying the observable structure during imaging and needs to be well characterized before extension of the technique to more complex or unknown structures. We have chosen to characterize the effects of the experimental parameters in contact mode AFM, and to extend this to Tapping Mode, or intermittent contact mode, AFM.[4] For the thiol-Au system, the only sample parameter varied is the carbon chain length, which was varied from one (the sulfur-methyl case) to greater than 14. The choice of tip material (Si versus Si_3N_4, coated versus uncoated) plays a major role, particularly in the adhesion forces involved in imaging.[5] The largest set of parameters can best be described as imaging parameters. For contact mode AFM these include: force magnitude and direction (repulsive versus adhesive; lateral versus normal), feedback signal and gains, scan rate and direction, and monitored signal (feedback error, z-axis change, or lateral force). For the intermittent contact mode, additional parameters of cantilever resonant frequency, drive frequency and amplitude, feedback mode (amplitude, phase or frequency), and the phase shift as an additional imaging signal are added.

The other prong of this project is based on imaging of the more complex and less studied SAM system of alkyl phosphates on Al (with the native oxide). This system is more representative of commercially interesting SAMs than the thiol-Au system; but with much less known about it from previous investigations. In the phosphate on Al system the phosphate monolayer self-assembles on a thin film of oxide on Al, thus allowing for chemical bonding quite different from that of a noble metal such as gold. We use Al thermally evaporated onto glass slides in moderate vacuum. Several questions about this system are being addressed. One is the effect of the Al surface properties (i.e. roughness, grain size,

grain structure) on the assembly and conformity of the monolayer. As in the thiol-Au system, the effects of varying chain length on microstructure and properties is also being investigated. An interesting parameter which appears to be playing an important role in the self-assembly process is time. (i.e.. How long the substrate remains in the phosphate solution for coating). This system also exhibits an interesting structure on the 10 to 100nm scale (dependant on chainlength) in addition to the expected molecular structure. An example of this is illustrated in Fig. 1. These studies allow us to not only better understand the structure and properties of the SAMs, but also to better understand and control the tip-sample interactions and optimization of the imaging process. This understanding is allowing us to begin local mechanical modification and mechanical property measurements using the AFM probe.

References

1. H. Sellers, A. Ulman, Y. Shnidman, J. E. Eilers, *J. Am. Chem. Soc.*, 115(1993)9389-9401.
2. Schonenberger, C.; Jorritsma, J.; Sondag-Huethorst, J.A.M.; Fokkink,L. G. J. *J. Phys. Chem.* 99(1995)3259-3271.
3. Gang-yu Liu, Miguel B.Salmeron, *Langmuir*, 10(1994)367-370.
4. W. A. Ducker, R.F. Cook, D.R. Clark, *J. Appl. Phys.*, 67(1990)4045
5. Ross C. Thomas, J. E. Houston, Richard M. Crooks, Taisun Kim, Terry A. Michalske, *J. Am. Chem. Soc.*, 117(1995)3830-3834

FIG 1 - AFM phase image of a dodecyl-phosphate layer on Al (with the native oxide) (1μm x 1μm).

SURFACE ROUGHNESS MEASUREMENTS OF VANADIUM-CONTAMINATED FLUIDIZED CRACKING CATALYSTS BY ATOMIC FORCE MICROSCOPY

H. Kinney*, M.L. Occelli** and S.A.C. Gould***

*Claremont McKenna College, Claremont, CA 91711
**Georgia Tech Research Institute, Atlanta, GA 30332
***Keck Science Center, Claremont Colleges, Claremont, CA 91711-5916

For this study we have used a contact mode atomic force microscope[1,2] (AFM) to study to topography of fluidized cracking catalysts (FCC), before and after contamination with 5% vanadium[3]. We selected the AFM because of its ability to well characterize the surface roughness of materials down to the atomic level. It is believed that the cracking in the FCCs occurs mainly on the catalysts top 10-15 μm suggesting that the surface corrugation could play a key role in the FCCs microactivity properties. To test this hypothesis, we chose vanadium as a contaminate because this metal is capable of irreversibly destroying the FCC crystallinity as well as it microporous structure. In addition, we wanted to examine the extent to which steaming affects the vanadium contaminated FCC. Using the AFM, we measured the surface roughness of FCCs, before and after contamination and after steaming.

We obtained our FCC (GRZ-1) from Davison. The FCC is generated so that it contains and estimated 35% rare earth exchaged zeolite Y, 50% kaolin and 15% binder. Three groups of dried FCCs were prepared, a control group and two groups contaminated by a solution of vanadyl naphthenate in toluene. Both vanadium rich FCC groups were calcined at 540° C for 10 hours, however one group was then steamed at 760° C for 5 hours with 100% steam. Microspheres from all three groups were sprinkled onto a steel disk which had been covered with a thin film of epoxy and placed in the microscope. Table 1 lists mean surface roughness for each of the three groups. Figures 1-5 show some key features our results.[3,4]

The data from the uncontaminated FCCs (Fig. 1) showed a surface that is extremely rough. We found the clay mixtures produces large pits and crevices, often on the order of several microns deep (Fig. 1). We saw numerous examples of large pits with jagged terraces 200-300 nm in height which could act as possible docking sites for hydrocarbon chains. Table 1 shows the mean surface roughness (Rms) of 287 [nm] on the 5x5 [μm] images. The surface was also covered with large oval shaped platelets, 100-200 nm in length and 30-50 nm in width. At the finest detail, we were occasionally able to image the surface with atomic resolution.[3,4]

The data from the vanadium contaminated FCCs (Fig. 2-5) showed what appeared to be islands of and coatings of vanadium. The valleys and crevices found in the control group data appear to be filled including the channels that were found between platelets. Table 1 shows only slight differences (105.5 [nm] vs. 80.5 [nm] on the 5x5 [μm] images suggesting that while the steaming may decrease surface roughness, overall, the vanadium is the largest contributing factor to reducing the surface corrugation. Since Vanadium is known to reduce the catalytic activity of FCCs, its presence within the pores of the FCCs suggests the contamination physically blocks the openings into the microsphere where the catalysis occurs.[5]

References

1. G. Binnig, C.F. Quate, Ch. Gerber, ***Phys. Rev. Lett.***, **56**,930 (1986).
2. Nanoscope III, Digitial Instruments, Santa Barbara, CA.
3. M.L. Occelli, S.A.C. Gould, and B. Drake, ***Proc. Int. Congr. on Advances in FCC,*** Amer. Chem Soc. 1994, pg 271.
4. S.A.C. Gould and M.L. Occelli, ***Proc. Microscopy and Microanal.*** (1995) 424.
5. The authors would like to thank the W.M. Keck Foundation (H.K.) and Digital Instruments of Santa Barbara, CA (SACG) for their contributions to this study.

Table 1: Mean surface roughness and standard deviationof 5μm x 5μm images for 3 types of FCC

Surf. type	R_{max}(μm)	R_a(μm)	R_q(μm)
FCC	2.33	0.283	0.243
FCC w/V	1.28	0.1055	0.093
FCC w/V & steamed	1.16	0.0805	0.068

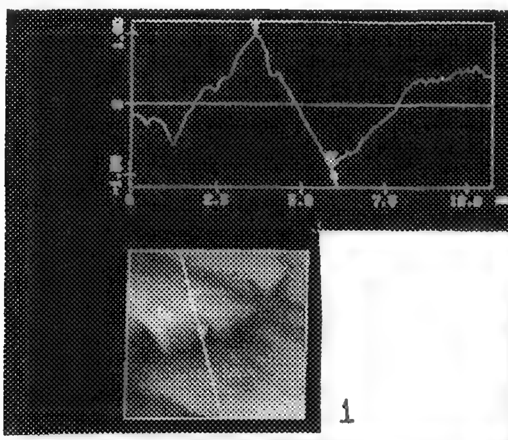

1

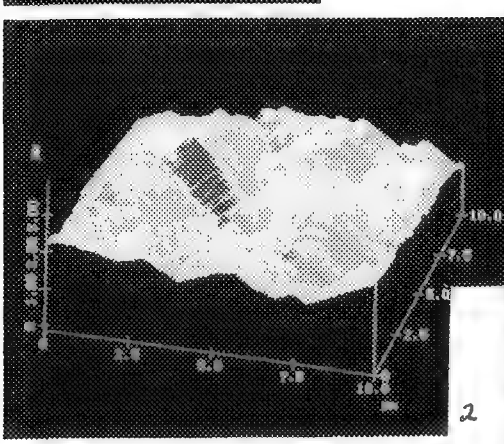

2

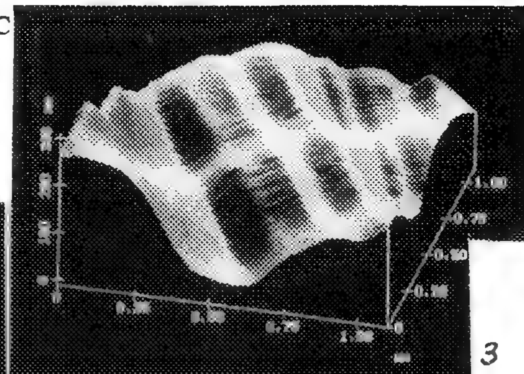

3

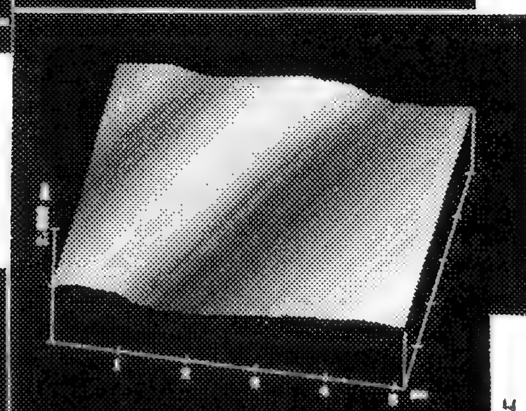

4

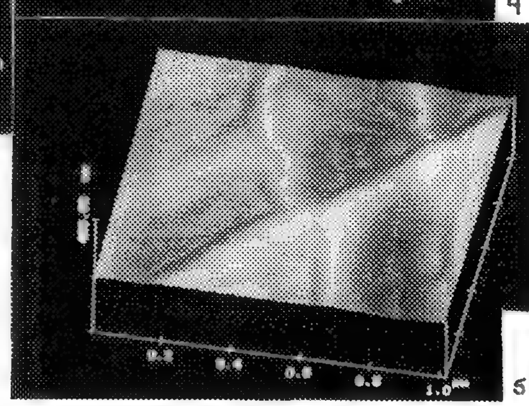

5

Figure 1. X-section of large scale atomic force microscope (AFM) image of FCC surface showing extent of large corrugation. The horizontal size of the image is 10 by 10 μm.
Figure 2. Large scale AFM image of V-contaminated FCC surface: 10 x 10 μm. Note how the vanadium coats the surface.
Figure 3. Large scale AFM image of V-contaminated FCC surface : 1 x 1 μm. Note V island structure.
Figure 4. Large scale AFM image of V contaminated FCC surface after steaming: 5 by 5 μm.
Figure 5. Large scale AFM image of V contaminated FCC surface after steaming: 1 x 1 μm.

HIGH-PRECISION CALIBRATION OF A SCANNING-PROBE MICROSCOPE (SPM) FOR MANUFACTURING APPLICATIONS

Donald A. Chernoff[a], Jason D. Lohr[a], Douglas Hansen[b], and Michael Lines[b]
[a]Advanced Surface Microscopy, Inc., Indianapolis, IN
[b]MOXTEK, Inc., Orem, UT

Introduction. For ordinary SPM (Scanning Probe Microscope) work, accuracy of XYZ length measurements of about 5% is acceptable. This is accomplished by periodic calibration checks (and adjustments, if required). Measurement of critical dimensions such as feature width and spacing on integrated circuits or compact discs requires much higher accuracy. For example, the new DVD (digital video disc) standard calls for a mean track pitch of 740 nm with a maximum allowable jitter (range) of 30 nm. To achieve a range of 30 nm, the standard deviation should be 10 nm or less. According to the gage-maker's rule, the measurement tool should be 4x more precise than the object being measured, so we need a standard deviation of 2.5 nm. This report describes the combined use of a new type of calibration standard and new software to meet these requirements.

Materials. Recently, MOXTEK has produced 1- and 2-dimensional holographic gratings as calibration standards for use with SEMs (Scanning Electron Microscopes). These consist of a Silicon substrate with a patterned photoresist, overcoated with a tungsten thin film. Fabrication and verification of these standards is described in a companion paper by Hansen et al. The holographic exposure process assures uniform feature spacing over the entire specimen area, with an expected accuracy of 0.1%. Subsequent processing steps increase edge roughness and may degrade the absolute accuracy. An independent measure of pitch (having 1 std.dev. accuracy of .33%), indicates that there is no detectable pitch variation across the entire specimen area, and the mean pitch found typically agrees within 0.5 nm with the as-exposed target value. When used in a SEM, the guaranteed accuracy is 1% (1 std.dev.), due to edge roughness. However, the SPM method described here greatly reduces the effects of edge roughness and we believe the accuracy of the mean pitch can be stated as .33% (1 std.dev.). We used a 288-nm pitch, 1-dimensional grating as the calibration reference for this work.

Methods. We operated a NanoScope III/Dimension 3000 large sample SPM in contact mode. We captured 15-µm wide images of the unknown (compact disc) and reference specimens. In order to reduce uncertainty due to edge roughness and other irregularities that may exist in these objects, we computed average cross-sections, using essentially all of the data in each image. These cross-sections show the height profile transverse to the track or grating axis. We analyzed the cross-sections using Advanced Surface Microscopy's SPM Calibrator software, which has the special attribute of reporting feature locations with a precision equivalent to .03-.1 pixel. At this level of precision, otherwise subtle nonlinearities stand out. We used additional software to remove the nonlinearities and calculate corrected feature locations and pitch values for the unknown specimen.

Results. The raw pitch values for the reference standard had mean = 296.4 nm and standard deviation = 4.4 nm. The pitch as a function of position in the frame showed a systematic variation across the frame (figure 1). We used these data with our linearization software to calculate a new length scale

for this scan size. We applied the new scale to calculate corrected pitch values both for the reference standard (as a self-consistency check) and for the compact disc specimens. After this correction, the pitch standard deviation for the reference was 1.1 nm and there was no systematic trend as a function of frame position (figure 1). (It is interesting to note that 1 nm is approximately 1/30 pixel for this size image.) Compact disc #1 had mean 744 nm and std. dev. 27 nm and did not meet the DVD specification. Disc #2 had mean 736 nm and std. dev. 6.8 nm and was in spec. If we had used the traditional SPM measurement technique of recording pitch based on pixel to pixel measurements of raw images, it would have been difficult to distinguish these two specimens and to discover which was out of spec.

Summary. We have demonstrated a new methodology for calibrating SPM images. The key innovations include: the use of a highly uniform, sub-micron pitch standard; the calculation of feature positions with sub-pixel precision; and replacement of the nonlinear raw length scale with a corrected, linear length scale. We have applied this method to a manufacturing problem requiring careful metrology.

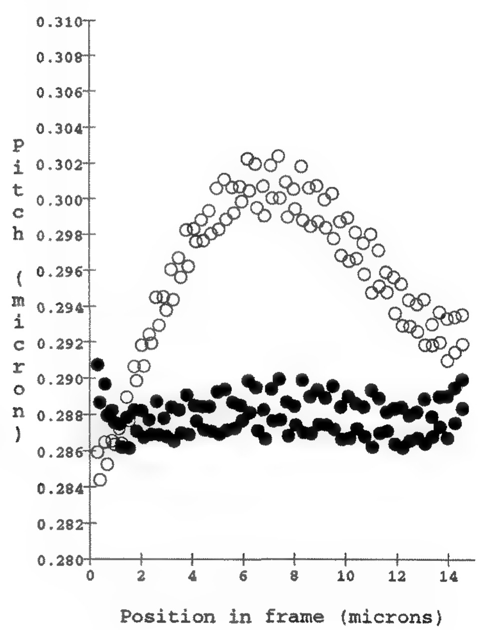

Figure 1. Pitch values for calibration standard. Open circles = Raw pitch. Filled circles = Corrected pitch. The total range of the Y axis approximates 1 pixel in the original image.

Round Robin AFM Study of Dealkalized Float Glass

K. A. Gesner, W. E. Votava, and J. F. Varner
NYS College of Ceramics at Alfred University-Alfred, NY 14802

An extensive study of the surfaces of glass treated in a variety of ways was undertaken at the New York State College Of Ceramics At Alfred University over the past 1.5 years. As the project progressed it became evident that glass surfaces can be very difficult to image because of a variety of factors including, static charge buildup, humidity, and tip reflections, to mention a few. Also, because many of the calibrations and scan parameters are specified by the operator, there is great potential for variability to occur between two or more AFM systems. To study the impact of the variations between operators and instruments, a round robin experiment was initiated, and five identical samples were distributed among five different facilities for AFM analysis; two microscopes were manufactured by Topometrix® and three by Digital Instruments®.

A dealkalized float glass sample was used for this experiment. The dealkalized float glass used was made by exposing both the air and tin sides of the glass to SO_2 gas for 30 minutes at 600°C Additionally, the SO_2 had 20% H_2O vapor mixed with it to provide a humid atmosphere.[1] Figure 4 is a schematic representation of the apparatus used for the dealkalization experiments.

Images were collected using each type of instrument for both the air and tin surfaces. A sample preparation procedure was sent to each person to insure that each sample was treated the same before examination with the AFM. That preparation included swabbing each sample with methanol, drying with a lint free cloth, and dusting with dry compressed air just prior to imaging. All the images collected for this study were scanned in air using contact mode over a 5 x 5 micrometer area.

The images collected by the two Topometrix® instruments for the air and tin surfaces are presented in figures 1 and 2. Similar features are detected by the two different instruments on the air surfaces, and fewer, but similar, surface features are observed on the tin surfaces.

Figure 3 represents images for the air surface, collected from three different AFMs manufactured by Digital Instruments®. Similar features are observed by each instrument and these are similar to the features previously seen in figures 1 and 2.

All five instruments detected more features on the air surfaces, and the features observed, both raised and depressed, are of similar geometry. Similarities exist between the image features seen from each manufacturer; they are just presented with different techniques. The images in figures 1 and 2 are leveled and shaded while figure 3 has only been leveled.

1. U. Senturk, "Effects of Dealkalization on Surface-Related Mechanical Properties of Alkalisilicate Glasses" PhD. Thesis, NYS College of Ceramics, Alfred University, Alfred, New York (1996).

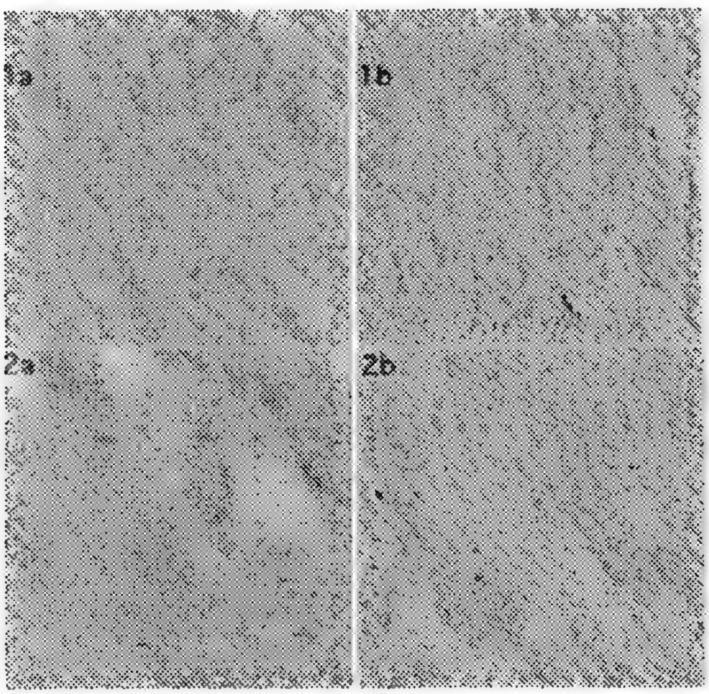

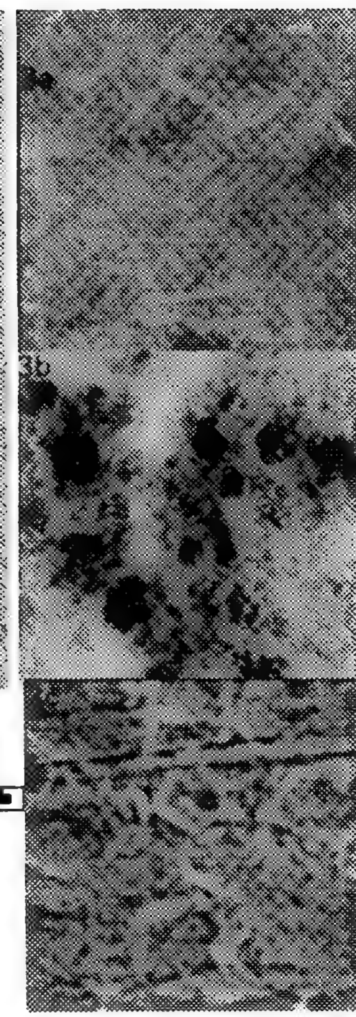

4

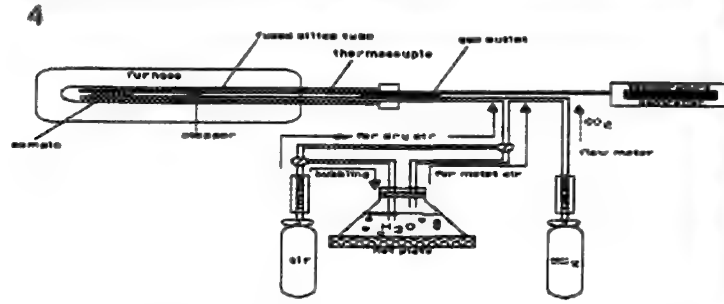

Fig. 1 AIR side. SO_2 treated with 20% H_2O for 30 minutes at 600 °C. Imaged using a Topometrix Explorer TMX 2000, a) NYSCC at Alfred University, Alfred, NY, b) Xerox Corporation, Webster, NY

Fig.2 TIN side. SO_2 treated with 20% H_2O for 30 minutes at 600 °C. Imaged using a Topometrix Explorer TMX 2000, a) NYSCC at Alfred University, Alfred, NY, b) Xerox Corporation, Webster, NY

Fig. 3 AIR side. SO_2 treated with 20% H_2O for 30 minutes at 600 °C. Imaged using a Nanoscope II from Digital®, a) Corning Incorporated, Corning, NY, b) Texas A & M University, College Station, TX, c) Laboratory for Laser Energetics, Rochester, NY

Fig. 4 Experimental apparatus used for dealkalization treatments of float glass

IMAGING OF SURFACE-ADHERENT HUMAN-BLOOD PLATELETS BY ATOMIC-FORCE MICROSCOPY (AFM)

N. Murthy, J. G. White and G. H. R. Rao

Departments of Laboratory Medicine and Pathology and Pediatrics, University of Minnesota Medical School, University of Minnesota, UMHC Box 490, 420 Delaware Street S.E., Minneapolis, Minnesota 55455

Studies in our laboratory over the past three decades have explored platelet ultrastructural morphology by light microscopy as well as transmission, scanning and low-voltage, high-resolution scanning electron microscopy. Unlike these optical microscopes, scanning probe microscopes measure real space images of cells on flat surfaces. In brief, the AFM works by scanning a very sharp conducting tip (SiN) over the surface of a conducting biological membrane. Cantilivers used for probing were short tipped with thin legs (0.22 nm spring constant). Scanning was done with the J size scanner (150 x 150 u scan area). The difficulty in achieving high resolution images of biological samples relates to the damage caused by the probing tip in spite of its minute force on delicate biological cell surface membranes. In the present study we have evaluated surface topography of fixed resting and activated platelets using AFM. Resting platelets were treated with cytochalasin B to prevent actin filament assembly shape change prior to being placed on polylysine-coated grid surfaces. The platelets were fixed immediately after stabilization on grids and preliminary studies indicated that their discoid shape was well preserved. AFM images were recorded with a multimode atomic force instrument (Nanascope AFM, Digital Instruments, Inc.). To obtain height profile as well as corrugations of plasma membrane surfaces, images were recorded in the contact mode (Nanascope 4.1 software). Images of resting platelets reveal the typical discoid appearance characteristic of resting platelets. Higher magnification of the platelet surface shows the fine corrugated appearance observed previously with low-voltage, high-resolution scanning electron microscopy (LVHR-SEM) (Figs. 1,2). Openings of the exposed surface into channels of the open canalicular system were also well shown by this technology (Figs. 3,4). Examination of fully activated platelets on the grid surfaces revealed images similar to those that have been observed previously by LVHR-SEM. Pseudopods extending from the central body of the cells were typical of dendritic forms, while many platelets have filled spaces between the pseudopods and transformed into spread forms. Earlier studies suggested the utility of this technique for measuring the elastic and repulsive forces of the platelet membrane glycocalyx. In this regard, preliminary studies done in our laboratory suggest that this technique may be useful to monitor attractive and repulsive forces involved in ligand-receptor interactions.

REFERENCES

1. J.G. White and W. Krivit: Blood 26 (1965) 554
2. J.G. White et al: British Journal of Haematology 90 (1995) 633
3. M. Radmacher et al: Science 257 (1992) 1900
4. M. Fritz, et al: Biophysical Journal 66 (1994) 1328

ACKNOWLEDGMENTS

The authors gratefully acknowledge the use of microscopy facilities at the Center for Interfacial Engineering (CIE). This work was supported by funds from the National Institutes of Health (HL11880, HL49556) and CIE.

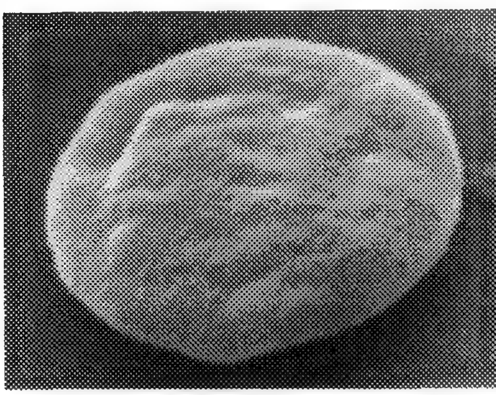

FIG.

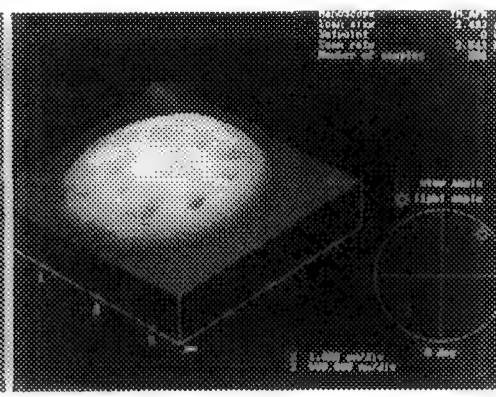

FIG. 2

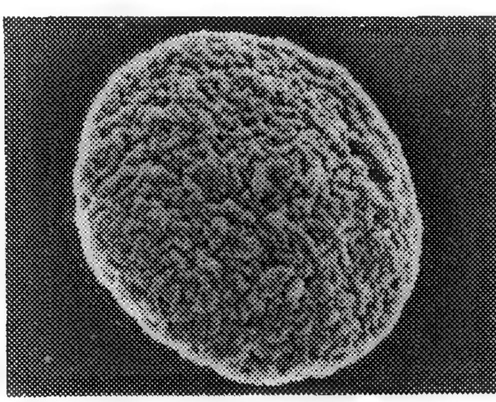

FIG.3

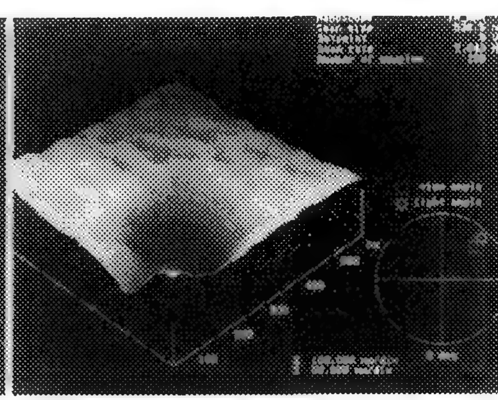

FIG.4

Fig. 1. Resting platelet imaged by SEM
Fig. 2. Resting platelet imaged by AFM
Fig. 3. Resting platelet by low-voltage, high-resolution EM
Fig. 4. Higher magnification of platelet membrane by AFM

QUANTITATIVE SCANNED PROBE MICROSCOPY

J. C. Russ[1,2], P. J. Scott[1,3]
[1] Research Department, Rank Taylor Hobson, Ltd., 2 New Star Road, Leicester, UK
[2] Dept. of Materials Science & Eng., North Carolina State Univ., Raleigh, NC, USA
[3] School of Manuf. & Mech. Eng., Univ. of Birmingham, Edgbaston, Birmingham, UK

The great advantage of the atomic force microscope and related technologies (tunneling current, near field optical, tips that oscillate vertically or laterally, etc.) has been simplicity of design. Vertical deflection of a reference tip on a cantilevered probe is detected by light scattering and used to shift the sample in the z direction to restore tip position. The output is generally in the form of surface images rather than measurements with high dimensional accuracy. Atomic scale resolution is achievable but lower magnification imaging is more difficult.

Piezo devices used for x-y and z axis control have a limited range of motion and are noisy, nonlinear and subject to creep. Piezo displacement is not simply a function of voltage, or of the time integral of current, but depends upon many factors including rate and distance of motion, and internal resistance and capacitance in the device. It is possible in principle to calibrate such a system using a reference grid standard, but even this is highly dependent on scanning speed (different in the x, y, z directions) and will not provide quantitative z information. The result is that AFM scans are not rectilinear and dimensional accuracy or even reproducibility is not achieved in the basic design which interprets the electrical signals to the piezo drives to yield position information. Since most interest to date in using AFM results has been for imagery, these defects have not raised serious limitations. Attempts to add precision interferometers to the x, y and z motions of the sample have significant influence on the cost and complexity of the basic instrument, and do not address the issues of noise, speed and range. The piezo-scanned AFM has scan speeds and range (area covered and magnitude of vertical relief) that are quite limited, due both to the limitations of the piezo design and (for the z direction) the shape of the reference tip, which must provide clearance for features on the surface.

Many of these limitations can be overcome by designing the scanned probe microscope for the primary purpose of relatively low magnification (large scan area) quantitative surface imaging and measurement (Morrison, 1995). A flexure-mounted, voice coil driven scanning mechanism of metrology quality is mounted so that a diamond-tipped stylus can be raster scanned across a stationary specimen. Scans of large areas (up to 1 mm^2) can be rapidly performed (50 seconds) with a maximum vertical motion range of up to 200 μm. Images are recorded as 500x500 arrays of points, and are suitable for quantitative measurement of surface form and finish for metrology applications (with full NAMAS traceability).

The diamond tip is mounted on a hollow aluminum tube giving 10mm clearance for surface relief. The total stylus mass is 5 mg and the force on the sample is 1 mN, which allows scanning speeds of 10 mm/s with the tip remaining always in contact with the surface. Reading the tip position with an optical pickup provides measurements with 1 μm lateral resolution. Optical sensors are used to measure both x and y positions. Resolution for the vertical measurements is 3 nm with an absolute accuracy of 10nm. Software correction is included for the horizontal offset of the stylus due to its arcuate motion. Software correction to remove mean surface elevation and slope can also be optionally applied. The Talyscan® instrument is interfaced to a PC, which provides flexible selection of scan areas and dynamic ranges, as well as a variety of display and analysis possibilities and a standard file format for user access. Image displays of the surface include range images (grey scale or color coded), isometric surface displays with hidden line removal, contour plots of the surface, rendered surface views, user-selectable profiles, etc. Figure 1 shows examples of typical applications. The low applied force and large scanning range makes the technique suitable for studies of metals, ceramics, polymers, coatings, and many other materials.

Metrology measurements of the surfaces include 14 amplitude, spatial, hybrid and functional parameters developed through a European Commission BCR research funded project, co-ordinated by The Centre for Metrology research group at The University of Birmingham UK. These parameters have been well studied and used to characterize a variety of real surfaces of industrial and scientific interest (BCR Report, 1993).

They have been agreed to by 37 European companies as a basis for 3D assessment and are currently under consideration by ANSI, ISO and other standards groups. Additional characterization techniques using fractal geometry (Russ, 1994) and topographic analysis (Scott, 1995) can also be applied to the data. The fractal dimension can be computed in several ways to reveal the scaling of statistically self-similar structures that are often present on natural surfaces, and to reveal directional anisotropy in the scaling. Topographic analysis uses a network graph of peaks, depressions, ridges, valleys and saddle points to describe the connectability of valleys and other large-scale surface structures. These tools extract properties that correspond more directly to what a human viewer "sees" in examining surfaces, and may be important for a variety of surface studies.

BCR Report EUR 15178 EN (1993) "The development of methods for the characterisation of roughness in three dimensions" ISBN 0 7044 1313 2

E. Morrison (1995) "A Prototype Scanning Stylus Profilometer for Rapid Measurement of Small Surface Areas" Int. J. Mach. Tools Manufact. 35(2):325-331

J. C. Russ (1994) Fractal Surfaces, Plenum Press, New York

P. J. Scott (1995) "Recent Advances in Areal Characterization" IX Intern. Oberflächenkolloq., Techn. Univ. Chemnitz-Zwickau, 151-158

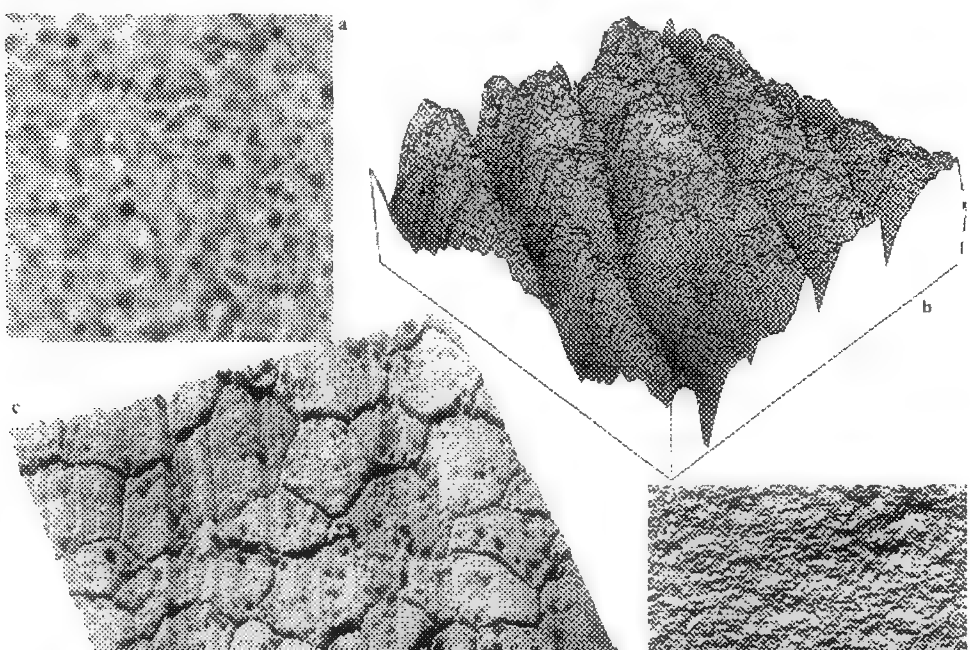

Figure 1. Example presentation modes and applications: a) grey scale (color coded) range image of 1 mm^2 surface of injection molded plastic; b) isometric line display of a plastic replica of human skin (original is in color); c) isometric rendered display of extruded aluminum with surface markings and grain boundaries; d) rendered vertical view of paint surface.

Scanning Probe Microscopy of Polymers in the Field Emission SEM

J. Brostin
Kimberly-Clark Corporation, Roswell, Ga 30076-2199

The field emission SEM (FESEM) is well suited for imaging polymer and other non-conductive surfaces. High resolution SEM images can be obtained without the application of a conductive coating when operated at low accelerating voltages. Compositional imaging in the backscattered electron mode is facilitated at low voltages by the incorporation of a microchannel plate (MCP) detector. The MCP equipped FESEM has been shown to be phenomenally sensitive to very small differences in average atomic number. Compositional contrasts are achieved in polymer and other low-Z composites that differ only in oxygen content. Those systems that completely lack intrinsic contrast can be differentially stained with ruthenium tetroxide vapors[1].

These capabilities make the FESEM an ideal platform for locating phases and/or subtle features for scanning probe microscopy (SPM). Transparent, thin coatings or very fine, heterogeneously dispersed structures that cannot be readily located or observed with conventional light optics can generally be seen in the FESEM. In order to integrate FESEM and SPM technology, Topometrix[2] has developed the Observer™ SPM that can be operated within the specimen chamber of the SEM. This system includes an airlock for rapid specimen exchange, and dual piezo drives for positioning both the specimen and the probe for proper alignment to the electron beam. The Observer™ can be operated in scanning tunneling (STM) and most atomic force (AFM) scanning modes. Using the 2 micron scanner, the Hitachi S4500 FESEM[3] can be operated with a GW microchannel plate[4] fully inserted. The geometry of the SPM requires a fixed 27 mm working distance in the S-4500 SEM and does cause some signal attenuation. Other than this, the operation of the SEM is unaffected by the use of the SPM.

Figure 1 shows a silicon nitride probe scanning the fracture edge of a thin polysaccharide coating on a polypropylene film substrate. Even in this secondary electron image, the compositional contrast between the two polymer phases is noted. Figure 2 shows the contact mode AFM image of this fracture edge. Note that a dispersed crystalline phase is clearly visible not only on the surface, but on the fractured edge of the coating, as well. Based on the AFM data, the polysaccharide coating is estimated to be 180 nm.

References

1 Brostin, J. Compositional Imaging of Polymers using a Field Emission Scanning Electron Microscope with a Microchannel Plate Backscattered Electron Detector *Scanning* Vol 17 (1995) 327-329.

2 Topometrix Corporation, 5403 Betsy Ross Drive, Santa Clara, Ca 95054-1162

3 Nissei Sangyo America, Hitachi Scientific Instruments, 755 Ravendale Drive, Mountain View, California 94043.

4 GW Electronics, Inc., 6981 Peachtree Industrial Boulevard, Norcross, Georgia, 30092

1 2

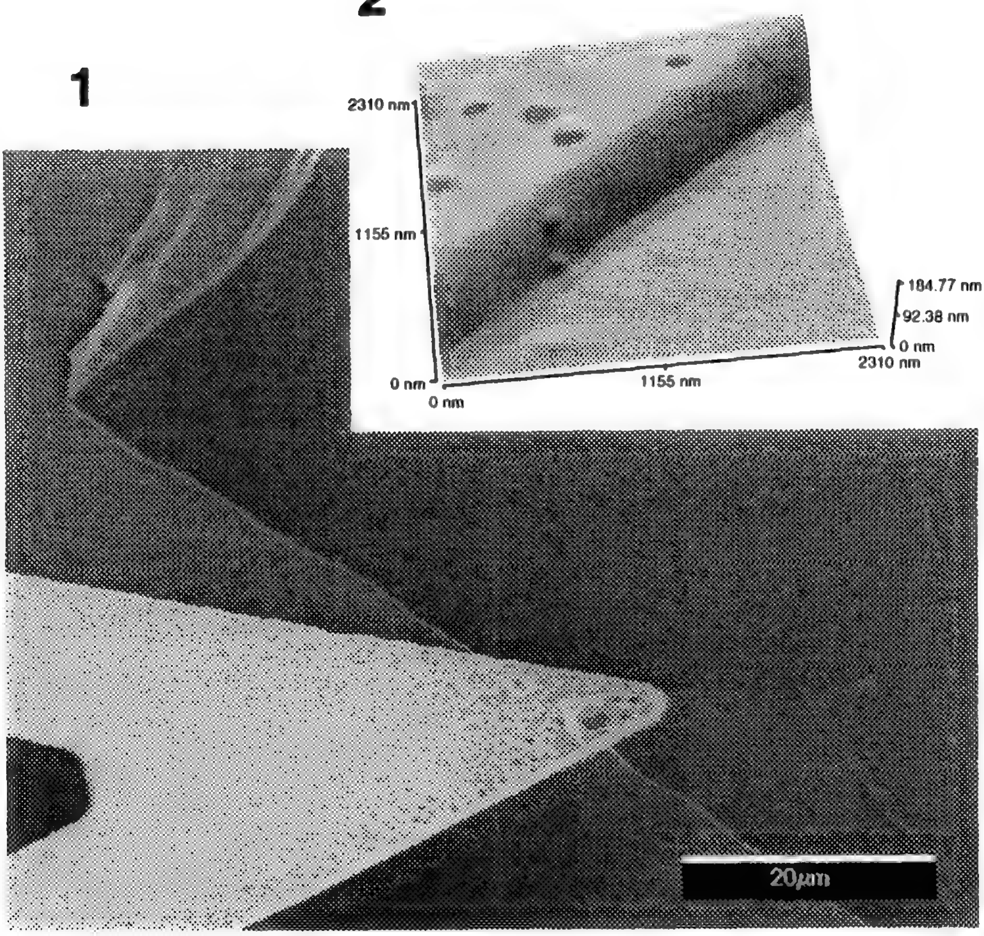

FIG. 1 FESEM image of AFM probe scanning edge of peeled, thin coating (1.0 KV)
FIG. 2 AFM image of coating fracture edge indicating film thickness of ~ 180 nm

NEW INSIGHTS INTO THE RAS ONCO-PROTEIN AND ITS INTERACTIONS WITH THE RAF-1-1 KINASE

Sharon Campbell , Helen Mott, Sheng Zhong, Jonelle Drugan & John Carpenter

Department of Biochemistry and Biophysics, U. of North Carolina, Chapel Hill, NC 27599-7260

The Ras proteins are members of a large superfamily of nucleotide-binding proteins that cycle between active GTP- and inactive GDP-bound states. They are positively regulated by guanine nucleotide exchange factors (GEFs) that promote formation of the active GTP-bound state and negatively regulated by GTPase activating proteins (GAPs) that stimulate formation of the inactive GDP-complexed protein. Structural mutations that activate Ras oncogenic potential either impair GAP-stimulated GTPase activity or promote enhanced intrinsic nucleotide exchange. The net result of either biochemical effect is to favor elevated levels of Ras-GTP *in vivo*.

We are investigating selected Ras variants containing substitutions at conserved sites thought to be important for guanine nucleotide binding, GTP hydrolysis, GTP/GDP inter-conversion and protein recognition, to better understand the role of these conserved amino acids in Ras-mediated signal transduction. Recent studies conducted at the U. of North Carolina will be presented, where we have characterized a novel activating mutation in Ras using multi-dimensional NMR spectroscopy and established a region involved in direct interaction with guanine nucleotide exchange factors. (1,2)

Another research focus involves elucidation of how activated forms of Ras recognize and stimulate downstream cellular targets. It is now known that Ras proteins function as molecular switches that orchestrate the transmission of growth promoting signals from a wide array of membrane-bound receptors to the transcriptional machinery in the nucleus of the cell. A critical downstream target of Ras is the Raf-1 serine/threonine kinase. Studies conducted in our laboratory provide evidence that Ras mediates activation of Raf-1 through two distinct binding sites in the Raf-1 N-terminal regulatory domain. (3,4) While extensive structural information exists on the first of the two Ras interacting sites in Raf-1, little is known about the second Ras binding site. We have recently conducted a series of biochemical and cell biology studies to establish the functional significance of this second and distinct Ras binding site. (4) In addition, we are examining the structural features of this second Ras:Raf-1 interaction site, the Raf-1 cysteine-rich domain, using heteronuclear NMR spectroscopy. (5)

The cysteine-rich domain of Raf-1 is a zinc finger 'like' motif that shares considerable homology to zinc coordinating domains found in a number of cell signaling enzymes that require lipids for activation. The structural and functional properties of the Raf-1 cysteine-rich domain and related motifs are poorly understood compared to other well documented protein domains such as src homology 2 (SH2) and 2 (SH3) domains. The zinc ions most likely provide a structural scaffold to stabilize residues involved in both protein-protein and protein-lipid interactions, that are likely to play a critical role in the activation of the Raf-1 kinase. In order to better understand the role of domain in Ras-mediated activation of Raf-1 and how the ligand specificity of this domain differs from that of related cysteine-rich domains, we have determined the solution structure of the Raf-1 cysteine-rich domain using heteronuclear multi-dimensional NMR. (5) We show that there are differences between this structure and the structures of two domains from protein kinase C (PKC). These PKC domains do not bind Ras, but interact with diacylglycerol (or mitogenic phorbol esters) and phosphatidylserine. The structural differences are confined to the regions of the domains that are involved in binding phorbol ester or Ras, respectively. Since it is a common ligand, we expect the binding site for

phosphatidylserine to be in a region where the structures of both the Raf-1 and PKC domains are similar. The structure of the Raf-1 cysteine-rich domain represents an example of this family of domains that does not bind diacylglycerol or phorbol esters and provides a framework for investigating its interactions with its physiological activators, such as the Ras oncoprotein.

References

1. L.A. Quilliam et al., *PNAS* (1995) **92**, 1272-1276.
2. L.A. Quilliam et al., *Journal of Biological Chemistry*, (in press).
3. T.R. Brtva et al., *Journal of Biological Chemistry*, (1995) **270**, 9809-9812.
4. J. K. Drugan et al., *Journal of Biological Chemistry*, (1996) **271**, 233-267.
5. H. Mott et al., (submitted).

6. This research was supported by NIH grants R29 CA 64569-01 and RO1 CA70308-1 to SLC and was conducted in collaboration with the laboratory of C.J. Der at the U. of North Carolina

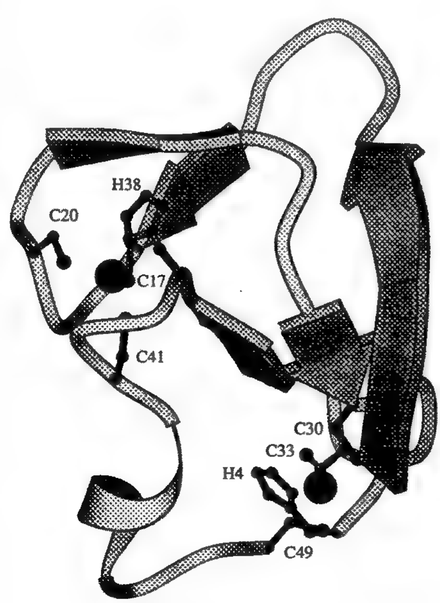

Raf-1 Cysteine-Rich Domain

MAGNETIC-RESONANCE INVESTIGATIONS OF BLOOD: FROM HEMOGLOBIN TO LYMPHOCYTE MIGRATION

C. Ho*

*Department of Biological Sciences, Carnegie Mellon University, Pittsburgh, PA 15213

We have applied various nuclear magnetic resonance (NMR) techniques, from high-resolution solution-state NMR spectroscopy to magnetic resonance imaging MRI), to investigate blood components such as hemoglobin and T-cells. We are interested in the structure-function relationship in human normal adult hemoglobin (Hb A) and in tracking the movement of T-cells in live rats. In this presentation, we shall give a brief summary of our approach and recent experimental results.

We have recently developed an expression system to produce authentic Hb A in Escherichia coli.[1] With our Hb A expression plasmid (pHE2) (Fig. 1), we are in a position to produce any desired hemoglobin in E. coli. We are carrying out a study to learn the rules governing oxygen affinity and cooperativity of the oxygen binding process in hemoglobin. We have constructed several recombinant hemoglobins which exhibit varying degrees of oxygen affinity and cooperativity (as measured by the Hill coefficient).[2,3] We have used high-resolution ^{1}H-NMR spectroscopy to investigate the tertiary structural features of the heme pockets and the structural features in the $\alpha_1\beta_1$ and $\alpha_1\beta_2$ subunit interfaces of these recombinant hemoglobins. From a comparison of the structural features and the functional properties of a number of novel hemoglobins, we hope to understand the relationship between structure and function well enough to be able to design several hemolgobins with the desired properties for hemoglobin-based oxygen carriers. In this talk, we shall present some of our recent findings in our hemoglobin research.

Recently, we have succeeded in incorporating dextran-coated iron-oxide particles (MRI contrast agents) into rat T-cells by endocytosis. These labeled T-cells exhibit normal functional properties as those of unlabeled or native T-cells.[4] Thus, we can apply MRI techniques to track the movement of these iron-oxide labeled T-cells in a live animal such as a rat[5]. In this presentation, we shall give a summary of our recent results. An immediate goal of this research is to develop this approach into a non-invasive method to detect early signs of acute graft rejection in human organ transplantation.

Magnetic resonance is a tool which can be used to investigate biological systems from molecules to humans.

References

1. T-J. Shen et al., Proceedings of the National Academy of Sciences USA, 90 (1993) 8108.
2. H.-W. Kim et al., Proceedings of the National Academy of Sciences USA, 91 (1994) 11547.
3. H.-W. Kim et al., Journal of Molecular Biology, 248 (1995) 867.
4. T. C. Yeh et al., Magnetic Resonance in Medicine, 30 (1993) 617.

5. T. C. Yeh et al., Magnetic Resonance in Medicine, 33 (1995) 200.
6. The author gratefully acknowledges the use of facilities at the Pittsburgh NMR Center for Biomedical Research which is supported by a grant from National Institutes of Health (RR-03631). This work is supported by research grants from the National Institutes of Health (HL-24525 and RR-10962) and a research grant from the Whitaker Foundation.

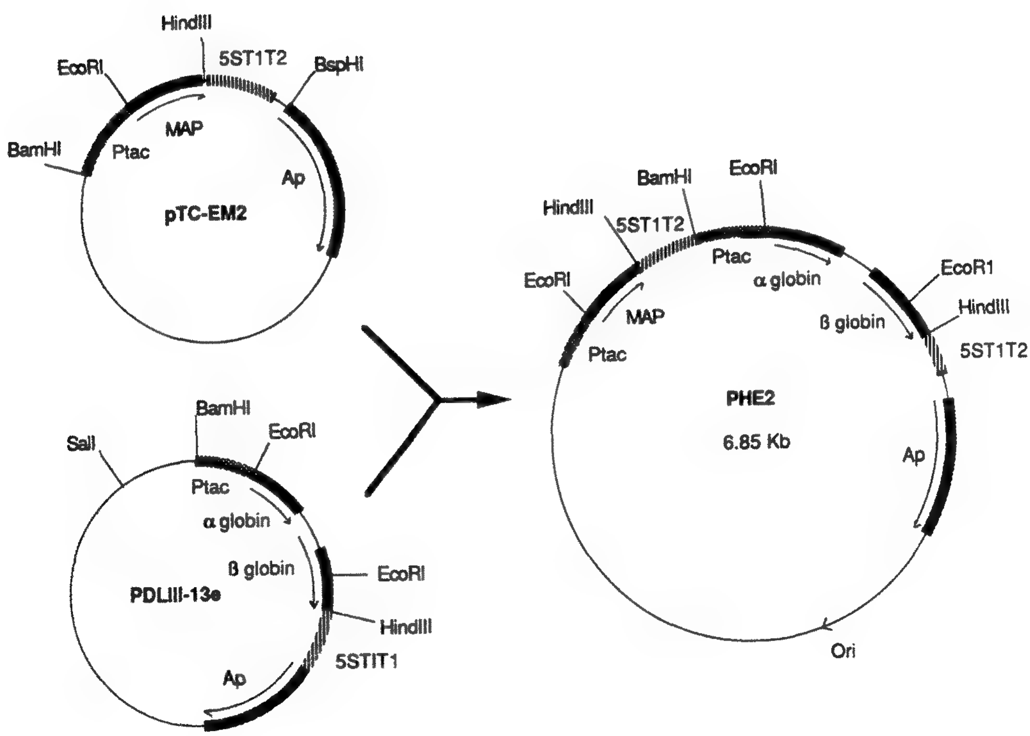

FIG. 1 Construction of a plasmid for the expression of human α- and β-globin genes and methionine aminopeptidase (MAP) gene in E. coli. (after Ref. 1).

Effects of Carbogen Inhalation on Tumor Oxygenation : Comparison of Magnetic Resonance and Oxygen Electrode Measurements

G.S. Karczmar, J.N. River, H.A. Al-Hallaq, M.Z. Lewis, H. Oikawa, D.A. Kovar

Department of Radiology, University of Chicago, Chicago, Illinois, 60637

Introduction : Radiotherapy is most effective in tumors in which the tissue concentration of oxygen is high. The potential of tumor oxygenating treatments (i.e., treatments which increase tumor oxygenation as an adjunct to radiotherapy; '***TOX's***') to substantially improve tumor response to therapy has been clearly demonstrated in animal models and in some studies of cancer patients. However, despite some initial successes, the ability of TOX's to help a large percentage of cancer patients has been disappointing. The reasons for this are not clear because there is currently no method which is routinely used to image the effects of TOX's on tumor oxygenation with high resolution and accuracy. Development of improved TOX's and optimization of their clinical application would be significantly advanced by such measurements.

Previous work in this laboratory[1-3] and other laboratories[4-5] has demonstrated that Magnetic Resonance (MR) can be used to detect effects of TOX's on tumor blood oxygenation, based on the BOLD effect (blood oxygen level dependent contrast).[6] Deoxyhemoglobin is paramagnetic while oxyhemoglobin is diamagnetic. Changes in blood oxygen affect the balance between oxyhemoglobin and deoxyhemoglobin and thus the magnetic susceptibility of blood vessels. High levels of blood deoxyhemoglobin increase the linewidth of the water resonance and decrease T_2*; low levels of deoxyhemoglobin decrease linewidth and increase T_2*. However it is extravascular oxygen tension which affects response to radiation. To date, there is no direct evidence that changes in T_2* reflect changes in extravascular tumor oxygen tension. Here we compare changes in T_2* during carbogen (95% O_2 / 5% CO_2) inhalation measured by MR with changes in extravascular oxygen tension measured by oxygen microelectrode.

Methods : Mammary adenocarcinomas were implanted in the flanks of F344 female rats. The tumors were studied when they were approximately 1 cm in diameter. Animals were anesthetized with ketamine and rompun.

Microelectrode measurements were made using a Non-Clarke style electrode with a 500 micron tip (Diamond General, Ann Arbor, MI) at a single point before, during, and after inhalation of carbogen. The electrode was then moved to a new position and the process was repeated.

Spectroscopic images were obtained at 4.7 Tesla before, during and after inhalation of carbogen. This produced a high resolution spectrum of the water resonance in each pixel which could be used to accurately determine changes in linewidth. Tumors used for MR and oxygen microelectrode studies came from the same stable tumor line and were similar in size and age.

Results : **Figure 1** shows a plot of electrode current at a single point in the tumor against time as the breathing gas is switched between air and carbogen twice. The maximum increase of 400 pA is equivalent to a 66 mm Hg increase in oxygen tension. Significant increases in the peak height

of the MR water signal (**Figure 2**) were detected during inhalation of carbogen. Increases in the integral of the signal were much smaller. Thus increased peak height reflects increased T_2*.

Tumor oxygen tension increased during carbogen inhalation in 60% of the tracks (in 6 tumors). The increase in pO_2 during carbogen inhalation in all tumors (and all tracks) studied averaged 32 ± 18 mm of Hg (the standard error is given). In a similar series of tumors (n=8) an average increase of 12% in T_2* was detected during carbogen inhalation.

Discussion : The data demonstrate that increases in tumor oxygen tension occur under the same conditions as increases in the T_2* of the water proton MR signal. Thus MR measurements correlate well with increased tumor extravascular oxygen tension. MR BOLD effect measurements could play an important role in assessment, design, and application of new cancer treatments.

Acknowledgments : This work was supported by Grants R29CA52008-01A1 and 5R21CA66132-02.

References :

1. G.S. Karczmar, et al, Soc. Magnetic Resonance in Medicine Abstract #830, Berlin, 1992.
2. G.S. Karczmar, et al.. *NMR in Biomedicine* 7: 3 - 11, 1994.
3. V. Yu. Kuperman, et al. Magnetic Resonance in Medicine **33**: 318-325, 1995.
4. S.P. Robinson et al.. International Journal of Radiation Oncology, Biology and Physics **33**: 855-859, 1995.
5. S.K. Lemieux, et al. Radiological Soc. North America Abstract #137, Chicago, 1995.
6. Ogawa S, Lee TM, Kay AR, and Tank DW. PNAS USA **87**:9868-9872, 1990.

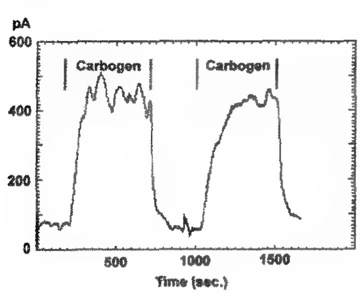

Figure 1

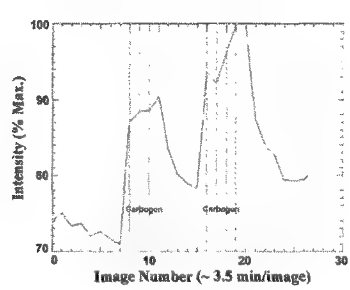

Figure 2

Figure 1. Change in microelectrode current during inhalation of carbogen (1 mm Hg ~ 6 pA). Carbogen was turned on and off twice.

Figure 2. Changes in MR signal peak height during inhalation of carbogen. Carbogen was turned on and off twice.

SPECTROSCOPIC IMAGING OF HUMAN DISEASE

D.J. Meyerhoff

Department of Radiology and Magnetic Resonance Unit DVA Medical Center, University of California San Francisco, San Francisco, CA 94121

Magnetic Resonance Imaging (MRI) observes tissue water in the presence of a magnetic field gradient to study morphological changes such as tissue volume loss and signal hyperintensities in human disease. These changes are mostly non-specific and do not appear to be correlated with the range of severity of a certain disease. In contrast, Magnetic Resonance Spectroscopy (MRS), which measures many different chemicals and tissue metabolites in the millimolar concentration range in the absence of a magnetic field gradient, has been shown to reveal characteristic metabolite patterns which are often correlated with the severity of a disease. In-vivo MRS studies are performed on widely available MRI scanners without any "sample preparation" or invasive procedures and are therefore widely used in clinical research. Hydrogen (^{1}H) MRS and MR Spectroscopic Imaging (MRSI, conceptionally a combination of MRI and MRS) measure N-acetylaspartate (a putative marker of neurons), creatine-containing metabolites (involved in energy processes in the cell), choline-containing metabolites (involved in membrane metabolism and, possibly, inflammatory processes), lactate (the end product of anaerobic metabolism), and several amino acids ((e.g., alanine, glutamine, glutamate, γ-amino butyric acid (GABA)) with a typical spatial resolution of about 1 ml. Phosphorus MRS and MRSI measure nucleotidetriphosphates and phosphocreatine (both involved in cellular energy processes), and intermediates of phospholipid metabolism with a minimum spatial resolution of about 10 ml.

MRS and MRSI are technically more demanding than MRI due to the low concentration of interesting metabolites, suppression of the much more intense water signal, spatial localization, and preservation of metabolite-characteristic resonance frequencies. However, over the last several years a number of clinical applications have emerged which have the potential to become important contributors to decision making in patient care and management.[1,2,3] These include the use of spectroscopic imaging in epilepsy, Alzheimer's disease, HIV infection, brain cancer, stroke, multiple sclerosis, and metabolic encephalopathies and myopathies.

Mesial temporal lobe epilepsy (TLE) patients typically have seizures originating from a single epileptogenic focus in the temporal lobe. Patients who do not respond to medical therapy may undergo surgery to remove the seizure focus. Implanted EEG is the gold standard for lateralizing seizure foci, but it is invasive and risky. MRI is used successfully in lateralizing a unilateral epileptogenic focus when tissue loss in the seizure focus is present. However, MRI is less successful in correctly lateralizing the seizure focus in the absence of tissue loss. ^{1}H MRSI allows reliable lateralization of the seizure focus, also in those cases in which temporal lobe tissue loss is not present or not detectable by MRI (Fig. 1).

Alzheimer's disease (AD) is a common cause of death and dementia. While the ultimate clinical objective in AD research is to develop effective therapy, methods of diagnosing AD early in the course of the disease with any certainty and of distinguishing AD from other causes of dementia are non-existent. The unique ability of ^{1}H and ^{31}P MRS and MRSI to detect neuron damage and membrane alterations has been found to be useful in addressing these clinical problems. AD shows a pattern of cerebral metabolite distributions which may help to distinguish it from other dementing illnesses.

HIV-associated dementia (HAD) is a major cause of dementia in young adults. HIV enters the central nervous system (CNS) early in the course of infection, but its neurological and morphological effects on the brain are manifest only in relatively late stages of the disease, often associated with AIDS. No diagnostic test is available to determine reliably the degree and progression of HIV infection in the CNS. ^{1}H MRS and MRSI have promise in the early detection of neuronal damage due to HIV infection, and in monitoring the effects of therapy and disease progression on the brain.

In brain tumor diagnosis, MRS and MRSI may provide useful pre-surgical information and may assist in treatment of brain tumors by identifying regions of necrosis and tumor regrowth. Recent research suggests that malignant brain tumors may be differentiated from benign brain tumors and low- from high-grade tumors on the basis of certain ^{1}H metabolite patterns. MRS' clinical role in assessing cancers outside of the brain and their treatment is more controversial.

For the medical management of acute stroke, ^{1}H MRSI provides unique diagnostic and prognostic information: acute NAA loss appears to delineate brain regions of final tissue loss, while characteristic metabolite patterns identify potentially salvageable brain tissue.

References

1. D.J. Meyerhoff et al., Magnetic Resonance Spectroscopy. Chapter in *Magnetic Resonance Imaging of the Body,* Second Edition. Editors: C.B. Higgins, H. Hricak, and C.A. Helms, Raven Press, New York (1992). Third Edition (in press).
2. G.B. Matson and M.W. Weiner, Spectroscopy. Chapter in *Magnetic Resonance Imaging,* Second Edition. Editors: D.D. Stark and W.G. Bradley, Jr., Mosby-Year Book, St. Louis, MO (1992). Third Edition (in press).
3. B. Ross and T. Michaelis, Clinical applications of magnetic resonance spectroscopy. *Magnetic Resonance Quarterly* 10:191-247 (1994).

CONTROL

TLE PATIENT

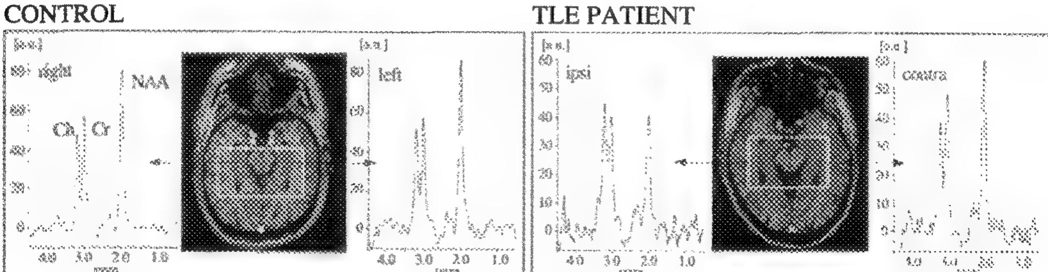

FIG 1: MRI and ^{1}H MRSI brain spectra from the temporal lobes of a control (left box) and a patient with right-sided mesial temporal lobe epilepsy (TLE) (right box). In the control, the NAA signal dominates the signals from creatine (Cr) and choline (Ch), and no differences between spectra from left and right temporal lobes are apparent. In the TLE patient, the MRI does not show any tissue loss in the temporal lobes. However, the NAA signal from the right temporal lobe (left on MRI) is obviously decreased compared to the Cr and Ch signals in the same spectrum and relative to the NAA signal on the contralateral side. This correctly lateralizes the seizure focus to the patient's right temporal lobe.

AN OVERVIEW OF FUNCTIONAL MAGNETIC-RESONANCE IMAGING

Xiaoping Hu, Tuong Le, Seong-Gi Kim and Kamil Ugurbil
Center for Magnetic Resonance, University of Minnesota, Minneapolis, MN 55455

In the past few years, one of the most significant developments in magnetic resonance imaging (MRI) is the use of MR imaging to non-invasively map human cortical function without the use of exogenous contrast agents[1-3]. Since its introduction in 1992, functional magnetic resonance imaging (fMRI) has emerged as a powerful tool for studying neuronal function and generated an enormous amount of interest among neuroscientists, NMR scientists, and clinicians. The purpose of this paper is to outline the principle of fMRI and the associated technical issues and illustrate the utility of fMRI with representative applications.

The basis of fMRI is the blood oxygenation level dependent (BOLD) contrast which is derived from the fact that deoxyhemoglobin is paramagnetic and changes in the local concentration of deoxyhemoglobin within the brain lead to alterations in the magnetic resonance signal. Neuronal activation within the cerebral cortex causes an increase in blood flow without a commensurate increase in oxygen extraction. Consequently, the capillary and venous deoxyhemoglobin concentrations decrease, leading to an increase in T2* and T2. This increase is reflected as an elevation of intensity in T2*- and T2-weighted MR images.

Despite the success of many reported BOLD fMRI studies, controversy pertaining to the exact origin of the functional signal in the MR images still remains. Recent studies have revealed that activation maps are dominated by large vessel contributions, particularly at low magnetic fields and at short echo times. One cause of the large vessel contribution is signal enhancement due to increased flow during activation; this enhancement could be reduced by using low flip angle sequences and by using reordered data acquisition. Calculations and experiments evaluating the vascular origin of the BOLD effect were performed by a number of groups. Numerical results indicated that the BOLD phenomenon was dependent on vessel size, and increased linearly on the main magnetic field magnitude (B_0) for large vessels and quadratically with B_0 for small vessels. In agreement with these calculations, high resolution studies illustrated that most of the high intensity task-related changes in the functional image are associated with large venous vessels and coexist together with smaller but detectable contributions from gray matter areas devoid of large vessels. More recently, an initial signal decrease in T2*-weighted images was observed, mirroring results from optical imaging studies and validating the fMRI methodology.

As a result of the field dependence of the fMRI contrast, studies performed at 4 Tesla are more sensitive to neuronal activation. A study conducted by Turner et al. has demonstrated that the contrast at 4 Tesla with a TE of 25 ms was approximately 3 times that at 1.5 Tesla and 40 ms. In addition to the increased contrast, high field also provides better signal-to-noise ratio. Despite the apparent advantage of the high field strength, other factors should be taken into account. T2* is shorter at higher fields, attenuating the overall image intensity and making echo-planar imaging more difficult. Furthermore, the physiological related noise can be more pronounced at high field if it is dominated by the respiration-induced susceptibility effects. These factors may slightly offset the advantage of high field strength. Furthermore, since most clinical systems are operating at 1.5 Tesla, fMRI studies will continue to be performed at that field strength.

FMRI relies on the detection of localized changes in signal intensity in T2*(or T2)-weighted images. Ideally, only intensity changes related to neuronal activation should be detected. In practice, many other sources contribute to the image-to-image intensity fluctuation, leading to artifacts in the resultant functional maps. These sources include system instability, subject movement, as well as normal physiological motions. Artifacts due to gross motion have been recognized as one possible source of false activation, and spatial registration of images can be beneficial in reducing these

artifacts. In addition to possible gross motion of subject, however, a major source of signal fluctuations is brain motion and other effects caused by respiration and cardiac pulsation and these effects cannot be readily eliminated. Several techniques have been proposed to reduce physiology related signal variation in fMRI. A navigator echo technique was adopted for fMRI to account for the global effects of breathing. and is able to reduce the signal fluctuation substantially. However, it only reduces the phase-encoding artifacts in a single image and does not directly correct the image-to-image variations. For echo-planar imaging, temporal filtering that suppresses the frequencies corresponding to the cardiac pulsation and respiration, respectively, has been described. The success of the filtering approach, however, relies on the periodicity of the physiological motion and on the ability to acquire images fast relative to the physiological pulsation. Furthermore, the filtering approach may distort the signal changes arising from neuronal activation. Recently a new technique based on retrospective estimation to correct for physiological fluctuation is developed. This approach reduces the signal fluctuation by as much as 80% without relying on the periodicity of physiological motion and fast image acquisition and without distorting the functional signal.

In functional imaging, T2*-weighted images are acquired consecutively while the subject alternate between various neuronal states. To quantitate the spatial extent and intensity of the changes in the T2*-weighted images, data analysis techniques are used. Currently, two techniques have been widely utilized. The first is the student t-test which is used in fMRI to assess the statistical significance of image intensity change between the baseline and activation periods. A significance level is then set to select pixels with significant change for further processing. A functional map is generated based the relative change (i.e. difference/baseline) or based on the Z value which corresponds to the t-statistic (i.e. difference/standard deviation). Another widely used approach is the cross-correlation technique. With this technique, a correlation template is first generated based on the stimulation paradigm and some knowledge of the hemodynamic response of the brain. Subsequently, the correlation between the time course of each pixel and the template is calculated and pixels are thresholded based the correlation coefficient. A map representing the correlation coefficient can then be generated. While the two techniques are similar in nature, they have some differences. The correlation approach is more flexible in that the hemodynamic response can be readily accounted for. However, it is not straightforward to assess the statistical significance based on the correlation coefficient. Recent work by Friston et al has provided a possible theoretical basis for the statistical significance in correlation analysis; however it has not been widely accepted.

To illustrate the utility of fMRI, several representative examples are described. Initial fMRI studies were conducted with photic stimulation; functional activation maps of the visual cortex were generated[1-2]. These studies were soon followed by studies of the motor function[3-4]. Subsequently, cognitive functions, such as language[5] and memory, were studied successfully, demonstrating the ability of fMRI in studying cognitive activities. In addition to functions of the cerebrum, fMRI has also been used to study the cerebellar involvement in a number of tasks.

In summary, while still in its infancy, fMRI represents a major breakthrough in neuroimaging and is becoming a widely accepted tool for studying neuronal function. However, technical development are still needed to make it more robust and reliable.

1. S. Ogawa et al., *PNAS*, 89 (1992) 5951.
2. K. K. Kwong et al., *PNAS*, 89 (1992) 5675.
3. P. A. Bandettini et al., *Magn Reson Med*, 25 (1992) 390.
4. S.-G. Kim et al., *J Neurophysiol*, 69 (1993) 297.
5. R. M. Hinke et al., *NeuroReport*, 4 (1993) 675.
6. This work is supported by the National Institutes of Health (grant RR08079).

GREEN FLUORESCENT PROTEIN: USE OF GFP-CHIMERAS IN THE ANALYSIS OF MICROTUBULE-ASSOCIATED PROTEIN 4 DOMAINS AND MICROTUBULE DYNAMICS

J.B. Olmsted,* K.R. Olson,* M.L. Gonzalez-Garay,** and F. Cabral**

*Department of Biology, University of Rochester, Rochester, NY 14627
**Department of Pharmacology, University of Texas Medical School, Houston, TX 77225

Green Fluorescent Protein (GFP) is an endogenous 27 kDa fluorophore of the jellyfish, *Aequorea victoria*. Chalfie et al. first described the exogenous expression of this molecule in bacteria, and its utility as a reporter in higher eukaryotes.[1] Potential applications of GFP have been expanded through the construction of variants with enhanced brightness and/or different spectral properties.[2,3,4]

We have explored using GFP for the analysis of the real-time behaviors of microtubules and their associated proteins. Constructs of microtubule-associated protein 4 (MAP 4) or β-tubulin were generated in pRC/CMV vectors and used in either transient or stable transfection assays in a variety of cultured cell lines (3T3, PtK1, BHK, CHO, Cos). The GFP-chimeras were visualized using conventional fluorescence microscopy and confocal laser scanning microscopy. Unusual features of the GFP reporter are that fluorescence intensity increased 2-10 fold upon illumination, and that phototoxicity was low.

GFP alone distributed uniformly throughout the cytoplasm and nucleus of cells (Fig. 1). Cells transfected with constructs in which GFP was linked at the C-terminus of β-tubulin showed typical microtubule arrays (Fig. 2), and cells continued to divide normally. These patterns resembled those seen by conventional immunofluorescence microscopy of tubulin, or following microinjection of tubulin molecules covalently tagged with other fluorophores (e.g., rhodamine). Full length GFP-MAP 4 bound to microtubules, and microtubule organization appeared normal (Fig. 3). In contrast, the basic domain of MAP 4 alone caused extensive reorganization of microtubules (Fig. 4). Further analyses with constructs encoding other MAP 4 domains suggested that various regions of this MAP could significantly alter microtubule organization.[5]

To investigate the dynamics of the GFP-tagged proteins, time-course analyses were performed using confocal microscopy. Images were typically obtained at a single Z-axis from 2 or 3 scans (each 0.8 sec) and recorded every 10 to 30 sec. At attenuated powers (1-10%) of the Kr-Ar laser 488 nm line, GFP showed very little photobleaching over a prolonged period of recording (5-10 minutes) and cells remained viable. Plots of microtubule ends showed that microtubules decorated with full-length MAP 4 underwent rapid growth and shrinkage (Fig. 5). In contrast, microtubules decorated with the basic domain of MAP 4 were relatively static; microtubules in bundles moved and grew, but rarely shortened (Fig. 6). The low toxicity and stability of the GFP tag, the availability of spectral variants, and the biological activity of the GFP chimeras now enable direct correlations to be made between MAP behavior and microtubule dynamics.

References

1. M. Chalfie et al., *Science*, 263 (1994) 802
2. R. Heim et al., *Proc. Natl. Acad. Sci. USA*, 91 (1994) 12501
3. S. Delgrave et al, *Bio/Technology*, 13 (1995) 151
4. R. Heim and R.Y. Tsien, *Curr. Biol.*, 6 (1996) 178
5. K. R. Olson et al., *J. Cell Biol.*, 130 (1995) 639
6. The authors gratefully acknowledge the use of confocal microscopy facilities at SUNY Buffalo, and the assistance of Dr. Robert Summers in obtaining images. This work was supported by the National Institutes of Health (GM 22214 to JBO and CA 52962 to FC).

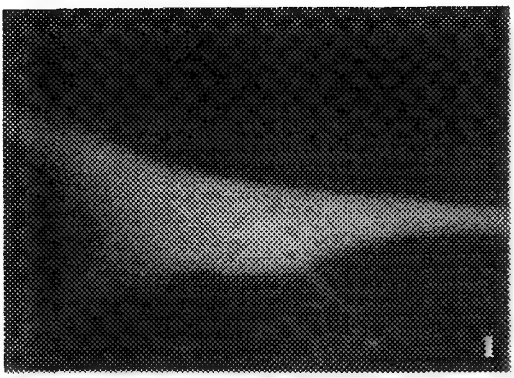

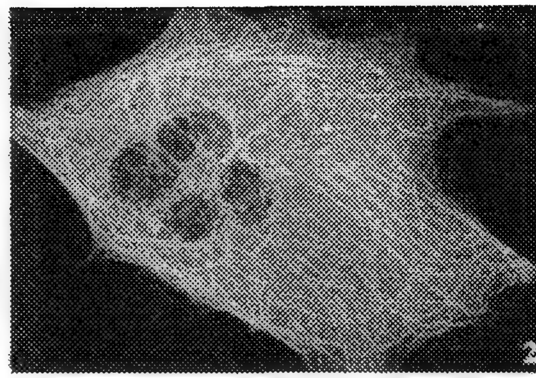

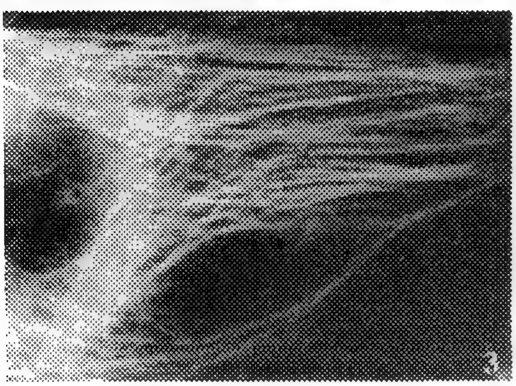

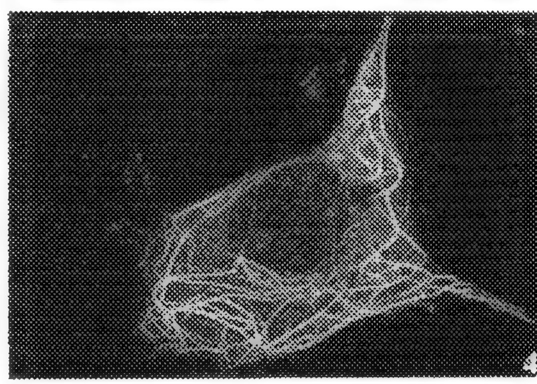

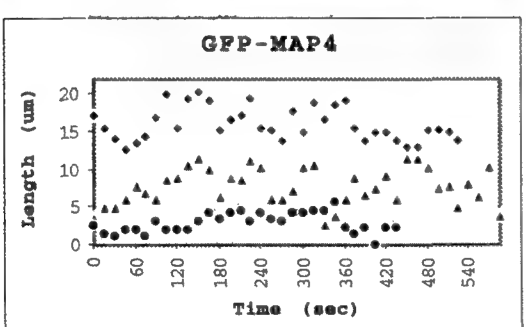

5

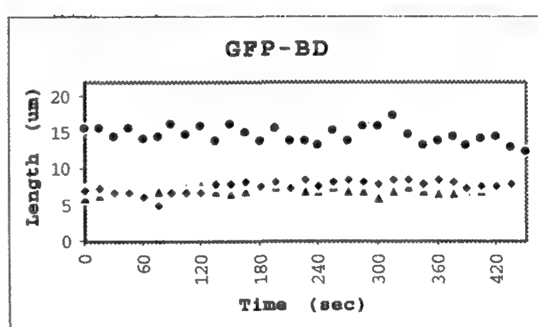

6

FIG. 1 Conventional fluorescence microscopy of a living BHK cell transfected with GFP alone
FIG. 2 Confocal microscopy of a living L cell transiently transfected with GFP-β tubulin
FIG. 3 Conventional fluorescence microscopy of a living CHO cell stably transfected with GFP-MAP 4
FIG. 4 Confocal microscopy of a living BHK cell transfected with GFP-MAP 4 basic domain (BD)
FIG. 5 GFP-MAP 4 dynamics in three BHK cells
FIG. 6 GFP-BD dynamics in three BHK cells

EMERGING APPLICATIONS OF FLUORESCENCE SPECTROSCOPY TO CELLULAR IMAGING: LONG-LIFETIME METAL-LIGAND PROBES, MULTI-PHOTON EXCITATION, LIGHT QUENCHING, AND LIFETIME IMAGING

J. R. Lakowicz

University of Maryland at Baltimore, Department of Biochemistry and Molecular Biology, 108 N. Greene Street, Baltimore, Maryland 21201

The applications of advanced concepts in fluorescence spectroscopy are increasing rapidly due to developments in probe chemistry and optical technology. In this talk we describe recent developments and their applications to cellular imaging.

While there exists thousands of fluorescent probes, almost all display lifetimes from 1 to 10 ns. These ns decay times are comparable to that found for cellular and tissue autofluorescence, which typically limits the sensitivity of most measurements. The lanthanides display long decay times, but their emission is unpolarized and cellular labeling is difficult. To circumvent these difficulties we are developing metal-ligand complexes as typified by $Ru(bpy)_3$ and its conjugtable derivatives (Figure 1). The asymmetrical complexes display high anisotropy. The high anisotropy, combined with decay times of 400 ns or longer (Figure 2) results in probes capable of measuring microsecond macromolecular hydrodynamics.[1,2] The use of long lived probes allows gated detection to avoid the prompt autofluorescence. Additionally, the metal-ligand probes are highly photostable.

In fluorescence microscopy it is difficult to quantify the intensity due to the unknown probe concentration at each point in the image and the effects of photobleaching. This laboratory[3] and others[4,5] have developed fluorescence lifetime imaging microscopy (FLIM) in which the image contrast is based on the decay time at each point in the image. The ns decay times of most fluorophores results in moderately complex instrumentation for FLIM.[3-5] However the development of red absorbing and long-lifetime probes can result in all solid-state FLIM instruments, based on gatable CCD detectors and solid state light sources (Figure 3).

The availability of ps and fs laser sources has resulted in the possibility of two-photon excitation, which is now used to obtain intrinsic "confocal" 3D imaging. In recent reports we have shown that three-photon excitation is possible with a number of fluorophores, including the calcium probe Indo-1.[6,7] Three-photon excitation of Indo-1 can be accomplished near the peak of the Ti:Sapphire tuning curve at 845 nm (Figure 4). Remarkably the intensity with three-photon excitation is only about 50-fold less than with two-photon excitation (Figure 5).

We will also describe the phenomena of light quenching (Figure 6). This phenoman can be used to control the excited state population and orientation.[8] This seemingly exotic topic is already being used to provide "confocal" imaging, where the modulated signal originates only in the region of beam overlap.[9-10] In summary, cellular imaging capabilities are improving due to a combination of emerging technologies.

References

1. E. Terpetschnig et al., (1995) *Biophys. J.*, 68:342-350.
2. E. Terpetschnig et al. (1995) *Anal. Biochem.*, 227:140-147.
3. J.R. Lakowicz et al. (1994) *Cell Calcium*, 15:7-27.
4. A. Periasamy et al. (1995) *Microscopy & Analy.*, March, 33-35.

5. A. Periasamy et al. (1995) *J.M.S.A.*, 1(1):13-23.
6. I. Gryczynski et al. (1995) *Photochem. Photobiol.*, 62(4):804-808.
7. H. Szmacinski et al. (1996) *Biophys. J.*, 70:547-555.
8. I. Gryczynski et al. (1994) *J. Phys. Chem.*, 98:8886-8895.
9. S.W. Hell et al. (1995) *J. Microscopy*, 180(2):RP1-RP2.
10. C.Y. Dong et al. (1995) *Biophys. J..*, 69:2234-2242.

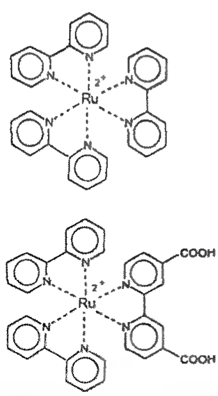

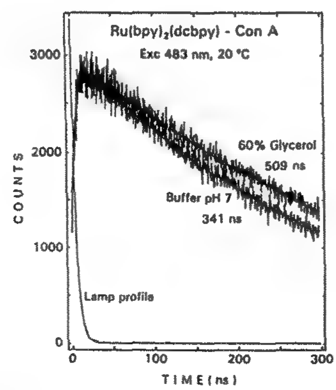

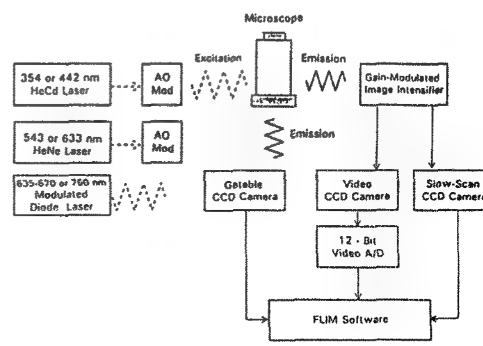

Figure 1. Chemical structure of $[Ru(bpy)_3]^{2+}$ and of $[Ru(bpy)_2(dcbpy)]$.
Figure 2. Intensity decays of $[Ru(bpy)_2(dcbpy)]$ conjugated to Concanavalin A.
Figure 3. Possible future FLIM instrument configurations.

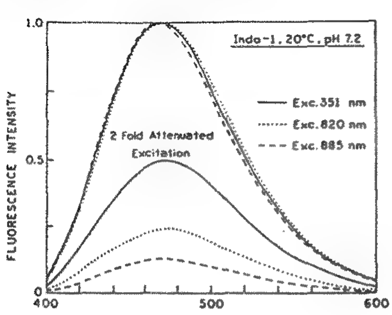

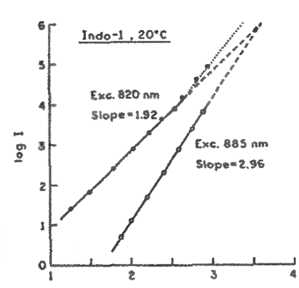

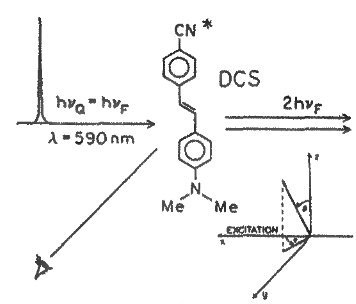

Figure 4. Emission spectra of Indo-1 for excitation at 351, 820 and 885 nm. Also shown are the emission spectra for each excitation wavelength with a two-fold attenuation of the incident light using a neutral density filter.
Figure 5. Dependence of the emission intensity of Indo-1 on laser power at 820 and 885 nm. The dotted line at 820 nm shows the slope at higher laser power. The laser power is in mW.
Figure 6. Intuitive description of light quenching.

LARGE-CLUSTER AND COMBINED FLUORESCENT AND GOLD IMMUNOPROBES

Richard D. Powell,* James F. Hainfeld,* Carol M. R. Halsey,* David L. Spector,** Shelley Kaurin,** Jennifer McCann,** Roger Craig,† Fredric S. Fay,† and Kathryn E. McNamara†

* Nanoprobes, Incorporated, Stony Brook, NY 11790
** Cold Spring Harbor Laboratory, 1 Bungtown Road, Cold Spring Harbor, NY 11724
† University of Massachusetts Medical Center, Biomedical Imaging Group, Worcester, MA 01605

Two new types of covalently linked, site-specific immunoprobes have been prepared using metal cluster labels, and used to stain components of cells. Combined fluorescein and 1.4 nm "Nanogold"[1] labels were prepared by using the fluorescein-conjugated tris (aryl) phosphine ligand (**1**) and the amino-substituted ligand (**2**) in the synthesis of the Nanogold cluster. This cluster label was activated by reaction with a 60-fold excess of *sulfo*-Succinimidyl-4-*N*-maleimido-cyclohexane-1-carboxylate (*sulfo*-SMCC) at pH 7.5, separated from excess cross-linking reagent by gel filtration, and mixed in ten-fold excess with Goat Fab' fragments against mouse IgG (obtained by reduction of $F(ab')_2$ fragments with 50 mM mercaptoethylamine hydrochloride). Labeled Fab' fragments were isolated by gel filtration HPLC (Superose-12, Pharmacia). A combined Nanogold and Texas Red label was also prepared, using a Nanogold cluster derivatized with both (**2**) and its protected analog (**3**): the cluster was reacted with an eight-fold excess of Texas Red sulfonyl chloride at pH 9.0, separated from excess Texas Red by gel filtration, then deprotected with HCl in methanol to yield the amino-substituted label. This was conjugated to goat anti-mouse Fab' fragments using the above procedure.

The fluorescein/Nanogold probe was used to label a pre-mRNA splicing factor in HeLa cell nuclei, as a secondary antibody against a monoclonal primary antibody specific for the SC35 splicing factor.[2] Specific staining was observed by confocal laser scanning microscopy (Fig. 2(a)), in which measured fluorescence intensities were approximately one-half of those found with a commercially available FITC-labeled secondary IgG antibody, and by transmission electron microscopy with silver enhancement (HQ Silver, Nanoprobes)(Fig. 2(b)).

Combined fluorescein/Nanogold anti-mouse Fab' was also used to label vinculin and pericentrin in smooth muscle cells, as a secondary probe for monoclonal antibodies against these proteins.[3] Specific staining was observed by fluorescence microscopy with deconvolution analysis.[4] Measured fluorescence intensities were 0.4 relative to a commercially available fluorescein-labeled IgG secondary antibody. For vinculin, some specific staining was also observed by electron microscopy with silver enhancement. These results indicate that these reagents provide a unique method for visualizing the same molecules at both the fluorescence and the EM level.

Functionalized platinum and palladium clusters 2 to 3 nm in diameter were prepared by reduction of an eight-fold excess of metal acetate with a mixture of the functionalized 1,10-phenanthroline ligands (**4**) and (**5**), followed by air oxidation of the surface metal atoms.[5] Platinum clusters prepared in this manner are shown in Fig. 5. These large clusters were conjugated to goat anti-mouse Fab' fragments using the procedure described above; conjugates were isolated by gel filtration HPLC (Superose-12, Pharmacia). These conjugates were readily silver enhanced: in immunoblots, they exhibited sensitivities equal to Nanogold conjugates, detecting as little as 10 pg of mouse IgG immobilized on nitrocellulose membrane. These larger labels were clearly visible in the electron microscope at 35,000X magnification in the immunolocalization of SC35 in HeLa cells; Nanogold was not visualized under these conditions.

References

1. Hainfeld, J. F., and Furuya, F. R., *J. Histochem. Cytochem.* 40 (1992) 177.
2. Spector, D. L., Fu, X.-D., and Maniatis, T.; *EMBO J.*, 10 (1991) 3467.
3. Moore, E. D. W., et al ; *Nature*, 365 (1993) 657.

4. Coggins, L. W., and Fay, F. S.; in "Computer Methods and Programs in Biomedicine;" Vol. 22, p. 69; Elsevier Publishers, New York, NY (1986).
5. (a) Schmid, G.; Morun, B., and Malm, J.-O.; *Angew. Chem. Int. Ed. Eng.*, 28 (1989) 778; (b) Schmid, G., et al; *J. Amer. Chem. Soc.*, 115 (1993) 2046.
6. This work was supported by NIH grants 2R44GM48328 and 2R44GM49564.

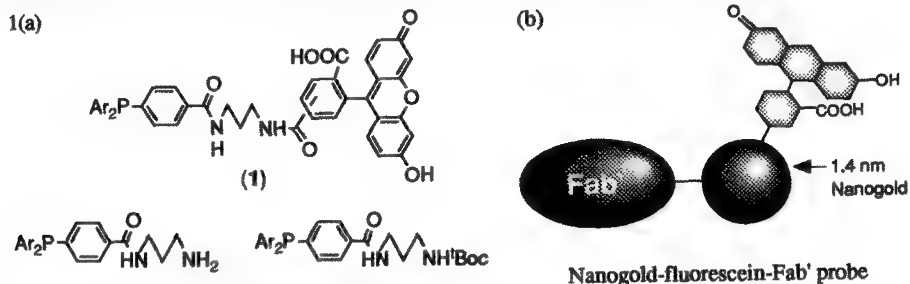

Nanogold-fluorescein-Fab' probe
(all moities covalently attached)

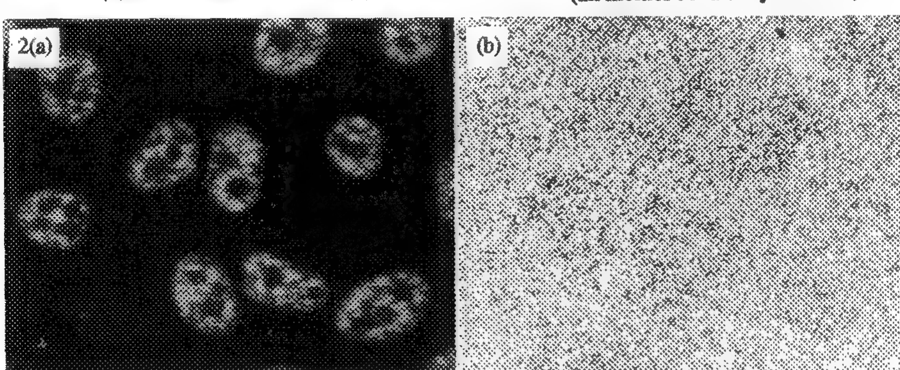

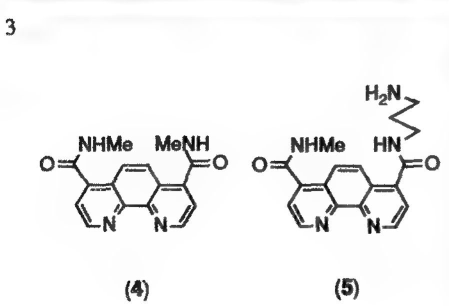

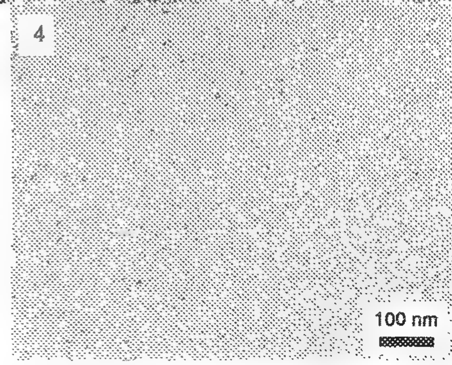

FIG. 1. (a) Ligands used for combined fluorescent /gold labels; (b) Fluorescein/Nanogold-Fab'.
FIG. 2. (a) Confocal laser scanning micrograph of HeLa cells labeled with anti-SC35 monoclonal primary antibody, detected with fluorescein/Nanogold-labeled goat Fab' anti-mouse antibody fragment (X 400) (b) Electron micrograph after silver enhancement (X 18,000).
FIG. 3. 1,10-phenanthroline ligands for preparation of large platinum/palladium cluster complexes.
FIG. 4. Transmission electron micrograph of large platinum clusters (Original mag. X 75,000).

NOVEL LABELING METHODS FOR EM ANALYSIS OF ULTRATHIN CRYOSECTIONS

John M. Robinson*, Toshihiro Takizawa**

*Department of Cell Biology, Neurobiology, and Anatomy Ohio State University, Columbus, OH 43210
**Department of Anatomy, Jichi Medical School, Tochigi, Japan

Ultrathin cryosections are the most favorable material for localization of intracellular antigens with particulate probes (e.g., colloidal gold) in post-embedding immunocytochemistry. Cryosections are prepared under the most benign conditions as compared to embedding samples in various kinds of plastic media. Typically, higher labeling efficiencies can be achieved with ultrathin frozen sections than with plastic sections.[1]

We have utilized human neutrophils, the most abundant type of leukocyte, as a model system to explore labeling procedures for ultrathin cryosections. These labeling procedures can serve as alternative or complementary approaches to the traditional colloidal gold label. Neutrophils are characterized by the presence of numerous granules in their cytoplasm. For many years, the model for neutrophil structure has held that there are two granule types in these cells, the so-called azurophilic and specific granules. We have described an additional cytoplasmic compartment with unusual properties in neutrophils.[2] This compartment is characterized by the presence of the enzyme alkaline phosphatase (Fig. 1). We have developed a method in which we can detect the cytochemical activity of this enzyme on ultrathin cryosections and then localize additional proteins by means of immunocytochemistry on the same section (Fig. 2). With this method, we have shown that alkaline phosphatase is in a compartment distinct from the specific granule where previously it had been thought to reside.[3]

Even though ultrathin cryosections are an excellent substrate for EM-level immunocytochemistry, there are certain limitations to this approach. One potential problem that has been noted relates to the limited ability of colloidal gold to penetrate into sections.[4] The degree of penetration of colloidal gold-immunoprobes relates to the size of the particles. Indeed, there is an inverse relationship between particle size and labeling density.[5] We have used 1.4-nm gold particles conjugated to Fab fragments as the secondary antibody. These very small particles are subsequently visualized following a silver enhancement procedure. The 1.4-nm particles can be used alone or in conjunction with standard colloidal gold in double-label preparations (Fig. 3). Using 1 - 2 μm thick cryosections, instead of ultrathin cryosections, we demonstrate that 1.4-nm immunoprobes penetrate into cryosections much better than do 5- and 10-nm colloidal gold particles (Fig. 4 - 6). These results illustrate the usefulness of alternative labeling procedures for ultrathin cryosections.

References

1. G. Griffiths and H. Hoppeler, J Histochem Cytochem, (1986) 34: 1389.
2. T. Kobayashi and J.M. Robinson, J Cell Biol, (1991) 113: 743.
3. T. Takizawa and J.M. Robinson, J Histochem Cytochem, (1993) 41: 1635.
4. J.W. Slot et al., Am J Anat, (1989) 185: 271.
5. T. Takizawa and J.M. Robinson, J Histochem Cytochem, (1994) 42: 1615.

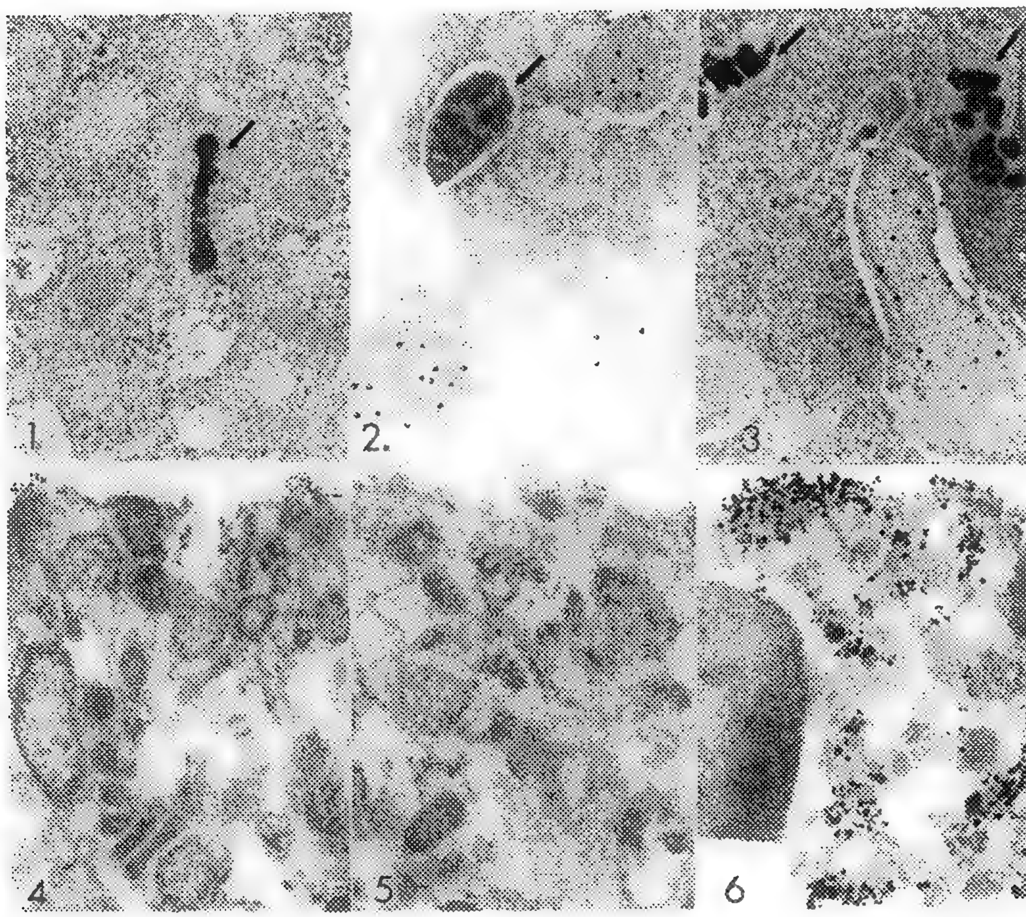

FIG. 1 Pre-embedding enzyme cytochemical localization of alkaline phosphatase to a unique compartment (arrow) in human neutrophils.
FIG. 2 Localization of alkaline phosphatase (arrow) by enzyme cytochemistry and lactoferrin by immunogold labeling in the same ultrathin cryosection.
FIG. 3 Localization of complement decay accelerating factor with 1.4-nm immunogold and silver enhancement (arrow) and lactoferrin with 15-nm colloidal gold.
FIG 4 Detection of lactoferrin with 10-nm colloidal gold in a thick cryosection. Localization restricted to granules at the cut surface.
FIG. 5 Detection of lactoferrin with 5-nm colloidal gold in a thick cryosection. Localization restricted to granules at the cut surface.
FIG. 6 Detection of lactoferrin with 1.4-nm immunogold and silver enhancement in a thick cryosection. Specific labeling is found throughout the section.

HIGH PERFORMANCE NANOGOLD™-*IN SITU* HYBRIDZATION AND ITS USE IN THE DETECTION OF HYBRIDIZED AND PCR-AMPLIFIED MICROSCOPICAL PREPARATIONS

G. W. Hacker,* I. Zehbe,** J. Hainfeld,*** A.-H. Graf,**** C. Hauser-Kronberger,* A. Schiechl,* H. Su,***** and O. Dietze*

* Institute of Pathological Anatomy, Salzburg General Hospital, Muellner Hauptstr. 48, A-5020 Salzburg, Austria
**Department of Pathology, University Hospital, S-751 85 Uppsala, Sweden
***Nanoprobes, 25 East Loop Drive, Suite 124, Stony Brook, NY 11790-3355
****Department of Obstetrics and Gynecology, Salzburg General Hospital, A-5020 Salzburg
*****Department of Histology and Embryology, Fourth Military Medical University, Xi'an, Shaanxi, PR China

In situ hybridization (ISH) with biotin-labeled probes is increasingly used in histology, histopathology and molecular biology, to detect genetic nucleic acid sequences of interest, such as viruses, genetic alterations and peptide-/protein-encoding messenger RNA (mRNA). *In situ* polymerase chain reaction (PCR) (PCR *in situ* hybridization = PISH) and the new *in situ* self-sustained sequence replication-based amplification (3SR) method even allow the detection of single copies of DNA or RNA in cytological and histological material. However, there is a number of considerable problems with the *in situ* PCR methods available today: False positives due to mis-priming of DNA breakdown products contained in several types of cells causing non-specific incorporation of label in direct methods, and re-diffusion artefacts of amplicons into previously negative cells have been observed. To avoid these problems, super-sensitive ISH procedures can be used, and it is well known that the sensitivity and outcome of these methods partially depend on the detection system used.

A series of manuscripts dealing with highly sensitive ISH, PCR and 3SR procedures, combined with immunogold-silver staining (IGSS) methods and silver acetate autometallography has been published by our group.[1-11] Nanogold™ is a new gold label covalently bound to macromolecules with several advantages compared to colloidal gold[12]. A new unpublished modification uses a combination of ISH with streptavidin-Nanogold™ which is more sensitive than other conventional ISH procedures (such as peroxidase- or alkaline phosphatase-based systems). Cervical cancers usually contain very low copy numbers of human papillomavirus (HPV). We have chosen ten low-copy-number cases of cervical cancers which were HPV-16-positive in conventional solution phase PCR performed in DNA material obtained from routine paraffin sections. Serial sections were then hybridized with a commercial streptavidin-biotin-peroxidase-complex ISH technique (PathoGene-kits, Enzo, NY, USA) and our new streptavi-

din-Nanogold™-ISH with silver acetate autometallography. With standard streptavidin-biotin-peroxidase-complex ISH, HPV-16 DNA was found in only one of these ten cases. The new Nanogold™-modification showed the presence of HPV-16 hybrids in five of these cases. Detection was not 100 %, but far clearer and better than with other techniques.

The new streptavidin-Nanogold™-ISH technique resulted in black staining of the structures containing the DNA or RNA sequence in question distinctly standing out against the unlabeled background tissue (Fig. 1). Very low-copy specimens gave a punctuate staining appearance. Such preparations can also be transferred to the electron microscope and may therefore be used to evaluate specific nucleic acid sequence harbouring, e.g. virus-infected cells at the ultrastructural level.

We also used the new streptavidin-Nanogold™-ISH technique after *in situ* PCR and *in situ* 3SR and obtained strong labeling of HPV-16-DNA and mRNA in SiHa cell cultures known to contain one copy of HPV-16 DNA only.

References

1. G.W. Hacker et al., J. Histotechnol. 11(1988)213.
2. I. Zehbe et al., *Anticancer Res.* 12(1992)2165.
3. G.W. Hacker et al., *Chinese Med. J.* 106(1993)83.
4. G. Danscher et al., *J. Histotechnol.* 16(1993)201.
5. I. Zehbe et al., *Cell Vision* 1(1994)20.
6. G.W. Hacker et al., *Cell Vision* 1(1994)30.
7. I. Zehbe et al., *Cell Vision* 1(1994)46.
8. I. Zehbe et al., *Cell Vision* 1(1994)163.
9. G.W. Hacker et al., in *Modern Methods in Analytical Morphology*, J. Gu and G.W. Hacker, eds., New York, NY: Plenum-Press (1994)19.
10. I. Zehbe et al., *Cell Vision* 2(1995)240.
11. G.W. Hacker et al., *Cell Vision* 2(1995)247.
12. J.F. Hainfeld and F.R. Furuya, *J. Histchem. Cytochem.*40(1992)177.

13.This work was funded by the Medical Research Society of Salzburg, Austria, and the Lions Cancer Foundation, Uppsala, Sweden.

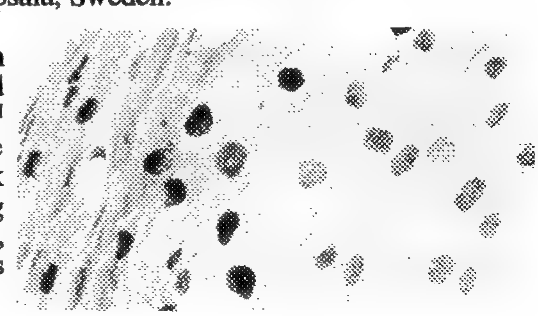

FIG. 1 Condyloma accuminatum hybridized for HPV-6/11 and detected with the streptavidin-Nanogold™ technique and silver acetate autometallography. Strong black staining is seen in cells expressing higher copy numbers of HPV DNA, and greyish or punctuate staining is seen in cells with low copy numbers.

GOLD LIPOSOMES

James F. Hainfeld

Biology Department, Brookhaven National Lab., Upton NY 11973

Lipids are an important class of molecules, being found in membranes, HDL, LDL, and other natural structures, serving essential roles in structure and with varied functions such as compartmentalization and transport. Synthetic liposomes are also widely used as delivery and release vehicles for drugs, cosmetics, and other chemicals; soap is made from lipids. Lipids may form bilayer or multilammellar vesicles, micelles, sheets, tubes, and other structures. Lipid molecules may be linked to proteins, carbohydrates, or other moieties. EM study of this essential ingredient of life has lagged, due to lack of direct methods to visualize lipids without extensive alteration. OsO4 reacts with double bonds in membrane phospholipids, forming crossbridges. This has been the method of choice to both fix and stain membranes, thus far. An earlier work described the use of tungstate clusters (W_{11}) attached to lipid moieties to form lipid structures and lipid probes.[1]

With the development of gold clusters, it is now possible to covalently and specifically link a dense gold sphere[2] to a lipid molecule; for example, reacting a mono-N-hydroxysuccinimide Nanogold cluster with the amino group on phosphatidyl ethanolamine. Examples of a gold-fatty acid and a gold-phospholipid are shown in Fig. 1.

Dipalmitoyl phosphatidylethanolamine-Nanogold (DPPE-Nanogold, Fig. 1b), which has C_{16} hydrophobic tail chains, was obtained from Nanoprobes, Inc.[3], and made into vesicles. Dried DPPE-Nanogold (10 nmoles) was resuspended in 0.5 ml methanol. 20 ml was transferred to a test tube and dried with a nitrogen stream. 50 ml water was added and the tube sonicated for 10 min in a bath unit at room temperature. A drop was applied to thin carbon supported by a holey film on an EM grid. After 1 min, the solution was wicked, rinsed with 20 mM ammonium acetate several times, wicked, and quick frozen in liquid nitrogen slush. The sample was then freeze dried overnight, brought to room temperature, transferred to the EM under vacuum, and inserted into the specimen stage which was cooled to -130° C. The samples were observed in the high resolution Brookhaven Scanning Transmission EM (STEM) operating in darkfield mode.[4]

Several interesting lipid forms were observed, including small micelles (Fig. 2), and bilayer vesicles that had apparently broken so that single and double layers were displayed (Fig. 3). Since no other unlabeled lipid was used, and the labeling was virtually quantitative, nearly every lipid molecule appeared with a gold cluster. Hexagonal close packing was observed in these regular arrays, with spacings of ~ 2.5 nm. This is approximately the diameter of the gold cluster, whose gold core is 1.4 nm, with an organic shell of total diameter of 2.7 nm. However, this is somewhat more than a typical spacing between phospholipids in native bilayers, which is ~ 1.3 nm.[5]

These methods provide a way of producing regular gold sphere monolayers, or other lipid structures. For biology, they might be intercalated into membranes to follow membrane movement, or used in reconstituted membrane-protein structures to study lipid distribution. They also provide a way to directly visualize liposomes, even at the light microscope level, via silver enhancement.[6]

References

1. J.F. Hainfeld, J.J. Lipka, and F.E. Quaite, J. Histochem. Cytochem. 38(1990)1793.

2. J.F. Hainfeld and F.R. Furuya, J. Histochem. Cytochem. 40(1992)177.
3. Nanoprobes, 25 East Loop Rd, Ste. 124, Stony Brook, NY 11790.
4. J.S. Wall, J.F. Hainfeld, and M.N. Simon, EMSA Bulletin 21(1991)81.
5. L. Stryer, in *Biochemistry* (1975).
6. J.F. Hainfeld and F.F. Furuya, in *Immunogold silver staining: Principles, methods and applications.* M. A. Hayat, ed., CRC Press, New York (1995)71.
7. The author would like to thank M. Simon, B. Lin, and F. Kito of the BNL STEM facility, and F. Furuya for synthesis and helpful discussions. This work was supported by NIH grant RR 01777 and US Dept of Energy, OHER.

1A

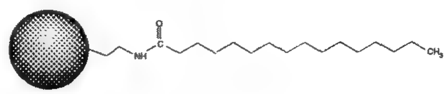

Fatty Acid - gold

1B

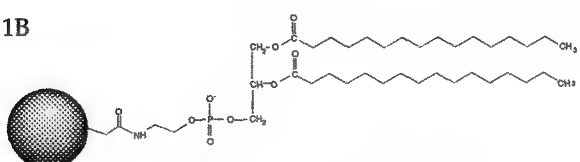

Dipalmitoyl phosphatidylethanolamine-Nanogold

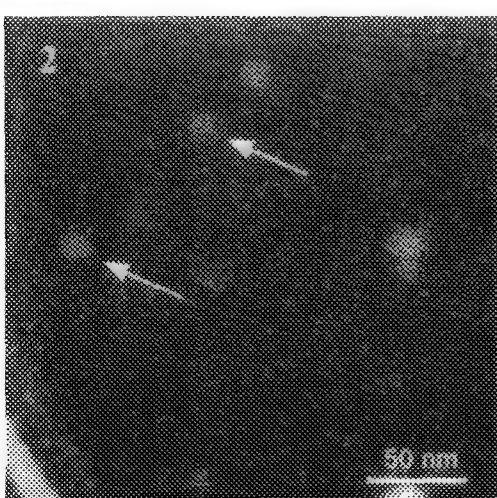

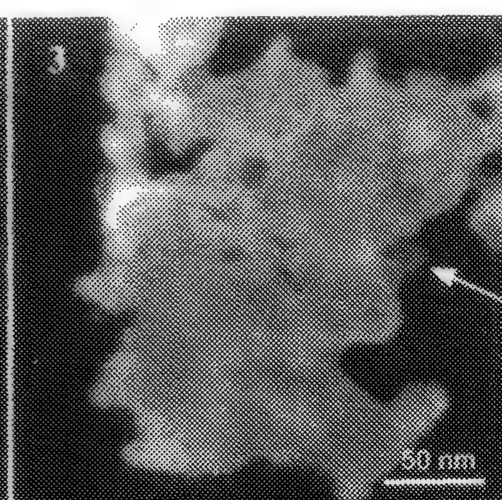

Fig. 1. Schematic drawing of gold-lipids. A. Fatty acid (palmitoyl, C_{16})-gold ; B. Phospholipid (DPPE, C_{16})-gold.
Fig. 2. Darkfield STEM micrograph of unstained gold-lipid micelles (arrows), made from DPPE-gold, with diameters of ~14 nm.
Fig. 3. Darkfield STEM micrograph of unstained gold-lipid bilayer, made from DPPE-gold; arrow points to single lipid layer region.

GREEN FLUORESCENT PROTEIN (GFP) AS A TRACER DYE FOR CELL MOVEMENTS IN DEVELOPING ZEBRAFISH EMBRYOS

T. Murakami, O.G. Doerre, L.D. Peachey, and E.S. Weinberg

Department of Biology, University of Pennsylvania, Philadelphia, PA 19104

Fluorescent dyes have been extremely useful in determining cell lineages in the developing zebrafish embryo. For example, injection of FITC-dextran into blastomeres has allowed the determination of a tissue fate map at late blastula[1] and a description of cell movements during gastrulation[2]. Here we describe the use of green fluorescent protein (GFP) as a tracer dye for cell movements in developing early zebrafish (*Danio rerio*) embryos. Since GFP was purified and cloned from the jellyfish *Aequorea victoria*, it has attracted great attention from biologists as an in vivo tracer and a reporter gene[3,4]. The protein requires no cofactors or substrates for its fluorescence. This property allows one to inject GFP DNA constructs or in vitro synthesized GFP mRNA into individual cells which can then be expected to continuously synthesize the protein, thus obviating the dilution and bleaching effects often observed when fixed amounts of fluorescent tracer dyes are injected into dividing cells. We inserted a GFP coding sequence into CS2+[5], a vector which perimits the transcription of the inserted sequence in eukaryotic cells and can also be used for efficient in vitro synthesis of RNA encoding the inserted open reading frame. We demonstrated that when GFP-CS2+ DNA is injected into one cell at the 1–4 cell stage, strong fluorescence is observed in approximately 5% of the cells at mid- to late-blastula stage (4–5 hours post-fertilization). As development proceeds through the blastula and gastrula stages in the GFP-CS2+ injected embryos, the total number of fluorescent cells increases approximately 6-fold, arranged in a clonal manner, reaching a peak in the 13 hour neurula. Expression can also be detected in almost every 24 hour embryo, although in a reduced number of cells. In contrast, when we inject GFP RNA into one cell at the 1–4 cell stage, most if not all of the cells are fluorescent in the blastula. Cells continue to fluoresce for at least the first 30 hours of development. This result indicated that GFP mRNA might be a suitable tracer of cell lineage and movement in the zebrafish embryo.

We applied the use of GFP mRNA to study the movement of cells that ectopically express the homeodomain transcription factor zOtx1[6]. *Otx1* is expressed in the presumptive forebrain and midbrain at the gastrula stage of zebrafish embryos[6], as is the case in other vertebrate embryos. Embryos injected with RNA encoding zOtx1 appear to have gastrulation defects indicative of abnormal cell movements. We traced the movements of the descendents of cells that ectopically express *zOtx1* by co-injecting RNAs encoding zOtx1 and GFP into single cells at the 16 cell stage. Bright fluorescence from GFP could be detected in a subpopulation (approximately 5–10%) of cells in the 5 hour blastula (Fig. 1a,d). When embryos were injected solely with GFP mRNA (Fig. 1d–f), descendents of the marked cells completed normal epiboly movements and eventually, at 12 hours, were dispersed throughout the head and trunk of the embryo. In contrast, descendents of cells injected with both zOtx1 and GFP RNAs did not disperse normally in the 5 hour and 8 hour embryos (Fig. 1a,b), and at 12 hours, the marked cells appeared to be excluded from the trunk and head (Fig. 1e). These fluorescent cells formed aggregates on the surface of the yolk, or between the trunk and yolk. Most of the zOtx1-injected embryos developed fairly normally despite the highly aberrant cell movements of those cells actually containing the ectopic *zOtx1* RNA. Cell movements in embryos injected with RNA encoding zOtx1 protein lacking were identical to those of embryos injected solely with GFP RNA. These results indicate the efficacy of GFP as a tracer to study cell movements in the zebrafish embryo and also a possible role of zOtx1 in restriction of cell movements and promotion of cell adhesion.

References

1. Kimmel, C.B., Warga, R.M. and Schilling, T.F. (1990) Development 120: 581–594.
2. Warga, R.M. and Kimmel, C.B. (1990) Development 120: 569–580.
3. Prasher, D.C., Eckenrode, V.K., Ward, W.W., Prendergast, F.G., and Cormier, M.J. (1992) Gene 111: 229–233.
4. Chalfie, M., Tu, Y., Euskirchen, G., Ward, W.W., and Prasher, D.C. (1994) Science 263: 802–805.
5. Turner, D.L. and Weintraub, H. (1994) Genes and Dev. 108: 569–580.
6. Li, Y, Allende, M., Finkelstein, R., and Weinberg, E.S. (1994) Mech. Dev. 48: 229–244.

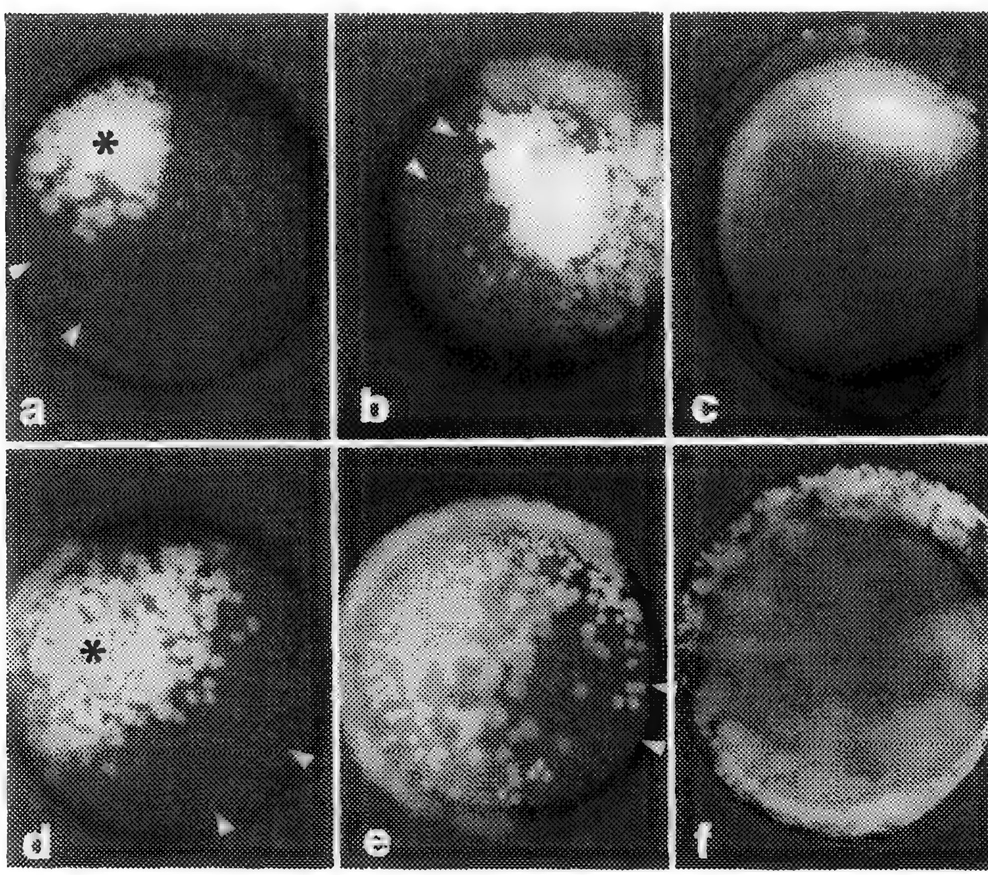

FIG. 1 Fluorescence microscopy of two representative zebrafish embryos injected with GFP and zOtx1 RNAs (a–c) or solely with GFP RNA (d–f) at 5 (a, d), 8 (b, e) and 12 (c, f) hours post-fertilization. Asterisks indicate GFP expressing cells. Arrowheads indicate the leading edges of epiboly movements.

IMMUNOGOLD-SILVER STAINING (IGSS) OF AGAROSE EMBEDDED (NCP) BVDV-INFECTED CELL SUSPENSIONS

C.E. Hearne and H. Van Campen

Department of Veterinary Sciences, University of Wyoming, Laramie, WY 82071

The use of pre-embedding immunogold-silver staining (IGSS) in electron microscopy of cell culture monolayers has been reported by various authors and its usefulness to localize antigens has been documented.[1,2,3] Embedding cell suspensions or cell fractions for IGSS can require time-consuming centrifugation steps. Embedding cell suspensions in agarose simplifies IGSS processing and embedding procedures.

Bovine turbinate cells (BTs) were grown to confluence in $25cm^3$ culture flasks. BTs were infected with a non-cytopathic strain (ncp) of bovine viral diarrhea virus (BVDV) while control cells were sham inoculated. At 18 h pi, cells were detached with trypsin. All following procedures were carried out at RT. The cells were fixed for 30 min in 2.0% paraformaldehyde + 0.2% glutaraldehyde in 0.1 M phosphate buffer, pH 7.4, and rinsed 3 times in 0.1 M phosphate buffer, pH 7.4 (each centrifuged for 10 min at 300g). The cells were resuspended in 1 ml of buffer, transferred to an eppendorf tube and centrifuged for 10 min at 300g. The excess buffer was removed, 1-2 drops of warm, molten 1.0% agarose added, and the mixture centrifuged for 1 min at 300g to pellet the cells to the tip of the tube. The solidified cell-agarose mixture was removed, cut into $<0.5mm^3$ pieces, and placed in phosphate buffer.[4]

IGSS procedures were carried out according to Nanoprobes, Inc.[5] Cell-agarose blocks were quenched for 5 min in 0.02 M glycine in 0.01 M PBS, pH 7.4, rinsed 3 times with PBG buffer containing 0.01 M PBS, pH 7.4, + 0.138 M NaCl + 0.002 M KCl + 0.5% BSA + 0.1% high purity gelatin, and treated for 60 min with 0.01 PBS, pH 7.4, + 0.1% saponin + 5.0% normal goat serum (NGS). The blocks were incubated for 60 min with the primary antibody, 20.10.6 MAb, washed with PBG buffer + 1.0% NGS and incubated for 60 min with secondary antibody conjugated with 1.4nm Nanogold (Nanoprobes, Inc., Stoney Brook, NY). After washing in PBG buffer + 1.0% NGS and multiple distilled water washes, the blocks were silver enhanced in the dark for 8 min using HQ Silver Enhancement Kit (Nanoprobe, Inc., Stoney Brook, NY) followed by multiple water washes. They were transferred to 0.1 M phosphate buffer, pH 7.4, Post-fixed for 30 min in 2.0% glutaraldehyde in 0.1 M phosphate buffer, pH 7.4 and rinsed 3 times in phosphate buffer. The blocks were treated with 0.1% OsO_4 in phosphate buffer for 30 min, rinsed in water multiple times, and en bloc stained for 60 min with 1.0% uranyl acetate in acetate buffer, pH 5.0. Following rinses in water, the blocks were dehydrated through a graded series of ethyl alcohol, infiltrated, and embedded in polybed-araldite resin (Polysciences, Inc., Warrington, PA), polymerized, sectioned with a Diatome diamond knife using a Reichert Ultracut, and viewed with a Philips 410 LS transmission electron microscope at 40 KV.

Figure 1 illustrates results obtained with the uninoculated control BT cells embedded in agarose. Minimal background labeling is noted (arrows). Figure 2 illustrates the location of non-structural protein, p125. Labeling is present on the cytosol of cells infected with a non-cytopathic BVDV.

The results indicate a time-saving advantage using agarose embedded cell suspensions for immunogold-silver staining investigations. This is an alternative to IGSS cells that grow in monolayers as well as those that grow in suspensions.

References:

1. Tao-Cheng, J.-H. and V.A. Tanner, Proc. 52nd Ann MSA Meeting, (1994) 306.
2. Burry, R.W., in Immunogold-silver Staining: Principles, Methods, and Applications, M.A. Hayat, ed., CRC Press, Boca Raton, FL (1995) 217.
3. Marchetti, A. and G. Bevelacqua, in Immunogold-silver Staining: Principles, Methods, and Applications, M.A. Hayat, ed., CRC Press, Boca Raton, Fl (1995) 275.
4. B. Plantholt, EMSA Bulletin, (1985) 15(2): 106.
5. Nanogold(TM) product information pamphlet, Rev.1.3 (2/93), Nanoprobes, Inc., Stoney Brook, NY.
6. The authors wish to thank Dr. E.J. Dubovi, New York State Diagnostic Laboratory, Cornell University, Ithaca, NY for providing the MAb 20.10.6 used in this investigation.

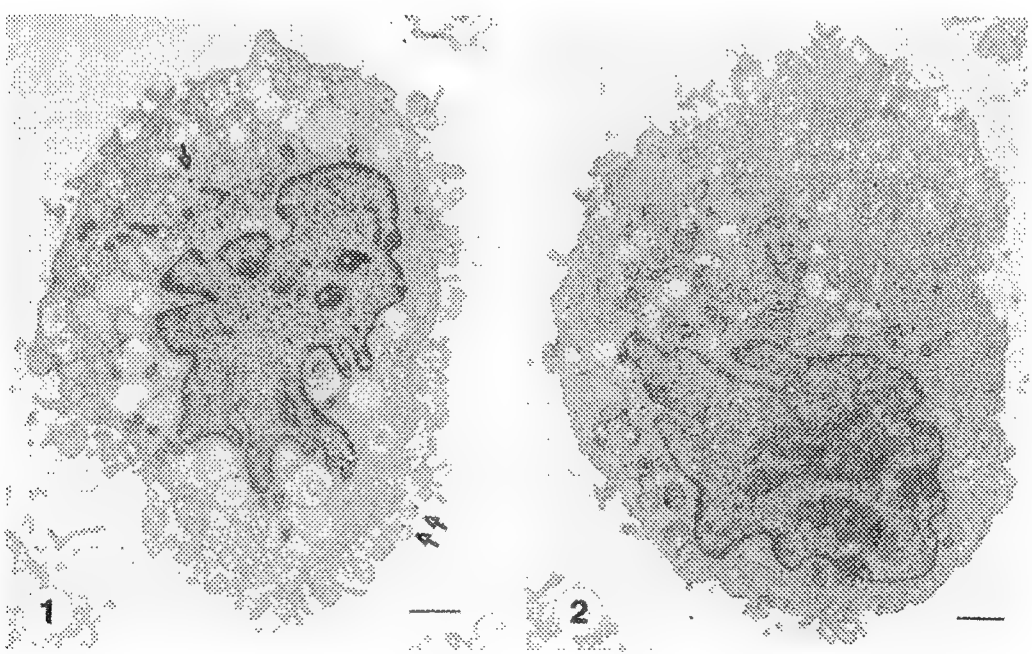

FIG. 1 Immunogold-silver stained uninoculated BT cells embedded in agarose. Bar = 1 micron.

FIG. 2 Immunogold-silver stained (ncp) BVDV infected BT cells embedded in agarose. Bar = 1 micron

CCD CAMERAS FACILITATE THE IMAGING OF SMALL GOLD PARTICLES IN IMMUNOGOLD-LABELLED ULTRATHIN CRYOSECTIONS

C.A. Ackerley*, L.E. Becker*, A. Tilups*, J.T. Rutka**, and J.F. Mancuso***

*Department of Pathology, Hospital for Sick Children, Toronto, Ontario, Canada
**Department of Neurosurgery, Hospital for Sick Children, Toronto, Ontario, Canada
***Advanced Microscopy Techniques, Danvers, MA

Immunogold labelled ultrathin cryosections have proven themselves invaluable in subcellular localizations of many epitopes. As there are no embeddents to block an antibody's access to an epitope beyond physical size or chemical alteration by primary fixation, immunogold labelling density is increased dramatically with smaller (>5nm) gold-ligand complexes. Takizawa and Robinson have elegantly demonstrated penetrations in excess of 1μm using 1.4nm gold-Fab conjugates, while 5nm IgG gold particles only partially penetrated the surface and 10nm IgG gold particles labelled the surface[1]. In order to visualize the 1.4nm gold-Fab particles silver enhancement was required leading one to doubt the viability of doing any quantitation.

Modern CCD cameras provide an effective alternative method of data collection to photographic plates with their ability to record 1000 x 1000 pixel digital images. Using a simple sharpen filter and contrast enhancement, 1.4nm gold Fab particles are easily resolved on thin films. Problems arise when using this small a particle on conventionally stained immunogold labelled cryosections. Standard preparation techniques employ the use of neutral uranyl acetate followed by embedding in methyl cellulose containing uranyl acetate at a concentration of 0.2%. Using this protocol and conventional photographic techniques we were able to localize two different isoforms of myelin basic protein, one to the intraperiod line[2] and the other to the major dense line[3] using 3nm gold-Fab particles. At conventional electron doses (usually in excess of 30 pa/cm^2 on the phosphorus screen) the specimen "clears" due to etching by the electron beam which sometimes results in a fine uniform granular precipitate not unlike 1.4nm gold-Fab particle in size and density. On a positive note some enhancement of these particles does occur at these electron doses due to the positive staining of the protein on the gold particle by the uranyl acetate.

To access the potential of using small immunogold particles and imaging them with a CCD a glial fibrillary acid protein (GFAP) expressing astrocytoma cell line was fixed in 4% paraformaldehyde in 0.1M phosphate buffer PH 7.4. The cells were then pelleted, embedded in gelatin, and cryoprotected with 2.3M sucrose. Ultrathin cryosections were then triple labelled with an antibody against GFAP (10nm gold), either α-actinin or β-spectrin (3nm gold), and CD44 (1.4nm). To minimize contamination due to the "clearing" effect at conventional electron doses staining with neutral uranyl acetate was omitted and the uranyl acetate concentration in the methyl cellulose was decreased to 0.05% uranyl acetate. Specimens were never submitted to electron doses greater than 2 pa/cm^2 on the phosphorus screen. Images were captured with the CCD and the contrast enhanced. They were then sharpened using a sharpen filter and examined on the computer monitor. Following this procedure images of the same area were recorded on plate film for comparative purposes.

There was little or no difference between the image obtained from the CCD and the photographic plate for all intensive purposes. The major change was the ease in obtaining an acceptable image. Where the CCD images were obtained in seconds, photographic plate

development and printing with reasonable contrast from such low density negatives were both tedious and time consuming.

The unenhanced 1.4nm gold-Fab was visible but this was probably due to the fact that CD44 is an external epitope[4] and some positive staining of the protein associated with the gold had occurred. α-actinin and β-spectrin were easily distinguished in the dense cytoplasm of the astrocytic processes using 3nm gold-Fab particles as was the GFAP labelled with 10nm-IgG gold. When 1.4nm gold-Fab particles were used with antibodies against cytoplasmic epitopes they were not detected.

The use of unenhanced 1.4nm gold-Fab particles has potential in quantitative studies involving plasma membrane constituents. Comparative quantitative studies will be done involving a number of gold-ligand systems. Of importance was the ease at which gold particles as small as 1.4nm could be detected using the CCD. As the images are already digitized this will aid in any particle density determinations.

REFERENCES:

1. T. Takizawa and J.M. Robinson, J. Histochem and Cytochem 42 (1994) 1615-1623.
2. J. McLaurin, C.A. Ackerley, and M.A. Moscarello, J. Neurosci Res 35 (1993) 618-628.
3. M. Yon et al, J. Neuroimmunol (1996) in press.
4. N. Gingrah, C.A. Ackerley, and M.A. Moscarello, Neuroreport 2 (1992) 441-444.

Dye sublimation print of triple labelled astrocytoma tissue culture cell captured with CCD camera. 1.4nm gold particles which label CD44 are easily distinguished (arrowheads) along the plasma membrance. 3nm particles which label β-spectrin are seen on portions of the inner membrance (arrows). A 10nm particle which labels GFAP is seen in the upper left corner of the micrograph. Bar equals 50nm.

UV-EXCITED FLUOROPHORE IMAGES OBTAINED WITH IR EXCITATION

D. Wokosin, V.F. Centonze, and J.G. White

Integrated Microscopy Resource, University of Wisconsin

The widespread use of two-photon excitation fluorescence imaging has been somewhat inhibited by the necessity to use large, expensive, high-power, short-pulse lasers. These ultra-short pulse lasers are used as an excitation source in a raster scanning configuration to provide sufficient peak power density in a lens focal volume to generate detectable two-photon absorption events for rapid imaging. Biological studies often benefit from multiple fluorescent labels and multi-labelled samples often require different excitation wavelengths for adequate excitation of the various colored fluorophores. This is achieved inexpensively with the three Krypton Argon laser lines in standard confocal imaging systems, but multiple two-photon excitation lasers--if available-- would be a very expensive system. The lasers commonly used for two-photon imaging are tuneable, but this is not a non-trivial and time consuming process. The tuning range on these lasers allows good access to the blue-emitting and green-emitting fluorophores via two-photon excitation; however, we have found that a fixed-wavelength, compact, pulsed infrared source at 1047nm can image a variety of commonly used biological fluorophores (blue-emitting, green-emitting, and red-emitting), even though they have disparate single-photon excitation peak wavelengths.

The technique of two-photon excitation fluorescence imaging[1] provides an elegant alternative to confocal imaging for optical sectioning of fluorescent samples. Fluorophore excitation is confined to the section being observed in two-photon excitation fluorescence imaging. Fluorophore excitation in the bulk of the sample is avoided since the excitation wavelength is around twice the excitation peak wavelength of the fluorophore being observed. The probability of two-photon absorption events is proportional to the square of the excitation intensity; therefore, two-photon events rapidly fall off away from the lens focal volume, thereby essentially eliminating fluorophore excitation outside of the focal volume. Thus, only the fluorophore being observed is excited with a consequent reduction of total fluorophore bleaching and potential phototoxicity; in addition, this obviates the need for a blocking aperture to reject out-of-focus interference. In contrast, confocal imaging produces fluorophore excitation throughout the sample and out-of-focus interference is removed by inserting a blocking aperture in the emission path.

We have developed a two-photon imaging system that uses an all-solid-state, mode-locked Nd:YLF laser operating at the fixed wavelength of 1047nm. This laser was supplied by Microlase, Ltd. (Scotland) and produces 300 femtosecond pulses at a repetition rate of 120 Mhz and a mean power of 300 mw. The laser is coupled to a Bio-Rad MRC 600 used as a laser scanning system that is attached to a Nikon Diaphot 300 inverted microscope. We have found that the 1047nm wavelength gives good excitation of many of the commonly used red-emitting fluorophores such as Cy 3 and rhodamine. In addition, the green fluorophore, fluorescein, can also be excited, although not as well as the red-emitting fluorophores. Fortuitously, we are also able to excite several UV emitting fluorophores, such as the DNA stains DAPI and Hoescht 33258. It is most likely that these fluorophores are excited by three-photon excitation fluorescence[3]. Figure 1 shows a DAPI stained *Caenorhabditis elegans* embryo. This image is a projection of optical sections where each optical section image was integrated for one minute. We have therefore found that it is possible to excite a wide range of fluorophores with a single excitation wavelength of 1047nm using both two-photon excitation and three-photon excitation fluorescence microscopy. This opens up the prospect of being able to view multiple-labelled specimens with a single, IR excitation source.

This work was supported by NIH Grant P41 RR00570-25A to the Integrated Microscopy Resaource.

References

1 W. Denk et al. *Science* **248**:73 (1990)
2 D.L. Wokosin et al. *Proc. SPIE,* (1996) in press.
3 I. Gryczynski et al. *Photochem. Photobiol* **62**:804 (1995)

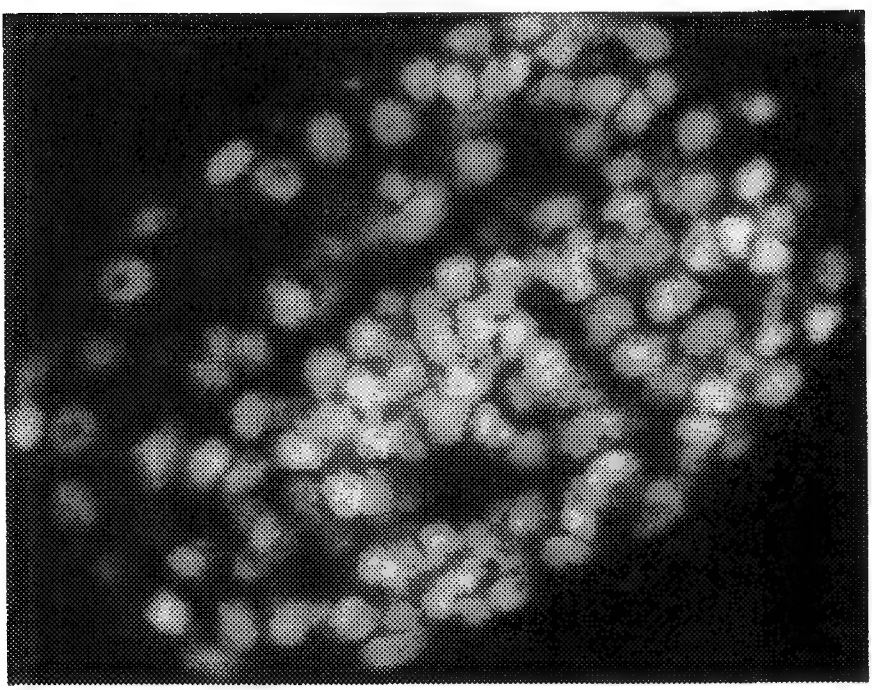

Image of a DAPI-stained whole-mount embryo of *Caenorhabditis elegans* revealing the nuclei. This image was obtained using 1047nm excitation and using a Nikon X60 N.A. 1.4 objective lens. The image is a projection of four optical sections.

VISUALIZATION OF INDIVIDUAL ASTROCYTES IN THREE-DIMENSIONAL CEREBELLAR TISSUES USING GREEN FLUORESCENT PROTEIN

M. D. Andersen*, D. H. Szarowski**, J. N. Turner***, and W. Shain****

* Department of Biomedical Engineering, Rensselear Polytechnic Institute, Troy, NY & Wadsworth Center, Albany, NY
** Wadsworth Center, Albany, NY
*** Wadsworth Center, Albany, NY, Department of Biomedical Engineering, Rensselear Polytechnic Institute, Troy, NY& School of Public Health, University at Albany, Albany, NY
**** Wadsworth Center, Albany, NY & School of Public Health, University at Albany, Albany, NY

The central nervous system is a complex structure traditionally studied through selective stains and two-dimensional images of fixed tissues. A long term goal of this laboratory is the study of dynamic cellular interactions in three dimensional tissues such as organotypic cultures. Due to the large volume of tissue, traditional microscopy methods contain excessive out-of-focus data making it difficult to observe clearly specific cellular interactions. The visualization of morphological changes in specific cells in living, three-dimensional tissues is commonly done with vital dyes. An alternate approach is labeling individual astrocytes with Green Fluorescent Protein (GFP) and injecting them into organotypic cultures.

GFP is a naturally fluorescent protein originally isolated from the jellyfish *Aequorea victorea.*[1] To label individual astrocytes, LRM55 astroglial cells were transfected with GFP using calcium phosphate. The percentage of stable transfectants was low (< 1%) resulting in expression of varying amounts of GFP, as seen in Figs 5 and 6. Approximately 60 clones were screened, and three of the most fluorescent cell lines were maintained for further experiments.

Cerebellar organotypic cultures, 400-µm thick, were prepared from 14-day old rat pups. Sagittal sections were sliced around the midline and maintained at the air media interface similar to the methods described by Stoppini et al.[2] The cultures appear to sustain normal morphology, and maintain their laminar structure (Fig 1,2). Organotypic cultures were fixed and stained for glial fibrillary acidic protein (GFAP) to accurately describe normal astroglial cell morphology. As seen in Fig 3, the radial glia are apparent and cultures appear to maintain normal morphology. Fluorescing astrocytes exhibiting varying morphologies were imaged throughout the depth of the slice; however, due to the large data sets, analysis was generally limited to a volume depth of < 100 µm.

In order to visualize individual astrocytes in three dimensional tissues, fluorescently labeled cells were injected into cerebellar organotypic cultures. Varying numbers of cells (10-1000) were injected using a Hamilton syringe in conjunction with a micro-manipulator. The organotypic cultures were then grown in culture for different periods of time prior to imaging with a scanning confocal microscope. As seen in figure 4, the transfected cells are visible in the cerebellar tissues.

References

1. Chalfie et al., *Science*, (1994) 802.
2. Stoppini et al., *J. Neurosci. Meth.*, (1991)173.
3. This work was partially supported by NIH (RR10957 and RR01219).

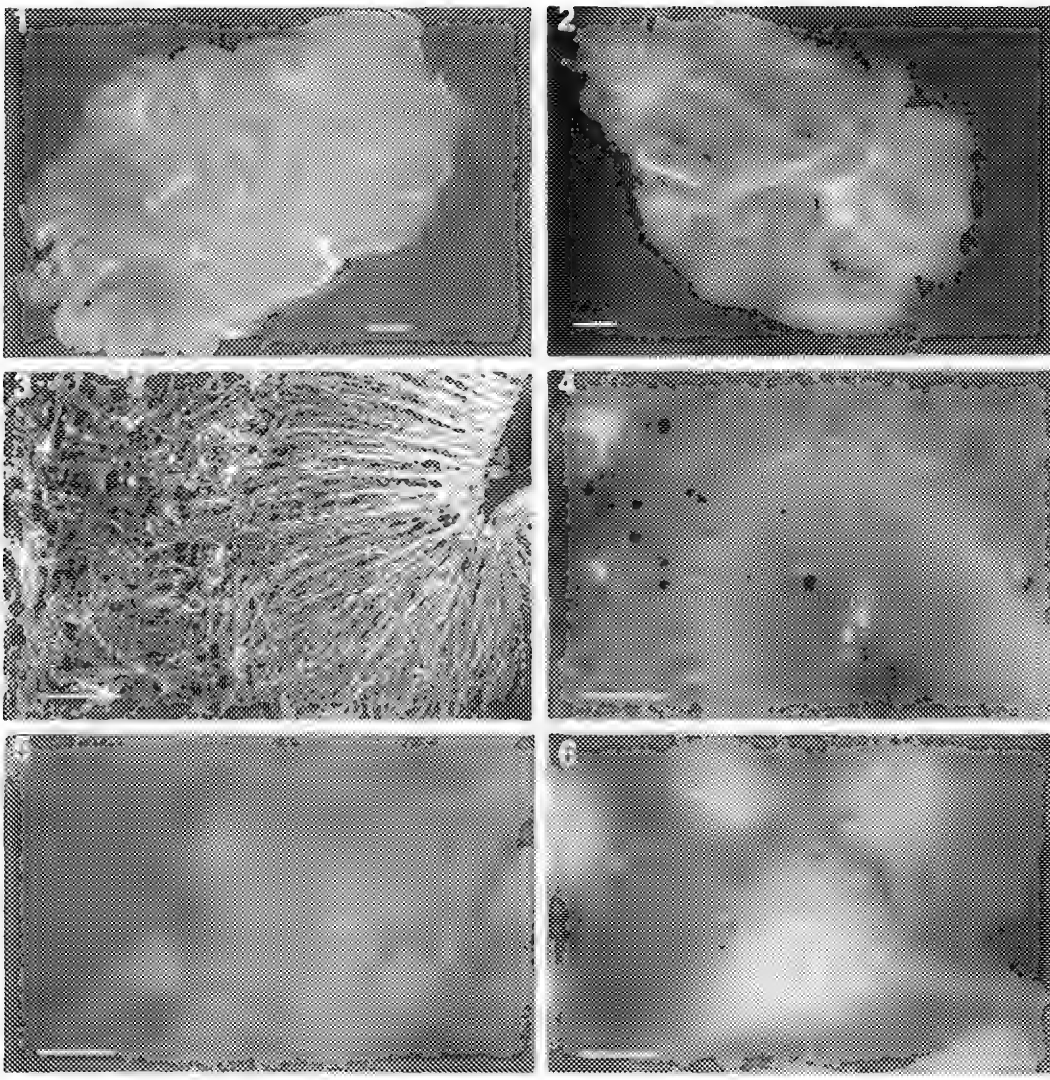

FIG 1 Cerebellar organotypic culture at 0 days in vitro, scale bar = 500μm
FIG 2 Cerebellar organotypic culture at 7 days in vitro, scale bar = 500 μm
FIG 3 Cerebellar culture stained for GFAP at 0 days in vitro, scale bar = 50 μm
FIG 4 Cerebellar culture with injected cells expressing GFP, scale bar = 100 μm
FIG 5 GFP-tranfected cells with low fluorescence, scale bar = 25 μm
FIG 6 GFP-transfected cells with high fluorescence, scale bar = 25 μm

TRANSMISSION ELECTRON MICROSCOPIC COMPARISON OF OSMIUM VS OSMIUM WITH POTASSIUM FERRICYANIDE SECONDARY FIXATIVES AND THE IMPACT OF SECONDARY FIXATIVE TEMPERATURE ON TISSUE PRESERVATION/CONTRAST QUALITY

J. W. Horn*, B. J. Dovey-Hartman**, and V. P. Meador*

*Lilly Research Laboratories, Eli Lilly & Company, 2001 W. Main St., Greenfield, IN 46140
**Schering-Plough Research Institute, P.O. Box 32, Lafayette, NJ 07848

Osmium tetroxide (OsO_4) is a universally used secondary fixative for routine transmission electron microscopic evaluation of biological specimens. Use of OsO_4 results in good ultrastructural preservation and electron density but several factors, such as concentration, length of exposure, and temperature, impact overall results. Potassium ferricyanide, an additive used primarily in combination with OsO_4, has mainly been used to enhance the contrast of lipids, glycogen, cell membranes, and membranous organelles. The purpose of this project was to compare the secondary fixative solutions, OsO_4 vs. OsO_4 with potassium ferricyanide, and secondary fixative temperature for determining which combination gives optimal ultrastructural fixation and enhanced organelle staining/contrast.

Fresh rat liver samples were diced to ~1 mm^3 blocks, placed into porous processing capsules/baskets, preserved in buffered 2% formaldehyde/2.5% glutaraldehyde solution, and rinsed with 0.12 M cacodylate buffer (pH 7.2).[1] Tissue processing capsules were separated (3 capsules/secondary fixative solution) and secondarily fixed (table) for 90 minutes.[2 & 3] Tissues were buffer rinsed, dehydrated with ascending concentrations of ethanol solutions, infiltrated, and embedded in epoxy resin. Ultrathin sections were cut, mounted on copper grids, stained, and evaluated with a transmission electron microscope.

Hepatocytes from all 4 test groups had good to very good ultrastructural preservation. The following table provides results.

Group #	Secondary Fixative Solution	Temperature	Preservation Quality	Electron Density
1	2%OsO_4	Room Temperature	Very good	Moderate
2	2%OsO_4	On ice	Good	Moderate
3	1%OsO_4 / 1.5% FeCN	Room Temperature	Good	Moderate
4	1%OsO_4/ 1.5% FeCN	On ice	Very Good	Dense

Cells preserved with 1%OsO_4/1.5% FeCN on ice (group #4) had the best overall ultrastructural quality and electron density compared with the other 3 groups (Figs. 1 - 4). The criteria for evaluation were image sharpness of membranous and non-membranous structures and staining density over a range of magnifications. Individual hepatocellular structures, such as smooth and rough endoplasmic reticulum, mitochondria, nuclei, plasma membrane, golgi, chromatin, and lipid droplets, within group #4 were very well preserved and densely stained. This secondary fixative produced slightly better results over group #1; the main determining factor was preservation of lipid droplets and mitochondria cristae/matrix. Group #4 had intact lipid droplets and well defined mitochondrial matrix, whereas Group #1 had washed-out lipid droplets and slightly undefined mitochondrial matrix. Groups #2 and #3, although well preserved, had less densely stained organelles. Group # 2 did not have well defined glycogen, lipid droplets, and mitochondrial matrix. Group #3 had well stained glycogen but lipid droplets did not stain and mitochondrial matrix was poorly preserved and stained.

References

1. M. A. Hayat, *Fixaton for Electron Microscopy*, Academic Press, 1981.
2. M. A. Hayat, Stains and Cytochemical Methods, Plenum Press, 1993.
3. J. Turek, Technical Section, *Fall MSEM Newsletter*. (1984) 22.

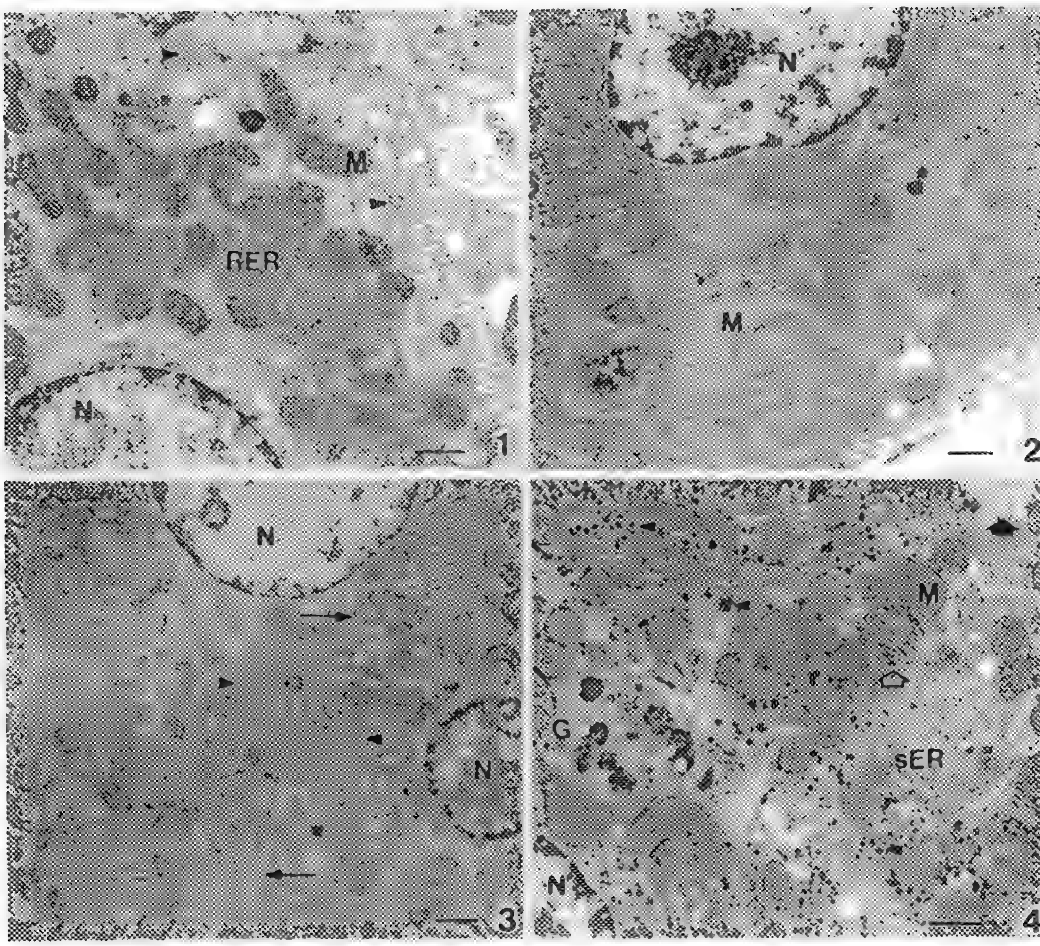

Fig. 1 Rat hepatocytes secondarily fixed with 2% OsO_4 at room temperature. Mitochondria are well fixed and staining is moderate (M). Glycogen (arrowheads) is densely stained and membranous structures are moderately stained and well fixed (Nucleus = N, Rough Endoplasmic Reticulum = RER). Bar = 1 µm

Fig. 2 Rat hepatocytes secondarily fixed with 2% OsO_4 on ice. Mitochondria are well fixed and moderately stained (M), glycogen is not stained, and membranous structures are well fixed and moderately stained. Bar = 1 µm

Fig. 3 Rat hepatocytes secondarily fixed with 1% OsO_4/1.5% FeCN at room temperature. Membranous structures, such as smooth endoplasmic reticulum (arrowheads), rough endoplasmic reticulum (arrows), and nuclei (N), are well fixed and moderately stained. Bar = 1 µm

Fig. 4 Rat hepatocytes secondarily fixed with 1% OsO_4/1.5% FeCN on ice. Mitochondria cristae and matrix are densely stained and very well preserved (M), lipid droplet (solid arrow), glycogen (arrowheads), rough endoplasmic reticulum (hollow arrow), and other membranous structures, such as nucleus (N) and smooth endoplasmic reticulum (sER), are densely stained and fixed. Bar = 1 µm

CRYOHOMOGENIZATION OF LIVER TO MAKE IN VITRO PREPARATIONS OF ROUGH ENDOPLASMIC RETICULUM AND OTHER ORGANELLES

A. Kent Christensen

Department of Anatomy and Cell Biology, University of Michigan Medical School, Ann Arbor, MI 48109-0616

Cell fractionation has been used for many years to isolate organelles for biochemical study.[1,2] Typically, fresh tissue is homogenized in a suitable buffer, and the various size-classes of organelles are then isolated by differential centrifugation. One of the common fractions is the microsomal fraction, which consists largely of vesiculated rough and smooth endoplasmic reticulum, and of Golgi elements.

In the past we have investigated bound polysomes on the rough endoplasmic reticulum (RER) by electron microscopy[3], and have used cell fractionation and EM to study the orientation of ribosomes in polysomes bound to rough microsomal vesicles.[4] However, the value of the cell fractionation material in our work has been limited by the small size of the microsomal vesicles, which are produced by vesicular fragmentation of the endoplasmic reticulum during tissue homogenization. For our work we need in vitro preparations in which the RER retains its cisternal form, rather than being fragmented into small vesicles. This report describes a method we have devised that can yield relatively intact RER in vitro.

Part of a fresh liver lobe from an anesthetized rat was quickly diced into pieces roughly 5 mm in diameter, which were promptly frozen in liquid nitrogen (LN). A mortar and pestle were brought to LN temperature (-196°C), and the frozen tissue pieces were ground into a fine powder at that temperature (cryohomogenization). This pulverization produced powder grains whose surfaces consisted of cells that had been cleaved, but their cytoplasm remained in place and was undamaged by the cleavage, because of the extremely low temperature. The powder was transferred (in LN) to a small petri dish, which was allowed to warm in a cold room. As the material approached 0°C, cold homogenization buffer (triethanolamine[2], 0.5 M sucrose) was added to the powder, and the solution was mixed by gentle pipetting (Pipetman). During this process, nuclei and cytoplasmic organelles from the broken cells at the surface of the grains passed into the medium. Formaldehyde, in buffer, was added to make 2%, and the homogenate was fixed for an hour at 4°C. The powder "grains" and most of the cell nuclei and other larger debris were then centrifuged (cold Eppendorf) into a pellet, and the supernatant was subsequently centrifuged (14,000 RPM for 15 min) to produce an organelle pellet. Both pellets received a further hour of fixation in 2.5% glutaraldehyde buffered with 0.1 M *s*-collidine, and were then detached from the microtubes, postfixed with osmium tetroxide, diced, dehydrated, embedded in Epon-Araldite, sectioned, stained, and then viewed by light and electron microscopy.

The organelle pellet appeared quite homogeneous, and contained abundant mitochondria, endoplasmic reticulum and other organelles. Figures 1 and 2 show the appearance of RER in the pellet. The clumps of RER usually consisted of several cisternae, which exhibited varying degrees of swelling. The occasional surface views of bound polysomes seen on the RER membranes (Fig. 2) appeared normal, resembling those in liver tissue sections.[5]

We have not yet tried to separate these in vitro organelles by fractional centrifugation, or to test their biochemical capabilities. Most of our intended EM uses will not require separation. One might

anticipate that these organelles, before fixation, would have had substantial functional competence, since freezing and thawing have been used as a method[6] to prepare "permeabilized cells", which generally retain the ability to synthesize proteins, and transport them from the RER to the Golgi.[7]

1. S. Gaetani et al. (1983), *Meth. Enzymol.* 96:3.
2. P. Walter, G. Blobel (1983), *Meth. Enzymol.* 96:84.
3. A. K. Christensen et al. (1987), *Am. J. Anat.* 178:1.
4. A. K. Christensen (1994), *Cell Tissue Res.* 276:439.
5. G. Dallner et al (1966), J. Cell Biol. 30:73, 97.
6. A. Lepers et al. (1990), *Biochimie* 72:1.
7. C. J. M. Beckers et al. (1989), *Meth. Cell Biol.* 31:91.

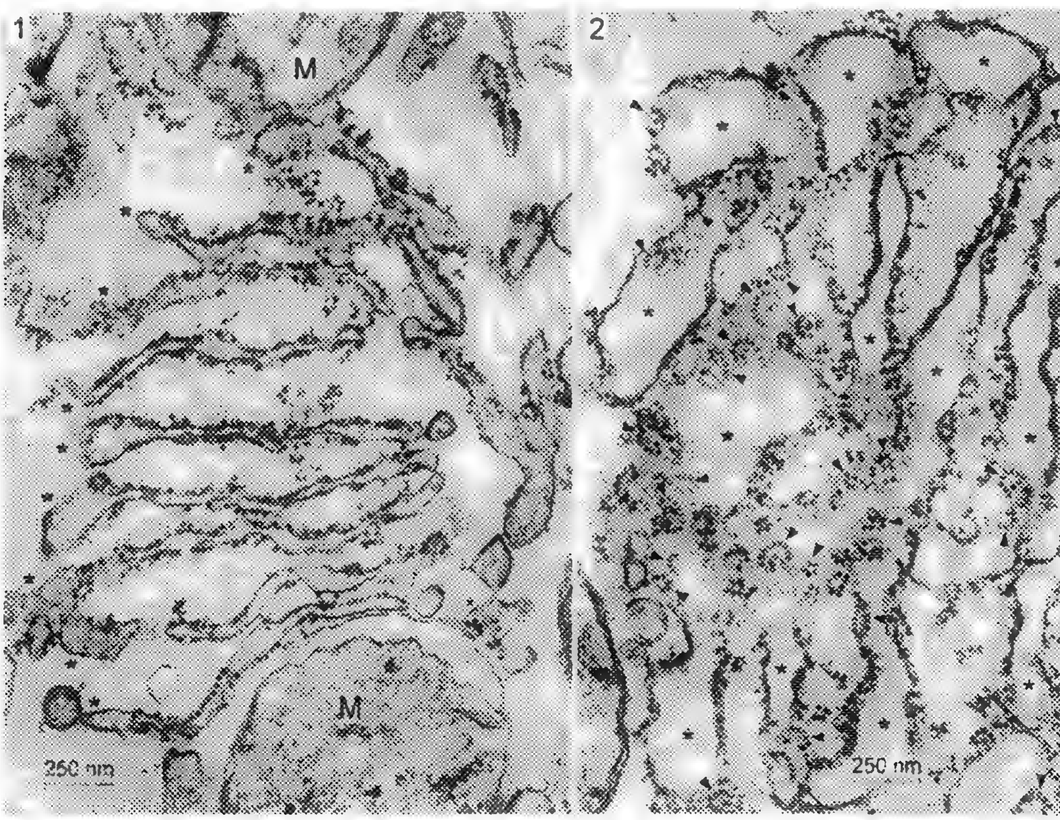

FIG. 1. -- In vitro rough endoplasmic reticulum (RER) in the organelle pellet. This clump of RER consists of 9 cisternae (asterisks), with ribosomes (seen as dark dots) on the outer surface of their membranes. These RER cisternae show less swelling than is usual in these preparations. M, mitochondria.

FIG. 2. -- Several RER cisternae (asterisks), showing the variable swelling that is common. Some of the RER membranes are sectioned obliquely, allowing bound polysomes (arrowheads) to be seen in surface view on the gray, obliquely-sectioned membranes.

AN IMPROVED METHOD FOR PREPARATION AND STEREO IMAGING OF NEGATIVE-STAINED PHOSPHOLIPID VESICLES BY FIELD-EMISSION STEM

Robert P. Apkarian,* Stephen Lee,[1] Fredric M. Menger [1]

Integrated SEM & Microanalytical Facility,* Department of Chemistry[1]. Emory University, Atlanta GA 30322

The method of application of negative stains and the subsequent chemical interaction with various types of phospholipids affect vesicle morphology. Temperature, pH, stain concentration, and the method by which the vesicle solution is applied to the grid necessitates a systematic study.[1] We have developed a method for spray mounting and uranyl acetate (UA) staining of extruded vesicles composed of dilauroylphosphatidylcholine (DLPC, 95%) and dimyristoylphosphatidylcholine (DMPC, 5%) from which we could acquire quality stereo images with high resolution field emission STEM.

The vesicles were prepared by 19 passes through a low pressure extruder containing a 0.1 μm polycarbonate membrane filter. After extrusion, 0.5 ml of vesicle solution was diluted with 3.5 ml of 0.1μm filtered water and vortexed. The concentration of diluted phospholipid was 1.35 mM. The vesicle solution and 2 % UA stain in Milli-Q purified deionized water were mixed at room temperature 1:1 v/v. The UA solution was first prepared at 2X the desired concentration (4%) and sonicated into aqueous solution for at least 15 min. Before mixing with the vesicle solution, the UA was diluted to the desired 2% concentration and run through a 0.1 μm filter. The solution of vesicles and 2% UA were vortexed to insure good mixing. The final surfactant concentration in the stain mixture was 0.675 mM. The stained vesicle solution was immediately drawn into capillary tubes and spray mounted onto carbon stabilized formvar coated grids using an EFFA sprayer (E.F. Fullam, Inc.). Grids, as well as Si chips used for HRSEM imaging, were loaded into the Denton DV-602 chromium sputter coater, pumped to at least 1 x 10^{-7} torr overnight, and coated with a 1 nm fine-grain Cr film before imaging in a Topcon DS-130F in-lens SEM/STEM.[2]

The standard drop method for applying a vesicle solution onto a grid was tested for comparison purposes. Distinctly delineated droplets and well dispersed vesicles were consistently imaged by STEM when the spray mounting technique was employed (Fig.1), but not with the standard method. Unbound stain, which resulted in contaminant deposition during STEM imaging, was removed by overnight high vacuum storage. Easily located profiles of specific vesicles within a droplet facilitated 100,000-300,000 x stereo STEM recordings (Fig.2). The 3-dimensional morphology of vesicles imaged by stereo STEM revealed torroidal and macaroni-shell shaped structures ranging 50-150 nm in diameter with a narrow size distribution around 100 nm. Occasionally vesicles displayed concentric multilamellar stacking. HRSEM and STEM correlated the frequently observed donut shaped torroidal vesicles (Fig. 3).

The osmotic effect of the stain addition on vesicle stability must be considered when presenting a morphological description. However stereo STEM and HRSEM have provided a rapid method by which observed UA stained DLPC/DMPC liposomes retained a spherical motif and contained a region that corresponded to the central internally trapped aqueous volume. Whereas TEM imaging represents a spherical vesicle as a circular profile, stereo STEM provided 3-D images.[3] Additionally HRSEM contained SE-I topographic contrasts of the UA stained vesicle surface. Both HRSEM and stereo STEM imaging modes will be extended by cryopreparation and cryo-staging in the near future.

References:
1. S. Lukac and A. Perovic, 1985. J. Coll. and Interface Sci. 103:2, 586.
2. R.P. Apkarian et al., 1993. Proc. 51st Ann. Meeting MSA. 608.
3. V.S. Kulkarni et al., 1995. USA Microsc. and Anal. 10, 13.
4. This research was supported in part by NIH grant GM21457 to F.M. Menger.

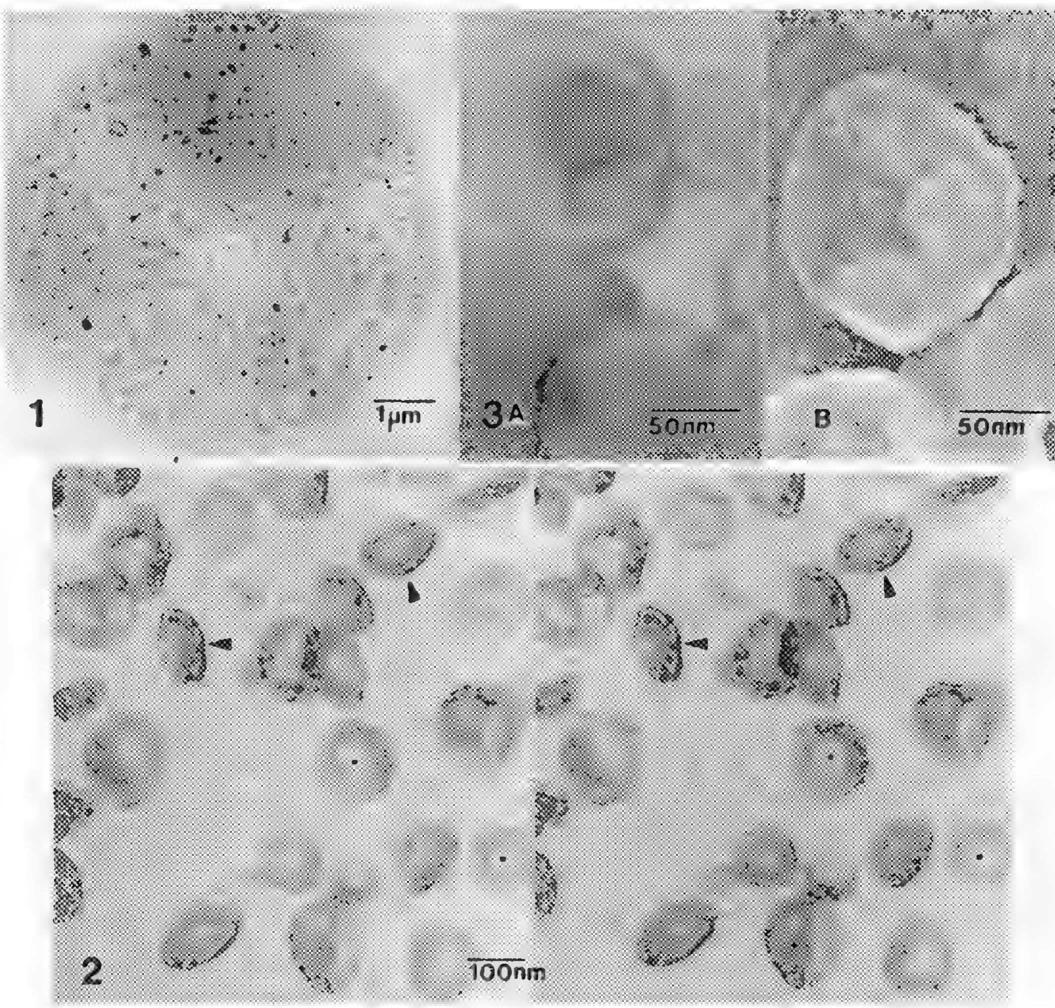

FIG. 1--Spray mounted vesicle droplet on carbon-formvar coated grid imaged by STEM.
FIG. 2--Stereo STEM of torroidal (*) and macaroni shell (arrows) shaped DLPC/DMPC vesicles.
FIG. 3--a. HRSTEM and b. HRSEM display topographic contrasts of vesicles with internal volume region. Note UA particlates on vesicle surface in 3b.

VISUALIZATION AND ANALYSIS OF CAPSID DIMORPHISM IN HEPATITIS B VIRUS TO 17 Å RESOLUTION BY CRYO-ELECTRON MICROSCOPY

A. Zlotnick[1], N. Cheng[1], J.F. Conway[1], F.P. Booy[1], A.C. Steven[1], S.J. Stahl[2], and P.T. Wingfield[2]

1 Laboratory of Structural Biology, 2 Protein Expression Laboratory, National Institute of Arthritis, Musculoskeletal and Skin Diseases, National Institutes of Health, Bethesda, MD 20892

Hepatitis B virus (HBV) is an enveloped virus with an icosahedral capsid. Its homodimeric capsid protein assembles into particles of two sizes - one with T=3 icosahedral symmetry (90 dimers), the other with T=4 symmetry (120 dimers)[1,2]. Both sizes of particle are found *in vivo*[3] as well as in expression systems[1-3]. We have developed an *in vitro* assembly system using purified, bacterially expressed, capsid proteins[2,4]. Capsids assembled from different protein constructs were studied by cryo-electron microscopy[5] using a Philips CM20 microscope equipped with a field emission gun operating at 120 keV.

Capsids assembled from the different protein constructs were assayed by cryo-electron microscopy and sucrose gradient fractionation. Cryo-electron microscopy was required to identify the two different sizes of capsids and the small population of misshapen particles, and also to ascertain the quality of the gradient fractionation (Figure 1, 2). The protein constructs lacked the predominantly basic C-terminal 34 amino acids of the full-length capsid protein (183 amino acids), and were further truncated between residues 138 and 149. Constructs terminating between residue 140 and 149 assembled into mixtures of T=3 and T=4 particles; the smallest construct (138 residues) did not form capsids. The proportion of T=3 capsids increased systematically with larger deletions from the C-terminus. A 149 residue protein formed < 10% of T=3 capsids, while 85% of the particles formed by a 140 residue protein had T=3 morphology.

Icosahedrally averaged image reconstructions were calculated to 17 Å resolution for the 147-residue capsid protein[4]. To achieve this resolution required correction of the contrast transfer function and combining data from a defocus pair of micrographs (Figure 1, 2). There were sufficient numbers of T=3 and T=4 particles in the same field to allow both reconstructions to be calculated from a single defocus pair. In surface shaded views (Figure 3), the boundaries of the constituent dimers can be clearly seen, and the quaternary structures of the two capsids compared. The individual dimers and the arrangement of dimers around their icosahedral fivefold axes are almost identical, whereas the quasi-sixfold arrangements of dimers are distinctly different.

1) R. A. Crowther, *et al.* (1994). Cell 77, 943-950.
2) P. T. Wingfield, *et al.* (1995). Biochemistry 34, 4919-4932.
3) J. M. Kenney, *et al.* (1995). Nature Structure 3, 1009-1019.
4) A. Zlotnick, *et al.* (1996). Biophys. J. 70, A364.
5) F.P. Booy, *et al.* (1991). Cell 64, 1007-1015.

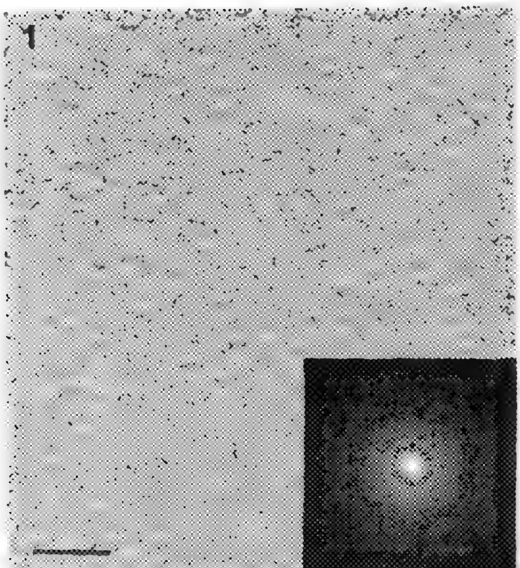

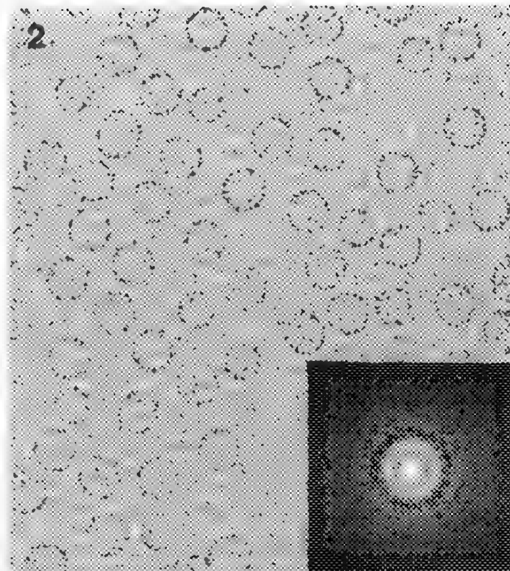

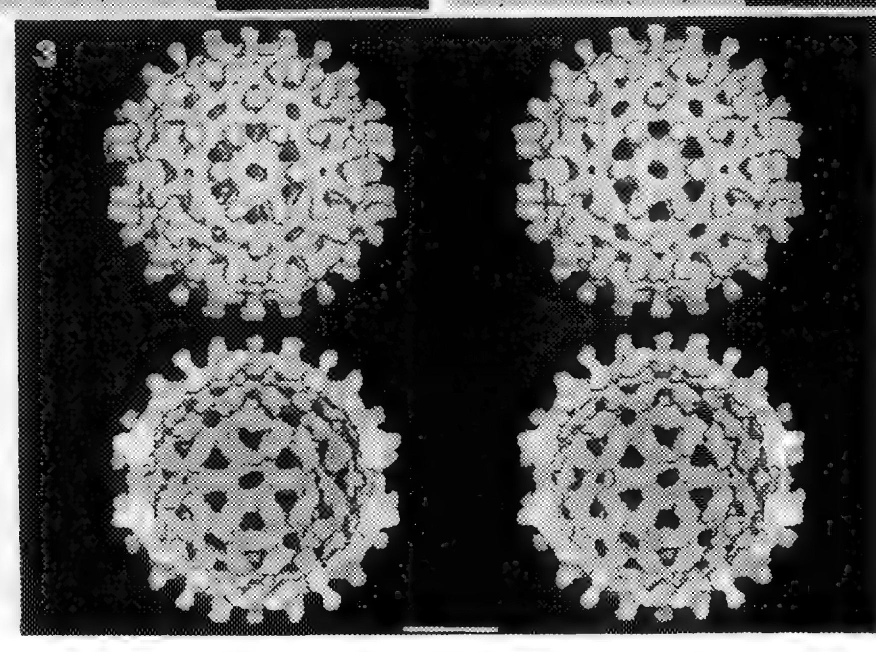

FIG. 1 Cryo-EM of T=3 and T=4 (15:85 ratio) HBV capsids. Optical diffraction (inset) shows that the first zero in the contrast transfer function (CTF) is at (17 Å)$^{-1}$. Scale bar = 500 Å.

FIG. 2 Cryo-EM of the same field taken further from focus. The first CTF zero is at (28 Å)$^{-1}$.

FIG. 3 A stereo-pair of a three dimensional image reconstruction of the HBV T=4 capsid (viewed down the icosahedral two-fold axis) at 17 Å resolution. Scale bar = 100 Å.

LOW-TEMPERATURE LOW-VOLTAGE SCANNING ELECTRON MICROSCOPY (LTLVSEM) OF UNCOATED FROZEN BIOLOGICAL MATERIALS: A SIMPLE ALTERNATIVE

G. G. Ahlstrand

Minnesota Ag. Experiment Station, University of Minnesota, 495 Borlaug Hall, St. Paul, MN 55108.

INTRODUCTION. Scanning Electron Microscopy (SEM) of biological materials, e.g. plants, fungi, insects, bacteria, host-pathogen interactions, and food systems, requires sample stabilization. Conventional strategies of chemical fixation (e.g. buffered glutaraldehyde, paraformaldehyde, osmium tetroxide), dehydration (ethanol or acetone series), critical point drying (CPD) and metal coating (Au/Pd) in a sputter coater or vacuum evaporator are often by applied.[1] However, delicate biological materials may not withstand the stress of conventional preparation and acquire artifact such as collapse or shrinkage of cells or loss of soluble components (Fig 1a). Sophisticated devices and techniques are available which quick-freeze (<1.0 s), metal coat and transfer specimens under vacuum into the SEM.[2] Herein I describe a simple, inexpensive alternative in which fresh biologicals are frozen slowly (< 1.5 min.) on an SEM cold stage, imaged directly without metal coating (Fig 1b) at low SEM acceleration voltage (kV), and defrosted if needed with nitrogen gas (N_2). **METHODS.** Fresh biological samples are affixed to aluminum stubs with carbon double sided tape and/or carbon conductive paint. The cold stage (Fig 2), pre-cooled to -160°C by circulating liquid nitrogen (LN), is withdrawn from the SEM stage (Philips 500) into the specimen exchange chamber which is then vented to atmospheric pressure with dry N_2. The chamber door is opened briefly to room air, the stub is quickly clamped onto the cold stage, the chamber is vacuum pumped and the cold stage is reinserted into the SEM, (< 30 s.). On humid days, frost crystals may form on the sample during these procedures. (Fig. 3a). To defrost sample surfaces, the SEM sample chamber is vented to atmospheric pressure using dry N_2 (but not opened to room air), immediately pumped down to high vacuum (< 5 min.) while sample stub remains inside SEM in full contact with cold stage. Stage temperature is monitored by thermocouple. SEM is operated at 1.5 kV with beam current maximized. **DISCUSSION.** The SEM must be operated at low kV for which no or very little uncoated sample charging occurs. In conventional SEM (tungsten filament) operating at 1.5 kV, gun brightness and image signal to noise are low. To maximize beam current incident onto sample: **1.** Set gun emission control to highest value to maximize gun current output. **2.** Use larger objective lens apertures of 200-400 µm: however, depth-of-focus considerations may warrant use of smaller apertures e.g. 100 µm (Fig. 4). **3.** Use largest SEM spot size compatible with required resolution. **4.** Set filament closer to aperture in gun Wehnelt cap. In conventional SEM operated at 1.5 kV, resolution is not optimized and useful magnifications are limited to ≤ 5,000X. The N_2 gas warms the ice crystals enough so they quickly sublimate away (Fig. 3b). Some sample warming occurs (≤ -130° C) but no appreciable freeze-drying results and samples cool back down to -160° C within minutes during pump down.

REFERENCES

1. M.T. Postek et al., *Scanning Electron Microscopy*, Ladd Research Industries, Inc. (1980).
2.A.W. Robards & U.B. Sleytr, *Low Temperature Methods in Biological Electron Microscopy*, *Practical Methods in Electron Microscopy*, editor: Audrey M. Glauert, Elsevier, Amsterdam (1985).

FIGURE CAPTIONS

Fig. 1a. The powdery mildew *Erysiphe graminis* 24 hours post-inoculation onto leaf of barley, *Hordeum vulgare*, chemically fixed, CPD, viewed at 12 kV. Note partially collapsed appressoria (A), spore walls. (S). 1b. LTLVSEM: Note smooth, fully turgid appressorial wall and spore.
Fig. 2. Philips cold stage is cooled via ball & socket contact with LN cooled cryo head.
Fig. 3a. LTLVSEM: Pinto bean, *Phaseolus vulgaris pinto*, leaf epidermal cells (C) and trichome (T) contaminated by frost crystals (F). 3b. Same area after application of N_2 gas defrost.
Fig. 4. LTLVSEM: Sequence of developing trichomes (T) on *Arabidopsis thaliana* (ecotype WS) leaf primordia. A 100 µm objective aperture was used for greater depth of field.
Fig. 5. LTLVSEM: Shoot apical meristem of the English Ivy *Hedera helix* L.
Fig. 6a. LTLVSEM: Fly eye, *Drosophila melanogaster* . 6b. Close up view.

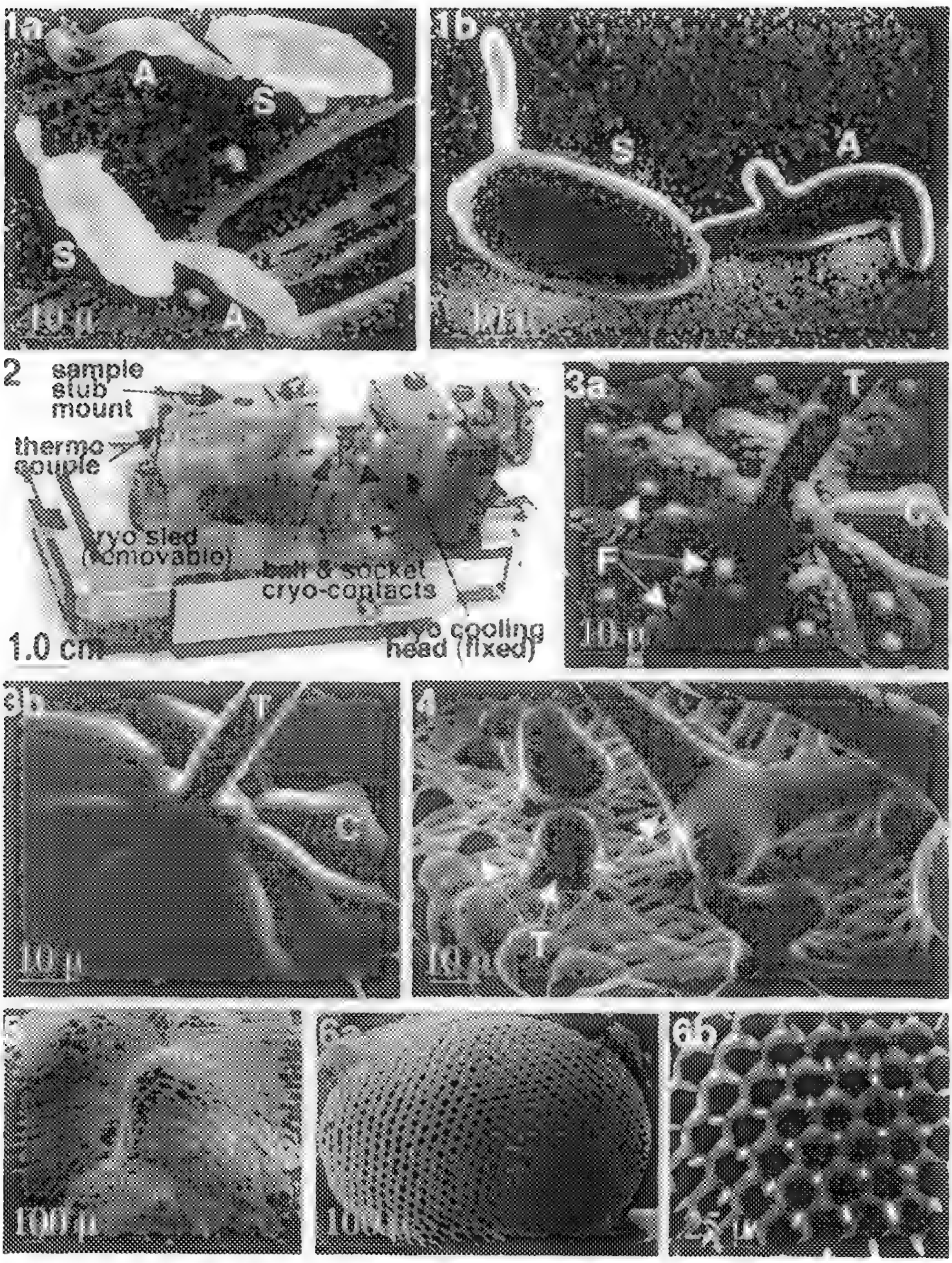
1a
A
S
S
A
10 µ
1b
S
A
2
sample
stub
mount
thermo
couple
cryo sled
(removable)
ball & socket
cryo-contacts
cryo cooling
head (fixed)
1.0 cm
3a
T
C
F
10 µ
3b
T
C
10 µ
4
T
10 µ
5
100 µ
6a
100 µ
6b
25 µ

DEVELOPMENT OF A CRYOSECTION EM AUTORADIOGRAPHY TECHNIQUE AND ITS APPLICATION FOR THE SUBCELLULAR LOCALIZATION OF RECEPTORS

C.-L. Na,* H. K. Hagler, ** and K. H. Muntz*

*Program in Biomedical Engineering, UT Southwestern Medical Center at Dallas, Dallas, TX 75235
**Department of Pathology, UT Southwestern Medical Center at Dallas, Dallas, TX 75235

Recent progress in immunocytochemistry and cryo-techniques has made it possible to study receptor localization at the subcellular level. For many receptor-ligand systems suitable antibodies are not available and it would be more appropriate to use radioligands to study these receptors. Although fresh frozen sections have been widely used in light microscopy (LM) autoradiography studies, to our knowledge, no one has established a technique using electron microscope (EM) autoradiography with ultrathin frozen sections.

Unlike conventional EM approaches which can extract many biological molecules during dehydration and plastic embedding steps, we have adopted the method of Tokuyasu combined with LM autoradiography protocol for frozen sections to develop a new EM autoradiography technique using ultrathin frozen sections.[1,2] Heart blocks were fixed in 2% periodate-lysine-paraformaldehyde (PLP) and 0.1% glutaraldehyde (GA), sucrose infused, and frozen in liquid nitrogen. They were sectioned in a Reichert Ultracut S cryo-microtome equipped with a Reichert FCS cryo-unit. Ultrathin frozen heart sections were incubated in the ß-adrenergic receptor radioligand ^{125}I-iodocyanopindolol (ICYP) and embedded in methyl cellulose (MC) to prevent structural damage from air drying. They were overlaid with a layer of Butvar B-98 film to keep sections from rewetting in the developing process. Autoradiograms obtained using this technique showed that developed silver grains and subcellular structural detail were similar to those obtained from conventional plastic EM autoradiography (Fig. 1a and 1b). In addition, the PLP fixation and MC embedding did not induce any increase in nonspecific binding to ICYP and ICYP diffusion in labeled sections. These findings suggest that it is feasible to establish the cryo-EM autoradiography technique.

Currently, we are determining the resolution (half distance) of developed silver grains from a line source.[3] Briefly, ^{125}I-bovine serum albumin (^{125}I-BSA) spread and dried to a thickness of 50-100 nm was fixed in GA and washed in distilled water to remove un-fixed ^{125}I-BSA. The film was removed and sandwiched between 20% gelatin blocks. 0.5 mm^3 blocks were prepared with the ^{125}I-BSA film oriented perpendicular to the block face. These cryosections were cut and prepared on grids as described above. Line source autoradiographs were developed in D-19 after a 10 day exposure (Fig. 2a). Preliminary resolution analysis shows that our technique has a half distance value between 110 nm and 170 nm using line source sections exposed for 10 days (Fig. 2b).

The development of this new technique will make it possible to study subcellular localization of various receptors and other biological molecules of interest in vitro without using conventional plastic EM preparations or conventional immunocytochemical approaches.

References

1. K. T. Tokuyasu, *Immunolabeling for electron microscopy* , Elsevier: Amsterdam (1984)71.
2. M. M. Zhao and K. H. Muntz, *Circ Res* 73(1993)943.
3. M. M. Salpeter et al., *J Cell Biol* 72(1977)161.

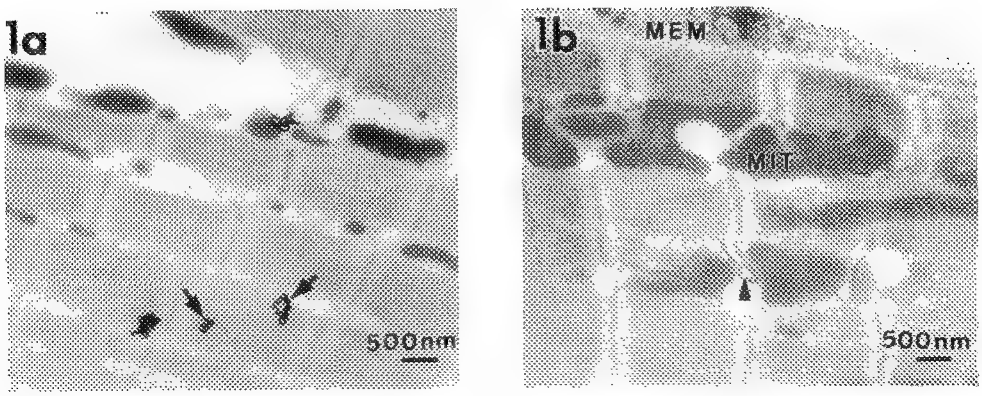

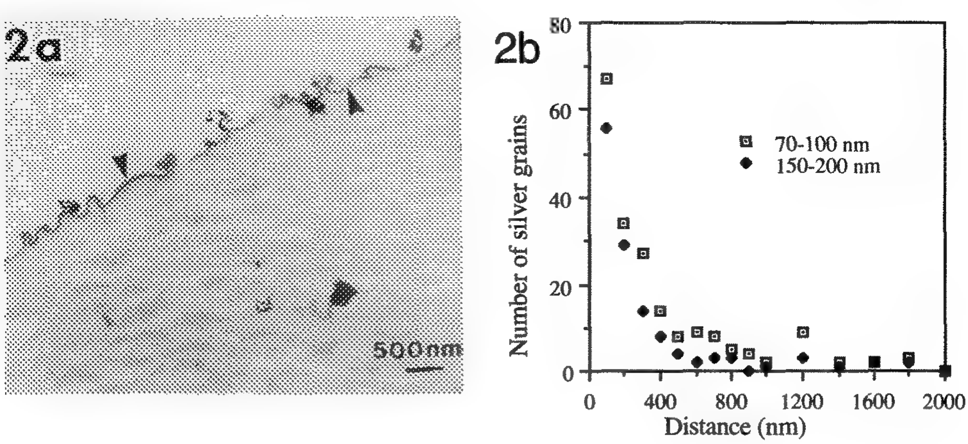

FIG. 1 (a) Silver grains (arrow) as well as myofibrils and T-tubules are observed on an ultrathin frozen rat heart section (100 nm thick) after 70 pM ^{125}I-ICYP incubation and 30 day exposure at 4 °C. (b) Background EM autoradiograph of a cardiac myocyte shows well preserved plasma membrane (MEM), cristae of mitochondria (MIT) and a longitudinal section of T-tubule (arrow). FIG. 2 (a) Line source EM autoradiographs after 10 day exposure. Developed silver grains as well as the line source (arrowhead) can be identified on this micrograph. (b) A histogram shows the silver grain distribution along line source sections 70-100 nm and 150-200 nm in thickness.

LOCALIZATION OF CALCIUM IN PORCINE EPIDERMIS USING ELECTRON ENERGY LOSS SPECTROSCOPY (EELS)

Manoj Misra*, Krisda Siangchaew** and Matthew Libera**

*Unilever Research, 45 River Road, Edgewater, NJ 07020
**Dept. of Materials Science and Engineering, Stevens Institute of Technology, Hoboken, NJ 07030

The properties of biological systems are often governed by variations in the distribution of trace (0.01-0.1%) constituents. The importance of calcium ions for differentiation and proliferation of keratinocytes *in vitro* is well known[1]. The situation *in vivo* warrants study. A major contribution to that study involves the determination of calcium ion distribution in the stratified layers of the epidermis. We describe here the first study to localize and verify calcium distribution in chemically fixed porcine skin using EELS.

Freshly dissected porcine skin is processed according to Menon and Elias[2]. Briefly, tissue fixed in a buffer containing 90 mM potassium oxalate and formaldehyde/glutaraldehyde is post fixed in 1% osmium tetroxide containing 2% potassium pyroantimonate. Control specimens are prepared without pyroantimonate treatment. Tissue dried in a graded series of acetone is embedded in Spurr resin and 30-40 nm sections are cut. Stained and unstained sections are examined using a Philips CM 20 FEG TEM equipped with parallel electron energy loss spectrometer (Gatan EELS) and a spectrum imaging system (EMiSpec). The microscope is used in STEM mode for the EELS work and second difference spectra are acquired.

A typical micrograph from a control tissue (Fig. 1a) exhibits only layers of stratum corneum (SC) and stratum granulosum (SG) and no evidence of granulation. A micrograph of pyroantimonate treated tissue (Fig. 1b) exhibits the presence of granular dense deposits in the SG. These deposits are found in nuclear and intracellular regions and at the cell membrane. Interestingly, the desmosomes (as seen in Fig. 2) and SC (as seen in the bottom of Fig. 1) appear free of such deposits. The presence of calcium is established in certain granular deposits and along the cell membrane from the spectra (Fig. 3). However, not all the intra-cellular granular deposits appear to contain calcium.

We have localized the distribution of calcium in porcine epidermis and have also established that not all the granular deposits contain calcium. Efforts are currently underway to determine the composition of such deposits. Also, cryo-fixation and freeze drying techniques are being used to attempt a more representative mapping of the *in vivo* distribution of calcium[3].

References

1. J. A. Fairley, *Arch Dermatol.*, *124* (1988), 443.
2. G. Menon and P. Elias, *Arch. Dermatol.*, *127* (1991), 57.
3. R. D. Leapman, et al., *Ultramicroscopy*, *49* (1993), 225.

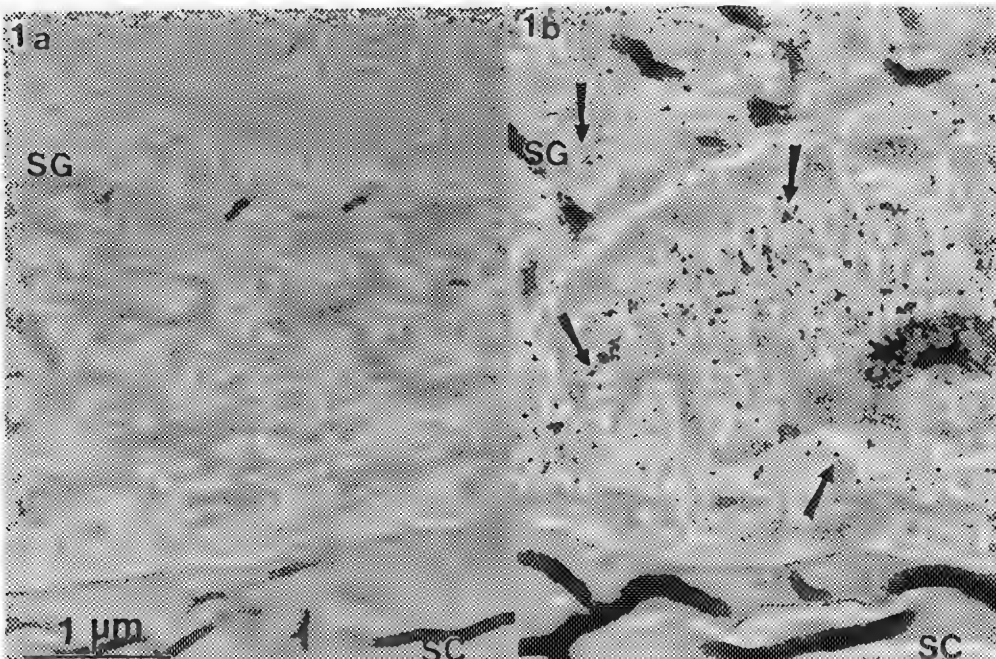

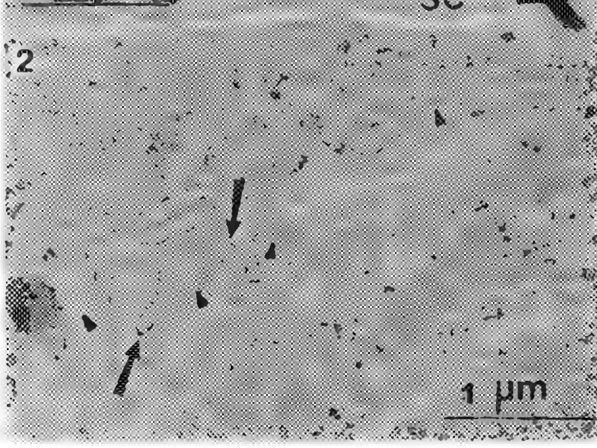

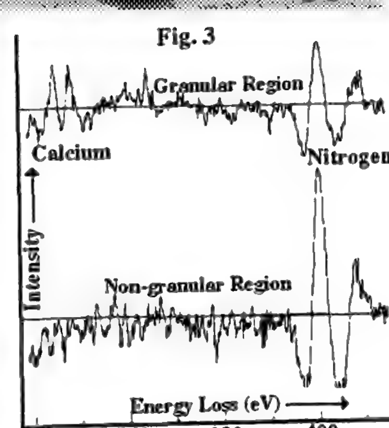

Fig. 1: A micrograph from a control tissue showing layers of stratum corneum and stratum granulosum (a). Presence of dense granular deposits (arrows) in stratum granulosum is seen in pyroantimonate treated tissue (b).

Fig. 2: Granular dense deposits along cell wall (arrows), which are not present at desmosomes (arrowheads).

Fig. 3: Second difference EELS spectrum only from the deposits showed the presence of Ca.

ENERGY FILTERING TRANSMISSION ELECTRON MICROSCOPY OF TRANSFECTED DNA.

Marek Malecki

Integrated Microscopy Resource, National Institutes of Health Biotechnology Resource. Madison, Wisconsin, 53706

Energy filtering transmission electron microscopy (EFTEM) relies upon spatial separation of imaging electrons based upon their energy within an energy loss spectrum (Ottensmeyer 1986). In particular, EFTEM allows contrast enhancement in the zero loss mode and element mapping with electron spectroscopic imaging. These capabilities find a new application in studies of transgenesis in which constructs, probes, and antibodies are marked with organometallic clusters. Since the basic routes of intracellular trafficking of the transfected DNA have become recognized along with the crucial role played by nuclear pores as the selection gates (Malecki et al. 1995, Malecki and Skowron 1995), the current research is pursued by means of ultramicroscopy.

Two strategies were developed for ultrastructural imaging of the transfected plasmid DNA with EFTEM. In both strategies, the transfected cells were cryo-immobilized, embedded in Lowicryl K4M, and sectioned; plasmid constructs, transfection complexes containing nuclear localization signals, and transfection procedures were described previously (Malecki 1995). In the first strategy, the plasmid DNA was covalently conjugated to Nanogold (Nanoprobes) prior to transfections. In the second strategy, the unmodified plasmid DNA was detected by polymerase chain reaction (PCR) in situ hybridization (ISH) (Nuovo 1991, Yap and McGee 1991) with digoxigenin incorporated into the probe (Konat et al. 1991) and labeled with the antibody marked with Nanogold (Hainfeld et al. 1992). For multiple labeling, attempts were made to use boron (Barth et al. 1986) and iron as reporters for spectroscopic imaging. The samples were imaged in the Zeiss 912 operated at 120kV and equipped with the Omega in-column energy spectrometer or in the Jeol 3010 operated at 300kV and equipped with the Gatan post-column energy filter (GIF).

These new strategies for EFTEM imaging allowed us to demonstrate directly, that the nuclear localization signal present on the transfection complex resulted in the nuclear import of the plasmid DNA. In the first strategy, the reporter - Nanogold was directly linked to the transfected DNA. Nanogold, a cluster of 67 gold atoms, had 1.4nm diameter. This feature led to improved spatial resolution as compared to that obtained with larger colloidal gold beads (Richardson et al. 1988). In the second strategy, unmodified plasmids were used; therefore their physiological behavior was uncompromised, but they were detected by PCR ISH. Similarly to detection of the viral DNA (Nuovo 1991), the sensitivity of PCR ISH should allow us detection of single copy genes within the cell ultrastructure.

References. Barth RF, Alam F, Soloway AH, Adams DM, Steplewski Z, 1986. Hybridoma 5: S43. Hainfeld J, Furuya FR, and Carbone K, 1992. Proc. 50th Ann. Mtg EMSA : 526. (Bailey GW, Bentley J, and Small JA, eds.) San Francisco Press, San Francisco, CA. Konat G, Laszkiewicz I, Bednarczuk T, Kanoh M, and Wiggins RC 1991. J. Meth. Cell and Mol. Biol. 3: 64. Malecki M, Skowron P, and Ris H, 1995. Abstracts of Scanning 95 Mtg Sup.1: 16. Malecki M, 1995. In: Science of specimen preparation for microscopy. 1:1. (Malecki M and Roomans G, eds.) SMI Press, Chicago, IL. Malecki M and Skowron P, 1995. Mol.Biol. Cell 6: 1823. Nuovo GJ, 1991. Am.J. Pathol. 139: 847. Ottensmeyer 1986. Ann. NY Acad Sci. 483: 339. Richardson WD, Mills AD, Dilworth SM, Laskey RA, and Dingwal C, 1988. Cell 52: 655. Yap EPH and McGee JOD, 1991. Nucleic Acid Res. 19: 15.

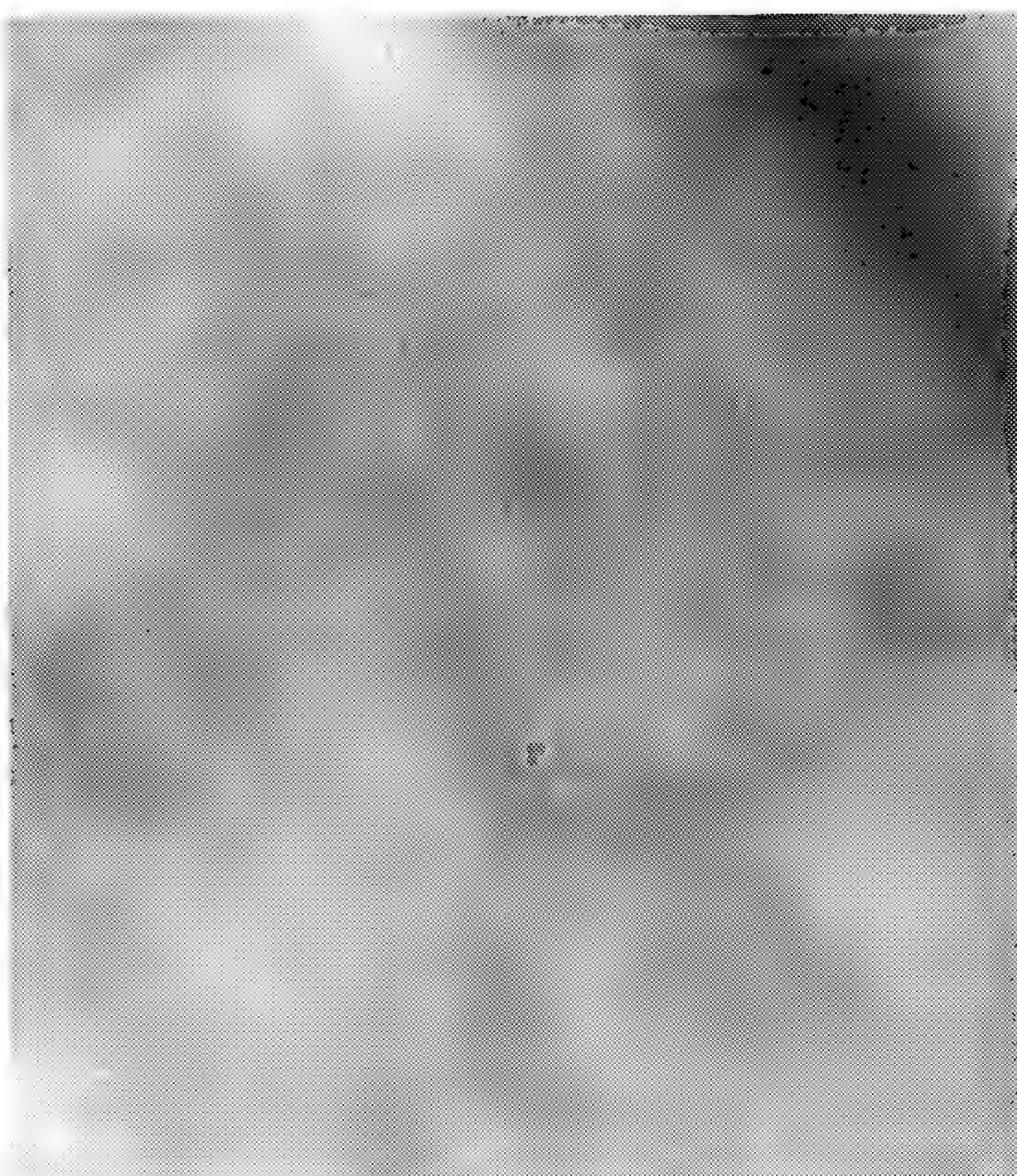

Figure legends. The plasmid DNA / Nanogold present within the nucleus of the cultured human glial cell after transfection within a complex containing nuclear localization signal. Image recorded in the Zeiss 912 operated at 120kV, 140000x magnification, with the Omega spectrometer set for zero loss, 10eV window.

RAPID MICROWAVE PROCESSING OF SKELETAL MUSCLE FOR TRANSMISSION ELECTRON MICROSCOPY

S.A. Smith* and A. Martella*

*Department of Pathology, Electron Microscopy Laboratory, Hennepin County Medical Center, Minneapolis, MN 55415

Rapid tissue processing for transmission electron microscopy is a desired goal in a clinical EM laboratory. Reducing the time from tissue submission to examination in the electron microscope shortens turnaround time for diagnosis. Microwave enhanced tissue processing will accomplish these goals.

Microwave technology reduces the time for tissue fixation and processing and may improve overall results.[1,2] Fixation times can be reduced from minutes to seconds and resin polymerization from hours to minutes.[3,4] Dehydration and infiltration steps can also be reduced, so that microwave rapid tissue processing can yield ultrathin sections from unfixed tissue in three hours.[5]

Three microwave protocols to process skeletal muscle biopsies are compared to standard processing. The protocols test the efficacy of microwave fixation, dehydration, and resin infiltration and polymerization. Protocol #1 uses microwave enhanced 4:1 formaldehyde/glutaraldehyde primary fixation followed by routine processing for remaining steps. Protocol #2 uses microwave primary fixation and 2% OsO_4 post-fixation followed by routine processing. Protocol #3 uses microwave enhanced processing for entire procedure. Protocol #4 uses the standard processing technique.

Study of 10 muscle samples shows that sharper membrane definition, improved contrast of glycogen, clearer delineation of myofibrils, and excellent preservation of sarcotubular systems are the results from the use of microwave processing compared to standard processing (Figures 1-4). The turnaround time from tissue acquisition to diagnosis is markedly reduced. Improved tissue fixation and enhanced preservation of morphology are emerging as significant benefits from microwave processing of skeletal muscle.

References

1. Login GR, Dvorak AM. Methods of microwave fixation for microscopy. *Progr Histochem Cyctochem* 1994;27:72-94
2. Leong AS-Y. Microwave technology for morphological analysis. *Cell Vision* 1994;1:278-288
3. Giammara BL. Microwave embedment for light and electron microscopy using epoxy resins, LR White, and other polymers. *Scanning* 1993;15:82-87
4. Demaree RS Jr, Giberson RT, Smith RL. Routine microwave polymerization of resins for transmission electron microscopy. *Scanning* 1995;17(Suppl V)
5. Giberson RT, Smith RT, Demaree RS. Three hour microwave tissue processing for transmission electron microscopy: From unfixed tissue to sections. *Scanning* 1995;17(Suppl V)
6. The authors gratefully acknowledge the technical assistance of Cathy Kuehner, Kerstin Halverson, and Frida Maiers.

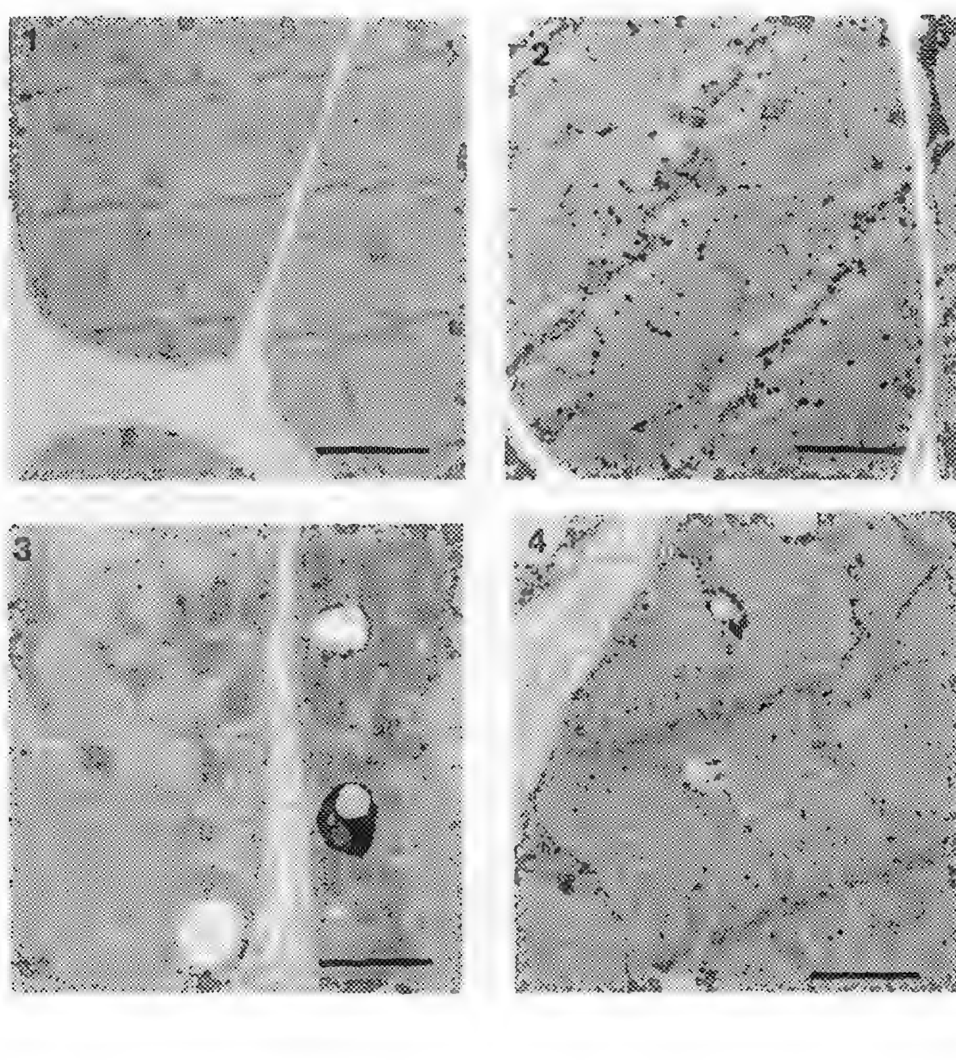

Fig. 1 Skeletal muscle processed routine method. (Bar = 1 μm)

Fig. 2 Same biopsy as Fig. 1 utilizing microwave fixation (4:1 formaldehyde/glutaraldehyde fixation at 37° for 2.5 minutes in microwave) followed by routine technique. (Bar = 1 μm)

Fig. 3 Skeletal muscle processed routine method. (Bar = 1 μm)

Fig. 4 Same biopsy as Fig. 3 utilizing microwave technique for all steps (2.5 minutes initial fixation, 2.5 minutes OsO_4 post-fixation, 6 minutes dehydration, 45 minutes resin infiltration, 75 minutes resin polymerization). (Bar = 1 μm)

THE BASIS FOR FIBRINOGEN CEDAR RAPIDS (γ R275C) FIBRIN NETWORK STRUCTURE

J.P. DiOrio*, M. W. Mosesson**, K. R. Siebenlist**, J.D. Olson†, J. F. Hainfeld§, J. S. Wall§

* Baxter Healthcare Corporation, Round Lake, IL 60073
** Sinai Samaritan Med Ctr, Univ Wisc Med Schl-Milw Clin Campus, Milwaukee, WI 53201
† University of Iowa, Iowa City, Iowa 52242
§ Biology Department, Brookhaven National Laboratory, Upton, NY 11973

Fibrinogen 'Cedar Rapids' is a heterozygous dysfibrinogenemia characterized by delayed and abnormal fibrin polymerization. The specific molecular defect (γ R275C) is relatively common[2], but in only one case, fibrinogen Tokyo II[3], has the ultrastructural basis for defective clot formation been determined. This report reflects similar structural studies on Cedar Rapids fibrinogen and fibrin. Crosslinked fibrinogen molecules and fibrils, were prepared at 1 mg/ml in the presence of factor XIIIa (100 u/ml). When γ chains had become ~10 to 20% crosslinked to γ dimers, samples were diluted with Hepes buffered saline, pH 7, to a fibrinogen concentration of 5 to 10 µg/ml. Three µl was then injected into 3 µl buffer on a carbon-coated EM grid, the specimen allowed to attach for one minute, fluid-exchanged several times with 150 mM NH_4 acetate solution, frozen in liquid nitrogen, freeze-dried, and imaged at the Brookhaven STEM facility using a 40 kv probe focused at 0.25 nm. Fibrin for scanning EM (SEM) was formed directly on carbon-formvar coated gold grids. Clots that had formed overnight were fixed with 2.5% glutaraldehyde in 0.1 M Hepes, pH 7 buffer containing 0.2% tannic acid, washed with buffer, dehydrated, $C0_2$ critical point dried, coated with 7.5 nm platinum, and imaged in a JOEL Field Emission SEM operated at 5 kV.

XIIIa-mediated intermolecular crosslinking of fibrinogen at its γ chain crosslinking site occurs as a consequence of self-association at a constitutive D domain site ('γXL'). This interaction results in linearly aligned 45 nm fibrinogen molecules (Fig. 1 'a'; Fig. 2, 'e') that form double-stranded fibrils (Fig 2, 'd') joined by covalently crosslinked γ chains extending transversely between each fibril strand[1]. Fibrinogen fibrils show 22.5 nm periodicity due to a half-staggered molecular arrangement. In addition to γXL, there is a constitutive self-association site ('D:D') situated at the outer end of each D domain which contributes to end-to-end molecular alignment of fibrinogen molecules within each fibril strand. Upon thrombin-catalyzed conversion of fibrinogen to fibrin, FPA release exposes an N-terminal site ('E_A') that interacts with a constitutive site in each D domain ('D_a') to drive fibrin 'D:E' assembly. One direct consequence of fibrin D:E assembly is acceleration of the γ chain crosslinking rate between aligned γXL sites, and this can be used as an indicator of the D:E association process.

As assessed by crosslinking rates, Cedar Rapids fibrinogen had a normal γXL association reaction, yet formed polymeric structures that were not well organized like normal crosslinked fibrinogen fibrils (cf. Fig. 1, 'b', 'c' and Fig. 2, 'd'). Instead, it formed aggregates of poorly aligned molecules, with occasional short double-stranded stretches ('c'), probably reflecting the presence of a subpopulation of functionally normal molecules. Like fibrinogen Tokyo II, this behavior indicates defective end-to-end association at D:D sites resulting in aberrant fibrinogen assembly. Although Cedar Rapids fibrin had a normal D:E assembly rate, it formed a defective clot structure characterized by extensively branched relatively thick fibers with a lower fiber density than normal, with frequent tapering terminal fibers (cf. Figs. 3 and 4). The greater widths of Cedar Rapids fibers probably reflect the slowed kinetics of fibrin assembly, whereas increased branching is probably due to impaired D:D sites that permit fibrin molecules to more frequently extend outward from linearly propagating strands, thus favoring formation of branch points.

References

1. M. W. Mosesson et al., J Struct Biol 115:88, 1995
2. R. F. Ebert (ed.), *Index of Variant Human Fibrinogens*, CRC press, 1994
3. M. W. Mosesson et al., *J Clin Invest* 96:1053, 1995

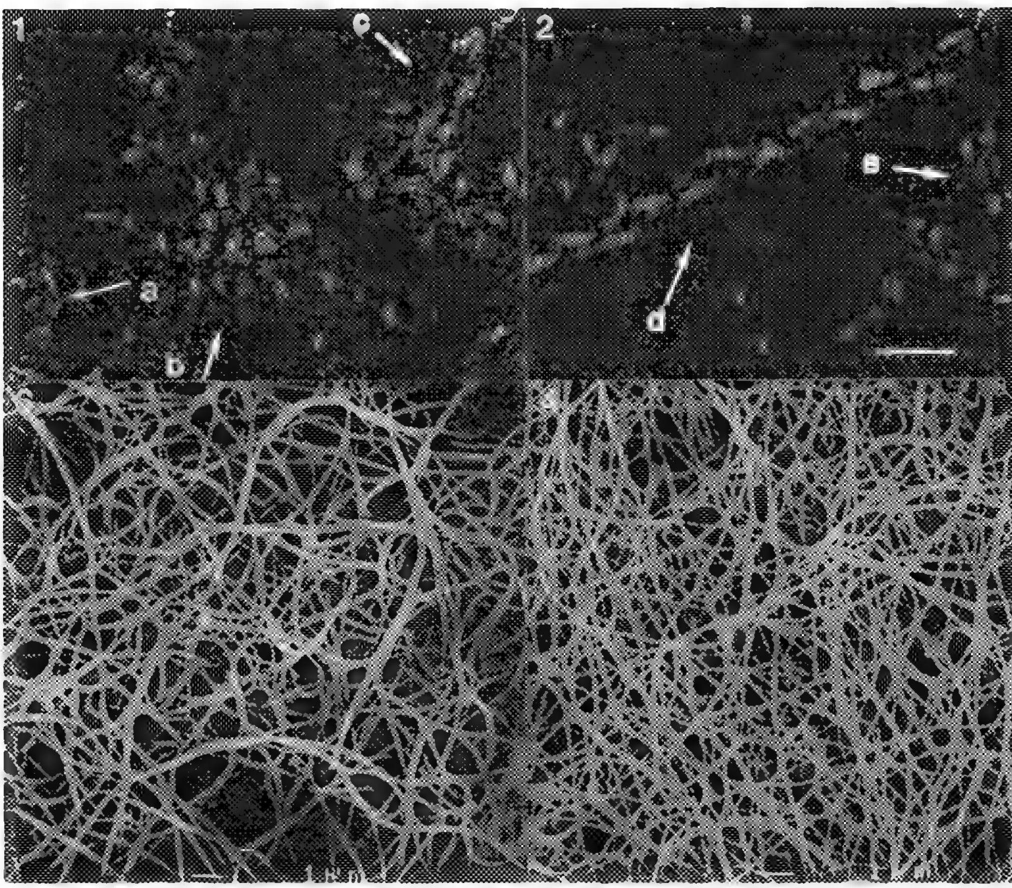

Fig. 1 STEM image of factor XIIIa-crosslinked Cedar Rapids fibrinogen.
Fig. 2 STEM image of factor XIIIa-crosslinked normal fibrinogen. Bar, 45 nm for Figs 1 and 2.
Fig. 3 SEM image of Cedar Rapids fibrin. A fibrinogen concentration of 500 µg/ml was used in order to obtain an adequate matrix fiber density. Bar, 1 µm.
Fig. 4 SEM image of normal fibrin prepared at a fibrinogen concentration of 50 µg/ml. Bar, 1 µm.

ULTRASTRUCTURAL STUDY OF HUMAN FETAL APPENDIX: A "Novel" Cytoplasmic Organelle

K. M. Siddiqui, Ph.D*. Southern Research Institute (SRI), Birmingham, AL

*Current Address: Bioscience Department, Zeneca Pharmaceuticals, P.O. Box 15437, Wilmington, DE 19850-5437

Vermiform appendix (VA) present in humans and other vertebrates may have a similar function to gut-associated lymphoepithelial tissue (GALT). The function of GALT in the gastrointestinal tract (GIT) is well documented. The functional significance of VA, as a "lymphoid" tissue in developing human fetus has not been established. However, VA is the narrowest part of GIT that protrudes from the base of cecum at the ileocecal juncture. Several diseases such as chronic appendicitis, mucocele, argentaffin carcinoma, and developmental diverticula causing inflammation are associated with VA (Delikaris, et al., 1983). An agenesis of VA and complications associated with it in a child born to a mother who had taken thalidomide during her pregnancy has been documented (Bremner & Mooney, 1978). These pathologies and also occurance of appendicitis with cystic fibrosis (Bockman, 1983) suggest a functional significance, and warrants a close observation of VA in human fetuses. On the other hand, studies detailing the subcellular architecture and characterization of various cell types of it have been limited, partly because it is difficult to fix. To over come the fixation problem, a pre-fixation with 1% acrylaldehyde for 30 min provided an excellent preservation of cells, cytoplasmic organelles, and the granules.

Tissue specimens were obtained from legally aborted human fetuses of 13 to 17 weeks of gestation period from the Medical Center of University of Alabama at Birmingham, Al. Soon it was realized that the regular glutaraldehyde fixation failed to provide desireable results. Therefore, a 1.0% acrylaldehyde solution was injected into the lumen of appendix specimen for 30 min.at 4°C. The remainder of glutaraldehyde fixation and transmission electron microscopy procedure was followed as described by Siddiqui (1977). Thin sections of gold/grey reflections were cut, and observed under Hitachi HU-12 transmission electron microscope. Selected areas were photographed.

The identification, and characterization of individual cell types have been limited to the shape, size, and presence or absence of secretory granules and cytoplasmic organelles. Toluidine blue stained thick sections exhibited an undulated mucosal lining without villi. The absence of the villi suggests that VA is not involved in the absorption processes. The ultrastructural data exhibited several differentiated goblet, apocrine and un-differentiated basal proliferative cells (Figs.1, 2, 3, 4, and 5), and also absorptive, secretory, endocrine type cells (Figs. 6-12), constitute the mucosa. Furthermore, the apocrine cells are noted in discharging a substantial apical portion of cytoplasm containing coarse granules into the lumen (Fig. 1). Also, just beneath the reconstituting apical cell membrane, an Oval/U-shaped complex or body (OU-Body) has invariably been seen in all the apocrine type cells (Figs. 2, 3, and 4). This is the first time this body/complex is being reported. It's structural conformity as well as functional significance to the developing fetus needs to be explored further. Basal mucosa nurtures various endocrine type cells, some of them have not been reported previously. For instance, one of the cell-type (Fig. 9) contained both mucigen type large electron lucent granules similar to goblet cells and also relatively small but electron dense compact granules. This cell type has not been reported in the literature. In addition, several secretory type cells differing in the density and size of their granules have been commonly noted at the basal areas. Presence of these various types of secretory cells lead to suggest that human fetal VA plays perhaps some important role in modulation of its growth and possibly the growth of the adjacent cecum and colon tissues.

References:

Delikaris, P., et al. (1983), Dis Colon. 26(6):374-376.
Bremner, D.N..and Mooney, G. (1978), The Lancet, 1:826.
Bockman, D.E. (1983), Arch. Histol. Jpn., 46(3):271-292.
Siddiqui, K.M. (1977), Ph.D. Thesis. The University of Texas, Austin.

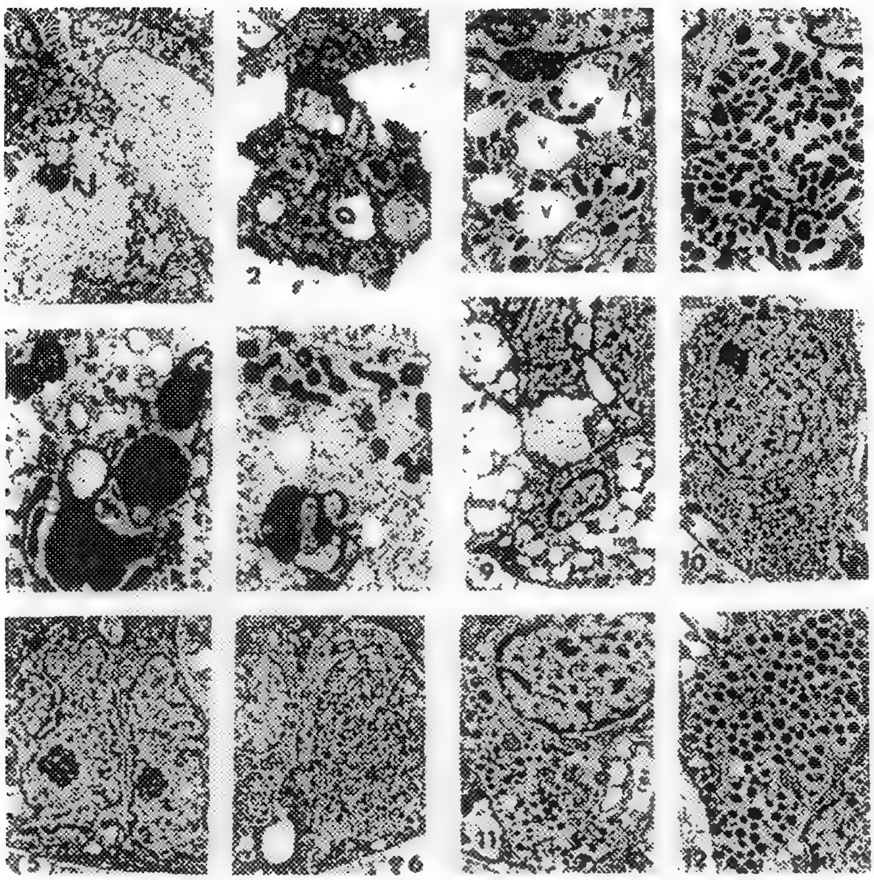

Fig. 1: An appocrine-type cell shows apical cytoplasm (C) is being pinched off into lumen (Lu). OU-body (curved arrow). ~x8000. **Fig.2:** Several thecae of OU-body filled with un-identified substance (I). Microvilli (mv). Desmosomes (DS). ~x33,000. **Fig.3:** A pronounced form of OU-body; it's thecae are filled with an un-identified electron-dense substance. ~x50,000. **Fig.4:** Another formation of the OU-body. Mitochondria (M) and cisternae of rough endoplasmic reticulum (rer) surround the OU-body. Lumen (Lu). ~x22,000. **Fig. 5**: Two basal proliferative epithelial cells with indented nuclei (N), and nucleoli (Nu). Basal lamina (arrow). ~x8,000. **Fig. 6**: Two autocrine cells show subnuclearly located pleomorphic tightly-packed electron-dense granules. Rough endoplasmic reticulum (rer). Nucleus (N). Mitochondrion (M). ~x9,000. **Fig. 7:** Electron-dense pleomorphic membrane bound granules, and also large vesicles (V). Nucleus (N). Nucleolus (Nu). Polysomes (p). ~x31,000. **Fig. 8:** Pleomorphic mostly elliptical and un-bound granules. Nucleus (N). Mitochondrion (M). Basal lamina (arrow). ~x22,000. **Fig.9**: Cell shows compact electron-dense, and large mucigen-type (mg) granules. Nucleus (N). Basal lamina (arrow). ~x10,000. **Fig. 10:** Cell shows electron-dense un-bound granules, and cluster of mitochondria (M). Basal lamina (arrow). ~x11,000. **Fig. 11**: A cell with pleomorphic electron-dense compact granules, and cisternae of dilated rough endoplasmic reticulum (rer). Nucleus (N). Patchy chromatic (pg). Mitochonria (M). Basal lamina (arrow). ~x11,000. **Fig. 12**: This cell shows electron-dense homogeneous granules. Free-ribosomes (r). Fine filaments (f). Mitochondria (M). ~x44,000.

COMPARATIVE ULTRASTRUCTURAL STUDY OF CAMEL, COW, AND HORSE NEUTROPHIL

N. Hailat*, S. Lafi*, Z. Bataineh***, O. Al-Rawashdeh*, and Fakhri Al-Bagdadi**

*Department of Clinical Veterinary Sciences, **Department of Basic Veterinary Sciences, Faculty of Veterinary Medicine, ***Department of Anatomy, Faculty of Medicine, Jordan University of Science and Technology (Irbid, Jordan)

The ultrastructure of Arabian camel, cow, and horse neutrophils in peripheral blood was studied in order to provide detailed description of its constituents and to determine the similarities and the differences between these three species. Peripheral blood was taken from the three animals, centrifuged and the pellets were fixed in glutaraldehyde, dehydrated and embedded in Spurr's resin. Silver sections were mounted on copper grids and viewed by Zeiss electron microscope and microphotographs were taken.

Camel's neutrophils were found to have smoother cell surface with small number of short pseudopodia (Fig. 1). The horse's neutrophil had longer pseudopodia while the cow's neutrophil had a large number of small ridges instead. The size of the cell in camel was larger than that in cow and horse. The nucleus of camel's neutrophil appeared less irregular compared with that of cow's and horse's, with marginated non-patchy chromatin, and with abundant heterochromatin.

The cytoplasm of the neutrophils of the three species was loaded with coarse, electron dense granules, which vary in size and shape (Fig. 1). In the camel's neutrophil, the granules are larger in number compared with that of cow, but smaller in size. This difference was less prominent compared to that of horse (Fig. 1). The granules in camel were irregular in shape, ranging from circular to drum-shaped, with few football like granules with electron lucent center, similar in shape to those in eosinophils[1]. The neutrophil in the three species had few mitochondria, a small golgi apparatus and no clear profiles of smooth or rough endoplasmic reticulum. The distinct variation in the morphology, and number of granules in the neutrophil of camel, compared to those of the cow and the horse granules, suggest different structure and function or different stage of maturation.

Granules with irregular shape, ranging from circular to drum-shaped were reported in sheep and human neutrophil[1,2,3]. It was reported that cows have an additional type of granules which is not present in sheep. The presence of these granules in camel's neutrophils suggest the involvement of this cell type, like in other species, in phagocytosis. However, further study regarding histochemical characterization of these granules is still needed.

References

1. L. Weis, Blood. In Histology, Cell and Tissue Biology, 5th ed. Elsevier Biomedical, New York (1983) 454.
2. O. Slauson, et al, Inflammation and Repair. In: Mechanisms of Disease, 2nd ed. Williams and Wilkins, Baltimore, (1990) 200.

3. M. Brown, Blood and bone marrow. In: Textbook of Veterinary Histology, 3rd ed. D. Dellmann, and M. Brown, Eds., Lea & Febiger, Philadelphia, (1987) 77.
4. The authors gratefully acknowledge the use of facilities at Yarmouk University for Electron Microscopy.

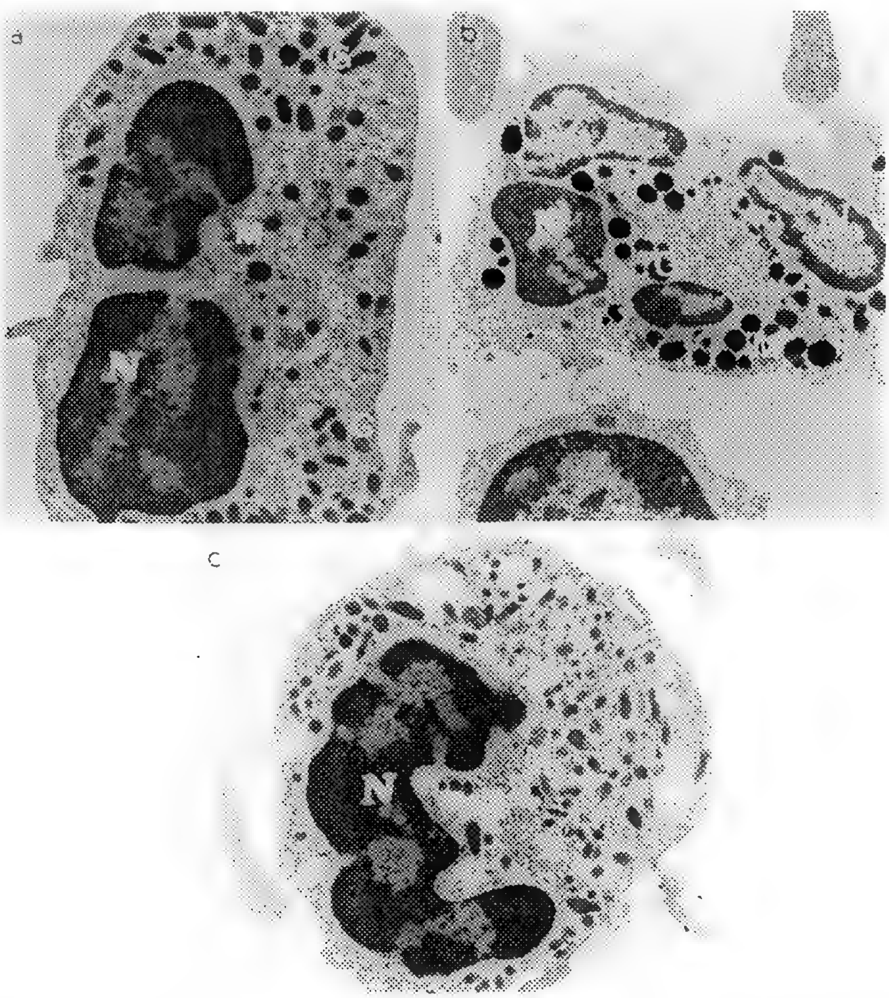

Figure 1 Shows electron micrographs of camel(a), cow(b), and horse(c) neutrophil. Granules(G), Nucleus(N), Mitochondria(M). Figure 1 = x 12800.

NATURE OF CAVEOLAE IN THE ENDOTHELIAL CELLS OF TOAD URINARY BLADDERS

A.J. Mia,* J. Ford,* L.X. Oakford,** and T. Yorio**

*Jarvis Christian College, Highway 80, Hawkins, TX 75765
**University of North Texas Health Science Center at Fort Worth, TX 76107

Intact toad urinary hemibladder sacs have been in use for many years as a membrane model for experimental studies of transepithelial aqueous transfer under osmotic gradient.[1,2] The toad bladder tissue is composed of several cell types. Recently, we reported the presence of a large concentration of caveolae in the granular epithelial cells of toad urinary bladders.[3] Caveolae are microstructures which arise by invagination of the plasma membrane on the cytoplasmic side of the cell.[3,4] Currently, we report the presence of caveolae in endothelial cells of toad urinary bladder.

Urinary hemibladder sacs were excised from doubly-pithed toads, *Bufo marinus*, fixed using 1% glutaraldehyde in PIPES, postfixed in 1% osmium tetroxide, dehydrated and embedded in epon blocks. Ultrathin sections were exposed to uranyl acetate and lead citrate for transmission electron microscopy. In some cases, the bladder sacs were tied up at the ends of glass tubes and equilibrated in aerated Ringer's solution for 30 min prior to experimental procedures.

Figure 1 is an ultrathin cross-sectional view showing a group of endothelial cells (en) surrounding a blood capillary containing a large concentration of caveolae (arrows) distributed along the margins of the plasma membranes. Most caveolae in these cells occur singly around the entire plasma membrane of a cell but at times they may be seen in clusters. Although most caveolae are seen localized at the plasma membrane, many of them occur deep within the cytoplasm (arrowheads). These endothelial cells often contain multivesicular bodies (curved arrows) in addition to coated pits (short arrow). A count of the caveolae from a large single cell indicates the presence of over 75 caveolae along the cell borders in addition to those present within the deeper region of the cytosol. This may account for their number to be in thousands per endothelial cell when considering its length and diameter. Since caveolae have been known to be involved in many cellular processes including transcytosis, potocytosis, signal-transduction and receptor-mediated endocytosis, their increased presence in the endothelial cells of toad urinary bladders may provide an excellent model to investigate the role of caveolae in these cellular processes.

References

1. D. R. DiBona, Am. J. Physiol.245 (1983)C297.
2. A. J. Mia et al., Tissue& Cell, 23(1991)161.
3. A. J. Mia et al., FASEB J.10(1996)A172.
4. K. G. Rothberg et al., Cell, 68(1992)673.
5. Supported by grant DAMD17-95-C-5086.

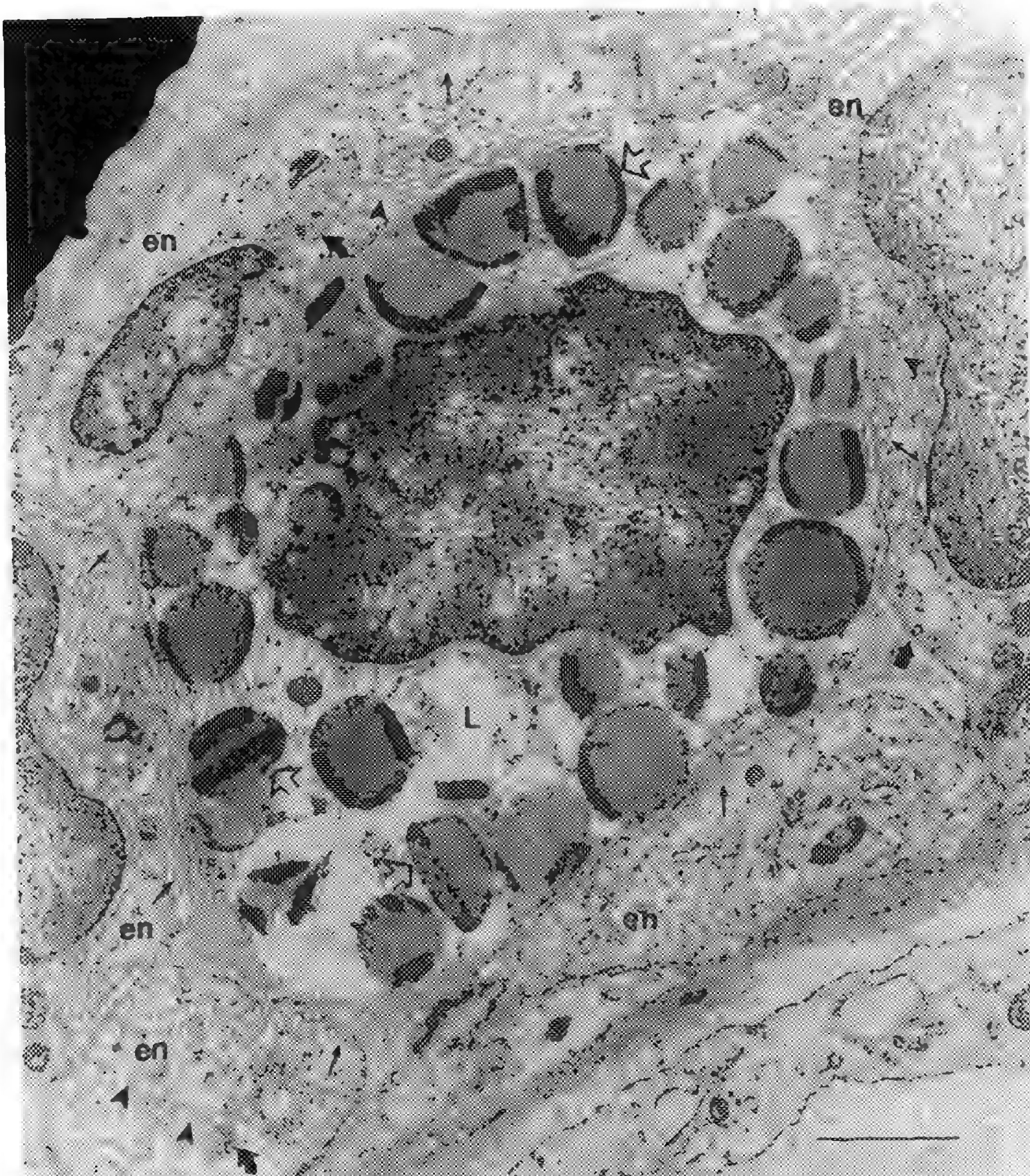

Figure represents TEM of toad urinary bladder showing caveolae (arrows) in the endothelial cells (en) surrounding a leucocyte (L) with specific granules containing polyhedral crystals (open arrows). For additional details see text. Bar= 1µm.

MODULATION OF TUBULAR MICROSTRUCTURAL SELF-ASSEMBLY IN GALACTOSYLCERAMIDES: INFLUENCE OF *N*-LINKED FATTY ACYL CHAINS

Vitthal S. Kulkarni and Rhoderick E. Brown

The Hormel Institute, University of Minnesota, 801 16th Avenue NE, Austin, MN 55912

Our recent studies have indicated that aqueous dispersions of galactosylceramides (GalCers) containing nervonoyl [$24{:}1^{\Delta 15\ (cis)}$] acyl chains, which constitute the major unsaturated acyl moieties in bovine brain GalCer, form tubular bilayers[1,2]. In an effort to define the structural parameters that modulate tubule formation, we synthesized a series of GalCers having successively shorter *cis* monounsaturated acyl chains than the tubule-forming 24:1 GalCer and investigated the resulting microstructural self-assemblies by freeze fracture and deep etch electron microscopy.

GalCers having *N*-linked erucic [$22{:}1^{\Delta 13\ (cis)}$], eicosenoic [$20{:}1^{\Delta 11\ (cis)}$], or oleic [$18{:}1^{\Delta 9\ (cis)}$] acyl chains were synthesized and purified as previously reported for 24:1 GalCer[2]. Dispersions were prepared by hydrating dry lipid at >90°C with phosphate buffer (pH 6.6) followed by vigorous vortexing and three freeze-thaw cycles. Samples were cryo-fixed from room temperature (22°C) by plunging into liquid propane cooled by liquid nitrogen, were fractured in a Balzers 300 freeze fracture apparatus at -120°C, and were etched for 6 min. at -100°C. Replicas were produced by shadowing with carbon-platinum at 45° and with carbon at 90° and then were cleaned with 50% Nochromix® in sulfuric acid prior to viewing with a JEOL 100S electron microscope.

Figure A shows the cylindrical microstructures that form in a subfraction of bovine brain GalCer containing only nonhydroxy fatty acyl chains of which 67% are nervonate [$24{:}1^{\Delta 15\ (cis)}$]. The diameters of the undulating, cochleate cylinders ranged from 100 to 150 nm with lengths exceeding 1000 nm. $22{:}1^{\Delta 13\ (cis)}$ GalCer assembled into cylindrical microstructures (Fig. B) but their smaller diameters (25-35 nm) were consistent with bilayer tubule formation and the long, smooth tubules self-aligned into large aggregates or bundles. In contrast, $20{:}1^{\Delta 11\ (cis)}$ GalCer formed a more random array of helically-twisted, ribbon-like structures (Fig. C) with diameters of 40-50 nm and helical pitches of 80 nm. In $18{:}1^{\Delta 9\ (cis)}$ GalCer, a variety of microstructures formed including multilamellar cylindrical bilayers, sheet-like structures, and giant, multilamellar, spherical assemblies (Fig. D, E, & F).

This study clearly shows that the self-assembly of GalCers into tubular microstructures is influenced both by hydrocarbon chain-length asymmetry and by the *cis* double bond position in the amide-linked fatty acyl chains. When the hydrocarbon chain-length asymmetry is reduced and the *cis* double bond is near the middle of the acyl chain (as in $18{:}1^{\Delta 9\ (cis)}$GalCer), then a variety of microstructures form. Lengthening the acyl chain while moving the *cis* double bond closer to the terminal methyl group of the adjacent sphingoid base chain results in high-axial, cylindrical microstructures (as described above). Differential scanning calorimetric measurements indicate that relatively strong intermolecular interactions exist in the GalCers upon assembly into high-axial cylinders and tubules[3].

[Support: USPHS grant GM45928 and the Hormel Foundation]

References:

1. V. S. Kulkarni et al., *Proc. Microscopy and Microanalysis* 1995, 944-945.
2. V. S. Kulkarni et al., *Biophys. J.* 69 (1995), 1976-1985.
3. V. S. Kulkarni and R. E. Brown, (1996) in preparation.

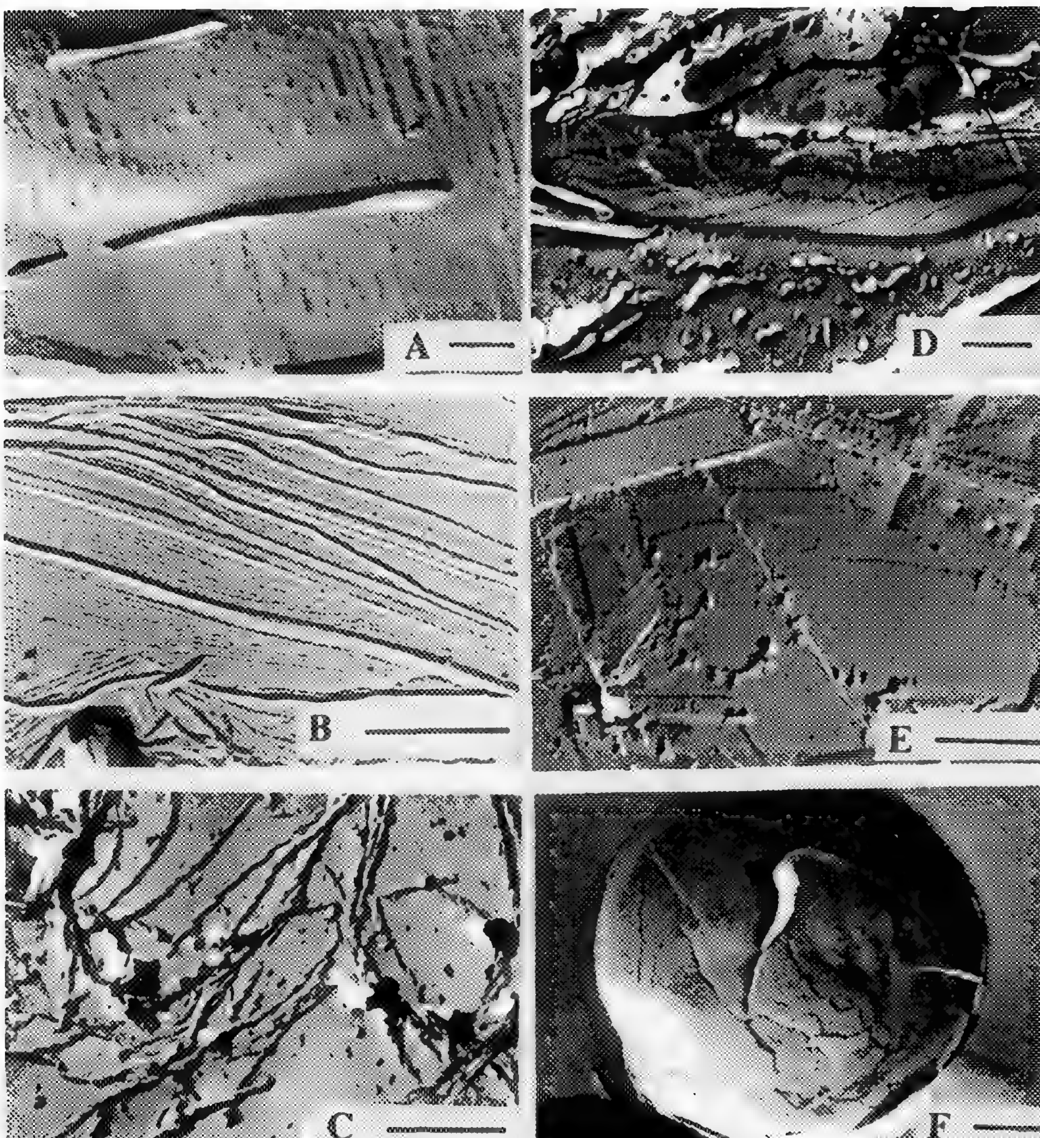

Electron micrographs of freeze-fractured and deep-etched GalCer dispersions cryo-fixed from 22°C. Panel **A** shows bovine brain GalCer containing nonhydroxy acyl chains; Panel **B** shows $22{:}1^{\Delta 13\,(cis)}$ GalCer; Panel **C** shows $20{:}1^{\Delta 11\,(cis)}$ GalCer; Panels **D**, **E**, and **F** show $18{:}1^{\Delta 9\,(cis)}$ GalCer. In each panel, the bar = 500 nm.

FUNGIFORM AND CIRCUMVALLATE PAPILLAE VOLUMES IN THE PIG

A. Singh, A. Mack, and W. P. Ireland

Department of Anatomy and Physiology, Atlantic Veterinary College, Charlottetown, PE C1A 4P3

Taste buds on the porcine tongue have not been quantitated.[1] The morphometric information would be useful in investigation of nutrition-related issues both in human beings and animals.

The tongue specimens were obtained from three, 6-month-old, castrated, male pigs immediately after they were killed in a local abbatoir. The organs were fixed in 10% buffred formalin, and the fungiform and circumvallate papillae were mapped and counted. Mapping was done by drawing an outline of the dorsal aspect of the specimens and marking the approximate positions of fungiform (dorsal and lateral) and circumvallate papillae. Samples from each tongue were harvested from dorsal, lateral and dorsal root regions. These samples were processed in a tissue processor [Model 166MP; Fischer Scientific]. Paraffin-embedded samples were *serially* sectioned at 15 μm, and stained with hematoxylin and eosin in a stainer [Varistain; Shandon]. The samples were embedded in such a manner that mucosal surface was cut in a plane transverse to long axis of the tongue. The sections were examined at 100X with a light microscope, and the image was projected on the monitor of an image analysis machine [Bioquant IV; R & M Biometrics] by a television camera attached to a microscope. For quantitation, a fungiform papilla was selected and its area that extended over adjacent (2-3) sections was measured using Bioquant; accompanying this measurement were the counts of the taste buds located in the papilla. Sterio rule was invoked when performing the latter task.[2] Counting of the buds in circumvallate papillae was somewhat difficult because of a dense population of these structures in the papilla. Thus a papilla volume, number of its taste buds and density of its taste buds was estimated.[3] Data on volume of the porcine fungiform and circumvallate papillae is presented here that was calculated by using Cavalieri's direct estimator of volume from the sections.[3]

A significant difference was noted in the lingual papillae volumes as depicted in Fig. 1. Dorsal fungiform papillae were revealed to be significantly smaller (0.28 mm^3) than those located on lateral border (0.735 mm^3). However, the average circumvallate papillae volume was the largest (15.1 mm^3) among the studied papillae.

Taste papillae would possibly play a role in diet selection.[4] In addition, the pig is a superior animal model for human nutrition-related investigations because both species are omnivorous.

References

1. A. Singh and W.P. Ireland, *Anatomia Histologia Embryologia*, 17(1988)376.
2. D.C. Sterio, *Journal of Microscopy*, 134(1984)127.
3. H.J.G. Gundersen et al., *Acta Pathologica Microbiologica Immunologica scand*, Suppl., 96(1988)379.
4. J.M. Forbes, *Voluntary Food Intake and Diet Selection in Farm Animals*. CAB International. p. 254.

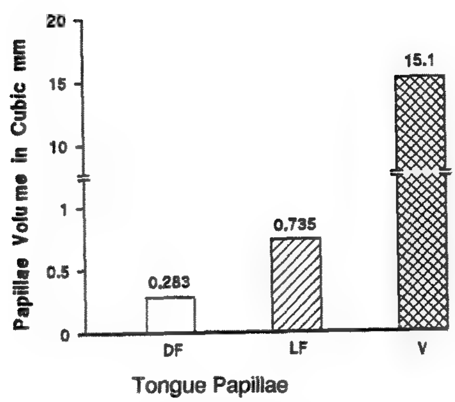

FIG. 1. Histogram to depict volume of the pig lingual papillae. DF = Dorsal fungiform papillae; LF = Lateral fungiform papillae; V = Circumvallate papillae.

COSMETOLOGY TREATMENTS ON HUMAN HAIR: AN SEM STUDY

D.F. Bowling

Electronics Department, Patterson Career Center, 118 East First Street, Dayton, OH 45402 (513) 226- 8012

High school cosmetology students study the methods and effects of various human hair treatments, including permanents, straightening, conditioning, coloring and cutting. Although they are provided with textbook examples of overtreatment and numerous hair disorders and diseases, a view of an individual hair at the high resolution offered by an SEM provides convincing evidence of the hair's altered structure. Magnifications up to 2000X provide dramatic differences in perspective. A good quality classroom optical microscope can be very informative at lower resolutions.

Students in a cosmetology class are initially split into two groups. One group is taught basic controls on the SEM (focus, magnification, brightness, contrast, specimen X, Y, and Z axis movements). A healthy, untreated piece of hair is initially examined on the SEM. The second group cements a piece of their own hair on a stub. The samples are dryed quickly using heat or vacuum while the groups trade places and activities.

As cosmetology students tend to practice what they learn, many of them employ straighteners, permanents, and conditioners in their hair. As each sample is marked by student initials under the stub, observations are personalized and the teacher can ask each student to confirm the observations by stating what treatments were used. Samples with special treatments can also be prepared in advance for subsequent imaging.

Figures 1 -3 are SEM images of hair. Figure 1 reveals a split end condition, called Trichoptilosis, which requires oil treatment to soften and lubricate the strands, and cutting of the ends themselves. Figure 2 shows a knotted hair condition called Trichorrhexis, which is a dry, brittle condition . The hair breaks easily and there is a brush- like spreading out of the fibers of individual strands. Softening the hair with conditioners helps this condition. Figure 3 reveals a beaded hair condition called Monilethrix, where the hair tends to break between the beads or nodes. Various scalp and hair treatments may correct this condition.

References

1. Milady's Standard Textbook of Cosmetology, Milady Publishing Company, Albany, NY (1995)
2. The author gratefully acknowledges the support provided by Wright Laboratory, Wright- Patterson Air Force Base, and the Cosmetology Department at Patterson Career Center.

Figure 1 Split End (Trichoptilosis)

Figure 2 Knotted Hair (Trichorrhexis)

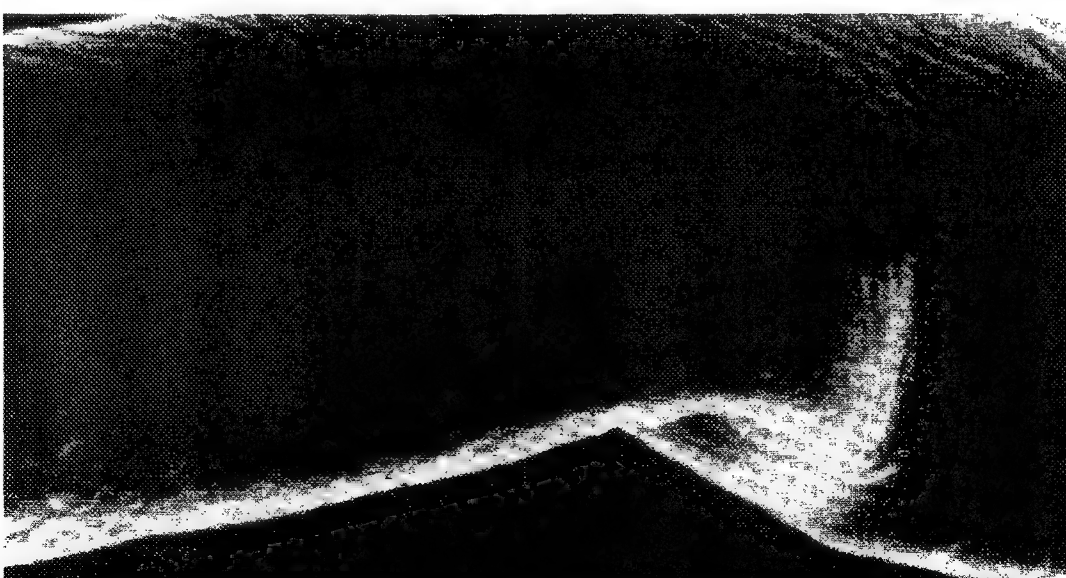

Figure 3 Beaded Hair (Monilethrix)

STRUCTURE of III-V OXIDES

Z. Liliental-Weber, M. Li,* G. S. Li,* C. Chang-Hasnain,* and E.R. Weber**

Materials Science Division, Lawrence Berkeley National Laboratory, Berkeley, Ca 94720
* Electrical Engineering and Computer Science Department, UC Berkeley, Berkeley, CA 94720
**Material Science Dept, UC Berkeley, Berkeley, CA 94720

The lack of high-quality native oxides on the III-V compounds has hindered the development of III-V integrated circuits and optoelectronic technology. Recently it was shown [1,2] that stable oxides can be formed in the III-V compounds rich in Al, such as $Al_xGa_{1-x}As$ similarly as it was done in Si technology by the reaction of $Al_xGa_{1-x}As$ with H_2O vapor (in N_2 carrier gas) at elevated temperatures (~400-450°C). The high quality of these oxides was attributed to the formation of stable AlO(OH) and Al_2O_3 compounds. However, this conclusion was not definitive, since several Al rich compounds were proposed as well. In addition, it was never clarified whether the excess As created in this process has any role in the stabilization of these oxides, in reducing leakage current or in impurity diffusion. Moreover there is concern as to the quality of the oxide/GaAs interfaces created by lateral oxidation of an intermediate AlGaAs layer.

In this study $Al_xGa_{1-x}As$/GaAs layers with different Al contents and different thicknesses were studied by cross-sectional transmission electron microscopy (TEM). Five periods of $Al_{0.7}Ga_{0.3}As$/GaAs quantum wells with thickness of 42/38 nm were grown by MBE on a GaAs substrate, followed by 38 nm thick $Al_xGa_{1-x}As$ graded layer (changing x from 0 to 1), then a 210 nm AlAs layer, and again a 38 nm thick graded layer of $Al_xGa_{1-x}As$ (changing x from 1 to 0), finally a 66 nm thick top layer of GaAs. Special lithographic masks were applied to form round dotes with 100 nm diameter. Wet oxidation (described above) was applied to such structures for 20 min. TEM was used to study these samples in cross-section. Uniform oxidation of the AlAs layer was observed (Fig. 1) with much larger granularity in the surrounding $Al_xGa_{1-x}As$ graded layers. It appears that addition of Ga to AlAs leads to the formation of porosity of the oxidized layer. Quantum wells with lower Al content (x=0.7) were practically unaffected and remained crystalline in this process, confirming previous studies, that showed formation of these oxides related to the Al concentration [3]. Shrinking of the oxides by 7.5 nm was detected after wet oxidation (compare Figs. 2a, b and c). Accumulation of As on the top of the GaAs was also observed (Fig. 2 d) and confirmed by energy dispersive x-ray (EDX) spectrometry (compare Figs. 2d, e and f).

Selective area diffraction patterns obtained from the oxidized AlAs layers and their surrounding graded $Al_xGa_{1-x}As$ layers gave ring diffraction patterns consistent with the following interplanar distances: 4.5, 2.78, 2.41, 1.97, 1.52, 1.4, 1.1776, and 1.138 Å. Three of these rings (2.41, 2.02 and 1.41Å) were detected earlier [2] and were assigned to one of the phase of AlO(OH) mixed with one of the four (η, γ, χ, and δ) Al_2O_3 oxide. Taking into account all rings and their intensities it appears that these interplanar distances agree well with the γ-Al_2O_3 oxides. This is consistent with a recent finding by Guha et al [4]. However, at this point it is difficult to eliminate the presence of pure Al in these oxides since interplanar distances overlap with the oxides, and high resolution micrographs give a hint of the presence of small Al grains imbedded in the oxides. In addition to the ring pattern small arcs containing defined spots consistent with AlAs and As could be detected as well. High resolution electron microscopy shows As accumulation in a

form of small precipitates on the upper and lower interface of the graded $Al_xGa_{1-x}As$ and in the GaAs top layer in addition to As cumulation at the GaAs surface. The presence of As clusters in the GaAs would suggest similar properties for these layers as those observed in LT-GaAs. Therefore, the insulating properties after wet oxidation can be a combined properties of the oxides plus the GaAs rich in As. Further work is is progress to determine the role of As in these oxides which could be of great relevance for further development of III-V device technology.

1. A.R. Sugg, N. Holonyak, Jr., J.E. Baker, F.A. Kish, and J.M. Dallesasse, Appl. Phys. Lett., **58**. 1199 (1991).
2. A.R. Sugg, E.I. Cnen, N. Holonyak, Jr., K.C. Hsieh, J.E. Baker, and N. Finnegan, J. Appl. Phys., **74**, 3880 (1993).
3. F.A. Kish, S.J. Carracci, N. Holonyak, Jr., K.C. Hsieh, J.E. Baker, S.A. Maranowski, A.R. Sugg, and J.M. Dallesasse, J. Electr. Mat. **21**, 1133 (1992).
4. S. Guha, F. Agahi, B. Pezeshi, J.A. Kash, D.W. Kisker, and N.A. Bojarczuk, Appl. Phys. Lett., **68**, 906 (1996).

5. This research was supported by AFOSR-ISSA-90-0009. Z.L.W. would like to thank W. Swider for help with TEM sample preparation.

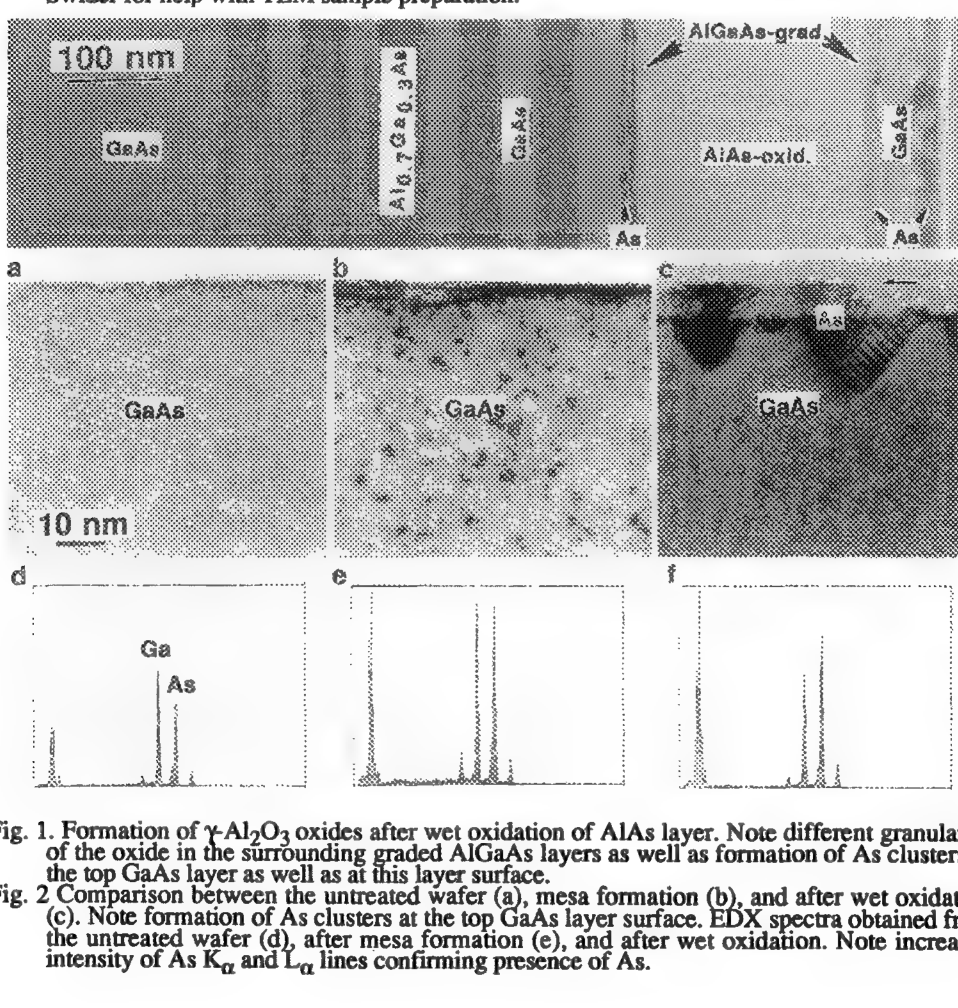

Fig. 1. Formation of γ-Al_2O_3 oxides after wet oxidation of AlAs layer. Note different granularity of the oxide in the surrounding graded AlGaAs layers as well as formation of As clusters in the top GaAs layer as well as at this layer surface.

Fig. 2 Comparison between the untreated wafer (a), mesa formation (b), and after wet oxidation (c). Note formation of As clusters at the top GaAs layer surface. EDX spectra obtained from the untreated wafer (d), after mesa formation (e), and after wet oxidation. Note increased intensity of As K_α and L_α lines confirming presence of As.

Using the Secondary Electrons (SE) of Scanning Electron Microscope with NIST's MONSEL-II Program to Obtain Improved Linewidth Measurements and Slope Angles of Line Edges on a MMIC GaAs Device

Richard G. Sartore

US Army Research Laboratory, AMSRL-PS-DC, Fort Monmouth, NJ 07703

In the evaluation of GaAs devices from the MMIC (Monolithic Microwave Integrated Circuits) program for Army applications, there was a requirement to obtain accurate linewidth measurements on the nominal 0.5 micrometer gate lengths used to fabricate these devices. Preliminary measurements indicated a significant variation (typically 10 % to 30% but could be more) in the critical dimensional measurements of the gate length, gate to source distance and gate to drain distance. Passivation introduced a margin of error, which was removed by plasma etching. Additionally, the high aspect ratio (4-5) of the thick gold (Au) conductors also introduced measurement difficulties. The final measurements were performed after the thick gold conductor was removed and only the barrier metal remained, which was approximately 250 nanometer thick platinum on GaAs substrate. The thickness was measured using the penetration voltage method [1]. Linescan of the secondary electron signal as it scans across the gate is shown in Figure 1. This linescan is an average of 5 linescans in the immediate vicinity to reduce noise levels. A SEM image of the area is shown in Figure 2. To obtain a rough estimate of the slopes of the gate lines at the edges, the sample was tilted to 75 degrees and the image in Figure 3 was obtained. From this figure a rough estimate of the sloped edges, using a protractor , was obtained, approximately 27 degrees, +/- 5 degrees.

A simulated linescan using NIST's MONSEL-II program [2-5] is shown in Figure 4, for the nominal values of 250 nanometer thick film with 30 degrees edge slope, with a beam diameter of 30nm. Subsequent simulations with MONSEL-II shows a noticeable shift of linescan peaks and valleys with slope angle variation and size of beam diameter. The linescan peaks can vary by 10% to 20% with slope angle variation of 30 degrees. based on simulation results. There is also a shift of the valley bottom that can vary by 10% or more from the position of the calculated bottom based on nominal values. Considering the simulation results, it is possible to develop a correlation of the position of the peaks and/or valleys for the edges and/or bottoms to the angle of the edge slope. Thus assuming that the relative accuracy of the NIST model is good, it should be possible to estimate the angle of the sloped edges from a linescan measurement and use these results to perform the necessary correction on the linwidth measurements.

The NIST MONSEL-II has enabled a higher degree of confidence in the identification of the top and bottom edges of the metallized line, using secondary electrons. In addition, based on the MONSEL-II simulation results, a rough estimated of slope angle can be obtained from the secondary electron signal.

1. R.G.Sartore, Scanning Microscopy Inc. Vol 1, No.1, (1987), p41-48
2. J.Lowney, Scanning, Vol.17, No. 5, p281-286, Sept/Oct 1995
3. J.Lowney, Microbeam Analysis, Vol. 4, pp131-136, 1995
4. J.Lowney, M. Postek and A.Vladar, Proc. MAS 1995, p343-344
5. J.Lowney, Scanning, in press
6. J.Lowney at NIST made the MONSEL-II program available and provided assistance in installation

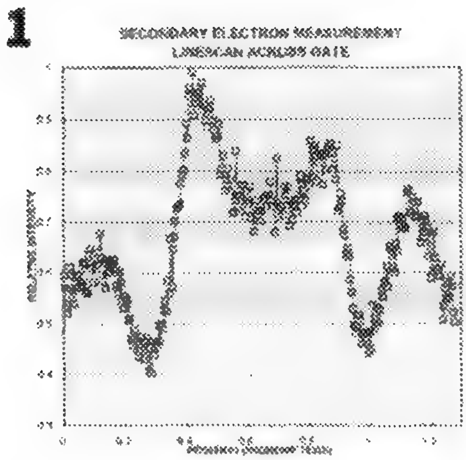

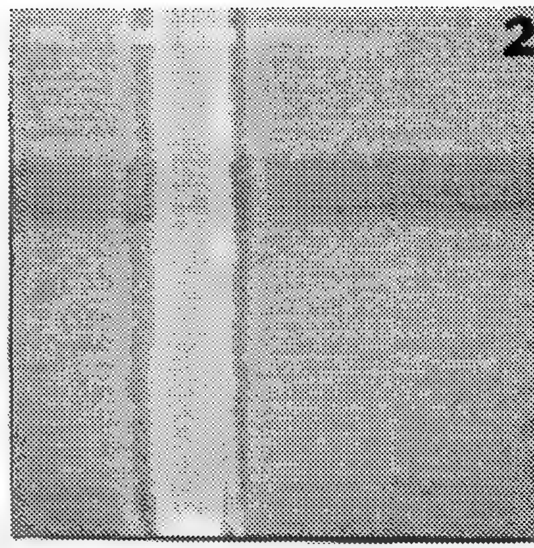

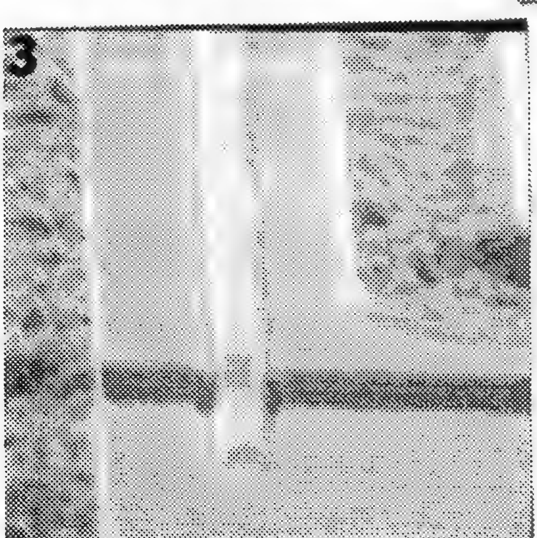

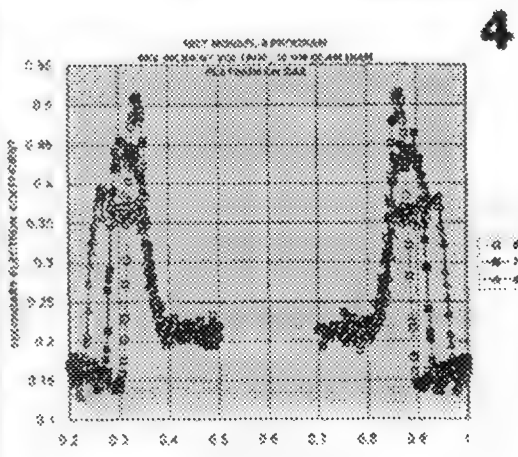

Figure 1. Linescan across a sub-micron gate at 20,000X magnification
Figure 2. SEM microphotograph of the area scanned in Figure 1
Figure 3. SEM microphotograph of the same gate in Figure 1&2 but at 75 degree tilt and 15,000X magnification
Figure 4. Results of MONSEL-II simulation at various slope angles with respect to substrate

NUCLEATION OF MISFIT AND THREADING DISLOCATIONS IN GaSb/GaAs(001) HETEROSTRUCTURE

W. Qian,*+ M. Skowronski,* R. Kaspi,** and M. De Graef*

*Department of Materials Science & Engineering, Carnegie Mellon University, Pittsburgh, PA 15213
**Wright State University, University Research Center, Dayton, OH 45435
+now at Department of Materials Science & Engineering, Northwestern University, Evanston, IL 60208

GaSb thin film grown on GaAs is a promising substrate for fabrication of electronic and optical devices such as infrared photodetectors. However, these two materials exhibit a 7.8% lattice constant mismatch which raises concerns about the amount of extended defects introduced during strain relaxation. It was found that[1,2], unlike small lattice mismatched systems such as $In_xGa_{1-x}As/GaAs$ or $Ge_xSi_{1-x}/Si(100)$, the GaSb/GaAs interface consists of a quasi-periodic array of 90° misfit dislocations, and the threading dislocation density is low despite its large lattice mismatch. This paper reports on the initial stages of GaSb growth on GaAs(001) substrates by molecular beam epitaxy (MBE). In particular, we discuss the possible formation mechanism of misfit dislocations at the GaSb/GaAs(001) interface and the origin of threading dislocations in the GaSb epilayer.

GaSb thin films with nominal thicknesses of 5 to 100 nm were grown on GaAs(001) by MBE at a growth rate of about 0.8 monolayers per second. The films were deposited at 550 °C with an antimony stabilized surface exhibiting a 1x3 reconstruction. At thicknesses below 10 nm, the GaSb layer consists of isolated, flat-topped islands with well defined {111} facets on each side (Fig.1). All the islands are elongated in the $[1\bar{1}0]$ direction, indicating that the Sb terminated $\{111\}_B$ facets grow faster than the Ga-terminated $\{111\}_A$ facets. The GaSb/GaAs(001) interface consists of a regular net of misfit dislocations which are primarily of 90° type, lying along [110] and $[1\bar{1}0]$ directions with Burgers vectors of $\mathbf{b} = \pm(a/2)[1\bar{1}0]$ and $\mathbf{b} = \pm(a/2)[110]$ (Fig.2). The measured misfit dislocation spacing, D = 5.8 ± .2 nm, is slightly larger than the predicted value of 5.5 nm for a fully relaxed system. Every dislocation is associated with two extra {111} planes located near the dislocation core which intersects with the interface along the [110] projection. Many small islands have perfect {220} moiré patterns (Fig.3), indicating that those islands are defect-free. Selected area electron diffraction pattern (Fig.4) reveals that there is about 0.6% residual compressive strain in the GaSb layer. Since 90° misfit dislocations are sessile on {111} planes, it is unlikely that each one of them is formed by the interaction of two 60° dislocations nucleating on particular {111} planes and gliding into the interface. We propose that misfit dislocations in the GaSb/GaAs(001) system are spontaneously nucleated at the edges of advancing {111} planes and glide inwards on the (001) plane until they reach their equilibrium position (Fig.5). GaSb forms a continuous film at thicknesses of 80 nm and above, with a typical threading dislocation density of $\sim 1\times10^{10}/cm^2$. The threading segments are associated with 60° misfit dislocations, which may either nucleate in the GaSb film at the later stages of island growth and glide into the interface along the {111} planes, or are introduced during coalescence of neighboring islands. Since the 90° misfit dislocations are not likely to thread on the {111} planes, these 60° ones are the main source of threading dislocations in the GaSb epilayer (Fig.6). In addition, the minority 60° misfit dislocations often cause half-period shifts between the neighboring 90° dislocation array (Fig.6) due to their mutual interactions[3,4]. This can be fully explained by the use of the Thompson tetrahedron[5].

References

1. A. Rocher, Solid State Phenomena, 19/20 (1991) 563.
2. C. Raisin, et al., Applied Surface Science, 50 (1991) 434.
3. S. Amelinckx, Phil. Mag., 1 (1956) 269.
4. J.G. Zhu and C.B. Carter, Phil. Mag. A 62 (1990) 319.
5. N. Thompson, Proc. Phys. Soc. B 66 (1953) 481.
6. Supported by the US Air Force Wright Laboratory under Contract No. F33615-95-C1619.

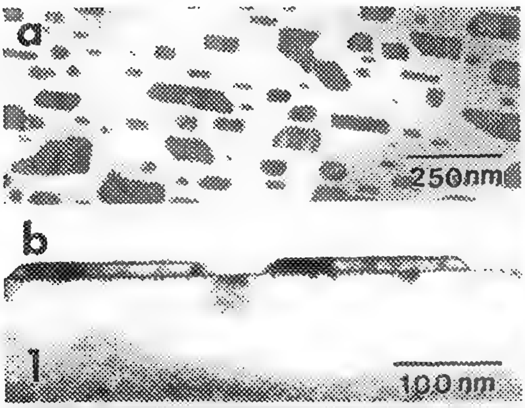

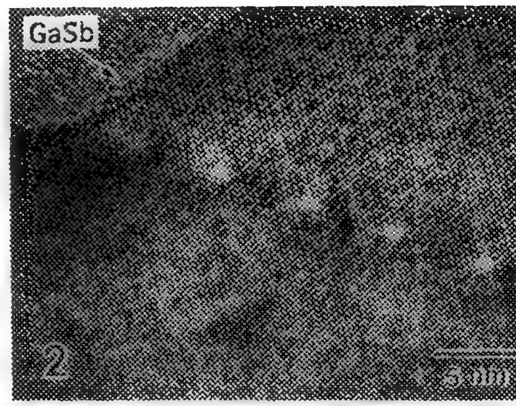

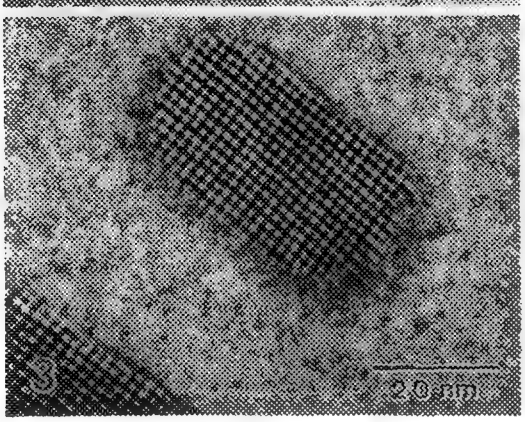

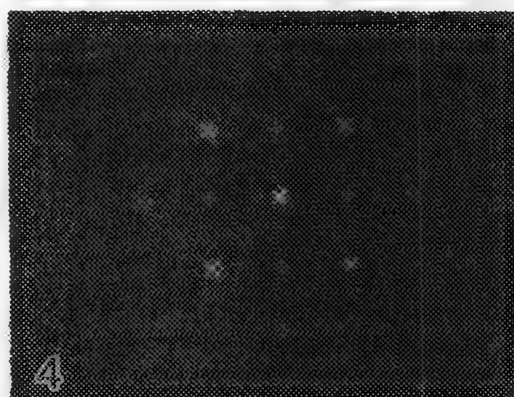

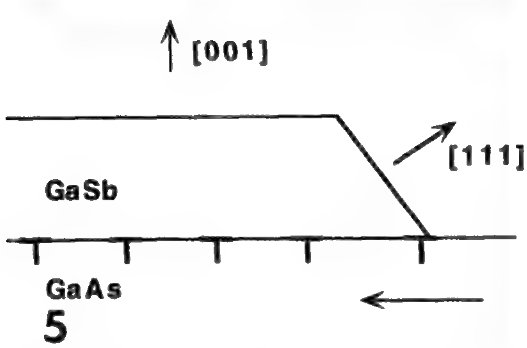

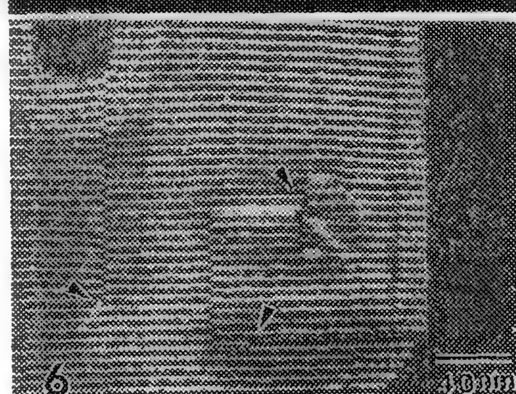

FIG.1 Plan-view (a) and cross-sectional (b) TEM micrographs of a 5 nm (nominal) GaSb layer on GaAs.
FIG.2 Lattice image of the 5 nm GaSb/GaAs interface along [110] show the 90° misfit dislocation array.
FIG.3 Many beam bright field image shows small islands with perfect {220} moiré patterns.
FIG.4 Selected area electron diffarction pattern from thin layer of GaSb on GaAs.
FIG.5 Schematic of a possible formation mechanism of the 90° misfit dislocation net.
FIG.6 Weak beam image of a 20 nm GaSb layer on GaAs shows misfit and threading dislocations.

EFFECTS OF SUBSTRATE ORIENTATION ON GROWTH OF EPITAXIAL LAYERS

Y. Hsu,* T. S. Kuan,* and W. I. Wang**

*Department of Physics, University at Albany, SUNY, Albany, NY 12222
**Department of Electrical Engineering, Columbia University, New York, NY 10027

Semiconductor superlattices or epitaxial overlayers have so far been grown mostly on (100)-oriented substrates. It has long been suspected that growth on surfaces such as (m11) could produce equally good or better epitaxial layers.[1] In this work, we have systematically tested the growth of multi- or single-layered structures, including the GaAs/AlAs, AlAs/Ge, and GaAs/Si systems, on surfaces of different orientations. The crystallinity and defect mechanisms in the layers grown on (100), (311), and (511) surfaces at different temperatures were compared. In most cases we found that (311) surfaces can produce epitaxial layers as good as on (100) surfaces.

Perfect lattice-matched GaAs/AlAs superlattices were grown on (311)A-, (311)B-, and (100)-oriented GaAs substrates. Superlattices with good layer morphology were achieved on all three surfaces at 600°C. Fig. 1(a) shows an image of a typical GaAs/AlAs superlattice grown on a (311)B surface. This superlattice exhibits sharp interface abruptness as indicated by the high-order satellites observed in the diffraction pattern in Fig. 1(b). High-resolution x-ray diffraction also revealed good crystalline quality in all these superlattices. However, by comparison of the total number of satellites observed and the intensity distribution among them, we were able to conclude that the growth on (311)A and (311)B surfaces gives rise to sharper interface abruptness than the growth on (100) surfaces.[2] High density of surface steps and terraces on (311) surfaces could lead to sharper interfaces between layers, maybe because the meandering of steps during growth is limited by the narrow terraces on this surface.

The growth of lattice-matched AlAs/Ge system behaved quite differently. They were grown on various GaAs substrates of different orientations at temperatures ranging from 415 to 500°C. All these AlAs/Ge superlattices contain a high density of stacking faults. Fig. 2(a) and (b) show these stacking faults in layers growth on (100) and (511)A surfaces, respectively. No stacking faults were ever found in GaAs/AlAs superlattices grown under optimum conditions. The formation of stacking faults in AlAs/Ge layers is attributed to impurity absorption by active Al atoms during growth. As growth temperature rises to 500°C, however, there is a significant change of stacking fault configuration. Stacking faults tend to form on {111} planes with high Schmid factors, indicating the presence of significant misfit strain at higher temperatures and the relief of strain by these stacking faults. No antiphase boundaries were detected in AlAs layers in all these superlattices.

GaAs epilayers grown on (311)- and (511)-oriented Si substrate at temperatures ranging from 480 to 540°C contain high density of dislocations because of the large lattice mismatch involved. The growth on (311) Si surfaces was observed to produce dislocations about 30% less than the growth on (511) surfaces. The misfit dislocations on (311) surfaces are mostly edge type, whereas more 60° dislocations are formed on (511) surfaces. The superior quality of (311) GaAs epilayer was also demonstrated by high resolution x-ray diffraction. The GaAs epitaxial layers grown on both (311) and (511) surfaces were found to tilt slightly (0.5° and 0.27°, respectively) away from the growth axes. It is believed that this slight orientation tilt serves to relieve misfit strain and thus the dislocation density is reduced. This orientation tilt has been reported to be much less in layers grown on (100)-oriented Si substrates.[3]

References

(1) K. F. Longenbach and W. I. Wang, APL **59**, 2427 (1991); H. Kroemer, MRS Symp. Proc. Vol. **67**, 3 (1986).
(2) Y. Hsu, W. I. Wang, and T. S. Kuan, to appear in JVST (1996).
(3) R. J. Matyi, J. W. Lee, and H. F. Schaake, J. Electron. Mater., **17**, 87 (1988).

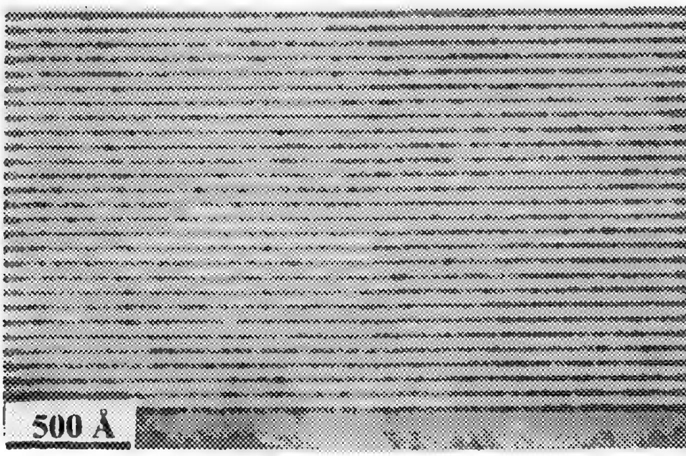

1(a) 1(b)

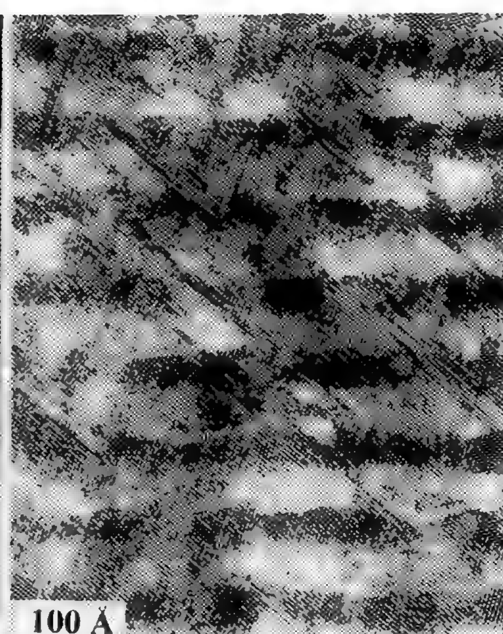

2(a) 2(b)

Fig. 1(a) Bright-field image of a GaAs/AlAs superlattice grown on a (311)B GaAs substrate at 600°C.
Fig. 1(b) Diffraction pattern of (a).
Fig. 2(a) Lattice image of a AlAs/Ge superlattice grown on a (100) GaAs substrate at 415°C.
Fig. 2(b) Lattice image of a AlAs/Ge superlattice grown on a (511)A GaAs substrate at 415°C.

THE INFLUENCE OF SURFACE ROUGHENING AND Si{111} FACETS ON LOW TEMPERATURE Si HOMOEPITAXY

O.P Karpenko and S.M. Yalisove

Department of Materials Science and Engineering, University of Michigan, Ann Arbor, MI 48109

Recent research in the area of low temperature (T<450°C) epitaxial growth of semiconductors has revealed a number of interesting phenomena which are not yet fully understood.[1] One such phenomena is the crystalline to amorphous phase transition which occurs during low temperature Si homoepitaxy. For low temperature Si homoepitaxy, crystalline growth is limited by a critical epitaxial thickness (h_{epi}), beyond which Si grows as an amorphous phase. It has been established that h_{epi} follows an Arrhenius relation with temperature, is preceded by an increase in surface roughness, and is affected by the presence of impurities and the substrate surface orientation.[2] Although the formation of amorphous Si is not fully understood, several models have been proposed to explain this phenomenon. One of these models suggests that Si amorphization is associated with surface roughening and the formation of Si{111} facets at the growth surface.[1] According to this model, h_{epi} should decrease as the density of Si{111} microfacets on the starting increases. This study provides evidence which strongly suggests that the breakdown in crystalline growth during low temperature Si homoepitaxy is intimately linked to the formation and presence of Si{111} facets at the growth front. It was found that surface roughening during low temperature Si(100) homoepitaxy leads to the formation of Si{111} facets and eventual breakdown of crystalline growth, and that the reduction in h_{epi} for growth on higher indexed Si{hkl} surfaces is correlated to an increase in the initial Si{111} facet density along these surfaces.

Surface roughening during low temperature Si(100) homoepitaxy was investigated using reflection high energy electron diffraction (RHEED) and cross-section transmission electron microscopy (TEM). The use of RHEED allowed *in-situ* real-time collection of structural information from the growth surface. In order to simplify analysis of the RHEED patterns, a simple kinematic diffraction model was used.[3] The kinematic RHEED model, used to measure surface roughening in the growth direction, was calibrated against cross section TEM analyses of Ge marker layer spreading (1/4ML Ge markers were introduced every ~150Å during growth).[2,3] For Si (100) homoepitaxy between 150°-275°C, RHEED analyses show that surface roughness, in the growth direction, increases rapidly with film thickness and saturates at a "critical" value prior to the crystalline to amorphous phase transition (see fig.1). The saturation of surface roughness was accompanied by the formation of Si{111} facets and twinning along Si{111} planes. It was also found that the initial roughening rate was temperature independent, and that the "critical" value at which roughness saturated increased rapidly with growth temperature.

A replica technique was developed to map the density of Si{111} facets along the starting surfaces of higher indexed Si{hkl} surfaces.[4] The replica technique involved cross-section and plan-view TEM analyses of $CoSi_2$ layers grown onto patterned Si(100) substrates. Based on these analyses it was established that $CoSi_2$ epitaxial orientation is dependent on Si surface orientation (see fig.2), and that $CoSi_2$(221) grains nucleate along Si{111} microfacets. This replica technique was then applied to determining the correlation between initial Si{111} facet density and the reduction in h_{epi} for growth on high indexed Si{hkl} surfaces. Both $CoSi_2$ and Si were grown on one-dimensionally patterned Si(100) substrates containing a number of well defined high-indexed Si(hkl) surfaces.[2,4] Analysis of the Si homoepitaxial films showed that a reduction in h_{epi} with increasing surface misorientation from Si(100) towards Si(111).[2] Analysis of $CoSi_2$ films suggests that Si{111} facet density increases with

Si surface misorientation (increasing $CoSi_2(221)$ grain density and decreasing $CoSi_2(221)$ grain size with incraesing surface misorientation).[4]

References

1. D.J. Eaglesham, J. Appl. Phys. **77**, 3597 (1995).
2. D.P. Adams and S.M. Yalisove, J. Appl. Phys. **76**, 5185 (1994).
3. O.P. Karpenko, D.J. Eaglesham and S.M. Yalisove (submitted to J. Appl. Phys.)
4. O.P. Karpenko and S.M. Yalisove (submitted to J. Appl. Phys.)

Figure 1

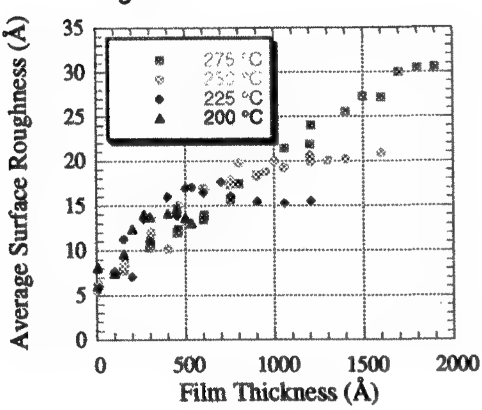

Figure 2

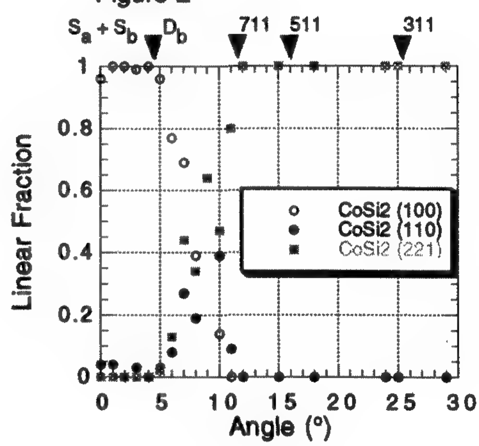

Figure 1 The scaling of surface roughness in the growth direction with film thickness, as measured by RHEED.

Figure 2 The dependence of $CoSi_2$ epitaxial orientation on Si surface orientation (the angle is measured between the $CoSi_2$/Si interface normal and Si(100).

Acknowledgment: The authors would like to thank David Eaglesham for useful discussions.

OBSERVATION OF PASSIVATED Al-1%Cu LINES USING ENVIRONMENTAL SCANNING ELECTRON MICROSCOPY (ESEM)

D.T. Carpenter*, D.A. Smith*, and J.R. Lloyd*

*Department of Materials Science and Engineering, Lehigh University, Bethlehem, PA 18018

Characterization of failure phenomena in passivated interconnects requires the ability to observe dynamic changes in buried lines (e.g. formation of electromigration voids or microstructural changes during an anneal). Conventional SEM cannot image passivated structures due to surface charging. HVSEM has been used with some success to image voids in metal lines under passivation, but it requires intensive specimen preparation and is not commercially available.[1,2] The present study is intended to determine whether ESEM is suitable for such dynamic experiments on passivated structures.

The lines were composed of Al-1%Cu and had a uniform thickness of 1.4 μm. All lines also had both an underlayer and an anti-reflective coating of Ti/TiN. The thickness of these layers varied slightly, but was typically around 600 Å. Observations were performed in an Electroscan model 2020 environmental scanning microscope with a LaB_6 thermionic source using the gaseous secondary electron detector (GSED) and water vapor as an imaging gas. Image quality changes with gas amplification of the SE signal and degradation of the beam by the gas, both of which are affected by beam energy, working distance, and chamber pressure in a complex manner. These data are therefore included with each micrograph.

Under 0.75 μm of passivation, voids could be easily distinguished as dark areas on the bright lines (Fig. 1). For the purpose of these exploratory experiments, voids were formed by resistance heating lines with a current density of ca. 7.5 MA/cm^2 until local melting occurred. Thermal expansion cracked the passivation, allowing molten metal to escape, leaving behind voids. Lines could be imaged even under 2 μm of glass, though with markedly poorer resolution (Fig. 2). The basis for this is as follows: the primary imaging signal consists of SE2 electrons (the entire surface is flat passivation, so the SE1 signal carries no useful information). The backscatter yield (η) increases with atomic number quite strongly for low Z materials and SE2 yield is proportional to η, so we expect Al to appear bright relative to SiO_2 and voids to appear dark (as long they are within the interaction volume). Lines appear brighter after passivation is removed, as expected, and smaller features are resolvable than when passivation is present (Fig. 3). Contrast may be enhanced due to the presence of Ti on the top surface of the lines.

Microstructural detail was visible in 0.75 μm-deep lines (Fig. 4), including particles of Al_2Cu (or θ-phase) and grain boundaries (GBs). θ-phase particles appear bright due to the relatively high Z of Cu, consistent with previous ESEM images of passivated lines.[3] It is surprising that GBs can be distinguished since the glass prevents formation of GB grooves (the usual source of GB contrast). Some GBs are decorated with elongated particles, probably Ti-Al intermetallics (formed by diffusion of Ti into Al grain boundaries). Undecorated GBs are visible due to slight variations in η with grain orientation (channeling contrast). Several examples of apparently anomalous contrast were also observed. Fig. 5a shows periodic contrast between neighboring 2 μm-deep lines in plan view. Fig. 5b shows the same area in cross section with contrast of the same periodicity appearing in empty space. A likely explanation for this contrast is the presence of surface fields or a charging effect.

These initial experiments have shown that ESEM is a very powerful tool for the analysis of passivated line structures. Future work will concentrate on optimizing the technique for *in situ* experiments.

[1] D.M. Follstaedt et al, *Mater. Res. Soc. Symp. Proc.* **225**, 225 (1991).
[2] M.C. Madden et al, *Mater. Res. Soc. Symp. Proc.* **265**, 33 (1992).
[3] D.A. Smith et al, *Ultramicroscopy* **51**, 328 (1993).

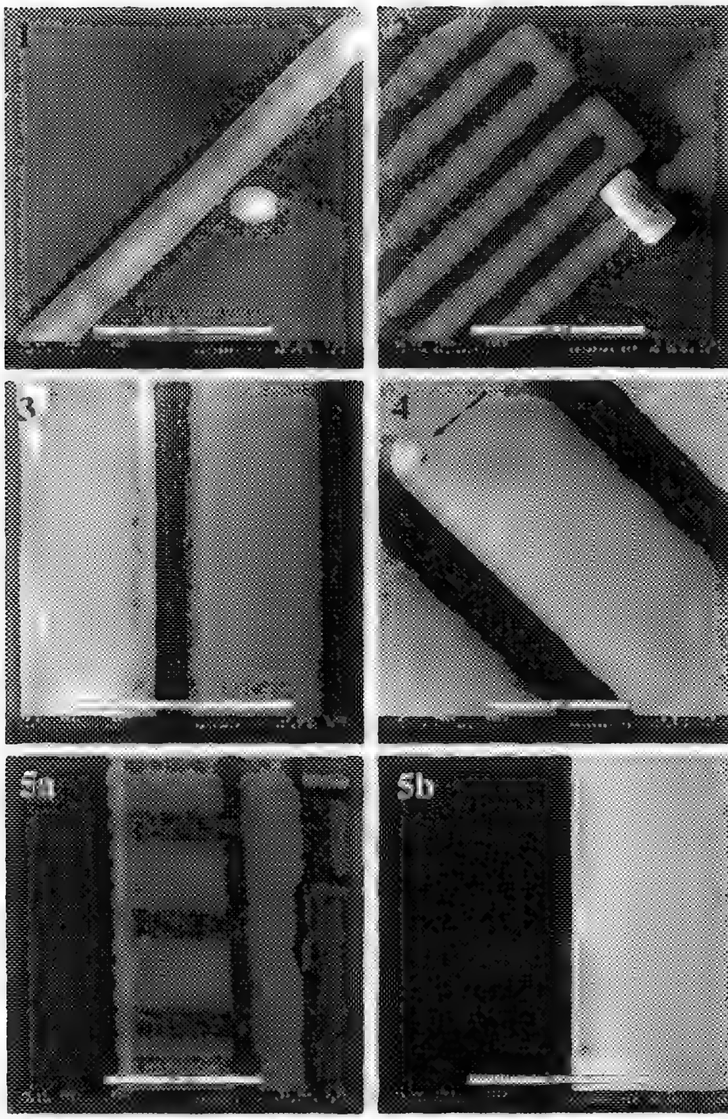

FIG. 1 - Voids in line under 0.75μm passivation (bar=15μm, 30 kV, 10 mm, 3 Torr)
FIG. 2 - Lines under 2μm passivation (bar=35μm, 30 kV, 9.9 mm, 3 Torr)
FIG. 3 - Line with passivation removed (left) next to line under 0.75μm passivation (bar=10μm, 30 kV, 10 mm, 3 Torr)
FIG. 4 - Grain boundaries and θ-phase (arrowed) under 0.75μm passivation (bar=5μm, 30 kV, 10 mm, 3 Torr)
FIG. 5 - Contrast between lines under 2μm passivation in (a) plan view (bar=50μm, 30 kV, 11.9 mm, 3 Torr) and (b) edge-on (bar=35μm, 10 kV, 6.3 mm, 3.5 Torr). Note identical periodicity.

Shallow Drain Extension by Angled Ion Implantation

Roger Alvis,* Scott Luning,* and Peter Griffin**
*Technology and Reliability Engineering, Advanced Micro Devices, Sunnyvale, CA
**Department of Electrical Engineering, Stanford University, Stanford, CA

In a technology driven enterprise, such as the semiconductor industry, pure research and development often overshadows manufacturing concerns. Typically, "discovery" is the result of miniaturization efforts with integration into existing process flows a secondary concern. However, it is often the case that fabrication of devices is complicated by next generations of technologies. Since revenue and profits are ultimately determined by the speed and ease with which a wafer may be processed, the streamlining of process flows assumes a certain level of importance. In this work, we describe the construction and microstructural characterization of a simple spacerless metal-oxide semiconductor (MOS) transistor with a self-aligned shallow drain extension.[1]

Transistor structures were fabricated at Stanford University's Center for Integrated Systems using a single masking step to pattern the gate mask for the self-aligned structures. A 200Å gate oxide was grown and a 3000Å polysilicon blanket film was subsequently deposited on the wafer. The polysilicon was patterned into an array of 2.0μm lines and 3.0μm spaces. Arsenic was implanted at 120keV with a nominal dose of 1e15 ions/cm^2 at 20° from normal incidence and rapid thermal annealed at 1000° C for 30 seconds (Fig. 1). Cross-sectional transmission electron microscopy and atomic force microscopy (TEM, XAFM) samples were prepared using standard metallographic procedures with the doped regions delineated by chemical etching.[2,3] A one-dimensionally calibrated process simulation was performed using Athena v.2.0.13, a commercial derivative of SUPREM IV.[4]

Direct comparison of TEM micrographs with the SUPREM plots immediately reveals a 325Å discrepancy between the predicted and measured overlap (Y_j) of the 5e18 arsenic ions/cm^3 etch contour and the edge of the gate (Fig. 2a,b). It is important to note that a similarly derived 1-D calibrated simulation on angled 35keV implants compared well with the TEM results, with Y_j in both cases showing negative overlap and agreeing to within 130Å. A closer inspection of the TEM analysis reveals there to be unexpected, "extra" contours located at the corner of the gate near the surface. Heavier delineation of the doped region and imaging by XAFM reveals an even greater Y_j (300Å) than the 75Å seen by TEM (Fig. 3). The 2-D distribution of the arsenic is evocative of a lightly-doped-drain (LDD) structure common to modern logic technologies.[5]

This microstructure may be attributed to the penetration and scattering of the arsenic ions through the corner of the gate mask, allowing ions to "fill-in" the shadowed region adjacent to the edge of the gate. Because of the relatively large range and straggle associated with 120keV arsenic ions (≈1000Å), a sufficient number of ions will emerge from the leeward side of the gate with lower energy to effect a shallow junction between the channel and the deeper drain junction.[6] Although it is likely that the drain extension is more lightly doped than the drain junction itself because of dose loss to the polysilicon gate, further quantitative 2-D analysis on the nano-scale is required. Nevertheless, the integration of this phenomenon advantageously into a process flow may reduce the minimum number of required steps by one-half and still retain the beneficial effects of the LDD.

References:
1. Patent Pending.
2. Maher and Zhang, *J. Vac. Sci. Techol. B* 12(1) 1994.
3. Alvis and Mantiply, *J. Vac. Sci. Techol. B* 14(1) 1996.
4. Alvis, Luning, Thompson, Griffin, and Sinclair, *J. Vac. Sci. Techol. B* 14(1) 1996.
5. Ogura, Tsang, Walker, Critchlow, and Shepard, *IEEE Trans. Elec. Dev.*, ED-27, 1980.
6. Sze, S. M., ed., *VLSI Technology*, McGraw-Hill, NY, 1983.

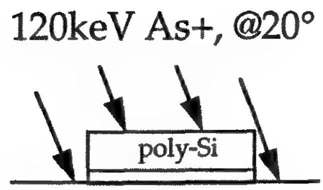

Figure 1: Schematic representation of self-aligned implant structure (not to scale).

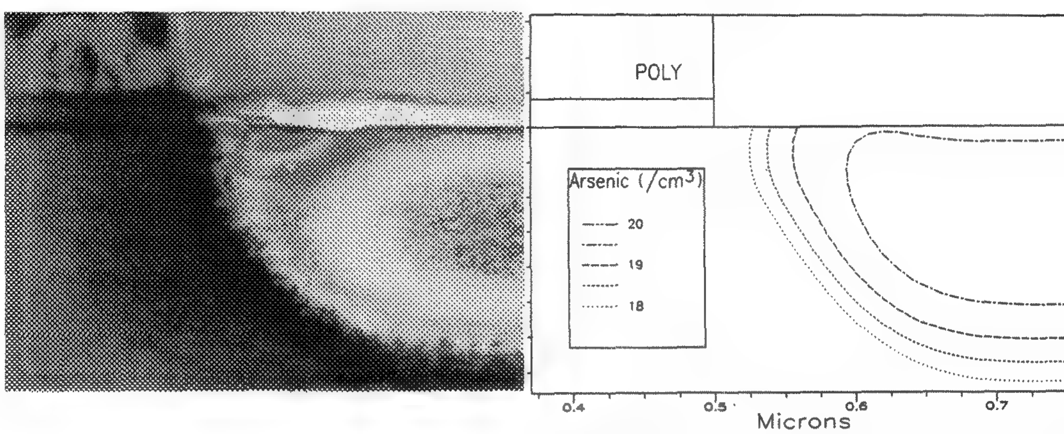

Figure 2a,b: TEM micrograph and corresponding SUPREM plot (same scale). Notice that the simulated microstructure predicts an undoped "shadowed" region which is not revealed in the micrograph.

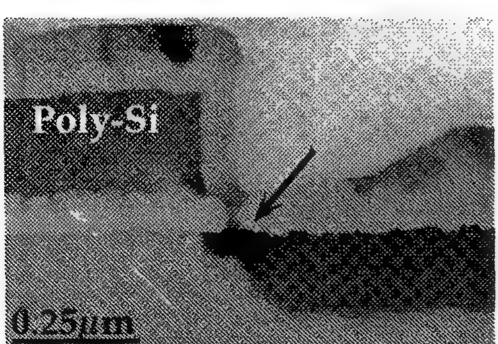

Figure 3: AFM imaging of cross-section allows for heavier etching than is possible with TEM and reveals a shallow junction extending from the drain, underlapping the edge of the gate.

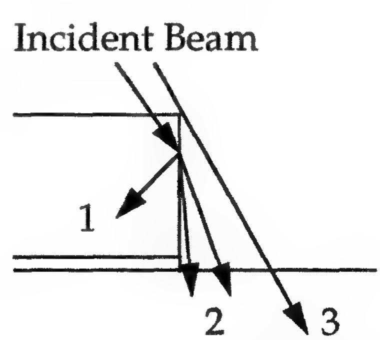

Figure 4: Schematic of gate corner detailing ion-mask interactions: 1) ion scatters into mask, 2) ion scattered from mask into shadowed region, losing energy, 3) ion implanted at incident energy (not to scale).

IMAGING FREE CARRIERS IN ELECTRONIC MATERIAL USING A SCANNING PROBE MICROSCOPE: SCANNING CAPACITANCE MICROSCOPY

A Erickson*, D Adderton*, T Day* and R Alvis**

*Digital Instruments, 520 E Montecito St., Santa Barbara, Ca 93103
**Advavced Micro Devices, One AMD Place, Sunnyvale, Ca 94088

The development of methods to measure electrical properties, which are suitable to directly yield the desired carrier distributions on a nanometer scale has greatly benefited from the development of scanning probe technology over the last decade. Scanning Probe Microscopes (SPMs) offer inherent two-dimensionality and have been shown to have applications ranging from Magnet force to electro-chemistry. We have used an SPM in contact mode to simultaneously measure topography (and therefore physical structure) and capacitance variations (due to an applied bias) of various electronic materials such as doped silicon, poly silicon, SiC, and III-V materials.

The technique aptly named Scanning Capacitance Microscopy (SCM) takes advantage of the fact that electrical carrier response to an applied electric field is largely dependent upon the local carrier concentration. Using a high 'Q' GHz resonant circuit, SCM measures capacitance variations due to an applied bias between the metalized nano-probe tip and semiconductor sample during scanning. Since these variations are directly related to dopant (carrier) concentration, the SCM generates a two-dimensional image with contrast corresponding to near-surface variations in carrier density. Because the measurement is done with an extremely sharp probe, we have been able to resolve features as small as 10nm, corresponding to attofarad (1e-18 farad) capacitance changes.

Dopant profile information and SCM data modeling have been presented previously by Erickson et.al. and Huang et. al. and this work continues to be a high priority for researchers in the field.{4,5} We have also used the tools features in a very practical way which does not require extensive theoretical modeling and large amounts of computer processing and simulation time. Because of the technique's sharp resolution of steep carrier gradients, such as pn junctions where essentially no free carriers are present, or local implant defects and grain boundaries where carriers may segregate and be inactive, we have been able to image loop defects with extremely high resolution and delineate effective gate lengths. The authors know of no other techniques which may directly image Leff. Furthermore, because of SCM's high range of dopant sensitivity (e15-e20 atoms/cm^3) structures such as LDDs are also imaged. Again this is the only tool which may do this type of measurement directly.

1. R. Subrahmanyan, J. Vac. Sci. Tech. B 10 (1), 358 (1992);
2. H. Cerva, Proc. 1st Intern. Workshop on the Meas. And Char. Of Ultra-Shallow Doping Profiles, Vol. 2, 286 (1991)
3. R Alvis, S Luning, L Thompson, R Sinclair and P Griffin, Proc. 3rd Intern. Workshop on the Meas. And Char. Of Ultra-Shallow Doping Profiles, Vol. 3, (1995)
4. A Erickson, L Sadwick, G Neubauer, J Kopanski, D Adderton, and M Rodgers, J. Elec. Mat. Feb. (1996)
5. Y Huang, C Williams, H Smith, Proc. 3rd Intern. Workshop on the Meas. And Char. Of Ultra-Shallow Doping Profiles, Vol. 3, (1995)

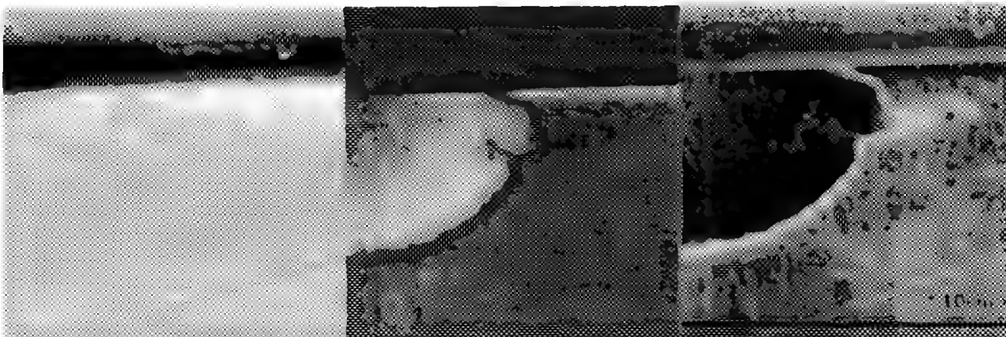

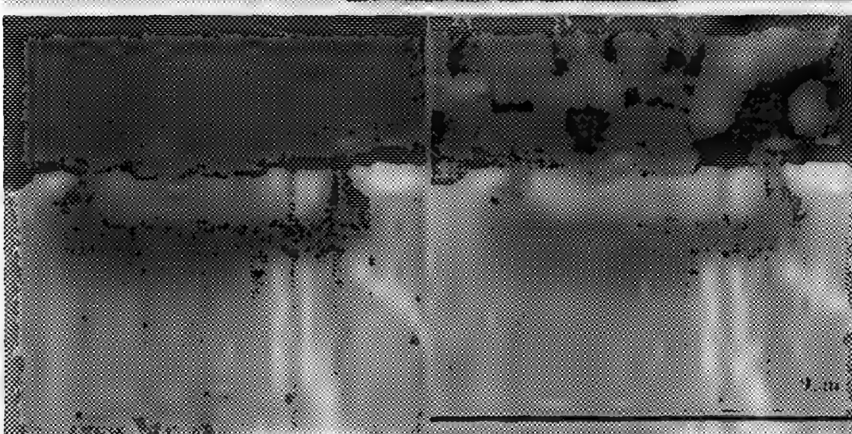

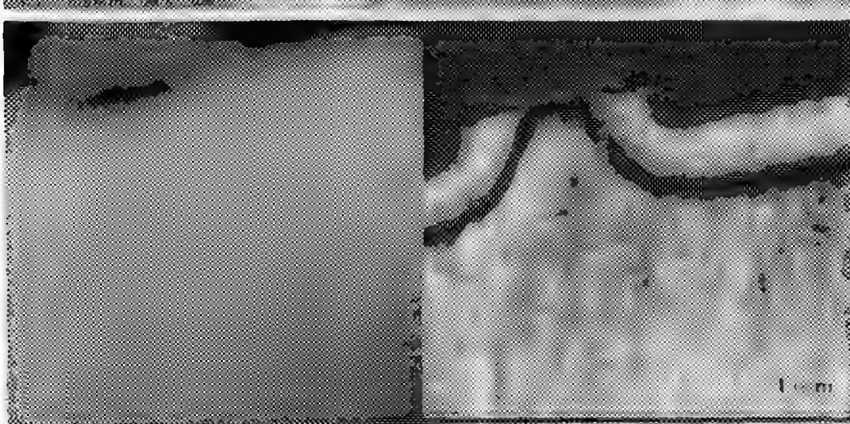

FIG. 1 Implant with defect. The above set are topography (left) capacitance (center) and subracted capacitance and topography (right).

FIG. 2 Complete p-channel MOSFET. Scanning capacitance image (left), topography and capacitance image (right).

FIG. 3 Close-up topography and capacitance scans of a 0.7μm gate MOSFET.

ELECTRON MICROSCOPY INVESTIGATION OF Si AND Mo FIELD EMITTERS COATED WITH DIAMOND POWDER BY DIELECTROPHORESIS

A. F. Myers, W. B. Choi, J. J. Cuomo, and J. J. Hren

Materials Science and Engineering Dept., North Carolina State University, Raleigh, NC 27695.

Silicon and molybdenum are commonly used to fabricate field emission devices, which have promising applications in the flat panel display and vacuum microelectronics industries. However, uncoated Si and Mo field emitters usually exhibit oscillating currents during extended operation due to surface contaminant adsorption and desorption. Coating these cathodes with diamond by microwave plasma chemical vapor deposition (MPCVD) has been shown to considerably improve the total electron emission current as well as to enhance the emission current stability [1]. A very simple, inexpensive technique for depositing high pressure, high temperature (HPHT) synthetic diamond powder on Si and Mo emitters was recently developed and also shows greatly enhanced current-voltage characteristics [2]. Since field electron emission from a cathode strongly depends on the emitter morphology, the diamond coating morphology and the diamond/Si and diamond/Mo interface microstructures were analyzed by electron microscopy.

Single-crystal <111>-oriented Si emitters 100-300μm in height were grown by a Si-Au eutectic vapor-liquid-solid technique, then chemically sharpened to form tips with a radius of curvature ≤ 30nm [3]. Mo emitters with tip radii of curvature ≤ 100nm were fabricated from 0.125mm diameter, <110>-textured Mo wire by electrochemical polishing in a KOH solution at 6-10Vdc. Diamond powder was deposited on the Si and Mo emitters by dielectrophoresis [2], which is defined as "the translational motion of neutral matter caused by polarization effects in a nonuniform electric field" [4]. Two types of diamond powder were deposited: synthetic HPHT intrinsic diamond powder (particle size ≤ 0.25μm) and HPHT Type Ib diamond powder (particle size ≤ 0.1μm), N-doped to about $10^{19}cm^{-3}$. Raman spectroscopy on these powders showed the presence of only sp^3-bonded carbon; no sp^2-bonded (graphitic) carbon was detected.

SEM revealed that the diamond particles were uniformly distributed over the emitter surface (FIGS. 1, 2). From HRTEM (see FIG. 3), an amorphous layer was found to exist at both the diamond/Si and diamond/Mo interfaces; this layer is most likely SiO_2 and MoO_3, respectively. An amorphous layer, probably due to impurities in the powder, also surrounded the intrinsic diamond particles, but was not observed in the Type Ib diamond powder coatings. FIG. 4 shows a Type Ib diamond particle on the surface of a Mo emitter. Selected area electron diffraction (SAED) indicated only the presence of polycrystalline diamond (FIGS. 5, 6); carbides did not form at the interface during dielectrophoresis diamond deposition, unlike in MPCVD deposition. Experiments are in progress to determine the effect of annealing on the interface structure of the coated emitters. Carbide layers are expected to form during the annealing, and to subsequently influence the electron emission properties.

As shown in FIGS. 7 and 8, coating both Si and Mo field emitters with diamond powder improved the electron field emission characteristics, compared to pure Si and Mo tips. Preliminary current-voltage (I-V) measurements on the annealed, coated emitters exhibited improved field emission characteristics over the unannealed, coated cathodes. The mechanism behind the enhanced electron emission is still a topic of great speculation and debate [1, 2].

References

1. See Proc. 7th Int. Vacuum Microelectronics Conf., in J. Vac. Sci. Tech. B **13** (1995).
2. W. B. Choi et al., Appl. Phys. Lett. **68**, 720 (1996).
3. E. I. Givargizov, J. Vac. Sci. Technol. B **11**, 449 (1993).
3. H. A. Pohl, *Dielectrophoresis*, (Cambridge University Press, Boston: 1978.)
5. The uncoated Si emitters were kindly provided by Dr. E. I. Givargizov and Dr. V. V. Zhirnov of the Institute for Crystallography in Moscow, Russia. The authors also wish to thank A. T. Sowers and R. J. Nemanich for performing the Raman spectroscopy.

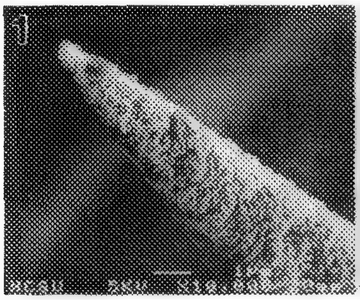

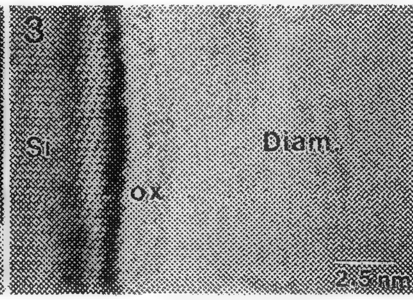

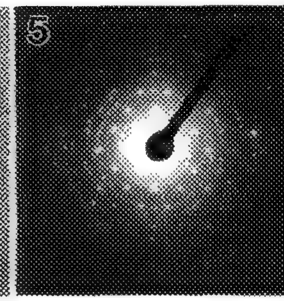

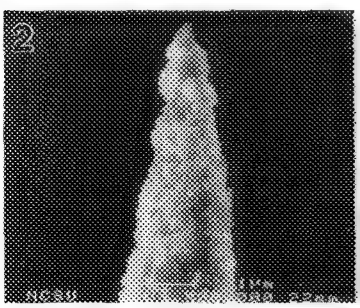

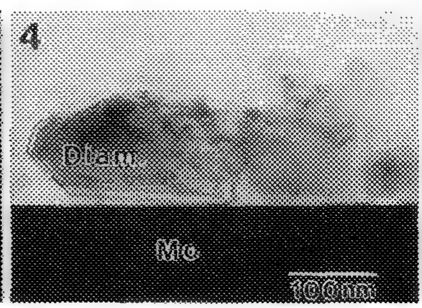

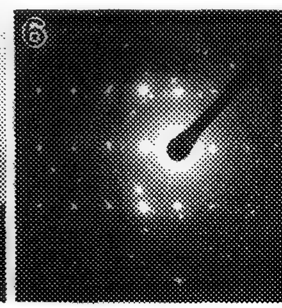

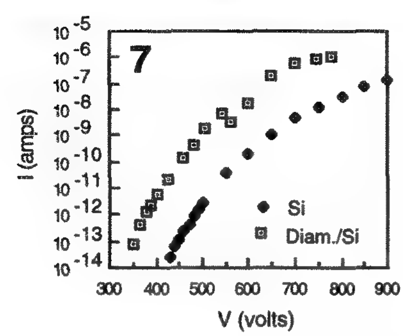

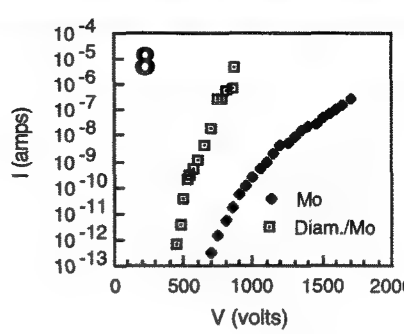

FIG. 1 – SEM image of a HPHT intrinsic diamond powder coated Si field emitter. Diamond particles are distributed uniformly over the surface of the emitter.
FIG. 2 – SEM image of a HPHT intrinsic diamond powder coated Mo field emitter.
FIG. 3 – HRTEM image of the intrinsic diamond/Si interface. Diamond (111) and Si (111) lattice fringes are visible. A thin amorphous SiO_2 layer coats the Si surface.
FIG. 4 – TEM image of Type Ib diamond particles on the surface of a Mo field emitter.
FIG. 5 – SAED pattern from the coated Si emitter tip, showing a polycrystalline diamond ring pattern superimposed on the Si <110> spot pattern.
FIG. 6 – SAED pattern from the region shown in FIG. 4. A polycrystalline diamond ring pattern is superimposed on the <112> diamond spot pattern from the large crystal in FIG. 4.
FIG. 7 – Field emission characteristics of an uncoated and intrinsic diamond powder coated Si emitter.
FIG. 8 – Field emission characteristics of an uncoated and Type Ib diamond powder coated Mo emitter.

TEM CHARACTERIZATION OF LPCVD Ta_2O_5 FILMS FABRICATED BY PRE-DEPOSITION RAPID THERMAL NITRIDATION

J.C. Park, J.M. Choi, J.W. Oh, J.T. Choi, S.S. Kim, H.M. Choi and S.B. Hahn

ULSI Research Center, LG Semicon, Co., Ltd., Cheongju, Korea 361-480

Chemical vapor deposited tantalum pentoxide (Ta_2O_5) films have been a promising dielectric material for a storage capacitor in high-density DRAM with three-dimensional cell architecture, due to its higher dielectric constant than that of conventional SiO_2 or Si_3N_4/ SiO_2 films. The effective dielectric constant of Ta_2O_5 films is influenced by the thickness of interfacial lower-dielectric SiO_2 layer which could be a native oxide or a thermally grown oxide during deposition and annealing.[1] In general, the capacitor with the thinner SiO_2 layer has the larger effective dielectric constant.[2] In this work, the capacitor structure films prepared with or without RTN treatment, which was performed to inhibit the growth of SiO_2, were studied by various TEM techniques.

Two samples were prepared to compare the characteristics of the Ta_2O_5 films fabricated with or without RTN treatment. Ta_2O_5 films were deposited on a phosphorus-doped polysilicon on a p-type silicon substrate by low pressure chemical vapor deposition (LPCVD). Then, RTN treatment was performed in NH_3 at 900°C for 60 sec for one sample and no treatment for the other. After deposition, both samples were rapid-thermal-annealed at 900°C for 60 sec in N_2O ambient for reducing leakage currents in the dielectric films.[3] Finally, TiN plate electrodes were deposited on Ta_2O_5 by reactive sputtering. Cross-section (XTEM) electron microscopy specimens were examined by using a high resolution electron microscopy (HREM), nanodiffraction and EDS techniques in CM200FEG ST-α operating at 200 keV.

Figure 1 shows the overview of the MOS capacitor structure consisting of TiN/ Ta_2O_5/ poly-Si/ SiO_2/ Si substrate. The interface of Ta_2O_5/ poly-Si is abrupt but slightly rough. HREM image of Ta_2O_5/ poly-Si in the sample prepared *without* RTN treatment in Figure 2 shows that there exists a ~3.2 nm thickness of a SiO_2 layer at the interface of Ta_2O_5/ poly-Si and that a ~5.5 nm thickness of the dielectric film is crystallized. HREM image of Ta_2O_5/ poly-Si in the sample prepared *with* RTN treatment in Figure 3(a) shows that the SiO_2 layer is still present in a non-uniform, <2.1 nm thickness at the interface of Ta_2O_5/ poly-Si, although a chemical etching was tried to remove before the deposition. On the other hand, the Ta_2O_5 film is ~ 6.2 nm thick and has its relatively more abrupt interface with TiN. From the lattice image and the nanodiffraction pattern of Ta_2O_5/ TiN films, it is indicated that the dielectric films are crystallized and that TiN may be epitaxially grown on the orthorhombic Ta_2O_5. An interesting point is that a very thick Ta_2O_5 layer looks like divided into two layers from a contrast point of view. However, the lattice image of another location in the same sample in Figure 3(b) shows that the bottom brighter layer (arrow head) consists of Ta_2O_5 plus SiO_2, which is also confirmed with EDS analysis. That constrast may be attributed to the very bumpy bottom interface of Ta_2O_5, which could be a leakage source.

The RTN treatment considerably reduces the thickness of SiO_2 layer from 3.2 to 2.1 nm, resulting in a decrease in the SiO_2 equivalent thickness of the capacitor films from 4.22 to 3.78 nm. That may be because the nitrogen in an annealing ambient prevents the polysilicon from being oxidised during Ta_2O_5 deposition and post-annealing.

References

1. C. Isobe and M. Saitoh, *Appl. Phys. Lett.*, 56 (1990) 907.
2. S. Kamiyama et al., *J. Electrochem. Soc.*, 140 (1993) 1617.
3 S C Sun and T F Chen, *Extended Abstracts of SSDM*, (1994) 655

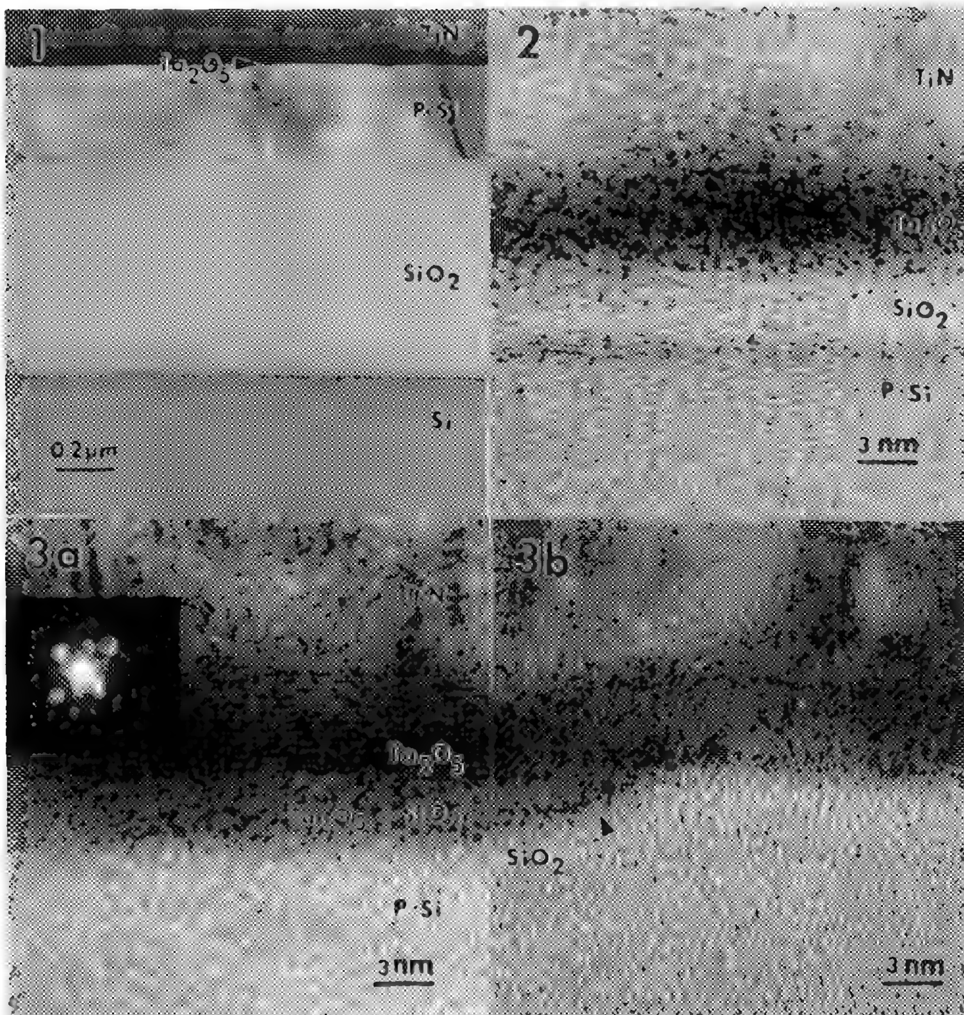

Figure 1.- Cross-section TEM micrograph of the Ta_2O_5 capacitor structure.
Figure 2 - HREM micrograph of the interface of Ta_2O_5 and polysilicon in the sample prepared *without* RTN treatment.
Figure 3 - HREM micrographs and nanodiffraction pattern of the interface of Ta_2O_5 and polysilicon in the sample prepared *with* RTN treatment.

SIMS DEPTH PROFILING AND DIRECT ION IMAGING OF A 16-MEGABIT DRAM

G. McMahon*, M. W. Phaneuf** and L. Weaver**

* Materials Technology Laboratory, NRCan, 568 Booth St., Ottawa, Ontario CANADA
** Chipworks Inc., 205 Catherine St., Ottawa, Ontario CANADA

The use of secondary ion mass spectrometry (SIMS) has long been established as a powerful tool for the analysis of microelectronic devices.[1] However, as newer fabrication technologies emerge, and device dimensions shrink, increasing demands are placed upon the SIMS analyst.

The present work illustrates how the depth profiling and direct ion imaging capabilities of a Cameca ims 4f SIMS can be exploited to determine the structure and dopant chemistry of a state-of-the-art 16 megabit DRAM (dynamic random access memory) device. The optical micrograph shown in Fig. 1 is an overview of a portion of the sense amplifiers located between two array blocks. In the centre of this area, p-type devices sitting in an n-well, surrounded on either side by n-type devices, all in a p-type substrate can be observed. The object of the study was to determine if a low concentration p-type implant is present below the n-type devices. For the depth profiling portion of the analysis, a Cs^+ primary ion beam with a net impact energy of 14.5 keV/atom was selected, and negative ions were detected from a 62 μm diameter region centrally located within a 200 x 200 μm rastered area. Although a smaller analysis and rastered area would have been preferred, the resultant decrease in the boron (B, a p-type dopant) secondary ion intensity would have raised the detection limits of B to a value higher than the peak B concentration in question. These experimental conditions therefore provide the best compromise for the simultaneous analysis of B, phosphorus and arsenic (P and As, both n-type dopants) with the detection limit levels and spatial resolution required for this work. The resulting depth profile encompassing both the n-type and p-type devices is shown in Fig. 2. A peak in the profile for B at a concentration of 2.5×10^{16} atoms/cm^3 is discernible below the total depth of the P and As source and drain implants. However, with this information alone, it cannot be unambiguously determined if the peak occurs only in the area under the n-type devices. Therefore, imaging depth profiles for B were acquired using an O_2^+ primary ion beam with a net impact energy of 4 keV/atom. Since B was the only element of interest in this case, the O_2^+ primary beam could be used, which provides an improvement of about five times in the B sensitivity. Images were acquired using a resistive anode encoder (RAE), a pulse counting, position sensitive computing device capable of localizing and counting ion intensity in the image plane of the detector. As spatial resolution was important in this portion of the study, the operating parameters were adjusted to give a spatial resolution of about 1 μm at a cost of decreasing the instrument's detection sensitivity. A cross-sectional image produced by integrating and slicing through the resulting stack of acquired images is shown in Fig. 3, which clearly shows the trench capacitors in the array on both sides whose increased ion intensity vis-a-vis the regions under the n-type devices is postulated to be the result of an oxygen enhanced secondary ion yield effect due to the oxide based capacitor dielectric surrounding each trench. A column of p-type source/drain/source triplets are visible at the top centre of the image. A selected area depth profile reconstructed from the area underneath the n-type devices is illustrated in Fig. 4. A peak in the B secondary ion intensity at the same depth as observed in Fig. 2 is reproduced, thus providing final proof that a p-type implant with a peak concentration of 2.5×10^{16} atoms/cm^3, as determined from the depth profiling portion of the study, is present below the n-type device regions. Additionally Fig. 3 confirms that this implant is present only under the n-type devices, and not under the central p-type devices.

1. A. Benninghoven et al., *SIMS VII,VIII,* John Wiley and Sons, Chichester (1990,1992) for example.

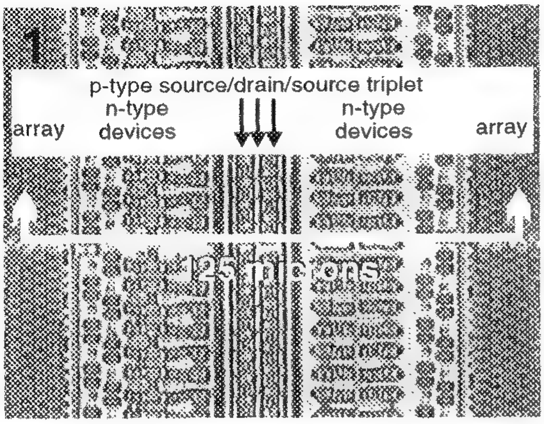

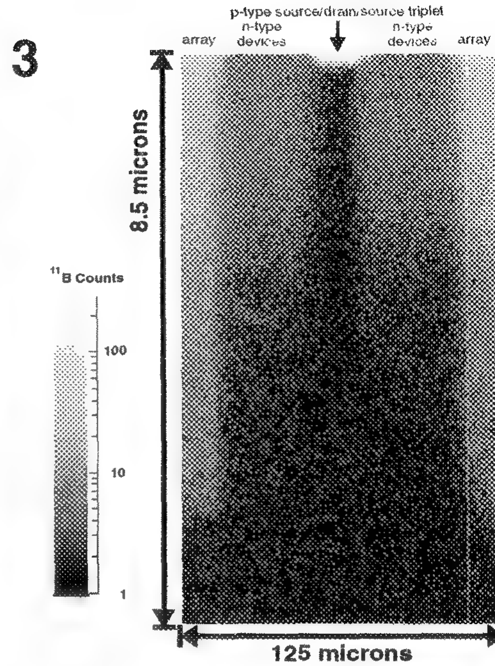

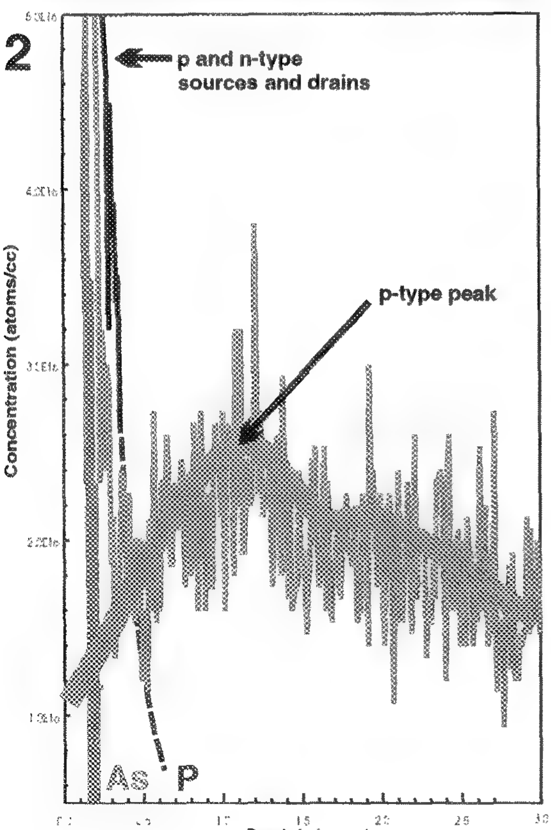

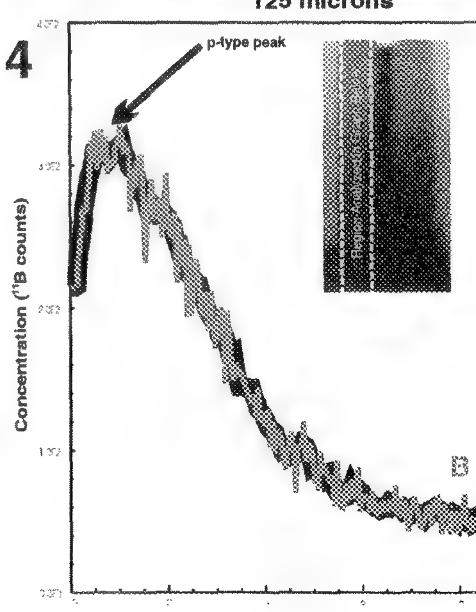

FIG. 1. Optical micrograph showing sense amplifiers between two array blocks of a 16M DRAM.
FIG. 2. SIMS depth profile from a 62.5 micron region of FIG. 1 containing both p & n-type devices.
FIG. 3. Cross-section produced by slicing imaging depth profiles of the region indicated in FIG. 1.
FIG. 4. Selected area depth profile reconstructed from the area beneath the n-type devices (inset).

THE SCANNING INFRA-RED MICROSCOPE (SIRM) : EVALUATING A NEW TOOL FOR MAPPING SUB-100NM DEFECTS IN SEMICONDUCTORS

L.Mule'Stagno[1,2] , J.C. Holzer[1], R.Falster[1], and P.Fraundorf[2]

1. MEMC Electronic Materials Inc., Materials Research Group, 501 Pearl Dr., St.Peters, MO 63376.
2. Physics Dept., University of Missouri-St.Louis, 8001 Natural Bridge Rd., St.Louis, MO 63121.

The manufacturing yield and reliability required of modern silicon micro-electronic devices has led to a need for wafer and device manufacturing processes which are immune to metallic contamination. To this end, various 'gettering' mechanisms have been developed in which unwanted metallic impurities are 'gettered' to regions of the wafer away from the active device layer. 'Internal (or intrinsic) gettering' is a method in which silicon-oxide defects are produced in the bulk of the wafer, with a near-surface defect-free zone (denuded zone). In the event of metallic contamination during high temperature device manufacturing steps, these bulk microdefects (BMDs) act as heterogeneous sites for metal-silicide precipitation during the cooling, and prevent precipitation of the metals in the device layer. For this reason it is essential to monitor the spatial distribution and density of bulk microdefects during device manufacturing.

The standard method by which the density is measured is termed cleave and etch. In this method cross-sectional cleaved strips of wafers are etched in one of a variety of etchant mixtures, and the distribution and density of BMDs is measured by optical microscopy. The disadvantages of this method are that it uses corrosive chemicals, it is destructive, and the accuracy of the result is highly dependent on the skill of the operator. If more accurate characterization of the defects is required TEM is the method of choice. However the amount of labor and cost involved makes this technique impractical for routine monitoring.

The Scanning Infra-Red Microscope (SIRM) and similar imaging systems take advantage of the fact that semiconductors are transparent to infra-red light to provide an alternative to cleaving and etching.[1,2,3] A schematic view of the SIRM is shown in Figure 1. It utilizes the principle of reflection scanning confocal microscopy to image inhomogeneities in the bulk of the specimen. A beam of infra-red light (1320nm wavelength) from a laser is expanded and then focused into the specimen, forming a probe with approximate dimensions of 1 micron wide by 7 microns long. Light will only scatter off precipitates of a different refractive index from the bulk. This scattered light is projected towards the detector lens which produces a magnified image of the probe on the detector. The pinhole is placed in front of the detector so that only light originating from the probe gets to the detector. This results in the rejection of out of focus light, and thus depth sectioning.

The specimen is placed on a table sitting on 3 piezo crystals and a stepper motor. The stepper motor provides the large movement necessary, while the piezo crystals are used to raster the specimen in any orthogonal axis. While it is rastered a gray level image is formed from the signal gathered at each point. A typical resulting image is shown in Figure 2. The BMDs appear as white dots if they are in Gaussian focus, or black dots if they are within the probe but outside Gaussian focus. Image analysis software is then used to count the number of particles which is then

interpolated into a bulk defect density. The typical defect densities in processed wafers range from 10^7 to 10^{10} defects/cm^3. The SIRM can measure all this range of densities, and even densities two orders of magnitude lower.

References:

1. Z.Laczik and G.R.Booker in *Altech 95, Analytical Techniques for Semiconductor Characterization*, vol 95-30, The Electrochemical Society, Pennington ,NJ 1995, pp140 .
2. M.A.Nokes and P.G.Borden , *Microelectronics Manufacturing Technology*, p 33, Nov 1991.
3. K.Moriya et al, J.Appl Phys., **66** (11), 1989, pp5267.

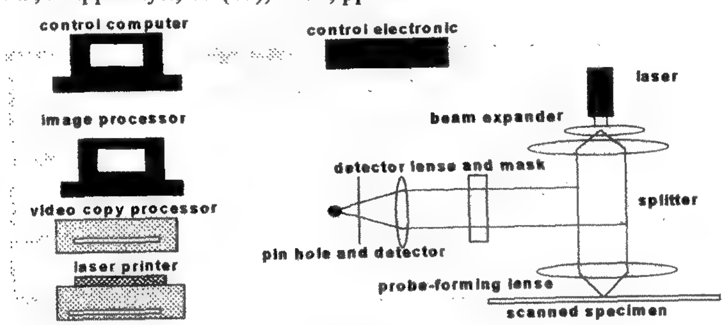

Fig 1 : Schematic diagram of the SIRM

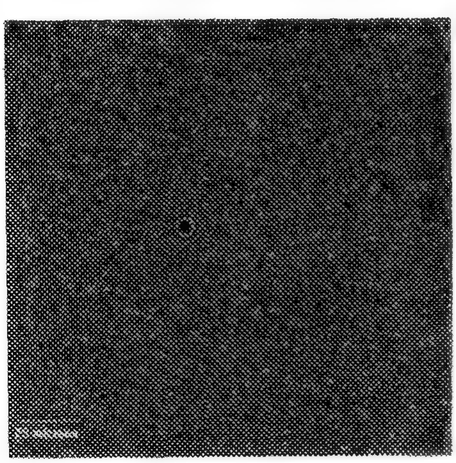

Fig 2 : Typical SIRM image of heavily precipitated specimen . The white dots are precipitates which are in Gaussian focus. The large objects are surface-related artifacts.

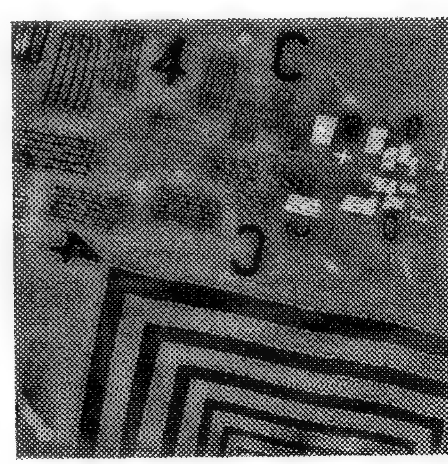

Fig3 : test SIRM image of a calibration grating. The pattern was etched on the surface of a wafer, which was then bonded to anothe silicon wafer. The SIRM is imaging the etch pattern, 300μm *below* the wafer surface.

STRUCTURE OF CONTACT SITES BETWEEN THE OUTER AND INNER MITOCHONDRIAL MEMBRANES INVESTIGATED BY HVEM TOMOGRAPHY

C.A. Mannella,* K.F. Buttle, K.A. O'Farrell**, A. Leith, M. Marko

Biological Microscopy and Image Reconstruction Resource, Division of Molecular Medicine, Wadsworth Center, Empire State Plaza, Albany, NY 12201-0509

Departments of Biomedical Sciences* and Biological Sciences,** University at Albany, Albany, NY

Early transmission electron microscopy of plastic-embedded, thin-sectioned mitochondria indicated that there are numerous junctions between the outer and inner membranes of this organelle.[1] More recent studies have suggested that the mitochondrial membrane contacts may be the site of protein complexes engaged in specialized functions, e.g., import of mitochondrial precursor proteins,[2] adenine nucleotide channeling,[3] and even intermembrane signalling.[4] It has been suggested that the intermembrane contacts may be sites of membrane fusion involving non-bilayer lipid domains in the two membranes.[5] However, despite growing interest in the nature and function of intramitochondrial contact sites, little is known about their structure.

We are using electron microscopic tomography with the Albany HVEM to determine the internal organization of mitochondria.[6] We have reconstructed a 0.6-μm section through an isolated, plastic-embedded rat-liver mitochondrion by combining 123 projections collected by tilting (+/- 70°) around two perpendicular tilt axes.[7] The resulting 3-D image has confirmed the basic inner-membrane organization inferred from lower-resolution reconstructions obtained from single-axis tomography.[6] Basically, the cristae are highly pleomorphic, consisting of cisternae connected by narrow, tubular extensions to each other and to the surface of the inner membrane. In the new reconstruction, it has also been possible to trace the outlines of the inner and outer membranes along the entire periphery of each 6-nm slice in the reconstructed volume (one of which is shown in Fig. 1). Fig. 2 is a surface view of the outer membrane. It has an undulating topography, composed of numerous "hills" typically 100-200 nm across and up to 50 nm high. Intermembrane contacts (arrows, Fig. 1) tend to occur at the base of the hills, are predominantly punctate (usually extending only 20-40 nm in any one direction), and have a surface density over $1000/\mu m^2$. While two distinct membranes are usually visible around the mitochondrial periphery in each section (arguing against membrane fusion), there are a few sites at which the outer and inner membranes appear to merge and fork or branch (arrows, Figs. 3,4). These apparent membrane fusions usually occur near sites where the inner membrane folds inward to form cristae.

References

1. C.R. Hackenbrock, *J. Cell Biol.*, 30(1966)269.
2. I. Van der Klei et al., *Microscopy Res. Tech.*, 27(1994)284.
3. D. Brdiczka, *Biochim. Biophys. Acta*, 1071(1991)291.
4. M.W. McEnery, *J. Bioenerg. Biomembr.*, 24(1992)63.
5. R. Van Venetie and A.J. Verkleij, *Biochim. Biophys. Acta*, 692(1982)379.
6. C.A. Mannella et al., *Microscopy Res. Tech.*, 27(1994)278.
7. C.A. Mannella et al., *Proc.53rd. Ann MSA Meeting*, (1995)740.

8. The authors gratefully acknowledge the support of NSF (grant MCB-9506113) and the Biomedical Resource Program of the NIH NCRR (grant RR01219).

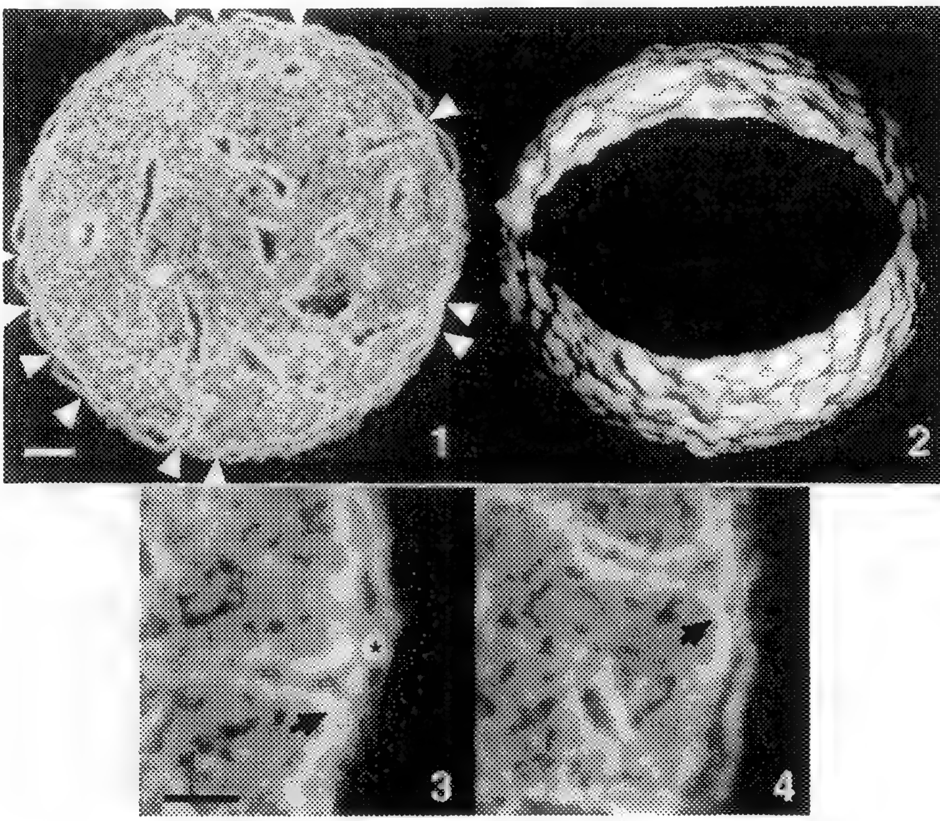

FIG. 1 Six-nm slice through the two-axis tomographic reconstruction of a rat-liver mitochondrion showing intermembrane contacts (arrows). Scale bar = 0.15μm.

FIG. 2 Surface of the outer mitochondrial membrane.

FIGS 3,4 Enlargement of regions on mitochondrial periphery, showing sites of apparent membrane fusion (arrows). (At the asterix is a gold particle used for alignment.) Scale bar = 100nm.

MICROSTRUCTURE OF GaAs NANOCRYSTALS FORMED INSIDE SINGLE CRYSTALLINE SILICON

Jane G. Zhu,* C. W. White,* J. D. Budai,* M. J. Yacamán,** and G. Mondragón**

*Oak Ridge National Laboratory, Solid State Division, Oak Ridge, TN 37831-6057
**Instituto de Fisica, UNAM, Mexico

Semiconductor nanocrystals exhibit novel properties that are important for electronic and opto-electronic device applications.[1] Many methods have been developed to synthesize semiconductor nanocrystals. Among them is the ion implantation technique,[2-4] which is compatible with the semiconductor technology. It has been recently reported that the compound semiconductor GaAs can be formed inside Si by sequential implantation of Ga and As and thermal annealing.[5]

In this study, GaAs nanocrystals were formed by sequential implantation of As and Ga, with the same dose of 1×10^{17} cm^{-2}, into (100) Si substrates at 550°C. The implantation energies were chosen so that the Ga and As ions are overlapped over a few hundred nanometers in depth. The samples were then annealed at 1000°C for 1 h in flowing Ar + 4%H_2 atmosphere to form GaAs precipitates. Transmission electron microscopy (TEM) has been used to study the microstructures of these samples.

The cross-sectional TEM image in Fig. 1 shows the GaAs precipitates formed inside the Si substrate implanted with As and then Ga. The sizes of GaAs crystallites range from several nanometers to several tens of nanometers. The GaAs precipitates are three-dimensionally aligned with the Si matrix. High-resolution electron microscopy (HREM) image in Fig. 2 shows that the small precipitates are faceted on {111} lattice planes. The lattice spacing of GaAs precipitates is about 3.5% larger than that of the Si matrix (i.e., 99.4% of the bulk GaAs), which indicates that this GaAs nanocrystal is under strain and stress.

The sequence of implantation of Ga and As has significant effect on the formation GaAs particles. Much larger GaAs precipitates are formed in samples implanted with Ga first and then As under the same annealing conditions, as shown in Fig. 3(a). A dramatic influence of implantation sequence on the nanocrystal sizes has also been observed for the GaAs nanocrystals formed in amorphous SiO_2. Electron diffraction shows that the lattice constant of these large precipitates is about that of the bulk material. Dislocations are formed in the matrix due to ion implantation damage. Since the ion species were implanted at 550°C, the Si substrate was never amorphorized during implantation, and the crystal orientation of GaAs is well aligned with the single crystal Si matrix. Figure 3(b) shows that some dislocations in Si are terminated at the GaAs precipitates and the surface of the substrate.

References

1. See, for example, "Microcrystalline and Nanocrystalline Semiconductors," edited by R. W. Collins, et. al, Mater. Res. Soc. Symp. Proc. **358**, (1995).
2. H. A. Atwater, et al., Mater. Res. Soc. Symp. Proc. **316**, 409 (1994).
3. C. W. White, et al., J. Appl. Phys. **79**, 1876 (1996).
4. J. G. Zhu, et al., J. Appl. Phys. **78**, 4386 (1995).
5. C. W. White, et al., to be published in Appl. Phys. Lett. (1996).
6. This research was sponsored by the Division of Materials Sciences, U.S. Department of Energy, under contract DE-AC05-96OR22464 with Lockheed Martin Energy Research Corp., and supported in part by an appointment to Oak Ridge National Laboratory Postdoctoral Research Associate Program administered jointly by Oak Ridge National Laboratory and the Oak Ridge Institute for Science and Education.

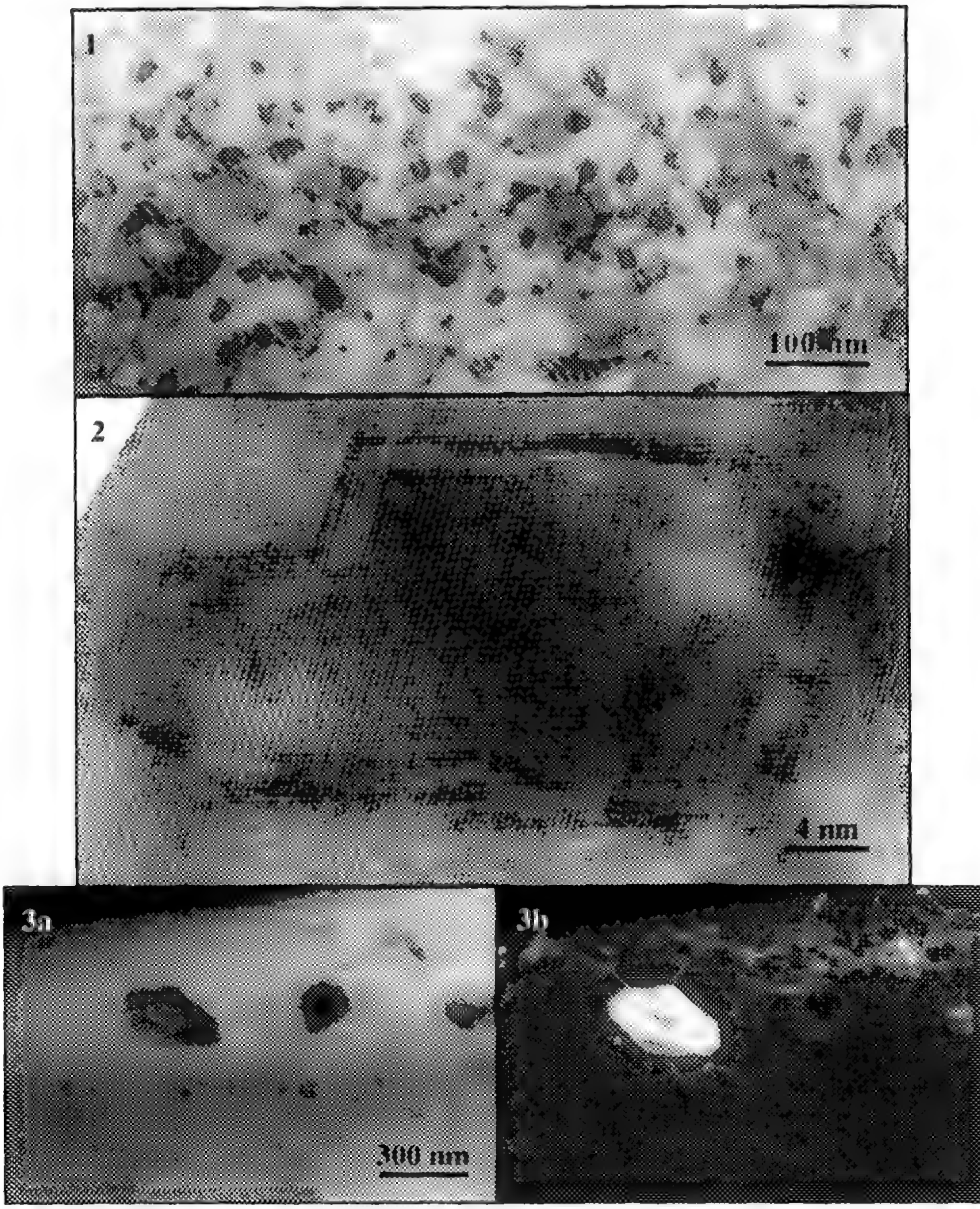

Fig. 1. Cross-sectional TEM image of GaAs nanocrystals inside a Si substrate.
Fig. 2. HREM image of a faceted GaAs particle in Si matrix.
Fig. 3. Dark-field images of the same area from a sample with large GaAs precipitates to show (a) the GaAs precipitates and (b) dislocations surrounding the precipitates.

ANOMALOUS STRAIN PROFILES OF SHORT-PERIOD SEMICONDUCTOR-SUPERLATTICE STRUCTURES AS MEASURED FROM HREM IMAGES

M.D. Robertson,* and J.M. Corbett

Guelph-Waterloo Program for Graduate Work in Physics, University of Waterloo, Waterloo, Ontario, Canada N2L 3G1

Recently, there has been considerable interest in the measurement of lattice strains at the nanometre level using high resolution electron microscopy (HREM) techniques. In particular, techniques based on the measurement of the displacements of lattice fringes from processed images derived from the individual Fourier components of the original CCD image have been successful in accurately reproducing the strain profiles present in semiconductor and metal heterostructures.[1,2,3] In order to isolate the information associated with a given reflection, Fourier-filter masks of approximately the first Brillouin zone in size are positioned on the desired reflection in the digital diffractogram and all the Fourier frequencies not located within the masks are removed. This procedure assumes that only information associated with a given reflection is contained within the masks. However, if Fourier information from more than one main reflection is present in the masks then artifacts may arise in the measured strain distribution.

For example, consider the strain analysis performed on a GaAs / AlAs superlattice structure[4] using the CUSUM approach[2,3] (Fig. 1) in which the cumulative sum of the deviations of the lattice-fringe spacings from the average value is plotted against pixel position. Fig. 1a is a 128x512 pixel HREM image of about 6 periods from a 20 period superlattice structure. Fig. 1b displays the [002] Fourier-filtered lattice-fringe image and Fig. 1c presents the [002] CUSUM curve based on the lattice fringes of Fig. 1b. If the slopes of the CUSUM plot were interpreted in the usual way[2,3], the lattice mismatch between the GaAs and AlAs layers would be determined to be 1.76(0.14)%. This interpretation is clearly incorrect since the system is nearly lattice matched, with mismatch between the two layers expected to be only 0.12%. In order to understand this anomalous strain measurement, consider the selected-area-electron-diffraction pattern obtained from all twenty periods of the superlattice shown in Fig. 2. Each reflection consisted of a main diffraction spot and a series of satellite spots due to the periodicity of the superlattice structure. The limits of the first Brillouin zone in the [001] direction for the [002] reflection are marked by the arrows. Note that satellite spots from the [000] main reflection were present within a first Brillouin zone sized mask centred on the [002] reflection. Since information from two separate reflections was present within the Fourier-filter mask, artifacts are expected in the measured strain profile (as observed). Note that the percentage difference in the spacing between the two sets of satellite reflections, normalized to the [002] main reflection, is 1.7(0.2)%; the same value as determined by the CUSUM strain analysis technique.

Due to the presence of this strain artifact, the standard interpretation of the vertices present in the CUSUM plot as demarking the positions of the interfaces between the two sets of materials is no longer valid. However, the average period, as determined by the separation of the vertices, was measured to be 4.0(0.1) nm which agreed very well with the value of 4.02(0.1) nm from electron diffraction results. This superlattice period corresponded to 7.10(0.02) lattice spacings, a non-integer value which explains why the positions of the two overlapping sets of satellites from the [000] and [002] primary reflections did not precisely coincide.

This particular strain measurement anomaly is only expected for short-period-semiconductor superlattices where the envelope functions associated with the main diffraction spots overlap. In longer period structures, the envelope function narrows significantly thereby eliminating overlap and reliable strain measurements can be obtained.[3]

---

* Current address: Applied & Engineering Physics, F7 Clark Hall, Cornell University, Ithaca, NY 14850

References

1. M.J. Hytch and P. Bayle, in *Proc. 13th Int. Congr. on Electron Microscopy* **2A**, B. Jouffrey and C. Colliex, (Eds.), Les Éditions de Physique, Les Ulis, France, (1994) 129.
2. M.D. Robertson et al., *Ultramicroscopy*, **58** (1995) 175.
3. M.D. Robertson et al., *Micron*, (1996) in press.
4. The sample was provided by L. Wasileski and J. McCaffrey of the National Research Council of Canada.

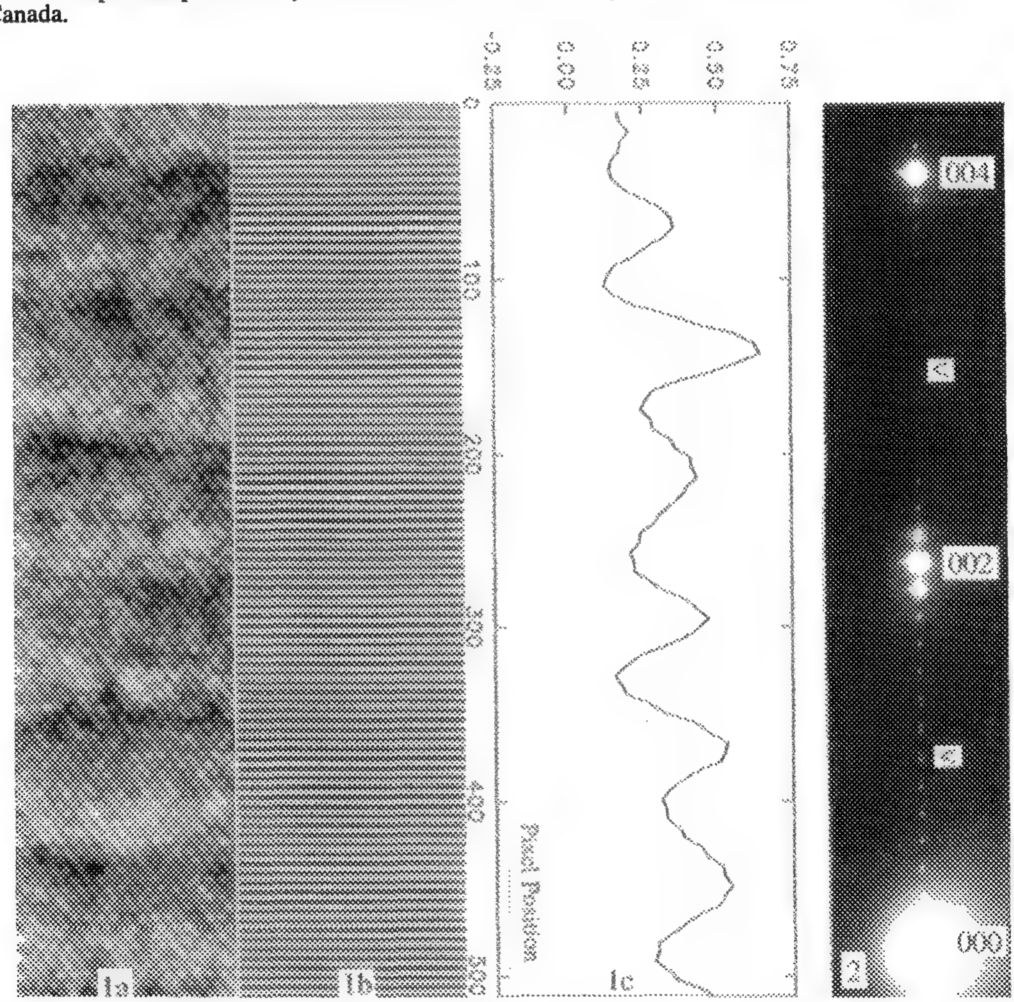

Fig. 1 (a) 128x512 pixel HREM image of six periods of a 20 period AlAs / GaAs superlattice.
(b) [002] Fourier filtered lattice-fringe image of the region displayed in (a).
(c) [002] CUSUM plot based on the lattice-fringe data presented in (b).

Fig. 2 Selected-area-electron-diffraction pattern obtained from all 20 periods of the AlAs superlattice. Only reflections along the [001] direction are displayed.

TEM OBSERVATIONS OF HYDROGEN NANOBUBBLES IN IMPLANTED AMORPHOUS SILICON

K.M. Jones, D.L. Williamson*, S. Acco** and M.M. Al-Jassim
National Renewable Energy Laboratory, 1617 Cole Blvd., Golden, CO 80401
* Department of Physics, Colorado School of Mines, Golden, CO 80401
** Debye Institute, Utrecht University, P.O. Box 8000, 3508 TA Utrecht, The Netherlands

Over the last two decades extensive studies on the optical and electrical properties of hydrogenated amorphous Si (a-Si:H) have been reported. However, less attention was given to the structural characterization of this material partly due to the insensitivity to hydrogen of structural probes such as x-rays and electron diffraction. From a recent set of experiments, results on the solubility limit of hydrogen in a special type of a-Si:H and the characterization of hydrogen induced complexes or nanobubbles has been reported.[1] In this study, we report TEM observations of the structural morphology of hydrogen related defects that support these recent measurements obtained by secondary ion mass spectrometry (SIMS) and small-angle x-ray scattering (SAXS).

a-Si:H thin films for solar cells and other applications are produced by a variety of methods. In each case, the deposited films are usually not homogeneous as they have been found to contain low-density inhomogenities in the size range of 1-10 nm.[2] These defects are commonly referred to as microvoids or hydrogen-rich clusters. The densities of these defects have been observed to change with deposition parameters, thermal treatment and H concentration. In order to separate the role of thermal treatment and H concentration from deposition conditions, an amorphous Si sample (a-Si) produced by ion implantation was used in this study. The a-Si was first prepared by Si ion implantation at various energies ranging from 0.5 to 17 MeV into a 75 μm-thick double-polished Si wafer. The thickness of the a-Si layer was measured by FTIR to be ~ 8 μm. This amorphized state, without H incorporated, was recently shown by SAXS to be homogeneous on a nm length scale, in spite of a known density deficit of 1.8%.[3] The hydrogen was then introduced into the a-Si by implanting H_2^+ at energies ranging from 50 to 500 keV/amu with a total dose of 3.0×10^{18} cm^{-2}, leading to peak concentrations near 20 at.% and a maximum depth of 6.5 μm. In the as-implanted state, SAXS measurements of this sample showed no indication of nanoscale inhomogeneties. The sample was then annealed for 4 hours in steps at temperatures ranging from 200 to 550°C and SAXS demonstrated the appearance and systematic growth of nanoscale features above 300°C.[1] The TEM cross-sections of the sample were prepared by standard dimple polishing followed by Ar ion milling at LN_2 temperatures. The TEM analysis was performed in a Philips CM-30 STEM operating at 300 kV. The SAXS, SIMS, and TEM were performed on the *same* sample.

Figure 1 compares a low magnification cross-sectional TEM image of the sample after the 500°C 4 hour anneal and the corresponding SIMS H depth profile of the as-implanted state. The peaks in the SIMS profile and the light bands in the TEM image designate the different implant energies and the distribution of H. The electron scattering efficiency difference from peak-to-valley delineates the hydrogen-rich bands as shown in figure 2. SAXS measurements taken after the 500°C 4 hour anneal revealed the volume-fraction-weighted average radius of the nanobubbles to be 1.25 nm.[1] Detailed HREM investigation was performed to study their size and distribution. HREM images (figure 3) taken in the H-rich bands show that the bubble sizes expand with increasing H concentration towards the peaks of the H distribution. Within these peak regions the nanobubbles appear spherical with diameters of 2.0-3.0 nm, in excellent agreement with the SAXS. As was suggested,[1] annealing produces precipitation or clustering of the H (presumably as H_2) only in some fraction of the layer corresponding to the peaks in the profile where the local H solubility is exceeded. It is in these areas that the direct observation of the size, morphology and distribution of H nanobubbles in this material were obtained by TEM.

1

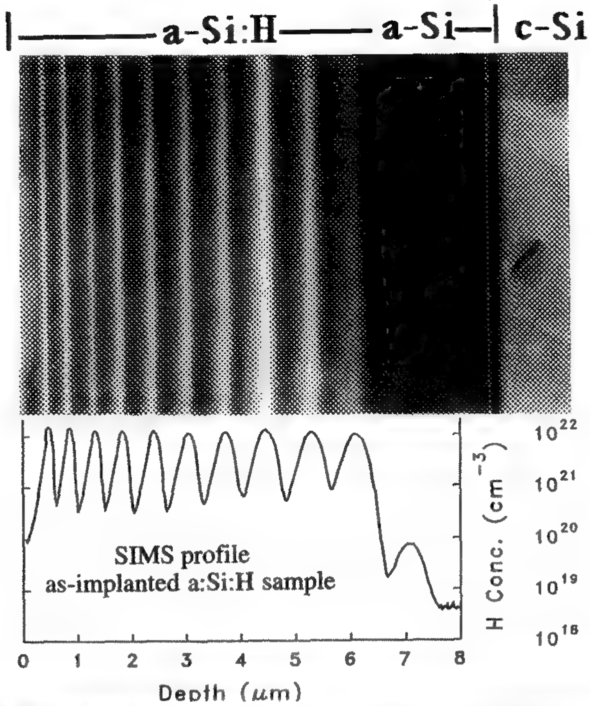

2

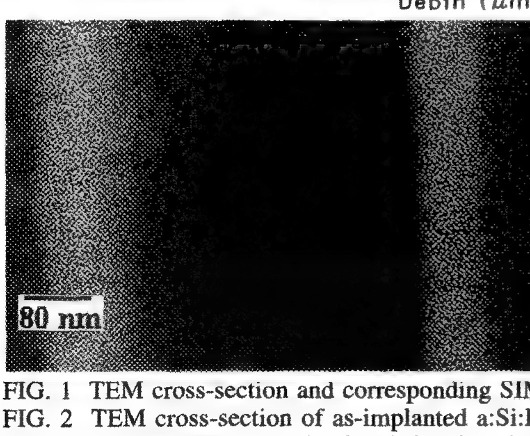

3

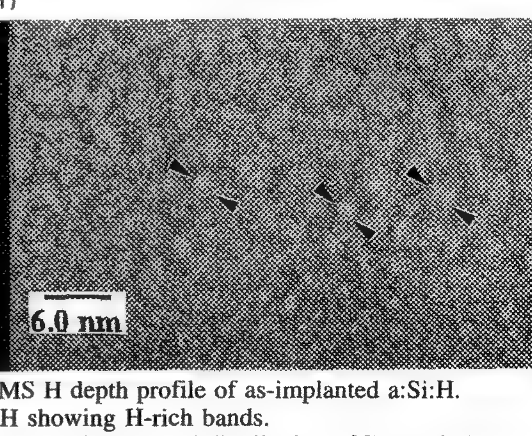

FIG. 1 TEM cross-section and corresponding SIMS H depth profile of as-implanted a:Si:H.
FIG. 2 TEM cross-section of as-implanted a:Si:H showing H-rich bands.
FIG. 3 HREM image of H-rich band showing size, morphology and distribution of H nanobubbles.

The SIMS depth profile measured by A. Carnera is gratefully acknowledged.

References

1. S. Acco, D.L Williamson, P.A. Stolk, F.W. Saris, M.J. van den Boogaard, W.C Sinke, W.F. van der Weg, S. Roorda, and P.C. Zalm, Phys. Rev. B **53**, 4415 (1996).
2. D.L. Williamson, Mat. Res. Soc. Symp. Proc. **377**, 251 (1995).
3. D.L. Williamson, S. Roorda, M. Chicoine, R. Tabti, P.A. Stolk, S. Acco, and F.W. Saris, Appl. Phys. Lett. **67**, 226 (1995).

This work was supported by the U.S. Dept. of Energy under contract number DE-A362-83CH10093

ELECTRON HOLOGRAPHY OF P-N JUNCTIONS

B.G.Frost, D.C.Joy, L.F.Allard, and E.Voelkl

Oak Ridge National Laboratory, Oak Ridge, TN 37831-6064 and
EM Facility, University of Tennessee, Knoxville, TN 37996-0810, USA

A wide holographic field of view (up to 15 μm in the Hitachi-HF2000) is achieved in a TEM by switching off the objective lens and imaging the sample by the first intermediate lens.[1] Fig.1 shows the corresponding ray diagram for low magnification image plane off-axis holography. A coherent electron beam modulated by the sample in its amplitude and its phase is superimposed on a plane reference wave by a negatively biased Möllenstedt-type biprism.

Our holograms are acquired utilizing a Hitachi HF-2000 field emission electron microscope at 200 kV. Essential for holography are a field emission gun and an electron biprism. At low magnification, the excitation of each lens must be appropriately adjusted by the free lens control mode of the microscope. The holograms are acquired by a 1024 by 1024 slow-scan CCD-camera and processed by the "Holoworks" software.[2] The hologram fringes indicate positively and negatively charged areas in a sample by the direction of the fringe bending (Fig.2). Thus we directly recognize p and n regions of a semiconductor by the fringe bending of the interference fringes. Fig.3 shows a reconstructed phase distribution of the image wave. This phase distribution represents the electric potential projected on the image plane. The electric potential comprises the mean inner potential of the sample (i.e. variations in thickness) and the potential due to electric fields (e.g. doping of the semiconductor). Though it is in principal possible to separate the phase caused by the inner potential from the phase caused by the field distribution, as shown by Gajdardziska and McCartney,[3] it is still difficult to evaluate the correct voltage at the junction because the phase strongly depends on the alignment of the microscope.

The different displays of the reconstructed phase distribution in Fig.3 allow us to analyze the potential distribution and the electric field as well. In a first approximation the electric field lines are perpendicular to equiphase lines which are contour lines of the electric potential. These field lines are schematically drawn. Since the thickness of this sample is nearly uniform, the phase inside represents the potential distribution of the p-n junction. The band on the left side shows the phase without contour lines. The line scan was taken in this part.

1. Frost,B.G. et al., Submitted to Ultramicroscopy.
2. Voelkl,E. et al., Journal of Microscopy, 180 (1995) 39.
3. Gajdardziska-Josifovska,M., McCartney,M.R., Ultramicroscopy, 53 (1994) 291.
4.We thank B.Cunningham from IBM/Fishkill for the semiconductor sample.
This work was performed at the Oak Ridge National Laboratory, supported by the Laboratory Directed R&D Program of Oak Ridge National Laboratory, managed for the DOE by Lockheed Martin Energy Research, under contract DE-AC05-84OR214000.

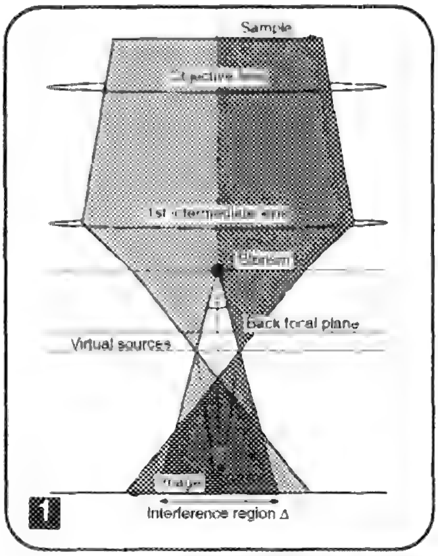

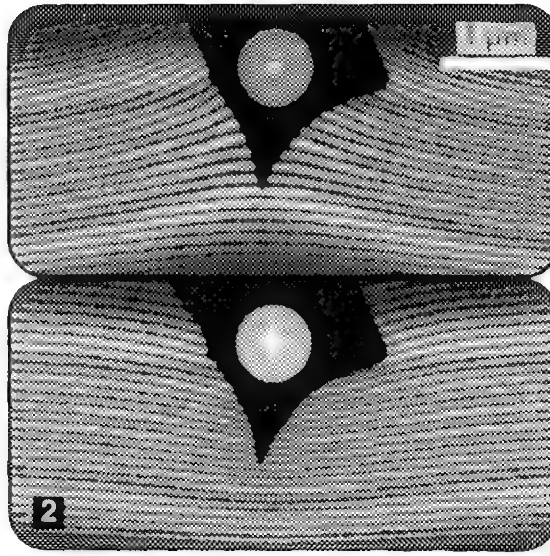

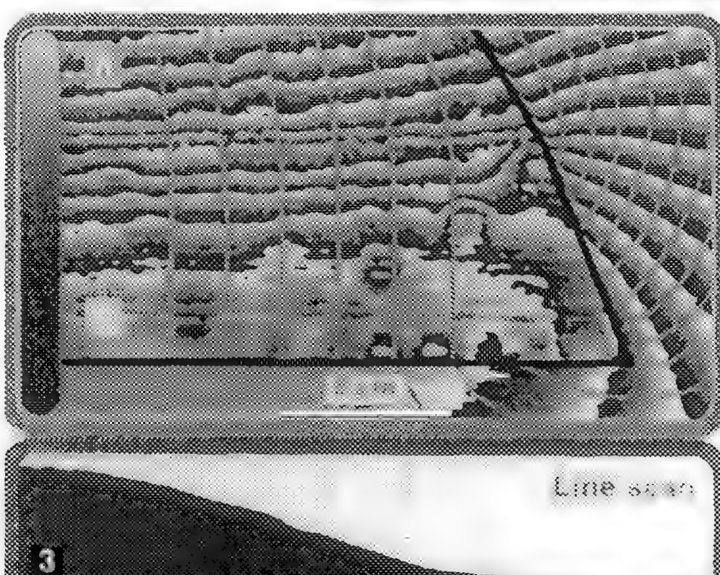

Fig.1: Ray path for off-axis image plane holography at low magnification with biprism between first and second intermediate lenses.
Fig.2: Top: Interference fringes are bent towards negatively charged particle. Bottom: Interference fringes are bent away from positively charged particle.
Fig.3: Measured potential distribution of pn junction. Electric field lines are perpendicular to equipotential lines. Band on the left side shows potential without contour lines.

DETERMINATION OF ARSENIC ATOM DISTRIBUTION IN ARSENIC DOPED SILICON USING HOLZ LINE ANALYSIS

Y.Kikuchi*, N.Hashikawa**, F.Uesugi**, E.Wakai***, K.Watanabe****, and I.Hashimoto**

*Process Development Division, Fujitsu Limited, 1-1, Kamikodanaka,4-chome, Nakahara-ku, Kawasaki 211-88,Japan.
**Department of Physics, Science University of Tokyo, 1-3 Kagurazaka, Shinjuku-ku, Tokyo ,162 , Japan
***Department of Materials, Science and Engineering, Japan Atomic Energy Research Institute, Tokai-Mura, Naka-Gun, Ibaraki-Ken 319-11, Japan
****Tokyo Metropolitan Technical College, 1-10-40 Higashiohi, Shinagawa-ku,Tokyo 140, Japan

In order to measure the concentration of arsenic atoms in nanometer sized regions of arsenic doped silicon, the HOLZ analysis is carried out under the exact [011] zone axis observation. In previous papers,[1,2] it is revealed that the position of two bright lines in the outer SOLZ structures on the [011] zone axis is little influenced by the crystal thickness and the background intensity caused by inelastic scattering electrons, but is sensitive to the concentration of As atoms substitutional for Si atomic site. As the result, it becomes possible to determine the concentration of electrically activated As atoms in silicon within an observed area by means of the simple fitting between experimental result and dynamical simulation. In the present work, in order to investigate the distribution of electrically activated As in silicon, the outer HOLZ analysis is applied using a nanometer sized probe of TEM equipped with a FEG.

Czochralski-grown <100> orientated p-type Si wafers with a resistivity of 10 Ω cm are used for the experiments. The As^+ implantation is performed at a dose of $5.0\times10^{15}cm^{-2}$ at 25keV. A subsequent annealing is carried out at 1000℃ for 10sec. As shown in an [011] cross sectional TEM photograph (Fig 1), it is possible to avoid the evolution of residual defects under the anneal condition. CBED patterns from an [011] cross sectional direction are obtained by using a Hitachi HF2000 TEM operated at 100kV with a probe size of ~5nm. Fig2 shows the CBED pattern at a depth of 140nm below the surface. The two bright lines in the $(\overline{11},13,\overline{11})$ SOLZ reflection indicated in Fig2 are used for the quantitative analysis at several depths.

Figs.3(a) and (b) show the $(\overline{11},13,\overline{11})$ SOLZ structure at the depth of 10nm and 60nm, respectively. It is apparent that the distance between the two bright lines for the 10nm depth is wider than that for the 60nm one, though the intensity of line for the 10nm depth is indistinct to some extent. On the other hand, it is also found that there is little difference between the SOLZ structure below the 60nm depth. From these results and fitting simulation, it is found that the electrically activated As atoms with the concentration of about 5% distribute in the region shallower than 60nm.

References

1. N.Hashikawa et al., *Philos.Mag.Lett.*,(1996), in press.
2. N.Hashikawa et al., *phys.stat.sol.(a).*,**154**,No.2,(1996) in press.

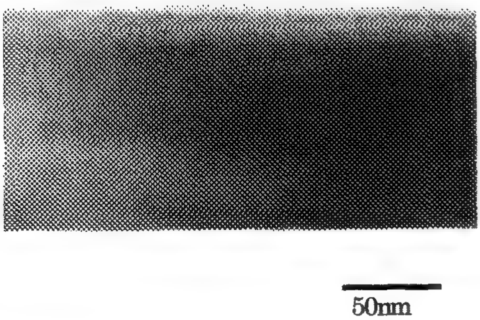

Silicon Surface
Arsenic atoms doped layer

Fig.1 A [011] cross sectional TEM photograph after a 10 sec anneal at 1000℃.

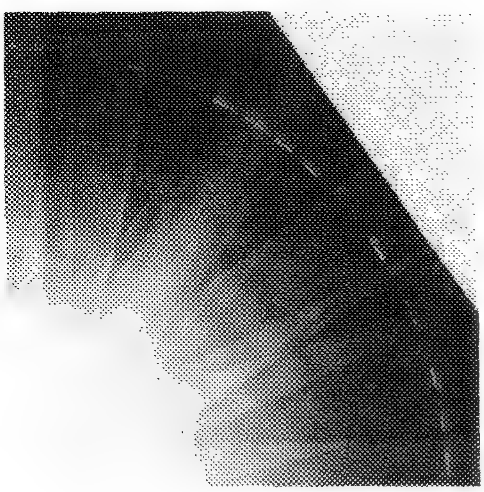

($\bar{1}\bar{1}$,13,$\bar{1}\bar{1}$) SOLZ reflection

Fig.2 CBED patterns from a [011] cross sectional direction.

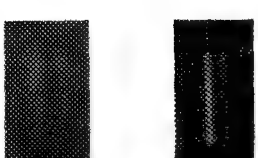

(a) 10nm depth (b) 60nm depth

Fig.3 ($\bar{1}\bar{1}$,13 $\bar{1}\bar{1}$) SOLZ reflections in the region of such depths below the surface as 10nm (a) and 60nm (b), respectively.

TIME-RESOLVED HIGH-RESOLUTION ELECTRON MICROSCOPY OF STRUCTURAL TRANSFORMATION IN NANOCRYSTALLINE ZnO FILMS

T. Kizuka and N. Tanaka

Department of Applied physics, School of Engineering, Nagoya University
Furo-cho, Chikusa-ku, Nagoya, 464-01, Japan

Mechanical properties of polycrystalline materials become anomalous when the grain size and grain boundary length decrease to nanometer scale. For example, ductility and toughness increase significantly in nanometer-grained ceramics (nanocrystalline ceramics).[1] Ductility increases due to appearance of fine-grained-superplastic deformation. Grain boundary migration and interface migration are fundamental processes of the superplastic deformation. Structural transformation of fine grains is a factor which limits the toughness in polycrystalline ceramics because the transformation relaxes internal strain. The behavior of grain boundaries and interfaces, such as diffusion bonding and Czochralski-type crystal growth at ambient temperature, can be analyzed by a time-resolved high-resolution electron microscopy (TRHREM) developed by Kizuka et al.[2,3]

In the present study, grain boundary migration and successive transformation of crystal structure in nanocrystalline ZnO were investigated by TRHREM.

Zinc oxide was vacuum-deposited on air-cleaved (001) surfaces of sodium chloride at 200°C. TRHREM was carried out at room temperature using a 200-kV electron microscope (JEOL, JEM2010) equipped with a high sensitive TV camera and a video tape recorder. The spatial resolution of the system was 0.2 nm at 200 kV and the time resolution was 1/60 s. Electron beam irradiation density was 30 A/cm^2

Polycrystalline films, in which grain size ranged from 3 to 10 nm, were obtained by the vacuum-deposition. Crystal structure of the films was the wurtzite type structure of ZnO with lattice constants of a=0.325nm and c=0.521nm. Grain boundary migration was enhanced by the increase of atomic diffusion due to electron beam irradiation.

Figure 1 shows a time-sequence series of high-resolution images showing grain boundary migration and transformation of the crystal structure. Orientation relationship for fig. 1a and 1e are shown in fig. 2a and 2b, respectively. The grain boundary (GB) between a crystallite A and a crystallite B is a [10.0] axis tilt grain boundary with a rotation angle of 120° (fig. 1a). The polarity of the wurtzite ZnO along the c-axis direction was taken into account the angle. The crystallites A and B contain stacking faults (SF) on $(00.1)_{A,B}$ planes. The lattice misfit between $(01.1)_A$ plane and $(00.2)_B$ plane at the GB is 5.3% (fig. 2a). The GB migrates and crystal structure transforms from the wurtzite type structure into the a zinc blend type structure that is a cubic structure with a lattice constant of a=0.462nm near the GB and surface (fig. 1b, C). Two interfaces (IF) form at the structural transformation. Subsequently the crystallite C grows and the interface between the crystallite B and the crystallite C migrates (fig. 1b-d). Finally the crystallite B transforms into the crystallite C completely (fig. 1e-f). The lattice misfit between $(01.0)_A$ plane and $(111)_C$ plane at the IF is 0.36% (fig. 2b). Thus the lattice misfit reduces from 5.3% to 0.36% after the grain boundary migration and the structural transformation. It is concluded that the lattice misfit strain of the grain boundary is attributed to the structural transformation.[4]

References

1. J. Karch et al., Nature, **330**(1987)556.
2. T. Kizuka et al., Phil. Mag. Lett., **69**(1994)135.
3. T. Kizuka et al., Proc. ICEM13, p369 (1994).
4. Financial supports were provided to the present study from Yazaki Memorial Foundation for Science and Technology and Research Foundation for the Electrotechnology of Chubu. The present study is partly supported by Grant-In-Aid of the Ministry of Education, Science and Culture, Japan.

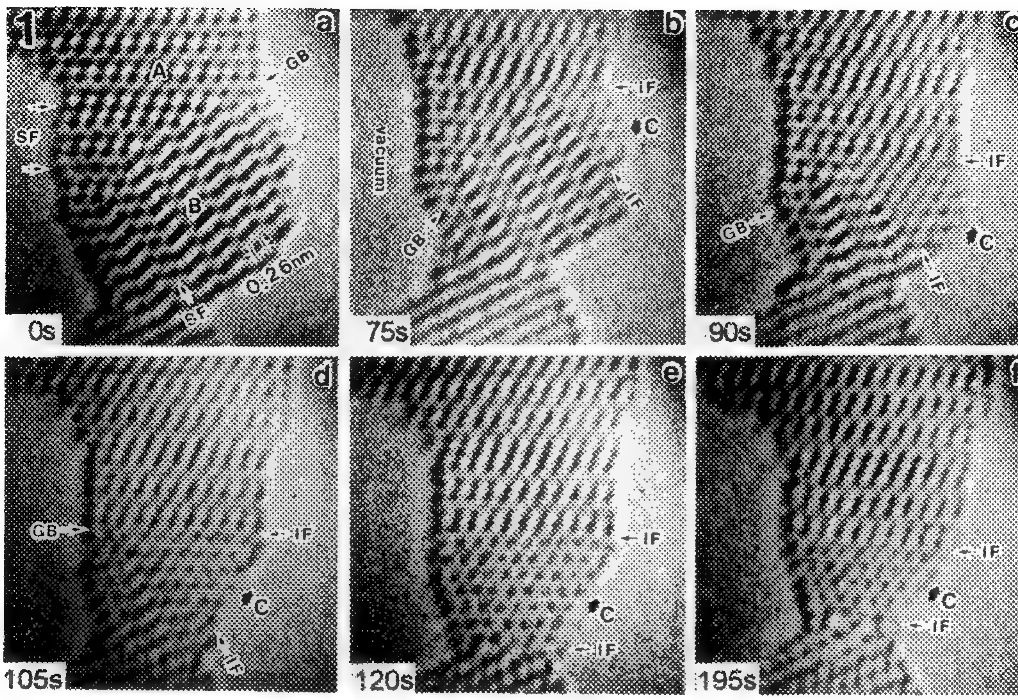

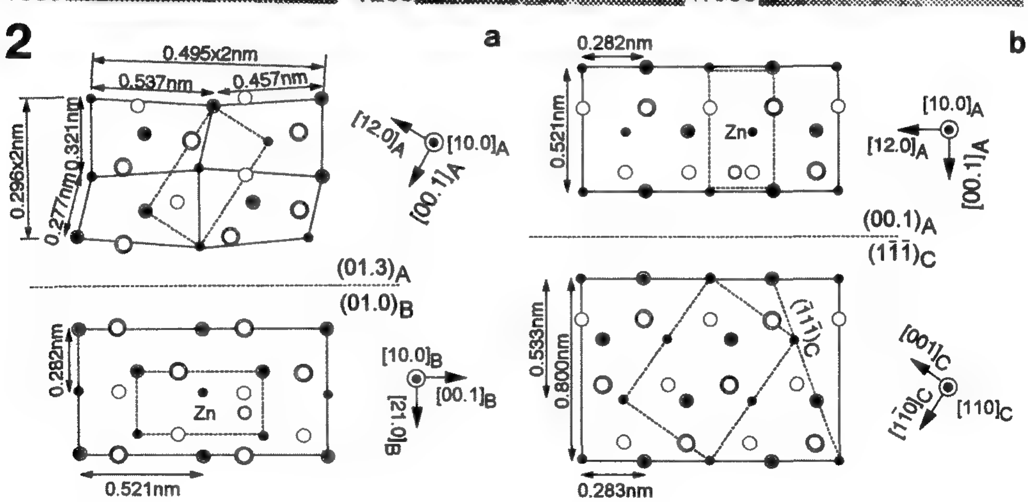

FIG. 1 - A time-sequence series of high-resolution images of grain boundary migration and transformation of the crystal structure in nanocrystalline ZnO.

FIG. 2 - Orientation relations at the grain boundary in fig.1a (a) and the interface in fig.1e (b).

TIME-RESOLVED HIGH-RESOLUTION ELECTRON MICROSCOPY OF NANOMETER-SCALE ELECTRON BEAM PROCESSING OF PbTe FILMS

T. Kizuka and N. Tanaka

Department of Applied physics, School of Engineering, Nagoya University
Furo-cho, Chikusa-ku, Nagoya, 464-01, Japan

Various kinds of nanometer scale processings are required to produce advanced materials, for example, nano-structured electric devices. Electron beam processing at nanometer scale using STEM and TEM, such as drilling and line-writing, is recently interested as a most useful method.[1,2] Details of structural change during the processing should be elucidated at atomic resolution in order to establish the processing. In the present work we have processed lead telluride (PbTe) films with nanometer electron beam in a high-resolution transmission electron microscope and *in-situ* observed the variation of atomic arrangements during the processing.

PbTe of 99.99% was vacuum-deposited on air-cleaved (001) surfaces of sodium chloride at room temperature. Time-resolved high-resolution electron microscopy was carried out at room temperature using a 200-kV electron microscope (JEOL, JEM2010) equipped with a high sensitive TV camera and a video tape recorder. The spatial resolution of the system was 0.2 nm at 200 kV and the time resolution was 1/60 s. Electron beam irradiation density was 120 A/cm^2 at the processing and the observation.

Figure 1 shows a time-sequence series of high-resolution images of drilling in the PbTe film. The hole of 1.0 nm, 1.5 nm, 3.0 nm and 3.5 nm in diameter can be obtained when the beam irradiation is terminated at fig. 1 (c), (d), (e) and (f), respectively. The size of the hole can be controlled at atomic scale by adjusting the beam irradiation, showing a superiority of the present method to any other method.

Figure 2 shows atomic structural change at an edge-surface of a hole in the drilling. Figure 3 shows the image simulation of the positions of atomic columns at a step (S) and a kink (S*) in an edge-surface. The structural model for the simulation is also shown. The contrast at the kink (S*) is lower than that at the step (S). The positions of steps and kinks in the high-resolution images are identified from the simulation and shown by triangle arrows in fig. 2. First, atoms desorp from non-melting surface and steps are formed (fig. 2a-b, arrows). Next, atoms at steps and kinks desorp preferentially and hole is enlarged (fig. 2c-e, triangle arrows). The width of the terrace becomes narrower after the steps and kinks migrate right and left and finally move to one side, showing that atoms diffuse at steps and kinks. The processing speed is limited by the desorption speed of atoms at the weak-bonded positions. The mechanism of nanometer electron beam processing is summarized as follows. First most of surface atoms get the threshold energy enough to diffuse due to primary knock-on with the electrons of 200 kV. Next the atoms desorp to vacuum when they get the threshold energy enough to desorp to vacuum from weak-bonded positions such as steps, kinks and isolated positions at surface.[3]

References

1. M. E. Mochel et al., Appl. Phys. Lett., **42**(1983)392.
2. T. Kizuka et al., Phil. Mag. **A71**(1995)631.
3. Financial supports were provided to the present study from Yazaki Memorial Foundation for Science and Technology and Research Foundation for the Electrotechnology of Chubu. The present study is partly supported by Grant-In-Aid of the Ministry of Education, Science and Culture, Japan

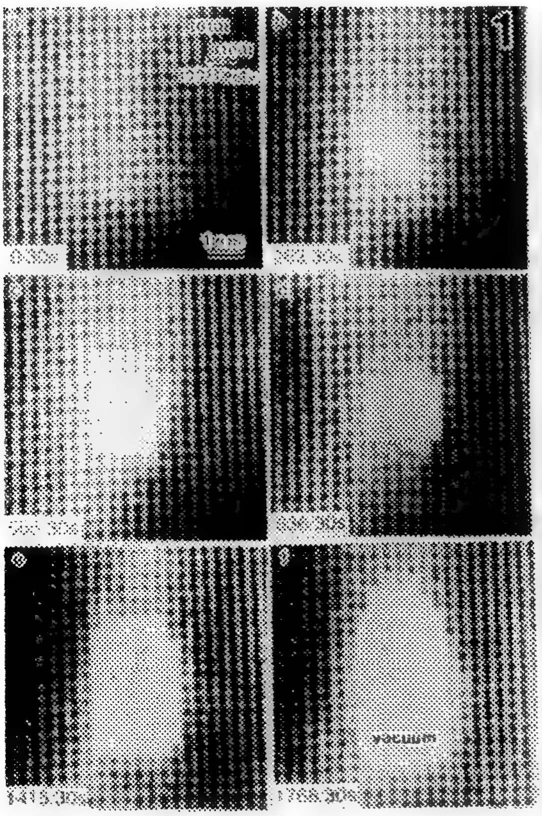

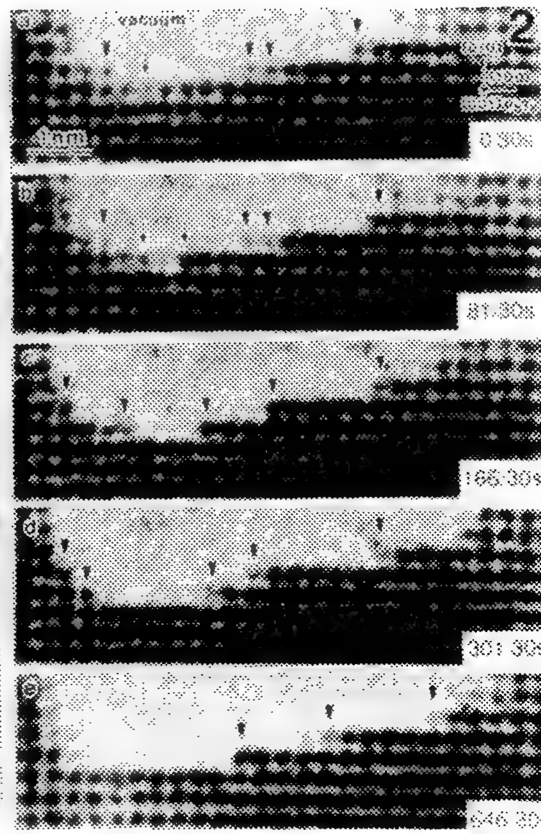

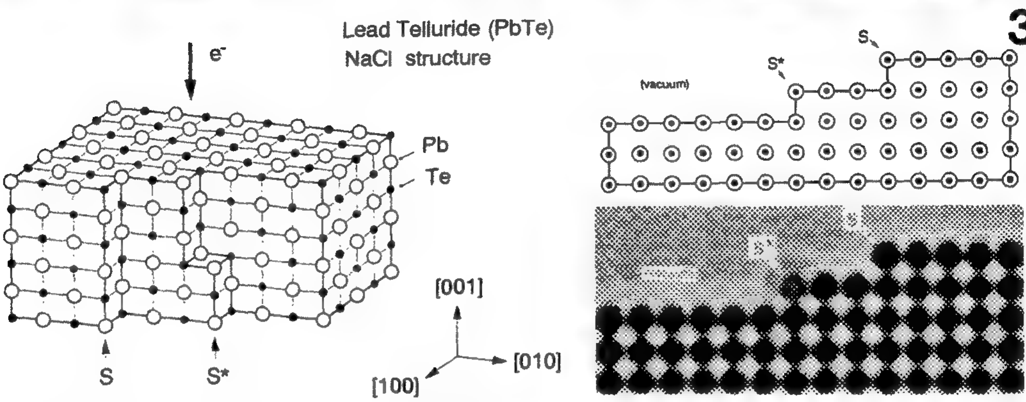

FIG. 1 - A time sequence series of high-resolution images of drilling in the PbTe film.
FIG. 2 - A time sequence series of high-resolution images of structural change at an edge- surface of a hole in the drilling.
FIG. 3 - The image simulation of the positions of atomic columns at a step (S) and that at a kink (S*) in an edge-surface

CROSS-SECTIONAL TIME-RESOLVED HIGH-RESOLUTION ELECTRON MICROSCOPY OF EPITAXIAL GROWTH OF Au ON MgO

T. Kizuka and N. Tanaka

Department of Applied Physics, School of Engineering, Nagoya University
Furo-cho, Chikusa-ku, Nagoya, 464-01, Japan

Vapor phase epitaxial growth techniques are indispensable for production of thin film electric devices. Various structural analyses have been attempted to evaluate the epitaxial growth. Conventional transmission electron microscopy (CTEM) is a most useful method. In particular, it is known that a plan-view time-resolved CTEM of *in-situ* vacuum-deposition in a microscope can analyze each process of epitaxial growth.[1] The nucleation in vacuum-deposition was also *in-situ* observed by a time-resolved high resolution electron microscopy (TRHREM).[2] However many unresolved problems still remain in the studies of the epitaxial growth because it is difficult to observe the epitaxial interfaces less than a few nanometer under appropriate conditions. Much more advanced techniques are required for electron microscopy to obtain detailed information.

In the present study, a TRHREM for the cross-sectional observation was developed to elucidate the epitaxial growth process in vacuum-deposition.

Gold (Au) was vacuum-deposited on (001) surfaces of the magnesium oxide (MgO) substrates at room temperature in a specimen chamber of a 200-kV high-resolution electron microscope (JEOL, JEM2010).[3] Growing process was *in-situ* observed cross-sectionally by TRHREM at spatial resolution of 0.2 nm and at time resolution of 1/60 s using a high sensitive TV camera and a video tape recorder.

Figure 1 shows a time-sequence series of high-resolution images showing epitaxial growth of Au on the MgO substrate. Illustrations of the growth process and atomic arrangement for fig. 1b-d are shown in fig. 2. First, a step of one atom height was observed on a $(001)_{MgO}$ clean surface before the deposition (fig. 1a; an arrow). One Au cluster as an 'embryo' formed at the beginning of the deposition (fig. 1b). This shows that Au atoms impinging on the surface diffused along the step and then nucleated with each other. The number of the constituent atoms in the cluster was less than 30. The cluster showed structural fluctuation. Orientation relation between the cluster and the substrate also changed frequently. The structural fluctuation stopped and an epitaxial orientation, $(001)[100]_{Au}//(001)[100]_{MgO}$, fixed when the number of the atoms increased more than 90 (fig. 1c). It was reported by Kizuka et al. that the interface having the epitaxial orientation was the most stable between the Au cluster and the MgO substrate.[4] The external shape of the cluster changed to a tetragonal pyramid surrounded with a $(001)_{Au}//(001)_{MgO}$ interface and four $\{111\}_{Au}$ surfaces. The epitaxial orientation was kept when the tetragonal pyramid grew. Obviously, growth mode of the present Au/MgO system is an island growth mode. A top corner of the island was truncated with a $(001)_{Au}$ plane and four corners at the bottom were also truncated with $(100)_{Au}$ and $(010)_{Au}$ planes (fig. 1d). The island grew along the direction parallel to $(001)_{MgO}$ surface after the height of the island was more than 3 nm. The island coalesced with neighboring islands when the deposition further continued. The epitaxial orientation at the interface kept even at the coalescence.

In conclusion, the present observation shows that the cross-sectional TRHREM is a new method to analyze the vapor phase epitaxial growth processes.[5]

References

1. G. Honjo et al., phys. stat. sol. **a55**(1979)353.
2. K. Takayanagi, et al., Jpn. J. Appl. Phys., **26**(1987)1957.
3. The attachment for vacuum-deposition in the electron microscope was produced by Mr. K. Kumazawa at the Workshop of department of Applied Physics at Nagoya University.
4. T. Kizuka et al., Z. Phys., **D26**(1993)S58.
5. Financial supports were provided to the present study from Yazaki Memorial Foundation for Science and Technology and Research Foundation for the Electrotechnology of Chubu. The present study is partly supported by Grant-In-Aid of the Ministry of Education, Science and Culture, Japan.

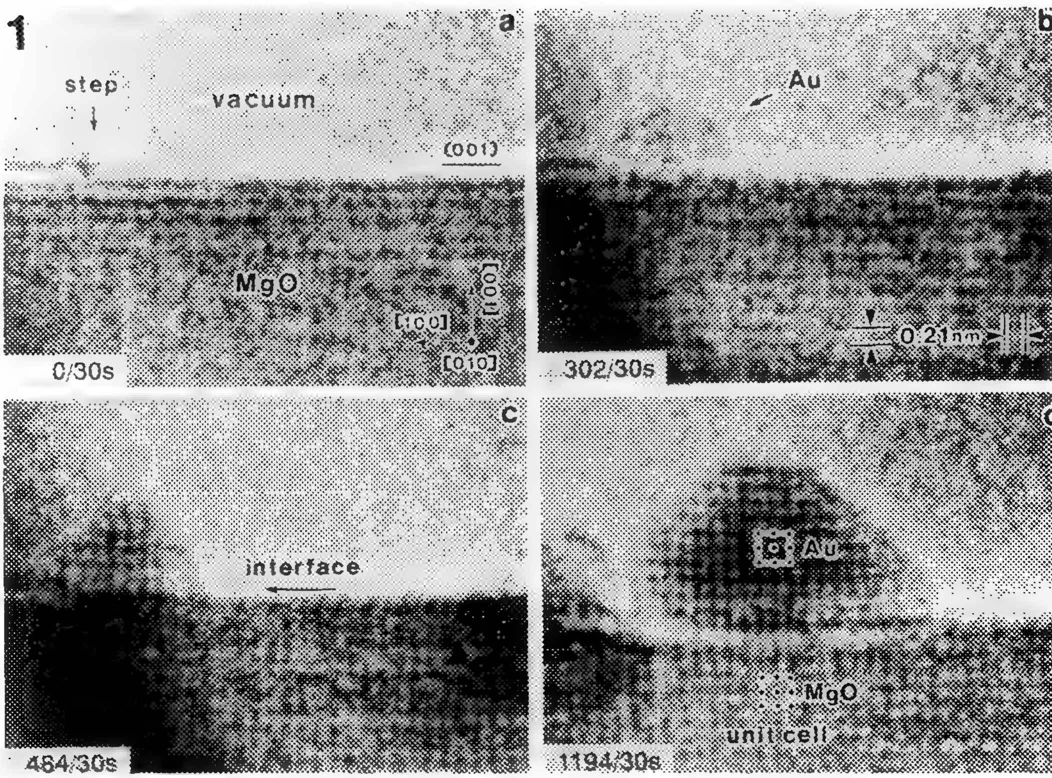

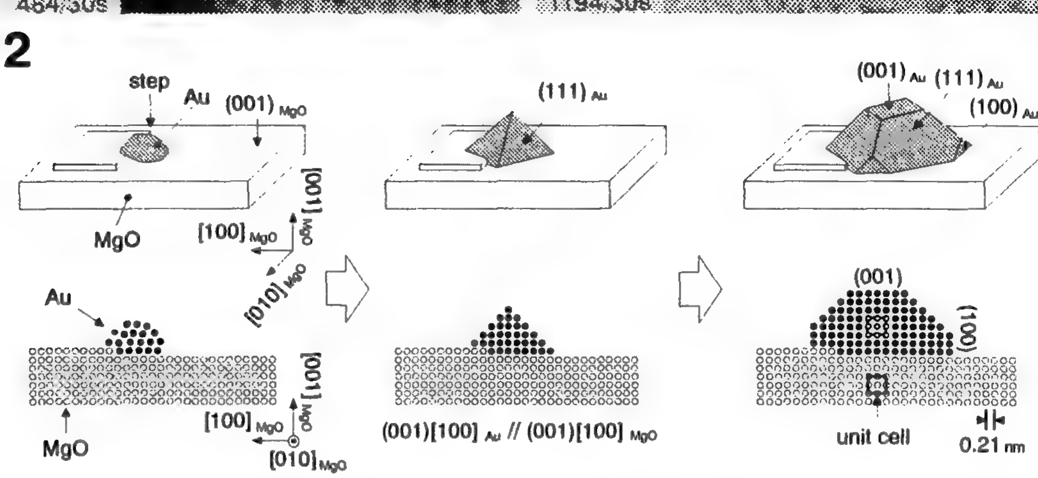

FIG. 1 - A time-sequence series of high-resolution images showing epitaxial growth of Au on a MgO substrate.

FIG. 2 - Schematic illustrations of the growth process and atomic arrangement for fig. 1.

DYNAMIC OBSERVATION OF A SURFACE RECONSTRUCTION OF Au-DEPOSITED Si PARTICLE

T.Kamino,* T.Yaguchi,* M.Tomita,** and H.Saka***

*Hitachi Instruments Engineering Co., Ltd., 882 Ichige, Hitachi-naka, Ibaraki, 312 Japan
** Instrument Division, Hitachi Ltd., 882 Ichige, Hitachi-naka, Ibaraki, 312 Japan
***Dept. of Materials Science and Engineering and Department of Quantum Engineering, Nagoya Univ. , Chikusa-ku, Nagoya, 464-01 Japan

Metal deposition is one of the most effective methods to reconstruct the surface structure of Si, and a number of studies using electron microscopes have been carried out.[1] Endo et al. have studied Au-deposited Si(111) surface by ultra-high vacuum(UHV) scanning electron microscope(SEM) , and obtained SEM images of 7×7 and 5×2-Au structure at 600℃.[2] Ozawa et al. have observed Au - deposited Si(111) surface by UHV-transmission electron microscope(TEM) and observed the formation of 5×2-Au structure at 700℃.[3] Marks et al. have studied the structure of Au-deposited Si(111) surface to reconstruct electronic potential on the surface.[4]

Recently, we developed a direct heating type- specimen heating holder[5] consists of two heating elements. for use with a conventional analytical TEM, and applied to an in-situ study of the surface reconstruction of Au-deposited Si at high temperature. A schematic drawing of the heating holder is shown in Fig. 1. Tungsten wire with a diameter of 25μm was used as the heating elements. The upper heating element was used for metal deposition, in this case Au, and lower one for the heating of substrate material, in this case Si. The microscope used in the study is a H-9000NAR analytical TEM operated at 300kV. The spherical and chromatic aberration coefficients of the objective lens were 0.69 and 1.4mm, respectively, and the TEM image resolution was 0.175nm.

A series of high resolution electron microscopy(HREM) images of Au clusters during deposition on the surface of Si particle are shown in Fig. 2. The surface of Si particle had been covered with 1.0~1.5nm thick native oxide layer(a). The deposition of Au was carried out without removing the oxide layer. The deposition of Au was stopped as the cluster grew to about 5nm in diameter. The Si particle was then heated up to about 1050℃. During the heating, the oxide layer on the Si surface became thinner, and Au clusters showed rapid movement on the surface of Si. Facetting of the surface of Si was observed during the heating. Figure 3 shows the surface structure before(a) and after the heating(b). The facetting took place on {111},{311}, {001} and {211}. Reconstruction of the facetted surface was also dynamically observed . An example of the reconstruction took place on (001) is shown in Fig. 4.

References

1. S. Ino : Proc. NATO Advanced Research Workshop, June 15-19(1987) Netherlands, NATO ASI Series B188(Plenum, New York, 1988) 3
2. A. Endo et al. : Proc. of the 12th Int. Congr. for Electron Micros. 304(1990)
3 S.Ozawa et al. : Proc. of the 12th Int. Congr. for Electron Micros. 340(1990)
4. L.D.Marks et al. : Proc. of the 13th Int. Congr. for Electron Micros.1015 (1994)
5. T. Kamino et al. : Microscopy Microanalysis Microstructure 4 (1993) 127

1

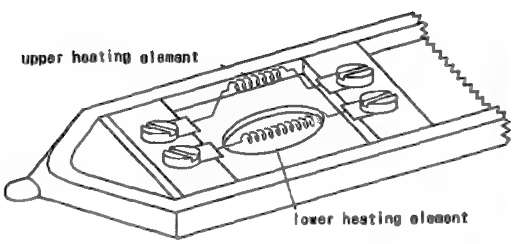

2a

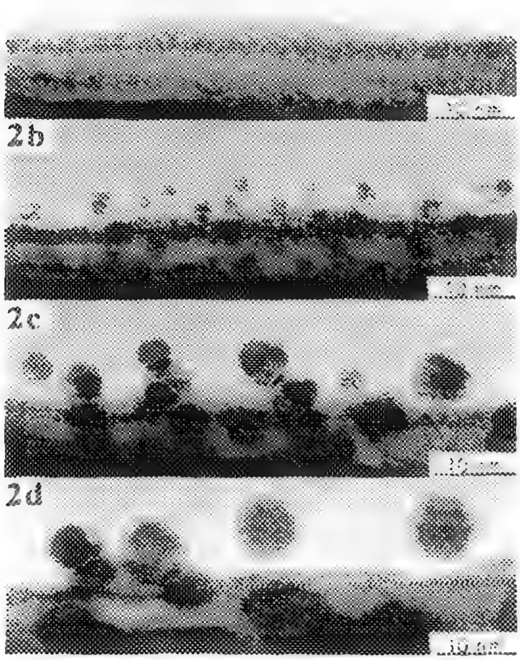

3a

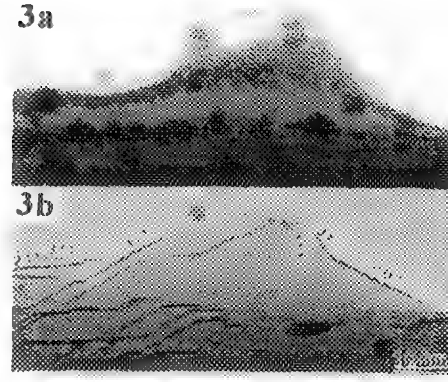

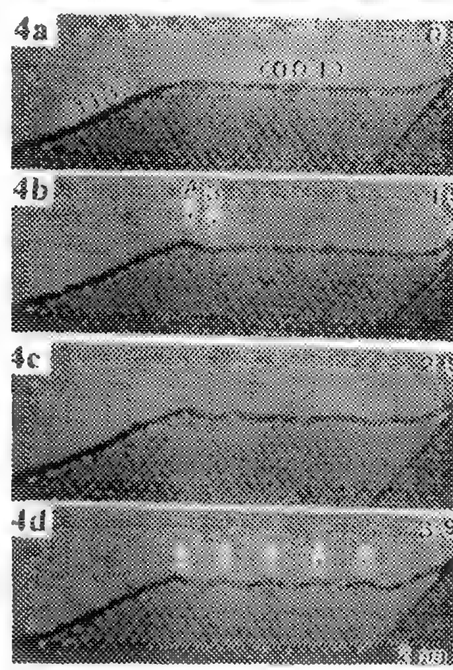

FIG. 1 Schematic drawing of specimen heating holder with two heating elements.
FIG. 2 Series of high resolution electron microscopy images of Au clusters during deposition.
FIG. 3 Surface structure before(a) and after the heating (b).
FIG. 4 Dynamic observation of the reconstruction of the facetted surface of Si.

IN SITU TEM OBSERVATIONS OF MELTING IN NANOSIZED EUTECTIC Pb-Cd INCLUSIONS EMBEDDED IN Al

S. Hagège[1], U. Dahmen[2], E. Johnson[3], A. Johansen[3] and V.S. Tuboltsev[3]

[1]CECM-CNRS, 15, rue Georges Urbain, F94407 Vitry sur Seine Cedex, France
[2]National Center for Electron Microscopy, LBNL B72, Berkeley CA 94720
[3]Niels Bohr Institute, Ørsted Laboratory, University of Copenhagen, Denmark

Small particles of a low-melting phase embedded in a solid matrix with a higher melting point offer the possibility of studying the mechanisms of melting and solidification directly by in-situ observation in a transmission electron microscope. Previous studies of Pb, Cd and other low-melting inclusions embedded in an Al matrix have shown well-defined orientation relationships, strongly faceted shapes, and an unusual size-dependent superheating before melting [e.g. 1,2].

In the present study we have examined the shapes and thermal behavior of eutectic Pb-Cd inclusions in Al. Pb and Cd form a simple eutectic system with each other, but both elements are insoluble in solid Al [3]. Ternary alloys of Al (Pb,Cd) were prepared from high purity elements by melt spinning or by sequential ion implantation of the two alloying additions to achieve a total alloying addition of up to 1at%. TEM observations were made using a heating stage in a 200kV electron microscope equipped with a video system for recording dynamic behavior.

Inclusions in the size range of 1 to 60nm were observed in as-prepared material, exhibiting nearly cuboctahedral shape and characteristic internal structure. Figure 1 shows that particles were comprised of two parts, meeting along a planar interface, and distinguished by their different moiré fringe contrast. Analysis of selected area diffraction patterns revealed the presence of two phases consistent with fcc Pb and hcp Cd, respectively. The orientation relationship between Cd, Pb and Al was one of parallel planes and directions, i.e.

$$0001_{Cd} \parallel 111_{Pb} \parallel 111_{Al} \qquad \text{and} \qquad 2\bar{1}\bar{1}0_{Cd} \parallel 0\bar{1}1_{Pb} \parallel 0\bar{1}1_{Al}.$$

These orientation relationships are the same as those found in the binary monotectic systems Al-Pb and Al-Cd [1,2]. The observed moiré fringe contrast allowed the Pb and Cd parts of the inclusions to be easily identified. The planar interface between Pb and Cd was parallel to the common close-packed planes. The inclusion shape can be thought of as made from two partial inclusions of Pb and Cd, joined together along their common close-packed plane. Each of the two segments corresponds closely in shape and orientation relationship to the equilibrium shapes observed in binary Al-Pb and Al-Cd systems.

Melting of individual inclusions was observed directly by in-situ TEM as the sample was heated through the eutectic temperature at a rate of about 1°C per minute. Melting began at an indicated 251°C, within experimental accuracy of the eutectic temperature (248°C). In sharp contrast to the behavior of Pb inclusions in binary Al-Pb alloys, there was no evidence of superheating, and no dependence on particle size was observed. Figure 2 shows a typical melting sequence taken from a video recording at a nominal temperature of 252°C. The time in seconds is given in each figure. Melting is seen to be initiated at the triple junction between Cd, Pb and Al. The V-shaped liquid-solid interface always formed nearest to the rounded {100} truncation on the cadmium side of the particle with a contact angle of about 70°. The melting front was found to extend slowly from the initial point of nucleation in an irregular process, eventually enveloping the whole inclusion. Between (c) and (d) the liquid groove is seen to shrink as the melting front envelops the Pb side of the particle, as seen at the bottom right in (d). This behavior was observed reproducibly on several

different samples and inclusions. During cooling, solidification did not occur until about 35° below the bulk melting point. In contrast to melting, solidification took place in a burst within less than one video frame (1/30 s). The strain due to the volume contraction was clearly visible as black lobes which were observed to decay over a period of about 20s.

References
1. L. Gråbæk, J. Bohr, E. Johnson, A. Johanson, L. Sarholt-Kristensen and H.H. Andersen Phys. Rev. Lett. 64, 934 (1990)
2. D.L. Zhang, K. Chattopadhyay and B. Cantor, J. Mat. Sci. 26, 1531 (1991)
3. S. Hagége and U. Dahmen, Phil. Mag. Lett., submitted
4. This work is supported by the Director, Office of Energy Research, Office of Basic Energy Sciences, Materials Sciences Division of the U.S. Department of Energy under Contract No. DE-ACO3-76SFOOO98.

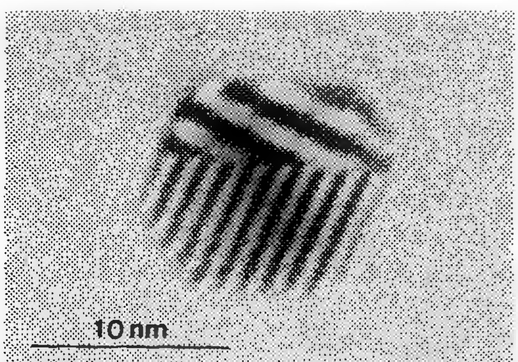

Figure 1 left: TEM micrograph showing Pb-Cd bimetal inclusion of eutectic composition embedded in Al. The moiré fringes show that the particle is composed of a hexagonal Cd and a cubic Pb segment joined along a planar interface.

Figure 2 below: Melting sequence taken from a dark field video recording during heating to the eutectic temperature. Melting is seen to initiate at the triple line between Pb, Cd and Al and advance along a V-shaped groove (see arrows).

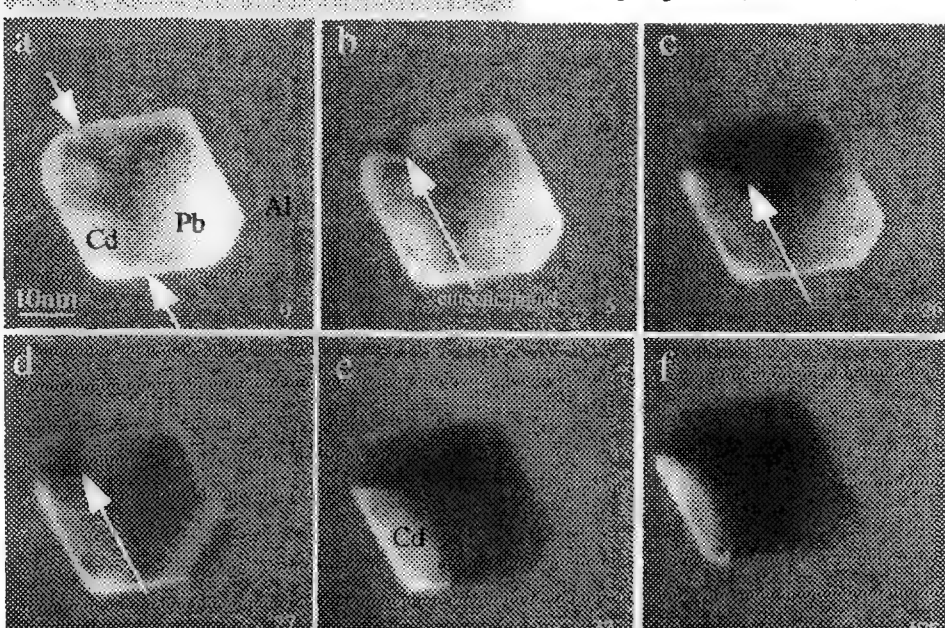

IN-SITU INVESTIGATION OF ION-IMPLANTATION EFFECTS ON RADIATION-INDUCED SEGREGATION IN NI-AL ALLOYS

M.J. Giacobbe [a,b], N.Q. Lam [b], P.R. Okamoto [b], N.J. Zaluzec [b], and J.F. Stubbins [a]

[a] Dept. of Nuclear Engineering, University of Illinois at Urbana-Champaign, Urbana, IL 61801
[b] Materials Science Division, Argonne National Laboratory, Argonne, IL 60439

In-situ experiments using the HVEM (high voltage electron microscope)/Tandem accelerator facility at Argonne National Laboratory were performed to determine the effects of 400-keV Zr^+ and 75-keV Ne^+ implantation on electron radiation-induced segregation (RIS) in Ni-9at.%Al at 550°C and 450°C, respectively. The alteration of RIS kinetics by Ne implantation was studied at two different doses. A highly-focused 900-keV electron beam, which produces a radial defect flux away from the beam center, was used to induce segregation of Al atoms in the opposite direction via the inverse-Kirkendall effect. Within the irradiated zone, Al enrichment drives the formation of γ'-Ni_3Al precipitates, and the radial segregation rate of Al was monitored by measuring the growth of the precipitate zone.

When a thin film is subject to a focused, electron beam, a non uniform defect distribution is produced [1]. The effective beam diameter, D_o, is defined by $I_T = I_o(\pi D_o/2)^2$ where I_T is the total electron current and I_o is the peak electron flux. For a beam with a Gaussian profile, D_o is related to the standard deviation, σ, by $D_o = 2\sqrt{2}\sigma$. Previous HVEM irradiations in Ni-Al alloys [1-5] have shown the segregation of Al against the vacancy flux, resulting in Al enrichment at the beam center. When the solubility limit is reached, nucleation and subsequent growth of a γ'-Ni_3Al zone occur, which provides a direct measure of the segregation rate.

Two types of irradiation were conducted: (i) electrons only and (ii) ion implantation followed by electron irradiation. In case (ii), small γ'-Ni_3Al zones were pre-formed by electron irradiation before ion implantation to act as reference markers during and after ion bombardment. The ion energies were chosen so that all incident ions were implanted in the observation zone (1800Å) The electron beams in this investigation were elliptical in nature and, therefore, assumed to possess a bi-gaussian shape described by $I(x,y) = I_o \exp\{-(x/a_o)^2 - (y/b_o)^2\}$ where $a_o = \sqrt{2}\,\sigma_a$ and $b_o = \sqrt{2}\,\sigma_b$ (σ_a and σ_b are defined as the standard deviation of the beam profile along the major and minor axes, respectively). The dimensions of the precipitate zones were normalized to a_o and b_o along these axes and can thus be displayed on the same scale.

Typical micrographs of γ'-Ni_3Al zones in both (i) and (ii) types of irradiation are given in Figure 1. The effect of 400-keV Zr^+ implantation on RIS at 550°C is demonstrated in Figure 2. After Zr implantation to a dose of 10^{15} Zr/cm^2, γ'-Ni_3Al precipitate growth was similar to the standard irradiation with electrons only. The effects of 2.5 and 4.2x10^{15} Ne/cm^2 on Al segregation are shown in Figure 3, and the results indicate that increasing Ne implantation fluence results in decreased γ'-Ni_3Al precipitate growth.

It has been previously reported that Zr, much like Ti, acts as a strong vacancy trapping site in the reduction of void swelling in austenitic stainless steels [6,7]. The results from Zr implantation here contradict the suggestion that it acts as a strong vacancy trapping site, since the radial segregation of Al was not changed by the presence of 10^{15} Zr/cm^2. Hence, an undetermined mechanism may be responsible for the suppression of void swelling in Zr doped steels. The presence of Ne in Ni-9at.%Al, on the other hand, altered RIS kinetics, gradually reducing the precipitate growth with increasing Ne implantation dose. This effect suggests that Ne atoms may act as strong defect trapping sites, reducing the number of defects free to participate in RIS.

References

1. N.Q. Lam and P.R. Okamoto, in *Solute-Defect Interaction: Theory and Experiment*, eds. S. Saimoto et al. (Pergamon Press, Toronto, 1986) 307.
2. M.J. Giacobbe, N.Q. Lam, P.R. Okamoto, and J.F. Stubbins Mat.Res.Soc.Symp.Proc (1995) in press.
3. N.Q. Lam and P.R. Okamoto, in *Effects of Radiation on Materials: Twelfth International Symposium*, ASTM STP 870, eds. F.A. Garner and J.S. Perrin (ASTM, Philadelphia, 1985) 430.
4. N.Q. Lam and P.R. Okamoto, J. Nucl. Mater. **133-134**, 430 (1985).
5. N.Q. Lam and P.R. Okamoto, Mat. Res. Soc. Symp. Proc. **41**, (1985) 241; N.Q. Lam, P.R. Okamoto, and G.K. Leaf, Mat. Res. Soc. Symp. Proc. **74** (1987) 523.
6. Y. Katano, K. Nakata, S. Jitsukawa, T. Aruga, and Shiraisi, J. Nucl. Mater. **133-134**, 530 (1985).
7. K. Nakata, T. Kato, and I. Masaoka, J. Nucl. Mater. **148**, 185 (1987).

8. The authors would like to thank B. Kestel, E. Ryan, S. Ockers, L. Funk, and C. Allen for their experimental assistance. This work was supported by US DOE under contract BES-MS W-31-109-Eng-38 and DEP at ANL.

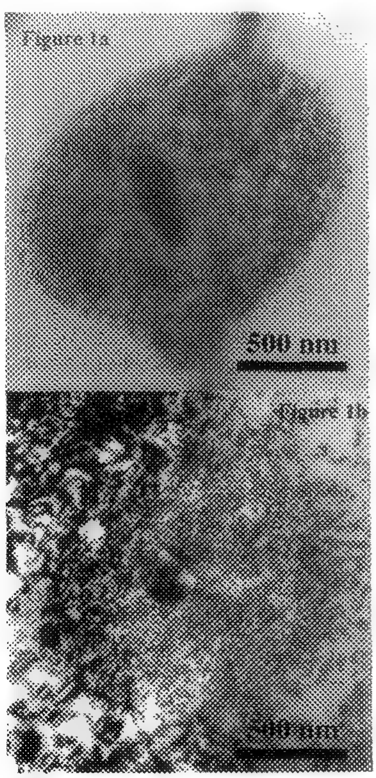

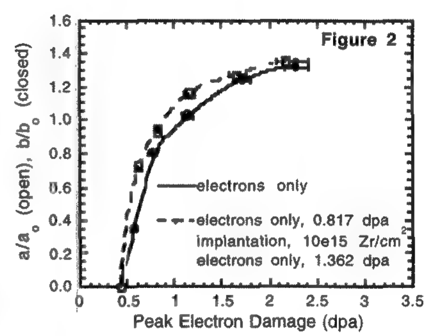

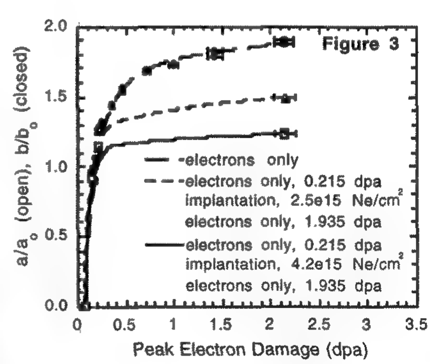

Fig. 1a γ'-Ni_3Al zone after electron irradiation at 550°C to 2.18 dpa.

Fig. 1b γ'-Ni_3Al zone after implantation of 10^{15} Zr/cm^2 and electron irradiation at 550°C to 1.67 dpa.

Fig. 2 γ'-Ni_3Al growth curves for 900-keV electron and pre-implanted 400-keV Zr^+ ion/900-keV electron irradiations at 550°C. Peak electron damage rates ranged from 5.68-7.24x10^{-4} dpa/s.

Fig. 3 γ'-Ni_3Al growth curves for 900-keV electron and pre-implanted 75-keV Ne^+ ion/900-keV electron irradiations at 450°C. Peak electron damage rates ranged from 5.68-6.03x10^{-4} dpa/s.

Structural Investigation of B+ Ion Implantation Induced Amorphization in Polycrystalline Ni Thin Films

P.C. Liu,** N.J. Zaluzec,* P.R. Okamoto,* and M. Meshii**

*Materials Science Division, Argonne National Laboratory, Argonne, IL 60439
**Department of Materials Science and Engineering, Northwestern University, Evanston, IL 60208

High fluence metalloid ion implantation have been shown to induce amorphous phase formation in transition metals systems.[1,2] In this study Electron Energy Loss Spectroscopy (EELS) and Energy Filtered Selective Area Electron Diffraction (EFSAED) techniques have been employed along with conventional TEM to characterize the structural and electronic changes resulting from B+ ion implantation into polycrystalline Ni thin films.

Polycrystalline Ni thin films of thickness ~500Å have been prepared by evaporating pure Ni (99.99%) onto commercial Bioden R.F.A. acetyl cellulose films in a vacuum of 5 x 10^{-6} Torr at room temperature. The TEM samples are obtained by dissolving the underlying acetyl cellulose layer using acetone wetting from below the TEM grids. The resulting films exhibit a continuous, non-textured fcc polycrystalline rings pattern with an average grain size of 17 ± 4 nm. Ion implantation was performed in an implantation chamber using 50 keV B^+ ions directed at normal incidence to the Ni TEM samples. The sample configuration consists of a ~500Å Ni energy degrader films on the 100 mesh Cu grids situated in front of the polycrystalline Ni thin films on the 300 mesh Cu grids. Such configuration maintains optimum efficiency of B^+ ion implantation while producing a more homogeneous profile. After a total incident dose of 4.22×10^{17} ions/cm^2, the implanted polycrystalline Ni thin films was transferred to the Philips EM420 electron microscope equipped with a Gatan (M-607) serial EELS detector for structural characterization.

During implantation part of the Ni film was shadowed by the 100 mesh Cu grids supporting the energy degrader films, hence providing a direct comparison of implanted and controlled regions on the same specimen (Fig. 1). In the implanted regions the transformation from crystalline (A) to amorphous (B) phase was confirmed by the presence of diffuse halos in EFSAED patterns (Fig. 2a, 2b). TEM observation shows that some grain growth occurred during the implantation process. Crystal grains in the implanted regions, while fewer in number, tend to be larger in size relative to those in the controlled region's. EFSAED analysis[3,4] shows that the first amorphous halo appears in the same position as the Ni (111) peak, while the second halo peak appears in-between the Ni (022) and (113) peaks (Fig. 3). The radial distribution function G(r) for the implanted region extracted from the Fourier sine transform shows a broadening in the dispersion of the nearest neighbor shell relative to that of the controlled region (Fig. 4). The successive near neighbor shells for implanted regions also shows extensive overlapping and broadening effect. EELS low loss studies reveals that the two plasmon peaks for the controlled regions, at 20.0 and 26.8 eV, respectively, converge to a single plasmon peak with peak energy loss of 23.8 eV (Fig. 5). Similar broadening effect is also found in Ni $L_{2,3}$ core loss edges (Fig. 6). Since the two plasmon peaks are indicative of the plasma-like and interband transition which characterize the valence electrons excitation in Ni polycrystals,[5] the convergence to a single plasmon peak show that the smearing of the valence electron band states is associated with the highly disordered structures resulted from the implantation process. An understanding of this effect will lead to a deeper understanding into C-A transition phenomena, and may provide a way to measure the volume fraction of the amorphous phase.

References

1. B.Rauschenbach and V.Heera, Zentralinstitut fur Kernforschung Rossendorf, 630 (1988) 1-29.
2. B.Rauschenbach, G.Otto, K.Hohmuth, and V.Heera, J. Phys. F: 17 (1987) 2207-16.
3. M.Saunders et al., Ultramicroscopy, 60 (1995) 311-323.
4. D.J.H.Cockayne, and D.R.McKenzie, Acta Cryst., A44 (1988) 870-878.
5. D.L.Misell, and J.A.Atkins, Phil. Mag., 27 (1973) 95-106.
6. The authors would like to thank E.Ryan, P.Baldo and L.Funk for their assistances with experiments. This work was supported by US. DoE under contract BES-MS W-31-109-Eng-38 and DEP at ANL.

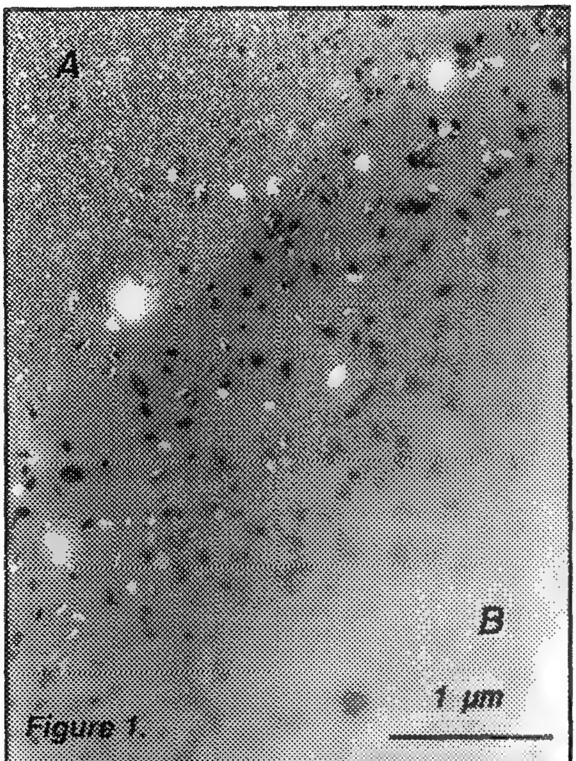

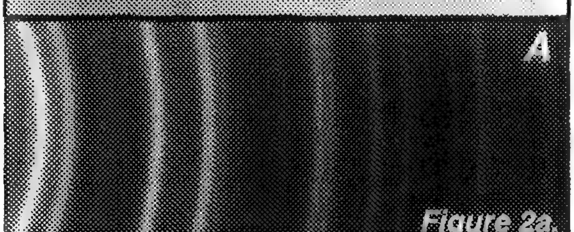

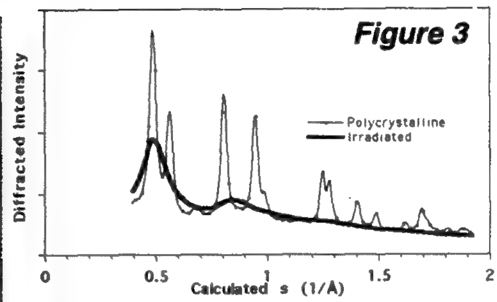

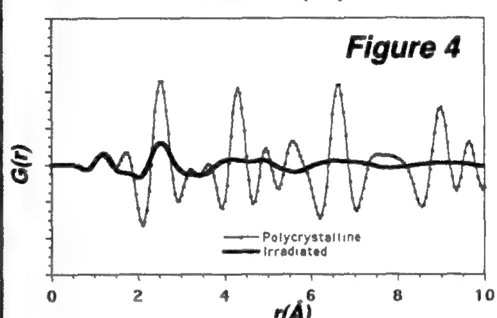

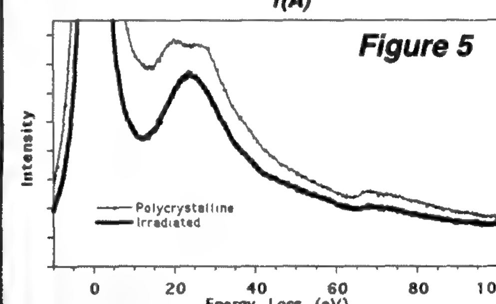

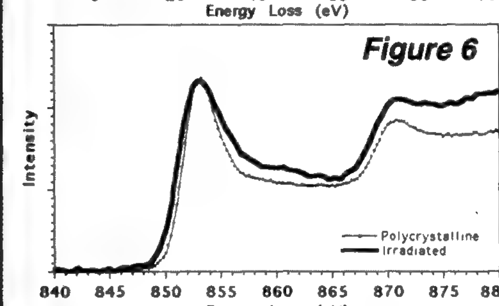

Fig. 1 TEM BF image showing both controlled and B^+ implanted regions in Ni polycrystal thin film.
Fig. 2 EFSAED patterns taken from (2a) controlled regions A, (2b) implanted regions B.
Fig. 3 EFSAED experimental intensity profile as a function of calibrated diffraction vector s.
Fig. 4 Fourier transformed radial distribution function G(r) for controlled and implanted regions.
Fig. 5 EELS low loss spectrum showing changes in going from controlled to implanted regions.
Fig. 6 EELS core loss spectrum showing the corresponding changes in Ni $L_{2,3}$ inner shell edges.

EFFECT OF ELECTRON IRRADIATION ON THE 3C–4H TRANSFORMATION IN A Co-Fe ALLOY

Charles W. Allen * and Hirotaro Mori **

*Materials Science Division, Argonne National Laboratory, Argonne, IL 60439 USA
**Research Center for UHVEM, Osaka University, Suita, Osaka 565 Japan

In general, irradiation of materials by high energy electrons, protons or neutrons has been shown to stabilize the existing microstructure against subsequent martensitic transformation. Alloys which have been studied include the binary intermediate phases NiTi [2, 3] and $Ni_{63}Al_{37}$ [4] and ternary phases between $Cu_{37.5}Al_{62.5}$ and $Cu_{63.6}Al_{36.4}$ [5, 6] as well as the intermetallic $Cu_{69.01}Al_{17.92}Zn_{12.17}$ [7, 8, 9]. In these materials, the martensitic transformations are known to be sensitive to small changes in chemical composition and to the degree of long range order. In addition, one should expect the kinetics of martensitic transformations to be sensitive to other forms of structural damage introduced during irradiation also. This spectrum of irradiation-induced phenomena renders the interpretation of results in studies of such concentrated binary and ternary phases rather complicated, therefore.

We present here the preliminary results of a study of the effect of electron irradiation on the character of the martensitic transformation in a relatively dilute terminal solid solution of Co+5.75 wt pct Fe, similar in composition to that employed for studies of the transformation mechanism itself [10]. The effect of the solute Fe is to depress the equilibrium Co-transformation temperature and to modify the transformation, which in Co is fcc–hcp, to one of the type fcc–dhcp; that is, the transformation is between the three-layer stacking sequence of the cubic structure (ABC), known as 3C, and the four-layer stacking sequence of the di-hexagonal structure (ABAC), known as 4H. The transformation involves only the glide of groups of Shockley-like partial dislocations [10, 11, 12] and is one of the family of simple martensitic transformations often called shear transformations. While electron irradiation may modify to some extent the degree of short range order in such an alloy, its predominant effect is surely the formation of faulted Frank-type dislocation loops, which may be expected to impede the shear transformations (that is, to stabilize the existing structure) by acting as barriers to the glide of the necessary transformation dislocations. The effect of the presence of Frank loops on nucleation of such a transformation is perhaps less predictable. The loops enclose intrinsic or extrinsic stacking faults, the introduction of which is the structural essence of the transformation. However, the irradiation-induced loops themselves are sessile; that is, the transformation cannot propagate by glide of the loops in the fault plane; only by climb. The transformation occurring in this manner would not be martensitic.

The subject alloy was prepared by arc melting and hot rolling by the Materials Preparation Center of Ames Laboratory. 3 mm disks were cut by EDM, lapped to about 200 mm thickness, annealed for 2 h at 915°C in an evacuated Vicor tube and air cooled to room temperature, resulting in predominantly 3C material. Some of the specimens were subsequently quenched in LN_2 to produce a significant volume fraction the 4H structure within 3C. Thin foils were prepared by jet thinning at -15°C in a perchloric acid-alcohol electrolyte.

Preliminary experiments were performed at the Research Center for Ultra-High Voltage Electron Microscopy at Osaka University. The threshold of electron energy to produce displacement damage in this alloy is estimated to be between 400 and 500 kV. At an electron energy of 2 MeV, the displacement cross-section for electron damage in this material is approximately 75 barns (1 barn = 10^{-24} cm^2). Heating of one of the quenched specimens (large volume fraction of 4H) in an Hitachi H-800B operated at 200 kV (well below threshold for displacement damage) revealed that the 4H–3C transformation occurred over the range 120–400°C in the electron transparent areas of the specimen. A similar specimen was subjected to 2 MeV electron irradiation (well above threshold for displacement damage) in the Hitachi H-3000 at room temperature for more than 1 h with the electron beam substantially defocussed over the entire electron transparent region. The specimen was subsequently heated but failed to observably transform until about 600°C. A specimen which was initially predominantly 3C was irradiated in a similar manner also at room temperature, followed by cooling in an Oxford helium-cooled double tilt holder. No transformation to the 4H structure was observed in this specimen even on cooling to an indicated temperature of 16 K. Both experiments seem to demonstrate qualitatively the profound effect that the damage structure produced by electron irradiation can have on these simple martensitic transformations. In the interpretation of results of related earlier studies involving intermetallics, the

contribution of irradiation-induced structural defects (not associated with disordering) to the stabilization phenomenon was totally ignored, which, in view of the qualitative results presented here, seems to be thoroughly unjustified.

A more thorough study of this phenomenon is being pursued which attempts to quantify the transformation retardation effect. The major problem in doing so stems from the well known fact that such martensitic transformations are significantly retarded due to surface relaxation and possibly surface contamination effects in thin regions of foil specimens.

Acknowledgment

The preliminary experiments in this study were performed under a Japan Society for the Advancement of Science (Short Term) Fellowship (CWA) in the Research Center for Ultra-High Voltage Electron Microscopy, Osaka University. One of he authors is grateful to Professors H. Mori and H. Nishihara of UHVEM Center for their hospitality during this brief visit and to Bernard Kestel of Argonne National Laboratory for his indispensible assistance in the TEM specimen preparation.

References

1. Electron Microscopy Center for Materials Research is supported by U. S. Department of Energy, BES-Materials Sciences, under Contract W-31-109-Eng-38.
2. T. Hoshiya, T. S. Den, H. Ito, H. Itami, and S. Takamura, 1986, *Proceedings of the International Conference on Martensitic Transformations* 1986 (Japan Institute of Metals), p. 685.
3. K. Tsuchiya and S. Ohnuki, Private Communications.
4. S. Muto and D. Schryvers, J. Alloys and Compounds, 199 (1993) 1–6.
5. Y. Nakata,T. Tadaki, and K. Shimizu, *International Meeting on Advances in Materials* (Pittsburgh, PA: Materials Research Society, vol. 9) p. 231.
6. K. Tsuchiya and K. Marukawa, *Proceedings of the International Symposium on Shape Memory Materials* (Beijing: International Academic Publishers, 1994) 314–318.
7. A. Tolley and M. Ahlers, Scripta Metall., 23 (1989) 2117.
8. A. Tolley, Radiat. Effects Defects Solids, 128 (1994) 229.
9. A. Tolley, M.-P. Macht, M. Müller, C. Abromeit and H. Wollenberger, Phil. Mag. A, 72 (1995) 1633–1647.
10.T. Waitz and H. Kamthaler, Phil. Mag. A, in press.
11.C. Allen and K. Liao, Phys. Stat. Sol. (a), 74 (1982) 673.
12.C. W. Allen, H. R. Kolar and J. C. H. Spence, *Proceedings of the International Conference on Martensitic Transformations* 1986 (Japan Institute of Metals) 186–191.

IRRADIATION-INDUCED PRECIPITATION IN DIRECT-AGED ALLOY 625

M.G. Burke and R. Bajaj

Bettis Atomic Power Laboratory, Westinghouse Electric Corp., West Mifflin, PA 15122

Direct-aged alloy 625 (DA-A625) is a precipitation-hardened nickel-base superalloy with good mechanical properties and excellent corrosion resistance. Its superior stress corrosion cracking (SCC) performance makes it a candidate material for applications in light water reactors where resistance to irradiation-assisted SCC (IASCC) is important.[1] This alloy derives its strength from the intragranular precipitation of fine DO_{22} - ordered γ'' precipitates. These precipitates have a disc-like morphology and are crystallograhically related to the γ matrix such that the [001] axis of the precipitates are oriented parallel to <100> directions in the matrix. This alloy is generally solution-annealed then aged within the temperature range ~600 to 750°C. In direct-aging, the alloy is immediately aged at ~ 660°C for 80 h following hot-working. In addition to the γ'' precipitates, intergranular $M_{23}C_6$, M_7C_3, M_6C, or MC carbides can form in this material.

To evaluate the effect of neutron irradiation on the microstructure and IASCC behavior of Alloy 625, specimens in the direct-aged condition were neutron-irradiated at 370°C and 265°C to a fluence of ~10^{20} neutrons/cm^2 (E > 1 MeV).[1] Conventional thin-foil specimens were prepared using 20% $HClO_4$ - 80% CH_3OH at ~-40°C, and subsequently examined in Philips CM12 and CM30 analytical electron microscopes.

Direct-Aged Alloy 625: This material was characterized by the presence of a uniform distribution of fine (~15 nm in length) γ'' precipitates throughout the matrix. Two of the 3 {100} variants of the γ'' precipitates are evident in the dark-field transmission electron micrograph of Fig. 1. In addition to the intragranular precipitates, many grain boundaries were decorated with fine, discrete γ'' precipitates. Intergranular carbides, primarily $M_{23}C_6$ and some M_7C_3, were observed at ~40% of the grain boundaries, Fig. 2. Dislocations, present as a result of thermomechanical processing, served as preferential nucleation sites for the γ'' precipitates.

Neutron Irradiated at 370°C: Neutron irradiation resulted in the formation of fine dislocation loops, "black spot" damage, and stacking fault tetrahedra, Fig. 3. Selected area electron diffraction (SAED) revealed the presence of additional reflections in the 1/3 and 2/3 (220) positions in [001], [110] and [111] zones which were associated with the formation of a new metastable phase in Alloy 625. A dark-field TEM image of this phase and the associated SAED pattern are shown in Fig. 4. Analysis of electron diffraction data indicates that this phase is consistent with a body centered orthorhombic Pt_2Mo-type structure.

Thermally aged at 370°C: The microstructure of the thermally aged material was identical to that of the direct-aged (control) material. Aging at 370°C for times equivalent to the duration of the irradiation (~1000 h) did not result in measurable coarsening of the γ'' precipitates nor induce the formation of the Pt_2Mo-type precipitates. SAED patterns showed no evidence of diffuse scattering phenomena associated with a precursor phase, Fig. 5.

Neutron Irradiated at 265°C: Unlike the material irradiated at 370°C, no discrete precipitate reflections from the Pt_2Mo-type phase were present in the electron diffraction patterns. The fine γ'' precipitates were clearly evident in this material, although dark-field micrographs showed indications of some radiation-induced "damage" or structure within the precipitates, Fig. 6. Electron diffraction patterns obtained from this material showed a ring of diffuse intensity which intersected the 1/3 and 2/3 (220) positions, Fig.7. This scattering is consistent with the initial stages of formation of the metastable phase observed at 370°C. Similar effects have been observed in the study of phase transformations in Ni-Mo alloys.[2]

References

1. R. Bajaj et al. in *7th Int'l. Symp. on the Environment-Sensitive Behavior of Materials--Water Reactors,* eds. G.P. Airey et al., (NACE, 1995) 1093.
2. S.K. Das and G.Thomas, *Phys. Stat. Sol.(a),* 21 (1974) 177.

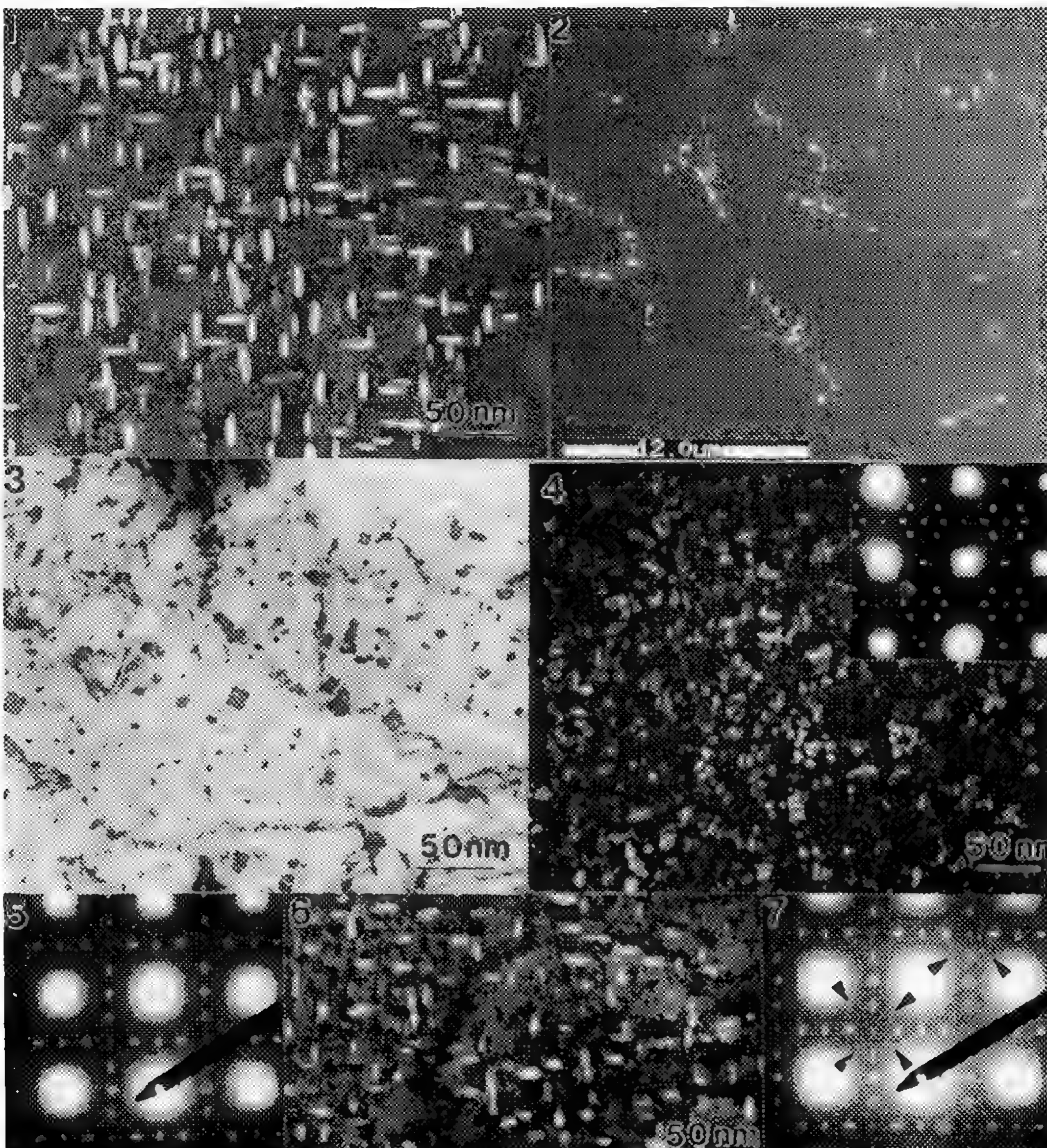

FIG. 1. [001]-oriented dark-field transmission electron micrograph of 2 {100} variants of γ″ in DA-A625.
FIG. 2 Secondary electron image of intergranular carbides present in DA-A625.
FIG. 3 Dislocation loops, "black spot" damage and stacking fault tetrahedra in irradiated DA-A625.
FIG. 4 Dark-field image of new Pt_2Mo-type precipitates in irradiated DA-A625; [001] SAED pattern.
FIG. 5 [001] SAED pattern of DA-A625 aged at 370°C for 1000 h.
FIG. 6 [001]-oriented dark-field micrograph of 2 {100} γ″ variants in sample irradiated at 265°C.
FIG. 7 [001] SAED pattern of DA-A625 irradiated at 265°C; note diffuse rings intersecting ⅓ & ⅔ (220) positions (arrowed).

GPB ZONES AS A PRECURSOR FOR S′ PRECIPITATION IN Al-BASED MATRICES

[1]V. Radmilovic, [1]S. Ratkovic, [2]G.J. Shiflet, and [3]U. Dahmen

[1]University of Belgrade, Dept. of Physical Metallurgy, Belgrade, Yugoslavia
[2]University of Virginia, Charlottesville, VA, USA
[3]University of California, National Center for Electron Microscopy, LBL, Berkeley, CA, USA

In the pseudo-binary Al-Al_2CuMg alloy, the Cu/Mg-rich precipitation zones (GPB) are able to cause considerable hardening of the matrix. The hardening is apparently not very sensitive to the zone size or degree of ordering[1]. According to Silcock[1] these zones are cylindrical, 1-2 nm in diameter and 4 nm long. They are also formed during the early stage of aging at 190°C and are followed by nucleation of S′ precipitates with {210} habit plane. Overaging occurs by the further formation and growth of S′ with a corresponding re-solution of GPB zones[2,3]. Since the discovery of GP zones (reach in Cu) in Al-Cu alloys by Guinier and Preston, the structure of these zones, even at atomic level, has been studied extensively[4,5]. However, there are very few studies of GPB zone structure and crystallographic relationship with Al matrix. In this paper results using atomic resolution electron microscopy on the GPB zone size, structure and crystallographic orientation relationship with Al matrix are reported.

An electron micrograph of GPB zone at atomic resolution is shown in Fig. 1a, in {100} zone axis for Al-Cu-Mg alloy aged 16 hrs at 190°C. The bright dots have been interpreted as the rows of Al atoms in the matrix. The arrays of bright dots denoted by C correspond to planes of Cu atoms in GPB zone laying close to <110> directions. Based on Yoshida′s assumption for the GP zones[5], it seems that the Cu layer behaves as a dislocation loop, which is responsible for the distortion field in the Al matrix. Because of the complexity of GPB crystal structure, modeling and the contrast calculation is performed on limited scale, but was good enough to indicate the correspondence between simulated and experimental images. Inside some of the clusters an ordering in <102> direction takes place (Fig. 1a). It may be possible that ordering within the clusters along <102> can represent the initiation of the S′ phase. By subsequent aging for 72 hrs at 190°C GPB zone transforms into well developed S′ particle (Fig. 1b). In Al-Li-Cu-Mg based alloys these clusters has not been observed, in spite of the use of aging treatment which result in their formation in Al-Cu-Mg alloy. This is in agreement with observations of other authors[2], who proposed absence of dislocation loops as favorable sites for Cu/Mg rich cluster formation due to the high binding energy between vacancies and Li atoms[6], which prevents vacancy supersaturation and collapse into loops and dislocation climb to helices. Instead, S′-phase in Al-Li-Cu-Mg alloy nucleates on the δ′/Al matrix interface (Fig. 2a) and on matrix dislocations (Fig. 2b). Because of the negligible misfit between the matrix and δ′, this interface would not be expected to serve as a favorable site for S′ nucleation. However, during the growth of Al_3Li (δ′) excess Cu and Mg concentrations occur at the growth front[7]. This coupled with the excess vacancies released when Li adds to the δ′ particle[2] result in favorable conditions for S′ precipitation[7].

1. J.M. Silcock, J. Inst. Metals, 89 (1960-61) 203.
2. H.M. Flower and P.J. Gregson, Mater. Sci. Tech., 3 (1987) 81.
3. G.C. Weatherly, Ph.D. Theses, Univer. Cambridge, U.K., (1966).
4. T. Sato and T. Takahashi, Scripta Met., 22 (1988) 941.
5. H. Yoshida, Scripta Met., 22 (1988) 947.
6. S. Ceresara, A. Giarda, and A. Sanchez, Phil. Mag., 35 (1977) 97.
7. V. Radmilovic, G. Thomas, G.J. Shiflet and E. A. Starke, Scripta Met., 23 (1989) 1141.

8. This work was supported by the Director, Office of Basic Energy Sciences, Materials Scien
Division, US Department of Energy, under contract DE-AC3-76SF00098.

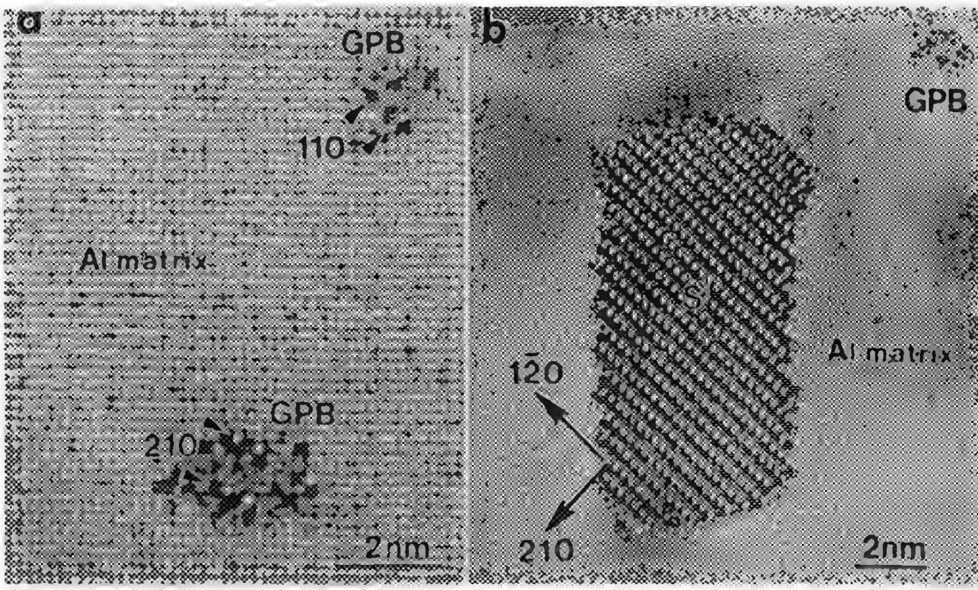

Fig. 1 . a) HREM of aluminum matrix and Cu/Mg rich clusters in Al; b) Well developed S′ particl [001] zone axis.

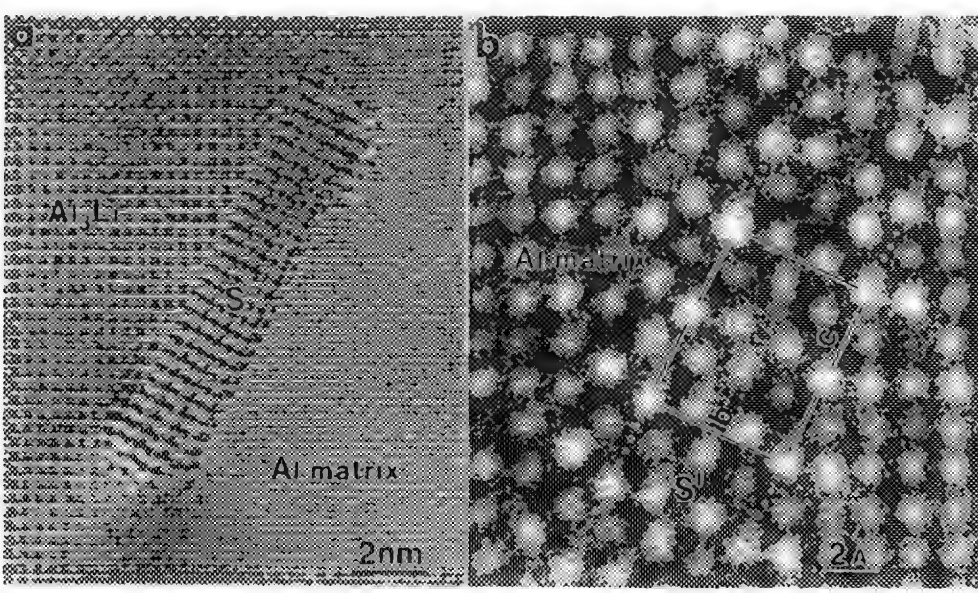

Fig. 2. a) S′ precipitate at δ′/Al matrix interface in Al-Cu-Mg alloy; [001] zone axis. b) precipitate of the unit cell height, formed on dislocation.

TEM STUDY OF PRECIPITATION IN A NiAl-3Ti-0.5Hf SINGLE-CRYSTAL ALLOY

A. Garg, R. D. Noebe, J. M. Howe*, A. W. Wilson* and V. Levit**

NASA Lewis Research Center, Cleveland, OH 44135
* Dept. of Materials Science and Engineering, University of Virginia, Charlottesville, VA 22903
** Dept. of Materials Science and Engineering, University of Florida, Gainesville, FL 32611

Three directionally solidified NiAl single-crystal alloys, NiAl-3Ti, NiAl-0.5Hf and NiAl-3Ti-0.5Hf (at.%), were grown by a Bridgeman technique using high purity alumina crucibles. The ingots were homogenized for 32h at 1644 K followed by aging for 6h at 1255 K and finally furnace cooled under an argon atmosphere. This heat treatment was found to be very effective in dissolving Hf-rich interdendritic particles that were present in the as-cast structure, and at the same time it produced fine second-phase precipitates in the alloy.

Samples for transmission electron microscopy (TEM) were prepared from 3 mm diameter cylinders electro-discharge machined from the heat-treated ingots. Slices sectioned from the cylinders were mechanically ground and electrochemically thinned in a twin-jet Tenupol-3 polisher. Microstructural and energy-dispersive X-ray spectroscopy (EDXS) studies were conducted in a Philips 400T TEM equipped with a double tilt goniometer and a KEVEX Si/Li X-ray detector.

TEM microstructures of the NiAl-3Ti and NiAl-0.5Hf samples were featureless except for the presence of some random dislocations. No homogeneous precipitation was observed in either of the two alloys suggesting that 3 at.% Ti in the first alloy and 0.5 at.% Hf in the second alloy were in solid solution in the NiAl matrix. The microstructure of the NiAl-3Ti-0.5Hf alloy was, however, very different and showed a high density of precipitates. A TEM bright-field image of the alloy close to a $<001>_{NiAl}$ zone-axis is presented in Fig. 1(a). It shows a high density of fine precipitates (size ~ 5-50nm) distributed uniformly throughout the foil, and some coarse precipitates (size ~ 100-700nm) nucleated preferentially on dislocations on $\{100\}_{NiAl}$ planes. The coarse precipitates were always associated with precipitate free zones. The fine precipitates, shown at a higher magnification in Fig. 1(b), clearly exhibited a plate-shape morphology with associated coherency strain. Using EDXS, electron diffraction (Fig. 1(c)) and trace analysis these fine precipitates were identified as Ni_2AlTi Heusler phase ($L2_1$, a = 0.587nm) formed on the $\{100\}_{NiAl}$ planes with a cube-on-cube orientation relationship. Two types of coarse precipitates were found to nucleate on dislocations; edge-on plates (marked T, size ~ 100-250nm) and almost equiaxed precipitates (marked H, size ~ 200-700nm). These precipitates were also found to be Heusler phases; T: Ni_2AlTi, H: Ni_2AlHf ($L2_1$, a = 0.608 nm). Both of these phases are formed by further ordering of the B2 structure of NiAl (ordered BCC, a = 0.289nm) during cooling[1,2]. The lattice misfits of the Ni_2AlTi and Ni_2AlHf phases with the NiAl matrix are 1.5 % and 5.2 %, respectively. Due to large misfit of the Ni_2AlHf phase, a square network of misfit dislocations of spacing ~ 5.6nm was often observed at the Ni_2AlHf/NiAl interface, which made its presence unmistakable and unique.

Dislocation segments lying along the $<110>_{NiAl}$ directions were often unstable and found to sharply bend along the $<100>_{NiAl}$ directions, giving them a zigzag appearance (arrows in Fig 1(a)). Preferred nucleation of the Ni_2AlTi precipitates on such segments produced a saw-tooth appearance. In several regions of the foil, a dense precipitation of large Ni_2AlTi plates and some Ni_2AlHf

precipitates were observed along the <110> directions in a $<001>_{NiAl}$ zone-axis (Fig 2). This is believed to be due to preferential nucleation of the Ni_2AlTi precipitates possibly on prismatic dislocation loops.

A high density of fine precipitation as seen in Fig. 1(a) is expected to enhance the creep properties of NiAl single crystals significantly and is under investigation.

References

1. R. D. Field et al., *Scripta Metallurgica*, 23(1989)1469.
2. N. C. Tso and J. M. Sanchez, *MRS Symp. Proc.*, Vol. 133(1989)63.

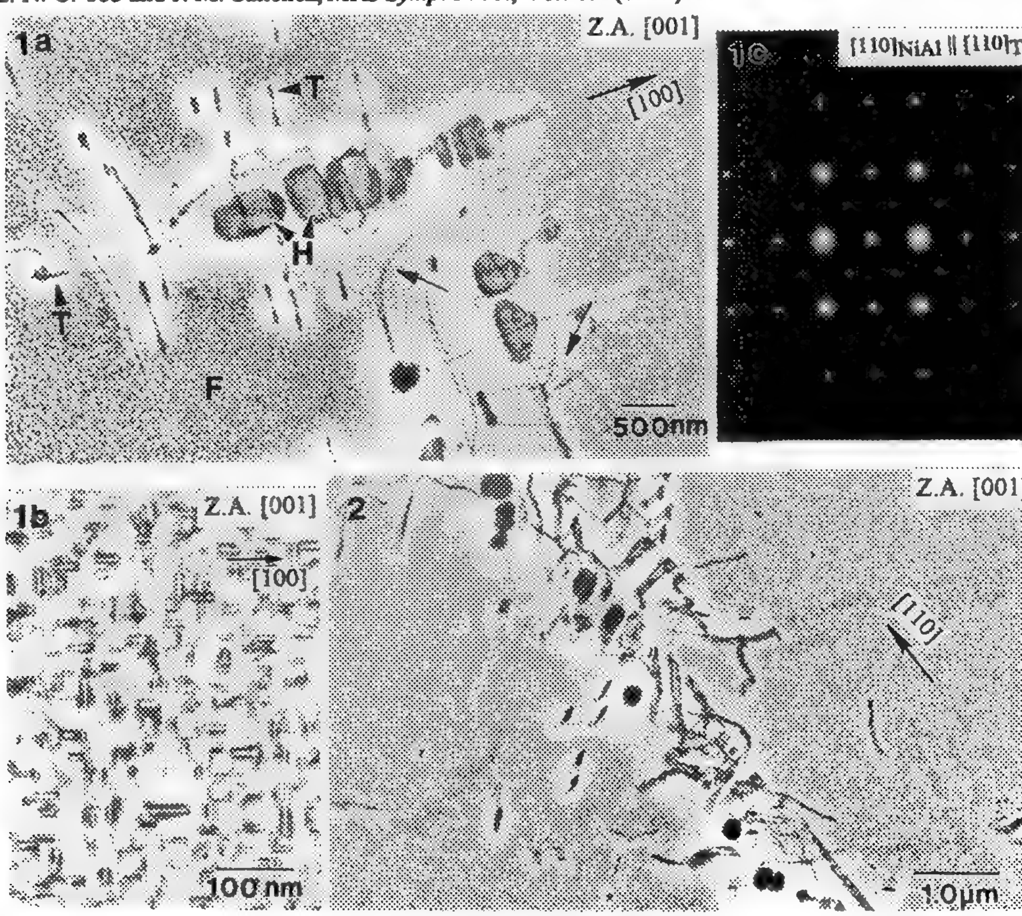

Fig. 1 (a) General microstructure of the NiAl-3Ti-0.5Hf single-crystal alloy in the as-heat treated condition. A higher magnification view of region F and its SADP are shown in (b,c), respectively.
Fig. 2 Preferential precipitation of large Ni_2AlTi plates and equiaxed Ni_2AlHf phase along a <110> direction in a $<001>_{NiAl}$ zone-axis.

CHARACTERIZATION OF REACTIVE PHASE FORMATION IN SPUTTER-DEPOSITED Ni/Al MULTILAYER THIN FILMS USING TRANSMISSION ELECTRON MICROSCOPY

G. Lucadamo*, K. Barmak*, and C. Michaelsen**

* Department of Materials Science and Engineering, Lehigh University, Bethlehem, PA 18015
** Institute of Materials Research, GKSS Research Center, 21502 Geesthacht, Germany

The subject of reactive phase formation in multilayer thin films of varying periodicity has stimulated much research over the past few years. Recent studies have sought to understand the reactions that occur during the annealing of Ni/Al multilayers.[1,2] Dark field imaging from transmission electron microscopy (TEM) studies in conjunction with *in situ* x-ray diffraction measurements, and calorimetry experiments (isothermal and constant heating rate), have yielded new insights into the sequence of phases that occur during annealing and the evolution of their microstructure.

In this paper we report on reactive phase formation in sputter-deposited 1Ni:3Al multilayer thin films with a periodicity Λ (the combined thickness of an aluminum and nickel layer) from 2.5 to 320 nm. A cross-sectional TEM micrograph of an as-deposited film with a periodicity of 10 nm is shown in figure 1. This image shows diffraction contrast from the Ni grains and occasionally from the Al grains in their respective layers. As the periodicity of the layers is increased, the polycrystalline nature of the layers become clearer with the grains at 80 nm having heights equal to layer thickness. When the periodicity is increased further, the grains become columnar as observed in a Λ=160 nm as-deposited film shown in figure 2.

Free standing films were subsequently annealed at constant heating rates in a calorimeter furnace. A characteristic differential scanning calorimetry (DSC) trace for a 10 nm film heated to 800 K at 20 K/min is shown in figure 3. The trace exhibits a gradual heat release leading to a sharp, exothermic peak followed by a less pronounced peak. Both exotherms correspond to the formation of the intermetallic compound. Separate hot-stage x-ray diffraction studies of 10 nm multilayers indicated the formation of the tri-aluminide ε phase, $NiAl_3$ at approximately 490 K near the maximum of the first peak.[3]

In addition to the identification of the phases that appear during annealing, information regarding the morphology of the intermetallic grains is useful to fully describe the transformation process. Isothermal calorimetry performed at 460 K on free-standing 10 nm multilayers revealed that the transformation process yielded a bell shaped curve. This is indicative of a nucleation and growth type process and can be interpreted by applying the Johnson-Mehl-Avrami theory.[4] The result is a value for n, the Avrami exponent, which varies between 0.5 and 4, depending on the nucleation rate and growth mechanisms and morphology. We obtained an Avrami exponent of 2.9 for our film with Λ = 10 nm.

A cross-sectional sample of a multilayer with this periodicity on a sapphire substrate annealed to 445 K at 20 K/min in the DSC is shown in figures 4a and b. A dark field image formed by selecting one of the spots corresponding to the intermetallic phase, $NiAl_3$, reveals that the grains are long and flat and constrained to a height approximately equal to the original periodicity. One interpretation of n = 2.9 consistent with the observed transformed microstructure would involve nuclei forming at a constant rate with two dimensional interface controlled growth laterally in the plane of the interface. The initial growth to full height in the direction normal to the interface is assumed to be too small to contribute to the heat signal.[5]

References

1. E. Ma et al., J. Appl. Phys. 69 (1991) 2211.
2. A. S. Edelstein et al., J. Appl. Phys. 76 (1994) 7850.
3 K. Barmak et al., Mat. Res. Soc. Symp. Proc. 382 (1995) 33.
4. J.W. Christian, *The Theory of Phase Transformations in Metals and Alloys*, Pergamon Press, New York, 1981, 542.
5. The authors gratefully acknowledge the financial support of Lehigh University, NSF DMR-9458000, and the support of Deutsche Forschungsgemeinschaft through SFB 371.

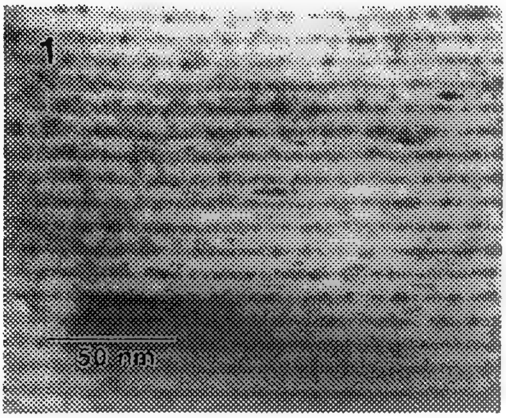

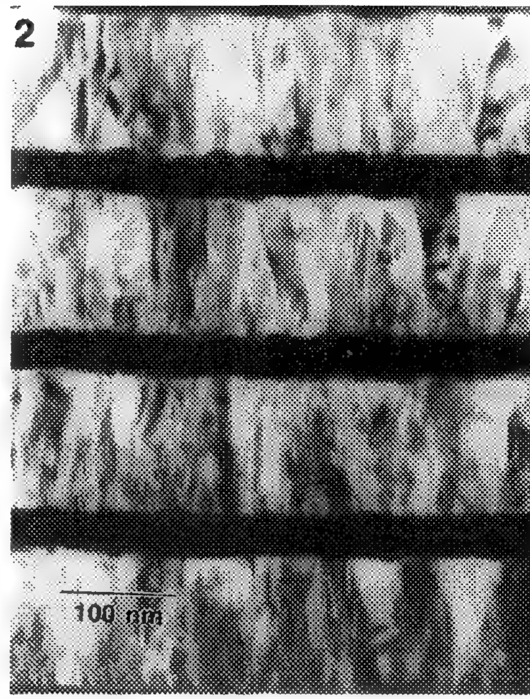

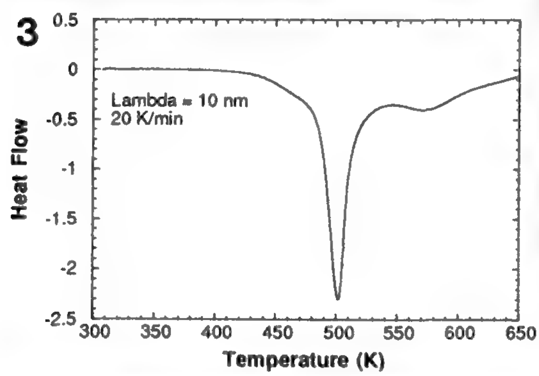

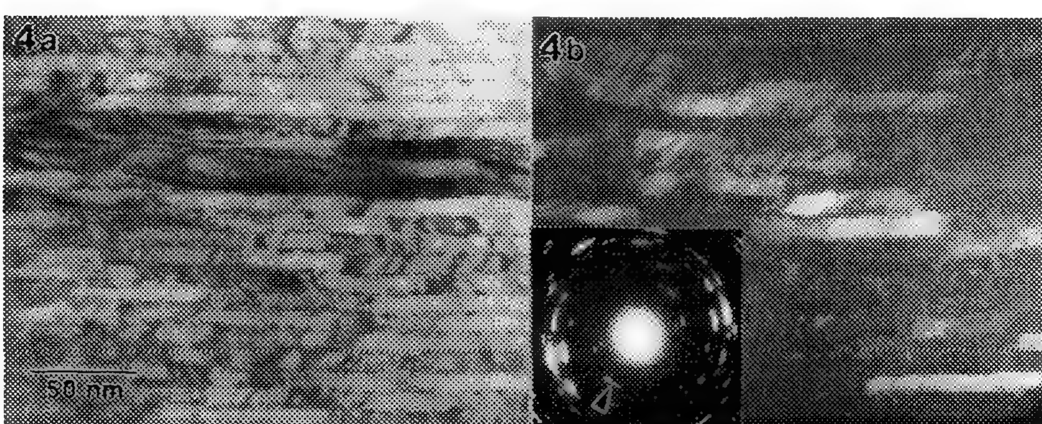

Fig. 1 - Cross-sectional TEM micrograph of an as-deposited 1Ni:3Al multilayer film with $\Lambda = 10$ nm.
Fig. 2 - Cross-sectional TEM micrograph of an as-deposited 1Ni:3Al multilayer film with $\Lambda = 160$ nm.
Fig. 3 - DSC trace for a 10 nm 1Ni/3Al multilayer heated at 20 K/min.
Fig. 4 - Cross-sectional TEM micrograph of a 1Ni:3Al multilayer film with $\Lambda = 10$ nm reacted to 445 K at 20 K/min, (a) bright field, (b) dark field using intermetallic ring.

LARGE-ANGLE CONVERGENT-BEAM ELECTRON-DIFFRACTION STUDY OF COHERENT PRECIPITATES AND DECORATED DISLOCATIONS

J.M.K. Wiezorek and H.L. Fraser

The Ohio State University, Department of Materials Science and Engineering, 2041 College Rd., Columbus, OH 43210;

Conventional methods of convergent beam electron diffraction (CBED) use a fully converged probe focused on the specimen in the object plane resulting in the formation of a CBED pattern in the diffraction plane. Large angle CBED (LACBED) uses a converged but defocused probe resulting in the formation of 'shadow images' of the illuminated sample area in the diffraction plane. Hence, low-spatial resolution image information and high-angular resolution diffraction information are superimposed in LACBED patterns which enables the simultaneous observation of crystal defects and their effect on the diffraction pattern[1]. In recent years LACBED has been used successfully for the investigation of a variety of crystal defects, such as stacking faults, interfaces and dislocations[2]. In this paper the contrast from coherent precipitates and decorated dislocations in LACBED patterns has been investigated. Computer simulated LACBED contrast from decorated dislocations and coherent precipitates is compared with experimental observations.

The computer program used for the LACBED simulations assumed isotropic elasticity theory and the kinematical theory of electron diffraction, and has been used successfully before[3]. Cylindrical displacement fields have been employed to model the effects of coherent precipitates on the contrast in the LACBED patterns. The experimental LACBED work has been performed on TiAl and TiNi specimens prepared by standard electropolishing techniques with a Philips CM30 transmission electron microscope (TEM) operating at 300 kV in the nanoprobe mode following standard practice for LACBED[4]. The dark field LACBED simulations presented in Figs 1(a) and (b) display the characteristic distortion of an excess line by a dislocation for a value of **g.b**=2, i.e. a displacement of the reflection contour producing two minima, and are in agreement with previously reported simulations[3,6]. The contrast from the precipitate decorated dislocation shown in the simulation of Fig 1(c) is more complicated than for the undecorated dislocations and cannot be explained by applying the Cherns-Preston rules[5]. Fig 2 compares simulated LACBED contrast from coherent precipitates of two different sizes and for three different values of misfit between the matrix and the precipitate. Clearly, the distortion of the reflection contour is symmetrical and the number of minima produced by the contour displacements increases with both the precipitate size and the amount of misfit. Since the displacement field of the precipitate for the case shown in Fig 1(c) is symmetrical the contribution from the Burgers vector of the dislocation can be determined as the difference between the number of minima in the distorted contour on either side of the contour crossing defect[3]. The experimentally observed detail in the bright field LACBED disk of Fig 3 displays contrast characteristics expected for a decorated dislocation. The distorted contour exhibits four minima above the defect location (indicated by arrow) and three minima below the defect which is consistent with a value of **g.b**=1. The experimental observations from a small Al_2O_3 precipitate in a TiAl foil (Fig 4(a) and (b)) are consistent with the contrast characteristics of the simulations of Fig 2 and Fig 2(e) in particular. The experimentally observed LACBED contrast from the dislocation dipole shown in Fig 4(c) agrees very well with previously reported dynamic simulations[6] and strongly resembles that of the precipitate in Fig 4(b). Thus, it can be concluded that the simulations presented in this paper correctly predicted the contrast characteristics of dislocation, decorated dislocation and coherent precipitates in isotropic and moderately anisotropic crystals. It appears that LACBED patterns are sensitive to the long range behavior rather than the short range details of the strain field which complicates distinction between different types of defects. Hence, LACBED studies of defects ought to be accompanied by conventional defect imaging in order to avoid misinterpretation.

References

1. M. Tanaka and M. Terauchi, Convergent Beam Electron Diffraction (Tokio:JEOL Ltd), 1985
2. D. Cherns, J. de Physique IV Colloque C7, supplément au J. de Physique III, 3, 1993, p2113
3. J.M.K. Wiezorek, A.R. Preston, S.A. Court, H.L. Fraser and C.J. Humphreys, Phil. Mag. A, 69, 1994, p285
4. R. Vincent, J. Electron Microscopy Technique, 13, 1989, p40
5. D. Cherns and A.R. Preston, Proc. 11th ICEM, Kyoto, (Tokyo:JSEM) 1986, p721
6. M. Tanaka, M. Terauchi and T. Kaneyama, Convergent Beam Electron Diffraction-II (Tokio:JEOL Ltd), 1988
7. Useful discussion with Dr. A.R. Preston and financial support from the NSF are acknowledged.

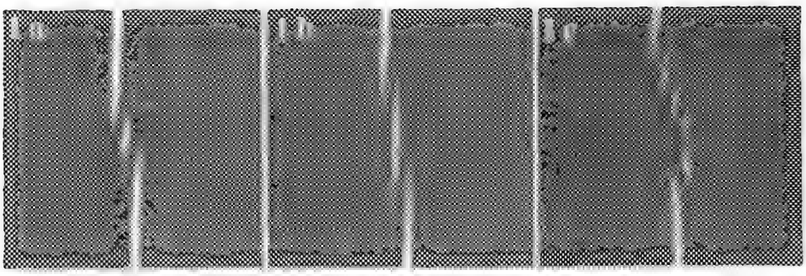

FIG. 1
Dark field LACBED simulations for a (a) screw, (b) edge and (c) decorated edge dislocation, **g.b**=2, precipitate radius r=10nm, misfit ∂=3%.

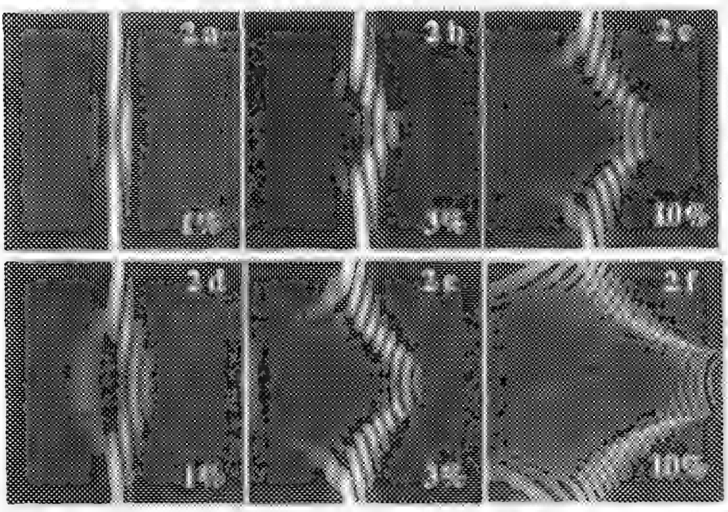

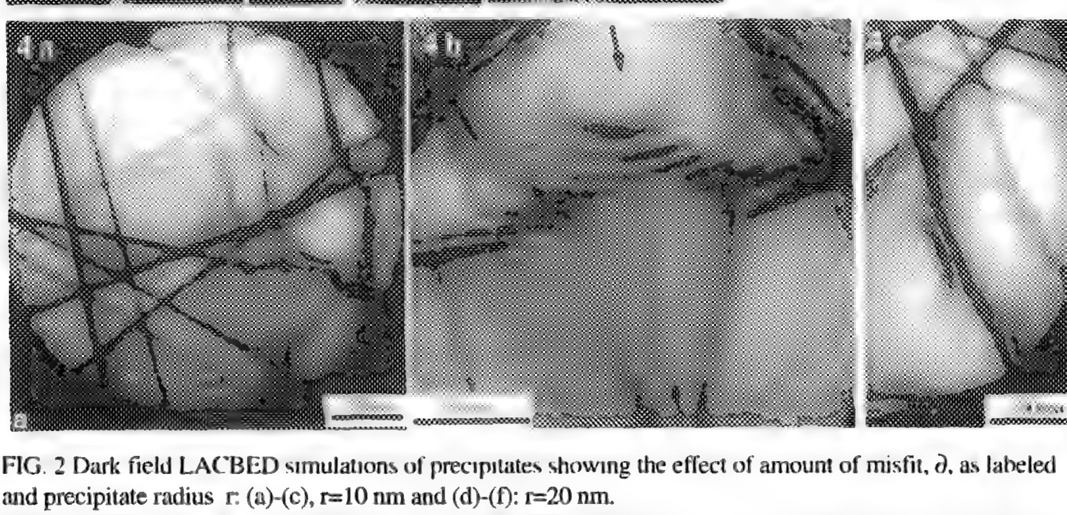

FIG. 2 Dark field LACBED simulations of precipitates showing the effect of amount of misfit, ∂, as labeled and precipitate radius r: (a)-(c), r=10 nm and (d)-(f): r=20 nm.

FIG. 3 Detail of experimental bright field LACBED disk obtained for a decorated dislocation in TiNi foil.

FIG. 4 (a) 600nm diameter bright field LACBED disk from a TiAl foil containing a 40 nm diameter precipitate, (b) detail of precipitate contrast and (c) contrast obtained for a dislocation dipole in the same TiAl foil.

HIGH-RESOLUTION OBSERVATIONS OF METASTABLE γ' PRECIPITATION IN Al-15at.%Ag

N. V. Larcher and I. G. Solórzano

Department of Materials Science and Metallurgy, Cath. University of Rio de Janeiro
C.P. 38008 - Gávea, 22452 Rio de Janeiro, Brazil.

It is currently well established[1] that, for an Al-Ag alloy quenched from the α phase and aged within the metastable *solvus*, the aging sequence is: supersaturated $\alpha \rightarrow$ GP zones $\rightarrow \gamma' \rightarrow \gamma$ (Ag_2Al). While GP zones and plate-shaped γ' are metastable phases, continuously distributed in the matrix, formation of the equilibrium phase γ takes place at grain boundaries by discontinuous precipitation (DP). The crystal structure of both γ' and γ is hcp with the following orientation relationship with respect to the fcc α matrix: $\{0001\}_{\gamma',\gamma} // \{111\}_{\alpha}$, $<1120>_{\gamma',\gamma} // <110>_{\alpha}$.

The mechanisms and kinetics of continuous matrix precipitation (CMP) in dilute Al-Ag alloys have been studied in considerable detail. The quantitative description of DP kinetics, however, has received less attention. The present contribution reports the microstructural evolution resulting from aging an Al-Ag alloy with Ag content higher than those previously reported in the literature, focusing the observations of γ' plate-shaped metastable precipitates.

The alloy used for this investigation, Al-15at.%Ag, was prepared from high purity components by induction melting under purified Ar followed by chill-cast. Slabs, intended for both SEM and TEM studies, were cold rolled and then heat-treated according to the following sequence: solution treatment at 540°C for 3h, followed by quenching in ice-water and finally an isothermal aging at several temperatures ranging from 250 to 400°C. The solution treatment generated a fully recrystallized microstructure with a grain size of about 60 μm. After thinning in a 30% nitric acid/methanol solution at -30°C and cleaning by low-angle Ar ion beam bombardment at 2 kV, the samples were examined in a Jeol 200 CX and in a Topcon 002B TEM operating at 200kV.

A general view of the resulting microstructure from a solution anneal-quenching-and-aging treatment is shown in Fig. 1. It can be seen that the aging conditions have allowed the generation of both continuous and discontinuous precipitate products. The continuous matrix precipitation (CMP) of γ' rapidly takes place and grows in a plate-like shape with size and interplate distance proportional to the aging temperature, as shown in Fig. 2.

Detailed HREM observations of γ' precipitates have revealed some evidence of solid state branching mechanism occurring during the plate growth process. Fig. 3a shows two edge-on plates at the contact region. The small objective aperture (OA) used here has allowed enough diffracted beams to generate a lattice image while it has still been possible to resolve some local strain field contrast, suggesting the presence of misfit dislocations. With a large OA, the image of the same area (Fig. 3b) shows, in fact, some local bending of the atomic planes necessary to accommodate the misfit. This observation has not been mentioned in the literature and invites further investigation.[2]

References:

1. G. Lorimer in *Precipitation Processes in Solids*, The Metall. Soc. of AIME. (1978) 87.
2. The authors are indebted to Prof. W. Gust at Max Planck-Institut, Stuttgart, Germany, for providing the alloy and to Prof. J. B. Vander Sande at MIT, Cambridge, USA, for providing HREM facilities. This research is supported by CNPq and FINEP (Brazil).

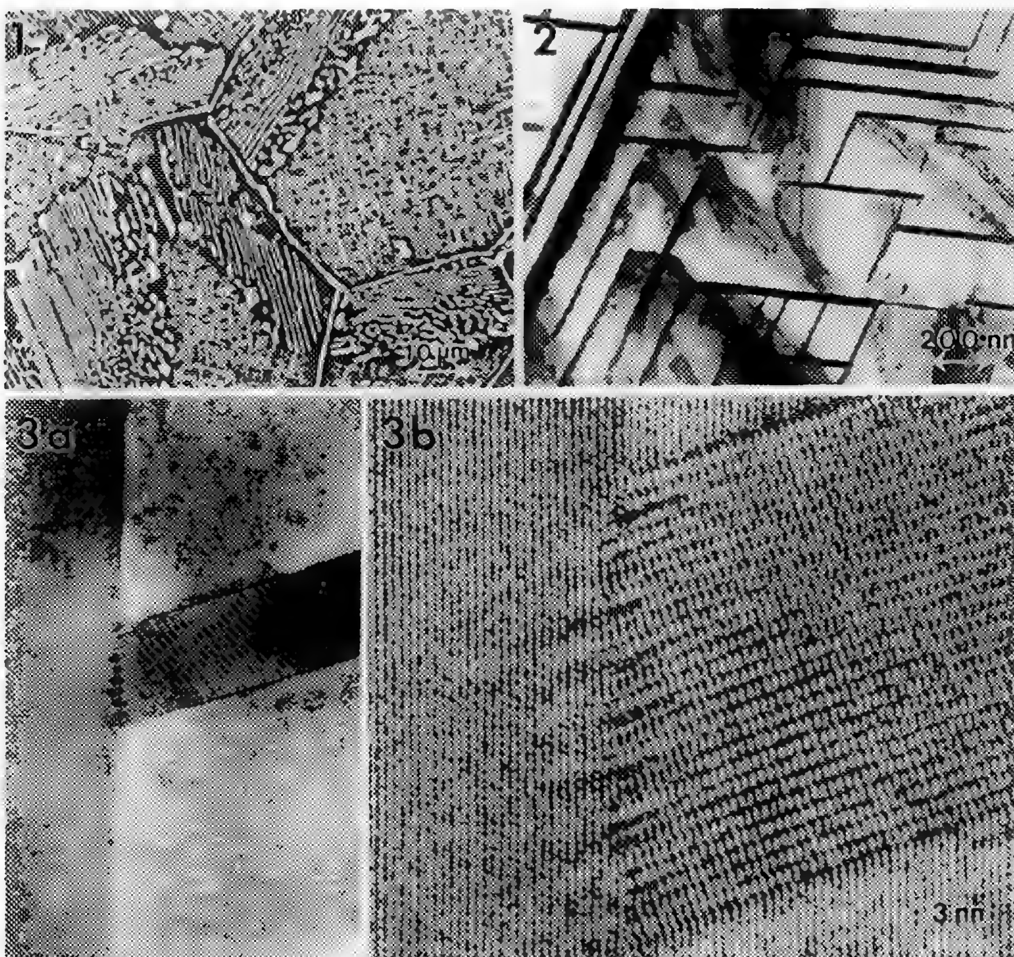

Fig. 1 - Microstructure after aging at 400°C/3h showing DP and CMP products. SEM
Fig. 2 - Continuous matrix precipitation of γ' after aging at 350°C/3h TEM
Fig. 3a - Lattice image with strain field contrast at two γ' plate junction.
3b - HREM showing local atomic plane bending at the γ' junction.

HIGH-RESOLUTION ELECTRON-MICROSCOPY INVESTIGATION ABOUT EFFECT OF STRESS ON FORMATION OF ω–PHASE CRYSTALS IN β–TITANIUM ALLOYS

E. Sukedai, M. Shimoda+, A. Fujita*, H. Nishizawa* and H. Hashimoto

Faculty of Engineering, Okayama University of Science, Okayama 700, Japan
+: Graduate School, Okayama University of Science, Okayama 700, Japan
*: Undergraduate School, Okayama University of Science, Okayama 700, Japan

ω–phase particles formed in β–titanium alloys (bcc structure) act important roles to their mechanical properties such as ductility and hardness. About the ductility, fine ω–phase particles in β–titanium alloys improve the ductility, because ω–phase crystals becomes nucleation sites of α–phase and it is well known that (β+α) duplex alloys have higher ductility(1). In the present study, the formation sites and the formation mechanism of ω–phase crystals due to external stress and aging are investigated using the conventional and high resolution electron microscopy.

A β–titanium alloy (Ti15Mo5Zr) was supplied by Kobe Steel Co., and a single crystal was prepared by a zone refining method. Plates with {110} surface were cut from the crystal and were pressured hydrostatically, and stressed by rolling and tensile testing. Specimens for aging with tensile stress were also prepared from Ti20Mo polycrystals. TEM specimens from these specimens were prepared by a twin–jet electron–polishing machine. A JEM 4000EX electron microscope operated at 400kV was used for taking dark field and HREM images.

Fig. 1 shows a HREM image of a specimen pressurized hydrostatically at 1.5GPa and an ω–phase structure can be seen. The average size is about 5nm x 3nm. Fig.2 shows a deformation twin boundary, introduced by a tensile test. Analysis of its diffraction pattern indicates that the operated twin system is {112}<111> one. The HREM image shows ω–phase structures are formed along the wide range of twin boundary. It seems that the twin boundary due to this deformation twin system is suitable for the formation site of ω–phase crystals. Small ω–phase particles also can be seen in HREM images of a specimen rolled to 5% reduction,. These results mentioned above suggest the compressive stress has an important role to form ω–phase crystals. This conclusion seems to be reasonable, because when ω–phase are formed, the volume of the specimen decreases(2). Fig.3 shows some results from a specimen, which was rolled to 5% reduction and then aged for 14.4ks at 623K. Fig.3(a) shows a dark field image. Dislocation lines can be seen clearly. Fig.3(b) shows a dark field image taken using a diffraction spot of ω–phase crystals, and the contrasts corresponding to dislocation lines shown in Fig.3(a) also can be seen. As compared Figs.3(a) with (b), it is found that ω–phase crystals precipitate at the dislocation lines. It is found that dislocation lines become one of the formation sites of ω–phase crystals in aging process. Fig.4 shows the result about the effect of stress operated in the aging process. Figs.4(a) and (b) show dark field images of Ti20Mo alloy aged for 12.6ks without stress and with a tensile stress of 412MPa, respectively. The comparison between both images indicates the density of ω–phase particles in Fig.4(b) is higher than that in Fig.4(a). It seems that a tensile stress activates the nucleation process of ω–phase transformation during the aging.

References:
(1) C. Ouchi, H. Suenaga and Y. Kohsaka: *6th World Conference on Titanium, Les Editions de Physique*, (1988), 819.
(2) F. Brotzen, E. L. Harmon Jr. and A. R. Troiano: Trans AIME 203 (1955) 413.

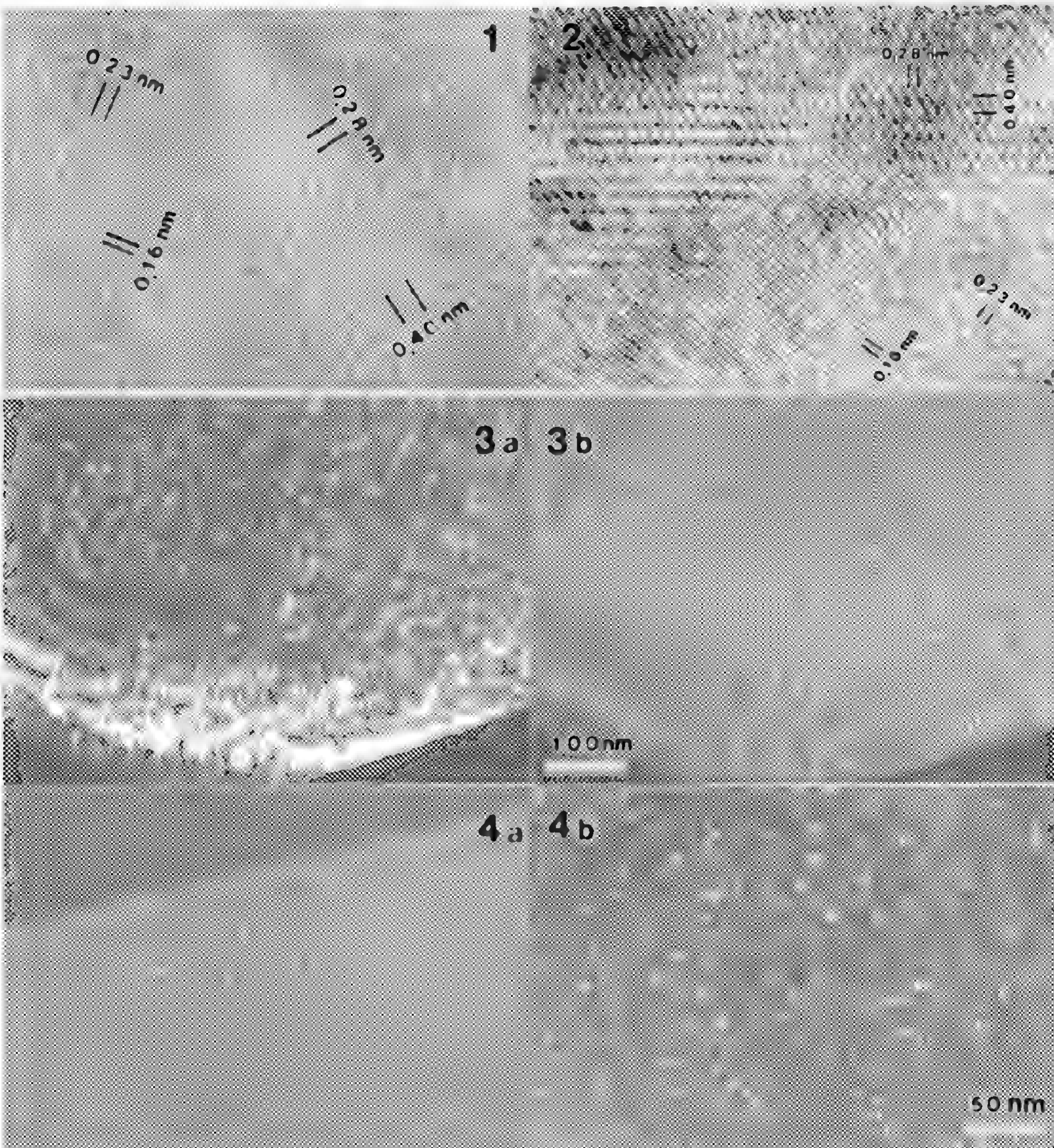

FIG.1 A HREM image of Ti15Mo5Zr, pressurized hydrostatically at 1.5GPa.
FIG.2 A HREM image of a twin boundary in Ti15Mo5Zr deformed by tension. ω–phase structure can be seen along the wide range of twin boundary. M: matrix, T: twin band.
FIG.3(a) A dark field image of a specimen, rolled to 5% reduction and then aged at 623K. (b) A dark field image at the same place, taken using an ω–phase spot. White ellipsoids are ω particles.
FIG.4 Dark field images of Ti20Mo alloy aged for 12.6ks without stress in (a) and with a tensile stress in (b).

CHARACTERIZATION OF PRECIPITATES OF Ti_3Al IN A TITANIUM ALLOY

X.D. Zhang*, J.M.K. Wiezorek*, D.J. Evans† and H.L. Fraser*

* The Ohio State University, Department of Materials Science and Engineering, 2041 College Rd., Columbus, OH 43210;
† Materials Directorate, Wright Laboratory, WL/MLLM, Wright Patterson AFB, OH 45433;

A two phase alpha-beta titanium alloy, Ti-6Al-2Mo-2Cr-2Sn-2Zr-0.2Si (Ti-6-22-22S), has recently been reconsidered as a high temperature material for aircraft engine applications. This alloy exhibits specific strength and fracture toughness superior to those of Ti-6Al-4V. However, similar to other alpha-beta titanium alloys, microstructural stability is one of the major concerns regarding industrial application of Ti-6-22-22S, since changes of the microstructure during long term high temperature exposure significantly affect the performance of components[1]. Two types of precipitates have been observed in Ti-6-22-22S alloys, namely silicides and alpha 2-Ti_3Al [2]. The presence of intermetallic precipitates, such as alpha 2-Ti_3Al, in the parent alpha matrix has been reported to result in brittle behaviour of the alpha-beta alloys due to the formation of intense planar slip bands[3]. The present paper presents results of the characterization of intermetallic alpha2-Ti_3Al precipitates in the alpha phase by methods of scanning and transmission electron microscopy (SEM and TEM respectively).

The samples studied here have been exposed to a commercial heat treatment which previously has been shown to generate alloys with properties particularly suitable for fracture critical applications[4]. The three steps of this heat treatment involved (i) a beta solution treatment, (ii) an (alpha + beta)-solution treatment and (iii) aging. The characteristic microstructure of Ti-6-22-22S after the heat treatment consists of alpha platelets in a Widmanstätten orientation with transformed beta phase as shown in the SEM micrographs of Fig. 1. The higher magnification detail depicted in Fig. 1(b), reveals that the transformed beta phase contains thin acicular alpha plates which formed during the final aging stage of the heat treatment. The many-beam bright field TEM micrograph shown in Fig. 2(a) details the Widmanstätten-like microstructure with the constituent phases as labeled. Interestingly, under many-beam imaging conditions the alpha matrix exhibits mottled contrast, (Fig. 2(b)). Long time exposure selected area diffraction patterns (SADP) have been obtained from the alpha phase region for the $[0001]_\alpha$ and $[11\bar{2}0]_\alpha$ zone axes (Fig. 3). These SADP clearly reveal the presence of superlattice reflections which can be indexed consistent with alpha2-Ti_3Al phas. A comparison of a conventional two-beam bright field and an off-axis dark field micrograph of the alpha phase is presented in fig. 4. The line defect imaged in fig. 4 can be used as a recognizable landmark. Unlike the many-beam image of Fig. 2(a), the conventional two-beam bright field image of Fig. 4(a) shows uniform contrast. The dark field image (Fig. 4(b)) has been formed using a superlattice reflection from the alpha 2-Ti_3Al phase and revealed a homogenous dispersion of small strongly diffracting speckles which correspond to second phase precipitates. Thus, it can be concluded that the mottled contrast observed under many-beam conditions for the alpha phase regions is due to small alpha 2-Ti_3Al precipitates about 1.0-2.0 nm in size and distributed uniformly throughout the alpha matrix. Furthermore, the reasonably large number density of these very small alpha 2-precipitates is consistent with the SADP obtained from the alpha phase regions (Fig. 3).

The observed dispersion of small, brittle intermetallic precipitates is expected to have a detrimental effect on the fracture performance of Ti-6-22-22S. Hence, it is important to ascertain the origin of this precipitation phenomenon. The results of investigations of the alpha2 precipitates by high spatial resolution microanalysis and high resolution electron microscopy, which are currently in progress, will also be presented.

References

1.G. W. Kuhlman, K. A. Rohde and A. K. Chakrabarti, Proc. of 7th Int. Titanium Conf., San Diego, 1992
2.D. J. Evans, T. F. Broderick, J. B. Woodhouse and J. R. Hoenigman, Proc. of 8th Int. Titanium Conf., Birmingham, 1995

3. A. P. Woodfield, P. J. Postans, M. H. Loretto and R. E. Smallman, Acta Met. , 36, 1988, p507
4. J. R. Wood and H. R. Phelps, Proc. of 123rd TMS Meeting, San Francisco, 1994
5. Financial support for this research from the Air Force Wright Laboratory, Materials Directorate, is gratefully acknowledged.

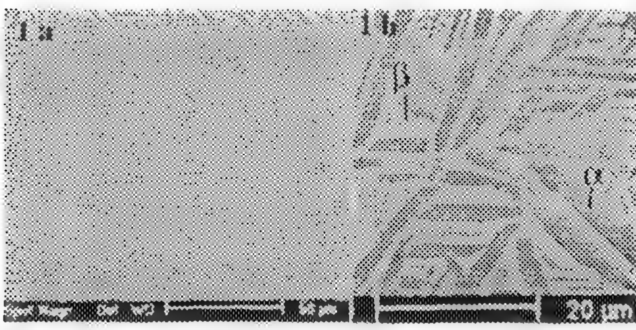

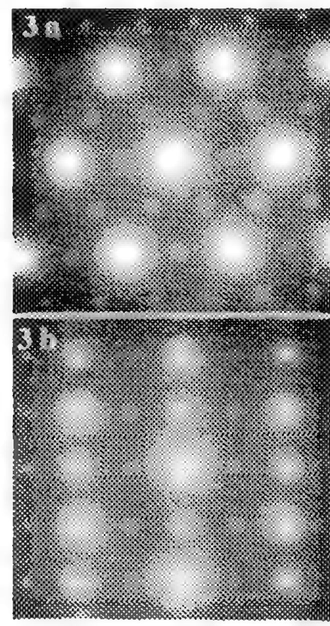

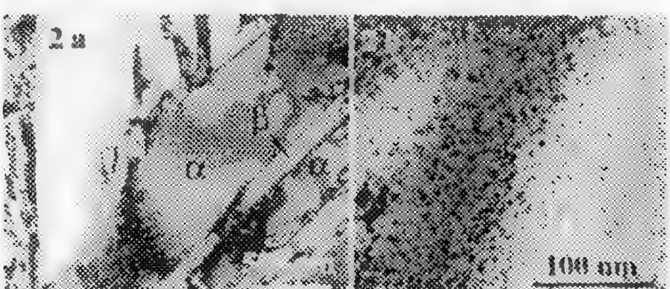

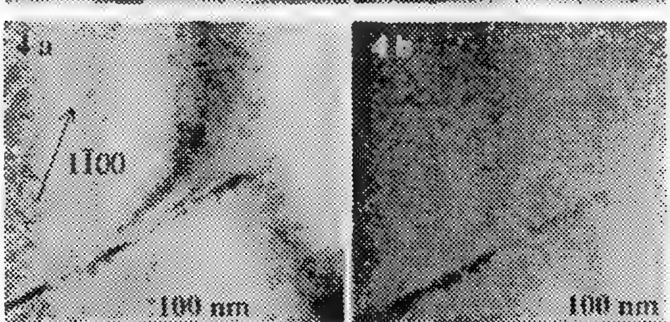

FIG. 1 Back scatter electron SEM micrographs of the alloy microstructure: (a) overview and (b) detail. The darker and brighter regions correspond to the alpha and beta regions respectivly.
FIG. 2 Many beam bright field TEM micrographs: (a) overview and (b) detail of the alpha phase region.
FIG. 3 SADP from the alpha phase region at the [0001] and $[11\bar{2}0]$ zone axes.
FIG. 4 (a) Two beam bright field and (b) off-axis dark field micrographs, where the latter employed a superlattice reflection for image formation.

MICROSTRUCTURE OF AGED Ni-Mo (Ni/Mo = 4) ALLOYS CONTAINING Al

Elaine Shen, Charlie R. Brooks and E. A. Kenik†

Materials Science and Engineering Department, The University of Tennessee, Knoxville, TN 37996, †Metals and Ceramics Division, Oak Ridge National Laboratory, Oak Ridge, TN 37831-6376.

Ni-rich Ni-Mo alloys containing around 20 at. % Mo exist as a face-centered cubic, short-range ordered (SRO), solid solution (α) above around 868 °C, and transform to a long-range ordered (LRO), body-centered tetragonal structure (β) upon cooling slowly to below this temperature. Upon quenching, the α is retained, which can then be converted to β upon aging below 868 °C. The formation of the β structure induces considerable strengthening (e.g., the hardness doubles), but is accompanied by embrittlement.[1]

A commercial alloy based on this composition is Hastelloy B2, and precautions are exercised in its use to prevent ordering and hence embrittlement. In a continuing effort to develop Ni-Mo alloys strengthened by ordering but with usable toughness, we have been examining the addition of Al to the base Ni-25 at. % Mo composition. Specimens containing 2, 5, 7 and 9 at. % Al, with Ni/Mo = 4.0, were made by arc melting the appropriate amounts of a Hastelloy B2 alloy and Al. The buttons were melted several times under an argon atmosphere. They were sealed in evacuated quart tubes and homogenized for several hours around 1100 °C, then water quenched. The buttons were sectioned into small specimens which were then aged. Thin discs were electrochemically thinned locally to electron transparency. They were examined in a Philips CM12 electron microscope with EDXA capabilities.

A convenient way to follow the structural decomposition of α is to examine the 001 electron diffraction pattern (referred to the fcc lattice). In the as-quenched condition, the retained α has a SRO structure which produces diffuse spots at the locations shown in Fig. 1a. As the α decomposes to a fine dispersion of LRO β domains, superlattice spots appear and the SRO spots weaken (see Fig. 1b). Finally, a well developed LRO diffraction pattern appears (Fig. 1c). In this paper, we present examples of the 001 patterns and associated microstructures characteristic of the Ni-Mo-Al alloys.

In the Hastelloy B2 base alloy, only SRO spots (as in Fig. 1a) were found in the as-quenched condition. Upon aging, the α decomposed into a fine β domain structure. In the alloys containing Al, the microstructure did not show α, probably due to inadequate cooling rate, but consisted of a fine microstructure, such as shown in Fig. 2a. The 001 diffraction patterns (Fig. 2b) indicate a microstructure of DO_{22} domains. In the as-quenched condition, the hardness was typically 430 Vickers. Upon aging the 7 % Al alloy for 100 h at 750 °C, the microstructure (Fig. 3a) appears similar to that of the as-quenched condition. The 001 diffraction pattern in Fig. 3b shows that the microstructure consists of domains of Ni_2Mo and DO_{22}. In this aged condition, the hardness has increased to about 590 Vickers.[2]

References
1. C. R. Brooks, J. E. Spruiell and E. E. Stansbury, Int. Metall. Rev., 29, 210 (1984).
2. Research at the Oak Ridge National Laboratory (ORNL) SHaRE User Facility was partially supported by the Division of Materials Science, U. S. Department of

Energy under contract DE-AC05-96OR22464 with Lockheed Martin Energy Research Corp. and DE-AC05-76OR00033 with Oak Ridge Associated Universities.

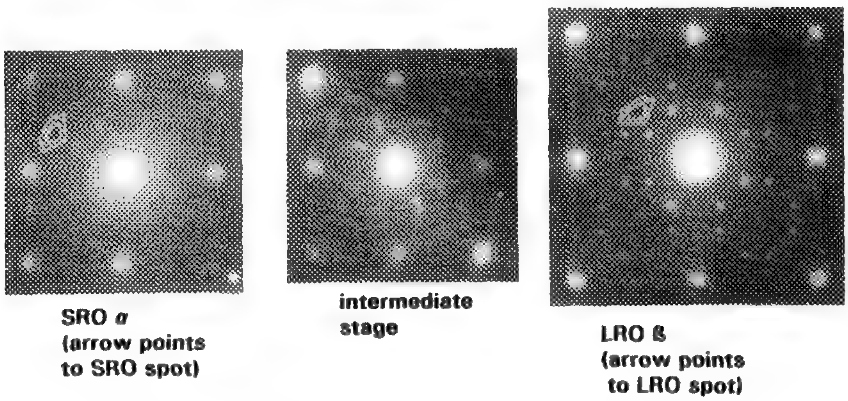

FIG. 1. 001 electron diffraction patterns for Ni-20 at. % Mo.

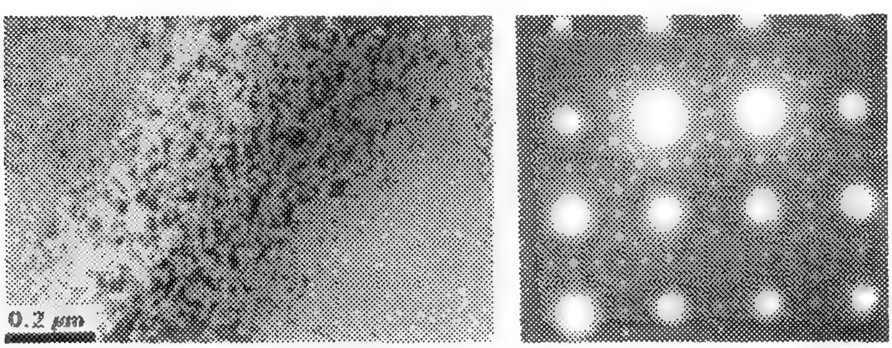

FIG. 2. Microstructure and diffraction pattern for as-quenched 7 at. % Al alloy.

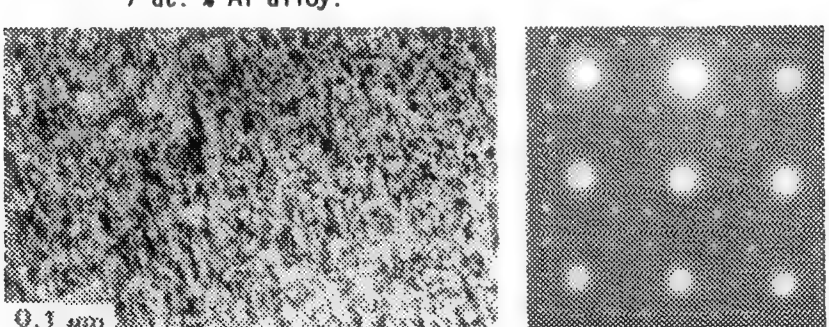

FIG. 3. Microstructure and diffraction pattern for the 7 at. % Al alloy aged for 100 h at 750 °C.

PARTITIONING BEHAVIOR OF ALLOYING ELEMENTS IN PWA 1484

M. K. Miller, L. S. Lin*, A. D. Cetel*, H. Harada° and H. Murakami°

Metals and Ceramics Division, Oak Ridge National Laboratory, Oak Ridge, TN 37831-6376; *Pratt and Whitney, Materials Engineering, East Hartford, CT 06108; °National Research Institute for Metals, Tsukuba 305, Japan.

In order to achieve a desired set of properties, such as high creep strength and oxidation resistance, a variety of alloying elements are typically added to commercial nickel-based superalloys. Since single crystal superalloys do not require the inclusion of alloying elements to improve the grain boundary properties, there is significant scope in optimizing the composition and heat treatment of these alloys. The effectiveness of these alloying elements depends on their level and location in the different phases present in the microstructure. Therefore, it is desirable to be able to accurately measure and theoretically predict their distribution within the microstructure.

The partitioning behavior of the alloying elements in nickel-based superalloy PWA 1484 has been determined with the atom probe field ion microscope. These results have been compared with predictions generated from the "Alloy Design Program". This computer program is based on regression analysis.[1] Of particular interest were the characterization of the partitioning behavior of hafnium between the γ' L_{12}-ordered precipitates and the γ disordered face centered cubic matrix and the clustering behavior of the rhenium atoms in the γ matrix.

The nominal composition of the single crystal PWA 1484 material used in this investigation was Ni-10.5 at. % Co, 6% Cr, 1.3% Mo, 2.0% W, 12.9% Al, 3.0% Ta, 0.04% Hf and 1.0% Re. All compositions quoted are given in atomic percent. The superalloy was examined after a standard heat treatment of 4 h at 1304°C, 4 h at 1079°C and 24 h at 704°C. Specimen temperatures of between 50 and 60K and a pulse fraction of 20% were used for the compositional determinations in the ORNL energy-compensated atom probe field ion microscope.[2]

The average compositions of the γ' precipitates and the γ matrix were experimentally determined in the atom probe and are shown in Table 1. A series of estimates of the compositions of the γ and γ' phases was also determined with the use of the model specifically for the nominal composition of this PWA 1484 alloy. The results for each of the 3 stages of the heat treatment for the γ and γ' phases are summarized in Table 2. It should be noted that the volume fraction of the γ' phase increases with decreasing temperature. In all cases, the expected partitioning of the alloying elements between the γ and γ' phases was found. In particular, the experimental atom probe and the model results both indicate that Co, Cr, Mo, W and Re partition to the γ phase and Ni, Al, Ta and Hf partition to the γ' phase. The partitioning factors (defined as the ratios of the concentrations of the elements in the γ and γ' phases) were determined from the atom probe results and the model and are summarized in Table 3. The atom probe results for Co, Mo, W, Al, Hf and Re are in reasonable agreement with the model. The results for chromium appear to be slightly over predicted and those of tantalum are slightly under predicted by the model. However, it is also possible that the equilibrium compositions had not been fully attained after 24 h at 704 °C in the real material. As in previous atom probe studies of this and other nickel-based superalloys, no solute enrichments were observed at the γ - γ' interfaces in the atom probe compositional data, Fig. 1, and no evidence of local enrichments were evident in the field ion images, Fig. 2.

The distribution of rhenium in the γ matrix was investigated by examination of the atom-by-atom data chains and by applying two statistical tests, namely the mean separation method and the Johnson and Klotz ordering parameter to the atom probe data.[2] In contrast to previous atom probe results,[3] neither method was able to detect the presence of rhenium clusters in the γ matrix and there was no evidence of clustering in the field ion images.[4]

1. H. Harada, K. Ohno, T. Yamagata, T. Yokokawa and M. Yamazaki, *Superalloys 1988*, eds. S Reichman, *et al.*, The Metallurgical Society, Warrendale, (1988) 733.
2. M.K. Miller and G.D.W. Smith, *Atom Probe Microanalysis: Principles and Applications to Materials Problems*, Materials Research Society, Pittsburgh, PA (1989).
3. D. Blavette, P. Caron and T. Khan, *Scripta Metall.*, **20** (1986) 1395.
4. Research partially supported by the Division of Materials Sciences, U.S. Department of Energy under contract DE-AC05-96OR22464 with Lockheed Martin Energy Research Corp. and through the SHaRE Program under contract DE-AC05-76OR00033 with Oak Ridge Associated Universities.

TABLE 1. Phase compositions experimentally measured in the atom probe.

γ phase	Co	Cr	Mo	W	Al	Ta	Hf	Re
Average	22.8	16.9	2.8	3.2	3.2	0.28	0	3.7
γ′ phase	Co	Cr	Mo	W	Al	Ta	Hf	Re
Average	6.1	2.1	0.9	2.6	23.5	6.2	0.08	0.27

TABLE 2. Predictions of the phase compositions by the linear regression model.

γ phase	Co	Cr	Mo	W	Al	Ta	Hf	Re
1304°C	10.6	5.98	1.30	2.03	12.9	2.99	0.03	1.00
1079°C	13.6	10.0	2.14	2.44	8.20	1.32	0.01	1.93
704°C	25.5	19.7	2.94	2.54	1.74	0.54	0	3.13
γ′ phase	Co	Cr	Mo	W	Al	Ta	Hf	Re
1304°C	8.63	2.20	0.33	1.34	15.7	7.75	0.13	0.09
1079°C	7.86	2.38	0.55	1.67	17.1	4.47	0.06	0.18
704°C	5.59	1.42	0.75	1.86	16.6	3.81	0.05	0.29

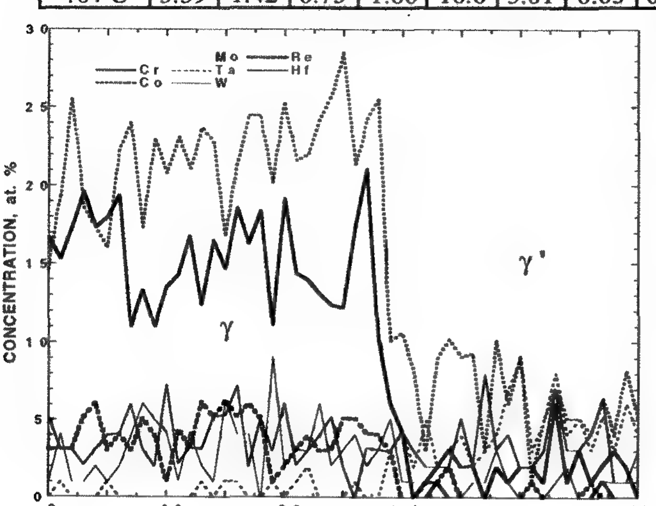

FIG. 1. Composition profile through a γ - γ′ interface.

TABLE 3. Comparison of the partitioning factors of γ : γ′ compositions determind from the atom probe experiments and the 704°C results from the linear regression model.

Preference γ	γ′	Atom Probe	Model
Co		3.7 : 1	4.6 : 1
Cr		8.0 : 1	13.8 : 1
Mo		3.1 : 1	3.9 : 1
W		1.2 : 1	1.4 : 1
	Al	1 : 7.3	1 : 9.5
	Ta	1 : 22.1	1 : 7.0
	Hf	1 : ∞	1 : ∞
Re		13.7 : 1	10.8 : 1

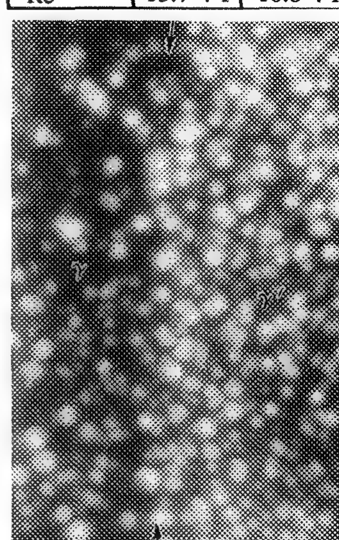

FIG. 2. Field ion micrograph of PWA 1484 after the three stage heat treatment.

INVESTIGATION OF AERMET100 SEGREGATION BEHAVIOR DURING CASTING AND HOMOGENIZATION BY QUANTITATIVE ELECTRON MICROSCOPY AND THERMODYNAMIC/KINETIC MODELING

H.E. Lippard, C.E. Campbell, V.P. Dravid, G.B. Olson

Department of Materials Science & Engineering, Northwestern University, Evanston, IL 60208, USA

Dendritic segregation of alloying elements during solidification results in non-uniform chemical and mechanical properties of steels.[1] Homogenization can reduce the composition imbalances and restore uniformnity of mechanical properties . AerMet100 is a high alloy steel produced in wrought forms by Carpenter Technology, Inc. for applications requiring a combination of high strength, high fracture toughness, and resistance to stress corrosion cracking. The nominal composition is (wt%) 13.4% Co, 11.1% Ni, 3.1% Cr, 1.2% Mo, 0.23% C, and the balance Fe. Recent studies of cast and homogenized AerMet100 have demonstrated the mechanical properties approaching the high levels of wrought AerMet100. Optimization of a homogenization treatment for elimination of the microsegregation developed during solidification was completed using thermodynamic/kinetic modeling and quantitative energy dispersive spectrometry (EDS) in scanning electron microscopy.

The as-cast alloy has the classic fern-like dendritic structure shown in Figure 1. The primary dendrite arm spacing was 150-400 μm and the secondary arm spacing was 70-110μm. The DICTRA simulation code modeled the microsegregation of the complete alloy composition from the liquid state to a completely solid austenite phase and assumed no further segregation would occur while cooling to room temperature.[2,3] EDS line profiles from a Hitachi S-4500 SEM across the secondary dendrite arm spacing of the as-cast material were conducted and compared to the DICTRA simulations. Figures 2 and 3 show the excellent agreement between the simulations and experiments for the principal segregants chromium and molybdenum.

The homogenization treatment must reduce composition variations to less than 5% across the secondary dendrite arm spacing. Homogenization treatments were conducted at 1177°C (2061°F) for 14 and 36 hours. Molybdenum microsegregation was 14% after the 14 hour homogenization treatment while chromium microsegregation is less than 5%. The 36 hour homogenization treatment reduces microsegregation to less than 5% for all elements. Figures 4 and 5 display the DICTRA predictions and experimental results of the high and low microsegregant compositions across a 100μm secondary arm spacing. DICTRA simulations predicted slower homogenization than observed experimentally.

Macrosegregation of chromium and molybdenum to the casting core was severe and was not reduced by the homogenization treatments for microsegregation. Figure 6 shows the macrosegregation level of the casting core compared to the casting body. The poster will highlight the role of quantitative EDS in the SEM for solving such microsegregation problems.

References

1. M.C. Flemings et al., *Journal of the Iron and Steel Institute*, (1970) 371.
2. B. Sundman, *CALPHAD*, 9 (1985) 153.
3. A. Engström, *Metall. Mater. Trans*, 25A (1994) 1127.
4. This work was supported by ARO Grant # DAAH04-93-G-0471/P01 and an NSF Graduate Fellowship (HL).

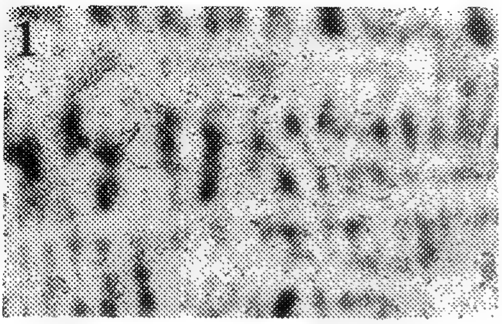

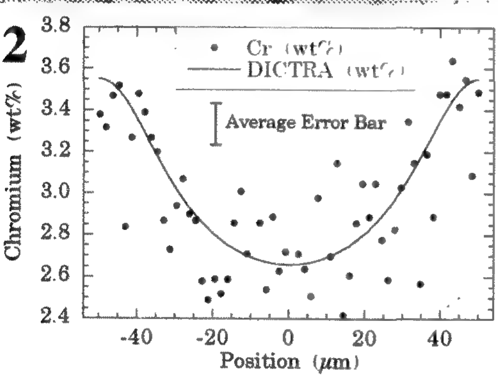

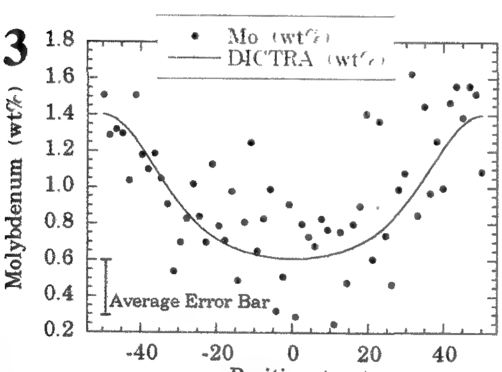

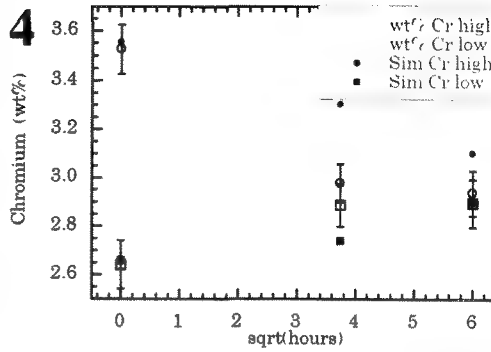

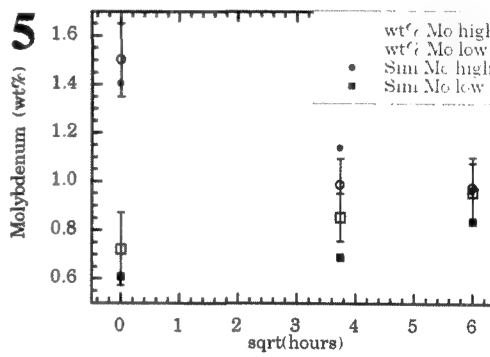

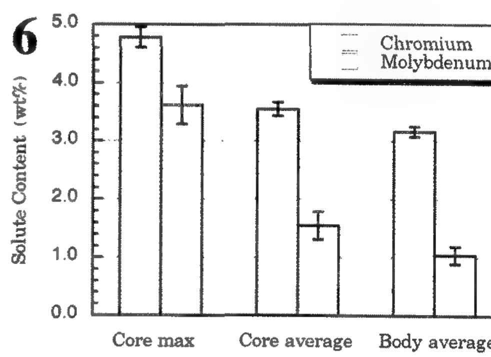

FIG. 1. - Secondary dendrite structure of as-cast AerMet100 .
FIG. 2. - Comparison of experimental and predicted chromium microsegregation across a 100μm secondary dendrite arm.
FIG. 3. - Comparison of experimental and predicted molybdenum microsegregation across a 100μm secondary dendrite arm.
FIG. 4. - Maximum chromium composition difference across a 100μm secondary dendrite arm as a function of √(time).
FIG. 5. - Maximum chromium composition difference across a 100μm secondary dendrite arm as a function of √(time).
FIG. 6. - Macrosegregation of chromium and molybdenum to the casting core.

TEM MICROSCOPICAL EXAMINATION OF THE MAGNETIC DOMAIN BOUNDARIES IN A SUPER DUPLEX AUSTENITIC-FERRITIC STAINLESS STEEL

By G. Fourlaris*, T. Gladman*, M. Maylin**, R. Lane** and G. D.Papadimitriou***

* School of Materials , The University of Leeds, Leeds LS2 9JT, U.K.
** Defence Research Agency, Holton Heath, Poole , Dorset, BH16 6JU, U.K.
*** National Technical University of Athens, Lab. of Physical Metallurgy, 15780 Athens, Greece

It is well known that, due to the good corrosion resistance[1] certain grades of stainless steels have significant applications in marine environments. For the development of certain large naval structures, in addition to the good corrosion resistance, other requirements are imposed such as high strength and toughness coupled with suitable magnetic characteristics.

It has been demonstrated in an earlier publication [2] that significant improvements in the coercivity , maximum induction and remanence values can be achieved , by using a 2205 type Duplex austenitic -ferritic stainless steel (DSS) instead of the low alloy medium carbon steels currently being used. These improvements are achieved in the as received 2205 material, and after small amounts of cold rolling have been applied, to increase the strength. In addition, the modification of the duplex austenitic-ferritic microstructure, via a heat treatment route, results in a finer austenite 'island' dispersion in a ferritic matrix and provides an attractive option for further modification of the magnetic characteristics of the material[3]. However, the 2205 type DSS exhibits "marginal" corrosion protection in a marine environment, so that a study has been undertaken to examine whether the beneficial effects exhibited by the 2205 DSS, are also present in a 2507 type super-DSS.

A 2507 type austenitic-ferritic super DSS was subjected to modest amounts of cold rolling reductions, with a view to achieving a 0.2% proof strength value of at least 700 MPa, coupled with an elongation of at least 20%. Samples of this steel were subjected to SEM and TEM examination, following the cold rolling experiments. In addition, magnetic property assessment was also carried out, in a static field, using as a reference for comparison the properties exhibited by a medium carbon low-alloy steel. In Figure 1, an SEM micrograph is presented, showing the general details of the elongated lath austenitic-ferritic microstructure. The microstructure consists only of austenite and ferrite in equal proportions. This has also been verified by TEM examination, where it can be seen that both regions exhibit a high dislocation density (Fig.2). The magnetic hysteresis loop, under a static field, is presented in Figure 3, where the hysteresis loop of a 817M40 type medium carbon low alloy reference steel of equivalent strength is also presented, to illustrate the significant differences observed in both the low maximum magnetisation value and the low coercivity achieved in the 2507 steel. It can be concluded that the presence of high amounts of ferromagnetic ferrite in the duplex microstructure does not prevent the steel from exhibiting very weak magnetic behaviour. An explanation for this behaviour can be found in the TEM micrographs of the magnetic domains present only within the ferromagnetic ferrite (Fig.4). The particular technique used for imaging the magnetic domain boundaries involved the operation of the TEM microscope in the Low magnification mode with the objective lens very weakly excited, so that in the vicinity of the sample the magnetic field is negligibly small. In Figure 4 the magnetic domain boundaries appear as bands of alternate light and dark contrast only within the ferritic regions.

It has been demonstrated that significant reductions in the maximum magnetic induction and coercivity values can be achieved when a 2507 super DSS is substituted for the conventional type of low alloy medium carbon steel. Such behaviour is due to the lamellar interwoven austenitic-ferritic microstructure that in addition provides the steel with excellent corrosion resistance and suitable mechanical properties for a marine environment. The super-DSS 2507 has very similar magnetic properties, strength, and toughness to those of the DSS 2205, but has significantly superior corrosion resistance.

References.
1. J.O.Nilsson, *Mater.Sci.Technol.*,(1992), **8**, 685.
2. G.Fourlaris and T.Gladman ,*Proc.51st Annual meeting of MSA*, (1993), 1048.
3. G.Fourlaris and T.Gladman ,*Electron Microscopy*, (1994), **2B**, 1177.
4.This work is supported by Procurement Executive , Defence Research Agency, U.K.

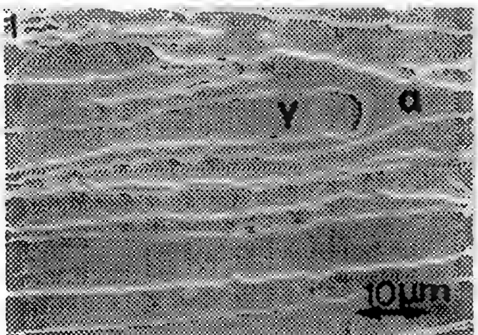

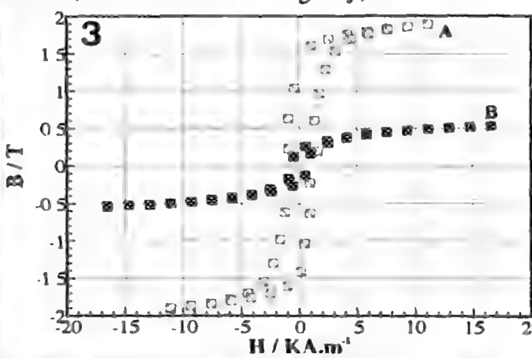

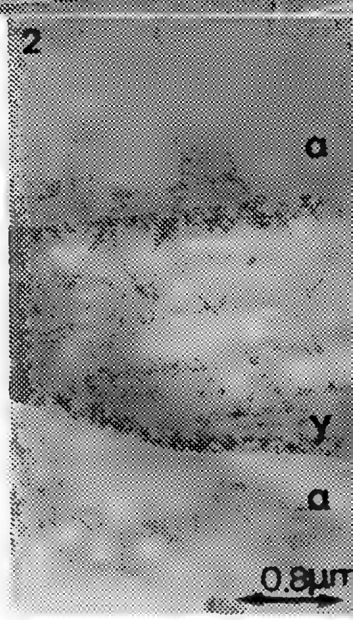

FIG.1:SEM micrograph of the 2507 type super DSS steel microstructure after 3% cold rolling.
FIG.2 : Bright field TEM micrograph of the duplex austenitic-ferritic microstructure.
FIG.3: Magnetic hysteresis loops of (**A**) the 817M40 type steel quenched and tempered at 675°C, and (**B**) of the 2507 type super DSS after 3% cold rolling.
FIG.4 : Low magnification bright field TEM micrograph of the magnetic domain boundaries within the ferritic lath regions of the 2507 type super DSS microstructure.

AN APPLICATION OF A METHOD FOR CORRELATING MECHANICAL PROPERTY CHANGES WITH MICROSTRUCTURAL CHANGES IN ION-IRRADIATED SPECIMENS

P. M. Rice and R. E. Stoller

Metals and Ceramics Division, Oak Ridge National Laboratory, P.O. Box 2008, Oak Ridge, TN 37831-6376

A method for correlating mechanical property changes and microstructural changes as a function of depth in ion irradiated specimens has been applied to a series of model pressure vessel steels. The technique employs nanoindentation with very small indent depths, on cross sectional specimens, to measure changes in hardness with sub-micron spatial resolution. Conventional TEM imaging of the cross sectional specimens allows the investigation of the defect microstructure as a function of depth below the original irradiated surface. For ion irradiations (implantations) the dose varies as a function of depth in the specimen and can be calculated with reasonable accuracy using TRIM calculations. Thus changes in both hardness and defect microstructure can be measured and correlated, over a range of doses, from a single specimen.

The technique has been applied to a set of model ferritic pressure vessel alloys to study the effect of various solutes on embrittlement. 2.5 MeV He ion irradiation was used to produce qualitatively similar microstructural features to those created in a nuclear reactor environment allowing the study to be carried out without the added complications associated with radioactive specimens. Figure 1a is an SEM image showing a set of nano-indents that starts on the left, beyond the end of range of the ions which is easily seen as the dark band. The indents eventually cross the thin oxide that marks the original irradiated surface (the white line) and enter the Fe electroplating seen here as the fine grained material at the bottom of the images. Figure 1b is a higher magnification SEM image of the same indents showing the three-sided pyramid shaped indents reflective of the Berkovich diamond used in nanoindenting. Each of these residual indents is the result of a multipule indent process. The first indent is 50nm deep to acquire the sub-micron resolution hardness data, and the second is twice as deep (thus twice as wide) to clearly mark the position of the shallower indent before moving to the next position. Figure 2a is a bright-field TEM micrograph showing the defect microstructure of the entire irradiated region of an Fe + low N alloy, taken with **g** = {330} such that the dislocation loops appear dark. Figure 2b is a plot of the actual change in hardness, ΔH, as a function of depth below the original irradiated surface at the same scale, and for the same alloy shown in figure 2a.

Comparing the results for alloys containing differing amounts of solutes allows some insight into the relative importance of each element in embrittlement, as well as defect nucleation and growth. All the copper free alloys showed a delayed onset of hardening with dose in contrast to the copper containing alloys which showed a super linear hardening with initial dose. Copper has proved to be the most significant embrittling agent, but it's apparent ability to suppress He bubble formation, even at very high He concentrations could prove useful. The addition of manganese with the copper significantly increased the hardening and also seemed to negate copper's ability to suppress He bubble formation. The addition of high concentrations of interstitial solutes, such as nitrogen and carbon, likewise seem to negate copper's ability to suppress He bubble formation. The entire technique will be discussed in detail, as well as the results from the application of the technique to the set of nine alloys irradiated with 2.5 MeV He ions. Insights into solute-defect interactions determined as a result of the technique, such as the very strong Cu-vacancy interaction, will also be discussed.

This research was performed at the ORNL SHaRE User Facility and was sponsored by the Division of Materials Sciences, U.S. Dept. of Energy and the Office of Nuclear Regulatory Research, U.S. Nuclear Regulatory Commission under interagency agreement DOE 1886-8109-8L with the U.S. Dept. of Energy under contract DE-AC05-960R22464 with Lockheed Martin Energy Research Corp., and by an appointment of P. M. Rice to the ORNL Postdoctoral Research Associates Program administered jointly by ORNL and Oak Ridge Institute for Science and Education.

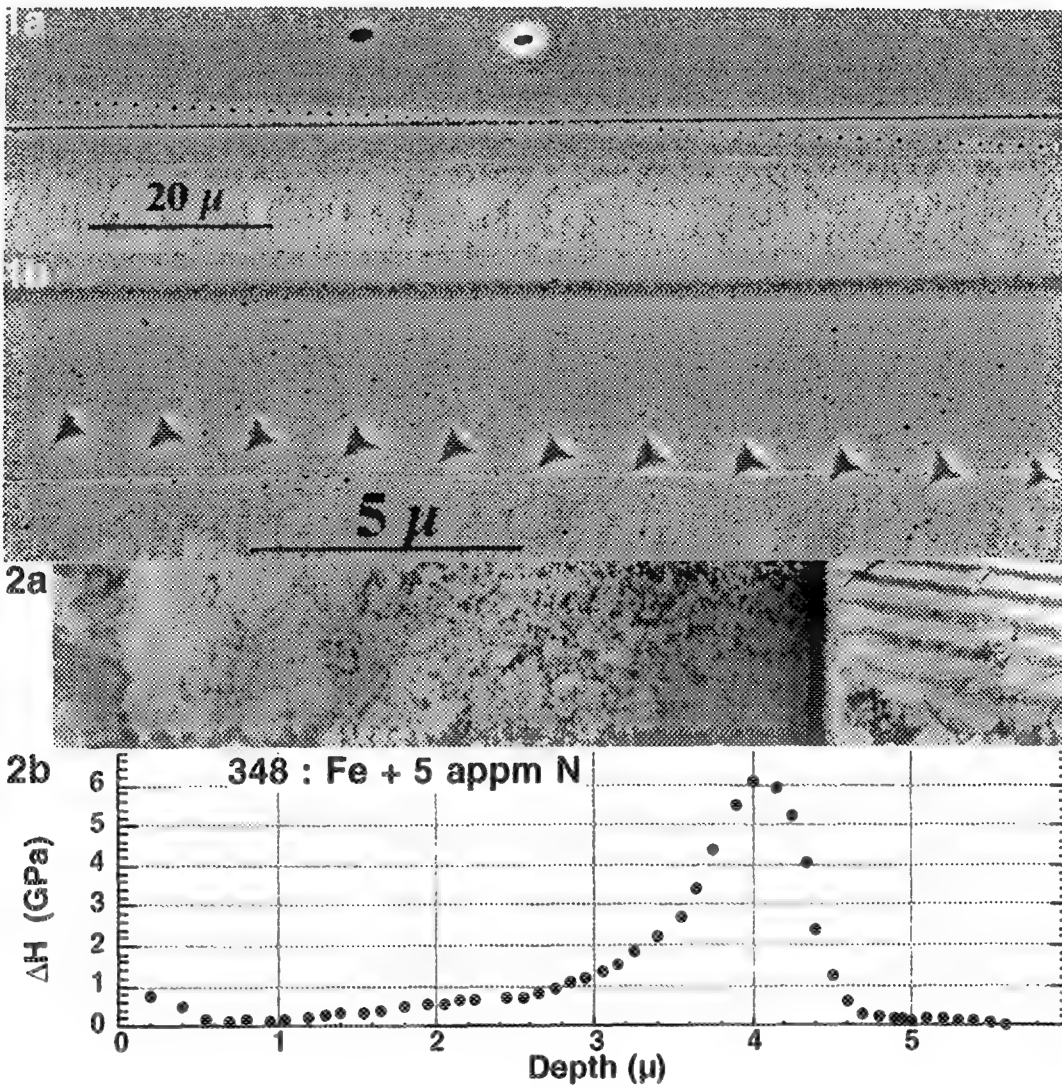

Fig. 1.- SEM images of a typical nanoindentation run on an Fe + high N alloy.
(a)low magnification SEM image to show an entire run starting, at the left, beyond the end of range of the He ions (dark band) and ending, on the right, beyond the original surface (white line).
(b) a higher magnification SEM image of the same indent run. The three sided pyramid shape of the indents is reflective of the Berkovich diamond indenter used in nanoindenting.These indents are twice as large as the indents used to measure the hardness with sub-micron spatial resolution.
Fig. 2(a).- A TEM image of the entire irradiated region of the Fe + low N alloy. Dislocation loops appear as dark spots. The scale is the same as the plot shown in 2(b)
Fig. 2(b).- Plot of the change in hardness, ΔH, as a function of depth below the original surface for the same low N alloy shown in (a).

TRANSMISSION ELECTRON MICROSCOPY STUDIES OF SOLID-STATE REACTIONS IN SPUTTER-DEPOSITED Nb/Al MULTILAYER THIN FILMS

F. Ma, S. Vivekanand, K. Barmak and C. Michaelsen*
Department of Materials Science and Engineering, Lehigh University, Bethlehem, PA 18015
* Institute of Materials Research, GKSS Research Center, D-21502 Geesthacht, Germany

Solid state reactions in sputter-deposited Nb/Al multilayer thin films have been studied by transmission and analytical electron microscopy (TEM/AEM), differential scanning calorimetry (DSC) and X-ray diffraction (XRD). The Nb/Al multilayer thin films for TEM studies were sputter-deposited on $(1\bar{1}02)$ sapphire substrates. The periodicity of the films is in the range 10-500 nm. The overall composition of the films are 1/3, 2/1, and 3/1 Nb/Al, corresponding to the stoichiometric composition of the three intermetallic phases in this system.

Figure 1 is a TEM micrograph of an as-deposited film with periodicity $\Lambda = d_{Al} + d_{Nb} = 72$ nm, where d's are layer thicknesses. The polycrystalline nature of the Al and Nb layers with their columnar grain structure is evident in the figure. Both Nb and Al layers exhibit crystallographic texture, with the electron diffraction pattern for this film showing stronger diffraction spots in the direction normal to the multilayer. The X-ray diffraction patterns of all films are dominated by the Al(111) and Nb(110) peaks and show a merging of these two peaks with decreasing periodicity.

DSC has been used to determine the phase formation sequence and annealing conditions of films for TEM studies. Figure 2 is a constant heating rate DSC run for free-standing films with 143 nm periodicity and 3/1 Nb/Al ratio. There are three exothermic peaks marked as A, B and C. A is determined to be the nucleation and growth to coalescence of $NbAl_3$, peak B is the normal growth of the $NbAl_3$ layer until the consumption of one or both reactants and peak C is the concurrent formation of the superconducting A15 phase $Nb_{3+x}Al$ and the sigma phase $Nb_{2+y}Al$.

Figure 3a and b are paired bright field (BF)/dark field (DF) micrographs for the film with the same periodicity and composition as the sample shown in figure 1 but annealed at 650K for 15 minutes. Comparison of the electron diffraction patterns from the as-deposited film and the annealed film indicates that the $NbAl_3$ phase has formed. The dark field image shows the formation of the $NbAl_3$ phase along the Nb/Al interface and its preferential growth along the Al-Al grain boundaries.

In order to get quantitative composition profiles (along or cross an interface) of partially or fully reacted films analytical electron microscopy (AEM) in a dedicated scanning transmission electron microscope has been used. Since $NbAl_3$ is a line compound in the Nb-Al system, it can be used as a standard of known composition to determine the Cliff-Lorimer k-factor. This k-factor relates the concentrations of constituents and intensities of their respective energy dispersive peaks via $C_{Nb} / C_{Al} = k_{NbAl} I_{Nb} / I_{Al}$. Nb(L) and Al(K) intensities have been used for this composition analysis, because their energies are close and the errors due to background subtraction are smaller. Figure 4 is a plot of $k_{Nb(L)Al(K)}$ vs. $I_{Nb(K)}$. The extrapolation of the line in figure 4 to zero Nb(K) intensity yields $k_{NbAl} = 0.448$. This value is in close agreement with the experimental k value of 0.446 determined by using the Horita et al.'s method for absorption correction[1] and also in agreement with the value of 0.489 calculated using the model of Zaluzec[2]. Figure 5 is a TEM micrograph of the films used for this k-factor determination. The as-deposited periodicity of the film was 72 nm, and the film was annealed to 1025 K at a constant heating rate of 20°C/min. The only phase present in figure 5 is the $NbAl_3$ intermetallic.

References

1. Z. Horita et al., *Ultramicroscopy*, **35** (1991) 27.
2. N. Zaluzec, *Analytical Electron Microscopy*, D.B. Williams and D.C. Joys Eds., San Francisco Press, CA, (1985) 237.
3. The authors thank Dr. Kevin Coffey for the deposition of the films. Financial support from NSF through DMR-9308651 is gratefully acknowledged.

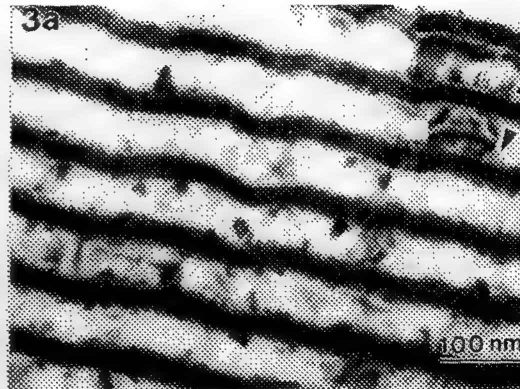

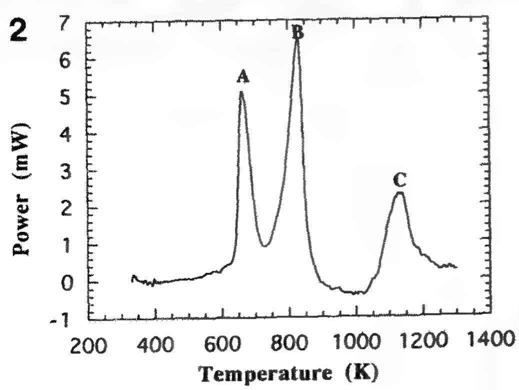

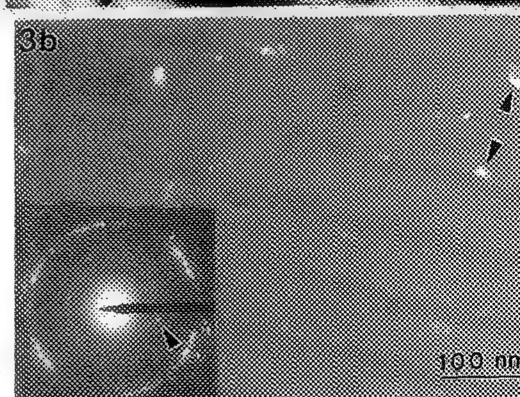

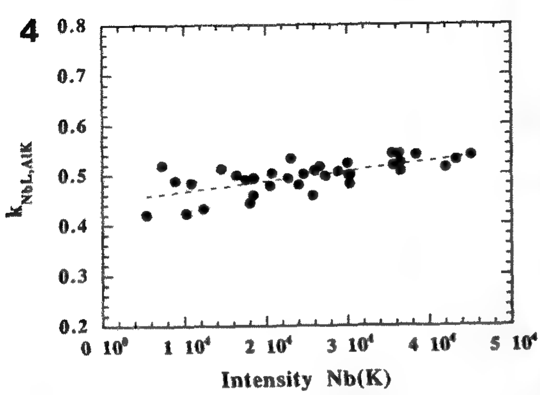

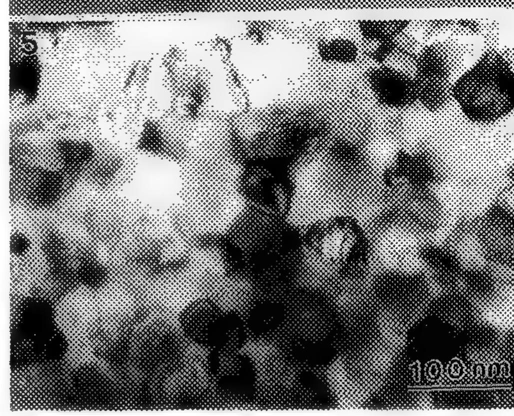

FIG. 1 TEM micrograph of an as-deposited 1Nb/3Al multilayer thin film with a periodicity of 72 nm.

FIG. 2 Heat-flux DSC trace for 3Nb/1Al multilayer thin film with Λ =143 nm annealed at 20°C/min.

FIG. 3 TEM micrographs of a 1Nb/3Al multilayer with Λ = 72 nm annealed at 650 K for 15 minute
(a) bright-field, (b) centered-dark-field using the inner diffraction rings unique to $NbAl_3$.

FIG. 4 Cliff-Lorimer k-factor for the Nb-Al system versus Nb(K) line intensity for each analysis point.

FIG. 5 Bright-filed TEM micrograph of a 1Nb/3Al multilayer annealed to 1025 K.

EFFECT OF Pt CONTENT ON COMPOSITIONAL SEGREGATION IN Co-Cr-P-Pt/Cr MAGNETIC THIN FILMS

J-H. Choi*, C. M. Sung*, K. H. Shin**, L. F. Allard***

*Center for Advanced Materials, University of Massachusetts at Lowell, Lowell, MA 01854
**Department of Advanced Materials Engineering, Korea Advanced Institute of Science & Technology, Seoul 130-012, KOREA
***High Temperature Materials Laboratory, Oak Ridge National Laboratory, Oak Ridge, TN 37831

Co/Cr alloys are among the most prominent materials for ultra-high density longitudinal magnetic recording media.[1,2] The recording and magnetic properties of the materials are related to their microstructure. It has been found that compositional segregation (CS) of the Co phase at the grain boundaries, and physical separation of Co/Cr phases are effective in producing low noise media due to low intergranular exchange coupling.[1] A series of Co/Cr alloy magnetic thin films were prepared by DC sputtering and studied using high-resolution transmission electron microscopy (HRTEM) coupled with energy dispersive x-ray spectroscopy (EDS). $Co_xCr_yP_zPt_w/Cr$ alloy thin films were deposited on circumferentially textured Ni-P/Al substrate. This substrate geometry was used to get better magnetic properties without substrate bias.[3] A Hitachi HF-2000 field emission TEM was used for imaging and to provide a 1 nm beam for high spatial resolution EDS analysis.

A TEM micrograph (Figure 1) of $Co_{83.2}Cr_{4.0}P_{12.8}/Cr$ film shows that the average grain size is about 120 nm long x 25 nm wide. The grains are in the form of slightly decoupled chains extending over several grains. The physical separation at the grain boundary was not clear across the sample. Figure 2a shows the TEM micrograph of $Co_{75.3}Cr_{3.9}P_{13.0}Pt_{7.8}/Cr$ film. Dislocations near the grain boundary which could decrease the exchange coupling between grains were observed. A schematic diagram of Figure 2a is shown in Figure 2b with grain (GR) and grain boundary (GB). EDS data in Figures 2c and 2d indicate that the grain boundary segregation of Co phase is greater when compared to the prior sample and is uniform throughout the sample. TEM micrographs show that this sample has clear physical separations compared to other samples with different Pt content. Figure 3 shows the TEM micrograph of $Co_{75.3}Cr_{3.9}P_{13.0}Pt_{7.8}/Cr$ film. The right insert in Figure 3 is a FFT image. Figure 4 shows the TEM micrograph of $Co_{67.2}Cr_{3.1}P_{10.9}Pt_{18.8}/Cr$ film. The average size of grains is unchanged and the decoupled chain structure still exists even with varying the Pt content. EDS data indicate that the grain boundary segregation is not uniform throughout the sample, and some of areas have very low Cr content when Pt content is at 18.8 at. %. This indicates that Co and Cr phases are randomly distributed. Depending upon the Pt content, the orientation of the magnetic layer changes from random orientation, at 13 at. %, to preferred (0002) at 20 at. % in the CoCrPt/Cr films.[4] It was also noted that the physical separations are not homogeneous across the sample when Pt content is at 18.8 at. %.

We conclude that the compositional segregation of Co phase at the grain boundary was at its maximum when Pt content was between 7.8 at. % -18.8 at. %. It has been demonstrated that the Pt content in Co-Cr-Pt-P alloys can be used to control the compositional segregation, which results in improved magnetic and recording properties.

References

1. T. Yogi, et. al., IEEE Trans. Magn., 26 (1990) 2271
2. M. Futamoto, et. al., IEEE Trans. Magn., 27 (1991) 5280
3. K. H. Shin, et. al., Proc. of IEEE Meeting, 1995
4. P. Glijer, et. al, J. Appl. Phys., 73 (1993) 5563
5. Research sponsored by the High Temperature Materials Laboratory User Program, DOE Office of Transportation Technologies, under contract DE-AC05-96OR22464 with Lockheed Martin Energy Research Corp.

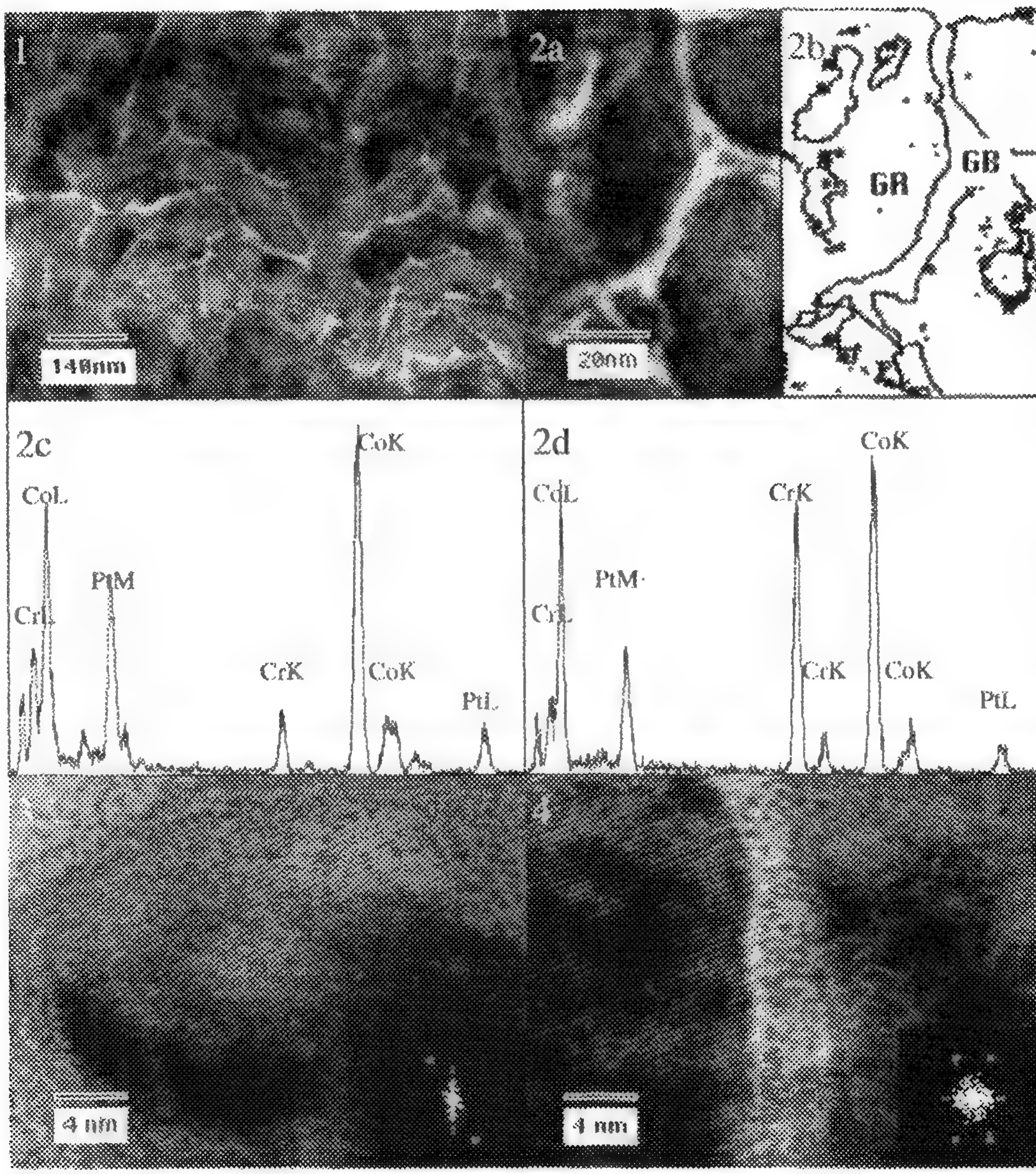

Figure 1 TEM micrograph of $Co_{83.2}Cr_{4.0}P_{12.8}$/Cr film.

Figure 2a-2d TEM micrograph (2a), schematic diagram (2b) and EDXS data (2c and 2d) of $Co_{75.3}$-$Cr_{3.9}P_{3.0}Pt_{7.8}$/Cr film showing dislocations and compositional segregation.

Figure 3 TEM micrograph and EDXS data of $Co_{75.3}Cr_{3.9}P_{13.0}Pt_{7.8}$/Cr film right insert is FFT image.

Figure 4 TEM micrograph and EDXS data of $Co_{67.2}Cr_{3.1}P_{10.9}Pt_{18.8}$/Cr film which show random orientation.

IN SITU REVERSED DEFORMATION OF PREFATIGUED ALUMINUM SINGLE CRYSTALS IN THE HVEM

M. A. Wall* and M. E. Kassner**

*M.L. TECH
**OREGON STATE UNIVERSITY

Utilizing a technique describe earlier by Wall[1] et al., prefatigued aluminum single crystals oriented for single slip, were cyclically deformed in the HVEM operating at 1.5Mev by deforming in mutually perpendicular "X and Y" directions. Deforming in X and Y avoids foil buckling and allows for shear reversal (fatigue). Initial observations are reported here and will aid in the understanding of the micro-mechanisms of cyclic deformation.

In situ specimens extracted from prefatigued single crystals (560 cycles, strain amplitude of 1.2 X 10^{-3} at 77K) were oriented in such a manner as to facilitate imaging primary dislocations, b=[0,1,-1], on the primary (111) slip plane. The (111) plane is inclined 25° about the [0,1,-1] direction to increase the projected length of these dislocations for viewing on the TEM screen. The [0,1,-1] direction is also contained in the plane of the specimen foil and is 45° to the tensile axes. The specimens are then tilted to a [1,1,-1] diffracting condition. Nonperforated specimens were prepared by a technique described by Kassner[2]. Specimens were then alternately deformed along mutually perpendicular tensile axis in the HVEM.

The results from an experiment are illustrated in figure 1. A more complete description of this experiment is reported by Kassner et al.[3]. Figure 1a, During X, loading screws A and B move within the channel and leave the foil at the surface. Screws G,H and I are formed from loops expanding from the lower bundle. Figure 1b, During Y loading screws H and G begin reversal in the channel. Loop K begins to expand from the middle dipole bundle. Figure 1c, H reverses motion during another cycle of X loading. Screws Q, P and N, which formed from loops expanding from the upper bundle, move within the channel and leave the foil at the surface. Loop R expands out of the lower dipole bundle. Edges L and M move into the viewing area and leave screw components on the surface of the foil.

The complete experiment provided several observations. First, the total plastic strain for edge and screw dislocations was calculated from the observation of 75 mobile dislocations. The results of these observations show a nearly equal contribution from screws and edges to the total strain. It appears that screws move first and easily reverse motion. Loops were frequently observed to bow out from dipole bundles and span the channels. Edges were also observed to traverse several channels leaving surface traces. Little or no cross-slip was observed. No foil bending was observed. During unloading of a cycle little or no back motion of dislocation was observed. This is consistent with a lack of back stress. No dipole flipping was observed under the conditions of these experiments. The stress to "break" dipoles is calculated and found to be comparable to the flow stress

In conclusion we have performed successful and reproducible in situ reversed deformation experiments with little or no foil bending. The ability to perform these experiments will allow us to gain further insight of the fatigue process and the Bauschinger effect. The Bauschinger effect appears to be the result of lower obstacle density on reversal rather than an internal stress.

1. M. A. Wall and M. E. Kassner, Proc. MSA (1995)248.
2. M. E. Kassner et al., J. of Microscopy Technique. 5(1987)189.
3. M. E. Kassner et al., (to be published).

We wish to thank the National Center for Electron Microscopy at Lawrence Berkeley Laboratory for their support and the use of the HVEM.

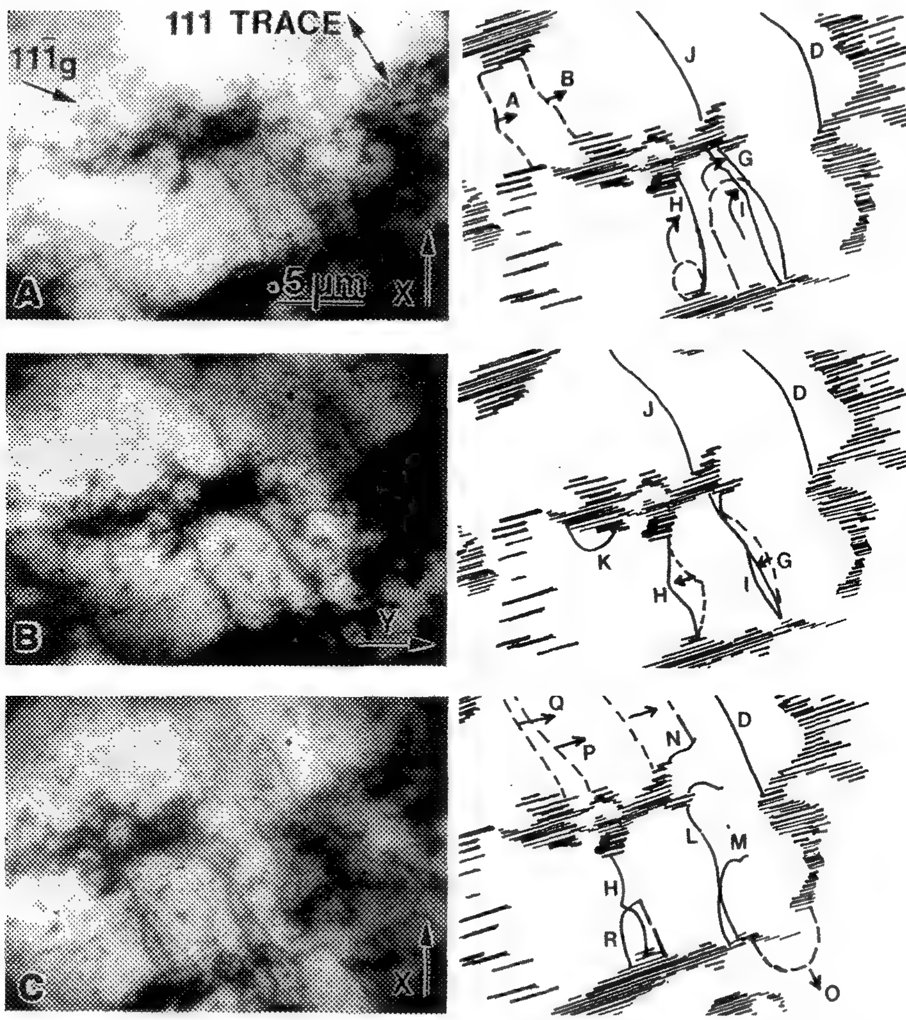

Fig. 1-(a) X axis tensile loading; (b) Y axis tensile loading; (c) X axis tensile loading.

ANOMALOUS BACKSCATTERED ELECTRON BEHAVIOR OF MoB AND Mo_5SiB_2 (T_2) PHASES IN AN AS-CAST Mo-B-Si ALLOY

J. H. Fournelle,* C. A. Nunes,**† and J. H. Perepezko**

* Department of Geology & Geophysics, University of Wisconsin-Madison, Madison, WI 53706 (johnf@geology.wisc.edu)
** Department of Materials Science & Engineering, Univ. of Wisconsin-Madison, Madison, WI 53706
† On leave from FAENQUIL/DEMAR, Lorena 12600-000 São Paulo Brazil

It is well established that backscattered electron (BSE) image contrast in SEM is primarily associated with differences in mean atomic number (Z) of the phases. The BSE coefficient increases with higher Z with slight dependence on beam energy (E_0), except for some materials at < 5 keV.[1]

We report here the anomalous BSE behavior of MoB and T_2 (Mo_5SiB_2) phases observed imaging a 60Mo-30B-10Si (at%) alloy with a CAMECA SX-50. Specifics of the material and EMPA are reported in a companion communication.[2] Mo-ss and Mo_3Si are also present. The drastic differences in BSE behavior are shown in Figures 1 (7 keV), 2 (15 keV) and 3 (25 keV). The material has not been coated; addition of 100 Å carbon does not change the observed behavior.

At 25 keV (Fig 3), MoB dendrites are the darkest phases present, the expected behavior based on their mean Z (Table 1). The T_2 matrix is gray, whereas smaller regions containing Mo+Mo_3Si have the greatest brightness. The T_2 phase also shows differences in gray levels in different regions. WDS analysis of T_2 phases show no significant compositional variations[2]; likewise, for the MoB. B and Si X-ray maps are shown in Figures 4 and 5. At 7 keV (Fig 1) some MoB dendrites demonstrate significant increases in backscattering, becoming whiter, with others remaining black and some of intermediate gray levels . Also differences in contrasts of different T_2 regions are observed. In the range of E_0 between 10 - 20 keV, some MoB dendrites are virtually indistinguishable from the surrounding T_2 phase (e.g., Figure 2).

Anomalous BSE behavior in the Al-Si system was reported by Ball, Wilson and Whitmarsh.[3] They reported an effect where the higher Z material (Si) showed a reduction in backscattered intensity with increasing E_0. There, however, the size of the silicon rods was small, ~0.25 µm, so the escape depth of backscatterd electrons was greater than the grain size. Hovington and others[4] used Monte Carlo modeling to reproduce this behavior in a small (0.25 µm) Si phase surrounded by Al, "the convolution between the interaction volume and the sample phases".

The phases we are reporting on are ≥ 25 times larger than the previously reported Al-Si phases. The MoB dendrites have an average width of 5 µm with variable lengths, and the continuous areas of T_2 are even larger — only the constant brightness Mo-ss+Mo_3Si phases are of small dimension. Monte Carlo simulations[5] suggest that the maximum depth of average backscattered electrons range from 0.15 (7 keV) to 1.1 µm (25 keV) for MoB, 0.1 to 0.83 µm for Mo, 0.3 to 3.2 µm for Mo3Si and 0.7 to 5.8 µm for T_2 (Table 1). The phenomenon we have observed cannot be explained by greater electron penetration since at 7 keV some of MoB dendrites are brighter than the surrounding T_2 which has a higher Z; with increasing E_0 and increasing electron penetration, MoB's resulting BS intensity should increase--not decrease. Nor can the differences in gray levels of T_2 in different regions of the sample be explained by this mechanism.

We suggest that electron channeling, with the (non-isotropic) phases of interest having different orientations relative to the electron beam, could possibly be responsible for the anomalous backscattered behavior.

References:

1. D. C. Joy, *Monte Carlo Modeling for Electron Microscopy and Microanalysis* (1995) Oxford Univ.
2. C. Nunes et al, MAS, these proceedings (1996)
3. M. D. Ball et al., Electron Microscopy Analysis, Inst. Phys. Conf. Ser.90 (1987) Ch. 7, 185-188.
4. P. Hovington et al., MAS Proceedings (1995), 351-352.
5. D. C. Joy, *JustBS* PC shareware computer program

Table 1

				Backscattered Electron Depth (μm)			
				Average		Maximum	
Phase	Z	At Wt	gm/cc	7 keV	25 keV	7 keV	25 keV
Mo	42.0	95.9	10.2	0.03	0.2	0.1	0.8
Mo_3Si	39.5	316	8.97	0.1	1.0	0.3	3.2
T_2	39.0	529	8.74	0.2	1.7	0.6	5.8
MoB	38.3	107	8.3	0.04	0.4	0.15	1.1

1. $T_2 = Mo_5SiB_2$
2. Mean Z's calculated by equation 6.2 in Joy (1995)
3. Densities used are the minima if more than one determination is available (e.g., MoB)
4. Backscattered electron depths (in microns) calculated using D. Joy's Monte Carlo simulation program "JustBS" with 2000-4000 trajectories

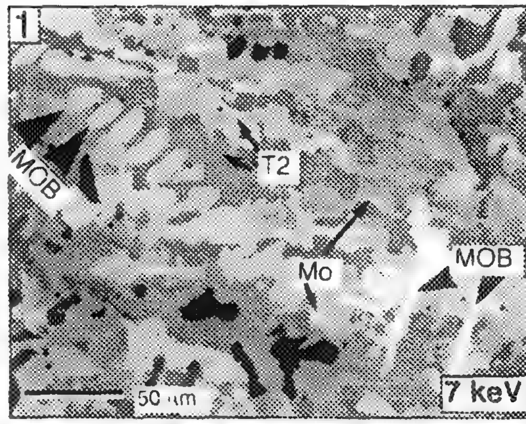

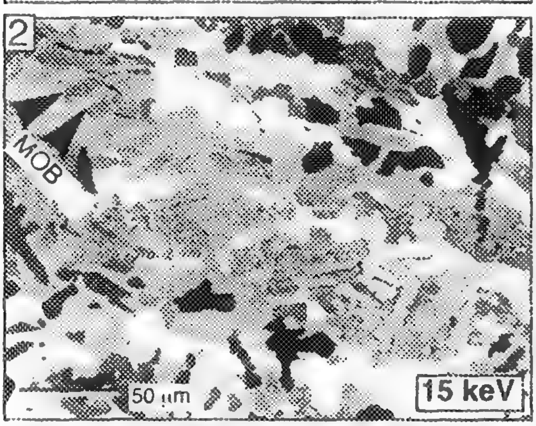

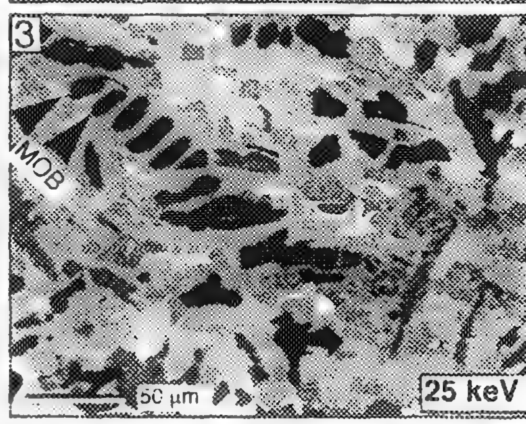

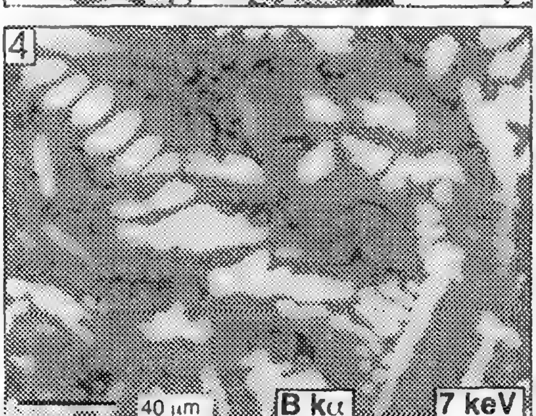

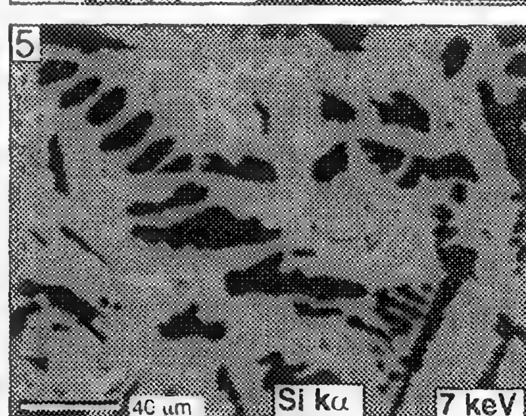

Figure 1-3. BSE images at 7, 15 and 25 keV of As-Cast 60Mo-30B-10Si alloy. Arrows indicate specific regions where MoB and T_2 anomalous BS contrasts are evident; Mo=Mo-ss+Mo_3Si
Figure 4-5. B kα (4) and Si kα (5) x-ray maps. Mo Mγ - B kα interference is negligible at these effectively low count collection conditions (512 x 512, 0.5 μm step, 100 ms 'dwell'; 7 keV, 20nA)

ENHANCED CONTROL OF ELECTROPOLISHING FOR THE PREPARATION OF THIN FOILS FOR TRANSMISSION ELECTRON MICROSCOPY: ARTIFICIAL AND MULTIPLE-PHASE MICRO-ELECTROPOLISHING

Peter J. Lee

Applied Superconductivity Center, University of Wisconsin-Madison, Madison, WI 53706

By rapidly changing voltage and current settings during electropolishing conditions can be set up for polishing otherwise difficult to polish multi-phase material. In addition a wider a more flexible range of polishing conditions can be obtained by manipulating the film build-up condition in micro-electropolishing that is normally outside the useful range of electropolishing.

Electropolishing may be broken down into two distinct processes: Macro-electropolishing or "smoothing" whereby large scale asperities are removed and Micro-electropolishing or "brightening" in which smaller (<1μm) irregularities are removed.[1] In "bath" (immersion) electropolishing both processes take place whereas in "jet" electropolishing the polishing mechanism is primarily micro-electropolishing. For micro-polishing to occur a thin solid film must be produced at the specimen surface.[2,3,4,5] In order for micro-electropolishing (sometimes called brightening or brilliance) there must be random removal of metal from the surface irrespective of features such as grain-boundaries, grain orientation and defects. A number of different theories have been applied to the exact process by which the film is formed and maintained and its composition[5,6,7,8] but again in simplistic terms as soon as the solid (typically) oxide layer is formed the removal rate is determined by the interaction between the solid film and the liquid layers rather than at the metal surface.

The optimum polishing conditions normally occur over a very restricted range of temperature, voltage and current density where film growth is balanced by film removal. Electropolishing rates and ideal polishing conditions are different for most metals and alloys,[10,11] and in composites and multi-phase materials the technique used is normally a difficult compromise. The tight balance of conditions often means that great care must be taken in creating stable and controlled electropolishing conditions. In multi-phase/component situations it can be very difficult and sometimes impossible to find a single polishing condition in which all phases are polished acceptably and at a similar rate. One alternative is to manually change the polishing conditions (i.e. current/voltage) during the polishing process to reflect the different optimum settings for the different phases and balance polishing rates with time spent under each condition. The disadvantages of this technique are that only one phase is optimally polished at any given time resulting in inferior polishing of the other phases, and, if the total polishing time is not known in advance (as is typically the case in TEM sample preparation) the ideal times for each polishing regime will not be known. In addition the solid film itself provides a problem in multi-phase material especially when the phases have very different oxidation rates[12], where the sub-film layer becomes enriched in the slower oxidizing element (e.g. Ag in Al-Ag[13,14] alloys and Cu in Al-Cu[15,16] alloys).

In order to provide more routine sample preparation for superconducting composites we have developed a new method of controlling micro-electropolishing.[17] We can set up "artificial" micro-electropolishing conditions that would normally be outside the "ideal" micro-electropolishing range (where film dissolution is balanced by film creation) by rapidly oscillating (≤1sec/level) between low current regimes where there is film build up and high current regimes where there is film removal. The periodic removal of the film by using the high current density level limits the level of sub-film species build up. The maximum film thickness can be controlled by both the current/voltage settings and times spent at each level. For our

multiple-phase samples the applied voltage across the electrochemical cell is rapidly changed ($\leq$0.1sec/level) using square wave steps between different current densities appropriate to different phases. Different material polishing rates can then be balanced by adjusting the time interval at each setting. The rapid cycling allows for balanced polishing rates irrespective of total time.

For typical electropolishing of Nb-Ti and Nb_3Sn superconductor composites with Cu matrices we use an electrolytic solution was 2 vol.% HF_{aq}, 5 vol.% H_2SO_{4aq} and 93 vol.% methanol at a temperature of ~-40C. We have found that extremely good specimens can be obtained by oscillating between 3-8mA mm^{-2} and 30-32mA mm^{-2}, even for transverese cross-sections of strand less than 0.1mm in diameter. For these specimens the oxide film can be controlled so that further surface cleaning (normally performed by ion beam thinning) is unnecessary. Balancing the polishing rates of Cu and the superconducting phase is performed by adjusting the duration at each current level, lowering the lower current level and increasing the time at that level increased the polishing rate for the superconductor and increasing the upper voltage level and increasing the time at that level increased the polishing rate for the Cu. Time intervals of 10ms for the upper current level and 20-100ms for the lower current have provided the best results so far.

References

1. W. J. Mc G. Tegart, The Electrolytic and Chemical Polishing of Metals in Research and Industry (2nd Edition), 1959.
2. R. Kirchheim, et al., *J. Electrochem. Soc.*, 128(1981)1027.
3. K. Kojima, and C. W. Tobias, *J. Electrochem. Soc.*, 120(1973)1026.
4. W. C. Elmore, *J. Appl., Phys.*, 10(1939)727.
5. B. Pointu and P. Poncet, *J. Electroanal. Chem.*, 123(1981)111.
6. T. P. Hoar and J. A. S. Mowat, *Nature,* 165(1950)64.
7. T. P. Hoar, in *Modern Aspects of Electrochemistry*, Butterworths, 2(1959)262.
8. M. Novak, et al., *J. Electrochem. Soc.*, 117(1970)733.
9. C. K. H. Dubose and J. O. Stiegler, *Rev. Sci. Instr.*, 38(1967)694.
10. I. J. Brammer and M. A. P. Dewey, *Specimen Preparation for Electron Metallography*, Blackwell Scientific, Oxford, (1966).
11. P. J. Goodhew, *Specimen Preparation in Materials Science, in Practical Methods in Electron Microscopy* Vol. 1, ed A. M. Glauert, North-Holland, (1972).
12. P. J. Lee, in *Analytical Electron Microscopy-1984*, D. B. Williams and D. C. Joy Eds, San Francisco Press, p. 69, 1984.
13. K. J. Sawley, et al., *J. Phys. D.*, 10, 1883, 1977.
14. P. L. Morris and H. J. Lamb, *J. Phys. D.*, 11, 273, 1978.
15. M. N. Thompson, et al., *Phil. Mag*, 35, 1537, 1977.
16. P. Doig and P. E. J. Flewitt, *J. Microsc.*, 110, 107, 1977.
17. Peter J. Lee, *United States Patent Number* 5,354,437, Oct. 11, 1994.
18. This work was supported by the US Department of Energy under Contract DE-FG02-91ER40643. The prototype electropolishing controller was constructed by Alexander A. Squitieri.

PERFECT TEM MEMBRANES BY FOCUSED ION BEAMS: A STRESS REDUCTION TECHNIQUE

John F. Walker,* James K. Odum,** and Peter D. Carleson**

*FEI–Europe Ltd, Brookfield Business Park, Cottenham, Cambridge CB4 4PS, England
**FEI Company, 7451 NE Evergreen Parkway, Hillsboro, OR 97124

With the realisation that the critical dimensions in integrated circuits are shrinking to the point where scanning electron microscopy (SEM) techniques are not sufficiently accurate for many applications, advanced semiconductor fabs are looking to the increased resolution and analytical functionality of transmission electron microscopy (TEM) in failure and process analysis. TEM sample preparation is traditionally labour-intensive and needs skilled technical support but, with the acceptance of focused ion beam (FIB) workstations, this preparation and subsequent analysis is now becoming more routine.[1-4] The reasons are: more reliable preparation with less risk of catastrophic breaking on unique specimens, highly site-specific preparation capable of viewing individual, sub-100 nm features, thin and uniform membranes even with tungsten plugs, and fast and easy preparation techniques.

The initial stages of sample preparation involves preparing a sub-100 μm sliver mounted on a TEM grid. When mounting this sliver on the grid, care must be taken to prevent any strain from being transferred to the silicon. However, grids are not perfect and glue can shrink on hardening and this can often leave some residual strain. While it is clearly better to prevent the cause of the strain (e.g., a distorted grid), and the conditions for achieving this are discussed, it is not always possible to completely eliminate it. If a residual strain is present, and the membrane is subsequently thinned locally by FIB, the strain concentrates there and compressive strain causes the membrane to buckle.

Analysis shows that a strain giving a particular radius of curvature on the initial sliver results in a radius of curvature proportionally smaller (i.e., greater curvature) on the FIB-thinned section. The curved section cannot be thinned further and would lead to an imperfect membrane which may or, more often, may not yield acceptable results. However, the strain can be released if two deep cuts are made perpendicular to the membrane on either side. This additional step of only a few minutes work visibly straightens the TEM section and allows further thinning. This represents a significant improvement in the reliability of the technique of TEM sample preparation using the FIB. While this technique has so far been specific to semiconductor applications, it could also be applied to the preparation of other sample types.

References

1. E.C.G. Kirk et al., Inst. Phys. Conf. Ser. No 100: Section 7, (1989) 501.
2. R. Hull et al., ECS, Reno, USA, May 1995.
3. J.F. Walker et al., MSA, Kansas City, USA, August 1995.
4. J.F. Walker et al., MNE, Aix-en-Provence, France, Sept 1995.

FIB SYSTEM FOR TEM SPECIMEN PREPARATION AND ITS APPLICATION

T.Yaguchi,* T.Kamino,* H.Koike,** T.Ishitani, ** and Y.Kitano ***

*Hitachi Instruments Engineering Co., Ltd.882 Ichige, Hitachi-naka,Ibaraki,312 Japan
** Instrument Division, Hitachi Ltd., 882 Ichige, Hitachi-naka,Ibaraki,312 Japan
***Dept. of Materials Science, Hiroshima Univ.1-3-1 Kagamiyama, Higashi−Hiroshima, Hiroshima,739 Japan

The transmission electron microscope(TEM) is one of the most powerful instrument in materials characterization, and various TEM specimen preparation methods have been developed.
It is known that Ar-etching method is most widely applied in the studies of high technology materials. However, it is time-consuming when a specific area is desired for examination. Because it is necessary to iterate through Ar-ion etching and TEM examination until the desired information is obtained.There is a great demand on a new specimen preparation technique that has high positional accuracy, reliability, and throughput.

Focused ion beam (FIB) milling has been proposed as a solution to the above requirements[1,2,3].
We have developed the FIB system (FB-2000) for SEM/TEM specimen preparation. An external view of the system is shown in Fig.1. The system is designed to use a compatible specimen holder (Fig.2) which allows both FIB milling and TEM observation without re-mounting the specimen.
The instrument has maximum accelerating voltage of 30kV and a minimum beam diameter of 10nm.
The FIB current density of $15A/cm^2$ is available.

The system was applied to the investigation of mechanically-alloyed(MA) powder particles of metals which were difficult to thin by any other methods. Powder particles were embedded in epoxy resin and glued onto the edge of a Ta plate (Fig.3). Scanning Ion Microscopic(SIM) image of epoxy resin embedded Mg-Zn powder particle after deposition of surface protection layer and before FIB milling is shown in Fig.4(a). The deposited material is a mixture of tungsten and carbon. The thickness of the layer was about 1μm. A tilted SIM image after several times of rough milling by a Ga ion beam with a diameter of 500nm is shown in Fig.4(b). After further milling by a FIB with a diameter of 30nm, a cross-sectional TEM image was observed using the H-9000NAR 300kV TEM (Fig.5). The image demonstrates good uniformity of specimen thickness. After further milling taking about 1 minute with the FIB of the same size as in the previous milling, the specimen was thin enough for HREM observation. HREM image from a part of the powder is shown in Fig.6. The lattice images of Mg (002) with a distance of 0.261nm are clearly observed .

References

1 H.Saka et al, Proc.13th Int. Cong. on Electron Microsc. 1, 1009(1994).
2 T.Ishitani et al., J.Electron Microsc. 322, **44**(1994).
3 J.F.Walker et al., Proc.Microscopy and Microanalysis, 518(1995).

1

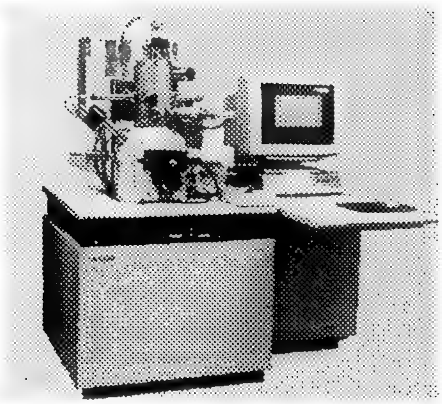

2

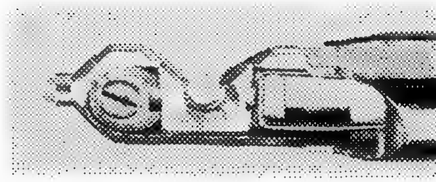

3

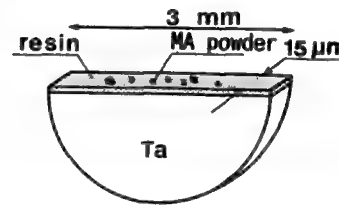

4a

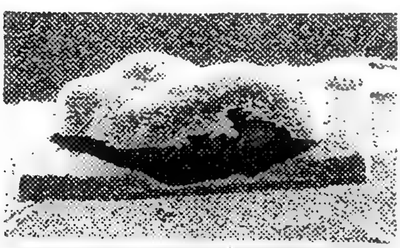

4b

5

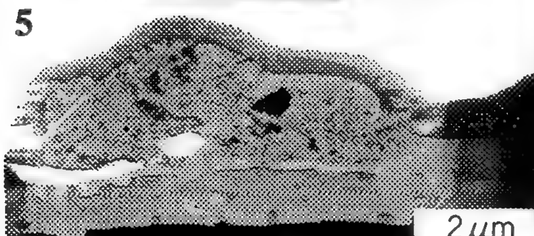

6

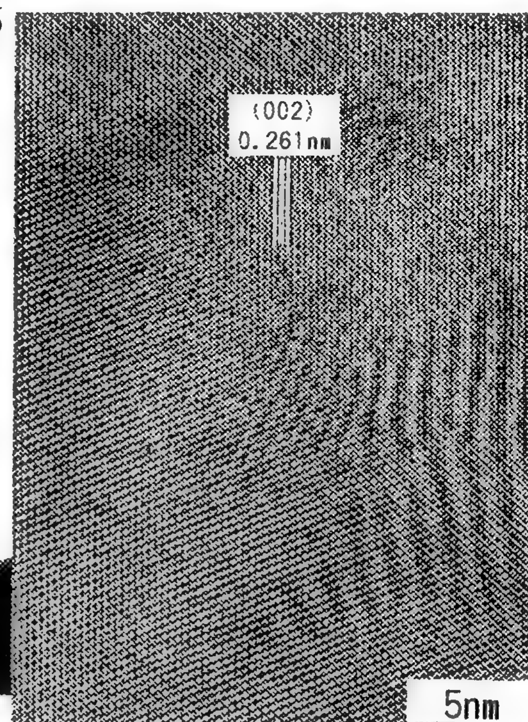

FIG.1 External view of the Hitachi FB-2000 focused Ion beam system.

FIG.2 Compatible specimen holder for FIB and TEM systems.

FIG.3 Schematic drawing of powder particles mounted by epoxy resin to a Ta plate.

FIG.4 SIM image of after deposition of carbon composite and before FIB cutting (a)and after several times of rough cutting by FIB(b).

FIG.5 Cross-sectional TEM image of the MA powder particle.

FIG.6 HREM image of the MA powder particle.

MATERIAL ANALYSIS TECHNIQUES USING THE ION MILL

J. P. Benedict, R. M. Anderson, S. J. Klepeis

ASG, IBM, Bldg 630, MS E-40, Hopewell Junction, N.Y. 12533-0999

Ion mills equipped with flood guns can perform two important functions in material analysis; they can either remove material or deposit material. The ion mill holder shown in Fig.1 is used to remove material from the polished surface of a sample for further optical inspection or SEM (Scanning Electron Microscopy) analysis. [1,2] The sample is attached to a polishing stud type SEM mount and placed in the ion mill holder with the polished surface of the sample pointing straight up, as shown in Fig 2. As the holder is rotating in the ion mill, Argon ions from the flood gun are directed down at the top of the sample. The impact of Argon ions against the surface of the sample causes some of the surface material to leave the sample at a material dependent, nonuniform rate. As a result, the polished surface will begin to develop topography during milling as fast sputtering materials leave behind depressions in the polished surface. [3] This topography can be maximized by having the Argon ions strike the polished surface at a high angle of 25 to 45 degrees or minimized by using a lower impact angle of 3 to 15 degrees. Using a low impact angle of 10 degrees, the thick carbon coating and heavy surface contamination on the sample in shown Fig 3 was removed. The impact angle was then increased to 25 degrees to delineate the different materials present at the surface by enhancing the surface topography , as shown in Fig 4.

The ion mill may also be used to sputter deposit materials on the surface of the sample for protection and delineation. The ion mill holder in Fig. 5 is used to deposit material on the surface of the sample for subsequent sample preparation. [4] Prior to ion milling, the sample is cleaned to remove any surface contamination and placed, facing up, beneath the target in the ion mill, as shown in Fig 5. During ion milling, Argon ions from the ion gun are directed up at a high angle, usually 35 to 40 degrees, at the bottom of the rotating target. The high impact angle of Argon ions against the surface of the target causes most of the ejected target material to strike the surface of the sample and thereby coating it. A composite layer containing layers of different materials can be deposited on the sample by stopping the mill, changing the target and then restarting the mill. A TEM cross section of a sputter deposited composite layer is shown in Fig. 6. In this sample, a marker layer of Titanium followed by a thick layer of SiO_2 was sputter deposited on the surface prior to cross sectioning. Notice that the Titanium, has outlined the surface oxide even along the steep sidewall, while the SiO_2 has protected the surface from damage during sample preparation. Because the deposition is the result of material being physically knocked off the surface of the target, any material that can be sputtered can be used as a target.

References

1. J.P. Benedict et al., *EMSA Bulletin*, 19, 2 (1989)74.
2. J.P. Benedict et al., *Mater. Res. Soc. Proc.* 254, (1992)121.
3. R.M. Anderson et al., *Mater. Res. Soc. Proc.* 254, (1992)141.
4. Gatan, *Gatan Model 600 Dual Ion Mill Instruction Manual*, Gatan:Warrendale, Pa. (1984)22

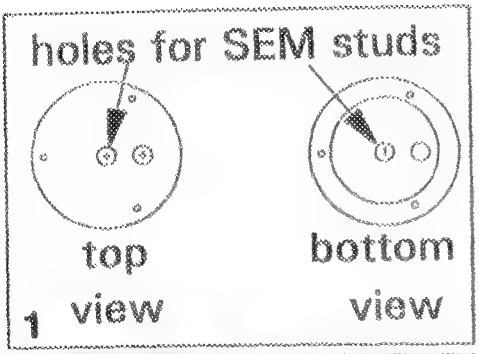

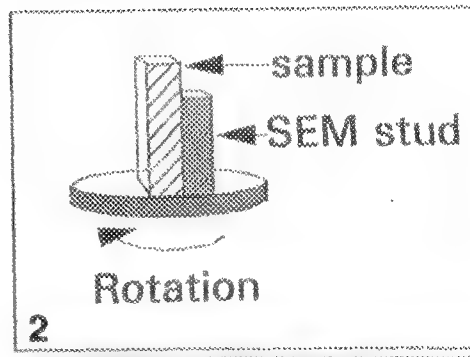

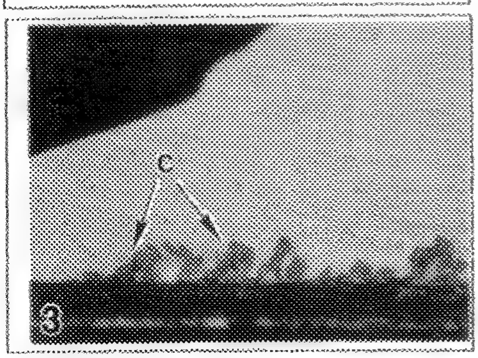

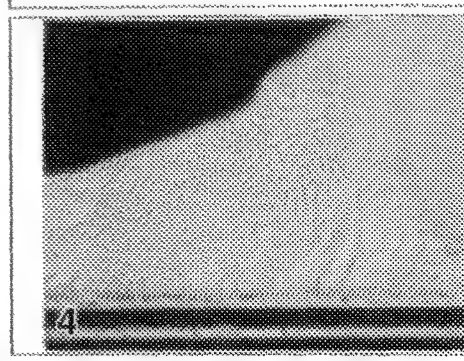

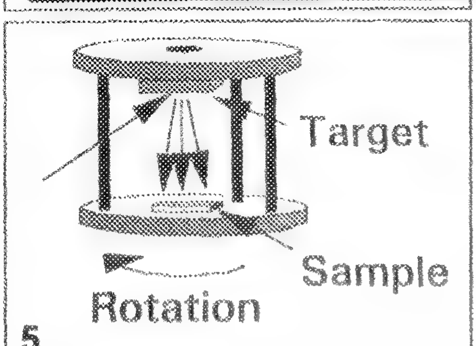

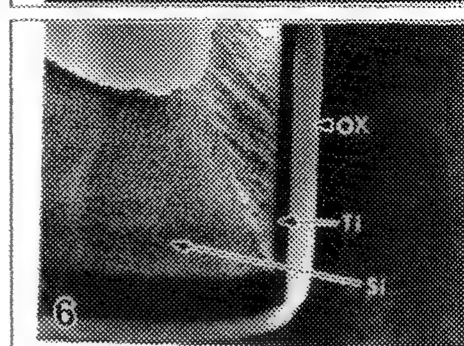

Fig. 1 Two views of ion mill holder which can use either pedestal or stud SEM mounts

Fig. 2 Sample on SEM stud is placed in holder with polished surface up.

Fig. 3 Optical photo showing heavy contamination (C) on the sample surface.

Fig. 4 Same sample after ion milling. Note the surface contamination is gone and surface features obscured by the contamination can now be clearly seen.

Fig. 5 Ion mill holder used to deposit material. Note the position of the sample relative to the target.

Fig. 6 TEM micrograph of surface oxide (OX) in Silicon substrate recess with Titanium (Ti) and Silicon (Si) on deposited on top. Note how well the Titanium has covered the sidewall.

NEW SPECIMEN HOLDERS FOR LOW-ANGLE ION MILLING OF TEM SPECIMENS

R. Alani and P.R. Swann

Gatan Research and Development, 6678 Owens Drive, Pleasanton, CA 94588, USA

The important role of milling angle in the preparation of ion milled TEM specimens can not be over emphasized. While higher milling angles produce more rapid milling of specimen surface, ion milling at glancing angles of about 5° or less has become increasingly popular because it produces higher quality specimens and fewer artifacts, especially specimens composed of materials which are difficult to mill. Specimens milled at higher angles are of lower quality and include surface roughness, limited thin areas and differential thinning rates for different constituents in specimen; low angle ion milling overcomes many of these problems.

A major requirement for low angle ion milling is a specimen holder with an appropriate line of sight capability. That is, the specimen holder must permit one or more ion beams to be directed against the specimen at angles down to 0°. The "single post specimen holder"[1] is an example of a specimen holder providing low angle ion milling capability. In this holder, specimens are seated on the top face of a pedestal, permitting the ion beam(s) to be directed at the top face of the specimen at milling angles down to 0°. However, such a holder does not permit two sided milling or removal of contaminants from the specimen underside. Accordingly, there is a need to develop ion milling specimen holders which permit simultaneous two-sided milling at very low angles down to 0°.

In this work, we report the design, construction and performance of such holders (see Fig. 1a,b). These holders consist of a pedestal having two extending specimen support arms adapted to engage a peripheral edge of a specimen. The support arms have a narrow profile such that at least a portion of the edge of the specimen remains unrestrained and spaced away from the pedestal. The spaced distance provides for line of sight clearance for the ion gun arrangement and permits the ion beams to impinge upon both sides of the specimen at very low angles of beam incidence down to 0°. The specimen is secured to the holders by seating in a recess in the support arms. In the glue type (Fig.1a), the securing means can be a low melting point wax. The wax is disposed in the recess in the support arms and the specimen is secured by melting the wax, seating the specimen and then cooling the wax. The wax also provides the advantage of a heat transfer medium to transfer heat from the specimen to the support arms; thus reducing ion beam induced heat damage effects. In the clamp type, the securing means is a spring type clamp and it can be used when specimen securing with wax is not desired. The clamping arm includes a clamping surface for engaging a peripheral edge of the specimen, a post extending from the clamping surface and a spring for biasing the clamping arm against the specimen support arm. Unlike screw type clamps, the spring maintains constant thermal contact force during heating or cooling of the specimen holder.

The new holders are adaptable for use in various ion milling systems and configurations. Particularly, they are quite suited for use in ion milling systems equipped with modulated ion beams[2] or any other mechanisms for sector ion milling. Sector ion milling is a well established technique for reducing differential milling rates of cross sectional type TEM specimen of multilayered materials. When the new holders are used in a precision ion polishing system (PIPS) with ion beam modulation[2], sector ion milling is carried out by switching the ion guns on/off. In other words, the gun(s) are "on" whenever the specimen holder is rotated to a position where there is line of sight clearance to the surface of specimen and the gun(s) turn "off" whenever, due to rotation, the support arms enter the path of the ion beams. As an example of specimens milled under this condition, Fig. 2 shows a cross sectional TEM image of a 14μm thick SiC film on a Si substrate. It can be seen that the entire SiC overlayer is electron transparent (taken at 120 KeV). Both the epoxy (used for cross sectioning) and the Si substrate are also labeled.

References

1. R. Alani, J.S. Jones and P.R. Swann, *MRS Symposium Proceedings* Vol. 119, 85, (1990)
2. R. Alani, R.G. Harper and P.R. Swann, *Proc. 50th. Ann. Meeting of EMSA*, 394, (1992)

Fig.1(a,b) Construction of new two-sided specimen holders for simultaneous ion milling on both sides of TEM specimens with milling angles down to 0°.

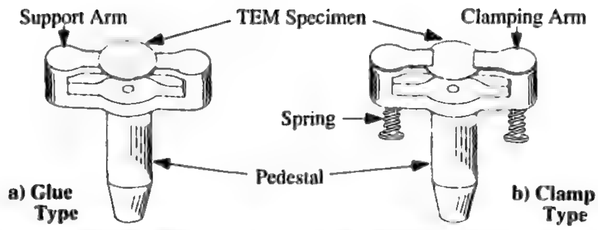

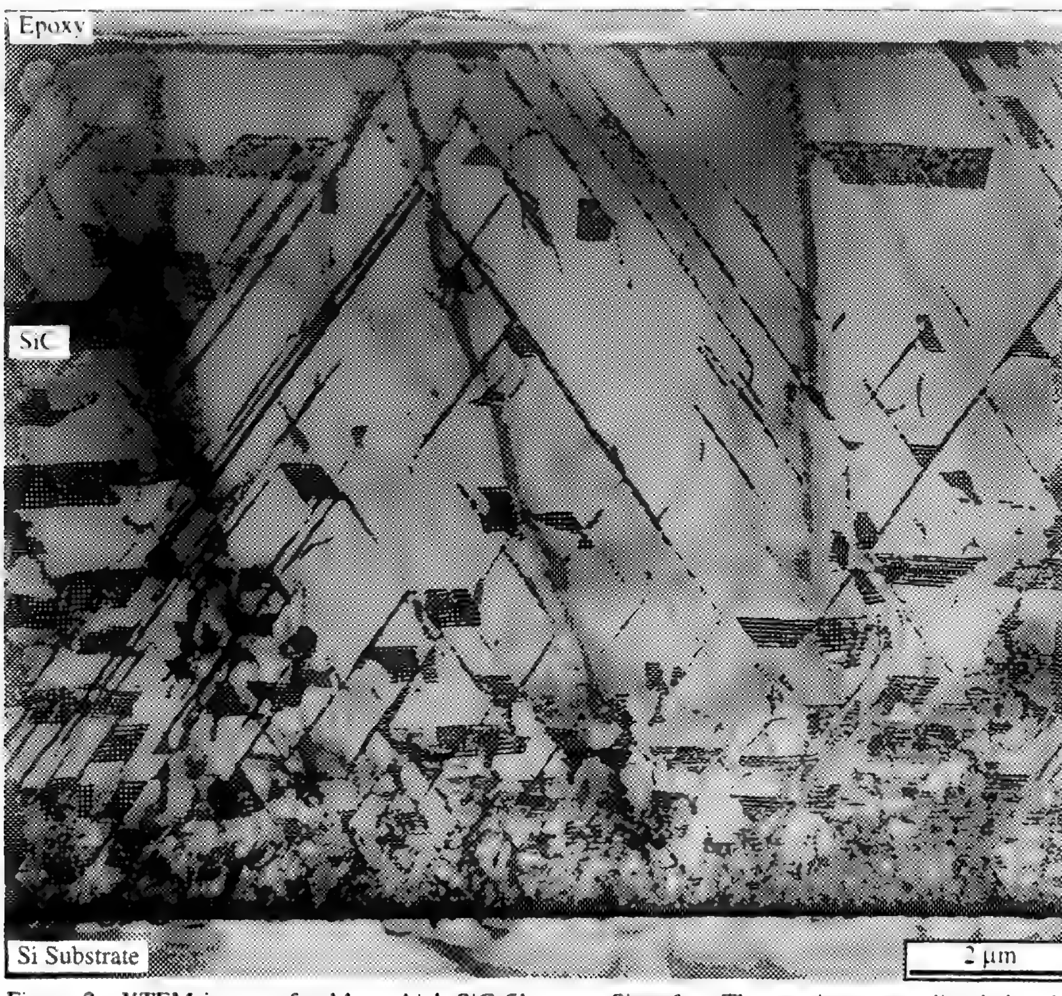

Figure 2. XTEM image of a 14µm thick SiC film on a Si wafer. The specimen was dimpled and mounted on a glue type specimen holder and milled in the PIPS using the ion beam modulation system, with an angle of 3° for the dimple side and 2° for the flat side. *(bulk wafer, courtesy of O. Kordina, L.-O. Bjorketun, L. Hultman, E.Jansen and J.-E.Sundgren, Linkoping University, Sweden)*

SPUTTER ETCHING FOR MICROSTRUCTURE EVALUATION OF SMALL-DIAMETER CORROSION-RESISTANT MP35N ALLOY WIRE

L. D. Hanke and K. Schenk

Materials Evaluation and Engineering, Inc., 13805 1st Avenue N, Plymouth, MN 55441

Metal alloy microstructures are characteristic of the material's mechanical and physical properties, including the key properties of strength and corrosion resistance. Microstructural evaluations typically use chemical etching to reveal the material's structure. For corrosion-resistant alloys, chemical etching can be difficult due to the inherent chemical resistance of the material. This is especially true for active-passive alloys, where the etching reaction is highly dependent on the final polishing and even the time delay between polishing and etching.

Chemical etching is further complicated for extremely fine microstructures and when two or more metals are joined in the sample. These factors are concerns for fine wires, such as those used in implantable medical devices. A common alloy for wires in many medical applications is a Co-Ni-Cr-Mo alloy, designated as MP35N. Wires with extremely small diameters are produced by severe drawing processes that result in very fine microstructures. The alloy is often used in composite wire products, such as an MP35N outer sheath containing a silver core. Wires are also commonly joined to dissimilar metal components by welding.

Successful chemical and electrochemical methods have been developed for monolithic MP35N wires, but with results that are not as reproducible as for more traditional metallographic evaluations. Composite-material wires and welds with dissimilar metals, however, are more difficult challenges with no satisfactory chemical etching alternatives in many cases.

An alternative method for revealing microstructures is ion sputter etching. Like chemical etching, ion sputtering removes material from a prepared sample surface. Material at locations with higher free energy, such as grain boundaries and slip bands, is more aggressively attacked than areas of lower free energy. Thus, etching delineates these features for observation by light microscopy or scanning electron microscopy.

Ion sputtering can be precisely controlled by varying the time, ion flux, and the ion source. This control allows fine structural features to be reliably revealed and repeatable etching results to be obtained from sample to sample. Furthermore, sputtering results are not significantly affected by passivation affects from polishing or galvanic effects from dissimilar metals.

In this investigation, experimental materials include: 0.005-in. diameter, monolithic MP35N alloy wires and 0.007-in. diameter composite wires with an MP35N alloy outer sheath covering a silver core. Traditional metallographic methods were used for sample preparation. Sputter etching was performed in an ultrahigh vacuum using a Xe^+ ion source. The monolithic wire was also etched chemically with a modified Kalling's Reagent .

For the monolithic wire, an excellent correlation is observed between the microstructures revealed by chemical etching (Figure 1) and sputter etching (Figure 2). Both methods clearly reveal the grain size and shape of the material and delineate slip bands in the grains.

The composite wire could not be etched by chemical methods to reveal a true microstructure. This difficulty is due to a combination of the extremely fine grain size and the galvanic affects of the dissimilar metals. Sputter etching was optimized to reveal the structure of the MP35N, Figure 3. The grain shape and size are clearly revealed by the sputter etching.

In summary, ion sputter etching is a feasible alternative to chemical etching for microstructure evaluations. This method is especially useful for extremely fine structures and for evaluation of samples with dissimilar metal couples.

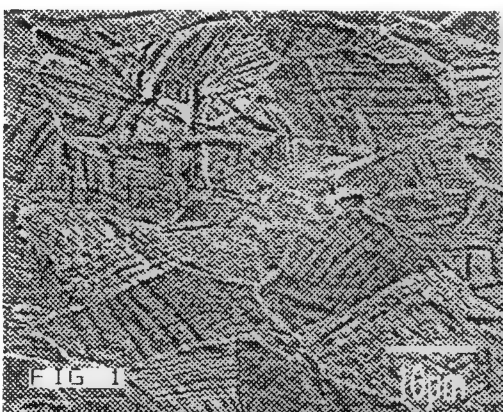

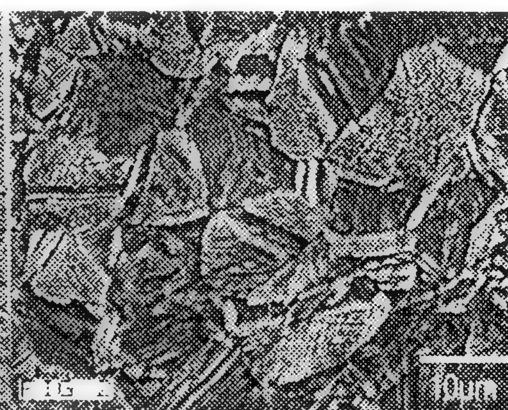

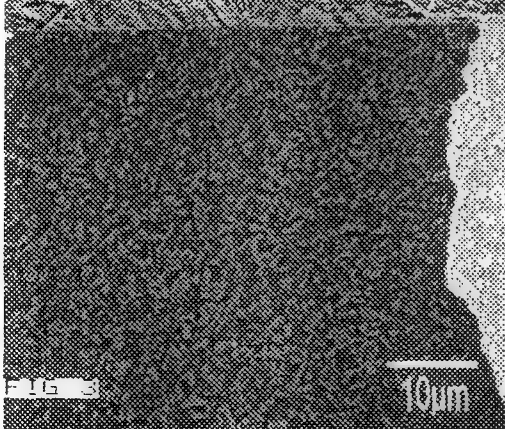

FIG. 1 Microstructure of MP35N wire, chemically etched.
FIG. 2 Microstructure of MP35N wire, ion sputter etched.
FIG. 3 MP35N microstructure in composite wire, ion sputter etched.

INDUSTRIAL APPLICATIONS OF TOF-SIMS IMAGING

Steven J. Pachuta

3M Corporate Research Laboratories, 201-2S-16 3M Center, St. Paul, Minnesota 55144

Time-of-flight secondary ion mass spectrometry (TOF-SIMS) has in recent years become a useful tool for surface analysis in industrial laboratories. All elements and isotopes, as well as many molecular entities, can be detected by SIMS, with most of the signal coming from the outer 10 - 20 Å of the surface. The initial penetration of TOF-SIMS into industry was as an improvement over existing quadrupole instruments, with higher mass range, mass resolution, and sensitivity. The coupling of TOF-SIMS with high brightness liquid metal ion sources greatly expanded the applicability of the technique, making chemical imaging of the outermost monolayers of a surface a routine experiment.

Several examples will be presented of TOF-SIMS imaging applied to real-world materials encountered in an industrial analytical laboratory. All results were obtained from a PHI-Evans TFS series instrument equipped with an FEI two-lens $^{69}Ga^{+}$ liquid metal ion gun (LMIG). When operated at 25 keV beam energy, a primary ion beam diameter of 2500 Å in continuous mode, and 1 - 2 µm in pulsed mode, can routinely be obtained.

Some useful applications of TOF-SIMS imaging have come from cross sectioning experiments in which the sample is either microtomed or embedded in epoxy and polished. The latter method is mainly applicable to inorganic systems. Fig. 1 shows a polished cross section of two algae-resistant roofing granules in which Cu-containing particles in the coating are mapped. The microtoming method has been found to be practical for preparing organic samples if great care is taken to keep the surface free from contamination during and after cutting. An image of a microtomed cross section of a 100 µm polypropylene film containing a fluorochemical melt additive is shown in Fig. 2.

Other systems in which TOF-SIMS imaging has proven useful include identification of debris on a magnetic recording head, determination of the spatial distributions of low-level dopants in fiber optic cross sections, imaging of inks and coatings on paper and polymer fibers, and imaging of microscratches in a coated polymer film. Imaging can also be used as an aid to depth profiling very small areas, such as coated SiC fibers of 15 µm diameter (Fig. 3).

TOF-SIMS can be a valuable complement to other microanalytical techniques, including energy dispersive x-ray spectroscopy (EDS), micro-infrared spectroscopy (IR), and optical microscopy. The spatial resolution of the LMIG is comparable to that obtainable with EDS, but SIMS has advantages in speed and sensitivity, and SIMS has much higher chemical specificity, including the ability to identify organic species. In comparison to IR, SIMS has higher spatial resolution, and it can provide additional chemical specificity--for example, molecular weight information. The surface sensitivity of SIMS is both an advantage and a disadvantage. Very thin features which are easily detectable by SIMS present difficulties to EDS and IR due to overwhelming signal from the underlying substrate and/or insufficient signal from the feature itself. On the other hand, there are frequently occasions when a small organic feature cannot be studied by SIMS due to a thin overcoating of a contaminant such as silicone oil. In these cases, the deeper analysis depth of IR and EDS is a clear advantage. Often a combination of SIMS with these near-surface techniques proves useful.

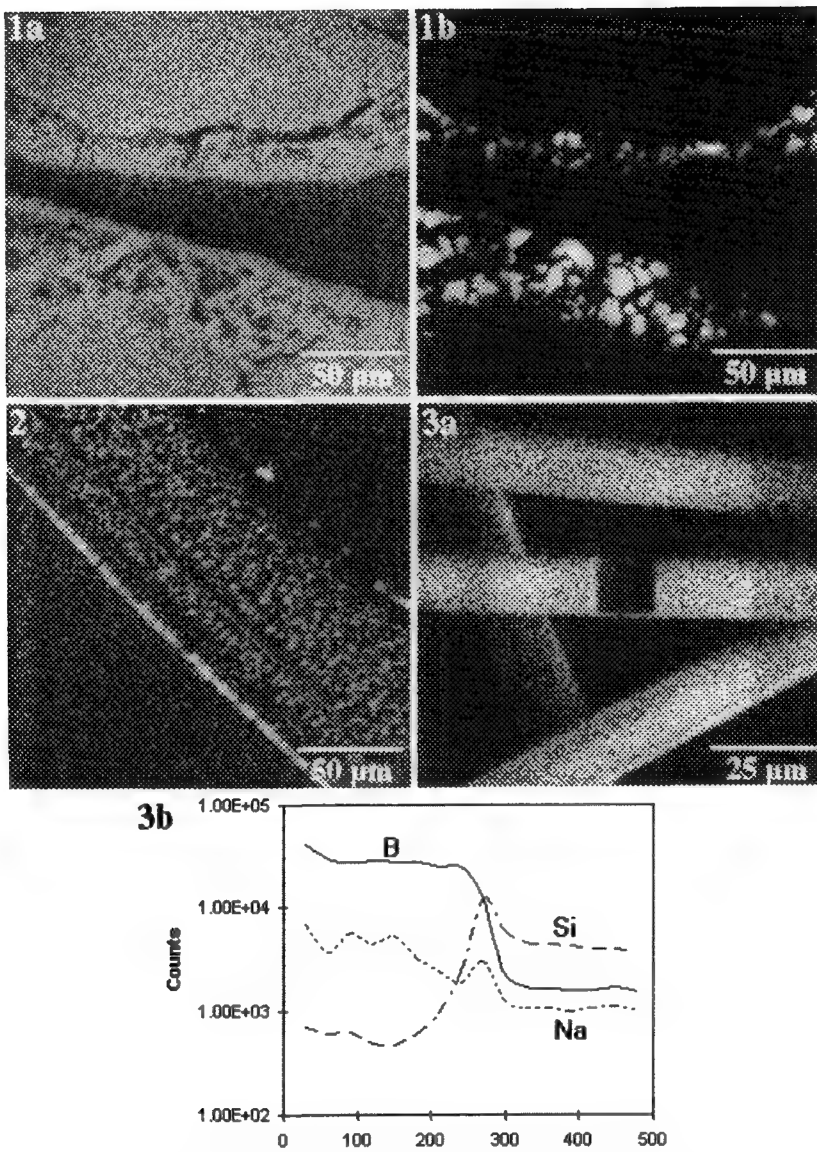

FIG. 1 SIMS images of two cross-sectioned roofing granules: (a) $^{27}Al^+$ from the base rock; (b) $^{63}Cu^+$ from particles used to impart algae-resistance.

FIG. 2 SIMS image of CF^+ from a microtomed cross section of a polypropylene film, showing a nonuniform distribution of fluorochemical.

FIG. 3 (a) SIMS $^{11}B^+$ image of BN-coated SiC fibers after sputter depth profiling a single fiber. Note the square crater, which appears dark due to removal of boron by sputtering. (b) Depth profiles of $^{11}B^+$, $^{23}Na^+$, and $^{28}Si^+$.

MOLECULE-SPECIFIC IMAGING OF BIOMATERIALS

N. Winograd

Department of Chemistry, Penn State University, 184 Materials Research Institute Building, University Park, PA 16802

The development of focused ion beams and time-of-flight SIMS have opened new possibilities for characterization of biomaterials. For some cases, laser postionization is important for further increasing the sensitivity of the analysis. Our group has been involved in finding methodologies and applications which could add to the repetoire of imaging methods available to biologists. Presently, these methods include fluorescence microscopy, confocal microscopy, scanning probe microscopies and autoradiography, to name just a few.

Sample preparation is a major issue for these materials. To achieve meaningful data it is essential to prepare an uncontaminated surface in vacuum that retains the original spatial composition of the target molecules. Although many elegant sample preparation methods have been developed in the electron microscopy community, the rules of the game for TOF-SIMS imaging are quite different since we are after chemical information rather than morphological information. To solve this problem we have developed several cryogenic sample handling techniques whereby a biomaterial (e.g. a single cell) is rapidly frozen in the laboratory. It is then introduced into the spectrometer at 77 K and subjected to freeze-fracture or microtoming as shown in the figure. Our results to date suggest that molecular imaging is indeed possible. We will show chemical maps for paramecia cultured in cocaine or dimethylsulfoxide and subsequently frozen and freeze-fractured.

The sensitivity of TOF-SIMS for molecular imaging may be exploited in a number of other applications. We have been involved in the chemical assay of 40 micron polystyrene spheres used as solid phase supports for combinatorial library synthesis. This approach has shown promise as a new drug discovery tool in the pharmaceutical industry. For these samples, a low molecular weight organic compound, a small peptide for example, is covalently linked to the sphere. The library is built by a combination of many steps using large numbers of beads. The beads are then assayed for biological activity. Using TOF-SIMS we can identify the composition of the bioactive chemical. Issues such as development of the proper linker chemistry, bead porosity, and sensitivity will be discussed. Moreover, we will present strategies from screening thousands of these beads in a single analysis.

A third issue involves signal enhancement using laser postionization. Of particular interest here is the recent development of high repetition rate ultra short pulsed Ti-Sapphire lasers. These fs-pulsed lasers photoionize fragile molecules with much less fragmentation than ns-pulsed lasers. The high repetition rate also allows image acquisition times to be improved by 2 orders of magnitude over previous capabilities. Recent examples of the use of this laser in imaging neutral molecules desorbed from surfaces will be presented.

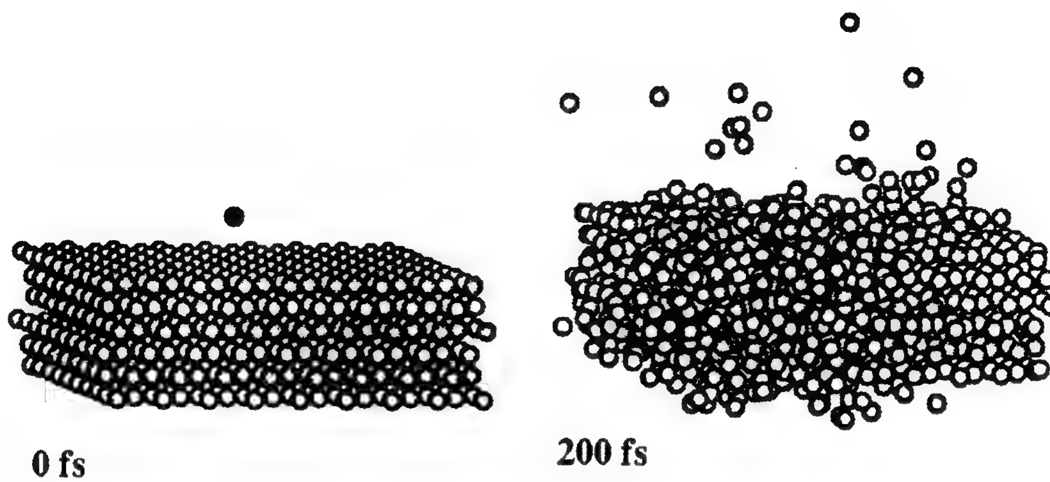
0 fs
200 fs

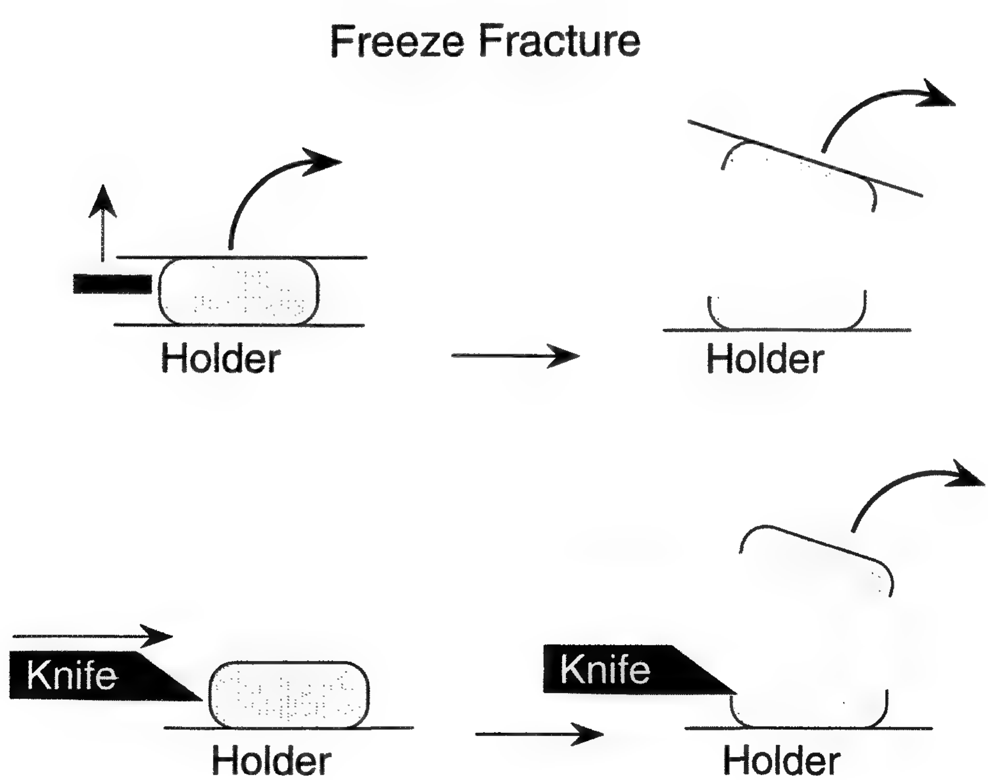
Freeze Fracture
Holder
Holder
Knife
Holder
Knife
Holder

CORRELATIVE TOF-SIMS AND FLUORESCENCE MICROSCOPY ANALYSES OF SURFACES USED TO CONTROL MAMMALIAN CELL FUNCTION

K.E. Healy,* C.H. Thomas,* A. Rezania,* P.J. McKeown,† C.D. McFarland,‡ and J.G. Steele‡

*Departments of Biological Materials, and Biomedical Engineering, Northwestern University Dental and Engineering Schools, Chicago, IL 60611-3008, USA
†Physical Electronics Incorporated, Eden Prairie, MN 55344
‡Division of Biomolecular Engineering, CSIRO, P.O. Box 184 North Ryde NSW 2113, Australia

A common theme in engineering surfaces for biomedical materials and devices is the control of cell behavior at the material-tissue interface. Multiple analytical techniques are required to fully characterize a material surface both prior to and after exposure to the biological environment. In addition, a full cadre of microscopy techniques are essential for understanding cell behavior to these surface engineered materials. At the heart of understanding the mechanisms that control cell function on solid materials is the adsorption of serum proteins, which ultimately dictates how a cell responds to a material. A great deal of complexity is introduced into the system by adsorbed proteins, since there are over 200 proteins in human blood, and that post adsorption changes in conformation could lead to altered function. Until recently it has been extremely difficult to correlate cell behavior with the initial surface chemistry of a material and the type of protein adsorbed to the surface. To provide further understanding of the way a cell interacts with solid materials, we have developed novel materials with patterned surface chemistry and characterized these materials using surface analytical techniques, including TOF-SIMS, and laser-based microscopy and spectroscopy techniques to assess preferential protein adsorption and cell adhesion.

Samples were prepared using photolithographic techniques as described previously.[1] The resulting surfaces contained 50μm wide regions of an aminosilane, N-(2-aminoethyl)-3-aminopropyl-trimethoxysilane (EDS), separated by 100μm wide regions of dimethyldichlorosilane (DMS), an alkyl silane [EDS/DMS: Figure 1]. Surfaces were characterized using static TOF-SIMS with imaging capabilities. Positive and negative images were acquired from patterned samples from a 200 x 200 μm area. The adsorption of serum glycoproteins, vitronectin (Vn) and fibronectin (Fn), to these surfaces was examined by immunofluorescent staining and laser confocal microscopy. Fetal bovine serum (FBS) depleted of either vitronectin (-Vn) or fibronectin (-Fn) were used to observe the effects of Vn and Fn on cell attachment and spatial distribution when exposed to EDS/DMS surfaces. Removal of Vn or FN from FBS was performed using an affinity column as described by Steele *et al.*[2] For each test group (FBS, -Vn, or -Fn) the spatial distribution of cells was determined at various time intervals using phase contrast light microscopy and time-lapse video microscopy.

Analysis of a patterned surface using TOF-SIMS with imaging identified the spatial location of the immobilized EDS and DMS. Figure 2 demonstrates that the CN^- fragment ion (m/z 26) indicative of EDS is preferentially localized on the EDS regions of the EDS/DMS sample. The position of the Si^- (m/z 28) fragment ion co-localized with the DMS chemistry. Vn preferentially adsorbed from FBS to the EDS portions of the patterned surface (Figure 3); however, Fn was not detected on the surface under similar adsorption conditions. This adsorption profile **exactly** mirrored the TOF-SIMS surface analysis, and cell attachment data (Figure 4). The removal of Vn from FBS resulted in little or no cell attachment (Figure 5), indicating Vn was required for bone cell attachment, spatial distribution, and subsequent mineralization (Figure 6) on the EDS regions of EDS/DMS patterned surfaces.

References

1. K. E. Healy, et al. *Biomaterials.* **1995,** *17*, 195-208.
2. J. G. Steele, et al. *J. Biomater. Sci. Polymer Edn.* **1993,** *5*, 245-257.

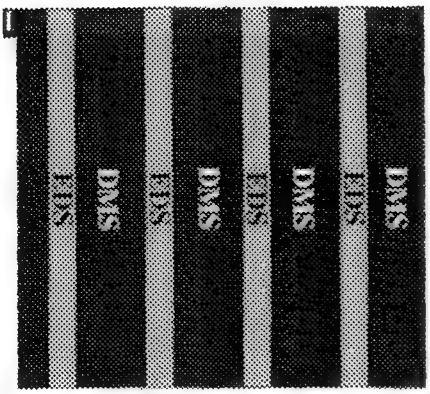

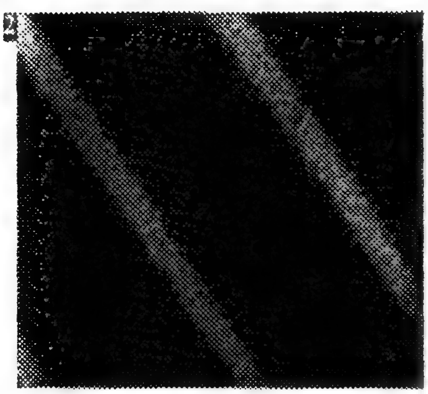

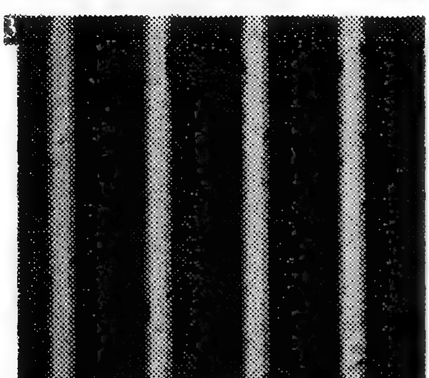

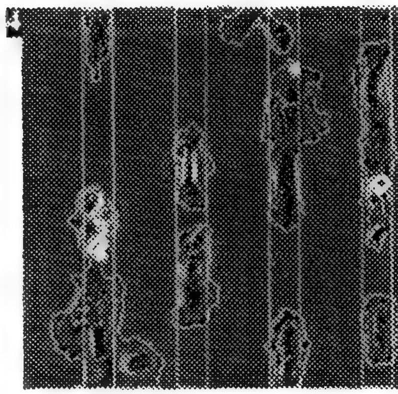

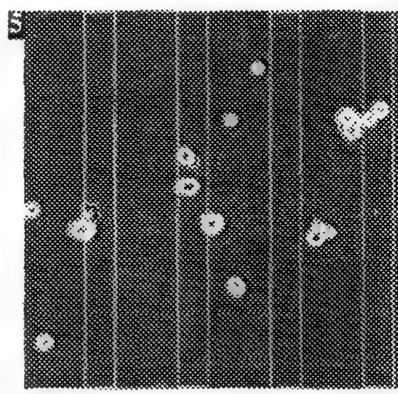

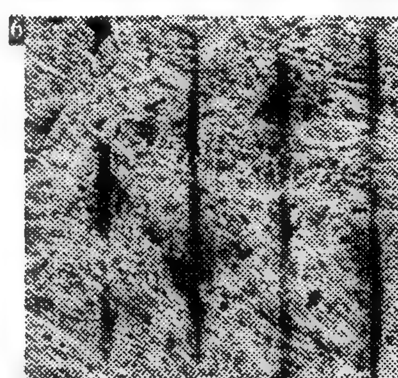

Fig. 1 Schematic of the EDS/DMS patterned substrate. EDS width = 50μm and DMS width = 100μm
Fig. 2 TOF-SIMS image of an EDS/DMS patterned substrate. Negative ion image of the CN (m/z 26) fragment attributed to EDS. Image has been enlarged.
Fig. 3 Confocal microscope image of adsorption of Vn onto an EDS/DMS patterned surface.
Fig. 4 Spatial distribution of primary bone cells in media containing 10% FBS for 2h.
Fig. 5 Lack of preferential spatial distribution for cells seeded in media with 10% -Vn serum for 2h.
Fig. 6 Preferential mineralization of tissue on the EDS regions of an EDS/DMS patterned surface, 15d.

MOLECULAR SURFACE IMAGING OF PARTICLES USING MICROPROBE TIME-OF-FLIGHT SECONDARY ION MASS SPECTROMETRY (TOF-SIMS)

R.W. Linton[1], T.F. Fister[2], S.S. Summers[1], G.S. Strossman[1,2], M.J. Holland[1], R.W. Odom[2]

[1]Department of Chemistry- CB3290, Univ. of North Carolina, Chapel Hill, NC 27599
[2]Charles Evans and Associates, Redwood City, CA 94063

The objective of this research is to develop imaging time-of-flight secondary ion mass spectrometry (TOF-SIMS) to characterize ultra-thin organic films on microscopic particles. An initial application is to evaluate the surface chemistry of polycyclic organic matter (POM) on combustion-generated particles as an area of fundamental interest in the assessment of the environmental fate and impact of carcinogenic pollutants.[1]

Controlled deposition of POM monolayers was achieved using either gas or solution phase coating on model particles such as silica, as well as on authentic environmental particles such as coal flyash or soot. Another aspect of the work was to monitor surface transformations of adsorbed POM involving photochemical degradation or reactions with gaseous pollutants such as nitrogen oxides. For the first time, variations in POM adsorption and reactivity have been probed as a function of particle type by the use of time-of-flight secondary ion mass spectrometry (TOF-SIMS) to perform surface analysis on single particles. Results using a pulsed gallium microbeam source on a TOF-SIMS indicated that 0.1 monolayer coverages of individual POM species can be detected as quasimolecular ions from single particles with diameters typically in the 5 µm range. Primary ion doses were $<10^{13}$ ions/cm^2 to minimize surface damage during a typical 10 min spectrum acquisition from an 40x40 µm image field. Correlation of *in situ* measurements using TOF-SIMS with traditional solvent extraction and chromatographic results, including LC or GC-MS, allowed for more detailed assessments of the sensitivity and quantitative capabilities of TOF-SIMS. The combination of monolayer analysis with microanalysis creates severe challenges to sensitivity since the total number of molecules within the analytical volume is so small ($< 10^7$ POM molecules on a 1µm^2 particle area)

This case study emphasizing the surface microanalysis of particles also serves to illustrate some general issues in the development of imaging TOF-SIMS, as is summarized below.

1. *Impact of Primary Source Characteristics.* The relative trade-offs involving pulse width and bunching of the primary beam were explored with respect to mass resolution, spatial resolution, and sensitivity.

2. *Sample Preparation.* Various solution deposition schemes were evaluated to achieve the best uniformity of coating when higher POM coverages were desired. Although the deposition apparatus is more complex, vapor phase adsorption is more relevant to authentic combustion processes and may provide more uniform particle coatings when low POM coverages are adequate. Particles less than 10 µm in diameter can be analyzed by transferring them to a silicon wafer. However, the electrostatic attraction may not be sufficient to hold particles firmly in place. Graphite and carbon planchets also were examined as substrates for particles. The carbon planchets have numerous limitations in that particles are difficult to locate optically because of the low substrate reflectivity, and POMs may migrate from the particles onto the planchet. Particles can be located more easily on the reflective surface of the polished graphite, but the stability of the adsorbed POM is still an issue. Larger particles can be pressed into indium foil, although questions remain about the integrity of the organic coating following this procedure. Other complications involve difficulties in locating and imaging particles on the rough surface of the foil, and the need to blank the high signal from the indium secondary ions to optimize ion counting statistics for the analyte signals. Another general issue in sample preparation is that the more volatile POMs may migrate from the particle surfaces or desorb during TOF-SIMS measurements. Such effects were reduced by using a liquid nitrogen cooled sample stage (<-50°C). For example, molecular ion signals from benz[a]anthracene (BaA) coated flyash remained at least 50% of their initial intensity after 2 hrs in the vacuum at low temperature, compared to a total loss of molecular ion signal after only 1 hr at ambient temperature.

3. *Topographic Artifacts*. There are inherent intensity variations across the particle diameter due to loc variations in effective primary ion current density and sputter yield, as well as possible chromatic contra due to local variations in the ion extraction field, reflecting sample topography. The off-normal incidenc of the ion beam also creates additional shadowing and smearing effects in the ion images.

4. *Surface Chemical Reactivity*. Both photodegradation and oxidation reactions of particle-associate POM have been observed *in situ*. For example, BaA formed photo-oxidation products such a benz[a]anthracenedione on silica (Fig. 1). TOF-SIMS results as a function of photo-irradiation time als allowed quantitative kinetic studies on single particles. Photoproducts were more difficult to detect on th less reactive coal flyash surfaces. However, hydroxylated products were suggested by TOF-SIMS studie immediately following the exposure of POM-coated flyash particles to gaseous nitrogen oxides.

5. *Quantitation and Sensitivity*. All of the above issues ultimately relate to questions involvin quantitation. For heterogeneous groups of particles, major concerns include variability in individu particle physical characteristics such as size, porosity and surface area, as well as chemical compositio variations that may influence the strength of adsorbate interactions and influence molecular sputter io yields. Spectrum normalization is essential, for example by ratioing to total secondary ion intensity or mass selected ion representative of the particle (e.g. $SiOH^+$ or deposited Ga^+ from the primary beam). Th later approach may be inadequate for mixtures with large inter-particle chemical heterogeneity such as co flyash. However, monotonic increases in normalized M^+ signals as a function of a specific POM' coverage on flyash (e.g., 0.02 to 3.0 monolayers of BaA) were observed, thereby establishing the hig detection sensitivity and potential for quantitative measurements using TOF-SIMS. Average coverage were verified independently by consideration of bulk surface area and utilizing solvent extraction an chromatographic analysis.

References
1. T.F. Fister et al., *Int. J. Mass. Spec. Ion Proc.*, 143(1995)87-111.
2. This work was funded by a Department of Energy SBIR grant.

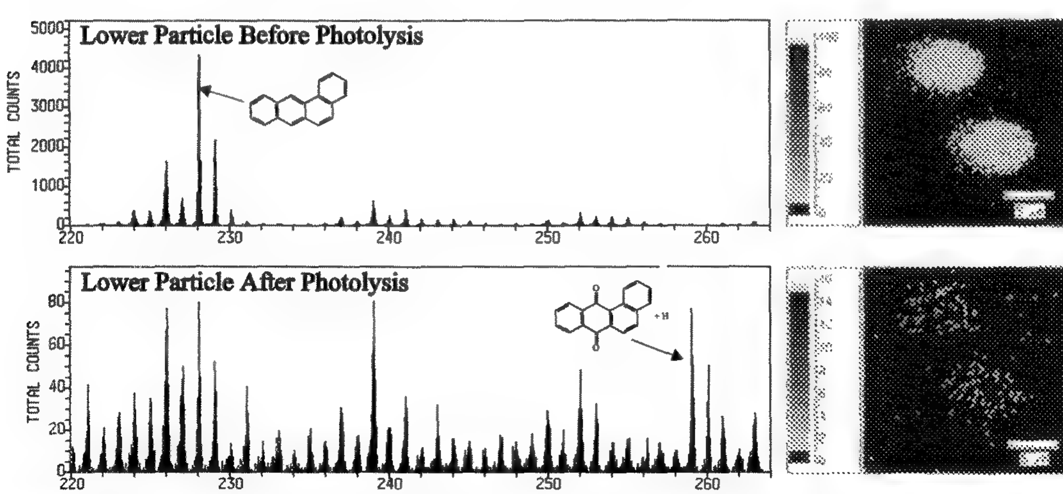

Figure 1. Examples of TOF-SIMS data of particles containing approximately 0.1 monolayers of Ba deposited from solution on silica particles, both before and after 15 min of photolysis. Images are of th molecular ions for the BaA (top) and its dione photoproduct (bottom) for individual particles in the 5μ diameter size range.

INTERFACIAL REACTIONS IN METAL MATRIX COMPOSITES REVEALED BY IMAGING SIMS

R. Levi-Setti, J.M. Chabala, W. Wolbach* and K.K. Soni**

Enrico Fermi Institute and Department of Physics, The University of Chicago, Chicago, IL 60637
*Department of Chemistry, Illinois Wesleyan University, Bloomington, IL 61702
**Corning Incorporated, Science and Technology Division, Corning, NY 14831

Secondary ion mass spectrometry (SIMS), often in its non-imaging manifestation, is a powerful analytical technique that has found numerous applications in the semiconductor, geochemistry and organic chemistry industries. Given its strengths, which often complement those of traditional electron-probe-based analyses, it is surprising that SIMS has not found a larger clientele among Researchers studying engineered and biological materials. To illustrate the power of high-spatial-resolution SIMS for the investigation of advanced materials, we summarize a series of experiments examining the microstructure and microchemistry of alloys reinforced with ceramic fibers.[1,2,3] The goals of this presentation are twofold: first, to notify the scientific community about the capabilities of imaging SIMS; and second, to elevate (hopefully) the study of metal-matrix composites via SIMS from an important but obscure engineering pursuit to a thriving profession. The principal advantages of the SIMS technique for this study are i) polished, bulk samples can be analyzed (i.e. thinning is not required); ii) the distribution of most elements and isotopes can be measured with submicrometer resolution; iii) the signal-to-noise is very good (essentially no background). The disadvantages are i) concentration quantification is difficult, ii) few SIMS instruments are commercially available that achieve the spatial resolution shown here.

Metal matrix composites are a new class of materials combining the separate benefits of ceramics and alloys. However, the incorporation of ceramic material into metal is complicated by reactions between the two, and by binders and additives that also may be included in the composite. We examined several composites with the University of Chicago scanning ion microprobe, an instrument that has been described to this society.[4] Briefly, a 40 keV, 25 pA Ga^+ primary ion beam was used, focused to a spot about 50 nm in diameter. An RF quadrupole mass filter was employed for SIMS analysis (a magnetic sector spectrometer is also available). Two composite samples, selected out of the many studied, are shown in the figure. Both samples are an Al-Si-Cu-Mg alloy in which alumina/silica fibers have been randomly embedded. The fibers were coated with a silica binder and calcined at 850°C, 3 h, before squeeze-casting at high temperature (~700°C) and pressure with the metal. Figures a,b are SIMS elemental maps of a polished cross section through a sample subjected to a "T5" heat treatment (200°C for 11 h). The ceramic fibers are the darker ovals/slashes running diagonally in Fig. a, an Al^+ map. The matrix, which is over 85 wt.% Al, is very bright in this map. The dark, submicrometer regions in the matrix are Si precipitations. The Mg distribution for this sample is very striking (Fig. b). Mg is present in the matrix as fine precipitates. The binder, which envelopes the fibers, has been attacked by Mg during the heat treatment; as a result, Mg has entered the binder and become uniformly and highly concentrated there. Very little Mg has penetrated into the fiber. Figures. c,d are maps of a second sample subjected to a hotter "T6" heat treatment (530°C for 6 h). A wide fiber, placed diagonally, bisects these maps. Because of the hotter heat treatment, Si from the fiber has been replaced by Al and Mg. Note that the Al concentration of portions of the fiber is similar to that of the metal matrix. The core of the fiber, darker in the Al^+ map, evidently has not been affected by the heat treatment. Mg, now nearly absent from the matrix, forms a thick coat about the fibers and has diffused at a low concentration into the fiber. Additional SIMS measurements, with data from other techniques, lead to a better understanding of the chemical reactions occurring during the processing of these materials.

References

1. R. Mogilevsky et al., *Mater. Sci. and Eng.*, A191 (1995) 209.
2. W.S. Wolbach et al., Submitted *J. Mater. Sci.*

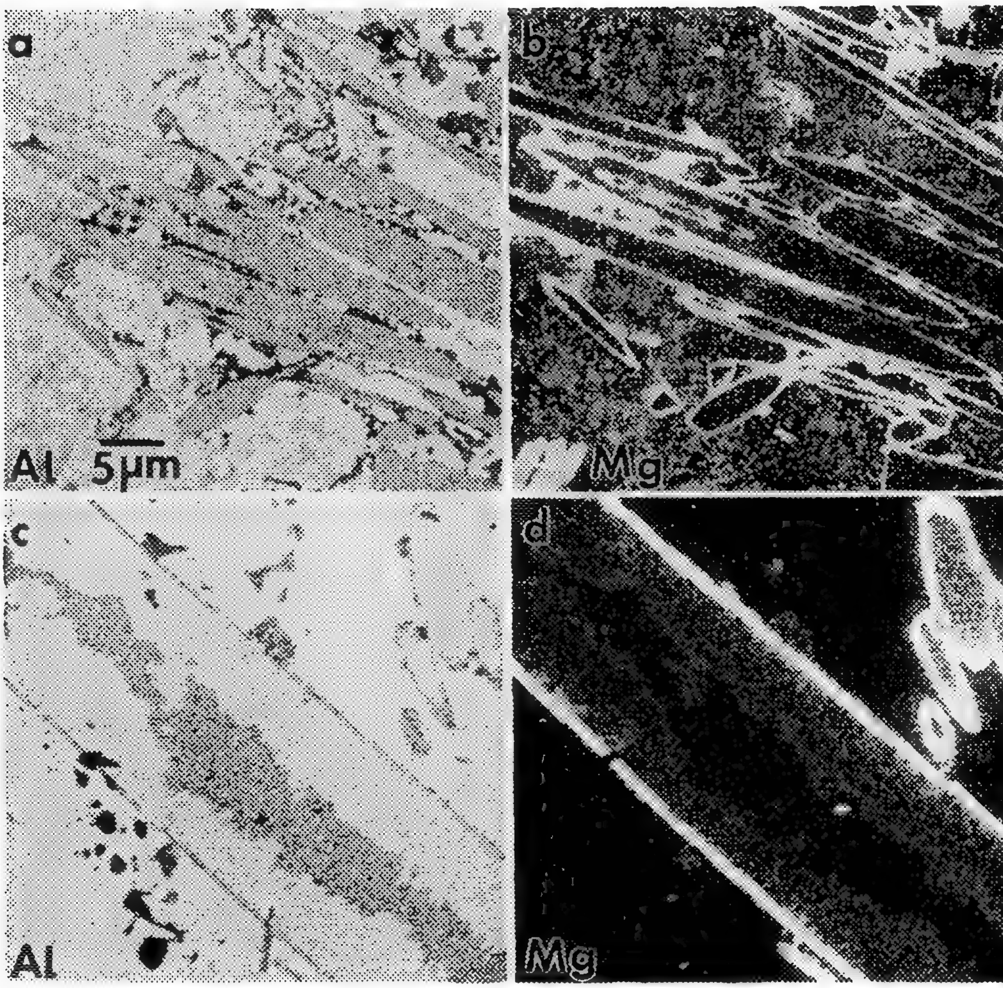

FIG. a SIMS Al^+ map of a cross section through a metal matrix composite, composed of alumina/silica fibers embedded in an Al alloy. The alloy has been given a T5 (low temp.) heat treatment.
FIG. b Mg^+ map of the area shown in a. Magnesium from the matrix has accumulated around the fibers.
FIG. c Al^+ map of a similar alloy, this time given a T6 (high temp.) heat treatment. A very wide fiber runs diagonally across the image. Aluminum from the matrix has entered the fiber; the core is unaffected.
FIG. d Mg^+ map of the area shown in c. Magnesium surrounds (at high concentration) the fibers and ha penetrated into the fiber. The core contains little Mg.

3. K.K. Soni et al., *J. Microscopy*, 177 (1995) 414.
4. J.M. Chabala et al., *Proc. 28th Ann. Microbeam Analysis Meeting*, New Orleans, LA, J. Friel, ed. (1994) 163.
5. This work was supported by a BP America Extramural research award and, in part, by the MRSEC Program of the NSF, award DMR-9400379. We thank Dr. S. Bryan for his assistance.

VOLUMETRIC RENDERING OF THREE-DIMENSIONAL (3D) SIMS DEPTH PROFILES

N.S. McIntyre, D.M. Kingston, P.A.W. van der Heide, M.L. Wagter, M.B. Stanley and A.H. Clarke
Surface Science Western, Western Science Centre, The University of Western Ontario, London, Ontario N6A 5B7 Canada

Dynamic secondary ion mass spectrometry (SIMS) can be used to uncover unique information about interfaces and whole structures which are "buried" within a solid. During a depth profile of a solid, a sequence of SIMS images is acquired for each element under study. The sequence is correlated into a vertical "stack" which contains digitised three dimensional (3D) elemental distributions. Although such distributions are distorted by surface roughness, preferential sputtering and SIMS matrix effects, there is still considerable structural information contained in the volume and much potential for further information retrieval as the above-mentioned distorting effects are addressed.

One of the major tools used to assess distributional information within the 3D volume has been visual rendering software. Using Sunvision software (Sun Microsystems Inc.) and a small workstation, images of the volume can be constructed which display pixels either in a "maximum value" perspective or in perspectives where the density of each phase can be adjusted to maximise structural detail. Several examples of the technique will be shown.

In one application, the corrosion of zirconium-2.5% niobium alloy in a nuclear reactor boiler circuit is being studied by SIMS imaging to determine the mechanisms by which hydrogen from the aqueous coolant gains access to the alloy phase. Such hydrogen ingress can result in the formation of brittle metal hydrides. Alloy surfaces removed from the reactor have been depth profiled by imaging SIMS. In Figures 1(a) and (b), vertical cross-sections of hydrogen and oxygen distributions have been extracted from stacks of the SIMS image depth profiles for the ions D^- and ZrO^-. Significant concentrations of hydrogen are found within all of the oxide surface layer; in addition, hydride layers are detected in the underlying metal. In Figures 2(a) - 2(c) 3D volume-rendered images of the hydrogen impart much added perspective to the structure of the corrosion layer; local "fingers" of oxide are seen to extend well beyond the main oxide front, and eventually connect with the hydride structures. An equivalent image of oxygen distribution (as ZrO^-) (not shown) also illustrates the finger-like distribution, but is less well-defined than for hydrogen.

A second example comes from a SIMS study of the interfacial structures formed during ultrasonic bonding on an aluminium-silicon alloy wire to a gold electrical contact surface. Figure 3(a) - 3(c) show volume-rendered SIMS 3D images of aluminium, silicon, and gold on one particular contact. The wire composition immediately at the bonded interface is very high in silicon. Aluminium is still present in surrounding regions of the metal and also appears to have alloyed with the gold contact surface.

Some corrections to SIMS depth profiles to account for topography and sputter effects will also be described.

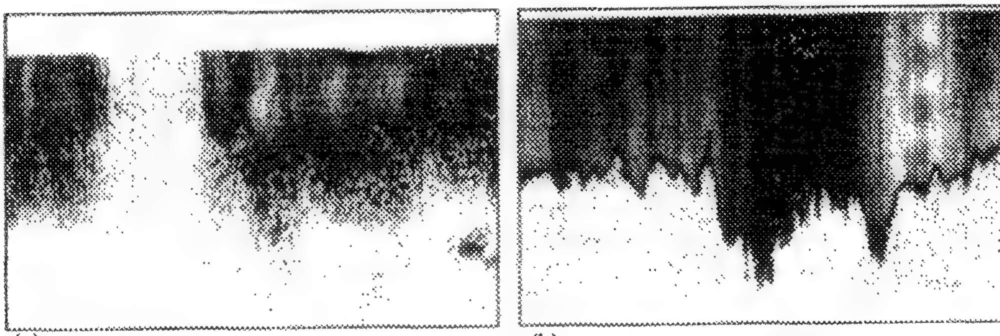

(a) (b)

FIG. 1 - SIMS image cross-sections for: (a) hydrogen (as D^-), and, (b) oxygen (as ZrO^-) within and beneath an oxide film on the surface of a Zr-Nb alloy. The images are the result of a transverse section through pixel volumes whose lateral dimensions are 150 μm and vertical dimensions are 20 μm. The very irregular interface between the oxide and metal phases seen in (b) is the result of composite contributions of roughness from the oxide surface and interface. Some hydrides located in the metal phase can be located in (a) (see arrow).

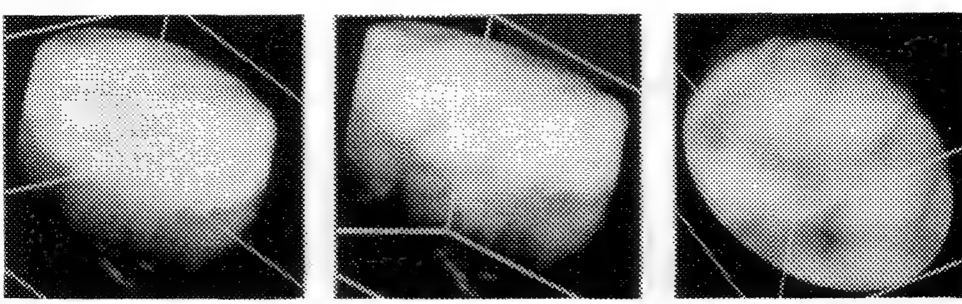

(a) (b) (c)

FIG. 2 - Volume representations of the hydrogen distribution in the above sample from three different perspectives. Hydride contributions can be located in the metal phase.

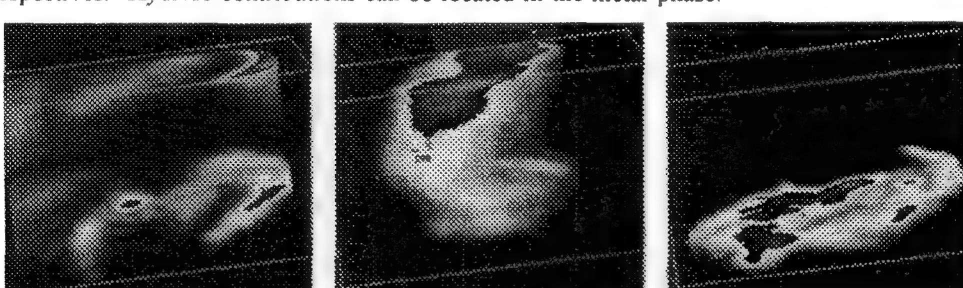

(a) (b) (c)

FIG. 3 - Volume representations of Al, Si and O as: (a) Al^-, (b) Si^-, and, (c) O^- in the region of an ultrasonic wire bond of Al-Si alloy onto a gold pad.

AUTHOR INDEX

AUTHOR INDEX

AUTHOR INDEX

AUTHOR INDEX

AUTHOR INDEX

AUTHOR INDEX

AUTHOR INDEX

AUTHOR INDEX

AUTHOR INDEX